Proceedings of the annual meeting of the French Society of Astronomy & Astrophysics

Mamadou N'Diaye, Arnaud Siebert, Nadège Lagarde, Olivia Venot, Kevin Baillié, Matthieu Bethermin, Eric Lagadec, Julien Malzac, Johan, Richard

▶ **To cite this version:**

Mamadou N'Diaye, Arnaud Siebert, Nadège Lagarde, Olivia Venot, Kevin Baillié, et al.. Proceedings of the annual meeting of the French Society of Astronomy & Astrophysics. SF2A, Jun 2023, Strasbourg, France. ⟨hal-04305648⟩

HAL Id: hal-04305648

https://hal.science/hal-04305648v1

Submitted on 27 Nov 2023

HAL is a multi-disciplinary open access archive for the deposit and dissemination of scientific research documents, whether they are published or not. The documents may come from teaching and research institutions in France or abroad, or from public or private research centers.

L'archive ouverte pluridisciplinaire **HAL**, est destinée au dépôt et à la diffusion de documents scientifiques de niveau recherche, publiés ou non, émanant des établissements d'enseignement et de recherche français ou étrangers, des laboratoires publics ou privés.

HAL Authorization

Proceedings of the annual meeting of the French Society of Astronomy & Astrophysics

Editors
M. N'Diaye, A. Siebert, N. Lagarde, O. Venot, K. Baillié, M. Béthermin, E. Lagadec, J. Malzac, J. Richard

Strasbourg - June 20-23, 2023

Sponsored by

Contents

Table of contents i

Foreword xi

List of participants xiii

SF2A — Plenary session 1

Astronomy and the European Open Science Cloud
M. Allen, B. Cecconi, M. Marchand, and A. Gonneau 3

Hot Corinos: the early organic molecular enrichment of the planet formation zones
M. De Simone 9

Strong magnetic fields discovered in red giant cores using seismology
S. Deheuvels, G. Li, J. Ballot, and F. Lignières 15

Challenges and limitations of future exoplanet space imagers
L. Leboulleux 19

COMMISSION FEMMES ET ASTRONOMIE DE LA SF2A : sexism and sexual harassment for European physicists
L. Manchon, R.-M. Ouazzani, I. Vauglin, C. Bot, S. Brau-Nogué, D. Briot, L. Ciesla, N. Lagarde, P. de Laverny, L. Leboulleux, et al. 25

The MICROSCOPE space mission to test the Equivalence Principle
G. Métris, M. Rodrigues, and J. Bergé 31

A brief review on Fast Radio Bursts
C. NG 37

Ice evolution during the star formation process: An IceAge JWST study of Chamaeleon I
J. A. Noble, and on behalf of the Ice Age team 43

Amas et groupes de galaxies dans l'ère des grands relevés 45

Mind the gap: A drastic change coming in our view of clusters brought by Euclid
G. Mahler 47

The Cosmological potential of high-redshift clusters with deep X-ray surveys
N. Cerardi, M. Pierre, P. Valageas, and C. Garrel 51

A UNIONS view of the brightest central galaxies of candidate fossil groups
A. Chu, F. Durret, A. Ellien, F. Sarron, C. Adami, I. Marquez, N. Martinet, T. de Boer, K. C. Chambers, J.-C. Cuillandre, et al. 55

Studying galaxy and hot gas interactions through cross-correlations of the thermal Sunyaev-Zeldovich effect and galaxy surveys
R. Kou, and J. Bartlett 59

© Société Française d'Astronomie et d'Astrophysique (SF2A) 2023

Galaxy clusters in MOND: the case of ultra diffuse galaxies in the Coma cluster
S. T. Nagesh, J. Freundlich, B. Famaey, and M. Bilek **63**

Unveiling the non-thermal radio emission in Galaxy Clusters and Future Prospects with the SKA
M. Pandey-Pommier, S. Paul, N. Roy, A. Marcowith, and B. Guiderdoni **67**

Investigating neutral hydrogen content in radio MOHEGs and prospects with the SKA
S. Wagh, M. Pandey-Pommier, N. Roy, M. Rashid, , A. Marcowith, S. Roy, C. Muthumariappan, R. Sethuram, and B. Guiderdoni **71**

Archéologie Galactique avec Gaia/DR3: un an après **75**

The spectroscopic data of the Gaia DR3 catalog: performance and use
P. A. Palicio **77**

s-process element abundances with the Gaia/GSP-spec catalogue
G. Contursi, P. de Laverny, A. Recio-Blanco, and P. A. Palicio **83**

Rewinding the history of high-mass X-ray binaries with Gaia
F. Fortin, F. Garcia, A. Simaz-Bunzel, S. Chaty, and E. Chassande-Mottin **87**

Can we decipher the dynamics of the Milky Way Disk from Gaia ?
Y. Khalil, B. Famaey, G. Monari, and A. Siebert **91**

New features of phase spiral from Gaia DR3
C. Li, A. Siebert, G. Monari, B. Famaey, and S. Rozier **95**

Hunting Na-rich stars among N-rich stars in the Galactic Halo
S. Martocchia, A. Savino, E. K. Grebel, C. Lardo, S. Martell, M. Shetrone, and N. Bastian **99**

The third version of the Gaia FGK Benchmark Stars
C. Soubiran, O. Creevey, N. Lagarde, N. Brouillet, P. Jofré, L. Casamiquela, U. Heiter, C. Aguilera–Gómez, S. Vitali, C. Worley, et al. **105**

Symbolic regression driven by dimensional analysis for the automated discovery of physical laws and constants of nature
W. Tenachi, R. Ibata, and F. I. Diakogiannis **107**

AS SKA-LOFAR and PNHE Workshop - Compact Objects: Observations and theory from radio to gamma **109**

Multi-wavelength studies on Fast Radio Bursts
C. NG **111**

Multi-wavelength light-curve fitting of young and millisecond pulsars
J. Pétri **115**

A new scenario for magnetar formation in a proto-neutron star spun up by fallback
P. Barrere, J. Guilet, R. Raynaud, and A. Reboul-Salze **119**

Identification of compact objects at the Galactic center
J. Berteaud, F. Calore, and M. Clavel **125**

Multi-wavelength emission of FR 0 radio galaxies at the subparsec scale
M. Boughelilba **129**

Multi-messenger observations with the KM3NeT telescope: search for high energy neutrinos coinciding with Fast Radio Bursts
F. Bretaudeau on behalf of the KM3NeT Collaboration **133**

Status of the NenuFAR Fast Radio Burst Program
V. Decoene, P. Zarka, C. Ng, N. Moukaddem, P. Gaspari, U. Laine, J.-M. Griessmeier, I. Cognard, F. Mottez, G. Voisin, et al. **137**

Using Vela X-1 to understand accretion and wind structure in High-Mass X-ray Binaries (HMXB)
C. M. Diez, V. Grinberg, F. Fürst, I. El Mellah, P. Kretschmar, S. Martínez Núñez, and A. Santangelo **143**

Extended emission in short gamma-ray bursts from fallback accretion
R. Duqué, C. Musolino, and L. Rezzolla **147**

MeV-GeV polarimetry with the Fermi-LAT: A first sensitivity estimate
A. Laviron, D. Bernard, and P. Bruel **155**

Numerical simulations of oblique electrospheres with realistic parameters based on "Pulsar ARoMa"
F. Mottez **159**

The hunt for Quasi-Periodic Eruptions
E. Quintin, and N. A. Webb **163**

Numerical modeling of dynamos in compact objects: magnetic field amplification and dissipation
M. Bugli, J. Guilet, R. Raynaud, A. Reboul-Salze, P. Barrère, A. Mignone, V. Berta, G. Mattia, and L. Del Zanna **167**

Open Science in Astronomy **169**

Open solar data, data products, and tools at MEDOC
E. Buchlin, S. Caminade, S. Parenti, B. Perri, F. Auchère, N. Traoré, K. Ashkar, and N. Dufourg **171**

Open Science and Astronomy
F. Genova **175**

Bien-être en astrophysique **181**

Improving well-being in astrophysics research
N. A. Webb, A. Allouch, C. Bot, N. Donati, J. Girardat, and S. Mei **183**

Partenariat Gemini SAF SF2A sur les collaborations amateurs professionnels **189**

A selection of astrometric binaries from Gaia-DR3 that could be double-lined spectroscopic binaries and eclipsing binaries
J.-L. Halbwachs, F. Kiefer, and Y. Lebreton **191**

Stellar occultations of the Lucy mission targets observed in France in 2022
A. Leroy, J. Desmars, F. Colas, T. Midavaine, G. Langin, and M. Grand **195**

RAPAS, PRO-AM NETWORK FOR THE SCIENTIFIC ALERTS, 2023 STATUS
T. Midavaine, W. Thuillot, M. Dennefeld, C. Buil, S. Neveu, M. Serrau, E. Barbotin, P. Barroy, Y. Delisle, P. Dupouy, et al. **199**

Citizen Science Time Domain Astronomy with Astro-COLIBRI
F. Schüssler, M. de Bony de Lavergne, A. Kaan Alkan, J. Mourier, and P. Reichherzer **203**

Planète Sciences and the Jean-Marc Salomon observatory in Buthiers, France: Citizen Science Projets
P. Barroy, M. Irzyk, J.-M. Vienney, Y. Delisle, P.-F. Rocci, D. Quéant, S. Neveu, M. Serrau, A. Lekic, D. Carlier, et al. **209**

Photometry of symbiotic stars: first results from an Am-Pro collaboration with Jaroslav Merc
A. Laouisset, E. Durand, T. Porte, M. Baylet, B. Delaveau, G. Malchirand, L. Sivet, J.-F. Coliac, S. Vasseur, P. Wullaert, et al. **213**

A Pro-Am collaboration to allow new discoveries at Mars
J. Lilensten, J. L. Dauvergne, C. Pellier, M. Delcroix, E. Beaudoin, and M. Vincendon **215**

V2-CEMN: identification of astrophysical X-ray sources
R. Eliott, and T. Hugo **219**

Cosmic Rays and Cosmology **221**

Search for diffuse gamma-ray emission from galaxy clusters with the Cherenkov Telescope Array
R. Adam, and the CTA consortium **223**

The impact of cosmic ray feedback on the reionisation of the Universe
M. Farcy, J. Rosdahl, Y. Dubois, J. Blaizot, and S. Martin-Alvarez **227**

Demain l'ELT! Stratégies d'observation, préparation des programmes scientifiques et synergies trans-instruments **231**

MOSAIC: the ELT optical and near-infrared Multi-Object Spectrograph
M. Puech, R. Pello, E. Prieto, M. Rodrigues, R. Sanchez-Janssen, G. Dalton, T. Contini, K. El Hadi, and the MOSAIC consortium **233**

MICADO spectroscopic mode for exoplanet characterization
P. Palma-Bifani, P. Baudoz, E. Huby, and G. Chauvin **239**

Solar System observations with the ESO Extremely Large Telescope
A. Delsanti, O. Groussin, S. Douté, F. Merlin, P. Rousselot, M. Roman, O. King, L. N. Fletcher, F. Clarke, B. Neichel, et al. **243**

L'égalité des genres en A&A: stéréotypes de genre dans l'enseignement **249**

The effect of gender stereotypes on academic performance: How our teaching methods affect girls' success
I. Vauglin, and R.-M. Ouazzani **251**

Status of women in astronomy: A Need for Advancing Inclusivity and Equal Opportunities
M. Pandey-Pommier, A. Piccialli, B. J. Wilkes, P. Hasan, S. Vargas Dominguez, A. S. Hassanin, D. Lazzaro, C. D. P. Lagos, J. Masegosa, L. Yang, et al. **255**

Latest insights on dust evolution **261**

Far-IR polarized emission in the Crab Nebula with SOFIA/HAWC+
J. Chastenet, I. Looze, B. Hensley, B. Vandenbroucke, M. Barlow, J. Rho, A. Ravi, H. Gomez, F. Kirchschlager, J. Macías-Pérez, et al. **263**

Dust properties in the millimeter to centimeter wavelength range: analysis of a sample of nearby galaxies
L. Correia, C. Bot, J. Chastenet, A. Rymar, and R. Paladini **267**

Impact of porosity and destructive effects on dust evolution using SPH simulations
S. Michoulier, and J.-F. Gonzalez **271**

Insight from laboratory measurements on dust in debris discs
J. Milli, O. Poch, J. B. Renard, J. C. Augereau, P. Beck, E. Choquet, J. M. Geffrin, et al. **275**

Dynamical study of the collapse of a cloud of gas and particles: what are the thermodynamical properties of the formed planetesimals?
P. Segretain, H. Méheut, and M. Moreira **279**

Origine de l'eau et de la vie: Quels défis astrophysiques et instrumentaux pour demain ? **283**

Origin of water and life: What astrophysical and instrumental challenges for tomorrow?
G. Chauvin, S. Raymond, D. Mouillet, J.-P. Berger, I. Boisse, E. Choquet, H. Cottin, X. Delfosse, M. Ferrari, E. Huby, et al. **285**

Water content trends in low-mass multiplanetary systems
L. Acuña, M. Deleuil, O. Mousis, T. A. Lopez, T. Morel, A. Aguichine, E. Marcq, and A. Santerne **289**

Preparation to future long-term space missions for exoplanets high contrast direct characterization
D. Mouillet, I. Laginja, and M. Ferrari **293**

Atelier général du PCMI **297**

Shaping the CO snowline in protoplanetary disks
S. Gavino, J. Kobus, A. Dutrey, S. Guilloteau, S. Wolf, J. K. Jörgensen, and R. Sharma **299**

Machine Learning to facilitate the study of complex organic molecules in hot cores
N. Kessler, T. Csengeri, D. Cornu, and S. Bontemps **303**

Discovery and study of the physical properties of massive stars precursors
M. Valeille-Manet, S. Bontemps, and T. Csengeri **307**

ATOMIS, an ALMA archive TOol for Molecular Investigations in Space
A. Coutens, S. Ben Hmida, and J.-M. Glorian **311**

Statistical analysis of the relative orientations between filaments and magnetic fields in star forming regions
J. Oers, I. Ristorcelli, K. Ferrière, and L. Montier **313**

Galaxy evolution in the era of JWST (atelier du PNCG) **315**

Preliminary results on JWST Cycle 1 GO #2180:The CircumGalactic Medium of NGC 891
J. Chastenet, I. Looze, M. Relaño, T. Williams, E. Xilouris, and the proposing team **317**

JWST probes the role of stellar mass and morphology in obscuring galaxies
C. Gómez-Guijarro **321**

Unveiling galaxy evolution with the COSMOS-Web survey
L. Paquereau, C. Laigle, H. J. McCracken, and M. Shuntov **325**

Probing the attenuation curve of $1 < z < 3$ galaxies with the JWST/CEERs program
L.-M. Seillé, V. Buat, V. Fernandez, and the CEERs team **329**

PNGRAM Géodésie Spatiale **333**

Modeling the lunar tides in INPOP
D. Baguet, N. Rambaux, A. Fienga, A. Briaud, H. Hussmann, M. Gastineau, X. Hu, J. Laskar, A. Mémin, and A. Stark **335**

NAROO program : Analysis of USNO Galilean observations 1967-1998
V. Robert, D. Pascu, J.-E. Arlot, and V. Lainey **339**

Constraints on Earth's core processes by space gravimetry
S. Rosat, H. Lecomte, and M. Mandea **343**

Frequency drift interferometry for stray light measurement on the LISA space instrument
A. Roubeau-Tissot, M. Lintz, M. Nardello, M. Pichot, and J.-P. Coulon **347**

Clairaut's equation extended to fast rotators
C. Staelen, and J.-M. Huré **351**

Atelier général du Programme National de Planétologie (PNP) **355**

Chemical characterisation of warm exoplanetary atmospheres: revelations from JWST about WASP-39b and much more
O. Venot, S.-M. Tsai, R. Veillet, B. Fleury, and M. Poveda **357**

Planet-gas interactions in debris disks: Observable structures
C. Bergez-Casalou, and Q. Kral **363**

Simulated methane clouds in the Titan troposphere with the Titan Planetary Climate Model
B. de Batz de Trenquelleon, P. Rannou, and S. Lebonnois **367**

Hydrodynamical modelling of tidal dissipation in gas giant planets at the time of space missions
H. Dhouib, C. Baruteau, S. Mathis, F. Debras, A. Astoul, and M. Rieutord **373**

High Temperature Measurement of Acetylene UV Absorption Cross Section for the Study of Hot Exoplanet Atmospheres
B. Fleury, M. Poveda, Y. Bénilan, and O. Venot **377**

A new scenario for the formation of planetary atmospheres
P. Huet, Q. Kral, and P. Thébault **381**

Modeling the recent (<5 Myrs) martian Ice Ages
J. Naar, F. Forget, E. Millour, A. Bierjon, L. Lange, E. Vos, and R. Vandemeulebrouck **387**

Multiwavelength observations of the exo-cometary dust around β pictoris.
P. Priolet, J.-C. Augereau, J. Milli, A. Matter, and J.-B. Le Bouquin **391**

NAROO program : Analysis of USNO Galilean observations 1967-1998
V. Robert, D. Pascu, J.-E. Arlot, and V. Lainey **395**

Atelier général du Programme National de Physique Stellaire (PNPS) **399**

Secular stability of the dipole-dipole interaction in magnetic binaries
C. Aykroyd, A. Bourgoin, C. Le Poncin-Lafitte, S. Mathis, and M.-C. Angonin **401**

Photocentre displacement of RHD simulations of AGB stars and correlation with stellar parameters
E. Béguin, A. Chiavassa, B. Freytag, A. Ahmad, and S. Uttenthaler **405**

Nebular spectra from Type Ia supernova explosion models compared to *JWST* observations of SN 2021aefx
S. Blondin, L. Dessart, D. J. Hillier, C. A. Ramsbottom, and P. J. Storey **409**

How much do magnetic fields impact stellar characterization?
P. I. Cristofari, and J.-F. Donati **413**

A landscape of main sequence cool stars activity thought photometric observations
L. Degott, F. Baudin, R. Samadi, C. Damiani, B. Perri, and C. Pinçon **417**

The scientific projects of the Interferometric Survey for Stellar Parameters with CHARA/SPICA
R. Ligi, D. Mourard, P. Bério, O. Creevey, S. Deheuvels, A. Domiciano de Souza, N. Ebrahimkutty, R. Iba, J. Jonak, N. Nardetto, et al. **421**

A magnetic field study in the envelope of cool evolved stars
L. Marinho, F. Herpin, H. Wiesemeyer, A. López-Ariste, A. Baudry, A. Asensio Ramos, and the PEPPER team **427**

How do (massive) binary stars form?
R. Mignon-Risse, M. González, and B. Commercon **431**

A new 12C+12C reaction rate from the STELLA collaboration: how to determine astrophysical parameters with nuclear experiments?
E. Monpribat, T. Dumont, A. Bonhomme, M. Heine, J. Nippert, and S. Courtin **435**

The GRAVITY view of the innermost regions of protoplanetary disks
K. Perraut, L. Labadie, J. Bouvier, and the GRAVITY Collaboration **439**

Do nonlinear effects disrupt tidal dissipation predictions in convective envelopes?
A. Astoul, and A. J. Barker **443**

Impact of the magnetic field on the stochastic excitation of p-modes
L. Bessila, and S. Mathis **445**

Measuring stellar rotation and activity with PLATO
S. N. Breton, A. F. Lanza, S. Messina, R. A. García, S. Mathur, A. R. G. Santos, L. Bugnet, E. Corsaro, and I. Pagano **447**

Improving stellar modeling with new precise nuclear reaction rates determined from nuclear experiment
T. Dumont, E. Monpribat, A. Choplin, A. Bonhomme, M. Heine, J. Nippert, and S. Courtin **449**

Detection of a steep height gradient of the rotational velocity in the low photosphere of the Sun
M. Faurobert, T. Corbard, B. Gelly, R. Douet, and D. Laforgue **451**

Studying brown dwarf dust cloud distributionthrough polarisation
E. González, B. Goldman, M. R. Zapatero Osorio, V. J. Sánchez Bejar, T. Henning, and J. Pitann **453**

Masses and luminosities of SB2 components deduced from OHP spectroscopic observations and Gaia-DR3 astrometric orbits
J.-L. Halbwachs, F. Kiefer, Y. Lebreton, F. Arenou, B. Famaey, P. Guillout, T. Mazeh, D. Pourbaix, and J.-B. Salomon **457**

Accretion properties of Class 0 protostars studied with near-infrared spectroscopy
V. Gouellec, T. Greene, L. Hillenbrand, and Z. Yates **459**

Magnetised winds in Transition Discs
E. Martel, and G. Lesur **461**

ASGARD: the realm of high angular resolution
M.-A. Martinod, D. Defrère, M. Ireland, S. Kraus, F. Martinache, and Asgard consortium **463**

Probing the secular evolution of embedded protoplanetary discs
J. Mauxion **465**

Using artificial intelligence to improve the performance of radiative hydrodynamics simulations
G. Radureau, C. Michaut, A. I. Comport, and R. Drouilly **467**

Near-infrared spectroscopic follow-up of Gaia ultra-cool dwarfs candidates
T. Ravinet, C. Reylé, A. Burgasser, R. L. Smart, J. G. Fernández-Trincado, and W. H. Moya **469**

Prédiction et suivi des signaux multi-messagers **473**

SVOM contribution to multi-messenger astronomy
J.-L. Atteia, B. Cordier, J. Y. Wei, and on behalf of the SVOM collaboration **475**

The impact of rotation and dynamos on the multi-messenger emission of core-collapse supernovae
M. Bugli, J. Guilet, T. Foglizzo, M. Obergaulinger, M. Reichert, M. Bendahman, S. El Hedri, and I. Goos **479**

Follow-up of gravitational waves alerts with IACTs using Astro-COLIBRI
M. de Bony de Lavergne, H. Ashkar, A. K. Alkan, J. Mourier, P. Reichherzer, F. Schüssler, and M. Seglar-Arroyo **483**

Probing binary evolution in accreting high-mass systems
F. Fortin, F. Garcia, A. Simaz-Bunzel, S. Chaty, and E. Chassande-Mottin **487**

Update in the search for close massive binary black holes: a list of new candidates
V. Foustoul, and N. A. Webb **491**

Predicting the electromagnetic signatures of pre-merger binary black holes
R. Mignon-Risse, P. Varniere, and F. Casse **495**

Jacobi captures : a first step in the formation of off-centered massive black hole binaries in dwarf galaxies
T. François, C. Boily, and J. Freundlich **499**

Sixième réunion des utilisateurs des télescopes français (TBL/OHP193) **501**

Spectro-imaging follow-up of gamma-ray burstswith the OHP/T193
B. Schneider, E. Le Floc'h, C. Adami, D. Turpin, S. Basa, D. Götz, J. T. Palmerio, A. Saccardi, S. D. Vergani, and B. Cordier **503**

A new NeoNarval pipeline with PyReduce
K. Thomson-Paressant, C. Gutteridge, C. Neiner, and C. Catala **507**

MISTRAL observations of the C/2022 E3 (ZTF) comet by the Aix-Marseille M2 students: first science results
C. Adami, E. Jehin, K. Aravind, Y. Ahmad, A. Roy, C. Carvajal-Bohorquez, M. Garnichey, M. Hasan, D. Hassaine, N. E. Jimenez de la Vega, et al. **511**

Spectroscopy of Transients with Mistral at OHP
M. Dennefeld **515**

Optical and X-ray variability in the active CGCG 077-102 NED02 galaxy
K. Parra Ramos, C. Adami, J. T. Harry, M. Ulmer, G. B. Lima Neto, and P. Amram **517**

MISTRAL@OHP observations of Bow-shock star candidates
D. Russeil, A. Zavagno, J. C. Bouret, C. Adami, and M. Dennefeld **519**

Observations of the XMM X-CLASS clusters of galaxies with MISTRAL at OHP
G. Soucail, N. Clerc, R. Cabanac, L. Paquereau, Q. Moysan, B. Altieri, and F. Sarron **521**

The future of micro- and nanosatellites for astronomy **523**

The French research Federation for nanosatellites in Universe and Earth Sciences
C. Neiner **525**

Transition environnementale : quels leviers d'actions pour réduire l'empreinte environnementale de l'astronomie ? **529**

Environmental transition: overview of actions to reduce the environmental footprint of astronomy
L. Leboulleux, F. Cantalloube, M.-A. Foujols, M. Giard, J. Guilet, J. Knödlseder, A. Santerne, L. Todorov, D. Barret, O. Berne, et al. **531**

Author Index **537**

SF2A 2023
M. N'Diaye, A. Siebert, N. Lagarde, O. Venot, K. Baillié, M. Béthermin, E. Lagadec, J. Malzac, J. Richard (eds)

Foreword

Nadège Lagarde, President of the SF2A

As the new president of the French Society of Astronomy and Astrophysics (Société Française d'Astronomie et d'Astrophysique - SF2A), it is an honour for me to write this foreword. As emphasized by my predecessors, the annual meeting of the SF2A is a highly significant event for our community, a place where permanent, doctoral and post-doctoral researchers can exchange their ideas and present to the whole community their new discoveries. The 2023 edition took place from June 20th to June 23rd in Strasbourg, having been efficiently prepared by members of the *Observatoire Astronomique de Strasbourg*, of the *Centre de données astronomiques de Strasbourg* and of the *Jardin des sciences de l'Université de Strasbourg*.

As every year, this meeting included the general assembly of our society, plenary sessions aimed at a large audience of professionals, workshops dedicated to various scientific issues, the young researcher and thesis price ceremony, events for schools and the public, discussions concerning societal subjects. This 2023 edition was a great success, with a record number of participants (more than 450) and marked a turning point in the way the conference was organised. For the first time, all the plenary lectures and workshops were accessible online. This enabled researchers who were unable to attend SF2A meeting in person to take an active part in the conference, sharing their work and exchanging views with other participants. This innovative approach is particularly important in the current context, where preserving the environment has become an absolute priority for everyone. I would like to thank the local organising committee for their exceptional efforts and remarkable efficiency in implementing this new format.

The programme of the plenary sessions was, as usual, very rich, with several high-quality presentations proposed by the various Programmes Nationaux and Actions Spécifiques of INSU-CNRS, covering a broad range of astrophysical topics, including news from Gaia and JWST, planetology, asteroseismology. Representatives of institutions (M. Giard for INSU, T. Bret-Dibat for CNES), the CNU (S. Mei), and the "sections" of CNRS (B. Famaey) and CNAP (D. Mourard) presented us a detailed view of the french research situation with crucial informations for the career. This whole session was concluded by a very interesting discussion with the community.

The place of women in the science community is a very important topics, specially in physics and astronomy and the SF2A meeting was an excellent opportunity to discuss it. R.-M. Ouazzani, who is in charge of *the SF2A's Women and Astronomy Committee*, gave us a presentation of the committee's latest activities. It is also very important to think about environmental issues. In this context, *the SF2A's Environmental Transition Committee* invited E. Guilyardi to give a presentation on integrating environmental issues into the conduct of research. The SF2A Board also wanted to highlight an important societal issue by inviting J.-G. Cuby to give a presentation on *"Astronomy on indigenous lands: the case of Maunakea"*. These three presentations attracted a great deal of interest from the community, as the very interesting discussions that followed showed.

The call for contributions to organise parallel sessions received a lot of answers, which allowed us to propose a very rich program, with meetings of the different *Programmes Nationaux* and *Actions Spécifiques* of

© Société Française d'Astronomie et d'Astrophysique (SF2A) 2023

INSU-CNRS and scientific meetings proposed by community members. Indeed, this year, not less than eighteen scientific workshops were organized on topical subjects, and three additional sessions were devoted to *"Gender equality in A&A: gender stereotypes in teaching"* ; *"Environmental transition: what levers for action to reduce the environmental footprint of astronomy?"* and to *"Well-being in astrophysics"*, each of which brought in specialists in these societal issues to enhance our thinking on these key subjects. This "record" number of sessions obviously reflects the great wealth and breadth of exchanges across thematic boundaries as well as the growing role played by this meeting and SF2A in animating our community and in initiating fruitful discussions and collaborations in a friendly and stimulating atmosphere. Finally, the SF2A annual meeting were concluded by our general assembly where the moral and financial reports were presented by the president and treasurer of the SF2A Council, N. Lagarde and K. Baillie. A vote from the members has complemented these presentations in Autumn 2023.

Three special moments usually illuminated the SF2A meeting. The first one was the "outreach" conference by Roland Lehoucq entitled *"Talking science through fiction"*. The second one was the SF2A prize ceremony. The laureate of the Thesis prize was **Marta de Simone** who presented her brilliant work concerning Hot corinos and the early organic molecular enrichment of the planet formation zones. The laureate of the young researcher price was **Laure Ciesla** for her work on the star formation history of galaxies based on their spectral emission. The laureate of the Camille Flammarion for scientific mediation (SF2A-SAF) was **Daniela Galarraga-Espinosa** for her participation in the *"Women in Sciences in Equador"* project. This ceremony was followed by a projection and a dinner-cocktail in the new and impressive planetarium of Strasbourg. Last but not least, an important moment of the week was the School project prize called "Découvrir l'Univers". I would like to highlight the incredible collaboration between the LOC and *Jardin des sciences de l'Université de Strasbourg*, who did an outstanding work in organising this prize. The jury was really impressed by the work of all the classes taking part in the competition. The highlight of the competition took place during the days when the competition participants were invited to a lecture given by Roland Le Houc.

I wish to thank the INSU-CNRS, the Observatoire de l'Université de Strasbourg, the "Centre de données astronomiques de Strasbourg" as well as the CNES, the CEA, the National Programs and Actions Spécifique of INSU-CNRS, for their financial and organisational support. We are extremely grateful to the University of Strasbourg for hosting our meeting. The 2023 edition was held in the beautiful city of Strasbourg, and I want to thank the Local Organising committee for the organisation, with a particularly beautiful conference diner on the historical site of the observatory. The Local Organizing Committee was chaired by Arnaud Siebert and composed of Mark Allen, Thibault Barnouin, Matthieu Bethermin, Paolo Bianchini, Lucie Correia, Pierre-Alain Duc, Jonathan Freundlich, Céline Halter, Yassin Khalil Rany, Frédéric Marin, Nicolas Martin, Mei Palanque, Emeline Ricciuti (JDS), Clément Stahl, Srikanth Togere Nagesh, Mathias Urbano, Karina Voggel and Milène Wendling (JDS). I would like also to thank all the members of the SF2A board who were all very active for preparing the meeting : Olivia Venot, Kévin Baillié, Arnaud Siebert, Johan Richard, Rhita-Maria Ouazzani, Julien Malzac, Mamadou N'Diaye, Eric Lagadec, Danielle Briot, Frédéric Pitout and Matthieu Berthermin. Together with the LOC members, they made the meeting a success. In addition to the rich program mentioned above (and somewhat detailed in these proceedings), embracing all of the astronomy research performed in France, the work of the LOC has also offered to all the participants many opportunities to meet and discuss beyond the limits of their own field of expertise.

See you next year in Marseille!

Nadège Lagarde, President of the SF2A

List of participants

ABELLO Margaux (e-mail: margaux.abello@oca.eu)
ACUNA Lorena (e-mail: acuna@mpia.de)
ADAM Remi (e-mail: remi.adam@oca.eu)
ADAMI Christophe (e-mail: christophe.adami@lam.fr)
AHMAD Adnan Ali (e-mail: adnan.ali.ahmad1998@gmail.com)
ALAGUERO Antoine (e-mail: antoine.alaguero@univ-grenoble-alpes.fr)
ALEI Eleonora (e-mail: elalei@phys.ethz.ch)
ALLAIN Tituan (e-mail: tituan.allain@univ-grenoble-alpes.fr)
ALLEN Mark (e-mail: mark.allen@astro.unistra.fr)
ALONSO PALICIO Pedro (e-mail: pedro.alonso-palicio@oca.eu)
AMRAM Philippe (e-mail: philiippe.amram@lam.fr)
AMSLER MOULANIER Alizee (e-mail: alizee.amsler@lam.fr)
ANDREU Audrey (e-mail: audrey.andreu@irap.omp.eu)
ARANGO Rafael (e-mail: rafael.arango-toro@lam.fr)
ARTHUR Léna (e-mail: arthur@apc.in2p3.fr)
ASTOUL Aurélie (e-mail: a.a.v.astoul@leeds.ac.uk)
ATTEIA Jean-Luc (e-mail: jean-luc.atteia@irap.omp.eu)
AUBERT Dominique (e-mail: dominique.aubert@astro.unistra.fr)
AUVRAY Isabelle (e-mail: iauvray@hotmail.com)
AYKROYD Christopher (e-mail: adrien.bourgoin1208@gmail.com)
BABUSIAUX Carine (e-mail: frederique.motte@univ-grenoble-alpes.fr)
BAGUET Daniel (e-mail: daniel.baguet@obspm.fr)
BAILLIE Kevin (e-mail: kevin.baillie@obspm.fr)
BALLET Jean (e-mail: jballet@cea.fr)
BARAFFE Isabelle (e-mail: ibaraffe@ens-lyon.fr)
BARNOUIN Thibault (e-mail: thibault.barnouin@gmail.com)
BARRÈRE Paul (e-mail: paul.barrere@cea.fr)
BARROY Pierre (e-mail: yorrab@hotmail.com)
BASA Stéphane (e-mail: stephane.basa@lam.fr)
BASTO Quentin (e-mail: quentin.basto@univ-lyon1.fr)
BAUMANN Matthieu (e-mail: matthieu.baumann@astro.unistra.fr)
BÉGUIN Elysabeth (e-mail: elysabeth.beguin@oca.eu)
BELKACEM Kevin (e-mail: kevin.belkacem@obspm.fr)
BERGER Jean-Philippe (e-mail: jean-philippe.berger@univ-grenoble-alpes.fr)
BERGEZ-CASALOU Camille (e-mail: camille.bergez@obspm.fr)
BERNE Olivier (e-mail: olivier.berne@irap.omp.eu)
BERTEAUD Joanna (e-mail: berteaud@lapth.cnrs.fr)
BERTRAND Tanguy (e-mail: tanguy.bertrand@obspm.fr)
BESSILA Leïla (e-mail: leila.bessila@cea.fr)
BETHERMIN Matthieu (e-mail: matthieu.bethermin@astro.unistra.fr)
BIANCHINI Paolo (e-mail: paolo.bianchini@astro.unistra.fr)
BIENAYME Olivier (e-mail: olivier.bienayme@orange.fr)
BISERO Sofia (e-mail: sofia.bisero@obspm.fr)
BLANCK Michel (e-mail: michelblanck68@aol.com)
BLONDIN Stéphane (e-mail: stephane.blondin@lam.fr)

© Société Française d'Astronomie et d'Astrophysique (SF2A) 2023

BOILY Christian (e-mail: christian.boily@astro.unistra.fr)
BOIRIN Laurence (e-mail: laurence.boirin@astro.unistra.fr)
BOISSE Isabelle (e-mail: isabelle.boisse@lam.fr)
BOISSIER Samuel (e-mail: samuel.boissier@lam.fr)
BOISSON Catherine (e-mail: catherine.boisson@obspm.fr)
BOMMIER Veronique (e-mail: V.Bommier@obspm.fr)
BONDUELLE Myriam (e-mail: myriam.bonduelle@univ-grenoble-alpes.fr)
BONFAND Melisse (e-mail: pgu4gb@virginia.edu)
BONNAREL François (e-mail: francois.bonnarel@astro.unistra.fr)
BOSELLI Alessandro (e-mail: alessandro.boselli@lam.fr)
BOSNJAK Zeljka (e-mail: Zeljka.Bosnjak@fer.hr)
BOT Caroline (e-mail: caroline.bot@astro.unistra.fr)
BOUCHE Nicolas (e-mail: nicolas.bouche@univ-lyon1.fr)
BOUCHET Tristan (e-mail: tristan.bouchet@cea.fr)
BOUGHELILBA Margot (e-mail: margot.boughelilba@gmail.com)
BOURET Jean-Claude (e-mail: jean-claude.bouret@lam.fr)
BOUTTARD Vincent (e-mail: vincent.bouttard@optique-unterlinden.com)
BRAU-NOGUE Sylvie (e-mail: sylvie.brau-nogue@irap.omp.eu)
BRET-DIBAT Thierry (e-mail: Thierry.Bret-Dibat@cnes.fr)
BRETAUDEAU Félix (e-mail: felix.bretaudeau@subatech.in2p3.fr)
BRIOT Danielle (e-mail: danielle.briot@obpm.fr)
BRON Emeric (e-mail: emeric.bron@obspm.fr)
BROUILLET Nathalie (e-mail: nathalie.brouillet@u-bordeaux.fr)
BROUTY Marianne (e-mail: marianne.brouty@astro.unistra.fr)
BRUANT Théo (e-mail: theo.bruant@etu.unistra.fr)
BRUNET Catherine (e-mail: catherine.brunet@astro.unistra.fr)
BRUNETTI Gianfranco (e-mail: gianfranco.brunetti@inaf.it)
BUCHLIN Eric (e-mail: eric.buchlin@ias.u-psud.fr)
BUGA Mihaela (e-mail: mihaela.buga@astro.unistra.fr)
BUGLI Matteo (e-mail: matteo.bugli@cea.fr)
BUGNET Lisa (e-mail: lisa.bugnet@ist.ac.at)
CABRAL Nahuel (e-mail: nahuel.cabral@univ-lyon1.fr)
CABRIT Sylvie (e-mail: sylvie.cabrit@obspm.fr)
CADRESSEN Nicolas (e-mail: nicolas.cadressen@lam.fr)
CAILLE Vincent (e-mail: vincent.caille@latmos.ipsl.fr)
CAMBRESY Laurent (e-mail: laurent.cambresy@astro.unistra.fr)
CANGEMI Floriane (e-mail: cangemi@apc.in2p3.fr)
CANTALLOUBE Faustine (e-mail: faustine.cantalloube@lam.fr)
CASTILLO Fabien (e-mail: fabien.castillo@etu.unistra.fr)
CECCARELLI Cecilia (e-mail: cecilia.ceccarelli@univ-grenoble-alpes.fr)
CECCONI Baptiste (e-mail: baptiste.cecconi@obspm.fr)
CERARDI Nicolas (e-mail: nicolas.cerardi@cea.fr)
CERQUI Valeria (e-mail: valeria.cerqui@obspm.fr)
CHAPIRON Alice (e-mail: achapiron@irap.omp.eu)
CHARLOT Patrick (e-mail: patrick.charlot@u-bordeaux.fr)
CHARNAY Benjamin (e-mail: benjamin.charnay@obspm.fr)
CHARPENTIER Paul (e-mail: Paul.Charpentier@irap.omp.eu)
CHARRIE Armelle (e-mail: acharrie@unistra.fr)
CHARRIE Nan-Mael (e-mail: nanma.charrie@gmail.com)
CHASTENET Jérémy (e-mail: jeremy.chastenet@ugent.be)
CHATY Sylvain (e-mail: sylvain.chaty@u-paris.fr)
CHAUVIN Gael (e-mail: gael.chauvin@oca.eu)
CHAVEROT Guillaume (e-mail: guillaume.chaverot@unige.ch)
CHEMERYNSKA Iryna (e-mail: chemerynskaira@gmail.com)
CHEMIN Laurent (e-mail: laurent.chemin@uantof.cl)

CHEVALLARD Jacopo (e-mail: jacopo.chevallard@physics.ox.ac.uk)
CHOQUET Elodie (e-mail: elodie.choquet@lam.fr)
CIESLA Laure (e-mail: laure.ciesla@lam.fr)
CLAEYSSENS Adelaide (e-mail: adelaide.claeyssens@astro.su.se)
CLENET Yann (e-mail: yann.clenet@obspm.fr)
COLLAS Esther (e-mail: esther.collas@astro.unistra.fr)
COLLET Brieuc (e-mail: brieuc.collet@lam.fr)
CONTINI Thierry (e-mail: thierry.contini@irap.omp.eu)
CONTURSI Gabriele (e-mail: gabriele.contursi@oca.eu)
CORNILLON Salomé (e-mail: salome.cornillon@etu.u-bordeaux.fr)
CORREIA Jean-Jacques (e-mail: jean-jacques.correia@univ-grenoble-alpes.fr)
CORREIA Lucie (e-mail: lucie.correia@astro.unistra.fr)
COSTES Jean (e-mail: jean.costes@lam.fr)
COUDRY Sabrina (e-mail: sabrina.coudry@universcience.fr)
COURTIN Régis (e-mail: regis.courtin@wanadoo.fr)
COUTENS Audrey (e-mail: audrey.coutens@irap.omp.eu)
COWAN Nicolas (e-mail: nicolas.cowan@mcgill.ca)
CREEVEY Orlagh (e-mail: orlagh.creevey@oca.eu)
CRIDA Aurelien (e-mail: crida@oca.eu)
CRISTOFARI Paul (e-mail: paul.cristofari@cfa.harvard.edu)
CUBY Jean-Gabriel (e-mail: cuby@cfht.hawaii.edu)
DALLIER Richard (e-mail: richard.dallier@subatech.in2p3.fr)
DARTOIS Emmanuel (e-mail: emmanuel.dartois@universite-paris-saclay.fr)
DAVID Lester (e-mail: lester.david@universcience.fr)
DE BATZ DE TRENQUELLÉON Bruno (e-mail: bruno.de-batz-de-trenquelleon@univ-reims.fr)
DE BONNIÈRES Michèle (e-mail: michele.debonnieres@gmail.com)
DE BONY DE LAVERGNE Mathieu (e-mail: mathieu.debony@cea.fr)
DE LAVERNY Patrick (e-mail: laverny@oca.eu)
DE SIMONE Marta (e-mail: Marta.DeSimone@eso.org)
DECOENE Valentin (e-mail: valentin.decoene@subatech.in2p3.fr)
DEGOTT Lucie (e-mail: lucie.degott@universite-paris-saclay.fr)
DEHEUVELS Sebastien (e-mail: sebastien.deheuvels@irap.omp.eu)
DELCAMP Simon (e-mail: simon.delcamp@univ-grenoble-alpes.fr)
DELEUIL Magali (e-mail: magali.deleuil@lam.fr)
DELFOSSE Xavier (e-mail: Xavier.Delfosse@univ-grenoble-alpes.fr)
DELSANTI Audrey (e-mail: audrey.delsanti@lam.fr)
DEMARS Dorian (e-mail: dorian.demars@univ-grenoble-alpes.fr)
DENNEFELD Michel (e-mail: dennefel@iap.fr)
DERRIERE Sébastien (e-mail: sebastien.derriere@astro.unistra.fr)
DERSON Etienne (e-mail: etienne.derson@hotmail.fr)
DESGRANGE Célia (e-mail: celia.desgrange@univ-grenoble-alpes.fr)
DESPOIS Didier (e-mail: despois.d@gmail.com)
DEWA Zirexe (e-mail: zeddemazi01@gmail.com)
DHOUIB Hachem (e-mail: hachem.dhouib@cea.fr)
DI FOLCO Emmanuel (e-mail: emmanuel.di-folco@u-bordeaux.fr)
DI MATTEO Paola (e-mail: paola.dimmatteo@obspm.fr)
DIEZ Camille (e-mail: camille.m.diez@gmail.com)
DITZ Patrick (e-mail: patrick.ditz@wanadoo.fr)
DOLAG Klaus (e-mail: kdolag@mpa-garching.mpg.de)
DOLIVA-DOLINSKY Amandine (e-mail: amandinedolinsky@gmail.com)
DONATI Noemi (e-mail: noemi.donati@hotmail.com)
DOUGADOS Catherine (e-mail: catherine.dougados@univ-grenoble-alpes.fr)
DOUTE Sylvain (e-mail: sylvain.doute@univ-grenoble-alpes.fr)
DUBOIS Pascal (e-mail: pascal.dubois67@gmail.com)

DUBOIS Yohan (e-mail: dubois@iap.fr)
DUC Pierre-Alain (e-mail: pierre-alain.duc@astro.unistra.fr)
DUCHESNE Frédéric (e-mail: freduch67@yahoo.fr)
DUCROT Elsa (e-mail: elsa.ducrot@cea.fr)
DUMONT Thibaut (e-mail: thibaut.dumont@iphc.cnrs.fr)
DUONG Tuan-Anh (e-mail: tuan.duong@cea.fr)
DUQUÉ Raphaël (e-mail: duque@physik.uni-frankfurt.de)
DURAKOVIC Amel (e-mail: durakovic@astro.unistra.fr)
DURAND Emilien (e-mail: emiliendurand771@yahoo.com)
DURRET Florence (e-mail: durret@iap.fr)
DUTREY Anne (e-mail: anne.dutrey@u-bordeaux.fr)
DVORKIN Irina (e-mail: dvorkin@iap.fr)
EL YAJOURI Meriem (e-mail: meriemyajouri@gmail.com)
ELLIEN Amaël (e-mail: a.r.j.ellien@uva.nl)
ESTEVE Frederic (e-mail: Frederic.Esteve@cnes.fr)
ESTEVEZ Dimitri (e-mail: dimitri.estevez@iphc.cnrs.fr)
EYER Laurent (e-mail: laurent.eyer@unige.ch)
FALCO Aurélien (e-mail: aurelienfalco@gmail.com)
FAMAEY Benoit (e-mail: benoit.famaey@astro.unistra.fr)
FARCY Marion (e-mail: marion.farcy@epfl.ch)
FASSENOT Thierry (e-mail: thierry.fassenot@etu.unistra.fr)
FAUROBERT Marianne (e-mail: marianne.faurobert@oca.eu)
FERRARI Marc (e-mail: marc.ferrari@lam.fr)
FLASSEUR Olivier (e-mail: olivier.flasseur@univ-lyon1.fr)
FLEURY Benjamin (e-mail: benjamin.fleury@lisa.ipsl.fr)
FLURY Manuel (e-mail: manuel.flury@wanadoo.fr)
FORTIN Francis (e-mail: fortin@apc.in2p3.fr)
FOSSE David (e-mail: d.fosse@cieletespace.fr)
FOUCHET Thierry (e-mail: thierry.fouchet@obspm.fr)
FOUJOLS Marie-Alice (e-mail: Marie-Alice.Foujols@ipsl.fr)
FOUSTOUL Vincent (e-mail: vincent.foustoul@irap.omp.eu)
FRANCOIS Thibaut (e-mail: thibaut.francois@astro.unistra.fr)
FRAY Nicolas (e-mail: nicolas.fray@lisa.u-pec.fr)
FREUNDLICH Jonathan (e-mail: jonathan.freundlich@astro.unistra.fr)
GABICI Stefano (e-mail: gabici@apc.in2p3.fr)
GALÁRRAGA-ESPINOSA Daniela (e-mail: danigaes@mpa-garching.mpg.de)
GAVINO Sacha (e-mail: sacha.gavino@nbi.ku.dk)
GENOVA Françoise (e-mail: francoise.genova@astro.unistra.fr)
GEROSA Fabiola Antonietta (e-mail: fabiola.gerosa@oca.eu)
GIARD Martin (e-mail: martin.giard@irap.omp.eu)
GODET Olivier (e-mail: ogodet@irap.omp.eu)
GODINAUD Leïla (e-mail: leila.godinaud@cea.fr)
GOLDMAN Bertrand (e-mail: bertrand.goldman@isunet.edu)
GOMEZ GUIJARRO Carlos (e-mail: carlos.gomezguijarro@cea.fr)
GONZALEZ Ezequiel (e-mail: ezequiel.gonzalez@community.isunet.edu)
GONZALEZ Jean-François (e-mail: Jean-Francois.Gonzalez@ens-lyon.fr)
GOOVAERTS Ilias (e-mail: ilias.goovaerts@lam.fr)
GRIECO Francesco (e-mail: Francesco.Grieco@UGent.be)
GRISHIN Kirill (e-mail: grishin@voxastro.org)
GRIVEAUD Philippine (e-mail: philippine.griveaud@oca.eu)
GROUFFAL Salomé (e-mail: salome.grouffal@lam.fr)
GUEBHART Tristan (e-mail: tristan.gueb@yahoo.fr)
GUÉRIN Frédéric (e-mail: frederic.guerin@free.fr)
GUERLET Sandrine (e-mail: sandrine.guerlet@lmd.ipsl.fr)
GUERRA Corentin (e-mail: corentin.guerra@obspm.fr)

GUILET Jérôme (e-mail: jerome.guilet@cea.fr)
GUILLARD Pierre (e-mail: pierre.guillard@gmail.com)
GUILLOT Sebastien (e-mail: sebastien.guillot@irap.omp.eu)
GUILYARDI Eric (e-mail: Eric.Guilyardi@locean.ipsl.fr)
GUIOT Pierre (e-mail: pierre.guiot@ias.u-psud.fr)
GUTTERIDGE Chloe (e-mail: chloe.gutteridge@obspm.fr)
HABART Emilie (e-mail: emilie.habart@ias.u-psud.fr)
HADID Lina (e-mail: lina.hadid@lpp.polytechnique.fr)
HALBWACHS Jean-Louis (e-mail: jean-louis.halbwachs@astro.unistra.fr)
HALTER Céline (e-mail: Celine.halter@astro.unistra.fr)
HAMEURY Jean-Marie (e-mail: jean-marie.hameury@astro.unistra.fr)
HARA Nathan (e-mail: nath.hara@gmail.com)
HÉBRARD Guillaume (e-mail: hebrard@iap.fr)
HEIDARI Neda (e-mail: heidari@iap.fr)
HELLOT Roger (e-mail: roger.hellot.astro@gmail.com)
HERBRETEAU Mathys (e-mail: mathys.herbreteau@ipsa.fr)
HERNANDEZ BERNAL Jorge (e-mail: jorge.hernandez-bernal@lmd.ipsl.fr)
HILL Vanessa (e-mail: Vanessa.Hill@oca.eu)
HOFFMANN Regine (e-mail: re.hoffmann@laposte.net)
HOUDAYER Pierre (e-mail: pierre.houdayer@obspm.fr)
HUBY Elsa (e-mail: elsa.huby@obspm.fr)
HUE Vincent (e-mail: vincent.hue@lam.fr)
HUET Paul (e-mail: paul.huet@obspm.fr)
HURTADO Norma (e-mail: norma.hurtado@cea.fr)
HUSSENOT-DESENONGES Thomas (e-mail: thomas.hussenot@ijclab.in2p3.fr)
IBATA Rodrigo (e-mail: rodrigo.ibata@astro.unistra.fr)
INART Enzo (e-mail: enzo.inart@etu.unistra.fr)
INES GOMEZ Ana (e-mail: anai_gomez@mat.ucm.es)
JACQUEMIN IDE Jonatan (e-mail: jonatan.jacqueminide@northwestern.edu)
JARRY Manon (e-mail: manon.jarry@irap.omp.eu)
JAZIRI Yassin (e-mail: yassin.jaziri@latmos.ipsl.fr)
JENN Matthieu (e-mail: matthieu.jenn@orange.fr)
JESSEL Vincent (e-mail: vega.lambdadraconis@gmail.com)
JIAO Yongjun (e-mail: yongjun.jiao@obspm.fr)
JORQUERA Sebastián (e-mail: sebastian.jorquera.c@ug.uchile.cl)
JOSSELIN Eric (e-mail: eric.josselin@umontpellier.fr)
JUSTE Vincent (e-mail: vincent.juste@iphc.cnrs.fr)
KASPER Markus (e-mail: mkasper@eso.org)
KATZ David (e-mail: david.katz@obspm.fr)
KEMPF Jean (e-mail: jean.kempf@irap.omp.eu)
KERVAZO Mathilde (e-mail: mathilde.kervazo@gmail.com)
KESSLER Nina (e-mail: nina.kessler@u-bordeaux.fr)
KHALIL Yassin Rany (e-mail: yassin-rany.khalil@etu.unistra.fr)
KIEFER Flavien (e-mail: flavien.kiefer@obspm.fr)
KIEFFER Nathan (e-mail: nathan.kieffer@ipsa.fr)
KLEIN Baptiste (e-mail: baptiste.klein@physics.ox.ac.uk)
KNÖDLSEDER Jürgen (e-mail: jknodlseder@irap.omp.eu)
KOU Raphaël (e-mail: raphael.kou@apc.in2p3.fr)
KOUACH Driss (e-mail: driss.kouach@obs-mip.fr)
KRAL Quentin (e-mail: quentin.kral@obspm.fr)
KRALJIC Katarina (e-mail: kraljic.kat@gmail.com)
KREIDER Christian (e-mail: christian.kreider@wanadoo.fr)
KRENCKER Tom (e-mail: tom.krencker@ipsa.fr)
KRUMACKER Edouard (e-mail: edouard.krumacker@gmail.com)
KURY Malou (e-mail: mkury10a@yahoo.com)

LAGADEC Eric (e-mail: elagadec@oca.eu)
LAGAGE Pierre-Olivier (e-mail: pierre-olivier.lagage@cea.fr)
LAGARDE Nadège (e-mail: nadege.lagarde@u-bordeaux.fr)
LAIBE Guillaume (e-mail: guillaume.laibe@ens-lyon.fr)
LAMAREILLE Fabrice (e-mail: fabrice.lamareille@ipsa.fr)
LAMBERT Julien (e-mail: julien@pulsr.sh)
LAMY Philippe (e-mail: philippelamy@latmos.ipsl.fr)
LANDAIS Gilles (e-mail: gilles.landais@unistra.fr)
LANGLOIS Maud (e-mail: maud.langlois@univ-lyon1.fr)
LAOUISSET Augustin (e-mail: augustin.laouisset@ipsa.fr)
LAPORTE Nicolas (e-mail: nl408@cam.ac.uk)
LAULHÈRE Christine (e-mail: christine.laulhere@orange.fr)
LAVAIL Alexis (e-mail: astro@lavail.net)
LAVIRON Adrien (e-mail: laviron@llr.in2p3.fr)
LE CAM Pierre (e-mail: plc@nocturno.fr)
LE FLOCH Bertrand (e-mail: bertrand.le-floch@u-bordeaux.fr)
LE GOUELLEC Valentin (e-mail: valentin.le.gouellec@gmail.com)
LE PETIT Franck (e-mail: Franck.LePetit@obspm.fr)
LE SAUX Arthur (e-mail: al598@exeter.ac.uk)
LEBLANC Francois (e-mail: francois.leblanc@latmos.ipsl.fr)
LEBOULLEUX Lucie (e-mail: lucie.leboulleux@univ-grenoble-alpes.fr)
LEBOUTEILLER Vianney (e-mail: vianney.lebouteiller@cnrs.fr)
LÈBRE Agnès (e-mail: agnes.lebre@umontpellier.fr)
LEBREUILLY Ugo (e-mail: ugo.lebreuilly@cea.fr)
LECA Jerome (e-mail: jerome.leca@rsacosmos.com)
LECLERC Armand (e-mail: armand.leclerc@ens-lyon.fr)
LECLERCQ Floriane (e-mail: floriane.leclercq@austin.utexas.edu)
LEHOUCQ Roland (e-mail: roland.lehoucq@cea.fr)
LEKIC Anica (e-mail: anica.lekic@ipsa.fr)
LEMOINE Jean-Michel (e-mail: jean-michel.lemoine@cnes.fr)
LENOBLE Romain (e-mail: romain.lenoble@ens-lyon.fr)
LEROY Arnaud (e-mail: arnaudastro@yahoo.fr)
LEROY Gavin (e-mail: gavin.leroy@cea.fr)
LEROY Nicolas (e-mail: nicolas.leroy@ijclab.in2p3.fr)
LESTEVEN Soizick (e-mail: soizick.lesteven@astro.unistra.fr)
LEWIS Joseph (e-mail: Joe.Lewis@uni-heidelberg.de)
LI Chengdong (e-mail: chengdong.li@astro.unistra.fr)
LIGI Roxanne (e-mail: roxanne.ligi@oca.eu)
LILENSTEIN Jean (e-mail: jean.lilensten@univ-grenoble-alpes.fr)
LINTZ Michel (e-mail: michel.lintz@oca.eu)
LOPEZ ARISTE Arturo (e-mail: Arturo.LopezAriste@irap.omp.eu)
LOPEZ SEPULCRE Ana (e-mail: ana.lopez-sepulcre@univ-grenoble-alpes.fr)
LOUP Cécile (e-mail: cecile.loup@astro.unistra.fr)
LOUYS Mireille (e-mail: mireille.louys@unistra.fr)
LOVIS Christophe (e-mail: christophe.lovis@unige.ch)
MAETZ Alain (e-mail: alainmaetz.am@gmail.com)
MAGGI Pierre (e-mail: pierre.maggi@astro.unistra.fr)
MAGNELLI Benjamin (e-mail: benjamin.magnelli@cea.fr)
MAHLER Guillaume (e-mail: guillaume.mahler@durham.ac.uk)
MAI Nicolas (e-mail: nicolas.mai@etu.unistra.fr)
MALBET Fabien (e-mail: Fabien.Malbet@univ-grenoble-alpes.fr)
MALZAC Julien (e-mail: julien.malzac@irap.omp.eu)
MANCHON Louis (e-mail: louis.manchon@obspm.fr)
MANGIAGLI Alberto (e-mail: mangiagli@apc.in2p3.fr)
MARCHAL Olivier (e-mail: olivier.marchal@astro.unistra.fr)

MARCHAND Manon (e-mail: manon.marchand@astro.unistra.fr)
MARCHIORO Julien (e-mail: julien.marchioro@apc.in2p3.fr)
MARCOWITH Alexandre (e-mail: Alexandre.Marcowith@umontpellier.fr)
MARET Sébastien (e-mail: sebastien.maret@univ-grenoble-alpes.fr)
MARIN Frédéric (e-mail: frederic.marin@astro.unistra.fr)
MARINHO Louise (e-mail: louise.marinho@u-bordeaux.fr)
MARQUES Joao (e-mail: joao.marques@universite-paris-saclay.fr)
MARTEL Étienne (e-mail: etienne.martel@sfr.fr)
MARTEL Michel (e-mail: beamichel@aol.com)
MARTINIEN Laurine (e-mail: laurine.martinien@univ-grenoble-alpes.fr)
MARTINOD Marc-Antoine (e-mail: marc-antoine.martinod@kuleuven.be)
MARTOCCHIA Silvia (e-mail: silvia.martocchia@uni-heidelberg.de)
MASNOU Jean Louis (e-mail: j4l5m6@orange.fr)
MATHIAS Philippe (e-mail: pmathias@irap.omp.eu)
MATHIS Stéphane (e-mail: stephane.mathis@cea.fr)
MAUREL Alice (e-mail: maurel@iap.fr)
MAUXION Jonah (e-mail: jonah.mauxion@univ-grenoble-alpes.fr)
MAYER Julia (e-mail: julia.mayer@ipsa.fr)
MAZOYER Johan (e-mail: johan.mazoyer@obspm.fr)
MEI Simona (e-mail: mei@apc.in2p3.fr)
MENARD Francois (e-mail: francois.menard@univ-grenoble-alpes.fr)
MERCIER Wilfried (e-mail: wilfried.mercier58@gmail.com)
METRIS Gilles (e-mail: gilles.metris@oca.eu)
MEUNIER Nadège (e-mail: nadege.meunier@univ-grenoble-alpes.fr)
MICHEL Laurent (e-mail: laurent.michel@astro.unistra.fr)
MICHOULIER Stéphane (e-mail: stephane.michoulier@univ-lyon1.fr)
MIDAVAINE Thierry (e-mail: thierrymidavaine@sfr.fr)
MIGNON-RISSE Raphaël (e-mail: raphael.mignon-risse@apc.in2p3.fr)
MILLI Julien (e-mail: julien.milli@univ-grenoble-alpes.fr)
MONARI Giacomo (e-mail: giacomo.monari@astro.unistra.fr)
MONPRIBAT Emma (e-mail: emma.monpribat@iphc.cnrs.fr)
MORAN Joseph (e-mail: moran@unistra.fr)
MOSSER Benoit (e-mail: benoit.mosser@observatoiredeparis.psl.eu)
MOTTE Frédérique (e-mail: frederique.motte@univ-grenoble-alpes.fr)
MOTTEZ Fabrice (e-mail: fabrice.mottez@obspm.fr)
MOUILLET David (e-mail: david.mouillet@univ-grenoble-alpes.fr)
MOURARD Denis (e-mail: denis.mourard@oca.eu)
MOURS Benoit (e-mail: benoit.mours@iphc.cnrs.fr)
MOUTARD Thibaud (e-mail: thibaud.moutard@lilo.org)
N'DIAYE Mamadou (e-mail: mamadou.ndiaye@oca.eu)
NAAR Joseph (e-mail: joseph.naar@lmd.ipsl.fr)
NEBOT-GOMEZ Ada (e-mail: ada.nebot@astro.unistra.fr)
NEINER Coralie (e-mail: coralie.neiner@obspm.fr)
NEVEU Stephane (e-mail: stephane.neveu@saf-astronomie.fr)
NG-GUIHENEUF Cherry (e-mail: cherry.ng-guiheneuf@cnrs-orleans.fr)
NIEMIEC Anna (e-mail: anna.niemiec@lpnhe.in2p3.fr)
NOBLE Jennifer (e-mail: jennifer.noble@univ-amu.fr)
NONY Thomas (e-mail: t.nony@irya.unam.mx)
NOTERDAEME Pasquier (e-mail: noterdaeme@iap.fr)
NOVAK Jerome (e-mail: jerome.novak@obspm.fr)
NUNEZ Arturo (e-mail: arturo.nunez@cea.fr)
OBERNOLTE Troy (e-mail: troy@obernolte.com)
OCVIRK Pierre (e-mail: pierre.ocvirk@astro.unistra.fr)
OERS Jonathan (e-mail: jonathan.oers@irap.omp.eu)
OERTEL Micaela (e-mail: micaela.oertel@obspm.fr)

OLIVEIRA Thomas (e-mail: thomas.oliveira@etu.unistra.fr)
OMONT Alain (e-mail: omont@iap.fr)
OUAZZANI Rhita-Maria (e-mail: rhita-maria.ouazzani@obspm.fr)
PALANQUE Mei (e-mail: m.palanque@unistra.fr)
PALMA-BIFANI Paulina (e-mail: paulina.palma-bifani@oca.eu)
PANEK Emilie (e-mail: panek@iap.fr)
PANTIN Eric (e-mail: eric.pantin@cea.fr)
PAQUEREAU Louise (e-mail: louise.paquereau@iap.fr)
PARC Léna (e-mail: lena.parc@unige.ch)
PARRA RAMOS Kethelin (e-mail: kethelin.ramos@usp.br)
PELLO Roser (e-mail: roser.pello@lam.fr)
PERALTA Raphael (e-mail: raphael.peralta@cea.fr)
PERRAUT Karine (e-mail: karine.perraut@univ-grenoble-alpes.fr)
PERRET Emmanuelle (e-mail: emmanuelle.perret@astro.unistra.fr)
PERRI Barbara (e-mail: barbara.perri@universite-paris-saclay.fr)
PETIT Pascal (e-mail: ppetit@irap.omp.eu)
PETRI Jerome (e-mail: jerome.petri@astro.unistra.fr)
PETRUCCI Pierre-Olivier (e-mail: pierre-olivier.petrucci@univ-grenoble-alpes.fr)
PETRUS Simon (e-mail: spetrus@npf.cl)
PHILIPOT Florian (e-mail: florian.philipot@obspm.fr)
PIANI Laurette (e-mail: laurette.piani@univ-lorraine.fr)
PILATE Quentin (e-mail: quentin.pilate@univ-tlse3.fr)
PINCON Charly (e-mail: charly.pincon@obspm.fr)
PISCHZUR Véronique (e-mail: veronique.pischzur4@gmail.com)
PITOUT Frédéric (e-mail: frederic.pitout@irap.omp.eu)
PLASSE Clara (e-mail: clara.plasse@cea.fr)
POMMIER Mamta (e-mail: mamtapan@gmail.com)
PORTE Thibaut (e-mail: thibaut.porte@ipsa.fr)
POURRÉ Nicolas (e-mail: nicolas.pourre@univ-grenoble-alpes.fr)
PRADIER Thierry (e-mail: thierry.pradier@iphc.cnrs.fr)
PRANTZOS Nicolas (e-mail: prantzos@iap.fr)
PRIOLET Philippe (e-mail: philippeprioletm@gmail.com)
PUECH Mathieu (e-mail: mathieu.puech@obspm.fr)
PUEYO Laurent (e-mail: pueyo@stsci.edu)
QUANZ Sascha (e-mail: sascha.quanz@phys.ethz.ch)
QUINTIN Erwan (e-mail: erwan.quintin@irap.omp.eu)
RADUREAU Gonzague (e-mail: gonzague.radureau-rebibo@oca.eu)
RAKOTONDRAINIBE Ny Avo (e-mail: ny-avo.rakotondrainibe@lam.fr)
RAMAMBASON Lise (e-mail: lise.ramambason@uni-heidelberg.de)
RAMBAUX Nicolas (e-mail: Nicolas.Rambaux@obspm.fr)
RAMESH Rameela (e-mail: rameela.davanagere@community.isunet.edu)
RAVINET Thomas (e-mail: thomas.ravinet@univ-fcomte.fr)
RAYMOND Sean (e-mail: rayray.sean@gmail.com)
REBOUL-SALZE Alexis (e-mail: alexis.reboul-salze@aei.mpg.de)
RECIO-BLANCO Alejandra (e-mail: arecio@oca.eu)
RENAUD Florent (e-mail: florent@astro.lu.se)
RENDON RESTREPO Steven (e-mail: srendon@aip.de)
REVOL Alexandre (e-mail: alexandre.revol@unige.ch)
REYLE Céline (e-mail: celine@obs-besancon.fr)
RICCIUTI Emeline (e-mail: e.ricciuti@unistra.fr)
RICHARD Johan (e-mail: johan.richard@univ-lyon1.fr)
RIGAUD Alexis (e-mail: alexis@pulsr.sh)
ROBERT Vincent (e-mail: vincent.robert@obspm.fr)
ROBIN Annie (e-mail: annie.robin@obs-besancon.fr)
ROCCI Pier-Francesco (e-mail: pierfrancesco.rocci@gmail.com)

RODRÍGUEZ MONTERO Francisco (e-mail: francisco.rodriguezmontero@physics.ox.ac.uk)
RODRIGUEZ Victor (e-mail: victor.rodriguez@etu.unistra.fr)
ROSAT Severine (e-mail: severine.rosat@unistra.fr)
ROSENBLATT Pascal (e-mail: pascal.rosenblatt@univ-nantes.fr)
ROUBEAU-TISSOT Amaël (e-mail: amael.roubeau-tissot@oca.eu)
ROULE Mathieu (e-mail: roule@iap.fr)
ROUMESY Maxime (e-mail: maxime.roumesy@univ-grenoble-alpes.fr)
ROZIER Simon (e-mail: simon_rozier@hotmail.fr)
RUSSEIL Delphine (e-mail: delphine.russeil@lam.fr)
RYAN Tim (e-mail: tim.ryan@gmx.net)
RYMAR Axel (e-mail: axel.rymar@universite-paris-saclay.fr)
SACCARDI Andrea (e-mail: andrea.saccardi@obspm.fr)
SAILLENFEST Melaine (e-mail: melaine.saillenfest@obspm.fr)
SAINRAT Thomas (e-mail: thomas.sainrat@iphc.cnrs.fr)
SALOME Philippe (e-mail: philipe.salome@observatoiredeparis.psl.eu)
SANSBERRO Inès (e-mail: ines.sansberro@lisa.ipsl.fr)
SANTERNE Alexandre (e-mail: alexandre.santerne@lam.fr)
SARRON Florian (e-mail: florian.sarron@irap.omp.eu)
SAUTRON Mattéo (e-mail: matteo.sautron@etu.unistra.fr)
SAVALLE Etienne (e-mail: savalle.etienne@hotmail.fr)
SCHAAFF André (e-mail: andre.schaaff@astro.unistra.fr)
SCHMIDT Carlo (e-mail: carlo.schimd@lam.fr)
SCHNEIDER Benjamin (e-mail: bschn@mit.edu)
SCHUSSLER Fabian (e-mail: fabian.schussler@cea.fr)
SEGRETAIN Paul (e-mail: paul.segretain@oca.eu)
SEILLÉ Lise-Marie (e-mail: lise-marie.seille@lam.fr)
SELSIS Franck (e-mail: franck.selsis@u-bordeaux.fr)
SERRE Marina (e-mail: marinaserre@icloud.com)
SERVILLAT Mathieu (e-mail: mathieu.servillat@obspm.fr)
SHAJI Aashiya Anitha (e-mail: aashiya.shaji@obspm.fr)
SHARMA Pooja (e-mail: pooja.sharma@ijclab.in2p3.fr)
SIEBERT Arnaud (e-mail: arnaud.siebert@astro.unistra.fr)
SIELLEZ Karelle (e-mail: karelle.siellez@utas.edu.au)
SIMON Christine (e-mail: christinesimon3@gmail.com)
SIMONNIN Adrien (e-mail: adrien.simonnin@oca.eu)
SLEZAK Eric (e-mail: eric.slezak@oca.eu)
SOLA Elisabeth (e-mail: elisabeth.sola@astro.unistra.fr)
SOUBIRAN Caroline (e-mail: caroline.soubiran@u-bordeaux.fr)
SOUCAIL Genevieve (e-mail: gsoucail@irap.omp.eu)
SOULAIN Anthony (e-mail: anthony.soulain@univ-grenoble-alpes.fr)
SPYROMILIO Jason (e-mail: jspyromi@eso.org)
SRIKANTH Togere Nagesh (e-mail: togerenagesh@astro.unistra.fr)
STAELEN Clément (e-mail: clement.staelen@u-bordeaux.fr)
STAHL Clément (e-mail: clement.stahl@astro.unistra.fr)
STEHLE Chantal (e-mail: chantal.stehle@obspm.fr)
STEHLIN Kathleen (e-mail: kathleen.stehlin@univ-fcomte.fr)
SULIS Sophia (e-mail: sophia.sulis@lam.fr)
SYX Antoine (e-mail: antoine.syx@iphc.cnrs.fr)
SZYMANSKI Damien (e-mail: evdszymanski@evc.net)
TABONE Benoît (e-mail: benoit.tabone@universite-paris-saclay.fr)
TATISCHEFF Vincent (e-mail: Vincent.Tatischeff@csnsm.in2p3.fr)
TAZAKI Ryo (e-mail: ryo.tazaki1205@gmail.com)
TENACHI Wassim (e-mail: wassim.tenachi@astro.unistra.fr)
THÉLIE Emilie (e-mail: emilie.thelie@astro.unistra.fr)
THEULÉ Patrice (e-mail: patrice.theule@univ-amu.fr)

THOMASSON Benjamin (e-mail: benjamin.thomasson@univ-grenoble-alpes.fr)
THOMSON-PARESSANT Keegan (e-mail: keegan.thomson-paressant@obspm.fr)
THOUVENIN Bruno (e-mail: bruno.thouvenin6@orange.fr)
THUILLOT William (e-mail: William.Thuillot@obspm.fr)
TISKYEH Joude (e-mail: Joudeastro@gmail.com)
TODOROV Lilia (e-mail: lilia.todorov@lam.fr)
TOUBOL Pierre-Bernard (e-mail: pierre@toubol.fr)
TRESSE Laurence (e-mail: laurence.tresse@lam.fr)
TURBET Martin (e-mail: martin.turbet@lmd.ipsl.fr)
URBANO Mathias (e-mail: mathias.urbano@astro.unistra.fr)
VALDIVIA Valeska (e-mail: valeska.valdivia.l@gmail.com)
VALEILLE-MANET Maxime (e-mail: maxime.valeille@outlook.fr)
VALENTIN Samuel (e-mail: samuel.valentin@etu.unistra.fr)
VALLUCCI-GOY Valentin (e-mail: valentin.goy@cea.fr)
VANCOELLIE Renaud (e-mail: renaud.vancoellie@etu.unistra.fr)
VANDAL Thomas (e-mail: thomas.vandal@umontreal.ca)
VASSEUR Serge (e-mail: hipparcos@outlook.com)
VAUGLIN Isabelle (e-mail: isabelle.vauglin@univ-lyon1.fr)
VEILLET Christian (e-mail: rapaiki@gmail.com)
VENOT Olivia (e-mail: olivia.venot@lisa.ipsl.fr)
VERGANI Susanna (e-mail: susanna.vergani@obspm.fr)
VINATIER Sandrine (e-mail: sandrine.vinatier@obspm.fr)
VIVIEN Hugo (e-mail: hugo.vivien@lam.fr)
VOGGEL Karina (e-mail: karina.voggel@astro.unistra.fr)
VOISIN Guillaume (e-mail: guillaume.voisin@obspm.fr)
VOLLMER Bernd (e-mail: Bernd.Vollmer@astro.unistra.fr)
WALCHSHOFER Pierre (e-mail: pwalcho@gmail.com)
WALLIANG Didier (e-mail: didier.walliang@gmail.com)
WEBB Natalie (e-mail: Natalie.Webb@irap.omp.eu)
WENDLING Milène (e-mail: milene.wendling@unistra.fr)
WOZNIAK Hervé (e-mail: herve.wozniak@umontpellier.fr)
ZAMBRANA PRADO Natalia (e-mail: natalia.zambranaprado@nasa.gov)
ZANNESE Marion (e-mail: marion.zannese@universite-paris-saclay.fr)
ZELLER Benoît (e-mail: bzastro@yahoo.fr)

Session S00

SF2A — Plenary session

SF2A 2023
M. N'Diaye, A. Siebert, N. Lagarde, O. Venot, K. Baillié, M. Béthermin, E. Lagadec, J. Malzac, J. Richard (eds)

ASTRONOMY AND THE EUROPEAN OPEN SCIENCE CLOUD

M. Allen[1], B. Cecconi[2], M. Marchand[1] and A. Gonneau[1]

Abstract. The European Open Science Cloud (EOSC) is an initiative to create a 'web of FAIR data' to enable open science. We present an overview of the astronomy-related activities that are contributing to the development of the EOSC. We highlight the participation of the Centre de Données astronomiques de Strasbourg (CDS) and the Observatoire de Paris in EOSC projects, and provide examples of how EOSC is already being used to support astronomy research and data sharing.

Keywords: Astronomical data bases, Virtual observatory tools, Gravitational waves, Standards, Open Science, Data sharing

1 Introduction

The vision of the European Open Science Cloud (EOSC) is to set up a 'web of FAIR data and services' to serve science in Europe. The first steps toward EOSC started in $\sim$ 2018 and current information about the development of EOSC is available on the EOSC Association web pages (`https://eosc.eu/`). The 'Strategic Research and Innovation Agenda' document available there, provides a detailed description of Open Science, the creation of the EOSC concept and its guiding principles, and it also identifies the challenges for its implementation and the potential impacts. The 'Multi-Annual Roadmap' defines a set of priorities for future investment in EOSC, with specific objectives.

Many consultations at European, national and institutional levels have contributed to the overall vision and development of EOSC. Phase 1 of EOSC (2018-2020) was a preparatory period, we are now in a 'convergence phase' (2021-2027), with the 'operational phase' expected to begin in 2027. In this article we summarise the astronomy-related activities that have been pursued at the Centre de Données astronomiques de Strasbourg (CDS*) and the Observatoire de Paris in the context of EOSC, highlighting examples of open science in astronomy and the use of EOSC services. The Action Spécifique Observatoires Virtuels (ASOV) also plays an important role of bringing the French actions toward the Virtual Observatory together, and information about the development of EOSC has been shared at ASOV events.

2 European projects supporting open science in astronomy

The CDS and the Observatoire de Paris are contributing to the development of Open Science in astronomy. The CDS is a Research Infrastructure providing services for reference data in astronomy. CDS participates in many initiatives for the promotion of Open Science at the national, european and international level. CDS recently became a Thematic Reference Centre of the French Recherche Data Gouv initiative, it leads many European Virtual Observatory projects and it is a major actor in the International Virtual Alliance (IVOA). CDS participates in EOSC via the EOSC Association memberships of CNRS and the Université de Strasbourg, and the CDS participation in European projects related to EOSC. The Observatoire de Paris is a member of the EOSC association since its inception. Observatoire de Paris teams are also contributing to international collaborations including similar Open Science and cloud-oriented developments, especially in Japan and in the USA. The development of EOSC and the associated projects is considered by Observatoire de Paris as strategic

[1] Université de Strasbourg, CNRS, Observatoire astronomique de Strasbourg, UMR 7550, F-67000 Strasbourg, France
[2] LESIA, Observatoire de Paris-PSL, CNRS, Sorbonne Université, Université Paris Cité, UMR 8109, F-92190 Meudon, France
*`https://cds.unistra.fr`

© Société Française d'Astronomie et d'Astrophysique (SF2A) 2023

for upcoming large scale research projects of the institution and the astrophysics science community. As a result, both the CDS and Observatoire de Paris contribute to the shaping of EOSC, at the national level through the *Collège EOSC*, grouping all the French EOSC members, under the umbrella of the French Ministry of Research, the European level of EOSC itself, and also the promotion of European activities at the international level.

2.1 ESCAPE

The European Science Cluster of Astronomy & Particle physics ESFRI research Infrastructure project (ESCAPE) addressed the Open Science challenges shared by ESFRI facilities. These included the astronomy and particle physics infrastructures: SKA, CTA, KM3Net, EST, ELT, HL-LHC, EGO/Virgo and FAIR as well as other pan-European research infrastructures (CERN, ESO, and JIVE) (Allen et al. 2022a). ESCAPE actions were focused on developing solutions for the large data sets handled by the ESFRI facilities. The CDS led a major work package of ESCAPE to "Connect ESFRI projects to EOSC through VO framework" (CEVO), with 16 partners including the astrophysics ESFRI and partners with expertise in the Virtual Observatory (CDS, University of Edinburgh, University of Heidelberg, INTA, INAF, Observatoire de Paris). The main task of this work was the implementation of the FAIR *'findable, accessible, interoperable, re-usable'* principles for ESFRI data through the Virtual Observatory, which was pursued by advancing the definition and adoption of common open IVOA standards for interoperability based on scientific requirements of the ESFRI and the astronomy community (Molinaro et al. 2021; Allen et al. 2022b). The results are described in the deliverable reports[†] of the CEVO work package.

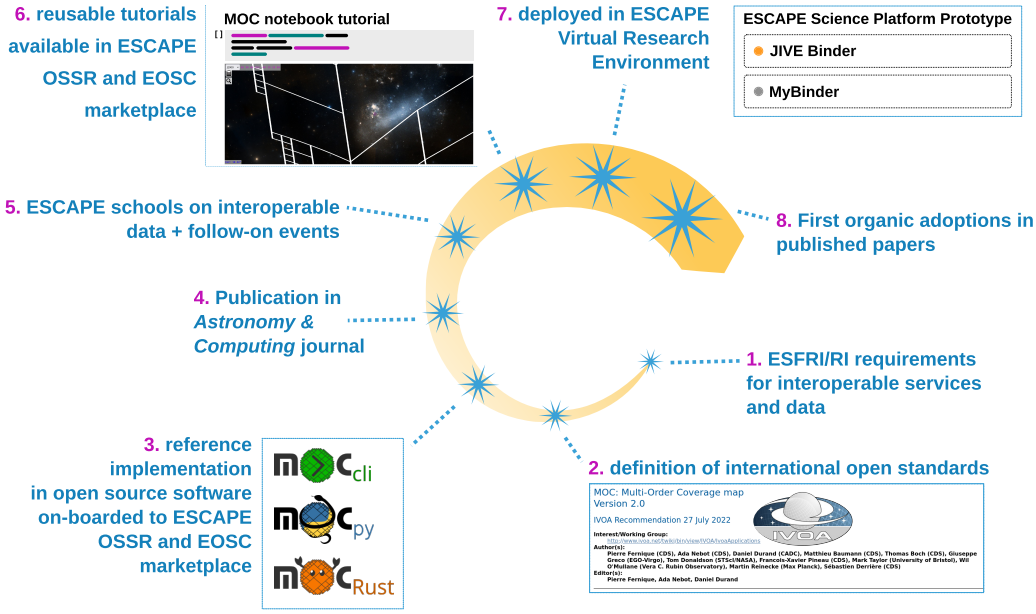

Fig. 1. The Open Science Cycle example of the EGO/Virgo science case in ESCAPE

Here we illustrate the results of the ESCAPE work with the example of the 'open science cycle' developed for the EGO-Virgo requirements. The cycle includes 8 steps from scientific requirements through re-usable notebooks fully integrated into EOSC, and then to community adoption:

1. Requirements for interoperable sky-area and temporal indexation were established, in particlar for managing sky areas in follow-up observations of gravitational wave events.

2. Standardisation was achieved with the acceptance of the MOC 2.0 IVOA recommendation (Fernique et al. 2022) following active participation of the partners in the IVOA.

3. The reference implementation of the MOC standard designed as a software suite in different languages – a command line interface MOCcli, a python library MOCpy (Baumann et al. 2023) and a Rust crate

[†]https://wiki.escape2020.de/index.php/WP4_-_CEVO

MOClibrust (Pineau & Baumann 2021) – to adapt to different users. This led to the release of open source software libraries which have been incorporated into visualisation tools (Baumann & Boch 2023), and on-boarded to the ESCAPE software repository (OSSR) and in the EOSC marketplace.

4. An Open Access refereed publication (Greco et al. 2022) disseminated the technical and scientific results generated by the new standards, tools and application.
5. A tutorial in the ESCAPE training event was based on the methods used for the publication, providing a real science case tutorial.
6. A Jupyter notebook implementation of the tutorial was created and was included into a collection of notebooks that has been on-boarded as a resource to the OSSR Marchand et al. (2023) and as a part of a tutorial suite directly included in the EOSC list of tutorials (Access and use of astronomy-related data from Python: a series of Jupyter notebooks tutorials).
7. Notebook tutorials are compatible with diverse deployments like the Binder interface implemented in ESCAPE Virtual Research Environment or *'devcontainers'* and Jupyter hub as used in the EOSC capabilities.
8. As a result, the first scientific papers explicitly referencing the MOC standard or one of the reference implementation software start to appear, some directly linked to gravitation wave follow-up science Chaudhary et al. (2023), and others from different astronomical domains, e.g. Wang et al. (2023); Rankine et al. (2023); Sweijen et al. (2023).

2.2 EOSC Pillar

The EOSC Pillar project (`https://www.eosc-pillar.eu`) conducted a program around the topic of building EOSC from national contributions. One of the astronomy-related activities that was selected as a thematic use-case was the on-boarding of the CDS SIMBAD service to EOSC. The support of the EOSC Pillar project was important for establishing the CDS as a 'service provider' in the EOSC Portal. The CDS SIMBAD service was then 'on-boarded' so that the service is made findable in the EOSC Portal[‡].

2.3 EOSC Future

The EOSC Future project (`https://eoscfuture.eu`)brought together the e-Infrastructures and Science Cluster communities to build a first implementation of EOSC. One of the astronomy activities in the project led by the CDS was to integrate the documentation about the CDS VizieR publishing process into the EOSC training materials. A tutorial[§] outlining the steps of publishing the data connected with refereed astronomy journal articles was prepared, and on-boarded to EOSC. This tutorial demonstrates how the already established CDS processes for publishing data in astronomy journals leads to the records being visible in the EOSC Marketplace without additional actions by the authors. This work consolidates the ESCAPE work of on-boarding the Virtual Observatory registry to EOSC, and Fig 2 shows the different paths for journal papers, VO services and general services can take to become visible in the EOSC system. Furthermore, a set of python notebook tutorials[¶] based on the ESCAPE 'Science with interoperable data schools' have also been made sustainable (Marchand et al. 2022) and on-boarded as part of the EOSC Future project, see also Fig 1.

3 Using EOSC in Astronomy projects

The main entry point of EOSC, when looking for resources is the EOSC Marketplace[‖], which is gathering all resources available in EOSC (services, data, publications...). A service provider interface is also available to register their services. The activities have focused on the five types of "generic services", which are basic bricks to be used to implement distributed digital infrastructures: (i) *Cloud Computing*, (ii) *Cloud Storage*, (iii) *Persistent Identifiers* and (iv) *Authentication and authorization infrastructure (AAI).*

[‡] `https://search.marketplace.eosc-portal.eu/search/service?q=SIMBAD`
[§] `https://search.marketplace.eosc-portal.eu/trainings/eosc.cds.6a0826b29f1f93ceed88ecf0de4e764c`
[¶] `https://search.marketplace.eosc-portal.eu/trainings/eosc.cds.0d5c7d6448cae721c84e6884f19f5f0b`
[‖] `https://marketplace.eosc-portal.eu`

Fig. 2. Paths for astronomy resources to become visible in the EOSC Marketplace/Portal. i) Published papers with associated data in the CDS VizieR service become visible in EOSC via the successive harvesting of the metadata by the Virtual Observatory registry, the EUDAT B2FIND service, and the integration of B2FIND in EOSC. ii) Similarly Virtual Observatory services in general are harvested by EUDAT B2FIND and hence become visible in EOSC. iii) There is also the possibility of directly on-boarding services, such as has been done for the CDS SIMBAD, with the CDS as the EOSC 'service provider'.

Several use cases have been explored by teams at the Observatoire de Paris, through various projects, namely, ESCAPE, Europlanet, FAIR-IMPACT, NenuFAR and VAMDC:

- The institution was a beneficiary of the ESCAPE project, and thus participated to the developments, through its contribution to the CTA (Cherenkov Telescope Array) project. The NenuFAR team was invited to many ESCAPE meetings for their expertise in low frequency radioastronomy, providing in-kind contribution. Currently, the Observatoire de Paris team has set up a prototype based on ESCAPE developments to run Jupyter notebooks on the local computing cluster. This prototype is aiming at providing a working and training infrastructure for teams willing to develop and deploy their pipeline is an environment, which can be scaled up to EOSC.

- Within the last Europlanet project (EPN2024RI, `https://doi.org/10.3030/871149`), the VESPA (Virtual European Solar and Planetary Access, Erard et al. 2020) team, lead by Observatoire de Paris, has been exploring EOSC services, thanks to the support of the EOSC-Hub project. Their VESPA-Cloud project (Cecconi et al. 2020) has been selected as an "Early Adopter Program", and received direct support from EGI for set up virtual machines on several cloud computing environments available through EOSC (namely: CC-IN2P3 and CESNET). The cloud computing virtual machines are used during the VESPA providers training workshop, and the team is consider using the virtual server in a production context soon. VESPA is also using the Eduteams AAI (`https://eduteams.org`, provided by GÉANT) to provide access to their gitlab server.

- The Observatoire de Paris is a funded participant of the FAIR-IMPACT project (`https://doi.org/10.3030/101057344`). In this project, the team at Observatoire de Paris is prototyping the use of ontologies in astronomy to enhance the semantic interoperability within EOSC.

- The NenuFAR (New Extension in Nançay Upgrading LOFAR) instrument is a small scale pathfinder of SKA (Square Kilometer Array), running at lower frequencies. Its team is facing a data management challenge (producing 1 to 2 PB of reduced data per year). It is supported by the DICE-EOSC project, with the provisioning of cold storage on tapes, for a total volume of 10 PB. The host infrastructure is located in Germany (MPCDF), and is part of EUDAT/B2SAFE. The sustainability of this setup has been discussed, and a volume of 1PB/yr of new data will be stored for free, thanks to an agreement between the NenuFAR team and the MaxPlanck Institüt für RadioAstronomie.

- VAMDC (Virtual Atomic and Molecular Data Center, `https://vamdc.org`) is a long standing project with uses the EUDAT (`https://eudat.eu`) services and well as Zenodo (`https://zenodo.org`) repository for minting PIDs and storing results from their Query Store.

For most of those development, support from an EOSC-funded institution was available and really helped to level up the skills of the teams involved. We list below a set of calls available (as of fall 2023) for onboarding EOSC:

- DICE-EOSC: `https://www.dice-eosc.eu/call-service-requests`

- EGI-ACE: `https://www.egi.eu/egi-ace-open-call/`
- EOSC-Future: `https://eoscfuture-grants.eu`
- EOSC-Portal: `https://eosc-portal.eu/eosc-early-adopter-programme`
- FAIR-IMPACT: `https://fair-impact.eu/fair-impact-open-calls-support`

4 Conclusions

EOSC is being developed as a major part of Open Science in Europe. Its interactions with the astronomy field are bidirectional: astronomy projects are connecting existing services, tutorials and datasets to the EOSC so that they become part of the wider data sharing framework, and astronomy projects can benefit from the more general services offered to the whole scientific community through the EOSC. We have shown that the connection of the astronomical VO to the EOSC enables the integration of a large amount of resources to the EOSC using a system that is already well established in astronomy. These efforts represent an investment for the future where we expect EOSC will provide new capabilities for data-sharing. It is clear that engagement with these initiatives is essential so that the input and needs of the astronomical community are taken into account in the on-going shaping of the EOSC.

The ESCAPE project has received funding from the European Union's Horizon 2020 research and innovation programme under Grant Agreement no. 824064. The EOSC Future project is co-funded by the European Union Horizon Programme under Grant Agreement no. 101017536. The Europlanet-2024 Research Infrastructure project has received funding from the European Union's Horizon 2020 research and innovation programme under grant agreement No 871149. This work used the EGI Infrastructure with the dedicated support of IN2P3-IRES and CESNET- MCC. The FAIR-IMPACT project has received funding from the European Union Horizon Programme under grant agreement No 101057344.

References

Allen, M., Lamanna, G., Espinal, X., et al. 2022a, in Astronomical Society of the Pacific Conference Series, Vol. 532, Astronomical Society of the Pacific Conference Series, ed. J. E. Ruiz, F. Pierfedereci, & P. Teuben, 113

Allen, M. G., Amodeo, S., Bonnarel, F., et al. 2022b, in Bulletin of the American Astronomical Society, Vol. 54, 2022n2i028

Baumann, M. & Boch, T. 2023, cds-astro/aladin-lite: 3.2.0

Baumann, M., Pineau, F.-X., Boch, T., & Marchand, M. 2023, cds-astro/mocpy: Release v0.13.0

Cecconi, B., Philippe, H., Shih, A., et al. 2020, in European Planetary Science Congress, EPSC2020–1015

Chaudhary, S. S., Toivonen, A., Waratkar, G., et al. 2023, Low-latency gravitational wave alert products and their performance in anticipation of the fourth LIGO-Virgo-KAGRA observing run

Erard, S., Cecconi, B., Le Sidaner, P., et al. 2020, Defense Science Journal, 19, 22

Fernique, P., Nebot, A., Durand, D., et al. 2022, MOC: Multi-Order Coverage map Version 2.0, IVOA Recommendation 27 July 2022

Greco, G., Punturo, M., Allen, M., et al. 2022, Astronomy and Computing, 39, 100547

Marchand, M., Amodeo, S., & Allen, M. 2022, working paper or preprint hal-03970692

Marchand, M. C., Amodeo, S., Baumann, M., et al. 2023, Access and use of astronomy-related data from Python : a series of Jupyter notebooks tutorials Zenodo 10.5281/zenodo.7547627

Molinaro, M., Allen, M., Bonnarel, F., et al. 2021, arXiv e-prints, arXiv:2111.14468

Pineau, F.-X. & Baumann, M. 2021, MOC Lib Rust, MOCCLi, MOCWasm and MOCSet, Release Notes: https://github.com/cds-astro/cds- moc-rust/blob/main/CHANGELOG.md

Rankine, A. L., Aird, J., Ruiz, A., & Georgakakis, A. 2023

Sweijen, F., Lyu, Y., Wang, L., et al. 2023, A&A, 671, A85

Wang, Y., Murphy, T., Lenc, E., et al. 2023, Monthly Notices of the Royal Astronomical Society, 523, 5661

SF2A 2023
M. N'Diaye, A. Siebert, N. Lagarde, O. Venot, K. Baillié, M. Béthermin, E. Lagadec, J. Malzac, J. Richard (eds)

HOT CORINOS: THE EARLY ORGANIC MOLECULAR ENRICHMENT OF THE PLANET FORMATION ZONES

M. De Simone[1,2]

Abstract. The earliest phases of a planetary system formation are represented by young warm protostars. Therefore, characterize the chemical content of young protostars is a crucial point in retrieving our origins. There the dust gets warm enough to release the molecules on the icy mantles into the gas phase and trigger a complex chemistry creating the so-called hot corinos, rich in interstellar complex organic molecules (iCOMs). However, after almost twenty year of studies, very few hot corinos have been discovered, and many of them show very different molecular spectra at millimeter wavelengths. Two straightforward question arise: i) What is the origin and nature of hot corinos? ii) How are iCOMs synthesized? To answer these questions, I investigated the protostellar binary system NGC 1333 IRAS 4A and its surroundings. I used i) VLA centimeter wavelengths observations toward the two protostars to investigate their chemical nature and history and ii) high-angular resolution observations with NOEMA, as part of the SOLIS (Seeds of Life in Space) Large Program, to study the chemical complexity of their molecular outflows. This contribution reports the main findings of my PhD Thesis work, that received the PhD prize from the SF2A. It was carried out at IPAG in Grenoble and it was part of the project Dawn of Organic Chemistry (DOC), funded by the European Research Council (ERC) under the grant No 741002.

Keywords: outflows, ISM, star formation, astrochemistry, shocks

1 Introduction

The formation of Solar-like stars goes through different stages, starting from a collapsing molecular core that evolves into a protostar, a protoplanetary disk, and eventually a planetary system. Together with the physical evolution, a chemical evolution takes place (see Figure 1.4)(Caselli & Ceccarelli 2012; Öberg & Bergin 2021). The discovery of iCOMs (interstellar Organic Molecules*, Herbst & van Dishoeck 2009; Ceccarelli et al. 2017) in the youngest phase of the formation of Solar-type stars, i.e., hot corinos (Ceccarelli 2004; Ceccarelli et al. 2007), raises a main important question: Is there a direct link between the first stages of Solar-like star formation and the latest ones? In other words, is the chemical complexity inherited from one stage to the other? Additionally, even though it has been thought for many years that the planets form in the protoplanetary disk stage (Class II, 10^7 yr), there have been recent evidences that shifted earlier the planet formation, already in the young protostellar stage (Class 0, 10^{4-5}yr) (Tychoniec et al. 2020; Sheehan & Eisner 2018; Segura-Cox et al. 2020). This enforces the importance of fully characterize, from a chemical point of view, the early stages of the formation of Solar-like stars, e.g., the protostellar one. However, protostars are really far to be chemically characterised.

2 Hot Corinos chemical diversity

The first sign of the presence of a rich organic chemistry in protostars comes in the early 2000 in the IRAS 16293-2422 source where abundant amounts of complex O- and N-bearing molecules were detected (Ceccarelli et al. 1998, 2000; Loinard et al. 2000; Cazaux et al. 2003). This was the first example of hot corino, a compact (< 100 au), hot (> 100 K), and dense ($>10^7$ cm^{-3}) region enriched in iCOMS, where the chemistry is dominated by the icy mantles sublimation. Since then, hot corinos were hunted at sub-mm wavelengths from single-dish to

[1] European Southern Observatory, Karl-Schwarzschild-Strasse 2, D-85748 Garching bei München, Germany
[2] Univ. Grenoble Alpes, CNRS, IPAG, 38000 Grenoble, France
*interstellar Complex Organic Molecules: saturated C-bearing molecules with more than six atoms and containing heteroatoms.

© Société Française d'Astronomie et d'Astrophysique (SF2A) 2023

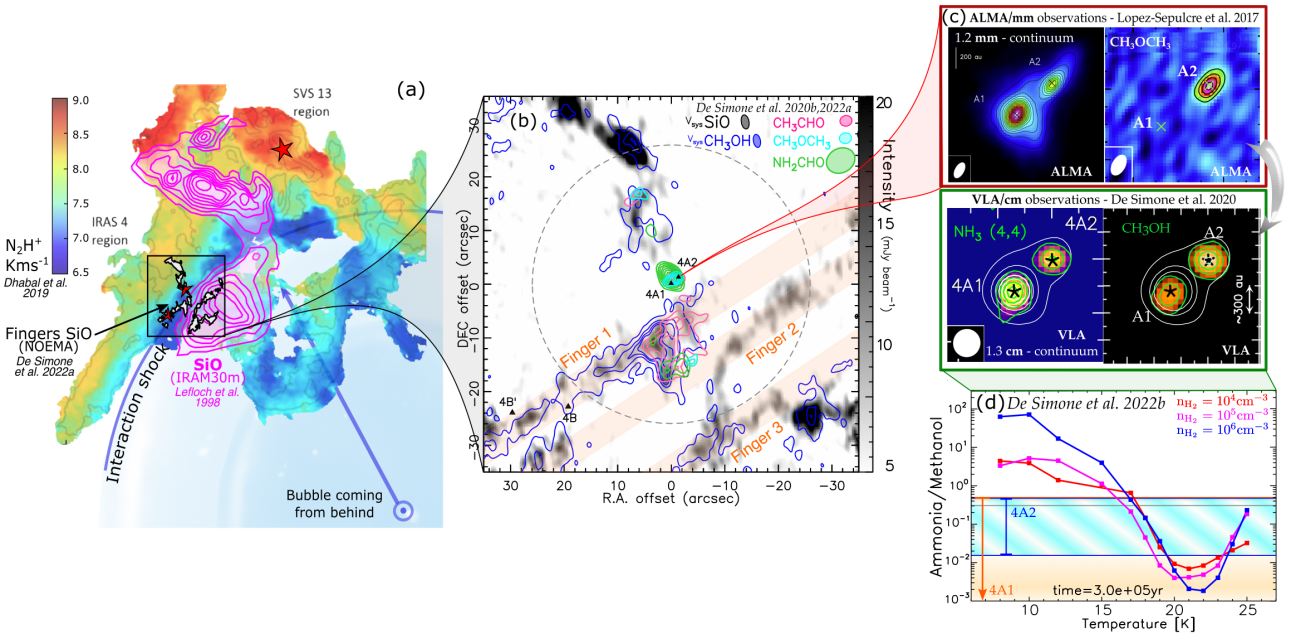

Fig. 1. *Panel (a)*: ***NGC 1333 shaped by a clashing bubble.*** N2H+ (1-0) velocity map of NGC 1333 south overlapped with SiO IRAM30m emission (magenta Dhabal et al. 2019; Lefloch et al. 1998), and SiO fingers (black De Simone et al. 2022). *Panel (b)*: ***Outflows rich in iCOMs and shocks tracing external interaction.*** iCOMs contour emission overlapped to SiO in greyscale in the IRAS 4A outflows observed with NOEMA/SOLIS (De Simone et al. 2020b, 2022). The shadowed area identify the three fingers. *Panel (c)*: ***Hot corino obscured by mm dust.*** IRAS 4A system observed in ALMA mm continuum (upper left) and mm lines (upper right) (López-Sepulcre et al. 2017), and with VLA NH_3 and CH_3OH lines (De Simone et al. 2020a; De Simone et al. 2022). *Panel d:* ***The ice mantle history.*** Theoretical prediction for NH_3/CH_3OH abundance ratio compared to the observed values (colored bands) (De Simone et al. 2022).

high sensitive interferometers, such us ALMA and NOEMA. However, after more than 20 years of search, only 25 iCOMs-rich hot corinos (40 with only CH_3OH) have been discovered (e.g., De Simone et al. 2017; Belloche et al. 2020; Bouvier et al. 2021; Yang et al. 2021). Additionally, several hot corinos in binary systems show very different millimeter molecular spectra (e.g., Yang et al. 2021; Codella et al. 2020b).

Several possibility may explain why hot corinos are so few and difficult to find, and why various protostellar system show such different molecular mm spectra: i) The dusty envelopes wrapping Class 0/I hot corinos could be optically thick enough to absorb the millimeter molecular lines and hide hot corinos. ii) Hot corinos are rare and the millimeter spectra reflect an intrinsic chemical diversity likely caused by a different history of the object. iii) the inner region is characterized by internal small scale substructures, such as disks, that can "protect" from the protostellar radiation. This implies that the temperature will drop not reaching the sublimation one, and the chemistry at play will change (Aikawa et al. 2020; Nazari et al. 2022; van Gelder et al. 2022).

Observational bias: The dust contribution

Several indirect evidences point that, at mm wavelengths, the dusty envelopes wrapping Class 0/I hot corinos could be optically thick (e.g., Miotello et al. 2014; Galván-Madrid et al. 2018; Galametz et al. 2019). Therefore, even if the mm wavelength is a perfect range to observe iCOMs thanks to the brightness of their emission, it can be not ideal to avoide optical thick dust effects. In order to test how much is the dust contribution at millimeter, me and my collaborators used a novel approach: we observed one of the simplest iCOMs, methanol (CH_3OH) at cm wavelength, with the JVLA interferometer, toward the IRAS 4A protostellar system, where only the source weaker in mm continuum, IRAS 4A2, shows mm iCOMs emission. We detected several methanol emission lines towards both sources with similar intensities (see Figure 1). With a non-LTE LVG analysis (Ceccarelli et al. 2003) we confirmed that methanol is tracing hot, dense gas in a compact region (about 70 au). Therefore, also IRAS 4A1, the source that at mm-wavelength lacks in iCOMs emission, has a hot corino region that was obscured by the thick mm dust. Additionally, we raised an important warning: the dust is affecting also the emission of IRAS 4A2, the known hot corino. Indeed, at 143 GHz we estimated a dust absorption of about

30%. That means that all the iCOMs abundances derived at mm wavelengths need to be taken with caution (De Simone et al. 2020a).

The protostellar ice mantle history

With these results we demonstrated that hot corinos can be few because hidden by the dust at mm wavelength. However, different hot corinos can still have different spectra. It is then crucial to measure the chemical composition of the ice mantles formed in the previous prestellar core phase to understand the chemical reservoir available for hot corinos. However, the direct study of the ice mantle composition in these young embedded sources is challenging. A possibility is to retrieve it indirectly by observing the ice mantle species when they are released in the gas phase in hot corinos. Among the major ice mantle species (Boogert et al. 2015; McClure et al. 2023), the critical tracers in the gas phase are NH_3 and CH_3OH, as they can be simultaneously observed with ground base telescope (JVLA), they can trace only the inner hot corino region, and they have very well known formation paths (Watanabe & Kouchi 2002; Rimola et al. 2014; Le Gal et al. 2014; Song & Kästner 2017; Tinacci et al. 2022). Aa a consequence, the NH_3/CH_3OH abundance ratio depends on the cloud temperature and density, and on the ice mantle formation timescale (Taquet et al. 2012; Aikawa et al. 2020).

Using JVLA we detected several lines of both CH_3OH and NH_3 toward the binaries IRAS 4A1 and 4A2, and IRAS 4B located 30" away from the binary. Using a non-LTE LVG analysis (Ceccarelli et al. 2003), as described in (De Simone et al. 2022), we derived the physical properties of the gas assessing that both species trace the hot corino region, and we derived their abundance ratio. Surprisingly, the three protostars show similar NH_3/CH_3OH value, that means that they went through the same chemical history. In other words, they were formed from a pre-collapse material with similar physical conditions. To quantify these physical conditions we run an astrochemical model (`grainoble;` Taquet et al. 2012; Ceccarelli et al. 2018) predicting the species abundance at different timescales, temperatures and densities of the pre-collapse material. Then we compared the predictions with the observations (Figure 1) and we found that to reproduce the observations, at the time of the icy mantle formation, the pre-collapse material should have been at about 17 K. However, at 70 au scales one would expect much lower temperature in a prestellar core (around 7 K Crapsi et al. 2007). On the other hand, the large- scale maps of Herschel-Planck (Zari et al. 2016) show that the average dust temperature of the south part of NGC 1333 is around 17 K. We then suggested that the three protostars did not have the usual dense and cold precollapse phase, as their mantles were mostly built during a relatively warm phase (dust temperature $\sim$17 K), which is characteristic of the less dense cloud material in NGC 1333 South (De Simone et al. 2022). In other words, something must have triggered a fast collapse and the protostars' formation.

3 The importance of the environment: outflows and shocks

The IRAS 4 protostars are located in the Perseus/NGC 1333 molecular cloud. As many star forming regions NGC 1333 is associated with filamentary structures, probably shaped by external triggers. In particular, the southern part, where IRAS 4 lie, show a clear velocity gradient blueshifted at the bottom and redshifted at the top (Figure 1) (e.g., Dhabal et al. 2018, 2019). Dhabal et al. (2019) hypothesized that this gradient could be due to a colliding "turbulent cell", a clash that could have triggered the birth of the protostars. However, no specific signatures of a clash, namely shocks, have been reported so far, leaving unanswered how and where the energy of this clash, if real, is dispersed.

Constraining iCOMs formation routes in molecular outflows

Using NOEMA observations from the SOLIS Large Program (Ceccarelli et al. 2017), I imaged the large scale (about 50", 15000 au) around the IRAS 4A protostars. The high angular resolution and high sensitivity observations allowed us to detect and image, for the second time ever after L1157-B1 (Codella et al. 2017, 2020a), several interstellar Complex Organic Molecules (iCOMs) in the IRAS 4A outflow (Figure 1): methanol tracing the whole lobes of the two outflows, acetaldehyde bright in the south-east lobe, dimethyl ether and formamide showing compact emission [4]. Analyzing the emission in different positions of the outflows, and focusing on methanol and acetaldehyde, we confirmed the presence of chemical differentiation, with the southeast lobe (driven by 4A1) brighter in iCOMs than the southwest-north (driven by 4A2). As explained in full details in De Simone et al. (2020b), comparing the observations with astrochemical model predictions we could test the formation path of acetaldehyde suggesting that it is synthesized in the gas phase by the reaction of atomic oxygen with ethyl radical.

Train of shocks as a signature of an unexpected clash

While analyzing the methanol emission in the IRAS 4A outflows, we noticed the presence of an elongated structure almost perpendicular to the outflow with a narrow spectral profile (FWHM∼1.5 km s^{-1}) peaking at the systemic velocity of the cloud. Similar structures were observed in SiO by Choi (2005) with the VLA, and by Lefloch et al. (1998) and Codella et al. (1999) with the IRAM 30m as a widespread SiO emission with unknown origin. To understand if these features were related, we analyzed the NOEMA/SOLIS observations of CH_3OH and SiO. We identified three parallel fingers separated by about 10" (∼3000 au), and chemically different with the northern Finger1 traced by both species, and the other two fingers traced only by SiO (in agreement with Choi 2005). Additionally the fingers are located in the large-scale blueshifted southern region of NGC 1333 (see Figure 1). Analyzing the methanol and SiO emission using a non-LTE LVG analysis (Ceccarelli et al. 2003) as described in (De Simone et al. 2022), we derived the gas properties and the SiO/CH_3OH abundance ratio in the fingers. We confirmed the observed chemical diversity, and we found that they are tracing high density ($> 10^5$ cm^{-3}) and high temperature (>80 K) material. However, what is their origin?
We investigated two possibilities: the fingers are tracing i) Kelvin Helmholtz instabilities or ii) a train of shocks. However, even if the former could reproduce the quasi periodicity of the fingers, it could not reproduce the observed gas density and temperature. Therefore, the only plausible possibility was a train of shocks, well justified by the presence of both SiO and methanol, known shock tracers (e.g., Bachiller et al. 1998, 2001; Arce et al. 2008; Codella et al. 2012), and by the derived gas physical condition. Comparing the observed CH_3OH/SiO abundance ratio with astrochemical model predictions we put constraint on when the shocks occurred in order to explain the observed chemical differentiation. We suggested that the northern finger is the youngest one and it happened at least 5000 yr after the next southern one. Therefore the three fingers could be the result of a successive train of shocks created by the clash of an expanding bubble coming from south-east and moving towards the IRAS 4A main cloud from behind (De Simone et al. 2022). Finally, we suggest that the widespread narrow SiO emission observed towards the NGC 1333 IRAS 4 and SVS 13 region with single-dish observations in the late 1990s (Lefloch et al. 1998; Codella et al. 1999) is due to unresolved trains of shocks like the SOLIS fingers. These shocks would be the signature of the interaction of the bubble giving rise to the IRAS 4A fingers and maybe the same bubble triggered prematurely the formation of the protostars in the filament, as suggested by the results on study of the ice mantle composition (as reported in Section 2; De Simone et al. 2022).

Acknowledgements: MDS thanks all the co-authors of the works presented in this proceeding (De Simone et al. 2020a,b; De Simone et al. 2022; De Simone et al. 2022), in particular the supervisors of the PhD thesis, Prof. C. Ceccarelli and Dr. C. Codella. This project has received funding within the European Union's Horizon 2020 research and innovation programme from the European Research Council (ERC) for the project "The Dawn of Organic Chemistry" (DOC), grant agreement No 741002.

References

Aikawa, Y., Furuya, K., Yamamoto, S., & Sakai, N. 2020, The Astrophysical Journal, 897, 110

Arce, H. G., Santiago-García, J., Jørgensen, J. K., Tafalla, M., & Bachiller, R. 2008, The Astrophysical Journal Letters, 681, L21

Bachiller, R., Guilloteau, S., Gueth, F., et al. 1998, Astronomy and Astrophysics, 339, L49

Bachiller, R., Pérez Gutiérrez, M., Kumar, M. S. N., & Tafalla, M. 2001, Astronomy and Astrophysics, 372, 899

Belloche, A., Maury, A. J., Maret, S., et al. 2020, Astronomy and Astrophysics, 635, A198

Boogert, A. C. A., Gerakines, P. A., & Whittet, D. C. B. 2015, Annual Review of Astronomy and Astrophysics, 53, 541

Bouvier, M., López-Sepulcre, A., Ceccarelli, C., et al. 2021, Astronomy and Astrophysics, 653, A117

Caselli, P. & Ceccarelli, C. 2012, Astronomy and Astrophysics Review, 20, 56

Cazaux, S., Tielens, A. G. G. M., Ceccarelli, C., et al. 2003, The Astrophysical Journal, 593, L51

Ceccarelli, C. 2004, ASP Conference Proceedings, 323, 195

Ceccarelli, C., Caselli, P., Fontani, F., et al. 2017, The Astrophysical Journal, 850, 176

Ceccarelli, C., Caselli, P., Herbst, E., Tielens, A. G. G. M., & Caux, E. 2007, Protostars and Planets V, 47

Ceccarelli, C., Castets, A., Loinard, L., Caux, E., & Tielens, A. G. G. M. 1998, Astronomy and Astrophysics, 338, L43

Ceccarelli, C., Loinard, L., Castets, A., Tielens, A. G. G. M., & Caux, E. 2000, Astronomy and Astrophysics, 357, L9

Ceccarelli, C., Maret, S., Tielens, A. G. G. M., Castets, A., & Caux, E. 2003, Astronomy and Astrophysics, 410, 587

Ceccarelli, C., Viti, S., Balucani, N., & Taquet, V. 2018, Monthly Notices of the Royal Astronomical Society, 476, 1371

Choi, M. 2005, The Astrophysical Journal, 630, 976

Codella, C., Bachiller, R., & Reipurth, B. 1999, Astronomy and Astrophysics, 343, 585

Codella, C., Ceccarelli, C., Bianchi, E., et al. 2020a, Astronomy and Astrophysics, 635, A17
Codella, C., Ceccarelli, C., Caselli, P., et al. 2017, Astronomy and Astrophysics, 605, L3
Codella, C., Ceccarelli, C., Lefloch, B., et al. 2012, The Astrophysical Journal, 757, L9
Codella, C., Podio, L., Garufi, A., et al. 2020b, Astronomy & Astrophysics, 644, A120
Crapsi, A., Caselli, P., Walmsley, M. C., & Tafalla, M. 2007, Astronomy and Astrophysics, 470, 221
De Simone, M., Ceccarelli, C., Codella, C., et al. 2020a, The Astrophysical Journal Letters, 896, L3
De Simone, M., Ceccarelli, C., Codella, C., et al. 2022, ApJ, 935, L14
De Simone, M., Codella, C., Ceccarelli, C., et al. 2022, Monthly Notices of the Royal Astronomical Society, 512, 5214
De Simone, M., Codella, C., Ceccarelli, C., et al. 2020b, Astronomy and Astrophysics, 640, A75
De Simone, M., Codella, C., Testi, L., et al. 2017, Astronomy and Astrophysics, 599, A121
Dhabal, A., Mundy, L. G., Chen, C.-y., Teuben, P., & Storm, S. 2019, The Astrophysical Journal, 876, 108
Dhabal, A., Mundy, L. G., Rizzo, M. J., Storm, S., & Teuben, P. 2018, The Astrophysical Journal, 853, 169
Galametz, M., Maury, A. J., Valdivia, V., et al. 2019, Astronomy and Astrophysics, 632, A5
Galván-Madrid, R., Liu, H. B., Izquierdo, A. F., et al. 2018, The Astrophysical Journal, 868, 39
Herbst, E. & van Dishoeck, E. F. 2009, Annual Review of Astronomy and Astrophysics, 47, 427
Le Gal, R., Hily-Blant, P., Faure, A., et al. 2014, A&A, 562, A83
Lefloch, B., Castets, A., Cernicharo, J., & Loinard, L. 1998, The Astrophysical Journal, 504, L109
Loinard, L., Castets, A., Ceccarelli, C., et al. 2000, Astronomy and Astrophysics, 359, 1169
López-Sepulcre, A., Sakai, N., Neri, R., et al. 2017, Astronomy and Astrophysics, 606, A121
McClure, M. K., Rocha, W. R. M., Pontoppidan, K. M., et al. 2023, Nature Astronomy, 7, 431
Miotello, A., Testi, L., Lodato, G., et al. 2014, Astronomy and Astrophysics, 567, A32
Nazari, P., Tabone, B., Rosotti, G. P., et al. 2022, A&A, 663, A58
Rimola, A., Taquet, V., Ugliengo, P., Balucani, N., & Ceccarelli, C. 2014, Astronomy and Astrophysics, 572, A70
Segura-Cox, D. M., Schmiedeke, A., Pineda, J. E., et al. 2020, Nature, 586, 228
Sheehan, P. D. & Eisner, J. A. 2018, The Astrophysical Journal, 857, 18
Song, L. & Kästner, J. 2017, The Astrophysical Journal, 850, 118
Taquet, V., Ceccarelli, C., & Kahane, C. 2012, Astronomy and Astrophysics, 538, A42
Tinacci, L., Germain, A., Pantaleone, S., et al. 2022, ACS Earth and Space Chemistry, 6, 1514
Tychoniec, L., Manara, C. F., Rosotti, G. P., et al. 2020, Astronomy and Astrophysics, 640, A19
van Gelder, M. L., Nazari, P., Tabone, B., et al. 2022, A&A, 662, A67
Watanabe, N. & Kouchi, A. 2002, The Astrophysical Journal, 571, L173
Yang, Y.-L., Sakai, N., Zhang, Y., et al. 2021, The Astrophysical Journal, 910, 20
Zari, E., Lombardi, M., Alves, J., Lada, C. J., & Bouy, H. 2016, Astronomy & Astrophysics, 587, A106
Öberg, K. I. & Bergin, E. A. 2021, Physics Reports, 893, 1

SF2A 2023
M. N'Diaye, A. Siebert, N. Lagarde, O. Venot, K. Baillié, M. Béthermin, E. Lagadec, J. Malzac, J. Richard (eds)

STRONG MAGNETIC FIELDS DISCOVERED IN RED GIANT CORES USING SEISMOLOGY

S. Deheuvels[1], G. Li[1,2], J. Ballot[1] and F. Lignières[1]

Abstract. We here provide a short summary of the first direct detection and measurement of magnetic fields in the cores of 24 red giants stars observed with the *Kepler* satellite (Borucki et al. 2010). For more detailed information, please see Li et al. (2022), Deheuvels et al. (2023), and Li et al. (2023).

Keywords: asteroseismology, stars: magnetic fields, stars: interiors, stars: evolution

1 Introduction

Magnetic fields affect stars throughout their lives. They are thought to play a crucial role in the redistribution of angular momentum within stars (e.g. Maeder & Meynet 2005). This impacts the rotational transport of chemical elements, and in turn the evolution of stars. Understanding the interaction between magnetic fields and rotation is thus a crucial step toward improving the precision to which stellar models can predict stellar ages. Until very recently, magnetic fields had been observed only at the surface of stars using spectropolarimetric observations (e. g. Donati & Landstreet 2009). The opacity of stellar matter had so far precluded direct detection of internal magnetic fields inside stars. Asteroseismology, which consists in the study of waves that propagate inside stars, is currently the only tool at our disposal to probe stellar interiors.

The seismology of red giant stars has become a crucial tool to test stellar physics. Red giant stars show extended convective envelopes, in which oscillation modes are stochastically excited, like in the Sun. For red giants, the frequency range of pressure (p) modes is comparable to that of gravity (g) modes. These two types of modes can thus couple, giving rise to so-called mixed modes, which probe both the envelope (where they behave as p modes) and the core (where they act as g modes). Since their detection in subgiants (Deheuvels & Michel 2010) and red giants (Beck et al. 2011), mixed modes have provided a wealth of information, for instance about their evolutionary status (Bedding et al. 2011), or their internal rotation (e.g. Beck et al. 2012, Deheuvels et al. 2012, Mosser et al. 2012). We here provide a short summary of how mixed modes were used to provide the first direct detection and measurement of magnetic fields in the cores of 24 red giants stars observed with the *Kepler* satellite (Borucki et al. 2010). For more detailed information, please see Li et al. (2022), Deheuvels et al. (2023), and Li et al. (2023).

2 Effects of magnetic fields on oscillation mode frequencies

To introduce the effects of magnetic fields on oscillation frequencies, it is convenient to first explain how they are impacted by rotation. By breaking the spherical symmetry of the star, rotation lifts the degeneracy between the frequencies of oscillation modes with same radial order n, same angular degree l, but different azimuthal orders m. This produces co-called *rotational multiplets* with $2l+1$ components. For slow rotators, such as red giants, the rotational multiplets are nearly symmetrical with respect to the central $m = 0$ component. Until very recently, deviations from the symmetry of multiplets had been observed only in p-dominated modes for certain red giants, owing to so-called near-degeneracy effects (Deheuvels et al. 2017).

The effects of magnetic fields on oscillation mode frequencies have been explored early on (Goossens 1972), and later extended to place constraints on the solar magnetic field (Gough 1990). They add to the effects of

[1] IRAP, Université de Toulouse, CNRS, CNES, UPS, 14 avenue Edouard Belin, 31400 Toulouse, France
[2] Institute of Astronomy, KU Leuven, Celestijnenlaan 200D, 3001 Leuven, Belgium

© Société Française d'Astronomie et d'Astrophysique (SF2A) 2023

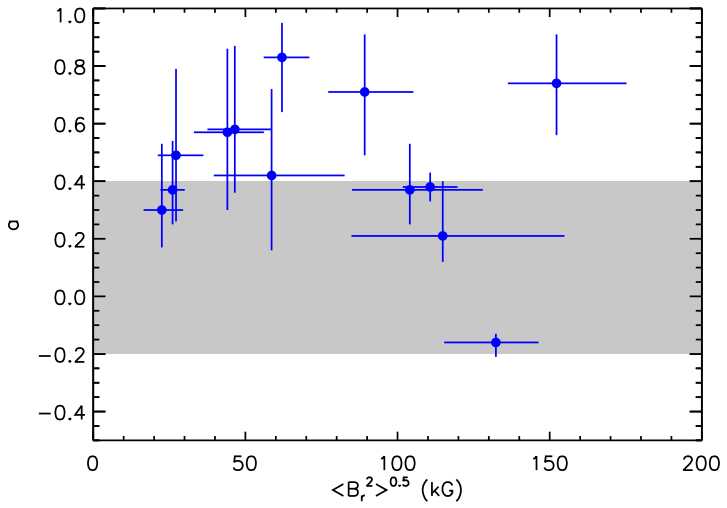

Fig. 1. Measured asymmetry parameter a as a function of the measured field strength for the 13 targets studied by Li et al. (2023). The gray shaded area shows the range of values of a covered by dipolar fields with various inclinations.

rotation by modifying the structure of rotational multiplets. Non-axisymmetric magnetic fields are known to produce up to $(2l+1)^2$ components per multiplet (Unno et al. 1989, Gough 1990), which can severely complicate the picture. For simplicity, most studies addressing this issue assumed specific configurations of the magnetic field. In particular, they commonly considered axisymmetric fields (aligned with the rotation axis), which do not modify the number of components in rotational multiplets, but can produce characteristic multiplet asymmetries. In this context, Hasan et al. (2005) showed that a dipolar axisymmetric field induces a highly-frequency-dependent perturbation to high-order g modes ($\delta\omega \sim \omega^{-3}$). The case of mixed modes in red giants was later addressed by Gomes & Lopes (2020), Mathis et al. (2021), and Bugnet et al. (2021), also assuming axisymmetric dipolar fields. Mathis et al. (2021) showed that the magnetic perturbations to mixed modes are dominated by contribution from the core field (i.e., by the effects on g-dominated modes), and Bugnet et al. (2021) explored the multiplet asymmetries caused by such magnetic fields. The effects on mixed modes of a dipolar field inclined with respect to the rotation axis were addressed by Loi (2021).

3 Detection of core magnetic fields in Kepler red giants using multiplet asymmetries

In Li et al. (2022) and Li et al. (2023), we detected clear asymmetries in the dipole multiplets of 13 red giants observed with *Kepler*. These asymmetries show features that closely correspond to what is expected in the presence of a core magnetic field: (i) they are stronger for g-dominated modes, (ii) they strongly decrease (in absolute value) as a function of frequency (the decrease is compatible with a dependency $\propto \omega^{-3}$), and (iii) they have the same sign for all multiplets in a given star (they are positive for 12 targets, and negative for only one star). We were able to safely rule out all known sources of multiplet asymmetries aside from magnetic fields. Indeed, we measured the internal rotation of these stars and found that they are all slow rotators, like other red giants. Also, the detected asymmetries cannot arise from near-degeneracy effects because they would then be stronger for p-dominated mixed modes, and also the asymmetries of consecutive modes would have alternate signs (Deheuvels et al. 2017).

To compare the detected asymmetries with theoretical magnetic perturbations, in Li et al. (2022) we generalized previous works to the case of magnetic fields with an arbitrary topology. We found that the average magnetic frequency shift of the components in a multiplet $\omega_{\rm B}$ can be expressed as $\omega_{\rm B} \propto \omega^{-3} \int_{\rm g} K(r)\overline{B_r^2}\,{\rm d}r$, where the weight function $K(r)$ depends on the core structure and $\overline{B_r^2}$ is a horizontal average of the square of the radial field. We showed that provided the ratio b between the magnetic shift $\omega_{\rm B}$ and the rotational shift $\omega_{\rm R}$ remains below unity, the effects of non-axisymmetry of the field on the oscillation modes remain negligible. In this case, the multiplet asymmetries can be expressed as $\delta_{\rm asym} = 3a\omega_{\rm B}$, where a corresponds to a horizontal average of B_r^2 weighted by the second order Legendre polynomial $P_2(\cos\theta)$, and thus depends on the geometry

of the field. We showed that a is maximal ($a = 1$) for a field entirely concentrated on the poles, and a is minimal ($a = -1/2$) for a field concentrated on the equator. This demonstrated that multiplet asymmetries can take on negative values, while previous theoretical studies, which considered particular field geometries, all predicted positive asymmetries. A purely dipolar field yields values of a ranging from $-1/5$ (when it is aligned with the equator) and $2/5$ (when it is aligned with the rotation axis). Mathis & Bugnet (2023) later specified the relation between the inclination angle of the dipolar field and the value of a.

We found that the above expressions were able to account very well for the detected asymmetries in the 13 *Kepler* red giants. By measuring $\omega_{\rm B}$ and a for these stars, we obtained measurements of the core field strengths ranging from 20 to 150 kG. We could also place constraints on the field topology. As shown in Fig. 1, the values of a we measured cover a large part of the possible range, which shows that there exists a wide diversity of field topologies in red giants cores. Also, for several stars, our measurements of a significantly exceed the maximal possible value for dipolar fields. This means that for these stars, the core field is more concentrated near the poles than a pure dipolar field aligned with the rotation axis.

4 Detection of strong core fields in Kepler red giants using g-mode periods

In the non-magnetic case, the periods of high-radial order g modes of degree l are nearly regularly spaced by the period spacing $\Delta\Pi_l$. A strong core magnetic field can produce significant deviations from this regularity (Loi 2020, Bugnet et al. 2021, Li et al. 2022). In Li et al. (2022), we showed that in this case, the period spacing $\Delta\Pi_l$ measured when ignoring magnetic effects is expected to be abnormally low (compared to other red giants) and non-constant with frequency. Several stars showing precisely these features had been identified in another context by Deheuvels et al. (2022). In Deheuvels et al. (2023), we found several other such stars and we showed that strong core fields account very well for the observations. The alternate explanation for these anomalies (so-called *buoyancy glitches*) was found to be very unlikely. We found minimal core fields in these stars ranging from 40 to 610 kG. These intensities are comparable to the critical field strength $B_{\rm c}$ above which the propagation of magneto-gravity waves are expected to be inhibited in the core (Fuller et al. 2015). The presence of core magnetic fields stronger than $B_{\rm c}$ was invoked by Fuller et al. (2015) to account for the unexpectedly low amplitudes of dipole mixed modes in about 20% of red giants (Stello et al. 2016), although this interpretation remains debated (Mosser et al. 2017). In Deheuvels et al. (2023), we found that the only star for which the measured field exceeds $B_{\rm c}$ shows mixed mode suppression at low frequency, which further suggests that this phenomenon might be related to strong core magnetic fields.

5 Origin and evolution of core magnetic fields

These first detections of internal magnetic fields bring direct observational constraints to investigate the origin of stellar magnetism. For stars in the mass range of our targets, the most commonly quoted origin is through dynamo action in the main-sequence convective core. The Ohmic dissipation time being longer than the lifetimes of the stars, such fields could persist long after the end of the main sequence. By assuming conservation of the magnetic flux, we found that the detected fields could be the remnants of main-sequence fields of a few kG. These estimates are lower but comparable to the field strengths predicted by numerical simulations of core convection (Brun et al. 2005) or by dynamo scaling laws (Bugnet et al. 2021). Another possibility is that these fields originate from fossil fields inherited from the stellar formation history.

Fig. 2 shows the measured field intensities as a function of the density of mixed modes, which is a good proxy for the evolution along the red giant branch (Gehan et al. 2018). We observe an overall decrease of the field strength with evolution. At first sight, one could have expected the contrary. Indeed, the core of red giants keeps contracting, which should produce an increase in the core field intensity, assuming conservation of the magnetic flux. In Deheuvels et al. (2023) and Li et al. (2023), we proposed that the observed decrease is related to the critical field strength $B_{\rm c}$, which itself decreases with evolution with a similar trend as the observed field strengths (see Fig. 2). The argument of Fuller et al. (2015) is that whenever the core field exceeds $B_{\rm c}$, mixed modes can no longer form. If it is indeed the case, we would then be unable to seismically detect the core field. The impact of a field stronger that $B_{\rm c}$ on global oscillation modes in red giants is currently a matter of debate (e.g., Rui & Fuller 2023).

We warmly thank the PNPS for giving us the opportunity to present these results at the SF2A days in Strasbourg, and for its valuable support to our project before we obtained a grant from ANR. We acknowledge support from from the project BEAMING ANR-18-CE31-0001 of the French National Research Agency (ANR) and from the Centre National d'Etudes Spatiales (CNES).

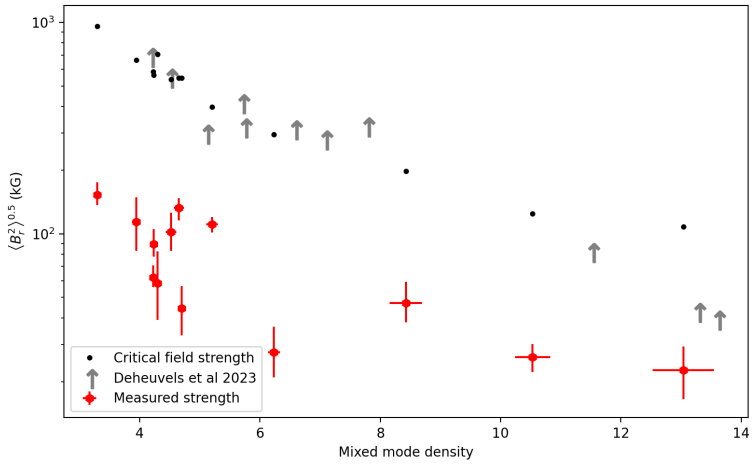

Fig. 2. Field strength as a function of mixed mode density, which is a proxy for evolution (stars evolve from left to right). The red hexagons are the field strengths of the 13 stars from Li et al. (2023), and the black dots are their critical field strengths. The grey vertical arrows show the lower limits of the field strengths reported by Deheuvels et al. (2023). Figure from Li et al. (2023)

References

Beck, P. G., Bedding, T. R., Mosser, B., et al. 2011, Science, 332, 205
Beck, P. G., Montalban, J., Kallinger, T., et al. 2012, Nature, 481, 55
Bedding, T. R., Mosser, B., Huber, D., et al. 2011, Nature, 471, 608
Borucki, W. J., Koch, D., Basri, G., et al. 2010, Science, 327, 977
Brun, A. S., Browning, M. K., & Toomre, J. 2005, ApJ, 629, 461
Bugnet, L., Prat, V., Mathis, S., et al. 2021, A&A, 650, A53
Deheuvels, S., Ballot, J., Gehan, C., & Mosser, B. 2022, A&A, 659, A106
Deheuvels, S., García, R. A., Chaplin, W. J., et al. 2012, ApJ, 756, 19
Deheuvels, S., Li, G., Ballot, J., & Lignières, F. 2023, A&A, 670, L16
Deheuvels, S. & Michel, E. 2010, Ap&SS, 328, 259
Deheuvels, S., Ouazzani, R. M., & Basu, S. 2017, A&A, 605, A75
Donati, J. F. & Landstreet, J. D. 2009, ARA&A, 47, 333
Fuller, J., Cantiello, M., Stello, D., Garcia, R. A., & Bildsten, L. 2015, Science, 350, 423
Gehan, C., Mosser, B., Michel, E., Samadi, R., & Kallinger, T. 2018, A&A, 616, A24
Gomes, P. & Lopes, I. 2020, MNRAS, 496, 620
Goossens, M. 1972, Ap&SS, 16, 386
Gough, D. O. 1990, in Lecture Notes in Physics, Berlin Springer Verlag, Vol. 367, Progress of Seismology of the Sun and Stars, ed. Y. Osaki & H. Shibahashi, 283
Hasan, S. S., Zahn, J. P., & Christensen-Dalsgaard, J. 2005, A&A, 444, L29
Li, G., Deheuvels, S., Ballot, J., & Lignières, F. 2022, Nature, 610, 43
Li, G., Deheuvels, S., Li, T., Ballot, J., & Lignières, F. 2023, arXiv e-prints, arXiv:2309.13756
Loi, S. T. 2020, MNRAS, 493, 5726
Loi, S. T. 2021, MNRAS, 504, 3711
Maeder, A. & Meynet, G. 2005, A&A, 440, 1041
Mathis, S. & Bugnet, L. 2023, A&A, 676, L9
Mathis, S., Bugnet, L., Prat, V., et al. 2021, A&A, 647, A122
Mosser, B., Goupil, M. J., Belkacem, K., et al. 2012, A&A, 548, A10
Mosser, B., Pinçon, C., Belkacem, K., Takata, M., & Vrard, M. 2017, A&A, 600, A1
Rui, N. Z. & Fuller, J. 2023, MNRAS, 523, 582
Stello, D., Cantiello, M., Fuller, J., et al. 2016, Nature, 529, 364
Unno, W., Osaki, Y., Ando, H., Saio, H., & Shibahashi, H. 1989, Nonradial oscillations of stars (Tokyo: University of Tokyo Press) (University of Tokyo Press)

SF2A 2023
M. N'Diaye, A. Siebert, N. Lagarde, O. Venot, K. Baillié, M. Béthermin, E. Lagadec, J. Malzac, J. Richard (eds)

CHALLENGES AND LIMITATIONS OF FUTURE EXOPLANET SPACE IMAGERS

L. Leboulleux[1]

Abstract. The James Webb Space Telescope was not even launched yet when the Astro2020 Decadal Survey American report recommended the development of what is now called the Habitable World Observatory, also mentioned by the Voyage 2050 European report. This future space telescope, at 11 billions dollars and at least 6 m diameter, should allow, around 2040, the characterization of at least 25 exoplanets similar to Earth and orbiting around main sequence stars, with the hope of discovering one where life could have developed. This objective represents a technological challenge since it requires the design of spectro-imagers able to access very high contrasts ($10^{-8} - 10^{-10}$) at low angular separations (smaller than 100 mas). This proceeding and the talk it is associated to address various obstacles that remain to be overcome in order to one day allow HabWorld to reach its ultimate performance.

Keywords: exoplanets, Habitable World Observatory, HabWorld, instrumentation, high-contrast imaging

1 Introduction

Every ten years, the National Academies of Sciences, Engineering, and Medicine (NASEM) publish recommendations for large science projects in various fields. In space astronomy for instance, the Chandra-X ray Observatory and the Hubble Space Telescope followed the "Astronomy and Astrophysics for the 1980s" NASEM report, the Spitzer Space Telescope issued from the 1991 "The Decade of Discovery in Astronomy and Astrophysics" report, and more recently, the Next Generation Space Telescope, now known as the James Webb Space Telescope (JWST), was recommended by the 2001 "Astronomy and Astrophysics in the New Millennium" report (Gardner et al. 2023). In 2010, the "New Worlds, New Horizons" NASEM report recommended to push forward the research in dark energy with the so-called Nancy Grace Roman Space Telescope (RST), a telescope that will be launched around 2028. Its science goal was extended to the field of exoplanet imaging and characterization, with the first detection of exoplanets in reflected light. It is now also equiped with a coronagraphic instrument able to detect and characterize planets down to $200 - 300$ mas from their host star and with contrasts down to $10^{-8} - 10^{-9}$ ($R \sim 50$ at 700 nm) (Bailey et al. 2023). In 2021, a new decadal report was released: the "Pathways to Discovery in Astronomy and Astrophysics for the 2020s" recommended the development of the so-called Habitable World Observatory (HabWorlds). This new large space mission should be able to characterize 25 Earth-like planets with separations of $20 - 50$ mas, contrasts down to 10^{-10} at mid to high spectral resolution ($200 - 5000$ at 500 nm) (Vaughan et al. 2023; Roberge et al. 2021; Gaudi et al. 2021, 2020).

With these two future space missions, the scientific requirements reach values that have never been accessed before, from space and from the ground. As a comparison, they imply a gain in contrast of a factor 10^5, and a gain in angular separation of a factor 20 compared to the JWST constraints. In addition to the difficulty to access such extreme performance in perfect conditions, it is highly deteriorated as soon as conditions are non perfect. As an example, one of the key phases in the JWST launch was the segment phasing of its primary mirror: 18 hexagonal segments had to be aligned from a few microns to 30 nm RMS of aberration, a complex operation that took one month to be completed. If HabWorlds, whose primary mirror will probably also be segmented, is aligned down to 30 nm RMS, its contrast will be maintained over 10^{-6}, far from its requirements. Compared to the JWST or other telescopes, the technological breakthrough must concern both the absolute performance and its robustness to realistic conditions.

This proceeding is dedicated to describing methods and tools that are developed or under development to access high contrasts at small angular separations (section 2) and, despite non perfect conditions (section 3), maintain such a performance over time and observation conditions (section 4).

[1] Univ. Grenoble Alpes, CNRS, IPAG, 38000 Grenoble, France

© Société Française d'Astronomie et d'Astrophysique (SF2A) 2023

2 Performance: coronagraphy and wavefront control for (non) dummies

The access to high contrasts in exoplanet imaging or spectroscopy requires the assembly of multiple components, set up in pupil planes, focal planes, or out of pupil planes. The general principle is illustrated in Fig. 1 and is made of a coronagraph, which can be combined with a wavefront control system, with the ultimate objective of removing the starlight in the area of interest of the detector plane.

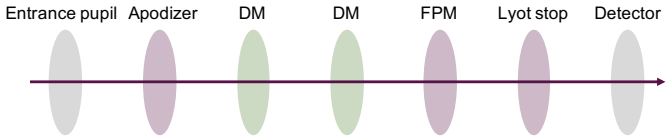

Fig. 1. Scheme of a typical high-contrast imaging system. Purple: components associated with coronagraphy, Green: components associated with wavefront control. DM stands for Deformable Mirror and FPM for Focal Plane Mask.

The coronagraph is made of up to three passive components :
- An apodizer (pupil plane) that reshapes the wavefront to modulate its intensity in the focal plane,
- A Focal-Plane Mask (FPM) that blocks the starlight along the optical axis,
- A Lyot stop (pupil plane) to remove the high-order star signal, not stopped by the FPM.

The apodizer and the FPM, if they exist, can be amplitude or phase masks, and a large variety of combinations are possible depending on the type of masks. Fig. 2 (left) introduces a few of these combinations, with no mention of the existence of a Lyot stop. For a more exhaustive list, please refer to Ruane et al. (2018). Fig. 2 (right) also illustrates this diversity with three cases: 1) a shaped pupil (amplitude apodizer, no FPM, no Lyot stop, see also Kasdin et al. 2003; Carlotti et al. 2011) optimized for a 18 segment pupil to dig a circular $1\lambda/D$-large dark zone localized at $8.3\lambda/D$, 2) an apodized pupil Lyot coronagraph (amplitude apodizer, FPM, and Lyot stop, see also Aime et al. 2002; Soummer et al. 2006; N'Diaye et al. 2016) to access high contrasts from 3 to $10\lambda/D$, and 3) an apodized vortex coronagraph (amplitude apodizer, phase FPM, and amplitude Lyot stop, see also Carlotti 2013; Fogarty et al. 2017) to access high contrasts from 3 to $10\lambda/D$.

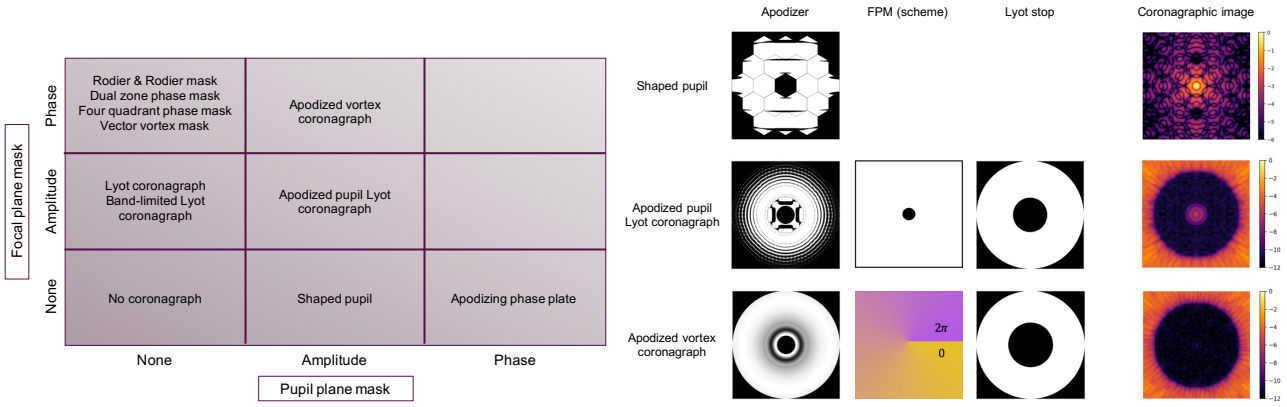

Fig. 2. (left) Non exhaustive list of coronagraphs classified by their types of focal plane and pupil plane masks. (right) Examples of coronagraphs and their associated coronagraphic images (no aberration added). The shaped pupil is taken from Leboulleux et al. (2022d) and the apodized pupil Lyot coronagraph and the apodized vortex coronagraph from Mazoyer et al. (2018a); N'Diaye et al. (2015); Fogarty et al. (2017). The focal-plane images are in logarithmic scales.

In addition of a coronagraph, a wavefront control system enables to reach higher contrasts at small angular separations by reshaping the wavefront with one or two Deformable Mirrors (DM). One DM is set in a pupil plane for phase control, but with one single DM, only half of the detector interest zone can be controled. A second DM can be installed out of pupil plane to access amplitude control and a symetric dark area. Due to the limited number of actuators, phase and amplitude are controlled with a small spatial sampling, which makes this tool usable only for small dark zones at close angular separations: with a 34-actuators across the diameter DM, the dark hole cannot go further than $17\lambda/D$. More details, with the descriptions and references of the diverse methods, can be found in Jovanovic et al. (2018) (see also figure 4 for illustration).

3 Limitations

Coronagraphs, no matter their ultimate performance, are highly sensitive to unperfect conditions. Fig. 3 illustrates a few of them for space operations, in the case of a shaped pupil compatible with a 18 segment pupil designed to access an ultimate contrast of 7×10^{-9} between 6 and $13\lambda/D$:

• When the pupil is complexified, for instance here with spiders added on the architecture: this is the reason why HabWorlds is considered off-axis, to avoid a complex pupil with spider and central obstruction.

• With global tip-tilt misalignments (or pointing error or jitter): they are particularly problematic in case of a FPM since the starlight leaks off the FPM at small angular separations.

• With phasing errors: on HabWorlds, a contrast of 10^{-10} imposes the phasing errors to remain below 10pm rms, which is not accessible yet in labs.

• With a mask shift or misalignment.

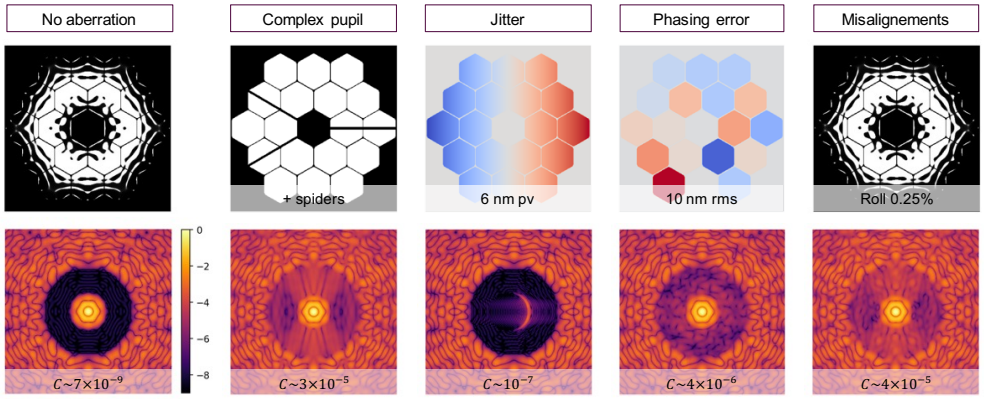

Fig. 3. Examples of aberrations and their impact on the coronagraphic image with a 18-segment pupil combined with a shaped pupil. From left to right: no aberration, spiders added on the pupil, tip or jitter (a FPM has been added in the coronagraphic system), segment phasing errors, apodizer vertical shift.

The high-contrast and high-angular separation performance can then not be accessed without a robust aberration mitigation. This mitigation can take two forms:

• Cure: diagnosing the sources of errors (wavefront sensing or WFS) and correcting them (wavefront sensing or WFC) with adaptive components,

• Prevention: optimizing the instrument to make it insensitive to errors.

4 Robustness: prevention or cure?

4.1 Cure

Curing relies on two steps:

• a diagnosis of the aberrations or WFS. Reconstructing the errors, static or dynamic, is complex and several methodologies and tools have been developed so far. They are not described in the proceeding and for more information please refer to Jovanovic et al. (2018).

• a correction of the aberrations or WFC. Several methods have also been developed, all of them requiring the use of adaptive components (Snik et al. 2018).

As phase control tools, DMs (Blanco et al. 2022; Bowens-Rubin et al. 2021) have been used since the beginning of adaptive optics (Chauvin 2018) and can enable to compensate for the aberrations and recover the performance. One of its latest application is the combination of two DMs and its use through the Active Correction of Aperture Discontinuities to compensate for both aperture complexity (spiders) and phase errors (segment phasing misalignements) on a space coronagraphic system (Mazoyer et al. 2018a,b). If DMs have so far never been used in space (except on specific experiments on balloon missions, see Morgan et al. 2019), the Nancy Grace Roman Space Telescope will be the first space telescope equipped of two deformable mirrors (Mennesson et al. 2022). As an alternative for phase control, one can cite the spatial-light modulator (SLM) technology (Kühn & Patapis 2022; Kühn et al. 2018) which can be used, between other applications, as a continuous and

low- to high-order programmable pupil phase mirror, despite being limited by its requirement to reflect linear polarized light. More recently, investigations have been ongoing to identify adaptive amplitude components. The use of Digital Micro-mirror Devices (DMD) is currently under study: the component tested at IPAG, for instance, is built as a matrix of small square mirrors that can be controlled in tip-tilt and flipped between two positions, one of them used as a transmissive direction towards the detector, the other one rejecting the light out of the optical system. It can then be used to get programmable binary apodizations (Carlotti et al. 2023; Leboulleux et al. 2022a; Carlotti et al. 2018).

Fig. 4 illustrates the use of 1) two DMs to mitigate the impact of phasing errors in the coronagraph dark region, 2) one DMD to recover the contrast in the coronagraph dark region despite missing segments.

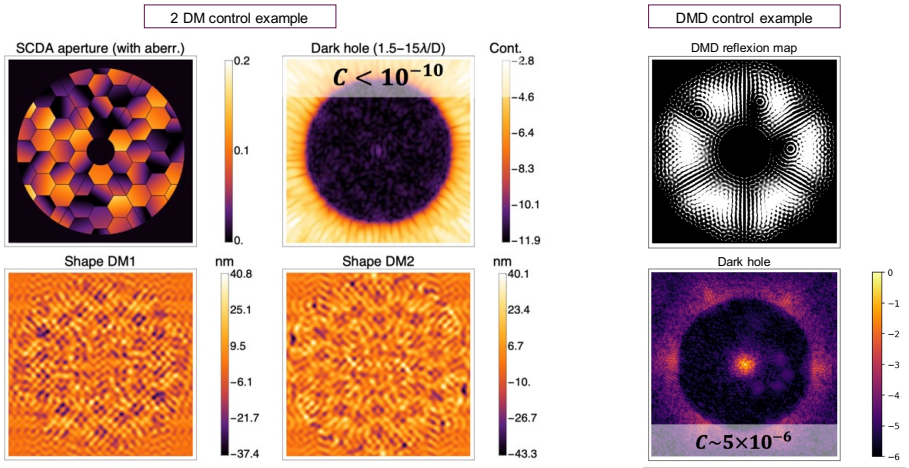

Fig. 4. Examples of aberration mitigation with adaptive components: 1) use of two deformable mirrors to recover the dark hole despite segment phasing errors with the ACAD-OSM methodology (simulation from Mazoyer et al. (2018a)), 2) use of a DMD to recover the dark hole despite missing segments (experimental image from Carlotti et al. (2023)).

4.2 Prevention

An alternative approach is to create a high-contrast system that is passively blind to or robust to aberrations by design, meaning optimized to remain performant (high contrast at small angular separations) despite a range of aberrations. As aberrations have a high impact on the performance, the robustness is a key aspect of the design study. Different methods have been proposed so far to increase the system robustness, combined with different coronagraphs: to reduce the impact of low-order aberrations on vortex coronagraphs (Fogarty et al. 2020), scalar vortex coronagraphs (Desai et al. 2022), or apodized pupil Lyot coronagraphs (N'Diaye et al. 2015), or Lyot stop shifts on apodized pupil Lyot coronagraphs (Nickson et al. 2022).

Let's focus on one example only, with a fully analytical construction: Leboulleux et al. (2018); Laginja et al. (2021) introduce the Pair-based Analytical model for Segmented Telescopes Imaging from Space (PASTIS) to evaluate the impact of phasing errors on the coronagraphic PSF and performance. In the PASTIS formula, a specific factor appears, as a weight factor of all other factors: the PSF of one segment only. If this weight factor, so the PSF of the segment, increases, then the contrast is easily deteriorated by segment-level aberrations. On the opposite, if the PSF of the segment is minimal, then the contrast is less impacted by any segment-level aberration. This assessment led to the Redundant Apodized Pupil (RAP) concept Leboulleux et al. (2022b,c): optimizing the segment and multiplying this apodization to mimic the pupil segmentation enable to obtain a high-contrast region that remains stable over a large range of segment-level aberrations, like segment phasing errors. Fig. 5 illustrates this concept and its robustness for a 10^{-6}-contrast dark zone between 5.5 and $12\lambda/D$.

5 Conclusions

The field of high-contrast imaging is the environment of many ongoing studies, that could not be all covered in this proceeding. The list of scientific requirements, with contrast and angular separations, is here far from exhaustive, since the planet photon flux, spectroscopy, polarimetry, or compatibility to post-processing methods

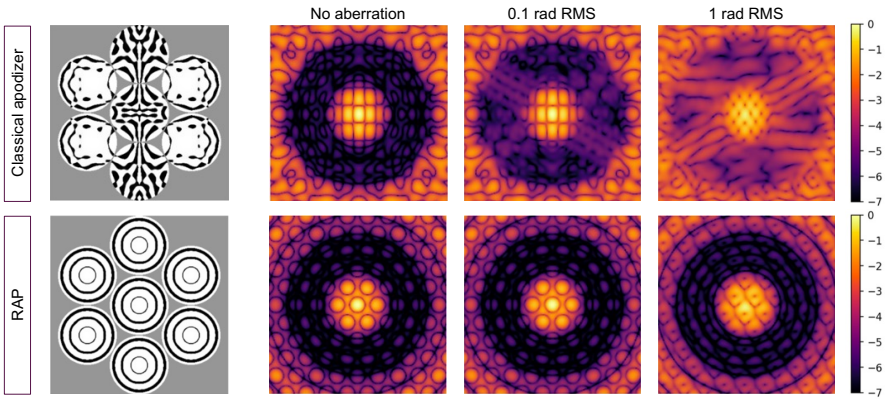

Fig. 5. Robustness of RAP design for segment-phasing errors on a Giant Magellan Telescope-like pupil (7 circular segments): (left) two apodizing phase plate maps, with π-shift between black and white areas, the top apodizer is classically optimized, the bottom one is redundantly optimized; (right) associated coronagraphic PSFs with increasing segment phasing errors (figure from Leboulleux et al. (2022b)).

were not even mentioned so far. Even with these requirements left on the side, the future scientific and technological ambitions for the Nancy Grace Roman Space Telescope and the Habitable Worlds Observatory demand multiple and complex instrumentation developments and research. Between others (Laginja et al. 2022; Mazoyer et al. 2019), in France, one can mention the development of several highly performant high-contrast testbeds, such as the Très Haute Dynamique one (THD2, Potier et al. 2019), the Segmented Pupil Experiment for Exoplanet Detection (SPEED, Martinez et al. 2023), the Marseille Imaging Testbed for High Contrast (MITHiC, El Morsy et al. 2022), or the High Contrast Module testbed (HCM, Hours et al. 2022).

These developments are necessary to overcome the limitations of current instruments and access rocky exoplanets. In space, the most efficient coronagraphs can currently not go deeper than contrasts of $\sim 10^{-5}$ at several hundreds of mas, and DMs have never been tested in space telescope, except for balloon missions. The Nancy Grace Roman Space Telescope and the Habitable Worlds Observatory are then setting ambitious objectives both in terms of science targets but also for first technological demonstrations.

The author thanks the SF2A organization committees (SOC and LOC) who made this conference a large success. She is also grateful for the help and references provided by colleagues, including Marie Ygouf, Elodie Choquet, Johan Mazoyer, Mamadou N'Diaye, Pierre Baudoz, and Alexis Carlotti.

References

Aime, C., Soummer, R., & Ferrari, A. 2002, A&A, 389, 334

Bailey, V. P., Bendek, E., Monacelli, B., et al. 2023, arXiv e-prints, arXiv:2309.08672

Blanco, L., Behara, N., Valenzuela, J., & Kasper, M. 2022, in Society of Photo-Optical Instrumentation Engineers (SPIE) Conference Series, Vol. 12185, Adaptive Optics Systems VIII, ed. L. Schreiber, D. Schmidt, & E. Vernet, 121856B

Bowens-Rubin, R., Hinz, P., Kuiper, S., & Dillon, D. 2021, in Society of Photo-Optical Instrumentation Engineers (SPIE) Conference Series, Vol. 11823, Techniques and Instrumentation for Detection of Exoplanets X, ed. S. B. Shaklan & G. J. Ruane, 118231R

Carlotti, A. 2013, A&A, 551, A10

Carlotti, A., Baccar, S., Leboulleux, L., et al. 2023, in Adaptive Optics for Extremely Large Telescopes VII (AO4ELT7)

Carlotti, A., Mouillet, D., Correia, J.-J., et al. 2018, in Society of Photo-Optical Instrumentation Engineers (SPIE) Conference Series, Vol. 10706, Advances in Optical and Mechanical Technologies for Telescopes and Instrumentation III, ed. R. Navarro & R. Geyl, 107062M

Carlotti, A., Vanderbei, R., & Kasdin, N. J. 2011, Optics Express, 19, 26796

Chauvin, G. 2018, in Society of Photo-Optical Instrumentation Engineers (SPIE) Conference Series, Vol. 10703, Adaptive Optics Systems VI, ed. L. M. Close, L. Schreiber, & D. Schmidt, 1070305

Desai, N., Llop-Sayson, J., Bertrou-Cantou, A., et al. 2022, in Society of Photo-Optical Instrumentation Engineers (SPIE) Conference Series, Vol. 12180, Space Telescopes and Instrumentation 2022: Optical, Infrared, and Millimeter Wave, ed. L. E. Coyle, S. Matsuura, & M. D. Perrin, 121805H

El Morsy, M., Vigan, A., Lopez, M., et al. 2022, A&A, 667, A171

Fogarty, K., Mawet, D., Mazoyer, J., et al. 2020, in Society of Photo-Optical Instrumentation Engineers (SPIE) Conference Series, Vol. 11443, Society of Photo-Optical Instrumentation Engineers (SPIE) Conference Series, 114433Y

Fogarty, K., Pueyo, L., Mazoyer, J., & N'Diaye, M. 2017, AJ, 154, 240

Gardner, J. P., Mather, J. C., Abbott, R., et al. 2023, PASP, 135, 068001

Gaudi, B., Roberge, A., Habex Team, & Luvoir Study Team. 2021, in Bulletin of the American Astronomical Society, Vol. 53, 0301

Gaudi, B. S., Seager, S., Mennesson, B., et al. 2020, arXiv e-prints, arXiv:2001.06683

Hours, A., Carlotti, A., Mouillet, D., et al. 2022, in Society of Photo-Optical Instrumentation Engineers (SPIE) Conference Series, Vol. 12185, Adaptive Optics Systems VIII, ed. L. Schreiber, D. Schmidt, & E. Vernet, 121852E

Jovanovic, N., Absil, O., Baudoz, P., et al. 2018, in Society of Photo-Optical Instrumentation Engineers (SPIE) Conference Series, Vol. 10703, Adaptive Optics Systems VI, ed. L. M. Close, L. Schreiber, & D. Schmidt, 107031U

Kasdin, N. J., Vanderbei, R. J., Spergel, D. N., & Littman, M. G. 2003, ApJ, 582, 1147

Kühn, J., Patapis, P., Lu, X., & Arikan, M. 2018, in Society of Photo-Optical Instrumentation Engineers (SPIE) Conference Series, Vol. 10706, Advances in Optical and Mechanical Technologies for Telescopes and Instrumentation III, ed. R. Navarro & R. Geyl, 107062N

Kühn, J. G. & Patapis, P. 2022, Appl. Opt., 61, 9000

Laginja, I., Robles, P., Barjot, K., et al. 2022, in Society of Photo-Optical Instrumentation Engineers (SPIE) Conference Series, Vol. 12185, Adaptive Optics Systems VIII, ed. L. Schreiber, D. Schmidt, & E. Vernet, 121853A

Laginja, I., Soummer, R., Mugnier, L. M., et al. 2021, Journal of Astronomical Telescopes, Instruments, and Systems, 7, 015004

Leboulleux, L., Carlotti, A., Curaba, S., et al. 2022a, in Society of Photo-Optical Instrumentation Engineers (SPIE) Conference Series, Vol. 12188, Advances in Optical and Mechanical Technologies for Telescopes and Instrumentation, 121884J

Leboulleux, L., Carlotti, A., & N'Diaye, M. 2022b, A&A, 659, A143

Leboulleux, L., Carlotti, A., N'Diaye, M., et al. 2022c, A&A, 666, A91

Leboulleux, L., Carlotti, A., N'Diaye, M., et al. 2022d, in Society of Photo-Optical Instrumentation Engineers (SPIE) Conference Series, Vol. 12188, Advances in Optical and Mechanical Technologies for Telescopes and Instrumentation, 121881S

Leboulleux, L., Sauvage, J.-F., Pueyo, L. A., et al. 2018, Journal of Astronomical Telescopes, Instruments, and Systems, 4, 035002

Martinez, P., Beaulieu, M., Gouvret, C., Spang, A., & Marcotto, A. 2023, The Messenger, 190, 55

Mazoyer, J., Baudoz, P., Belikov, R., et al. 2019, in Bulletin of the American Astronomical Society, Vol. 51, 101

Mazoyer, J., Pueyo, L., N'Diaye, M., et al. 2018a, AJ, 155, 7

Mazoyer, J., Pueyo, L., N'Diaye, M., et al. 2018b, AJ, 155, 8

Mennesson, B., Bailey, V. P., Zellem, R., et al. 2022, in Society of Photo-Optical Instrumentation Engineers (SPIE) Conference Series, Vol. 12180, Space Telescopes and Instrumentation 2022: Optical, Infrared, and Millimeter Wave, ed. L. E. Coyle, S. Matsuura, & M. D. Perrin, 121801W

Morgan, R., Douglas, E., Allan, G. W., et al. 2019, Micromachines, 10, 366

N'Diaye, M., Pueyo, L., & Soummer, R. 2015, ApJ, 799, 225

N'Diaye, M., Soummer, R., Pueyo, L., et al. 2016, ApJ, 818, 163

Nickson, B. F., Por, E. H., Nguyen, M. M., et al. 2022, in Society of Photo-Optical Instrumentation Engineers (SPIE) Conference Series, Vol. 12180, Space Telescopes and Instrumentation 2022: Optical, Infrared, and Millimeter Wave, ed. L. E. Coyle, S. Matsuura, & M. D. Perrin, 121805K

Potier, A., Baudoz, P., Galicher, R., Huby, E., & Singh, G. 2019, arXiv e-prints, arXiv:1910.09064

Roberge, A., Fischer, D., Peterson, B., et al. 2021, in Bulletin of the American Astronomical Society, Vol. 53, 332

Ruane, G., Riggs, A., Mazoyer, J., et al. 2018, in Society of Photo-Optical Instrumentation Engineers (SPIE) Conference Series, Vol. 10698, Space Telescopes and Instrumentation 2018: Optical, Infrared, and Millimeter Wave, ed. M. Lystrup, H. A. MacEwen, G. G. Fazio, N. Batalha, N. Siegler, & E. C. Tong, 106982S

Snik, F., Absil, O., Baudoz, P., et al. 2018, in Society of Photo-Optical Instrumentation Engineers (SPIE) Conference Series, Vol. 10706, Advances in Optical and Mechanical Technologies for Telescopes and Instrumentation III, ed. R. Navarro & R. Geyl, 107062L

Soummer, R., Aime, C., Ferrari, A., et al. 2006, in IAU Colloq. 200: Direct Imaging of Exoplanets: Science & Techniques, ed. C. Aime & F. Vakili, 367–372

Vaughan, S. R., Gebhard, T. D., Bott, K., et al. 2023, MNRAS, 524, 5477

SF2A 2023
M. N'Diaye, A. Siebert, N. Lagarde, O. Venot, K. Baillié, M. Béthermin, E. Lagadec, J. Malzac, J. Richard (eds)

COMMISSION FEMMES ET ASTRONOMIE DE LA SF2A : SEXISM AND SEXUAL HARASSMENT FOR EUROPEAN PHYSICISTS

L. Manchon[1], R.-M. Ouazzani[1], I. Vauglin[2], C. Bot[3], S. Brau-Nogué[4], D. Briot[5], L. Ciesla[6], N. Lagarde[7], P. de Laverny[8], L. Leboulleux[9], N. Nesvadba[8], J. Malzac[4] and O. Venot[10]

Abstract. The Commission des Femmes en Astronomie performed a detailed analysis for the sub-population of European physicists of the recent international survey of sexism and sexual harassment in science, conducted by the polling institute IPSOS for the L'Oréal Foundation for Women in Sciences, with the help of the association *Femmes et Sciences*. This study confirms, similarly to the results obtain for the international sample, the ubiquitous nature of sexism and sexual harassment in European physics communities, with 88% of the women taking part in the study having been victim of sexism at least once in their career, and 54 % of sexual harassment. The survey clearly documents the impact of sexual misconducts on physical and mental health. We finally demonstrate the failure of the institutions to fight sexual violence, as only 5% of the victims seek help within their institution.

Keywords: Astronomy & Astrophysics, Gender inequalities, Sexism, Sexual harassment

1 Introduction

The Commission Femmes et Astronomie of the SF2A (Société Française d'Astronomie et d'Astrophysique of the French astronomical Society; hereafter CF2A) is an instance created in 2020 to address questions related to gender equality within the French astronomical community. The Commission has twelve members, of which five members are currently - or were at some point - also part of the SF2A Council: I. Vauglin, R.-M. Ouazzani*, C. Bot, S. Brau-Nogué, D. Briot*, L. Ciesla, N. Lagarde*, P. de Laverny, L. Leboulleux, N. Nesvadba, J. Malzac* and O. Venot*. The main goals of the Commission are to promote gender equality in Astronomy & Astrophysics in France, fight against sexual and gender-based violence, support gender-focused outreach actions, etc. In this scope, the commission conducted last year a study (Ouazzani et al. 2022) showing that, in a sub-set of 8 astronomy and astrophysics institutes, women represented around 25 % of the total staff for the year 2021. They also show that this number decreases with increasing level of responsibility or income.

Parallel to the work of the Commission, the polling institute IPSOS was contracted by the *Fondation L'Oreal* for Women in Science†, in association to the Association *Femmes et Sciences*‡ to conduct an international survey on sexism and sexual harassment in Sciences §. Following a large call for participation, opened between the 26th

[1] LESIA, Observatoire de Paris, PSL Research University, CNRS, Université Pierre et Marie Curie, Université Denis Diderot, 92195 Meudon, France
[2] Univ Lyon, Université Lyon1, ENS de Lyon, CNRS, CRAL UMR5574, F-69230 Saint-Genis-Laval, France
[3] Université de Strasbourg, CNRS, Observatoire Astronomique de Strasbourg, UMR7550, F-67000 Strasbourg, France
[4] IRAP, Université de Toulouse, CNRS, UPS, CNES, Toulouse, France
[5] Observatoire de Paris, 61 avenue de l'Observatoire, 75014 Paris, France
[6] Aix-Marseille Univ., CNRS, CNES, LAM, 13388 Marseille Cedex 13, France
[7] Laboratoire d'Astrophysique de Bordeaux, Univ. Bordeaux, CNRS, B18N, allée Geoffroy Saint-Hilaire, 33615 Pessac, France
[8] Université Côte d'Azur, Observatoire de la Côte d'Azur, CNRS, Laboratoire Lagrange,F-06304 Nice, France
[9] Univ. Grenoble Alpes, CNRS, IPAG, 38000 Grenoble, France
[10] Université de Paris Cité and Univ Paris Est Creteil, CNRS, LISA, F-75013 Paris, France
*Members of the SF2A council.
†https://www.fondationloreal.com/fr
‡https://www.femmesetsciences.fr/
§`https://www.fondationloreal.com/fr/nos-programmes-pour-les-femmes-et-la-science/stillsearching`

© Société Française d'Astronomie et d'Astrophysique (SF2A) 2023

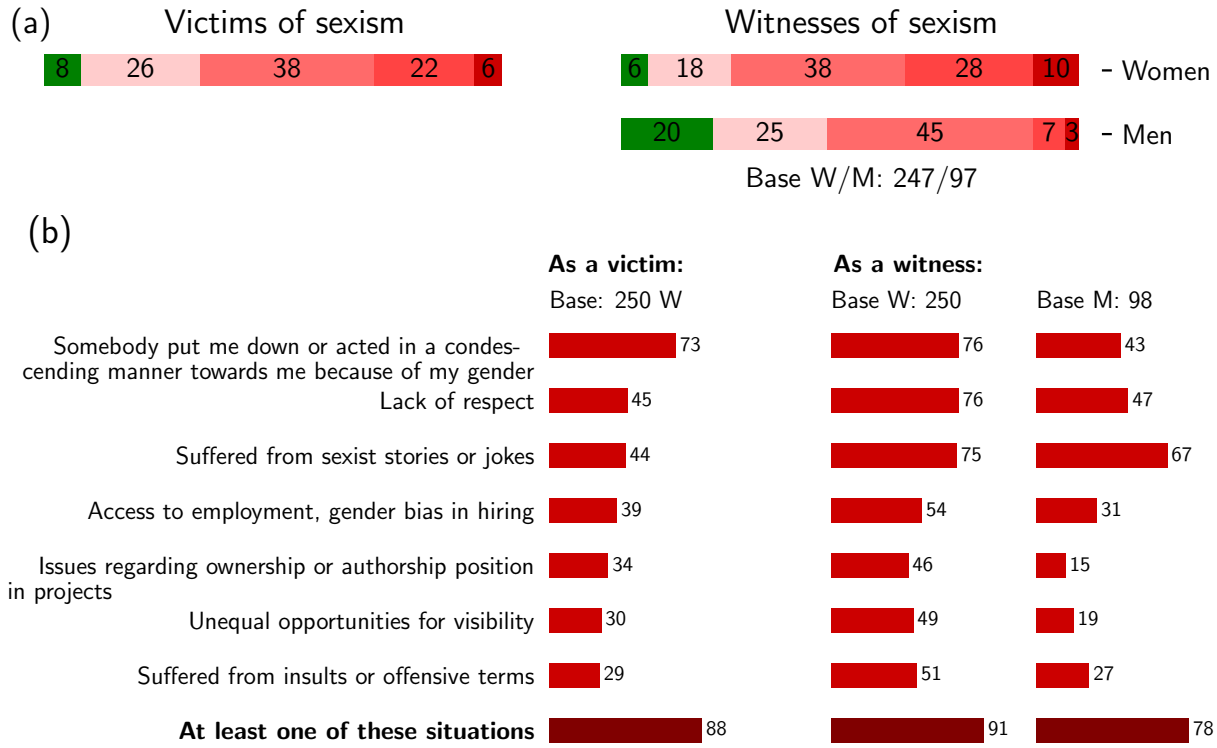

Figure 1. Row (a): Answer to the questions *"Rate the extent to which each of the following statements is representative of your experience in your academic/research career. I have personally experienced situations of sexism"* (left histogram) or *"I have witnessed situations of sexism"* (right histograms). Possible answers are "Never" (green), "At least once" (light pink), "On occasion" (pink), "Quite frequently" (light red), "Very frequently" (red). Numbers are percentage of the base number. **Row (b):** Answers to the question *"Have you personally ever experienced [witnessed] any of the following situations in your career within academia/research? Think about all the situations you experienced, both online and offline."*. Answers of the female victims (who "have personally experienced") are represented on first histogram. Answers from the female or male witnesses (who "have personally witnessed") are represented on the last two histograms. Number are percentage of the base of women or men.

of July and 16$^{\text{th}}$ of September 2022, they gathered answers from 5184 researchers (among which 76% of women) in 117 countries and over 50 institutions. The respondents include scientists with temporary or permanent position, students, and retired scientists, from 18 up to 70 years old. The vast majority of the respondents belong to a public academic institution (68% in the complete sample). Most of the scientists (80% for women and 85 % for men) consider that, overall, they are satisfied with their job. Yet, this study reveals the ubiquitous nature of sexism in science, as 84 % of women surveyed reported to have personally experience sexism in their carrier. This number remains similar on all continents, in all research fields. Half of the women interrogated in this study also reported to have been victims of sexual harassment with 2/3 regretting a negative impact on their career and around 70% denouncing the silence of their colleagues.

Starting from this data-set, the CF2A aimed at having a more precise look on the sexism and sexual harassment in the French astronomical community. Since the data-set does not give details about the sub-field of research, we did not have direct information on "astronomers", and therefore we chose to focus only on the physicists interviewed. Similarly, the sub-set of French physicists was too small, so we decided to extend the study to European physicists. This choice is also motivated by the fact that researchers in our community, especially young colleagues, regularly move from one country to another, in particular in Europe. Then, they may be concerned by the quality of working conditions in Europe. In the end, we have in our data-set 356 European physicists, among which 70% are women.

Section 2 of this proceeding is dedicated to sexism, and Sect. 3 to sexual harassment among European physicists. In Sect. 4 we investigate the impact of sexism and sexual harassment on the victims and their career. Finally, we discuss the limitation of the study and conclude in Sect. 5.

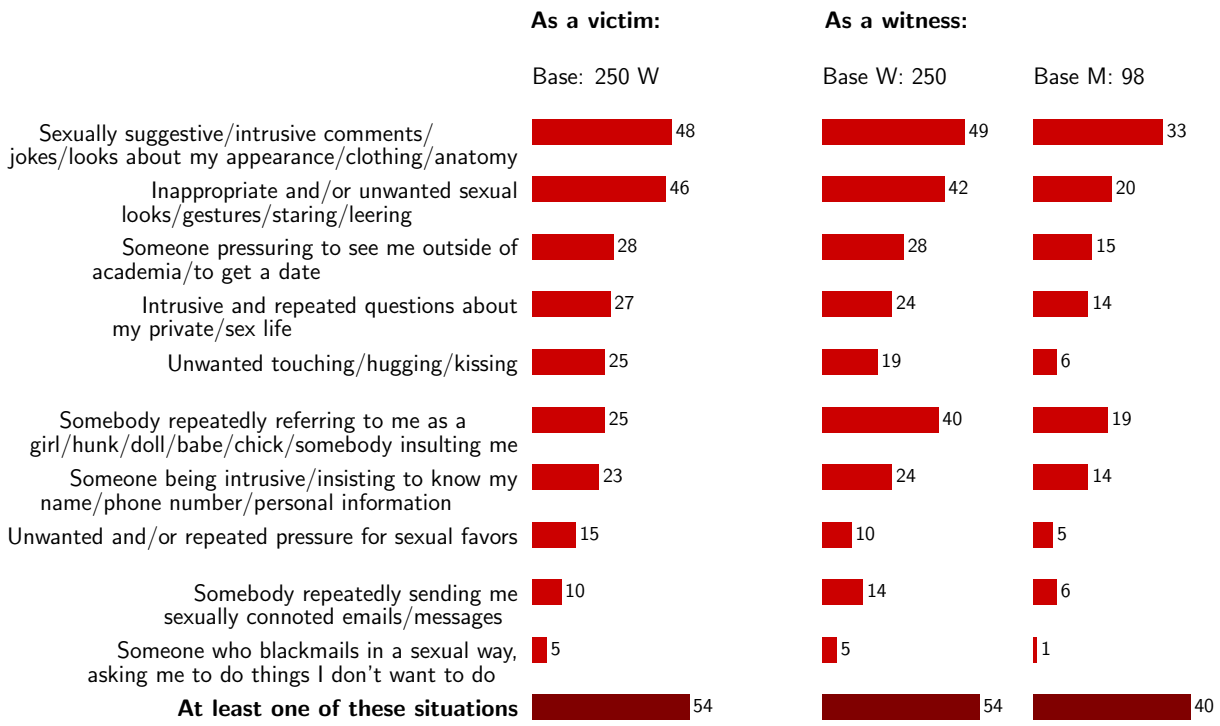

Figure 2. Answers to the question *"Have you personally ever experienced [witnessed] any of the following situations in your career within academia/research?"*. Answers of the female victims (who "have personally experienced") are represented on first histogram. Answers from the female or male witnesses (who "have personally witnessed") are represented on the last two histograms. Number are percentage of the base of women or men.

2 Sexism

French law defines sexism as any conduct related to a person's sex, which has the purpose or the effect of violating their dignity or creating an intimidating, hostile, degrading, humiliating or offending environment (Article L1142-2-1, Code du travail & Article 6 bis, *loi de 1983**). Such conduct can be sexist jokes, insults regarding gender, unequal access to employment, etc. First, the pollsters have asked scientists in the sample to tell if and how often they had experienced or witnessed sexism. Answers are summarized in Fig 1, row (a). The first striking conclusion that emerges from these answers is that almost every women who answered faced sexism at some point in their scientific career, and around one third more than once. This number is similar to the world average recalled in introduction. The slight excess may not be statistically relevant as our sub-sample is much smaller than the total sample. In the men's responses, quite an important fraction have never witness sexism in their work environment, a number at odds with what women declare.

Then, pollsters asked whether respondents had personally experienced or witnessed precise situations among a list of seven that can be qualified as situations of sexism. The results for victims and witnesses are summarized in Fig. 1, row (b). Such a question aims at knowing if a situation of sexism is correctly identified by victims or witnesses. This is actually the case, because, in each cases (victim/witness, female/male), the percentage of respondents declaring that they never faced a sexism situation is similar to the percentage that never faced one of the precise situation listed in Fig. 1, row (b). As before, men tend to witness less sexism situation compare to women ($\sim$ 80% compare to $\sim$ 90%). However, this numbers are very high and reveal quite an accurate sensitivity to sexism from men. It would be interesting to have some insight on the evolution of these numbers, in order to see if men become more and more aware of sexism.

Except for condescending acts that around 75% of victims experience, all other situations are experienced

*while the *code du travail* rules contracts in the private sector, it is the *loi de 1983, portant droits et obligations des fonctionnaires* which applies to public servants

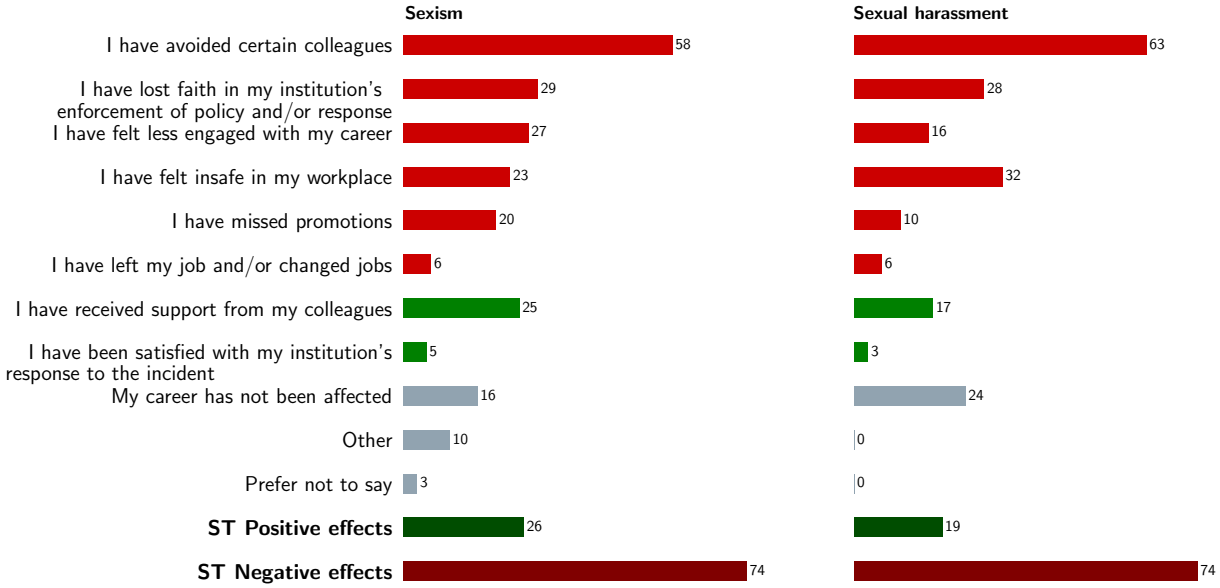

Figure 3. Answers to the question *"About the situation(s) you experienced personally: How has it affected you/ your career?"*. Results for victims of sexism (resp. sexual harassment) are displayed in the left (resp. right) histogram. Red bars code for negative consequences, green bars for positive consequences, and grey for no effect.

in a very homogeneous way, and at a very high level (> 30%). This homogeneity is also found with women who witness those situations, while men report much less issues with ownership or authorship and visibility opportunities. Women who experience sexism do not experience only one of these situations. Indeed 56% of the victims report that they have personally experience at least three situations listed in Fig. 1, row (b), and this number rises to 69 % percent among witnesses.

For half of the victims of sexism, the facts occurred at the beginning of their career, while only 5% have experience sexism only at the top of their career. 44% declare they have faced sexism all along their career. The victims have experience situations of sexism, for 47% less than 2 years ago, and for 71% less than 5 years ago. It stresses that, while the #metoo movement may have raised awareness on sexism, these situations still persist afterward.

3 Sexual harassment

The French legal definition of sexual harassment have been refined over time. First defined as repeated sexist behaviour (see above legal definition of sexism), it is now assimilated to the fact of using any form of serious pressure, even if not repeated, with the real or apparent aim of obtaining an act of a sexual nature, whether this is sought for the benefit of the perpetrator or for the benefit of a third party (Article L1153-1, Code du travail & Article 6 ter, *loi de 1983*). This definition is supplemented by the case law of the Orléans Court of Appeal, which characterizes the ambient or environmental sexual harassment, as a situation where "without being directly targeted, the victim is subjected to provocations and obscene or vulgar jokes which become unbearable for her (Orléans Court of Appeal, 2017).

In a symmetric way as they did for sexism, pollsters investigated perception of sexual harassment in science. 46% of European women physicists declare that they have been victims of sexual harassment, and 20% frequently. The situation is identically seen as female witness. Contrary to sexism, men strongly underestimate the occurrence of sexual harassment as only 27 % report having witnessed such conduct. When they are interrogated on precise situations, more women and men declare that they have experienced or witness situation of sexual harassment, as summarized in Fig. 2. Indeed, while 46% of women declared they had seen or faced sexual harassment when they are questioned on their perception, this number rises to 54% when they are asked to identify precise situations. Similarly, only 27% of men felt they had witnessed sexual harassment, while they are 40% when concrete situations are explicitly described. It reveals that a lot of work remains to be done on raising awareness of both women and men on sexual harassment.

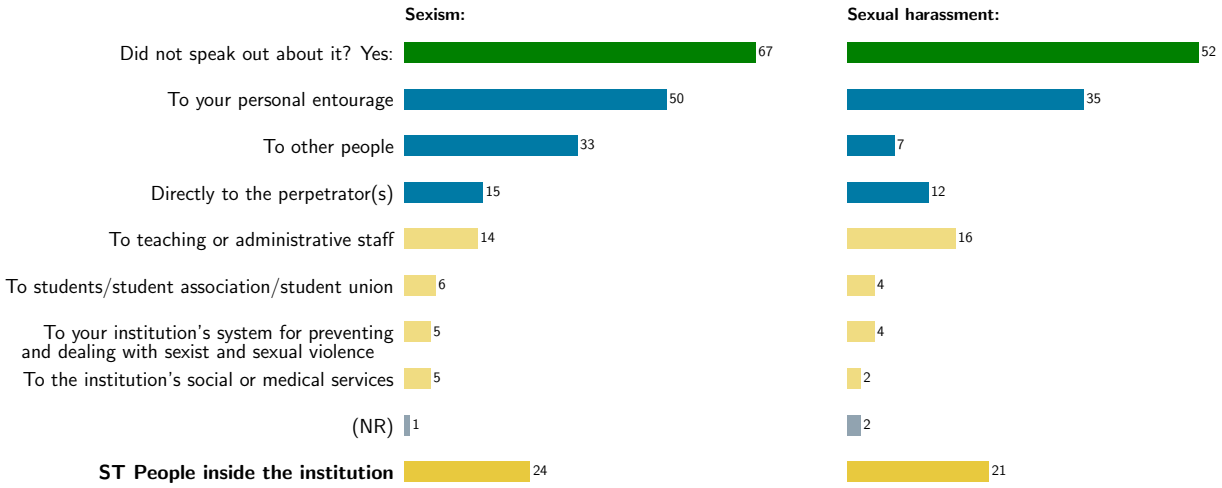

Figure 4. Answers to the question *"To whom did you speak out about the incident you experienced (when it happened or later)"*. Results for victims of sexism (resp. sexual harassment) are displayed in the left (resp. right) histogram. Numbers are percentages of the victims who spoke. Blue bars code for people inside the institution and yellow bars code for people inside the entourage of the victim.

It appears that women in lower hierarchical positions experience sexual harassment at a higher rate, and this is more the case than for sexism. Among the victims, 74 % have been harassed at the beginning of their career, and this number is still to 14% when the victim obtains her first responsibilities. This is also stressed by the fact that only 27 % experience sexual harassment during their whole career, when they were 44% for sexism. Similarly to sexism, the #metoo movement did not end the culture of sexual harassment that pervades in the scientific community.

4 Consequences

After quantifying the occurrence of sexism and sexual harassment in the scientific community, pollsters focused on assessing what are the consequences on the victims and on the perpetrators.

Sexism and sexual harassment induce stress, anxiety and uneasiness. In some cases victims feels vulnerable, scared and physically threatened. This is not without effect on the career of the victims. These consequences, as perceived by the victims, are summarized in Fig. 3. We can see that both sexism and sexual harassment induce protective reaction from the victim, such as avoiding the perpetrator -or groups where hostile sexist environment develop-, or by leaving their job. Sexism and sexual harassment also lead to loss of motivation, victims feeling less involved in their work or in the progress of their career. Loss of motivation is more pronounced for victims of sexism than of sexual harassment. The survey also shows that exposure to sexism reduces more self-confidence than sexual harassment. The reason may be that when sexist conducts become more and more serious, the feeling of injustice outweighs powerlessness and prompts action.

Interrogating the impact of sexist behaviours on the career also shows that institutions have not succeeded yet in having their employees feel protected against sexist and sexual violence. Very few victims ($\sim 5\%$) are satisfied with the answer of their institution, and around 30 % have lost faith in its ability to enforce its own rules. This is also visible when the victims have been asked to tell to whom they spoke if they spoke. The answers are summarized in Fig. 4 and show that, among the victims who spoke, less than 1/4 spoke to someone in their institution and very few ($\sim 5\%$) to the listening unit, dedicated to fight sexist conducts. This reflects, either the fact that these units are poorly known, or they are thought to be inefficient. This question also reveals that the more serious the facts are, the less victim speak.

5 Discussion and conclusion

We re-investigated an international survey lead by the L'Oréal Foundation and the IPSOS polling institute, on sexism and sexual harassment in the scientific community, focusing on the category of European physicists.

This sub-sample is thought to be the one that corresponds the best to the French astronomers community, while keeping a large enough data-set that leads to statistically significant conclusions. This study reveals that sexism and sexual harassment may be seen as characteristics of the culture that pervades in scientific communities. Indeed, around 9 European women physicist out of 10 declare they have been victim of sexism at least once in their scientific career, and half have been victim of sexual harassment. Such conducts severely diminish the self-confidence of the victims, make them avoid certain colleagues and even make them feel physically threatened. Despite the legal obligation of employers to ensure the safety of their employees on their workplace, victims often feel they are left on their own to deal with the situation. Among the women who do speak out, only $\sim 24\%$ seek help inside the institution, while the other confide to their personal entourage or try to face directly the perpetrator.

This study and the original poll still suffer from some limitations. Despite its international aspect, 64% of the respondents are European, and 68% of them are French. Such imbalance may induce geographical or cultural biases in the assessment of sexism and sexual harassment in science. Such disparities can lead to very small sample when too many conditions are consider, which made us prefer the category "European physicist" (365 respondents) to the one of "French physicists" (204 respondents). However, these possible biases may not be too strong because, as soon as a subset is large enough, for all the questions of the poll answers are display a distribution consistent with the distribution obtain for the complete sample.

Since personal data are protected, we could not have access to the answers of each respondent individually, but only to aggregated results in the form of percentage of each answer, for each category. This prevented us from conducting the analysis further because we cannot investigate the correlations between different answers. For instance, around 10% of the women who spoke after having been victim of sexual harassment notice a negative impact on their professional journey. It would be very interesting to know if, for instance, these women are the one who spoke about the situation to the perpetrator. This cannot be done with the data we have at our disposal.

Finally, the survey has been conducted over the internet, and link to the poll was sent to 50 institutions in the world. This raises two problems. First, response to the poll is voluntary. The respondents may be more familiar with questions related to sexist and sexual violence, either because as witness, or as victims. Even if the respondents are only representative of 10% of the community -which is a very conservative assumption-, these results show that, it we take an institute composed of 100 members, around 9 of them have experienced sexism and 6 sexual harassment, and we, as a community, should not tolerate this. Secondly, some questions in the poll might have led to ambiguous answers from the respondents. To the question "how did speaking out impacted your professional journey" (possible answers: positively/negatively/no impact), many ($\sim 70\%$) say that it had no impact. Does it mean that sexism or sexual harassment continued (which would be negative), or that it stopped but the victim was not ostracized nor supported by their colleagues (but then it is in contradiction with so many respondents reporting they have suffered from sexism or sexual harassment during their whole career) ? It would be interesting to extend this quantitative survey with a qualitative study based on semi-structured interviews. It would allow an in-depth study of the consequences of sexual misconducts, as well as the motivations for action or inaction, what kind of actions, etc.

Regardless of these caveats, this poll, by its extent and the details of its questions, is particularly important, demonstrating for the first time the extent of sexist and sexual violence in science, all over the world and in all fields. We thank the L'Oréal Foundation for tackling the subject, in order to raise awareness of it and for taking action to put an end to it. This survey sets a starting point for studying the evolution of the importance of sexism and sexual harassment in Science.

All authors thanks Fédérico Vacas, Elisa Simonpietri and Alice Tetaz for providing us with detailed data for the European physicists who responded to the survey.

References

Ouazzani, R. M., Bot, C., Brau-Nogué, S., et al. 2022, in SF2A-2022: Proceedings of the Annual meeting of the French Society of Astronomy and Astrophysics. Eds.: J. Richard, ed. J. Richard, A. Siebert, E. Lagadec, N. Lagarde, O. Venot, J. Malzac, J. B. Marquette, M. N'Diaye, & B. Briot, 23–28

SF2A 2023
M. N'Diaye, A. Siebert, N. Lagarde, O. Venot, K. Baillié, M. Béthermin, E. Lagadec, J. Malzac, J. Richard (eds)

THE MICROSCOPE SPACE MISSION TO TEST THE EQUIVALENCE PRINCIPLE

G. Métris[1], M. Rodrigues[2] and J. Bergé[2]

Abstract. The MICROSCOPE mission tested the Weak Equivalence Principle (WEP) with an unprecedented precision of order 10^{-15}, two orders of magnitude better than the previous best lab experiments. While the WEP, the cornerstone of General Relativity (GR), does not sway, the decade-long problems faced by fundamental physics stay still: how can we unify GR with the Standard Model, and how can we explain the acceleration of the cosmological expansion? As most beyond-GR models predict a violation of the WEP, albeit at an unknown level, it remains critical to even better test the WEP. In this paper, we review the MICROSCOPE mission, give its final constraint on the WEP, and build on its experimental limitations to show how we could improve them by a further two-order of magnitude in the precision of the test of the WEP.

Keywords: Equivalence Principle, Differential accelerometer, Space Experiment, Eötvös ratio

1 Introduction

The universality of free-fall (UFF) has been recognised since Galileo rolled objects down inclined planes and found that, locally, they all undergo the same gravitational acceleration: all objects within the same gravitational field fall at the same rate, independently of their mass and composition. With Newton's second law, the UFF can be restated as the proportionality between the gravitational mass m_G and the inertial mass m_I, with the same proportionality constant for all bodies: this is the usual definition of the weak equivalence principle (WEP). The Equivalence Principle, as generalised by Einstein, was the starting point to general relativity (GR).

GR describes gravitation as the simple spacetime's curvature, while recovering Newton's description of gravitation as a classical inverse-square law force in weak gravitational fields and for velocities small compared to the speed of light. As a highly predictive theory, it has so far successfully passed all experimental tests (Will 2014; Ishak 2019). Standing next to GR, the Standard Model (SM) was built from the realisation that the microscopic world is intrinsically quantum.

Although both GR and SM leave few doubts about their validity in their respective regimes, scientists have been faced with difficulties for decades. Firstly, the question of whether GR and the SM should and could be unified remains open: major theoretical endeavours delivered models such as string theory, but still fail to provide a coherent vision of the world. Secondly, the unexpected dark matter and dark energy make up most of the Universe's mass-energy budget.

The WEP has been tested for four centuries with increased precision (Eötvös et al. 1922; Bessel 1832; Roll et al. 1964; Braginskii & Panov 1971; Schlamminger et al. 2008; Wagner et al. 2012; Williams et al. 2012; Viswanathan et al. 2018). The concept of a test in space emerged in the 1970s (Chapman & Hanson 1970; Everitt et al. 2003), motivated by the quiet environment that space can provide and by the benefit of test periods much longer than on-ground experiments. In 1999, ONERA (Office National d'Etudes et de Recherches Aérospatiales) and OCA (Observatoire de la Côte d'Azur) proposed the MICROSCOPE mission (MICRO-Satellite à Compensation de traînée pour l'Observation du Principe d'Equivalence) to CNES.

MICROSCOPE was finally launched in 2016. After successfully dealing with unexpected anomalies (Rodrigues et al. 2022a), the mission provided two and a half years of useful data. In 2017, a first analysis based on only 7% of the eventual science data allowed us to verify the WEP at 2×10^{-14} sensitivity level (Touboul et al. 2017, 2019). In 2022, the full data allowed us to improve that precision by one order of magnitude (Touboul et al. 2022b). In this paper, we first describe MICROSCOPE in Sect. 2. In Sect. 3, we describe the data processing and provide the upper bound provided by MICROSCOPE on the validity of the WEP.

[1] Université Côte d'Azur, Observatoire de la Côte d'Azur, CNRS, IRD, Géoazur, F-06560 Valbonne, France
[2] DPHY, ONERA, Université Paris Saclay, F-92322 Châtillon, France

© Société Française d'Astronomie et d'Astrophysique (SF2A) 2023

2 MICROSCOPE mission overview

2.1 WEP test experiment principle

The measurement relies on comparing the accelerations of two concentric bodies – cylinders in the case of MICROSCOPE – in orbit around the Earth. As shown in Fig. 1, the measurement is performed along the cylinders' X-axis, which is aligned with their main axis. In an inertial pointing configuration, it is pointing in the same direction of the Earth's gravity field vector once per orbit. In a perfect case, the difference of acceleration is proportional to the Eötvös parameter defined by the relative ratio of difference of gravitational-to-inertial masses m_{gj}/m_{ij} between two materials j:

$$\delta(2,1) = 2\frac{a_2 - a_1}{a_2 + a_1} = 2\frac{m_{g2}/m_{i2} - m_{g1}/m_{i1}}{m_{g2}/m_{i2} + m_{g1}/m_{i1}}, \tag{2.1}$$

where a_j are the acceleration undergone by the two bodies.

In MICROSCOPE, the test-masses are part of a double concentric accelerometer. The test-masses are finely controlled by electrostatic forces to be motionless with respect to the surrounding electrodes as illustrated in the right panel of Fig. 1. The forces applied by the set of electrodes are determined by the voltage applied on the test-mass and on each electrodes (Liorzou et al. 2022). The combination of these voltages with the geometry of the instrument defines the electrostatic forces and torques applied to each test-mass in order to counteract all the other effects that prevent the test-mass to stay motionless with respect to the satellite.

Thus, if a WEP violation exists, it can be detected as a signal with a well-known frequency (the orbital frequency $f_{\rm orb}$ in the case of Fig. 1) in the differential acceleration measured by the accelerometer (i.e., the difference of electrostatic force per unit mass between the two test masses). The measurement precision can be improved by rotating the satellite about the axis normal to the orbital plane. This increases the modulation frequency of the Earth's gravity vector projected onto the X-axis, to put it closer to the minimum of the instrumental noise. The WEP-violation frequency becomes $f_{\rm EP} = f_{\rm orb} + f_{\rm spin}$, with $f_{\rm spin}$ the rotation frequency of the satellite. Two spin frequencies have been used during the mission, leading to two test measurement data sets at $f_{\rm EP} \approx 0.9 \times 10^{-3}$ Hz and $f_{\rm EP} \approx 3.1 \times 10^{-3}$ Hz.

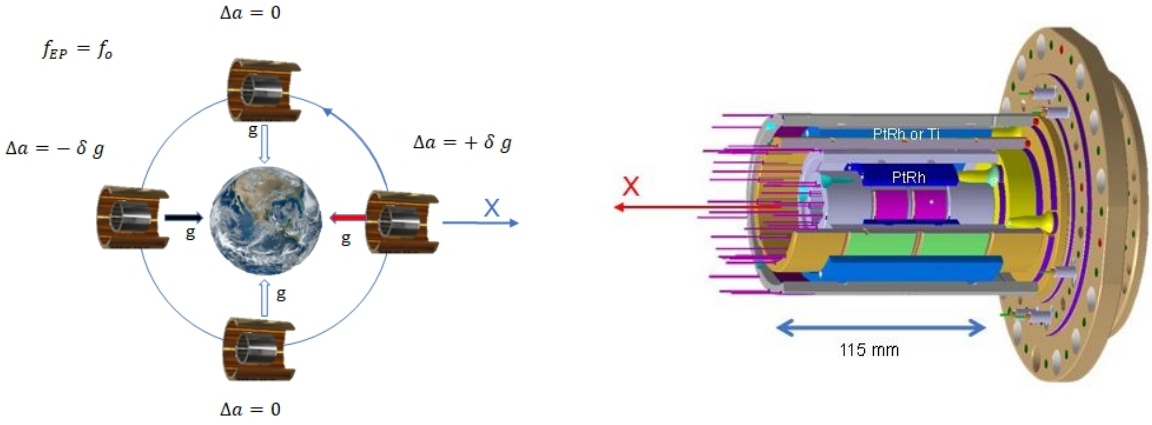

Fig. 1. Left: Experimental principle. **Right:** accelerometer core.

2.2 Payload

The payload (Liorzou et al. 2022) is composed of two identical differential accelerometers also called sensor units (SUs) except for the test-mass material. Each SU have two concentric hollow cylindrical test-masses surrounded by electrodes engraved on gold-coated silica parts. Each SU is connected to a front-end electronics unit (FEEU) which delivers the voltages to the test-masses and electrodes and transmits the data to the interface control unit (ICU). Each ICU connected to the FEEU contains all the digital electronics and software to operate the test-mass control servo-loops and data conditioning for the satellite and then the ground telemetry. The SU and the FEEU are integrated in a thermal cocoon placed at the core of the satellite which offers a micro-Kelvin stability around the measurement frequencies.

The first SU, called SUREF, comprises two test-masses of the same material: PtRh10 platinum-rhodium alloy containing 90% by mass of Pt ($A = 195.1$, $Z = 78$) and 10% Rh ($A = 102.9$, $Z = 45$). SUREF is dedicated to experiment and accuracy verification (in orbit or on ground within the data processing) as it is supposed to give a null signal at $f_{\rm EP}$. The second SU, called SUEP, comprises two test-masses of different material: the same PtRh10 alloy for the inner test-mass and an aeronautic titanium alloy (TA6V) for the outer test-mass with the atomic composition 90% of titanium ($A = 47.9$, $Z = 22$), 6% of aluminium ($A = 27.0$, $Z = 13$) and 4% of vanadium ($A = 50.9$, $Z = 23$). SUEP is dedicated to the WEP test.

2.3 Drag-free satellite

One of the challenges of the mission objectives is to make the satellite environment as quiet as possible for the payload to prevent any corruption of acceleration measurements.

The MICROSCOPE mission has been developed on the basis of scientific missions exploiting the CNES MYRIADE micro-satellite product line whose architecture comprises a platform with generic functional chains (energy, communication, computer, structure, etc.). Some adaptations and modifications were necessary to cope with the unusual performance requirements. Usually, the payloads of the MYRIADE satellites are located on the decoupled upper part of the platform but MICROSCOPE payload module has been accommodated at the centre of the spacecraft where it could take advantage of a more stable thermal environment (Fig. 2).

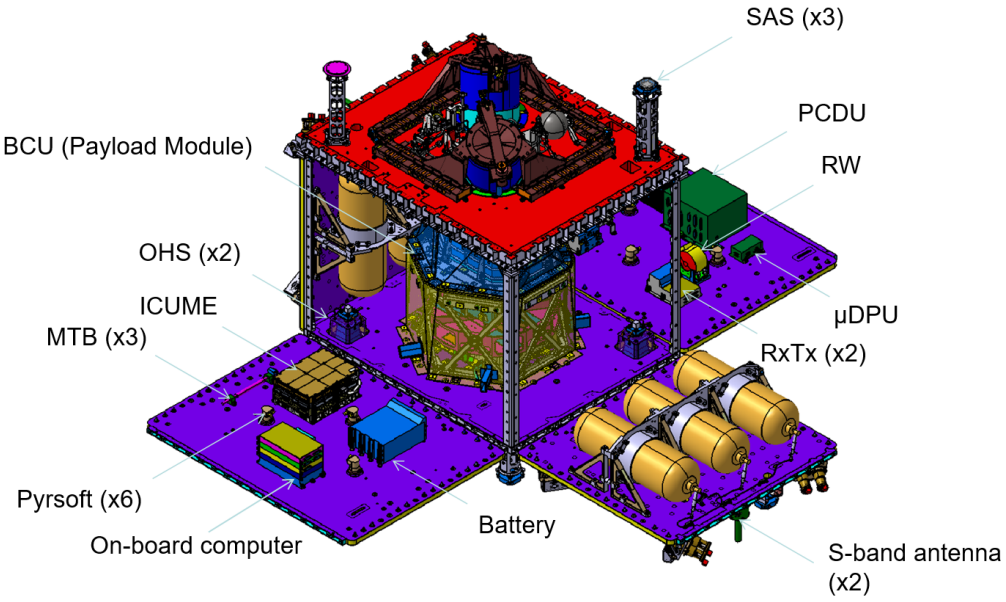

Fig. 2. The cube forming the satellite is open in the picture, the instrument T-SAGE is at the centre surrounded by the two 2×3 tanks of the cold gas propulsion system. Once closed the satellite cube measures $1.4\,\mathrm{m} \times 1\,\mathrm{m} \times 1.5\,\mathrm{m}$ and weighs about 300 kg.

The satellite thermal design has been optimised to offer the payload a tight temperature stability: the required stability around the WEP test frequency $f_{\rm EP}$ was set to 1 mK at the sensor unit interface and to 10 mK at the associated analog electronics interface. Active heaters did not operate during the science operations in order to avoid any interference with the payload measurements. Consequently, the thermal control on the satellite purely relied on passive methods: the dissipation of the electronic units was ensured by satellite external radiators. The in-orbit estimated thermal performance exceeded requirements and expectations. The payload was also shielded from the Earth and satellite magnetic field. In addition, the mechanical or electronic micro disturbances were minimised by a careful design and analysis to ensure an optimal environment: choice of multi-layer insulation (MLI) to minimise cracking, minimisation of current loops, study of thermoelastic deformations

to estimate internal gravitational effects...

To counteract non-gravitational forces and torques, an active control of accelerations and attitude of the satellite was implemented through the DFACS (Fig. 3). The DFACS used the scientific instrument itself as main sensor for delivering the linear as well as the angular accelerations hybridised with the star tracker measurements. The control laws for acceleration and attitude estimated the total forces and torques to be applied on the satellite which were transformed into eight micro-thrust commands sent to the cold gas propulsion system placed on two opposite walls of the satellite (Fig. 2). The DFACS in-orbit performances allowed to reduce the disturbances by 90 dB around $f_{\rm EP}$ leading to a controlled linear acceleration better than $3 \times 10^{-13}\,\mathrm{m\,s^{-2}}$, one order of magnitude better than expectation. The satellite attitude was controlled to better than 1 μrad at $f_{\rm EP}$ with an angular velocity stability better than $3 \times 10^{-10}\,\mathrm{rad\,s^{-1}}$ at $f_{\rm EP}$ in rotating mode, one order of magnitude better than expectation as well. The induced angular acceleration was controlled to better than $10^{-11}\,\mathrm{rad\,s^{-2}}$ at $f_{\rm EP}$, limiting centrifugal effects due to the off-centring of the test-masses.

Besides, the DFACS was able to receive additional external sine signals at particular frequencies in order to calibrate the instrument (differential scale factor, test-mass alignments and off-centerings, coupling between axes, non-linearity). Particular sessions were also dedicated to thermal sensitivities thanks to dedicated heaters.

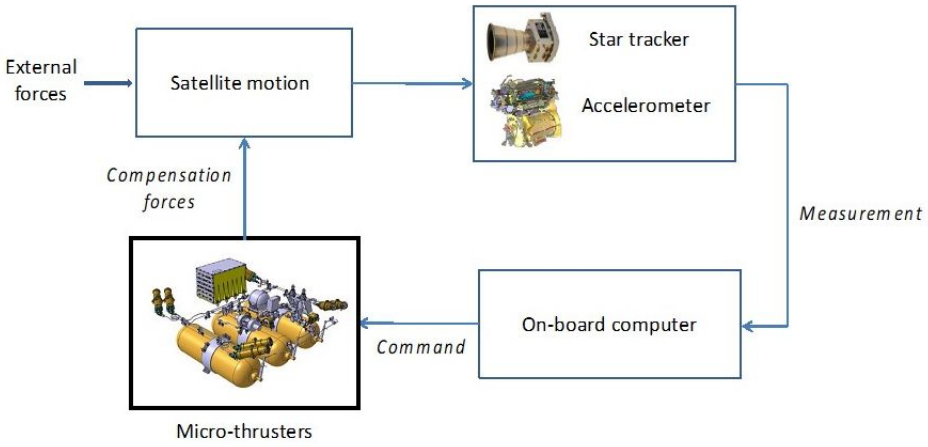

Fig. 3. Satellite Drag-Free and Attitude Control System

3 Data processing

3.1 Measurement equation

A single accelerometer (called inertial sensor) measures the difference of acceleration between the test-mass of the accelerometer and the centre of mass of the satellite. A differential accelerometer yields the difference $\vec{\Gamma}^{(d)} = \vec{\Gamma}^{(1)} - \vec{\Gamma}^{(2)}$ of two such accelerations for two test-masses. The accelerometers are not perfect, in the sense that we look for very small signals and thus any little defect can make deviate from an ideal response: they have bias, scale factors departing from unity, non-zero coupling between axes (Touboul et al. 2022c). Moreover, their orientation in the satellite, in space and with respect to the Earth's gravity field, is not perfectly known. That is why the measured differential acceleration $\vec{\Gamma}^{(d)}$ is not identical to the real one $\vec{\gamma}^{(d)}$, but is related to it as Touboul et al. (2022c):

$$\vec{\Gamma}^{(d)} = \vec{b}_0^{(d)} + \left[\mathbf{A}^{(c)}\right] \vec{\gamma}^{(d)} + 2\left[\mathbf{A}^{(d)}\right] \vec{\gamma}^{(c)} + \vec{n}^{(d)}, \tag{3.1}$$

where

- $\vec{b}_0^{(d)}$ is the difference of bias between the two inertial sensors;
- $\left[\mathbf{A}^{(c)}\right]$ is the common mode sensitivity matrix, close to the identity matrix, which includes scale factors, coupling between axes and global rotation common to the two sensors;

- $\left[\mathbf{A}^{(d)}\right]$ is the differential mode sensitivity matrix, very small, which takes into account the difference of characteristics of the two sensors;
- $\vec{\gamma}^{(c)}$ is the common mode acceleration which is mainly due to residual non-gravitational accelerations acting on the satellite and not on the enclosed test-masses; these non-gravitational accelerations include drag and radiation pressures and the thrust applied to the satellite which is servo-controlled in order to considerably reduce $\vec{\gamma}^{(c)}$ in the frequency band of interest;
- $\vec{n}^{(d)}$ is the (coloured) noise.

The potential WEP-violation signal, $\delta(2,1)\vec{g}$, is included in $\vec{\gamma}^{(d)}$ which also contains the gravity gradient and the differential angular acceleration due to the small residual off-centring between the two test-masses (Rodrigues et al. 2022a):

$$\vec{\gamma}^{(d)} = \delta(2,1)\vec{g}(O_{\rm sat}) + ([\mathrm{T}] - [\mathrm{In}])\vec{\Delta} + \vec{b}_1^{(d)}, \tag{3.2}$$

where

- $\vec{g}(O_{\rm sat})$ is the gravity acceleration;
- [T] is the gravity gradient tensor;
- [In] is the gradient of inertia matrix;
- $\vec{\Delta}$ is the off-centring vector from the centre of test-mass (1) to the centre of test-mass (2);
- $\vec{b}_1^{(d)}$ contains the differences between the other small (mainly non gravitational) perturbations acting on the two test-masses.

Only the axis of the cylindrical test-masses, called X, which is much more precise than the other axes is used to estimate the EP signal. Therefore Eq. (3.1) has to be projected onto the X-axis. This leads to numerous terms Rodrigues et al. (2022a) but some are negligible and others are calibrated and corrected (Touboul et al. 2022a). The remaining model used to analyse the measurements along the X-axis reads

$$\Gamma^{(d)}_{x,\rm corr} = \sum_{j=0}^{3} \alpha_j (t-t_0)^j + \delta_x g_x + \delta_z g_z + \Delta'_x S_{xx} + \Delta'_z S_{xz} + n_x^{(d)}, \tag{3.3}$$

where

- $\delta_x \approx A^{(c)}_{(1,1)}\delta(2,1)$ ($A^{(c)}_{(1,1)}$ being the scale factor along X) is very close to the Eötvös ratio;
- δ_z, a small fraction of $\delta(2,1)$, is in principle too small to be estimated but is included in the model to check the absence of anomaly;
- S_{xx} and S_{xz} are components of the matrix [S] which is the symmetric part of [T] − [In];
- Δ'_x (close to Δ_x) and Δ'_z (close to Δ_z) are "effective" components of the off-centring taking into account the sensitivity matrix;
- $\sum_{j=0}^{3} \alpha_j (t-t_0)^j$ is an empirical polynomial term aiming to absorb the effect of the bias and its slow drift (mainly due to thermal effects).

3.2 Results

The final results of the MICROSCOPE mission are based on eighteen sessions for SUEP and nine sessions for SUREF (Touboul et al. 2022a). A few sessions were discarded because of non-linearities at the beginning of the mission (before the control loop's electronics was upgraded) and a few others were discarded because of rare anomalies.

In practice, instrumental defects are parameterised by the $\overrightarrow{b}_1^{(d)}$ and $\overrightarrow{\Delta}$ vectors, as well as the $\left[A^{(d)}\right]$ and $\left[A^{(c)}\right]$ matrices in Eq. (3.3), with only some of their components impacting the projected acceleration (Rodrigues et al. 2022a,b). The estimation of Δ'_x and Δ'_z uses their couplings with the Earth gravity gradient, whose strong spectral line at $2f_{\rm EP}$ allows for a direct determination in science data based on an accurate Earth gravity model.

The final MICROSCOPE's constraint on the validity of the WEP is (Touboul et al. 2022b)

$$\delta(\mathrm{Ti},\mathrm{Pt}) = [-1.5 \pm 2.3\ (\mathrm{stat}) \pm 1.5\ (\mathrm{syst})] \times 10^{-15}, \tag{3.4}$$

where the statistical error is given at 1σ.

The reference instrument provided a null result, $\delta(\mathrm{Pt},\mathrm{Pt}) = [0.0 \pm 1.1\ (\mathrm{stat}) \pm 2.3\ (\mathrm{syst})] \times 10^{-15}$, showing no sign of unaccounted systematic errors in Eq. (3.4). As expected from its higher sensitivity, SUREF's result has a smaller statistical error than SUEP's. On the opposite, it has higher systematic errors (dominated by thermal effects), since they were estimated with less optimal sessions than SUEP's ones (Rodrigues et al. 2022b).

3.3 Beyond the WEP

MICROSCOPE was the first space-based laboratory dedicated to testing the WEP (Bergé 2023). Beside reaching its main goal, the mission also demonstrated technological advances (e.g. 6-degrees-of-freedom drag-free and attitude control) and provided an experience on the limits of the experiment. Furthermore, it allowed for state-of-the-art bounds on ultra-light dark matter and long-range fifth forces (Bergé et al. 2018). Additionally, it was shown that in principle, a MICROSCOPE-like experiment could constrain short fifth force models and screening mechanisms; nevertheless, MICROSCOPE itself was not designed for those experiments and gave only poor constraints (Bergé et al. 2022; Pernot-Borràs et al. 2021).

References

Bergé, J. 2023, Reports on Progress in Physics, 86, 066901

Bergé, J., Brax, P., Métris, G., et al. 2018, Physical Review Letters, 120, 141101

Bergé, J., Pernot-Borràs, M., Uzan, J.-P., et al. 2022, Classical and Quantum Gravity, 39, 204010

Bessel, F. W. 1832, Ann. Phys. Chem. (Poggendorf), 25, 401-17

Braginskii, V. B. & Panov, V. I. 1971, Zh. Eksp. Teor. Fiz., 61, 873-879

Chapman, P. K. & Hanson, A. J. 1970, in Proc. Conf. on Experimental Tests of Gravitation Theories, ed. R. W. Davies, JPL TM, 228

Eötvös, L., Pekár, D., & Fekete, E. 1922, Ann. Phys., 68, 11

Everitt, C. W. F., Damour, T., Nordtvedt, K., & Reinhard, R. 2003, Advances in Space Research, 32, 1297

Ishak, M. 2019, Living Reviews in Relativity, 22

Liorzou, F., Touboul, P., Rodrigues, M., et al. 2022, Classical and Quantum Gravity, 39, 204002

Pernot-Borràs, M., Bergé, J., Brax, P., et al. 2021, Physical Review D, 103, 064070

Rodrigues, M., Touboul, P., Métris, G., et al. 2022a, Classical and Quantum Gravity, 39, 204004

Rodrigues, M., Touboul, P., Métris, G., et al. 2022b, Classical and Quantum Gravity, 39, 204006

Roll, P. G., Krotkov, R., & Dicke, R. 1964, Annals Phys., 26, 442-517

Schlamminger, S., Choi, K.-Y., Wagner, T. A., Gundlach, J. H., & Adelberger, E. G. 2008, Physical Review Letters, 100, 041101

Touboul, P., Métris, G., Rodrigues, M., et al. 2019, Classical and Quantum Gravity, 36, 225006

Touboul, P., Métris, G., Rodrigues, M., et al. 2022a, Classical and Quantum Gravity, 39, 204009

Touboul, P., Métris, G., Rodrigues, M., et al. 2017, Physical Review Letters, 119, 231101

Touboul, P., Métris, G., Rodrigues, M., et al. 2022b, Physical Review Letters, 129, 121102

Touboul, P., Rodrigues, M., Métris, G., et al. 2022c, Classical and Quantum Gravity, 39, 204001

Viswanathan, V., Fienga, A., Minazzoli, O., et al. 2018, MNRAS, 476, 1877-1888

Wagner, T. A., Schlamminger, S., Gundlach, J. H., & Adelberger, E. G. 2012, Classical and Quantum Gravity, 29, 184002

Will, C. M. 2014, Living Reviews in Relativity, 17

Williams, J. G., Turyshev, S. G., & Boggs, D. H. 2012, Classical and Quantum Gravity, 29, 184004

SF2A 2023
M. N'Diaye, A. Siebert, N. Lagarde, O. Venot, K. Baillié, M. Béthermin, E. Lagadec, J. Malzac, J. Richard (eds)

A BRIEF REVIEW ON FAST RADIO BURSTS

C. NG[1]

Abstract. This is a brief, non-exhaustive review of Fast Radio Burst (FRB), a new category of radio transients originating from extragalactic distances. We discuss the key observational properties known so far and the scientific applications of FRBs. We summarize the FRB-related research in the French astrophysics community, and conclude by sharing some insights to the future of FRB science.

Keywords: Fast Radio Bursts, radio, transients

1 Introduction

Fast Radio Burst (FRB) is a recent astrophysical phenomenon, involving bright bursts ($<10^{44}\,\mathrm{erg\,s^{-1}}$) coming from extragalactic distances, currently observed in the redshift range from $z \sim 0.03$ to $z > 1$. They are extremely short in duration with bursts observed to last anything from tens of microseconds to several milliseconds, a fraction of the time it takes to blink an eye. The inferred event rate of FRB is high, of the order of 5000 events per sky per day above a fluence of 2 Jy ms (Champion et al. 2016; Keane & Petroff 2015), in other words, there is an FRB every few tens of seconds. The fact that FRBs are prolific, bright and extragalactic brings high hopes that we can use FRBs as a cosmological probe, for example, to study the intergalactic medium (Ravi et al. 2016) and find the missing baryons (Macquart et al. 2020).

The first FRB detection was made in 2007 (Lorimer et al. 2007), in the analysis of archival pulsar data taken in 2001. In the decade following, our knowledge of FRBs has been limited since only a few tens of cataclysmic FRBs were observed, constrained by the field-of-view (FOV) of single dish radio telescopes (e.g. Parkes, Arecibo) used for FRB studies at the time. Even though these are sensitive instruments, they can only see one point (or a few multi-beam positions) on the sky at a time. Since we did not know *a priori* when or where FRBs burst, plus the fact that in the early days all of them seemed to be cataclysmic, one-off, non-repeating bursts, it has been really difficult to study them.

Since 2018, the number of FRB discoveries has exploded thanks to the CHIME radio telescope in Canada (CHIME/FRB Collaboration et al. 2018). With the original design of a cylindrical transit telescope, CHIME has a FOV hundred times larger and this has proved to be a game changer for the FRB field, enabling hundreds of FRBs discoveries in the first years of the operation (CHIME/FRB Collaboration et al. 2021). However, while CHIME is undoubtedly a great survey instrument, it is not capable of localizing precisely where these FRBs come from. The localization uncertainty of CHIME is roughly 10" for the nearest one percent of sources it sees (e.g. Bhardwaj et al. 2021), but the region can be as large as 1 deg if the FRB was detected in the sidelobe (e.g. CHIME/FRB Collaboration et al. 2020b). Typically there are dozens of galaxies in a field of this size and so we cannot know exactly from which one did the FRB originate. To conduct proper host galaxy identification, we will need arcseond-level of spatial resolution provided by interferometer telescopes. A number of interferometers have recently joined the FRB field, including the Deep Synoptic Array (DSA) in the US and the Australian Square Kilometre Array Pathfinder (ASKAP) in Australia. These facilities have been responsible for the increase in localized FRBs in the last few years. To date, according to the Transient Name Server (TNS) database* there are more than 750 FRBs published, of which almost 40 have a host localization, in additional to a lot of more FRBs yet to be officially announced.

[1] Laboratoire de Physique et Chimie de l'Environnement et de l'Espace - Université d'Orléans/CNRS, 45071, Orléans Cedex 02, France
*TNS database search engine: `https://www.wis-tns.org/search`

© Société Française d'Astronomie et d'Astrophysique (SF2A) 2023

2 Key observational properties of FRBs

While most of the FRBs are one-off events, a small percentage of them have been seen to burst repeatedly. At the moment of writing, there are 51 published repeating FRBs, while a lot more are yet to be published. In CHIME/FRB Collaboration et al. (2023), the burst cadence of 46 repeating FRBs are compared and it appears that they tend to cluster in time and energy distribution. The repeaters either go into an active state where it emits brighter and more bursts or they stay quiet. FRB 20180916B is a particularly active FRB. Thanks to its high burst rate, a periodic activity window of about 16±0.15 days (∼4 days active followed by 12 days inactive) has been detected (CHIME/FRB Collaboration et al. 2020a). Periodic activity window has been established for one other repeating FRB 121102 at about 160 days (Rajwade et al. 2020; Cruces et al. 2021). The first CHIME/FRB catalog (CHIME/FRB Collaboration et al. 2021) consists of over 500 FRBs and it is the first large sample of FRBs detected under the same system thus representing a good starting point for population analysis. Using that, Pleunis et al. (2021a) reported statistically significant morphological differences between the repeaters and non-repeaters. Repeater bursts are intrinsically broader in width and narrower in bandwidth. However, it is not clear if the one-off FRBs are truly cataclysmic events, or if we just have not observed them when they repeat, or perhaps the repeated bursts are below the detection threshold of the telescope used.

The progenitor of FRB is another outstanding question. So far only one FRB has been unambiguously associated with the magnetar SGR 1935+2154 in our Milky Way (CHIME/FRB Collaboration et al. 2020b; Bochenek et al. 2020). In 2020, SGR 1935+2154 underwent a period of X-ray burst storm which lasted for hours. The high energy activity was detected by a number of X-ray (NICER, Chandra, XMM, Swift XRT) and Gamma ray (Swift BAT, Fermi, NuSTAR, Integral) telescopes (Mereghetti et al. 2020). FRB-like bursts were detected by two radio telescopes, namely CHIME and STARE2. The X-ray peaks lag the radio ones by 6.5 ms. Magnetar has always been one of the popular models of the FRB phenomenon, and this discovery adds a clear vote to that theory. However, as mentioned earlier, there appears to be multiple populations of FRBs. It would be hard to explain all the observed FRB properties, for example the periodic activity seen in FRBs 121102 and 20180916B, with the magnetar flare model. This FRB is also Galactic instead of extragalactic, and quite a bit less luminous than the bulk of the FRBs detected so far. Is it possible that SGR 1935+2154 is an exception rather than the rule? The answer is not conclusive. For all the other FRBs, no afterglow has been detected that can allow a progenitor association.

Nonetheless, almost 40 FRBs have been associated with a host galaxy. Most FRB hosts are star-forming, spiral galaxies, but there are also FRBs from more lenticular hosts. So far all hosts are located below z≈1, but this is most certainly sensitivity limited and as better telescope facilities come online we will be able to see further. Gordon et al. (2023) studied the overall properties of 23 highly-secure host galaxies of FRBs, involving six repeaters and 17 apparent non-repeaters. They find that FRB hosts have a median stellar mass of $\approx 10^{9.9}\,\mathrm{M}_\odot$, a mass-weighted age of ≈5.1 Gyr, and an ongoing star formation rate of $\approx 1.3\,\mathrm{M}_\odot\,\mathrm{yr}^{-1}$, while also noting a wide range in all properties. They report no statistically significant distinction between the hosts of repeaters and non-repeaters. We have to be careful when reading into this kind of analysis at a relatively early stage where the sample size remains modest. In fact, Mannings et al. (2021) presented examples of FRBs that are not located in the centre of their host galaxies but can, for instance, but on the spiral arms. That means an FRB associated with a star-forming galaxy does not necessarily imply that the FRB comes from the star-forming region. For example, FRB 20200120E in the M81 (star-forming galaxy) has been pin-pointed to a Globular cluster where there is little star forming (Kirsten et al. 2022). As an aside, a Globular cluster FRB makes a rather difficult case to reconcile with the magnetar model. In general, it seems that FRBs live in diverse local host environments and can come from various types of host galaxies.

3 Scientific applications of FRBs

FRBs are the shortest-duration extragalactic transients, and the most compact known extragalactic sources of electromagnetic radiation. This means we can potentially use FRB as a cosmological probe.

The dispersion measure of FRB (DM, not to be confused with Dark Matter) is arguably the most important observable of FRB studies, and it is a proxy for the distance of the FRB. The observed DM ($\mathrm{DM}_{\mathrm{obs}}$) includes the total line-of-sight electron-column densities, and can contain contributions from the host-galaxy interstellar medium (ISM), the circumgalactic medium (CGM), the intracluster medium (ICM) of intervening systems, the intergalactic medium (IGM), and the galactic halo of our Milky Way. FRBs act as a back-light and provide a clean signal for the study of these components which are very hard to probe otherwise, with no need for additional simulations.

Ravi et al. (2019) suggests that, with 1000 to 10,000 well localized FRBs, we would be able to make statistical detection and study the CGM, and understand whether all dark matter is composed of compact objects. There is already a study that has resolved the missing baryon problem (Macquart et al. 2020), and a recent detection of FRBs in the Abell cluster (Connor et al. 2023) could allow for the study of the ICM. With 10,000 to 100,000 FRBs, we might be able to measure the mean IGM density and study the magnetic field in the cosmic web, achieve a global detection of He-II deionization, and detect baryon acoustic oscillations in DM-space clustering. Finally, with 100,000 to 1 million FRBs, we might be able to improve the kinetic Sunyaev-Zel'dovich (kSZ) constraints on large-scale structure growth rate. Also, FRBs might provide the only means of measuring sub-ms time delays imparted by extragalactic lensing phenomena (Sammons et al. 2020).

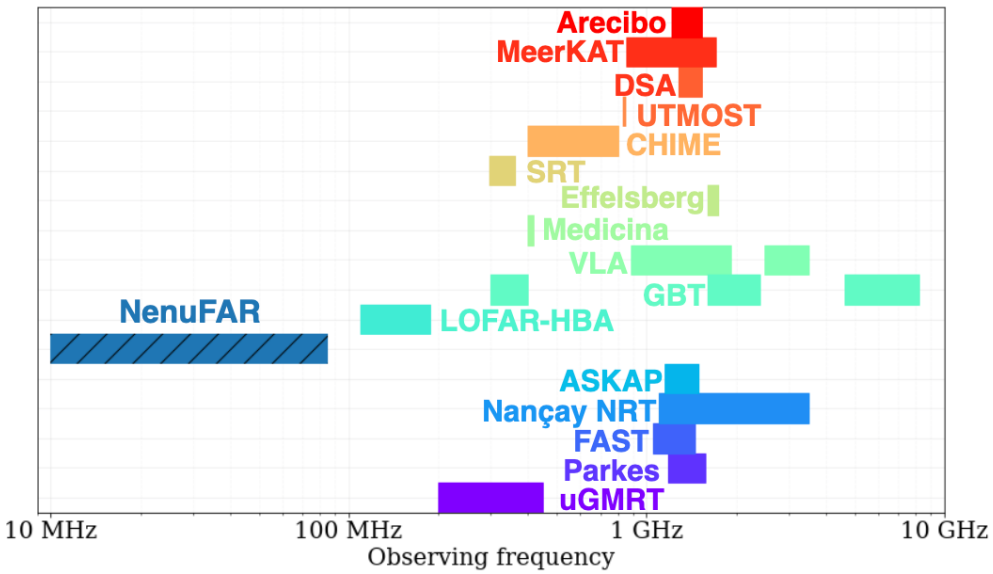

Fig. 1. A non-exhaustive list of radio telescope facilities that have detected FRB burst to-date, spanning as low as 110 MHz with the LOFAR-HBA to as high as 8 GHz with the Green Bank Telescope (GBT). We have an on-going FRB monitoring campaign with NenuFAR, which operates in a much lower frequency range of 10–85 MHz. Any future positive detections from NenuFAR will provide important clues regarding the emission mechanisms of FRBs.

4 The French FRB community

With these exciting prospects of FRB studies, we have in France a growing community, currently involving more than a dozen people across at least seven institutes. The largest focus of FRB work in France is in the domain of observations, led by researchers at the ORN[†], LPC2E[‡], SUBATECH[§] and LESIA[¶]. Notably, there is an on-going campaign with the Nançay Extension Upgrading LOFAR (NenuFAR) radio telescope to follow up repeating FRBs (Decoene et al. 2023). As shown in Fig. 1, FRBs have so far only been detected from 110 MHz (Pleunis et al. 2021b) up to 8 GHz (Zhang et al. 2018). With NenuFAR, we hope to open up a new window of FRB observations at the very low frequency range (10−85 MHz), which is important for understanding the emission mechanisms of FRBs. The NenuFAR FRB project currently monitors 15 sources with at least 500 observations taken and analysis on-going. It has been found that FRB emission at low frequencies can be systematically delayed by a few days after the higher frequency detections, at least in the case of FRB 20180916B between its CHIME and LOFAR signals (Pleunis et al. 2021b). This delay is perfect for triggering NenuFAR observations as soon as other telescopes at higher observing frequencies send out alerts of burst activities. Triggering capability is currently not available on NenuFAR but could have a relevant use case for FRBs and other transient studies. On the Nançay radio telescope (NRT), the Extragalactic Coherent

[†]ORN: Observatoire Radioastronomique de Nançay
[‡]LPC2E: le Laboratoire de Physique et Chimie de l'Environnement et de l'Espace
[§]SUBATECH: le laboratoire de Physique SUBAtomique et TECHnologies associées
[¶]LESIA: le Laboratoire d'études spatiales et d'instrumentation en astrophysique

Light from Astrophysical Transients (ECLAT) campaign has been monitoring 11 repeating FRBs since 2022. Thanks to the high sensitivity and time resolution of the NRT, seven FRBs have been detected. In one of the sources, dense forests of clustered microshots in the bursts have been observed. They can be extremely bright, occasionally exceeding a signal-to-noise of 1000 (Hewitt et al. 2023). These components have different dispersion measures, and they could be different burst types arising from different emission mechanisms, similar to what is seen in solar radio bursts. French astronomers are also involved in other international radio collaboration, for example, CHIME[‖] and MeerTRAP[**]. In additional to radio, there are efforts at IRAP[††] to study potential X-ray emission of FRBs, as well as neutrinos work at SUBATECH. There is also multi-wavelength follow-up work for example the Deeper Wider Faster (DWF)[‡‡] campaign being carried out at CEA[§§]. Finally, Machine Learning (ML) algorithms for FRB detections are being developed at LESIA and LPC2E. A number of theoretical studies of FRBs have also been presented by researchers from LUTH[¶¶] and LPC2E (see, e.g. Bonetti et al. 2016; Bentum et al. 2017; Mottez et al. 2020; Decoene et al. 2021; Voisin 2023).

5 Conclusion

Looking to the future of FRBs, I am optimistic that we will soon uncover the origin of FRBs, both in terms of their provenance and the physics of the emission mechanisms of these energetic bursts. I think the most important clues will be obtained from Multi-wavelength FRB observations (see, e.g. a review by Ng 2023). We will soon have a large sample of well localized FRBs. Upcoming next-generation radio telescope facilities including CHORD (Vanderlinde et al. 2019), DSA-2000 (Hallinan et al. 2019) and the Square Kilometre Array (SKA) will provide over 500 mas-localized FRBs per month. A critical challenge associated with this is how will the identification of host galaxies be able to keep up with this discovery rate? Finally, there is high hopes that we can use FRBs as cosmological probes for our Universe, for the studies of the missing baryons, galactic halo, setting constraints on Hubble constant (H_0), He-II reionization, lensing, IGM magnetic field, to name but a few. In summary, FRB is a young and fast growing field with a bright future and lots more discoveries to come.

References

Bentum, M. J., Bonetti, L., & Spallicci, A. D. A. M. 2017, Advances in Space Research, 59, 736

Bhardwaj, M., Gaensler, B. M., Kaspi, V. M., et al. 2021, ApJ, 910, L18

Bochenek, C. D., Ravi, V., Belov, K. V., et al. 2020, Nature, 587, 59

Bonetti, L., Ellis, J., Mavromatos, N. E., et al. 2016, Physics Letters B, 757, 548

Champion, D. J., Petroff, E., Kramer, M., et al. 2016, MNRAS, 460, L30

CHIME/FRB Collaboration, Amiri, M., Andersen, B. C., et al. 2021, ApJS, 257, 59

CHIME/FRB Collaboration, Amiri, M., Andersen, B. C., et al. 2020a, Nature, 582, 351

CHIME/FRB Collaboration, Amiri, M., Bandura, K., et al. 2018, ApJ, 863, 48

CHIME/FRB Collaboration, Andersen, B. C., Bandura, K., et al. 2023, ApJ, 947, 83

CHIME/FRB Collaboration, Andersen, B. C., Bandura, K. M., et al. 2020b, Nature, 587, 54

Connor, L., Ravi, V., Catha, M., et al. 2023, ApJ, 949, L26

Cruces, M., Spitler, L. G., Scholz, P., et al. 2021, MNRAS, 500, 448

Decoene, V., Kotera, K., & Silk, J. 2021, A&A, 645, A122

Decoene, V., Zarka, P., Ng, C., et al. 2023, in SF2A 2023: Proceedings of the Annual meeting of the French Society of Astronomy and Astrophysics, ed. M. N'Diaye, A. Siebert, N. Lagarde, O. Venot, K. Baillié, M. Béthermin, E. Lagadec, J. Malzac, & J. Richard, 137–141

Gordon, A. C., Fong, W.-f., Kilpatrick, C. D., et al. 2023, ApJ, 954, 80

Hallinan, G., Ravi, V., Weinreb, S., et al. 2019, in Bulletin of the American Astronomical Society, Vol. 51, 255

[‖] CHIME: `https://chime-experiment.ca/en`

[**] MeerTRAP: `https://www.meertrap.org`

[††] IRAP: the Institut de Recherche en Astrophysique et Planétologie

[‡‡] DWF: `https://www.swinburne.edu.au/research/centres-groups-clinics/centre-for-astrophysics-supercomputing/our-research/data-intensive-astronomy-software-instrumentation/deeper-wider-faster-program/`

[§§] CEA: Le Commissariat à l'énergie atomique et aux énergies alternatives

[¶¶] LUTH: le Laboratoire Univers et Théories

Hewitt, D. M., Hessels, J. W. T., Ould-Boukattine, O. S., et al. 2023, MNRAS

Keane, E. F. & Petroff, E. 2015, MNRAS, 447, 2852

Kirsten, F., Marcote, B., Nimmo, K., et al. 2022, Nature, 602, 585

Lorimer, D. R., Bailes, M., McLaughlin, M. A., Narkevic, D. J., & Crawford, F. 2007, Science, 318, 777

Macquart, J. P., Prochaska, J. X., McQuinn, M., et al. 2020, Nature, 581, 391

Mannings, A. G., Fong, W.-f., Simha, S., et al. 2021, ApJ, 917, 75

Mereghetti, S., Savchenko, V., Ferrigno, C., et al. 2020, ApJ, 898, L29

Mottez, F., Zarka, P., & Voisin, G. 2020, A&A, 644, A145

Ng, C. 2023, in SF2A-2023: Proceedings of the Annual meeting of the French Society of Astronomy and Astrophysics, ed. M. N'Diaye, A. Siebert, N. Lagarde, O. Venot, K. Baillié, M. Béthermin, E. Lagadec, J. Malzac, & J. Richard, 137–141

Pleunis, Z., Good, D. C., Kaspi, V. M., et al. 2021a, ApJ, 923, 1

Pleunis, Z., Michilli, D., Bassa, C. G., et al. 2021b, ApJ, 911, L3

Rajwade, K. M., Mickaliger, M. B., Stappers, B. W., et al. 2020, MNRAS, 495, 3551

Ravi, V., Battaglia, N., Burke-Spolaor, S., et al. 2019, Bulletin of the AAS, 51, https://baas.aas.org/pub/2020n3i420

Ravi, V., Shannon, R., Bailes, M., et al. 2016, Science, 354, 1249

Sammons, M. W., Macquart, J.-P., Ekers, R. D., et al. 2020, ApJ, 900, 122

Vanderlinde, K., Liu, A., Gaensler, B., et al. 2019, in Canadian Long Range Plan for Astronomy and Astrophysics White Papers, Vol. 2020, 28

Voisin, G. 2023, A&A, 675, A200

Zhang, Y. G., Gajjar, V., Foster, G., et al. 2018, ApJ, 866, 149

SF2A 2023
M. N'Diaye, A. Siebert, N. Lagarde, O. Venot, K. Baillié, M. Béthermin, E. Lagadec, J. Malzac, J. Richard (eds)

ICE EVOLUTION DURING THE STAR FORMATION PROCESS: AN ICEAGE JWST STUDY OF CHAMAELEON I

J. A. Noble[1] and on behalf of the Ice Age team[2]

Abstract. Icy grain mantles are the main reservoir for volatile elements in star-forming regions. The IceAge* Early Release Science program on the James Webb Space Telescope proposes to trace the evolution of pristine and complex ice chemistry in Chamaeleon I - a representative low-mass star-forming region - through various stages of star formation from dense cloud to protoplanetary disk. Observations towards the dense cloud made in summer 2022 using the NIRCam, NIRSpec and MIRI instruments provided high spectral resolution (R $\sim$ 1500-3000) and sensitivity (S/N $>$ 100) infrared spectra from 2.5 to 13 μm of two highly extincted background stars ($A_V < 100$).

Keywords: JWST, IR spectroscopy, star formation, molecular cloud

1 The IceAge Early Release Science program

The IceAge program McClure et al. (2017) is one of thirteen Early Release Science programs awarded Director's Discretionary observational time on the James Webb Space Telescope during the first six months of science operations. The IceAge program, led by PI Melissa McClure and co-PIs Adwin Boogert and Harold Linnartz, proposes to trace the evolution of pristine and complex ice chemistry in Chamaeleon I. This object was chosen as being a representative low-mass star-forming region containing – in close proximity – regions at various stages of star formation from dense cloud to protoplanetary disk. The program utilises the NIRCam, NIRSpec and MIRI instruments in a combination of imaging and spectral modes. The observed field of view in the Chamaeleon star forming region is shown in Fig. 1, a composite image obtained by combining NIRCam imaging filters.

2 First results from the IceAge program

The observations presented in this work were obtained in summer 2022 and are published in McClure et al. (2023). We summarise the results here. A combination of spectroscopy performed with the NIRCam, NIRSpec and MIRI instruments provided high spectral resolution (R $\sim$ 1500-3000) and sensitivity (S/N $>$ 100) infrared spectra from 2.5 to 13 μm of two highly extincted background stars ($A_V < 100$).

In this talk, we presented the first results of the IceAge program: a complete ice inventory towards the observed lines of sight, including derived column densities for expected ice species as well as the first detection of several species along lines of sight in a quiescent cold core (McClure et al. 2023). In summary, ice features attributable to the major ice components H_2O, CO_2, CO, NH_3, CH_4 and CH_3OH were observed towards NIR 38 and J110621 (see Fig. 1), background stars with A_V estimated at 60 mag and 95 mag, respectively, from archival data. Weaker ice features attributed to $^{13}CO_2$, ^{13}CO, OCN^-, OCS, as well as functional groups of complex organic molecules, were detected in a dense cloud for the first time. Profiles of the deeper ice bands, for example the $^{12}CO_2$ ice profile, indicate that moderate growth of the icy grains has occurred compared to the grain size distribution expected in the diffuse interstellar medium. An initial estimation of column densities for the observed ice species allows a constraint to be placed on the bulk budget of S, with S-bearing ice accounting for around 1 % of total S, while confirming the budgets of icy C and O to be around 19 % and N to be $\sim$ 13 %. There is some indication that the formation of complex molecules may begin in the water-rich ice mantle, prior to CO freeze-out.

[1] Physique des Interactions Ioniques et Moléculaires, CNRS, Aix Marseille Univ., 13397 Marseille, France
[2] PI M. K. McClure and co-PI H. Linnartz, Leiden Observatory, Leiden; co-PI A. C. A. Boogert, Institute for Astronomy/InfraRed Telescope Facility, Honolulu
*http://jwst-iceage.org/

© Société Française d'Astronomie et d'Astrophysique (SF2A) 2023

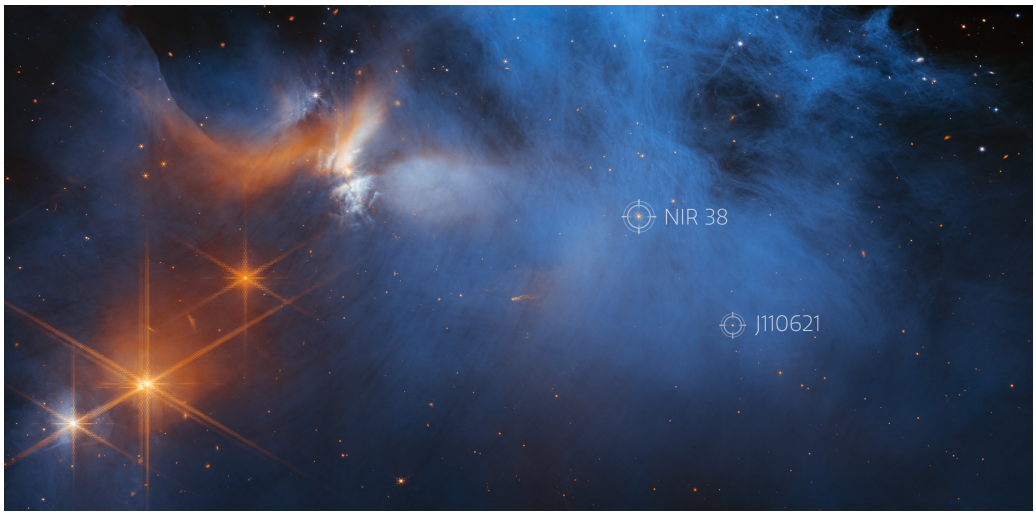

Fig. 1. Star-forming region Chamaeleon I, imaged by the JWST NIRCam instrument. The two highly extincted background stars targeted by the IceAge program are highlighted. This image was originally published in a press release on 23/01/23, available at: `https://esawebb.org/news/weic2303/`, to coincide with the publication of McClure et al. (2023). Image Credit: NASA, ESA, CSA, and M. Zamani (ESA/Webb); Science: M. K. McClure (Leiden Observatory), F. Sun (Steward Observatory), Z. Smith (Open University), and the IceAge ERS Team.

3 Conclusions and perspectives

This work presents the first results of the IceAge observational program targeting the Chamaeleon I star forming region. Since this talk, further results have been published, including NIRSpec observations of the class II edge-on protoplanetary disk HH 48 NE (Sturm et al. 2023). The perspectives for the rest of the IceAge program include mapping the spatial distribution of ices in the dense cloud down to $\sim$ 20-50 au to identify the onset of ice formation and determine the degree of chemical complexity achieved prior to star formation. Unravelling complex molecule formation and evolution during the star formation process requires the type of detailed, sensitive observations of interstellar ices now being performed with instruments on the JSWT. Ultimately, the IceAge program hopes to answer the question: how do complex organic molecules form in star-forming regions, and what are the chemical and physical processes responsible for this molecular complexity?

We acknowledge support from French Programme National 'Physique et Chimie du Milieu Interstellaire' (PCMI) of the CNRS/INSU with the INC/INP, co-funded by the CEA and the CNES.

References

McClure, M., Bailey, J., Beck, T., et al. 2017, IceAge: Chemical Evolution of Ices during Star Formation, JWST Proposal ID 1309. Cycle 0 Early Release Science

McClure, M. K., Rocha, W. R. M., Pontoppidan, K. M., et al. 2023, Nature Astronomy, 7, 431

Sturm, J. A., McClure, M. K., Beck, T. L., et al. 2023, arXiv e-prints, arXiv:2309.07817

Session S01

Amas et groupes de galaxies dans l'ère des grands relevés

SF2A 2023
M. N'Diaye, A. Siebert, N. Lagarde, O. Venot, K. Baillié, M. Béthermin, E. Lagadec, J. Malzac, J. Richard (eds)

MIND THE GAP: A DRASTIC CHANGE COMING IN OUR VIEW OF CLUSTERS BROUGHT BY EUCLID

G. Mahler[1, 2]

Abstract. Galaxy clusters are tracers of the matter density peaks in the cosmic web. They additionally provide efficient tests for cosmological models as they form via gravitational collapse in the expanding Universe. Identification of galaxy clusters from large extragalactic surveys (e.g., SDSS, ROSAT, Planck, SPT, DeCALS, KIDS, DES, VHS, LOFAR, ACT, HSC,) has proven to be a powerful way of detecting new clusters, potentially discovering new clusters acting as strong gravitational lenses. For nearly 30 years, the Hubble Space Telescope has remained the field's workhorse for appropriate modeling of individual clusters, with some renowned observing campaigns dedicated to them (e.g. LOCUSS, CLASH, Hubble Frontier Fields). In this article, I will discuss the upscale brought by Euclid, opening the statistical Era in cluster cosmology. With the launch schedule for summer 2023, we are on the verge of a significant transformation, which should boost the observed number of clusters to about two orders of magnitude and drastically affect our approach to cluster analysis. I will briefly discuss how this affects our way of doing astronomy as some pixels might never meet the human eye.

Keywords: subject, verb, noun, apostrophe

1 Introduction

Clusters of galaxies are located at the nodes of the cosmic filaments and represent the densest structures of dark matter; their merging history and evolution shape the properties of their mass distribution. They additionally provide efficient tests for cosmological models as they form via gravitational collapse in the expanding Universe. Identification of galaxy clusters from large extragalactic surveys (e.g., SDSS, ROSAT, Planck, SPT, DeCALS, KIDS, DES, VHS, LOFAR, ACT, HSC) has proven to be a powerful way of detecting new clusters, potentially discovering new strong gravitational lenses. Strong lensing galaxy clusters can play a key role in our understanding of the Universe, from mapping the distribution of matter in its densest regions, to the study of the earliest galaxies that they magnify.

An apparent discrepancy between the observed and expected number of giant arcs, known as the "arc statistics problem", has motivated studies of the correlation between strong lensing efficiency, cosmology, and cluster properties (see Meneghetti et al. 2013 for a review). Cosmological analyses reveal that the number of giant arcs is sensitive to Ω_m and σ_8 (Wambsganss et al. 2008; Li et al. 2006; Oguri et al. 2009; Boldrin et al. 2016), self-interacting dark matter cross section (Wyithe et al. 2001), primordial non-Gaussianity (D'Aloisio & Natarajan 2011), and dark energy (Bartelmann et al. 2003). Giocoli et al. (2012) found that halo concentration is the most important factor for the lensing cross sections for the production of large arcs, with more concentrated halos having larger strong lensing cross sections.

For nearly 30 years, the Hubble Space Telescope (HST) has remained the field's workhorse for appropriate strong lensing mass modeling of individual clusters, with some renowned observing campaigns dedicated to them (e.g. LOCUSS, CLASH, Hubble Frontier Fields). This Era might come to an end with the advent of Euclid, a space-based observatory, surveying the all-sky at nearly HST resolution and therefore offering direct access to modeling from the survey images themselves.

[1] Institute for Computational Cosmology, Durham University, South Road, Durham DH1 3LE, UK
[2] Centre for Extragalactic Astronomy, Durham University, South Road, Durham DH1 3LE, UK

© Société Française d'Astronomie et d'Astrophysique (SF2A) 2023

Origin	Nb of clusters	Survey area (deg^2)	Density ($\#/deg^2$)	Human time (hours)
Abell (Abell et al. 1989)	4 073	41 253	0.01	34
SDSS (Bahcall et al. 2003)	799	400	2	6.65
DES+unWISE (Wen & Han 2022)	151 244	5 000	30	1 260
Euclid (Euclid Collaboration et al. 2022)	2 000 000	15 000	400	16 666

Table 1. Non-exhaustive comparisons between previous sky surveys. The last column aims to grasp the necessary time needed to observe an image with the human eye. In this computation, I assumed that a cluster would be watched for 30 seconds. It clearly demonstrated the unrealistic expectation of looking at all clusters that Euclid will observe.

2 Euclid prospective

Euclid surveys aim to identify, catalog, and study the universe observing about 15 000 deg^2 with its imagers, VIS and NISP, and spectrographs (Racca et al. 2016). In comparison to previous studies, which identified potential strong-lensing line-of-sight, Euclid imaging should be able to provide at the same time, a full sky coverage and the necessary resolution to identify giant arcs as illustrated in Figure 1.

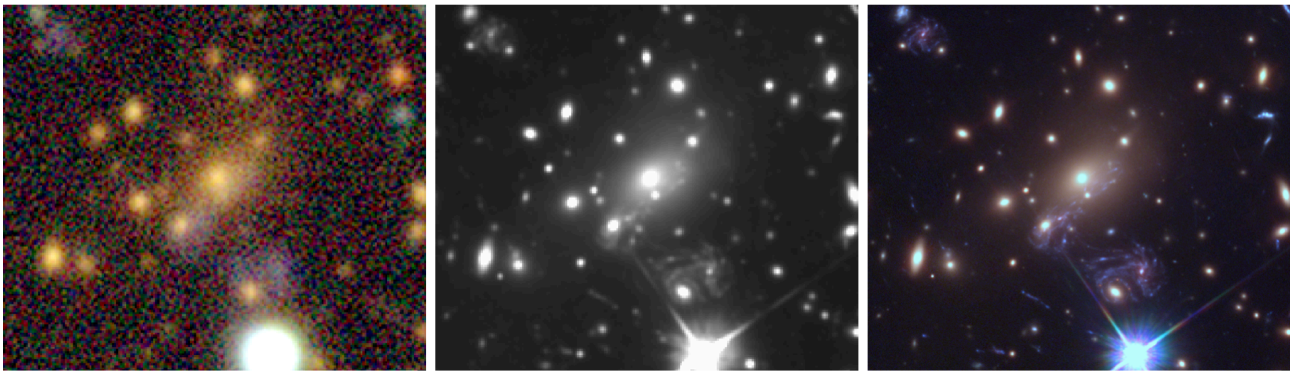

Fig. 1. Image of the famous multiply-imaged spiral galaxy hosting supernova Refsdal (Kelly et al. 2015). This image illustrated the resolution of the VIS instrument on board Euclid. **Left:** Field of view based on the DESI legacy survey, `https://www.legacysurvey.org/` **Middle:** Euclid mock VIS resolution (0.1' per pixel) images. **Right:** HST images using frontier fields data

The number of strong lensing clusters is estimated to be of the order of 10 000 (Boldrin et al. 2016). This is a dramatic change compared to the approximately 10^2 strong lensing clusters known today (see Fox et al. 2022 for the largest compilation grasping maybe aiming half of the known strong lensing cluster). This large upcoming dataset is challenging to review in the traditional visual inspection and is triggering a change of methods. Table 1 is trying to grasp the change of scale Euclid survey is presenting us, by looking at the time needed to watch all the clusters.

3 Conclusions

In summary, the forthcoming Euclid space observatory represents a significant breakthrough in observational astrophysics. It will substantially enhance our ability to study the universe with a tenfold increase in resolution, a vast expansion of surveyed regions, and the capability to probe cosmic phenomena at much greater distances compared to previous instruments like the Sloan Digital Sky Survey (SDSS).

However, this surge in data volume poses a challenge. To effectively utilize Euclid's observations, we must develop advanced software tools for data analysis. These tools are essential for analyzing a large dataset and extracting meaningful scientific information.

Furthermore, Euclid's capabilities demand a reevaluation of our existing modeling techniques. Current software may not handle the wealth of data Euclid will provide. Thus, as a community, we must adapt to

make the rise to this wealth of upcoming information. In essence, Euclid's launch signifies a pivotal moment in astrophysics.

The Legacy Surveys consist of three individual and complementary projects: the Dark Energy Camera Legacy Survey (DECaLS; Proposal ID #2014B-0404; PIs: David Schlegel and Arjun Dey), the Beijing-Arizona Sky Survey (BASS; NOAO Prop. ID #2015A-0801; PIs: Zhou Xu and Xiaohui Fan), and the Mayall z-band Legacy Survey (MzLS; Prop. ID #2016A-0453; PI: Arjun Dey). DECaLS, BASS and MzLS together include data obtained, respectively, at the Blanco telescope, Cerro Tololo Inter-American Observatory, NSF's NOIRLab; the Bok telescope, Steward Observatory, University of Arizona; and the Mayall telescope, Kitt Peak National Observatory, NOIRLab. Pipeline processing and analyses of the data were supported by NOIRLab and the Lawrence Berkeley National Laboratory (LBNL). The Legacy Surveys project is honored to be permitted to conduct astronomical research on Iolkam Du'ag (Kitt Peak), a mountain with particular significance to the Tohono O'odham Nation.

NOIRLab is operated by the Association of Universities for Research in Astronomy (AURA) under a cooperative agreement with the National Science Foundation. LBNL is managed by the Regents of the University of California under contract to the U.S. Department of Energy.

This project used data obtained with the Dark Energy Camera (DECam), which was constructed by the Dark Energy Survey (DES) collaboration. Funding for the DES Projects has been provided by the U.S. Department of Energy, the U.S. National Science Foundation, the Ministry of Science and Education of Spain, the Science and Technology Facilities Council of the United Kingdom, the Higher Education Funding Council for England, the National Center for Supercomputing Applications at the University of Illinois at Urbana-Champaign, the Kavli Institute of Cosmological Physics at the University of Chicago, Center for Cosmology and Astro-Particle Physics at the Ohio State University, the Mitchell Institute for Fundamental Physics and Astronomy at Texas A&M University, Financiadora de Estudos e Projetos, Fundacao Carlos Chagas Filho de Amparo, Financiadora de Estudos e Projetos, Fundacao Carlos Chagas Filho de Amparo a Pesquisa do Estado do Rio de Janeiro, Conselho Nacional de Desenvolvimento Cientifico e Tecnologico and the Ministerio da Ciencia, Tecnologia e Inovacao, the Deutsche Forschungsgemeinschaft and the Collaborating Institutions in the Dark Energy Survey. The Collaborating Institutions are Argonne National Laboratory, the University of California at Santa Cruz, the University of Cambridge, Centro de Investigaciones Energeticas, Medioambientales y Tecnologicas-Madrid, the University of Chicago, University College London, the DES-Brazil Consortium, the University of Edinburgh, the Eidgenossische Technische Hochschule (ETH) Zurich, Fermi National Accelerator Laboratory, the University of Illinois at Urbana-Champaign, the Institut de Ciencies de l'Espai (IEEC/CSIC), the Institut de Fisica d'Altes Energies, Lawrence Berkeley National Laboratory, the Ludwig Maximilians Universitat Munchen and the associated Excellence Cluster Universe, the University of Michigan, NSF's NOIRLab, the University of Nottingham, the Ohio State University, the University of Pennsylvania, the University of Portsmouth, SLAC National Accelerator Laboratory, Stanford University, the University of Sussex, and Texas A&M University.

BASS is a key project of the Telescope Access Program (TAP), which has been funded by the National Astronomical Observatories of China, the Chinese Academy of Sciences (the Strategic Priority Research Program "The Emergence of Cosmological Structures" Grant # XDB09000000), and the Special Fund for Astronomy from the Ministry of Finance. The BASS is also supported by the External Cooperation Program of Chinese Academy of Sciences (Grant # 114A11KYSB20160057), and Chinese National Natural Science Foundation (Grant # 12120101003, # 11433005).

The Legacy Survey team makes use of data products from the Near-Earth Object Wide-field Infrared Survey Explorer (NEOWISE), which is a project of the Jet Propulsion Laboratory/California Institute of Technology. NEOWISE is funded by the National Aeronautics and Space Administration.

The Legacy Surveys imaging of the DESI footprint is supported by the Director, Office of Science, Office of High Energy Physics of the U.S. Department of Energy under Contract No. DE-AC02-05CH1123, by the National Energy Research Scientific Computing Center, a DOE Office of Science User Facility under the same contract; and by the U.S. National Science Foundation, Division of Astronomical Sciences under Contract No. AST-0950945 to NOAO.

References

Abell, G. O., Corwin, Harold G., J., & Olowin, R. P. 1989, ApJS, 70, 1

Bahcall, N. A., McKay, T. A., Annis, J., et al. 2003, ApJS, 148, 243

Bartelmann, M., Meneghetti, M., Perrotta, F., Baccigalupi, C., & Moscardini, L. 2003, A&A, 409, 449

Boldrin, M., Giocoli, C., Meneghetti, M., et al. 2016, MNRAS, 457, 2738

D'Aloisio, A. & Natarajan, P. 2011, MNRAS, 415, 1913

Euclid Collaboration, Scaramella, R., Amiaux, J., et al. 2022, A&A, 662, A112

Fox, C., Mahler, G., Sharon, K., & Remolina González, J. D. 2022, ApJ, 928, 87

Giocoli, C., Meneghetti, M., Ettori, S., & Moscardini, L. 2012, MNRAS, 426, 1558

Kelly, P. L., Rodney, S. A., Treu, T., et al. 2015, Science, 347, 1123

Li, G. L., Mao, S., Jing, Y. P., et al. 2006, MNRAS, 372, L73

Meneghetti, M., Bartelmann, M., Dahle, H., & Limousin, M. 2013, Space Sci. Rev., 177, 31

Oguri, M., Hennawi, J. F., Gladders, M. D., et al. 2009, ApJ, 699, 1038

Racca, G. D., Laureijs, R., Stagnaro, L., et al. 2016, in Society of Photo-Optical Instrumentation Engineers (SPIE) Conference Series, Vol. 9904, Space Telescopes and Instrumentation 2016: Optical, Infrared, and Millimeter Wave, ed. H. A. MacEwen, G. G. Fazio, M. Lystrup, N. Batalha, N. Siegler, & E. C. Tong, 99040O

Wambsganss, J., Ostriker, J. P., & Bode, P. 2008, ApJ, 676, 753

Wen, Z. L. & Han, J. L. 2022, MNRAS, 513, 3946
Wyithe, J. S. B., Turner, E. L., & Spergel, D. N. 2001, ApJ, 555, 504

SF2A 2023
M. N'Diaye, A. Siebert, N. Lagarde, O. Venot, K. Baillié, M. Béthermin, E. Lagadec, J. Malzac, J. Richard (eds)

THE COSMOLOGICAL POTENTIAL OF HIGH-REDSHIFT CLUSTERS WITH DEEP X-RAY SURVEYS

N. Cerardi[1], M. Pierre[2], P. Valageas[3] and C. Garrel[4]

Abstract.

Since 2022, the ATHENA mission, selected in the ESA's Cosmic Vision Program, is undergoing a deep redefinition process due to budgetary constraints. However, in its current scope, this X-ray satellite is poised to unveil the high-z population of galaxy clusters with an unprecedented sensitivity compared to current telescopes. The high redshift population of clusters is a key lever arm to understand the evolution of dark energy - a goal that is complementary to many upcoming ground and space-based extragalactic surveys.

We consider two surveys designs to be carried out by the Wide Field Imager (WFI) of ATHENA, deriving simplified selection functions for both cases. Up to $z \sim 2$, we expect to recover thousands of clusters down to the low-mass (group) scale. We then perform a forward modelling of the theoretical cluster number counts into X-ray observable diagrams. We present cosmological forecasts for different cosmologies, emphasising the detection of high-z clusters will be crucial in obtaining independent constraints on dark energy. Such measurements with X-ray selected samples will only be possible with the launch of ATHENA in the 2030s.

Keywords: X-ray: galaxies: clusters, Cosmological parameters, Fisher forecasts

1 Introduction

At both early and late times, open questions remain in cosmology and challenge the standard cosmological model, namely ΛCDM. The recent and upcoming observatories (such as eROSITA, JWST, Euclid, Vera Rubin, CMB-S4...) are poised to bring a physical understanding on the natures of Dark Matter and Dark Energy (DE), as well as studying the inflation era.

Clusters of galaxies lie on the nodes of the cosmic web and as such are tracers of both the expansion of the Universe and the growth of structures. Therefore they naturally appear as cosmological probes, either through their number counts, their spatial clustering, or their gas fraction. The Halo Mass Function (HMF), used in number counts studies is particularly sensitive to Ω_m and σ_8 (see for instance Garrel et al. 2022). At high redshift, the sensitivity of the cluster population to the DE Equation of State (EoS) and to primordial non Gaussianities is increased (Majumdar & Mohr 2004; LoVerde et al. 2008). Galaxy cluster samples so far are restricted to the most massive end of the distribution, or to low-redshifts ($z < 1$). The next generation X-ray telescope ATHENA, to be launched in the late 2030s, is expected to reach unprecedented sensitivity. It will carry onboard a Wide Field Imager (WFI, Meidinger et al. 2017), able to run deep extragalactic X-ray surveys.

This study presents the forecasts for deep X-ray surveys achievable by ATHENA/WFI. We derive analytical selection functions and forecast the number of clusters to be detected. We furthermore study the cosmological potential of such samples by running a Fisher analysis, for the DE EoS and primordial non-Gaussianities. This work is extensively developped in Cerardi et al., 2023 (submitted).

[1] Université Paris Cité, Université Paris-Saclay, CEA, CNRS, AIM, F-91191, Gif-sur-Yvette, France
[2] Université Paris-Saclay, Université Paris Cité, CEA, CNRS, AIM, 91191, Gif-sur-Yvette, France
[3] Institut de Physique Théorique, Université Paris-Saclay, CEA, CNRS, F-91191 Gif-sur-Yvette Cedex, France
[4] Max Planck Institute for Extraterrestrial Physics, Giessenbachstrasse 1, D-85748 Garching, Germany

© Société Française d'Astronomie et d'Astrophysique (SF2A) 2023

Survey	Area (deg^2)	Depth (ks)	Nb of clusters in $0 < z < 2$	Nb of clusters in $1 < z < 2$
A	50	80	5500	940
B	200	20	11200	1400

Table 1. Survey designs modelled in this work. A and B share the same total exposure time ($\approx 9Ms$ for ATHENA/WFI).

2 Cluster population modelling

2.1 Cosmology

To model the cluster population, we take as fiducial cosmology the flat ΛCDM model with the values of Planck Collaboration et al. (2020). As ATHENA will operate in the late 2030s, we give Planck priors on h, Ω_b and n_s. We also want to test the constraining power of ATHENA on extensions of the standard model. In a first case, we write the DE EoS in the form $p/(\rho c^2) = w(a) = w_0 + w_a(1-a)$. In a second case, we consider deviations from Gaussianity in the primordial perturbation field. We focus here on non-Gaussianities of the local type, where the Bardeen potential is then expressed at lowest order with a quadratic term, parametrized by : $\Phi(x) = \phi(x) + f_{NL}^{loc}\left[\phi(x)^2 - \langle\phi\rangle^2\right]$. ϕ is a Gaussian field and f_{NL}^{loc} captures the amplitude of the non-Gaussian deviation. Followingly, cluster abundance is modelled following the HMF from Tinker et al. (2008).

2.2 Scaling relations

To convert the cluster mass* into ICM luminosity and temperature, we use the scaling relations formalism derived from XXL with HSC (Hyper Suprime-Cam) weak-lensing masses. We keep the slopes of the $T-M$ and $L-M$ fits from Sereno et al. (2020). The evolution parameters are set to self similarity, and the normalisations are refitted alone on the XXL C1 catalogue to ensure that (i) we recover the correct C1 number counts and (ii) it compensates for the weak-lensing mass bias.

We then transform the luminosity and temperature properties into count-rates, we assume throughout our study that the sensitivity of the ATHENA/WFI is equivalent to be five times that of XMM/EPIC(pn+mos1+mos2). We use the APEC model with the AtomDB database (Smith et al. 2001), and the response files of XMM/EPIC instruments to obtain the count-rate (CR) in the band [0.5–2] keV and the hardness-ratio (HR), the ratio of the count-rates in [1–2] keV and in [0.5–1] keV.

3 Detected cluster population

We then consider two survey designs that share the same exposure time ∼9 Ms. The first one, survey A, spans 50 deg^2 with a depth of 80ks, and the second one, survey B, is 4 times wider but 4 times shallower. In the band of interest, the particle background is assumed to be 2.5×10^{-7} c/s/arcsec^2, and the diffused X-ray backround is assumed to be the XMM one scaled to the ATHENA sensitivity: 4.08×10^{-6} c/s/arcsec^2. We then compute the completeness for both surveys, assuming that we detect clusters with a S/N ≥ 5 in a fixed aperture.

The so-defined selection functions are represented in the left panel of figure 1. At $z > 1$, ATHENA will detect clusters down to $2\times10^{13}\mathrm{h}^{-1}\mathrm{M}_\odot$ ($3.5\times10^{13}\mathrm{h}^{-1}\mathrm{M}_\odot$) for survey A (survey B), a population that will remain unprobed until ATHENA is launched. Combined with our fiducial cosmology, we can then forecast the expected number counts. The total numbers are given in table 1, and the right panel in figure 1 shows the distribution of these population as a function of redshift.

4 Cosmological forecasts

We derive cosmological forecasts for surveys A and B using a Fisher analysis. Assuming that the observations (i) are independant and (ii) follow a Poisson distribution, we can compute the Fisher matrix terms by :

$$F_{\alpha\beta} = \sum_i \frac{1}{\lambda_i}\frac{\partial\lambda_i}{\partial\theta_\alpha}\frac{\partial\lambda_i}{\partial\theta_\beta} \tag{4.1}$$

*here defined as $M_{500c} = 4\pi R_{500c}^3 500\rho_c/3$

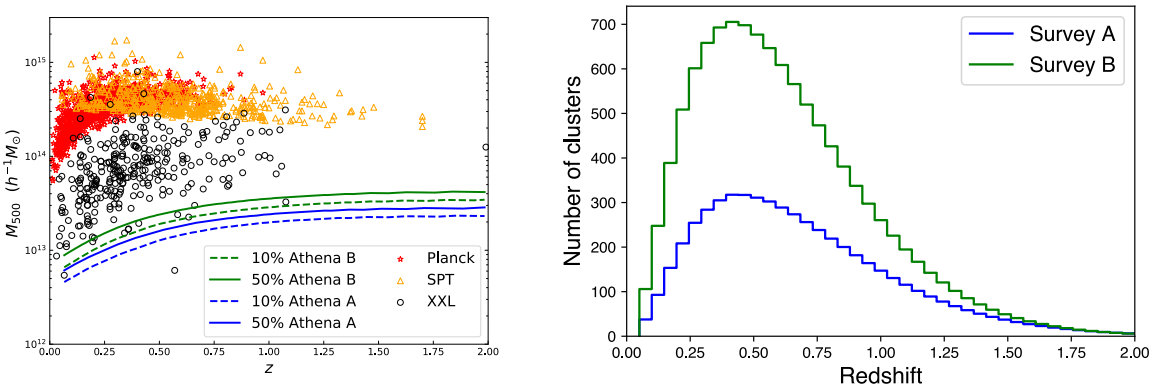

Fig. 1. Left: Mass detection limit for surveys A and B. The plain (dashed) lines represent the 50% (10%) detection limit in the $M_{500c} - z$ plane. A given cluster with mass above (resp. below) a line have a detection probability higher (resp. lower) than 50% in the corresponding survey design. The circles, stars and triangles denotes cluster samples from XXL (Adami et al. 2018), Planck SZ (Planck Collaboration et al. 2016) and SPT (Bleem et al. 2015), respectively. **Right:** Number counts for surveys A and B. Survey A has a density of clusters that is about twice the density in B, but the effect of the survey area dominates and B detects twice as many clusters as A (11200 vs 5500).

case	survey	$\Delta\Omega_m$	$\Delta\sigma_8$	Δw_0	Δw_a	Δf_{NL}
w_zCDM	A	0.025	0.015	0.32	1.25	
	B	0.016	0.0091	0.22	0.87	
Local primordial non Gaussianity	A	0.014	0.038			470
	B	0.0094	0.025			310

Table 2. Constraints derived from the Fisher analysis. 9 supplementary parameters (h, Ω_b, n_s, α_{TM}, β_{TM}, γ_{TM}, α_{LM}, β_{LM}, γ_{LM}) are included in the analysis and marginalised. The results quoted are the 1σ uncertainties, in $0.05 < z < 2$.

Inversing the Fisher matrix gives access to the covariance, hence the best achievable constraints. We always include in our analysis five cosmological parameters: Ω_m, σ_8, h, Ω_b, n_s; and 6 parameters of the T-M and L-M scaling relations: α_{TM}, β_{TM}, γ_{TM}, α_{LM}, β_{LM}, γ_{LM}. Given that Ω_m and σ_8 strongly influence cluster abundances, these parameters have no prior. We then provide cosmological forecasts either for the w_zCDM scenario, adding w_0 and w_a; or with primordial local non Gaussianities and the parameter f_{NL}^{loc}.

4.1 Forecasted constraints for surveys A and B

In table 2 we present the results of the Fisher analysis for each survey and each cosmological test. The results are marginalised over h, Ω_b, n_s and the scaling relations parameters. Thanks to its larger statistics, survey B outperforms survey A in all scenarii by a factor ≈1.4.

4.2 Impact of the high redshift counts

We now study the contribution of clusters at $z > 1$ in the analysis. We here focus on survey B as it is the most powerful survey, as seen in the previous section. We operate successives redshift-truncated analysis, as shown in figures 2 and 3, respectively for w_zCDM and local primordial non-gaussianities. In each panel, the outer-most ellipse encompasses $0.05 < z < 1$. The inner ellipses sequentially include the 5 remaining bins in the Fisher analysis. In each configuration, we observe that high-z bins induce a tilt of the ellipse, reducing the uncertainty for these parameters. Clusters at $z > 1$ only represents $\sim 15\%$ of the total sample, so that their statistical effect is not dominant. However, they help to break the degeneracy between parameters within the cluster abundance analysis for $z < 1$. This effect is very strong in the plane w_0–w_a: Δw_a shrinks by a factor ∼2.3. The same trend is observed for local primordial non-Gaussianities: clusters in $1 < z < 2$ improve the constraints on f_{NL}^{loc} by a factor ~ 2.6.

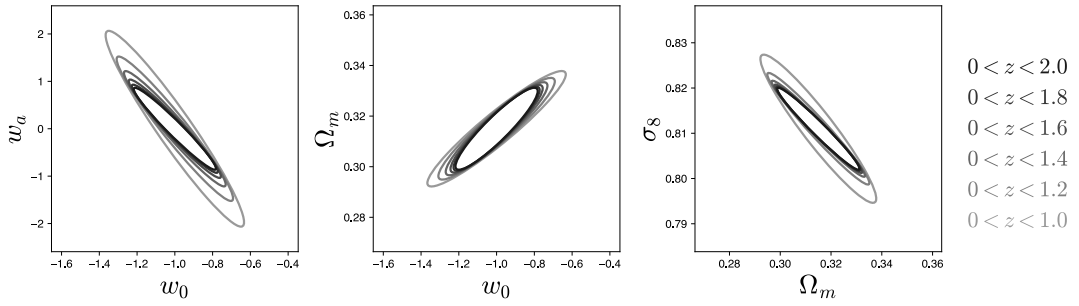

Fig. 2. w_zCDM

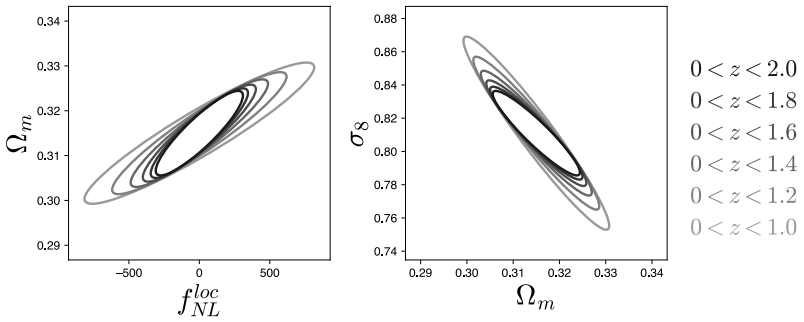

Fig. 3. Local primordial non Gaussianities

5 Conclusions

We studied the potential of high redshift clusters with deep X-ray surveys to be achieved by an ATHENA-like observatory. For two different survey designs, we derived selection functions and expected number counts for these surveys. The detected clusters populate a range of mass and redshift unprecedented with X-ray telescopes, up to $z \sim 2$. They contain critical cosmological information and breaks the degeneracy between parameters. High-redshift clusters are hence shown to be a very important component of the DE investigations. Their detection will require a powerful X-ray telescope of new generation such as ATHENA.

References

Adami, C., Giles, P., Koulouridis, E., et al. 2018, Astronomy & Astrophysics, 620, A5, arXiv:1810.03849 [astro-ph]

Bleem, L. E., Stalder, B., de Haan, T., et al. 2015, The Astrophysical Journal Supplement Series, 216, 27, arXiv:1409.0850 [astro-ph]

Garrel, C., Pierre, M., Valageas, P., et al. 2022, Astronomy & Astrophysics, 663, A3, arXiv:2109.13171 [astro-ph]

LoVerde, M., Miller, A., Shandera, S., & Verde, L. 2008, Journal of Cosmology and Astroparticle Physics, 2008, 014, arXiv:0711.4126 [astro-ph]

Majumdar, S. & Mohr, J. J. 2004, The Astrophysical Journal, 613, 41, publisher: IOP Publishing

Meidinger, N., Eder, J., Eraerds, T., et al. 2017, The Wide Field Imager Instrument for Athena, arXiv:1702.01079 [astro-ph]

Planck Collaboration, Ade, P. A. R., Aghanim, N., et al. 2016, Astronomy & Astrophysics, 594, A27, arXiv:1502.01598 [astro-ph]

Planck Collaboration, Aghanim, N., Akrami, Y., et al. 2020, Astronomy & Astrophysics, 641, A6, arXiv:1807.06209 [astro-ph]

Sereno, M., Umetsu, K., Ettori, S., et al. 2020, Monthly Notices of the Royal Astronomical Society, 492, 4528, arXiv:1912.02827 [astro-ph]

Smith, R. K., Brickhouse, N. S., Liedahl, D. A., & Raymond, J. C. 2001, The Astrophysical Journal, 556, L91, publisher: IOP Publishing

Tinker, J. L., Kravtsov, A. V., Klypin, A., et al. 2008, The Astrophysical Journal, 688, 709, arXiv:0803.2706 [astro-ph]

SF2A 2023
M. N'Diaye, A. Siebert, N. Lagarde, O. Venot, K. Baillié, M. Béthermin, E. Lagadec, J. Malzac, J. Richard (eds)

A UNIONS VIEW OF THE BRIGHTEST CENTRAL GALAXIES OF CANDIDATE FOSSIL GROUPS

A. Chu[1], F. Durret[1], A. Ellien[2], F. Sarron[3], C. Adami[4], I. Marquez[5], N. Martinet[4], T. de Boer[6], K. C. Chambers[6], J.-C. Cuillandre[7], S. Gwyn[8], E.A. Magnier[6], and A. W. McConnachie[8]

Abstract.

The formation process of fossil groups (FGs) is still under debate, and large samples of such objects are missing. With the aim to increase the sample of known FGs, analyse the properties of their brightest group galaxies (BGGs), and compare them with a control sample of non-FG BGGs, we extracted a sample of 87 FG and 100 non-FG candidates from a large spectroscopic catalogue. For all the objects with data available in UNIONS (initially the Canada France Imaging Survey, CFIS) in the u and r bands, and/or in an extra r-band processed to preserve all low-surface-brightness features (rLSB), we performed a 2D photometric fit of the BGG with GALFIT with one or two Sérsic components. We also analysed how the subtraction of the intracluster light (ICL) contribution modifies the BGG properties. From the SDSS spectra available for the BGGs of 65 FGs and 82 non-FGs, we extracted the properties of their stellar populations with Firefly.

We find that morphologically, a single Sérsic profile can fit most objects in the u band, while two Sérsics are needed in the r and rLSB bands, both for FGs and non-FGs. Non-FG BGGs cover a larger range of Sérsic index n. FG BGGs follow the Kormendy relation (mean surface brightness versus effective radius) previously derived for almost 1000 brightest cluster galaxies (BCGs), while the majority of non-FG BGGs are located below this relation, with fainter mean surface brightnesses. This suggests that FG BGGs have evolved similarly to BCGs, while non-FG BGGs have evolved differently. The above properties can be strongly modified by the subtraction of the ICL contribution. On the other hand, based on spectral fitting, the stellar populations of FG and non-FG BGGs do not differ significantly.

Keywords: fossil groups, brightest group galaxies

1 Introduction

Fossil groups (FGs) were discovered by Ponman et al. (1994). They are particular groups of galaxies with high X-ray luminosities but with fewer bright galaxies than most groups or clusters of galaxies. Jones et al. (2003) later provided a commonly accepted definition of FGs based on three conditions: their X-ray luminosity is at least $L_X = 10^{42}\ h_{50}^{-2}$ erg s^{-1}, their brightest group galaxy (BGG) is two magnitudes brighter than other group members, and the distance between the two brightest galaxies is smaller than half the group virial radius. The formation mechanism of FGs is still under debate: they can be the remnants of early mergers, or be a short temporary stage of group evolution.

Adami et al. (2020) carried out a statistical study of FGs, based on photometric redshifts, and concluded that FGs were most probably in a poor environment. Several studies have shown that the role of the BGG is

[1] Sorbonne Université, CNRS, UMR 7095, Institut d'Astrophysique de Paris, 98bis Bd Arago, 75014, Paris, France
[2] Anton Pannekoek Institute for Astronomy & GRAPPA, University of Amsterdam, Science Park 904, 1098 XH Amsterdam, The Netherlands
[3] IRAP, Institut de Recherche en Astrophysique et Planétologie, Université de Toulouse, UPS-OMP, CNRS, CNES, 14 avenue E. Belin, F-31400 Toulouse, France
[4] Aix-Marseille Univ., CNRS, CNES, LAM, Marseille, France
[5] Instituto de Astrofísica de Andalucía, CSIC, Glorieta de la Astronomía s/n, 18008, Granada, Spain
[6] Institute for Astronomy, University of Hawaii, 2680 Woodlawn Drive, Honolulu HI 96822, USA
[7] Université Paris-Saclay, Université Paris Cité, CEA, CNRS, AIM, 91191, Gif-sur-Yvette, France
[8] Herzberg Astronomy and Astrophysics, National Research Council, 5071 West Saanich Road, Victoria, BC, Canada, V9E2E7

© Société Française d'Astronomie et d'Astrophysique (SF2A) 2023

crucial to explain the lack of bright galaxies in FGs. We gathered a large sample of candidate FGs from the groups detected by Tinker* from SDSS data, aiming to increase the number of known FGs, analyse the physical properties of the BGGs of FGs and compare them to those of non-FGs and clusters.

2 The sample, data and method

Tinker has made catalogues available that contain data for 559,038 galaxies, providing positions, spectroscopic redshifts from the SDSS survey, k-corrected and evolution-corrected (to z=0.1) g and r band absolute magnitudes, galaxy stellar masses, and total halo masses. For each galaxy, the group to which it belongs is indicated.

We eliminated all the galaxies that were alone in a group and obtained a catalogue of 201,007 galaxies that were at least in a pair. We then selected the galaxies belonging to groups where the magnitude difference in the r band between the brightest and second-brightest galaxy was at least 2 mag, and for which the distance between these two galaxies was smaller than half the virial radius, r_{vir}. We thus obtained a catalogue of 2453 galaxies.

From the above catalogue, we extracted a list with the brightest galaxy of each group, and this led to a catalogue of 1112 galaxies that may be considered as BGGs. This means that most groups were made of pairs. In order to avoid considering objects that could not be real groups, such as isolated galaxies with a few small satellites, we added a condition on the halo mass: $M_{halo} > 10^{13}$ $M_{\odot}$, giving 87 FG candidates. We note that for most of these FGs we have no X-ray information, so they are FG candidates.

In order to compare the properties of BGGs of FGs with those of non-FGs, we built a catalogue of non-FGs in a similar way, but imposing a magnitude difference between the brightest and second-brightest galaxies smaller than 2. This condition, together with that of $M_{halo} > 10^{13}$ $M_{\odot}$, gave 100 non-FG candidates.

Most of the FGs are in the [0.02,0.12] redshift range, with only five FGs in the [0.12,0.18] range.

We searched for images of the 87 FG candidates in the UNIONS image database (DR3) in the u and r bands. Images were retrieved from the DR3. We found images for 35 FGs in the u band and for 25 FGs in the r band, among which 12 FGs having both u and r band images. We also retrieved UNIONS images in the u, r, and rLSB bands for a subsample of 30 non-FGs.

Chu et al. (2022) showed that subtracting the contribution of intracluster light (ICL) could modify the properties derived for BCGs. Therefore, with the aim of estimating how subtracting the ICL could modify the properties derived for the BGG, we also exploited the r band images processed to preserve all low-surface-brightness (LSB) features (hereafter referred to as rLSB). These images were obtained using an observing technique that is optimised for LSB surveys at CFHT.

The 2D profile of each BGG was fit with GALFIT (Peng et al. 2002) with a single Sérsic model and with a double Sérsic model. GALFIT initial parameters were obtained with SExtractor using a bulge + disk model. A mask and a point spread function were created following the method described in Chu et al. (2021). The choice between a single and double Sérsic model was made based on the statistical F-test (Margalef-Bentabol et al. 2016) and the computed p-value, which indicates whether or not complexifying the model is necessary by increasing the number of degrees of freedom. As the current sample has the same resolution as that of Chu et al. (2022), we adopt the same p-value limit to distinguish between the two different models: $P_0 = 0.15$.

3 Morphological properties of the BGGs

Table 1. 2D profile model distribution of BGGs of FGs and non-FGs.

	FG				Non-FG			
	u	r	rLSB	rLSB-ICL	u	r	rLSB	rLSB-ICL
One-Sérsic	29	2	9	3	27	6	14	6
Two-Sérsic	6	23	10	16	3	24	16	24

The numbers of BGGs of FGs and non-FGs for which one Sérsic law (S1) or two Sérsic laws (S2) are needed to fit their 2D profiles in the various bands are given in Table 1. For FGs, we can see that in the u band, most BGGs can be fit with a single Sérsic (83%). In contrast, a major part of the profiles in the r band require two

*https://www.galaxygroupfinder.net/catalogs

components (92%). If we now consider the BGGs from the rLSB data, only 53% require two Sérsics. Comparable results are obtained for non-FG BGGs, and the difference between FGs and non-FGs is not significant in view of the dispersion.

We computed the ICL contribution and subtracted it from the BGGs to see how the Sérsic parameters changed. If we look at Table 1, we can see that only 3 FG BGGs out of 19 (16%) can be fit with a single Sérsic, and for non-FG BGGs, 6 out of 30 BGGs (20%) are fit with a single Sérsic. The subtraction of the ICL contribution therefore does not make the second Sérsic component disappear, as already observed by Chu et al. (2022). Unexpectedly, we find more BGGs of FGs and non-FGs that are better modelled by two-Sérsic profiles on ICL-subtracted rLSB images than on rLSB images.

The only clear difference that we find between the physical properties of FGs and non-FGs is that FG BGGs are intrinsically brighter. This may be due to a selection bias, as our sample of FG BGGs is overall brighter than our sample of non-FG BGGs, but may indicate that, in a given group-mass range, FG BGGs are indeed brighter and most of the mass of the group is concentrated in the BGG.

A full discussion of these properties can be found in Chu et al. (2023).

4 Kormendy relation

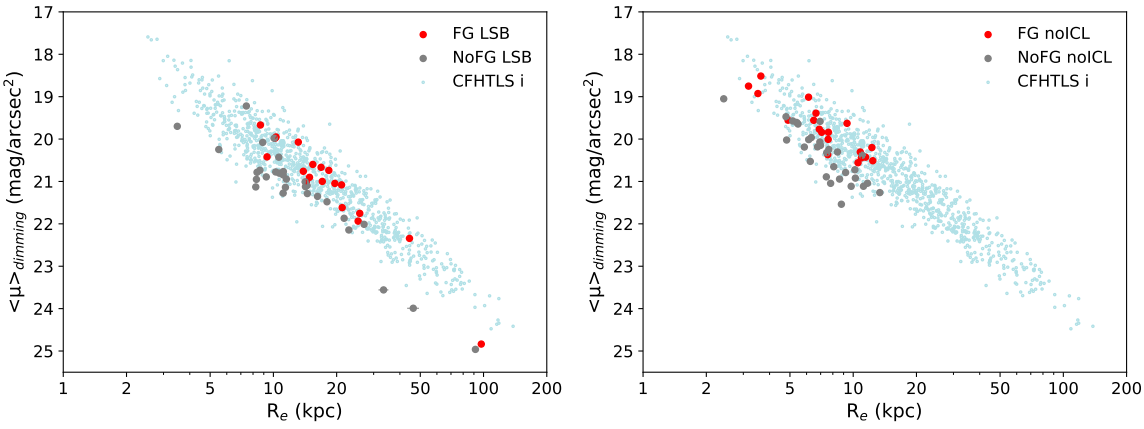

Fig. 1. Kormendy relation for FGs in red and Non-FGs in grey, superimposed on the relation found for almost one thousand BCGs by Chu et al. (2022) in cyan. Both plots are obtained in the rLSB band, the left plot without ICL subtraction and the right plot after ICL subtraction. The points for FGs and non-FGs have been shifted from the r to the i band, and all points are corrected for cosmological dimming.

We now consider the relation found by Kormendy (1977) (mean effective brightness $< \mu >$ as a function of effective radius R_e), which can be fit with the following law:

$$< \mu >= (a \pm \sigma_a) \times log(R_e) + (b \pm \sigma_b).$$

We find the dispersion to be smaller for FGs than for non-FGs in all bands, and the relations in u and r are parallel within the dispersion. With the exception of the rLSB band, the slopes are larger for non-FGs than for FGs, but in view of the dispersion this difference is not significant.

If we compare the Kormendy relations found here for FGs and non-FGs to those of Chu et al. (2022), we see that FGs are located on this relation, while the majority of non-FGs are located below the relation, and this is true both before and after ICL subtraction.

The BGGs of FGs appear to have properties more similar to those of BCGs than to those of non-FG BGGs, suggesting that BGGs in FGs and BCGs have followed a comparable evolutionary path, while non-FGs have evolved somewhat differently, reaching fainter surface brightnesses.

5 Influence of the ICL contribution

We compared the values of the various physical parameters galaxy by galaxy before and after ICL subtraction. The ICL contribution was estimated with `DAWIS` (Detection Algorithm with Wavelets for Intracluster light

Studies; Ellien et al. 2021), a wavelet-based algorithm optimised for the detection and characterisation of LSB structures in deep optical images.

For FGs, we find that the ICL increases the effective radius by a mean factor of 3.7, and the ICL adds light to the BGG by up to 1.3 mag. With ICL, the mean surface brightness can be up to 5 mag arcsec^{-2} brighter, with a mean at 1.3, and the Sérsic index n tends to be larger (by 2.8 on average). There seems to be a bimodality in the Sérsic index histogram. The peak at $n < 2$ comes from BGGs that were better modelled with two Sérsic profiles before and after ICL subtraction, and the peak at $n > 3$ originates from 1-Sérsic profile BGGs on LSB images that become 2-Sérsic BGGs after ICL subtraction.

For non-FGs, the ICL increases the effective radius by a mean factor of 2.4 and the absolute magnitude with ICL is up to 1.2 mag brighter. The mean surface brightness before subtraction of the ICL can be up to 1.2 mag arcsec^{-2} fainter, with a mean of about 0.8, and the Sérsic index n tends to be larger with ICL, with a large dispersion from one BGG to another.

When the ICL is subtracted, the Sérsic index distributions become comparable for FGs and non-FGs, and the distributions of the properties of BGGs obtained for FGs and non-FGs after ICL subtraction become more comparable to those measured in the r filter.

We can note that BGGs on r images appear bigger, brighter, with fainter mean surface brightnesses and higher Sérsic indices than on rLSB-ICL images. This illustrates the fact that ICL somewhat modifies the apparent morphological properties, and that its contribution should be carefully subtracted before analysing the physical properties of BCGs and BGGs, as already underlined by Chu et al. (2022).

6 Stellar populations of BGGs

We retrieved the spectra of the FG and non-FG BGGs of our sample in the SDSS. Among the 87 FGs, 9 spectra were not available, leaving us with 78 BGGs. Among the 100 non-FGs, 4 spectra were not available, and so we analysed 96 spectra. We fit these spectra with Firefly (Wilkinson et al. 2017) and eliminated the spectra corresponding to AGN as classified by the SDSS: 13 in FGs and 14 in non-FGs. This was done because it is difficult to extract stellar populations from spectra dominated by an AGN. The AGN fractions are very similar between BGGs of FGs and non-FGs, namely 20% and 17%, respectively. We were therefore left with 66 FG BGG and 82 non-FG BGG spectra. As Wilkinson et al. (2017) showed that Kroupa and Salpeter IMFs gave comparable results, we limited our analysis to a Kroupa IMF. We used the STELIB and MILES stellar libraries to estimate the robustness of our results.

We find that 76% and 71% of the total stellar mass of FG and non-FG BGGs, respectively, was already formed 8 Gyr ago based on the STELIB library. These percentages become 61% and 66% for the MILES library. These results agree with the fact that BGGs of FGs and non-FGs have very similar colours. The stellar populations of FG and non-FG BGGs cannot be distinguished with this relatively straightforward analysis.

7 Conclusions

Although the morphological properties of FG and non-FG BGGs somewhat differ, FG BGGs having properties comparable to those of cluster BCGs, their stellar populations do not. We emphasize the importance of taking into account the ICL contribution when analysing the morphological properties of BCGs.

References

Adami, C., Sarron, F., Martinet, N., & Durret, F. 2020, A&A, 639, A97
Chu, A., Durret, F., Ellien, A., et al. 2023, A&A, 673, A100
Chu, A., Durret, F., & Márquez, I. 2021, A&A, 649, A42
Chu, A., Sarron, F., Durret, F., & Márquez, I. 2022, A&A, 666, A54
Ellien, A., Slezak, E., Martinet, N., et al. 2021, A&A, 649, A38
Jones, L. R., Ponman, T. J., Horton, A., et al. 2003, MNRAS, 343, 627
Kormendy, J. 1977, ApJ, 218, 333
Margalef-Bentabol, B., Conselice, C. J., Mortlock, A., et al. 2016, MNRAS, 461, 2728
Peng, C. Y., Ho, L. C., Impey, C. D., & Rix, H.-W. 2002, The Astronomical Journal, 124, 266
Ponman, T. J., Allan, D. J., Jones, L. R., et al. 1994, Nature, 369, 462
Wilkinson, D. M., Maraston, C., Goddard, D., Thomas, D., & Parikh, T. 2017, MNRAS, 472, 4297

SF2A 2023
M. N'Diaye, A. Siebert, N. Lagarde, O. Venot, K. Baillié, M. Béthermin, E. Lagadec, J. Malzac, J. Richard (eds)

STUDYING GALAXY AND HOT GAS INTERACTIONS THROUGH CROSS-CORRELATIONS OF THE THERMAL SUNYAEV-ZELDOVICH EFFECT AND GALAXY SURVEYS

R. Kou[1] and J. Bartlett[1]

Abstract. In addition to dark matter, massive halos also contain galaxies and hot gas. These latter two components interact and influence each other. On the one hand, galaxies and stars therein form from gas, cooling towards the halo center. On the other hand, galaxies also influence the gas dynamics through a number of feedback processes, including stellar radiation, supernovae, and AGN feedback. In order to study these feedback processes and to understand the effect of the environment (mainly the gas thermodynamics) on the galaxy stellar population, it is useful to measure the joint distribution of galaxies and hot gas. In our study, we cross-correlate the thermal Sunyaev-Zeldovich (tSZ) map provided by the Planck satellite with the CMASS galaxy sample from BOSS. Binning galaxies on stellar mass, we can more finely study the interactions between gas and galaxies. Making use of the halo model formalism, we model the gas distribution inside galaxy halos and determine how its pressure depends on galaxy stellar mass. We find a hint that the gas pressure decreases slightly in the vicinity of the most massive galaxies, which could help to constrain feedback models.

Keywords: cosmology, Sunyaev-Zeldovich, galaxies, gas, cosmic microwave background

1 Introduction

The large-scale structure of the Universe is organized through a set of halos and filaments which form through the gravitational collapse of dark matter. The gas distribution then follows the underlying dark matter field, as do galaxies, which form in dark matter halos. The galaxy and gas distributions are closely linked to each other since galaxies (and their stellar populations) form from the cooling of gas in the dark matter halos. Moreover, after a galaxy has formed, there are many interactions between the stars and the gas therein, so that the gas dynamics is also affected by the processes occurring in the galaxy. Those processes are referred to as "feedback" effects and include gas ionization and ejection due to stellar radiation, supernovae and Active Galactic Nuclei (AGN) feedback. In our study, we aim at probing the joint distribution of galaxies and gas and at providing clues about whether the gas dynamics depends on the host galaxy's stellar population. We study galaxy and hot gas interactions through the cross-correlation of the thermal Sunyaev-Zeldovich (tSZ) effect and a galaxy survey. Section 2 presents the data that we use and how the measurements are performed. We then describe our modeling in Sect. 3. Finally, we present and discuss the results in Sect. 4.

2 Data and Measurements

2.1 The galaxy catalog

We use the CMASS galaxy sample (Alam et al. 2015), which is a subsample of the BOSS survey and released in the Sloan Digital Sky Survey's data release 12. In order to study the impact of stellar population on the galaxy and gas distributions, we define four subsamples from CMASS defined by stellar mass thresholds: $\log M_*/M_\odot > 10.8$, $\log M_*/M_\odot > 11.1$, $\log M_*/M_\odot > 11.25$, and $\log M_*/M_\odot > 11.4$. Note that these are all very high stellar masses, as CMASS was constructed with approximately constant (and actually high) stellar

[1] Université Paris Cité, CNRS, Astroparticule et Cosmologie, F-75013 Paris, France

© Société Française d'Astronomie et d'Astrophysique (SF2A) 2023

masses. The stellar masses estimates that we use come from the Portsmouth stellar population synthesis code (Maraston et al. 2013), which fits the observed galaxy spectral energy distributions.

The catalogs are then turned into *HEALPix*[*] (Górski et al. 2005; Zonca et al. 2019) maps, applying weights to take into account a number of observational effects, as described in Anderson et al. (2014).

2.2 The tSZ map

The hot gas distribution can be studied thanks to the tSZ effect, which is a distortion of the CMB spectrum due to the interaction of CMB photons with energetic electrons in the hot, ionized intra-halo gas (circumgalactic medium, or CGM). In this study, we use the Compton-y parameter map provided by Planck Collaboration et al. (2016) in the 2015 *Planck* data release.

2.3 Power spectra estimation

For each galaxy subsample, we estimate its power spectrum and its cross-spectrum with the Compton-y map. In the case of full sky coverage, the cross-correlation of two maps a and a' can be estimated using,

$$C_\ell^{aa'} = \frac{1}{2\ell+1} \sum_{m=-\ell}^{\ell} a_{\ell m} a'^{*}_{\ell m}, \tag{2.1}$$

where $a_{\ell m}$ denotes the coefficients of the spherical harmonic decomposition of map a and the asterisk indicates complex conjugation. However, in practice we do not observe the full sky, which introduces a mixing between the multipoles. This is taken into account by the *NaMaster*[†] code from Alonso et al. (2019), that we use for the estimation of the auto and cross-correlation power spectra.

Finally, we subtract the shot noise from the galaxy power spectra (no noise needs to be removed for the cross-correlations since the noise in the galaxy and Compton-y maps is not correlated), correct for the cosmic infrared background contamination, and estimate a Gaussian covariance matrix, all as described in more detail in Kou & Bartlett (2023).

3 Modeling

3.1 Line-of-sight projection

Using the Limber approximation (Limber 1953), the angular power spectra can be modeled as line-of-sight integrals over redshift, z:

$$C_\ell^{AB} = \int \frac{dz}{c} \frac{H(z)}{\chi(z)^2} W_A(z) W_B(z) P^{AB}\left(k = \frac{\ell}{\chi(z)}, z\right), \tag{3.1}$$

where H is the Hubble function, c is the speed of light, χ is the comoving distance, P^{AB} is the three-dimensional power spectrum of tracers A and B, and W_A and W_B are the kernels for the different probes. For the galaxies and the Compton-y parameter, those kernels are,

$$W_g(z) = \frac{1}{n_{\rm tot}} \frac{dn}{dz} \tag{3.2}$$

$$W_y(z) = \frac{1}{1+z}, \tag{3.3}$$

with $\frac{dn}{dz}$ the galaxy redshift distribution and $n_{\rm tot}$ the total number of galaxies in the sample.

[*] http://healpix.sf.net
[†] https://github.com/LSSTDESC/NaMaster

3.2 Halo model

The three-dimensional power spectrum, P^{AB}, is modeled using the halo model formalism (for a review, see Cooray & Sheth 2002). In this model, all matter, galaxies and gas are assumed to reside in dark matter halos. The dark matter distribution is then described by two main quantities: the halo mass function and the halo bias, for which we use functions derived from numerical simulations (Tinker et al. 2008, 2010). Once the dark matter distribution is (statistically) fixed, we need to describe how galaxies and gas populate the halos.

3.2.1 Halo Occupation Distribution (HOD)

We split galaxies between centrals and satellites and use the following HOD modeling (Zheng et al. 2005),

$$\langle N_{\rm c}|M\rangle = \frac{1}{2}\left[1+\mathrm{erf}\left(\frac{\log M-\log M_{\rm min}}{\sigma_{\log M}}\right)\right] f_{\rm inc}(M) \tag{3.4}$$

$$\langle N_{\rm s}|M\rangle = \langle N_c|M\rangle \left(\frac{M-M_0}{M_1}\right)^{\alpha_g} \mathcal{H}(M>M_0), \tag{3.5}$$

where $\langle N_{\rm c}|M\rangle$ (resp. $\langle N_{\rm s}|M\rangle$) is the number of central (resp. satellite) galaxies in a halo of mass M, $\mathcal{H}$ and erf are the Heaviside and the error functions, M_0, M_1, $M_{\rm min}$, $\sigma_{\log M}$, α_g are free parameters, and $f_{\rm inc}$ is a function introduced by More et al. (2015) to take into account the fact that CMASS is incomplete at low stellar mass. In practice, M_0 and α_g are fixed to reduce degeneracies, and only M_1, $M_{\rm min}$ and $\sigma_{\log M}$ are varied (see Kou & Bartlett 2023, for more detail).

3.2.2 Gas distribution profile

As for the galaxies, we need to describe how the gas is distributed inside a halo. We therefore use the pressure profile $P_{\rm e}(r|M)$ from Arnaud et al. (2010) with the parameters from Planck Collaboration et al. (2013),

$$P_{\rm e}(r|M) = 1.65(h/0.7)^2\,\mathrm{eV\,cm^{-3}}E^{8/3}(z)\left(\frac{(1-b_{\rm h})M_{500c}}{3\times10^{14}(0.7/h)M_\odot}\right)^{2/3+\alpha_p} p[r|(1-b_{\rm h})M_{500c}], \tag{3.6}$$

where h is the reduced Hubble constant, $E(z)=H(z)/H_0$, $\alpha_p=0.12$, M_{500c} is the mass of a halo defined such that the halo is a spherical region with average density equal to 500 times the critical density of the Universe. Finally, p is the gas distribution profile, taken as a generalized Navarro-Frenk-White profile (Navarro et al. 1997), and $b_{\rm h}$ is the so-called hydrostatic mass bias. This latter parameter probes the amplitude of the pressure profile and it is the only one that we leave free in our fits.

4 Results and Discussion

For each stellar mass bin, we run a MCMC analysis using the *emcee*[‡] (Foreman-Mackey et al. 2013) sampler to fit our model to the observations.

We constrain the hydrostatic mass bias and find that it is either constant or slightly increasing ($1-b_h$ decreases) with galaxy stellar mass (see the blue curve in Fig. 1). Since we use this bias parameter as a proxy to study the gas dynamics, we also show directly the inferred halo-bias weighted thermal pressure as the orange curve in Fig. 1. Similarly, we find a hint that the gas pressure is slightly lower around high stellar-mass galaxies. This could suggest that these galaxies have exhausted their supply of gas through the formation of stars, or that strong feedback has ejected the gas out of the halos. This kind of measurement can therefore be used to test galaxy evolution and feedback models. More results, especially about how galaxies populate their halos depending on the stellar mass of the observed galaxies, can be found in Kou & Bartlett (2023).

5 Conclusion

The distributions of galaxies and gas are strongly correlated due to the way galaxies form and to the interactions between the stellar population of galaxies and gas, known as feedback effects. Using the cross-correlation of

[‡]https://emcee.readthedocs.io/

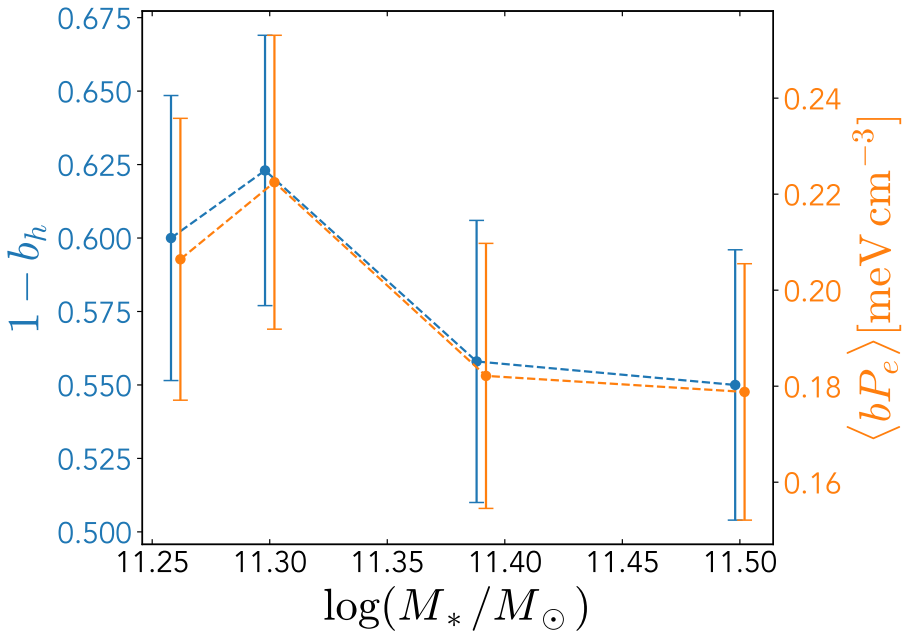

Fig. 1. Hydrostatic mass bias (blue) and halo-bias weighted thermal pressure (orange) as a function of galaxy median stellar mass. The two sets of error bars are shifted along the x-axis for visualization.

CMASS galaxies and the tSZ effect map provided by the *Planck* collaboration, we studied the joint distribution of gas and galaxies. Binning the galaxies by stellar mass, we find that the gas pressure decreases slightly in the vicinity of galaxies with the highest stellar mass. Reproducing this kind of study with the next generation surveys will make it possible to test more precisely galaxy formation, evolution and feedback processes.

References

Alam, S., Albareti, F. D., Allende Prieto, C., et al. 2015, ApJS, 219, 12
Alonso, D., Sanchez, J., Slosar, A., & LSST Dark Energy Science Collaboration. 2019, MNRAS, 484, 4127
Anderson, L., Aubourg, É., Bailey, S., et al. 2014, MNRAS, 441, 24
Arnaud, M., Pratt, G. W., Piffaretti, R., et al. 2010, A&A, 517, A92
Cooray, A. & Sheth, R. 2002, Phys. Rep., 372, 1
Foreman-Mackey, D., Hogg, D. W., Lang, D., & Goodman, J. 2013, PASP, 125, 306
Górski, K. M., Hivon, E., Banday, A. J., et al. 2005, ApJ, 622, 759
Kou, R. & Bartlett, J. G. 2023, A&A, 675, A149
Limber, D. N. 1953, ApJ, 117, 134
Maraston, C., Pforr, J., Henriques, B. M., et al. 2013, MNRAS, 435, 2764
More, S., Miyatake, H., Mandelbaum, R., et al. 2015, ApJ, 806, 2
Navarro, J. F., Frenk, C. S., & White, S. D. M. 1997, ApJ, 490, 493
Planck Collaboration, Ade, P. A. R., Aghanim, N., et al. 2013, A&A, 550, A131
Planck Collaboration, Aghanim, N., Arnaud, M., et al. 2016, A&A, 594, A22
Tinker, J., Kravtsov, A. V., Klypin, A., et al. 2008, ApJ, 688, 709
Tinker, J. L., Robertson, B. E., Kravtsov, A. V., et al. 2010, ApJ, 724, 878
Zheng, Z., Berlind, A. A., Weinberg, D. H., et al. 2005, ApJ, 633, 791
Zonca, A., Singer, L., Lenz, D., et al. 2019, Journal of Open Source Software, 4, 1298

SF2A 2023
M. N'Diaye, A. Siebert, N. Lagarde, O. Venot, K. Baillié, M. Béthermin, E. Lagadec, J. Malzac, J. Richard (eds)

GALAXY CLUSTERS IN MOND: THE CASE OF ULTRA DIFFUSE GALAXIES IN THE COMA CLUSTER

S. T. Nagesh[1], J. Freundlich[1], B. Famaey[1] and M. Bilek[2]

Abstract. Modified Newtonian dynamics (MOND) postulates a deviation from Newtonian gravity in the low acceleration regime. It is an alternative to dark matter that enjoys much success on galaxy scales, but not on galaxy cluster scales. A fundamental aspect of this paradigm is the violation of the strong equivalence principle (SEP). The SEP states that the internal dynamics of a system, on scales much smaller than the variations of the external gravitational field itself, should be independent of this external field; its violation induces that galaxies experiencing an external field should behave differently than their isolated counterparts. Observations of ultra-diffuse galaxies (UDGs) in galaxy cluster environments provide an opportunity to test MOND in the presence of an external field, especially since UDGs have significantly low internal acceleration. Recent work compared the line-of-sight stellar velocity dispersions of 11 UDGs in the Coma cluster and found that they were higher than the MOND predictions including the external field effect. Tidal forces in the cluster environment may provide an explanation for this discrepancy. Here, we present 36 simulations of Coma cluster UDGs launched from different distances from the center on different orbits in the MOND framework to test if tidal heating can inflate the velocity dispersion to match the observations. We find that tidal disruption near the cluster center renders inadequate to inflate the velocity dispersion of these UDGs to the observed levels whilst retaining their structural properties. This sets interesting constraints on any further development of the paradigm.

Keywords: gravitation - dark matter - galaxies: evolution - galaxies: clusters: general - galaxies: clusters: individual: Coma - galaxies: kinematics and dynamics

1 Introduction

Modified Newtonian Dynamics (MOND), proposed by M. Milgrom in 1983 (Milgrom 1983b) in an attempt to circumvent the then incipient dark matter paradigm, postulates that systems with Newtonian gravitational accelerations $g_N < a_0$, where $a_0 = 1.2 \times 10^{-10}$ ms^{-2} (Gentile et al. (2011)) deviate significantly from Newtonian behaviour. Under these conditions, the true gravity g will essentially be $g = \sqrt{a_0 g_N}$, where g_N is the Newtonian acceleration.

MOND has been surprisingly successful over the years in explaining many galactic scale phenomena, like the detailed shape of galaxy rotation curves using just the baryonic matter distribution of the galaxy. It accounts for wiggles (also known as Renzo's rule) observed in the rotation curves (Sancisi (2004); Famaey & McGaugh (2012); Banik & Zhao (2022)). MOND has been successful in predicting various scaling relations such as the baryonic Tully-Fisher relation (BTFR; Milgrom (1983a)) and its local analogue, the radial acceleration relation (RAR) which relates acceleration due to baryons g_{bar} with the dynamical observed acceleration g_{obs} at all radii (McGaugh (2016); Lelli et al. (2017)).

A fundamental aspect of the modified gravity version of MOND is the 'external field effect' (EFE), which is a manifestation of the breaking of the strong equivalence principle (SEP) in this paradigm. In simple words, if a system with internal acceleration g is embedded in a constant external gravitational field g_e such that $g < g_e$, then the external field effect influences the internal dynamics of the system. The internal acceleration of such a system deviates from the isolated MOND case ($g = \sqrt{a_0 g_N}$) towards a Newtonian behaviour ($g \propto g_N$), which should have a signature in observations and can thus be tested. For example, any rotationally (or pressure)

[1] Université de Strasbourg, CNRS, Observatoire astronomique de Strasbourg, UMR 7550, F-67000 Strasbourg, France
[2] LERMA, Observatoire de Paris, CNRS, PSL Univ., Sorbonne Univ., 75014 Paris, France

© Société Française d'Astronomie et d'Astrophysique (SF2A) 2023

supported isolated galaxy with $g < a_0$ should exhibit a MOND behaviour and fall on the RAR, while systems under the influence of the EFE should deviate from the RAR. The isolated systems should indeed have a higher rotational velocity (velocity dispersion) as compared to their counterparts around a massive host with a strong external field. This is however true only at equilibrium.

Ultra diffuse galaxies (UDG) are very low-surface brightness objects with large effective radii. UDGs inside galaxy clusters have therefore very low internal accelerations which makes them ideal candidates for testing the MOND paradigm as a possible alternative to dark matter. Freundlich et al. (2022) studied the velocity dispersions of 11 UDGs in the Coma cluster and compared them with the predictions of MOND. The gravity from the cluster is expected to lower the internal gravitational accelerations of the UDGs due to the EFE, thus lowering their velocity dispersions, but the observed line-of-sight (l.o.s) velocity dispersions are higher than expected, and instead are actually in good agreement with the predictions of MOND in isolation, as if there was no EFE. The authors discussed several scenarios that could possibly explain this discrepancy:

1. The UDGs are undergoing their first infall onto the cluster and/or they are heated by tides.
2. They are surrounded by baryonic dark matter, such as moleculr hydrogen.
3. They have higher stellar masses than estimated from their photometry.
4. The MOND critical acceleration depends on the depth of the gravitational potential (the 'EMOND' hypothesis).
5. The MOND effects would depend on the trajectory of the system (modified inertia).
6. The EFE is screened in galaxy clusters within the parent modified gravity theory.
7. MOND is in fact an effective scaling relation emerging in the classical dark matter framework.

The first scenario can be tested using N-body simulations. Building on this work, we present here the results of numerical simulations of UDGs orbiting in the Coma cluster, in the MOND framework. We study their dynamical properties, compare them with observations, and subsequently try to assess whether these UDGs do pose a challenge to MOND or not.

2 Numerical methods

2.1 Coma cluster in MOND

From the X-ray emitting hot gas density, the cumulative mass profile is calculated assuming hydrostatic equilibrium and that the gas is isothermal. The Newtonian mass profile and the corresponding acceleration $a_C(R)$ are converted to MOND mass $M_C(R)$ using a simple interpolation function. All this is done in Eqs. 13 - 15 of Freundlich et al. (2022). The Newtonian mass profile is converted into a MOND mass profile using the simple interpolation function, We use the resulting cumulative mass profile, normalise it, and numerically invert the normalised function to generate a distribution function. We sample 10^5 particles of equal mass from this distribution and distribute them spherically symmetrically up to 5 Mpc from the center. These particles have masses of 4.18×10^9 $M_\odot$ and are kept static during the simulation. Their purpose is to generate the potential of the Coma cluster through which the UDGs move.

2.2 UDGs in MOND

UDGs at the start of the simulations are approximated by Sérsic spheres with a mass of 10^7 $M_\odot$, a Sérsic index 1.0 and an effective radius of 1.5 kpc. These parameters correspond to the medians of those indicated in Freundlich et al. (2022). A crucial aspect of our simulations was to ensure that the UDGs were in equilibrium given the EFE generated by the Coma cluster at their respective launch distances. This was achieved by using Eq. 25 of Freundlich et al. (2022), namely setting the internal accelerations of the UDGs after accounting for the EFE due to the Coma cluster.

Once the initial conditions for the cluster and the UDGs are set, we use the phantom of Ramses (POR; Lüghausen et al. 2015; Nagesh et al. (2021)) code to run the simulations. POR is a patch to the original RAMSES code (Teyssier (2002)) which implements a MOND Poisson solver alongside the already existing Newtonian one,

thus enabling the users to run simulations in both Newtonian gravity and MOND. A user manual describing the procedure to setup, run, and analyse disc galaxies in MOND using POR is available online *.

UDGs were launched into the Coma cluster at 1, 1.2, 1.4, 1.6, 1.8, 2.0 Mpc from the cluster center and, for each distance, with eccentricities of 0, 0.2, 0.4, 0.6, 0.8, and 0.99. In total, this results in 36 simulations which are run for 5 Gyr with outputs each 100 Myr.

3 Results

Particle data are extracted from the simulation outputs using EXTRACT_POR, barycentre subtracted, and analysed. In this on-going project, we have performed multiple analyses on the simulated UDGs, but we present here the most important one.

As mentioned in Section 1, a tension between the observed l.o.s. velocity dispersion and the MOND-predicted l.o.s. velocity dispersion was noted by Freundlich et al. (2022). We calculated the l.o.s. velocity dispersion, σ_{los}, in projection in the direction of the z axis/into the xy plane, for all simulated UDGs at the apocentre of their orbits and compared it with the MOND-predicted velocity dispersion in isolation, σ_{iso}. σ_{los} is calculated using Eq. 22 of Banik et al. (2020), and σ_{iso} is computed using methods described in Sec. 3.2.1 Freundlich et al. (2022). The latter estimates used Sérsic fit parameters obtained with GALFIT (Peng et al. 2010) at the corresponding times.

Fig. 1 shows the ratio $\sigma_{los}/\sigma_{iso}$ for the simulated UDGs at the apocentres of their orbits. These UDGs are launched at different distances from the cluster center and with different eccentricities. Dashed lines indicate that the UDGs are disrupted, which is defined as when they lose 80% of the mass within their initial tidal radius. The σ_{los} profiles of UDGs on orbits with $e < 0.6$ remain significantly below the isolated MOND limit. Although the UDG launched at 1 Mpc is disrupted due to tides, it still does not reach the isolated MOND limit. In contrast to the latter, quite a few UDGs on orbits with $e \geq 0.6$ reach the isolated MOND limit, but most of them are disrupted. The only UDG in our sample that has an inflated σ_{los} without being disrupted has an initial distance $R = 1.6$ Mpc and $e = 0.99$ (see bottom right plot). The shape of the σ_{los} profiles vary from $\sigma_{\rm los}$ declining with r to remaining flat to flaring up in the outskirts. An increase of σ_{los} towards the centre has been observed in the sample UDGs, and has been shown to be consistent with theoretical profiles including a radial anisotropy (for example, see Fig. 9 of Freundlich et al. (2022)). An increase in σ_{los} has also been observed in the profile of DF44 (van Dokkum et al. 2019; Freundlich et al. 2022).

4 Conclusions

Fig. 1 shows that UDGs need to be disrupted in order to have an inflated l.o.s. velocity dispersion, but the UDGs in the sample studied by Freundlich et al. (2022) have structural parameters like effective radius, and Sérsic index compatible with equilibrium. The analyses done so far thus indicate that it is quite difficult for the UDGs to survive a pericentric passage through the cluster and retain their structural properties whilst inflating their velocity dispersion to the isolated MOND prediction, which the observations seem to conform to. However, the detectability of the simulated UDGs still needs to be checked by constructing surface brightness maps and comparing them with observations. It is however important to note that the observations have large error bars and that the theoretical σ_{los} is within these error bars for some UDGs. Future observations could better constrain the σ_{los} values, which might increase or decrease the tension between theory and observations. With a few more tests, analyses, and simulations, we hope to conclude whether tidal disruption could possibly reconcile the observations with theoretical predictions or not.

References

Banik, I., Thies, I., Candlish, G., et al. 2020, ApJ, 905, 135

Banik, I. & Zhao, H. 2022, Symmetry, 14, 1331

Famaey, B. & McGaugh, S. S. 2012, Living Reviews in Relativity, 15, 10

*https://bitbucket.org/SrikanthTN/bonnPoR/src/master/

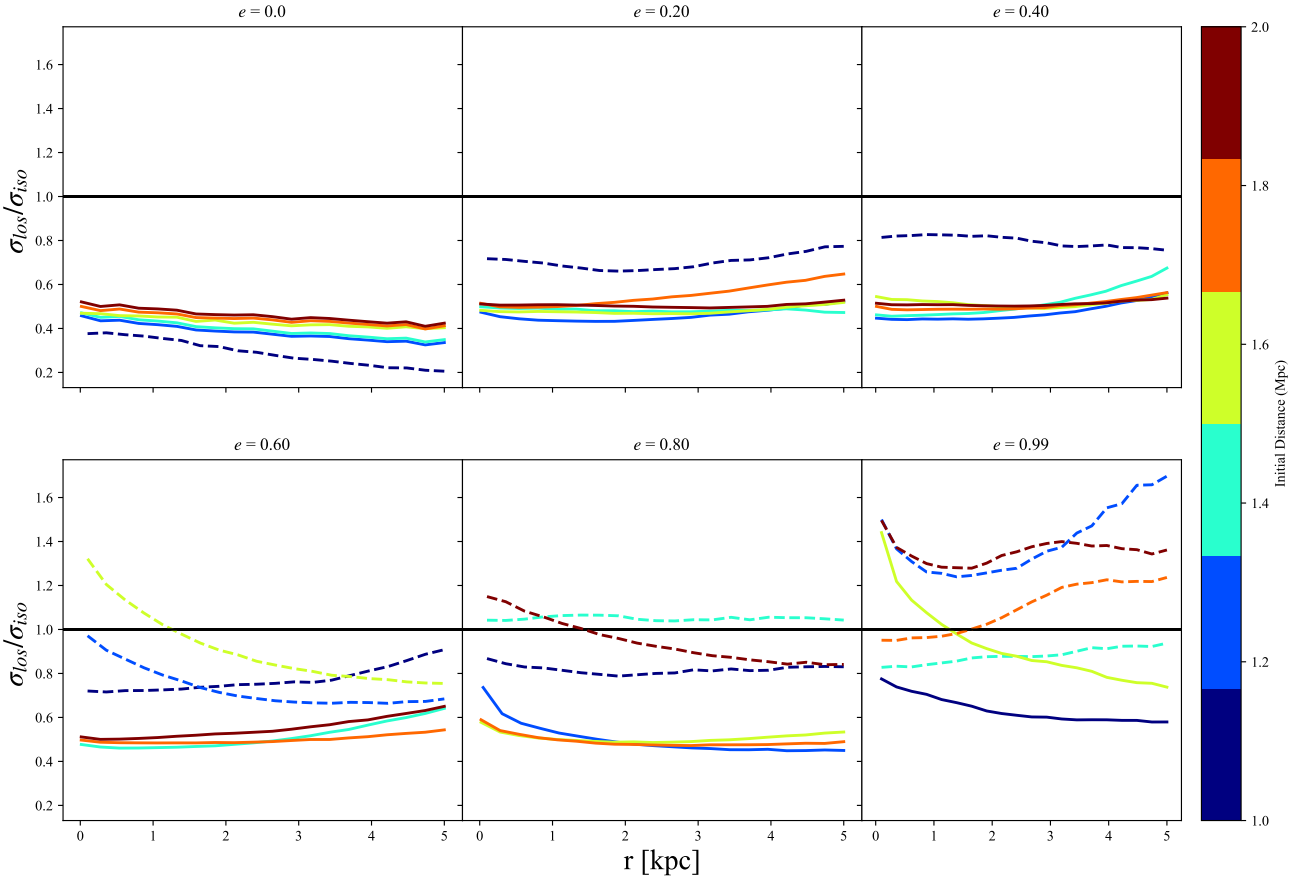

Fig. 1. Ratio between the simulated l.o.s. velocity dispersion, σ_{los}, and that predicted by MOND, σ_{iso}, for UDGs launched on orbits with different initial distances (cf. colorbar) and eccentricities ($e = 0, 0.2, 0.4, 0.6, 0.8, 0.99$). Dashed lines indicate that the UDG is disrupted or under disruption. The black solid line marks where $\sigma_{los} = \sigma_{iso}$.

Freundlich, J., Famaey, B., Oria, P.-A., et al. 2022, A&A, 658, A26

Gentile, G., Famaey, B., & de Blok, W. J. G. 2011, A&A, 527, A76

Lelli, F., McGaugh, S. S., Schombert, J. M., & Pawlowski, M. S. 2017, ApJ, 836, 152

Lüghausen, F., Famaey, B., & Kroupa, P. 2015, Canadian Journal of Physics, 93, 232

McGaugh, S. S. 2016, ApJL, 832, L8

Milgrom, M. 1983a, ApJ, 270, 371

Milgrom, M. 1983b, ApJ, 270, 365

Nagesh, S. T., Banik, I., Thies, I., et al. 2021, Canadian Journal of Physics, 99, 607

Peng, C. Y., Ho, L. C., Impey, C. D., & Rix, H.-W. 2010, AJ, 139, 2097

Sancisi, R. 2004, in International Astronomical Union Symposium no. 220, Vol. 220, Dark Matter in Galaxies, ed. S. Ryder, D. Pisano, M. Walker, & K. Freeman (PASP), 233

Teyssier, R. 2002, A&A, 385, 337

van Dokkum, P., Wasserman, A., Danieli, S., et al. 2019, ApJ, 880, 91

SF2A 2023
M. N'Diaye, A. Siebert, N. Lagarde, O. Venot, K. Baillié, M. Béthermin, E. Lagadec, J. Malzac, J. Richard (eds)

UNVEILING THE NON-THERMAL RADIO EMISSION IN GALAXY CLUSTERS AND FUTURE PROSPECTS WITH THE SKA

M. Pandey-Pommier[1,2], S. Paul[3], N. Roy[4], A. Marcowith[2] and B. Guiderdoni[5]

Abstract. Galaxy clusters are the most massive structures in the universe that are held together by their gravity. They harbor various forms of non-thermal diffuse radio emissions at their cores, including radio halos, mini-halos, relics, and reactivated fossil plasma sources known as 'phoenixes.' The detection of these non-thermal radio emissions at radio wavelengths has been challenging in the past due to their steep spectral nature and low surface brightness. In the last decade, surveys conducted with SKA pathfinder telescopes like LOFAR, uGMRT, and Australian SKA Pathfinder (ASKAP) have revolutionized the study of cluster-scale radio emissions. These surveys have doubled the number of detected radio halos and mini-halos, with masses as low as $\sim 10^{14}$M$_\odot$ and up to a redshift of 0.9. These breakthroughs have enabled the development of high-resolution numerical models for radio emissions and advanced our understanding of the cosmic magnetic fields associated with galaxy clusters. In this paper, we present statistical results from surveys conducted in the last decade and highlight the pivotal role of the Square Kilometer Array (SKA) in advancing our knowledge of galaxy clusters, particularly at higher redshifts.

Keywords: galaxies: clusters: general- galaxies: clusters: intracluster medium- non-thermal radio emission

1 Introduction

Galaxy clusters reside at the crossroads of cosmology and the astrophysics of large-scale structure formation and galaxy evolution in the Universe. These dense gravitationally bounded structures provide favorable conditions for collisions, mergers, or interactions between galaxies within their Intracluster medium (ICM). These interactions give rise to turbulence and heating-up of the ICM to temperatures up to tens of millions of degrees (several keV per particle), thereby emitting in the soft X-ray regime via thermal bremsstrahlung radiation. In addition to the thermal emission, the ICM is also known to host non-thermal synchrotron radiation emitting predominantly at MHz-range in the radio regime. Diffuse radio emission has been detected in a considerable number of galaxy clusters and groups, revealing the presence of pervasive cosmic magnetic fields and relativistic particles in the large-scale structure of the Universe. Since the radio emissions in galaxy clusters are faint with steep spectral properties ($\alpha \sim -1.3$), their observations are largely limited by the instrument sensitivity and the frequency of observation, leading to a dearth of information, more so for lower-mass $M_{500} = 10^{14}$M$_\odot$ and higher redshift ($z > 0.5$) systems. The recent commissioning or upgrade of several large radio telescope arrays, particularly at the low-frequency bands (< MHz), aided by the development of advanced calibration and imaging techniques, has helped in achieving unparalleled image quality and revolutionized the study of cluster-scale radio emission, thanks to the availability of high-performance computing facilities to handle large survey data set processing. In this paper, we provide a summary of the contributions made by SKA pathfinders, including LOFAR, uGMRT, and ASKAP, over the last decade in uncovering various types of cluster radio sources through dedicated surveys and individual studies. Additionally, we explore the potential of SKA in the discovery of diffuse radio emission in clusters and cosmic web filaments.

[1] CNRS/Laboratoire Univers et Particules de Montpellier, Université de Montpellier LUPM CC 072 - Place Eugène Bataillon 34095 Montpellier Cedex 5, France

[2] University Catholic of Lyon, 10, place des Archives 69288 Lyon Cedex 02, France

[3] Department of Physics, Pune University, Pune 411007, India

[4] Department of Physics, Indian Institute of Science, Bangalore 560012, India

[5] Univ Lyon, Univ Lyon1, Ens de Lyon, CNRS, Centre de Recherche Atsrophysique de Lyon UMR5574, F-69230, Saint-Genis Laval, France

© Société Française d'Astronomie et d'Astrophysique (SF2A) 2023

2 Advancements in Radio emission Classification and Detection Statistics in Galaxy Clusters with the SKA pathfinders and prospects with the SKA

Recent advancements in survey sensitivities achieved by SKA pathfinders, reaching levels as low as $\sim$ 0.1 mJy/beam, have opened up exciting possibilities in the study of radio emissions within galaxy clusters. These improvements have led to the detection of a greater number of radio sources at frequencies $<$ 144 MHz, shedding light on a previously unknown population of sources. These discoveries are particularly significant in the context of low-mass galaxy cluster systems, where masses hover around $\sim 10^{14}$M$_\odot$ as illustrated in Figure 1 (left panel) extracted from (Paul et al. 2023). The compilation of comprehensive datasets from both earlier observations and more recent ones (for a review, see van Weeren et al. 2019 and references therein, Botteon et al. 2022; Cassano et al. 2013; Cuciti et al. 2018; Hoang et al. 2022; Paul et al. 2023) suggests a correlation for $P_{1.4GHz} - M_{500}$ with the BCES bisector slope for ($\alpha_{new} = 3.56 \pm 0.22$). This follows a pattern similar to the previously established correlation ($\alpha = 3.70 \pm 0.56$) by Cassano et al. (2013). With the $P_{1.4GHz} - M_{500}$ correlation plot Figure 1 (left panel), it is apparent that there is a dearth of data points for cluster masses below $M < 4 \times 10^{14}$ M$_\odot$. These results emphasize the need for more extended observation times, preferably exceeding 8 hours, or achieving microJy level sensitivity through advanced arrays like the SKA to probe the properties of radio haloes in clusters at the lower end of the mass spectrum more comprehensively.

Further, the enhancement in detection statistics has led to more refined source classification schemes based on the intrinsic properties of these sources. These newly identified source populations predominantly consist of radio haloes (larger than 500 kiloparsecs) or mini-haloes (smaller than 500 kiloparsecs), often found in poor clusters, groups of galaxies, and ultra-steep spectrum sources (Botteon et al. 2022; van Weeren et al. 2019). In Figure 1 (Right panel), we present statistics reflecting the increased detection of radio emissions within clusters with respect to the redshift over the last decade, primarily through the use of SKA pathfinders, notably the LOTSS survey initiated in 2014 (Shimwell et al. 2019). Compared to surveys conducted until 2013, there has been a remarkable 54% increase in the number of detected radio haloes and mini-haloes in the last decade. Furthermore, there is a noticeable peak in the formation period of galaxy clusters, occurring at a redshift of approximately $z \sim 0.2$ to $z \sim 0.3$, which is consistent with recent surveys from PLANCK, SPT, and ACT (Bartalucci et al. 2019). In addition, these improved detection statistics have allowed us to identify rare haloes (8) in the $0.6 < z < 0.9$ range and 1 mini-halo up to $z = 0.6$ for the first time. Nevertheless, these detections are scarce, and SKA will significantly contribute to the discovery of thousands of haloes beyond $z > 0.6$ (Cassano et al. 2013). Consequently, the combination of enhanced detection statistics, along with improved theoretical insights, will facilitate the refinement of radio emission mechanisms in galaxy clusters and their classification schemes by incorporating their detailed intrinsic properties.

We gratefully acknowledge the support of the Indo-French Centre for the Promotion of Advanced Research (Centre Franco-Indien pour la Promotion de la Recherche Avancée) under project 6504-3.

References

Bartalucci, I., Arnaud, M., & et al. 2019, A&A, 628

Botteon, A., Shimwell, T. W., Cassano, R., et al. 2022, arXiv e-prints, arXiv:2202.11720

Cassano, R., Ettori, S., Brunetti, G., et al. 2013, ApJ, 777, 141

Cuciti, V., Brunetti, G., van Weeren, R., et al. 2018, A&A, 609, A61

Hoang, D. N., Brüggen, M., Botteon, A., et al. 2022, A&A, 665, arXiv:2206.04666

Paul, S., Kale, R., Datta, A., & et al. 2023, JApA, 44, 38

Shimwell, T. W., Tasse, C., Hardcastle, M. J., et al. 2019, A&A, 622, A1

van Weeren, R. J., de Gasperin, F., Akamatsu, H., et al. 2019, Space. Sci. Rev., 215, 16

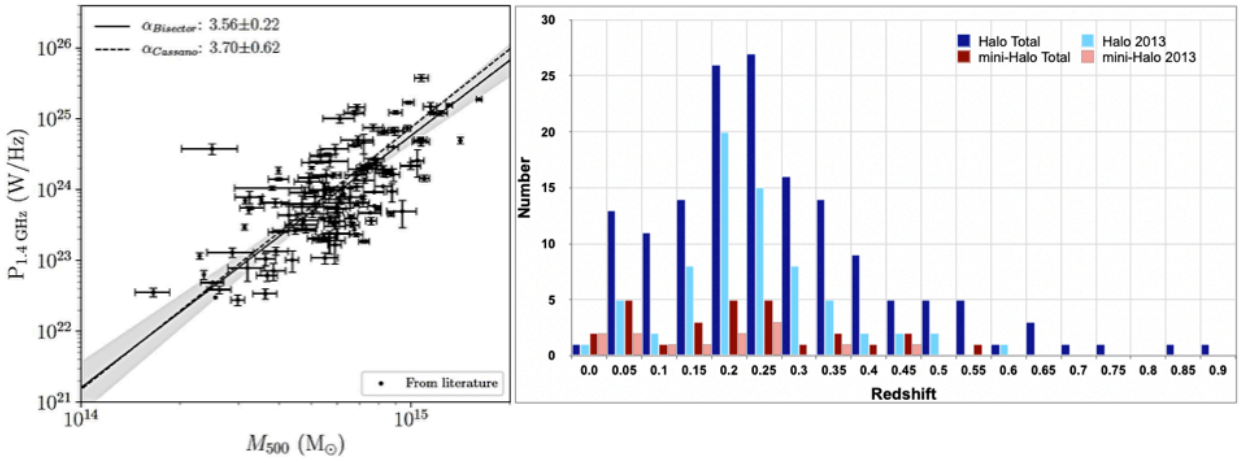

Fig. 1. Left Panel: Radio halo power plotted against mass M_{500} of all the radio halos observed so far and extracted from (Paul et al. 2023). The halo radio power here is scaled to 1.4 GHz, assuming the spectral index of -1.3 wherever no spectral index information is available in the literature. Right Panel: Radio halo and mini-halo detection statistics across redshift: pre-2013 versus recent surveys.

SF2A 2023
M. N'Diaye, A. Siebert, N. Lagarde, O. Venot, K. Baillié, M. Béthermin, E. Lagadec, J. Malzac, J. Richard (eds)

INVESTIGATING NEUTRAL HYDROGEN CONTENT IN RADIO MOHEGS AND PROSPECTS WITH THE SKA

S. Wagh[1], M. Pandey-Pommier[2,3], N. Roy[1], M. Rashid,[1], A. Marcowith[2], S. Roy[4], C. Muthumariappan[5], R. Sethuram[5] and B. Guiderdoni[6]

Abstract. Most of the interstellar matter in galaxies occurs in the form of cold neutral hydrogen (H I) gas, which is the primary fuel for star formation. Observations of the H I 21-cm line absorption help understand the kinematics of gases, the overall star formation activities within the galaxies, and their interaction with the neighbouring environment. This paper presents the first systematic H I study of radio MOlecular Hydrogen Emission Galaxies (MOHEGs). These massive galaxies show FRI/II type radio morphology, high-luminosity molecular hydrogen emission, and weak Polycyclic Aromatic Hydrocarbon (PAH) emission indicative of a low star formation rate. Neutral hydrogen (H I) column density down to 10^{20} cm^{-2} is detected in 50% (7/14) galaxies within our sample at a distance of a few kiloparsec scales from the nearest neighbours. Our results suggest that radio MOHEGs are deficient in H I, and various factors, such as nuclear radio activities in central regions, the density of their environment (low or high), the evolutionary stage of these galaxies, play a role in regulating the presence of neutral gas. Next-generation radio telescopes such as the Square Kilometre Array (SKA) and pathfinder instruments will not only trace the evolution of H I 21-cm absorbers systems from nearby up to intermediate redshift Universe at unprecedented depths but also revolutionize our understanding of galaxy evolution across different environments, gas inflows-outflows, interaction with the intragalactic medium, and probe the era of galaxy evolution at the cosmic noon ($1 < z < 3$).

Keywords: Galaxies: absorption lines - Galaxies: evolution - Galaxies: Interstellar medium

1 Introduction

Recent studies from the IR Spitzer telescope have revealed an exciting class of 17 (FR-I and FR-II) radio MOlecular Hydrogen Emission Galaxies (radio MOHEGs) at redshift $z < 0.22$. These galaxies have ample amounts of molecular hydrogen gas masses ($\sim 10^{10}$ M$\odot$), though they are inefficient at star formation, suggesting that the molecular gas is kinematically unsettled and turbulent. The star formation in these galaxies is critically affected due to molecular gas heating, preventing the gas from cooling down to form stars. These galaxies show a significantly larger L(H_2) /L(PAH) ratio (0.03-4 or greater) as compared to normal star-forming galaxies. The pure rotational and ro-vibrational H_2 transitions give rise to H_2 luminosities of the order of 10^{40}-10^{42} ergs^{-1}, along with a relatively weak IR continuum emission L(H_2)/L(IR) $>10^{-3}$, that acts as the primary coolant for the warm molecular phase of the ISM, with a very short cooling timescale ($\sim 10^4$ years) (Ogle et al. 2010). In addition, these galaxies belong to galaxy clusters or close interacting pairs or groups. The high observed molecular mass may be linked to gas-rich galaxy collisions/interactions or cooling flows, which drive gas into the central less gas-rich environments in radio galaxies (Ogle et al. 2007).

[1] Department of Physics, Indian Institute of Science, Bangalore 560012, India
[2] CNRS/Laboratoire Univers et Particules de Montpellier, Université de Montpellier LUPM CC 072 - Place Eugène Bataillon 34095 Montpellier Cedex 5, France
[3] University Catholic of Lyon, 10, place des Archives 69288 Lyon Cedex 02, France
[4] National Centre for Radio Astrophysics - Tata Institute of Fundamental Research, Ganeshkhind, Pune 411007, Maharashtra, India
[5] Indian Institute of Astrophysics, II Block, Koramangala, Bangalore 560034, India
[6] Univ Lyon, Univ Lyon1, Ens de Lyon, CNRS, Centre de Recherche Atsrophysique de Lyon UMR5574, F-69230, Saint-Genis Laval, France

© Société Française d'Astronomie et d'Astrophysique (SF2A) 2023

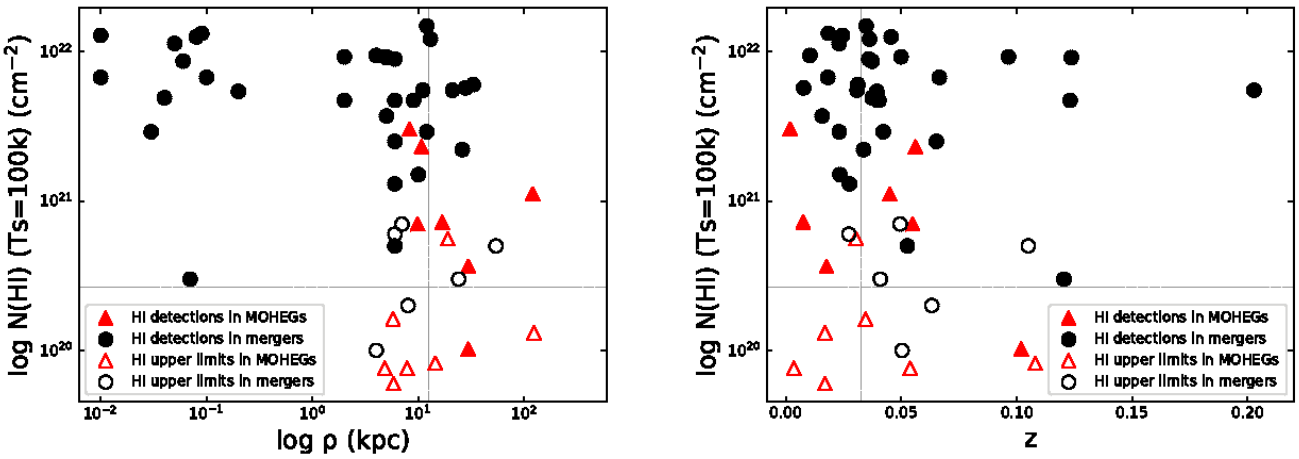

Fig. 1. Neutral hydrogen column densities of the radio MOHEG sample sources along with a sample of mergers following the same distribution as a function of interaction distance between the nearest neighbour (left panel) and redshifts (right panel). The dotted lines represent median values derived from the MOHEG sample. The median N(H I) value is 2.64 x 10^{20} cm^{-2}, the median redshift is 0.03241, and the median separation is 12.58272 kpc.

Moreover, it is not only the H_2 gas abundance but also the atomic gas in galaxies that plays a significant role in star formation and galaxy evolution. It acts as an important intermediary component in the baryon cycle, a reservoir of the raw fuel for star formation, and leads to the formation of H_2 gas via exothermic processes. It is inferred from previous studies that extended atomic gas in the disc regions of the gas-rich systems is highly exposed to distortions caused by tidal interactions, ram pressure stripping, and merging activities in dense environments (Yun et al. 1994; Brown et al. 2017). In addition, the atomic gas is also heated up by chemical, radiative, and mechanical feedback linked with star formation activities (Cox & Smith 1974; Wolfire et al. 1995). The imprints of such interactions can be studied through H I 21cm absorption line studies. It can complement the emission line surveys to trace the evolution of the atomic gas component in and around galaxies. The H I absorption features depend on the strength of the background radio continuum and are independent of the distance of the source. The H I 21-cm optical depth-integrated over velocity is proportional to the column density of neutral hydrogen, N(H I) cm $^{-2}$ is given by,

$$N_{HI} = 1.82 \times 10^{18} \frac{T_s}{f_c} \int \tau d\nu \ \ (cm^{-2}) \tag{1.1}$$

where T_s (K) is the spin temperature of the gas, f_c is the fraction of the background radio source covered by the absorbing gas (Rohlfs & Wilson 2000).

In this paper, we discuss the importance of studying cold neutral gas content in radio galaxies rich in molecular hydrogen to probe the role of atomic hydrogen gas in explaining the influence of surrounding environments on galaxy evolution over cosmic timescales. In § 2, we present the results of our study of neutral hydrogen gas distribution in the radio MOHEGs and their dependence on the galaxy properties. The prospects of SKA in studying the H I properties of MOHEGs type galaxies are discussed in § 3, and the conclusion of this work is discussed in § 4.

2 N(H I) and kinematics

The H I column density in galaxies serves as a crucial indicator of their gas content, offering valuable insights into various aspects such as morphology, gas composition, dynamical activities, and interactions with their neighbouring environments. Additionally, it allows us to investigate the locations of active star formation and provides information on the kinematics of gas within these galaxies. In our study, we calculated the average N (H I) for our MOHEG sample. The results presented are based on the H I data taken from the literature. The H I column density within our sample ranges from $\approx 6 \times 10^{19}$ cm^{-2} to 3.03 $\times 10^{21}$ cm^{-2}, assuming a spin

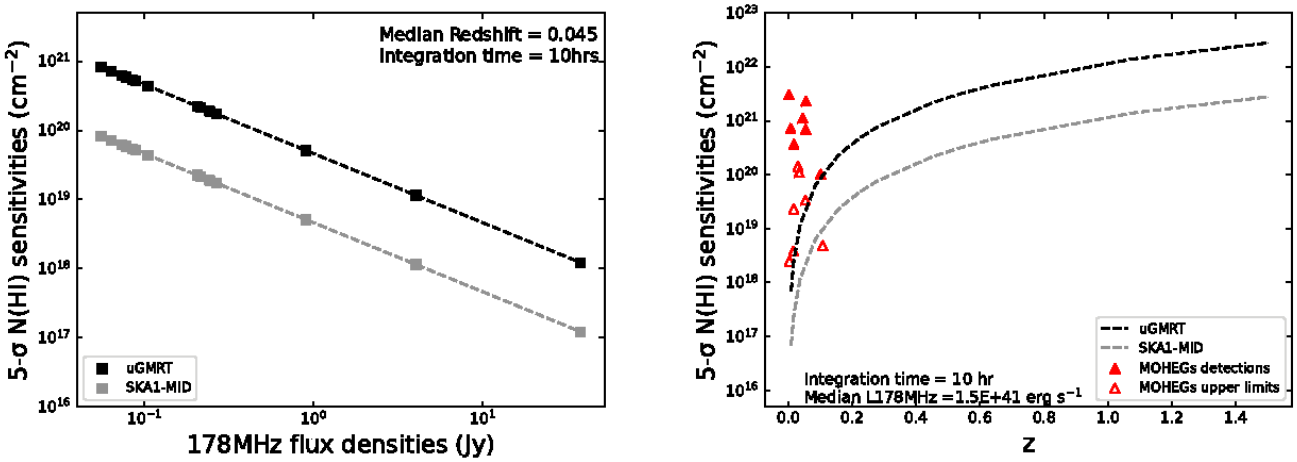

Fig. 2. 5σ N(H I) absorption sensitivities for MOHEGs-type sources for SKA1-MID (grey line) and uGMRT (black line) for 10hrs integration times with respect to the 178MHz flux densities (left panel) and redshifts (right panel). The radio MOHEGs sample is plotted in red triangles.

temperature of 100K. Existing data in the literature suggests that the average column density for the H I disk in spiral galaxies typically falls around 10^{20} cm^{-2} (Wang et al. 2016; Serra et al. 2012). Consequently, MOHEGs exhibit a wide range of column densities; however, only 50% of galaxies in our sample show neutral hydrogen detection, with H I column densities reaching as low as 10^{20} cm^{-2}. We suggest that the radio MOHEGs are class of galaxies engaged in merging stages, with N(H I) values a factor of 18 lower compared to the merger sample, where the median N(H I) $\sim 5 \times 10^{21}$ cm^{-2} (Dutta 2019), refer Figure 1. Furthermore, there is no specific trend in the H I column density distribution concerning the nearest neighbour distance and redshift for both samples. This result suggests that radio MOHEGs are deficient in atomic hydrogen compared to merging galaxies at similar redshifts and distances due to their dense neighbouring environment, leading to enhanced gas stripping. Understanding the link between H I absorption properties and the feedback mechanisms that trigger or quench star formation in galaxies is essential for investigating the turbulence generated in the cold hydrogen gas and the interplay between atomic and molecular gas in explaining the properties of these galaxies during mergers within the intergalactic medium (Wagh et al. 2023).

3 SKA HI survey and prospects

In Figure 2, we plot the sensitivity for H I detections in MOHEG-type sources at different flux densities, observation times, and redshifts for the SKA1-MID and uGMRT. We used the extrapolated values at 178 MHz flux densities and the median redshift of the total MOHEGs sample to compute the flux densities of the background continuum sources (Ogle et al. 2010), using a power-law scaling of -0.7 spectral index (a typical value for radio galaxies). The theoretical RMS noise was calculated for a given integration time at a 5 km s^{-1} channel width for all the instruments (Blyth et al. 2015; Bharti & Bagla 2022; Maddox et al. 2021; Braun et al. 2019). The 5σ sensitivity limits on H I detections for different instruments at different integration times are plotted in Figure 2. For a reasonable integration time up to $\sim$ 10 hrs on a strong background continuum source, we will detect sources with N(H I) column densities as low as $\sim 10^{17}$ cm^{-2} for the SKA1-MID bands, whereas we will be limited to $\sim 10^{18}$ cm^{-2} with the uGMRT. Further, due to the narrow band observations and poor sensitivities (mJy-level) offered by the SKA precursor instruments, H I detections in MOHEGs-type galaxy samples have been limited to the z $\sim$ 0.2 range, however; upcoming telescopes like SKA1-MID can detect much deeper and fainter absorption features (a factor of 2 and above better) with the same integration times as shown in Figure 2 panel 2. These plots suggest that in shallow surveys, SKA1-MID will efficiently detect N(H I) column densities up to a redshift of z $\sim$ 1.5 for a bright population of background sources, thereby probing the cosmic noon regime where star formation activities show a peak. SKA will thus discover a new class of low-column-density absorbers around galaxies with extended or compact morphologies based on their surrounding environments.

4 Conclusions

In this study, we systematically investigated the neutral hydrogen gas in radio MOHEGs using the H I 21-cm absorption line and assessed the prospects for conducting such studies with the SKA and pathfinder telescopes. The key results of our work are summarized below:

- Radio MOHEGs exhibit a deficiency in atomic hydrogen, with a median value of 2.64 x 10^{20} cm^{-2}, compared to merging galaxies at similar redshifts. This deficiency can be attributed to their dense neighbouring environments, which lead to reduced H I gas quantities due to tidal forces, stripping, and strangulations.
- There exists no clear correlation between H I gas column densities and the galaxy properties below z $\sim$ 0.2.
- The SKA is poised to efficiently detect low column density features, enabling the tracing of the complete gas cycle from disks to the intergalactic medium (IGM), including tails and filaments that indicate the phases (pre-, post-, ongoing) of merger events and AGN-induced feedback mechanisms. Importantly, it will provide comprehensive data to trace the entire evolution of H I from the current epoch up to the cosmic noon within a reasonable observation time, allowing us to probe the star formation history of the universe.

We gratefully acknowledge the support of the Indo-French Centre for the Promotion of Advanced Research (Centre Franco-Indien pour la Promotion de la Recherche Avancée) under project 6504-3.

References

Bharti, S. & Bagla, J. S. 2022, Journal of Astrophysics and Astronomy, 43, 95

Blyth, S., van der Hulst, T. M., Verheijen, M. A. W., et al. 2015, in Advancing Astrophysics with the Square Kilometre Array (AASKA14), 128

Braun, R., Bonaldi, A., Bourke, T., Keane, E., & Wagg, J. 2019, arXiv e-prints, arXiv:1912.12699

Brown, T., Catinella, B., Cortese, L., et al. 2017, MNRAS, 466, 1275

Cox, D. P. & Smith, B. W. 1974, ApJ, 189, L105

Dutta, R. 2019, Journal of Astrophysics and Astronomy, 40, 41

Maddox, N., Frank, B. S., Ponomareva, A. A., et al. 2021, A&A, 646, A35

Ogle, P., Antonucci, R., Appleton, P. N., & Whysong, D. 2007, ApJ, 668, 699

Ogle, P., Boulanger, F., Guillard, P., et al. 2010, ApJ, 724, 1193

Rohlfs, K. & Wilson, T. L. 2000, Tools of radio astronomy

Serra, P., Oosterloo, T., Morganti, R., et al. 2012, MNRAS, 422, 1835

Wagh, S., Pandey-Pommier, M., Roy, N., & et al. 2023, MNRAS, submitted

Wang, J., Koribalski, B. S., Serra, P., et al. 2016, Monthly Notices of the Royal Astronomical Society, 460, 2143

Wolfire, M. G., Hollenbach, D., McKee, C. F., Tielens, A. G. G. M., & Bakes, E. L. O. 1995, ApJ, 443, 152

Yun, M. S., Ho, P. T. P., & Lo, K. Y. 1994, Nature, 372, 530

Session S02

Archéologie Galactique avec Gaia/DR3: un an après

SF2A 2023
M. N'Diaye, A. Siebert, N. Lagarde, O. Venot, K. Baillié, M. Béthermin, E. Lagadec, J. Malzac, J. Richard (eds)

THE SPECTROSCOPIC DATA OF THE GAIA DR3 CATALOG: PERFORMANCE AND USE

P. A. Palicio[1]

Abstract. Galactic Archaeology has experienced a great advance in the last decade thanks to the development of large surveys like APOGEE, LAMOST and GALAH. The *Gaia* mission (ESA) has contributed to this revolution by providing precise astrometric and photometric data for more than one billion stars, radial velocities for the bright subset of them and, since *Gaia* DR3, the stellar parameters and chemical abundances of 5.6 million sources observed by the on-board RVS spectrograph. The extraction of the atmospheric parameters and composition for such an unprecedented large volume of stars has been possible thanks to the implementation of the GSP-Spec module in the *Gaia* pipeline. In this work, we describe the performance of GSP-Spec and present its output to the community. We demonstrate the quality of the GSP-Spec data and provide a guide of best practices for its correct usage, as well as illustrate some scientific applications.

Keywords: stars: fundamental parameters – stars: abundances – methods: data analysis – Galaxy: stellar content

1 Introduction

Gaia is the most advanced astrometric mission to date (Perryman et al. 2001; Gaia Collaboration et al. 2016). Since its launch in December 2013, it has continued the legacy of Hipparcos (Perryman & Hassan 1989) by providing positions, parallaxes and proper motions with errors of few microns. In addition to the astrometry, *Gaia* provides the line-of-sight velocities of a subset of bright stars whose spectra have been collected by the on-board Radial Velocity Spectrograph (Katz et al. 2004, RVS), which operates in the wavelength domain of the near infra-red calcium triplet (846-870 nm) with a resolution of 11,500 (Cropper et al. 2018). This full kinematic information for *Gaia* sources was included, for first time, as part of the second data release (Gaia Collaboration et al. 2018, *Gaia* DR2), in which the astrometry and line-of-sight velocities were extended and updated in the subsequent *Gaia* eDR3 (Gaia Collaboration et al. 2021) and *Gaia* DR3 (Gaia Collaboration et al. 2023b) data releases, respectively. On the contrary, the stellar parameters, chemical abundances and other valuable information extracted from the RVS spectra were not publicly available until the latest *Gaia* data release. Thus, *Gaia* DR3 constitutes the first data-set containing the results of the GSP-Spec module (Recio-Blanco et al. 2023) –one of the eighth Data Processing and Analysis Consortium (DPAC) collaboration unit (CU8) modules – devoted to the analysis of the RVS combined spectra and currently incorporated to the *Gaia* pipeline. Since *Gaia* has been continuously observing the sky for years in more stable conditions compared to ground-base telescopes, it allows a more homogeneous treatment of the spectra and modelling of the systematics. This results in the largest stellar spectroscopic characterisation catalog ever published, totalling almost 5.6 million *Gaia* sources. From the scientific point of view, this characterisation is key for understanding the structure of the Milky Way. In particular, the chemical abundances shed light on Galaxy formation and evolution through the composition of the individual stars, since they are synthesised in the stellar interior and pollute the inter-stellar medium (ISM) through different channels. The relative contribution of these channels leads to a characteristic footprint that preserves the information of the birthplace of the stars. For example, it is well known the thick disc stars show higher [α/Fe] abundances compared to its thinner counterpart (Lee et al. 2011), while stars accreted from satellites tend to be α-poor compared to these born in the Milky Way

[1] Université Côte d'Azur, Observatoire de la Côte d'Azur, CNRS, Laboratoire Lagrange, Bd de l'Observatoire, CS 34229, 06304 Nice cedex 4, France

© Société Française d'Astronomie et d'Astrophysique (SF2A) 2023

with the same metallicity (Nissen & Schuster 2010). In this work, we describe the performance of the GSP-Spec module and summarise its main products, with special emphasis on the treatment of the output data for the proper usage on scientific applications. Finally, we illustrate some novel results already published made with GSP-Spec data.

2 The GSP-Spec module

2.1 The GSP-Spec architecture

As mentioned in the previous section, GSP-Spec is one of the modules included in the *Gaia* pipeline for the analysis of the RVS spectra. In contrast to other modules, it uses no additional input information (i.e., parallaxes, photometry, extinction, etc.) for performing the analysis. GSP-Spec encompasses two distinct workflows with different architecture, MatisseGauguin and the supervised machine learning algorithm ANN. The former incorporates various sub-modules to tackle multiple tasks, while the latter comprises three layers to analyse the spectra: an input layer with 800 neurons, an intermediate layer containing a variable number of neurons ranging from 50 to 100, and an output layer of four neurons.

While both workflows yield the four basic atmospheric parameters (effective temperature $T_{\rm eff}$, surface gravity logg, global metallicity [M/H] and global alpha abundance [α/Fe]) and their respective quality flags as output, only MatisseGauguin provides additional information concerning the chemical composition and the inter-stellar absorption through the estimates of thirteen chemical abundances, the cyanogen equivalent width and two diffuse inter-stellar bands (DIBs).

The structure of the MatisseGauguin module is summarised in Fig. 4 of Recio-Blanco et al. (2023). Given an input RVS spectra, a decision tree called DEGAS gets an initial estimation of the atmospheric parameters. Then, the Matisse algorithm updates this seed by performing a multi-regression method until it converges. The output parameters of Matisse are refined by the Gauguin module, which implements a Gauss-Newton algorithm that computes the dimension in the parameter space that minimises the difference between the observed and the synthetic spectra. If needed, this process is repeated to get a satisfactory subtraction of the continuum, especially for cool stars, by performing a sigma-clipping procedure based on the comparison of the observed and the interpolated synthetic spectra. The quality of this fitting is quantified by the $\log \chi^2$ parameter, included in the final output. Previously to its ingestion in the pipeline, the Matisse algorithm had been trained with the synthetic grid to optimise the b-functions, required for determining the weight of each pixel during the application stage.

Once the stellar parameters are determined, the Gauguin algorithm is re-implemented for the extraction of the chemical abundances from individual lines, adding an extra normalisation routine focused on the spectral region near the considered line (Santos-Peral et al. 2020). The algorithm stops when the iteration step is smaller than one hundredth the step of the abundance grid. Finally the DIB and the cyanogen parameters are determined by an iterative Gaussian profile fitting algorithm.

In order to account for the flux error of the input spectra, the whole procedure described above is repeated fifty times using different random realisations of the input spectra, whose distortion depends on their signal-to-noise ratio. We consider the median of the outputs of all of these realisations as estimators, while the 16 and 84th percentiles are associated with the uncertainty. For those elements with multiple lines, we combine the individual abundances from each line by computing their weighted mean, in which the weight is determined by the inverse of their uncertainties. A more detailed explanation involving the rejection of bad estimates can be found in Section 6.8 of Recio-Blanco et al. (2023).

2.2 The synthetic spectral grids

As mentioned in the previous section, MatisseGauguin uses grids of synthetic spectra as reference for determining the stellar parameters and the chemical abundances. These grids were generated with the version 19.2 of the TURBOSPECTRUM code (Plez 2012) assuming the MARCS atmospherics models (Gustafsson et al. 2008) and the list of atomic and molecular lines of Contursi et al. (2021). As Fig. 1 illustrates, the four-dimensional grid used in the determination of the atmospheric parameters contains more than fifty thousand spectra spanning the range 2750 K $\leq T_{\rm eff} \leq$ 8000 K, -0.5 dex $\leq$ logg $\leq$ 5.5 dex, -0.5 dex $\leq$ [M/H] $\leq$ 5.5 dex, -0.4 dex $\leq [\alpha/{\rm Fe}] \leq$ 0.8 dex with steps of $\Delta T_{\rm eff}$ = 250K, Δlogg = 0.5 dex, Δ[M/H] = 0.25 dex and $\Delta[\alpha/{\rm Fe}]$ = 0.1 dex. Once a synthetic spectrum is generated, it is degraded to the RVS resolution (11,500) and re-sampled using a wavelength step of 0.03 nm within 876.0 and 870. nm to mimic the observed spectra.

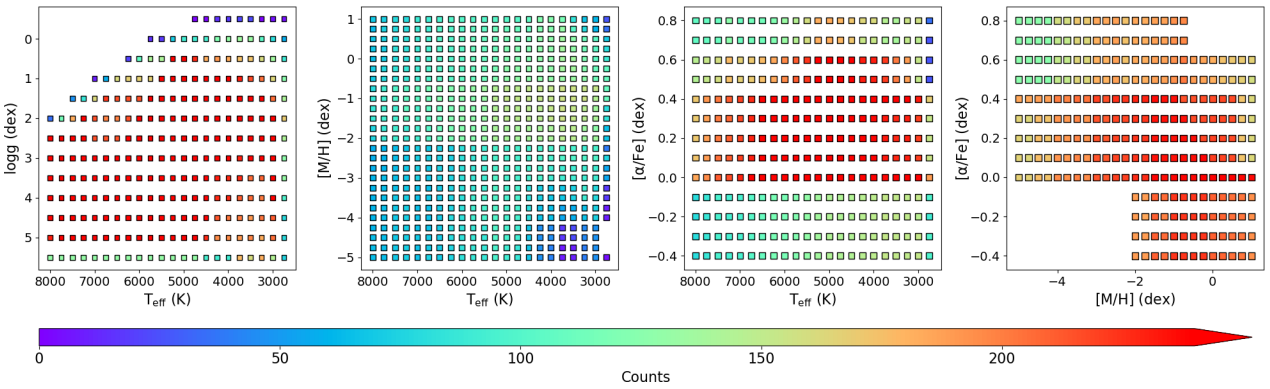

Fig. 1. Distribution of the nodes of the four-dimensional synthetic grid in different projections. **Left:** Number of synthetic spectra simulated in the logg vs. T_{eff} plane. **Middle-left:** Number of synthetic spectra per node in the [M/H] vs. T_{eff} plane. **Middle-right:** Distribution of synthetic spectra in the [α/Fe] vs. T_{eff} plane. **Right:** [α/Fe] vs. [M/H] diagram with the number of synthetic spectra in this projection.

Regarding the abundance determination, a five-dimensional grid is computed for each chemical element by considering 9-10 possible values of the individual abundance, generally ranging from -2.0 dex to $+2.0$ dex with the exception of the α elements, whose range of values depends on the metallicity to mimic that of the Milky Way. Compared to the four-dimensional grid described above, these five-dimensional grids are more restricted in the atmospheric parameter space, excluding the cool stars and the very metal poor (¡-3 dex) regime among other variations. However, the synthetic grids associated with the Fe, Ti and Ca abundances contain the nodes at such low metallicites. In total, the number of synthetic spectra for each individual element ranges from $\sim 470,000$ to almost $591,000$ for the mentioned Fe, Ti and Ca cases.

2.3 The line list

GSP-Spec makes use of a compilation of atomic and molecular lines summarised in Contursi et al. (2021). After an exhaustive evaluation based on the dependence of these lines with the abundance, the existence of blends with other chemical species, and the consistency with lines of the same element, we reduce the initial list to 49 lines of 12 different elements: N, Mg, Si, S, Ca, Ti, Cr, Fe, Ni, Zr, Ce and Nd.

For each line in the final list, we consider a wavelength domain where the flux variation correlates with the abundance in the simulated spectra of Arcturus, Procyon, and solar-like stars. Similarly, we define a broader wavelength domain for the extra normalisation (referred as *second normalisation* in Recio-Blanco et al. 2023) associated with each line (see Section 2.1). For consecutive lines of the same elements, in which common abundance and/or second normalisation windows are applicable, we tested whether the inclusion in a shared wavelength domain improves the results or not. Furthermore, in the specific case of the calcium triplet, abundances are determined by exploring both sides of the line wings while excluding the core to avoid NLTE effects. This results in an 'effective" number of lines of 33. After testing multiple combinations of abundance and second normalisation windows, the final limits for these wavelength domains are summarised in Table B.1 of Recio-Blanco et al. (2023).

3 GSP-Spec data availability

The running of the GSP-Spec module was performed at the Data Processing Centre CNES (DPCC) in Toulouse (France), where it analysed almost seven million sources with fifty repetitions each due to the error propagation (see Section 2.1). It required more than one hundred thousand computing hours spread on 2,100 cores, resulting in a total execution time of one hundred and fifty hours. Among the total volume analysed, approximately 1.3 million sources were discarded during the validation of the processing stage, leading to the released sample of 5.6 million stars.

Similarly to other *Gaia* products, the tables with the GSP-Spec output have been ingested into the *Gaia*

archive*. More precisely, the results of MatisseGauguin are located in the GAIADR3.ASTROPHYSICAL_PARAMETERS table while these of ANN can be found in the supplementary GAIADR3.ASTROPHYSICAL_PARAMETERS_SUPP table, where the parameters associated with each module can be identified by the subfix of the field names. As usual, these data is accessible by performing an ADQL query on the *Gaia* archive web-site (see Appendix B of Gaia Collaboration et al. (2023a) for examples of queries with scientific purposes).

4 Calibration

The comparison of the GSP-Spec results with these from large ground-based surveys like APOGEE-DR17 (Abdurro'uf et al. 2022), GALAH-DR3 (Buder et al. 2021) and RAVE-DR6 (Steinmetz et al. 2020) reveals some trends with the GSP-Spec parameters that must be corrected. The giants analysed by GSP-Spec show a significant bias in logg compared to that reported in literature, while their global metallicity [M/H] seems to be under-estimated. On the contrary, dwarf stars show good agreement in surface density but an excess of global metallicity. No significant bias has been observed in effective temperature. In order to account for the mentioned discrepancies, we propose a polynomial correction based on the measured value of logg of the form

$$parameter_{calibrated} = parameter_{uncalibrated} + \sum_{n=0}^{N} p_n (logg_{uncalibrated})^n \tag{4.1}$$

where N is the degree of the polynomia and the coefficients p_n can be found in Table 3 of Recio-Blanco et al. (2023), where an additional calibration for the metallicies of stars in open clusters has been provided. Similarly, analogous corrections have been suggested for the the global $[\alpha/Fe]$ and the individual chemical abundances, with the exception of [Zr/Fe], [Nd/Fe] due to low number statistics, and of [Ce/Fe] because of an offset in the solar value. These calibrations are, however, restricted to specific ranges of logg. For the particular case of the [α/Fe], [Ca/Fe] and [S/Fe] estimates, other corrections based on the effective temperature $T_{\rm eff}$ are provided.

Since the corrections proposed above were obtained for a selection of stars that spans a wide range in logg or $T_{\rm eff}$, other calibrations for more specific samples in the parameter space might improve the agreement with the literature (for example, see the case of the [Mg/Fe] abundance of Spitoni et al. 2023). In any case, we recall the calibration of GSP-Spec parameters is mandatory for their correct usage. Additional resources for the calibration of GSP-Spec parameters can be found in the *Gaia* DR3 web-page†.

5 Flagging system

Both the MatisseGauguin and the ANN workflows return a string of integer numbers, called *flags*, encoding the quality of their respective outputs. In total, a system of 41 flags is adopted for the GSP-Spec output, in which only the first twelve are common to both workflows (the remaining 29 are exclusive to MatisseGauguin). These 41 flags can be group into three families concerning the spectral features (first 13 flags), the chemical abundance determination (the next 26 flags) and the cyanogen/DIB fittings (last 2 flags). In general, flag values range from "0" for the high quality parameters to "9" for the bad estimates (sometimes removed from the table). Since their definition is quite technical, we provide here a brief description of the first family and refer to Section 8 in Recio-Blanco et al. (2023) for a more detailed explanation of the whole set.

The first three flags *vbroadT*, *vbroadG* and *vbroadM* indicate the bias induced by the rotational velocity of the star on the atmospheric parameters $T_{\rm eff}$, logg and [M/H], respectively. We evaluated these biases by simulating the broadening effects on a set of synthetic spectra, which is used as input of GSP-Spec. As a result, this artificial rotation leads to values of $T_{\rm eff}$, logg and [M/H] different from the nominal ones (see Figure 2 for an example). Depending on the level of such distortion, a flag from "0" to "2" is assigned to the stellar parameter. In the same way, the biases induced by the errors in the line-of-sight velocity correction were explored following a similar procedure but using shifted synthetic spectra instead of broadened ones. The quantification of these biases are summarised in the next three flags *vradT*, *vradG* and *voadM* for the $T_{\rm eff}$, logg and [M/H], respectively.

The *fluxNoise* flag is associated with the bias induced by the flux error of the input spectra, which was explored by observing the dispersion of the four atmospheric parameters $T_{\rm eff}$, logg, [M/H] and [α/Fe] along the fifty random realisations mentioned in Section 2.1. The *extrapol* flags determines the quality of the solution

*https://gea.esac.esa.int/archive/

†https://www.cosmos.esa.int/web/gaia/dr3-gspspec-metallicity-logg-calibration

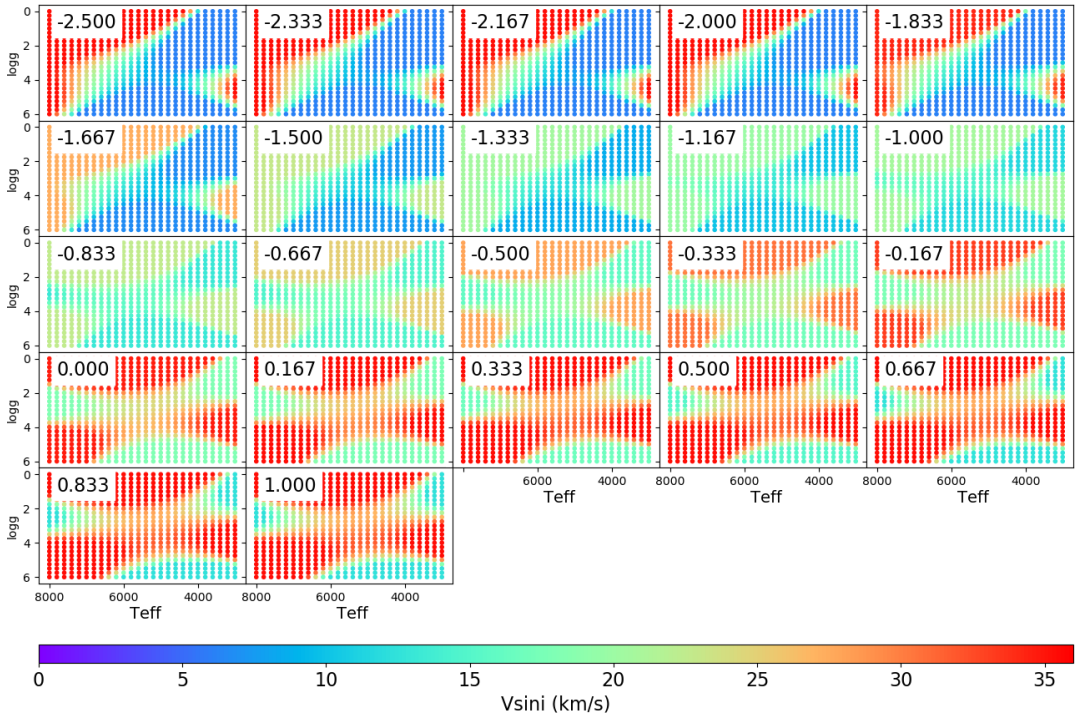

Fig. 2. Limiting rotational velocity values $Vsini$ (colour-code) in the Kiel diagram leading to a *vbroadT* flag equal to zero (i.e., a bias of $\Delta T_{\rm eff} < 250$ K). Each subpanel corresponds to the metallicity $[M/H]$ indicated in the upper left corners.

found by MatisseGauguin or ANN depending on the distance to the borders of the training grids, and it was used to exclude some sources with bad estimations from the *Gaia* archive during the post-processing phase.

There are four flags related to undesired features in the RVS spectra: *negativeFlux* and *nanFlux* informs about the presence of pixels with negative or NaN fluxes, respectively. Similarly, *nullFluxErr* is equal to nine if no flux error is provided by the input spectra, leading to a zero-variance atmospheric parameter estimations during the random realisation stage; while the *emission* flag is nine if the CU6 has detected an emission line in the spectra.

In the cool regimes, where there are many molecular absorption lines, the estimation of the atmospheric parameters is specially difficult, resulting in an unphysical combination of $T_{\rm eff}$ and logg values. For these stars, we assign a non-zero *KMgiantFlag* value and artificially set their effective temperatures and surface gravities to 4250 ± 500 K, 1.5 ± 1 dex, respectively. As for the calibrations (cf. Section 4), the usage of the flags previously introduced is mandatory for the correct application of the GSP-Spec data and avoid misleading results. As an initial recommendation, we suggest selecting the stars with the first thirteen flags equal to zero and adjusting the initial guess as needed.

6 Scientific application of GSP-Spec

Since the publication of the GSP-Spec products with *Gaia* DR3, many groups have been exploiting this information for scientific purposes. For sake of exemplification, we have selected few of them to illustrate the quality of the GSP-Spec parametrization and the multiple possibilities of its application. Gaia Collaboration et al. (2023a) constitutes one of the major compilation of examples of usages of GSP-Spec data. Their analysis of accreted structures identified in the energy vs. angular momentum reveal a chemical pattern consistent with their *ex-situ* origin, showing a deficiency of α-elements compared to the Milky Way stars at the same metallicity (Nissen & Schuster 2010). Similarly, they explored the chemistry of the kinematic and dynamic structures reported in previous works, such as the ridges in the velocity profile (Ramos et al. 2018), the spiral in the Z-V_Z plane (Antoja et al. 2018), and the over-densities in the action space J_R vs. L_Z (Trick et al. 2019; Trick 2022), to find clear correlations between the location of the stars in these structures and their chemical composition. By selecting massive stars in the Kiel diagram, Gaia Collaboration et al. (2023a) observed spatial inhomogeneities

in the Galactic Plane revealing the presence of spiral arms, being the innermost ones more metal rich than the external arms. This connects with the work of Poggio et al. (2022), who analysed the spatial distribution of three populations classified as bright giant stars by GSP-Spec to find an excess of metallicity in these regions where the spiral arms are observed. They also report a varying metallicity gradient with azimuth for their sample of old stars. Analysing the α-element abundances, Spitoni et al. (2023) found an evidence of a third infall of gas that triggered the star formation in the solar vicinity 2.7 Gyr ago, likely related to the pericenter passage of the Sagittarius dwarf galaxy. This model can also explain the trend of the cerium abundances with metallicity studied in Contursi et al. (2023), who found a good agreement between the GSP-Spec [Ce/Fe] estimates and these reported in literature, even though the latter might show some systematics. They also reported radial and vertical gradients for the [Ce/Fe] and [Ce/H] abundances.

7 Conclusions

Gaia DR3 constitutes the largest all-sky chemical survey ever published, with atmospheric parameters and chemical abundances for nearly 5.6 million sources. This was possible thanks to the implementation of the GSP-Spec module in the *Gaia* pipeline, which automatised the analysis of the combined, velocity-corrected spectra given as input from the CU6. As a result, it provided very competitive data compared to large ground-base spectroscopic surveys, although calibration and filtering are required for its correct application. A wide variety of scientific results has already been published using the GSP-Spec catalog, including the evidence of a recent gas infall, the metallicity excess in the spiral arm regions, as well as the gradients in the distribution of heavy elements among others .

I acknowledge the invitation from the organisation of the "Archéologie Galactique avec *Gaia*/DR3: un an après" session, as part of the French Astronomy and Astrophysics Society (SF2A) meeting held in Strasbourg (France). I thank the financial support from the Centre national d'études spatiales (CNES). This work presents results from the European Space Agency (ESA) space mission Gaia. Gaia data are being processed by the Gaia Data Processing and Analysis Consortium (DPAC). Funding for the DPAC is provided by national institutions, in particular the institutions participating in the Gaia MultiLateral Agreement (MLA).

References

Abdurro'uf, Accetta, K., Aerts, C., et al. 2022, ApJS, 259, 35
Antoja, T., Helmi, A., Romero-Gómez, M., et al. 2018, Nature, 561, 360
Buder, S., Sharma, S., Kos, J., et al. 2021, MNRAS, 506, 150
Contursi, G., de Laverny, P., Recio-Blanco, A., & Palicio, P. A. 2021, A&A, 654, A130
Contursi, G., de Laverny, P., Recio-Blanco, A., et al. 2023, A&A, 670, A106
Cropper, M., Katz, D., Sartoretti, P., et al. 2018, A&A, 616, A5
Gaia Collaboration, Brown, A. G. A., Vallenari, A., et al. 2018, A&A, 616, A1
Gaia Collaboration, Brown, A. G. A., Vallenari, A., et al. 2021, A&A, 649, A1
Gaia Collaboration, Prusti, T., de Bruijne, J. H. J., et al. 2016, A&A, 595, A1
Gaia Collaboration, Recio-Blanco, A., Kordopatis, G., et al. 2023a, A&A, 674, A38
Gaia Collaboration, Vallenari, A., Brown, A. G. A., et al. 2023b, A&A, 674, A1
Gustafsson, B., Edvardsson, B., Eriksson, K., et al. 2008, A&A, 486, 951
Katz, D., Munari, U., Cropper, M., et al. 2004, MNRAS, 354, 1223
Lee, Y. S., Beers, T. C., An, D., et al. 2011, ApJ, 738, 187
Nissen, P. E. & Schuster, W. J. 2010, A&A, 511, L10
Perryman, M. A. C., de Boer, K. S., Gilmore, G., et al. 2001, A&A, 369, 339
Perryman, M. A. C. & Hassan, H. 1989, ESA Bulletin, 58, 77
Plez, B. 2012, Turbospectrum: Code for spectral synthesis, Astrophysics Source Code Library
Poggio, E., Recio-Blanco, A., Palicio, P. A., et al. 2022, A&A, 666, L4
Ramos, P., Antoja, T., & Figueras, F. 2018, A&A, 619, A72
Recio-Blanco, A., de Laverny, P., Palicio, P. A., et al. 2023, A&A, 674, A29
Santos-Peral, P., Recio-Blanco, A., de Laverny, P., Fernández-Alvar, E., & Ordenovic, C. 2020, A&A, 639, A140
Spitoni, E., Recio-Blanco, A., de Laverny, P., et al. 2023, A&A, 670, A109
Steinmetz, M., Guiglion, G., McMillan, P. J., et al. 2020, AJ, 160, 83
Trick, W. H. 2022, MNRAS, 509, 844
Trick, W. H., Coronado, J., & Rix, H.-W. 2019, MNRAS, 484, 3291

SF2A 2023
M. N'Diaye, A. Siebert, N. Lagarde, O. Venot, K. Baillié, M. Béthermin, E. Lagadec, J. Malzac, J. Richard (eds)

S-PROCESS ELEMENT ABUNDANCES WITH THE GAIA/GSP-SPEC CATALOGUE

G. Contursi[1], P. de Laverny [1], A. Recio-Blanco [1] and P. A. Palicio[1]

Abstract. The study of *s*-process elements allows to constrain and better understand the nucleosynthesis within AGBs. These evolved stars indeed release *s*-process elements at their surface through successive Third Dredge Ups.

On another hand, Galactic Archaeology relies on the study of a large amount of stars in order to statistically characterise the different Galactic stellar populations. It is in this context that the Gaia DR3 offers a huge step forward since such chemical abundances associated with accurate astrometric data have been published for an unprecedented number of stars. Thanks to such data derived from the analysis of RVS spectra by the *GSP-Spec* module, we have explored the Galactic content in neutron-capture elements (Ce, Nd) and the importance of those elements in the stellar evolution.

GSP-Spec Ce abundances cover several stellar populations (AGB and giants) while Nd abundances are available only on AGB stars. Therefore, combining Ce and Nd abundances, we found a good correlation between those two elements in AGB stars. We also found a relation between *s*-process abundances and atmospheric parameters of the stars showing the production of Ce and Nd by the AGB. We compared our *GSP-Spec* abundances with AGB models.

In addition, Gaia DR3 cerium abundances can be used to trace the Galactic content of the Milky Way. For instance, we found a flat trend in [Ce/Fe] vs [M/H] in the Milky way disc. We also computed horizontal gradient from field stars as well as from open clusters. We also found cerium in the halo within accreted systems and one globular cluster.

Keywords: Galaxy: abundances, disc, halo, evolution - Stars: abundances, evolution, AGB and post-AGB

1 Introduction

Our understanding of the Milky Way has made a great leap forward thanks to the different data releases of the Gaia mission. The third release (Gaia Collaboration et al. 2023) consists in a major and unique step since it includes a large variety of new data products including, in particular, extensive characterisation of the *Gaia* sources. In this context, the General Stellar Parametrizer from Spectroscopy module (*GSP-Spec*, hereafter, see Gaia Collaboration, Recio-Blanco et al. 2022) has estimated atmospheric parameters (effective temperature $T_{\rm eff}$, surface gravity $\log(g)$, global metallicity [M/H], abundances of α-elements with respect to iron [α/Fe]) as well as individual chemical abundances of up to a dozen of elements* for about 5.6 millions stars which have been observed by the Radial Velocity Spectrometer (RVS hereafter, Katz et al. 2022). The *GSP-Spec* module also provides quality flags (*flags_gspspec* hereafter) related to the parametrization or the determination of the individual abundances.

Among these 13 chemical elements, three are produced by neutron captures in the inner layers of some specific stages of stellar evolution: Zirconium (Z = 40), Cerium (Z = 58) and Neodynium (Z = 60). According to the seminal work of Burbidge et al. (1957), neutron capture occurs through two main processes: the rapid (*r*-) and slow (*s*-) processes (slow and rapid referring to the time-scale of the neutron captures with respect to the β-decay).

The formation sites of the *s*-process are well understood. When looking at the distribution of Solar abundances, three peaks located around the atomic mass number A=90, 138 and 208 are found. Sr, Y and Zr

[1] Université Côte d'Azur, Observatoire de la Côte d'Azur, CNRS, Laboratoire Lagrange, Bd de l'Observatoire, CS 34229, 06304 Nice cedex 4, France

*see `https://www.cosmos.esa.int/web/gaia/iow_20210709`. These elements are: N, Mg, Si, S, Ca, Ti, Fe I, Fe II, Ni, Zr, Ce, and Nd.

© Société Française d'Astronomie et d'Astrophysique (SF2A) 2023

represent the first peak; Ba and Ce the second and Pb the third ones. Even though all these elements are mainly formed via s-process (Prantzos et al. 2018), their formation sites can differ. Indeed, the *s*-process can be decomposed in three sub-processes, each one populating a different peak (see Kappeler et al. 1989, and references therein). Low- and intermediate-mass AGB stars at Solar metallicity produce the so-called *main* *s*-process such as Ce and Nd thanks to neutrons produced mainly by the ^{13}C(α,n)^{16}O reaction (Bisterzo et al. 2015, e.g.). This reaction takes place in the so-called ^{13}C-pocket, between the H and He burning shells. This ^{13}C pocket is formed through a sequence reaction ^{12}C(p,γ)^{13}N(β^+)^{13}C thanks to the partial mixing of protons from the convective H-rich envelope into the ^{12}C region during the third dredge-up. The ^{22}Ne(α, n)^{25}Mg reaction also contributes to the convective thermal pulse.

This work is composed as follows. Section 2 describes the study of the *GSP-Spec* Ce abundances in the Milky Way while Sect. 3 presents Ce and Nd *GSP-Spec* abundances focusing on AGB. Finally, the conclusions of this work are presented in Sect. 4.

2 Cerium content of the Milky Way

In this section, we investigate the cerium content of the Milky Way, based on the *GSP-Spec* abundances. Cerium abundances are determined from a triplet of Ce II lines centred around 851.375 nm (in vacuum). An example of this cerium feature is provided in Fig. 9 of Gaia Collaboration, Recio-Blanco et al. (2022). More details about this work can be found in Contursi et al. (2023).

2.1 Sample selection

Among the about 5.6 million of stars having chemo-physical parameters derived by the *GSP-Spec* module, there are 103 948 stars with a Ce abundance, whatever the *flags_gspspec*. By selecting a specific combination of these flags, we obtained a sample of 29 941 stars with high-quality Ce abundances. This sample contains some AGB stars. As evoked in the introduction, AGB stars are among the main producers of *s*-process elements such as Ce. We then removed those stars from the sample as they can be polluted by internal production. *s*-process elements on AGB stars parametrized by *GSP-Spec* are investigated in the next section.

We then end up with a sample of 7397 stars to investigate the Ce content of the Milky Way. 90% of this sample have $|Z_{max}| < 0.7$ kpc and 85% have a total velocity < 70 km/s, confirming their belonging to the disc.

2.2 [Ce/Fe] versus [M/H] trend

We illustrate the [Ce/Fe] trend with respect to metallicity in the top panel of Fig. 1. We found a rather flat trend at a mean level of [Ce/Fe]$\sim$0.2 dex for metallicities varying between $\sim$-0.7 up to $\sim$+0.3 dex. A similar behaviour and mean level of [Ce/Fe] is reported by Forsberg et al. (2019), based on 277 stars (red triangles in Fig. 1, top panel). This flat trend is also in agreement with Reddy et al. (2006) (178 stars), Battistini & Bensby (2016) (365 stars) and Delgado Mena et al. (2017) (orange diamonds in Fig. 1, top panel, 653 stars. Note that those stars have $T_{\rm eff} > 5300$ K and $S/N > 100$ according to their Sect. 4), although these authors report a lower [Ce/Fe] level (around $\sim$+0.0 dex), probably resulting from different calibrations and/or reference scales. Finally, it is worth noting that, in the low metallicity regime ([M/H] < -0.8 dex), the working sample is probably not statistically representative.

The bottom panel of Fig. 1 shows the [Ce/Ca] abundance ratio versus [Ca/H]. Orange dots illustrate again the running mean [Ce/Ca] abundance, using bins of 0.07 dex in [Ca/H]. Error bars are the associated standard deviation for each bin. For values of [Ca/H] larger than $\sim$-0.7 dex (low statistics blurring the trend at lower metallicities), we found a slight increasing [Ce/Ca] abundance with increasing [Ca/H] (δ[Ce/Ca]/δ[Ca/H] = $0.087^{\pm 0.013}$), similar to the trend of the high-Ia population of Griffith et al. (2021) (this population representing their thin disc low-[Mg/Fe] distribution). It is important to note that Griffith et al. (2021) used Mg abundances from APOGEE DR16 data, while the α-element reference is Ca in our study.[†] This continuous increase of [Ce/Ca] could be the consequence of the later contribution of AGB stars (main producers of *s*-process elements, as cerium) in the Galactic chemical evolution history with respect to SN II (producers of α-elements as Ca). Moreover, we point out that we also found a rather flat distribution of [Ce/Ca] ratio for [Ca/H] > 0.1 dex whereas Griffith et al. (2021) report a strong decrease. This is due to the different trend of our Ca abundances

[†]We adopted Ca instead of Mg as several of the *High-Quality Sample* stars do not have *GSP-Spec* magnesium abundances.

and their Mg ones. Actually, their [Mg/Fe] remains constant for positive metallicities, contrary to the continuous decrease of our [Ca/Fe], as it can be seen in Fig.25 of Recio-Blanco et al. (2022). This continuous decrease is more in agreement with Galactic evolution models that predict a similar decrease of any [α/Fe] ratios with [M/H](see also Spitoni et al. (2022)). We also note that our [Ce/Ca] is systematically higher than that of Griffith et al. (2021), probably because of the different reference scales adopted.

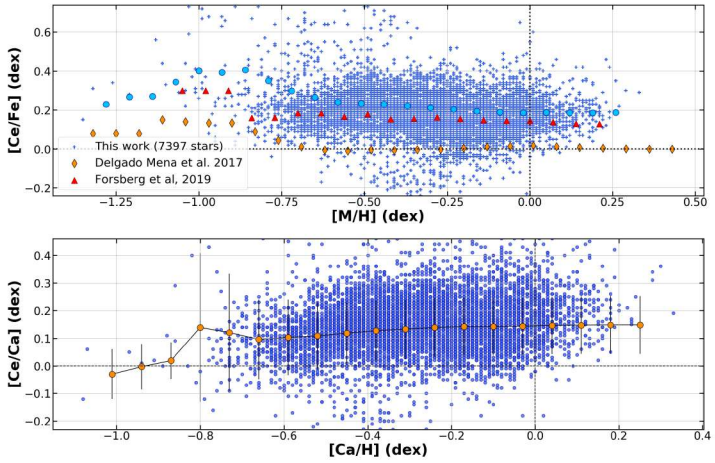

Fig. 1. Top panel: Cerium and iron abundances ratio for the *High-Quality Sample* with respect to the metallicity. Red triangles and orange diamonds are mean [Ce/Fe] ratios for the stars of F19 and Delgado Mena et al. (2017), respectively (computed per bins of 0.07 dex). Sky blue points the mean of our data per bin of 0.07 dex in [Ca/H]. **Bottom panel**: [Ce/Ca] versus [M/H]. Orange dots correspond to the mean of the measurements per bin of 0.07 dex and the error bars correspond to the standard deviation in each bin.

3 Production of Ce and Nd in AGB stars

We define a working sample of 19 544 AGB stars having high-quality Ce and/or Nd abundances (17 765 stars with Ce abundances and 3 490 with Nd abundances, 1 711 stars having both Ce and Nd abundances), selected by applying a specific combination of the *GSP-Spec* quality flags.

We first confirmed that the majority of the working sample is composed of AGB stars by estimating their absolute magnitude in the K-band and their properties in a Gaia-2MASS diagram. We also checked that these stars are oxygen-rich AGBs, as assumed during the *GSP-Spec* parameterisation.

Fig. 2 shows a high positive correlation between the Ce and Nd abundances (Pearson correlation coefficient = 0.75). The associated dispersion is rather large since it is dominated by the Nd measurement uncertainties, the Nd II line being more difficult to analyse. Such a correlation confirms the quality of the derived abundances since it is actually expected as both elements belong to the *s*-process second peak and hence have a similar nucleosynthetic origin. We also remark that colour-coding this correlation with $T_{\rm eff}$ clearly shows the enhancement of the Ce and Nd abundances for cooler stars, i.e. for more evolved stars on the AGB. This illustrates the successive mixing episodes enriching the AGB surface in s-process elements formed deeper in their stellar interior.

We then compared the observed Ce and Nd abundances with FRUITY and Monash AGB yields and found that the higher Ce and Nd abundances can not be explained by AGBs of mass higher than 5 $M_{\odot}$. On the contrary, the yields predicted by both models for AGB with an initial mass between $\sim$1.5 and $\sim$2.5 $M_{\odot}$ and metallicities between $\sim$-0.5 and $\sim$ 0.0 dex are fully compatible with the observed *GSP-Spec* abundances.

Note that more details about this work can be found in Contursi et. al, in prep.

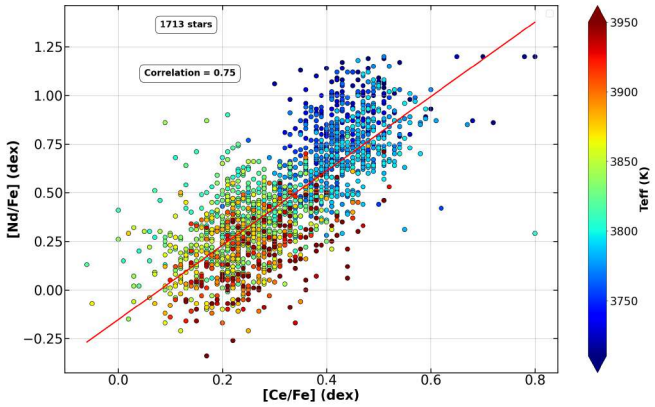

Fig. 2. Correlation between Ce and Nd abundances for AGB stars colour-coded by their $T_{\rm eff}$. The slope of the red line is 1.91 while the standard deviation is 0.44 dex. The Pearson correlation coefficient is also reported.

4 Conclusions

The Gaia DR3 is the first whole-sky spatial spectroscopic survey. Among the 5.6 million of stars parametrized by the *GSP-Spec* module, some of them have abundances of elements formed through neutron capture: cerium and neodymium.

We first investigate the cerium content of the Milky Way and found a relatively flat trend with the metallicity. We compared it with litterature measurements.

On the other hand, we investigated the Ce and Nd abundances in AGB stars parametrized by *GSP-Spec* and found higher abundances of these elements for cooler stars (i.e. in more advanced stages for a given $\log(g)$ and [M/H]).

All those results show the excellent quality of the Gaia DR3 data and are in agreement with our understanding of the production sites of these elements as well as their evolution through the Galactic chemical evolution history.

References

Battistini, C. & Bensby, T. 2016, A&A, 586, A49
Bisterzo, S., Gallino, R., Käppeler, F., et al. 2015, MNRAS, 449, 506
Burbidge, E. M., Burbidge, G. R., Fowler, W. A., & Hoyle, F. 1957, Reviews of Modern Physics, 29, 547
Contursi, G., de Laverny, P., Recio-Blanco, A., et al. 2023, A&A, 670, A106
Delgado Mena, E., Tsantaki, M., Adibekyan, V. Z., et al. 2017, A&A, 606, A94
Forsberg, R., Jönsson, H., Ryde, N., & Matteucci, F. 2019, A&A, 631, A113
Gaia Collaboration, Vallenari, A., Brown, A. G. A., et al. 2023, A&A, 674, A1
Gaia Collaboration, Recio-Blanco, A., Kordopatis, G., de Laverny, P., et al. 2022, arXiv e-prints, arXiv:2206.05534
Griffith, E., Weinberg, D. H., Johnson, J. A., et al. 2021, ApJ, 909, 77
Kappeler, F., Beer, H., & Wisshak, K. 1989, Reports on Progress in Physics, 52, 945
Katz, D., Sartoretti, P., Guerrier, A., et al. 2022, arXiv e-prints, arXiv:2206.05902
Prantzos, N., Abia, C., Limongi, M., Chieffi, A., & Cristallo, S. 2018, MNRAS, 476, 3432
Recio-Blanco, A., de Laverny, P., Palicio, P. A., et al. 2022, arXiv e-prints, arXiv:2206.05541
Reddy, B. E., Lambert, D. L., & Allende Prieto, C. 2006, MNRAS, 367, 1329
Spitoni, E., Recio-Blanco, A., de Laverny, P., et al. 2022, arXiv e-prints, arXiv:2206.12436

SF2A 2023
M. N'Diaye, A. Siebert, N. Lagarde, O. Venot, K. Baillié, M. Béthermin, E. Lagadec, J. Malzac, J. Richard (eds)

REWINDING THE HISTORY OF HIGH-MASS X-RAY BINARIES WITH GAIA

F. Fortin[1], F. Garcia[2], A. Simaz-Bunzel[2], S. Chaty[1] and E. Chassande-Mottin[1]

Abstract. High-mass X-ray binaries (HMXBs) are stellar couples that undergo mass exchange between a massive star and a compact object. They represent a peculiar phase in the life of massive stars in binaries, which is preceeded by a supernova event as well as mass transfer episodes. These mechanisms interplay in the evolution of massive stars and need to be constrained to better understand how these binaries may be the progenitors of compact mergers seen by LIGO/Virgo.

Gaia has observed more than 100 HMXBs in the Milky Way. By combining the knowledge we already have on those systems, thanks to the building of a new and up to date catalogue, with the exquisite astrometric measurements from Gaia EDR3, we are able to put constraints to the strength of the natal kick imparted to HMXBs during a supernova event, as well as find out where precisely they were born in the Galaxy. Gaia is thus a precious tool for Galactic archeology and the ecology of massive stars, from their birth to their endpoint as compact binaries.

Keywords: binaries: general; stars: formation; stars: evolution; astrometry; stars: kinematics and dynamics; stars: neutron; stars: black holes;

1 Introduction

High-mass X-ray binaries are stellar couples composed of a compact object –usually a neutron star (NS) and seldom a black hole (BH) – accreting from a massive O-B companion ($M \geq 8\,M_\odot$, see a broad review in Chaty (2022)). Mass transfer can occur through a decretion disk around a Be companion in BeHMXBs (Rivinius et al. 2013), or via intense stellar wind from an evolved, supergiant companion in sgHMXBs (Chaty 2013).

X-ray binaries have been observed for more than 60 years now, yet they require multiwavelength observations as well as time series to be properly constrained. Hence, we still unveil new systems today and keep observing known ones to better constrain their properties: orbital periods, spectral type of the companion, nature of the compact object, etc. Not only they are of interest because of the extreme, high-energy physics of accretion-ejection they display, they also are of key importance in the scope of stellar evolution. It is likely that most massive stars spend at least part of their lives in binaries, and by the end of their lives some could be the progenitors of compact mergers now seen by LIGO/Virgo (and later by LISA).

Gaia has been surveying the whole sky to produce a huge astrometrical database that allow us to precisely locate sources within the Milky Way, and may help to understand the role of HMXBs in the Galactic ecology. It is high time we have an updated view of the population of X-ray binaries in our Galaxy in a modern, community-driven database. This HMXB catalogue (Fortin et al. 2023), available online*, is designed to be a starting base for population studies and and tool to help with targeting the right HMXBs to revisit in observing time proposals. I will present the catalogue in Section 2, then review how it has already been used to valorize astrometric data from Gaia by probing the past history of those HMXBs, inferring their natal kick (Section 3) and finding their birthplace in the Milky Way (Section 4).

[1] Université Paris Cité, CNRS, Astroparticule et Cosmologie, F-75013 Paris, France
[2] Instituto Argentino de Radioastronomía (CCT La Plata, CONICET; CICPBA; UNLP), C.C.5, (1894) Villa Elisa, Buenos Aires, Argentina
*https://binary-revolution.github.io/HMXBwebcat/

© Société Française d'Astronomie et d'Astrophysique (SF2A) 2023

2 The catalogue of HMXBs in the Galaxy from the INTEGRAL to the Gaia era

The latest catalogue dedicated to Galactic HMXBs was compiled by Liu et al. (2006), a few years after the launch of the *INTEGRAL* satellite. Back then, the census counted 114 HMXBs and candidates in the Milky Way. However, *INTEGRAL* was particularly adapted to the observation of HMXBs and even discovered a new subclass, the obscured sgHMXBs, thanks to its sensitivity in hard X-rays. Hence, in the past 17 years, *INTEGRAL* has triggered many multi-wavelength followup campaigns to identify hard X-ray sources and constrain their nature (Fortin et al. 2018).

All of this observational knowledge, produced by independent teams of researchers over many years, is not easy to collect together in a coherent and updated database because of the many new systems discovered each year and new constraints brought on their nature and intrinsic parameters (orbital period, companion spectral type, presence of pulsations...). It is necessary to have an accurate picture of the current population of X-ray binaries if we want to be able to link them to the growing population of compact binaries, and bring constraints to the evolutionary mechanisms that govern the life of massive stars.

2.1 Building an updated database

For this work, we have extensively used the services of the Centre de Données Astronomiques de Strasbourg (CDS), mainly Simbad and Vizier. First, we retrieved the last HMXB catalogue from Liu et al. (2006), that we supplemented by adding hard X-ray sources detected by INTEGRAL (Bird et al. 2016). We crossmatched the two catalogues, and at this stage kept all INTEGRAL sources labelled either HMXB, LMXB or CV since misidentification is common.

Then, we queried Simbad for all sources labelled "HXB", and performed a spatial selection on the plane of the sky to discard extragalactic sources (which are densely clustered in their host galaxies, contrary to Galactic HMXBs which are mainly spread whithin the Galactic plane). After crossmatching the Simbad HMXBs with the sample from Liu et al. (2006) and Bird et al. (2016), we added 66 new candidates to review.

At this point, we performed an individual, minute search in the literature for each source to retrieve the original references for already published data on their parameters, find out if anything new was publised since the last catalogues and confirm they are indeed HMXBs. For this, we queried NASA's ADS using a combination of a variety of keywords. This process is quite lengthy but necessary to ensure the quality of the data presented in the catalogue and have a proper track of references for each listed parameter.

Finally, we performed a semi-automatic search for counterparts of each HMXB at various wavelengths, including the detections from Gaia EDR3 in order to also retrieve a distance estimation whevever possible. This allows us to precisely locate HMXBs whithin the Galaxy, as shown in Figure 1 (left panel).

2.2 Contents of the catalogue and availability

At the time of publication, the finished catalogue counted 153 HMXBs in the Milky Way (Fortin et al. 2023). That was a 33% increase compared to the sample in Liu et al. (2006), or a 100% increase if we limit to the confirmed systems (hard X-ray detection and early spectral type confirmed for the optical counterpart). 111 HMXBs had a Gaia counterpart, which offer an unprecendented opportunity to precisely locate them whithin the Milky Way. We compiled astrometric information, orbital data, spectral types and spin periods, which allows us to draw the most up to date picture of the Galactic HMXB population.

The catalogue is hosted at the CDS in a fixed version; but in order to take into account new discoveries (or correct the few mistakes that are unavoidable on such a large, manually built database), we host the catalogue on an independent website, HMXBwebcat[†]. The database itself is hosted on our GitHub collaboration, and is able to receive updates from the community as new observations are performed. This is why, at the time of writing, the catalogue now counts 159 HMXBs and the numbers keep steadily growing. New versions of the catalogue are published regularly, with a track reccord of each modifications to ensure continuity. The database can be browsed directly in a navigator, or downloaded in various formats to be explored (we recommend Topcat).

[†]`https://binary-revolution.github.io/HMXBwebcat/index.html`

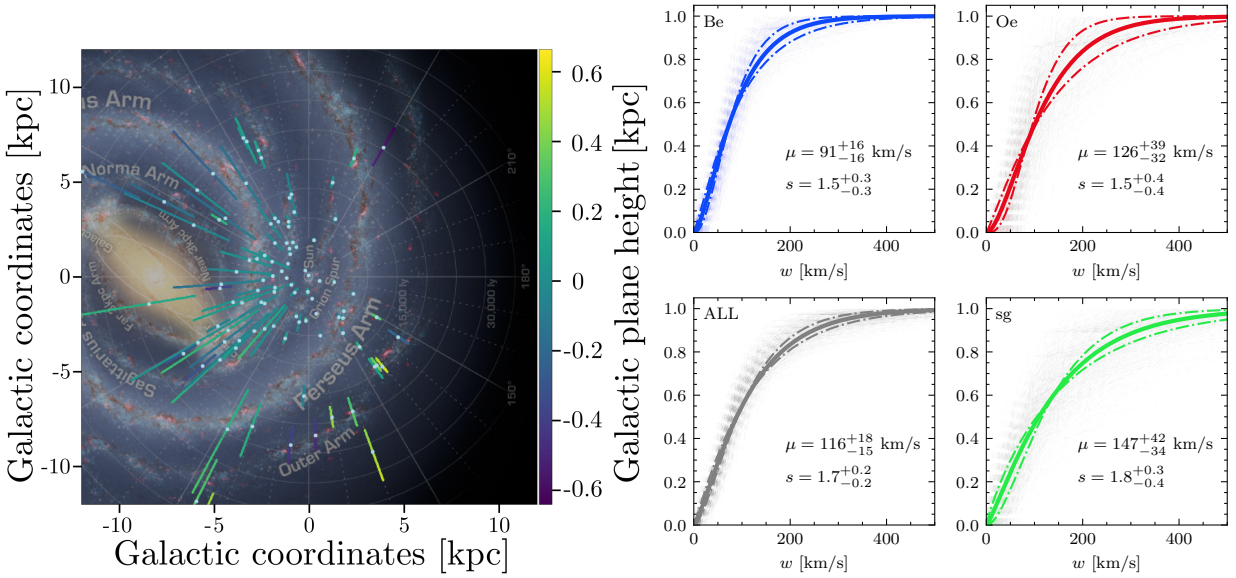

Fig. 1. Left: Face-on view of the Galactic HMXBs seen by Gaia Right: Cumulative distribution of neutron star kicks in Galactic HMXBs.

3 Constraints to neutron star kicks in HMXBs

All the HMXBs present in the catalogue contain a compact object, and most of them are NSs. Hence, most of HMXBs, prior to their X-ray phase, underwent a supernova event. Not only the explosion induces a sudden mass loss that affects the orbit of the binary, the supernova may happen with a certain degree of asymetry, kicking the center of mass in a random direction and adding to the eccentricity of the system. Because we have compiled intrinsic parameters such as orbital periods, eccentricities and stellar masses in HMXBs, and retrieved astrometric measurements from Gaia, it is possible to observe the effects of this natal kick in HMXBs and thus allow us to estimate the strength of the supernova explosion and its effect on the binaries.

The information on the natal kick is indeed contained within the peculiar velocity of HMXBs, which is the proper motion corrected for the Galactic co-rotation velocity. Hence, we can compute the peculiar velocity of HMXBs on the condition of them having a precise distance determination from Gaia data (Bailer-Jones et al. 2021) as well as having an independent radial velocity measurement. The peculiar velocity is used as an input the the equations that describe the effects of an asymetric supernova explosion on the center of mass of a binary system (Brandt & Podsiadlowski 1995; Kalogera 1996). Using Monte-Carlo Markov-Chain simulations, we can compute the posterior probability of the natal kick strength in each of the neutron stars of our HMXB sample. Because a complete set of orbital parameters, masses and astrometry of high quality are necessary, we were able to perform this on 35 Galactic HMXBs.

On top of deriving the kick strength for each system, we agregated those results to get average kick distributions across sub-types of HMXBs, namely the BeHMXBs, OeHMXBs (slightly more massive than Be) and sgHMXBs (Figure 1, right panel).

4 Finding the birthplace of HMXBs in the Milky Way

For the few HMXBs that have exquisite astrometry and radial velocity measurements, it is possible to look even further back in time to search for their birthplace in the Milky Way. Not only this would provide an estimation of their age, this can also give an estimation of the initial masses of the stars whithin the binaries, which is of prime importance to understand what is the population of star that are the progenitors of HMXBs.

We are looking for birthplaces in the Galactic spiral arms as well as the open clusters in the Galaxy. Recent publications, also using Gaia EDR3 astrometry, bring very good constraints on the shape, pitch angle and rotation velocity of the spiral arms (Castro-Ginard et al. 2021), and the precise location of 2000 open clusters whithin the Milky Way (Cantat-Gaudin et al. 2018). To find birthplace candidates, we integrate the motion of the HMXBs, clusters and spiral arms 100 Myr back in time and look for spatio-temporal coincidences.

When a coincidence is found, the time at which it happened provides an estimation of the time since supernova. In the case of a candidate birthplace in a cluster, since we have access to the age of the cluster via isochrone fitting, we can assume the binary formed at the same time as the cluster and thus have access to the full age of the binary. Combined with the knowledge of the time since supernova, and currently measured mass of the companion star, we can infer the initial masses of the two stars, the mass gained by the companion during the initial mass transfer as well as the pre-supernova mass of the primary star.

5 Conclusion

The building of an up to date catalogue of Galactic HMXBs lead to getting an accurate view of their population, and is a tool that can be used in various ways to explore the history and ecology of X-ray binaries in the Milky Way. Combined with recent astrometric data from Gaia, we can constrain the evolution of massive binaries from their formation (Fortin et al. 2022a) up to the supernova event that preceeds the X-ray phase (Fortin et al. 2022b). Multiple other evolutionary mechanisms punctuate the life of massive stars in binaries, e.g. the common envelope event, and are of prime importance to understand how massive stars reaching the endpoint of their lives coalesce as double compact systems.

Gaia is thus a precious tool for Galactic archeology. HMXBs, that involve massive stars right at their birth as binaries, are contributors to the Galactic ecology as they may impact their environement throughout multiple phases of their lives, either via intense stellar winds, jets, X-rays, supernova explosion as well as kilonova ejecta, that feeds the interstellar medium with heavy elements from the r-process.

The authors were supported by the LabEx UnivEarthS, Interface project I10, "From evolution of binaries to merging of compact objects" and Interface project "Binary rEvolution". The authors would like to thank Thierry Foglizzo, Jérôme Guillet and Thomas Tauris for fruitful discussions. This research has made use of the SIMBAD database, operated at CDS, Strasbourg, France. This work has made use of data from the European Space Agency (ESA) mission *Gaia* (`https://www.cosmos.esa.int/Gaia`), processed by the *Gaia* Data Processing and Analysis Consortium (DPAC, `https://www.cosmos.esa.int/web/Gaia/dpac/consortium`). Funding for the DPAC has been provided by national institutions, in particular the institutions participating in the *Gaia* Multilateral Agreement.

References

Bailer-Jones, C. A. L., Rybizki, J., Fouesneau, M., Demleitner, M., & Andrae, R. 2021, AJ, 161, 147

Bird, A. J., Bazzano, A., Malizia, A., et al. 2016, ApJS, 223, 15

Brandt, N. & Podsiadlowski, P. 1995, MNRAS, 274, 461

Cantat-Gaudin, T., Jordi, C., Vallenari, A., et al. 2018, A&A, 618, A93

Castro-Ginard, A., McMillan, P. J., Luri, X., et al. 2021, A&A, 652, A162

Chaty, S. 2013, Advances in Space Research, 52, 2132

Chaty, S. 2022, Accreting Binaries; Nature, formation, and evolution

Fortin, F., Chaty, S., Coleiro, A., Tomsick, J. A., & Nitschelm, C. H. R. 2018, A&A, 618, A150

Fortin, F., García, F., & Chaty, S. 2022a, A&A, 665, A69

Fortin, F., García, F., Chaty, S., Chassande-Mottin, E., & Simaz Bunzel, A. 2022b, A&A, 665, A31

Fortin, F., García, F., Simaz Bunzel, A., & Chaty, S. 2023, A&A, 671, A149

Kalogera, V. 1996, ApJ, 471, 352

Liu, Q. Z., van Paradijs, J., & van den Heuvel, E. P. J. 2006, A&A, 455, 1165

Rivinius, T., Carciofi, A. C., & Martayan, C. 2013, A&A Rev., 21, 69

SF2A 2023
M. N'Diaye, A. Siebert, N. Lagarde, O. Venot, K. Baillié, M. Béthermin, E. Lagadec, J. Malzac, J. Richard (eds)

CAN WE DECIPHER THE DYNAMICS OF THE MILKY WAY DISK FROM GAIA ?

Y. Khalil[1], B. Famaey[1], G. Monari[1] and A. Siebert[1]

Abstract. The unprecedented data from the Gaia mission have revealed the complex structure of the phase-space of the Milky Way (MW) disk over a larger volume than ever before. These data should help us in the search for a complete dynamical model of the MW. We concentrate here on in-plane motions and on what they can teach us about the present-day non-axisymmetric structures of the MW Disk. In the joint presence of the central bar and spiral arms, it is particularly hard to analytically compute velocities of stars for the whole phase-space domain from a distribution function (DF) satisfying the linearized collisionless Boltzmann equation. However, the conservation of the DF in infinitesimal phase-space patches following the Hamiltonian flow allows us to compute the current DF by integrating orbits backward in time to an axisymmetric equilibrium state. In this way, we can construct a DF in the joint presence of the bar and spiral arms, and confront the models to Gaia data with observables computed with the DF. Here, we show preliminary results on the effects of the bar alone, and lay down our plans for the exploration of the space of parameters of the models to establish realistic dynamical non-axisymmetric models for the MW disk, and hopefully decipher the dynamics of the MW's spiral arms.

Keywords: Galaxy: kinematics and dynamics, Galaxy: fundamental parameters, Galaxy: structure, Galaxy: Disk, Galaxy: solar neighborhood

1 Introduction

The third data release of Gaia (DR3, Gaia Collaboration et al. 2023b) has been an important milestone in offering full 6D phase-space information for stars of the Milky Way (MW) disk over a larger volume than ever before (Gaia Collaboration et al. 2023a). Whilst stellar vertical motions have revealed in recent years a disequilibrium of the Galactic disk (Antoja et al. 2018, 2023), possibly related to a subtle interplay between external peturbations and internal non-axisymmetries (Li et al. 2023), the richness of the information contained solely within the in-plane motions of stars has not been fully exploited yet. In principle, these in-plane motions should allow us to get a precise dynamical mapping of the Galactic parameters setting the location, kinematics and dynamics of the most important non-axisymmetric structures of the MW disk namely, the bar and the spiral arms.

So far, different tracers and observations are far from converging on parameters describing the placement of each spiral arm segment in the MW disk. In particular, the observed geometry and extension of the arms may differ. The so-called Local arm, for example, has been found by Gaia Collaboration et al. (2023a) and Poggio et al. (2021), tracing young stars, to be more extended and to have an intermediary pitch angle if compared to Vázquez et al. (2008), where this arm heads outwards to the Perseus arm, or to Xu et al. (2021), where the Local arm heads inwards to the Carina-Sagittarius arm. Similar debates exist regarding the Perseus arm and Outer arm with respect to their position in the disk and pitch angle. Perhaps most strikingly, the pitch angle of the Perseus arm has been found around 24° in Levine et al. (2006), compatible with results of Poggio et al. (2021), and around 9° in Reid et al. (2019). These examples may illustrate the challenges in accurately tracing the spiral arms of the MW from photometry alone, and using the unprecedented dynamical information from Gaia could help obtaining independent constraints.

The detailed mapping of velocity space in the immediate neighbourhood of the Sun (the 'local velocity field', herafter LVF) has long revealed a complex structure in the radial (v_R) vs azimuthal (v_ϕ) velocity plane where it presents a complex configuration of overdensities called moving groups (Eggen 1958; Blaauw 1970),

[1] Observatoire Astronomique de Strasbourg, Université de Strasbourg, UMR 7550, F-67000 Strasbourg, France

© Société Française d'Astronomie et d'Astrophysique (SF2A) 2023

most of those being nowadays thought to be related to the orbital resonances with the bar and spiral arms of the Galaxy (Dehnen 1998, 2000; Famaey et al. 2005; Antoja et al. 2011). In particular, the so-called Hercules moving group, creating a bimodality in the local velocity distribution at low v_ϕ and positive v_R, has traditionally been associated with resonances from the Galactic bar, although some debates are still going on about which resonance to associate it to. For the other moving groups, things are even less clear, as they have been associated to various possible resonances with spiral arms (Sellwood 2010; McMillan 2011; Pompéia et al. 2011), as well as with high-order modes of the bar (Monari et al. 2019).

Regarding the mean non-axisymmetrtic motions of stars in a larger volume around the Sun (the 'extended velocity field', hereafter EVF), pioneering work has been carried out by Siebert et al. (2011) who uncovered a significant Galactocentric radial velocity gradient within a distance range limited to 2 kpc from the Sun, with data from the RAVE survey. This velocity map was explored in Siebert et al. (2012) to constrain the parameters of a Lin-Shu density wave logarithmic spiral model, notably its amplitude, pattern speed, pitch angle and number of arms. The best model found was two-armed with a location compatible with the Local and Perseus arm placements and a pattern speed of 18.6 km/s/kpc. It was noted by Monari et al. (2014) that the Galactic bar could also contribute to the gradient. With the Gaia Data Release 2 (Gaia DR2), parameters of a two-armed logarithmic spiral model were again constrained in Eilers et al. (2020): the constrained model was found to be compatible with the location of Local and Outer Arms, not giving any dynamical evidence for the Perseus arm, and with a lower pattern speed of 12 km/s/kpc. More recently, in Gaia Collaboration et al. (2023a), a full map of the average Galactocentric radial velocities of late-type RGB stars from Gaia DR3 has been produced. One can clearly identify a distinguishable signature of the Galaxy's bar in the central regions, while other spiral-induced features seem to appear in the outskirts. It is therefore clear that a combination of the influence of the Galactic bar and spiral arms should be able to explain the main features of such a Galactocentric radial velocity map.

In the following, we describe briefly in section 2 the Gaia DR3 data subsets that we will use to confront the model at two scales: in the vicinity of the Sun (the LVF) and an extended region about 4 kpc from the Sun (the EVF). The bar model is described in 3 together with our modelling technique. In section 4 we compare the data to a bar model (without spiral arms) that already describes reasonably well the data in the LVF, similarly to the earlier results of Monari et al. (2019), but not in the EVF. We conclude in 5 on discussing the upcoming addition of spiral arms and the perspectives of this work.

2 Gaia DR3 data

From the Gaia DR3 RVS data we select stars for which we compute the positions in Galactocentric Cartesian coordinates, $\mathbf{x} = (x, y, z)$ and velocities in Galactocentric Cylindrical coordinates, $\mathbf{v} = (v_R, v_\phi, v_z)$. The coordinate transformations from original Equatorial coordinates to Galactocentric coordinates depend on the Sun's position and velocity. For the Sun's position, we set: $\mathbf{x}_\odot = (8.275\,\mathrm{kpc}, 0, 15.29\,\mathrm{pc})$, with x from GRAVITY Collaboration et al. (2021), and z from Widmark & Monari (2019). For the Sun's velocity we use $\mathbf{v}_\odot = (9.3\ \mathrm{kms}^{-1}, 250.2\ \mathrm{kms}^{-1}, 7.2\ \mathrm{kms}^{-1})$.

We select stars within $|z| < 200\,\mathrm{pc}$, and we consider them close enough to the plane to analyze their planar motion within the $z = 0$ plane. For the LVF, we consider 909 666 stars within $r = \sqrt{(x - x_\odot)^2 + (y - y_\odot)^2} <$ 200 pc, whereas, for the EVF, we consider 12 740 039 stars within $4\,\mathrm{kpc} < x < 12\,\mathrm{kpc}$ and $-4\,\mathrm{kpc} < y < 4\,\mathrm{kpc}$. The stars of the LVF are used to study the number density distribution of stars in velocity space in the vicinity of the Sun, so we work with a 2-dimensional histogram on the (v_R, v_ϕ)-plane. The stars of the EVF are used to study the radial velocity v_R map. The data for the disk sample of Gaia DR3 data are shown in the top panels of Figure 1.

3 Model

For a joint system of bar and spiral arms with different pattern speeds there is no easy analytical description for the distribution function (DF) satisfying the linearized collisionless Boltzmann equation for the whole phase-space domain. To overcome this difficulty, we will use in our work the backwards integration method developed by Vauterin & Dejonghe (1997). Many works explored this method, notably to study the MW bar dynamics. For instance, in Dehnen (2000), the bar's pattern speed was explored with this method and compared to the LVF obtained at the time from Hipparcos data. More recently, in Monari et al. (2019), this method was used to relate the resonances of various modes of the bar to many features of the LVF from Gaia data.

The backwards integration method is based on the conservation of the DF in infinitesimal phase-space patches following the Hamiltonian flow, which allows us to compute the current DF by integrating orbits backward in time to an axisymmetric equilibrium state, where analytical expression for the DF are well established. In this way, we can construct a DF in the joint presence of the bar and spiral arms, and confront the models to Gaia data with observables computed with the DF, mainly number denssity of stars in velocity space and median velocities as a function of position in the disk. We can therefore in principle explore the space of parameters of the models to establish realistic dynamical non-axisymmetric models for the MW Disk and hopefully decipher the complex non-axisymmetric structure of the disk.

In our model, we first impose a background axisymmetric potential and DF for the disk. For the time being, we then add a bar which grows smoothly. The bar potential, defined by a combination of three Fourier modes ($m = 2, 4, 6$), is described in Thomas et al. (2023) and inspired from the model of Portail et al. (2017), known to match fairly well the kinematics of the inner Galaxy. The main parameters, beyond the amplitude of the modes, are the pattern speed, $\Omega_{\rm bar}$ and the angle of the bar's major axis in Galactocentric coordinates ϕ_b.

4 Results

Here, we set $\Omega_{\rm bar} = 38\,{\rm kms}^{-1}{\rm kpc}^{-1}$ and $\phi_b = 28^\circ$ (Monari et al. 2019) and display the results of this bar-only model in the bottom panels of Figure 1. Comparing the left panels of Figure 1, we confirm the results of Monari et al. (2019), namely that many features of the LVF can be reproduced by the bar alone. Comparing the right panels, though, it is clear that the EVF is not reproduced in the outer Galaxy. Nevertheless, it is reasonably well recovered by the bar-only model (bottom-right panel) for the region within $x < 8$ kpc and $y < 2$ kpc, although some features are definitely missing even in this region.

5 Perspectives

Especially in regions beyond the Sun, the EVF obtained from our bar-only model clearly indicates the necesarry inclusion of spiral arms in the model, in accordance with the precedent analysis in Siebert et al. (2012), and more recently in Eilers et al. (2020). The challenge is however to recover the EVF without destroying the already pretty satisfactory LVF. Hopefully, the inclusion of spiral arms would even improve the LVF, in regions corresponding to the Hyades and Sirius moving groups (Dehnen 1998, 2000; Famaey et al. 2005; Antoja et al. 2011; Bernet et al. 2022). Further development of quantitative metrics to compare model to data will allow us to explore the parameter space for spiral arms in a joint model with the bar, and more generally, to constrain parameters of the Galaxy potential, including both axisymmetric and non-axisymmetric internal structures.

References

Antoja, T., Figueras, F., Romero-Gómez, M., et al. 2011, MNRAS, 418, 1423
Antoja, T., Helmi, A., Romero-Gómez, M., et al. 2018, Nature, 561, 360
Antoja, T., Ramos, P., García-Conde, B., et al. 2023, A&A, 673, A115
Bernet, M., Ramos, P., Antoja, T., et al. 2022, A&A, 667, A116
Blaauw, A. 1970, in The Spiral Structure of our Galaxy, ed. W. Becker & G. I. Kontopoulos, Vol. 38, 199
Dehnen, W. 1998, AJ, 115, 2384
Dehnen, W. 2000, AJ, 119, 800
Eggen, O. J. 1958, MNRAS, 118, 65
Eilers, A.-C., Hogg, D. W., Rix, H.-W., et al. 2020, ApJ, 900, 186
Famaey, B., Jorissen, A., Luri, X., et al. 2005, A&A, 430, 165
Gaia Collaboration, Drimmel, R., Romero-Gómez, M., et al. 2023a, A&A, 674, A37
Gaia Collaboration, Vallenari, A., Brown, A. G. A., et al. 2023b, A&A, 674, A1
GRAVITY Collaboration, Abuter, R., Amorim, A., et al. 2021, A&A, 647, A59
Levine, E. S., Blitz, L., & Heiles, C. 2006, Science, 312, 1773
Li, C., Siebert, A., Monari, G., Famaey, B., & Rozier, S. 2023, MNRAS, 524, 6331
McMillan, P. J. 2011, MNRAS, 418, 1565
Monari, G., Famaey, B., Siebert, A., Wegg, C., & Gerhard, O. 2019, A&A, 626, A41
Monari, G., Helmi, A., Antoja, T., & Steinmetz, M. 2014, A&A, 569, A69

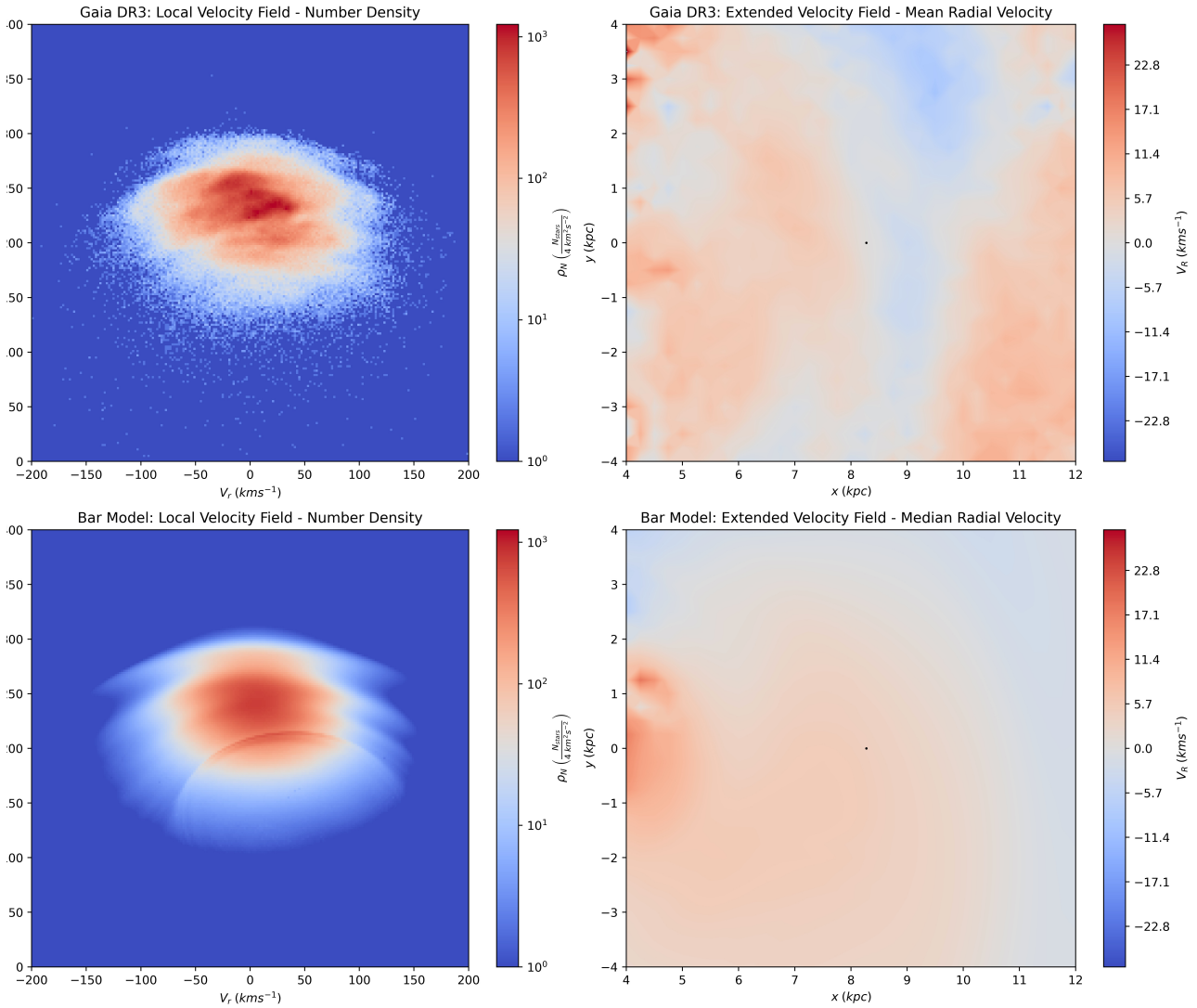

Fig. 1. Top panels: Gaia DR3 data. Bottom panels: Bar-only model. The left panels display the 2-dimensional histogram of the number density of stars for the LVF in the (v_R, v_ϕ)-plane in the Solar neighbourhood, for squared 2 kms^{-1} bins. The right panels display the median Galactocentric radial velocity map for the EVF in the Galactic plane seen face-on, binned in squared 250 pc bins. The small black dot represents the Sun's position in the Galactic plane, which rotates anti-clockwise. It is clear that the bar alone reproduces many features of the LVF but not the detailed shape of the EVF, especially in the outer Galactic disk.

Poggio, E., Drimmel, R., Cantat-Gaudin, T., et al. 2021, A&A, 651, A104
Pompéia, L., Masseron, T., Famaey, B., et al. 2011, MNRAS, 415, 1138
Portail, M., Gerhard, O., Wegg, C., & Ness, M. 2017, MNRAS, 465, 1621
Reid, M. J., Menten, K. M., Brunthaler, A., et al. 2019, ApJ, 885, 131
Sellwood, J. A. 2010, MNRAS, 409, 145
Siebert, A., Famaey, B., Binney, J., et al. 2012, MNRAS, 425, 2335
Siebert, A., Famaey, B., Minchev, I., et al. 2011, MNRAS, 412, 2026
Thomas, G. F., Famaey, B., Monari, G., et al. 2023, arXiv e-prints, arXiv:2309.05733
Vauterin, P. & Dejonghe, H. 1997, MNRAS, 286, 812
Vázquez, R. A., May, J., Carraro, G., et al. 2008, ApJ, 672, 930
Widmark, A. & Monari, G. 2019, MNRAS, 482, 262
Xu, Y., Hou, L. G., Bian, S. B., et al. 2021, A&A, 645, L8

SF2A 2023
M. N'Diaye, A. Siebert, N. Lagarde, O. Venot, K. Baillié, M. Béthermin, E. Lagadec, J. Malzac, J. Richard (eds)

NEW FEATURES OF PHASE SPIRAL FROM GAIA DR3

C. Li[1], A. Siebert[1], G. Monari[1], B. Famaey[1] and S. Rozier[2]

Abstract. Disc stars from the Gaia DR3 RVS catalogue are selected to explore the phase spiral in the Galaxy. The data reveal a two-armed phase spiral pattern in the local $z - v_z$ plane inside the solar radius, which appears clearly when colour-coded by $\langle v_R \rangle(z, v_z)$: this is characteristic of a breathing mode that can in principle be produced by in-plane non-axisymmetric perturbations. The phase spiral pattern becomes single armed outside the solar radius. When a realistic analytic model with a steadily rotating bar and 2-armed spiral arms as perturbation is used to perform particle test integrations, no phase-spiral is perceptible in the (z, v_z) plane. Finally, we show as a proof of concept how a toy model of a time-varying non-axisymmetric in-plane perturbation with varying pattern speed can produce a strong two-armed phase-spiral. We conclude a time-varying strong internal perturbation together with an external vertical perturbation could perhaps explain the transition between the two-armed and one-armed phase-spirals around the Solar radius.

Keywords: Galaxy: kinematics and dynamics – Galaxy: evolution – Galaxy: structure – Galaxy: disc

1 Introduction

The phase spiral structure in the vertical position and velocity (z, v_z) plane of the Milky Way is one of the most important discoveries since the launch of the Gaia mission (Gaia Collaboration et al. 2016). This feature was first revealed in the solar vicinity with a population of stars sharing similar Galacto-centric radii and azimuthal angles (Antoja et al. 2018). Usually, the phase spiral is supposed to be generated by an external perturber such as a dwarf galaxy merging with the Milky Way. Binney & Schönrich (2018), for instance, developed a toy model based on the impulse approximation to show that the perturbation imposed by an intruder (such as a dwarf galaxy or some dark matter subhalo) can cause a prominent phase spiral in $\langle v_\phi \rangle(z, v_z)$. A concurrent explanation of the phase spiral associates it with internal mechanisms within the disc. In particular, Khoperskov et al. (2019) used an N-body simulation of an isolated Milky Way-type galaxy to show that the vertical oscillations driven by bar buckling can generate phase spirals in the solar neighbourhood.

Recently, using Gaia DR3 observations of inner disk stars, Hunt et al. (2022) spotted a two-armed spiral feature in $\rho(z, v_z)$ when stars are binned by guiding radius R_g and θ_ϕ, the conjugate angle of the action J_ϕ. Interestingly, they also found such a two-armed phase spiral in an isolated simulation. Recently, the framework of the shearing box approximation was adopted by Widrow (2023) to investigate the response of a disc to an impulsive excitation in the presence of self-gravity of the disc and swing amplification.

In light of the recently discovered two-armed phase spiral inside the solar radius, which can be produced by internal plane-symmetric perturbations, this paper aims at analysing what kind of phase spiral could potentially be produced by the bar and spiral arms of the Galaxy. We then compare the data, for the time being at the *qualitative* level, to test-particle simulations in a galactic potential with different bar and spiral arms perturbations added on top of a self-consistent background axisymmetric model.

2 Phase space spirals with Gaia DR3

Figure 1 shows the density plot of the sample stars in the $z - v_z$ phase space binned by the value of their angular momentum J_ϕ. The resulting density $\rho(z, v_z)$ is then smoothed by convolution with a Gaussian filter of width

[1] Université de Strasbourg, CNRS, Observatoire astronomique de Strasbourg (ObAS), UMR 7550, 67000 Strasbourg, France
[2] School of Mathematics, University of Edinburgh, Kings Buildings, Edinburgh, EH9 3FD, UK

© Société Française d'Astronomie et d'Astrophysique (SF2A) 2023

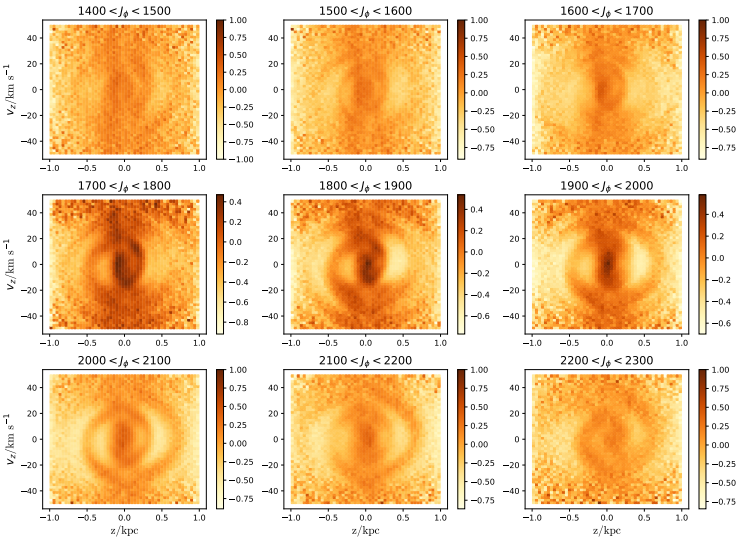

Fig. 1. The phase space density plot for our selected Gaia RVS sample data. The plotted quantity is the relative overdensity w.r.t. an average local density, following a procedure introduced in the text in detail. Only one armed phase spirals are seen in different J_ϕ intervals.

$4\,\Delta$pix, yielding the smoothed density $\bar{\rho}(z, v_z)$. We then plot the overdensity $\hat{\rho} = \rho(z, v_z)/\bar{\rho}(z, v_z) - 1$. Different panels correspond to different azimuthal action bins, which is an increasing function of the guiding radius R_g: $J_\phi = R_\mathrm{g} \times v_\mathrm{c}(R_\mathrm{g})$.

A single spiral pattern appears clearly in most panels, although this is not clear for the three innermost (lowest angular momenta) bins due to the large scatters of the data points in these bins. This one-armed phase spiral, as discussed thoroughly in the literature, could be related to a bending mode in the local and outer Galaxy, which could be triggered by the impact of the Sagittarius dwarf galaxy (e.g., Binney & Schönrich 2018; Bland-Hawthorn & Tepper-García 2021).

Several previous works have shown that the phase spiral can sometimes appear more clearly, and with different characteristics, either in the $\langle v_R \rangle(z, v_z)$ and $\langle v_\phi \rangle(z, v_z)$ maps (e.g. Antoja et al. 2018; Binney & Schönrich 2018; Bland-Hawthorn & Tepper-García 2021). Figure 2 therefore displays the mean Galactocentric radial velocity maps $\langle v_R \rangle(z, v_z)$ in different J_ϕ bins. The results are particularly interesting in the inner Galaxy. The first four panels, with $1400\,\mathrm{km\ s^{-1}kpc} < J_\phi < 1800\,\mathrm{km\ s^{-1}kpc}$, indeed show clear *two-armed* spiral patterns. When $J_\phi > 1800$ km s^{-1} kpc (next five panels), only one-armed spiral features can be seen in the plots, as in the density maps of Fig. 1. The two-armed phase-spiral pattern corresponds to a breathing wave (e.g., Widrow 2023) and is a strong hint for another perturbation mechanism than the perturbation causing the one-armed spiral in the outer disc (Hunt et al. 2022).

3 Modelling predictions under perturbations

3.1 Results for steadily rotating perturbations

Figure 3 shows the phase space maps of $\rho(z, v_z)$ (top row) and $\langle v_R \rangle(z, v_z)$ (bottom row) for different positions along the disc at $T = 1.5$ Gyr for a steadily rotating bar model. Unlike the observational data, the density plot $\rho(z, v_z)$ shows no spiral arm features among different azimuthal action intervals. Furthermore, the $\langle v_R \rangle(z, v_z)$ plots do not show any sign of phase spirals either. The distribution of $\langle v_R \rangle(z, v_z)$ is smooth within the central region of the $z - v_z$ plane and gets progressively noisy outwards. We did test the pseudo stars phase space properties for other snapshots at various time steps in the simulation: there are no phase spiral structures either in the (z, v_z) plane, whether it is in density or colour-coded by velocities.

3.2 Time-varying strong bar toy-model

To demonstrate that such two-armed phase spirals can *in principle* be produced by plane-symmetric perturbations, we now explore a toy-model of a strong bar with a time-varying pattern speed. We consider a bar with a large initial pattern speed and let the pattern speed decrease with time. The bar model we use in this toy-simulation is from Sormani et al. (2022). The initial pattern speed is $\Omega_\mathrm{b} = -88\,\mathrm{km\ s^{-1}\,kpc^{-1}}$ at $T = 0$ Gyr.

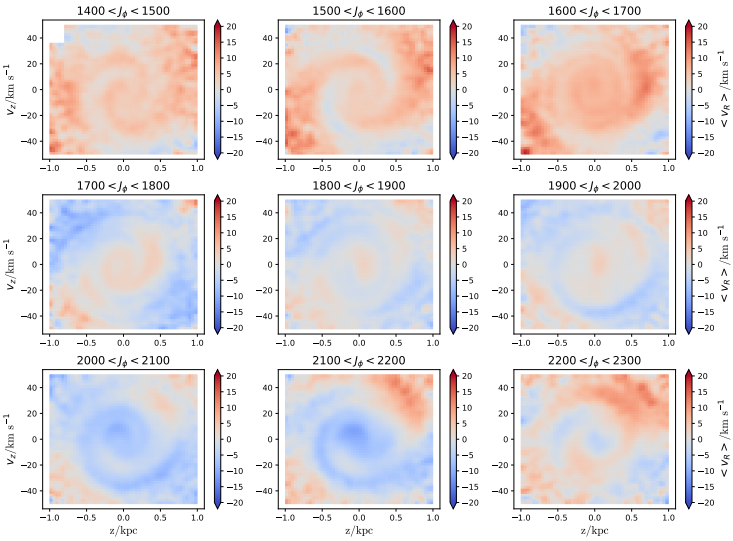

Fig. 2. The phase space plot colour-coded by $\langle v_R \rangle$ for our selected Gaia RVS sample data. Two armed phase spirals are clearly seen inside the solar radius when $J_\phi < 1800\,\mathrm{km\ s^{-1}kpc}$. The phase spiral pattern becomes single armed when $J_\phi > 1800\,\mathrm{km\ s^{-1}kpc}$.

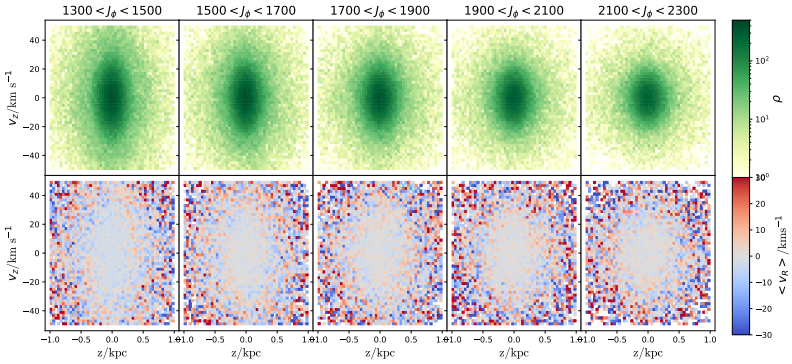

Fig. 3. Maps of $\rho(z, v_z)$ (top) and $\langle v_R \rangle(z, v_z)$ (bottom) for the model including a bar and spiral arms with constant pattern speeds, at $T = 1.5$ Gyr. Both the density $\rho(z, v_z)$ and $\langle v_R \rangle(z, v_z)$ show no spiral arm features.

Then it immediately starts to decrease and reach $\Omega_\mathrm{b} = -35\,\mathrm{km\ s^{-1}\,kpc^{-1}}$ at $T = 6$ Gyr. Meanwhile, the mass and radial profile of the bar are set to be multiplied by factors 2.5 and 1.5 respectively, which roughly simulates the growth of the bar. We then integrate test particle orbits for 8 Gyr. This extreme model is not meant to represent the real Milky Way in any way, but is rather meant, as a proof of concept, to strongly disturb the disk in a plane-symmetric way whilst not letting the pseudo stars settling within the potential of the perturber whose pattern speed constantly varies with time.

Figure 4 then shows the $z - v_z$ phase space density of the pseudo stars at $T = 3.0$ Gyr in the upper panels and $T = 3.5$ Gyr in the lower panels. It shows clear 2-armed spiral features in the first two panels at $T = 3.0$ Gyr. We also tested constant pattern speed bar models with the same spiral arm potential as in this model, and only this one produced the bisymmetric phase spiral, which is strong evidence that a bar with varying pattern speed is likely the culprit generating perturbations to the disc stars that lead to a 2-armed phase space spiral structure. The same pattern can also be seen in $\langle v_R \rangle(z, v_z)$ at $T = 3.0$ Gyr in the first panel.

4 Conclusions

In this work, we investigated the Gaia phase spiral structure based on observational data from Gaia DR3. We see a clear two-armed phase spiral structure in the inner disc in the $\langle v_R \rangle(z, v_z)$ map. On the contrary, only a one-armed phase spiral structure is clearly seen in the $\rho(z, v_z)$ plots. In order to analyse the possible origin of the two-armed phase spiral structure, we used test particle simulations to investigate how such perturbations affect the vertical phase space structure of the Galactic disc.

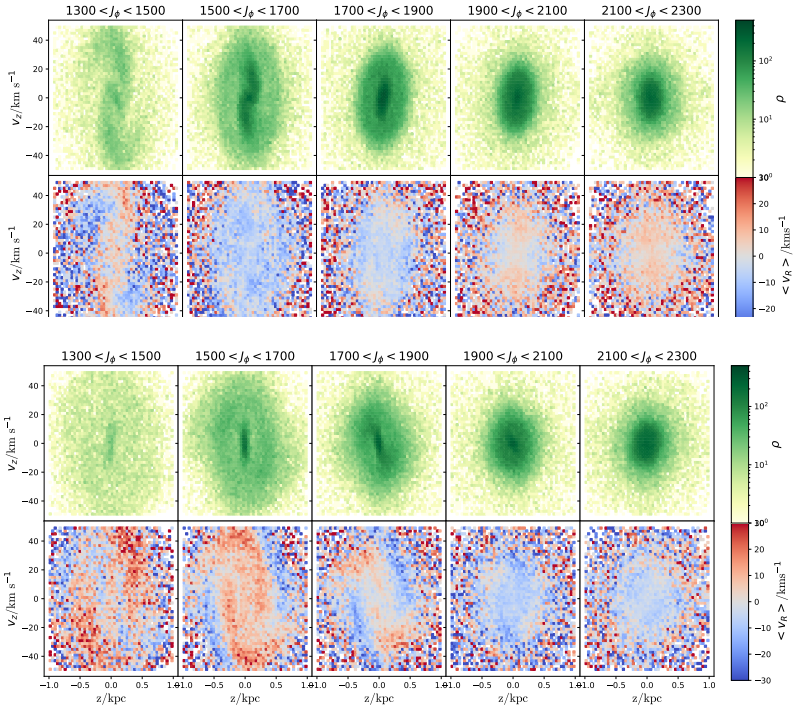

Fig. 4. Maps of $\rho(z, v_z)$ and $\langle v_R \rangle(z, v_z)$ for test particles in the model with decreasing bar pattern speed, at $T = 3.0$ Gyr (upper grid) and $T = 3.5$ Gyr (lower grid). In each grid, the top row shows the density $\rho(z, v_z)$ and the bottom row $\langle v_R \rangle(z, v_z)$. The density plot $\rho(z, v_z)$ shows clear 2-armed spiral features in the first two panels at $T = 3.0$ Gyr. The 2-armed spiral feature can also be seen in the first panel of $\langle v_R \rangle(z, v_z)$. At $T = 3.5$ Gyr, the 2-armed spiral feature in $\rho(z, v_z)$ is eliminated but still clear in $\langle v_R \rangle(z, v_z)$.

First, we showed that a realistic bar and spiral arm pattern with constant amplitude and pattern speed generates, as expected, non-zero mean v_R values across the disc, while the mean v_z remains null because the perturbations are plane-symmetric. The subtraction of the mean v_z values in the North and South hemisphere above and below the Galactic plane demonstrate, as expected too, that the Galaxy undergoes a breathing mode, which is particularly visible in the inner Galaxy. However, this breathing mode only translates itself in an inclination of the $z - v_z$ ellipsoid but does not show any sign of a two-armed phase spiral.

Therefore, we also tested the ability to disturb the disc with a stronger bar with varying pattern speed, not allowing the pseudo stars to settle in the potential of the perturber due to a constantly evolving potential. In this toy-model, we find that the phase space density $\rho(z, v_z)$ does show clear 2-armed spiral features, which is strong evidence that a bar with a decreasing pattern speed is able to produce a 2-armed phase spiral. This result suggests that the pattern speed of the bar might not be constant over time in the real Galaxy. We note that it takes a long time to produce these two-armed phase spirals and that the phase spiral features appear from inside-out, probably related to the growth of the bar.

References

Antoja, T., Helmi, A., Romero-Gómez, M., et al. 2018, Nature, 561, 360
Binney, J. & Schönrich, R. 2018, MNRAS, 481, 1501
Bland-Hawthorn, J. & Tepper-García, T. 2021, MNRAS, 504, 3168
Gaia Collaboration, Prusti, T., de Bruijne, J. H. J., et al. 2016, A&A, 595, A1
Hunt, J. A. S., Price-Whelan, A. M., Johnston, K. V., & Darragh-Ford, E. 2022, MNRAS, 516, L7
Khoperskov, S., Di Matteo, P., Gerhard, O., et al. 2019, A&A, 622, L6
Sormani, M. C., Gerhard, O., Portail, M., Vasiliev, E., & Clarke, J. 2022, MNRAS, 514, L1
Widrow, L. M. 2023, MNRAS, 522, 477

SF2A 2023
M. N'Diaye, A. Siebert, N. Lagarde, O. Venot, K. Baillié, M. Béthermin, E. Lagadec, J. Malzac, J. Richard (eds)

HUNTING NA-RICH STARS AMONG N-RICH STARS IN THE GALACTIC HALO

S. Martocchia[1], A. Savino[2], E. K. Grebel[1], C. Lardo[3], S. Martell[4], M. Shetrone[5] and N. Bastian[6,7,8]

Abstract. Globular clusters (GCs) provide stars to the halo as a result of two-body interactions and tidal forces exerted by the Galactic gravitational field. Therefore, to understand how the Galactic halo formed, it is crucial to estimate what fraction of the halo field stars are GC escapees. Identifying characteristic chemical patterns in halo stars is a promising approach, because GCs have unique chemical fingerprints, with concurrent and correlated enrichment in N and Na. Large existing surveys such as, e.g. APOGEE and SEGUE-1/2, use N enrichment to identify GC escapees. However, N enrichment is a necessary but insufficient condition, due to mixing processes affecting the N enhancement. To test this method, we report here the estimation of Na abundances of a sample of ∼30 N-rich Galactic Halo giant stars with high-resolution VLT/UVES and HET/HRS spectroscopy. Indeed, if a N-rich star in the halo is a GC escapee, it should also show Na enhancement. We find that less than 30% of our N-rich sample is also Na-rich, as expected from GC stars peculiar chemistry. Our analysis shows that the majority of N-rich stars in the Galactic Halo are likely not of GC origin and that previous works have possibly overestimated the fraction of GC stars in the halo by a factor of ∼3. We conclude that (i) future surveys need to take into account several elements (N, Na, C) in order to reliably identify GC escapees in the MW, (ii) our results support recent works suggesting that the disruption of GCs plays a minor role in the build-up of the MW stellar halo.

Keywords: galactic halo formation, chemically peculiar stars, globular clusters, abundances, spectroscopy

1 Introduction

Understanding how the halo of the Milky Way (MW) formed is still a complex problem to solve. Crucial insights are obtained thanks to globular clusters (GCs), ancient and massive agglomerate of stars that represent the fossil record of galaxy formation (e.g., Brodie & Strader 2006, Kruijssen et al. 2019). The MW hosts at least 160 GCs (Baumgardt & Vasiliev 2021) which lose their stars into the halo, disk or bulge due to the interaction with the gravitational potential of the MW, as well as internal relaxation processes. GC stars can be easily chemically tagged because almost all GCs host multiple stellar populations (MPs) in the form of star-to-star light element abundance variations (e.g., Gratton et al. 2012). Indeed, GCs are composed of ∼30-40% stars with comparable elemental abundances of field stars at the same metallicity, while up to ∼70% show enhanced N, Na and He together with depleted abundances of C and O (e.g., Bastian & Lardo 2018). Hence, knowing what fraction of the halo is represented by GCs stars provides an important piece of the puzzle for understanding the formation history of our Galaxy. Former spectroscopic surveys such as SEGUE, APOGEE, and Gaia−ESO provide large datasets to identify field stars exhibiting MPs. Existing attempts for finding GC escapee stars mainly rely on identifying chemical anomalies in C and N (SEGUE and APOGEE, e.g. Martell et al. 2011;

[1] Astronomisches Rechen-Institut, Zentrum für Astronomie der Universität Heidelberg, Mönchhofstraße 12-14, D-69120 Heidelberg, Germany
[2] Department of Astronomy, University of California Berkeley, Berkeley, CA, 94720, USA.
[3] Dipartimento di Fisica e Astronomia, Università degli Studi di Bologna, Via Gobetti 93/2, 40129, Bologna, Italy.
[4] School of Physics, University of New South Wales, Sydney NSW 2052, Australia.
[5] University of California Observatories, University of California Santa Cruz, Santa Cruz, CA 95064, USA.
[6] Astrophysics Research Institute, Liverpool John Moores University, 146 Brownlow Hill, Liverpool L3 5RF, UK.
[7] Donostia International Physics Center (DIPC), Paseo Manuel de Lardizabal, 4, 20018, Donostia-San Sebastián, Guipuzkoa, Spain.
[8] IKERBASQUE, Basque Foundation for Science, 48013, Bilbao, Spain.

© Société Française d'Astronomie et d'Astrophysique (SF2A) 2023

Schiavon et al. 2017; Koch et al. 2019), although some studies using Mg and Al were also reported (e.g. Lind et al. 2015; Fernández-Trincado et al. 2017). These works found a large population of N-rich stars both in the halo (∼2-3%, Martell et al. 2011) and in the bulge (∼7% for stars at [Fe/H]< −1, Schiavon et al. 2017) of the MW, suggesting that these stars might be originated from GCs. N is a good tracer to identify stars that were formed in a GC because the variations exhibited by this element extend to the main sequence (Harbeck et al. 2003) as do the O and Na variations (D'Orazi et al. 2010), indicating that the origin of N inhomogeneities cannot be explained entirely by evolution along the red giant (RG) phase. However, N is not an ideal element to search for GC escapees because RG stars can modify their surface abundances of C, N, and O via mixing processes (e.g., Karakas & Lattanzio 2014; Lagarde et al. 2019). Additionally, Bekki (2019) showed that other processes might lead to N enrichment (such as pollution from asymptotic giant branch stars) and concluded that the vast majority of N-rich stars are not of GC origin, both in the bulge and halo. Another way to identify chemically peculiar stars formed in GCs is to use either Na or Al abundances, as these elements are not altered by mixing. Among Na and Al, the best tracer of GC escapee stars is Na, because large Na variations of up to one dex are exhibited by GC stars at any metallicity, while the Al spread in GCs is sensitive to metallicity (Carretta et al. 2009). Unfortunately, neither the Gaia-ESO nor the APOGEE surveys can be used to systematically detect Na-enriched stars. For instance, the APOGEE spectral band contains two Na lines that become undetectable at [Fe/H]< −0.7 (Mészáros et al. 2015). On the other hand, only the UVES spectra of the Gaia-ESO survey (only 10% of the survey) have Na lines, and only a small fraction of them target halo giant stars.

In this paper, we then estimate the Na abundances of a sample of red giant stars in the Galactic Halo with high resolution spectra. The majority of the sample are selected to be rich in N, through the measurement of the strength of the CN, a molecular band located in the UV part of the spectra (at ∼3883Å), tracer of N abundance (Martell & Grebel 2010; Martell et al. 2011). The goal of this study is to determine whether the CN-rich stars also show a Na enhancement and in which fraction, in order to verify how well a N enrichment is able to trace and identify stars with GC origin. Section 2 will briefly describe the data and analysis, while in Section 3 we will present the results. We will conclude in Section 4 and refer the interested reader to a forthcoming paper (Martocchia et al., in prep) for more details and discussion on this study.

2 Data & Analysis

The data used in this analysis consist of optical spectra of 47 red giant stars of the Galactic Halo, selected from the Sloan Extension for Galactic Understanding and Exploration (SEGUE) sample of the SDSS (Yanny et al. 2009). Giants were selected in the Hertzprung-Russell diagram, which was built from the effective temperatures $T_{\rm eff}$ and gravities log(g) estimated by the SEGUE Stellar Parameters Pipeline (SSPP) of the SDSS (Rockosi et al. 2022). The SSPP also offers other stellar parameters such as the metallicity [Fe/H]. We refer the interested readers to Martell & Grebel (2010) and Martell et al. (2011) for more details about the selection. Our stars have 4800 ≤$T_{\rm eff}$≤ 5300 K and 1.5 ≤log(g)≤ 3.2 dex, and span a wide range in metallicity, i.e. −1.8 ≤[Fe/H]≤ −0.9 dex. In total, we collected spectra of 10 stars with VLT/UVES (R∼ 70,000, spectral coverage from ∼ 4700Å−6900Å) and spectra of 40 stars with the HET/HRS (R∼ 15,000, ∼ 6000Å−7900Å). These stars have Gaia DR3 G-band magnitudes from 14.6 to 17.2 mag (Gaia Collaboration et al. 2023).

Sodium abundances were computed by fitting the observed spectra with synthetic templates around the Na I lines at 6154.22Å and 6160.74Å. To calculate synthetic spectra, we adopted the atmospheric parameters from the SSPP ($T_{\rm eff}$, log(g) and [Fe/H]), while we assumed a microturbulent velocity v_t = 2 km/s for all the stars. Atomic and molecular line lists were taken from the most recent Kurucz compilation*. Model atmospheres were calculated with the ATLAS9 code (Castelli & Kurucz 2004) using an α-enhanced composition ([α/Fe]= +0.3 dex) for each star in the sample. Model spectra were generated using SYNTHE (Kurucz 2005) and then fitted to the observed spectra with a χ^2 minimisation algorithm to find the model that best fits our data. All the steps mentioned above were performed with the python routines `iSPy3`†. To estimate the errors associated with the abundance measurements, we consider a typical error of ±100 K in $T_{\rm eff}$, an error of ±0.2 dex in log(g), an error of ±1 km/s in the microturbulent velocity, and an error of ±0.2 dex in [Fe/H]. The errors were calculated as in in Martocchia et al. (2021).

*`http://wwwuser.oats.inaf.it/castelli/linelists.html`
†`https://github.com/soerenslarsen/ISPy3`

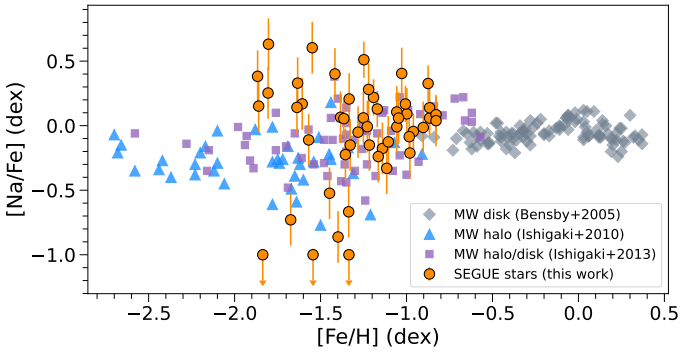

Fig. 1. [Fe/H] vs. [Na/Fe] of stars in the MW disk and halo from the literature. Blue triangles indicate stars in the MW halo from Ishigaki et al. (2010), while purple squares are stars in the halo and disk from Ishigaki et al. (2013). Grey diamonds represent MW disk stars from Bensby et al. (2005) while our sample is displayed with orange circles. Arrows indicate the upper limits on the estimated abundances.

3 Results

Figure 1 shows the estimated Na abundances as a function of the metallicity [Fe/H] for our sample stars, indicated as filled orange circles, compared to other field stars in the MW halo and disk from the literature. Blue triangles indicate halo stars from Ishigaki et al. (2010), while purple squares are halo and disk stars from the Ishigaki et al. (2013) sample. Grey diamonds represent thick and thin disk stars from Bensby et al. (2005). Arrows indicate the upper limits on the estimated abundances. Fig. 1 shows that the [Na/Fe] abundances of our SEGUE sample are mainly consistent with the bulk of stars in the MW halo, except for a few stars that are Na-richer. Na-rich stars within our sample are selected comparing their [Na/Fe] abundances with those of the GCs as a function of metallicity. Indeed, the left panel of Figure 2 shows [Fe/H] versus [Na/Fe] of our SEGUE sample (orange filled circles) compared with stars in 17 MW GCs, indicated as blue filled squares, from the sample of Carretta et al. (2009). Na-rich stars are selected at a threshold of [Na/Fe]$= +0.3$ dex (for [Fe/H]< -0.85), which roughly corresponds to the dip of the bimodal distributions of the Na abundances of GCs, in bins of 0.25 dex in [Fe/H]. More details will be reported in the forthcoming paper. In both panels of Fig. 2, the selection is represented by a green solid line within a grey shaded area. From this selection, we find that 8 stars are Na-rich. The right panel of Fig. 2 displays the CN indices (at 3883Å) of our sample stars as a function of [Na/Fe]. CN indices are calculated from the SDSS spectra with the formula reported in Martocchia et al. (2021). CN-rich stars are estimated according to the method reported in Martell et al. (2011), i.e. taking into account that we are mixing stars with different luminosities and metallicities and that this has an effect on the CN index. Additionally, as we are interested in stars that might have a GC origin, CN-rich stars are also selected to be poor in Carbon (see again, Martell et al. 2011). CN-rich (and C-poor) stars are indicated as red open squares in the right panel of Fig. 2. We found that only 8 stars out of 30 CN-rich stars are Na-rich, hence less than 30% of CN-rich stars in our sample seem to have a GC origin.

Finally, thanks to unprecedented data provided by Gaia DR3 (Gaia Collaboration et al. 2023), we were able to estimate the integrals of motion of our stars and compare them with those of the MW GCs. We assume that if a star is a GC escapee, it still retains the same orbital properties of the GC it belonged to in the past, as the gravitational potential of the MW did not significantly evolve in the last ~ 5 Gyr. Hence, we compared the energy, the angular momentum, the radial and vertical actions of our stars with those of the MW GCs, whose parameters were taken from Baumgardt & Vasiliev (2021). The orbital properties of both stars and GCs were calculated following the method and prescriptions reported in Savino & Posti (2019). As a preliminary result, we found no kinematical associations among our SEGUE stars and the MW GCs. A more detailed discussion on the method and its caveats will be provided in the forthcoming paper.

4 Conclusions

We estimated the Na abundances of a sample of field stars in the MW halo that are mainly CN-rich (i.e., rich in N). We found that less than 30% of our CN-rich stars are also enhanced in Na, by comparing their Na abundances with those of stars within GCs. Hence, we conclude that the majority of CN-rich stars in the Galactic Halo

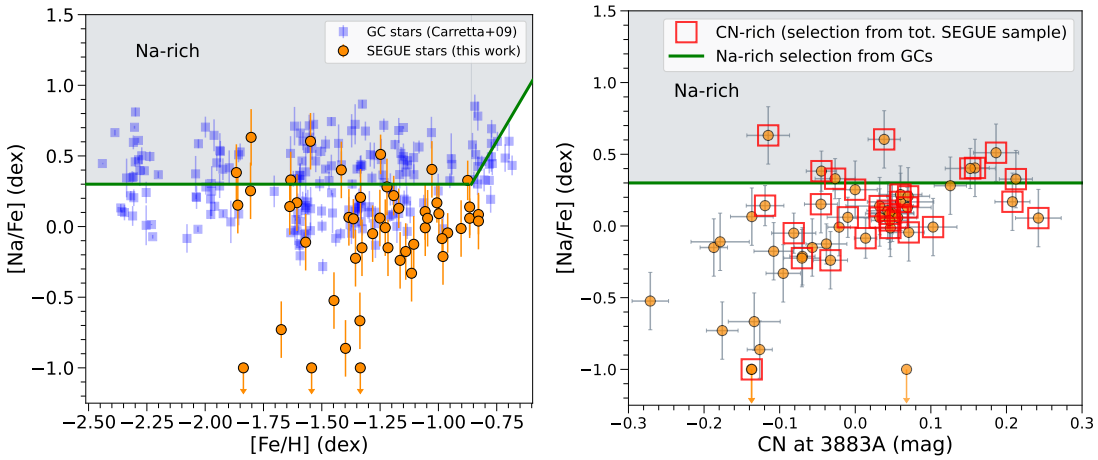

Fig. 2. *Left panel*: [Na/Fe] versus [Fe/H] for our SEGUE sample (orange filled circles) compared to stars in MW GCs from Carretta et al. (2009), indicated with blue filled squares. The green solid line indicates the selection of Na-rich stars, also represented by the grey shaded area. *Right panel*: CN at 3883Å as a function of [Na/Fe] for the stars in our sample. Red open squares represent CN-rich stars according to the selection from Martell et al. (2011).

are likely not of GC origin. Previous works (e.g., Martell et al. 2011) found that the halo is composed of 2-3% of GC stars based on CN-rich selected stars. We argue that this fraction was likely overestimated by a factor of ~ 3, although a more accurate number will need to be confirmed by future larger surveys, based on both N and Na abundances. Additionally, our results agree with recent simulation works finding that the disruption of GCs plays a minor role in the assembly of the MW halo (e.g., Reina-Campos et al. 2020).

SM was supported by a Gliese Fellowship at the Zentrum für Astronomie, University of Heidelberg, Germany. SM also thanks Radboud University and the Coma Cluster thanks to which part of this analysis was carried out.

References

Bastian, N. & Lardo, C. 2018, ARA&A, 56, 83
Baumgardt, H. & Vasiliev, E. 2021, MNRAS, 505, 5957
Bekki, K. 2019, MNRAS, 490, 4007
Bensby, T., Feltzing, S., Lundström, I., & Ilyin, I. 2005, A&A, 433, 185
Brodie, J. P. & Strader, J. 2006, ARA&A, 44, 193
Carretta, E., Bragaglia, A., Gratton, R., & Lucatello, S. 2009, A&A, 505, 139
Castelli, F. & Kurucz, R. L. 2004, ArXiv Astrophysics e-prints
D'Orazi, V., Lucatello, S., Gratton, R., et al. 2010, ApJ, 713, L1
Fernández-Trincado, J. G., Zamora, O., García-Hernández, D. A., et al. 2017, ApJ, 846, L2
Gaia Collaboration, Vallenari, A., Brown, A. G. A., et al. 2023, A&A, 674, A1
Gratton, R. G., Carretta, E., & Bragaglia, A. 2012, A&A Rev., 20, 50
Harbeck, D., Smith, G. H., & Grebel, E. K. 2003, AJ, 125, 197
Ishigaki, M., Chiba, M., & Aoki, W. 2010, PASJ, 62, 143
Ishigaki, M. N., Aoki, W., & Chiba, M. 2013, ApJ, 771, 67
Karakas, A. I. & Lattanzio, J. C. 2014, PASA, 31, e030
Koch, A., Grebel, E. K., & Martell, S. L. 2019, A&A, 625, A75
Kruijssen, J. M. D., Pfeffer, J. L., Reina-Campos, M., Crain, R. A., & Bastian, N. 2019, MNRAS, 486, 3180
Kurucz, R. L. 2005, Memorie della Societa Astronomica Italiana Supplementi, 8, 14
Lagarde, N., Reylé, C., Robin, A. C., et al. 2019, A&A, 621, A24
Lind, K., Koposov, S. E., Battistini, C., et al. 2015, A&A, 575, L12
Martell, S. L. & Grebel, E. K. 2010, A&A, 519, A14
Martell, S. L., Smolinski, J. P., Beers, T. C., & Grebel, E. K. 2011, A&A, 534, A136

Martocchia, S., Lardo, C., Rejkuba, M., et al. 2021, MNRAS, 505, 5389
Mészáros, S., Martell, S. L., Shetrone, M., et al. 2015, AJ, 149, 153
Reina-Campos, M., Hughes, M. E., Kruijssen, J. M. D., et al. 2020, MNRAS, 493, 3422
Rockosi, C. M., Lee, Y. S., Morrison, H. L., et al. 2022, ApJS, 259, 60
Savino, A. & Posti, L. 2019, A&A, 624, L9
Schiavon, R. P., Zamora, O., Carrera, R., et al. 2017, MNRAS, 465, 501
Yanny, B., Rockosi, C., Newberg, H. J., et al. 2009, AJ, 137, 4377

SF2A 2023
M. N'Diaye, A. Siebert, N. Lagarde, O. Venot, K. Baillié, M. Béthermin, E. Lagadec, J. Malzac, J. Richard (eds)

THE THIRD VERSION OF THE GAIA FGK BENCHMARK STARS

C. Soubiran[1], O. Creevey[2], N. Lagarde[1], N. Brouillet[1], P. Jofré[3], L. Casamiquela[4], U. Heiter[5], C. Aguilera–Gómez[6], S. Vitali[3], C. Worley[7] and D. de Brito Silva[3]

Abstract. The Gaia FGK Benchmark Stars (GBS) are reference stars carefully selected for the calibration and the validation of atmospheric parameters massively determined from large-scale spectroscopic surveys. Their Teff and logg are determined independently of spectroscopy, through the fundamental relations based on angular diameters, bolometric fluxes, parallaxes and masses. An initial version of the GBS comprising 34 stars was presented by Heiter et al. (2015). We now introduce the third version, GBS V3, which comprises ∼200 stars.

Keywords: stars: late-type, stars: fundamental parameters, stars: atmospheres, standards, surveys

1 Introduction

Gaia needs to anchor its stellar astrophysical parameters on a set of well-characterised stars spanning the HR diagram and the full metallicity range. Similarly, spectroscopic surveys that massively derive atmospheric parameters and abundances (e.g. RAVE, GALAH, Gaia ESO, WEAVE,..) need reference stars to assess and calibrate their results. We expect atmospheric parameters and abundances from these different origins to be consistent. The GBS were defined to address these needs. They also contribute to improve stellar models from observational constraints.

2 Method

We start with a sample of 201 stars with a known angular diameter. Teff and logg are deduced from the Stefan-Boltzmann law and Newton's law of gravitation:

$$T_{\rm eff} = \left(\frac{F_{\rm bol}}{\sigma}\right)^{0.25} (0.5\,\theta_{\rm LD})^{-0.5} \tag{2.1}$$

$$g = \frac{GM}{(0.5\,\theta_{\rm LD}/\pi)^2} \tag{2.2}$$

Interferometric angular diameters $\theta_{\rm LD}$ are taken from the JMDC catalogue (Duvert 2016) and Salsi et al. (2020). Bolometric fluxes $F_{\rm bol}$ are determined using fluxes compiled from VOSA (Bayo et al. 2008), extinction values from the 3D map of Vergely et al. (2022) and the SED fitting method developed by Creevey et al. (2015). Parallaxes π are mostly from Gaia DR3, or Hipparcos for the brightest stars. Masses are computed with the SPInS code (Lebreton & Reese 2020) operated with both sets of stellar evolution tracks BaSTI and STAREVOL.

[1] Laboratoire d'Astrophysique de Bordeaux, Univ. Bordeaux, CNRS, Pessac, France
[2] Université Côte d'Azur, Observatoire de la Côte d'Azur, CNRS, Laboratoire Lagrange, Nice, France
[3] Instituto de Estudios Astrofísicos, Facultad de Ingeniería y Ciencias, Universidad Diego Portales, Santiago, Chile
[4] GEPI, Observatoire de Paris, PSL Research University, CNRS, Sorbonne Paris Cité, Meudon, France
[5] Observational Astrophysics, Department of Physics and Astronomy, Uppsala University, Sweden
[6] Instituto de Astrofísica, Pontificia Universidad Católica de Chile, Santiago, Chile
[7] School of Physical and Chemical Sciences – Te Kura Matū, University of Canterbury, Christchurch, New Zealand

© Société Française d'Astronomie et d'Astrophysique (SF2A) 2023

Teff and luminosities determined from $F_{\rm bol}$, $\theta_{\rm LD}$ and π are used as input for SPInS, with [Fe/H] from high-resolution spectroscopy. Our validation tests showed that the determination of masses from evolutionary tracks can be rather uncertain for some giants.

The resulting Teff and logg were assessed by comparing them to other determinations of similar quality. We identify a subset of 165 GBS of the best quality, with uncertainties on Teff and logg better than 2% and 0.1 dex respectively. Their Kiel diagram is shown on Fig. 1. We have used this subsample to assess Teff and logg obtained by high-resolution and high signal-to-noise spectroscopy (PASTEL catalogue), by medium-resolution spectroscopy (APOGEE, GALAH and Gaia-ESO surveys), and by Gaia photometry and spectroscopy. This has revealed some issues in spectroscopic values that need to be investigated.

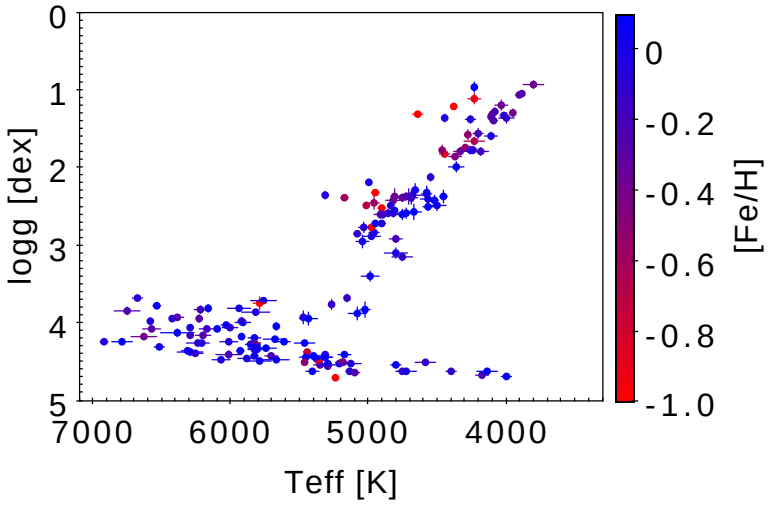

Fig. 1. Kiel diagram with fundamental Teff and logg of the 165 GBS with uncertainties better than 2% and 0.1 dex respectively. The colour scale is related to spectroscopic metallicities from the literature.

3 Conclusions

GBS V3 show significant improvements with respect to previous versions due to: (1) the larger number of stars, ∼200 instead of ∼40, resulting from our systematic search of high quality angular diameters based on interferometric measurements, (2) more accurate Teff and logg, resulting from better parallaxes which now mostly come from Gaia DR3, (3) more precise and homogeneous Fbol values, owing to the methodology of SED fitting applied to a combination of photometric and spectrophotometric data, including measurements made on XP spectra from Gaia DR3, with extinctions deduced from a state-of-the-art 3D map of the solar neighbourhood. This new set of well-characterised stars is a powerful tool for the calibration of parametrisation methods. We are now determining the chemical abundances of these stars from a large set of high quality spectra.

References

Bayo, A., Rodrigo, C., Barrado Y Navascués, D., et al. 2008, A&A, 492, 277
Creevey, O. L., Thévenin, F., Berio, P., et al. 2015, A&A, 575, A26
Duvert, G. 2016, VizieR Online Data Catalog, II/345
Heiter, U., Jofré, P., Gustafsson, B., et al. 2015, A&A, 582, A49
Lebreton, Y. & Reese, D. R. 2020, A&A, 642, A88
Salsi, A., Nardetto, N., Mourard, D., et al. 2020, A&A, 640, A2
Vergely, J. L., Lallement, R., & Cox, N. L. J. 2022, A&A, 664, A174

SF2A 2023
M. N'Diaye, A. Siebert, N. Lagarde, O. Venot, K. Baillié, M. Béthermin, E. Lagadec, J. Malzac, J. Richard (eds)

SYMBOLIC REGRESSION DRIVEN BY DIMENSIONAL ANALYSIS FOR THE AUTOMATED DISCOVERY OF PHYSICAL LAWS AND CONSTANTS OF NATURE

W. Tenachi[1], R. Ibata[1] and F. I. Diakogiannis[2]

Abstract. Given the abundance of empirical laws in astrophysics, the rise of agnostic and automatic methods to derive them from data is of great interest. This concept is embodied in symbolic regression, which seeks to identify the best functional form fitting a dataset. Here we present a protocol for deducing both physical laws but also the constants of nature appearing in those with their associated units. Our method is grounded in the Physical Symbolic Optimization framework, which integrates dimensional analysis with deep reinforcement learning. We showcase our approach on a panel of equations from (astro)-physics.

Keywords: Symbolic regression, Dimensional Analysis, Reinforcement learning

1 Introduction

Physical theories, including astrophysical ones, often originate from empirical laws. Typically, physicists observe phenomena, derive empirical laws, and then formulate overarching theories that encompass these laws, e.g., Newton's law of universal gravitation Newton (1687) which describes both the movement of objects on Earth and the movement of planets themselves. However, with the rise of deep learning, many empirical laws are now represented as neural networks, complicating their integration into broader theories. While neural networks are indispensable for modeling complex or high-dimensional data, such as images, there are instances where these models can be distilled into simpler analytical expressions (see e.g., Tenachi et al. (2023a)), bridging the gap between empirical laws and theoretical understanding.

Our research project aims to build a method for agnostically bridging this gap. In Section 2, we briefly summarize how we employ dimensional analysis alongside reinforcement learning to derive physical analytical expressions through our Physical Symbolic Optimization framework detailed in Tenachi et al. (2023b). Subsequently, in Section 3, we introduce a protocol to simultaneously identify concise physical laws and the constants that should appear in those with appropriate units such that the resulting law is accurate, succinct, and adheres to dimensional analysis principles.

2 Recovering physical laws

Symbolic regression (SR) consists in the inference of a free-form symbolic analytical function $f : \mathbb{R}^n \longrightarrow \mathbb{R}$ that fits $y = f(\mathbf{x})$ given $(\mathbf{x}, y)$ data. It is distinct from numerical parameter optimization procedures in that it consists in a search in the space of functional forms themselves by optimizing the arrangement of mathematical symbols (e.g. x, $+$, $-$, $\times$, $/$, sin, exp, log, ...).

Here we adopt the Physical Symbolic Optimization (Φ-SO) framework detailed in Tenachi et al. (2023b) which was built from the ground up for physics. In this framework, the search space is reduced by leveraging physical units constraints (e.g., cos is dimensionless, velocity $+$ length$/\square \iff \square$ is a time etc.) and proposing physically meaningful expressions only. Φ-SO relies on a recurrent neural network (RNN) to generate multiple trial analytical expressions. Fit quality of these expressions can then be assessed against data. The best expressions are then reinforced and the process is repeated until the RNN converges and yields a set of high quality expressions.

[1] Université de Strasbourg, CNRS, Observatoire astronomique de Strasbourg, UMR 7550, F-67000 Strasbourg, France
[2] Data61, CSIRO, Kensington, WA 6155, Australia

© Société Française d'Astronomie et d'Astrophysique (SF2A) 2023

Φ-SO was evaluated using a standard benchmark of 120 equations from the Feynman Lectures on Physics (Feynman et al. 1971) following the `SRBench` procedure (La Cava et al. 2021), with the objective of accurately recovering the expressions from their associated datasets. It achieved state-of-the-art performance in the presence of noise (exceeding 0.1%) and showed robust performances even in the presence of substantial (10%) noise.

3 Composing natural constants

For new scientific discovery, there are instances where the appropriate free parameters and their corresponding units are not immediately evident. In such situations, we propose a protocol wherein Φ-SO is allowed one free parameter for each input variable, sharing the same units, and another free parameter reflecting the units of the output variable. Specifically, for an SR problem consisting in the deduction of y from $\{x_1, ...x_n\}$, we would permit the inclusion of $\{\theta_y, \theta_{x_1}, ...\theta_{x_n}\}$ as free constants. This grants Φ-SO the flexibility to selectively combine or omit these free parameters to construct new parameters that align with dimensional analysis constraints. In this setup, we demonstrate that Φ-SO can adeptly resolve the SR challenges outlined in Table 1, yielding both the precise symbolic expressions and their corresponding physical constants with accurate units.

Case	Expression
Ideal Gas Law	$P = \frac{nRT}{V}$
Free Fall Terminal Velocity	$v_t = \sqrt{\frac{2mg}{\rho A C_d}}$
Classical Gravity	$F = \frac{Gm_1m_2}{r^2}$
Black Body Photon Count	$n = 1/(e^{\frac{h\nu}{k_bT}} - 1)$

Table 1. Target expressions. Input variables are colored in red with recovered natural constants to recover left in black.

For illustration, Φ-SO successfully derives the equation describing the equation of state of an ideal gas $P = C\frac{nT}{V}$ with $C = \frac{\theta_P\theta_V}{\theta_n\theta_T}$ having units $M.L^2.T^{-2}.K^{-1}.N^{-1}$ effectively rediscovering the ideal gas constant usually denoted by R. Similarly, Φ-SO is able to recover the expression for the terminal velocity of a free falling object as a function of its mass m, its surface area A and the density of the medium it traverses ρ as $v_t = \sqrt{C\frac{m}{\rho A}}$ by unveiling its proportionality to the square root of an acceleration $\sqrt{C}$, formulated by Φ-SO as $\sqrt{\theta_{v_t}/\sqrt{\theta_A}}$, corresponding to the Earth surface gravity $\sqrt{g}$ and other scale factors.

Interestingly, while the discussion on interpretability often revolves around the agnostic recovery of functional forms (as in our main study Tenachi et al. (2023b)), incorporating dimensional analysis introduces fresh perspectives. Specifically, it offers a method to agnostically determine the most straight forward units of the degrees of freedom such that these units are the simplest combination of the problem's natural units, and that the resulting expression is not only predictive but also physically sound and concise.

Code availability

The documented code for the Φ-SO algorithm along with demonstration notebooks are available on GitHub github.com/WassimTenachi/PhySO.

RI acknowledges funding from the European Research Council (ERC) under the European Unions Horizon 2020 research and innovation programme (grant agreement No. 834148).

References

Feynman, R. P., Leighton, R. B., Sands, M., et al. 1971, The Feynman lectures on physics, Vol. 1-3 (Addison-Wesley Reading, MA)

La Cava, W., Orzechowski, P., Burlacu, B., et al. 2021, in Proceedings of the Neural Information Processing Systems Track on Datasets and Benchmarks, ed. J. Vanschoren & S. Yeung, Vol. 1 (Curran)

Newton, I. 1687, Philosophiae Naturalis Principia Mathematica

Tenachi, W., Ibata, R., & Diakogiannis, F. I. 2023a, arXiv e-prints, arXiv:2305.16845

Tenachi, W., Ibata, R., & Diakogiannis, F. I. 2023b, arXiv e-prints, arXiv:2303.03192

Session S03

AS SKA-LOFAR and PNHE Workshop - Compact Objects: Observations and theory from radio to gamma

SF2A 2023
M. N'Diaye, A. Siebert, N. Lagarde, O. Venot, K. Baillié, M. Béthermin, E. Lagadec, J. Malzac, J. Richard (eds)

MULTI-WAVELENGTH STUDIES ON FAST RADIO BURSTS

C. NG[1]

Abstract. Multi-wavelength (MW) observations of Fast Radio Bursts (FRBs) is a key avenue to uncover the yet-unknown origin(s) of these extragalactic signals. In this proceeding, we discuss the need for precise localization to conduct MW studies. We present a number of theoretical predictions of MW counterparts and mention a few examples of on-going MW campaigns.

Keywords: Fast Radio Bursts, radio, transients, multi-wavelength

1 Introduction

FRBs are short (μs to ms), bright ($<10^{44}\,\mathrm{erg\,s^{-1}}$) bursts from extra-galactic distances ($z \sim 0.03$ to $z > 1$). They can potentially be used as cosmological probes, for example, to study the intergalactic medium (Ravi et al. 2016) and find the missing baryons (Macquart et al. 2020). See Ng (2023) for a brief review of the current status of the FRB field.

Since the discovery of the first FRB in 2007 (Lorimer et al. 2007), the origin(s) of FRBs remains a highly contentious topic. MW observations is arguably the only unambiguous way to solve this puzzle. Despite a number of MW efforts in the literature, FRBs have thus far only been detected between 110 MHz (Pleunis et al. 2021) and 8 GHz (Zhang et al. 2018). There is not yet any definitive detections at wavelengths other than radio, except the FRB-like signal detected from the Galactic magnetar SGR 1935+2154 (CHIME/FRB Collaboration et al. 2020; Bochenek et al. 2020; Mereghetti et al. 2020). To-date, about 40 FRBs* have been localized to a host galaxy, showing diverse host galaxy properties and local environments (Gordon et al. 2023; Mannings et al. 2021).

Fig. 1 attempts to summarize various types of MW studies, with the two main motivations being the detection of counterparts and the identification of host galaxies. There are two categories of counterparts:

- Prompt / bona fide: Counterpart just before or near the same time as the FRB.
- Associated / latent / afterglow: Counterpart well before or after the FRB, typically associated to the environment, or source, and does not have to be with the exact burst.

A positive detection of either bona-fide or associated counterparts can help set constraints on the model of the emission mechanisms and tell us what the progenitor might be. For host identification, the goal is essentially to locate the FRB to a host galaxy, derive the redshift, spectral properties, age, metallicity and other relevant information. Apart from providing us with a better understanding of the FRB environment, these information are also crucial for conducting cosmological studies using FRBs as probes.

2 The need for localization

Before doing any multi-wavelength study, we need to have a precise idea of where the FRB is located. Most standalone radio telescopes do not have good enough localization capability to tell which host galaxy the FRB came from, except for the closest sources. Take the CHIME radio telescope as an example. When it first

[1] Laboratoire de Physique et Chimie de l'Environnement et de l'Espace - Université d'Orléans/CNRS, 45071, Orléans Cedex 02, France
*See the Transient Name Server (TNS) database `https://www.wis-tns.org/search` for up-to-date numbers.

© Société Française d'Astronomie et d'Astrophysique (SF2A) 2023

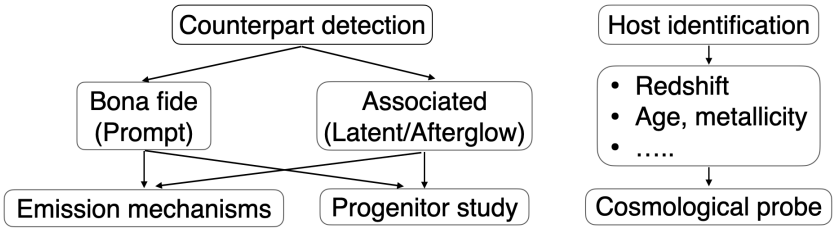

Fig. 1. A schematic of the various types of MW follow-up discussed in this proceeding.

detected the Galactic magnetar SGR 1935+2154, the localization uncertainty was large (about 1 deg) as it was seen from the sidelobe (CHIME/FRB Collaboration et al. 2020). Fortunately, the relatively low Dispersion Measure (DM) of this source set tight constraints on the distance. With the same two bursts detected by X-ray telescopes (Mereghetti et al. 2020), it was clear that they are from the same source. For the closest ∼1% of CHIME FRB discoveries, it is possible to use their low DMs to set upper limit to the redshifts, reduce chance coincidence and in turn, pinpoint the host galaxy. This was the case for the first publication of the M81 FRB (Bhardwaj et al. 2021), at least before the European VLBI Network (EVN) looked at it and further improved the localization (Kirsten et al. 2022; Marcote et al. 2022). Note that closer by FRBs also tend to be brighter (although not necessarily), which means the localization uncertainties can be reduced thanks to the high signal-to-noise detections.

To achieve proper localization we will need interferometric telescopes, which can provide precision of around 0.1 arcsec and allow a confident association of host galaxy (see, e.g. the analysis conducted with the Very Large Array (VLA) Chatterjee et al. 2017). With a larger scale interferometer such as the EVN, we can have of the order of 1 mas localization capability, meaning we can tell exactly which part of the host galaxy did the FRB originate (Kirsten et al. 2022). However, the EVN has a small field-of-view and coordinating observations with it is an intensive operation. Its time allocation is heavily subscribed and we will definitely not be able to use EVN for every single FRB. On the positive side, a number of next generation radio facilities are coming online. CHIME is commissioning two outrigger stations located in Hat Creek (∼1000 km baseline from CHIME) and Green Bank (∼3000 km baseline) in the US. Once operational, CHIME will be able to achieve ∼100 mas-localization for all its FRBs. In the near future, CHORD (Vanderlinde et al. 2019), DSA-2000 (Hallinan et al. 2019), the Square Kilometre Array (SKA) and BURSTT (Lin et al. 2022) will provide of the order of 500 FRBs per month each with milliarcsecond-level localization uncertainty.

3 Theoretical counterpart expectations

Theorists have predicted a number of bona-fide and associated counterparts for FRBs. Here we will discuss a few examples:

3.1 Bona-fide counterparts

There are two main models for prompt counterparts. In the synchrotron maser emission model, relativistic ejecta runs into a slower moving medium. The flare collides with an ion shell and the shell decelerates through shock waves which gives rise to an FRB burst (see, e.g. Metzger et al. 2019). In this model, we would also get incoherent emission in hard energy (gamma ray and X-ray). The other model involves a classic Magnetar flare, where the trapped fireball also emits thermal X-ray and comptonization (see, e.g. Thompson & Duncan 1995; Lu et al. 2020). The Galactic magnetar SGR 1935+2154 might be an example of this.

3.2 Associated counterparts

A wide range of possibilities have been proposed in the literature, spanning pretty much the entire spectrum from radio, optical, X-ray, gamma ray to even gravitational waves (GW):

- Radio: Persistent radio source (PRS) associated with a magnetar pulsar nebula has been suggested. This is particularly relevant given a few FRBs have been found to co-locate with PRS (Law et al. 2022).
- Optical: If FRBs are associated with neutron stars, we might expect associated supernova explosions some time in the past since neutron stars are primarily born in core-collapse supernovae (Margalit & Metzger

2018). Since the environment around the progenitor is initially very dense, we would probably have to wait at least a decade or so between the initial supernova and the time when the environment has dissipated enough for an FRB to be seen. One could look into archival data for a supernova association, but the risk of getting false chance associations could be quite high.

- X-ray: Synchrotron maser emission from persistent X-ray / Ultra Luminous X-ray Sources (ULX)-like objects has been suggested (Sridhar et al. 2021a; Deng et al. 2021). This is probably going to be difficult to detect given the extragalactic distances of FRBs. One would need very sensitive X-ray telescopes and detections might only be feasible for the brightest sources.

- Gravitational waves (GW) / Gamma ray: Short gamma ray burst (GBR) from neutron star mergers is a possible albeit rare formation channel for magnetars (Margalit et al. 2019; Wang et al. 2020; Sridhar et al. 2021b). FRB can be formed from the interaction of the magnetospheres of the neutron stars as they inspiral towards each other. It has been proposed that in this model, we could get an FRB preceding an associated GW event. Alternatively, if a stable, long-lived neutron star is formed after the merger, an FRB can be produced through the kilonova ejecta. In this case we will need to wait a few weeks or so for the FRB to go through this less dense, rapidly expanding media.

4 Examples of MW campaigns

MW campaigns are logistically challenging and require coordination from the community. The detection of bona-fide counterparts is particularly tricky because time is critical. One has to get on source basically in real-time of the FRB burst. On the other hand, associated counterpart detections have less of a rush as emission is expected on longer timescales. There are a number of approaches in the literature:

- Take a radio telescope as the master and employ facilities at other wavelengths to shadow it, for example in the case of MeerKAT+MeerLITCT (Bloemen et al. 2016). It is probably a good idea to pick a radio telescope that has already seen FRBs in the past, to have a better chance of success!

- A reversed search, where a radio telescope is used to to shadow, for example, Swift/XRT (see, e.g. Nicastro et al. 2021). This is probably applicable for smaller, less heavily subscribed radio telescopes.

- A large-scale campaign coordinating many telescopes across the spectrum to observe the same program together. A great example is the Deeper Wider Faster (DWF)[†] project.

- Search archival data of other wavelengths at the positions of known FRBs to see if there is any associated counterparts from further back in time (see, e.g. Ashkar et al. 2023).

In order to facilitate these time-critical follow-up studies, CHIME publishes quasi-real time alerts for FRB discoveries via the framework of VOEvents[‡] on a (free) subscription basis. As the CHIME real-time FRB pipeline detects a candidate, it will be sent to a database and the VOEvent will be published by the Comet broker, which is an implementation of the VOEvent The Transport Protocol broadcasts machine-reachable messages over the Internet to any observatories or send out human-readable emails. The end-to-end processing is very fast. VOEvents can be received by other telescopes within about 30 seconds of an FRB detection in CHIME. This service has been available since October 2021. So far, over 1800 alerts have been published to over 100 subscribers from over 60 institutes.

For the study of host galaxy identification and classification, it typically involves conducting coordinated photometric and spectroscopic follow-up observations. This type of follow up also has no rush but obtaining observing time on telescopes sensitive enough to observe the host galaxy is not always for granted. So far, most of these follow-up studies are conducted on a case by case basis, targeting individual FRB one at a time. Nonetheless, a more coordinated effort has been initiated by the Fast and Fortunate for FRB Follow-up (F^4)[§] collaboration. They have signed agreement with a number of FRB discovery radio experiments (e.g. CHIME, CRAFT, AstroFlash, MeerTRAP), to take all their arcsecond-localized FRBs and go to telescopes at other

[†]DWF: `https://www.swinburne.edu.au/research/centres-groups-clinics/centre-for-astrophysics-supercomputing/our-research/data-intensive-astronomy-software-instrumentation/deeper-wider-faster-program/`

[‡]CHIME VOEvents: `https://www.chime-frb.ca/voevents`

[§]F^4: `https://sites.google.com/ucolick.org/f-4`

wavelength to identify the hosts. They have partnerships with the Keck, Gemini, Magellan, ESO/VLT, Hubble, ALMA, Chandra, and the VLA.

5 Conclusion

Multi-wavelength observation is arguably the only unambiguous way to identify counterparts for FRBs. So far FRBs have only been detected in radio (110 MHz–8 GHz), except one FRB-like signal from the Galactic magnetar SGR 1935+2154. Multi-wavelength observations require coordinated community effort, and a number of on-going campaigns are summarized in this proceeding. Low-DM FRBs have a better chance of having multi-wavelength detections and are possibly worth prioritizing for follow-up studies. We will hopefully soon arrive at the era of many (well-)localized FRB events, and at which point, there will also be potential synergies with publicly available catalogues, for example, PanSTARRS, SDSS, DESI, Rubin/LSST, Euclid, SPHEREx, etc, for host galaxy studies.

References

Ashkar, H., Bouhaddouti, M. E., Fegan, S., & Schüssler, F. 2023, PoS, ICRC2023, 555

Bhardwaj, M., Gaensler, B. M., Kaspi, V. M., et al. 2021, ApJ, 910, L18

Bloemen, S., Groot, P., Woudt, P., et al. 2016, in Society of Photo-Optical Instrumentation Engineers (SPIE) Conference Series, Vol. 9906, Ground-based and Airborne Telescopes VI, ed. H. J. Hall, R. Gilmozzi, & H. K. Marshall, 990664

Bochenek, C. D., Ravi, V., Belov, K. V., et al. 2020, Nature, 587, 59

Chatterjee, S., Law, C. J., Wharton, R. S., et al. 2017, Nature, 541, 58

CHIME/FRB Collaboration, Andersen, B. C., Bandura, K. M., et al. 2020, Nature, 587, 54

Deng, C.-M., Zhong, S.-Q., & Dai, Z.-G. 2021, ApJ, 922, 98

Gordon, A. C., Fong, W.-f., Kilpatrick, C. D., et al. 2023, ApJ, 954, 80

Hallinan, G., Ravi, V., Weinreb, S., et al. 2019, in Bulletin of the American Astronomical Society, Vol. 51, 255

Kirsten, F., Marcote, B., Nimmo, K., et al. 2022, Nature, 602, 585

Law, C. J., Connor, L., & Aggarwal, K. 2022, ApJ, 927, 55

Lin, H.-H., Lin, K.-y., Li, C.-T., et al. 2022, PASP, 134, 094106

Lorimer, D. R., Bailes, M., McLaughlin, M. A., Narkevic, D. J., & Crawford, F. 2007, Science, 318, 777

Lu, W., Kumar, P., & Zhang, B. 2020, MNRAS, 498, 1397

Macquart, J. P., Prochaska, J. X., McQuinn, M., et al. 2020, Nature, 581, 391

Mannings, A. G., Fong, W.-f., Simha, S., et al. 2021, ApJ, 917, 75

Marcote, B., Kirsten, F., Hessels, J., et al. 2022, in European VLBI Network Mini-Symposium and Users' Meeting 2021, Vol. 2021, 35

Margalit, B., Berger, E., & Metzger, B. D. 2019, ApJ, 886, 110

Margalit, B. & Metzger, B. D. 2018, ApJ, 868, L4

Mereghetti, S., Savchenko, V., Ferrigno, C., et al. 2020, ApJ, 898, L29

Metzger, B. D., Margalit, B., & Sironi, L. 2019, MNRAS, 485, 4091

Ng, C. 2023, in SF2A-2023: Proceedings of the Annual meeting of the French Society of Astronomy and Astrophysics. Eds.: M. N'Diaye,, ed. M. N'Diaye, A. Siebert, N. Lagarde, O. Venot, K. Baillié, M. Béthermin, E. Lagadec, J. Malzac, & J. Richard, ???–???

Nicastro, L., Guidorzi, C., Palazzi, E., et al. 2021, Universe, 7, 76

Pleunis, Z., Michilli, D., Bassa, C. G., et al. 2021, ApJ, 911, L3

Ravi, V., Shannon, R., Bailes, M., et al. 2016, Science, 354, 1249

Sridhar, N., Metzger, B. D., Beniamini, P., et al. 2021a, ApJ, 917, 13

Sridhar, N., Zrake, J., Metzger, B. D., Sironi, L., & Giannios, D. 2021b, MNRAS, 501, 3184

Thompson, C. & Duncan, R. C. 1995, MNRAS, 275, 255

Vanderlinde, K., Liu, A., Gaensler, B., et al. 2019, in Canadian Long Range Plan for Astronomy and Astrophysics White Papers, Vol. 2020, 28

Wang, F. Y., Wang, Y. Y., Yang, Y.-P., et al. 2020, ApJ, 891, 72

Zhang, Y. G., Gajjar, V., Foster, G., et al. 2018, ApJ, 866, 149

SF2A 2023
M. N'Diaye, A. Siebert, N. Lagarde, O. Venot, K. Baillié, M. Béthermin, E. Lagadec, J. Malzac, J. Richard (eds)

MULTI-WAVELENGTH LIGHT-CURVE FITTING OF YOUNG AND MILLISECOND PULSARS

J. Pétri[1]

Abstract. Since the launch of the Fermi γ-ray telescope, several hundred radio-loud γ-ray pulsars have been detected, some belonging to the millisecond pulsars and some part of the young pulsar population (with spin periods longer than 30 ms). Observing simultaneously pulsed radio and γ-ray emission from these stars helps to constrain the geometry and radiation mechanisms within their magnetosphere and to localize the photon production sites. In this work we show how time-aligned γ-ray light curve fitting of young and millisecond pulsars constrain their magnetospheric configuration, namely the magnetic axis and line-of-sight inclination angles. To this end, we assume a dipole force-free magnetosphere where radio photons emanate from high altitudes above the polar caps and γ-rays originate from the pulsar striped wind. Further constraints were obtained from radio polarization measurements, if available, following the rotating vector model, including aberration and retardation effects. We are currently extending our analysis to thermal and non-thermal X-ray emission using observations from several X-ray telescopes. Preliminary results applied to a bright pulsar show that the non-thermal X-rays are produced between 20% and 55% of the light cylinder radius.

Keywords: neutron stars, magnetic fields, rotation, pulsars, radio emission, γ-rays, X-rays

1 Introduction

The multi-wavelength pulsed emission of pulsars is very sensitive to their global geometry constrained by the angles between the rotation axis and the magnetic dipole moment and between the rotation axis and the line of sight. Several works in the past showed that a simultaneous radio and γ-ray light-curve fitting is valuable to pin down the geometry. For instance Pétri (2011) showed that in the framework of a force-free split-monopole solution, simple analytical expressions for the radio time lag and the γ-ray peak separation can be derived. Refinements with a dipolar force-free magnetosphere model have been given by Benli et al. (2021) for millisecond pulsars and by Pétri & Mitra (2021) for young pulsars. Other useful constraints on the emission sites come from detailed radio polarization observations if available. However, polarization data from millisecond pulsars are difficult to interpret because of the presence of strong non dipolar fields at the photon production sites. In section 2 the phase-aligned γ-ray light curve fitting is studied whereas in section 3 the thermal and non-thermal X-rays are fitted. Conclusions are drawn in section 4.

2 Gamma-ray light-curve fitting

To fit the γ-ray light-curves of pulsars, we distinguish between millisecond and young pulsars because for the latter, the radio emission altitude corresponds to regions where the magnetic field is essentially dipolar and good radio polarization data are available. Therefore, thanks to the rotating vector model (Radhakrishnan & Cooke 1969), it is possible to infer the radio emission height and to relate the magnetic obliquity to the observer line of sight inclination angle.

[1] Université de Strasbourg, CNRS, Observatoire astronomique de Strasbourg, UMR 7550, F-67000 Strasbourg, France.

© Société Française d'Astronomie et d'Astrophysique (SF2A) 2023

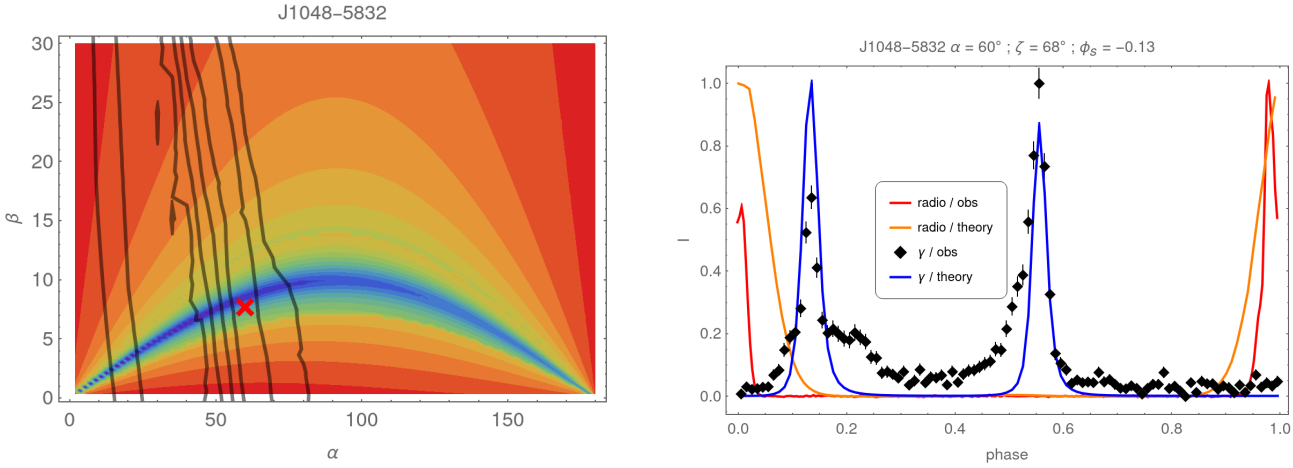

Fig. 1. Best fit for the young pulsar J1048-5832. On the left panel, the log χ^2 contour plots, in colour contours for radio polarization fits, and in solid coloured lines for γ-ray light-curves. The red cross indicates the best joined radio/γ-ray fit. On the right panel, the associated γ-ray light-curve for the geometry given by the red cross.

2.1 Young pulsars

In our first sample of pulsars (Pétri & Mitra 2021), we selected those with periods larger than 30 ms and with good quality γ-ray pulse profiles from the Fermi/LAT second pulsar catalogue (Abdo et al. 2013). These are non-recycled young pulsars some of them with good linear polarization data. Next, we computed a full atlas of radio and γ-ray pulse profiles depending on the magnetic axis obliquity and line of sight inclination with respect to the neutron star rotation axis. By applying a χ^2 fitting technique to the γ-ray data, we were able to pin down accurately the magnetosphere geometry. Further constrains were obtained from radio polarization measurement following the rotating vector model, including aberration and retardation effects.

Fig. 1 shows an example of best fit for PSR J1048-5832. It is a γ-ray pulsar of period 124 ms with very good quality radio polarization data. It shows two narrow and prominent γ-ray pulses. The radio polarisation data give a relation between α and $\beta = \zeta - \alpha$ as shown in the left panel whereas the γ-ray fit is shown on the right panel with $\alpha = 60°$ and $\zeta = 68°$ with an offset of $\phi_s = -0.13$.

2.2 Millisecond pulsars

In our second sample (Benli et al. 2021), we selected millisecond pulsars (MSPs) with good γ-ray pulse profile also from the second pulsar catalogue. Contrary to the young pulsars, the polarization data are not usable to fit to the rotating vector model because for millisecond pulsars, the light-cylinder radius is much smaller and small scale surface multipole components can strongly affect the polarization position angle. Thus for MSPs we can only rely on the time lag between the γ-ray and the radio pulse profile and on the γ-ray pulse separation.

As an example, Fig.2 shows results for PSR J0030+0451, a MSP with $P = 4.87$ ms possessing a double pulse profile in γ-rays. As can be seen on the left panel, the best fit to the γ-ray light curve was obtained by fixing $\alpha = 70°$, $\zeta = 60°$ and an offset $\phi_s = -0.07$. The right panel shows a crescent shape polar cap and an almost circular polar cap as described by Riley et al. (2019).

3 X-ray light-curve fitting

To complete the multi-wavelength study we need to address the thermal and non-thermal X-ray emission. The former is produced by heating the neutron star surface due to particle bombardment from the magnetosphere or internal heat. Pulsed emission is expected when the polar cap are hotter than the rest of the surface. The location and the size of these polar caps depend on the magnetic field structure in the crust. The latter radiation emanates from higher altitudes within the magnetosphere.

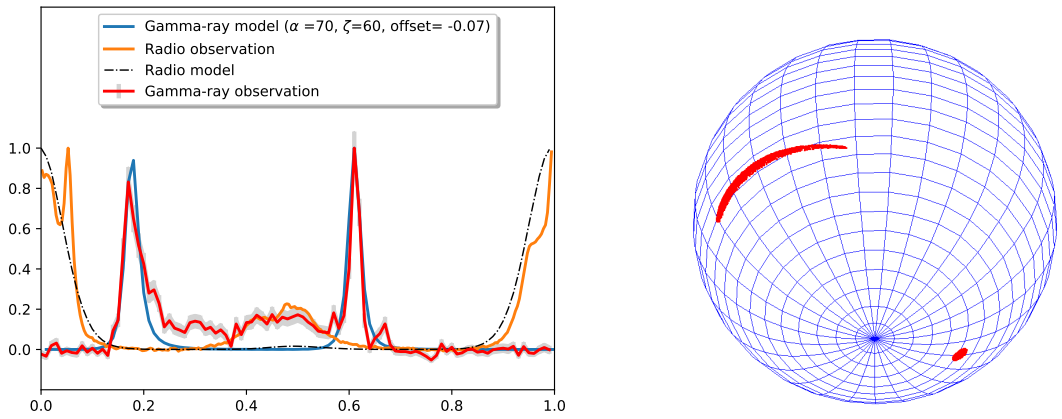

Fig. 2. Best fit for the millisecond pulsar J0030+0451 on the left panel and hot spot geometry from an off-centred dipole plus a small scale surface dipole on the right panel.

3.1 Thermal X-ray

The NICER mission is dedicated to constrain the mass and radius of neutron stars by modelling the pulse profile in the thermal X-ray band. A handful millisecond pulsars have already been investigated by several groups (Riley et al. 2019; Miller et al. 2019). They found the shape, size and location of the hot spots, of which they are usually two. For PSR J0030+0451, they found two hot spots located in the same hemisphere. If the magnetic field is dipolar, this is a strong hint of an off-centred dipole geometry. Moreover the crescent shape of one of this spot suggests the presence of a small scale surface dipole on top of one polar cap, right panel of fig. 2. Base on this idea and on the γ-ray light-curve fits as shown in the previous section, we were able to confirm the line of sight inclination angle of $\zeta \approx 54^\circ$ and the obliquity about $\alpha = 70^\circ$, (Pétri et al. 2023). Therefore phased-aligned γ-ray light-curve studies independently of the thermal X-ray studies agree each other on the same geometry which is thus a robust result. With this first success, we plan to investigate several other NICER pulsars for instance PSR J0740+6620 for which a detailed investigation have already been published by Riley et al. (2021) and Miller et al. (2021).

3.2 Non thermal X-ray

Contrary to the previous energy bands, radio, γ and thermal X-ray, the non-thermal X-ray emission sites and mechanisms are still largely unconstrained. In a last investigation, based again on the γ-ray phased aligned light-curve modelling, we selected young and radio-loud γ-ray pulsars that are also bright in non-thermal X-rays, above 1-2 keV. PSR J2229+6114 is a particularly good candidate. Its geometry is known from Pétri & Mitra (2021) and has been re-explored recently using the third pulsar catalogue 3PC (Smith et al. 2023). Our best fit is shown on the left panel of Fig. 3. Only the X-ray emission altitude and extension need to be fixed. To this end, we computed a comprehensive atlas of X-ray pulse profiles based on the slot gap model, assuming emission only along the separatrix within the light-cylinder. X-ray data are available from NICER (1–10 keV), RXTE (9.4–22.4 keV) and NuSTAR (3–10 keV). The X-ray pulse profiles are compatible with curvature radiation of the primary beam from an emission height in $r/r_{\rm L} \in [0.2, 0.55]$ and an obliquity $\alpha \in [45^\circ, 50^\circ]$. Moreover the line of sight inclination agrees with γ-ray fit $\zeta \in [34^\circ, 48^\circ]$. The right panel of fig. 3 shows the fit obtained with RXTE.

4 Conclusions

We find good agreement between our emission model and the time-aligned single- or double-peaked γ-ray pulsar observations. We deduce the magnetic inclination angle and the observer line-of-sight with respect to the rotation axis within a small error bar. The distinction between radio-loud or radio-quiet γ-ray pulsars or only radio pulsars is entirely related to the geometry of the associated emitting regions.

The high-altitude polar cap model combined with the striped wind represents a minimalistic approach able to reproduce a wealth of γ-ray pulse profiles for the whole population of pulsars. Based on self-consistent

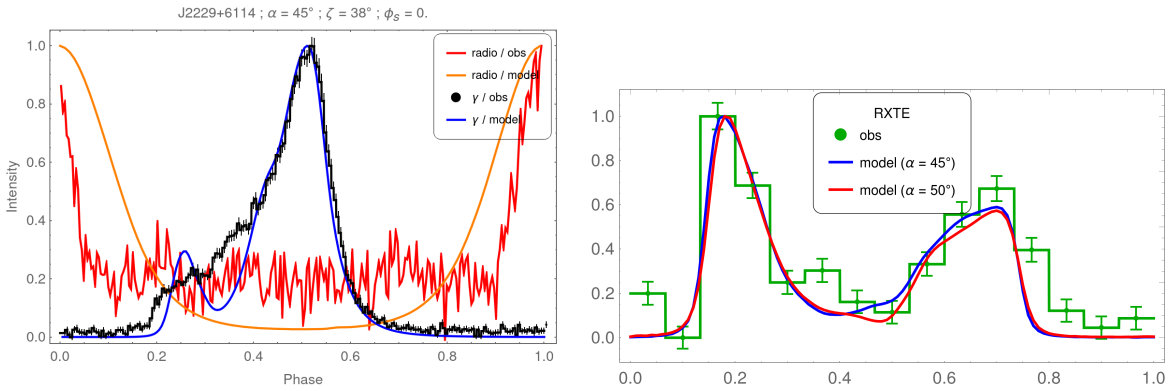

Fig. 3. Best fit of PSR J2229+6114 using the 3PC for γ-rays on the left panel and using the RXTE data in the range 9.4–22.4 keV on the right panel.

force-free simulations, it gives a full geometrical picture of the emission properties without resorting to detailed knowledge of the individual particle dynamics and energetics. For the first time it becomes possible to localize with high confidence the non-thermal X-ray emission sites within the magnetosphere.

This work has been supported by the CEFIPRA grant IFC/F5904-B/2018 and ANR-20-CE31-0010.

References

Abdo, A. A., Ajello, M., Allafort, A., et al. 2013, ApJS, 208, 17
Benli, O., Pétri, J., & Mitra, D. 2021, A&A, 647, A101
Miller, M. C., Lamb, F. K., Dittmann, A. J., et al. 2019, ApJL, 887, L24
Miller, M. C., Lamb, F. K., Dittmann, A. J., et al. 2021, ApJ, 918, L28
Pétri, J. 2011, MNRAS, 412, 1870
Pétri, J., Guillot, S., Guillemot, L., et al. 2023, arXiv:2309.03620
Pétri, J. & Mitra, D. 2021, A&A, 654, A106
Radhakrishnan, V. & Cooke, D. J. 1969, Ap. Lett., 3, 225
Riley, T. E., Watts, A. L., Bogdanov, S., et al. 2019, ApJL, 887, L21
Riley, T. E., Watts, A. L., Ray, P. S., et al. 2021, ApJ, 918, L27
Smith, D. A., Bruel, P., Clark, C. J., et al. 2023, arXiv:2307.11132

SF2A 2023
M. N'Diaye, A. Siebert, N. Lagarde, O. Venot, K. Baillié, M. Béthermin, E. Lagadec, J. Malzac, J. Richard (eds)

A NEW SCENARIO FOR MAGNETAR FORMATION IN A PROTO-NEUTRON STAR SPUN UP BY FALLBACK

P. Barrere[1], J. Guilet[1], R. Raynaud[2] and A. Reboul-Salze[3]

Abstract. The origin of magnetar magnetic field is a challenging question. In situ magnetic field amplification by dynamo action is a promising process to generate ultra-strong magnetic fields in fast-rotating progenitors. It is, however, unclear whether the fraction of progenitors harboring fast core rotation is sufficient to explain the entire magnetar population. To address this point, we investigate a new scenario for magnetar formation from a slow rotating progenitor, in which a slow-rotating proto-neutron star is spun-up by the supernova fallback. We show that this can trigger the development of the Tayler-Spruit dynamo while other dynamo processes are disfavored. In this proceeding, we present an analytical model of our scenario and three dimensional numerical simulations of the Tayler-Spruit dynamo. We find that the generated magnetic field intensities are close to those expected in magnetars and our simulations demonstrate the existence of the Tayler-Spruit dynamo in the frame of this scenario. Thus, our scenario provides a new promising approach to form magnetars from slow-rotating progenitors.

Keywords: magnetars, supernovae, magnetohydrodynamics (MHD), instabilities, methods: numericals

1 Introduction

Magnetars are isolated young neutron stars characterized by the most intense magnetic fields known in the Universe, which power a wide diversity of outstanding emissions. Under the assumption of a magnetic dipole braking, the observations of the rotation period and its derivative, i.e. the spin-down, show that magnetars harbor a typical surface magnetic dipole of $\sim 10^{14} - 10^{15}$ G (Rea et al. 2012; Olausen & Kaspi 2014). Magnetars with a millisecond rotation period may also be at the origin of extreme explosions, which are more energetic than typical supernovae : (i) hypernovae (e.g. Duncan & Thompson 1992; Gompertz & Fruchter 2017; Metzger et al. 2011, 2018) via a magnetorotational explosion (e.g. Dessart et al. 2008; Obergaulinger & Aloy 2022; Bugli et al. 2021, 2023), and (ii) superluminous supernovae through a delayed energy injection from the spin-down luminosity (e.g. Woosley 2010; Inserra et al. 2013; Nicholl et al. 2013).

The formation of magnetar magnetic field is therefore a critical question to understand magnetar activity and extreme explosions. Two scenarios invoke the amplification of the magnetic field via a dynamo action during the early stages of the proto-neutron star (PNS): the convective dynamo scenario (e.g. Thompson & Duncan 1993; Raynaud et al. 2020, 2022) and the magnetorotational instability (MRI) scenario (e.g. Reboul-Salze et al. 2021, 2022; Guilet et al. 2022). They both suppose a PNS with a millisecond rotation period which stems from the rotation of the progenitor core. However, it is still uncertain whether there is a large enough fraction of fast rotating progenitor cores to explain the formation of whole magnetar population, which represents $\sim 10 - 40\,\%$ of the young neutron star population (e.g. Kouveliotou et al. 1994; Beniamini et al. 2019).

This proceeding presents a new magnetar formation scenario in which the PNS rotation is determined by the fallback accretion and the magnetic field amplified via the Tayler-Spruit dynamo (Barrère et al. 2022, 2023). This dynamo is driven by the instability of a toroidal magnetic field, called the Tayler instability (Tayler 1973; Goossens & Tayler 1980; Goossens 1980; Goossens et al. 1981) and was first modelled by Spruit (2002). An alternative modelling is proposed Fuller et al. (2019) to tackle critics of Spruit's model (see Denissenkov & Pinsonneault 2007; Zahn et al. 2007). This mechanism is usually invoked in the context of angular momentum transport in stellar radiative zones (e.g. Eggenberger et al. 2005, 2019; Cantiello et al. 2014; Griffiths et al. 2022) and we apply it in the context of magnetar formation for the first time (Barrère et al. 2022, 2023).

[1] Université Paris-Saclay, Université Paris Cité, CEA, CNRS, AIM, 91191, Gif-sur-Yvette, France
[2] Université Paris Cité, Université Paris-Saclay, CEA, CNRS, AIM, 91191, Gif-sur-Yvette, France
[3] Max Planck Institute for Gravitational Physics (Albert Einstein Institute), 14476 Potsdam, Germany

© Société Française d'Astronomie et d'Astrophysique (SF2A) 2023

2 New magnetar formation model (Barrère et al. 2022)

As illustrated in Figure 1, our magnetar formation scenario begins $\sim 10\,$s after the collapse of the progenitor core when a fraction of the initially ejected matter which is still gravitationally bound to the PNS is accreted onto the PNS surface. This fallback accretion is found to be asymmetric (Chan et al. 2020) and the matter is expected to have an angular momentum comparable to the Keplerian angular momentum (Janka et al. 2022). The PNS surface is therefore spun up, which creates a differential rotation with the PNS surface rotating faster than the core. We argue that the other dynamo mechanisms are disfavored* and that only the Tayler-Spruit dynamo development is triggered: (i) the differential rotation shears the axisymmetric poloidal magnetic field B_r into an axisymmetric toroidal magnetic field B_ϕ (ii) until the latter becomes Tayler unstable, which creates a perturbed non-axisymmetric field $\delta B_\perp$ and (iii) generates B_r via a non-linear induction characterized by the azimuthal component of the electromotive force E_ϕ. The dynamo loop amplifies the magnetic field until a turbulent dissipation due to the instability balances the growth of the magnetic field, which makes the dynamo saturate. Two descriptions of the saturation mechanisms have been proposed: that of (Spruit 2002) and (Fuller et al. 2019), which are both still keenly discussed in particular due to the difficulty in finding the dynamo in direct numerical simulations (Denissenkov & Pinsonneault 2007; Zahn et al. 2007; Petitdemange et al. 2023; Barrère et al. 2023).

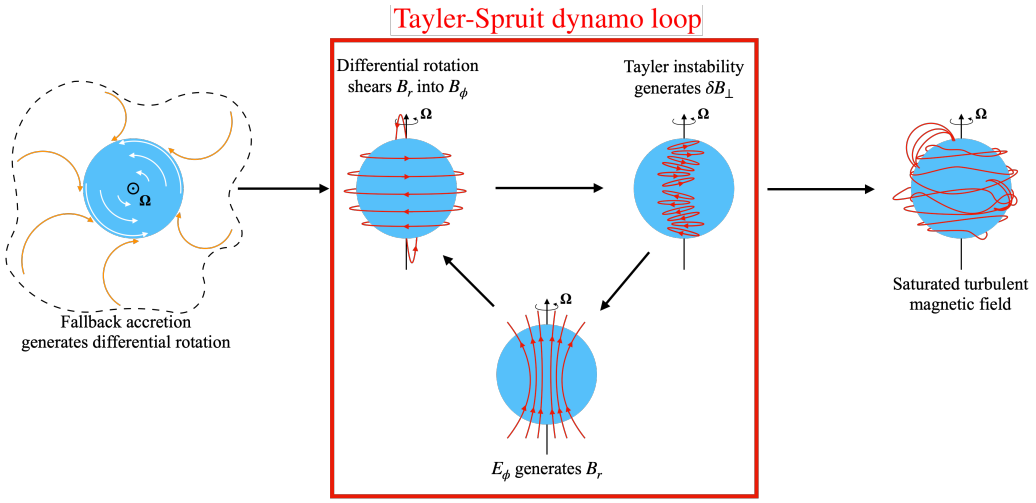

Fig. 1. Schematic representation of the different stages of our magnetar formation scenario. The dashed line encloses the region of the fallback (orange arrows). Red and white lines represent the magnetic field lines and fluid motions, respectively. Ω and E_ϕ stand for the angular rotation frequency and the azimuthal component of the electromotive force, respectively. B_ϕ and B_r are the axisymmetric azimuthal and radial magnetic fields, and $\delta B_\perp$ is the non-axisymmetric perpendicular magnetic field.

To check the plausibility of this scenario to form magnetars, we built a one-zone model. It consists in a system of average time evolution equations for the rotational properties of the PNS: average rotation rate Ω and shear rate q, and different components of the magnetic field: B_ϕ, B_r, $\delta B_\perp$ using the formalism of Fuller et al. (2019) to describe the Tayler-Spruit dynamo. The integration of these equations for specific values of the total accreted mass (which is equivalent to choose a value for the PNS final rotation rate) show a time evolution of the magnetic field which is consistent with the phases of our scenario from the shearing to the saturation (see Fig. 2 and 3 in Barrère et al. 2022). To define a proxy for the saturated magnetar magnetic field, we used the maximum magnetic intensity reached (plus signs in figure 2) and the magnetic intensity when $q = 0$, i.e. when all the rotation becomes rigid due to angular momemtum transport (cross signs in figure 2). We see that the measured saturated B_ϕ (in blue) and B_r (in green) are close to the analytical predictions of Fuller et al. (2019) (in solid line) and that the saturated B_r crosses the regions of magnetic fields expected for magnetars (in darkgrey) for rotation periods $\lesssim 28\,$ms (or a total accreted mass $\gtrsim 10^{-2}\,\mathrm{M}_\odot$), which is then the lower rotation

*Indeed, the PNS interior is expected to be mostly stably stratified when the fallback occurs (Hüdepohl 2014) and the MRI only develops when the rotation rate decreases with the radius.

period limit to form magnetars with our scenario. In the same figure, a comparison is also made with the predictions of Spruit (2002), from which we can also infer a lower limit for rotation period of ~ 8 ms. Our model therefore predicts that strong enough magnetic fields can be generated to form magnetars in our scenario.

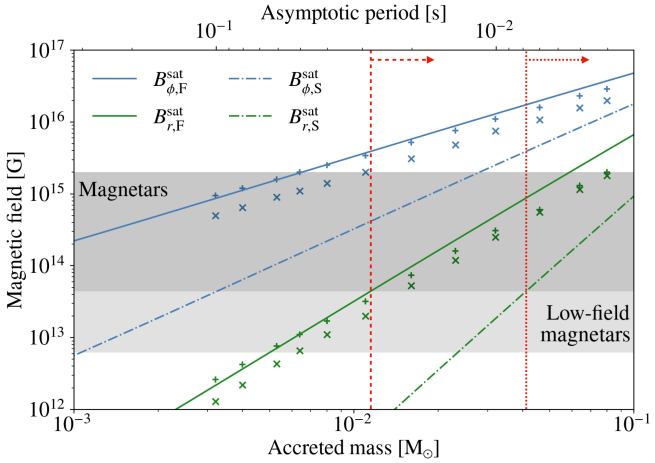

Fig. 2. Different characteristic timescales as a function of the accreted mass: winding (black), Tayler instability (dark blue), and dynamo (red). The green line represents the sum of the three timescales. The shear rate is set at $q = 1$. The green crosses represent the entire amplification time obtained by integrating the evolution equations. The red vertical line shows the lower limit of the accreted mass to form a magnetar with a radial field stronger than $B_Q \equiv m_e c^2/e\hbar \simeq 4.4 \times 10^{13}$ G using the predictions of Fuller et al. (2019).

3 3D numerical simulations (Barrère et al. 2023)

The promising results of the semi-analytical model of Barrère et al. (2022) encourages further studies of our scenario, especially through numerical simulations. Indeed, a numerical study would test whether the Tayler instability can sustain a dynamo, in particular in the framework of our scenario. In the case where the Tayler-Spruit dynamo is present, numerical simulations would also provide information about the geometry the magnetic field and the scaling law it follows.

We performed three-dimensional (3D) direct numerical simulations of a stably stratified and electrically conducting Boussinesq fluid with the pseudo-spectral code MagIC (Wicht 2002; Gastine & Wicht 2012). The fluid has a constant density $\rho = 3.8 \times 10^{14}\,\mathrm{g\,cm^{-3}}$ (which corresponds to a proto-neutron star mass of $M = 1.4\,\mathrm{M_\odot}$) and evolves between two concentric spheres of radius $r_i = 3$ km and $r_o = 12$ km, rotating at the angular frequencies Ω_i and $\Omega_o = 200\,\mathrm{rad\,s^{-1}}$, respectively. The imposed differential rotation is characterized by the Rossby number $Ro \equiv 1 - \Omega_i/\Omega_o > 0$, which is varied between 0.125 and 1.2. In all the simulations, we keep fixed the other dimensionless control parameters: the shell aspect ratio $\chi \equiv r_i/r_o = 0.25$, the thermal and magnetic Prandtl numbers $Pr \equiv \nu/\kappa = 0.1$ and $Pm \equiv \nu/\eta = 1$, respectively, the Ekman number $E \equiv \nu/(d^2\Omega_o) = 10^{-5}$, and the ratio of the Brunt-Väisälä to the outer angular frequency $N/\Omega_o = 0.1$. The coefficients ν, κ, η, and $d \equiv r_o - r_i$ are respectively the kinematic viscosity, the thermal diffusivity, the resistivity, and the shell width. The magnetic energy is measured by the Elsasser number $\Lambda \equiv B^2_{\rm rms}/(4\pi\rho\eta\Omega_o)$.

The performed simulation are all gathered in a diagram which displays the average magnetic energy during the saturated state of the dynamo (measured by the Elsasser number) as a function of the input differential rotation (represented by the Rossby number). This diagram, called *bifurcation diagram*, (plot on the left in figure 3) shows different branches represented by different colours. Following the bifurcation diagram, when Ro is low, the flow can not amplify an initially weak magnetic field ($\Lambda = 1 \times 10^{-4}$) until $Ro \sim Ro_{\rm W} = 0.65$ is reached, where an exponential amplification occurs until saturation at $\Lambda \sim 3 \times 10^{-1}$. This dynamo branch (in black) is driven by an hydrodynamic instability, which occurs for $Ro \gtrsim Ro_{\rm hyd} = 0.177$. For $Ro \gtrsim 0.8$, the magnetic field undergoes a non-linear growth and transitions to another dynamo branch (in green) at $\Lambda \sim 10$. Restarting from nearby saturated states, the branch can be extended to $Ro \sim 0.37 < Ro_{\rm W}$, which betrays the subcriticality of the branch. Finally, a stronger branch at $\Lambda \sim 80$ (in red) can be reached by starting with a strong magnetic field of $\Lambda \sim 10$ and be maintained to $Ro \sim Ro_{\rm D} = 0.19$. These three main solutions not only

differs by their magnetic strength but also by their geometry (see snapshots on the right of 3): equatorial, hemispherical, and dipolar (i.e. equatorially symmetric magnetic field), respectively.

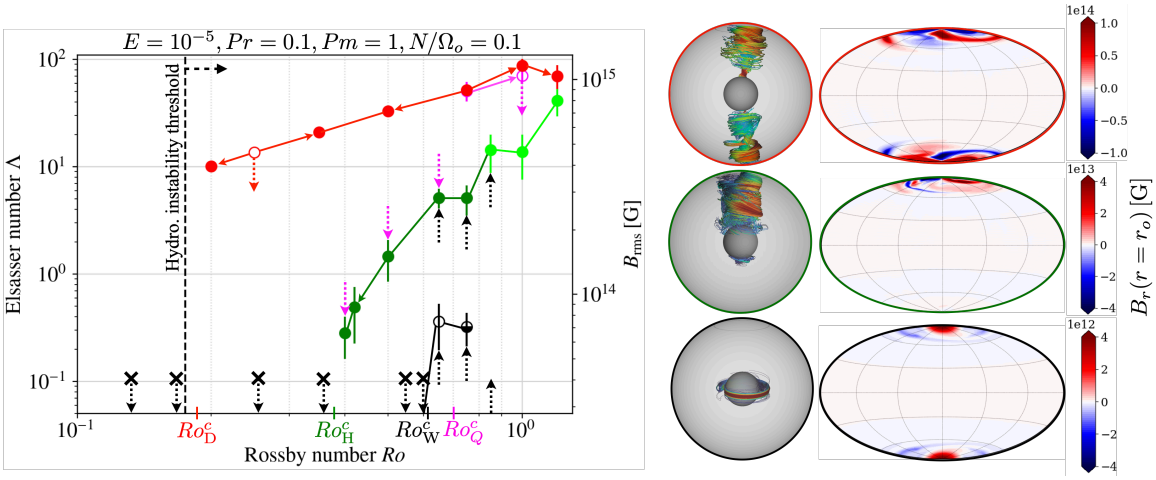

Fig. 3. Left: Bifurcation diagram of the time and volume averaged Elsasser number (and rms magnetic field) versus the Rossby number. Distinct dynamo branches are represented: dipolar (red), quadrupolar (mauve), hemispherical (green), and kinematic (black) whose respective thresholds are $Ro^c_{\rm D} \sim 0.19$, $Ro^c_{\rm Q} \sim 0.7$, $Ro^c_{\rm H} \sim 0.37$, and $Ro^c_{\rm W} \sim 0.62$. The hydrodynamic instability is triggered for $Ro^c_{\rm hyd} > 0.177$. Dark green circles are stationary hemispherical dynamos and light green ones display parity modulations. Black crosses indicate failed dynamos, empty circles metastable solutions. Arrows attached to circles indicate the initial condition of the associated simulation. The black half empty circle specifies that the solution was found to be metastable in a simulation and stable in another. The error bars indicate the standard deviation. **Right:** snapshots of the magnetic field lines and surface radial fields associated to the different main dynamo branches at $Ro = 0.75$: dipolar (top), hemispherical (middle), and kinematic (bottom).

Furthermore, we show that both hemispherical and dipolar dynamos are driven by the Tayler instability: (i) the magnetic field is clearly dominated by its axisymmetric toroidal component, (ii) snapshots of the perturbed magnetic field and magnetic energy spectra show a kink-shape instability (i.e. $m = 1$ perturbation), and (iii) the transition from the kinematic to the hemispherical branch occurs when the axisymmetric toroidal field exceeds the critical strength of the Tayler instability (see Barrère et al. 2023). Finally, the measure of the shear rate in our simulations shows that the hemispherical and dipolar branches follow the respective theoretical predictions of Spruit (2002) and Fuller et al. (2019).

4 Conclusions

To conclude, we propose a new magnetar formation scenario, in which the magnetic field amplified by the Tayler-Spruit dynamo in a slowly rotating and weakly magnetized PNS spun up by fallback. The semi-analytical modelling of our scenario built in Barrère et al. (2022) predicts that our scenario can form magnetars for PNS spun up to $\lesssim$ 28 ms rotation periods, which is greater than the expected rotation period for proto-magnetars born in typical supernovae (e.g. Vink & Kuiper 2006). Our numerical study in Barrère et al. (2023) demonstrates the existence of two distinct Tayler-Spruit dynamos which differ by their magnetic field strength, equatorial symmetry (hemispherical and dipolar), and scaling law. Besides, the study shows that both theoretical predictions of Spruit (2002) and Fuller et al. (2019) can be found in direct numerical simulations. This study is therefore complementary with Petitdemange et al. (2023), which finds a dynamo similar to the Tayler-Spruit dynamo of Spruit (2002) but in the context of stellar radiative zones and so with an opposite differential rotation. Finally, by extrapolating our results for the dipolar branch to $q \sim 1$ as in Barrère et al. (2022), we obtain a magnetic dipole of $B_{\rm dip} \sim 3.2 \times 10^{14}$ G, which falls right in the magnetar range (Olausen & Kaspi 2014). Extended parameter studies of the impact of the stratification and the resistivity on the dynamo will be needed to better constrain the astrophysical implications and test the theoretical predictions. Overall, by deepening our understanding on the complex dynamics of the Tayler-Spruit dynamo, our results are of particular importance in the domains of dynamo theory, stellar evolution modelling and magnetar formation.

This research was supported by the European Research Council through the ERC starting grant MagBURST No. 715368 and the PNPS and the PNHE programs of CNRS/INSU, co-funded by CEA and CNES. Numerical simulations have been carried out at the CINES on the Jean-Zay supercomputer (DARI project A0130410317). We are grateful to H.-T. Janka for his contribution to the article Barrère et al. (2022) and T. Foglizzo, A. Igoshev, L. Petitdemange, C. Gissinger, and F. Daniel for useful discussions.

References

Barrère, P., Guilet, J., Raynaud, R., & Reboul-Salze, A. 2023, arXiv e-prints, arXiv:2306.12296
Barrère, P., Guilet, J., Reboul-Salze, A., Raynaud, R., & Janka, H. T. 2022, Astron. Astrophys., 668, A79
Beniamini, P., Hotokezaka, K., van der Horst, A., & Kouveliotou, C. 2019, Mon. Not. Astron. R. Soc., 487, 1426
Bugli, M., Guilet, J., Foglizzo, T., & Obergaulinger, M. 2023, Mon. Not. Astron. R. Soc., 520, 5622
Bugli, M., Guilet, J., & Obergaulinger, M. 2021, Mon. Not. Astron. R. Soc., 507, 443
Cantiello, M., Mankovich, C., Bildsten, L., Christensen-Dalsgaard, J., & Paxton, B. 2014, Astrophys. J., 788, 93
Chan, C., Müller, B., & Heger, A. 2020, Mon. Not. Astron. R. Soc., 495, 3751
Denissenkov, P. A. & Pinsonneault, M. 2007, Astrophys. J., 655, 1157
Dessart, L., Burrows, A., Livne, E., & Ott, C. D. 2008, Astrophys. J. Lett., 673, L43
Duncan, R. C. & Thompson, C. 1992, Astrophys. J. Lett., 392, L9
Eggenberger, P., den Hartogh, J. W., Buldgen, G., et al. 2019, Astron. Astrophys., 631, L6
Eggenberger, P., Maeder, A., & Meynet, G. 2005, Astron. Astrophys., 440, L9
Fuller, J., Piro, A. L., & Jermyn, A. S. 2019, Mon. Not. Astron. R. Soc., 485, 3661
Gastine, T. & Wicht, J. 2012, Icarus, 219, 428
Gompertz, B. & Fruchter, A. 2017, Astrophys. J., 839, 49
Goossens, M. 1980, Geophysical and Astrophysical Fluid Dynamics, 15, 123
Goossens, M., Biront, D., & Tayler, R. J. 1981, Astrophys. Space Sci., 75, 521
Goossens, M. & Tayler, R. J. 1980, MNRAS, 193, 833
Griffiths, A., Eggenberger, P., Meynet, G., Moyano, F., & Aloy, M.-Á. 2022, Astron. Astrophys., 665, A147
Guilet, J., Reboul-Salze, A., Raynaud, R., Bugli, M., & Gallet, B. 2022, Mon. Not. Astron. R. Soc., 516, 4346
Hüdepohl, L. 2014, PhD thesis, Technical University of Munich, Germany
Inserra, C., Smartt, S. J., Jerkstrand, A., et al. 2013, Astrophys. J., 770, 128
Janka, H.-T., Wongwathanarat, A., & Kramer, M. 2022, Astrophys. J., 926, 9
Kouveliotou, C., Fishman, G. J., Meegan, C. A., et al. 1994, Nature, 368, 125
Metzger, B. D., Beniamini, P., & Giannios, D. 2018, Astrophys. J., 857, 95
Metzger, B. D., Giannios, D., Thompson, T. A., Bucciantini, N., & Quataert, E. 2011, Mon. Not. Astron. R. Soc., 413, 2031
Nicholl, M., Smartt, S. J., Jerkstrand, A., et al. 2013, Nature, 502, 346
Obergaulinger, M. & Aloy, M. Á. 2022, Mon. Not. Astron. R. Soc., 512, 2489
Olausen, S. A. & Kaspi, V. M. 2014, Astrophys. J.s, 212, 6
Petitdemange, L., Marcotte, F., & Gissinger, C. 2023, Science, 379, 300
Raynaud, R., Cerdá-Durán, P., & Guilet, J. 2022, Mon. Not. Astron. R. Soc., 509, 3410
Raynaud, R., Guilet, J., Janka, H.-T., & Gastine, T. 2020, Sci. Adv., 6, eaay2732
Rea, N., Israel, G. L., Esposito, P., et al. 2012, Astrophys. J., 754, 27
Reboul-Salze, A., Guilet, J., Raynaud, R., & Bugli, M. 2021, Astron. Astrophys., 645, A109
Reboul-Salze, A., Guilet, J., Raynaud, R., & Bugli, M. 2022, Astron. Astrophys., 667, A94
Spruit, H. C. 2002, Astron. Astrophys., 381, 923
Tayler, R. J. 1973, Mon. Not. Astron. R. Soc., 161, 365
Thompson, C. & Duncan, R. C. 1993, Astrophys. J., 408, 194
Vink, J. & Kuiper, L. 2006, Mon. Not. Astron. R. Soc., 370, L14
Wicht, J. 2002, Physics of the Earth and Planetary Interiors, 132, 281
Woosley, S. E. 2010, Astrophys. J. Lett., 719, L204
Zahn, J. P., Brun, A. S., & Mathis, S. 2007, Astron. Astrophys., 474, 145

SF2A 2023
M. N'Diaye, A. Siebert, N. Lagarde, O. Venot, K. Baillié, M. Béthermin, E. Lagadec, J. Malzac, J. Richard (eds)

IDENTIFICATION OF COMPACT OBJECTS AT THE GALACTIC CENTER

J. Berteaud[1,2], F. Calore[1] and M. Clavel[2]

Abstract. Unresolved point sources, namely millisecond pulsars (MSPs), are thought to contribute to an enigmatic signal detected in γ rays: the Galactic Center Excess. The detection of these sources at longer wavelengths will shed light on this long-standing puzzle, also related to dark matter. We present our recent progress in our search for MSPs among yet unidentified X-ray sources: 1. Infrared data helped us to identify compact objects among a large sample of promising X-ray MSP candidates; 2. A dedicated X-ray spectral analysis revealed contamination of our initial sample by a population of cataclysmic variables; 3. Finally, we are also conducting radio observations aiming at detecting millisecond pulsations.

Keywords: pulsar, compact objects, multi-wavelength, Galactic center

1 Introduction

The γ-ray sky has been observed by the *Fermi* Large Area Telescope (LAT) for almost 15 years. It shows a bright emission towards the Galactic plane and numerous point sources all across the sky that can be masked in order to study the diffuse emission alone. The latter is a linear combination of emissions from π^0 decay, Bremsstrahlung (both spatially correlated with the interstellar medium), inverse Compton scattering (with the interstellar radiation field), the huge *Fermi* bubbles and an extragalactic isotropic emission. However, towards the Galactic center, this standard model of diffuse γ-ray emission does not correctly reproduce the *Fermi* data without accounting for a signal of mysterious origin, dubbed the Galactic Center Excess (GCE). Goodenough & Hooper (2009) discovered this signal less than one year after the launch of the LAT and claimed to have found a possible sign of dark matter annihilation into γ rays toward the Galactic center, by analyzing the spectral shape and the spatial distribution of the photons detected by the LAT. Two years later, Abazajian (2011) showed that the spectrum of the GCE was also compatible with the one of globular clusters, known to host a large population of millisecond pulsars (MSPs), suggesting that these highly magnetized and fast rotating neutron stars could be the origin of the excess. Further studies suggested that the emission was extended (Calore et al. 2015; Daylan et al. 2016), coming from the bulge (Bartels et al. 2018a; Macias et al. 2018) and at least partly from point sources (Calore et al. 2021; List et al. 2021). Not only would the discovery of MSPs towards the Galactic center improve our understanding of the GCE and its relation to dark matter, but it would also *e.g.* constrain the models of free electron density in the Milky Way and allow astrophysicists to test the gravitational potential of the region. Moreover, with its high density and profusion of massive stars, the Galactic center is the perfect place to look for compact objects (COs).

2 Simulation and X-ray detectability of the Galactic bulge MSP population

In Berteaud et al. (2021), we performed a Monte Carlo simulation* of the Galactic population of MSPs, which we supposed to be made of two components: the disk and the bulge. The former is well constrained from observations and we used the spatial distribution and γ-ray luminosity function (GLF) found by Bartels et al. (2018b) who used the data of $\sim$ 100 MSPs detected by the LAT and accounted for the sensitivity threshold of the telescope. The existence of a population in the bulge is speculative and is the putative origin of the

[1] LAPTh, CNRS, USMB, F-74940 Annecy, France
[2] Université Grenoble Alpes, CNRS, IPAG F-38000 Grenoble, France
*Available on Zenodo: `https://doi.org/10.5281/zenodo.7446997`

© Société Française d'Astronomie et d'Astrophysique (SF2A) 2023

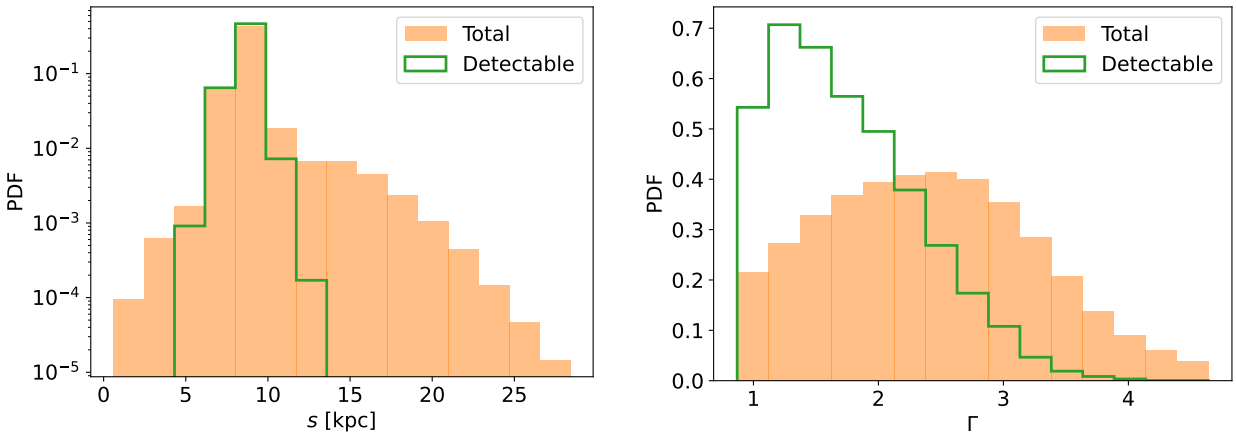

Fig. 1. *Left:* Probability density function (PDF) of the distance s of simulated MSPs in the global population (orange) and in the X-ray detectable one (green). *Right:* Same as left but for the X-ray spectral index Γ.

GCE. We used the spatial distribution of the excess found by Bartels et al. (2018a) and the same GLF as in the disk for our simulation. We constructed a γ-to-X emission model and obtained a population of $\sim$ 14 000 sources in our region of interest (ROI, $|l|, |b| < 3°$) with an absorbed X-ray flux $F_{\rm X}^{\rm abs}$ between 10^{-22} and 10^{-12} erg/cm^2/s. About a hundred of them, with a negligible contribution from the disk, have $F_{\rm X}^{\rm abs}$ larger than the detection threshold the *Chandra* X-ray observatory, meaning that this telescope could have detected some bulge MSPs in past observations. According to our simulation, these sources would be located at 5.2/11.9/8.5 kpc at minimum/maximum/on average and would be rather hard compared to the global population, as can be seen in figure 1.

3 Millisecond pulsars candidates

3.1 Multi-wavelength selections

In Berteaud et al. (2021), we also selected MSP candidates in the *Chandra* Source Catalog. Among non-variable, non-extended objects with a rather hard emission, we excluded those with a *Gaia* counterpart either too close (< 5.2 kpc) or too far (> 11.9 kpc) from us. The association between *Chandra* and *Gaia* sources is not known *a priori* and we performed a geometrical cross-match between both catalogs, *i.e.* we considered as counterparts two sources for which the angular separation is less than the error radius of the X-ray source. With this method, we identified more than 3100 MSP candidates in our ROI, *i.e.* more than what was expected from the simulation, demonstrating that the X-ray data do not exclude the MSP origin of the GCE. Therefore, we recently made additional cuts on our selection, following the idea that the optical, ultraviolet (UV) and infrared (IR) light from MSPs should not be bright, and anyways highly absorbed if in the bulge. Again, we performed geometrical cross-matches (accounting for the counterpart error when relevant) and we excluded those sources with optical, UV and strong IR emission, while the ones with faint IR emission were tagged as potential COs, according to the criterion of Lin et al. (2012):

$$\log_{10}(F_{\rm X}/F_{\rm IR}) > 0.5, \tag{3.1}$$

where $F_{\rm X}$ and $F_{\rm IR}$ are the unabsorbed X-ray and the IR flux. About 1400 sources survived these selections and more than 50 of them were tagged as CO candidates.

3.2 Cumulative X-ray spectrum

Most of the candidates mentioned above are too faint to perform a dedicated spectral analysis. Therefore, we combined the X-ray spectra of our $\sim$ 1400 sources in order to shed light on the general properties of this population. The cumulative X-ray spectrum of our candidates shows a prominent line between 6 and 7 keV, that we interpreted as an iron K-shell line. This feature is characteristic of cataclysmic variables (CVs), a type

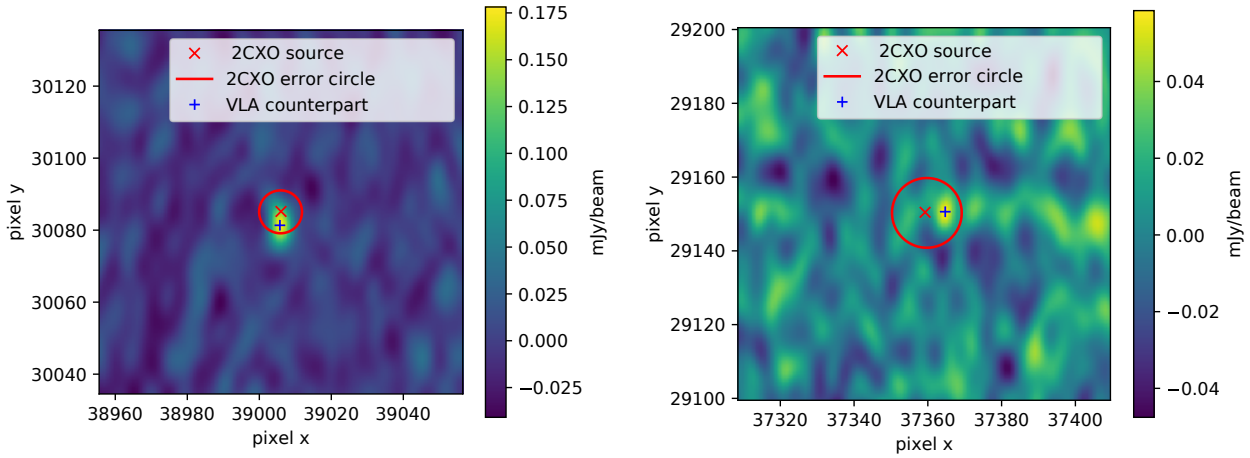

Fig. 2. Identification of the radio counterpart of 2 MSP candidates detected in X-rays in VLA imaging data (colored background). The positions and error circles of the *Chandra* (2CXO) sources are shown by the red crosses and circles. The blue cross indicates the position of VLA sources whose distance from the MSP candidate is less than the radius of the error circle.

of CO, which are probably the dominant sources in our ROI (Hong et al. 2009; Jonker et al. 2011). Given the selections that we made, we expected to have included CVs among our MSP candidates. Further investigations will be necessary to disentangle both kinds of sources. Nonetheless, we also created the cumulative spectrum of the sources tagged as potential CO, which encouragingly did not present the same line feature. Moreover, its spectral shape is compatible with the cumulative spectrum of simulated detectable MSPs.

3.3 Radio counterparts

In order to complete the counterpart search that we described in section 3.1, we analyzed unpublished radio imaging data collected from 28h of observations of the Very Large Array (VLA) in the region $|l| < 1°$, $-1° < b < 2°$ (PI: M. Kerr). Unlike optical, UV and IR light, the radio emission of MSPs is especially strong. We used a source detection algorithm, `PyBDSF`[†], in $\sim$ 20-arcsec boxes around the $\sim$ 900 candidates covered by the VLA observations to identify radio sources in the vicinity of our MSP candidates and required the distance between the X-ray and the VLA sources to be less than the *Chandra* error radius in order to consider a match. Each match was then carefully inspected. Some of the sources detected by `PyBDSF` were actually noise, others were spatially extended. For the rest, we made sure, by looking for their position in VizieR, that we did not miss any potential counterparts. With this method, we identified promising MSP candidates: 5 with only X-ray and radio emission, plus one tagged as CO. In figure 2, we show the radio image of two of them. The non-detections of the other candidates cannot rule out their pulsar nature, given the noise level of the VLA image.

4 Radio timing follow-ups

4.1 Theory

The radiometer equation is a useful tool to calculate the minimal detectable flux of a pulsar $S_{\rm min}$ as a function of parameters of the radio telescope used for the observation, the duration of the observation $T_{\rm obs}$, the pulsar period P and its observed pulse width $w_{\rm obs}$:

$$S_{\rm min} \propto \sqrt{\frac{w_{\rm obs}}{T_{\rm obs}(P - w_{\rm obs})}}. \tag{4.1}$$

$w_{\rm obs}$ increases with the dispersion measure (DM) of the pulsar, *i.e.* its column density of free electrons. With a flux smaller than $S_{\rm min}$, the pulsations, characteristic of this type of source, would be indistinguishable from

[†] `https://pybdsf.readthedocs.io/en/latest/`

noise. This equation tells us that the hardest pulsation detections are for pulsars with high DMs, with short periods and low fluxes, which is a pretty accurate definition of bulge MSPs. Calore et al. (2015) indeed showed that current radio surveys are not sensitive enough to the population of bulge MSPs. Hence, deep targeted observations are needed. We used the radiometer equation to calculate the minimal detectable period of the 6 promising MSP candidates from section 3.3, knowing their radio flux thanks to `PyBDSF` and their DM was calculated with `PSRDist` Bartels et al. (2018b), assuming either a distance of 5.2 or 8.5 kpc. We used these results to support several radio observational proposals.

4.2 Observations and data analysis

We obtained about 50h of observations with Parkes and the Green Bank Telescope and performed the pulsation search with `PRESTO`[‡]. For bright pulsars, their signal is usually seen at all wavelengths, during the whole observation, and `PRESTO` finds well-defined period and period derivative. The data analysis is ongoing and preliminary results are encouraging.

5 Conclusions

The Galactic center is the perfect place to look for COs. The existence of a population of MSPs in this region is supported by the discovery of an excess of γ rays and their detection would be a major breakthrough in various domains of physics. We have developed a novel method to select MSP candidates in the direction of the Galactic center, starting from *Chandra* observations. We found more than 1400 X-ray sources with neither optical, nor UV, nor strong IR counterparts. A vast majority of them do not have IR counterparts at all, while the rest respect the CO criterion (equation 3.1). The cumulative X-ray emission of all candidates revealed the presence of CVs in our selection, while the population of potential CO does not seem to be polluted by these sources. Finally, 6 of our sources were also detected in radio, making them very promising candidates for follow-up studies. We obtained more than 50h of timing observations for these targets, and we are currently working on the data analysis. Results will be published in a near future.

JB acknowledges financial support from the Programme National des Hautes Energies of CNRS/INSU with INP and IN2P3, co-funded by CEA and CNES, from the 'Agence Nationale de la Recherche', grant number ANR-19-CE310005-01 (PI: F. Calore), and from the Centre National d'Etudes Spatiales (CNES).

References

Abazajian, K. N. 2011, Journal of Cosmology and Astroparticle Physics, 2011, 010, aDS Bibcode: 2011JCAP...03..010A

Bartels, R., Storm, E., Weniger, C., & Calore, F. 2018a, Nature Astronomy, 2, 819, aDS Bibcode: 2018NatAs...2..819B

Bartels, R. T., Edwards, T. D. P., & Weniger, C. 2018b, Monthly Notices of the Royal Astronomical Society, 481, 3966

Berteaud, J., Calore, F., Clavel, M., et al. 2021, Physical Review D, 104, 043007, arXiv: 2012.03580

Calore, F., Cholis, I., & Weniger, C. 2015, Journal of Cosmology and Astroparticle Physics, 2015, 038, aDS Bibcode: 2015JCAP...03..038C

Calore, F., Donato, F., & Manconi, S. 2021, Physical Review Letters, 127, 161102, arXiv:2102.12497 [astro-ph, physics:hep-ph]

Daylan, T., Finkbeiner, D. P., Hooper, D., et al. 2016, Physics of the Dark Universe, 12, 1, aDS Bibcode: 2016PDU....12....1D

Goodenough, L. & Hooper, D. 2009, Possible Evidence For Dark Matter Annihilation In The Inner Milky Way From The Fermi Gamma Ray Space Telescope, Tech. rep., publication Title: arXiv e-prints ADS Bibcode: 2009arXiv0910.2998G Type: article

Hong, J., van den Berg, M., Grindlay, J. E., & Laycock, S. 2009, The Astrophysical Journal, 706, 223

Jonker, P. G., Bassa, C. G., Nelemans, G., et al. 2011, The Astrophysical Journal Supplement Series, 194, 18, aDS Bibcode: 2011ApJS..194...18J

Lin, D., Webb, N. A., & Barret, D. 2012, The Astrophysical Journal, 756, 27

List, F., Rodd, N. L., & Lewis, G. F. 2021, Physical Review D, 104, 123022, arXiv:2107.09070 [astro-ph, physics:hep-ph]

Macias, O., Gordon, C., Crocker, R. M., et al. 2018, Nature Astronomy, 2, 387, aDS Bibcode: 2018NatAs...2..387M

[‡] `https://github.com/scottransom/presto`

SF2A 2023
M. N'Diaye, A. Siebert, N. Lagarde, O. Venot, K. Baillié, M. Béthermin, E. Lagadec, J. Malzac, J. Richard (eds)

MULTI-WAVELENGTH EMISSION OF FR 0 RADIO GALAXIES AT THE SUBPARSEC SCALE

M. Boughelilba[1]

Abstract. Fanaroff-Riley (FR) 0 radio galaxies are a new class of radio galaxies. These sources are usually weaker but much more numerous than the well-established class of FR I and FR II radio galaxies. In particular, they are observationally very close to the FR I radio galaxies, with the exception of the lack of extended radio emission. We propose a lepto-hadronic jet model, focusing on the core emission region, with parameters close to equipartition, combined with an advection-dominated accretion flow model. This model was successfully used for the FR I galaxy M87 in order to explain its quiet core emission. This combined model is able to reproduce the multiwavelength FR 0 data, both for the gamma-ray undetected sources, as well as the two sources recently associated with a Fermi-LAT detection.

Keywords: Relativistic jets, Particle astrophysics, Active galactic nuclei, High energy astrophysics, Gamma-ray sources

1 Introduction

Based on their radio morphology, radio galaxies are usually classified as either faint edge-darkened Fanaroff-Riley type I (FR I) or bright edge-brightened type II (FR II) galaxies. Recently, a new type of radio galaxy has gained popularity, named FR 0 galaxies (Baldi et al. 2018). From the radio perspective, FR 0s are similar to FR Is, except for the lack of extended emission (i.e. on a kiloparsec scale). Optical and X-ray observation (Torresi et al. 2018), confirm the similarity of the nuclear properties of the two classes. In the high-energy domain, the detection of gamma rays FR 0s (namely LEDA 55267 and LEDA 58287) has recently been reported in Paliya (2021). As of now the population is characterized by a redshift $z \leq 0.05$, radio sources located at maximum 2" from the optical centre, a minimum FIRST flux of 5 mJy at 1.4 GHz. FR 0s are shown to be in the order of ~ 5 times more numerous than the FR I radio galaxies in the local Universe, making them the dominating jet population there (Baldi & Capetti 2009, 2010). Several hypotheses have been proposed so far, to explain the lack of extended radio emission from FR 0s (Baldi et al. 2019; Garofalo et al. 2010; Garofalo & Singh 2019). We propose that the true nature of this jet population is linked to their broadband spectral energy distribution (SED). Here, we compare the broadband emission of FR 0s to FR Is, and in particular to M87 as one of the most detailed studied archetypal FR I galaxy.

2 Broadband SED

Following Merten et al. (2021) we collected available data from 114 FR 0s. The gamma-ray data of LEDA 55267 and LEDA 58287 are taken from Paliya (2021). We also collected data of 216 FR I sources listed in the FRICAT (Capetti et al. 2017) in the same way. These data are compared to M87's quiet core emission from 2017 (EHT MWL Science Working Group et al. 2021) and its multiwavelength flaring state. We use the average fitted values and uncertainties reported all together in MAGIC Collaboration et al. (2020). Figure 1 shows the resulting broadband SEDs of FR 0s as compared to those of M87 and all the other FR Is, all scaled to the mean distance of FR 0s (i.e $z \sim 0.04$). What stands out in this comparison is the extreme similarity between M87's quiet core emission and the spectral behaviour of FR 0s, at all wavelengths. A model that reproduces the radio-to-gamma-ray quiet core emission of M87 in a one-zone setup was proposed by Boughelilba et al. (2022). This model focuses on the central region of the AGN, with a jet emission region of a few gravitational radii. Given the compactness of the FR 0s and the SED similarities, we explore here the same type of model for the FR 0 source class.

[1] Universität Innsbruck, Institut für Astro- und Teilchenphysik, 6020 Innsbruck, Austria

© Société Française d'Astronomie et d'Astrophysique (SF2A) 2023

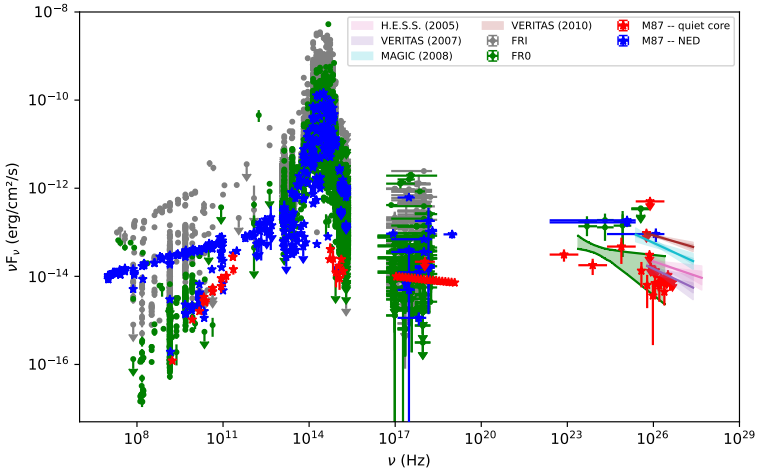

Fig. 1. Broadband SED of FR Is (grey dots), FR 0s (green dots and green butterfly), M87 in its 2017 quiet state (red stars). The blue star symbols are the SED of M87 with all the observations available in the NED. The butterfly plots in the very-high-energy gamma-ray range are the power-law spectra fitted to observations of the flaring state of M87 with H.E.S.S (Aharonian et al. 2006, pink region), VERITAS (Acciari et al. 2008; Aliu et al. 2012, purple and brown regions respectively) and with MAGIC (Albert et al. 2008; MAGIC Collaboration et al. 2020, cyan region). The fluxes from FR Is and M87 have been rescaled from their mean distance to the mean distance of FR 0s.

3 Model

We consider a continuous cylindrical jet of radius $R'_{\rm em}$ containing primary relativistic electrons and protons that are isotropically and homogeneously distributed in the comoving jet frame, and follow a power-law energy spectrum cutting off exponentially, such that the spectral number density $n'_{e,p}(E') \propto E'^{-p_{e,p}} e^{-E'/E'_{\rm max,e,p}}$ cm^{-3}, for $E' \geq E'_{\rm min,e,p}$ (where e,p denotes the electrons or the protons, respectively). The primary particles are continuously injected into the emission region, where they experience energy losses caused by various interactions. Specifically, we consider photo-meson production, Bethe-Heitler pair production, inverse-Compton scattering, γ-γ pair production, decay of all unstable particles, synchrotron radiation (from electrons and positrons, protons, and $\pi^{\pm}$, $\mu^{\pm}$ and $K^{\pm}$ before their respective decays), and particle escape.

We model Advection-Dominated Accretion Flows (ADAFs, Rees et al. 1982; Ichimaru 1977; Narayan & Yi 1995; Abramowicz et al. 1995) as described in Boughelilba et al. (2022). ADAFs exist only when the accretion rate is sufficiently low ($\dot{m} = \dot{M}/\dot{M}_{\rm Edd} \leq 0.01$, where $\dot{m}$ is the mass accretion rate scaled to the Eddington accretion rate). The quantities governing the accretion flow depend on the plasma parameter β, which is the ratio between the gas and the total pressure (i.e., the sum of the magnetic and gas pressure), on the viscosity α and on the heating fraction δ_e which represents the fraction of viscous energy directly transmitted to the electrons of the plasma. Furthermore, we take $\dot{m} = \dot{m}_{\rm out}\,(R/R_{\rm out})^s$, where $R_{\rm out}$ is the outer radius of the ADAF and is associated with an accretion rate $\dot{m}_{\rm out}$, and s is the mass-loss parameter (Blandford & Begelman 1999).

4 Results

The ADAF spectrum is calculated for the two gamma-ray detected sources, as well as for the 23 other sources where X-ray data are available. The resulting SED is a combination of the ADAF component, the jet component and the host galaxy's modified blackbody. FR 0s' jets are expected to be less powerful than FR Is' and only mildly relativistic (Giovannini et al. 2023). Therefore the relative jet bulk velocity is set to $\beta_{\rm j} = 0.55$, and a jet inclination with respect to the line of sight of 20°. A summary of the ADAF and jet parameters is given in Table 1. In Figure 2, we present the SED of the two gamma-ray detected sources (LEDA 55267 and LEDA 58287) and their multiwavelength models for a jet magnetic field strength of 25 G from left to right respectively. As described above, the 23 subthreshold sources with X-ray data possess a modelled ADAF and a jet. All the 112 subthreshold sources are modelled with the same jet parameters. For each source, the observed flux is displayed in Figure 3 in faint purple. The average SED of the population is represented with the darker, wider purple curve. The steady-state jet power is estimated by $L'_{\rm jet,ss} = \pi R'^2_{\rm em} \Gamma_{\rm j}^2 \beta_{\rm j} c \sum_i u'_i$ where $u'_{\rm i}$ is the energy density of

Table 1. Model parameters. $n'_{\mathrm{inj,e(p)}}$ is the electron (proton) number density injection rate. The minimum Lorentz factor of the primary electrons and protons is set to $\gamma' = 1$. R_{S} is the Schwarzschild's radius.

Parameters	$B = 25\,\mathrm{G}$	$B = 50\,\mathrm{G}$
α	0.1	0.1
β	0.99	0.99
s	0.1	0.1
R_{out}	$5 \times 10^3\, R_{\mathrm{S}}$	$5 \times 10^3\, R_{\mathrm{S}}$
δ_e	5×10^{-3}	5×10^{-3}
$\dot{m}(R = R_{\mathrm{out}})$	$(6 - 20) \times 10^{-4}$	$(1 - 4) \times 10^{-3}$
R'_{em} (cm)	4.0×10^{15}	1.2×10^{15}
$E'_{\mathrm{max,e}}$ (MeV)	$(8.0 - 15) \times 10^3$	8.0×10^3
$E'_{\mathrm{max,p}}$ (GeV)	$(2 - 5.5) \times 10^9$	$(1.5 - 4) \times 10^9$
$p_{\mathrm{e}} = p_{\mathrm{p}}$	1.7	1.7
$u'_{\mathrm{part,ss}}/u'_{\mathrm{B}}$	$(3.5 - 21) \times 10^{-2}$	$(1 - 4.8) \times 10^{-1}$
$L'_{\mathrm{jet,ss}}$ (erg s^{-1})	$(3.1 - 3.6) \times 10^{43}$	$(1.1 - 1.5) \times 10^{43}$

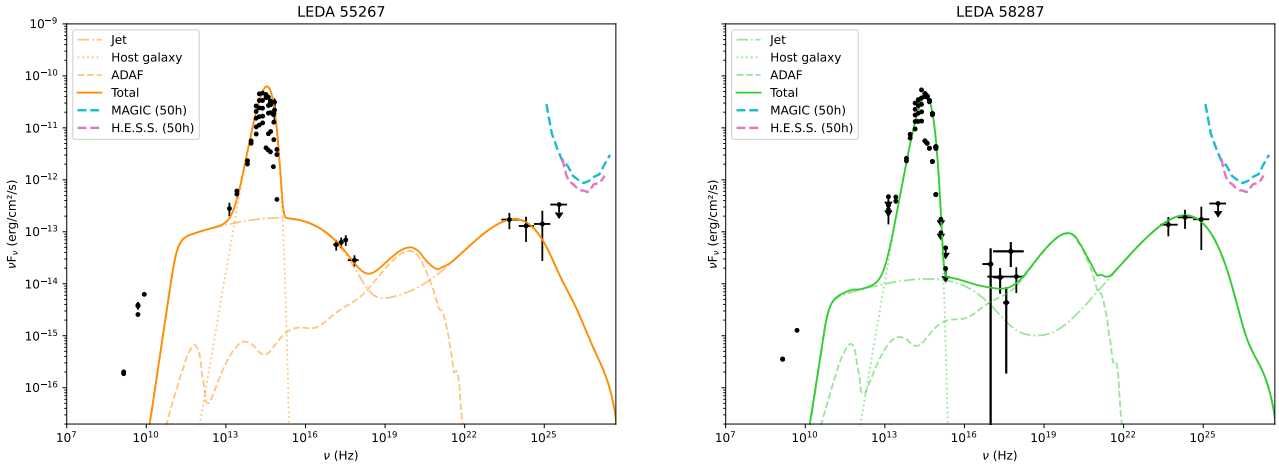

Fig. 2. Left: SED and models for a magnetic field strength of 25G in the jet for LEDA 55267. **Right:** For LEDA 58287. The dotted line is the modified blackbody modelling the host galaxy emission, the dashed line is the emission coming from the ADAF, the dash-dotted line is the total jet's emission and the solid line represents the total emission of the source and is the sum of the three components. The differential fluxes sensitivities for 50 hours of observation with MAGIC (Aleksić et al. 2016) and H.E.S.S (Holler et al. 2015) are shown with the cyan and pink dashed lines respectively.

radiation, electrons, protons ($u'_{\mathrm{part,ss}}$) and magnetic field (u'_{B}) respectively. Overall, the jet composition is very close to equipartition.

5 Conclusion

We found that the broadband SED of FR 0s is extremely similar to the archetypal FR I, M87, during its quiet steady state (described in detail in EHT MWL Science Working Group et al. 2021). The similarity goes from the core radio emission to the X-ray band, and up to gamma-rays for two individual sources detected in the high-energy band. We found that a compact subparsec-scale jet-flow emission region is able to explain the nuclear multiwavelength SED of FR 0s, provided that a magnetic field strength of $25 - 50\,\mathrm{G}$ is reached in the core region. The jet of FR 0s is mildly relativistic, with a velocity $\beta_{\mathrm{j}} c = 0.55\, c$, which is consistent with the value obtained by Giovannini et al. (2023) when observing the core of FR 0s in comparison to FR Is.

This work acknowledges financial support from the Austrian Science Fund (FWF) under grant agreement number I 4144-N27. MB

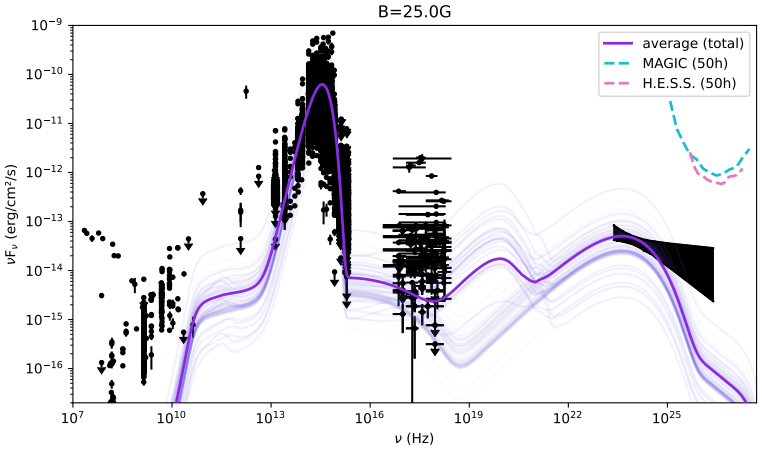

Fig. 3. SEDs of the 112 sources that are not individually detected in the gamma-ray band, and models for a magnetic field strength of 25G in the jet. The faint purple lines are the individual fluxes of the 112 sources (see main text for details) and the solid purple line is the average of the 112 models. The differential fluxes sensitivities for 50 hours of observation with MAGIC (Aleksić et al. 2016) and H.E.S.S (Holler et al. 2015) are shown with the cyan and pink dashed lines respectively.

has for this project received funding from the European Union's Horizon 2020 research and innovation program under the Marie Sklodowska-Curie grant agreement No 847476. The views and opinions expressed herein do not necessarily reflect those of the European Commission.

References

Abramowicz, M. A., Chen, X., Kato, S., Lasota, J.-P., & Regev, O. 1995, ApJ, 438, L37
Acciari, V. A., Beilicke, M., Blaylock, G., et al. 2008, ApJ, 679, 397
Aharonian, F., Akhperjanian, A. G., Bazer-Bachi, A. R., et al. 2006, Science, 314, 1424
Albert, J., Aliu, E., Anderhub, H., et al. 2008, ApJ, 685, L23
Aleksić, J., Ansoldi, S., Antonelli, L. A., et al. 2016, Astroparticle Physics, 72, 76
Aliu, E., Arlen, T., Aune, T., et al. 2012, ApJ, 746, 141
Baldi, R. D. & Capetti, A. 2009, A&A, 508, 603
Baldi, R. D. & Capetti, A. 2010, A&A, 519, A48
Baldi, R. D., Capetti, A., & Giovannini, G. 2019, MNRAS, 482, 2294
Baldi, R. D., Capetti, A., & Massaro, F. 2018, A&A, 609, A1
Blandford, R. D. & Begelman, M. C. 1999, MNRAS, 303, L1
Boughelilba, M., Reimer, A., & Merten, L. 2022, ApJ, 938, 79
Capetti, A., Massaro, F., & Baldi, R. D. 2017, A&A, 598, A49
EHT MWL Science Working Group, Algaba, J. C., Anczarski, J., et al. 2021, ApJ, 911, L11
Garofalo, D., Evans, D. A., & Sambruna, R. M. 2010, MNRAS, 406, 975
Garofalo, D. & Singh, C. B. 2019, ApJ, 871, 259
Giovannini, G., Baldi, R. D., Capetti, A., Giroletti, M., & Lico, R. 2023, A&A, 672, A104
Holler, M., de Naurois, M., Zaborov, D., Balzer, A., & Chalmé-Calvet, R. 2015, in International Cosmic Ray Conference, Vol. 34, 34th International Cosmic Ray Conference (ICRC2015), 980
Ichimaru, S. 1977, ApJ, 214, 840
MAGIC Collaboration, Acciari, V. A., Ansoldi, S., et al. 2020, MNRAS, 492, 5354
Merten, L., Boughelilba, M., Reimer, A., et al. 2021, Astroparticle Physics, 128, 102564
Narayan, R. & Yi, I. 1995, ApJ, 452, 710
Paliya, V. S. 2021, ApJ, 918, L39
Rees, M. J., Begelman, M. C., Blandford, R. D., & Phinney, E. S. 1982, Nature, 295, 17
Torresi, E., Grandi, P., Capetti, A., Baldi, R. D., & Giovannini, G. 2018, MNRAS, 476, 5535

SF2A 2023
M. N'Diaye, A. Siebert, N. Lagarde, O. Venot, K. Baillié, M. Béthermin, E. Lagadec, J. Malzac, J. Richard (eds)

MULTI-MESSENGER OBSERVATIONS WITH THE KM3NET TELESCOPE: SEARCH FOR HIGH ENERGY NEUTRINOS COINCIDING WITH FAST RADIO BURSTS

F. Bretaudeau on behalf of the KM3NeT Collaboration[1]

Abstract. The KM3NeT experiment is a next-generation neutrino telescope, consisting of two separate detection structures, organised as arrays of light sensors, and immersed in the depths of the Mediterranean Sea. The two detectors are the Oscillation Research with Cosmics in the Abyss (ORCA detector), located off the coast of France and the Astrophysics Research with Cosmics in the Abyss (ARCA detector), off the coast of Sicily. Identical in the design but differing by scale, these two detectors observe neutrino interactions in the sea water through Cherenkov light produced by the interaction products at different energy ranges. Specifically, ORCA aims at detecting atmospheric neutrinos to study their oscillation parameters, while ARCA will focus at higher energies on astrophysical neutrinos and the characterisation of their sources. Among the latter topic, Fast Radio Bursts (FRB) are good candidates for multi-messenger emissions due to the huge energy involved in their burst. I will present the method and criteria of a multi-messenger analysis intended to search for spatial and temporal coincidences of astrophysical neutrino signals from KM3NeT with FRBs. The search uses a FRB catalogue of around 800 sources among which 14 occured in the period ranging from January 2020 to March 2021, and were visible from the KM3NeT site.

Keywords: astrophysics, neutrino, multi-messenger, FRB, KM3NeT

1 Introduction

Starting with the detection of the first galactic supernova SN1987A, seen both in photons and neutrinos, and followed later by the first binary neutron star merger (Abbott et al. 2017), seen in gamma rays and gravitational waves, the astronomy has entered the multi-messenger era. Since then, several distant events of the Universe have been monitored in more than one channel of observation (Greus & Losa 2021), so-called *Universe messengers*. Observing an event in several channels is highly interesting, as different emissions have different production processes and tell a different story of their source. Until recently, the most favored messenger is the photon, coming at various energies along the electromagnetic spectrum. In the 2000's, a very puzzling type of emission has been detected in the radio band, the Fast Radio Burst (FRB) (Zhang 2022). A colossal amount of energy emitted coherently over a very short period of time (less than a millisecond), coming from extragalactic distances, is definitely intriguing but has not been fully yet explained. A way to increase our knowledge of FRBs and their sources is to use multi-messenger observations implying a FRB and another type of messenger, like the multi-wavelength observation of FRB20200428* and a Hard X-Ray burst coming from the magnetar SGR1935+2154 (Andersen et al. 2020). Along with electromagnetic radiations, gravitational waves and cosmic rays, neutrinos are a newly observed type of cosmic messengers that are showing a growing interest in the field of astrophysics. Travelling extragalactic distances without being impeded, carrying direct information of their production mechanisms, neutrinos are a privileged channel to understand the sources that produced them. A large-volume neutrino telescope, the KM3NeT experiment, is being built in the Mediterranean Sea, and will be able to conduct surveys of the sky, real-time analyses and high energy neutrino searches for multi-messenger purposes (Aiello et al. 2023). Although the detector is not fully built yet, the infrastructure already allows for data taking and analyses. This work is focused on the selection of neutrino events that originate from the same time and location in the sky as FRBs that have been observed already and could be correlated to them. After introducing the KM3NeT experiment, and stating the characteristics of a possible dual emission of neutrinos and FRBs, the strategy of this analysis will be presented.

[1] Subatech, 44300 Nantes, France
*FRB are registered as their observation time, in the format *FRBYYYY-MM-DD*

© Société Française d'Astronomie et d'Astrophysique (SF2A) 2023

2 The KM3NeT Experiment

KM3NeT is a large volume neutrino detector, plunged at the bottom of the Mediterranean Sea, continuously monitoring the flux of neutrinos coming from both the atmosphere and the more distant Universe. The signal from neutrinos is catched through the Cherenkov light emitted by ultrarelativistic neutrino interaction products in the sea water. The KM3NeT telescope is able to recover both the energy and direction of the interacting neutrino (Adrián-Martínez et al. 2016). The experiment is composed of two different detectors, equal in design and differing only by scale, in order to probe two different energy ranges at the best possible sensitivity. As can be seen on Fig. 1, ORCA (Oscillation Research with Cosmic in the Abyss) focuses on lower energies and the detection of atmospheric neutrinos to understand further the neutrino oscillations, whereas ARCA (Astrophysics Research with Cosmic in the Abyss) targets higher energies in search for astrophysical sources. The Cherenkov radiation is collected by PMTs, grouped in Digital Optical Modules (DOMs). DOMs each have 31 PMTs and are arranged by 18 in strings, held straight by an anchor at the bottom and a buoy at the top. The strings, called Detection Units, are 200 m high in ORCA and separated on the seabed by 20 m, and 700 m high in ARCA and separated by 90 m. Both detectors are in the deep sea, shielded from atmospheric particles by 2400 m of water in the case of ORCA and 3500 m for ARCA. The construction of the detectors started in 2015 and by this decade KM3NeT will be the largest instrumented volume for neutrino detection in the Northern Hemisphere. It follows the ANTARES experiment, that took data from 1999 to 2022, but thanks to the larger infrastructure will be more sensitive on the whole energy range (see the effective volumes of the two experiments in Fig. 1). Although the detector is under construction, and only reaching 13% of the foreseen final size, its design allows to conduct data taking and physics analyses, implying a limited sensitivity. The energy range covered by ARCA and ORCA is unprecendented (Adrián-Martínez et al. 2016), from the GeV to the PeV, allowing to work on different topics. First, atmospheric neutrinos produced by cosmic rays in the atmosphere in the range from 1 GeV to 100 GeV are very abundant, and by accumulating statistics one can constrain neutrino oscillation parameters and determine the neutrino mass ordering (Gupta et al. 2022). Then, at higher energies (above the TeV) fluxes of atmospheric neutrinos are less important, allowing to study astrophysical neutrinos and constraining models of their sources. Recently, the first neutrino observations were made by IceCube, on neutrino-emitting galaxies NGC 1048 and TXS 0506+056 (Kurahashi et al. 2022), or an evidence of the Galactic Plane signal in the neutrino channel (Sclafani & Huennefeld 2023). KM3NeT will have access to different astrophysical sources in the Southern Hemisphere, notably the Galactic Center. It will be therefore essential to work together with telescopes located in the South, like the Square Kilometer Array, in order to combine surveys of the experiments, send and receive alerts. Additionally, KM3NeT can detect a Supernova thanks to its large flux in the MeV range (Aiello et al. 2021), and is also sensitive to some exotic sources (Aiello et al. 2022). The pointing capabilities of KM3NeT at high energies can be used to search for multi-messenger observations, connecting a neutrino emission with another transient emission like a Fast Radio Burst.

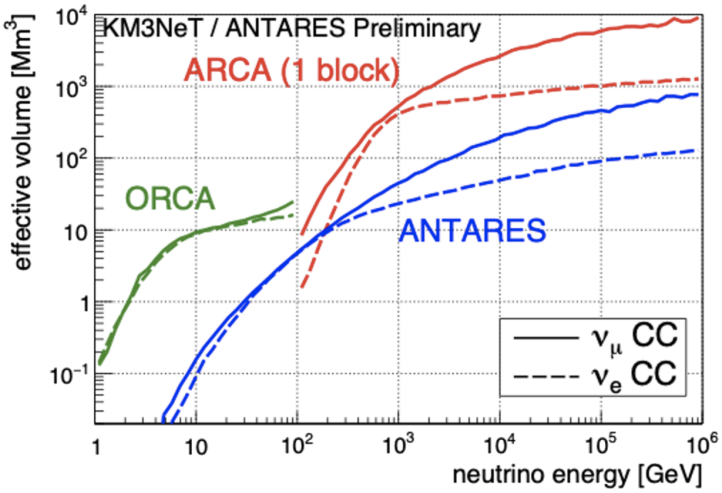

Fig. 1. Planned effective volumes of the detectors of KM3NeT, ORCA and ARCA, compared to the actual effective area of ANTARES. Credit: Hallmann, Steffen, KM3NeT collaboration meeting, Bari, 16/06/17.

3 Fast Radio Bursts in the Multi-Messenger Context

Since the first detection in 2007, several hundreds of FRBs have been observed, from which a few properties on the progenitors have been derived such as the duration, fluence, dispersion measure, rotation measure and scattering. They encode the properties of the bright coherent bursts coming from extra-galactic distances, emerging from a mechanism that has an environment with an energetic, dense, perturbed and magnetized plasma (Zhang 2022). This plasma is therefore a possible source of hadronic accelerations and by conventional processes, like the photopion process (Metzger et al. 2020), source of high energy neutrinos. In addition, thanks to the first and only multi-wavelength detection of the FRB 20200428, associated with the galactic magnetar SGR1935+2154, models of neutrino production from magnetars have emerged. From these models, it is possible to extrapolate the expected neutrino fluxes and energies and to optimise the neutrino analysis for events similar to the ones associated with SGR1935+2154 (see sketch on Fig. 2 for the possible production sites near the magnetar). Eventually, the analysis conducted needs to be as model-independent as possible, since FRB sources are not constrained yet. The Cut-and-Count analysis is then well suited for this purpose.

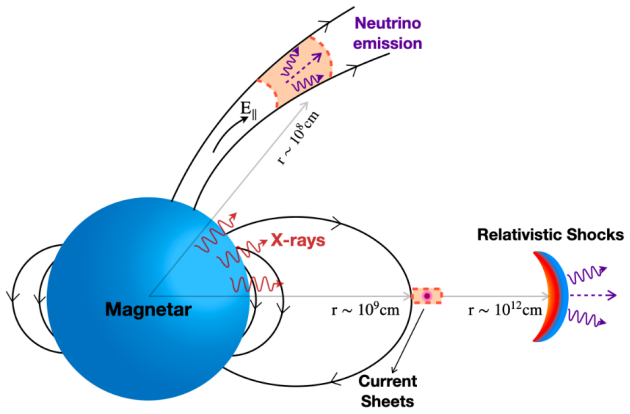

Fig. 2. Sketch of three neutrino production sites from the surroundings of a magnetar: the magnetosphere (top), current sheets region and relativistic shocked region. Neutrinos are propagating along the purple arrows. Metzger et al. (2020).

4 Analysis Strategy

The data used in this analysis consists of up-going muon neutrino event candidates recorded from January, 1st 2021 to March 31st, 2022. The ORCA detector being under construction, only 6 detection units were running, about 5% of the final size of ORCA. During this period, 43 FRBs were detected from various radiotelescopes, 14 of which were visible from the site of KM3NeT. In order to correlate in time the FRB and possible neutrino signal, a time window of 1000 s was chosen, centered around the FRB. To be properly model-independent and to have a significant correlation, the method put forward is the binned Cut-and-Count analysis (see references in Aiello et al. 2023). An ON zone is defined around the FRB direction, as well as an OFF zone. The OFF zone is the declination band (or elevation band in some cases) centered around the FRB declination (elevation), having a similar background as the ON zone. It is used to compute the background, from data scrambled in time (thus the arrival direction is also scrambled), and then re-scaled to the size of the ON zone. Cuts are performed on both the dataset and the corresponding simulation that is used to estimate the signal. Namely, the size of the ON region is one parameter, and the probability of the event to be an astrophysical neutrino, expressed in terms of a classifier (*Boosted Decision Tree*) score, is the other one. The tool used to optimize the two cuts in this low-signal environment is the Model Rejection Factor (Hill & Rawlins 2003). A certain value of the factor is computed from the Feldman-Cousins average upper limit (Feldman & Cousins 1997), using the classifier score and ON region size pair, and by scanning over this two-parameter space the optimal parameter pair is found where the factor is minimized. The analysis is prepared in blinded mode, on simulated rather than real data. The optimization results before un-blinding the data (and then using events from the ON region instead of simulations) are shown in Fig. 3, where the 14 bursts studied are shown in the all-sky map, along with their ON regions that have been optimized. The radii range from 5° to 13°, which can be considered large

but are explained by the lack of statistics in this small region of the sky, and in such a reduced time window.

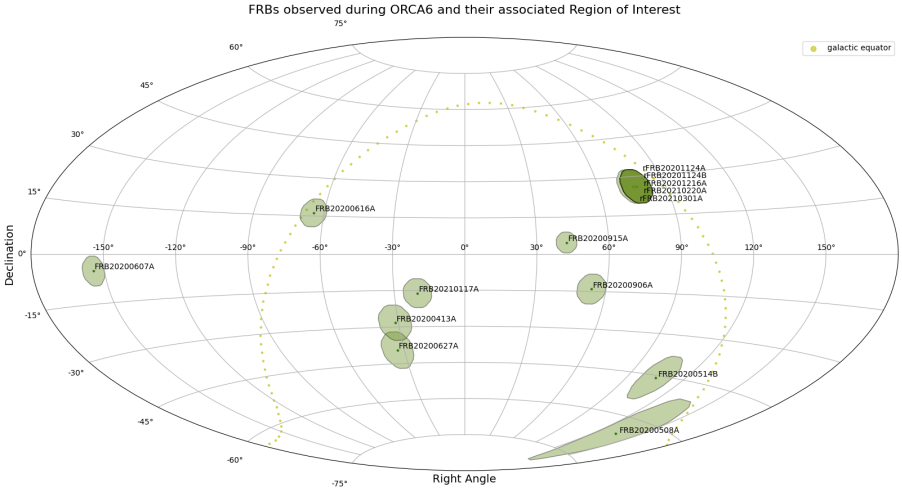

Fig. 3. Skymap, in equatorial coordinates, of the 14 studied FRBs. Green disks around the direction of FRBs represent the regions from where neutrinos could be associated to significant signal. Yellow dots indicate the Galactic Equator.

5 Conclusions

A short presentation of the experiment KM3NeT has been made. The analysis strategy for the neutrino-FRB correlated observations has been presented, leading to the optimization result presented. The un-blinding of the data will be realized shortly to obtain the result of the analysis. Eventually, the analysis will complement those of IceCube (Aartsen et al. 2018; Abbasi et al. 2023) and ANTARES (Albert et al. 2018), searching in several years of neutrino data and finding no significant coincidence with FRB observations. In the future, the analysis can be improved, on the one hand by the increase of statistics and size of KM3NeT and on the other hand by the increase of the FRB detection rate. Indeed, there is an estimate of about 5000 FRB per sky per day (Connor et al. 2016), with only a fraction of them detected by radiotelescopes today. The arrival of the Square Kilometer Array (SKA) in the scope of the radio detection experiments will allow to detect a much larger part of this large population of FRBs.

References

Aartsen, M. G., Ackermann, M., Adams, J., et al. 2018, Science, 361, eaat1378
Abbasi, R., Ackermann, M., Adams, J., et al. 2023, The Astrophysical Journal, 946, 80
Abbott, B. P., Abbott, R., Abbott, T. D., et al. 2017, The Astrophysical Journal Letters, 848, L12
Adrián-Martínez, S., Ageron, M., Aharonian, F., et al. 2016, Journal of Physics G, 43, 084001
Aiello, S., Albert, A., Garre, S. A., et al. 2022, The European Physical Journal C, 82
Aiello, S., Albert, A., Garre, S. A., et al. 2023, Contributions of KM3NeT to ICRC2023
Aiello, S., Albert, A., Garre, S. A., et al. 2021, The European Physical Journal C, 81
Albert, A., André , M., Anghinolfi, M., et al. 2018, Monthly Notices of the Royal Astronomical Society, 482, 184
Andersen, B. C., Bandura, K. M., Bhardwaj, M., et al. 2020, Nature, 587, 54
Connor, L., Lin, H.-H., Masui, K., et al. 2016, Monthly Notices of the Royal Astronomical Society, 460, 1054
Feldman, G. J. & Cousins, R. D. 1997, Physical Review D, 57, 3873
Greus, F. S. & Losa, A. S. 2021, Universe, 7, 397
Gupta, A., Majumdar, D., & Halder, A. 2022, Modern Physics Letters A, 37
Hill, G. C. & Rawlins, K. 2003, Astroparticle Physics, 19, 393
Kurahashi, N., Murase, K., & Santander, M. 2022, Annual Review of Nuclear and Particle Science, 72, 365
Metzger, B. D., Fang, K., & Margalit, B. 2020, The Astrophysical Journal Letters, 902, L22
Sclafani, S. & Huennefeld, M. 2023, Observation of high-energy neutrinos from the Galactic plane
Zhang, B. 2022, The Physics of Fast Radio Bursts

SF2A 2023
M. N'Diaye, A. Siebert, N. Lagarde, O. Venot, K. Baillié, M. Béthermin, E. Lagadec, J. Malzac, J. Richard (eds)

STATUS OF THE NENUFAR FAST RADIO BURST PROGRAM

V. Decoene[1], P. Zarka[2, 3], C. Ng[4], N. Moukaddem[1], P. Gaspari [4], U. Laine[1], J.-M. Griessmeier[4,3], I. Cognard[4,3], F. Mottez[5], G. Voisin[5], R. Dallier[1], L. Martin[1] and the NenuFAR team

Abstract. The New Extension in Nançay Upgrading LOFAR (NenuFAR) telescope is a newly commissioned SKA pathfinder targeting very low frequencies. The nearly 2000 dual polarized and phased antennas allow for very sensitive observations in the $10 - 85$ MHz range. Therefore, it is very well suited for the hunt of Fast Radio Bursts (FRB) in this frequency domain, where noise, dispersion, and scattering effects can become quite challenging to handle in order to achieve the detection of these extra-galactic events. Since the start of the early science phase of the instrument, a FRB Program is conducted in order to detect, or at least, constrain the existence of FRBs at the very low frequencies. The detection strategy relies on the monitoring of already known and repeating sources. Currently, the program has accumulated more than 2000 h over 11 promising repeaters. No detection has been achieved yet, but the data analysis is still ongoing. In this proceeding, we present the observation and analysis strategies.

Keywords: Fast Radio Burst, Low Frequency Radioastronomy

1 Introduction

Fast Radio Bursts (FRBs) are a new class of extra-galactic radio transients discovered about ten years ago, and for which the origin and physical mechanisms remain unknown yet (Lorimer et al. 2007). In that respect, many radio observatories are trying to observe and characterize these events, however, their nature, very brief events and mostly non-repeating, makes this task challenging (Spitler et al. 2016; Amiri et al. 2019). On the other hand, many theoretical developments have been made with a great profusion of models (Voisin 2021), despite that, the sparsity of the observations does not allow for constraining them robustly yet (Platts et al. 2019). So far, FRBs have been detected from several GHz down to 110 MHz (Pleunis et al. 2021a), and this program intents to observe them below 85MHz. This goal is particularly challenging because of the dilution of the signal during the propagation over the great distances travelled by the radio emissions (Sokolowski et al. 2018; Pleunis et al. 2021b). In particular, the scattering is expected to reach a few seconds at the frequencies of NenuFAR, hence drastically reduces the signal intensities. Nevertheless, the detection and characterization of already known and new FRBs in the low frequency domain can provide critical information on the FRB physics and populations. Hence, it can unveil a bit more the origin of the FRBs, and add new constraints for the many models currently existing (Shannon et al. 2018). Furthermore, this program on NenuFAR represents a pathfinder program for future FRB searches at low frequency at the dawn of the construction of the SKA. Towards this goal we have already performed numerous observations of already known FRB repeaters, as well as blind zenith observations, and Galactic magnetar survey (SGR1935+2154). We present here the progress made so far on the analysis of the data, and the remaining works ahead of us to detect or constrain FRBs in the frequency band of NenuFAR.

2 Observations

The observation strategy of the FRB Program relies on the high sensitivity at low frequency provided by the radio telescope NenuFAR, and the choice of targets. We detail in this section these two aspects of the program.

[1] SUBATECH, IN2P3-CNRS, Nantes U., IMT Atlantique, Nantes, France
[2] LESIA, Observatoire de Paris, CNRS, PSL, Sorbonne U., U. Paris Cité, Meudon, France
[3] ORN, Observatoire de Paris, CNRS, PSL, U. Orléans, Nançay, France
[4] LPC2E, U. d'Orléans, CNRS, Orléans, France
[5] LUTH, Observatoire de Paris, CNRS, PSL, Sorbonne U., U. Paris Cité, Meudon, France

© Société Française d'Astronomie et d'Astrophysique (SF2A) 2023

2.1 NenuFAR (New Extension in Nançay Upgrading LOFAR)

NenuFAR is a low-frequency radio array located at the Nançay Radio Observatory, designed as a SKA pathfinder. It consists in 1938 dual polarization antennas hierarchically distributed in mini arrays (MA) of 19 antennas in a hexagonal tile pattern, with a step of 5.5 m between any two antennas inside the MA. 96 of these MA are concentrated in a 400 m core and 6 are located at distances up to 3 km. All MA are analog phased with delay lines, and the digital pointing of the whole array is performed quasi-continuously within the analog MA beam. The antennas operate between the Earth ionospheric cut-off at ~ 10 MHz and the radio FM band at ~ 85 MHz. The angular resolution from the core only varies between 2.9° and 0.5°. The two linear polarization (NE-NW) of each antenna are connected in parallel to several receivers, allowing to operate in four distinct modes: a standalone beam-former, a waveform capture mode, a standalone imager and an upgraded LOFAR station mode combining NenuFAR and the International LOFAR Telescope through the Nançay LOFAR station (FR606). The NenuFAR frequency resolution is $\mathrm{d}f \sim 195$ kHz with a time resolution of $\mathrm{d}t \sim 5$ µs, which can be numerically channelled down to $\mathrm{d}f \sim 100$ Hz at a cost of a lower time resolution $\mathrm{d}t \sim 10$ ms. Finally, the sensitivity of NenuFAR varies from 130 mJy at 15 MHz to 9 mJy at 85 MHz for one hour integration time with a frequency bandwidth of $\mathrm{d}f = 10$ MHz. This makes NenuFAR one of the most sensitive radio telescopes below 85 MHz (Zarka et al. 2020).

2.2 Strategy and targets

The FRB Program observes on a regular basis about 12 FRB repeaters among a total of 50 repeaters discovered worldwide. The choice of these targets is constrained by their visibility in the sky of NenuFAR, their dispersion measure (DM) as low as possible, their fluence as high as possible and scattering as small as possible. The program also surveys the Galactic magnetar SGR1935+2154, progenitor of a possible Galactic FRB signal in 2020 (Andersen et al. 2020). The complete list of targets is given in Table 1, with their parameters and total observation time. A number of pulsars (B0329+54, B0809+74, B2217+47, B1919+21, and B1508+55) are also monitored prior to some observations, in order to assess the radio-telescope capabilities at the time of the observation. Furthermore, it conveniently provides a way to test the analysis pipelines. Usually, each FRB observation last for about 4 h in order to collect enough signal across the frequency band, taking into account the dispersion delay.

Targets	Positions	DM	Fluence	Peak flux	RM	Obs (h)
FRB20180916B	$(01:58:00, +65:44:00)$	350	$2-30$	$0.5-4$	-114.6	592.77
FRB20200120E	$(09:57:56.7, +68:49:32)$	87.2	2	1.8	-28.3	179.38
FRB20181030A	$(10:54:07, +73:44:26)$	103.5	$7-30$	3.2		302.60
FRB20180814A	$(04:22:22, +73:04:00)$	190	$10-60$	1		380.74
FRB20180908B	$(12:32:00, +74:12:00)$	196	2.7	0.6		66.50
FRB20220912A	$(23:09:09.6, +48:42:00)$	219.5	$10-779$	$6-181$	$+0.6$	80.22
FRB20190303A	$(13:53:00, +48:15:00)$	222	$2-3$	0.5	-499.9	105.91
FRB151125	$(01:31:00, +30:58:48)$	273	2450	0.54		95.55
FRB190907	$(08:09:00, +46:16:00)$	311	1.7	0.3		42.76
SGR1935+2154	$(19:34:55.68, +21:53:48.2)$	332.7	480k	110k	112.3	105.18
FRB20181017A	$(22:06:00, +08:50:34)$	240	31	89		67.64
FRB20121102A	$(05:32:09, +33:05:13)$	560	0.11	0.03	10^5	6.96
FRB20190425A*	$(10:39:18, +21:33:36)$	128.2	31.6	18.6		20.64
FRB20181223C*	$(07:32:30, +27:34:48)$	112.5	2.84	1.36		23.87
Zenith pointing	local zenith	blind search	-	-	-	115.94
Total						2186.66

Table 1. List of targets and their observational parameters, derived from detection achieved at higher frequencies by other instruments (e.g. CHIME, LOFAR, PARKES...). Position are given in (α h:m:s, δ deg:m:s), DM values in pc.cm^{-3}, fluences in Jy.ms, peak flux Jy in and RM in rad.m^{-2}. FRB20190425A and FRB20181223C are non repeaters events.

Two observation modes are used for all observations: an incoherent time-frequency mode and the PULSAR mode developed and used by the Pulsar Program of NenuFAR (Bondonneau et al. 2021). For specific targets (considered as promising), the frequency range is increased, in order to cover the full range of NenuFAR. These

promising targets are: FRB20180916B (a periodic repeater), FRB20181030A (a high fluence, low DM repeater), and SGR1935+2154 (a possible FRB source).

Time-frequency mode:

- incoherent observation mode: no de-dispersion
- frequency range: $35.4 - 72.7\,\mathrm{MHz}$, and an extended mode: $12 - 85\,\mathrm{MHz}$
- time and frequency resolutions: $\mathrm{d}t = 21\,\mathrm{ms}$, $\mathrm{d}f = 1.52\,\mathrm{kHz}$
- data rate: $\sim 60\,\mathrm{GB/h}$ ($\sim 120\,\mathrm{GB/h}$ in extended mode)
- output: time-frequency dynamic spectra

PULSAR mode:

- coherent de-dispersion through all sub-bands
- frequency range $35.4 - 72.7\,\mathrm{MHz}$
- time and frequency resolutions: $\mathrm{d}t = 21\,\mathrm{ms}$, $\mathrm{d}f = 195\,\mathrm{kHz}$
- data rate $< 1\,\mathrm{GB}$ per observations
- output: standard PULSAR mode output (psrfits)

3 Analysis

The analysis of the data from the time-frequency mode follows a distinct procedure from the Pulsar Mode. The goal envisioned is to design a dedicated FRB detection pipeline benefiting from the incoherent observation mode to extract fine features from the FRB spectrum and the time series. The flexibility provided by the incoherent time-frequency spectra (intensity and polarization) allows for testing and implementing new detection strategies and techniques.

3.1 Time-Frequency mode

The strategy followed by the group is standard: a first step consists in cleaning and reducing the data, followed by a second step of refined cleaning and production of de-dispersed time series, and finally a third step to detect the bursts in the obtained time series. The first processing step in the treatment of the time-frequency data is called the "pre-processing". It consists in the mitigation of the RFI, the correction of the instrument response in time and frequency, and the incoherent de-dispersion at the repeater's expected DM within each 195 kHz sub-band. Then the data are integrated over each sub-bands. This strategy cleans the data with remaining fluctuations below the percent level, and reduces significantly the size of the data. The reduction factor is ~ 64, leading to data volumes of $\sim 2 - 5\,\mathrm{GB}$ for a typical observation duration of 4 h, depending on the observation mode. The post-processing step is designed to leave some flexibility after the pre-processing in order to test various refined cleaning tools. Currently, the code consists of frequency and time cleaning methods, a high-pass filter and a frequency comb method. Each tool can be optimized through a few parameters in order to adapt to the quality and the topology of the data. At the end, the time-frequency data are de-dispersed over a range of DM values and integrated over frequencies to produce the time series. Furthermore, the spikes can be flagged depending on their width and signal-to-noise-ratio (SNR). These data can be directly plotted and analyzed to search for bursts, as illustrated on Fig. 1. The burst search focuses on the analysis of the time

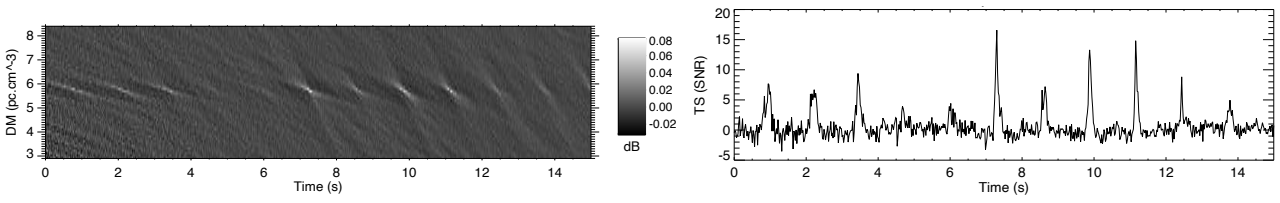

Fig. 1. Detection of single pulses from the pulsar B0809+74. *Left:* DM vs. time plane, where the butterfly shapes associated to all single pulses are clearly visible. *Right:* corresponding time series at the best DM value, where single pulses are detected with signal-to-noise-ratio between 5 and 15. The detection is achieved by using the time-frequency analysis procedures of the FRB Program on time-frequency data.

series via the detection of typical butterfly shapes in the DM vs. time plane. However, due to the length of the observations, the brevity of the expected signals and its scattering, the signal is likely to be buried in the

noise. To counter that, a dedicated code helps to discriminate the different peaks present in the data. The code smooths the time series by applying a median filter followed by a convolution of the series with a trapezoid function. Then, it proceeds to search in the DM vs. time plane for clusters of peaks with the "friends of friends" algorithm*. The classification based on the SNR allows for displaying in details the detected peaks, which are then discriminated by eye. The complete detection pipeline has been successfully tested on pulsar observations and FRB simulations (Zarka & Mottez 2016).

3.2 PULSAR mode

The Pulsar Mode analysis has been developed and is maintained by the people involved in the Pulsar Program of NenuFAR (Bondonneau et al. 2021). It provides a robust and independent search strategy for FRB signals. Furthermore, the data analysis is automated and quickly assesses the potential of each observation. The procedure for the analysis is summarized below:

1 normalize the data with respect to the median and the median absolute deviation for each frequency and time window of 10 s
2 clean the data at DM=0: loop, 4 times, over this sequence:
   – compute standard deviation of each data block
   – target blocks with standard deviation fluctuations over $3\,\sigma$
   – compute standard deviation of each data block integrated over time
   – target time integrated blocks with standard deviation fluctuations over $3\,\sigma$
   – compute standard deviation of each data block integrated over frequencies
   – target frequency integrated blocks with standard deviation fluctuations over $3\,\sigma$
   – replace targeted blocks with a synthetic noise following the statistical properties of the data
3 clean the data with RFIFIND (PRESTO Ransom (2001))
4 produce the time series (PRESTO), with reference channel set at the highest frequency for the de-dispersion. One time series is produced for each DM value tested
5 search for bursts (or pulses) with single_pulse_search.py: search for bursts above given $n\,\sigma$ values through a running window with different widths

4 Summary and future prospects

The FRB Program on NenuFAR started during the Early Science Phase of the commissioning of the instrument in 2018. Since then, it regularly observed a list of FRB repeaters already characterized by radio telescopes at higher frequencies. The targets are selected based on their low DM and scattering values, in order to maximize their detection in the frequency band of NenuFAR. The observation strategy is also based on two distinct observation mode: time-frequency and coherent de-dispersion (PULSAR mode). Up to now more than 2000 h of observations have been accumulated, and the analysis is still ongoing. The analysis strategy relies on the two distinct observation modes, for which two distinct analysis are conducted. The time-frequency analysis, while being more flexible, is not automated, unlike the PULSAR mode analysis. These two independent analysis modes can cross-validate any potential discovery robustly. Several improvements and prospects are envisioned, among which we plan to conduct joint observations with the Nançay Radio Telescope for constraining the multi-wavelength emission of FRBs. In addition, real time search algorithms directly fed at the receiver outputs will be deployed soon. The complete analysis of all the data is still undergoing.

The FRB mystery at low frequencies is not unveiled yet, but every observation done with NenuFAR drives us closer to the answer.

References

Amiri, M. et al. 2019, Nature, 566, 235

Andersen, B. C. et al. 2020, Nature, 587, 54

Bondonneau, L. et al. 2021, Astron. Astrophys., 652, A34

Lorimer, D. R. et al. 2007, Science, 318, 777

Platts, E. et al. 2019, Phys. Rept., 821, 1

Pleunis, Z. et al. 2021a, Astrophys. J. Lett., 911, L3

*see: `https://github.com/simongibbons/pyfof`

Pleunis, Z. et al. 2021b, Astrophys. J. Lett., 911, L3
Ransom, S. M. 2001, PhD thesis, Harvard University
Shannon, R. M. et al. 2018, Nature, 562, 386
Sokolowski, M. et al. 2018, Astrophys. J. Lett., 867, L12
Spitler, L. G. et al. 2016, Nature, 531, 202
Voisin, G. 2021, Proceedings SF2A-2021, 405
Zarka, P. & Mottez, F. 2016, Proceedings SF2A-2016, 347
Zarka, P. et al. 2020, URSSI GASS 2020, J01

SF2A 2023
M. N'Diaye, A. Siebert, N. Lagarde, O. Venot, K. Baillié, M. Béthermin, E. Lagadec, J. Malzac, J. Richard (eds)

USING VELA X-1 TO UNDERSTAND ACCRETION AND WIND STRUCTURE IN HIGH-MASS X-RAY BINARIES (HMXB)

C. M. Diez[1,2], V. Grinberg[3], F. Fürst[1], I. El Mellah[4,5], P. Kretschmar[1], S. Martínez Núñez[6] and A. Santangelo[2]

Abstract. The spectral and timing behaviour of high-mass X-ray binaries (HMXBs) offers a unique opportunity for the investigation of accretion onto compact objects and of wind structure in massive stars. The bright and persistent neutron star HMXB Vela X-1 is one of the key systems for such studies. It has a complex clumpy stellar wind, prominent cyclotron resonant scattering features (CRSFs) and thus high magnetic field. We analyse two new observations taken with *NuSTAR* and *XMM-Newton* at orbital phases ∼0.68–0.78 and ∼0.36–0.52. We follow the evolution of spectral parameters down to the pulse period time-scale to model the continuum and local absorption variability. Modelling *NuSTAR* data, we observe parameter correlations that are flux dependent and imply a change in properties of the Comptonising plasma. The observed drop of the CRSF energy following a strong flare may indicate a change in the accretion geometry. The strong variability of the absorption observed along the orbit is due to the presence of a large-scale wind structure, such as accretion- and photoionisation wakes, combined with the variable line of sight as the neutron star moves along the orbit. However, the main spectral features of the stellar wind are imprinted on the spectrum at lower energies than those covered by *NuSTAR*. We thus also present time- and absorption-resolved *XMM-Newton* spectral analysis based on our *NuSTAR* results and that we use to disentangle emission and absorption features imprinted onto the intrinsic spectrum by the wind.

Keywords: X-rays binaries, neutron stars, stellar winds, outflows

1 Introduction

1.1 The Vela X-1 system

The bright and persistent eclipsing HMXB Vela X-1 is one of the key sources for stellar wind analyses. We refer to the review by Kretschmar et al. (2021) and references therein for more details about the orbital parameters of the Vela X-1 system that we mention here. The system consists of a B0.5 Ib supergiant, HD 77581 (Hiltner et al. 1972), and an accreting neutron star with an orbital period of ∼9 d. Due to a small orbital separation of $\sim 1.7\,R_\star$ between the two components, the neutron star is deeply embedded in the stellar wind of its supergiant companion and significantly influences the surrounding material via X-ray radiation. The strong stellar wind with a mass loss rate of $\sim 10^{-6} M_\odot\,\mathrm{yr}^{-1}$ (Giménez-García et al. 2016) drives the accretion of material onto the neutron star and the pulsating X-ray emission characterised by a variable pulse period of 283 s.

The system is seen almost edge-on from the Earth which facilitates its analysis through the observation of eclipses in the light curves and allows us to span different geometries of the wind as modified by the orbital motion of the accreting neutron star. In particular, we can measure the absorption as function of the orbital phase, which was found to be highly variable in the past (see the overview Fig. 5 of Kretschmar et al. 2021).

[1] European Space Agency (ESA), European Space Astronomy Centre (ESAC), Camino Bajo del Castillo s/n, 28692 Villanueva de la Cañada, Madrid, Spain
[2] Institut für Astronomie und Astrophysik, Universität Tübingen, Sand 1, 72076 Tübingen, Germany
[3] European Space Agency (ESA), European Space Research and Technology Centre (ESTEC), Keplerlaan 1, 2201 AZ Noordwijk, The Netherlands
[4] Université Grenoble Alpes, CNRS, IPAG, Grenoble, France
[5] Departamento de Física, Universidad de Santiago de Chile, Av. Victor Jara 3659, Santiago, Chile
[6] Instituto de Física de Cantabria (CSIC-Universidad de Cantabria), E-39005, Santander, Spain

© Société Française d'Astronomie et d'Astrophysique (SF2A) 2023

There is a typical decrease after the eclipse followed by a steep increase when the neutron star is in inferior conjunction (around orbital phase ∼0.5). However, no identical values for the absorption can be found at the same orbital phases at different times implying changes in the structure of the wind.

1.2 Absorption from the stellar wind

Theoretical hydrodynamical models (Manousakis et al. 2012) suggest a wake structure, known as the accretion wake, trailing the neutron star and is attributed to its supersonic motion around the companion star. Additionally, the ionisation of the wind by the X-ray source leads to the formation of a photoionisation wake, where local and large-scale instabilities with filamentary structures occur (Blondin et al. 1990). The presence of those wakes, in particular when they cross or block our line of sight, deeply affects the average X-ray emission from the neutron star by absorbing photons at low energies ($\lesssim 10$ keV). Short-term variability of the flux and spectral parameters have been associated to the clumpiness of the companion wind by many authors (e.g. Martínez-Núñez et al. 2014; Grinberg et al. 2017), in particular to local absorption by or accretion of clumps.

1.3 CRSFs

Due to the intense magnetic field of the neutron star ($\sim 10^{12}$ G , Kreykenbohm et al. 2008) in Vela X-1, electrons are accelerated off the neutron star's surface along the magnetic field lines. Since electrons are quantised intro Landau levels, incoming photons can excite them to higher levels. The excited electrons then emit photons (cyclotron radiation) as they spiral around the magnetic field lines with the peak of the emission at the frequency (or energy) of its orbit, known as the cyclotron frequency (or energy), and corresponding to the energy gap between the Landau levels. Consequently, resonant scattering of incoming X-ray photons against electrons embedded in the magnetic field can occur and appears as an absorption line called cyclotron line or CRSF at the cyclotron energy. The CRSFs are called fundamental if the resonance is between the ground state and the first Landau level, harmonics for higher levels. In the spectrum of Vela X-1, two cyclotron lines have been confirmed (e.g. Kreykenbohm et al. 2008): a prominent harmonic line at ∼55 keV and a weaker fundamental line at ∼25 keV.

2 Our analysis

2.1 The datasets

Vela X-1 was observed in our targeted campaigns on 10–11 January 2019 by *NuSTAR* and on May 3–5 May 2019 by both *XMM-Newton* and *NuSTAR*, referred as observation I and observation II respectively (see Fig.1). For the first observation we have a total exposure of ∼36 ks with *NuSTAR* covering $\phi_{\rm orb} \approx 0.68$–$0.78$ when the wakes cover our line of sight. For the second observation we have ∼40 ks with *NuSTAR* and ∼109 ks with *XMM-Newton*, covering $\phi_{\rm orb} \approx 0.36$–$0.52$ during the onset of the wakes on our line of sight. Data from FPMA and FPMB (onboard *NuSTAR*) and from EPIC-pn (onboard *XMM-Newton*, timing-mode) were analysed during this work. The *XMM-Newton* EPIC-pn suffered from important pile-up that we corrected during the extraction of the data.

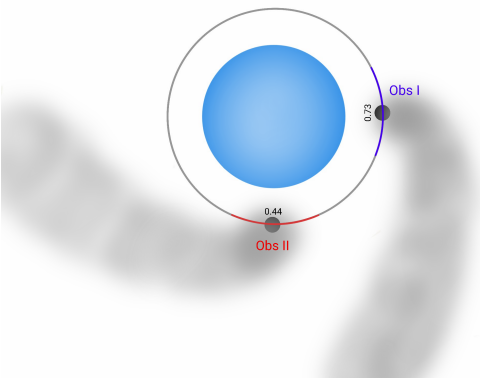

Fig. 1. Sketch of Vela X-1 showing the orbital phases covered during the two observations. In this image, the observer is located facing the system at the bottom of the picture. Figure from Diez et al. (2022).

We first extracted the *XMM-Newton* EPIC-pn and *NuSTAR* time-averaged spectra for both observations to constrain the parameters of our model before proceeding to the time-resolved spectroscopic analysis. The quality of the data was good enough with both observatories that we could extract a spectrum for each pulse of the neutron star giving us access to very short term variability in the spectral parameters (see e.g. Fig 4).

2.2 Partial covering model

For this work, we used a partial covering model. The covering fraction CF quantifies the clumpiness of the wind and ranges from 0 (X-ray source not covered) to 1 (source fully obscured). This enables us to assess both the emission from the neutron star and the absorption from the stellar wind separately as can be seen from Fig. 2. The neutron star's continuum consists of a powerlaw with a high-energy Fermi-Dirac cutoff, two cyclotron lines CRSF,F (fundamental) and CRSF,H (first harmonic), the FeKα and FeKβ lines inherent to accreting pulsars at 6.4 keV and 7.1 keV respectively, and a 10 keV feature to account for an emission-like feature in the spectrum at this energy (for more details, see Diez et al. 2022). We also modelled a plethora of ionisation lines present in the *XMM-Newton* EPIC-pn spectra of the source between 0.5 and 4 keV (see Fig. 3).

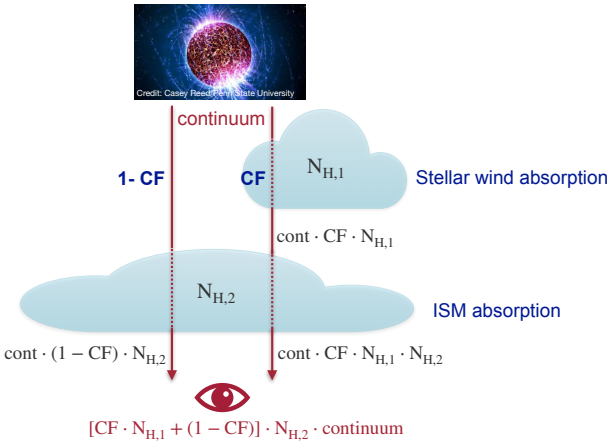

Fig. 2. Scheme of the partial covering model used in this work. The X-ray emitting source is at the top of the figure and the observer is located at the bottom. $N_{H,1}$ is the hydrogen absorption column density of the stellar wind, $N_{H,2}$ the hydrogen absorption column density of the interstellar medium between the source and the Earth fixed at its known value (NASA's HEASARC N_H tool `https://heasarc.gsfc.nasa.gov/cgi-bin/Tools/w3nh/w3nh.pl`). Figure from Diez et al. (2022).

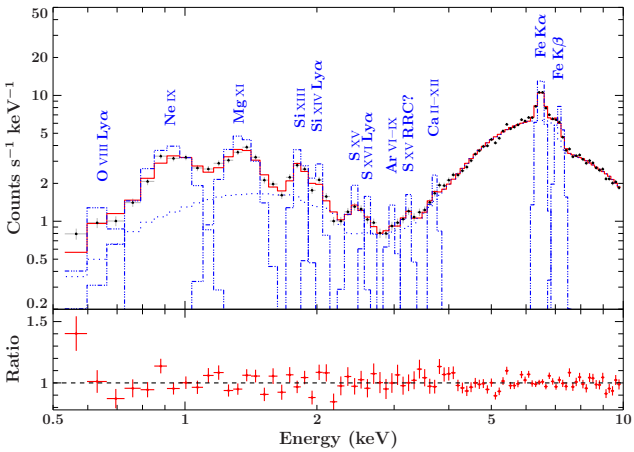

Fig. 3. Example of an *XMM-Newton* EPIC-pn spectrum (black datapoints). The individual model components including all lines detected in this dataset are indicated by blue dot-dashed Gaussians and the absorbed continuum by the blue dotted line. Figure from Diez et al. (2023).

3 Conclusions

In this work, we analysed two observations of the HMXB Vela X-1 shortly before the neutron star is in inferior conjunction and at late orbital phases when the wakes obscure our line of sight (Diez et al. 2022, 2023). We cover a broad X-ray range from 0.5 keV to 78 keV thanks to the simultaneous *XMM-Newton* and *NuSTAR* coverage we obtained for the second observation, the first one was covered by *NuSTAR* only. Using a partial covering model, we performed a detailed study of the CRSFs and observed flux/time dependent correlations among the spectral parameters of our model.

3.1 CRSFs

We confirmed the negative correlation between photon index and flux but could not confirm a previously seen positive correlation between flux and energy of the first harmonic CRSF (Fürst et al. 2014). We therefore question the accretion regime of Vela X-1 which may lie between sub- and super-critical regimes in this observation. However, we observed a drop in the CRSFs energies following a strong flare. This could be explained by a

restructuring of the accretion column and consequently to a change in the location of the CRSF producing region due to sudden strong accretion of material.

3.2 Clumpy wind

The newly obtained constraints at high-energies permitted by *NuSTAR* enables us to trace the onset of the wakes in Vela X-1 using the *XMM-Newton* simultaneous coverage. This is the first time that we have such a detailed view of the wind on a broad X-ray band and with high-time resolution, down to the pulse period of the neutron star of ∼283 s. The wakes are characterised by a rise of the absorption column density $N_{\rm H,1}$ as well as local absorption variability (see Fig. 4). There are also orbital dependencies between spectral parameters, which are observational evidences of overlapping and accretion of clumps.

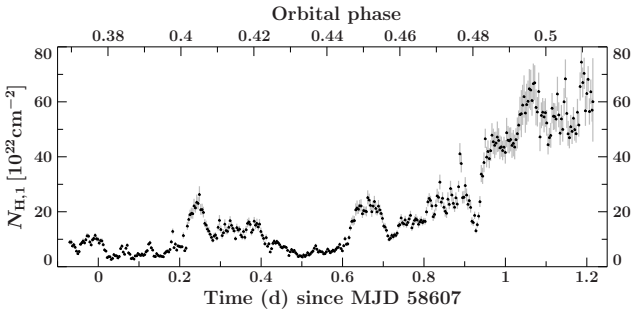

Fig. 4. Absorption column density $N_{\rm H,1}$ of the stellar wind as function of time (bottom axis) or orbital phase (top axis). Each point is integrated over a pulse period (∼283 s) of the neutron star. Figure from Diez et al. (2023).

3.3 Nature of the absorbers

We also conducted a high-resolution spectroscopy of the multiple fluorescent emission lines present in the Vela X-1 system (Lyα lines of O, Ne, Mg, Si and S) which show a strong photoionisation of the wind. The presence of those lines at different absorption phases implies that the sources of emission originate from both local absorbers close the neutron star (clumps) and large-scale structures (photoionisation wake).

3.4 Perspectives

From the *XMM-Newton* observation, only EPIC-pn data were explored so far. The analysis of the simultaneous *XMM-Newton* RGS data in a future work is crucial as blending with neighbouring elements with EPIC-pn can happen. Moreover, a similar analysis on other HMXBs is also in progress in order to put constraints on a bigger sample of sources and find common absorption behaviours between different HMXBs. Last but not least, the recently launched *XRISM* and upcoming *Athena* will be of utmost importance for this study thanks to their high-resolution instruments enabling a detailed X-raying of the stellar wind.

The research leading to these results has received funding from the Bundesministerium für Wirtschaft und Energie under the Deutsches Zentrum für Luft- und Raumfahrt Grants 50 OR 1915, from the European Union's Horizon 2020 Programme under the AHEAD2020 project (grant agreement n. 871158) and from the ESA Archival Research Visitor Programme.

References

Blondin, J. M., Kallman, T. R., Fryxell, B. A., & Taam, R. E. 1990, ApJ, 356, 591
Diez, C. M., Grinberg, V., Fürst, F., et al. 2023, A&A, 674, A147
Diez, C. M., Grinberg, V., Fürst, F., et al. 2022, A&A, 660, A19
Fürst, F., Pottschmidt, K., Wilms, J., et al. 2014, ApJ, 780, 133
Giménez-García, A., Shenar, T., Torrejón, J. M., et al. 2016, A&A, 591, A26
Grinberg, V., Hell, N., El Mellah, I., et al. 2017, A&A, 608, A143
Hiltner, W. A., Werner, J., & Osmer, P. 1972, ApJ, 175, L19
Kretschmar, P., El Mellah, I., Martínez-Núñez, S., et al. 2021, A&A, 652, A95
Kreykenbohm, I., Wilms, J., Kretschmar, P., et al. 2008, A&A, 492, 511
Manousakis, A., Walter, R., & Blondin, J. M. 2012, A&A, 547, A20
Martínez-Núñez, S., Torrejón, J. M., Kühnel, M., et al. 2014, A&A, 563, A70

SF2A 2023
M. N'Diaye, A. Siebert, N. Lagarde, O. Venot, K. Baillié, M. Béthermin, E. Lagadec, J. Malzac, J. Richard (eds)

EXTENDED EMISSION IN SHORT GAMMA-RAY BURSTS FROM FALLBACK ACCRETION

R. Duqué[1], C. Musolino[1] and L. Rezzolla[1]

Abstract. Through a set of GRMHD simulations of BNS mergers, we reveal a long-lived phase of fallback accretion onto the merger remnant, totaling a mass of $\gtrsim 10^{-3} M_\odot$ over a time scale of hundreds of seconds. The accretion luminosity and timescale of the fallback points to the possibility that EM radiation from this inflow could explain long-term emission from BNS mergers, for example the extended emission of short GRBs. We devise a simple electromagnetic emission model based on the thermodynamical state of this material expected from its heating by r-process nucleosynthesis using the neutrino transport scheme of our GRMHD simulations. We find that this fallback material can shine in the gamma-rays and X-rays with luminosities $\gtrsim 10^{48}$ erg/s for hundreds of seconds. We predict that this emission is spectrally softer than prompt emission and that it ends in an exponential cutoff, features reminiscent of extended emission in GRBs. Finally, our findings suggest that the radiation from the fallback flow can impact the other electromagnetic signals from binary compact mergers, in particular the kilonova transient.

Keywords: GRMHD – Compact objects – Gravitational waves – Gamma-ray bursts

1 Introduction

The merging* of binary compact objects is a complex phenomenon involving many different physical processes, making them a great laboratory for many branches of physics and astrophysics (Baiotti & Rezzolla 2017). Nonetheless, the inspiral and merging processes are deterministic and determined by the parameters of the binary. In particular, the characteristics of the different outflows launched in the merger and their electromagnetic (EM) signals are fully determined by these binary parameters. The EM signals from binary neutron-star (BNS) mergers, as historically exemplified by the GW170817 event (The LIGO Scientific Collaboration et al. 2017; Abbott et al. 2017a), are an integral part of the rich phenomenology of short GRBs, that was explored before the GW era (e.g., Berger 2014; D'Avanzo 2015). All these signals likely arise from distinct outflows from the merger and the ideal tool to study the correspondence between outflows and EM signals is first-principle general-relativistic magnetohydrodynamical (GRMHD) simulations followed by adequate post-processing to implement the emission models of the EM counterparts.

In this contribution, we focus on the extended emission episodes of short GRBs (Norris & Bonnell 2006), that cover two recurring features in short GRBs observed in the gamma-ray and X-ray bands. Gamma-ray extended emission, first discovered in the prototypical GRBs 050724 and 060614 (Barthelmy et al. 2005; Gehrels et al. 2006), is a episode of gamma-ray emission that can last for hundreds of seconds after the prompt emission of short GRBs and that is of lower luminosity and softer spectrum than the parent prompt (a.k.a, "the spike"). It is present in 2–25% of short GRBs depending on the instrument.

The extended emission in the X-ray band was discovered in a sample of *Swift* sGRBs where the extended near-flat X-ray emission is suggested to be the X-ray counterpart of the extended emission in the gamma-rays (Kagawa et al. 2015). The X-ray extended emission has a similar duration (up to hundreds of seconds) and often features an exponential cutoff. X-ray extended emission is found in approximately 20–50% of short GRBs detected by *Swift* (Kisaka et al. 2017; Kagawa et al. 2019). In short GRBs with measured redshift, the

[1] Institut für Theoretische Physik, Goethe Universität Frankfurt am Main, D-60323 Frankfurt am Main, Germany

*The material of this contribution is drawn from a larger work on the extended emission of short gamma-ray busts in the light of a numerical study of fallback accretion in compact binary mergers, that is to be published shortly (Musolino, Duqué and Rezzolla, 2023).

© Société Française d'Astronomie et d'Astrophysique (SF2A) 2023

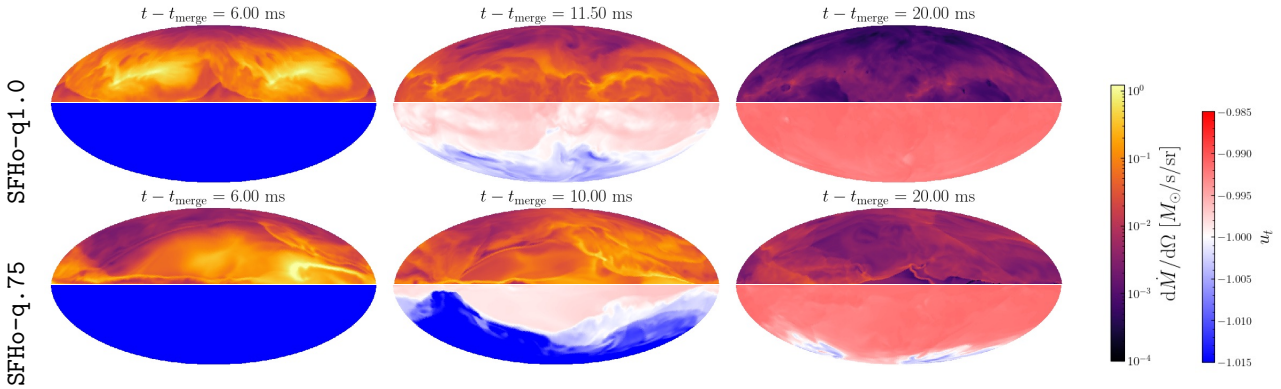

Fig. 1. Snapshots of the material flowing through a sphere at $R_d = 300\,M_\odot$ at various times of the simulation. **Upper panels:** `SFHo-q1.0` system. **Lower panels:** `SFHo-q.75` system. **Upper hemispheres:** mass flux per unit solid angle. **Lower hemispheres:** u_t of the flowing material. The three columns correspond to different times during the evolution, as reported in Fig. 2.

luminosities of extended emission episodes in the X-rays spans from 10^{46} to 10^{49} erg/s in the *Swift*/XRT band (Kisaka et al. 2017). The total output of extended emission episodes can largely exceed that of the prompt emission, suggesting a large reservoir of energy active on long timescales.

Extended emission in short GRBs has been understood through various pictures, invoking the launching of a second jet by the black hole (BH) central engine (Barkov & Pozanenko 2011), or radiation from a proto-magnetar central object (Bucciantini et al. 2012) or from material falling back after the burst (Kisaka & Ioka 2015). Indeed, the ejection of material that remains gravitationally bound to the central object and falls back on long time-scales seems to be ubiquitous in explosive events, from tidal disruption events (TDEs, Krolik & Piran 2012) to BNS mergers (Ishizaki et al. 2021).

In this contribution, we deepen the the study of extended emission from the fallback of merger ejecta using high-performance multi-physics numerical simulations including a novel scheme for neutrino transport.

2 A GRMHD study of long-term fallback episodes in BNS mergers

We perform state-of-the-art numerical relativity simulations of the binary inspiral and merger phases using the EinsteinToolkit framework (Löffler et al. 2012), the higher-than-second order accurate GRMHD module `FIL` (Most et al. 2019) and the recently developed moment-based neutrino transport module `FIL-M1` (Musolino & Rezzolla 2023). The inclusion of neutrino transport allows us to more accurately track the temperature and composition of the ejected and bound material, which are affected by weak interactions. We study four different systems with different mass ratio $q < 1$ and equation of state (EoS). For conciseness, we present here only two binary systems, both with the SFHo EoS (Hempel & Schaffner-Bielich 2010), a chirp mass equal to the estimated value for the GW170917 event (Abbott et al. 2017b), and two mass ratios $q = 1$ (system `SFHo-q1.0`) and $q = 0.75$ (`SFHo-q0.7`) consistent with the data from GW170817.

In Fig. 1, we present snapshots of the material outflowing from the merger at a distance of $R_d = 300\,M_\odot$ from the merger, at various times of our simulations of the two `SFHo` systems. The time-component of the material's four-velocity, u_t, determines whether the material is gravitationally bound or unbound, with a threshold at $u_t = -1$, as used in the color bar. Fig. 1 shows that the material initially ejected is unbound (left panel), and then progressively the ejecta is more and more bound. In addition, the front of bound material progresses from the equatorial region up to the polar directions, and ends up by filling the whole sphere. We also find that, while the early unbound ejecta is strongly anisotropic perhaps due to the tidal tails, the bound ejecta is quite isotropic. This can be seen at the maximum of bound mass ejection (middle panels), and even more at the later times (right panels). Comparing the upper and lower panels, we find that the asymmetry in the binary accentuates the anisotropy of the early unbound ejecta, as expected from its effect on the tidal tails, but has an opposite effect on the bound material, which is found to be even more isotropic than in the symmetric case. By analyzing the ejection latitudes θ of all the bound material detected in the simulation domain, we can confirm that the ejecta is isotropic, as suggested by the snapshots shown here.

In Fig. 2, we present the mass ejection history of our two systems, and we report the times at which the BH forms in the post-merger phase. This figure allows to confirm the trends found in the snapshots. For the

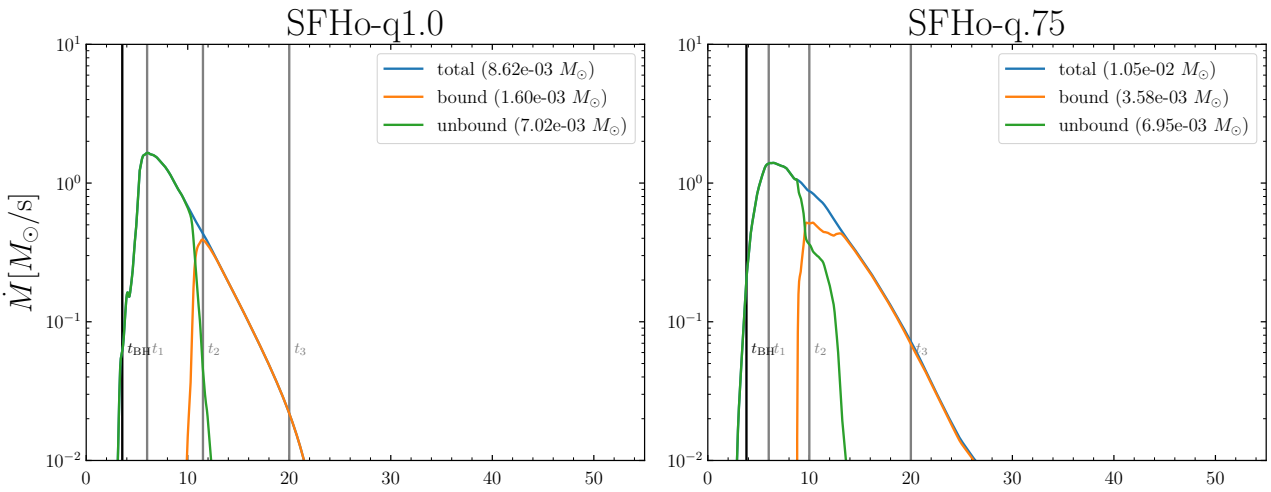

Fig. 2. Mass ejection history of two of our four simulations. All times are measured from the merger time, and the mass flux is separated into bound (orange), unbound (green) and total mass flux (blue). The legends report the total mass measured in all three categories. For all systems, the vertical gray lines mark the moments where the snapshots of Fig. 1 are taken. The time of BH formation is also marked, in black.

two `SFHo` systems, there is a sharp transition from unbound to bound ejection $\sim 10\,$ms post-merger. In the asymmetric binary, the decay of bound ejection is less steep than in the symmetric binary. Overall, the ejection episode is short-lived, due to the prompt collapsing of the BH $t_{\rm BH} \sim 4\,$ms post-merger and the very small disk mass $M_{\rm disk} \sim 2\,\%M_{\rm rem}$ susceptible of carrying our longer ejection. For the two prompt-collapse systems (`SFHo`), we find that asymmetry favors bound ejection, which is 19 % and 33 % of the total in the symmetric and asymmetric systems respectively.

This transition in time from unbound to bound suggests that the fallback material will remain *underneath* the unbound flow, with some physical separation. Inspecting the velocities of the bound and unbound component shows that, indeed, they should be well separated in the subsequent evolution, with consequences on the eventual radiation we explore in Sec. 4.

The dynamics of the bound matter on long-time scales cannot be followed exactly in our simulations for obvious computational reasons. Therefore, we consider Newtonian free-fall dynamics in the gravity filed of the remnant object, with the orbital period being $t_{\rm FB} = \frac{\pi}{\sqrt{2}} M |1+u_t|^{-3/2}$ for material with velocity u_t. Using the period of Newtonian orbits is justified by the length of the fallback orbits, since we are interested in timescales of hundreds of seconds. We determine the mass $M_{\rm rem}$ of the merger remnant using a quasi-local integral on the apparent horizon surface as determined by the vanishing of a null geodesic congruence expansion, or simply by measuring the gravitational field at a given distance using the metric components. We that these two methods agree to within 2%.

We find that the bond material in our simulations has fallback times up to hundreds of seconds. Together with the total mass of bound ejecta ($\gtrsim 10^{-3}\,M_\odot$, Fig. 2), this shows that the bound material can potentially contribute to a fallback episode on the remnant object and a long-term EM emission. To predict the fallback accretion rate, we study the the distribution of orbital energy ($\epsilon = -1 - u_t < 0$) per unit mass in the debris, denoted by $\mathrm{d}\epsilon/\mathrm{d}m_{\rm FB}$. Remarkably, this function is flat for a large range of energies, particularly, near the $\epsilon = 0$ bound, as hypothesized as early as Rees (1988); Evans & Kochanek (1989); Phinney (1989) in the study of fallback of debris from TDEs. Under this hypothesis, one has $\frac{\mathrm{d}m_{\rm FB}}{\mathrm{d}t_{\rm FB}} = \frac{\mathrm{d}m_{\rm FB}}{\mathrm{d}\epsilon}\frac{\mathrm{d}\epsilon}{\mathrm{d}t_{\rm FB}} \propto \frac{\mathrm{d}m_{\rm FB}}{\mathrm{d}\epsilon} \times t_{\rm FB}^{-5/3}$, such that the fallback accretion rate follows a power-law with $\dot{m}_{\rm FB} \propto t^{-5/3}$. This hypothesis was then indirectly confirmed by some later observations of TDEs (e.g., Komossa 2015). Our results thus show that, in addition to the tidal ejecta, the bound material of other origin such as from the merger itself and disk winds also verify this hypothesis.

Computing the fallback accretion rate confirms the power-law decay $\dot{m}_{\rm FB} \propto t^{-5/3}$, as had already been obtained in previous numerical studies of compact object mergers with various numerical schemes (Rosswog 2007; Chawla et al. 2010; Kyutoku et al. 2015). We here further confirm these results, and trace the origin

of the $t_{\rm FB}^{-5/3}$ behavior to the energy distribution of the ejecta. Using a crude conversion of accretion rate to luminosity, $L_{\rm acc} \sim 0.1 \times \dot{m}_{\rm FB} c^2$, we find that this inflow could sustain luminosities $L \gtrsim 10^{47}\,{\rm erg/s}$ for up to $\sim 1000\,{\rm s}$. This encourages us to better understand the radiation arising from this fallback accretion and its eventual observational signatures, as we do in Sec. 3.

3 From fallback accretion to extended emission in short GRBs

The fallback accretion rate determined in Sec. 2 is largely super-Eddington, such that a finer model for the fallback dynamics is required. In addition, one must account for the nucleosynthetic processes in the ejecta that contribute to the radiation from the fallback. To overcome the limitation in computational power, we derive a semi-analytical model to determine the fallback dynamics, from which a model for the radiation can be subsequently derived.

The material that falls back with $t_{\rm FB} \gtrsim 100\,{\rm s}$ has very eccentric orbits. Thus, we simplify our analysis by considering the inflow-outflow dynamics to be purely radial, in free-fall, with density and radial velocity fields $\rho(r,t)$ and $v(r,t)$ independent of the radial direction, following the isotropy of the ejecta underlined previously. The electron fraction of the material does depend on the latitude, and we will account for this in the determination of the fallback radiation below. In this free-fall flow, one can derive the following consistency equation connecting the density at any space-time point to that at a fiducial radius R_d:

$$\rho(R_1,t_1) = \left(\frac{R_d}{R_1}\right)^2 \rho(R_d, t_1 + t_{\rm FF}(R_1,R_d)) \times \left[1 + v_{\rm FF}(R_1,R_d)\frac{\partial t_{\rm FF}}{\partial R_i}(R_1,R_d)\right] \tag{3.1}$$

where $t_{\rm FF}(R_i,R_f)$ and $v_{\rm FF}(R_i,R_f)$ are the Newtonian free-fall time and free-fall velocity from radius R_i to R_f.

We solve for the density $\rho(r,t)$ with its non-trivial dynamics by enforcing the power-law fallback accretion rate $\dot{m}_{\rm FB} \propto t^{-5/3}$ at $R = R_d$, and using Eq. 3.1 to find the density throughout the ejecta. This, in turn, allows us to locate the photosphere, at radius $R_\phi(t)$, in the fallback flow. This is the position of the photosphere *within the fallback flow*, not accounting for the eventual unbound material above the flow.

At these early stages post-merger, the r-process nucleosynthesis is already well underway and the material opaque (e.g., Lippuner & Roberts 2015; Tanaka et al. 2020), though exact opacity calculations at these early times lack in the literature. Adopting a low opacity of $\kappa = 0.5\,{\rm cm^2/g}$, we find that for timescales up to $t \sim 10^5\,{\rm s}$, the photosphere coincides with the leading edge of ejecta, before starting to recede within the ejecta. We find the same with an opacity as low as $\kappa = 0.1\,{\rm cm^2/g}$. Therefore, we conclude that the radiation arising from the ejecta on these timescales comes from the leading-edge material, and we consider a black-body emission spectrum from this emitter. To capture the temperature time evolution $T_\phi(t)$ of this material accounting for r-process nucleosynthesis and expansion cooling, we run the `SkyNet` nuclear reaction network (Lippuner & Roberts 2017), with initial temperature and electron fraction determined from the neutrino scheme of our simulations, and with a density evolution at the photosphere according to our semi-analytical model $\rho(R_\phi(t),t)$.

In Fig. 3 (right panel), we report the bolometric, X-ray and gamma-ray luminosities of the fallback radiation according to our model. We considered the fallback material picked from latitude $\theta = 15\,{\rm deg}$ in the inflow. The initial Y_e of that material, also marked, is determined from our M1 scheme. The dotted line is the bolometric luminosity from the fallback accretion one would deduce from a naive conversion from the fallback rate $L_{\rm acc} = \eta \dot{m}_{\rm FB} c^2 \propto t^{-5/3}$, with an efficiency of $\eta = 10\%$.

First of all, we notice that the duration and luminosity of this radiation component are significant and on the level of extended emission in short GRBs (see Sec. 1). Second, we find that, through a non-trivial interplay between the photospheric radius and temperature evolution, the bolometric luminosity displays a power-law decay with near-constant slope $\alpha \sim -8/3$, which is steeper than the decay of $\dot{m}_{\rm FB} \propto t^{-5/3}$.

Because of the temperature's decreasing with time (we find $T_\phi \propto t^{-1}$, as in Wanajo et al. 2014; Lippuner & Roberts 2015), the radiation is mainly output first in the gamma-ray band, then in the X-ray band. In all bands, the luminosity follows three segments. At very early times, the blackbody temperature exceeds the energy band, such that the Rayleigh regime applies with $L_\gamma \sim R_\phi^2 T_\phi \propto t^{1/3}$. This near-constant segment of the light curve is apparent in the X-ray band in Fig. 3. Once the blackbody temperature reaches the observing band, at $t \sim 1\,{\rm s}$ for the gamma-rays, the luminosity follows the bolometric with $L_\gamma \propto t^{-8/3}$. Finally, the black-body peak frequency leaves the band, and an exponential cutoff is seen. In practice, the earlier segment of this sequence in the gamma-rays and the later segment in the X-ray are expected to be outshined by the prompt and the forward-shock afterglow respectively.

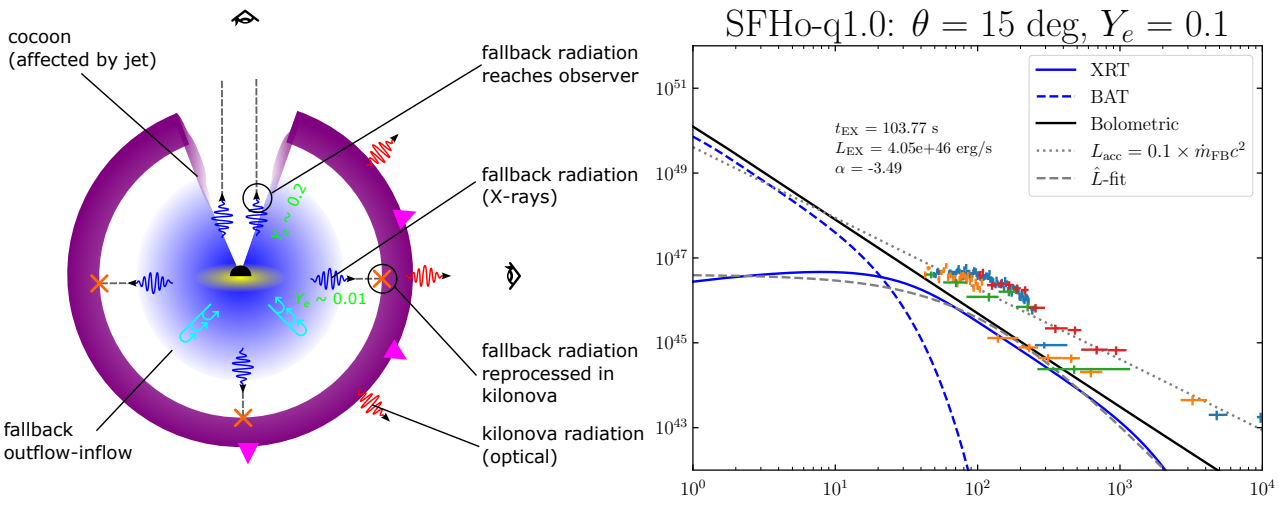

Fig. 3. Left: A schematic view of our model for the electromagnetic signature of the fallback flow. The fallback outflow-inflow (blue) is ejected underneath the unbound material (purple), where the kilonova signal is emitted (red photons). The fallback material emits X-rays (blue photons), that can either be absorbed and reprocessed in the kilonova ejecta (equatorial direction), or reach a distant observer by passing through the free way opened by the jet launched post-merger (polar direction). In this case, the fallback radiation appears as high-energy extended emission. **Right:** Radiation arising from the fallback flow as per our model of blackbody emission from the photosphere heated up by r-process nucleosynthesis (Sec. 3). The temperature evolution was determined from the r-process heating starting from the Y_e value measured at in the fallback flow, at the latitude indicated. We present the luminosity in the *Swift*/BAT and *Swift*/XRT bands (colored solid and dashed lines, respectively) and the bolometric luminosity (black solid line). We also present the luminosity derived from the accretion rate (gray dotted line) and the best-fit model of a flat-power-law light curve to the XRT luminosity (gray dashed line). Finally, we show the XRT data for some GRBs with extended emission in the source frame, arbitrarily scaled in flux to compare with our model (colored points, see text for the list of GRBs, data from Evans et al. 2007, 2009).

4 Discussion

4.1 A new high-energy emission component in BNS mergers

Our study suggests the general scenario for fallback radiation described in cartoon form in Fig. 3 (left panel).

On low-latitude or polar views of the binary merger, the fallback radiation to escape to a distant observer through the cavity opened by the jet or the lower optical thickness of the cocoon, i.e., a relatively low-density region where the jet has deposited energy in its interaction with the ejecta Bromberg et al. 2011; Matsumoto & Masada 2019. This makes up for a hitherto unconsidered emission component in BNS mergers, and a contender to explain the extended emission in short GRBs.

Indeed, the thermal spectrum and quickly decreasing hardness ratio of the radiation in our model reproduces an essential feature of extended emission in short GRBs: the relatively softer spectrum with respect to the parent prompt (Barthelmy et al. 2005; Gehrels et al. 2006; Kaneko et al. 2015). Moreover, the ratio of extended-emission energy to prompt energy in the gamma-rays varies in a large range, from $E_{\rm EE}/E_{\rm prompt} \lesssim 0.1$ to $\gtrsim 40$ (e.g. Bostancı et al. 2013; Kagawa et al. 2019). Beyond the uncertain geometrical factors that will condition the visibility of the fallback radiation in our scenario, our picture attributes these emissions to two distinct flows in BNS mergers, with energy output that are somewhat unrelated. Also, the initial Y_e of the bound material determines the temperature evolution and thus the time of the cutoff in the gamma-ray extended emission luminosity. The duration of the extended emission episode is thus, in our picture, weakly correlated with prompt emission temporal features, which remains to be explored in extended emission catalogs.

Turning to the X-ray component of extended emission, we note that the exponential cutoff, generally attributed to a black-hole spin-down in second-jet scenarios (Kagawa et al. 2015, 2019), is due in our picture to the crossing of the black-body peak frequency in the X-ray band. Again, this will occur sooner or later according to the heating rate in the bound material, such that we expect no strong correlation with the temporal properties

of the prompt emission.

To compare our model for extended emission with observations, we follow Kisaka et al. (2017) in fitting the *Swift*/XRT photometry expected from our model with a plateau of duration $t_{\rm EX}$ and luminosity $L_{\rm EX}$ followed by a power-law decay with a temporal index denoted by α. We find that the luminosity and durations of the plateau segment correspond to the clustering of the events reported in the Kisaka et al. (2017) catalog of events with redshift data. However, we find that the temporal slope is shallower than the $-40/9 \sim -4.4$ favored by Kisaka et al. (2017) corresponding to the second-jet model Kisaka & Ioka (2015). Indeed, we find the shallower $\alpha \sim -3.5$ in the case reported in Fig. 3 and in others, consistently with the temporal decay of the bolometric luminosity discussed previously.

To further ground our fallback emission model in the observations of extended emission, we place on the light-curve plots in Fig. 3 the data from extended emission in short GRBs 080905A, 080919, 150831A and 160821B. These were selected among the Kisaka et al. catalog to present a shallower decrease than the $-40/9$ that they use for their fits. This comparion shows that these shallow-decaying events are consistent with our model. Further, the data suggest that extended emission episodes show a variety of decay rates[†], implying that the universal $-40/9$ slope is not applicable, and that a diversity of physical mechanisms (such as fallback accretion and secondary BH jets) can be at the origin of the extended emission phenomenon. This non-uniqueness of the physical origin of extended-emission X-ray components is in line with the apparent bimodality in the duration and luminosity of these phenomena (Kisaka et al. 2017).

Finally, our picture for extended emission decouples the duration of the extended emission from the timescales of the small-scale physics near the remnant, in contrast with the magnetar and secondary-jet models (e.g., Barkov & Pozanenko 2011; Kisaka & Ioka 2015). Indeed, these models require the magnetar to shine (and to survive) of the jet to emit for as long as the emission lasts, up to hundreds of seconds. In our case, it is only the single and very short-lived process (the ejection of bound material over $t_{\rm ej} \lesssim 100\,{\rm ms}$) that results in a long-lived emission episode. The characteristics of this emission is largely set only from the very early post-merger dynamics. We have yet to study how this reconciles with the statistics of the duration of extended emission episodes.

4.2 Effect of the radiation from within the kilonova

Conversely, on high-latitude or equatorial directions, the fallback radiation is trapped by the kilonova material, and will not reach a distant observer. However, it will be absorbed and reprocessed, energizing the kilonova. Depending on the the radiative efficiency of the fallback flow and on the efficiency of reprocessing of this radiation into the kilonova emission, this effect can change the kilonova luminosity by roughly $\eta_{\rm FB} = m_{\rm FB}/m_{\rm KN}$, the ratio of fallback mass to unbound mass. This maximum ratio can reach $\sim 50\,\%$, though the effect on the kilonova luminosity is expected to be much less due to the low radiative and reprocessing efficiencies.

In the case of GW170817, Gill et al. (2019) used a series of GRMHD simulations to determine how long the remnant should have lasted to eject the large mass of lanthanide-poor (a.k.a, blue) component of the ejecta inferred from the kilonova signal ($M_{\rm blue} \sim 2 \times 10^{-2}\,M_\odot$; e.g., Perego et al. 2017; Villar et al. 2017). They concluded to a long-lived remnant collapsing after $t_{\rm collapse} \gtrsim 1\,{\rm s}$, a long timescale in apparent contradiction with the absence of very heavy elements in the kilonova composition (Perego et al. 2022), and possibly with the early launching of the jet in this system. Furthermore, simulations of BNS mergers suggest that only long-lived remnants are capable of ejecting this large mass of blue material (Fujibayashi et al. 2020). The proposal of a magnetar to energize the ejecta, softening the constraint on the blue mass (Metzger et al. 2018), likely also meets the challenge of the early launching of a jet by the magnetar. In this context, we note that energy injection from the fallback flow into the kilonova ejecta as described in our picture could contribute to alleviating the large-blue-mass constraint, and reconcile the data from GW170817 with a short-lived remnant able to launch a jet. We leave the investigation of this solution to future work.

5 Conclusion

Thanks to GRMHD simulations of the merger of binary neutron stars with neutrino transport, we have carried out a detailed study of the bound material ejected in the merger and post-merger phases. This component of the outflow is scarcely considered, and we reveal that it can have important a significant observational

[†]Some are very shallow (e.g., GRBs 060801, 061006, 100724A, 090426), others shallow (e.g, our selection of GRBs), others steep (e.g., GRBs 071227, 081023, 160821B).

signature in the gamma-ray and X-ray bands akin to extended emission episodes of short gamma-ray bursts, shining from within the expanding ejecta with luminosities $\sim 10^{50}\,\mathrm{erg/s}$ over hundreds of seconds.

On lines-of-sight aligned with the binary's polar axis, looking through the funnel punched by the relativistic jet, this emission component is indeed a good candidate for the extended-emission of short gamma-ray bursts. On significantly misaligned lines-of-sight, this radiation is another source of energy injected into the ejecta and contributing to the kilonova counterpart. We see this process as a further complication in the inference of ejecta properties (e.g., mass and velocity) from kilonova data.

While the posr-processing of our simulations make simplifications in order to reach the actual light curve predictions for this emission component, the existence of this fallback flow is a robust result of our simulations, and the overall flux level of its radiation ($L \gtrsim 10^{46}\,\mathrm{erg/s}$) is largely determined by the mass of bound material, which is robustly determined from our simulations. Finally, the sharp cutoff of the radiation in the high-energy bands, due to the fast cooling of the ejecta, is an expected effect regardless of the details of the ejection.

RD, CM and LR are supported by the European Research Council Advanced Grant "JETSET: Launching, propagation and emission of relativistic jets from binary mergers and across mass scales" (grant no. 884631).

References

Abbott, B. P. et al. 2017a, Astrophys. J. Lett., 848, L13
Abbott, B. P. et al. 2017b, Phys. Rev. Lett., 119, 161101
Baiotti, L. & Rezzolla, L. 2017, Rept. Prog. Phys., 80, 096901
Barkov, M. V. & Pozanenko, A. S. 2011, MNRAS, 417, 2161
Barthelmy, S. D., Chincarini, G., Burrows, D. N., et al. 2005, Nature, 438, 994
Berger, E. 2014, Annual Review of Astron. and Astrophys., 52, 43
Bostancı, Z. F., Kaneko, Y., & Göğüş, E. 2013, MNRAS, 428, 1623
Bromberg, O., Nakar, E., Piran, T., & Sari, R. 2011, Astrophys. J., 740, 100
Bucciantini, N., Metzger, B. D., Thompson, T. A., & Quataert, E. 2012, MNRAS, 419, 1537
Chawla, S., Anderson, M., Besselman, M., et al. 2010, Phys. Rev. Lett., 105, 111101
D'Avanzo, P. 2015, Journal of High Energy Astrophysics, 7, 73
Evans, C. R. & Kochanek, C. S. 1989, Astrophys. J. Lett., 346, L13
Evans, P. A., Beardmore, A. P., Page, K. L., et al. 2009, MNRAS, 397, 1177
Evans, P. A., Beardmore, A. P., Page, K. L., et al. 2007, A&A, 469, 379
Fujibayashi, S., Shibata, M., Wanajo, S., et al. 2020, Phys. Rev. D, 101, 083029
Gehrels, N., Norris, J. P., Barthelmy, S. D., et al. 2006, Nature, 444, 1044
Gill, R., Nathanail, A., & Rezzolla, L. 2019, Astrophys. J., 876, 139
Hempel, M. & Schaffner-Bielich, J. 2010, Nuclear Physics A, 837, 210
Ishizaki, W., Ioka, K., & Kiuchi, K. 2021, Astrophys. J. Lett., 916, L13
Kagawa, Y., Yonetoku, D., Sawano, T., et al. 2019, Astrophys. J., 877, 147
Kagawa, Y., Yonetoku, D., Sawano, T., et al. 2015, Astrophys. J., 811, 4
Kaneko, Y., Bostancı, Z. F., Göğüş, E., & Lin, L. 2015, MNRAS, 452, 824
Kisaka, S. & Ioka, K. 2015, Astrophys. J. Lett., 804, L16
Kisaka, S., Ioka, K., & Sakamoto, T. 2017, Astrophys. J., 846, 142
Komossa, S. 2015, Journal of High Energy Astrophysics, 7, 148
Krolik, J. H. & Piran, T. 2012, Astrophys. J., 749, 92
Kyutoku, K., Ioka, K., Okawa, H., Shibata, M., & Taniguchi, K. 2015, Phys. Rev. D, 92, 044028
Lippuner, J. & Roberts, L. F. 2015, Astrophys. J., 815, 82
Lippuner, J. & Roberts, L. F. 2017, Astrophys. J., Supp., 233, 18
Löffler, F., Faber, J., Bentivegna, E., et al. 2012, Class. Quantum Grav., 29, 115001
Matsumoto, J. & Masada, Y. 2019, Mon. Not. R. Astron. Soc., 490, 4271
Metzger, B. D., Thompson, T. A., & Quataert, E. 2018, Astrophys. J., 856, 101
Most, E. R., Papenfort, L. J., & Rezzolla, L. 2019, Mon. Not. R. Astron. Soc., 490, 3588
Musolino, C. & Rezzolla, L. 2023, arXiv e-prints, arXiv:2304.09168
Norris, J. P. & Bonnell, J. T. 2006, Astrophys. J., 643, 266

Perego, A., Radice, D., & Bernuzzi, S. 2017, Astrophys. J. Lett., 850, L37

Perego, A., Vescovi, D., Fiore, A., et al. 2022, Astrophys. J., 925, 22

Phinney, E. S. 1989, in Proceedings of the 136th Symposium of the International Astronomical Union, held in Los Angeles, U.S.A., July 25-29, 1988, Vol. 136, The Center of the Galaxy, ed. M. Morris, 543

Rees, M. J. 1988, Nature, 333, 523

Rosswog, S. 2007, MNRAS, 376, L48

Tanaka, M., Kato, D., Gaigalas, G., & Kawaguchi, K. 2020, MNRAS, 496, 1369

The LIGO Scientific Collaboration, the Virgo Collaboration, Abbott, B. P., et al. 2017, Astrophys. J. Lett., 848, L12

Villar, V. A., Guillochon, J., Berger, E., et al. 2017, Astrophys. J. Letters, 851, L21

Wanajo, S., Sekiguchi, Y., Nishimura, N., et al. 2014, Astrophys. J., 789, L39

SF2A 2023
M. N'Diaye, A. Siebert, N. Lagarde, O. Venot, K. Baillié, M. Béthermin, E. Lagadec, J. Malzac, J. Richard (eds)

MEV-GEV POLARIMETRY WITH THE FERMI-LAT: A FIRST SENSITIVITY ESTIMATE

A. Laviron[1], D. Bernard[1] and P. Bruel[1]

Abstract. A measurement of MeV-GeV linear polarization would provide information about the emission mechanisms of gamma-ray sources, especially pulsars and AGNs (active galaxy nuclei). The *Fermi* Large Area Telescope (*Fermi*-LAT) detects gamma rays between $\sim 20\,\mathrm{MeV}$ and $\sim 300\,\mathrm{GeV}$, using their conversion into an electron-positron pair, with the linear polarization affecting the distribution of the azimuthal direction of the pair. Measuring this azimuthal direction is extremely challenging due to the multiple scattering of the electron-positron pair in the detector. We present the current effort to extract the polarization information from the *Fermi*-LAT data, including recent developments on the simulation implementation and the event reconstruction and selection. This allows us to estimate the expected sensitivity to linear polarization of the *Fermi*-LAT, and we apply this to the Vela pulsar.

Keywords: Gamma-ray, Polarimetry, Pulsar

1 Introduction

Pulsars were discovered in 1967 as pulsating radio sources Hewish et al. (1968). They were quickly interpreted as magnetized, rotating neutron stars. The *Fermi* Large Area Telescope reported 294 pulsars detected in the GeV range*, making pulsars a significant fraction of the known gamma-ray sources. Their gamma-ray emission has a spectral shape of a power-law with sub-exponential cutoff at an energy of a few GeV (Smith et al. 2023). If the radio emission is thought to originate from the polar cap, the gamma-ray emission cannot escape that part of the magnetosphere because of the $\gamma - B \rightarrow e^+e^-$ absorption by the intense magnetic field (Abdo et al. 2010). The gamma-ray emission therefore comes from an outer part of the magnetosphere, but the exact location of that emission region and the radiative processes at play are still debated. The polarization signature of these different emission processes and emission regions differ significantly (Harding & Kalapotharakos 2017), with curvature radiation emitted within the light cylinder predicted to be more polarized than synchrotron emission from the striped wind.

In the MeV to GeV energy range, the dominant interaction process of gamma rays with matter is $e^+ - e^-$ pair production. This process is inherently sensitive to linear polarization: the bisector φ of the azimuthal angles of the electron and positron is preferentially perpendicular to the polarization direction, as can be seen in Figure 1 (left). The φ distribution, called in the following "polarigram", therefore has a cosine modulation, as can be seen in Figure 1 (right). One of the minima of the polarigram is the polarization angle φ_0 and the amplitude of the modulation A is proportional to the polarization fraction P,

$$\mathrm{P} = A/A_{100}\ , \tag{1.1}$$

where A_{100} is the modulation of a 100 % polarized source.

The *Fermi*-LAT (Atwood et al. 2009) is a gamma-ray space telescope, using pair production and observing in the $\sim 20\,\mathrm{MeV}$ to $\gtrsim 300\,\mathrm{GeV}$ energy range. It is composed of two main subsystems: a tracker to measure the direction of the incoming gamma ray and a calorimeter to measure its energy. It was designed to optimize the effective area and angular resolution throughout its energy range, but not its polarization sensitivity. Previous polarimetry attempts using information provided by the standard *Fermi*-LAT reconstruction were not

[1] Laboratoire Leprince-Ringuet, CNRS/IN2P3, Ecole polytechnique, Institut Polytechnique de Paris, 91120 Palaiseau, France
*https://confluence.slac.stanford.edu/display/GLAMCOG/Public+List+of+LAT-Detected+Gamma-Ray+Pulsars

© Société Française d'Astronomie et d'Astrophysique (SF2A) 2023

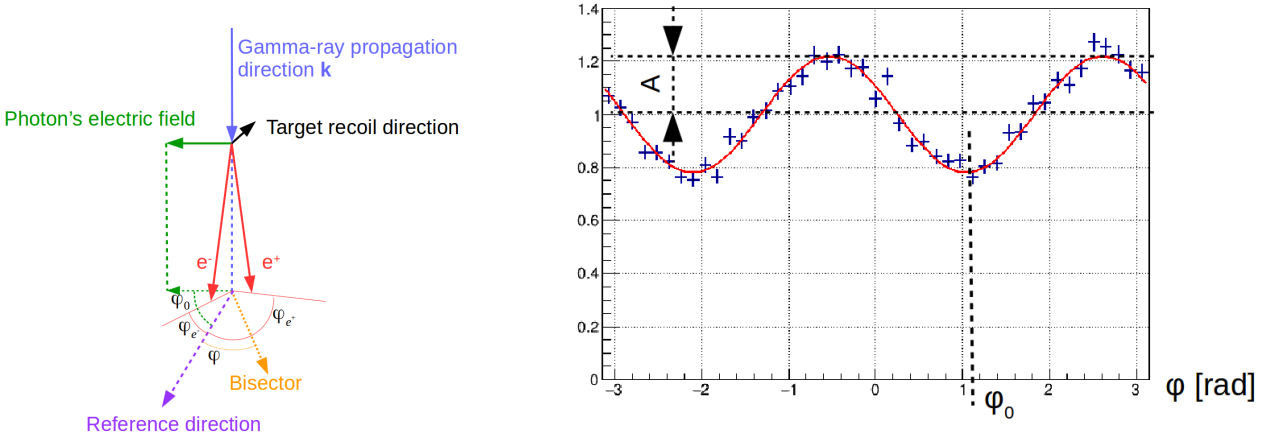

Fig. 1. Left: diagram of pair production. Right: distribution of φ angles, called a polarigram. The distribution minimum φ_0 is the polarization angle, the amplitude A is related to the polarization fraction.

successful (Giomi et al. 2017). Here we present a new approach to *Fermi*-LAT polarimetry based on the work of Bernard (2022). It relies on a dedicated event reconstruction that is described in Section 2. To develop this method, we performed Monte-Carlo simulations of the full LAT detector using Gleam (Atwood et al. 2009), a simulation software based on Geant4 (Agostinelli et al. 2003). The physics list of the Geant4 simulation has been modified to use the 5-dimensional, polarized Bethe-Heitler gamma-ray conversion model (Bernard 2018). Section 3 presents the results and a preliminary polarization sensitivity estimate applied to the Vela pulsar.

2 Methodology

The *Fermi*-LAT tracker is composed of 4×4 towers. Each tower contains 18 detector layers, each layer being composed of two single-sided silicon strip detectors, one dedicated to the measurement of the x coordinate and the other to the y coordinate†. For that purpose, they are electrically segmented along one direction with strips separated by 0.228 mm. The top 12 layers have a thin tungsten converter (3.5 % radiation length, 0.1 mm) and compose the Front section of the tracker. The Back section of the tracker consists of 4 layers with a thicker tungsten converter (18 % radiation length, 0.72 mm). The *Fermi*-LAT standard event reconstruction algorithm, named Pass 8 (Atwood et al. 2013), first groups contiguous strips that triggered into clusters in each silicon plane. Then it combines clusters to form tracks that are fitted to extract their direction. Next, it chooses the best track, that we call "the Pass 8 track" in the following, to reconstruct the incident gamma-ray direction.

The main challenge in pair-production polarimetry is the multiple Coulomb scattering of the electron and positron by the detector material, especially near the gamma-ray conversion point. Multiple scattering increases with the amount of material crossed. Therefore, as was found in Bernard (2022), the azimuthal angle can be computed from the first two layers of the event, the conversion layer and in the layer just below the conversion layer, called hereafter the "layer below conversion". Within the detector layer, the conversion happens either in the silicon detectors or in the tungsten converter, where multiple scattering is greater. By construction, the Pass 8 reconstructed z conversion coordinate is located in either the upper or lower silicon detector of the conversion layer. The majority of "upper detector" events are tungsten conversions. "Lower detector" events represent only 5.5 % of all events at 100 MeV, but 76 % of them are silicon conversions, expected to be much more sensitive to polarization. We will therefore report their measured modulation amplitudes separately.

In order to compute a pair azimuthal angle from the cluster information, we need one point in the conversion layer, and two points (corresponding to the crossing points of the electron and positron) in the layer below conversion. We select events that have at least one cluster (in either x or y) and at most one cluster in x and one cluster in y in the conversion layer. In the layer below conversion, we use events that have two clusters in either x or y and either one or two clusters in the other direction. This leads to two configurations that are shown in Figure 2. We name them according to their number of possible azimuthal angles (NPAA). The one schematized in Figure 2 (left) is called NPAA1. It has two x coordinates for the electron and positron

†In the LAT frame, the x and y axes span the silicon detectors plane and the z axis points towards the LAT boresight.

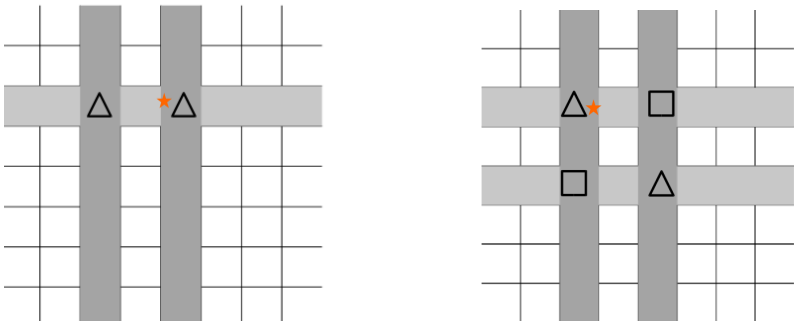

Fig. 2. Cluster configurations in the layer below conversion. Light grey represents the y clusters and dark grey the x clusters. The orange star represents the coordinates of the Pass 8 track in that plane. The black triangles and squares represent the sets of (x, y) positions that we may use to compute an azimuthal angle. Left: NPAA1 (there is one cluster in either x or y). Right: NPAA2 (there are two clusters in both x and y, yielding two possible azimuthal angles).

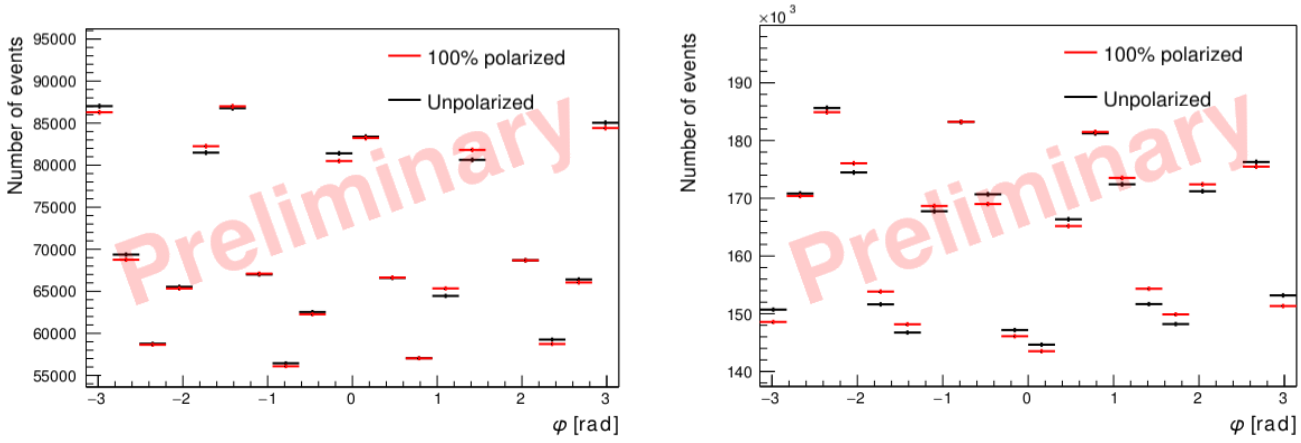

Fig. 3. Distribution of φ azimuthal angles, for a 100 % polarized source in red and a 0 % polarized source in black. Only Front-converted and upper detector events are shown. Left: distribution for NPAA1 events. Right: NPAA2 events.

and a single y coordinate, leaving a single possible pair azimuthal angle, computed using the coordinates in the conversion layer and the two xy coordinates indicated by black triangles. The event configuration shown in Figure 2 (right) has two x coordinates and two y coordinates. This results in an ambiguity: we could compute an azimuthal angle using either the two coordinates indicated by the black triangles or by the black squares. We therefore call these events NPAA2. In that case, we use the azimuthal angle computed from the pair possibility that is closer to the Pass 8 track.

3 Results

In order to estimate the *Fermi*-LAT sensitivity to polarization, we first measure the modulation amplitude A_{100} (defined in Eq. 1.1) for each event configuration. To do so, we simulate gamma rays from the celestial coordinates of the Vela pulsar (J2000 R.A. = 128.84 °, Dec = − 45.18 °). Simulations are performed at three energies: 50 MeV, 100 MeV and 200 MeV. For each energy, we simulate an unpolarized source (0 % polarized), and a fully polarized source (100 % polarized, polarization angle of 0 °). Figure 3 shows examples of polarigrams, for 100 MeV, Front-converted and "upper detector" events, NPAA1 (left) and NPAA2 (right). These distributions do not show the cosine modulation because they are dominated by the x-y structure of the LAT tracker.

Ratios (bin-to-bin) of the polarized distribution to the unpolarized distribution are shown in Figure 4. For the sake of simplicity, we refer to these ratios as polarigrams. We fit these ratios with a cosine function to extract the modulation amplitudes A_{100}. The amplitudes of Front, upper detector events are 0.77 ± 0.16 % for NPAA1 events and 1.20 ± 0.11 % for NPAA2 events (respectively 1.72 ± 0.35 % and 2.54 ± 0.35 % for Front, lower detector events). We observe that modulations of NPAA1 events are smaller than those of NPAA2 events, because the

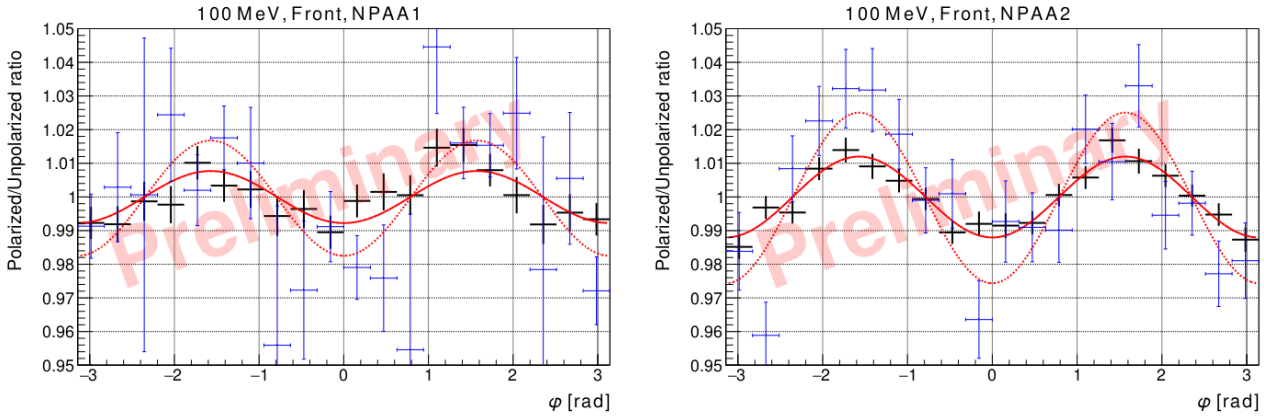

Fig. 4. Polarigrams of Front-converted events at 100 MeV. Thin blue line (fitted by red dashed line): "lower detector" events. Thicker black line (fitted by red continuous line): "upper detector" events. Left: NPAA1. Right: NPAA2.

azimuthal angles reconstructed in NPAA1 events are less precise. As expected, the "lower detector" events are much more sensitive to polarization. Finally, the modulation of Back events (not shown here) is compatible with zero. These overall low numbers are not surprising since the LAT was not designed for polarimetry. The modulation amplitudes vary slightly with energy. These results are comparable with those obtained with a simplified model of the *Fermi*-LAT in Bernard (2022). Our simulations at 50 MeV, 100 MeV and 200 MeV are at the center of three logarithmic energy bins in the range 35 MeV to 283 MeV. In that energy range, the observed Vela pulsar count spectrum is almost flat, and the expected number of photons is $\sim 2 \times 10^6$ for 15 years of observation. Under these assumptions, we obtain an uncertainty on the measured linear polarization fraction of $\sigma_{\rm P} \simeq 20\,\%$.

4 Conclusions

We have presented a new analysis that allows us to obtain for the first time a non-zero sensitivity to linear polarization with *Fermi*-LAT. This result is enabled by directly using the tracker cluster information rather than the output of the standard event reconstruction. Using simulations, we measure modulation amplitudes up to 2.5 % in the energy range between ~ 30 MeV and ~ 300 MeV and estimate the expected sensitivity to the linear polarization of the Vela pulsar to be about 20 % with 15 years of data. The next step of this study is to extend the investigated energy range. We will then apply the analysis to *Fermi*-LAT data.

The *Fermi*-LAT Collaboration acknowledges support for LAT development, operation and data analysis from NASA and DOE (United States), CEA/Irfu and IN2P3/CNRS (France), ASI and INFN (Italy), MEXT, KEK, and JAXA (Japan), and the K.A. Wallenberg Foundation, the Swedish Research Council and the National Space Board (Sweden). Science analysis support in the operations phase from INAF (Italy) and CNES (France) is also gratefully acknowledged. This work performed in part under DOE Contract DE-AC02-76SF00515.

References

Abdo, A. A., Ackermann, M., Ajello, M., et al. 2010, ApJS, 187, 460.

Agostinelli, S., Allison, J., Amako, K., et al. 2003, Nucl.Instrum.Meth., 506, 250.

Atwood, W. B., Abdo, A. A., Ackermann, M., et al. 2009, ApJ, 697, 1071.

Atwood, W., Albert, A., Baldini, L., et al. 2013, arXiv:1303.3514.

Bernard, D. 2018, Nucl.Instrum.Meth., 899, 85.

Bernard, D. 2022, Nucl.Instrum.Meth., 1042, 167462.

Giomi, M., Bühler, R., Sgrò, C., et al. 2017, 6th International Symposium on High Energy Gamma-Ray Astronomy, 1792, 070022, arXiv:1610.06729.

Harding, A. K. & Kalapotharakos, C. 2017, ApJ, 840, 73.

Hewish, A., Bell, S. J., Pilkington, J. D. H., et al. 1968, Nature, 217, 709.

Smith et al. ApJS submitted (2023), arXiv:2307.11132.

SF2A 2023
M. N'Diaye, A. Siebert, N. Lagarde, O. Venot, K. Baillié, M. Béthermin, E. Lagadec, J. Malzac, J. Richard (eds)

NUMERICAL SIMULATIONS OF OBLIQUE ELECTROSPHERES WITH REALISTIC PARAMETERS BASED ON "PULSAR AROMA"

F. Mottez[1]

Abstract. The structure of neutron stars electrospheres covering a large range of realistic parameters is investigated thanks to the development and use of a numerical simulation code named *Pulsar ARoMa*.

Keywords: neutron star, electrosphere, pulsar, numerical simulation

1 Introduction

The environment of a neutron star is that of an electrically conductive, highly magnetized, rotating sphere (the star). In the absence of high-energy radiative phenomena leading to the creation of electron positron pairs, these environments are structured by two opposing domes made up of particles of a given charge, and a belt surrounding the star made up of particles of opposite charge (see figure in Krause-Polstorff & Michel 1985).

These structures are known as electrospheres, due to their large charge differences. When the magnetic field has an axis of symmetry, and this is not aligned with the axis of rotation of the sphere/star, we speak of an oblique electrosphere. Simulations of aligned electrospheres were produced as early as 2000-2010. They are reviewed in (Cerutti & Beloborodov 2017). By contrast, simulations of oblique electrospheres are rare. To the best of my knowledge, only one article presents them, without giving any details (McDonald & Shearer 2009). I present simulations of oblique electrospheres produced very recently, with the aim of describing kinetic processes as accurately as possible, without making MHD or force-free field assumptions.

2 Method

These simulations are carried out using a specific code. It is governed by an algorithm combining aspects of particle-type codes (PIC), and Vlasov-type codes (with 3 dimensions in space, and one in momentum). Electromagnetic fields are calculated on a spherical grid, by decomposing the functions into spherical vector harmonics for the angular part, and Chebychev polynomials over a set of nested domains for the radial part. The implementation is similar to that of Pétri et al. (2002).

The relativistic motion of the particles is obtained by solving a relatively little-known relativistic equation, which I have re-demonstrated, adapted to very strong, moderate or zero magnetic fields. It is inspired from a method already used for the simulation of non-relativistic plasmas (Mottez et al. 1998; Mottez 2008). The rendering of motion in the case of strong magnetic fields is that of the particle guiding-center. The loss of particle energy caused by radiation associated with the curvature of their trajectory is taken into account, but the associated rate of high-energy photons is not calculated. As a result, we do not yet provide a radiation map of the electrosphere.

The choice of stationary solutions considerably speeds up calculations. A typical simulation takes less than an hour with a MPI run involving 3 processes on a Intel Core i7. There are no reduced sizes, a simulations can be run with realistic parameters.

As we like to give everything a name, I've named this code "Pulsar ARoMa" for *Pulsars' Asymmetric Rotating Magnetospheres*.

[1] LUTH, Observatoire de Paris, PSL Research University, CNRS 5 place Jules Janssen, 92190 Meudon, France.

© Société Française d'Astronomie et d'Astrophysique (SF2A) 2023

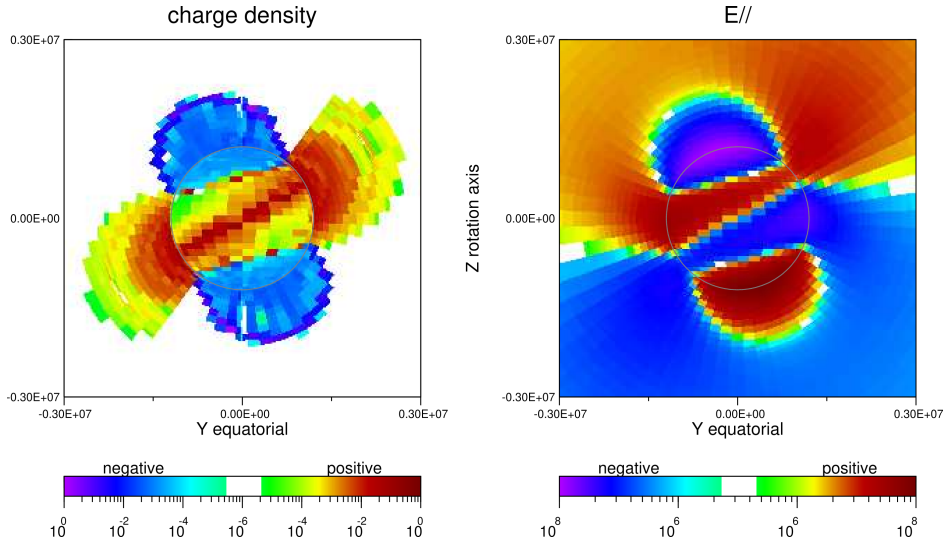

Fig. 1. Charge density and parallel electric field of an electrosphere. The figure shows the values at the star's surface (inside the circle that represents it), and in a meridian plane (outside this circle). Star radius: 12 km. Dipolar magnetic field, surface value: 10^9 G, rotation period: 10 ms. Rotation axis vertical. The magnetic axis is inclined 30 degrees to the rotation axis. Logarithmic scales in cold colors for negative values, in warm colors for positive values. System of units used: CGS.

3 First results

I have simulated electrospheres of neutron stars with a range of magnetic fields and rotation periods that is typical of millisecond pulsars, standard pulsars, and neutron stars beyond the "death line", i.e. neutron star that have not enough rotational energy to power a pulsar. I found that the electrospheric structure of oblique pulsars is similar to those of aligned pulsar. It is composed of two domes above the magnetic axis of symmetry, and a belt of opposite charge surrounding the magnetic equator. Nevertheless, their shape is influenced by the rotational effects: the domes and the belt are not symmetric relatively to the magnetic axis.

An example of an electrosphere with a plasma composed of electrons and protons is shown in fig. 1. We have seen that particle energies reach high values. Their Lorentz factors are shown in fig. 2. This suggests that for neutron stars in the regime of high rotational and magnetic energies, the electrons have sufficiently high energy to produce gamma rays via synchro-curvature radiation, and possibly electron-positron pairs (Voisin et al. 2018). A pulsar is therefore a potentially viable solution, as soon as radiation effects are included in the *Pulsar AroMa* code.

4 Outlook

When the particles in an electrosphere are energetic enough to emit gamma rays that generate pairs of electrons and positrons, the star's environment changes from electrosphere to pulsar magnetosphere (oblique or aligned). Ultimately, the aim is to adapt this code to pulsar simulation, with the inclusion of an explicit computation of high energy emissions, electron-positron pair creation, and general relativity effects.

I would like to thank Silvano Bonazzola and Guillaume Voisin for their help and support.

References

Cerutti, B. & Beloborodov, A. M. 2017, Space Sci. Rev., 207, 111

Krause-Polstorff, J. & Michel, F. C. 1985, A&A, 144, 72

McDonald, J. & Shearer, A. 2009, ApJ, 690, 13

Mottez, F. 2008, Journal of Computational Physics, 227, 3260

Mottez, F., Adam, J. C., & Heron, A. 1998, Computer Physics Communications, 113, 109

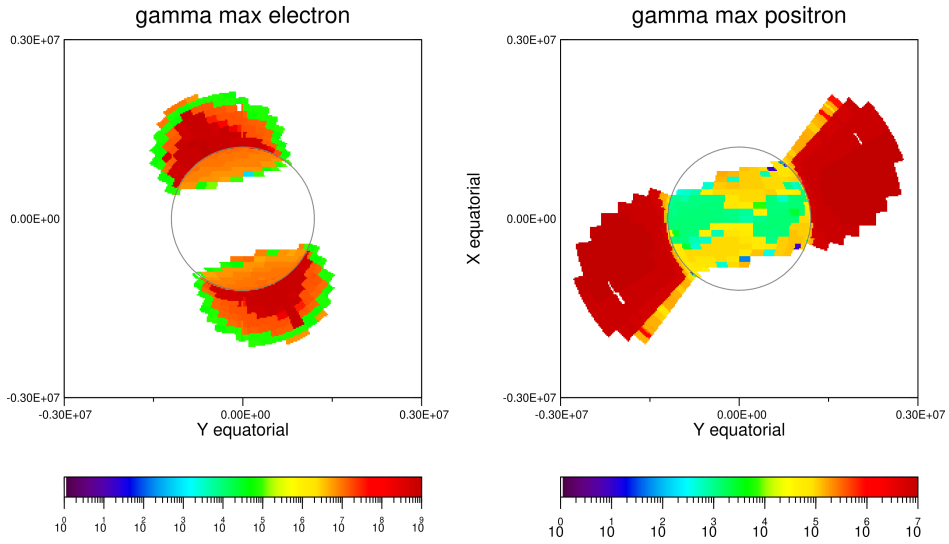

Fig. 2. Same simulation. Left: maximum Lorentz factor reached by electrons. Right, maximum Lorentz factor for positrons.

Pétri, J., Heyvaerts, J., & Bonazzola, S. 2002, A&A, 384, 414
Voisin, G., Mottez, F., & Bonazzola, S. 2018, MNRAS, 474, 1436

SF2A 2023
M. N'Diaye, A. Siebert, N. Lagarde, O. Venot, K. Baillié, M. Béthermin, E. Lagadec, J. Malzac, J. Richard (eds)

THE HUNT FOR QUASI-PERIODIC ERUPTIONS

E. Quintin[1] and N. A. Webb[1]

Abstract. Quasi-Periodic Eruptions (QPEs) are the latest addition to the ever-growing family of extragalactic transients. The first QPE source was discovered in 2019, with a current total of four known sources (with two additional candidates). From an observational standpoint, they appear as repeated ∼2h-long bright bursts of thermal X-rays, with a regular quasi-periodic pattern between peaks in most of them (but not all). They appear to be linked to Tidal Disruption Events (TDEs, when an inbound star gets disrupted by the tidal forces of a Super-Massive Black Hole). Several models have been suggested, trying to account for the complex observed behaviour of these puzzling objects, but they all fall short in some aspects. Understanding these peculiar objects might help us constrain the physics of super-Eddington accretion (that happens in both TDEs and QPEs), and thus the growth of Super-Massive Black Holes. I summarize here the current state of the art of the study of QPEs, and its most recent developments. I present a new QPE candidate, Tormund, that was found as part of a larger endeavour aimed at data-mining the current and past multi-instrument X-ray archives to unearth previously-undetected transient events.

Keywords: galaxies: nuclei - accretion, accretion disks - black hole physics

1 Introduction

One of the current open questions in astrophysics is that of the growth of Super-Massive Black Holes (SMBHs). The very existence of SMBHs with $M_{BH} >\sim 10^9 M_\odot$ at redshift $z >\sim 6$ (when the Universe was less than one billion years old), as revealed by the detection of luminous very high-z quasars (e.g. Wang et al. 2021), challenges theoretical models for early BH formation and evolution as it appears difficult to reach such high masses in such a short timescale (e.g. Volonteri 2010). The proposed scenarios include intermediate-mass black hole (IMBH, in the $\sim 10^2$-$10^5 M_\odot$ range) progenitors continously accreting at their Eddington rate (i.e. the maximum rate for standard accretion models), or less massive seeds experiencing shorter-lived super-Eddington accretion events. Mergers could also play an important role (see e.g. Volonteri et al. 2021, for a review). From an observational point of view, future space-based gravitational wave observatories are needed to detect SMBH binaries leading to mergers and, at present, we need to rely on electromagnetic observations to make progress in the field of SMBH growth and evolution. As such, increasing the sample size of super-Eddington accretors can be of paramount importance to deepen our understanding of SMBH growth and evolution.

There are various astrophysical objects that can exhibit super-Eddington accretion. One of these are Tidal Disruption Events (TDEs, e.g. Gezari 2021). TDEs correspond to the destruction of a star by a massive black hole due to the tidal forces. This results in orbiting stellar debris, that create a temporary accretion disc around the super-massive black hole (SMBH). This then leads to a transient outburst, lasting several months, reaching super-Eddington levels. While TDEs are being intensely studied, the precise phenomena at play are still somewhat unclear. One seemingly independent phenomenon could help us understand TDEs: quasi-periodic eruptions (QPEs).

2 Our current understanding of QPEs

QPEs were first discovered in 2019 in GSN 069(Miniutti et al. 2019). To date, only four bona fide QPE sources are known, with one strong candidate. These sources are characterised by intense bursts of soft X-rays, lasting

[1] IRAP, 9 avenue du Colonel Roche, 31400 Toulouse, France

© Société Française d'Astronomie et d'Astrophysique (SF2A) 2023

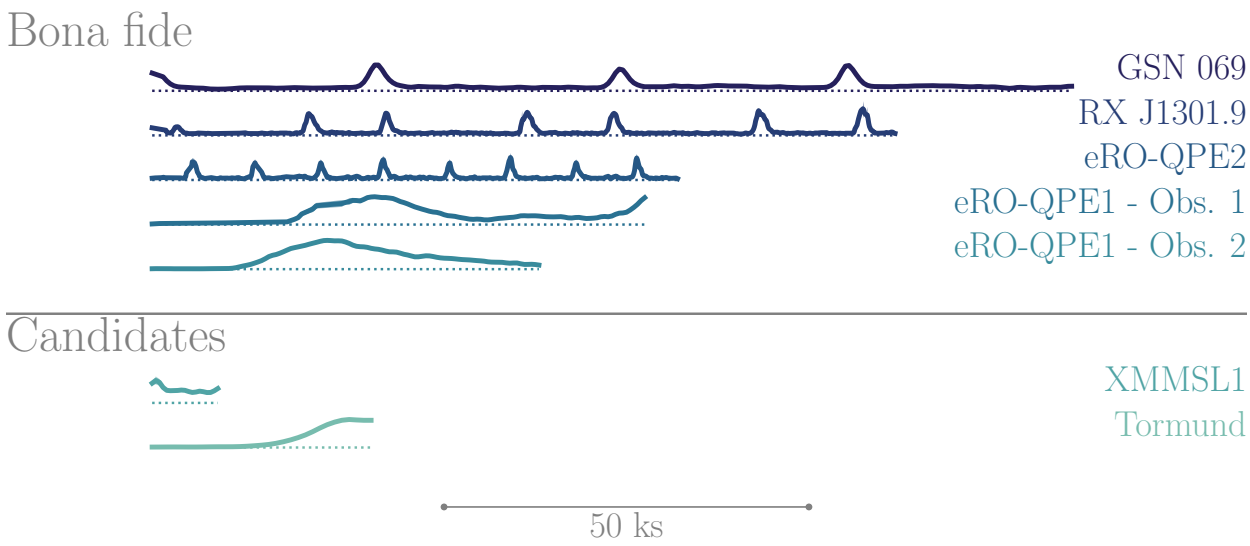

Fig. 1. Qualitative overview of the difference in the shape of the *XMM-Newton* 0.2–2 keV lightcurves of the known QPE bona fide sources (top) and candidates (bottom) (Miniutti et al. 2019; Giustini et al. 2020; Arcodia et al. 2021; Chakraborty et al. 2021; Quintin et al. 2023). The lightcurves are normalized by their respective peak count-rate value, to allow comparison of their shapes. The time axis is common to all lightcurves, with the scale shown at the bottom. The first observation of eRO-QPE1 finished with a large amplitude burst that was cropped here for visualization purposes - it reached about 5 times higher than the previous peaks of the same observation.

about an hour and repeating every few hours, showing thermal emission with temperatures of $\sim$ 50 eV in quiescence, and reaching $\sim$100 eV at the peak. These peaks can repeat in regular or irregular patterns. They are transient on longer timescales, for example the QPEs in GSN 069 being observed over the course of $\sim$1 year only, then disappearing with a rebrightening of the quiescent state, and finally appearing again a few months later with a different pulse profile (Miniutti et al. 2023a,b). Finally, QPEs appear observationally correlated with TDEs. Out of the five known QPEs, two show a link with past X-ray TDEs. This is unlikely to be a coincidence considering the rarity of TDEs (rate of $\sim 6 \times 10^{-5}$ yr^{-1} galaxy^{-1}, van Velzen et al. 2020).

The precise phenomena at play in QPEs are still unclear, and several models have been suggested to explain their properties. They all try to encompass the observational link with TDEs. The first type of model is based on different sorts of instabilities in the transient accretion flow from a TDE (e.g. Śniegowska et al. 2023). The second type of model uses a partial TDE, with a remaining body orbiting the black hole and interacting with the disk (e.g. Franchini et al. 2023). The last type of model corresponds to repeated tidal strippings of an orbiting white dwarf (e.g. Wang et al. 2022). Intense monitoring of the known sources, as well as additional detections and observations of new QPEs are necessary to discriminate between the models and understand the nature of QPEs. With this aim, and as part of an ongoing study on the systematic exploitation of multi-instrument X-ray archives, we searched for new QPE candidates previously missed in archival data.

3 Tormund: a new QPE candidate

3.1 Data mining

This search for QPEs is a part of a larger endeavour, part of the XMM2Athena project (Webb et al. 2023), which aims at making full use of the archival X-ray data (see Quintin et al. to be sub. for details). The general idea is that the best way to reveal the long-term variability of an object is to sample its evolution as intensively as possible. For this purpose, we cross-matched the largest available X-ray catalogs, and systematically computed the XMM-Newton upper limits for all non-XMM sources that lay in the XMM-Newton observational footprint. This led to a catalog of $\sim$ 1M X-ray sources, that has two applications. First, we can compare any new XMM-Newton detection to the archival data, allowing to automatically detect transient events. This is the STONKS pipeline, that is currently being embedded in the XMM-Newton pipeline (Quintin et al. to be sub.). The second application is that we can directly data mine the catalog in search of objects of interest, using the available

properties. This was used for instance to find a new candidate pulsating ultra-luminous X-ray source (another type of super-Eddington accretor) through its long-term variability (Quintin et al. 2021).

In order to find QPEs, we looked for short-term variable, soft X-ray sources for which the position matched the centre of galaxies present in the GLADE+ catalogue (Dálya et al. 2022). This allowed us to detect known QPEs (which confirms the efficiency of the method), and a new QPE candidate, 4XMM J123856.3+330957.

3.2 Tormund's properties

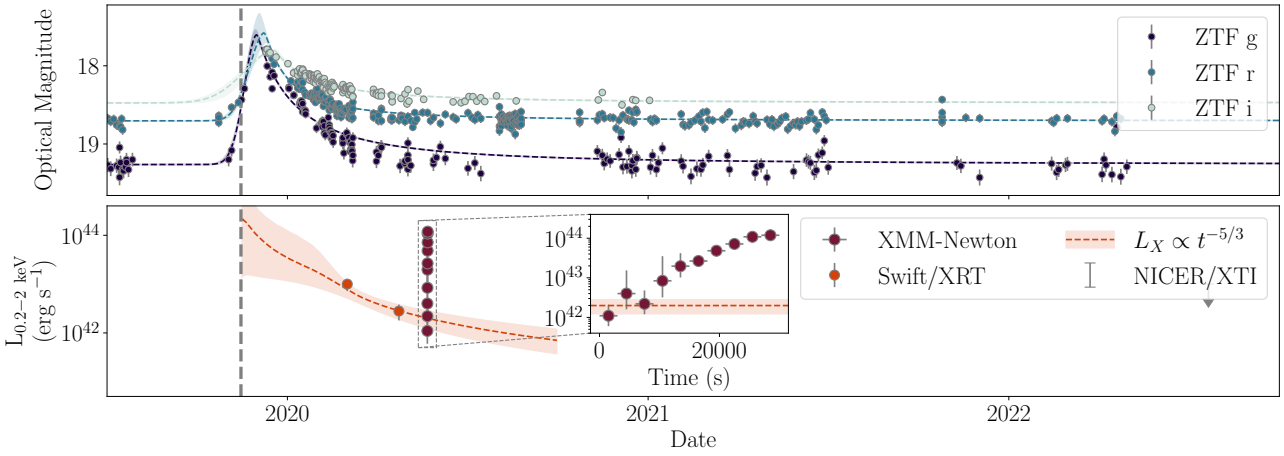

Fig. 2. Long-term lightcurves of AT 2019vcb, nicknamed Tormund (extracted from Quintin et al. 2023). *Top panel:* ZTF monitoring of the source, showing the optical TDE in the g, r and i bands. *Bottom panel:* X-ray long-term lightcurve of Tormund, with the inset showing the short-term eruption during the XMM-Newton observation. The orange dashed line and shaded region correpond to the confidence region of a $\propto t^{-5/3}$ X-ray decay using only the two Swift data points, showing that the beginning of the XMM-Newton observation is consistent with this expected behaviour.

The full details of the study of this object are presented in Quintin et al. (2023). This source was originally detected as an optical transient event: AT 2019vcb. It was observed first by the Zwicky Transient Facility (ZTF, Bellm 2014) on November 15, 2019 (ZTF19acspeuw, nicknamed Tormund), and then by ATLAS (ATLAS19bcyz) and Gaia (Gaia19feb) a few days later. With an amplitude of ∼1 magnitude and a decay over about 100 days, it was classified as a TDE. Such a discovery led to two follow-ups: an optical spectrum, that allowed to confirm its TDE nature and revealed numerous broad emission lines, consistent with a H+He TDE (see Fig. 1 in Hammerstein et al. 2022). Using the `MOSFiT` TDE model (Guillochon et al. 2018), the black hole mass was also estimated at $M_{\mathrm{BH}} \approx 8.3^{+0.8}_{-0.7} \times 10^7\,\mathrm{M}_\odot$. The second follow-up was in X-rays, with two Swift exposures and one by XMM-Newton. The Swift data points and the beginning of the XMM-Newton observation are consistent with the expected $F_X \propto t^{-5/3}$ emission (see envelope in Fig. 2), with a soft thermal emission. However, in the second half of the XMM-Newton observation, the source underwent an extreme rebrightening.

In less than 15ks, the source luminosity increased from $\sim 3\times10^{42}$ erg s^{-1} to $\sim 10^{44}$ erg s^{-1}, and its temperature rose from ∼50 eV to ∼120 eV. This behaviour is similar to the other known long-timescale QPE source, eRO-QPE1 (Arcodia et al. 2022) – with the exception that the short duration of the observation prevented from observing an entire flare. A late optical spectral follow-up, once the TDE was over, allowed to rule out the presence of an AGN that could have powered this variability. Such variability amplitudes and timescales are not expected from X-ray TDEs, which show fairly steady decay with mild short-term variability (typically factors of ∼5 in ∼days). As a consequence, we argued that Tormund was a strong QPE candidate.

3.3 Consequences on QPE models

As a strong QPE candidate, the existence of this source has several consequences on our understanding of QPEs in general:

- This source is the third QPE source which is associated with a TDE, bringing the fraction of TDE-linked QPE to three out of five. This allows to definitely exclude the hypothesis that this correlation is fortuitous, and confirms the need to account for an initial TDE in the QPE formation models

- This is the first QPE source for which the initial TDE was detected in visible light, and thus for which the time of disruption could be precisely constrained (as opposed to deduced from variability from anterior archival flux values, for the other two sources). This allows in turn to put constraints on the formation time of QPEs, which must be below 6 months. This is remarkably short for models that require a circularization of a remnant through emission of gravitational waves, which should require longer formation times.
- This QPE is the brightest (both in terms of quiescent and peak flux), has the longest rise timescale, and the largest black hole mass of the known sample. This is puzzling, as such a scaling does not seem to exist in TDEs (Gezari 2021), and might thus provide us insight on the different physical mechanisms at play.

4 Conclusions

The study of QPEs is a very recent field, and a lot is still yet to be understood. Systematic and in-depth exploitation of the archives may allow us to discover more of these rare objects, and intense multi-wavelength long-term monitoring of the few that are known is necessary. As they seem to provide an *in-situ* probe of the inner accretion-powered engine of TDEs, understanding them might give us the keys to understand TDEs, and thus constrain super-Eddington accretion models.

Some of this work was done as part of the XMM2ATHENA project. This project has received funding from the European Union's Horizon 2020 research and innovation programme under grant agreement n°101004168, the XMM2ATHENA project. EQ and NAW acknowledge the CNES who also supported this work.

References

Arcodia, R., Merloni, A., Nandra, K., et al. 2021, Nature, 592, 704, arXiv:2104.13388 [astro-ph]

Arcodia, R., Miniutti, G., Ponti, G., et al. 2022, Astronomy & Astrophysics, 662, A49, publisher: EDP Sciences

Bellm, E. 2014, in The Third Hot-wiring the Transient Universe Workshop, eprint: arXiv:1410.8185, 27–33, conference Name: The Third Hot-wiring the Transient Universe Workshop Pages: 27-33 ADS Bibcode: 2014htu..conf...27B

Chakraborty, J., Kara, E., Masterson, M., et al. 2021, The Astrophysical Journal, 921, L40, aDS Bibcode: 2021ApJ...921L..40C

Dálya, G., Díaz, R., Bouchet, F. R., et al. 2022, Monthly Notices of the Royal Astronomical Society, 514, 1403

Franchini, A., Bonetti, M., Lupi, A., et al. 2023, Astronomy and Astrophysics, 675, A100, aDS Bibcode: 2023A&A...675A.100F

Gezari, S. 2021, Annual Review of Astronomy and Astrophysics, 59, 21, aDS Bibcode: 2021ARA&A..59...21G

Giustini, M., Miniutti, G., & Saxton, R. D. 2020, Astronomy & Astrophysics, 636, L2, publisher: EDP Sciences

Guillochon, J., Nicholl, M., Villar, V. A., et al. 2018, The Astrophysical Journal Supplement Series, 236, 6, publisher: American Astronomical Society

Hammerstein, E., Velzen, S. v., Gezari, S., et al. 2022, The Astrophysical Journal, 942, 9, publisher: The American Astronomical Society

Miniutti, G., Giustini, M., Arcodia, R., et al. 2023a, Astronomy & Astrophysics, 674, L1, publisher: EDP Sciences

Miniutti, G., Giustini, M., Arcodia, R., et al. 2023b, Astronomy & Astrophysics, 670, A93, publisher: EDP Sciences

Miniutti, G., Saxton, R. D., Giustini, M., et al. 2019, Nature, 573, 381, aDS Bibcode: 2019Natur.573..381M

Quintin, E., Webb, N. A., Guillot, S., et al. 2023, Astronomy and Astrophysics, 675, A152, aDS Bibcode: 2023A&A...675A.152Q

Quintin, E., Webb, N. A., Gúrpide, A., Bachetti, M., & Fürst, F. 2021, Monthly Notices of the Royal Astronomical Society, 503, 5485, aDS Bibcode: 2021MNRAS.503.5485Q

van Velzen, S., Holoien, T. W.-S., Onori, F., Hung, T., & Arcavi, I. 2020, Space Science Reviews, 216, 124, arXiv:2008.05461 [astro-ph]

Volonteri, M. 2010, The Astronomy and Astrophysics Review, 18, 279, arXiv:1003.4404 [astro-ph]

Volonteri, M., Habouzit, M., & Colpi, M. 2021, Nature Reviews Physics, 3, 732, aDS Bibcode: 2021NatRP...3..732V

Wang, F., Yang, J., Fan, X., et al. 2021, The Astrophysical Journal Letters, 907, L1, arXiv:2101.03179 [astro-ph]

Wang, M., Yin, J., Ma, Y., & Wu, Q. 2022, The Astrophysical Journal, 933, 225, aDS Bibcode: 2022ApJ...933..225W

Webb, N. A., Carrera, F. J., Schwope, A., et al. 2023, XMM2ATHENA, the H2020 project to improve XMM-Newton analysis software and prepare for Athena, publication Title: arXiv e-prints ADS Bibcode: 2023arXiv230310097W

Śniegowska, M., Grzedzielski, M., Czerny, B., & Janiuk, A. 2023, Astronomy & Astrophysics, 672, A19, publisher: EDP Sciences

SF2A 2023
M. N'Diaye, A. Siebert, N. Lagarde, O. Venot, K. Baillié, M. Béthermin, E. Lagadec, J. Malzac, J. Richard (eds)

NUMERICAL MODELING OF DYNAMOS IN COMPACT OBJECTS: MAGNETIC FIELD AMPLIFICATION AND DISSIPATION

M. Bugli[1,2], J. Guilet[2], R. Raynaud[2], A. Reboul-Salze[3], P. Barrère[2], A. Mignone[1], V. Berta[1], G. Mattia[4] and L. Del Zanna[4]

Abstract. The amplification of magnetic fields via dynamo mechanisms is a fundamental process that not only shapes the dynamics of stars, but also deeply affects the evolution of compact objects from their formation throughout their activity. Understanding how magnetic fields are dissipated and amplified in the environment surrounding neutron stars and black holes can thus disclose the connection between the properties of the central object and the multi-messenger emission related to the accretion process. We present results from recent studies aimed at quantifying the properties of dynamo-generated magnetic fields in proto-neutron stars and their potential impact on the explosion and the neutrino and gravitational waves signals emitted at the formation of the compact object. We also show how mean-field dynamos can modify the dynamics of accreting black holes, as weak magnetic seeds are amplified to strong large-scale fields that can reshape the properties of the accretion flow. Finally, we present some recent models of resistive relativistic jets and high-order numerical schemes for (relativistic) magnetohydrodynamics (RMHD) that showcase the importance of reducing the numerical dissipation of magnetic fields observed in simulations, thus enhancing the robustness of their predictions.

Keywords: magnetic fields, neutron stars, black holes, dynamo, MHD, numerical algorithms

1 Introduction

The combination of rapid rotation and large-scale magnetic fields provides the perfect conditions to power-up high-energy astrophysical sources such as gamma-ray bursts, compact binaries and accreting black holes. However, the large scale separation between the sites where amplification (or dissipation) of magnetic fields takes place and the accretion flows (or relativistic jets) from compact objects still poses a serious challenge for numerical models. In the following we present a series of recent results from (general relativistic) MHD models of accreting compact objects that demonstrate the challenges and main features of simulations of astrophysical plasmas within (or in proximity) of either proto-neutron stars (PNS) or black holes.

2 Multi-scale approach: PNS dynamos and magneto-rotational explosions

While the exact origin of the large-scale magnetic fields of magnetars remains uncertain, a possible scenario is represented by the action of dynamos occurring within a still-forming PNS during the gravitational collapse of a massive star. Using global MHD models exploring different layers of the PNS, we showed how PNS convection can efficiently amplify weak small-scale magnetic seed up to magnetar-like levels ($\sim 10^{15}$ G; Raynaud et al. 2020) and lead to significant emission of gravitational waves (GW; Raynaud et al. 2022). The magnetorotational instability can also take over as driving dynamo mechanism (Guilet et al. 2022), producing large-scale magnetic fields with dynamics that resemble typical mean-field dynamo processes (Reboul-Salze et al. 2021; Reboul-Salze et al. 2022). Finally, the fallback of material onto the PNS can trigger the onset of the Tayler instability, exciting

[1] Dipartimento di Fisica, Università di Torino, via Pietro Giuria 1, 10125 Torino, Italy
[2] Université Paris-Saclay, Université Paris Cité, CEA, CNRS, AIM, 91191, Gif-sur-Yvette, France
[3] Max Planck Institute for Gravitational Physics (Albert Einstein Institute), Potsdam, D-14476, Germany
[4] INFN, Sezione di Firenze, Via G. Sansone 1, I-50019 Sesto Fiorentino, Italy

© Société Française d'Astronomie et d'Astrophysique (SF2A) 2023

large-scale non-axisymmetric perturbations and closing dynamo cycle (Barrère et al. 2022, 2023). All these dynamo models predict the amplification of magnetic fields with a multipolar and generally non-axisymmetric spatial structure. Bugli et al. (2021) explored the effects that such fields could have on core-collapse supernovae, showing that aligned dipolar fields are the most efficient at launching bipolar outflows (also in 2D; see Bugli et al. 2020). Moreover, magnetic fields can quench the onset of rotationally-driven instabilities and suppress the corresponding multi-messenger signatures (Bugli et al. 2023).

3 Sub-grid modeling: black hole accretion disks and resistive jets

An alternative approach to the investigation of magnetic fields amplification and dissipation are sub-grid models. An example is given by the *mean-field dynamo* closure, where unresolved small-scale fluctuation of velocity and magnetic fields produce both a large-scale electromotive force and an enhanced turbulent dissipation Brandenburg & Subramanian (2005). Accretion disks and relativistic jets can be highly affected by such dynamics (Mattia & Fendt 2020, 2022). When applied to the general relativistic (GR) MHD framework (Bucciantini & Del Zanna 2013), a mean-fied dynamo can reshape the properties of accretion disks around black holes. The emergence of dynamo waves (Bugli et al. 2014) can not only induce large-scale non-axisymmetries in the gas accreting onto the black hole (Del Zanna et al. 2022), but also amplify an initially weak magnetic seed and reproduce results from ideal GRMHD models (Porth et al. 2019) that include from the beginning intense magnetic fields (Tomei et al. 2020, 2021). The effects of numerical dissipation on the properties of astrophysical flows in simulations (which are unavoidable in all grid-based models) can be mitigated by using explicit prescriptions for the turbulent resistivity. Mattia et al. (2023) showed how reproducibility of MHD simulations of relativistic jets increases significantly when the resistive RMHD regime is adopted. Moreover, a substantial decrease of numerical magnetic dissipation can be obtained using high-order integration schemes (Berta et al. 2023), which increase the effective resolution of a given model and can produce large speedups w.r.t. $2^{\rm nd}$-order methods.

4 Conclusions

We presented results from a series of studies that focus on the modeling of magnetic field amplification and dissipation in accreting compact objects. Our results showcase the importance of connecting all the scales relevant for both the magnetic field dynamics and the astrophysical outflow evolution, highlighting also the common traits that can characterize different stages of the activity of a compact object.

References

Barrère, P., Guilet, J., Raynaud, R., & Reboul-Salze, A. 2023, MNRAS, 526, L88
Barrère, P., Guilet, J., Reboul-Salze, A., Raynaud, R., & Janka, H. T. 2022, A&A, 668, A79
Berta, V., Mignone, A., Bugli, M., & Mattia, G. 2023, sub. to JCP
Brandenburg, A. & Subramanian, K. 2005, Phys. Rep., 417, 1
Bucciantini, N. & Del Zanna, L. 2013, MNRAS, 428, 71
Bugli, M., Del Zanna, L., & Bucciantini, N. 2014, MNRAS, 440, L41
Bugli, M., Guilet, J., Foglizzo, T., & Obergaulinger, M. 2023, MNRAS, 520, 5622
Bugli, M., Guilet, J., & Obergaulinger, M. 2021, MNRAS, 507, 443
Bugli, M., Guilet, J., Obergaulinger, M., Cerdá-Durán, P., & Aloy, M. Á. 2020, MNRAS, 492, 58
Del Zanna, L., Tomei, N., Franceschetti, K., Bugli, M., & Bucciantini, N. 2022, Fluidika, 7, 87
Guilet, J., Reboul-Salze, A., Raynaud, R., Bugli, M., & Gallet, B. 2022, MNRAS
Mattia, G., Del Zanna, L., Bugli, M., et al. 2023, arXiv e-prints, arXiv:2308.09477
Mattia, G. & Fendt, C. 2020, ApJ, 900, 59
Mattia, G. & Fendt, C. 2022, ApJ, 935, 22
Porth, O., Chatterjee, K., Narayan, R., et al. 2019, ApJS, 243, 26
Raynaud, R., Cerdá-Durán, P., & Guilet, J. 2022, MNRAS, 509, 3410
Raynaud, R., Guilet, J., Janka, H.-T., & Gastine, T. 2020, Science Advances, 6, eaay2732
Reboul-Salze, A., Guilet, J., Raynaud, R., & Bugli, M. 2021, A&A, 645, A109
Reboul-Salze, A., Guilet, J., Raynaud, R., & Bugli, M. 2022, A&A, 667, A94
Tomei, N., Del Zanna, L., Bugli, M., & Bucciantini, N. 2020, MNRAS, 491, 2346
Tomei, N., Del Zanna, L., Bugli, M., & Bucciantini, N. 2021, Universe, 7, 259

Session S04

Open Science in Astronomy

SF2A 2023
M. N'Diaye, A. Siebert, N. Lagarde, O. Venot, K. Baillié, M. Béthermin, E. Lagadec, J. Malzac, J. Richard (eds)

OPEN SOLAR DATA, DATA PRODUCTS, AND TOOLS AT MEDOC

E. Buchlin[1], S. Caminade[1], S. Parenti[1], B. Perri[1,2], F. Auchère[1], N. Traoré[3], K. Ashkar[1] and N. Dufourg[4]

Abstract. MEDOC (Multi-Experiment Data and Operation Centre), initially created as a European data and operation centre for the SoHO mission, has grown with data from other solar physics space missions, from STEREO to SDO, and now Solar Orbiter. In addition to observational data, MEDOC also provides data products derived from observations (maps, catalogues...), tools for data analysis and interpretation, and numerical simulation results. We present the current and future MEDOC interfaces, including Application Programming Interfaces (APIs) and Virtual Observatory (VO) services, data formats, implementation of Digital Object Identifier (DOIs), and how they contribute making MEDOC data FAIR (Findable, Accessible, Interoperable, and Reusable).

Keywords: open data, archives, interfaces, tools, heliophysics

1 Introduction

The main scientific objectives of solar physics concern the physical mechanisms behind the Sun's internal structure, its magnetism, its atmosphere (in particular the corona) and its wind, as well as their variability. In addition, scientific understanding of these phenomena has applications for space weather, which seeks to understand how they can affect the Earth and human activities, and to anticipate them in order to mitigate their adverse effects.

The complexity of these phenomena, involving many physical fields and many temporal and spatial scales, requires the coordinated use of numerous datasets, covering long periods at high cadence, including measurements of different physical quantities, measurements covering several wavelength ranges, wide field of view observations and others at high resolution. Scientific data centres have an essential role to play in the data life cycle, by allowing the scientific community making the most of these data and exploiting them for optimal scientific return, thanks to their adhesion to the FAIR principles* for Findable, Accessible, Interoperable, and Reusable data and metadata.

MEDOC† (Multi-Experiment Data and Operations Centre) is a data and operations centre for space solar physics, set up in 1996 at the Institut d'Astrophysique Spatiale (IAS) by CNES and CNRS/INSU with the support of the Université Paris-Sud (now Université Paris-Saclay), for the ESA/NASA SoHO mission. Since then, it has received data from other missions and developed numerous value-added products and services. MEDOC's objective is to serve the solar physics and heliosphere scientific community by supplying data, tools, and services, and carrying out scientific operations for space missions in the discipline. MEDOC works in collaboration with the other French data centers and observations services (CNRS/INSU AA-ANO5 and/or ANO6) in heliophysics: CDPP (in-situ measurements), 3SOLEIL (ground-based observations), APIS, MASER, CLIMSO, and STORMS.

[1] Université Paris-Saclay, CNRS, Institut d'astrophysique spatiale, 91405, Orsay, France
[2] Dept. d'Astrophysique/AIM, CEA/IRFU, CNRS/INSU, Université Paris et Paris-Saclay, 91191 Gif-sur-Yvette Cedex, France
[3] DSI Group, Paris, France
[4] CNES, Toulouse
*https://www.go-fair.org/fair-principles/
†http://medoc.ias.u-psud.fr

© Société Française d'Astronomie et d'Astrophysique (SF2A) 2023

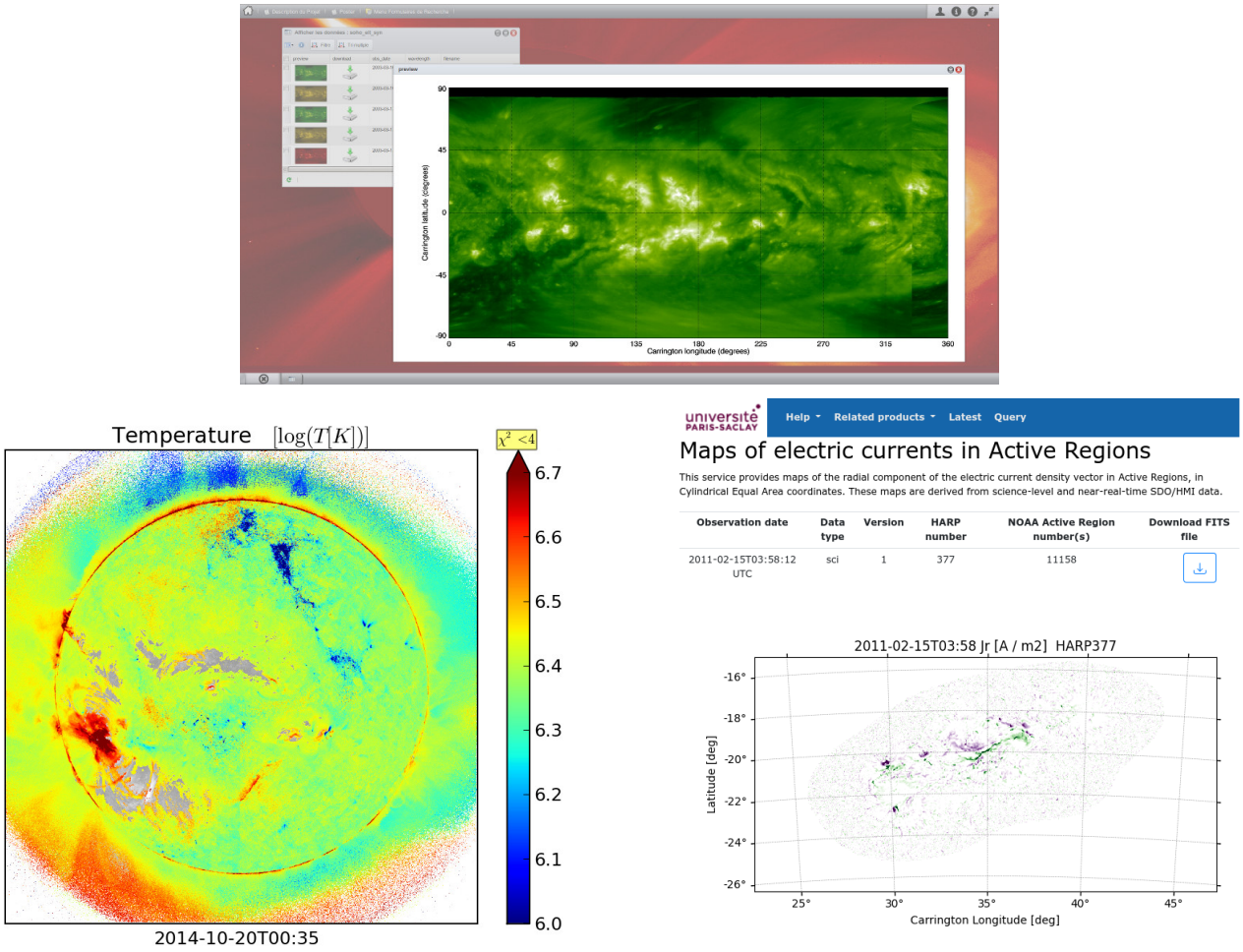

Fig. 1. Examples of derived data products at MEDOC: SoHO/EIT synchronous synoptic maps (top), temperature map of the corona (bottom left), and electric currents in active regions (bottom right). The latter is one of the four products provided by MEDOC to the ESA Space Weather portal.

2 MEDOC observation data and derived data products

MEDOC hosts data from SoHO (1995–), STEREO/SECCHI (2006–), SDO (2010–), TRACE (1998–2010) and other missions, for a total of more than 900 TB. It is also the main mission archive for the CNES PICARD mission (2010–2014), and will include Solar Orbiter data (2020–). From SoHO (1995), almost all solar physics data from space missions are open, with a proprietary period of no more than 3 to 6 months (if any) after telemetry reception, and this proved to be very useful for multi-instrument studies and collaboration. In the heliophysics community, reluctance to this policy, due either to fears about being scooped or to concerns about data quality, exists but is limited.

MEDOC also provides value-added, derived data products, that are computed from observational data stored at MEDOC, such as movies, spectral atlases, catalogs, maps of the thermal structure of the corona and of electric currents in active regions, synchronous synoptic maps of the photosphere and corona (see Fig. 1). Some of these are computed several times per day, just a few hours after the observation itself.

3 Interfaces for data access

The main web interface to data and derived data products is provided by the SiTools2 software developed for CNES (2010–2017) by the AKKA company, based on Java and ExtJS technologies (see Fig. 2). We have developed IDL and Python clients for the SiTools2 REpresentational State Transfer (REST) API, that can be used to analyse large datasets by scripts.

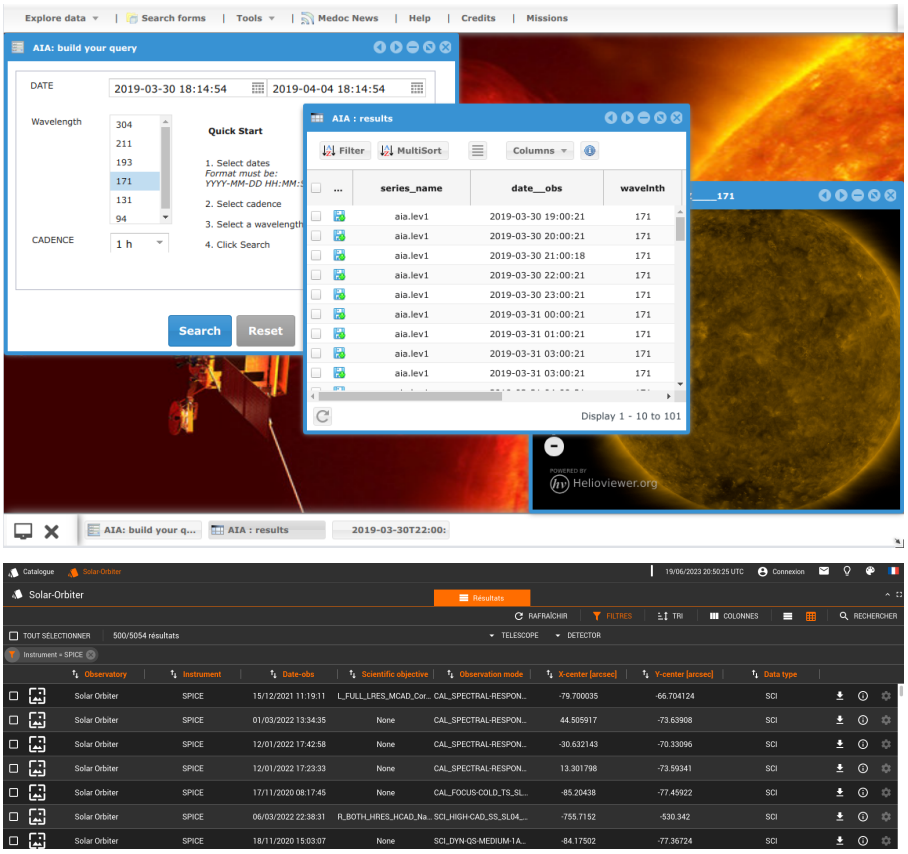

Fig. 2. Top: SiTools2 interface at MEDOC. Bottom: Solar Orbiter data in the current status of the REGARDS interface at MEDOC.

Since 2017, the CS company is developing REGARDS for CNES, as a successor of both SiTools2 and SIPAD (used in particular at CDPP). REGARDS has been installed at MEDOC, and several new functionalities had to be developed to adapt it to the local data archive context. REGARDS configuration and ingestion of Solar Orbiter data and other MEDOC datasets (see Fig. 2) are still ongoing (SDO data have hundreds of millions of records). As for SiTools2, MEDOC has developed a Python client for the REGARDS API, and REGARDS also provides an OpenSearch interface.

Some MEDOC-specific derived data products are also provided through a Virtual Observatory (VO) API with the EuroPlanet Table Access Protocol (EPN-TAP), thanks to a DaCHS server. These products have then been made available through several Virtual Observatories, such as VESPA (Virtual European Solar and Planetary Access, Erard et al. 2018, EuroPlanet 2024 Research Infrastructure) and Solar-VO (SOLARNET H2020 project).

Four products are provided to the ESA Space Weather Portal[‡], including web pages with latest data and query forms to the archive, and a custom API. By ESA request, the web page and API had to be protected by the ESA single-sign-on system, but registration is open to everyone. All datasets have a Space Physics Archive Search and Extract (SPASE, Roberts et al. 2018) description file, which has been submitted to ESA.

Finally, MEDOC hosts data output from some numerical simulations runs: solar wind profiles (hydrodynamic models from LPP and LESIA laboratories), a solar eruption (3D MHD, also from LPP and LESIA), and the Solar wind with cosmic rays scattering (3D MHD, from AIM laboratory). The custom web pages hosting these results are planned to be migrated to a new Galactica [§] node; Galactica is built following the International Virtual Observatory (IVOA) Theory Data Model.

[‡]`https://swe.ssa.esa.int/`
[§]`http://www.galactica-simulations.eu/db/`

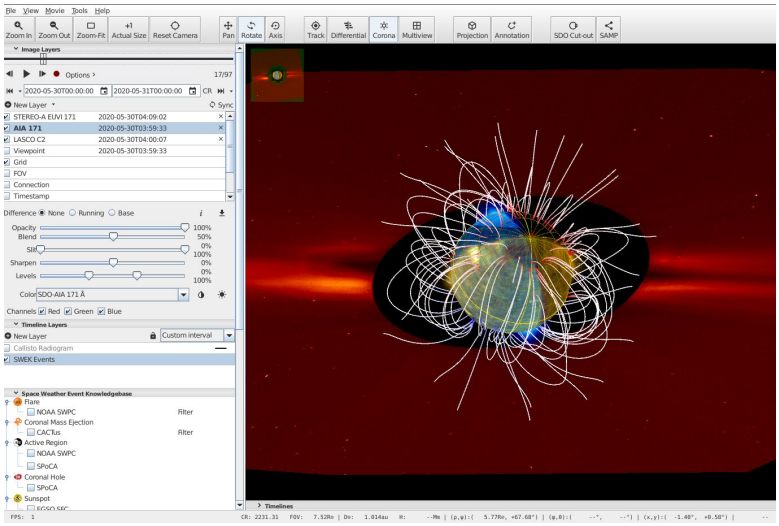

Fig. 3. HelioViewer Java client (JHelioViewer) with data from the MEDOC server, including coronal observations from several viewpoints, coronagraphic data, and magnetic field lines from a Potential Field Source Surface (PFSS) extrapolation.

4 Data exploration and visualization

The large data volumes available in heliophysics, with multi-scale data and an important time variability, make it very useful to have dedicated tools for multi-instrument data exploration and visualization. This is why ESA and NASA have jointly developed the HelioViewer system, including a JPEG 2000 Interactive Protocol (JPIP) server, and web and Java clients (among other clients developed by the scientific community); see Fig. 3 and Müller et al. (2017). MEDOC hosts a server instance, with a full mirror of the data (127 TB). The Java client has a Simple Application Messaging Protocol (SAMP) interface, allowing for example users to get FITS data directly from the ESA Solar Orbiter archive, and to combine them with other data in HelioViewer. A HAPI (Heliophysics data API, Weigel et al. 2021) functionality is in development, for the servers and clients, to provide a better way of exchanging information about data availability.

5 Conclusion

MEDOC provides open data and tools for the solar physics, heliophysics, and space weather communities. Data are using standard file formats (mainly FITS), and efforts are made to provide APIs and complete and useful metadata. Most datasets also have Digital Object Identifiers (DOIs), for their persistent identification. Efforts are made to adopt standards (in particular the IVOA ones), although much work is still to be done in the case of tools that are not fully compliant with these standards yet.

References

Erard, S., Cecconi, B., Le Sidaner, P., et al. 2018, Planet. Space Sci., 150, 65

Müller, D., Nicula, B., Felix, S., et al. 2017, A&A, 606, A10

Roberts, D. A., Thieman, J., Génot, V., et al. 2018, Space Weather, 16, 1899

Weigel, R. S., Vandegriff, J., Faden, J., et al. 2021, Journal of Geophysical Research (Space Physics), 126, e29534

SF2A 2023
M. N'Diaye, A. Siebert, N. Lagarde, O. Venot, K. Baillié, M. Béthermin, E. Lagadec, J. Malzac, J. Richard (eds)

OPEN SCIENCE AND ASTRONOMY

F. Genova[1]

Abstract. Open Science is rapidly developing, with a strong political support in France and in more and more other countries, as well as at the European and international levels. Many disciplinary fields are joining the endeavour. Astronomy has been one of the early pioneers of Open Science. Astronomers from all around the world are using data and tools provided by others in their daily research work, thanks to the Virtual Observatory data sharing framework and to the dedicated work of the data and service providers. It is essential for us to track the ongoing developments and to fully participate in them, to ensure that astronomy continues to be recognized as one of the important components of the rapidly evolving Open Science landscape. This paper discusses several hot topics which have been tackled by the Research Data Alliance, and how they interface with the way astronomy implements Open Science in its field, namely, the Global Open Research Commons, the evaluation of FAIR (Findable, Accessible, Interoperable, Reusable), and the necessary evolution of research evaluation.

Keywords: Open Science, Astronomy, Evaluation of research, Global Open Research Commons, FAIR,

1 Introduction

Astronomy has been a pioneer of Open Science and FAIR, with the FITS standard, first described by Wells, Greisen & Harten (1981), which links data together with the metadata enabling to reuse it, and the standards developed and maintained by the *International Virtual Observatory Alliance* (IVOA, `https://www.ivoa.net/`), which started in 2002, enabling astronomers to Find, Access and Interoperate data. One can also remind that the *Centre de Données astronomiques de Strasbourg* (Strasbourg astronomical Data Centre - CDS) was created in 1972 to serve the international astronomical community, and that the data from the *International Ultraviolet Explorer* (IUE, which was active from 1978 to 1996) had been downloaded in average five times already in 1994 (Wamsteker & Griffin 1995).

Thanks to the hard work of the data and tool providers and of the IVOA community, most data produced in astronomy are available in the Virtual Observatory data sharing framework, which enables the world-wide community to access and use it for their research. To remain relevant, the astronomical disciplinary data sharing framework has to continue to evolve because the scientific, technical, and political contexts in which it operates evolve.

This paper summarizes the current evolution of the Open Science context and the way astronomy has been tackling the data aspects of Open Science over the years, long before Open Science gained its prominent position in the political scientific landscape. Three among the challenges astronomy has to face in the current landscape will then be discussed.

2 The fast-evolving Open Science context

Open Science, which includes open publication, open data and now open software, has been a hot topic on the political agenda in France and at the European and international levels for a while. In France the *Loi pour une République numérique** (Law for a digital Republic), was published in 2016 with the aim to regulate the circulation of data and knowledge. The ministry in charge of research, currently called *Ministère de l'Enseignement Supérieur et de la Recherche* (MESR - Ministry of Higher Education and Research) is engaged in the *Plan*

[1] Université de Strasbourg, CNRS, Observatoire astronomique de Strasbourg, UMR 7550, 67000 Strasbourg, France
*`https://www.gouvernement.fr/action/pour-une-republique-numerique`

© Société Française d'Astronomie et d'Astrophysique (SF2A) 2023

national pour la Science Ouverte (PNSO - National Plan for Open Science). The initial version of the Plan[†], published in 2018, was built around three pillars: generalize open access to publications; structure research data and make it available through open access; and be part of a sustainable European and international open science dynamic. Its second version[‡], published in 2021, includes source codes produced by science and the necessary transformation of practices among its four paths: generalising open access to publications; structuring, sharing and opening up research data; opening up and promoting source code produced by research; and transforming practices to make open science the default principle.

The MESR implemented the *Comité pour la Science Ouverte* (CoSO - Committee for Open Science)[§] in 2018. The Recherche Data Gouv (`https://recherche.data.gouv.fr/en`) ecosystem was inaugurated in July 2022. It includes modules to support research teams on all issues linked to data, namely local data management clusters (*Ateliers de la Données*), thematic reference centres, resource centres and institutional reference centres, a repository to deposit and disseminate data (when no disciplinary repository is available) and a registry to search for data in Recherche Data Gouv and other repositories.

The European Union has also been engaged for a while in supporting Open Science. Open Science[¶] is an item of the *Our digital future* chapter of its Research and Innovation Strategy 2020-2024: "Open science is a policy priority for the European Commission and the standard method of working under its research and innovation funding programmes as it improves the quality, efficiency and responsiveness of research." The ambitions of the European Union's Open Science policy are open data with a reference to FAIR; the European Open Science Cloud (EOSC); new generation metrics; mutual learning exercise on open science – altimetrics and rewards; future of scholarly communication; rewards; research integrity and reproducibility of research results; education and skills; and citizen science.

There are also notable activities at the international level in support to Open Science, with strong, repeated statements of the G7/G8 Ministers of Research[‖], for instance this recent one, included in the declaration from their meeting held in Sendai in May 2023: "The G7 will collaborate in expanding open science with equitable dissemination of scientific knowledge and publicly funded research outputs including research data and scholarly publications in line with the Findable, Accessible, Interoperable, and Reusable (FAIR) principles." The G7 Open Science Working Group was established in 2016. The OECD published in 2006 its pioneering *Recommendations on access to research data from public funding* and updated it in 2021 (`https://www.oecd.org/sti/inno/open-science.htm`). UNESCO also produced its *Recommendation for Open Science* in 2021 (`https://www.unesco.org/en/open-science`).

3 Astronomy and Open Science

Astronomy has been a pioneer in the data aspects of Open Science. Sharing astronomical data as widely as possible was required because astronomy relies on multi-wavelength, and now multi-messenger observations and performs statistical studies on large numbers of objects, and because astronomical objects can be variable on a wide range of time scales. It is also important to ensure the maximum possible return on the large investments in space and ground based telescopes by enabling their data to be reused as widely as possible.

Thanks to the IVOA standards and to the fact that they are used by the data and tool providers, astronomical data appears to its users as a single, global, multipolar data infrastructure. The infrastructure is open, anyone can publish a data resource in it or develop a tool using the data. The infrastructure, and thus the hard work required to make it happen, is hidden from the end users since it provides seamless access to data and the VO-enabled tools are interoperable.

Work is indeed required at the disciplinary level to make the most of Open Science: the knowledge of science needs and data resides there. This work has to be interfaced with the generic developments. For instance, the IVOA chose from the start to develop its Registry of Resources using the OAI-PMH standard and the Dublin Core with disciplinary extensions (Hanisch et al. 2007) as the basis for the resource metadata. These standards are widely used, and this enabled the IVOA Registry to be included in the EUDAT B2FIND

[†] `https://www.ouvrirlascience.fr/national-plan-for-open-science-4th-july-2018/`

[‡] `https://www.enseignementsup-recherche.gouv.fr/fr/le-plan-national-pour-la-science-ouverte-2021-2024-vers-une-generalisation-de-la-science-ouverte-en-48525`

[§] `https://www.ouvrirlascience.fr/the-committee-for-open-science/`

[¶] `https://research-and-innovation.ec.europa.eu/strategy/strategy-2020-2024/our-digital-future/open-science_en`

[‖] `https://www.ouvrirlascience.fr/les-ministres-de-la-recherche-et-de-la-technologie-du-g7-sengagent-en-faveur-de-la-science-ouverte/`

(https://b2find.eudat.eu/) registry with no major issue, a first step to ensure the visibility of VO-enabled resources in the EOSC.

Many disciplines are joining the Open Science endeavour, some with significant resources and in domains seen as societal priorities. Astronomy continues to update its disciplinary data sharing framework to respond to science needs and technical evolution. The SKA Organisation for instance joined the IVOA in 2022, and collaborations have been established to deal at best with multi-messenger astronomy. We have to make sure that we identify among the numerous developments linked to Open Science in the general context those that we have to follow and to tackle to ensure that we remain relevant. Three examples are discussed in the next section.

4 Challenges for Astronomy in the current Open Science landscape - Three examples

These three examples have been selected because the author has been involved both at the disciplinary level and with building the link with activities at the general level, in particular, but not only, in the framework of the Research Data Alliance (RDA, https://www.rd-alliance.org/). The RDA is a community-driven initiative, an international organisation with the mission to build the social and technical bridges that enable open sharing and re-use of data. Its activities are developed by the community organised in Interest Groups (IG), which are addressing a topic on the medium/long term, and Working Groups (WG) which have 18 months to prepare a Recommendation which will then be submitted to the community before endorsement by the RDA Council. In September 2023 there were more than 100 active RDA Groups tackling a large variety of subjects.

4.1 Astronomy among the Global Open Research Commons

One of the RDA Interest Groups is dealing with *Global Open Research Commons*"** (GORCs). "Commons" are defined as a global trusted ecosystem that provides seamless access to high quality interoperable research outputs and services. The IG is working to reach a shared understanding of what a "Commons" is in the research data space; what functionality, coverage and characteristics does such an initiative require and how this can be coordinated at a global level. The first IG output is a Typology of the essential elements in a Commons (Jones et al. 2023). The IG also set up a Working Group *GORC International Model*††, which recently produced a model or framework to describe Commons attributes. Its Version 1 (Leggott et al. 2023) was submitted for comments to the RDA community in September 2023.

The usual examples of GORCs are the European Open Science Cloud (EOSC), the Australian Research Data Commons or the African Open Science Platform. From the definition of a GORC, it seemed that the IVOA could apply to be recognized as one of them, but it is very different from the examples cited above, since it does not manage services per se, except its Registry of Resources which is provided by several of its partners, in implementations which harvest each other to ensure that their content is aligned. Participating in the WG activities enabled to test the idea and to propose the IVOA as a possible GORC. The WG organised a series of presentations of GORCs, to identify common elements which could appear in the model. The IVOA was the first to be presented, and the WG agreed that it was to be considered as a GORC. Its characteristics have been considered as examples in the definition of the model displayed in Version 1.

4.2 FAIR in Astronomy

By developing and maintaining the Virtual Observatory, astronomy has been providing its community with a rare global, operational framework enabling data sharing and interoperability. Our disciplinary data sharing framework has to be interfaced properly with the systems which are progressively being established at the general level. The key aspect to enable interoperability with the general level are the Registry of Resources and vocabularies.

The FAIR guiding principles encountered a remarkable success since their publication in 2016 (Wilkinson et al. 2016): they provided a simple way to define and check essential characteristics to be fulfilled to efficiently share data. This is evident when one compares them for instance to the properties identified in the OECD "Guiding Principles" in 2007: openness, flexibility, transparency, legal conformity, protection of intellectual

**https://www.rd-alliance.org/groups/global-open-research-commons-ig
††https://www.rd-alliance.org/groups/gorc-international-model-wg

property, formal responsibility, professionalism, interoperability, quality, security, efficiency, accountability, sustainability. This list is well thought and covers a large palette of key aspects of data sharing, but the FAIR guiding principles provide a subset of essential guidelines, as well as a powerful mnemonic.

The report *Six Recommendations for implementation of FAIR practice* produced by the FAIR in practice Task Force of the European Open Science Cloud FAIR working group (European Commission, Directorate-General for Research and Innovation 2020) offers six recommendations on how FAIR can be turned into practice: (1) Fund awareness-raising, training, education and community-specific support; (2) Fund development, adoption and maintenance of community standards, tools and infrastructure; (3) Incentivise development of community governance; (4) Translate FAIR guidelines for other digital objects; (5) Reward and recognise improvements of FAIR practice; (6) Develop and monitor adequate policies for FAIR data and research objects. The necessary evolution of evaluation of research cited in (5) will be discussed in the next Subsection. These recommendations strongly emphasise the importance of community standards, governance and support for FAIR to be turned into practice. This aligns perfectly with the way the astronomy community has been implementing FAIR, by setting up the IVOA for gathering the relevant community at the international level to ensure the governance, definition and maintenance of the standards.

Any astronomer anywhere one the world – providing that they have access to the internet – can Find, Access, Reuse and Interoperate VO-enabled data and tools. For astronomers astronomical data are thus FAIR for their own needs. This is not necessarily true when considering the criteria defined by the RDA FAIR Data Maturity Model WG (FAIR Data Maturity Model Working Group 2020). A study performed during the ESCAPE Cluster project by F. Genova, F. Bonnarel and M. Molinaro showed that we can live with the criteria. The Virtual Observatory enables some of them "for free" once it is implemented on top of the data holdings. But we also found that we have issues with the priority levels assigned to criteria. There is for instance no "Essential" criterion among the Interoperability ones, whereas for us Interoperability has been one of the key IVOA driving forces – the IVOA six-monthly meetings are even called *the IVOA Interoperability Meetings*. The priority levels have been chosen by the RDA community, and the low ranking reflects the fact that very few disciplines have Interoperability as a priority or have been able to achieve it. Find is a dynamic process for us, with the persistent identifier, which appears prominently among the criteria, only one among many parameters. Three of the Reuse criteria refer to licenses: "metadata includes information about the license under which the data can be reused" is deemed essential, "metadata refers to a standard reuse license" and "metadata refers to a machine-understandable reuse license" are deemed important. Not all astronomical data found in the VO will have a reuse license attached. The data are however widely reused, usage being based on disciplinary ethics: cite what you use.

The astronomical community has thus to work in particular on defining and attaching licenses to the data and metadata it shares. Also the Interoperability criteria cite "FAIR-compliant vocabularies", to be used for data and metadata. We have to follow the activities on-going to define what a FAIR-compliant vocabulary is, and make sure that the IVOA vocabularies are compliant.

Even if it is time consuming for the individuals involved, we have to ensure that the discipline is actively represented in the committees and projects which tackle the evaluation of FAIR, to make sure that our point of view, which is the point of view of a legacy disciplinary data sharing framework which enables advanced functionalities and is widely used by its world-wide community, is considered.

4.3 Astronomy and the necessary evolution of evaluation of research

The evolution of research evaluation from being mostly bibliographic index-based is – at last! – being recognized as a priority at the international, European, national, and institutional levels. One can of course cite DORA (`https://sfdora.org/`), the Declaration on Research Assessment, which is a decade old in 2023. The fact that it has been well understood for some time now that the evolution of research evaluation is indispensable to enable Open Science has been a strong incentive to prioritize it, in particular in France and at the level of the European Commission. It is fully included in the Transforming Practices path of the Second French Plan for Open Science, which highlights the issue in two of the three measures it recommends: "Develop and value open science skills throughout the educational and career pathways of students and research staff" and "Value open science and the diversity of scientific productions in the assessment of researchers, of projects and of universities and research performing organizations." Rewards are also discussed among the ambitions of the European Union's open science policy, and evaluation, incentives and rewards are cited in a number of other international reference documents on Open Science.

Astronomy evaluation committees have had to face the issue somehow forever, since the recognition of the

work done by the astronomers involved in conceptualizing astronomical instruments has not always been an easy endeavour, to say the least, whereas these instruments are essential to the practice of astronomy. The scientists involved in the data and code aspects of the discipline encountered the same problem in their careers when these profiles emerged thanks to the early adoption of computing and digital data sharing by the discipline.

A recent evolution is the establishment of the Coalition for Advancing Research Assessment (CoARA – `https://coara.eu`) in December 2022. CoARA gathers research performing organisations which agree to work together to implement the changes described in the *Agreement for Reforming Research Assessment*. "The Agreement, Based on 10 commitments, establishes a common direction for research assessment reform, while respecting organisations' autonomy." As of 21 September 2023, 539 organisations have joined the Coalition, including more than 40 based in France, among which research organisations such as the CNRS, a number of Universities, the *Agence Nationale de la Recherche* (ANR) and the *Haut Conseil de l'évaluation de la recherche et de l'enseignement supérieur* (HCERES).

The RDA also recently set up an Interest Group to identify its role and value in the domain, the RDA Evaluation of Research Interest Group (`https://www.rd-alliance.org/groups/evaluation-research-ig`). "The Interest Group (IG) will be a value-added contribution to the organisations, including research organisations and universities, funders and policy makers who use the RDA as an international, neutral forum: it will enable them to discuss their proposals on the evolution of research evaluation with the (RDA) community, whose comments will help improve these proposals and make them more relevant and applicable. It will also be a high value-added contribution to the community of RDA data experts, who will benefit from better recognition of their activities. The IG will bring their voice to the attention of the organisations, funders and policy makers who participate in the RDA."

The author's experience from years of participation in and chairpersonship of disciplinary evaluation committee shows that the evolution of evaluation of research from being mostly bibliographic index-based is extremely difficult to put into practice, even in a discipline like astronomy which relies on research infrastructures, and which has a significant fraction of its research staff belonging to the *Corps des Astronomes et Physiciens*, whose missions include the so-called *tâches de service*(functional duties). The diversity of **research** tasks, products and profiles is not always fully recognized by the *Conseil National des Astronomes et Physiciens* and the CNRS committee in charge of evaluating astronomy. Legitimate research activities are not only those which produce publications. One still has to fully base evaluation on impact and not on bibliometric indicators. The evolution of science evaluation in astronomy, not only on the aspects linked to Open Science, is still a challenge, even when CNRS is fully involved in the process and is producing very relevant guidelines, since its requires a deep cultural evolution of the whole community. This should be a topic for the next *Exercice de Prospective* (Long Range Planning Exercise) of the discipline.

5 Conclusion

The examples discussed in these proceedings underline only a few of the challenges faced by the discipline in the fast-evolving Open Science context. We have to follow and participate in the on-going developments at all levels, institutional (in CNRS and in our Universities), national, European and international. In France for instance, it is very important to participate in the activities driven by the Committee for Open Science and engage in the Recherche Data Gouv endeavour. At the international level we have to make sure that IVOA is known and recognized, and bring key new topics to the IVOA so that its data sharing framework is properly interfaced with the general framework which is progressively being set up. Participation in EOSC and evaluation and adoption of the new possibilities offered by Artificial Intelligence when they can fit our needs are also among the key challenges linked to the position of astronomy in the Open Science context.

References

European Commission, Directorate-General for Research and Innovation 2020, Six Recommendations for implementation of FAIR practice by the FAIR in practice task force of the European open science cloud FAIR working group, Publications Office. https://data.europa.eu/doi/10.2777/986252

FAIR Data Maturity Model Working Group 2020, FAIR Data Maturity Model: specification and guidelines, Research Data Alliance. `https://doi.org/10.15497/RDA00050`

Hanisch, R., the IVOA Resource Registry Working Group, the NVO Metadata Working Group 2007, Resource metadata for the Virtual Observatory Version 1.12, International Virtual Observatory Alliance. `https://doi.org/10.5479/ADS/bib/2007ivoa.spec.0302H`

Jones, S., Leggott, M., Lopez Albacete, et al. 2023, GORC IG: Typology and Definitions (Version 1.01), Research Data Alliance. https://doi.org/10.15497/RDA00087

Leggott, M., Treloar, A., Woodford, C. J., et al. 2023, The Global Open Research Commons International Model, Version 1, Research Data Alliance. https://doi.org/10.15497/RDA00097

Wamsteker, W., & Griffin, R.E.M. 1995, Ap&SS, 228, 385

Wells, D.C., Greisen, E.W., & Harten, R.H. 1981, A&AS, 44, 363

Wilkinson, M.D., Dumontier, M., IJsbrand, J.A., et al. 2016, Scientific Data, 3, 16001

Session S05

Bien-être en astrophysique

SF2A 2023
M. N'Diaye, A. Siebert, N. Lagarde, O. Venot, K. Baillié, M. Béthermin, E. Lagadec, J. Malzac, J. Richard (eds)

IMPROVING WELL-BEING IN ASTROPHYSICS RESEARCH

N. A. Webb[1], A. Allouch[2], C. Bot[3], N. Donati[4], J. Girardat[5] and S. Mei[6]

Abstract. Following the *Well-being in astrophysics* survey conducted in France in early 2021, to establish how astrophysics researchers experience their careers (Webb et al. 2021), we organised another national workshop to help promote well-being in (French) astrophysics research. Thanks to the participation of three professionals (sociologists, psychologists), we covered areas such as improving social interactions, identifying and avoiding burn-out, understanding and negotiating the ever present competition in academia, as well as including a discussion on the race to publish. We summarise here some of the important points discussed during the workshop.

Keywords: careers, well-being

1 Introduction

Thanks to the survey *Well-being in astrophysics*, conducted in France in early 2021 to establish how French astrophysics researchers experience their careers (Webb et al. 2021), and subsequent workshops, it has become clear that there are several areas that can be improved to enhance well-being in French astrophysics. Amongst these are improving social interactions between colleagues, with or without hierarchical relationships, which in some cases are not always optimal. Section 2 describes the dynamics of different relationships and give some examples of how to improve them. Section 3 discusses the subject of the ever present competition in academia, which manifests itself throughout a career in research, from obtaining a PhD/post-doc/permanent positions or even a promotion, to the competition for grants/funding or even telescope time, and is considerable source for anxiety, especially in the younger generations. Understanding the role of competition is important in overcoming the harm that in can cause. Section 4 considers the stress associated with the (perceived) pressure to publish. Recently Park et al. (2022) published a paper suggesting that in part due to the pressure to publish, papers are becoming less *disruptive* and thus less innovative, with fewer major break-throughs. We explore the role of publications and how to proliferate innovation and avoid the race to publish. Finally Section 5 covers other sources of stress and the downward spiral that can lead to a burnout. We discuss the origin of burnout, identify the symptoms of burn-out, and examine ways that scientist can avoid it.

2 Social interactions

Positive interactions with our peers are very important. Firstly, they allow us to collaborate and work together in a profitable fashion, but they are also important for our mental health and well-being. Research is a field which places high demands on those who work in the domain, which in turn results in a high mental load. In general, researchers are high achievers, doing everything they can to do well, but which can lead exhaustion and suffering with a poor work-life balance.

Each and everyone of us have needs (Rojzman et al. 2015). We need to feel safe, to feel a part of society, to be appreciated and to have a sense of direction or a feeling of personal achievement. If these needs are not

[1] IRAP, Université de Toulouse, CNRS, CNES, 9 avenue du Colonel Roche, 31028 Toulouse, France
[2] Université de Picardie Jules Verne, CURAPP-ESS/CNRS, 10, Placette Lafleur BP 2716 80027 Amiens, France
[3] CDS, Université de Strasbourg, CNRS, Observatoire astronomique de Strasbourg, UMR 7550, 67000 Strasbourg, France
[4] ContactÜ, Rome, Italy
[5] Rue de la Musau, 67100 Strasbourg, France
[6] Université de Paris, CNRS, Astroparticule et Cosmologie, F-75013 Paris, France

© Société Française d'Astronomie et d'Astrophysique (SF2A) 2023

met, it can lead to anxiety or apprehension of being attacked, rejected, judged or even made to feel guilty. This can lead us to behave poorly with others in an aim to protecting ourselves, by rejecting colleagues, humiliating them, guilt-tripping them or generally treating them badly. These destructive reactions can also be applied to ourselves when neither our needs nor our fears are being recognized and addressed. This interplay between needs, responses and actions has been well summarised by Rojzman et al. (2015), see also Fig. 1.

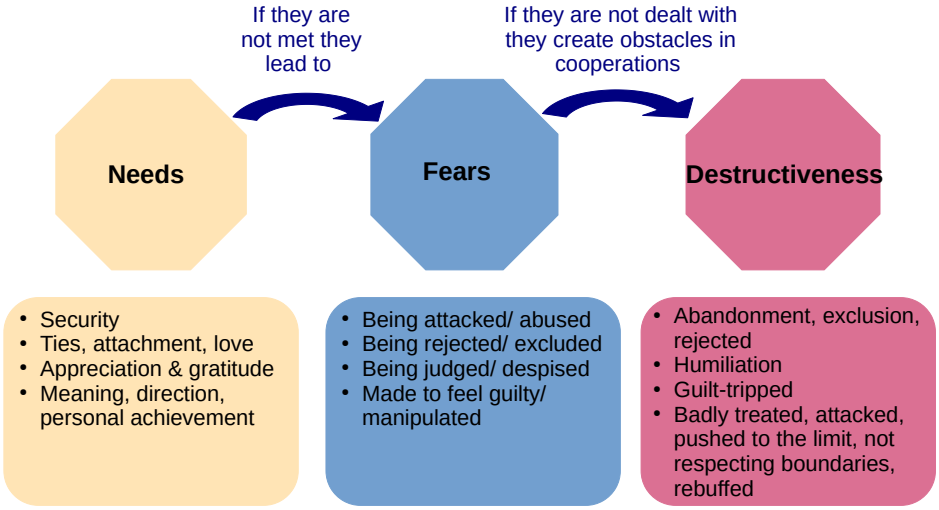

Fig. 1. Figure showing human needs, their fears if their needs are not met and the cruelty that can result if the fears are not dealt with, adapted from Rojzman et al. (2015).

Following a study of linguistic data from 200 tweets from each of nearly 130,000 Twitter users across more than 3,500 occupations, Armitage (2020) showed that researchers are less agreable than people from other professions. In order to improve our colleagues disposition and therefore improve interactions, ideally we should ensure that we acknowledge their contributions, appreciate their work and be vigilant that they are included, to ensure that their needs are being met, reducing anxiety and thus unpleasant behaviour.

During this session, a large part was dedicated to a practical session, which the vast majority of the participants found very effective. This was carried out in pairs, where participants were asked to discuss six questions, the first of which helped to serve as a reminder about what we love about our job. We were asked to consider on a personal level : What do we care most about about in our job? What is it that feeds our desire to work? What drives us or stimulates us or fascinates us in this job? What is the one thing that really speaks to us in this job? Afterwards we were asked to reflect on a moment during our professional lives that caused : intense stress or anxiety; complete exhaustion; utter helplessness. We were then asked to discuss what we felt like at that moment, what the effects were on us and what we said to ourselves. Following that we examined our fears and our apprehensions. Subsequently we were encouraged to reflect on what we needed at that moment to get through the event, what did we feel that we were missing to traverse the difficulty. We were then invited to reflect on the interplay between our needs, fears and our behaviour. Finally, we were asked to contemplate what we needed to help us at that moment. The exercise revealed, in an effective manner, the link between our emotions and behaviour, as well as allowing the participants to speak about subjects that are rarely discussed, which was also felt to be highly beneficial, see Section 3.

It should be noted that social therapy can help increase creativity and productivity and encourage collaborative efforts, important in avoiding stress related to academic careers, see Sections 3, 4 and 5. It can also help to encourage learning by example, decrease feelings of loneliness and isolation and reduce stress and anxiety. This is important for well-being and improving work output and therefore social therapy sessions maybe extremely beneficial in the workplace.

3 Competition in (astrophysics) research

Competition, real or perceived, is omni-present throughout the life of an academic. Competition exists in trying to get the highest grades, to get into the best schools, onto popular courses, in getting a PhD position and then getting post-doctoral jobs and then permanent positions. It exists well beyond that, in getting grants,

promotions, telescope/computing time, and even in getting our talks chosen to be presented at a conference, having the highest impact research and obtaining awards. A competition based system should logically lead to the best people being awarded grants or jobs. Competition can also help to prevent confirmation bias (Fang & Casadevall 2015), as different research teams work on similar research, thus all working to (dis)prove a hypothesis. It can also drive us to invest extra effort that we would not have done without the competition, and thus improve standards (e.g. DiMenichi & Tricomi 2015). But whilst competition can be a good thing, there are also drawbacks. Children rapidly perceive adult's anxiety when the children are faced with competition in school, and so they learn this anxious response to competition. Without supervision, academic competition can lead to aggression, anxiety, and frustration. We may become unduly stressed about losing status among peers, which can lead to undue focus on winning, extreme disappointment, and even low self-esteem. This competition can also lead to secrecy around results for fear of being scooped and scientists reluctant to share their work, impeding scientific progress (see e.g. Fang & Casadevall 2015, and references therein). Academic competitivity can also lead to competition to publish (see Sec. 4), reducing creativity and/or foster scientific misconduct as a result of trying to publish ever faster (e.g. Fang & Casadevall 2015).

So what can be done to help scientists overcome the stress related to competition? Leslie (2019) suggests that we should move towards collaboration rather than focussing constantly on competition. Big collaborations have produced some of the highest quality research, based on citations (e.g. Leslie 2019) and there have been calls for the Nobel Prize to be altered so that teams of researchers can be recognised, rather than the current maximum of three scientists, to take into account the way that research is moving towards large collaborations (Leslie 2019). In this way some of the stress associated with research is reduced, see Section 5, still allowing high class research to be done. Other things that can help overcome competition related stress is to talk about it, normalising it and making it easier to break-away from negative thoughts related to competition. This can also help us to create a connection with our peers (see Section 5). Finally scientists should provide support to their colleagues to help prepare for competition, encouraging the candidate and providing information on how to succeed, to ease the process and allow them to be more successful.

4 The publication race

One area of (astrophysics) research that can cause significant stress is the race to publish. Increasingly, publication rate has become one of the measures to evaluate researchers and projects, which can be at the origin of the pressure felt by researchers. However, not only does this lead to a very high volume of papers published per year, and therefore a large body of literature to keep up with, adding to the general research workload, it has been proposed that this pressure to publish may be inhibiting innovation (Park et al. 2022). The authors carried out a study using data from 45 million papers and 3.9 million patents from six large-scale datasets spanning six decades. The study used a new quantitative metric—the CD index—that characterises how papers and patents change networks of citations. They found that papers and patents are increasingly less likely to break with the past in ways that push science and technology in new directions. Park et al. (2022) state that this decline represents a shift in science and technology, that reinforces concerns about slowing innovative activity. They attribute this trend in part to reliance on a narrower set of existing knowledge, due to difficulties in following the vast number of papers published today. Whilst this paper has received some criticism concerning the metric and the methods, they are not the first people to address the problem and other authors have suggested that the competitivity in science can also reduce creativity e.g. Fang & Casadevall (2015). Park et al. (2022) also propose some interesting recommendations to improve creativity. They suggest that researchers should be encouraged to read widely, therefore sufficient time should be allocated to keep up with the rapidly expanding knowledge frontier, so universities (and other organisations) should forgo the focus on quantity, and instead reward research quality. Further, agencies should invest in riskier and longer-term individual awards that support careers and not specific projects, thus moving away from the publish or perish culture.

Whilst these actions maybe difficult to put into place in their entirety, it should be noted that in France the *High Council for the Evaluation of Research and Higher Education* (HCERES), the *French National Agency for Research* (ANR), the *Presidents of the French Universities* (CPU) and the *National Centre for Scientific Research* (CNRS) have all signed the San Francisco declaration (Declaration On Research Assessment - DORA) which states that there are many ways to contribute to our knowledge base and signatories are comitted to evaluating the quality and impact of new knowledge. This means that the publication of code, databases, etc as well as the contribution to community activities and scientific integrity should also be used in the evaluation of scientists. This means that work that is already being done will now be valued and it may help to relieve

some of the pressure felt and in some way improve the quality and impact of new science. Further, as noted in Sec. 3, a move towards collaborative science may also hold the key to reducing the publish or perish culture.

5 Burnout and how to avoid it

Burnout is rife in academia. In a recent online *Nature* poll, which ran from 7 to 15 November 2022, 75% of 1748 researchers from all career stages that replied to the survey, said that they had reduced their work hours since March 2020 (Forrester 2023). Of these 1311, 67% stated that the reason for this cut-back was that they felt burnt out. This amounts to 50% of the researchers responding to the survey. Whilst there are obviously biasses in who replied to the survey, this is a significant proportion of researchers.

Burnout is a state of exhaustion that affects you emotionally, physically, and mentally. Its origin lies in excessive and prolonged stress and can happen when you feel overwhelmed, emotionally drained, and unable to meet continual demands. If the stress continues, you can lose the interest and motivation that led you to take on the task initially. Therefore it is important to tackle the initial stress, with an aim to avoiding burnout.

There are numerous causes of stress, common ones are work, finances, relationships, parenting and day-to-day inconveniences. Stress can trigger the body's response to a perceived threat or danger, known as the fight-or-flight response. This causes hormones like adrenaline and cortisol to be released, which lead to changes in nervous functions, giving the body a burst of energy and strength. Once the stress is removed, the body returns to functionning normally, via the relaxation response. However, if the stress does not go away, remaining in the fight-or-flight state can cause damage to the body. Further, stress can also cause us to take up unhealthy habits, that could have a negative effect on health as well.

Stress affects people differently. It can cause behavioural changes in some, cognitive differences in others, emotional changes, physical effects or all of these, with the manifestation of many different symptoms (American Psychiatric Association 2013), indicated in the following paragraphs. Behavioral changes that can be signs of stress include :

- changes in eating
- clumsiness/forgetfulness
- not taking breaks
- working long hours
- functioning on 'auto-pilot'
- absenteeism
- withdrawal from others
- indecisiveness
- enhances alcohol/nicotine/ coffee intake
- temper outbursts
- avoiding things
- presenteeism
- rushing around
- over-checking
- reduced productivity
- poor self-care
- procrastinating
- reduced focus

Cognitive differences that can be signs of stress include 'thoughts that race', worrying, hopelessness, being over critical and over-ruminating. Typical thoughts include, "This is too much", "I can't cope", "They'll think badly of me", "This won't change", "I should be able to cope", "I must get this done", "I haven't got time".

Emotional changes that can be signs of stress include:

- irritability
- restlessness
- feeling overwhelmed
- unhappiness
- mood swings
- anxiousness
- often upset
- feeling overwhelmed
- feeling 'stuck in a rut'
- resentfulness
- tension in the body
- angriness
- feeling demotivated
- becoming disintrested

Physical signs of stress include:

- headaches
- nausea
- breathlessness
- blurred vision
- lump in your throat
- change in appetite
- muscle tension
- sweating
- shakiness
- dry mouth
- tingling feelings
- aches
- digestive problems
- diziness
- heart palpitations
- cold
- numbness
- pains

Stress can be either external, e.g. due to demands from work, see Fig. 2, or internal, when we become proccupied with thoughts such as memories, thoughts about the future, ideas about oneself, etc, see Fig. 3. These stresses have one of two responses, either 'eustress', which uses psychological and physical resources so that an objective can be reached and 'distress' that continues to use the resources even after the stress goes away, until the resources are depleted, leaving the individual exhausted (Lazarus 1966).

Fig. 2. Figure showing different types of external stressors, credit: contactÜ (`https://www.contactu.it/`).

Fig. 3. Figure showing different types of internal stressors, credit: contactÜ (`https://www.contactu.it/`).

Work-related stress is becoming more widely recognised, where many of the external stressors, see Fig. 2, can be present in the work place. Further, academics are often perfectionists (Levine 2008), a personality trait that can also favour stress, see Fig. 3. Hyper competitive work cultures (see Sec. 3), a lack of social support and a fear of losing ones job can make us feel like we need to sacrifice our well-being to succeed. This can lead to a vicious circle where work pressure, emotional demands and work-home conflicts can lead to exhaustion, which will reduce performance and our ability to rely on resources from our job (such as colleague support, team cohesion, supervisor support, etc) and increase our cynicism and therefore further decrease our job performance. Identifying your personal resources in work is essential to keeping a good balance. Identifying colleagues that you feel provide support and keeping regular contact with them, either by meeting for coffee, lunch or afterwork, or participating in team cohesion activities, or by reaching out to a supervisor, are all good resources to draw on to fight against stress caused from work, for example.

As we showed in Webb et al. (2021), 199 out of 276 respondents to the French National survey on well-being in astronomy stated that they work in excess of 40 hours per week and 88 out of 276 work in excess of 50 hours per week. Overwork is a significant factor in stress and it can be further amplified by short-term contracts that lack stability or security, accumulating managerial and supervisory tasks that significantly increase the workload without changing job title or salary and a lack of clarity about career opportunities and what is required to achieve a stable position. This overwork is one of the major factors in job burnout. Job burnout is defined as a result of chronic workplace stress that has not been successfully managed, and is characterised by:

1. exhaustion (feelings of energy depletion)
2. cynicism (increased mental distance from one's work and negativism related to one's work)
3. professional efficacy (a sense of ineffectiveness and lack of accomplishment)

Signs of a burnout include physical signs, including insomnia, headaches, pain and chronic tiredness. Psychological signs include depression, low self-esteem, anger and cynicism. Finally, behavioural manifestations of a burnout include absences at work, being late to work and isolating from colleagues. Whilst stress is the factor that can lead to burnout, it does not need to be the outcome. Burnout occurs when the action (fight-or-flight phase) triggered by the stress becomes continual and there is no relief phase. Then those suffering from stress are more prone to losing their coping resources and which stops them from reaching the relief (relaxing) phase. There are therefore significant differences between stress and burnout, see Table 5.

So how can we avoid burnout? There are several factors that can help protect us. As indicated above, we should develop social and emotional support from colleagues and supervisors. We must practice self-care, in order to achieve high levels of productivity and performance, and we must learn to know ourselves better,

Stress	Burnout
• Energetic, focussed	• Exhausted, fatigued
• Emotionally involved	• Emotionally drained
• Dynamic	• Detached and helpless
• Prone to anxiety disorders	• Prone to depressive disorders

Table 1. Comparison of the characteristics of stress and burnout.

manage our time, and find a safe space. Finally, it is important to choose which battles should be fought and when to let something go.

There are six steps that can be taken to avoid work-related burnout. First, make your own health a priority. Taking care of yourself is not an indulgent luxury, it is a matter of self-preservation. It is essential to find activities that can help you destress, it could be reading a book, going for a drink with friends, doing a sport that you enjoy, doing crafts, gardening, etc. Then it is essential to devote 20 minutes of the day to the activity(ies) that you enjoy, that stimulate the mind and body by activating other neural circuits and increase oxytocin production. Secondly, work on keeping stress levels down within the workplace with other colleagues who would like to do the same. This is helpful for the group but will also keep you accountable for taking care of yourself. Thirdly, also within the work place, recognise, both inwardly and publicly, saying things like "all of us are doing the best we can with the resources we have been given." In this way you are creating a psychologically safe place for yourself and others. Fourth, set a good example within the work place. If you are running from meeting to meeting and don't have enough time in the day to breathe, what message does that send? When colleagues are completely overwhelmed, you can encourage them to take regular breaks, to rest and rejuvenate and disconnect from work. Fifth, a common symptom (and cause) of job-related burnout is a disconnection between a person's values and the work they are doing. It is easy to forget what drew you to your career and your organization in the first place. When people have shared values and a connection, they are more likely to feel positively about their work. Discussions and team builiding activities can be a way to foster shared values and a connection to each other. Finally, as explained above, constant stress can lead to poor performance, which can lead to more stress and a downwards spiral. If you are aware that you or your colleagues are suffering in this way, it is time to talk to your supervisor, project manager, or other hierarchy and explain that without sufficient time to rest, you or your colleagues may no longer be able to continue, which would be detrimental to the work to be done.

These steps can help to improve well-being. However, if stress strongly affects your life, you should seek help from a mental health professional. A psychologist has the tools to support you and provide you with strategies to better manage states of stress. Don't wait to burn out before taking action.

The organisers of the June 2023 workshop on 'Well-being in Astronomy' are grateful to AA, ND and JG for their excellent contributions to the session. We are also grateful to the participants who provided some excellent feedback to the points raised and we also take the opportunity to thank the SF2A for their support.

References

American Psychiatric Association. 2013, Diagnostic and statistical manual of mental disorders: DSM-5^{TM}, 5th ed. (Arlington, VA, US: American Psychiatric Publishing, Inc.)

Armitage, C. 2020, Nature, 578, Dataviz

DiMenichi, B. C. & Tricomi, E. 2015, Front Psychology, 6, 1282

Fang, F. C. & Casadevall, A. 2015, Infection and Immunity, 83, 1229

Forrester, N. 2023, Nature, 615, 751

Lazarus, R. S. 1966, Psychological stress and the coping process, ed. A. P. Association (New York: McGraw Hill)

Leslie, K. 2019, THEGIST, May

Levine, I. S. 2008, Science, Mar., Careers

Park, M., Leahey, E., & Funk, R. 2022, The decline of disruptive science and technology

Rojzman, C., Rothenbuehler, I., & Rothenbuehler, N. 2015, La Thérapie Sociale, ed. C. Socia (Lyon: Chronique Sociale), 1–238

Webb, N. A., Bot, C., Charpinet, S., et al. 2021, in SF2A-2021: Proceedings of the Annual meeting of the French Society of Astronomy and Astrophysics, ed. A. Siebert, K. Baillié, E. Lagadec, N. Lagarde, J. Malzac, J. B. Marquette, M. N'Diaye, J. Richard, & O. Venot, 35–40

Session S06

Partenariat Gemini SAF SF2A sur les collaborations amateurs professionnels

SF2A 2023
M. N'Diaye, A. Siebert, N. Lagarde, O. Venot, K. Baillié, M. Béthermin, E. Lagadec, J. Malzac, J. Richard (eds)

A SELECTION OF ASTROMETRIC BINARIES FROM GAIA-DR3 THAT COULD BE DOUBLE-LINED SPECTROSCOPIC BINARIES AND ECLIPSING BINARIES

J.-L. Halbwachs[1], F. Kiefer[2,3] and Y. Lebreton[3,4]

Abstract. We present a selection of 41 bright astrometric binaries from the 3rd Gaia Data Release (Gaia-DR3) that could also be eclipsing binaries and double-line spectroscopic binaries (SB2s). By adding elements from SB2 orbits and photometric observations of eclipses to the astrometric orbital elements, it should be possible to obtain the masses and radii of the components of these binaries.

Keywords: binaries: spectroscopic, binaries: eclipsing, Astrometry, stars: fundamental parameters

1 Introduction

The masses, luminosities and radii of stars are fundamental parameters for studying the stellar interiors (Serenelli et al. 2021). The masses can be derived from the orbits of double-line spectroscopic binaries (SB2s), when the inclination of the orbit is given by an astrometric orbit. The luminosity ratio is derived from the SB2 orbital elements, the semi-major axis of the photocentric orbit and the trigonometric parallax. When the orientation of the orbit is almost on edge, the binary system can also be eclipsing, and it is possible to deduce the radii of the components. Such systems are rather rare, and generally have components so close together that their masses have been modified by mass exchanges. Fortunately, this situation is set to change thanks to the Gaia satellite.

The 3^{rd} Gaia Data Release (Gaia DR3) includes the orbital elements of nearly 165500 astrometric binaries (Gaia Collaboration et al. 2016; Halbwachs et al. 2023; Holl et al. 2023), most of which were previously unknown. Due to selection effects, the periods of these binaries are essentially between 30 and 2000 days, which puts them in a range where mass transfers are less frequent than in all eclipsing binaries. For these reasons, we decided to select the astrometric binaries of DR3 (i) which could show eclipses, (ii) which could be observed like SB2s with the 193 cm telescope (T193) of the Observatoire de Haute-Provence (OHP) equipped with the "Spectrographe pour l'Observation des PHénomènes des Intérieurs Stellaires et des Exoplanètes" (Sophie), and (iii) that could give masses accurate to 1 % or better.

2 Selection criteria

The objectives listed in the introduction will be translated into selection criteria as follows:

- As we want stars that can be observed from the OHP, we are restricting ourselves to declinations $\delta > 0°$.
- As we want stars that can be observed with T193/Sophie, the magnitude must be bright enough to obtain a good quality spectrum in less than an hour under poor weather conditions. So, $m_v < 10.40$ mag.
- To obtain radial velocities with Sophie, the spectral type must be later than A.

[1] Université de Strasbourg, CNRS, Observatoire astronomique de Strasbourg, UMR 7550, F-67000 Strasbourg, France
[2] Institut d'Astrophysique de Paris, CNRS/UMR7095, F-75014 Paris, France
[3] LESIA, Observatoire de Paris, PSL Research University, CNRS, Sorbonne Université, UPMC Univ. Paris 06, Univ. Paris Diderot Sorbonne Paris Cité, F-92195 Meudon, France
[4] Univ Rennes, CNRS, IPR (Institut de Physique de Rennes) - UMR 6251, F-35000 Rennes, France

© Société Française d'Astronomie et d'Astrophysique (SF2A) 2023

- To have a chance of getting masses to within 1 %, the astrometric orbit in Gaia DR3 must give $\sin^3 i$ more accurate than 1 % (i is the orbital inclination deduced from the Thiele-Innès elements, as explained in Halbwachs et al. 2023).
- For the binary to show eclipses, the projection of the minimum separation between the components must be less than the radius of the primary component. These radii may be overestimated, since they were derived neglecting the contribution of the secondary component to the total luminosity of the system. On the other hand, we have also overlooked the fact that, due to the size of the secondary component, a partial eclipse can occur when the orbit only grazes the primary component without passing in front of it.
- Stars with a combined astrometric and single-lined spectroscopic (SB1) solution in Gaia DR3 are only retained when a_0/a_1 is not in the range [0.9 , 1.1], in order to exclude the binaries with a component much brighter than the other, since such stars are probably not SB2s.

The masses and radii of the primary components were taken in the Gaia DR3 Main Sources catalogue (Gaia Collaboration et al. 2023). Taken together, these criteria give us a list of 41 targets that will be observed from the OHP starting in the second semester of 2023 to obtain their SB2 orbits.

3 Properties of the selected targets

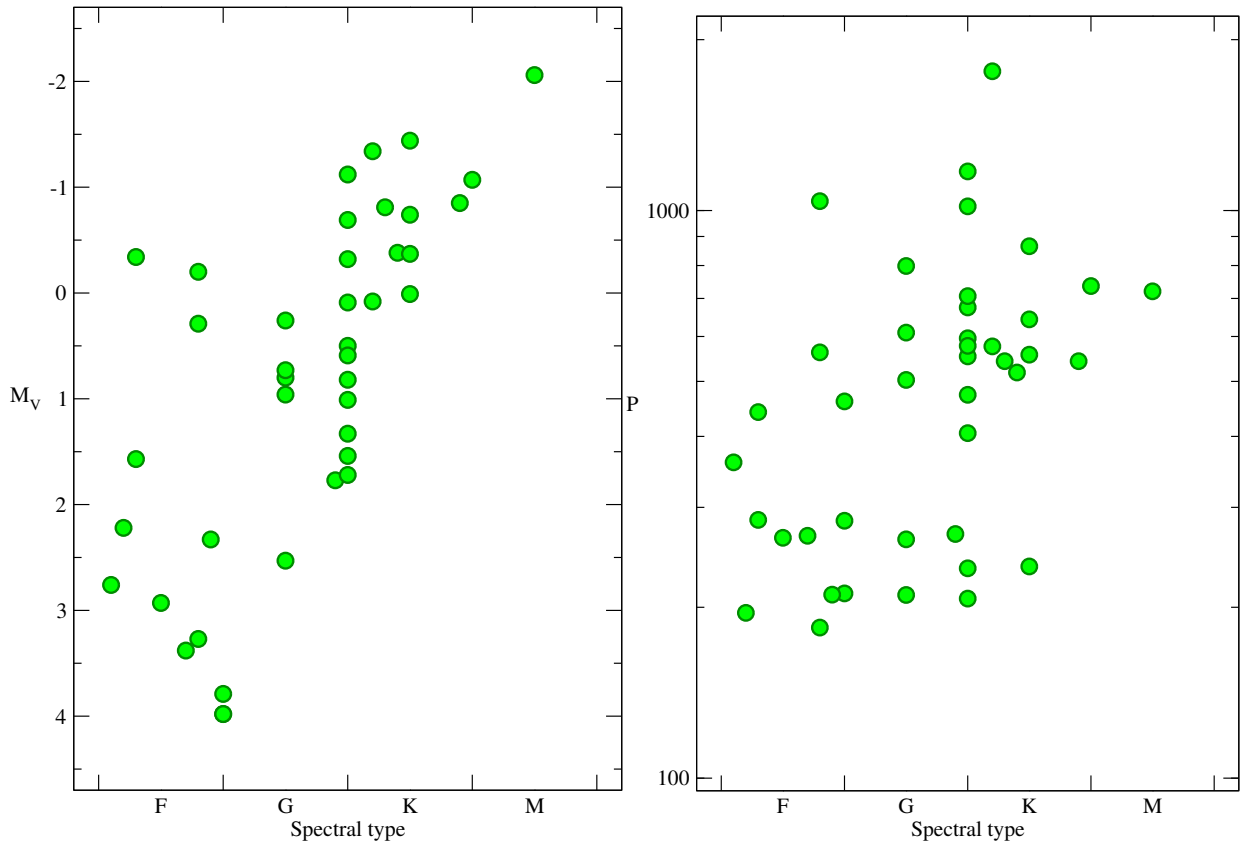

Fig. 1. Properties of the 41 binaries possibly eclipsing. **Left:** HR diagram. **Right:** Spectral type vs period diagram.

The main characteristics of our targets are shown in Figure 1. Their positions in the HR diagram (figure on the left) shows several types of stars: a dozen or so F-G dwarfs or sub-giants and about thirty or so giants, distributed between the clump, the asymptotic giant branch and the horizontal branch.

The periods of these binaries are shown in the figure on the right. We can see that the late–type stars, which are giants, have periods of several hundred days, which suggests that many of them have not been affected by mass transfer.

4 Programme organisation

First of all, we need to be sure that we can determine the masses of the components of these binaries, so that these stars are SB2s. For each star, this will require 1 or 2 observations from the OHP with the T193/Sophie. To be as effective as possible, these observations will be made at carefully chosen phases. Now that our project has been accepted*, observations begin this autumn 2023.

As soon as an SB2 has been detected, we will propose it for photometric observations with a view to observing eclipses. For this, we hope to be able to count on well-equipped amateur astronomers. To cover eclipses effectively, we will need observers spread out different longitudes, and working in the same wavelength ranges if possible. We will produce ephemerides announcing the corresponding epochs; because of the uncertainties affecting the periods of the DR3 orbits, these epochs will be at the beginning of time intervals of several days. Subsequently, once the orbits have been revised on the basis of radial velocity measurements, these intervals should narrow.

5 Conclusions

We have selected 41 targets whose spectra will be observed from OHP to detect SB2s, and then photometrically to detect eclipses. We hope that many amateur astronomers will be able to take part in this final part of the programme. Individuals or organisations wishing to join us are invited to contact us at jean-louis.halbwachs(at)astro.unistra.fr to receive eclipse ephemerides.

After a few years and the publication of DR4, it should be possible to produce a list giving the masses, magnitudes and radii of a few dozen stars of all types.

This work has made use of the SIMBAD database and of the Vizier facility, both operated at CDS, Strasbourg, France.

References

Gaia Collaboration, Prusti, T., de Bruijne, J. H. J., et al. 2016, A&A, 595, A1
Gaia Collaboration, Vallenari, A., Brown, A. G. A., et al. 2023, A&A, 674, A1
Halbwachs, J.-L., Pourbaix, D., Arenou, F., et al. 2023, A&A, 674, A9
Holl, B., Sozzetti, A., Sahlmann, J., et al. 2023, A&A, 674, A10
Serenelli, A., Weiss, A., Aerts, C., et al. 2021, A&A Rev., 29, 4

*The investigators in the OHP programme are Flavien Kiefer (principal investigator), Orlagh Creevey, Benoît Famaey, Patrick Guillout, Jean-Louis Halbwachs, Yveline Lebreton, Olivier Marchal, Tsevi Mazeh, Thibault Merle and Jean-Baptiste Salomon.

SF2A 2023
M. N'Diaye, A. Siebert, N. Lagarde, O. Venot, K. Baillié, M. Béthermin, E. Lagadec, J. Malzac, J. Richard (eds)

STELLAR OCCULTATIONS OF THE LUCY MISSION TARGETS OBSERVED IN FRANCE IN 2022

A. Leroy[1], J. Desmars[3,2], F. Colas[3], T. Midavaine[4], G. Langin[5] and M. Grand[5]

Abstract. As part of the development of a network of observers of stellar occultations by asteroids, we present our first results from observation campaigns carried out in 2022. The objects observed were the asteroids (15094) Polymele, (3548) Eurybates and (21900) Orus, targets of the LUCY mission. These observations were realised as part of a collaboration with the South West Research Institute. This document presents the observations performed by the network and preliminary results of these occultations.

Keywords: Occultations, Minor Planets , Asteroids, Methods : observational,Pro-am collaboration

1 Introduction

Stellar occultation is a powerful technique to get access to physical characteristics of small solar system bodies. This technique requires to observe the event on a thin band (large as the body) with multiple stations (telescope, camera and timing system). More stations are involved, more details on physical characteristics of the body are obtained. In that context, an equipped and trained network of observers is a clear advantage, in particular, thanks to the amateur community.

As part of the API pro-am, initiated by the Paris Observatory and following a first occultation expedition to Spain (Schnabel et al. 2022) (for the Lucy probe), we start to develop and equip a French team of occultation observers (Desmars et al. 2022). This team was made possible by the Comission des Techniques en Astronomie Amateur (CT2A) of the Société Astronomique de France (SAF, `https://saf-astronomie.fr/techniques-astronomie-amateur/`).

Following previous experiences in occultations, we identify that the need is to be organised and to offer high-quality dating equipment. In this context, we were funded by the Paris Observatory ProAm initiative in early 2022 for the purchase of Timebox (i.e. dating system). This document presents the four different campaigns of occultations we organised in France in 2022, involving targets of the LUCY mission.

These observations were realised as part of a collaboration between the South West Research Institute (PI Marc Buie - stellar occultation team), Paris Observatory (PI Josselin Desmars - Co-PI François Colas) and French national structures, the Société Astronomique de France (Commission CT2A - PI Thierry Midavaine) and the Association Française d'Astronomie (Section Sciences Participatives - PI Guillaume Langin - Co-PI Marie Grand).

2 The occultation events in France for 2022

The Lucy mission is a NASA spacecraft that will visit 6 trojan asteroids in 2027 and 2033. Stellar occultations are helpful to determine physical characteristics and position of these objects before the mission and in order to prepare their flybies. In that context, several occultation campaigns of these targets are organised all over the world by M. Buie (SWRI), the Lucy occultation project leader.

[1] Uranoscope de l'Ile de France, allée Camille Flammarion, 77220 Gretz-Armainvilliers
[2] Institut Polytechnique des Sciences Avancées, 63 boulevard de Brandebourg, 94200 Ivry-sur-Seine
[3] Observatoire de Paris, IMCCE, 77 avenue Denfert Rochereau, 75014 Paris
[4] Société Astronomique de France, 3 avenue Beethoven, 75016 Paris
[5] Association Française d'Astronomie, 17 rue Emile Deutsch de la Meurthe, 75014 Paris

© Société Française d'Astronomie et d'Astrophysique (SF2A) 2023

In 2022, four occultations by these targets were visible in France and we decided to take part of the campaign to train and prepare the French network. In addition, as the Eurybates occultation involving a relative bright star accessible to small telescopes or even DSLR, we have encouraged a large public from beginners to professional to participate. Thus, we have organised several webinars* presenting occultation and the way to observe it. At the same time, we set up a centralised data feedback system so that we could then have an overview of the results.

For the four occultations, we present preliminary analysis. All the data were collected by M. Buie (SWRI) who is leading the scientific analysis and who is in charge of publishing the results in forthcoming papers. Consequently, our results are partial and we only provide shape profile without dimension as an example of results that we obtained from these occultations.

2.1 Polymele 26/08/2022

The first occultation took place on August 26 and involved Polymele that occulted a magnitude 12.8 star. Polymele is a 29km-size trojan and it has a satellite, provisionally named Shaun, discovered during an occultation a few months earlier (Buie et al. 2022). In addition to Polymele, the secondary objective was to detect also the satellite. The occultation was visible in Portugal, Spain and France (Fig. 1 left). In addition to the main campaign in Portugal, 3 stations observed this occultation in France leading to 2 positive and 1 negative. These chords allow to obtain the ellipsoid shape profile of the asteroid (Fig. 1 right). The Northern chord shows a double event probably due to topographic features at the surface of the body. 7 other stations could have observed, but the sky was cloudy (no data). The satellite Shaun was not detected during this observation campaign.

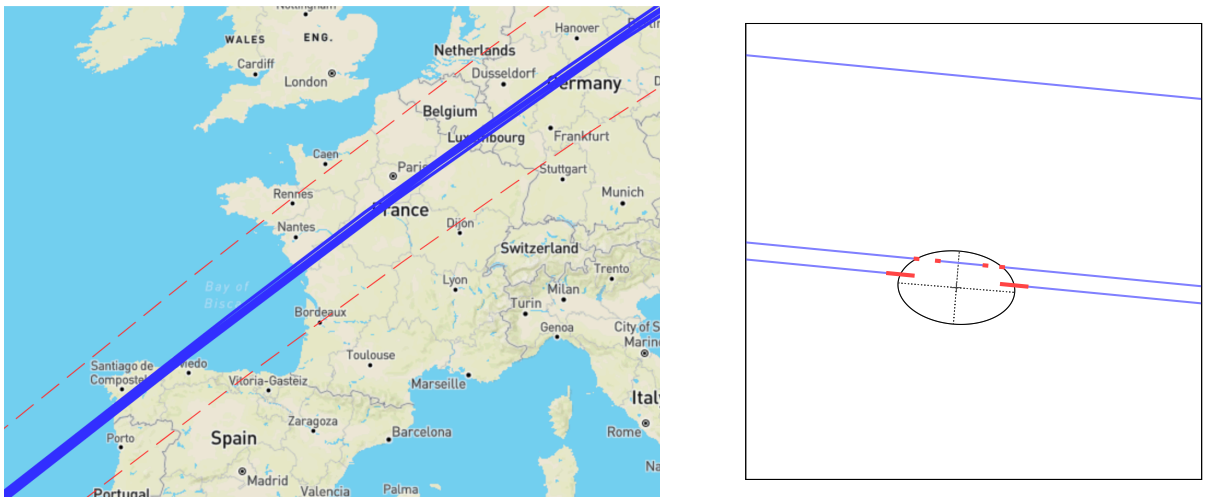

Fig. 1. Left: Occultation map by Polymele on 26/08/2022. Blue lines represents the body limits whereas the red lines represent the uncertainty on the path. **Right:** Shape profil of Polymele derived from the occultation assuming an ellipsoid.

2.2 Eurybates 23/10/2022

The second occultation involved Eurybates, a 64km-size trojan occulting a magnitude 8.7 star on October 23 (Fig. 2 left). This event was very interesting because of the brightness of the star making the occultation recordable with a small telescope or even a small telelens. For this occultation, AFA organised a huge campaign for the amateur community with the rallying of about 1000 observers. At the end, 340 persons made a report and because of bad weather all along the path most of them were under clouds. Despite the bad weather, the occultation was positive for 17 stations and negative for 44 stations. The preliminary analysis of the occultation

*See for instance, the AFA Youtube channel: `https://www.youtube.com/watch?v=Eo3hDbQLaVA`, `https://www.youtube.com/watch?v=8mQ7M-QRRxw` and `https://www.youtube.com/watch?v=SZTLtNOQuT8`

allows to derive the shape of Eurybates at the time of the occultation (Fig. 2 right). For this analysis, Eurybates is assumed to be an ellispoid whereas it is irregular, in particular some topographic features are revealed by the Southern positive chord. Note that, as for the other occultations, results are preliminary.

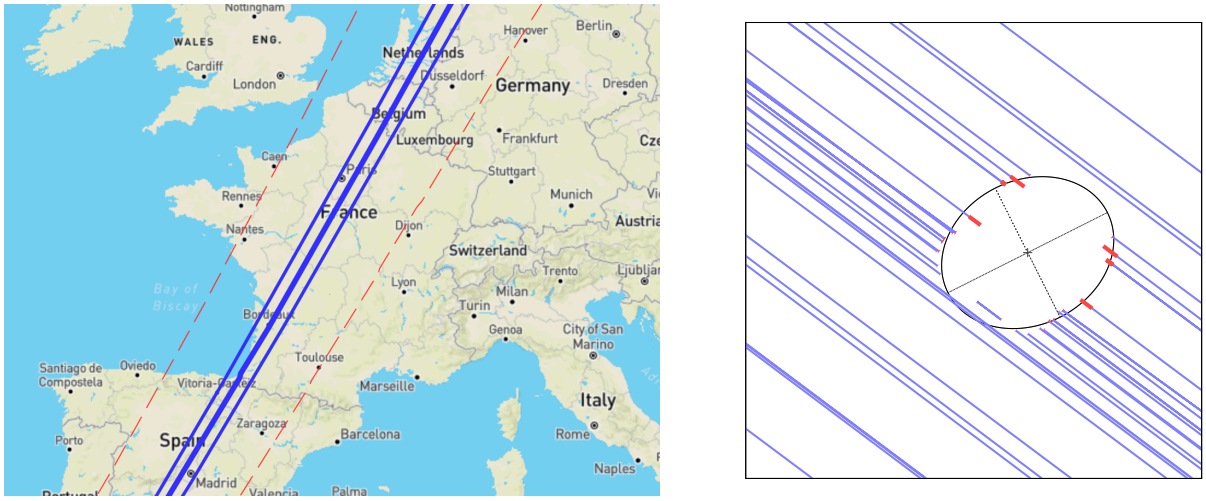

Fig. 2. Left: Occultation map by Eurybates on 23/10/2022. **Right:** Shape profile of Eurybates derived from the occultation assuming an ellipsoid.

2.3 Orus 16/12/2023

The third occultation was Orus, a 53km-size trojan, occulting a magnitude 14.8 star on December 16 (Fig. 3 left). The occultation was recorded on 12 stations with 9 positive and 3 negative. A preliminary analysis of the occultation allows to derive the shape profile presented in Fig. 3 right. The profile is done assuming an ellipsoid for Orus, whereas Orus is clearly irregular.

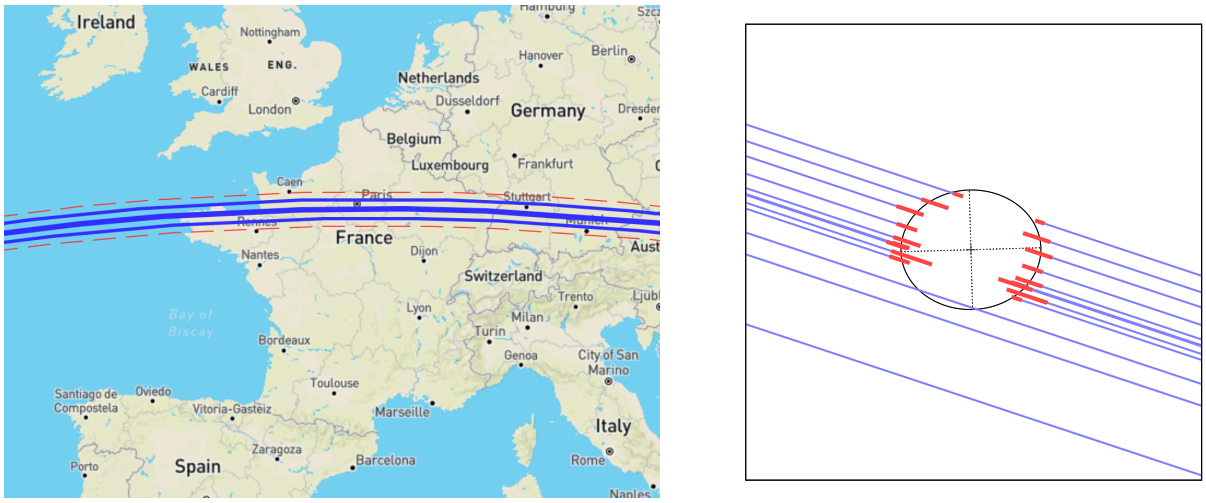

Fig. 3. Left: Occultation map by Orus on 16/12/2022. **Right:** Shape profile of Orus assuming an ellipsoid derived from the occultation.

2.4 Polymele 27/12/2023

The last event involved again Polymele that occulted a magnitude 14.4 star on December 27 (Fig. 4 left). Due to weather conditions, only one station reported a positive chord. Using one chord, we can only assume a spherical body with a specific size in order to derive the two possible solutions that fit to the chord (Fig. 4 right)

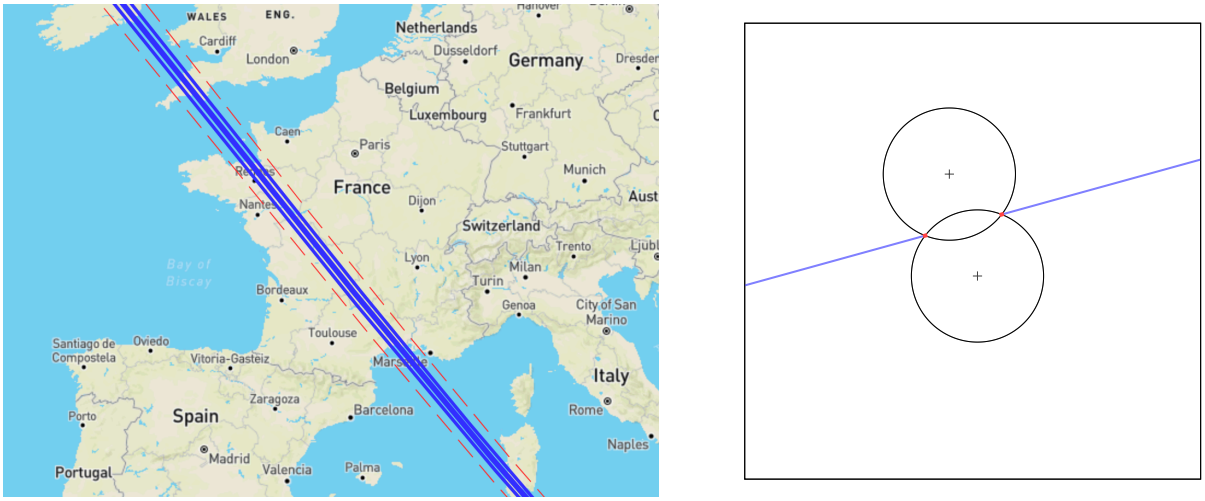

Fig. 4. Left: Occultation map by Polymele on 26/08/2022. **Right:** Shape profile of the two possible solutions derived from the occultation, assuming a spherical body.

3 Conclusions

In 2022, we organised and participated to four occultation campaigns in collaboration with the SouthWest Research Institute. They were all impressive success in term of coordination, participation and scientific results. This is validating the network we are developing. Thanks to the API PromAm initiative of Paris Observatory, we are equipping the amateur community for timing system, camera, etc. that are required to record high quality data of occultations. We have collected the data of the four campaigns and they will be analysed in details and scientific results will be published by the Lucy occultation project. All these occultations will help in a better knowledge of the Lucy targets and in the preparation of the flybies by the probe in 2027 and 2033.

We would like to thank all the observers who took part in these observation campaigns, as well as the Société Astronomique de France and the Association Française d'Astronomie. We would also like to thank Marc Buie for his predictions. We would also like to thank the Observatoire de Paris-PSL for its support in our Pro-Am collaboration, and the SF2A for allowing us to present our results during the Semaine Française de l'Astrophysique 2023.

References

Buie, M., Keeney, B., Levison, H., Olkin, C., & Lucy Occultations Team. 2022, in AAS/Division for Planetary Sciences Meeting Abstracts, Vol. 54, AAS/Division for Planetary Sciences Meeting Abstracts, 512.03

Desmars, J., Colas, F., Leroy, A., Midavaine, T., & Langin, G. 2022, in SF2A-2022: Proceedings of the Annual meeting of the French Society of Astronomy and Astrophysics. Eds.: J. Richard, ed. J. Richard, A. Siebert, E. Lagadec, N. Lagarde, O. Venot, J. Malzac, J. B. Marquette, M. N'Diaye, & B. Briot, 141–144

Schnabel, C., Marco, J., & Guhl, K. 2022, Journal for Occultation Astronomy, 12, 3

SF2A 2023
M. N'Diaye, A. Siebert, N. Lagarde, O. Venot, K. Baillié, M. Béthermin, E. Lagadec, J. Malzac, J. Richard (eds)

RAPAS, PRO-AM NETWORK FOR THE SCIENTIFIC ALERTS, 2023 STATUS

T. Midavaine[1], W. Thuillot[2], M. Dennefeld[3], C. Buil[4], S. Neveu[1,7], M. Serrau[1,7,5], E. Barbotin[6], P. Barroy[7], Y. Delisle[7], P. Dupouy[8], A. Leroy[7,9], J. M. Lopez[10], F. Losse[11], E. Maris[12], P. Martinez[1,13], C. Pantacchini[14] and A. Wünsche[15]

Abstract. This is an update of the RAPAS project (Reseau Amateurs Professionnels pour les Alertes Scientifiques) introduced last year during "Les Journées de la SF2A 2022" (Thuillot et al. 2022). Several projects on the ground and space are releasing all along the years alerts (ZTF, ASSAS-SN, ATLAS, CRTS,...). Gaia mission is the most emblematic example delivering Solar System Objects (SSO) new detections (Carry et al. 2021), Galactic or extragalactic variable alerts (Hodgkin et al. 2021). In addition, during the last years, other programs are transient events in the multimessenger domain (GW, GRB, X, Neutrinos, FRB,...) (Schüssler et al. 2023) where the optical counterpart is to be find in the field of the assumed designation accuracy. The RAPAS ProAm collaboration, funded by Paris Observatory in the frame of the multi-year Incentive Action Pro-Am (AIP), invited amateur french observatories to register to the RAPAS Gemini web site* all along 2022 and 2023 years. End of 2022, we equipped them with 25 set of filters we designed and manufactured meeting the three Gaia photometric spectral bands: G, Gbp and Grp. We are assessing the upper magnitude limit and the magnitude accuracy of each amateur observatory. In 2023 we are launching the design of two spectrograph prototypes able to deliver Spectral Emission Distribution (SED) of each detected alert to allow its first classification and characterization or reject false alerts. We are on the way to the 2024 and third year of the program to release an operational Pro-Am network.

Keywords: Gaia, Photometry, Astronomical Alerts, Transient Event Detection, Filters, Spectral Energy Distribution

1 Introduction

Observational programs generating astronomical alerts are increasing. These could be in a wide range of objects and signatures from new Solar System Objects (SSO), to Galactic Novae or eruptive stars, or even beyond to high energy transient events, far away in the deep extragalactic cosmos as Supernovae or Gamma Ray Bursts. These alerts are released either with optical instruments or with non optical surveys. In the case of optical

[1] Société astronomique de France, 3 rue Beethoven, 75016 Paris, France
[2] IMCCE-Paris Observatory, PSL Univ., CNRS, Sorbonne Univ., Lille Univ., 77 Av. Denfert Rochereau, 75014, Paris, France
[3] Institut d'Astrophysique de Paris, Sorbonne Université, CNRS, UMR 7095, 98 bis bd Arago, 75014, Paris, France
[4] Astronomical Ring for Access to Spectroscopy, ARAS Aude, France
[5] Dauban Grappa, observatoire de Dax, France
[6] Astroclub Charantais, France
[7] Télescope Jean-Marc Salomon, Buthiers, CPS Planète Sciences, France
[8] Observatoire de Dax, France
[9] Uranoscope de l'Ile de France, France
[10] Observatoire des Pises, France
[11] Observatoire de St Pardon de Conques, France
[12] CEPHEE73, club astronomique de Chambéry, France
[13] Adagio Observatoire de Belesta, France
[14] Observatoire de Benayes, France
[15] Observatoire des Baronnies Provençales, France
*RAPAS Gemini web page : `https://proam-gemini.fr/rapas/` (in French)

© Société Française d'Astronomie et d'Astrophysique (SF2A) 2023

data, the RA and Dec are usually accurately delivered except for SSO, where latencies between observations and inaccuracies in orbit model building provide a wider and wider field of research to recover it. In the case of non-optical alerts these could be released from Gamma ray or X ray space observatories, Cosmic ray and Neutrino detectors, Gravitational Waves Interferometers, or Radio waves telescopes. Inherent to the signal natures and related instrument, a wide inaccuracy basket is attached to the angular designation of the source, usually from 1 square degrees to several 10 square degrees, or even more ! Therefore, wide field of view and high magnitude upper limit optical instruments are required to find and classify optical counterparts. This is a task where amateurs with their availability and their networked instruments can efficiently contribute to the discovery of transient phenomenon and why we launch the RAPAS[†] project (Reseau Amateurs Professionnels pour les Alertes Scientifiques) in 2022. The monitoring of the phenomenon can then, be carried out by amateurs or mobilize large professional instruments thanks to this Pro-Am collaboration and organization.

2 Filter design and manufacturing

Gaia is releasing a very accurate catalog since 2016 with DR1 (Data Release 1), in June 2022 we got the latest update Gaia DR3, then Gaia DR5 is scheduled in 2028, and beyond the final release. This catalog deliver accurate 1.9×10^9 stars angular localization and photometric measurement thanks to the ideal space probe localization. The magnitude native measurements don't need any atmospheric corrections. Gaia introduces three interesting photometric bands: G, Gbp and Grp (Riello et al. 2021) given on Fig. 1.

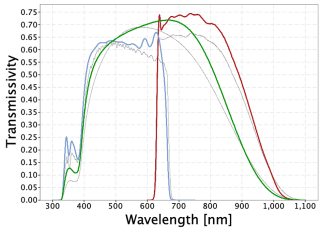

Fig. 1. Gaia photometric bands G band in green, Gbp in blue, Grp in red.

Before the RAPAS program we try to purchase the filters defining these very interesting bands. With these large bandwidth compare to standard UBVRI Johnson Cousins set, or Bessel filter set or ugriz set from the SDSS, we enhance the sensitivity of amateur telescopes. In using Gaia bandwidth we will be able to perform accurate photometric reductions in using the Gaia catalog. We realized in fact these filters do not exist. The Gaia G, Gbp, and Grp bands are resulting of the resistivity and thickness giving the quantum efficiency of three families of back-side illuminated CCD on the Gaia focal plane array, combined with a small prism for the Gbp and Grp bands. The Gaia team gives us the feedback that such filters had never been realized. In the framework of this project, proposed to Paris Observatory AIP fundings, we designed and manufactured such fitted filters in taking into account the spectral sensitivity dispersion we meet with amateur CCD or CMOS cameras and variables air mass. At the end of 2022 we got the delivery of 25 sets of the three filters we call A, B and C displayed on Fig. 2 with the effective spectral transmission on Fig. 3. These filters are 2mm thick and 50mm in diameter.

Fig. 2. Picture in transmission of the three filters A, B and C from left to right.

3 RAPAS network

With the first public presentation of the RAPAS project during the "2022 journées de la SF2A" (Thuillot et al. 2022) we invited amateurs to join our team and to register their observatory on the Gemini web site on the

[†]`https://rapas.imcce.fr` (in French)

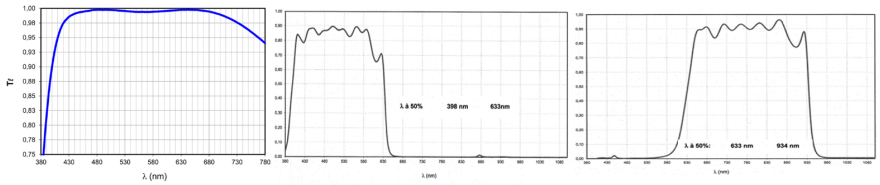

Fig. 3. Spectral transmission curves of the three filters A, B and C from left to right.

RAPAS topic. More than 30 observatories registered in october 2022 for our first workshop[‡] where we shared the detail of RAPAS project and how we will implement the characterization of the instrument set up equipped with the RAPAS set of filters. In September 2023 we are close to 50 observers registered. During this workshop we started the attribution of the 25 set of filters. Fig. 4 shows the location of the equipped observatories giving a wide spread over France to meet wide range of Longitudes and Latitudes and meet independent cloud coverages if any. The range of telescope diameters are from 200 mm to 820 mm.

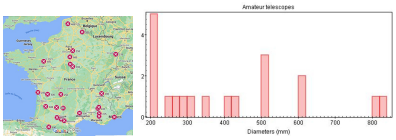

Fig. 4. French localization of the observatories equipped with RAPAS filters. The range of telescope diameters is from 200 mm to more than 800 mm displayed on the histogram on the right.

4 First photometric acquisitions

Step by step each observers perform the mounting of the filters. Due to the fact filters installations rely on various optical and mechanical interfaces this could be more or less easy. During the workshop we provided three fields of view from the Sky and Telescope paper (Everhart 1984) defining SA51, SA57 and SA68. It allows all along the year to get one of these field passing the meridian during the night. M. Serrau produced the Grappa catalog[§]. This is an extract of EDR3 Gaia catalog limited to all information necessary for astrometric and photometric reductions. In addition M. Serrau provides a process in using Prism V11 and Grappa catalog to extract and compare in any field the star flux with the Gaia catalog. This allows the construction of graph showing the fidelity between the measured flux with the filters A, B in C in versus the magnitude in respective G, Bbp and Grp bands. The standard deviation versus the magnitude is assessed. Several observers demonstrated upper limit magnitude above 20.

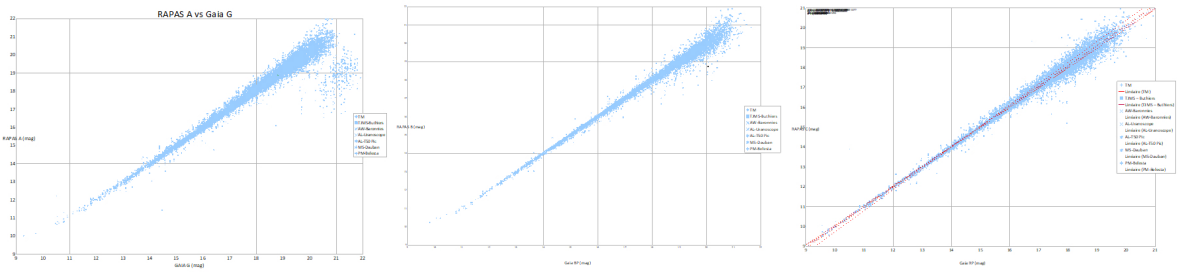

Fig. 5. Example of the data reduction of the measured flux with A, B, C filters vs respective G, Gbp, Grp (courtesy M. Serrau).

[‡]see `http://rapas.imcce.fr/RAPAS-atelier1.html` (in French)
[§]see `http://www.astrosurf.com/noctambule/CCD-GRAPPA/`(in French)

Mid of may 2023 we got the alert of a supernova discovered in M101 : SN2023ixf. This gave us a good opportunity to mobilise the starting RAPAS network on real case. It shows how, all along the weeks, the operational observers are available to acquire the field and to realise the data reduction. The Fig. 6 shows the light curves got with A B C filters and reduced with Gaia catalog in respective G Gbp and Grp versus time. We deliver also the curve of the G magnitude vs the colour index Gbp-Grp showing how the equivalent temperature of the source decrease with the magnitude.

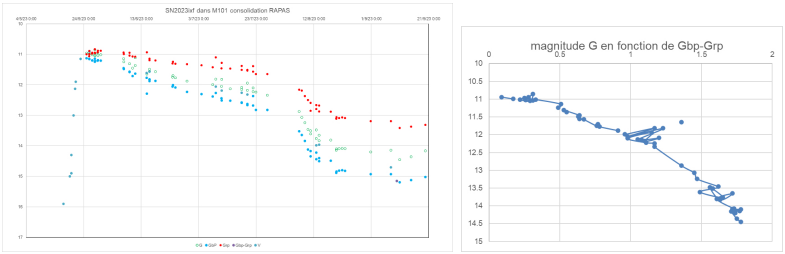

Fig. 6. Left: light curve of the SN2023ixf discovered in may 2023 in M101. Red dots for Grp magnitude got through filter C, green empty dots for G magnitude through filter A and blue dots for Gbp magnitude through filter B. **Right**: G magnitude vs colour index Gbp-Grp.

5 Spectral Energy Distribution

In 2023 we launch the spectroscopic task of the Rapas project. The purpose is following the detection and localization of an optical counterpart candidate to be able to provide a first characterization of the signature in getting the spectral energy distribution. We need to show how deep we may get this spectra with magnitude range up to 20. Therefore the trade off of such spectrograph have to limit the Resolution around 100 to get the targeted sensitivity. We have just launched the manufacturing of two prototypes relying on existing spectrograph Alpy 200 and StarEx VLR. On the Alpy 600 we replace the grism for a transmission blazed grating of 200 grooves per millimeter, giving an Alpy 200. And on the Star'Ex we replace the reflective grating 600g/mm with a 150g/mm one's. We schedule to assess the limiting magnitude and the effective resolution before the end of this year to allow according the target be able to detect : continuous spectra fitted to a Blackbody with a temperature measurement, continuous spectra not fitted to a Blackbody signature, monitor the temperature variability of the target, emission lines on the spectra, wide absorption lines, localize Balmer or Lyman lines break to get the target z, ...

Fig. 7. Alpy and Star'Ex spectrograph on the left and on the right respectively.

We would like to thank the Paris Observatory's API (Action Pluriannuel Incitative) Pro-Am for the funding that made these developments possible.

References

Carry, B., Thuillot, W., Spoto, F., & 42 more. 2021, A&A, 648, A96

Everhart, E. 1984, S&T, 67, 28

Hodgkin, S. T., Harrison, D. L., Breedt, E., & 108 more. 2021, A&A, 652, A76

Riello, M., De Angeli, F., Evans, D. W., & 39 more. 2021, A&A, 649, A3

Schüssler, F., de Bony de Lavergne, M., Alkan, A., & 2 more. 2023, Proc. 38th Intern. Cosmic Ray Conf. (ICRC2023)

Thuillot, W., Midavaine, T., Dennefeld, M., & 2 more. 2022, SF2A-2022: Proc. meeting French Soc. of Astron. and Astrophys., 149

SF2A 2023
M. N'Diaye, A. Siebert, N. Lagarde, O. Venot, K. Baillié, M. Béthermin, E. Lagadec, J. Malzac, J. Richard (eds)

CITIZEN SCIENCE TIME DOMAIN ASTRONOMY WITH ASTRO-COLIBRI

F. Schüssler[1], M. de Bony de Lavergne[1], A. Kaan Alkan[1,2], J. Mourier[1] and P. Reichherzer[3]

Abstract. Astro-COLIBRI is an innovative tool designed for professional astronomers to facilitate the study of transient astronomical events. Transient events - such as supernovae, gamma-ray bursts and stellar mergers - are fleeting cataclysmic phenomena that can offer profound insights into the most violent processes in the universe. Revealing their secrets requires rapid and precise observations: Astro-COLIBRI alerts its users of new transient discoveries from observatories all over the world in real-time. The platform also provides observers the details they need to make follow-up observations.

Some of the transient phenomena available through Astro-COLIBRI at accessible by amateur astronomers and citizen scientists. Some of the features dedicated to this growing group of users are highlighted here. They include the possibility of receiving only alerts on very bright events, the possibility of defining custom observer locations, as well as the calculation of optimized observation plans for searches for optical counterparts to gravitational wave events.

Keywords: multi-messenger, real-time, follow-up, citizen science

1 Introduction

Astro-COLIBRI (Reichherzer 2021, 2023) is a modern system created to help researchers study short-lived astrophysical events. It does this by collecting information about detections of different types of signals in real-time, all in one easy-to-use interface. Astro-COLIBRI brings together the data about these events with tools to plan and faciliate follow-up observations. This helps both professional and amateur astronomers learn more about the violent universe by using different types of observational data. Astro-COLIBRI can be used to study many different phenomena like flaring Active Galactic Nuclei (AGN), Gamma-ray Bursts (GRBs), Fast Radio Bursts (FRBs), Gravitational Waves (GWs), High-energy Neutrinos, Optical Transients (OT) including Supernovae (SN), and more. Aiming to combine information from different observatories and systems, Astro-COLIBRI encourages astronomers to work together and share their data. An overview of the context and place of Astro-COLIBRI fits in the bigger picture of time domain astrophysics is given in Fig. 1. The system connects to many sources of information that send out alerts about new discoveries and classifications of these short-lived events. It organizes this information and compares it with other time-critical and archival data. Each event is also linked to various external services and expert platforms. Specially designed tools help astronomers get ready to observe the most interesting events.

2 Alerts and notifications

One of the most prominent features of Astro-COLIBRI is the possiblity to receive alerts about new detections of transient phenomena in realtime on any smartphone. The free Android* and iOS† apps can be downloaded from the relevant app stores by anyone interested in following time domain astrophysics news. At first launch of the app, several onboarding screen will be displayed to guide the user through the app. The first such screen is interactive and allows for the selection of the various available notification streams. These are served by the

[1] IRFU, CEA, Université Paris-Saclay, Gif-sur-Yvette, France
[2] Laboratoire Interdisciplinaire des Sciences du Numérique, CNRS, Université Paris-Saclay, 91405 Orsay, France
[3] Department of Physics, University of Oxford, Oxford OX1 3PU, United Kingdom
*`https://play.google.com/store/apps/details?id=science.astro.colibri`
†`https://apps.apple.com/us/app/astro-colibri/id1576668763`

© Société Française d'Astronomie et d'Astrophysique (SF2A) 2023

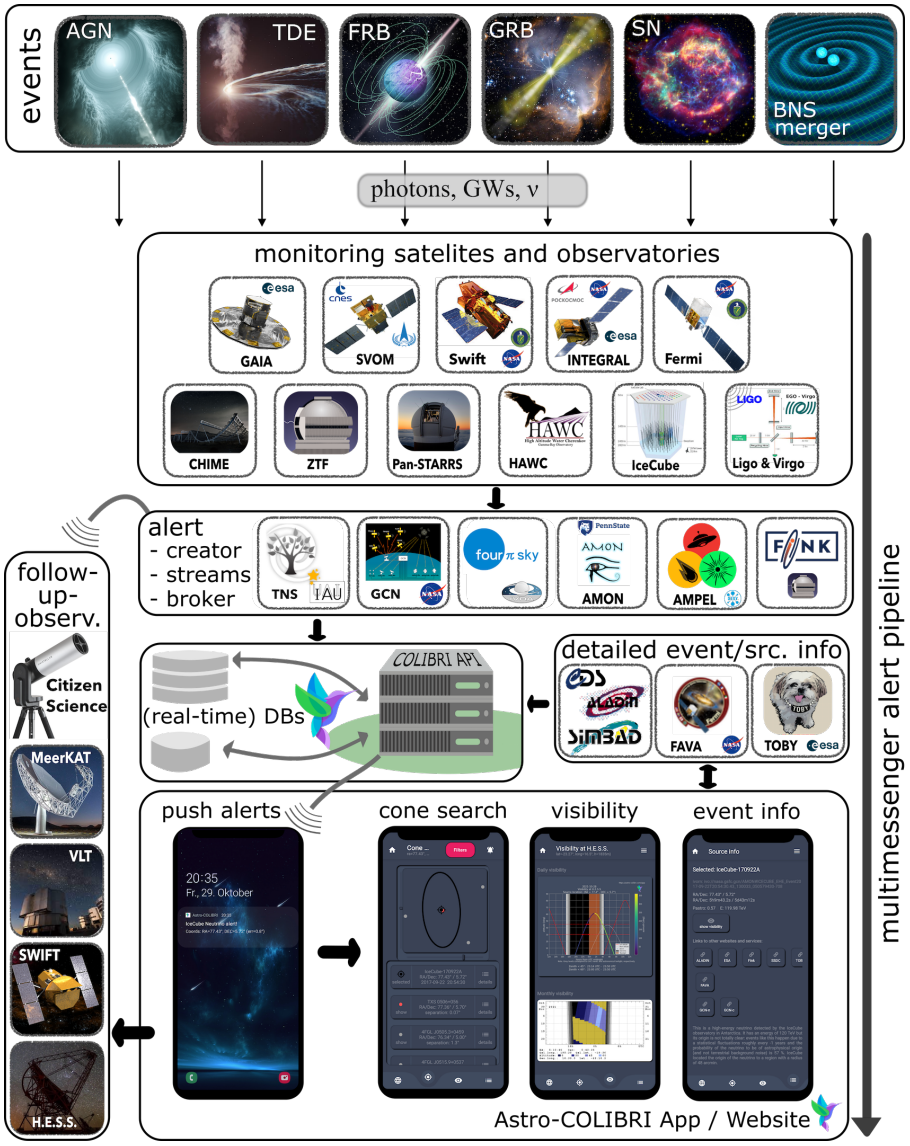

Fig. 1. Astro-COLIBRI is conveived as top-level platfrom fully integrated in the global multi-wavelength and multi-messenger landscape.

Google Firebase Cloud Messaging system and allow the recepetion of notifications in realtime. The available choices (v2.6.0 of the platform) are shown in Fig. 2. The same selection screen can also be found in the app menu, accessible via a button in the top right corner of the app.

Particularly interesting for amateur astronomers are the notification streams announcing the classification of bright optical transients. These are:

Bright optical transients (mag<18) Announcements of optical transients (SNe and other classified optical transients) with magnitudes < 18 at the time of the detection of the new source. Thus, the source evolution since this moment is not taken into accocunt directly. The notification stream is a subset of two more extensive categories, which announce supernovae and all other optical transients independent of their magnitudes.

Unistellar: bright and early optical transients These notifications announce the detection of candidate supernovae by the ZTF observatory and selected by the Unistellar Citizen Science program. Their magnitudes at the time of detection are usually required to be < 16.3. These events are thus accessible by

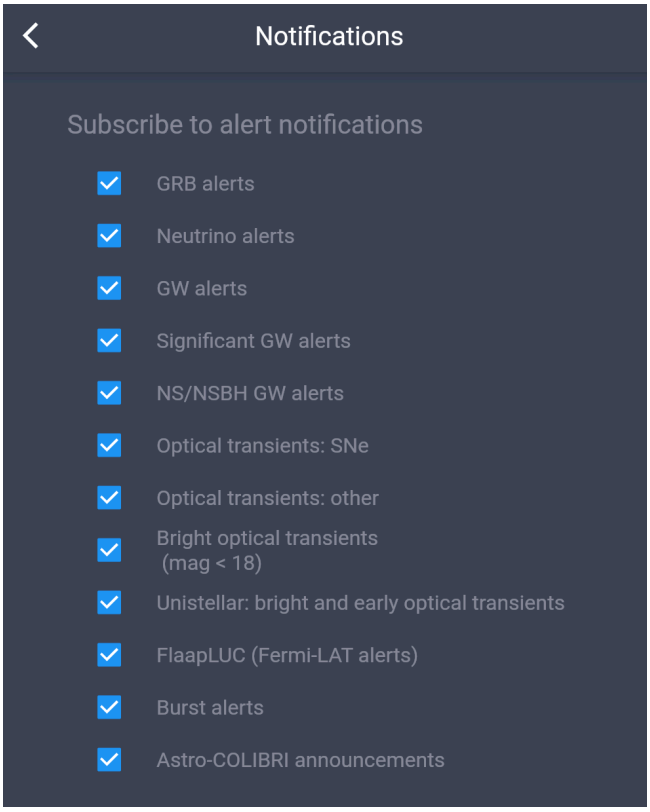

Fig. 2. Selection of realtime notification streams.

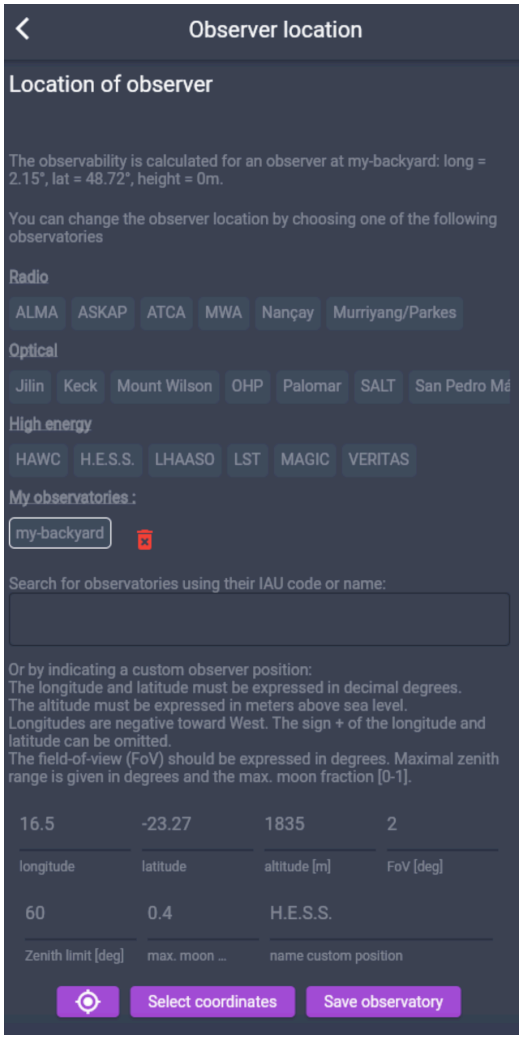

Fig. 3. Selection of follow-up observatories.

relatively small aperture telescopes. The selection procedure by the ALeRCE broker has large uncertainties due to the limited amount of information (e.g. typically only a single flux measurement exceeding the archival observations), the fraction of the events due to mis-classifications can thus be sizable.

3 Observatory selection

An important step towards follow-up observations of a particular event is the assessment of its observability at a given location that can be defined via the "Observer location" menu entry. This can be found in the app menu in the top right corner and on the web interface via the teardrop icon in the "personalize" area in the top row. Illustrated in Fig. 3, three complementary ways of selecting the observer location are available:

Pre-defined observatories: Grouped by wavelength range, a set of professional observatories around the globe are available for rapid selection.

Searches in the IAU database: Using a text field input with autocompletion, the user can search the database of the International Astronomical Union for additional observatories.

Custom observatories: Most useful for citizen scientists and amateur astronomers, custom locations can be defined. The user can either rely on the GPS position of his device or input the coordinates and parameters of his/her setup manually. A user account (that can be created for free only with a valid email address) is necessary to save the created entries for later use.

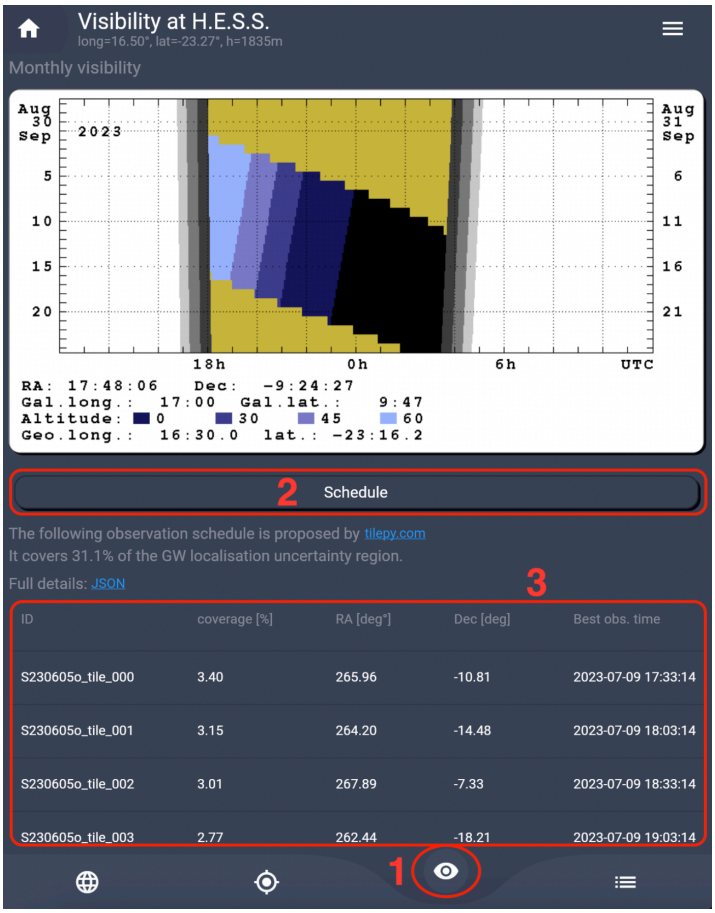

Fig. 4. Request of a GW follow-up schedule in the mobile Astro-COLIBRI app.

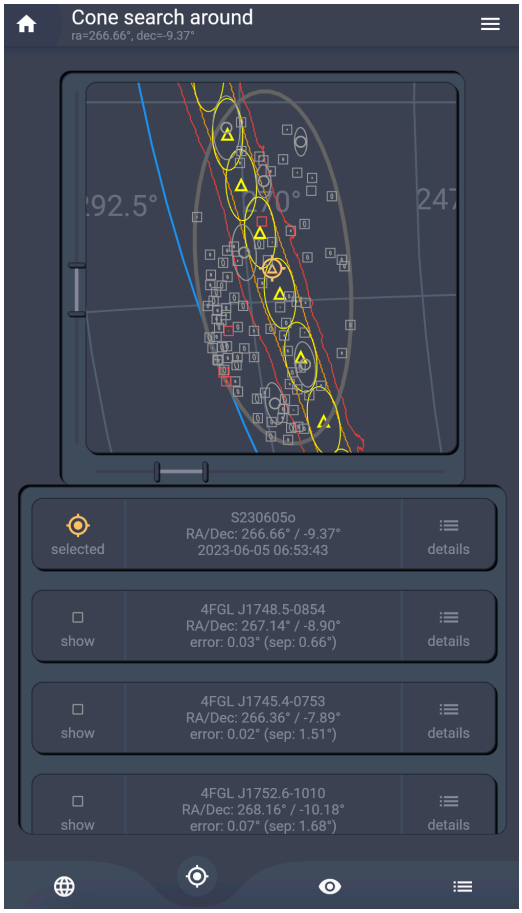

Fig. 5. Visualisation of the resulting observation plan.

4 Gravitational waves

Gravitational waves (GWs) and the associated multi-wavelength emissions allow unprecedented studies but are challenging due to the large localisation uncertainty regions provided by the gravitational wave interferometers. Follow-up observations aiming to localise the source of the GW emission thus require dedicated and optimized scheduling procedures. One such scheduling tool is *tilepy* (Schüssler et al. 2023), a packaged that has been developed within the H.E.S.S. collaboration (Ashkar et al. 2021). The code is publicly available (cf. tilepy@GitHub). In addition, Astro-COLIBRI is providing an open, cloud-based and ready-to-use installation at `https://tilepy.com` from which the scheduling calculation can be requested easily via an API endpoint.

Furthermore, the *tilepy* API has been integrated into the Astro-COLIBRI graphical interfaces. A typical use case can be described as: if matching the various user-defined filter criteria, Astro-COLIBRI users are notified upon the detection of a new GW event in real-time. They can verify all details and parameters of the event directly in the app. The localization of the event is displayed via two contours, representing 50 and 90% containments. For each GW event and each user-selected follow-up observatory, an optimized follow-up schedule can then be obtained directly in the app or via the web interface (cf. Fig. 4). The request can be submitted via a dedicated button (2) on the visbility screen (1). The derived observation positions are then automatically displayed in a table (3) and overlayed on the skymap, which allows one to check for possible related detections of transient events (e.g. a GRB, a high-energy neutrino, etc.). An example of this display is shown in Fig. 5. Finally, the details of the observation plan can be downloaded in JSON format.

5 Conclusions

Astro-COLIBRI offers a comprehensive and efficient solution for real-time multi-messenger astrophysics, enhancing the discovery potential and collaboration within the astronomy community and with citizen scientists around the world. By integrating various data resources and providing intuitive interfaces, Astro-COLIBRI enables amateur and professional astronomers to better understand and explore the nature of transient astrophysical events.

The Astro-COLIBRI development team welcomes comments and feedback from the community to further improve the platform and can be contacted at astro.colibri@gmail.com.

The authors acknowledge the support of the French Agence Nationale de la Recherche (ANR) under reference ANR-22-CE31-0012. This work was also supported by the Programme National des Hautes Energies of CNRS/INSU with INP and IN2P3, co-funded by CEA and CNES and we acknowledge support by the European Union's Horizon 2020 Programme under the AHEAD2020 project (grant agreement n. 871158).

References

Ashkar, H., Brun, F., Füßling, M., et al. 2021, JCAP, 2021, 045

Reichherzer, P., S. F. L. V. B. J. M. J. K. A. 2023, Galaxies, 11, 22

Reichherzer, P., S. F. L. V. Y. A. K. A. A. H. B. J. 2021, ApJS, 256, 5

Schüssler, F., Ashkar, H., de Bony de Lavergne, M., & Seglar-Arroyo, M. 2023, in 38th International Cosmic Ray Conference. July 26 - Aug 3, 2023. Nagoya, PoS(ICRC2023)1469

SF2A 2023
M. N'Diaye, A. Siebert, N. Lagarde, O. Venot, K. Baillié, M. Béthermin, E. Lagadec, J. Malzac, J. Richard (eds)

PLANÈTE SCIENCES AND THE JEAN-MARC SALOMON OBSERVATORY IN BUTHIERS, FRANCE: CITIZEN SCIENCE PROJETS

P. Barroy[1,2], M. Irzyk[1], J.-M. Vienney[1], Y. Delisle[1], P.-F. Rocci[1,3], D. Quéant[1], S. Neveu[1], M. Serrau[1,3], A. Lekic[1,3,4], D. Carlier[1], J.-B. Bellier[1], J.-P. Godard[1], C. Courson[1], M. Grandidier[1,4], F. Targa[1], J. Paufique[1 5], P. Traverse[1], J. Rodriguez[1], O. Desormiere[1] and T. Midavaine[1,3]

Abstract. Planète-Sciences is a French national association developing & managing a large professional-class telescope in an observatory for outreach and citizen science. This poster aims at presenting some of its capabilities and to inspire you to organize your own experiment or join in with those on offer.

Keywords: astronomy, citizen science, occultations, exoplanets, light curve, spectroscopy, asteroid, TJMS

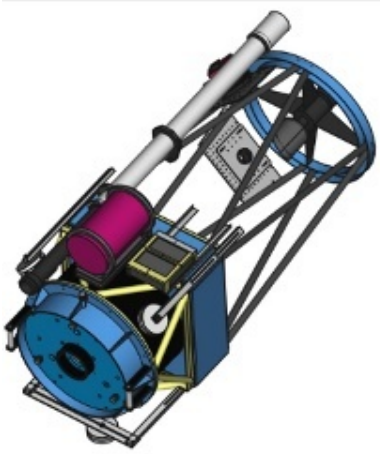

Fig. 1. Telescope Jean Marc Salomon schematic

1 Introduction

Planète Sciences (Planète-Sciences 2023) welcomes ∼100000 people each year for a wide range of activities, thanks to ∼80 salaried staff and ∼1000 volunteers. Planète Sciences manages an observatory, Centre d'Astronomie Jean-Marc Salomon (UAI code 199). Located in Buthiers near Malesherbes, the observatory is easily accessible to a large audience, by RER commuter train from Paris, Ile de France region, or from Loiret, Centre region, even though it has a relatively unspoilt sky (SQM ∼21 magnitudes per square arcsecond, seeing ∼2", Gâtinais regional nature park). Accommodation of groups of up to a few tens nearby can be provided by Buthiers leisure park. A 600 mm diameter telescope, the Télescope Jean-Marc Salomon (TJMS), is on site, as are a number of other instruments, mobile instruments for all kinds of astronomical activities (Sol'Ex, Coronado, Cassegrain, Newtonian), enabling mobile manipulations and easy accompaniment of novices in Pro-Am programs.

[1] PLANÈTE-SCIENCES, Observatoire JM Salomon, 73 rue des Roches, 77760 , Buthiers, France
[2] Université de Picardie Jules Verne, 80000 Amiens, France. mail: pierre.barroy@u-picardie.fr
[3] Société Astronomique de France 3, rue Beethoven, 75016 Paris
[4] IPSA, Institut Polytechnique des Sciences Avancées, 63 boulevard de Brandebourg 94200 Ivry-Sur-Seine, France
[5] European Southern Observatory,Karl-Schwarzschild-Str. 2, 85748 Garching bei Muenchen, Germany

© Société Française d'Astronomie et d'Astrophysique (SF2A) 2023

2 Main equipment

TJMS is a Newton-Cassegrain type telescope used mainly in Newton configuration, with a 2010 mm focal length and a 600 mm primary mirror (F/D∼3.35) recently re-illuminated (MCM 2021), with a pointing speed of 1.5°/s, and an estimated periodic error of 0.5" in 1 minute (MCMT electronics). Now equipped with 4 holding stages (the secondary mirror can be rotated in the direction of each easily), 3 of which have motorized focusing (Lacerta, FLI), the TJMS is instrumented with an Imaging chain, Spectroscopy and 2 Eyepiece-holding stages.

2.1 CMOS imaging chain

Behind a 3" Wynne ASA field corrector is a QHY 268 Pro acquisition camera, with integrated GPS enabling acquisitions at up to 50 frames per second. This camera is built around a Sony IMX571 monochrome CMOS sensor with 78% quantum efficiency, a 51000-electron well, low-gain readout noise, low dark current, and a very low power consumption. 7 filters are camera-ready with Gaia G, Grp and Gbp from the RAPAS (RAPAS 2023) program and Halpha, OIII, SII standard filters. Off-axis guiding is also included in this setup.

2.2 Spectroscopy

A Shelyak LISA spectroscope (Shelyak 2023) has been adjusted to the TJMS (reduction ×0.86). LISA is a High Brightness spectroscope ideal for weak objects : Novae & Supernovae, Planetary Nebulae, Comets, Symbiotic stars, Cataclysmic variables stars and galaxies. Its calibration module makes calibration very easy thanks to an Argon/ Neon lamp with a large number of emission lines over the main spectral range. This same module is equipped with a Tungsten lamp to produce flat fields. With a resolving power R∼500 to 1000 (depending on entrance slit, R∼700 at 35μm), its spectral range covers the visible range between 400 to 700 nm. An ASI294 MM PRO acquisition camera and ASI 174 mini-guiding cameras complete this setup.

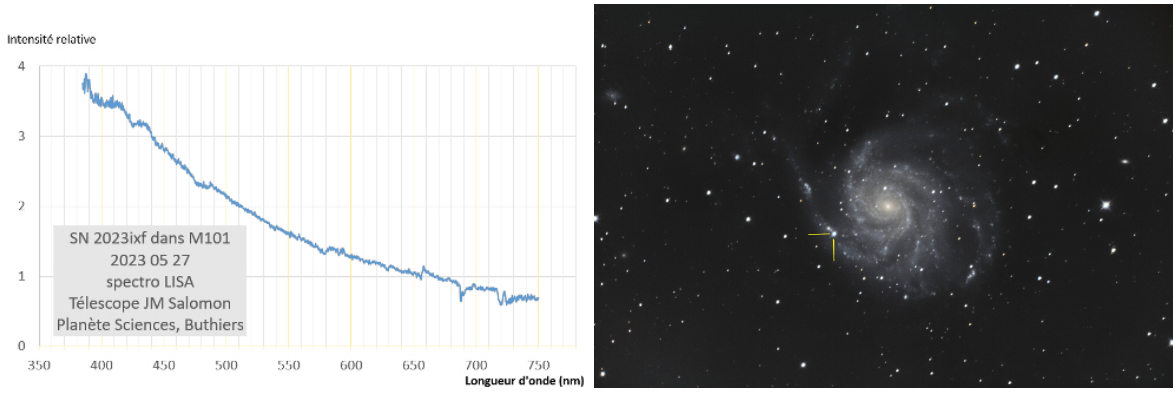

Fig. 2. Left: spectrum of supernova SN2023ixf in M101 galaxy (TJMS) **Right:** same supernova imaged (TJMS)

2.3 Examples of citizen Science at the Astronomy Center JM Salomon

In this observatory, many projects contributing to Sciences can be and are carried out. Asteroids (125718) Jemasalomon and (125592) Buthiers were discovered there on 2001-12-15 by J.-C. Merlin. For instance, we participate in regular stellar occultation campaigns. There have also been measurements of the occultation by Pluto of stars, which have helped understand the dynamics of the tenuous Pluto atmosphere (Meza et al. 2019), or by asteroids (LUCKYSTAR 2023), or by Trojan asteroids (LUCY 2023). There are regular contributions to Exoplanet research e.g. in Exoplanet Transit Database (ETD 2023) or Exoclock (EXOCLOCK 2023, Ariel space mission) (Kokori et al. 2023). Rotation curves of asteroids & Light curves of variable stars are also regularly tackled there (CdR/CdL 2023). There are also more recent participations in KiloNova Catcher, Binast, BESS, ARAS programs. We also welcome events (e.g., European Symposium on Occultation Projects 2019, Technical WeekEnds, Space-Camp 2023)

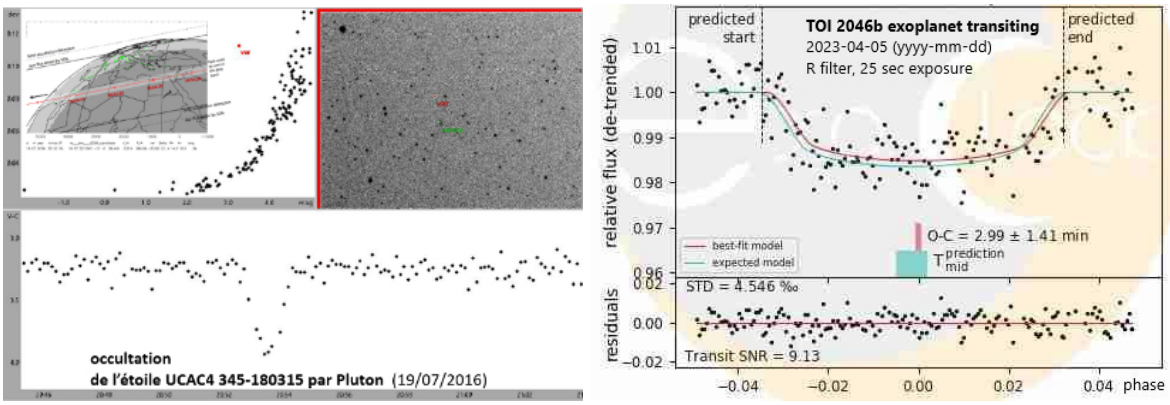

Fig. 3. Left: occultation of a star by Pluto (TJMS) **Right:** transit of Exoclock candidate TOI2046b (TJMS)

3 Conclusion

Recently a special group ("Comité de Promotion Scientifique" CPS) has been developped within Planète Sciences in order to accompany newcomers in experiments that could benefit professionnal astronomy.

Planète Sciences also encourages young people, either in clubs or in schools or universities and their teachers through various programmes (e.g. "Arpenter l'Univers") and can build new programmes. *Please, Come join us with your project/s !*

References

CdR/CdL. 2023, CdR/CdL, Courbes de rotation d'astéroïdes et de comètes, Courbes de luminosité d'étoiles variables régulières, `https://obswww.unige.ch/~behrend/page/cou.html`

ETD. 2023, Exoplanet Transit Database ETD, `http://var2.astro.cz/ETD/index.php`

EXOCLOCK. 2023, EXOCLOCK (ephemerides of transiting Exoplanets for the ARIEL space mission), `https://www.exoclock.space/`

Kokori, A., Tsiaras, A., Edwards, B., et al. 2023, ApJS, 265, 4

LUCKYSTAR. 2023, LUCKY STAR ERC project, `https://lesia.obspm.fr/lucky-star/`

LUCY. 2023, LUCY NASA Mission, Occultations from Ground, `https://lucy.swri.edu/occultations.html`

MCM. 2021, MCM Optique, `https://www.mcm-optique.com/`

Meza, E., Sicardy, B., Assafin, M., et al. 2019, A&A, 625, A42

Planète-Sciences. 2023, PLANETE SCIENCES section Astronomie, `https://www.planete-sciences.org/astro`

RAPAS. 2023, Réseau Amateurs Professionnels pour les Alertes Scientifiques, `https://rapas.imcce.fr/`

Shelyak. 2023, SHELYAK Instruments LISA, `https://www.shelyak.com/produit/pf0021vis-lisa-slit-visible/?lang=en`

SF2A 2023
M. N'Diaye, A. Siebert, N. Lagarde, O. Venot, K. Baillié, M. Béthermin, E. Lagadec, J. Malzac, J. Richard (eds)

PHOTOMETRY OF SYMBIOTIC STARS: FIRST RESULTS FROM AN AM-PRO COLLABORATION WITH JAROSLAV MERC

A. Laouisset[1,2], E. Durand[1,2], T. Porte[1,2], M. Baylet[1,2], B. Delaveau[1,2], G. Malchirand[2,3], L. Sivet[2,3], J.-F. Coliac[2], S. Vasseur[2], P. Wullaert[2], C. M. Tharakan[1], A. Lekic[1,2] and J. Merc[4]

Abstract. In October 2022, a collaborative mission was undertaken by the IPSA Vega association and the SAF Double Star Commission at the Saint-Véran Observatory. During this mission, the esteemed Czech astronomer, Jaroslav Merc, provided the association with a curated list of 8 symbiotic binary star targets for the specific purpose of observing flickering phenomena. We processed the data to make light curves and finally got results of flickering for some of them. The Pro-am collaboration is continuing in order to observe more symbiotic stars and participate in the Jaroslav's database.

Keywords: symbiotic stars, photometry, Pro-Am

1 Introduction

The Saint-Véran Observatory is situated in the Queyras mountains atop the Pic de Châteaurenard and is positioned at a lofty altitude of 2936 meters, with a geographical location at 44°41' 56" North latitude and 6°54' 30" East longitude. These observations were conducted utilizing a 500mm external telescope, which was augmented by a Ritchey-Chrétien telescope boasting a substantial diameter of 50 cm and a generous focal length of 4 meters (F/D = 8). Jaroslav Merc holds the position of astrophysicist-researcher at the Institute of Astronomy, Charles University, located in Prague, Czech Republic. His primary research focus centers on symbiotic binary systems and their associated celestial entities. His work extends to the comprehensive examination of their distribution within the Milky Way and extragalactic regions, as well as the intricate photometric and spectroscopic analysis of symbiotic candidates. Notably, he has established a comprehensive database dedicated to candidate and confirmed symbiotic stars.

The collaborative relationship between IPSA Vega and Jaroslav Merc was initiated at the Observatoire de Haute-Provence and the collaboration began during the SAF mission to Saint-Véran in October 2022. Within this context, Mr. Merc provided a list of 8 stars for observation, including AS 357, IRAS 20434+5052, KIC4918300, MV Cyg, StHa 185, V1760 Cyg, V335 Vul, and DT Psc. The preliminary findings from this Pro-Am collaboration are presented in the following proceeding.

2 Symbiotic stars and flickering

Symbiotic stars are a binary system consisting of a cold giant and a hot star, often a white dwarf or neutron star. A transfer of mass from the cold giant to the hot star causes observable activity called flickering, resulting in complex light curves and variable star spectra. These binary systems are either detached or semi-detached, with orbital periods ranging from 600 days to tens of years. The flickering in the light curves of symbiotic systems has a large amplitude and is most visible at shorter wavelengths, whereas the flickering of accretions alone is predominant in UV light. Observations show that flickering can only be detected transiently in the presence of accretion disks around hot components.

[1] IPSA (Institut Polytechnique des Sciences Avancées), 63 Bis Boulevard de Brandebourg - 94200 Ivry-Sur-Seine

[2] SAF (Société Astronomique de France) - Commission Etoiles Doubles, 3 rue Beethoven - 75016 Paris

[3] SAF (Société Astronomique de France) - Commission Jeunes, 3 rue Beethoven - 75016 Paris

[4] Astronomical Institute, Faculty of Mathematics and Physics, Charles University, V Holešovičkách, 180000, Prague, Czech Republic; jaroslav.merc@mff.cuni.cz

© Société Française d'Astronomie et d'Astrophysique (SF2A) 2023

3 First results and evidence of flickering

The light curves were generated using the Muniwin amateur software, and comparison stars which were sourced from the AAVSO. An ensemble photometry approach was employed, predominantly utilizing the U filter, as it offers enhanced visibility of the accretion phenomenon in symbiotic stars at this wavelength. It is worth noting that the observation of flickering necessitates the use of the shortest available wavelength.

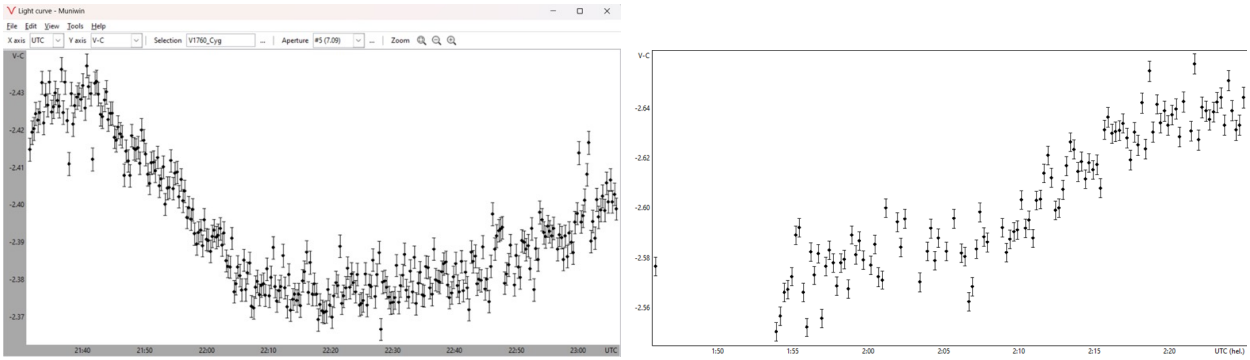

Fig. 1. Left: Lightcurve obtained with Muniwin software for V1760 Cyg showing a possible flickering in U-filter and 10s exposure time. **Right:** Lightcurve obtained with Muniwin software for MV Cyg showing a possible flickering in U-filter and 6s exposure time.

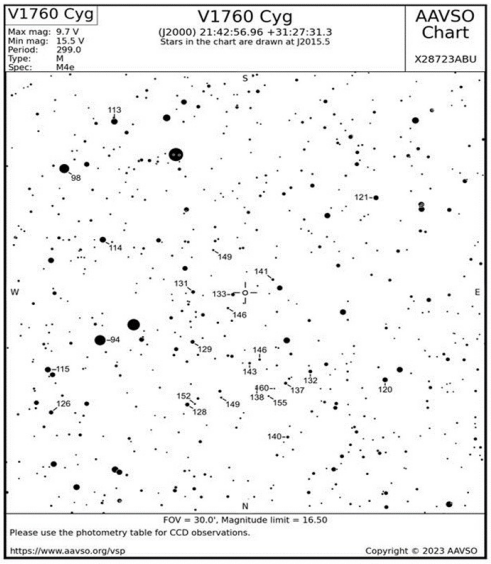

Fig. 2. AAVSO Chart for V1760 Cyg

4 Conclusions

Following consultation with the expert, the observed targets have been categorized as follows:

1. Stable or Non-variable Targets (No Flickering Observed): IRAS 20434+5052, KIC 4918300, StHa 185.
2. Targets Lacking Comparison Stars: DT Psc, EM AS 357.
3. Targets with Potential Flickering of Interest: V1760 Cyg, MV Cyg, and V335 Vul.

Another noteworthy target, V503 Her, has been suggested M. Merc for observation by IPSA Vega and SAF. Commencing in 2023 and extending into 2024, a comprehensive multi-wavelength follow-up will be initiated for these four designated targets. The team will engage in the acquisition of spectra utilizing LISA, contributing to the mutual Professional-Amateur collaboration with Mr. Merc.

SF2A 2023
M. N'Diaye, A. Siebert, N. Lagarde, O. Venot, K. Baillié, M. Béthermin, E. Lagadec, J. Malzac, J. Richard (eds)

A PRO-AM COLLABORATION TO ALLOW NEW DISCOVERIES AT MARS

J. Lilensten[1], J. L. Dauvergne[2], C. Pellier[3], M. Delcroix[2], E. Beaudoin[4] and M. Vincendon[5]

Abstract. Several features have been either predicted or briefly observed in the night upper atmosphere of Mars, namely, blue, green and red aurorae on one side, and high altitude cloud systems on the other. These cannot always be observed by the current armada of spacecrafts but may be revealed through a tremendous observational effort from the Earth. This can only be achieved by a strong international collaboration of astrophotographers and professional astrophysicists. In this article, we show what should be expected from positive observations, why the space instruments are not equipped to do these observations and how to coordinate this effort through a large Pro-Am collaboration.

Keywords: Mars, ionosphere, thermosphere, aurorae, clouds

1 Introduction

The planet Mars has always fascinated mankind. A lot of efforts have been devoted by several space agencies to reveal all its mysteries. Yet, the current set of space instruments are missing some features. The largest ones may partly escape their fields of investigation, especially if they are faint and if they occur at night. This is the case for at least two of them: the visible aurorae and the upper atmospheric night clouds. The incredible task force of astrophotographers could largely compensate for these shortcomings with ground based observations. This is what will be explored in this paper.

2 Visible Mars aurorae: predicted but not yet observed

In 2005, Bertaux et al. (2005) measured an enhancement of UV emissions in the upper atmosphere of Mars with the SPICAM (Bertaux et al. 2000) instrument on board Mars Express (ESA). Using an electron transport code (Lilensten et al. 2015), it was shown that this emission was due to electron precipitation of solar origin, with energies of a few tens of eV (Leblanc et al. 2008). Using the ASPERA-37 instrument, the same authors showed that the crustal magnetic fields, when organised into cusp-like structures, can accelerate solar wind electrons and trigger the observed UV aurorae. It also creates long-lived and active magnetic flux tubes (Dubinin et al. 2009) (altitude of typically 130 km, width of 20 to 150 km) in which the electron energy flux is of the order of 10^4 W.m^{-2}. An intriguing feature is that the UV auroral activity was observed on several subsequent orbits during more than two weeks, implying a stable existence of aurorae. Lately, structures called "plumes" were observed in the visible range up to 1000 km height for about 10 days at the morning terminator (Sánchez-Lavega et al. 2015). The authors suggest that these structures are due to ice particles reflecting solar radiation, mentioning auroral emissions as an alternative possibility. The NASA spacecraft MAVEN confirmed the Mars UV aurorae (Schneider et al. 2015) and could even analyse their behaviour during a strong space weather event (Schneider et al. 2018). In 2015 it was predicted experimentally and theoretically that the mars aurorae should also emit in the visible range (Lilensten et al. 2015). Indeed, the UV aurorae on Mars have a counterpart in the visible spectral range, specifically at 412 nm and 434 nm, i.e. in the blue part of the visible spectrum.

[1] Univ. Grenoble-Alpes, CNRS, IPAG, 38000 Grenoble, France
[2] Société de Planétologie des Pyrénées (S2P) 5 rue Gazan, 75014 Paris, France
[3] Commission des Observations planétaires, Société Astronomique de France, 3, rue Beethoven, 75016 Paris, France
[4] Université Paris-Saclay, LPS (UMR8502), 510 Rue André Rivière, 91400 Orsay, France
[5] Institut d'Astrophysique Spatiale, Université Paris Saclay, Orsay, France

© Société Française d'Astronomie et d'Astrophysique (SF2A) 2023

The Fox Duffendack Barker bands responsible for these emissions correspond to the $\tilde{A}^2\Pi_u - \tilde{X}^2\Pi_g$ transition of CO_2^+ and its blue part represents about 7% of the total production. Moreover, the presence of atomic oxygen should trigger red (630 nm) and green (557.7 nm) aurorae, similarly to the Earth ones. These emissions were predicted to happen mainly in the southern hemisphere above the magnetic anomalies (Acuña et al. 2001). Under the assumption of vertical magnetic field lines, the altitude of the maximum emission was predicted to occur around 140 km (blue and green) and 160 km (red) and higher in case the field lines are inclined. The first red line thermospheric Martian observation occurred on the dayside (Gérard et al. 2020) originating from solar radiation excitation.
One of the most exciting features in the blue, red and green aurorae prediction is that they should be visible with the naked eye. On the Earth, the definition of aurorae is quite fuzzy. In the absence of a given official intensity threshold to determine whether an emission is an aurora, one can simply state that a visible aurora occurs when it is visible to the naked eye. The thermospheric and ionospheric emissions at Mars should be visible with the naked eye, and therefore be quoted as visible aurorae.

3 Cloud system in the upper Martian atmosphere : Observed while not predicted.

The Red Planet is not the subject of continuous monitoring programs by professional ground-based astronomers. Only amateur astronomers carry out this work around periods of opposition. They contribute to several participatory science databases, such as ALPO Japan (`https://alpo-j.sakura.ne.jp/indexE.htm`) and PVOL (`http://pvol2.ehu.eus/pvol2/`). Driven by the above predictions of visible aurorae in the upper atmosphere of Mars, one of the co-authors of this work (JLD) gathered a group of 10 astrophotographers amateurs spread across all continents in 2018. They were connected to a group of astrophysicists in order to constitute a solid team. The idea is that when the Earth and Mars are in opposition, it should be possible to picture the Mars aurorae from the Earth at the beginning or at the end of the night. A good opposition occurs about every second year.
On November 17, 2020, 2 of the 10 observers were able to photograph Mars: Frenchmen Christophe Pellier and Emmanuel Beaudoin. Their data, acquired under excellent conditions, made it possible to follow a huge cloud structure located at the terminator for 3 hours in a row through different filters. The images show the formation emerging from the night, clearly separated from the terminator. Its evolution was followed until the sun rose beneath the cloud. The cloud dissipates shortly afterwards. What was observed here is atypical in two respects: not only is the cloud complex gigantic in relation to the planet, it is also located at an altitude of 92 km. This altitude is comparable to that of noctilucent clouds regularly observed on Earth at high latitudes around the summer solstices (Lilensten et al. 2022).
Detailed analysis of the photometric data showed that the cloud scatters light at all visible wavelengths, with a maximum in the red. This suggests that the light is scattered by dust, water ice or CO_2 particles. The dust hypothesis has been ruled out as incompatible with observations, but water and CO_2 are good candidates. Water ice clouds, for example, have already been observed at this altitude and in this season (Clancy et al. 2019; Stcherbinine et al. 2020). However, water is rare on Mars, and spectroscopic detections to date show that water ice crystals are usually very small at this altitude, with a typical size of around 0.1 to 0.5 μm. However, the photometric data obtained on November 17, 2020 suggest that they are rather larger particles of 1 to 2 μm, which would make this cloud atypical, beyond its unusual dimensions (Clancy et al. 2007; Montmessin et al. 2007; Vincendon et al. 2011; Määttänen et al. 2010; Clancy et al. 2019). CO_2, on the other hand, is abundant, and is the main component of the Martian atmosphere. Previously observed CO_2 clouds at these altitudes may be composed of ice crystals of this size. However, the observation was obtained outside the typical season for CO_2 clouds, and these are usually a few hundred km or even 1000 km across, but never 3000 km, which would also make this cloud an atypical event.
Such structures could originate in the cosmic rays through the nucleation of ice crystals at this altitude, especially as the structures observed are on the edge of a magnetic zone. However, it is rather hazardous to draw conclusions from a single set of observations.

4 Why are these features not observed from space?

Exploration of Mars by spacecraft constitute most of today's discoveries since the first successful flyby of Mars on 14 - 15 July 1965, by NASA's Mariner 4 (Branigan 1965). Today, three operational rovers operate on the surface of Mars, the NASA's Curiosity (Kerr 2012), and Perseverance (Stack et al. 2020) rovers, and the CNSA Zhurong

rover. Eight orbiters are currently operational: Mars Odyssey (Saunders et al. 2004), Mars Express (Schmidt 2003), Mars Reconnaissance Orbiter (Zurek & Smrekar 2007), Mars Orbiter Mission (Srivastava et al. 2015 and references herein), MAVEN (Leblanc et al. 2018 and references herein), the Trace Gas Orbiter (Metcalfe et al. 2018), the Tianwen-1 orbiter (Liu et al. 2020), and the Hope Mars Mission. The harvest of results from this fleet may lead to underestimation of the possibilities offered by observations from the surface of the Earth, but such observations have already revealed their potential for cloud characterisation (Parker et al. 1999; Erard 2000; Bell et al. 2001; Sánchez-Lavega et al. 2015).
Despite this series of efforts, neither the expected visible counterpart of aurorae nor a large upper atmospheric cloud system similar to that discussed in section 3 have been observed with these spacecrafts. The reasons could be:

- Both features are difficult to observe at a global scale from Mars orbit due to the limited field of view of these observations whose primary objective is high spatial sampling. Some spacecraft instruments are dedicated to the monitoring of Mars at global scale and low resolution (e.g., VMC onboard Mars Express, see Hernandez-Bernal et al. 2021). However, it is difficult to follow the dynamics of a given cloud or an aurora using such dataset obtained from a spacecraft moving along its orbit.
- In order to make these observations, one needs cameras with high sensitivities working in the visible range at night. When these spacecrafts were conceived, the visible aurorae were known, and therefore no-one imagined to propose such an expensive camera in the payload. This is a well identified problem in scientific research: Why should one spend a lot of money if there is no chance to make an observation?
- The phenomena discussed here look rare. In the field of surveillance, amateur observations from Earth can really make a difference.

5 Why are these features not observed by professional ground based telescope?

The only reason is that in order to get observation time on these large telescopes, one needs to answer to proposals ways in advance. The selected proposals receive dedicated times of observation. There is no guaranty that the allowed slots can fulfill the positive observation conditions dooming these proposal to failure. There is of course an alert mode, but even on alert, there is no guaranty of success. Only a long continuous observation of Mars can lead to achieve this challenge.

6 The solution ahead: Earth-based observations by astrophotographers

Amateur observations from Earth can make a contribution in several areas, namely (1) the large field of view (large-scale phenomena) and (2) the possibility of making many and continuous observations, seeing temporal evolution and identifying rare events. This is the case for the two features above. On 17 November 2020, Mars and Earth were close to each other with a relative distance of 0.55 AU. Mars solar longitude was 316°. This allowed observing the upper atmosphere of Mars from the Earth at a global scale over the course of several hours. This clearly demonstrates that observing Mars from Earth allows following cloud formation and dissipation over several hours with a broad field of view. The same argument applies to auroras. However, such an effort needs good conditions to be successful, namely:

- The two planets should be close to opposition. This condition is mandatory in order to see part of the Mars nightside from the Earth. The next opposition will occur in December, 2024.
- The number of observers should dramatically expand to reach a hundred scattered over all the continents. This permits to observe Mars 24 hours a day and to insure that there are permanently observers free of cloud cover.
- The observers should be equipped with several color filters. For the current 2020 observations, we used white, red, green blue and UV filters. These allowed to perform a spectrum analysis and to compare with radiative transfer calculations.
- As for the aurorae, the solar activity should be high in order maximize the chances. The solar wind usually screens the cosmic rays, but this effect is not sufficient to fully stop them and prevent the observation of upper atmospheric clouds. In December 2024, the solar activity will be close to its peak, providing perfect conditions.

7 Conclusions

The authors of this contribution are willing to coordinate such a large scale campaign: observing Mars from allover the Earth in order to make the first observation of the Mars visible aurorae, and / or to confirm the discovery of the upper atmospheric clouds and to help characterizing and understanding them. Should you be interested, please contact either Jean Lilensten (`jean.lilensten@univ-grenoble-alpes.fr`) or Jean-Luc Dauvergne (`jl.dauvergne@cieletespace.fr`). As for the 2022 paper, all the contributors will co-sign the resulting publication in case of positive detection.

This work has been funded by the National Program of Planetology (PNP) and the National program of Solar-Terrestrial physics (PNST), France. The discovery of the upper atmosphere cloud at Mars has been rewarded with the Gemini prize of the Société Astronomique de France (SAF) and the Société Francaise d′Astronomie et d′Astrophysique (SF2A).

References

Acuña, M. H., Connerney, J. E. P., Wasilewski, P., et al. 2001, Journal of Geophysical Research (Solid Earth), 106, 23403

Bell, J. F., I., Morris, R. V., Farrand, W. H., & Wolff, M. J. 2001, in Lunar and Planetary Science Conference, Lunar and Planetary Science Conference, 1484

Bertaux, J.-L., Fonteyn, D., Korablev, O., et al. 2000, planetary and space science, 48, 1303

Bertaux, J.-L., Leblanc, F., Witasse, O., et al. 2005, Nature, 435, 790

Branigan, T. L. 1965, The Physics Teacher, 3, 303

Clancy, R. T., Wolff, M. J., Smith, M. D., et al. 2019, Icarus, 328, 246

Clancy, R. T., Wolff, M. J., Whitney, B. A., Cantor, B. A., & Smith, M. D. 2007, Journal of Geophysical Research (Planets), 112, E04004

Dubinin, E., Fraenz, M., Woch, J., Barabash, S., & Lundin, R. 2009, Geophysical Research Letters,, 36, L08108

Erard, S. 2000, Planetary and Space Science, 48, 1271

Gérard, J. C., Aoki, S., Willame, Y., et al. 2020, Nature Astronomy, 4, 1049

Hernandez-Bernal, J., Sanchez-Lavega, A., del Rio-Gaztelurrutia, T., et al. 2021, Geophysical Research Letters, 48, e92188

Kerr, R. A. 2012, Science, 336, 1498

Leblanc, F., Martinez, A., Chaufray, J. Y., et al. 2018, Geophysical Research Letters, 45, 4685

Leblanc, F., Witasse, O., Lilensten, J., et al. 2008, Journal of Geophysical Research (Space Physics), 113, A08311

Lilensten, J., Bernard, D., Barthélémy, M., et al. 2015, Planetary and Space Science, 115, 48, solar wind interaction with the terrestrial planets

Lilensten, J., Dauvergne, J. L., Pellier, C., et al. 2022, Astronomy and Astrophysics, 661, A127

Liu, K., Hao, X., Li, Y., et al. 2020, Earth and Planetary Physics, 4, 384

Määttänen, A., Montmessin, F., Gondet, B., et al. 2010, Icarus, 209, 452

Metcalfe, L., Aberasturi, M., Alonso, E., et al. 2018, Space Science Reviews, 214, 78

Montmessin, F., Gondet, B., Bibring, J. P., et al. 2007, Journal of Geophysical Research (Planets), 112, E11S90

Parker, D. C., Beish, J. D., Troiani, D. M., Joyce, D. P., & Hernandez, C. E. 1999, Icarus, 138, 3

Sánchez-Lavega, A., García Muñoz, A., García-Melendo, E., et al. 2015, Nature, 518, 525

Saunders, R. S., Arvidson, R. E., Badhwar, G. D., et al. 2004, Space Science Review, 110, 1

Schmidt, R. 2003, Acta Astronautica, 52, 197

Schneider, N. M., Deighan, J. I., Jain, S. K., et al. 2015, Science, 350, 0313

Schneider, N. M., Jain, S. K., Deighan, J., et al. 2018, Geophysical Research Letters, 45, 7391

Srivastava, V. K., Kumar, J., Kulshrestha, S., et al. 2015, Advances in Space Research, 56, 671

Stack, K. M., Williams, N. R., Calef, F., et al. 2020, Space Science Review, 216, 127

Stcherbinine, A., Vincendon, M., Montmessin, F., et al. 2020, Journal of Geophysical Research (Planets), 125, e06300

Vincendon, M., Pilorget, C., Gondet, B., Murchie, S., & Bibring, J.-P. 2011, Journal of Geophysical Research (Planets), 116, E00J02

Zurek, R. W. & Smrekar, S. E. 2007, Journal of Geophysical Research (Planets), 112, E05S01

SF2A 2023
M. N'Diaye, A. Siebert, N. Lagarde, O. Venot, K. Baillié, M. Béthermin, E. Lagadec, J. Malzac, J. Richard (eds)

V2-CEMN: IDENTIFICATION OF ASTROPHYSICAL X-RAY SOURCES

R. Eliott[1] and T. Hugo[2]

Abstract. During the 2022-2023 academic year, the group V2-CEMN of the participative astronomy course at IPSA worked in collaboration with a high-energy astronomer, helping him on the development and scientific exploitation of a citizen science experiment, CLAXSON. CLAXSON is a website on which people classify a variety of astrophysical X-ray sources. Thanks to the *XMM-Newton* space observatory, more than 13000 observations have been collected and transformed into catalogues. CLAXSON uses these data and multiwavelength archival data for the users to classify sources. The main goal of this website is to categorise as much objects as possible to map the sky and to find some interesting objects such as ultraluminous X-ray sources and supermassive black holes in different environments, which can help understand the formation and growth of supermassive black holes. During this year, our group has worked on different aspects of the website. We realised a new tutorial for novice users, contributed to develop and validate an upgrade of the experiment consisting in the classification of ultraluminous X-ray sources, improved the visibility of the website by realising a presentation video and discussed about the new features to add to CLAXSON.

Keywords: Participative astronomy, CLAXSON, high-energy, X-ray binaries, black holes, classification

1 Introduction

Supermassive black holes ($M_{\rm BH} > 10^5 M_\odot$) are ubiquitously found in massive galaxies and contribute to the formation and evolution of galaxies in general, yet their formation and growth is still a largely open question (e.g. Volonteri 2010; Volonteri et al. 2021). They could have been formed by sustained episodes of super-Eddington accretion onto massive seeds, a phenomenon which has its local analogue in ultraluminous X-ray sources (e.g. Gladstone et al. 2009; Kaaret et al. 2017), or by the mergers of these seeds. Some scenarios hence imply the existence of intermediate-mass black holes ($10^2 M_\odot < M_{\rm BH} < 10^5 M_\odot$), which however remain exclusive in current observations with the exception of a few strong candidates detected through their emission in different wavelengths or in gravitational waves (e.g. Farrell et al. 2009; Lin et al. 2018; Chilingarian et al. 2018; Abbott et al. 2020). The advent of deep and large X-ray surveys such as the *XMM-Newton* catalogues (Jansen et al. 2001; Webb et al. 2020) recently opened new avenues to better collect, identify and analyse black holes over their entire mass range. This paper presents the participating astronomy website CLAXSON*, its purpose and how to use it. We then discuss about the V2-CEMN contribution to this website.

2 The website

On CLAXSON, everyone is able to learn how to categorise sources detected in X-rays. Three classes of sources are considered, namely Active Galactic Nucleus (AGN), stars and X-ray binaries. Categorising sources is necessary to accurately map the sky and provide training samples of known sources to feed automatic classification algorithms. More than a hundred thousand sources have been classified on the site, including two thousands by the V2-CEMN group. To classify a source, many parameters have to be considered (Figure 1) such as LoXO, LoXI and Galactic latitude. They respectively refer to the ratios between X-ray and optical or infrared fluxes of the source and the angle it describes with the Galactic plane. Snapshots are also provided to visualise the source in different wavelengths, allowing to classify sources at first sight. Finally, two graphics are shown†, namely the X-ray spectrum and light curve of the source. They are used to recognise various spectral shapes and variability behaviours.

[1] V2-CEMN, IPSA Toulouse, 40 Bd de la Marquette, 31000 Toulouse
[2] ICCUB, Universitat de Barcelona, C. Martíi Franquès, 1, 08028 Barcelona
*`https://xmm-ssc.irap.omp.eu/claxson`
†Some information might be missing for some sources, however snapshots are generally sufficient to classify them.

© Société Française d'Astronomie et d'Astrophysique (SF2A) 2023

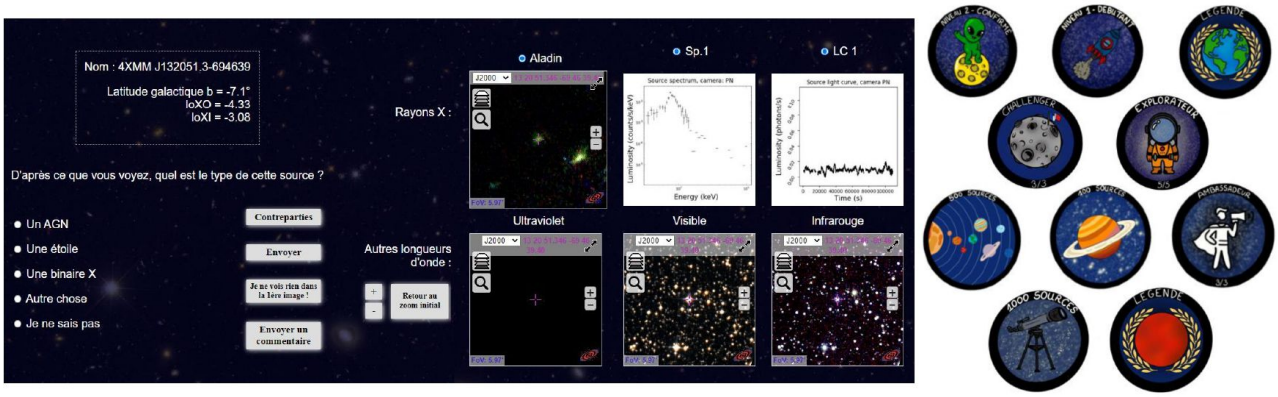

Fig. 1. Left: CLAXSON classification page. **Right:** The badges made by the V2-CEMN group.

3 Our contribution

Concerning our contribution to the website, we made an interactive tutorial for beginners. The purpose of this tutorial is to help beginners to understand the basics of classification and to start classifying. There are two versions of it, a long tutorial explaining the physics behind each parameter used to classify, and a shortened version focusing on the classification task. We also contributed to develop an upgrade of the website to include ultraluminous X-ray sources and our classifications were used to validate it. Some bugs of the website were also fixed in the process. We brainstormed about features to add to the site, such as awarded to users (increasing the gamification of the website) as shown in Figure 1. Finally, we have improved the visibility of the website by presenting it in a video format[‡].

4 Conclusion and outlook

To conclude, we have worked during the 2022-2023 academic year on the improvement of a participating astronomy website, named CLAXSON. The work we provided helped the research of Dr. Tranin. Over the last few years, such citizen science projects have been increasingly acknowledged as a great help to researchers, as illustrated by the success of other platforms such as Zooniverse[§]. The future is bright for CLAXSON: with more than 100,000 classifications and almost 500 sources classified by at least 15 users, the project is entering its scientific exploitation phase and a variety of subprojects are under development to focus on specific categories of X-ray sources. This goes hand in hand with continuous improvements in website features to have more users and enhance their experience.

References

Abbott, R., Abbott, T. D., & Abraham et al., S. 2020, Phys. Rev. Lett., 125, 101102
Chilingarian, I. V., Katkov, I. Y., & Zolotukhin et al., I. Y. 2018, ApJ, 863, 1
Farrell, S. A., Webb, N. A., Barret, D., Godet, O., & Rodrigues, J. M. 2009, Nature, 460, 73
Gladstone, J. C., Roberts, T. P., & Done, C. 2009, MNRAS, 397, 1836
Jansen, F., Lumb, D., & Altieri et al., B. 2001, A&A, 365, L1
Kaaret, P., Feng, H., & Roberts, T. P. 2017, ARA&A, 55, 303
Lin, D., Strader, J., & Carrasco et al., E. R. 2018, Nature Astronomy, 2, 656
Volonteri, M. 2010, A&A Rev., 18, 279
Volonteri, M., Habouzit, M., & Colpi, M. 2021, Nature Reviews Physics, 3, 732
Webb, N. A., Coriat, M., Traulsen, I., et al. 2020, A&A, 641, A136

[‡]https://www.instagram.com/reel/CoZyLyrqw4T/?utm_source=ig_web_copy_link&igshid=MzRlODBiNWFlZA==
[§]https://www.zooniverse.org/

Session S07

Cosmic Rays and Cosmology

SF2A 2023
M. N'Diaye, A. Siebert, N. Lagarde, O. Venot, K. Baillié, M. Béthermin, E. Lagadec, J. Malzac, J. Richard (eds)

SEARCH FOR DIFFUSE GAMMA-RAY EMISSION FROM GALAXY CLUSTERS WITH THE CHERENKOV TELESCOPE ARRAY

R. Adam[1] and the CTA consortium

Abstract. Galaxy clusters represent the last step of the formation of large-scale structures in the Universe. They are both useful cosmological probes and unique astrophysical laboratories. The clusters grow by accretion of surrounding structures and from the merging of subclusters, in very energetic events, eventually forming a diffuse gas phase made of a hot thermal component, but also leading to particle acceleration up to very high energies. One of the key science projects of the Cherenkov Telescope Array (CTA), the next generation array of imaging atmospheric Cherenkov telescopes, being built in La Palma (Spain) and Paranal (Chile), consists of the first unambiguous measurement of the diffuse gamma-ray emission associated with the interaction between the cluster cosmic rays protons and the thermal gas. Prospects for probing such a signal using CTA are discussed and we highlight what can be learned about cluster physics from such observations.

Keywords: Galaxy clusters, Intracluster medium, cosmic-rays, gamma-rays

1 Introduction

Galaxy clusters are the largest virialized structures in the Universe with masses up to 10^{15} $M_\odot$ (Voit 2005). The properties of their intracluster medium (ICM) are shaped by the hierarchical growth of structures through mergers and accretion. These dynamic events not only convert kinetic energy into heat but can also accelerate cosmic rays in the ambient magnetic fields (Brunetti & Jones 2014). Additionally, galaxies within these clusters may contribute to cosmic ray generation through active galactic nuclei (AGN) feedback and star formation processes (Fabian 2012).

Recent radio observations have provided direct evidence for the presence of cosmic ray electrons and magnetic fields in galaxy clusters (van Weeren et al. 2019). These observations have revealed various types of radio sources, including radio halos associated with cluster mergers and mini-halos in more relaxed clusters. Galaxy clusters are also expected to store cosmic ray protons (CRp) and heavier nuclei, injected into the ICM via various mechanisms. These CRp can interact with the thermal gas to produce gamma-ray emission (Dennison 1980; Blasi & Colafrancesco 1999), involving high-energy secondary electrons contributing to cluster-scale radio emission. Current theoretical models propose (re)acceleration of emitting electrons by turbulence and shocks, with the role of secondary electrons being debated. Cosmological simulations predict gamma-ray emissions but are subject to uncertainties in acceleration and transport physics (Enßlin et al. 2011; Brunetti & Jones 2014), emphasizing the importance of studying gamma-ray emissions from galaxy clusters.

The search for diffuse gamma-ray emissions from galaxy clusters has continued for over two decades (e.g., Reimer et al. 2003; Ackermann et al. 2014; Ahnen et al. 2016), but definitive detections are still pending, although some hints of a signal have been obtained towards the Coma cluster (Xi et al. 2018; Adam et al. 2021; Baghmanyan et al. 2022). Non-detections have constrained the CRp to thermal energy ratio to a few percent, challenging our understanding of these processes in the ICM, particularly when combined with radio data. Strict gamma-ray limits have also ruled out pure hadronic models for nearby radio halos and tested models involving the reacceleration of secondary particles, contributing to our comprehension of cosmic ray processes in galaxy clusters (Brunetti et al. 2017; Adam et al. 2021).

[1] Laboratoire Lagrange, Université Côte d'Azur, Observatoire de la Côte d'Azur, CNRS, Blvd de l'Observatoire, CS 34229, 06304 Nice cedex 4, France

© Société Française d'Astronomie et d'Astrophysique (SF2A) 2023

The Cherenkov Telescope Array (CTA) is the next-generation ground-based gamma-ray observatory*, offering exceptional sensitivity across a wide energy range (20 GeV to 300 TeV) and improved angular resolution (Cherenkov Telescope Array Consortium et al. 2019). CTA will operate from two locations, La Palma and Paranal, enabling observations of a significant portion of the sky. Its primary goals include the study of cosmic rays and dark matter. CTA will play a crucial role in searching for diffuse gamma-ray emissions from galaxy clusters, with one of the key projects focusing on the Perseus cluster, a promising target for such observations.

The Perseus cluster is a massive ($M_{500} \simeq 6 \times 10^{14}$ $M_\odot$) nearby (redshift $z = 0.017$) cluster with a dense core, with characteristics of a relaxed cool-core cluster. It hosts a radio mini-halo (e.g., Miley & Perola 1975; Gendron-Marsolais et al. 2020). Two cluster member AGNs, NGC 1275 and IC 310, have been identified as variable gamma-ray emitters (Abdo et al. 2009; Neronov et al. 2010). NGC1275 is the central galaxy and is associated with X-ray cavities, indicating significant feedback in the cluster center. Several other radio galaxies in the cluster were not detected in gamma rays but may still contribute to cosmic-ray injection into the ICM. The Perseus cluster is a prime target for gamma-ray searches due to its mini-halo in a very dense location, which concentrates hadronic collisions and secondary particle production. The cluster proximity implies that CTA can resolve the diffuse emission efficiently. Previous searches for gamma-ray emission in the Perseus cluster yielded no detection, setting upper limits on the cosmic-ray to thermal pressure ratio of about 1-2% (Ahnen et al. 2016).

Here, we summarize the current status of the study of the sensitivity of CTA to detect diffuse gamma-ray emission induced by cosmic rays from the Perseus cluster. The dark matter analysis was already discussed in Pérez-Romero & Consortium (2022) and the full analysis can be found in Cherenkov Telescope Array Consortium et al. (2023).

2 Modeling the diffuse gamma-ray emission

2.1 Modeling framework

The production of diffuse gamma-ray emission is expected due to the hadronic interaction between CRp and the thermal gas. We utilize the MINOT code (Adam et al. 2020), which calculates various observable ICM properties based on user-defined cluster conditions. Therefore we model the thermal gas density ($n_{\rm gas}(r)$) and pressure ($P_{\rm gas}(r)$), which provide the target particles and the thermal energy, respectively. Given the thermal gas model, we compute the X-ray and Sunyaev-Zel'dovich observables, which we use in combination with literature data (Churazov et al. 2003; Urban et al. 2014; Planck Collaboration et al. 2016), to calibrate the thermal model parameters. The thermal component is accurately described from the core to the outskirts and its uncertainties are negligible compared to the uncertainties associated with the non-thermal component. We consider the particle interactions to compute the gamma-ray production, but also the secondary cosmic-ray electrons. Assuming different models for the magnetic field strength profile, we compute the diffuse synchrotron emission arising from these electrons. The CRp population is modeled as a function of energy E (or momentum p) and radius r as

$$\frac{dN_{\rm CRp}}{dpdV}(E, r) = A_{\rm CRp}\ p^{-\alpha_{\rm CRp}}\ n_{\rm gas}(r)^{\eta_{\rm CRp}}, \tag{2.1}$$

where the normalization $A_{\rm CRp}$ is related to the parameter $X_{\rm CRp}$, i.e. the CRp to thermal energy fraction within the characteristic radius R_{500}. The two other parameters are $\eta_{\rm CRp}$ and $\alpha_{\rm CRp}$, the spatial scaling with respect to the gas density and the spectral index of the CRp.

2.2 Calibration of the model parameters

The three model parameters, $X_{\rm CRp}$, $\eta_{\rm CRp}$ and $\alpha_{\rm CRp}$, were estimated assuming two different scenarii. In the first scenario, we use the numerical simulation prediction (e.g., Pinzke & Pfrommer 2010) to set our model parameters to $X_{\rm CRp} = 10^{-2}$, $\eta_{\rm CRp} = 1$ and $\alpha_{\rm CRp} = 2.3$, i.e. the baseline model. In the second scenario, we assume that all the relativistic electrons arise from the same hadronic interactions that produce the gamma-rays, i.e. the (optimistic) pure hadronic model. We use the radio data from Pedlar et al. (1990); Gitti et al. (2002) to fit our model parameters and fix them to the best-fit values in the latter case.

*https://www.cta-observatory.org/

3 Simulation, analysis and results

3.1 Sky model and CTA simulations

In order to simulate CTA-like data to be analyzed, we constructed a sky model by considering the two cluster scenarios discussed above. The two AGNs NGC 1275 and IC 310 were included according to MAGIC observations assuming low-state emission (Aleksić et al. 2014; Ahnen et al. 2016). We also included the instrumental background using the standard instrument response function[†]. The event simulations were performed accordingly using the `ctools` software (Knödlseder et al. 2016), for 300h of observing time.

3.2 Analysis and results

We first analyze the simulations to test the upper limits that will be obtained by CTA, in the cluster parameter space, in the case of non-detection. This is done by performing a likelihood fit to the data to set an upper limit on the normalization $X_{\rm CRp}$, given $\eta_{\rm CRp}$ and $\alpha_{\rm CRp}$. The limits are reported in the right panel of Figure 1. CTA will improve the current MAGIC constraints by about an order of magnitude. We can also observe that in the case of non-detection, the pure hadronic scenario will be ruled out.

We then reconstruct the spectrum and profile of the cluster assuming our two different scenarios (Figure 1, left panel, in the case of the pure hadronic model). We can see that in optimistic cases, CTA will be capable of constraining accurately both the spectrum and the profile of the cluster, which are related to the acceleration and transport physics of cosmic rays, although we note significant degeneracy between $X_{\rm CRp}$ and $\alpha_{\rm CRp}$.

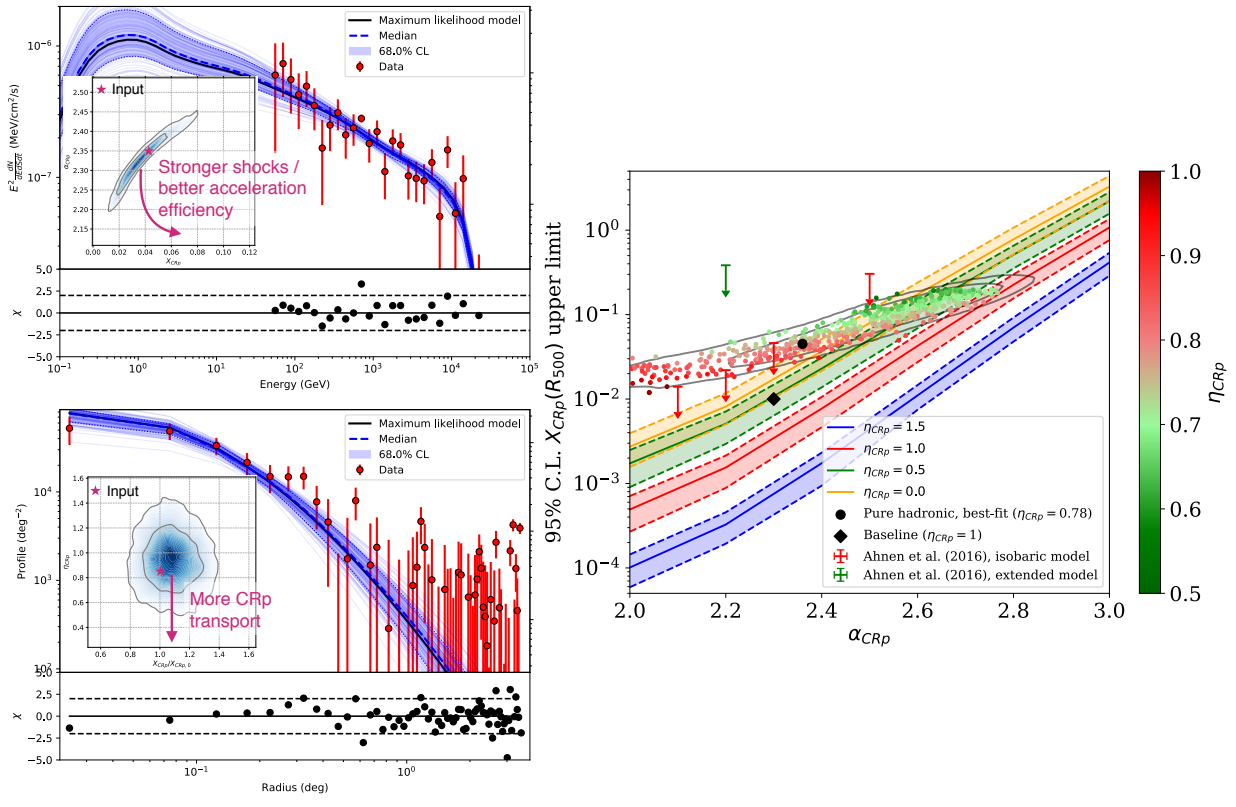

Fig. 1. Left: constraints on the spectrum (top) and profile (bottom) expected in the case of the best-fit pure hadronic model. **Right**: upper limits expected in the case of non-detection. The scattered points show the constraints on the pure hadronic model parameters, with colors indicating the value of $\eta_{\rm CRp}$, and the black point giving the best-fit model.

[†]Available at `https://zenodo.org/record/5163273#.Y5nebbKZNQ0`.

4 Conclusions

In this study, we investigated the sensitivity of CTA to detect diffuse gamma-ray emissions from the Perseus galaxy cluster. We considered contributions from cosmic rays. The contribution from dark matter annihilation/decay has already been discussed elsewhere (Pérez-Romero & Consortium 2022) and the full analysis can be found in Cherenkov Telescope Array Consortium et al. (2023).

We developed a model for gamma-ray emissions induced by CRp using the MINOT software. This model incorporated information about thermal gas pressure and density, magnetic field strength, and the spatial and spectral distribution of CRp. We calibrated these components based on existing literature data. CRp parameters were calibrated for different scenarios, including a baseline and pure hadronic model. Additionally, we considered the background sky, accounting for two point sources that would impact CTA observations. Lastly, we assessed CTA's sensitivity to detect diffuse gamma-ray emissions.

Our main findings regarding gamma-ray emission are as follows. 1) The pure hadronic model, calibrated with existing radio data, suggests about 5% of CRp energy relative to thermal energy within R_{500}, with uncertainties mainly due to limited radio data coverage and magnetic field uncertainties. 2) CTA is expected to improve current limits on the CRp content in the Perseus cluster by about one order of magnitude, reaching a constraint of around 3×10^{-3} within R_{500} in a standard scenario. 3) Assuming the pure hadronic model, CTA should detect the diffuse emission from the ICM with high significance, providing precise constraints on the CRp spectral index and spatial distribution. Thus, the CTA observations of Perseus will address key questions about particle acceleration and transport mechanisms in the ICM.

References

Abdo, A. A., Ackermann, M., Ajello, M., et al. 2009, ApJ, 699, 31
Ackermann, M., Ajello, M., Albert, A., et al. 2014, ApJ, 787, 18
Adam, R., Goksu, H., Brown, S., Rudnick, L., & Ferrari, C. 2021, A&A, 648, A60
Adam, R., Goksu, H., Leingärtner-Goth, A., et al. 2020, A&A, 644, A70
Ahnen, M. L., Ansoldi, S., Antonelli, L. A., et al. 2016, A&A, 589, A33
Aleksić, J., Antonelli, L. A., Antoranz, P., et al. 2014, A&A, 563, A91
Baghmanyan, V., Zargaryan, D., Aharonian, F., et al. 2022, Mon. Not. Roy. Astron. Soc., 516, 562
Blasi, P. & Colafrancesco, S. 1999, Astroparticle Physics, 12, 169
Brunetti, G. & Jones, T. W. 2014, International Journal of Modern Physics D, 23, 1430007
Brunetti, G., Zimmer, S., & Zandanel, F. 2017, MNRAS, 472, 1506
Cherenkov Telescope Array Consortium, Acharya, B. S., Agudo, I., et al. 2019, Science with the Cherenkov Telescope Array
Cherenkov Telescope Array Consortium, T., :, Abe, K., et al. 2023, arXiv e-prints, arXiv:2309.03712
Churazov, E., Forman, W., Jones, C., & Böhringer, H. 2003, ApJ, 590, 225
Dennison, B. 1980, ApJ, 239, L93
Enßlin, T., Pfrommer, C., Miniati, F., & Subramanian, K. 2011, A&A, 527, A99
Fabian, A. C. 2012, ARA&A, 50, 455
Gendron-Marsolais, M., Hlavacek-Larrondo, J., van Weeren, R. J., et al. 2020, MNRAS, 499, 5791
Gitti, M., Brunetti, G., & Setti, G. 2002, A&A, 386, 456
Knödlseder, J., Mayer, M., Deil, C., et al. 2016, A&A, 593, A1
Miley, G. K. & Perola, G. C. 1975, A&A, 45, 223
Neronov, A., Semikoz, D., & Vovk, I. 2010, A&A, 519, L6
Pedlar, A., Ghataure, H. S., Davies, R. D., et al. 1990, MNRAS, 246, 477
Pérez-Romero, J. & Consortium, C. 2022, in 37th International Cosmic Ray Conference, 546
Pinzke, A. & Pfrommer, C. 2010, MNRAS, 409, 449
Planck Collaboration, Aghanim, N., Arnaud, M., et al. 2016, A&A, 594, A22
Reimer, O., Pohl, M., Sreekumar, P., & Mattox, J. R. 2003, ApJ, 588, 155
Urban, O., Simionescu, A., Werner, N., et al. 2014, MNRAS, 437, 3939
van Weeren, R. J., de Gasperin, F., Akamatsu, H., et al. 2019, Space Sci. Rev., 215, 16
Voit, G. M. 2005, Reviews of Modern Physics, 77, 207
Xi, S.-Q., Wang, X.-Y., Liang, Y.-F., et al. 2018, Phys. Rev. D, 98, 063006

SF2A 2023
M. N'Diaye, A. Siebert, N. Lagarde, O. Venot, K. Baillié, M. Béthermin, E. Lagadec, J. Malzac, J. Richard (eds)

THE IMPACT OF COSMIC RAY FEEDBACK ON THE REIONISATION OF THE UNIVERSE

M. Farcy[1], J. Rosdahl[2], Y. Dubois[3], J. Blaizot[2] and S. Martin-Alvarez[4]

Abstract. The first billion years of the Universe are marked by a major transition: the Epoch of Reionisation. Both the reionisation of the intergalactic medium and the regulation of galaxy growth are ruled by feedback mechanisms, but the nature and the interplay of these feedback processes remain undetermined. Cosmic rays (CRs) are ubiquitous and provide a pressure support similar to that of gas, turbulence and magnetic fields, and therefore could have played a significant role in galaxy evolution. In this work, we investigate how cosmic rays regulate the growth of high-redshift galaxies, and if they play a role in the reionisation process by affecting the escape of hydrogen ionising photons from galaxies. For this purpose, we perform and analyse two radiation-magneto-hydrodynamics SPHINX cosmological simulations, with and without CR feedback. We find that CR feedback contributes to regulate star formation, but strongly delays the reionisation of the intergalactic medium. By smoothing the galactic gas distribution, CR feedback prevents ionising photons from escaping the interstellar medium, at any galaxy mass. In order to reconcile cosmic rays with the reionisation of the Universe, better understanding and constraining stellar feedback is required.

Keywords: galaxy evolution, cosmic ray feedback, epoch of reionisation

1 Introduction

To understand how our present-day Universe came into being, we have to look back to a few hundred thousand years after the Big Bang, during the Epoch of Reionisation. This epoch marks the last major transition of the Universe, from neutral to ionised. When the first stars and galaxies form, the radiation they emit photo-ionises their surrounding. With time, these bubbles of ionised hydrogen grow and overlap, which progressively makes the intergalactic medium (IGM) entirely ionised. This only happens if the hydrogen ionising radiation - also called Lyman Continuum (LyC) radiation - propagates through and out of the galaxies, i.e. if it escapes the interstellar medium (ISM) and reaches the IGM. In this scenario, the reionisation of the Universe is driven by the star formation rate density, the production of LyC photons by these stars, and the escape fraction of the LyC photons. Thanks to numerical simulations, it is now established that one of the key processes in regulating both star formation and the escape of ionising photons from galaxies is supernova (SN) feedback (Kimm et al. 2017; Trebitsch et al. 2017; Rosdahl et al. 2018). When the most massive stars explode as SNe, the energy and momentum released disrupt the star-forming clumps. This prevents and delays the formation of the next generation of stars, and also clears channels for photons to escape. However, while SN feedback is important to regulate star formation, it has been shown to be insufficient alone, suggesting that other feedback mechanisms are also important in galaxies (e.g. Hopkins et al. 2014). Another crucial source of feedback might be cosmic rays (CRs). Energetic charged particles accelerated in SN shock waves, CRs provide a significant non-thermal pressure support that can modify the gas kinematics. In particular, CRs have been shown to contribute to regulate star formation and to carry dense gas (e.g. Booth et al. 2013), which is where radiation is preferentially absorbed. The purpose of this work is to study the effect of CR feedback in the early Universe, and to determine if they play a role in the reionisation of the Universe by affecting the escape of ionising radiation from galaxies.

[1] Institute for Physics, Laboratory for Galaxy Evolution and Spectral Modelling, EPFL, Observatoire de Sauverny, Chemin Pegasi 51, 1290 Versoix, Switzerland
[2] CRAL, Université Lyon1, CNRS UMR 5574, ENS de Lyon, 9 avenue Charles André, F-69230 Saint-Genis-Laval, France
[3] Institut d'Astrophysique de Paris, CNRS UMR 7095, UPMC Univ. Paris VI, 98 bis boulevard Arago, F-75014 Paris, France
[4] Kavli Institute for Particle Astrophysics and Cosmology (KIPAC), Stanford University, Stanford, CA 94305, USA

© Société Française d'Astronomie et d'Astrophysique (SF2A) 2023

2 Cosmic ray feedback in the SPHINX simulations

In order to predict the effects of CR feedback on the reionisation history, it is required to 1) model a full cosmological volume that allows to track the ionisation state of the IGM and 2) capture ISM scales, where stars form and where CRs are injected. This is achieved in the SPHINX cosmological simulations (Rosdahl et al. 2018), that both resolve the ISM of tens of thousands of galaxies and the escape of radiation they emit. While the SPHINX simulations succeed in reproducing a reionisation history which is compatible with current observations, they need to boost the rate of supernovae by a factor of four (compared to what is derived from stellar population models, e.g. Kroupa 2001) to produce realistic galaxies. In this study, we want to alleviate the issue with the supernova rate, reducing the empirical boost and modelling the injection and transport of CR pressure instead. Using the RAMSES-RT code (Rosdahl et al. 2013; Rosdahl & Teyssier 2015), we perform two radiation-magneto-hydrodynamics (RMHD) SPHINX simulations, with and without CR feedback. Our two simulations have a box size of 10 comoving Mpc in width, a minimum cell width of 10 pc, and a dark matter mass of $2.5 \times 10^5\,\mathrm{M}_\odot$. Stars form as stellar particles (representing stellar populations) with an initial mass of $1000\,\mathrm{M}_\odot$, following the turbulent star formation prescription from Kimm et al. (2017). We use a mechanical SN feedback model in which multiple SN explosions are sampled between 3 and 50 Myr of the stellar particle lifetime (Kimm & Cen 2014; Kimm et al. 2015). One of our simulation is similar to the fiducial SPHINX from Rosdahl et al. (2018) at the exception that we use a magneto-hydrodynamics solver (Fromang et al. 2006) to evolve an initially uniform magnetic field, with an initial strength of 10^{-12} G at a scale of 1 comoving Mpc. This simulation, that we refer to as "Without CRs", includes the empirical four-fold SN boost, i.e. there are 4 SN explosions per $100\,\mathrm{M}_\odot$. The other simulation "With CRs" employs a more realistic SN feedback with 2 SN explosions per $100\,\mathrm{M}_\odot$, and injects 20% of the energy from each SN explosion (i.e. 2×10^{50} ergs) into non-thermal cosmic ray energy. The latter is transported via advection and diffusion following Dubois & Commerçon (2016); Dubois et al. (2019), with a diffusion coefficient $\kappa = 10^{28}\,\mathrm{cm}^2\,\mathrm{s}^{-1}$.

3 Effects of cosmic rays during the epoch of reionisation

In the following, we study how CR feedback regulates star formation and if it plays a role in reionisation by affecting the escape of ionising radiation from galaxies.

3.1 Star formation rate and UV luminosity function

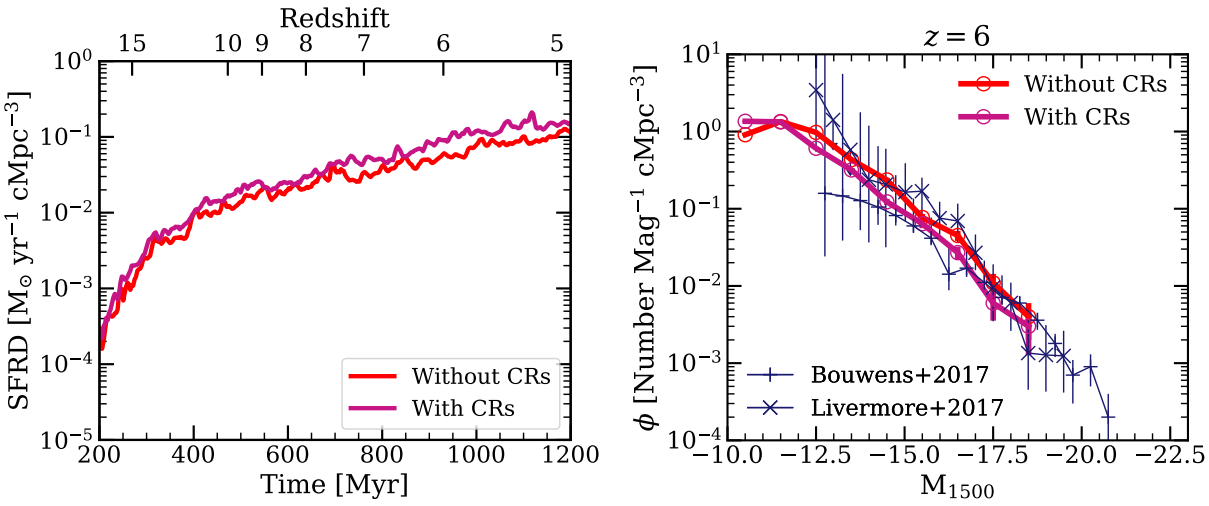

Fig. 1. Left: Star formation rate density as a function of time for the two simulations. The red curve corresponds to the simulation with the strong, boosted supernova feedback. The purple curve is the counterpart with a twice less boosted supernova rate, and including cosmic ray feedback instead. **Right:** Dust attenuated UV luminosity function at $z = 6$. The two simulations have similar star formation rate densities and luminosity functions, in agreement with observations from Bouwens et al. (2017) and Livermore et al. (2017).

In order to illustrate how star formation is regulated in our two simulations, Fig. 1 shows the star formation rate density as a function of time (left panel) and the dust-attenuated UV luminosity function at $z = 6$ (right panel). In all our plots, we show results for the simulation without CRs in red, and for the simulation with CR feedback in light purple. To derive the UV luminosity of the simulated galaxies (as well as to derive the escape fractions), we use the RASCAS code (Michel-Dansac et al. 2020). This post-processing radiative transfer code propagates photons such as UV or LyC photons, and integrate their optical depth to infer their probability of being absorbed or scattered. For UV photons, we take into account dust absorption which scales with the gas metallicity and the dust-to-metal ratio of the Small Magellanic Cloud, following Laursen et al. (2009).

The leftmost panel of Fig. 1 shows that the two feedback models produce a similar star formation rate density at any time, revealing that CR feedback plays the same role in regulating star formation at high redshift as the empirically boosted SN feedback. The rightmost panel of Fig. 1 confirms this conclusion, and additionally shows that the two simulations have a UV luminosity function in good agreement with the observations from Bouwens et al. (2017) and Livermore et al. (2017) shown in blue. This means that our two simulations produce a realistic amount of UV photons, and, consequently, a realistic amount of LyC photons.

3.2 Escape of LyC photons and reionisation

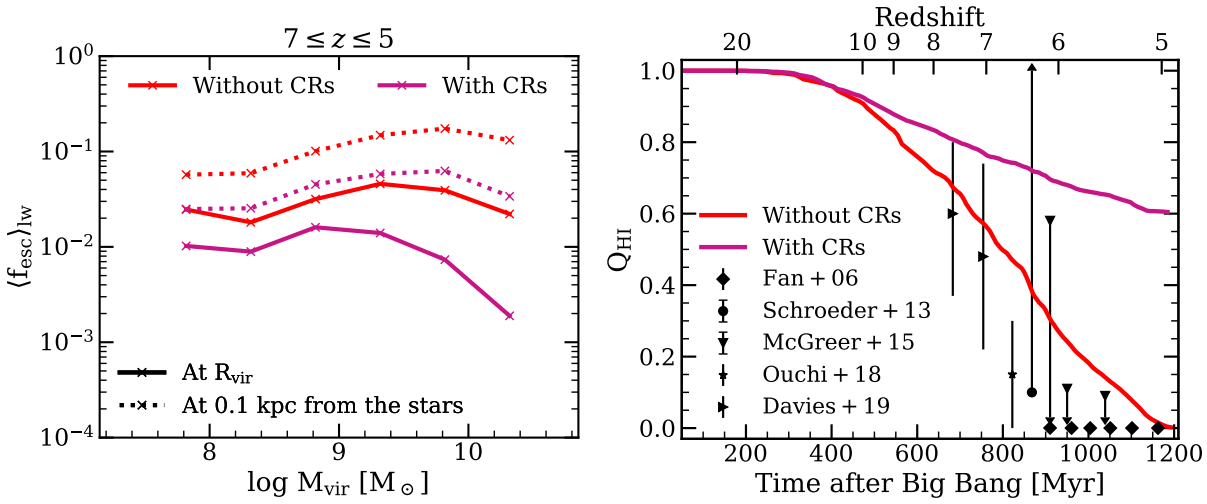

Fig. 2. Left: Luminosity-weighted mean escape fraction per bin of virial mass, from data stacked between $z = 7$ and $z = 5$. Dotted and solid lines respectively show f_{esc} at 0.1 kpc from the stellar particles and at the virial radius of the halos. **Right:** Time evolution of the neutral hyrdogen volume-filling fraction for the two SPHINX runs. Black points are observational estimates, for comparison (Fan et al. 2006; Schroeder et al. 2013; McGreer et al. 2015; Ouchi et al. 2018; Davies et al. 2019). As we do not expect to detect neutral gas by z=5, the simulation with CRs is in strong tension with observations, which is the consequence of CR feedback suppressing escape fractions.

Now that we established that our two simulations similarly regulate star formation and thus the intrinsic production of LyC photons, we want to determine how CRs impact LyC escape fractions and the reionisation of the Universe. We first focus on the left panel of Fig. 2, which shows the luminosity-weighted mean escape fraction f_{esc} as a function of virial mass, with data stacked from $z = 7$ to $z = 5$. The solid curves show f_{esc} measured at the virial radius of the halos, and reveal that CR feedback hampers the escape of ionising photons at any halo mass compared to the simulation without CRs. We also show in dotted lines the f_{esc} at an arbitrary distance of 0.1 kpc from the stellar particles, which is roughly in the ISM of galaxies in most halos. In the two simulations, less than 20% of the LyC photons go beyond 0.1 kpc from the stellar particles that emitted them. In other words, more than 80% of LyC photons are absorbed in the ISM, close to their emitting sources (as already found by Trebitsch et al. 2017). This is even worse for the simulation with CRs: only a few percents of LyC photons escape the ISM. Because CR pressure makes the gas distribution smoother, it increases gas column densities and make them less varying along different lines of sight, preventing LyC photons from escaping the ISM and reaching the IGM (see also Farcy et al. 2022). Therefore, the impact of CRs on the reionisation of the Universe is predominantly determined by the way CR feedback affects the escape fraction of LyC photons.

The right panel of Fig. 2 shows the volume-weighted fraction of neutral gas in the whole simulation volume as a function of time. Black data points correspond to observational estimates from Fan et al. (2006); Schroeder et al. (2013); McGreer et al. (2015); Ouchi et al. (2018); Davies et al. (2019). As found previously by Rosdahl et al. (2018) (with the same setup but without magnetic field), the SPHINX simulation with the boosted SN feedback is in good agreement with the observational estimates, i.e. it produces a realistic reionisation history. After $z = 6$, the fraction of neutral hydrogen drops and becomes extremely low ($Q_{\rm HI} \simeq 10^{-4}$ at $z = 5$) and the whole simulation volume can be considered as ionised. However, the picture becomes completely different with CR feedback, as a consequence from the lower escape fractions. From $z = 10$ and beyond, the fraction of neutral gas in the simulation with CRs starts to diverge with that of the fiducial SPHINX run and remains much higher at any time. The reionisation history in our simulation with CRs is delayed, and the neutral gas fraction is well above the observational estimates: at $z = 5$, 60% of the simulation volume is still not ionised.

4 Conclusions

We study the impact of cosmic ray feedback during the Epoch of Reionisation with two RMHD cosmological simulations, in volumes of 10 comoving Mpc in width and $\simeq 10\,$pc resolution. One simulation is a magneto-hydrodynamics analogue to the SPHINX simulations from Rosdahl et al. (2018), which uses an empirically boosted SN feedback. The other simulation uses a more realistic SN feedback and models CR feedback via the injection of CR energy at each SN event. With our choice of parameters for the CR energy injection and SN rate, we find that CR feedback suppresses star formation similarly as the calibrated strong SN feedback. This leads to a UV luminosity function at $z = 6$ in good agreement with observations, and as a consequence to a realistic production rate of LyC photons. In addition, we find that cosmic ray feedback prevents ionising radiation from escaping the ISM, which has the consequence of strongly delaying the reionisation of the inter-galactic medium. Therefore, the process of reionisation could be sensitive to the efficiency of cosmic ray feedback, and could be used in turn as an additional constraint on our models of stellar feedback.

We acknowledge support from the PSMN of the ENS de Lyon for the computing resources and access to the HPC resources of TGCC under the allocation 2022-A0120413449 made by GENCI. MF acknowledges funding from the Swiss National Science Foundation via a PRIMA Grant PR00P2 193577.

References

Booth, C. M., Agertz, O., Kravtsov, A. V., & Gnedin, N. Y. 2013, ApJ, 777, L16
Bouwens, R. J., Oesch, P. A., Illingworth, G. D., Ellis, R. S., & Stefanon, M. 2017, ApJ, 843, 129
Davies, R. L., Förster Schreiber, N. M., Übler, H., et al. 2019, ApJ, 873, 122
Dubois, Y. & Commerçon, B. 2016, A&A, 585, A138
Dubois, Y., Commerçon, B., Marcowith, A., & Brahimi, L. 2019, A&A, 631, A121
Fan, X., Strauss, M. A., Becker, R. H., et al. 2006, AJ, 132, 117
Farcy, M., Rosdahl, J., Dubois, Y., Blaizot, J., & Martin-Alvarez, S. 2022, MNRAS, 513, 5000
Fromang, S., Hennebelle, P., & Teyssier, R. 2006, A&A, 457, 371
Hopkins, P. F., Kereš, D., Oñorbe, J., et al. 2014, MNRAS, 445, 581
Kimm, T. & Cen, R. 2014, ApJ, 788, 121
Kimm, T., Cen, R., Devriendt, J., Dubois, Y., & Slyz, A. 2015, MNRAS, 451, 2900
Kimm, T., Katz, H., Haehnelt, M., et al. 2017, MNRAS, 466, 4826
Kroupa, P. 2001, MNRAS, 322, 231
Laursen, P., Sommer-Larsen, J., & Andersen, A. C. 2009, ApJ, 704, 1640
Livermore, R. C., Finkelstein, S. L., & Lotz, J. M. 2017, ApJ, 835, 113
McGreer, I. D., Mesinger, A., & D'Odorico, V. 2015, MNRAS, 447, 499
Michel-Dansac, L., Blaizot, J., Garel, T., et al. 2020, A&A, 635, A154
Ouchi, M., Harikane, Y., Shibuya, T., et al. 2018, PASJ, 70, S13
Rosdahl, J., Blaizot, J., Aubert, D., Stranex, T., & Teyssier, R. 2013, MNRAS, 436, 2188
Rosdahl, J., Katz, H., Blaizot, J., et al. 2018, MNRAS, 479, 994
Rosdahl, J. & Teyssier, R. 2015, MNRAS, 449, 4380
Schroeder, J., Mesinger, A., & Haiman, Z. 2013, MNRAS, 428, 3058
Trebitsch, M., Blaizot, J., Rosdahl, J., Devriendt, J., & Slyz, A. 2017, MNRAS, 470, 224

Session S08

Demain l'ELT! Stratégies d'observation, préparation des programmes scientifiques et synergies trans-instruments

SF2A 2023
M. N'Diaye, A. Siebert, N. Lagarde, O. Venot, K. Baillié, M. Béthermin, E. Lagadec, J. Malzac, J. Richard (eds)

MOSAIC: THE ELT OPTICAL AND NEAR-INFRARED MULTI-OBJECT SPECTROGRAPH

M. Puech[1], R. Pello[2], E. Prieto[2], M. Rodrigues[1], R. Sanchez-Janssen[3], G. Dalton[4], T. Contini[5], K. El Hadi[2] and the MOSAIC consortium

Abstract. MOSAIC is the future multi-object spectrograph for the ESO 39 meter Extremely Large Telescope, the ELT. We give here a brief summary of the project status, which has entered phase B1 with ESO in march 2023.

Keywords: Spectroscopy, ELT, galaxies, reionisation, inter-galactic medium, stellar populations, multi-messenger astronomy

1 MOSAIC at the ELT

The ESO's 39 meter Extremely Large Telescope (ELT) will see it first light in 2028 (see Spyromilio et al., this conference). Besides the four first light instruments (MICADO, see Clénet et al., this conference, HARMONI, see Bouché et al., this conference, MORFEO, see Douté et al. this conference, and METIS, see Pantin et al., this conference), two other instruments are planned as part of the ELT instrument roadmap, ANDES, a high-resolution spectrograph, and MOSAIC. MOSAIC [*†] is a versatile multi-object spectrograph dedicated to a large number of science cases for which multiplex capabilities are required (see e.g., Puech et al. 2018; Sánchez-Janssen et al. 2020).

MOSAIC will provide unique observational capabilities at the ELT, with multi-object observations at moderate spectral resolution. It is intended to make use of the entire Field of View available at the ELT (∼40 arcmin^2). The instrument will cover the optical and near-infrared domains with three observational modes. The requirements are the following:

- The MOS-VIS mode will provide integrated spectra of ∼200 objects at the same time, covering the ∼0.45-0.77 μm optical range with two bands. The spectra will be obtained using on-sky apertures of diameter 0.7 arcsec, with spectral resolution R>4000. Alternatively, it will possible to observe ∼70 objects at higher spectral resolution R∼18000 within two narrower windows of specific interest (see below);
- The MOS-NIR mode will provide integrated spectra of ∼200 objects at the same time, covering the ∼0.77-1.8 μm near-infrared range in a single band. The spectra will be obtained using on-sky apertures of diameter 0.6 arcsec, with spectral resolution R>4000. Alternatively, it will possible to observe ∼70 objects at higher spectral resolution R∼18000 within two narrower windows of specific interest (see below), including the CaT triplet;

[1] GEPI, Observatoire de Paris, PSL University, CNRS, 5 Place Jules Janssen, 92190 Meudon, France
[2] Aix-Marseille Université, CNRS, CNES, LAM (Laboratoire d'Astrophysique de Marseille) UMR 7326UMR7326, 38 rue Frédéric Joliot-Curie, 13388, Marseille, France
[3] STFC UK Astronomy Technology Centre, Royal Observatory, Blackford Hill, Edinburgh EH9 3HJ, UK
[4] Dept. Physics, University of Oxford, Keble Road, Oxford, OX1 3RH, UK; RAL, Space, Science and Technology Facilities Council, Harwell, Didcot, OX11 0QX, UK
[5] IRAP, Université de Toulouse III-CNRS, 9, avenue du Colonel Roche, BP 44346 - 31028 Toulouse Cedex 4, France
*http://www.mosaic-elt.eu/
†https://elt.eso.org/instrument/MOSAIC/

© Société Française d'Astronomie et d'Astrophysique (SF2A) 2023

- The mIFU mode will offer Integral Field Units for parallel observations of up to 8 extended objects, covering the same wavelengths that the MOS-NIR mode. The individual Field-Of-View of each IFU will be ∼2.5 arcsec in diameter, with hexagonal shape. Each spaxel (also hexagonal) will be 150mas on-sky, providing coarser spatial resolution compared to HARMONI, but optimised to reach higher surface brightness sensitivity for faint extended objects.

All MOSAIC modes will be assisted by Ground-Layer Adaptive Optics using both Natural and Laser Guide Stars. All modes are designed to provide the best possible survey speed, i.e., to minimize the amount of observing time necessary to reach the required signal-to-noise ratio for all targets in the large statistical samples required by the different MOSAIC science cases (see below and Puech et al. 2018, for further details).

While other ELT instruments will focus on exploiting the central part of the ELT focal plane, MOSAIC will exploit a much larger area (see Fig. 1). At this scale, one has to take into account the fact that the ELT focal plane is non-telecentric. For this reason, MOSAIC is developping an original stepped and tiled focal plane design (see Fig. 1) made of 300 segmented tiles, which can be individually oriented in space to provide local telecentricity. Three distinct families of tiles are being designed, corresponding to different sets of optical fibers/pick-off mirror they will carry, each of them addressing different observing modes: 100 tiles will carry optical fiber bundles suited for MOS-VIS observations (either at low or high spectral resolution), 100 will carry optical fiber bundles suited for MOS-NIR (either at low or high spectral resolution), and 100 other tiles will carry bundles suited for either MOS-VIS or MOS-NIR observations. This design will provide MOSAIC with the very interesting capability of observing in parallel different objects within the same field-of-view with different modes, within the limit of 200 objects at the same time. This will boost the observational efficiency of the instrument.

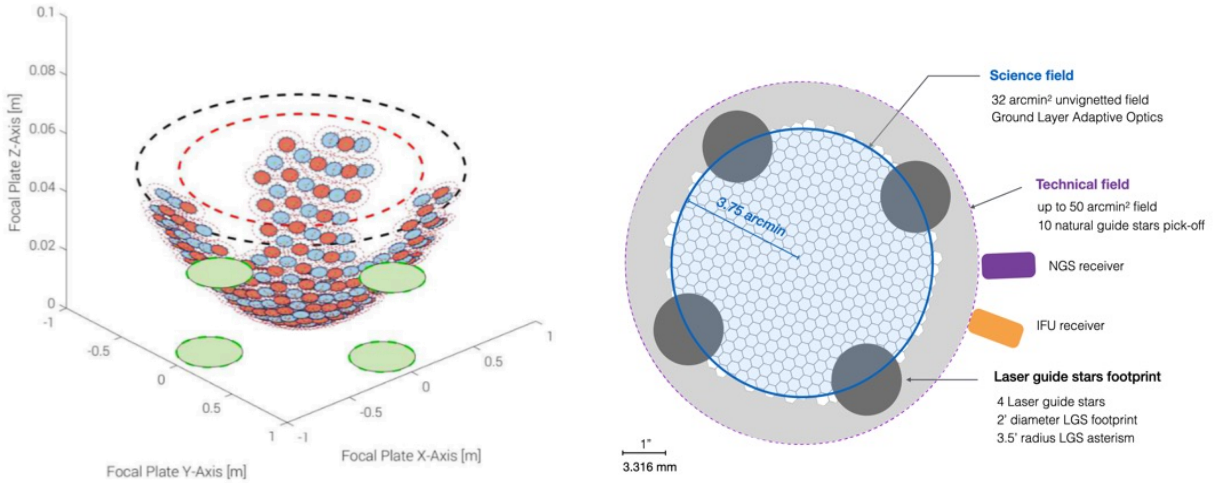

Fig. 1. Left: Illustration of the MOSAIC stepped and tiled focal plane design. The green circles represent the footprints of the 4 Laser Guide Stars, over which no scientific targets can be observed. The blue and red spots represent different families of tiles (see text), which are used to collect the light from different objects in the field-of-view and relay the light towards different observational modes. These tiles can be oriented in space so that telecentricity is locally recovered. **Right:** Top view of the MOSAIC focal plane concept. The tiles are represented by the white hexagones within the science field-of-view area. Their function is to collect the light from objects of interest and re-inject it within optical fiber bundles mounted beneath them. They can also redirect the light towards the 4 Natural Guide receivers or the 8 IFU receivers distributed on the focal plane edge, which will redirect the light towards the NIR spectrograph.

2 Status of the Project

The MOSAIC project was built on the legacy of three former E-ELT phase A instrument studies, EAGLE (Morris et al. 2012), OPTIMOS-EVE (Navarro et al. 2010), and OPTIMOS-DIORAMAS (Le Fèvre et al. 2010). MOSAIC completed its own Phase A conceptual study with ESO in 2016-17 (Morris et al. 2018). The project was largely reorganised in 2021-22 to prepare for a preliminary design phase (phase B, see Fig. 2). This important milestone was reached in march 2023. The consortium, with CNRS/INSU as lead technical

institute, signed over this summer an agreement for a Phase B1 study whose duration is 1.5 years, leading to a Specification and Architecture Review in 2024.

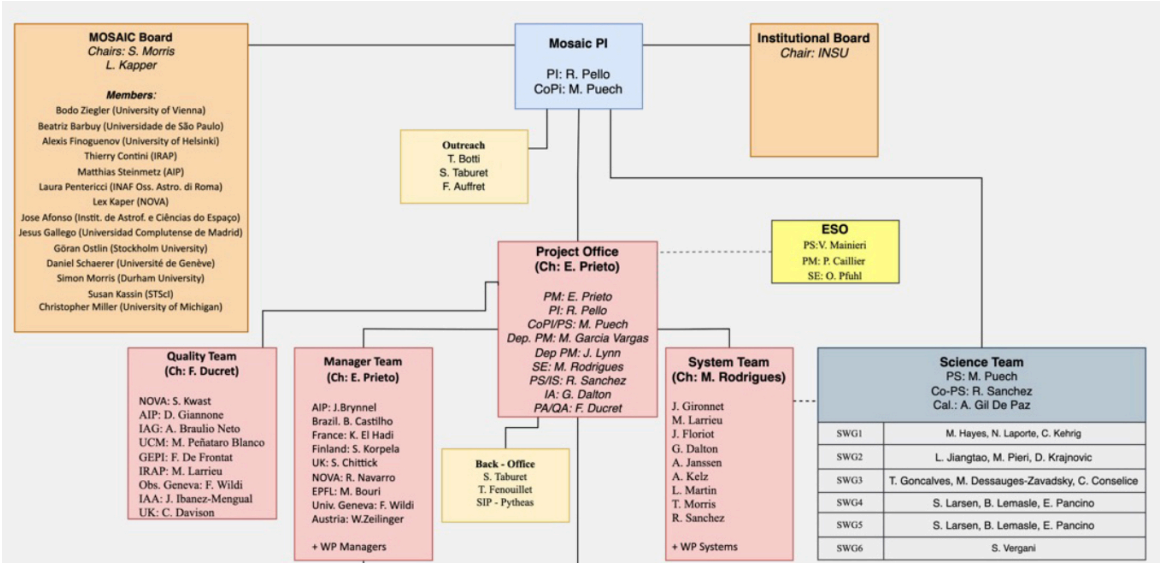

Fig. 2. Organigram of the MOSAIC project.

The particularity of MOSAIC (and ANDES), compared to other ELT instrument projects, is that ESO will not provide any hardware contribution, meaning that the consortium has to raise funding for both the human ressources and hardware procurement. The current budget is currently estimated to ∼750 ETP and 51 M€. Raising such ressources results in a quite large consortium of ∼ 350 members from 31 laboratories in 22 institutional partners spread over 14 countries. The consortium is still growing, since new partners are expected to complete the project budget in the coming years. French laboratories are leading several important Work Packages (WP) within the consortium: the NIR Spectrograph WP (LAM together with Spain), the m-IFU fiber link WP (GEPI), the optical relays WP (OCA/Lagrange), the Electronics and Instrumental Control System WP (IRAP), and the Science Software WP (LAM-GEPI).

The project is currently involved in a consolidation phase during which the partner contributions are reviewed and consolidated. The preliminary conclusions of this phase are suggesting that the MOS-VIS mode appears to be sufficiently mature to be further developped, with most of the required founds available, while the MOS-NIR and mIFU modes would require more founds to be raised (in particular for the detectors) and additional technological developments to be conducted. In this respect, several R&D actions are currently conducted or identified related to the NIR spectrograph camera, the focal plane positioner, or the possible implementation of an Atmospheric Dispersion Corrector. This might lead to a decision to develop the visible channels with a more agressive timeline (with a possible first light foreseen in ∼2031) compared to the NIR channels (∼2032).

The projects is currently also reviewing several design trade-offs:

- wavelength coverage in MOS-VIS: an extension towards the blue is studied with the goal of reaching 0.39μm. Several absorption lines of interest are indeed expected at these wavelength, which are important for the chemical characterization of stars. Other science cases would also benefit a lot of such an extension (e.g., tomography of the IGM, mass assembly). This extension is limited in efficiency by the current throughput of the ELT coating, which is optimised for near-infrared wavelengths;

- use (or not) of an ADC: several technical possibilites are currently studied (global ADC or individual ADC implemented within each individual optical path). Implementing an ADC increases the cost of the instrument but might lead to a simple opto-mecanical design of the optical relays and facilitates a reduction of the number of observing bands in the VIS.

These trade-offs should be finalised by the end of 2023.

3 MOSAIC surveys

All MOSAIC partners already agreed to pool the Guaranteed Time Observations (GTO) granted by ESO as a reward for building the instrument and share it to conduct ambitious and transformative surveys. Presently, the expected GTO consists on 65 nights for the FTE contribution, plus an additional reward for the hardware contribution, which remains to be negociated with ESO in the subsequent phases.

The large Science Team is reorganised into six Science Working Groups corresponding to the prominent MOSAIC science cases (see e.g. Puech et al. 2018; Sánchez-Janssen et al. 2020):

- First light galaxies and reionisation; In particular, MOSAIC will measure UV rest-frame spectra of the most distant galaxies, which is essential to assess their role in the reionisation of the Universe;
- Inventory of matter: MOSAIC will provide the first exhaustive census of matter at z∼3, combining measurements of the tomography of cold gas in the inter-galactic medium, of the abundances of metals in the haloes of galaxies, and of the dark matter content of z∼3-4 galaxies;
- Mass assembly of galaxies through cosmic time, focusing in particular on the spatially-resolved kinematics of low-mass galaxies out to z∼4 and on the stellar dynamics of massive galaxies at high redshifts;
- Stellar populations in and beyond the Milky Way, to unveil the past star formation and evolution history of galaxies, or probe low-metallicity stars in a variety of environnements;
- Transients and multi-messengers, to assess the possible role of MOSAIC in the identification and characterization of their electromagnetic counterparts.

The MOSAIC Science Team, which encompasses more than 290 colleagues from 14 countries, has started the long process of building the future MOSAIC surveys. This process starts by building Science Reference Projects, which will detail what are the foreseen observations with MOSAIC, along with observational considerations (e.g., possible choice of fields, number of visits, calibration requirements, etc.). These will be assembled into a MOSAIC red book at the end of phase B and will be used by the consortium to design Core Projects by the end of Phase D. These will be the building blocks of the MOSAIC surveys, which will be designed to adress the above science cases and provide the most transformational observations in the 2030 landscape. Important synergies with, e.g., other ELT instruments such as MICADO or HARMONI, but also with SKA are expected.

4 Conclusions

MOSAIC will provide the ELT with multi-object observations over a large patrol field, covering the optical and near-infrared wavelength range. MOSAIC is meant to be a multi-tasking instrument for the ELT and, in particular, an efficient follow-up machine for the most powerful space missions and ground-based experiments foreseen in the 2030 landscape (JWST, Euclid, Rubin, Roman, SKA, Athena and others). The MOSAIC project has started a phase B1 with ESO and is anticipating a first light in 2031-32.

We are grateful to the MOSAIC Science and Technical Teams, as well as to the MOSAIC team at ESO. We acknowledge the support received from the CNRS-INSU. This work benefited from the support of the the French National Research Agency (ANR) with the “Programme Investissement Avenir F-CELT (ANR-21-ESRE-0008)”, from the French program “CSAA-INSU”, the AMIDEX AAP-EQUIPEMENT, région SUD, and from region Ile-de-France through the ‘Domaine d’Intérêt Majeur ACAV+‘”.

References

Le Fèvre, O., Hill, L., Le Mignant, D., et al. 2010, The Messenger, 140, 34

Morris, S., Hammer, F., Jagourel, P., et al. 2018, in Society of Photo-Optical Instrumentation Engineers (SPIE) Conference Series, Vol. 10702, Ground-based and Airborne Instrumentation for Astronomy VII, ed. C. J. Evans, L. Simard, & H. Takami, 107021W

Morris, S. L., Cuby, J.-G., Dubbeldam, M., et al. 2012, in Society of Photo-Optical Instrumentation Engineers (SPIE) Conference Series, Vol. 8446, Ground-based and Airborne Instrumentation for Astronomy IV, ed. I. S. McLean, S. K. Ramsay, & H. Takami, 84461J

Navarro, R., Chemla, F., Bonifacio, P., et al. 2010, in Society of Photo-Optical Instrumentation Engineers (SPIE) Conference Series, Vol. 7735, Ground-based and Airborne Instrumentation for Astronomy III, ed. I. S. McLean, S. K. Ramsay, & H. Takami, 77352L

Puech, M., Evans, C. J., Disseau, K., et al. 2018, in Society of Photo-Optical Instrumentation Engineers (SPIE) Conference Series, Vol. 10702, Ground-based and Airborne Instrumentation for Astronomy VII, ed. C. J. Evans, L. Simard, & H. Takami, 107028R

Sánchez-Janssen, R., Hammer, F., Morris, S., et al. 2020, in Society of Photo-Optical Instrumentation Engineers (SPIE) Conference Series, Vol. 11447, Ground-based and Airborne Instrumentation for Astronomy VIII, ed. C. J. Evans, J. J. Bryant, & K. Motohara, 1144725

SF2A 2023
M. N'Diaye, A. Siebert, N. Lagarde, O. Venot, K. Baillié, M. Béthermin, E. Lagadec, J. Malzac, J. Richard (eds)

MICADO SPECTROSCOPIC MODE FOR EXOPLANET CHARACTERIZATION

P. Palma-Bifani[1], P. Baudoz[2], E. Huby[2] and G. Chauvin[1]

Abstract. MICADO is a general-purpose near-infrared spectro-imager that will, among others, observe exoplanets, aiming to understand their physics, formation, and evolution. This instrument will follow up the current discoveries to allow an unprecedented characterization of architecture, orbits, circumplanetary disks and moons formation, detection of molecules, and atmospheric studies. This will become feasible by using the gain in angular resolution to resolve chemical species in the atmospheres of young Jupiter-like exoplanets and even more mature planets. The ELT will be a highly oversubscribed instrument, which makes it evident that synergies with current and future facilities will be fundamental. Only the best-suited, well-justified, game-changer targets will be observed. During the first stage of this ongoing project, we constrain that the main limitations for performing exoplanet-related science will arise from the host star speckles field contamination. We aim to characterize the speckle noise for the long-slit spectroscopic mode in contrast, projected separation, and wavelength dependency, among others. In this context, we are developing a data reduction and analysis strategy, which we present here.

Keywords: ELT, MICADO, instrumentation, high-resolution spectroscopy, exoplanets, direct imaging

1 Introduction

MICADO will be one of the first-generation instruments at the Extremely Large Telescope (ELT) currently under construction by ESO. It is designed to be a versatile instrument promising to push science in various topics. Among its many applications, it will play a key role in unveiling the mysteries surrounding planetary-mass companions' formation, evolution, and physical properties. MICADO has exceptional capabilities, including astrometry, high contrast, spatial, and spectral resolution. Its spectroscopic mode is particularly captivating for the exoplanet community. It opens up possibilities for an in-depth understanding of young planets by studying their atmospheric chemistry, cloud dynamics, and physical properties, for example, the rotational period. As we look ahead, we aim to establish a meticulous data reduction methodology to be prepared when the time arrives to answer some of the fundamental questions we seek to address by targeting the most suitable exoplanets. In this document, we characterize the observing mode in section 2. We present our simulation framework for the spectroscopic mode of MICADO and describe our preliminary results in section 3 and to conclude, our closing remarks are in section 4.

2 Observing mode

MICADO provides two slits. The short slit will have a length of 3 arcsec and a width of 15 mas, while the long slit length will be 15 arcsec with a corresponding width of 20 mas. There will be three different modes allowing simultaneous spectroscopy in the following bands: IY, J, and HK. In this work, we use the long slit spectroscopic mode with the HK filter, which has a pixel scale of $\sim$4 mas and a spectral resolution of $\sim 20\,000$. For further details regarding the MICADO instrument and its components, we recommend referring to the ESO official webpage*

[1] Laboratoire Lagrange, Université Cote d'Azur, CNRS, Observatoire de la Cote d'Azur, 06304 Nice, France
[2] LESIA, Observatoire de Paris, PSL Research University, CNRS, Sorbonne Universités, UPMC Univ. Paris 06, Univ. Paris Diderot, Sorbonne Paris Cité, 5 place Jules Janssen, 92195 Meudon, France
*ESO/MICADO `https://elt.eso.org/instrument/MICADO/`

© Société Française d'Astronomie et d'Astrophysique (SF2A) 2023

MICADO has been designed in a particular way where the slit, located in the mask and aperture wheel, is before the air dispersion corrector (ADC). In practice, this means that for this particular operating mode, the ADC will be unavailable, and there will be a shift of the center of the point spread function (PSF) over wavelength (see equation 4 of Filippenko 1982). Given the slit's thin width (∼20 mas), to assure that all wavelengths of our science object will land inside the slit, the slit must stay aligned to the parallactic angle during observations. This will ensure that the atmospheric dispersion will be projected in the same direction as the slit length, and therefore, no information will be lost at short or long wavelength. Currently, two operational modes for spectroscopic observations can be considered considering the parallactic angle variation constraint: field tracking and pupil tracking.

1. **Field tracking**: This mode will use the de-rotator module of MICADO to rotate the slit to follow the parallactic angle variation between each exposure. In this mode, the diffraction effects from the spiders rotate over time while the field (center of the star and planet position) remains static with respect to the slit and the detector. This stabilization of the field keeping the planet well centered inside the slit is precised to about ∼3 mas every 15 minutes.

2. **Pupil tracking**: In this mode, the field rotates, and the spiders are fixed on the detector. The field selector (FS) within the SCAO system will compensate for the sky's rotation to keep the planet centered in the slit while the star is rotating. The precision will be about ∼6 mas every hour with no mandatory overheads.

3 Simulations setups and preliminary analysis

Many efforts are being carried out by different groups with the scope of realistically simulating MICADO detector defects and noise sources. One of the main Python packages being developed is ScopeSIM[†]. In this context, our current work is focused on constraining the limitations arising from our specific science case, where we aim to observe faint exoplanets close to bright stars. In a further stage, we plan to plug our simulations into ScopeSIM and, this way, account for all the instrument-related noise sources over the physical limitations.

To generate realistic datacubes where the point spread function (PSF) scales over wavelength, we use our internal Python code, MISTHIC, authored by Elsa Huby and Pierre Baudoz. The flux unit for a simulated PSF with MISTHIC is defined so that for each wavelength, the integrated cube slice value is constant, meaning that the total number of photons incident on the telescope is our fixed quantity. Therefore, we normalized each wavelength by the integration over both spatial dimensions and the final unit is proportional to the photon number. To test our simulations with a realistic science scene, we recreated the HR 8799 system. This is a known system with four directly imaged companions that have between 5 and 10 times the mass of Jupiter (Marois et al. 2010). We simulated the planetary system ephemerids on June 22nd, 2023, using the webpage WhereIsThePlanet[‡].

As shown in Figure 1, we first simulate the field of view, then position the slit and extract a corresponding 4D-datacube. The datacube is a function of the slit length and width, wavelength, and exposure time. For the simulation, we defined an integration time of 30 s per exposure and created 120 exposures. Integrating the planet over time results in the arc-shape projection in panel iii/ of Figure 1, which we show to visualize the rotation of the field with respect to the diffraction patterns of the spiders. A snapshot of the datacube at a fixed wavelength and integrated over the slit width is shown in panel iv/ of Figure 1.

For the star and planet e, we multiplied the simulated PSF over wavelength by a representative spectrum. For HR 8799 e we used an Exo-REM spectrum at T_{eff} = 1100 K, log(g) = 4 dex, [M/H] = 0 and a solar C/O ratio of 0.55, with an intrinsic wavelength resolution of ∼30 000 (Charnay et al. 2018) interpolated to a final resolution of 20 000. For HR 8799 A, the star, we used a Kurucz spectra at T_{eff} = 7500 K, log(g) = 4.5 dex, [M/H] = -0.5 (Castelli et al. 1997) with a low intrinsic wavelength resolution of ∼1 000 interpolated to a final resolution of 20 000. We added both spectra considering the speckle field and multiplying the planet intensity by 5.3×10^{-5}, the relative difference in flux to the host star at the K band (Bonnefoy et al. 2016).

To visualize the spectroscopic dimension of the cubes, in the top panel of Figure 2, we extracted a spectrum from the 4D-datacube, integrated over slit width and 13 mas length (spaxel of 20 mas x 13 mas), at time zero and located at slit length = 0.013 arcsec. We use arbitrary flux units for the moment. To start constraining

[†]ScopeSIM documentation: `https://scopesim.readthedocs.io/en/latest/index.html`
[‡]WhereIsThePlanet: `http://whereistheplanet.com`

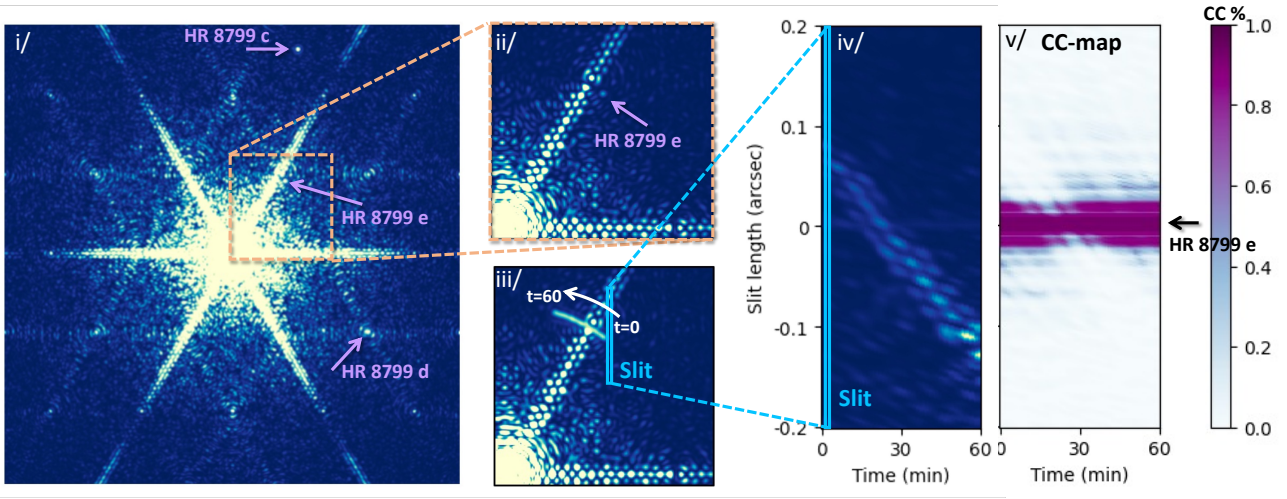

Fig. 1. HR 8799 system simulation using MYSTHIC. i/ The field view is centered on the star, where planets c, d, and e are inside the field of view. ii/ Zoom-in view centered on planet e, where the star speckles are observable. iii/ Same view as in ii/, but the planet is integrated over time for visualization, creating the image's bright arc shape due to the Field rotation. The slit is marked in blue at time position 0. iv/ Time versus slit length cut of our simulated datacube. The third dimension is wavelength, but for simplification, it is not shown in this diagram. The planet is visible as a faint horizontal line centered on the slit (slit length zero). The star speckles are brighter than the planet and cross over time in a diagonal. The slit for exposure zero is sketched for visualization purposes. v/ Cross-correlation map of the simulated datacube with a planetary spectrum. The intensity shows the agreement probability between the data for each pixel and the template used. The purple horizontal stripe shows the planet whose spectrum is intrinsically different from the speckles.

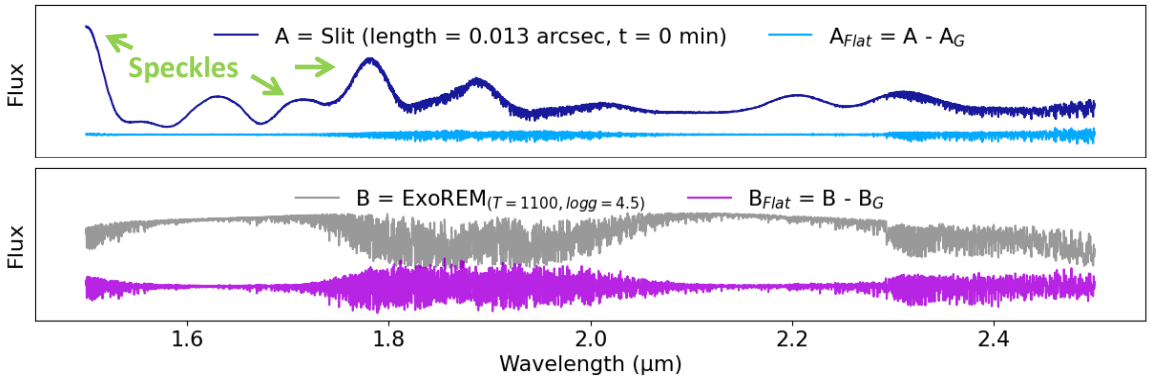

Fig. 2. Spectroscopic information of MICADO. Top panel: The pixel spectrum is extracted at 0.013 arcsec on the slit length dimension and at the first exposure (dark blue colored). The wavy behavior of the spectrum is due to the star speckles that contaminate the planet signal. The light blue colored spectrum is the A spectrum, flattened by applying a Gaussian filter with $\sigma = 10$. Bottom panel. It is the same as the top panel but for the injected planetary Exo-REM spectrum, which we use as template too, without star speckles contamination.

our detection and characterization capabilities by using this observing mode in MICADO, we implemented the cross-correlation (CC) method. Cross-correlation is a powerful tool for detecting molecular species and conducting planetary characterizations even when observations remain contaminated by the host star's residuals (Hoeijmakers et al. 2018) and is defined as:

$$CC = \frac{\sum(A_{\rm flat} \cdot B_{\rm flat})}{\sqrt{\sum(A_{\rm flat}^2) \cdot \sum(B_{\rm flat}^2)}} \tag{3.1}$$

In this equation, 'A' represents the spectrum for each given pixel of the datacube, while 'B' denotes the

template we compare to. The datacube signal and the template are flattened using a Gaussian filter with $\sigma = 10$ filtering most of the spectrum features lower than R = 2 000. As a first approach to evaluate this technique, we used the same injected planet e ExoREM spectrum for the cross-correlation. The overall CC signal in % units is shown in panel v/ of Figure 1. The central strip is the planet signal with a significance of ∼100 %, and the star speckles impact remains insignificant.

4 Closing remarks

Having validated the efficacy of the cross-correlation method through the HR 8799 e case, we will vary the separation and relative planet-star contrast, investigating detection capabilities as functions of separation and contrast and planet temperature. The scope is to understand the population of planets that we can target and particularly characterize with MICADO at the ELT. To explore the whole field of view angle dependency, we will systematically study the angle dependency from 0 to 180 degrees for all separations, corresponding to a projection of half an arc per simulation. This approach will allow us to explore whether specific on-sky angles could enhance observational efficiency. For MICADO, this is of high importance since the spiders of the PSF, where the intensity of the speckles is higher, cross at specific angles (see panel i/ in Figure 1). To improve our simulations, we must introduce several effects. Firstly, we need to account for zenith dependency to accurately reflect MICADO spectroscopic observations since, as stated before, the ADC module will not be used. Secondly, the influence of the temporal variation of the atmospheric turbulence and residuals, a dominant factor in ground-based astronomy, needs to be included, which in practice translates to the fact that speckles will not be static over time, and each exposure will have a slightly different speckle field. In addition, we are eager to explore how the characterization might evolve once we remove the star's speckles. We are studying routines to perform an adapted version of spectral deconvolution (Thatte et al. 2007).

Our ultimate objective is not merely detection but comprehensive characterization. Thus, our next milestone involves the integration of a Bayesian methodology, enabling a systematic analysis of the atmospheric studies of planetary mass companions using a grid of models and individual molecular templates. This will help us identify the limits of contrast, separation, and angular position. Furthermore, it will enable us to quantify the narrowing of error bars as we approach the more favorable observational conditions, marking a significant stride toward precise exoplanet characterization (temperature, surface gravity, metallicity, chemical abundances, isotopologues, clouds, radial and rotational velocities, spin-orbit alignment). Finally, with the overwhelming interest and dedication of the scientific community to the development and utilization of MICADO, it is evident that this instrument will be in high demand. Consequently, its usage should be carefully considered, avoiding blind exploitation. Thus, evaluating MICADO's potential within the broader framework of collaborations and synergies with existing and forthcoming astronomical facilities becomes imperative.

We thank the MICADO and MORFEO consortia for supporting this project.

References

Bonnefoy, M., Zurlo, A., Baudino, J. L., et al. 2016, A&A, 587, A58

Castelli, F., Gratton, R. G., & Kurucz, R. L. 1997, A&A, 318, 841

Charnay, B., Bézard, B., Baudino, J.-L., et al. 2018, The Astrophysical Journal, 854, 172

Filippenko, A. V. 1982, PASP, 94, 715

Hoeijmakers, H. J., Schwarz, H., Snellen, I. A. G., et al. 2018, A&A, 617, A144

Marois, C., Zuckerman, B., Konopacky, Q. M., Macintosh, B., & Barman, T. 2010, Nature, 468, 1080

Thatte, N., Abuter, R., Tecza, M., et al. 2007, MNRAS, 378, 1229

SF2A 2023
M. N'Diaye, A. Siebert, N. Lagarde, O. Venot, K. Baillié, M. Béthermin, E. Lagadec, J. Malzac, J. Richard (eds)

SOLAR SYSTEM OBSERVATIONS WITH THE ESO EXTREMELY LARGE TELESCOPE

A. Delsanti[1], O. Groussin[1], S. Douté[2], F. Merlin[3], P. Rousselot[4], M. Roman[5], O. King[5], L. N. Fletcher[5], F. Clarke[6], B. Neichel[1] and N. Thatte[6]

Abstract. By 2028, the first ever 39m-telescope will have its first light at the ESO Cerro Armazones site (Chile). The first generation instruments of the Extremely Large Telescope (ELT) will enable observations in imaging and spectroscopy that combines great sensitivity with an exquisite spatial resolution. We present several science cases for the ELT from the Solar System, involving comets, Main Belt Asteroids, Trans-Neptunian Objects (TNOs), and the giant planets (atmospheres and satellites).

Keywords: ESO ELT, Solar System, Observations, Inaging, Spectroscopy, Adaptive optics

1 Introduction

Today's major challenges in planetary science can be summarized in three points, as described in the NASA Planetary Science and Astrobiology Decadal Review 2023-2032 (`https://www.nationalacademies.org/our-work/planetary-science-and-astrobiology-decadal-survey-2023-2032`): 1) Origins: evolution of the protoplanetary disk, accretion in the Outer Solar System (how and when did the dwarf planets and cometary bodies form beyond the giant planets? etc.), origin of Earth and inner Solar System bodies, 2) Worlds and Processes: impacts and dynamics, solid body interiors and surfaces, atmospheres, exospheres and climate evolution, giant planets structure and evolution, etc. and 3) Life and habitability: exoplanets, searching for life elsewhere, etc. These questions can be tackled with the new ESO/ELT, thanks to the combination of the superb sensitivity of its instruments and the exquisite spatial resolution. Figure 1 displays the spatial sampling as a function of the distance from the Sun, as well as the apparent diameter in pixels with MICADO (Multi-AO Imaging Camera for Deep Observations) for some prominent objects. For instance, Jupiter's largest satellite Ganymede can be sampled over 1000 pixels, which gives us access to its fine geological structures at the surface (about 30km resolution, from a $\sim$10 mas spatial resolution) and enables long-term monitoring of the geological activity.

2 Comets and Main Belt Asteroids

The minor bodies of the Solar System (comets, main belt asteroids, interstellar objects, trans-Neptunian objects, Centaurs, satellites) are the residuals of planetary formation and hold clues on how and when the planets formed. Observations in imaging and spectroscopy in the visible and infrared domains lead to constraints on surface composition, shape models (and density determination), geological and composition heterogeneities (when the spatial resolution is satisfactory). For comets, the chemical composition of the coma can be unveiled.

The surface composition of the Main Belt Asteroids (mainly located between Mars and Jupiter) is already well constrained from extensive spectroscopic studies with 3m+ class telescopes since the '50s. The new contribution

[1] Aix Marseille Univ, CNRS, CNES, LAM, Marseille, France
[2] IPAG, Grenoble, France
[3] LESIA, Université Paris Cité, Observatoire de Paris, Université PSL, CNRS, Sorbonne Université, 5 place Jules Janssen, 92195 Meudon, France
[4] Institut UTINAM, UMR 6213 CNRS / Univ. Franche-Comté, OSU THETA, BP 1615, 25010 Besançon Cedex, France
[5] School of Physics and Astronomy, University of Leicester, UK
[6] University of Oxford, Keble Road, OX1 3RH, Oxford, UK

© Société Française d'Astronomie et d'Astrophysique (SF2A) 2023

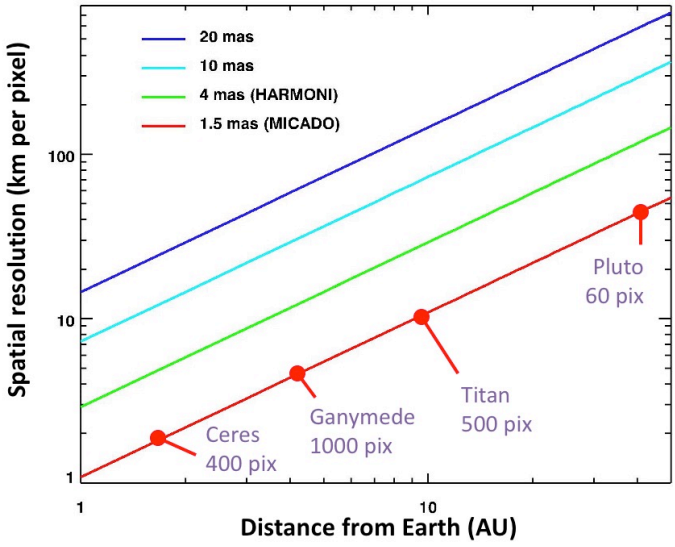

Fig. 1. Spatial sampling (km per pixel) as a function of distance from Earth (AU). The apparent diameter in pixels is given for some prominent objects using the MICADO imager 1.5 mas pixel scale. The final expected resolution (after deconvolution) should be about 10 mas.

of ELT to this domain would be to study the spectral properties of binary asteroids (more than 100 candidates) to constraint their formation mechanism. Also, the study of the shape and density of the asteroids in the 30-100km range in diameter would complete the existing dataset of objects larger than 100km (VLT+SPHERE/ZIMPOL, see Vernazza et al. 2021) and those <30km that were visited by various Space Missions. Figure 2 shows the largest asteroid Ceres, as seen by the NASA/Dawn mission (*in situ*) compared to a SIMCADO simulation of a MICADO image in the H band. The main geological structures can be easily identified.

Comets can be studied by different instruments. METIS (Mid Infrared ELT Imager and Spectrograph) will enable spectroscopic observations in the 3-13 μm range of the dust in the coma. Such observations are important for measuring the fraction of crystalline relative to amorphous silicates (indicative of the comet forming region) and can also be used to search for the presence of aliphatic and aromatic components in the dust (see e.g. Ootsubo et al. 2020, Icarus 338, 113450). ANDES (ArmazoNes high Dispersion Echelle Spectrograph) aiming at the 0.4-2.40 μm range will be a key tool for measuring isotopic ratios for different species in the coma (e.g. ^{14}N/^{15}N in N_2^+ or NH_2 , ^{12}C/^{13}C in CO^+, C_2 or CN). Such isotopic ratios are important tracers for the origin of comets.

3 Trans-Neptunian Objects (TNOs)

More than 3,500 objects have been discovered since the '90s (over ∼70,000 predicted) in the region beyond Neptune (also called the Kuiper Belt), the most famous of them being former planet Pluto. Typical apparent magnitudes peak over 20-22 in the visible and over 18-20 in the NIR: these objects are therefore extremely challenging to observe, even with 8-10-m class facilities. Despite an extensive observational effort from the community over 25 years, spectra are available in the vis-NIR for less than 100 objects and size and albedos for ∼150 objects (mainly using ESA/Herschel measurements with the radiometric method). From these early studies, three types of surfaces emerged: the methane/nitrogen dominated objects (mainly the largest bodies as Pluto, Eris and Makemake), the water ice dominated surfaces (such as Haumea, Orcus or Quaoar), and the "red matter" dominated surfaces, with a steep continuum in the visible and no ice absorption features in the NIR (although this "red matter" has not been fully identified so far). The latter class is populated with a significant fraction of objects with very low signal-to-noise ratio (SNR) spectra (in the J>19 range), blurring the surface composition interpretation, given the (apparent) lack of absorption features.

Although JWST will cast some light on the primitive ice content of a large number of TNOs, the ELT will provide the first spatially resolved data for the Kuiper Belt (besides Pluto and Arrokoth, targets from the NASA/New Horizons mission). HARMONI (High Angular Resolution Monolithic Optical and Near-infrared Integral field spectrograph) will enable the first surface composition contrast mapping of the largest dwarf

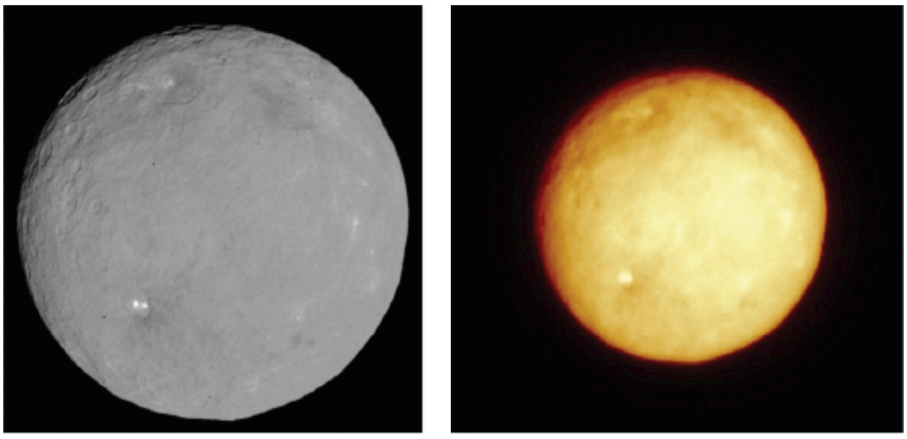

Fig. 2. The largest Main Belt Asteroid Ceres as seen *in situ* from NASA/Dawn mission (left) and simulated from SIMCADO for the ELT/MICADO 1.5 mas pixel scale mode in H band, from an apparent diameter of ∼600 mas (right). The simulated image was not deconvolved. The best spatial resolution that could be achieved after deconvolution should be around 10 mas.

planets in the 0.4-2.4 μm range at R∼3000, but will also allow us to reach any TNO in the J=18-22 magnitude range (above 1000 objects) with a 10-100 SNR NIR spectrum. Additional thermophysical information can be provided by both MICADO in its high resolution spectroscopy mode (up to R∼20,000) and HARMONI (up to R=17000 in the J, H and K bands). Figure 3 shows a HARMONI HSIM simulation of a ∼1300km TNO covered with various amounts of crystalline water ice.

The main breakthrough about TNOs will undoubtedly come from the study of binary (or multiple) systems by the combination of spatially resolved IFU NIR spectroscopy from HARMONI, with fine orbit determination in the astrometric mode of MICADO. The surface composition of both components will constrain the formation scenarios while the determination of the orbit parameters of the system will gives us access to the mass and density. While numerous known candidates can be targeted with ELT, the Vera-C.-Rubin Observatory will provide us with about 30,000 new TNOs in the next decade, offering new exciting science case opportunities for the ELT.

4 Satellites and atmospheres of the Giant Planets

The origin of the giant planets' satellites is still debated: were they formed *in situ* or captured? The known spatially resolved images show various stages of geological resurfacing (craters, cracks, etc.), and activity (plumes, volcanoes, etc.), while spectra can highlight the contrasts in surface composition (see for instance the VLT/SPHERE observations of Ganymede by King & Fletcher 2022 and references therein). All these features are tracers of their origin and further evolution. As illustrated in Fig. 4 for the Galilean satellites Io, Europa, Ganymede and Callisto, with an 8m imaging facility we have access only to partial information such as large physiographic provinces and contrasts (polar caps, bright/dark areas) and the very largest impact craters or volcanoes. With the ELT 12 mas typical spatial resolution (Fig. 4, second row) we can document the local terrain structure, small impact craters and rays from large craters, linae on Europa and small volcanoes on Io, while getting also the local spectral information when using HARMONI Integral Field spectroscopy. For Ganymede observations, a goal of 10 mas final spatial resolution (on deconvolved images) would give us a 30km scale on its surface, to be compared to the ∼20km achieved by NASA/Juno. We can therefore envision a high quality long term monitoring of the geological activity and features of Ganymede and the other satellites with the ELT instruments.

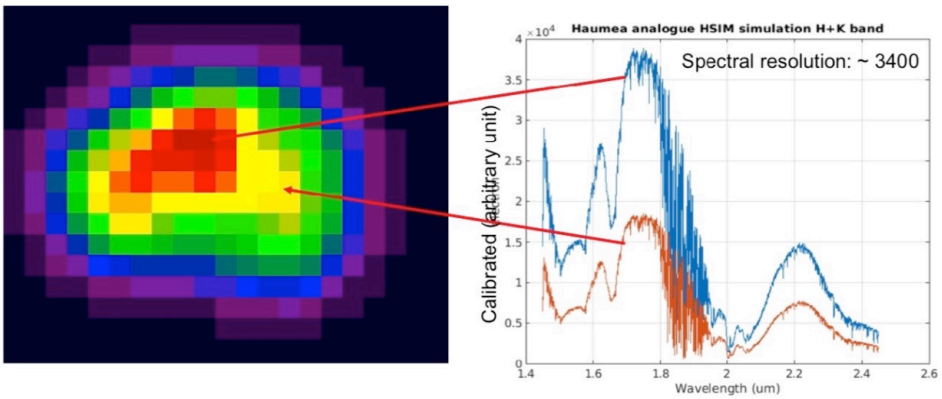

Fig. 3. HARMONI HSIM simulation of a ∼1300km body in the Kuiper Belt (left) covered with various amounts of crystalline water ice. The colors (from purple to red) show increasing signal intensity in instrument units. Such an object is not spatially resolved with existing facilities: the first contrast maps will be obtained with the ELT. The right panel shows the spectral extraction in the H+K band for 2 different pixels at R=3400.

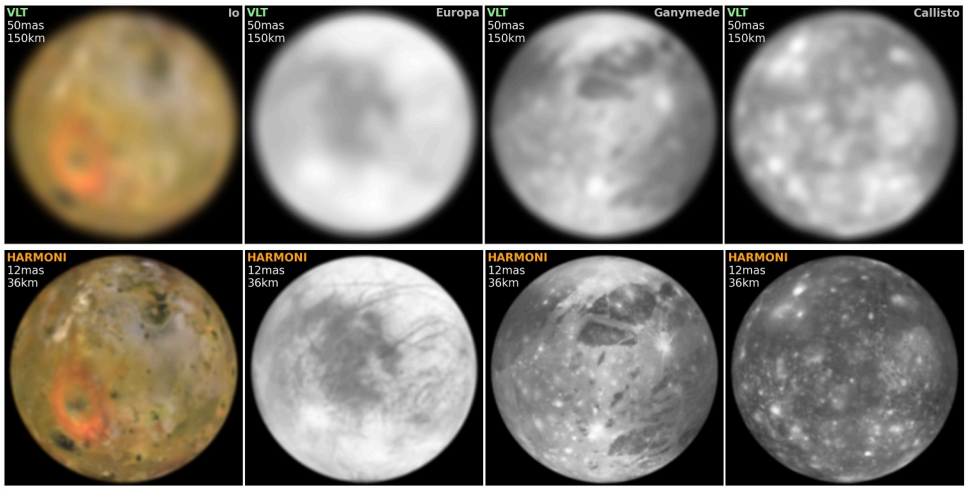

Fig. 4. The Galilean satellites Io, Europa, Ganymede, Callisto (from left to right) as seen from (top to bottom) VLT (50 mas spatial resolution) and ELT (12 mas spatial resolution). With the ELT/HARMONI instrument, each pixel will also contain the spectral information. The original U.S. Geological Survey (https://www.usgs.gov/) global mosaics of the moons, which are a combination of NASA/Galileo and Voyager images, were simply scaled in pixel size to the typical spatial resolution of each facility to visually illustrate the gain in resolution.

The atmospheres of giant planets provide a living laboratory to investigate large-scale fluid dynamics and physico-chemical phenomena. High resolution imaging will provide unprecedented clues to the atmospheric dynamics and global circulation, revealing detailed views of clouds, storms, vortices, and auroras and how these features move and change with time (thanks to long term monitoring with the same instruments). From spectroscopy, for instance, the finest spatial scales of tropospheric CH_4/H_2/aerosol distributions can become accessible for Neptune with HARMONI (and may be Uranus) taking advantage of the 825nm hydrogen collision induced absorption band. HARMONI Single Conjugate AO system is currently aimed at observing objects up to 2.5" in diameter, but in practice it might be able to deal also with larger diameter AO reference objects such as Uranus. Ice giants' observations will require mosaicing techniques to cover the explored regions.

5 Conclusions

The ELT will provide an exquisite set of instruments for observations with both a superb sensitivity and a fine spatial resolution to tackle the most exciting pending questions about the Solar System. We have to keep in mind that the ELT complexity will be substantially higher than for existing facilities, as regards operations (pointing, mirror stabilization, Adaptive Optics operations from both the telescope and the instruments, etc.), observations (hardware constraints, actual atmospheric conditions to be translated into observation performances, scheduling, etc), data volume management and analysis. The main challenge for us is to be prepared for: 1) refining AO capabilities for non-sidereal moving and extended targets of the Solar System, 3) image and spectral cubes analysis and deconvolution in particular in the framework of the ANR APPLY project by Neichel et al. on Point Spread Function (PSF) estimation for AO observations, 3) carefully defining phase 1 and 2 observations constraints for ESO for our Solar System targets. In this framework, the ELT Solar System Working Group aims at proposing relevant science cases for the various ELT instruments to be scientifically and technically prepared for the first light.

A. Delsanti, O. Groussin and S. Douté acknowledge funding from Programme National de Planétologie (PNP) of CNRS-INSU co-funded by CNES. F. Clarke and N. Thatte acknowledge support from UKRI grant ST/X002322/1. We would like to thank the organizers of the Strasbourg SF2A meeting and the organizers of the SF2A ELT workshop.

References

King, O. & Fletcher, L. N. 2022, Journal of Geophysical Research (Planets), 127, e2022JE007323

Vernazza, P., Ferrais, M., Jorda, L., et al. 2021, A&A, 654, A56

Session S09

L'égalité des genres en A&A: stéréotypes de genre dans l'enseignement

SF2A 2023
M. N'Diaye, A. Siebert, N. Lagarde, O. Venot, K. Baillié, M. Béthermin, E. Lagadec, J. Malzac, J. Richard (eds)

THE EFFECT OF GENDER STEREOTYPES ON ACADEMIC PERFORMANCE: HOW OUR TEACHING METHODS AFFECT GIRLS' SUCCESS

I. Vauglin[1] and R.-M. Ouazzani[2]

Abstract. Gender stereotypes have a strong impact on the academic performance of girls (and boys), at all levels of their school path. We aim at raising awareness on such biases, in order to prevent our teaching practices from perpetuating such stereotypes.

Keywords: gender stereotypes, education, gender equality

1 Introduction

At the wake of this third millennium, human societies are facing huge challenges among which climate changes, energy and water resources, pandemics, and the place of artificial intelligence. These challenges will require, at least partly, answers coming from progress in science and technology. We believe that all skills are needed to meet such huge challenges, and women have their role to play. However, girls' lack of interest in sciences has been a well-known problem for decades. While girls and boys are almost equally represented in the final year of high school, yet, as a representative example, women represent only a quarter of the members of the institutes of Astronomy and Astrophysics in France (Ouazzani et al. 2022). On the whole, the differences in educational choices between girls and boys hardly evolve over time. Equality between men and women is a major issue in the scientific fields of higher education and research; gender diversity in research teams leads to greater efficiency and more innovative teams. But the number of women in scientific and technological training and professions is still very low, and a cause for concern. The *Commission Femmes et Astronomie* of the SF2A organized a splinter session during the 2023 edition of its annual conference, which aim was to question the way we teach, which may be at the roots of poorer results and lower self-confidence among girls, increasing the risk of them dropping out of scientific education and careers. This proceeding tries to gather pieces of reflection which were presented then.

2 The shackles of stereotypes

Gender stereotypes are defined as "arbitrary characteristics based on preconceived ideas attributed to a group of people on the basis of their sex". It's an attribution of character traits that would determine the way individuals think and act according to their sex.

In 2015, not so long ago, an international study by the L'Oréal Foundation and Opinion Way highlighted the existence of such gender stereotypes affecting women in science. The survey shows that 67% of the 5032 Europeans questioned (50% women-50% men) believe that *"women do not have the required abilities to access high-level scientific positions"*. Why do they think this? Because they believe that *"women suffer from a lack of perseverance, rationality, practicality, rigor, scientific spirit and analytical skills"*.

[1] Univ Lyon, Univ Lyon1, Ens-Lyon, CNRS, Centre de Recherche Astrophysique de Lyon UMR5574, F-69230, Saint-Genis-Laval, France
[2] LESIA, Observatoire de Paris, PSL Research University, CNRS, Université Pierre et Marie Curie, Université Denis Diderot, 92195 Meudon, France

© Société Française d'Astronomie et d'Astrophysique (SF2A) 2023

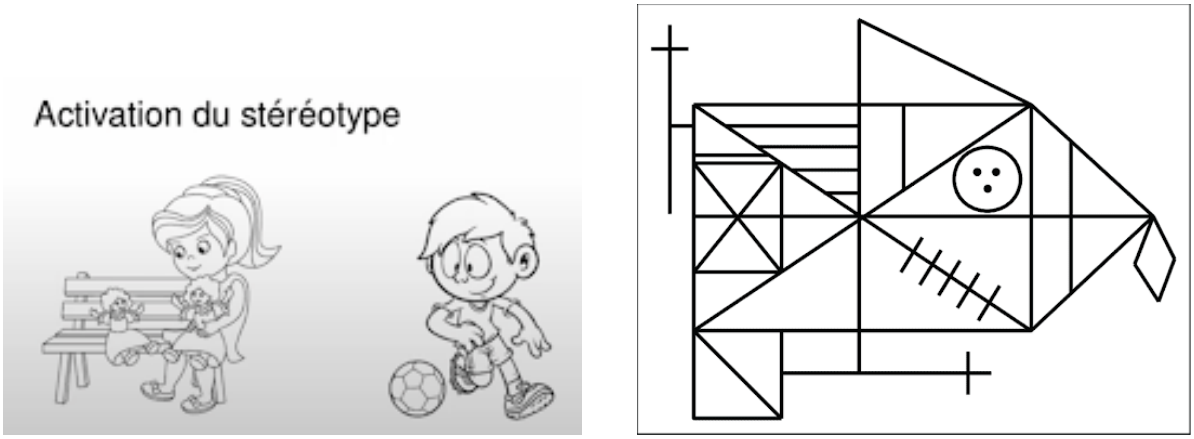

Fig. 1. Left: The colouring work assignment used for activation of the gender stereotype **Right:** The figure of Rey.

2.1 The impact of stereotypes in elementary school

A study by Neuville & Croizet (2007) was carried out on 79 CE2 children (34 boys, 45 girls aged 7 to 8), who were given arithmetics tests. Before taking the test, half the participants were given a coloring work that would activate the gender stereotype -typically a picture containing a scene were the characters would be illustrative of stereotyped behaviour, see fig. 1-, while the other half were given a neutral coloring work. The girls in the stereotype-activated group performed worse at the arithmetics test than the boys of their group, but also significantly worse than the girls in the other group for whom the stereotype had not been activated. The simple stereotype threat (*girls aren't good at science*) acts on the girls by "forcing them to confirm it" and thus leads the girls to perform below their real abilities in arithmetics.

2.2 The impact of stereotypes in middle school

The same year, Huguet & Regner (2007) carried out a study on 450 middle-school students. The task was to memorize and reconstruct Rey's figure - i.e. a drawing of a complex geometrical form, see fig. 1-. All the pupils took exactly the same test, under the same time conditions, corrected in the same way, by the same correctors (marked out of 44), the only difference being that half the pupils were told they would be taking a geometry test, while the other half were told they would be taking a drawing test. The girls who thought they were taking a geometry test didn't pass -with an average grade of 20.7-, while those who thought they were taking a drawing did -with average grade of 25.4-. As for the boys, while they got graded 23.7 in average when they thought they were taking a geometry test, they dropped to an average of 22.4 -i.e. 3 points lower than the girls!- when they thought they were taking a drawing test. Here again, the exercise presented as a geometry test activates, for the girls, the negative stereotype of which they are the target of, as well as the fear of confirming it. This fear represents an additional stress for the girls, which the boys don't have to deal with. The activated stereotype acts as a pressure on girls, leading to a drop in their performance compared to their results when it's not activated. It also affects boys, since their performance drops when they think they're doing artistic work.

The stereotype therefore has an impact on performance, starting in the earliest stages of primary and secondary school, in both good and bad pupils.

2.3 The impact of stereotypes at university

In 1999, Spencer et al. (1999) demonstrated an equivalent negative impact on students at the University of Michigan. A group of 67 students (36 women and 31 men) selected for being good at mathematics were offered to take a maths test presented as difficult. Half the group were told that previous results at this test had shown a difference in performance between women and men (the stereotype-activated group), while the other half were told that previous results showed that men and women performed equally well. As at younger age (see Sect. 2.1 and 2.2), the women in the stereotype-activated group performed worse than the men, while those in the non-stereotype-activated group performed on a par with the men. We can therefore see that, at all levels,

gender stereotypes affect the academic performance of girls and women, and sometimes boys and men when the counter-stereotype is activated.

A large number of studies have demonstrated the power of stereotypes on the groups they target. For example, still at university level, but concerning stereotypes which affect African-Americans, Steele & Aronson (1995) studied the stereotype that African-Americans are less skilled intellectually than other ethnic groups. They worked on standardized tests of verbal intelligence, used in the US for university admissions. They found that when the test was presented as a test of intelligence, the performance of black students was lower than that of white students (8.5 versus 12), but when the same test was presented as a problem-solving task, the performance of the two groups of students was similar (12.1 for black students versus 12.4 for white students). Again, as for women and maths, the authors highlight the negative stereotype the African-Americans suffer from, and the fear of confirming the stereotype, adding further stress that leads them to hinder their results.

2.4 And everywhere else

Bourguignon et al. (2007) have shown that implicit stereotype threat also operates outside the school context, more specifically, they have studied a group of 115 unemployed persons. The stereotype related to this group is that they are "lazy, apathetic and incompetent", and the unemployed persons are fully aware of this image projected on them. The study was based on tests including reading and understanding tasks and willingness to seek employment, and were presented either with the unemployed self-stereotype highlighted, or with the adult category mentioned. Again, participants for whom the unemployed stereotype was activated performed worse in reading understanding and expressed less job-seeking intentions than those for whom the adult category was mentioned. The activation of the stereotype associated with unemployed persons has negative consequences for their attempts to reintegrate the workforce. The power of stereotype threat generates stress, which in turn hinders their professional reintegration.

3 Awareness and stereotype falsification, a way to reduce the impact of stereotypes

Public education for all women is still a recent phenomenon. When we look at the history of women's education in France, we find that women were excluded from the education system until 1836. It was not until 1924 (less than 100 years ago) that women had the right to take the *Baccalauréat* -the high school diploma which gives access to university- hence keeping them out of the higher education system. Even then, many *grandes écoles* -elite higher education schools leading to business , public administration, and engineering jobs- remained closed to women for a long time. The prestigious *Ecole Polytechnique* was not admitting women until 1972 (50 years ago). It wasn't until 1975 that the *Haby* law made co-education compulsory, requiring the same teaching for boys and girls from kindergarten to 3rd grade. Prior to this law, textbooks and teaching was different for girls and for boys, and specifically the science ones. Hence, the idea that women are equally skilled and talented for sciences as men is still recent, and is not always a given. Therefore, girls and women still face images and messages which lead them to activate the stereotype that they are not good at sciences.

This is regularly reflected in the content of advertising campaigns. The French Ministry of Education (MEN) itself provides examples in its communication, with two posters for a recruitment campaign put up in May 2011 (see Fig. 2). The message is clear: men and women have received the same training, but a woman will find the job of her dreams, while a man has found a position that matches his ambitions. An equivalent campaign carried out by the *Institut National Supérieur du Professorat et de l'Education* -INSPE, French teachers' training school- in 2023 shows that things have not changed much in 12 years. Women are good at teaching at primary school, with small children, while men are more likely to teach in secondary school. Here again, even if they are provided with the same training, they don't have the same careers. It gives cause for concerns when the institution which is training the teachers, itself, conveys messages that are prompt to activate stereotypes.

So what can we do, as actors of the higher education system, and members of the scientific community? First of all, we, and our institutions (scientific institutes, universities, etc...), should screen our communication in order to remove totally stereotypical messages from all the contents we produce and broadcast. Various tools have been developed to do so, among which this guide for a stereotype-less public communication -in French-, edited by the higher council for equality*.

*see https://www.haut-conseil-egalite.gouv.fr/stereotypes-et-roles-sociaux/actualites/article/aujourd-hui-sort-en-librairie-le

Fig. 2. Left: Posters of a teacher recruitment campaign by MEN in 2011 **Right:** similar campaign by INSPE in 2013.

Also, in the classrooms, there are ways and techniques which one can apply when teaching so as not to activate gender stereotypes, and therefore reduce their impact on the performances of our female students. This set of techniques can be related to nudging. This concept comes from behavioral sciences: the idea is to propose adaptive designs of the environment, as ways to influence the behavior and decision making of groups of individuals ("Nudge Theory", Wikipedia). Applied to our problem, such strategies can help to counter-balance the negative impacts of stereotypes. It is called the stereotype falsification. It can take very simple forms, and be easy to implement in our daily teaching practices. Thanks to science historians, the works of female scientists are more and more coming out of the shadow. Therefore, one way to proceed is to try to cite female researchers (in a visible manner) and their results as often as possible when lecturing. Another way is to explicitly assert, for instance during the first day of class, when introducing yourself and the course, that you consider that men and women are equally skilled to thrive in sciences. We can take example from this maths teacher in a secondary school of the Grenoble Academy who has written above the blackboard in her classroom, in large letters, clearly visible to the whole class, "in mathematics, there is no difference in performance between women and men". Simple, easy and effective: her female students have some of the highest maths grades in the school.

4 Conclusion

Collecting a series of scientific studies, we have shown that diverse works in cognitive and behavioral sciences demonstrate that stereotype activation has deleterious effects on girls' performances in sciences, at all age. The anxiety generated by the implicit stereotype threat creates a pressure that leads to a drop in performance. To help girls and female students succeed in their school and career paths, we, teachers must be careful to give them the same conditions and resources as others. To do this, we must be careful not to activate gender stereotypes in our discourse, particularly before and during examinations.

IV and RMO thank all the members of the *commission femmes et astronomy* for their work and the organisation of the splinter session. A particular thank you goes to Marie-Blanche Mahourat for her contribution. They also warmly thank all the participants of the session, and specially Caroline Bot for having helped moderating the lively debates.

References

Bourguignon, D., Desmette, D., Yzerbyt, V., & Herman, G. 2007, Revue internationale de psychologie sociale, 123

Huguet, P. & Regner, I. 2007, Journal of educational psychology, 545

Neuville, E. & Croizet, J.-C. 2007, European journal of psychology of education, 307

Ouazzani, R. M., Bot, C., Brau-Nogué, S., et al. 2022, in SF2A-2022: Proceedings of the Annual meeting of the French Society of Astronomy and Astrophysics. Eds.: J. Richard, ed. J. Richard, A. Siebert, E. Lagadec, N. Lagarde, O. Venot, J. Malzac, J. B. Marquette, M. N'Diaye, & B. Briot, 23–28

Spencer, S., Steele, C., & Quinn, D. 1999, Journal of Experimental Social Psychology, 4

Steele, C. M. & Aronson, J. 1995, Journal of Personality and Social Psychology, 797

SF2A 2023
M. N'Diaye, A. Siebert, N. Lagarde, O. Venot, K. Baillié, M. Béthermin, E. Lagadec, J. Malzac, J. Richard (eds)

STATUS OF WOMEN IN ASTRONOMY: A NEED FOR ADVANCING INCLUSIVITY AND EQUAL OPPORTUNITIES

M. Pandey-Pommier[1,2], A. Piccialli[3], B. J. Wilkes[5], P. Hasan[6], S. Vargas Dominguez[7], A. S. Hassanin[8], D. Lazzaro[9], C. D. P. Lagos[10], J. Masegosa[11], L. Yang[12], D. Valls-Gabaud[13], J. Leibacher[14], D. J. Norman[15], J. Nastula[16] and A. Bamba[17]

Abstract. Women in the Astronomy and STEM fields face systemic inequalities throughout their careers. Raising awareness, supported by detailed statistical data, represents the initial step toward closely monitoring hurdles in career progress and addressing underlying barriers to workplace equality. This, in turn, contributes to rectifying gender imbalances in STEM careers. The International Astronomical Union Women in Astronomy (IAU WiA) working group, a part of the IAU Executive Committee, is dedicated to increasing awareness of the status of women in Astronomy and supporting the aspirations of female astronomers globally. Its mission includes taking concrete actions to advance equal opportunities for both women and men in the field of astronomy. In August 2021, the IAU WiA Working Group established a new organizing committee, unveiling a comprehensive four-point plan. This plan aims to strengthen various aspects of the group's mission, encompassing: (i) Awareness Sustainability: Achieved through surveys and data collection, (ii) Training and Skill Building: Focused on professional development, (iii) Fundraising: To support key initiatives, and (iv) Communication: Dissemination of results through conferences, WG Magazines, newsletters, and more. This publication provides an overview of focused surveys that illuminate the factors influencing the careers of women in Astronomy, with a particular focus on the careers of mothers. It highlights the lack of inclusive policies, equal opportunities, and funding support for women researchers in the field. Finally, we summarize the specific initiatives undertaken by the IAU WiA Working Group to advance inclusivity and equal opportunities in Astronomy.

Keywords: International Astronomical Union: Women in Astronomy- Gender Equality: bias- Career development: Marginalized Women Researchers

[1] CNRS/Laboratoire Univers et Particules de Montpellier, Université de Montpellier LUPM CC 072 - Place Eugène Bataillon 34095 Montpellier Cedex 5, France

[2] University Catholic of Lyon, 10, place des Archives 69288 Lyon Cedex 02, France

[3] Royal Belgian Institute for Space Aeronomy Planetary Aeronomy Ringlaan 3 Av. Circulaire 1180 Brussels Belgium

[4] Center for Astrophysics — Harvard & Smithsonian SAO Cambridge MA 02138-1516 Massachusetts (MA) United States

[5] Royal Society Wolfson Visiting Fellow, School of Physics, University of Bristol, United Kingdom

[6] Dept of Physics, Maulana Azad National Urdu University, Hyderabad, India 500034

[7] Universidad Nacional de Colombia Observatorio Astronómico Av. Carrera 30 # 45-03 Ciudad Universitaria Bogota Colombia

[8] Cairo University - Faculty of Science Astronomy, Space Science & Meteorology Department Cairo University - Faculty of Science - Astronomy Dep Giza 12613 Egypt

[9] Observatorio Nacional Coordenação de Pesquisas em Astronomia e Astrofisica R. Gal. Jose Cristino 77 São Cristóvão Rio de Janeiro, RJ 20921-400 Rio de Janeiro (RJ) Brazil

[10] University of Western Australia International Centre for Radio Astronomy Research 7 Fairway Crawley 6009 Western Australia (WA) Australia

[11] Inst de Astrofisica de Andalucía-CSIC Extragalactic Astronomy C/ Glorieta de la Astronomía 18008 Granada Spain

[12] Sun Yat-sen University School of Physics and Astronomy Tianqin Building 3401 Sun Yat-sen University, Zhuhai Campus Zhuhai 519082 Guangdong China, Nanjing

[13] Observatoire de Paris LERMA 61 Avenue de l'Observatoire 75014 Paris France

[14] 6631 North Donna Beatrix Circle Tucson 85718 Arizona (AZ) United States

[15] NOAO 950 North Cherry Ave Tucson AZ 85719 Arizona (AZ) United States

[16] Polish Academy of Sciences Space Research Center Bartycka 18 A 00-716 Warsaw Poland

[17] The University of Tokyo Department of Physics Hongo 7-3-1 Bunkyo-ku, Tokyo 113-1133 Kanto Japan

© Société Française d'Astronomie et d'Astrophysique (SF2A) 2023

1 Introduction

Worldwide, women researchers in the field of Astronomy face significant underrepresentation. Factors contributing to this situation include a lack of strong support for job applications, fewer opportunities, reduced participation in peer reviews for journals and funding proposals, fewer invitations to give colloquia compared to their counterparts at prestigious universities and in leadership roles on decision-making committees, caregiving, and family responsibilities (Piccialli et al. 2020). To address the gender imbalances at every career stage and promote international efforts to support women's careers in astronomy, the IAU Executive Committee (EC) established the Working Group for Women in Astronomy (IAU WiA) in 2003 (Cesarsky & Walker 2010). Over the past two decades, the WiA WG has organized various activities and events at IAU General Assemblies, including Women's Luncheons, Students Mentoring Sessions, and Special Talks, to raise awareness about the lack of inclusivity and equal opportunity women astronomers encounter in this field (Primas 2018; Norman 2021). Despite these efforts, the representation of women in the astronomy community has only marginally increased, and significant gender disparities persist in many parts of the world. To better understand the current status of women in astronomy, the acting IAU WiA WG conducted statistics of current IAU members data available at `https://www.iau.org/public/themes/member_statistics/`. The aim was to gather statistical information and show the current status of the representation of women in the field of astronomy worldwide (Pandey-Pommier et al. 2021).

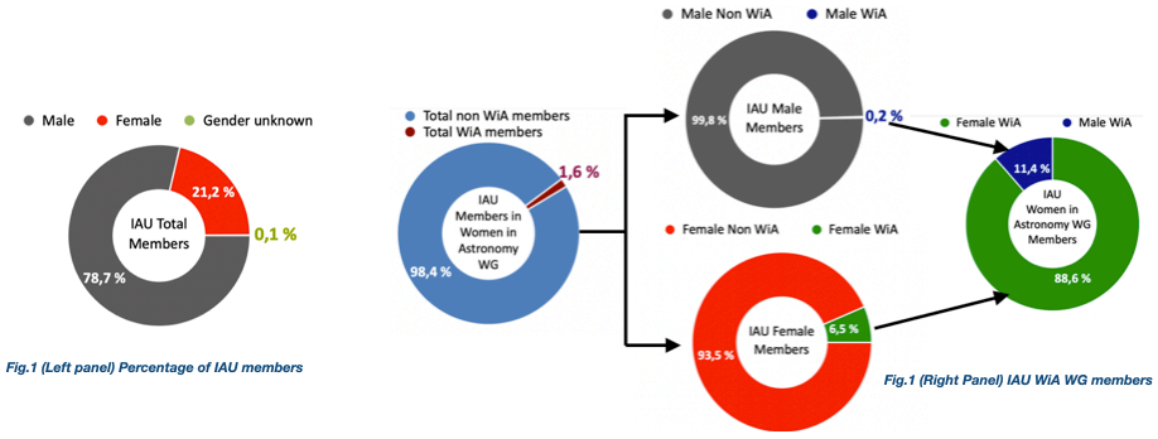

Fig. 1. IAU members and participants of WiA WG, adapted from (Pandey-Pommier et al. 2021)

The statistical analysis results shown in Figure 1 revealed that the IAU has less than $< 21\%$ female membership among its 12,000 total members, with fewer than $< 1.6\%$ actively participating in the WiA WG. Furthermore, only 29 countries have women actively participating in research activities, comprising $\leq 21\%$ of the total researchers in each country. Among these 29 countries, 18 are located in the European Union, while the remaining 11 are distributed across the Americas (4), Asia(4), Africa(1), Oceania(1), and the Middle East(1). These findings underscore the minimal participation of the overall astronomy community members to achieve gender balance within the field as well as the low global representation of women in astronomy, leading to a biased and discriminatory working environment.

2 Survey data and observation

To identify the critical factors influencing the underrepresentation and careers of women in Astronomy, raise awareness about the current working conditions for women astronomers, and emphasize the imperative need for global efforts to achieve inclusivity and gender balance in this field, M. Pommier conducted a comprehensive survey titled 'Working Conditions for Women in Astronomy', spanning over three years, beginning in 2019. This survey aimed to identify various factors, their proportions, and their impact on the representation of women in Astronomy (Pandey-Pommier et al. 2021). In this proceeding paper, we delve into the results obtained from this survey. The sections are organized as follows: Section 3.1 presents the findings on factors affecting the career growth of women astronomers, followed by Section 3.2, which discusses the 4-point action plan initiated by the IAU WiA WG to advance skill development and equal opportunity possibilities. Finally, in Section 4, we engage in a discussion about the changes in policies needed to support the career development of women in astronomy.

3 Results

A total of 750 participants from 58 countries took part in this survey, with more than $\geq 60\%$ of the respondents hailing from EU countries, followed by Americas($\sim 19\%$), Oceania($\sim 13\%$), Asia($\sim 4.5\%$), Africa($\sim 2.5\%$), and the Middle East($\sim 1\%$).

3.1 Factors affecting the career of women in Astronomy

Several factors have a significant impact on the careers of women in Astronomy, as illustrated in 2 with the most crucial:

- Family and Caregiving Responsibilities: related to caring for children and elderly family members.
- Bias Against Women Applicants, Especially Mothers: Discriminatory biases such as underpaid/unpaid contracts can affect the careers of women, particularly those who are mothers, during the application process.
- Social Stereotypes: Gender, marital status, race, and origin can lead to harmful social stereotypes that hinder career progression.
- Discrimination and Bullying: Discriminatory and bullying behaviors, both from older and younger colleagues, create hostile work environments.
- Lack of Funds, Role Models, and Support for Job Applications: Women applicants, especially mothers, often face challenges in securing necessary funding and workplace support leading to extended decades of fixed-term positions, that may be unethical working condition
- Unethical Work Evaluation: Unfair work evaluations may result in projects of non-permanent female members systematically being taken over by permanent members or given to younger male colleagues without consent.
- Lack of Family Support, Especially for Mothers: A lack of family support, particularly for mothers, can impact their ability to balance work and caregiving responsibilities.
- Sexual and Mental Harassment: Both older and younger colleagues can engage in sexual and mental harassment, further hindering career advancement.

The findings of this survey have identified eight crucial factors that significantly impact the careers of women astronomers at every stage, with all of these factors predominantly affecting the careers of mothers in this field while mostly 3 affect the careers of all (including women with no family responsibilities) the women in astronomy. This leads to a **systematic leaky pipeline effect in the career of women in Astronomy leading to underrepresentation and gender imbalance in this field**. It is thus imperative to urge policymakers to formulate inclusive policies to address these long-standing issues faced by women, particularly the challenges encountered by mothers, in academia. As of now the situation of mothers is poorly/inadequately addressed in hiring and evaluation committees policies. Consequently, this study underscores the urgent need for global efforts and increased awareness to achieve gender balance in the field of Astronomy and to collaborate with large international organizations dedicated to supporting women in STEM. (Pandey-Pommier et al. 2021).

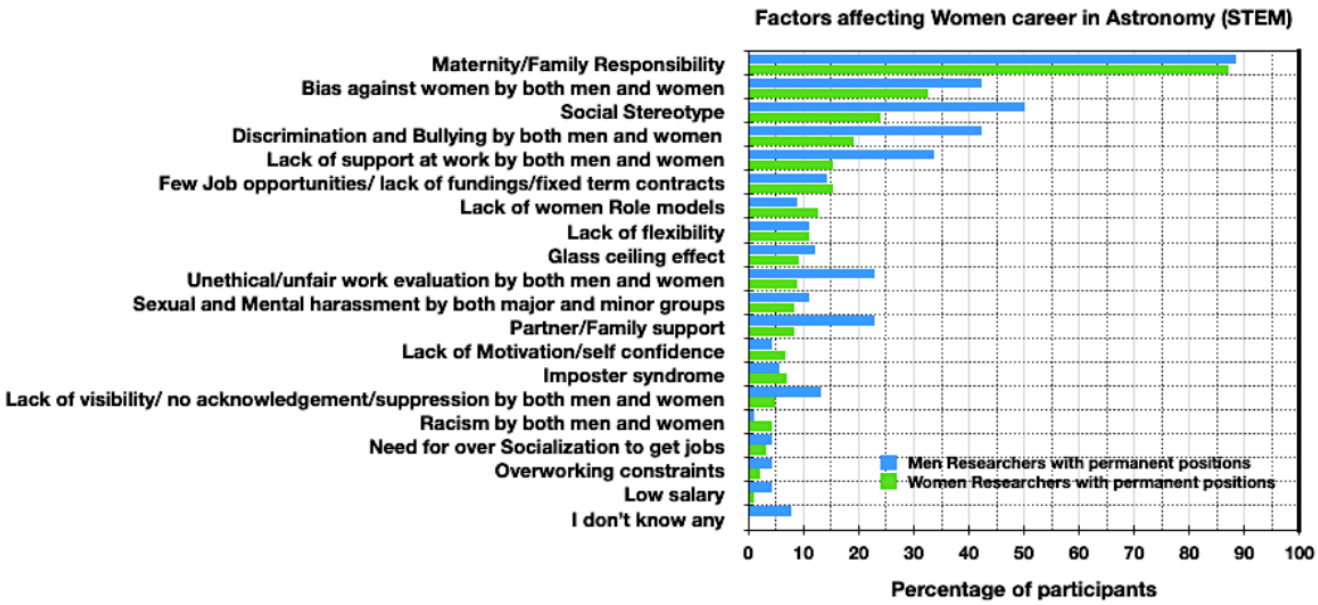

Fig. 2. Survey Results on factors affecting Women's Career in Astronomy and STEM fields, adapted from (Pandey-Pommier et al. 2021)

3.2 Activities initiated by the IAU WiA WG

Taking into account the marginalized and reduced job prospects for women in Astronomy, the Organizing Committee of the IAU WiA WG initiated a four-point action plan to advance the careers of women in Astronomy, **(ref. IAU WiA WG newsletters)**- `https://sites.google.com/view/iau-women-in-astronomy/home/iau-wia-ensemble-magazine-newsletter?authuser=2`, by creating:

- Awareness and Sustainability- This involves conducting surveys on the working conditions of women researchers, collecting statistical data from around the world, and highlighting gender balance issues within the IAU and the global astronomical community. Survey results are regularly featured in WG ENSEMBLE Magazine and annual reports, fostering a self-supporting and sustainable community(Pandey-Pommier 2022).

- Training and Skill Building- The focus here is on developing resources, gathering materials from other IAU offices, and conducting regular training programs to enhance the skills and professional development of female researchers worldwide(Hasan et al. 2022).

- Fundraising- This component aims to raise funds and offer financial support to women researchers at critical stages in their careers.

- Communication and Dissemination- This involves promoting the participation of women researchers worldwide by establishing communication channels on social media and organizing regular seminar series. These

seminars feature experts, both permanent and non-permanent female and male members (supporting careers of women in Astronomy), from a geographically diverse team with varying levels of experience (Pandey-Pommier 2022).

We have received global appreciation and support for these initiatives and ongoing activities from both permanent and non-permanent members of the worldwide community. Nevertheless, securing long-term funding is essential to sustain and further our efforts in promoting gender balance and ensuring healthy working conditions in the fields of astronomy and STEM.

4 Discussion and Future Prospects on Inclusivity and Equal Opportunities for Women in Astronomy

This study underscores the current working conditions of women in Astronomy worldwide which are affected by a lack of inclusive and equal opportunity work environment. The primary findings of our research are as follows:

- Marginalized representation of women astronomers (especially mothers) at the global level within the IAU membership and individual countries.
- Identification of eight major factors affecting the careers of women in Astronomy: maternity/family responsibilities, bias, stereotypes, discrimination/bullying, lack of funding, suppression of work, lack of support, and sexual/mental harassment. While all eight factors impact the careers of mothers, mainly three affect the careers of women without family and childcare responsibilities.
- Recognition of the challenges in addressing the "leaky pipeline effect" within research fields, highlighting the absence of proper policies to date. There is an urgent need for comprehensive policies to combat this long-standing issue, which contributes to gender imbalance in the field.
- A call for key policymakers, including funding agencies, universities/research organizations, and peer-reviewed journals, to implement inclusive and equal opportunity policies and criteria within their decision-making, hiring, and evaluation committees. These committees should comprise gender-balanced and diverse team members to comprehensively combat the "leaky pipeline effect " and other factors impacting women's careers in research. Particular attention needs to be paid to the situation of mothers who are working under reduced and non-inclusive opportunities or prolonged fixed-term contracts under unfair working conditions for several decades.

We gratefully acknowledge the support of the Indo-French Centre for the Promotion of Advanced Research (Centre Franco-Indien pour la Promotion de la Recherche Avancee) under project 6504-3.

References

Cesarsky, C. & Walker, H. 2010, Astronomy Geophysics, 2.33

Hasan, P., Pandey-Pommier, M., & et al. 2022, The IAU-Women in Astronomy Working Group and Inclusivity, 54

Norman, D. 2021, IAU Executive committee Women in Astronomy Working Group, Triennial Report (2019-2021)

Pandey-Pommier, M. 2022, IAU Executive committee Women in Astronomy Working Group, Triennial Report (2021-2022)

Pandey-Pommier, M., Gulisano, A. M., Saad, A., & et al. 2021, IAU WiA ENSEMBLE Magazine, 1

Piccialli, A., Rathbun, J., Levasseur-Regourd, A., & et al. 2020, Adv. Geosci., 169

Primas, F. 2018, IAU Executive committee Women in Astronomy Working Group, Triennial Report (2015-2018)

Session S10

Latest insights on dust evolution

SF2A 2023
M. N'Diaye, A. Siebert, N. Lagarde, O. Venot, K. Baillié, M. Béthermin, E. Lagadec, J. Malzac, J. Richard (eds)

FAR-IR POLARIZED EMISSION IN THE CRAB NEBULA WITH SOFIA/HAWC+

J. Chastenet[1], I. Looze[1,2], B. Hensley[3], B. Vandenbroucke[4], M. Barlow[2], J. Rho[5], A. Ravi[6], H. Gomez[7], F. Kirchschlager[1,2], J. Macías-Pérez[8], M. Matsuura[7], K. Pattle[2], N. Ponthieu[9], F. Priestley[7], M. Relaño[10,11], A. Ritacco[12,13] and R. Wesson[2]

Abstract. We present detection of dust polarized emission of the Crab Nebula (M 1) in the far-infrared, from SOFIA/HAWC+ observations, at 89 and 154 μm. After removing the signal from synchrotron emission, including its polarized component, we compute the average dust-only polarization in three dusty filaments, ranging from $\sim 3-9\%$. We constrain the grain temperatures and masses, assuming mixtures of silicate- and carbon-rich grains, using laboratory properties. Upper limits on the total dust mass in the Crab Nebula range from 0.027 to 1.0 $M_\odot$, and a fraction of carbon grains ranging from 0.2 to 70%.

Keywords: polarization, supernovae: individual: Crab, dust, emission, ISM: supernova remnants

This proceeding is an excerpt of the paper published by Chastenet et al. (2022). Please refer to the paper for more details.

1 Introduction

Supernovae (SNe) and supernova remnants (SNRs) affect the total dust budget of their host galaxy, be it in an effectively positive or negative sense. The formation of dust grains after these explosions could happen in the ejecta, thanks to the metal-rich environment that was birthed with the release of the elements formed in the progenitors (e.g., Barlow et al. 2010; De Looze et al. 2017; Chawner et al. 2020). But the shock waves sent out in the surrounding medium, that can rebound and run through the inner part of the SNR can be strong enough to fragment and destroy (newly) formed grains (e.g., Jones et al. 1994; Bocchio et al. 2016; Slavin et al. 2020; Kirchschlager et al. 2022).

The tensions between the observed and theoretical dust budget are often explained with the growth of dust grains in the dense interstellar medium (ISM), but this hypothesis comes with some caveats (e.g., Zhukovska et al. 2018; Galliano et al. 2021; Priestley et al. 2021). Another –or simultaneous– explanation could be that SNR destruction rates have been overestimated (e.g., Matsuura et al. 2009; Ferrara & Peroux 2021). These rates can vary depending on several parameters such as the size and composition (carbon- vs silicate-rich) of the considered grains, the energy released in the explosion, the density contrast of the dusty clumps where grains are found (e.g., Nozawa et al. 2007; Silvia et al. 2010; Micelotta et al. 2016; Kirchschlager et al. 2019).

[1] Sterrenkundig Observatorium, Ghent University, Krijgslaan 281-S9, B-9000 Gent, Belgium
[2] Dept. of Physics & Astronomy, University College London, Gower Street, London WC1E 6BT, UK
[3] Department of Astrophysical Sciences, Princeton University, Princeton, NJ 08544, USA
[4] Leiden Observatory, Leiden University, NL-2300 RA Leiden, Netherlands
[5] SETI Institute, 189 N. Bernardo Ave., Ste. 200, Mountain View, CA 94043
[6] Box 19059, Department of Physics, University of Texas at Arlington, Arlington, TX 76019, USA
[7] School of Physics and Astronomy, Cardiff University, Queens Buildings, The Parade, Cardiff CF24 3AA
[8] Univ. Grenoble Alpes, CNRS, Grenoble INP, LPSC-IN2P3, 53, avenue des Martyrs, 38000 Grenoble, France
[9] Univ. Grenoble Alpes, CNRS, IPAG, 38000 Grenoble, France
[10] Departamento Física Teórica y del Cosmos, Universidad de Granada, E-18071 Granada, Spain
[11] Instituto Universitario Carlos I de Física Teórica y Computacional, Universidad de Granada, E-18071 Granada, Spain
[12] INAF-Osservatorio Astronomico di Cagliari, Via della Scienza 5, 09047 Selargius, IT
[13] Laboratoire de Physique de l'École Normale Supérieure, ENS, PSL Research University, CNRS, Sorbonne Université, Université de Paris, 75005, Paris, France

© Société Française d'Astronomie et d'Astrophysique (SF2A) 2023

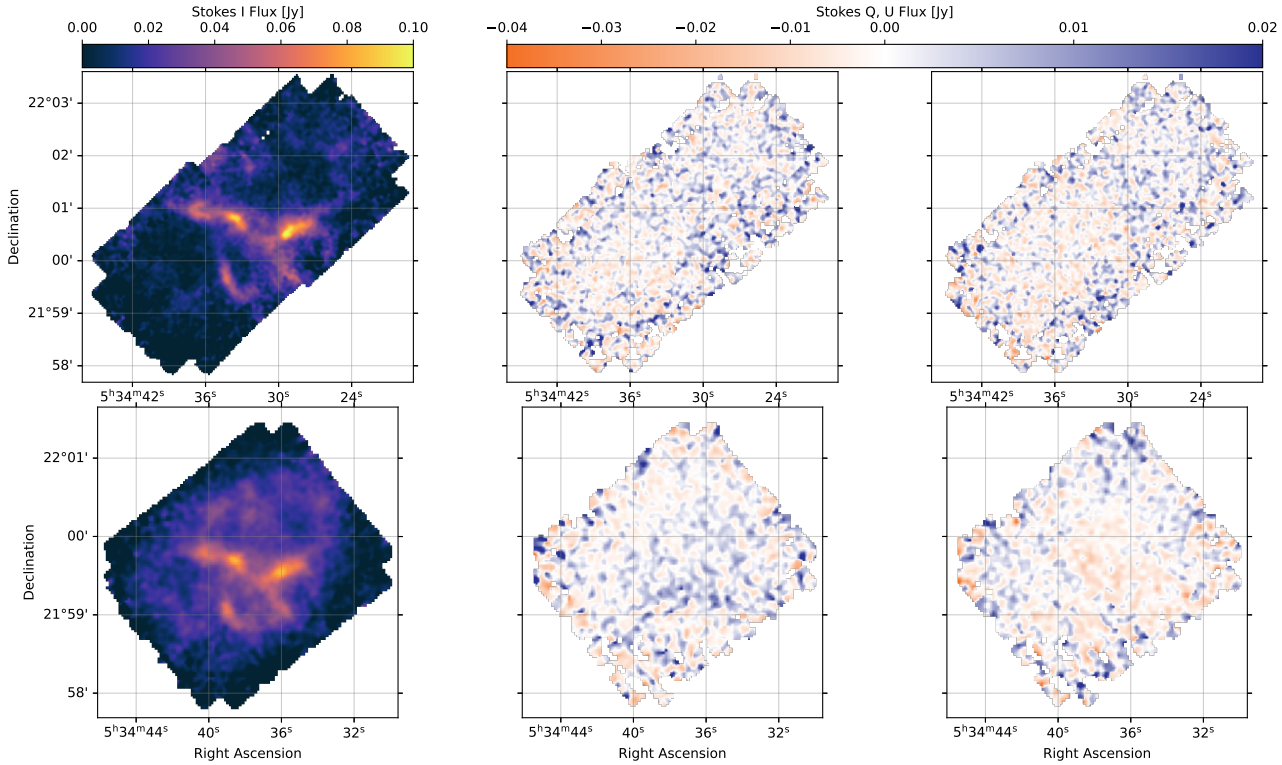

Fig. 1. *Left to right:* Stokes I, Q, and U parameters from SOFIA/HAWC+ observations in band C 89 μm (top) and band D 154 μm (bottom), at native resolutions, 7.8″ and 13.6″, respectively.

In this study, we use a new approach to constrain the mass, size, and composition of dust grains in a well-studied SNR, the Crab Nebula. Instead of performing spectral energy distribution fitting, we use polarization information and physical dust properties to derive grain temperatures and masses.

2 Data preparation and processing

2.1 New far-IR data, and radio synchrotron observations

The data was taken on September 2018 as part of the proposal 06_0193 (PI: De Looze). Observations were done in bands C (89 μm, FWHM $\sim$ 7.8″) and D (154 μm, FWHM $\sim$ 13.6″), using the HAWC+ instrument (Harper et al. 2018), on-board the Stratospheric Observatory for Infrared Astronomy (SOFIA; Temi et al. 2018) . We use the Level 4 data from the SOFIA pipeline for the Stokes vector (I, Q, U parameters), shown in Figure 1, but we calculate the debiased polarization using the modified asymptotic estimator as described in Plaszczynski et al. (2014). This allows a more robust estimate at low signal-to-noise ratios.

We use NIKA 150 GHz radio data (FWHM $\sim$ 18″) from Ritacco et al. (2018, , and reference therein) to estimate the synchrotron polarization parameters. We estimate the fraction of synchrotron emission in bands C and D from the results from De Looze et al. (2019), who fit a multi-component model to the infrared emission of the Crab. All their data products were estimated at the *Herschel*/SPIRE 500 resolution, which is $\sim$ 36″. We convolve and regrid our HAWC+ data to that same resolution.

2.2 Synchrotron radiation removal and dust-only polarization

The synchrotron radiation was shown to be significant in the Crab at far-IR wavelengths, between 20 and 35% by De Looze et al. (2019), and we need to remove it to focus on dust-only polarized emission. We use the NIKA radio data, where we consider that the measured emission is due to synchrotron radiation only, and estimate a synchrotron polarization fraction and angle. Assuming that the polarization fraction is constant

	$MgSiO_3$ amorphous	**$MgSiO_3$ glassy**	**Mg_2SiO_4**	**$Mg_{0.5}Fe_{0.5}SiO_3$**	**$Mg_{0.7}SiO_{2.7}$**
	Temperature [K]				
Silicates	$31.8 - 46.9$	$33 - 50$	$31.8 - 46.9$	31.45.1	33.450.9
Carbonaceous	$39 - 67.7$	$38.8 - 67.1$	$38.9 - 67.5$	$38.8 - 67$	$38.8 - 67$
	Total dust mass, upper limits [$M_\odot$]				
Estimate 1	$0.040 - 0.059$	$0.026 - 0.032$	$0.037 - 0.054$	$0.27 - 0.53$	$0.027 - 0.34$
Estimate 2	0.11	0.061	0.10	1.0	0.065
	f_{aC} [%]				
	$6 - 50$	$17 - 70$	$9 - 53$	$0.2 - 8$	$17 - 68$

Table 1. Dust grain temperatures, upper-limits on total dust mass in the Crab, and estimated fraction of carbon-rich grains for 5 types of silicate-rich grains. The ranges shown here cover all three ellipses encompassing dusty filaments, and the dust masses range additionally covers results for a range of zenith angle $45^\circ \leq \theta \leq 90^\circ$.

across wavelengths, we use the work from De Looze et al. (2019) to estimate the synchrotron contamination at the HAWC+ wavelengths, in all Stokes parameters.

3 Constraining dust properties

Given the only two accessible polarized measurements at 89 and 154 μm, we do not perform spectral energy distribution fitting. Instead, we proceed to constrain dust grain temperatures and masses step by step. Because of the limited number of data points, we are forced to make a number of assumptions to simplify the system of equations. We assume that

- the dust is a mixture of silicate- and carbon-rich grains;
- both grain species have the same size distribution, with radius ranging 0.1 μm $\leq$ a $\leq$ 5.0 μm, and an ellipsoid-shape distribution;
- carbon grains do not align with the magnetic field and do not produce polarized signal;
- all silicate-rich grains align with the same angle (0.1 μm being the lower limit for efficient alignment);
- grains have reached an equilibrium temperature and follow the blackbody emission.

We derive grain emissivities using laboratory measurements of the (n, k) refractive indices, and the simulation code COSTUUM (Vandenbroucke et al. 2020). We test 5 different silicate-rich species: $MgSiO_3$, amorphous and glassy, Mg_2SiO_4, $Mg_{0.5}Fe_{0.5}SiO_3$, and $Mg_{0.7}SiO_{2.7}$. The carbon material is assumed to be that discussed in the optECs model (Jones 2012a,b,c).

We first derive silicate grain temperature using the ratio of polarized emission between bands C and D, and assuming a blackbody emission. We then solve for the carbon grain temperature, by using the ratio of polarization fractions between bands C and D. Using these temperatures and the observations, we derive the dust surface density for each component, and the corresponding fraction of carbon grains. We tabulate these results in Table 1. We only show an extract of the results, covering variations between each dusty filament, and for varying zenith angle (one of the assumptions needed to simplify the equations).

We extrapolate the derived dust masses to estimate upper-limits on the total dust mass in the Crab using two methods: (i) scaling the total dust mass within the three ellipses, to the area of the ellipse in De Looze et al. (2019), and (ii) scaling the highest dust mass in the ellipse to the area of the ellipse in De Looze et al. (2019). By construction Estimate 2 in Table 1 is the highest, and very conservative.

4 Conclusions

With SOFIA/HAWC+ observations, we present detection of far-IR dust polarization in the Crab nebula, second confirmed detection in a SNR after Cassiopeia A. Using polarized emission at 89 and 154 μ, and after removing contamination from synchrotron polarization using radio data, we measure the (integrated) polarization fractions and angles in three dusty filaments, at the SPIRE 500 resolution (36″). We assume a mixture of silicate- and carbon-rich grains and using laboratory refractory indices, and solve a system of equations instead of fitting spectral energy distributions to derive dust grain temperatures, masses, and fraction of carbon grains. We find

that large grains ($a > 0.1$ μm in radius) must be present in the Crab Nebula, and that carbon- and silicate-rich species likely co-exist in this SNR.

JC acknowledges support from ERC starting grant #851622 DustOrigin. This research is based on observations made with the NASA/DLR Stratospheric Observatory for Infrared Astronomy (SOFIA). SOFIA is jointly operated by the Universities Space Research Association, Inc. (USRA), under NASA contract NNA17BF53C, and the Deutsches SOFIA Institut (DSI) under DLR contract 50 OK 0901 to the University of Stuttgart.

References

Barlow, M. J., Krause, O., Swinyard, B. M., et al. 2010, A&A, 518, L138
Bocchio, M., Marassi, S., Schneider, R., et al. 2016, A&A, 587, A157
Chastenet, J., De Looze, I., Hensley, B. S., et al. 2022, MNRAS, 516, 4229
Chawner, H., Gomez, H. L., Matsuura, M., et al. 2020, MNRAS, 493, 2706
De Looze, I., Barlow, M. J., Bandiera, R., et al. 2019, MNRAS, 488, 164
De Looze, I., Barlow, M. J., Swinyard, B. M., et al. 2017, MNRAS, 465, 3309
Ferrara, A. & Peroux, C. 2021, MNRAS, 503, 4537
Galliano, F., Nersesian, A., Bianchi, S., et al. 2021, A&A, 649, A18
Harper, D. A., Runyan, M. C., Dowell, C. D., et al. 2018, Journal of Astronomical Instrumentation, 7, 1840008
Jones, A. P. 2012a, A&A, 540, A1
Jones, A. P. 2012b, A&A, 540, A2
Jones, A. P. 2012c, A&A, 542, A98
Jones, A. P., Tielens, A. G. G. M., Hollenbach, D. J., & McKee, C. F. 1994, ApJ, 433, 797
Kirchschlager, F., Mattsson, L., & Gent, F. A. 2022, MNRAS, 509, 3218
Kirchschlager, F., Schmidt, F. D., Barlow, M. J., et al. 2019, MNRAS, 489, 4465
Matsuura, M., Barlow, M. J., Zijlstra, A. A., et al. 2009, MNRAS, 396, 918
Micelotta, E. R., Dwek, E., & Slavin, J. D. 2016, A&A, 590, A65
Nozawa, T., Kozasa, T., Habe, A., et al. 2007, ApJ, 666, 955
Plaszczynski, S., Montier, L., Levrier, F., & Tristram, M. 2014, MNRAS, 439, 4048
Priestley, F. D., De Looze, I., & Barlow, M. J. 2021, MNRAS, 502, 2438
Ritacco, A., Macías-Pérez, J. F., Ponthieu, N., et al. 2018, A&A, 616, A35
Silvia, D. W., Smith, B. D., & Shull, J. M. 2010, ApJ, 715, 1575
Slavin, J. D., Dwek, E., Mac Low, M.-M., & Hill, A. S. 2020, ApJ, 902, 135
Temi, P., Hoffman, D., Ennico, K., & Le, J. 2018, Journal of Astronomical Instrumentation, 7, 1840011
Vandenbroucke, B., Baes, M., & Camps, P. 2020, AJ, 160, 55
Zhukovska, S., Henning, T., & Dobbs, C. 2018, ApJ, 857, 94

SF2A 2023
M. N'Diaye, A. Siebert, N. Lagarde, O. Venot, K. Baillié, M. Béthermin, E. Lagadec, J. Malzac, J. Richard (eds)

DUST PROPERTIES IN THE MILLIMETER TO CENTIMETER WAVELENGTH RANGE: ANALYSIS OF A SAMPLE OF NEARBY GALAXIES

L. Correia[1], C. Bot [1], J. Chastenet[2], A. Rymar[3] and R. Paladini[4]

Abstract. Compared to the infrared and radio domains, there are very few observations of dust emission in the millimeter to centimeter wavelength range. The naive picture is that it is the thermal Rayleigh-Jeans emission from big grains. Yet resolved sub-mm and mm observations in our Galaxy and nearby galaxies have shown possible breaks in the emission law, or excess emission at long wavelengths. Laboratory measurements of dust analogs have shown more complex spectral emission laws as well with variations in temperature.
The aim of our study is to use the diversity of environments given by nearby galaxies to study dust emission at long wavelengths thanks to archival Planck and IRAS data.
One of the difficulties for these galaxies is that other foreground and background emission sources mix and often dominate the observed emission. We have to subtract the emission of these contaminating sources to obtain the dust-only emission of our targets.
Some preliminary SEDs of the sample of nearby galaxies are presented. The SEDs were fitted with a dust, free-free and synchrotron emissions model. I will present the dust properties we obtained and we will see whether the emission is consistent with the modified blackbody spectral shape or if we observe excesses or deficits of emission. These results will also be compared to those of distant galaxies.

Keywords: (sub-)millimeter emission, nearby galaxies, dust, SED

1 Introduction

Although dust constitutes a very small fraction of the mass of galaxies, its role in their evolution is significant. Dust abundance and composition reflect the chemical history of galaxies, so it is important to measure how they varie with the environment.
Information on dust composition, mass and temperature can be obtained from the analysis of its infrared (IR) emission up to millimeter wavelength. While the IR emission of galaxies has been extensively studied over the past 20 years, with space missions in the IR and ground-based antennas in the submillimeter, the millimeter to centimeter emission remains poorly observed and studied in comparison. It is, however, an interesting range to study, and the properties of dust at these long wavelengths remain relatively unconstrained.
The thermal emission of large dust grains is usually simply modeled by a modified black body, as it provides good fits to the spectral energy distribution (SED) in the far IR, but it may be more complicated than that. Dust emissivity in the (sub)-millimeter may be flatter than previously assumed, with a number of wavelength breaks and variations in shape and intensity with environmental conditions (temperature, density, ...). This can be explained by grains of different composition and/or by variations in the optical properties of the grains. Analysis of observations at long wavelengths can therefore provide information on the evolution of dust properties that can be compared from one galaxy to another.

[1] Strasbourg Astronomical Observatory, France
[2] Ghent University, Belgium
[3] Université Paris-Saclay, France
[4] IPAC, Caltech

© Société Française d'Astronomie et d'Astrophysique (SF2A) 2023

2 Sample selection

Ground-based observations of nearby galaxies in the mm to cm range provide observations with good spatial resolution but with large-scale filtering and sensitivity problems. In comparison, observations linked to the CMB such as Planck, allow to observe all the sky available, at low spatial resolution, but obtain the emission of the entire galaxy without filtering or sensitivity problems.
The IRAS and Planck satellites have mapped the entire sky, from the far-IR to microwaves. These observations give the emission of any sufficiently luminous galaxy in 10 photometric bands: 100μm for IRAS and 350μm, 550μm, 850μm, 1.3mm, 2.1mm, 3mm, 4.3mm, 6.8mm and 10mm for Planck. Some studies have exploited these data for the nearest, brightest and largest galaxies in the sky, such as the Magellanic clouds (Planck Collaboration et al. 2011) or even M33 (Tibbs et al. 2018) but a lot of nearby galaxies remain unstudied.
The sample of galaxies used in this paper is the same as the one of the IMEGIN project (Interpreting the Millimeter EMission of Galaxies *), a key project with IRAM's NIKA2 instrument, which observes 22 galaxies at higher resolution and up to 2 mm. These nearby galaxies (distance $\leq$ 30 Mpc) have a different morphological type, residing in distinct environments. In this paper, these nearby galaxies are observed at low-resolution but allow to cover a wide range of wavelengths, up to 10mm, to provide the integrated emission of these galaxies.

3 Modeling dust emission

3.1 Data processing

We start by the conversion of IRAS and Planck sky maps in the same unit (i.e. MJy/sr), the convolution of all maps over the whole sky at the same resolution (32', which is the lowest resolution in the sample, corresponding to the 10mm band) and the projection of the maps onto the same grid, at all frequencies.
Distinguishing galaxy emission in the millimeter to centimeter domain and at low resolution can be difficult: several foreground and background sources can dominate the emission of the galaxy, making it disappear. These sources, the cirrus emission from the Milky Way, the fluctuations in the cosmic microwave background, the zodiacal light and the emission from unresolved background galaxies in the field, need to be subtracted.
Figure 1 shows maps of the galaxy NGC891 in the 10 photometric bands. The central pixel surrounded in red for clarity, representing the galaxy, is completely dominated by emissions from foreground and background sources, and it is therefore necessary to subtract them.
After subtracting these emissions (see figure 2), the galaxy NGC891 is well detected, at least at shorter wavelengths, and more or less well detected at longer wavelengths.
These maps will be used to obtain galaxy fluxes in all bands in order to have the integrated spectral energy distribution for each galaxy.

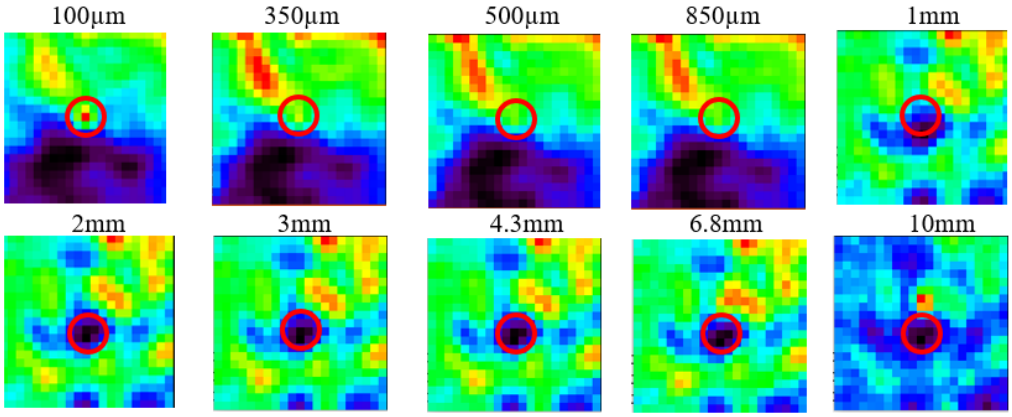

Fig. 1. Maps of NGC891 before subtraction of foreground and background emissions sources in the 10 photometric bands.

*https://irfu.cea.fr/dap/en/Phocea/Vie_des_labos/Ast/ast_visu.php?id_ast=4645

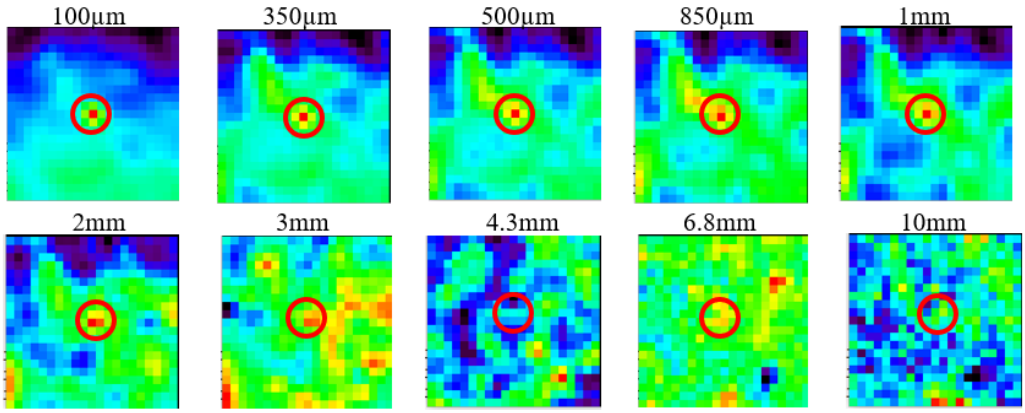

Fig. 2. Maps of NGC891 after subtraction of foreground and background emissions sources in the 10 photometric bands.

3.2 Adjusting infrared to microwave emission

We integrate the observed emission at the position of the galaxies and we subtract the average background emission measured in a surrounding region. The error on the galaxy flux is completely dominated by the uncertainties of the foreground and background subtractions, so the error on the measurements was measured by using the flux dispersion observed in the background region of the sky.
In the mm to cm range, the dust emission and the free-free emission of electrons from the ionized gas contribute to the total signal, which is then dominated by synchrotron emission in the radio range. Each of these components has a specific spectral shape, which is why we are able to disentangle and study them separately. To fit the SEDs of the sample of 22 nearby galaxies, we use a simplistic but phenomenological model to describe the shape and variations of dust emission, ionized gas and synchrotron emission. For that, we calculate the surface brightness S of the galaxy: $S_{galaxy} = S_{dust} + S_{free-free} + S_{synchrotron}$. In this model, the dust emission is a modified blackbody (equation 3.1Gordon et al. (2014)) and the ionized gas (equation 3.2) and synchrotron (equation 3.3) are power laws (Lequeux et al. 2004).

$$S_{dust} = \kappa(\beta) \times \Sigma_d \times B(T_d) \tag{3.1}$$

$$S_{free-free} = C_{ff} \times \lambda^{0.1} \tag{3.2}$$

$$S_{synchrotron} = Syn \times \lambda^{C_{syn}} \tag{3.3}$$

This model will enable us to deduce the actual physical characteristics of the dust (mass, temperature, β emissivity index) in each galaxy, and to compare them with the environment they represent (metallicity, gas mass, etc.). This modeling of the IR-cm emission will allow to see whether we reproduce the observed emission, or whether significant deviations from the model will be detected (excess or deficit).
To fit the simple model to the data, the models are integrated into the wide-band IRAS and Planck filters to best reproduce the observational data and the integrated models are fit to the data using MPFIT for each of the 22 nearby galaxy SEDs.

4 Results

Figure 3 gives two examples of SEDs observed for NGC0628 and NGC891, two galaxies of the sample, with the best model found by minimization. We superimposed radio data from SPECFIND V3.0, a radio continuum source catalogue (Stein, Y. et al. 2021) in blue. The DustPedia data corresponding to higher-resolution data for these galaxies are superimposed in green and appear to be compatible with our low resolution integrated SEDs and the best model found.
We can note that for galaxy NGC891, the SED of the galaxy can detect a small contribution of free-free emission compared to the galaxy NGC0628.
These SEDs best models give parameters of the dust, free-free and synchrotron emission, and will allow to study their properties, provide a global view of these nearby galaxies as point sources and quantify potential excesses of emission.

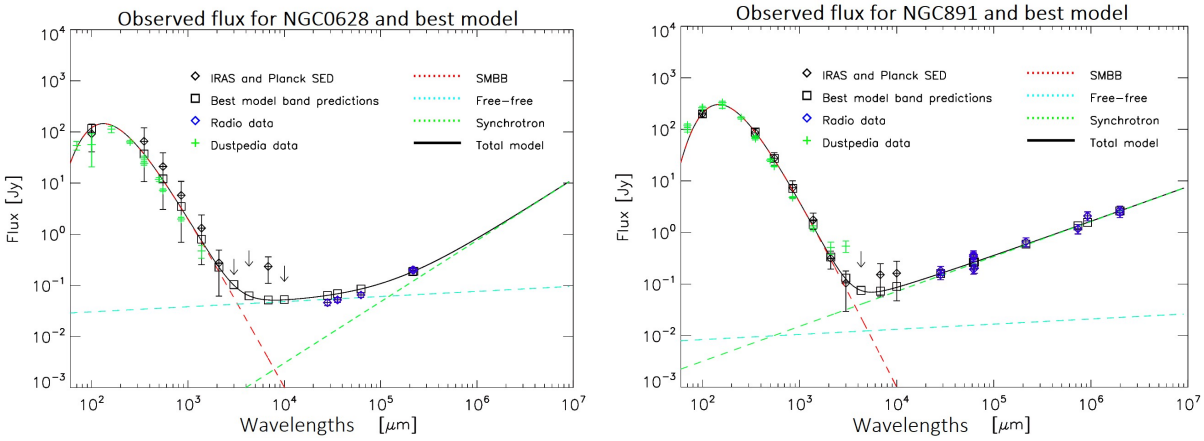

Fig. 3. Left: Spectral energy distribution of NGC0628. **Right:** Spectral energy distribution of NGC891. Black diamonds correspond to IRAS and Planck data, black squares to the best model fitting the data, blue diamonds to the radio data and green crosses to Dustpedia data. The dust model is shown in red dotted line, free-free emission in cyan dotted line, synchrotron emission in green dotted line and the total model in a blakc line.

5 Conclusions

To determine the dust properties in the millimeter to centimeter wavelegnth range, we analysed a sample of 22 nearby galaxies observed with IRAS and Planck in 10 photometric bands.
From the raw observations of these galaxies, we substrated the foreground and background emission sources that dominate the emission and prevented their detection at such low resolution.
We modeled infrared to centimeteter emission of sample of 22 nearby galaxies with a simple model of dust, ionized gas and synchrotron emission.
The next step will be to work on a potential existence of a significant excess or deficit of emission, like the one observed in the Small Magellanic Cloud (Bot et al. 2010).

References

Bot, C., Ysard, N., Paradis, D., et al. 2010, A&A, 523, A20
Gordon, K. D., Roman-Duval, J., Bot, C., et al. 2014, ApJ, 797, 85
Lequeux, J., Falgarone, E., & Ryter, C. 2004, , A&A
Planck Collaboration, Ade, P. A. R., Aghanim, N., et al. 2011, A&A, 536, A1
Stein, Y., Vollmer, B., Boch, T., et al. 2021, A&A, 655, A17
Tibbs, C. T., Israel, F. P., Laureijs, R. J., et al. 2018, MNRAS, 477, 4968

SF2A 2023
M. N'Diaye, A. Siebert, N. Lagarde, O. Venot, K. Baillié, M. Béthermin, E. Lagadec, J. Malzac, J. Richard (eds)

IMPACT OF POROSITY AND DESTRUCTIVE EFFECTS ON DUST EVOLUTION USING SPH SIMULATIONS

S. Michoulier[1] and J.-F. Gonzalez[1]

Abstract. In the theory of planetary formation, the process of how sub-μm to mm dust aggregates in protoplanetary discs grow into planetesimals is still poorly understood. A solution to overcome the fragmentation and radial drift barriers is to consider grain porosity (Garcia 2018). We have implemented a porosity evolution model in the SPH code Phantom based on Garcia (2018) and Garcia & Gonzalez (2020), with new destructive effects. With a disc model that reproduces observations, we show that porosity help grain growth as expected, allowing them to reach larger sizes. When fragmentation, bouncing and compaction are taken into account, it is still possible to form a thin disc of large dust in the mid-plane, with correct filling factors and sizes according to observations, something that can not be reproduced with compact grains.

Keywords: protoplanetary discs, planets and satellites: formation, methods: numerical

1 Introduction

Many ideas have been theorized to explain the formation of planets, yet none have been proven so far. Plenty of solutions have been proposed to form planets, mainly by forming dust traps via pressure maxima to create planetesimals, which are the building blocks of planet embryos. We can cite vortices (Barge & Sommeria 1995; Meheut et al. 2012), snow-lines (Kretke & Lin 2007; Vericel & Gonzalez 2020), or self-induced dust traps (Gonzalez et al. 2017; Vericel et al. 2021). Others classes of processes are based on instabilities, like the streaming instabilities (Youdin & Goodman 2005; Schäfer et al. 2017). Another solution is to consider more complex intrinsic properties of dust grains, namely their porosity. We have implemented a porosity evolution model that can be used in 3D simulations, developed by Garcia (2018) and Garcia & Gonzalez (2020), in the SPH code Phantom (Price et al. 2018). We also added new effects, mainly destructive, such as rotational disruption (Tatsuuma & Kataoka 2021; Michoulier & Gonzalez 2022), bouncing, and compaction during fragmentation. In this study, we will see how porosity and the different processes we added can affect the evolution of dust in discs compared to compact grains.

2 Models

2.1 Porosity and growth model

In order to take into account dust porosity, we use a slightly different and simplified version of the model derived by Garcia (2018) and Garcia & Gonzalez (2020), which contain all the details and equations about the evolution of porosity during growth. This model is based on the model from Suyama et al. (2008), Okuzumi et al. (2009), Okuzumi et al. (2012) and Kataoka et al. (2013). An aggregate is a collection of n monomers considered to be perfect compact spheres of mass m_0, size a_0 and intrinsic density ρ_s. The filling factor is defined as $\phi = \rho/\rho_\mathrm{s}$, i.e. the ratio between the aggregate's mean density and the intrinsic density of the monomers. The mass m, size s and mean density ρ of the grain can be computed as follows:

$$m = \rho V = \frac{4\pi}{3}\rho_\mathrm{s}\phi s^3. \tag{2.1}$$

[1] Universite Claude Bernard Lyon 1, CRAL UMR5574, ENS de Lyon, CNRS, Villeurbanne, F-69622, France

© Société Française d'Astronomie et d'Astrophysique (SF2A) 2023

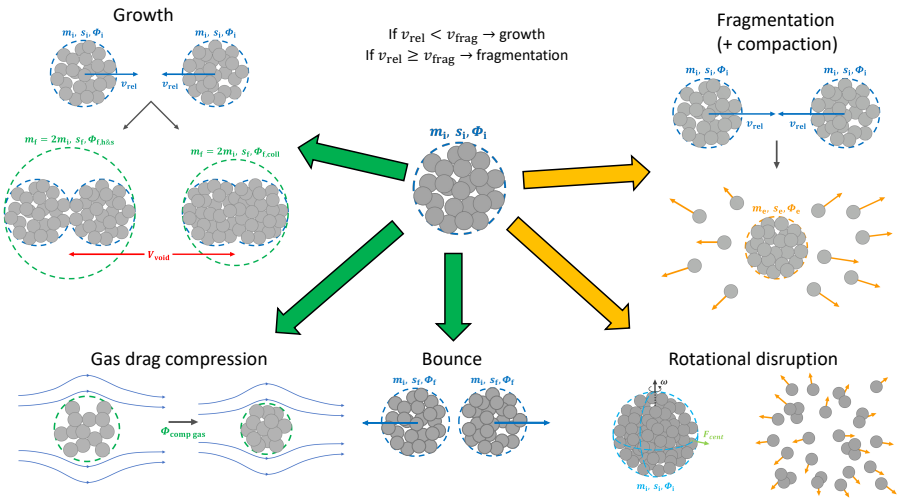

Fig. 1. Summary of some of the processes in our model a grain might undergo during its life. Some processes are destructive (yellow arrows), others lead to an increase or decrease of size, while the mass is conserved (green arrows).

The evolution of aggregates is driven by different regimes of expansion and compression depending on the mass of the grains. Grains can be in the "hit & stick" regime (see figure 1 left) or in collisional compression when masses increase. Independently of collisions, grains can also suffer static compaction (figure 1) due to gas flow (Kataoka et al. 2013). To model dust growth, we consider a locally uniform distribution of grain mass, where collisions occur between grains of identical mass m (Stepinski & Valageas 1996). Two grains collide with a relative velocity $v_{\rm rel}$ due to the gas turbulence transmitted to the dust by drag. This model was extensively used by Laibe et al. (2008), Gonzalez et al. (2015),Vericel et al. (2021). Moreover, grains can also bounce, when $\phi > 0.3$ (Wada et al. 2011; Shimaki & Arakawa 2012; Arakawa et al. 2023). Depending on $v_{\rm rel}$, the deformation can be elastic or plastic, the latter leading to compression. Some details on how bouncing is modeled are presented in Garcia (2018). The exact model will be presented in Michoulier & Gonzalez (in prep.).

2.2 Fragmentation, compaction and disruption

Lastly, to model fragmentation of dust aggregates, we use the model developed by Kobayashi & Tanaka (2010) and Garcia (2018), where the loss of mass is also a function of the fragmentation threshold $v_{\rm frag}$. The initial model supposes a constant filling during fragmentation. But Ringl et al. (2012) and Gunkelmann et al. (2016) have shown that the filling factor after fragmentation is approximately 1.5 to 2 times larger than the initial one. We have developed a model to take into account the compaction during fragmentation based on dust properties. The full model will also be presented in Michoulier & Gonzalez (in prep.). Finally, for the rotational disruption, we use the exact same model as the one detailed in Michoulier & Gonzalez (2022).

3 Results

For our simulations, we use the SPH code Phantom (Price et al. 2018) and the 1-fluid method. We use a disc model representative of observations (Williams & Best 2014). The mass of the star is set to $M_* = 1$ M$_\odot$, that of the disc to $M_* = 0.01$ M$_\odot$. The inner and outer radii are set to $r_{\rm in} = 10$ au and $r_{\rm out} = 400$ au, the disc aspect ratio is $H/r_0 = 0.0895$ with a reference radius $r_0 = 100$ au, $p = 0.75$, $q = 0.5$, and a turbulent viscosity parameter $\alpha = 5 \times 10^{-3}$. The external density profile decreases exponentially with a characteristic disc radius of $R_{\rm c} = 60$ au (see equation (298) in Price et al. 2018). For the dust, a typical dust-to-gas ratio of 1% is used. We use silicates with $\rho_{\rm s} = 2.7$ kg m^{-3}, a young modulus $\mathcal{E} = 72$ GPa (Yamamoto et al. 2014) and a surface energy of $\gamma_{\rm s} = 0.2$ J m^{-2} (Yamamoto et al. 2014; Kimura et al. 2020). The monomer size is fixed to 0.2 µm according to Tazaki & Dominik (2022), with different fragmentation thresholds $v_{\rm frag} = 5 - 10 - 20$ m s^{-1}.

Figures 2 and 3 show the results of six simulations at $t = 100$ kyr. GF-comp-Vf20 correspond to a simulation with growth and fragmentation with compact grains and $v_{\rm frag\,Si} = 20$ m s^{-1}, GF-a02-Vf20 is the same with porous grains with a monomer size of 0.2 µm. GBFc-a02-Vf10 and GBFc-a02-Vf20 correspond to simulations

with growth, fragmentation, bouncing and compaction and $v_{\mathrm{frag,\,Si}} = 10$ and 20 m s^{-1}. GBFcS-a02-Vf205 is GBFc-a02-Vf20 with a CO snow-line ($T = 20$ K) where $v_{\mathrm{frag,\,in}} = 20$ m s^{-1} and $v_{\mathrm{frag,\,out}} = 5$ m s^{-1} and GBFcD-a02-Vf20 is GBFc-a02-Vf20 with disruption. We can see on figure 2 showing the size s in the (r, z) plane that all cases produce thin discs in the inner regions, of the order of $15 - 20$ au thick at 100 au, except for GBFcS-a02-Vf205 where the disc is thicker due to the snow-line. We also note the outer region is thicker when porosity is taken into account. Large grains are located in the mid-plane, with sizes exceeding 100 µm. GF-a02-Vf20 and GBFc-a02-Vf20 are able to produce the largest grains, while GBFc-a02-Vf10 can't due to the lower fragmentation threshold that limit the grain size to 1 mm at maximum. Disruption (GBFcD-a02-Vf20) limits the maximum grain size compared to GBFc-a02-Vf20, as centimetre-sized aggregates are in this case harder to form. In the case of a snow-line, grains are not able to grow freely at distances larger than 100 au, where the CO snow-line is located, due to the very low v_{frag}. In the inner regions where v_{frag} is larger, dust grains larger than 1 mm are still formed with high filling factors. Figure 3 shows the radial size distribution colored with the

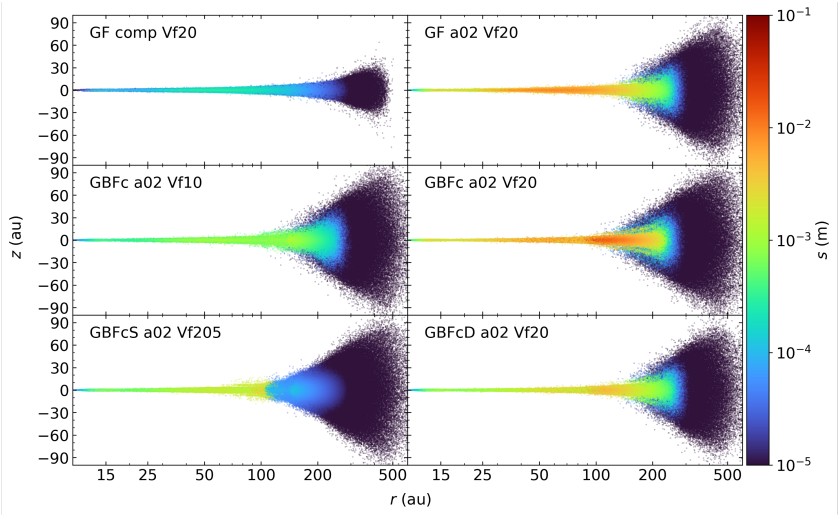

Fig. 2. Comparison between simulations in the (r, z) plane with growth and fragmentation with compact grains and $v_{\mathrm{frag\,Si}} = 20$ m s^{-1} (GF-comp-Vf20), the same with porous grains (GF-a02-Vf20), two simulations with growth, fragmentation, bouncing and compaction with $v_{\mathrm{frag,\,Si}} = 10$ and 20 m s^{-1} (GBFc-a02-Vf10 and GBFc-a02-Vf20). The last two are the same as GBFc-a02-Vf20. One with a CO snow-line (GBFcS-a02-Vf205) where $v_{\mathrm{frag,\,in}} = 20$ m s^{-1} and $v_{\mathrm{frag,\,out}} = 5$ m s^{-1}, the other one with disruption (GBFcD-a02-Vf20). The color gives the dust size.

filling factor ϕ. Simulation GF-comp-Vf20 with compact grains is not able to form grains of 1 mm anywhere in the disc. This is also the case of the simulation GBFc-a02-Vf10 where sizes of $1 - 2$ mm are barely reached between 30 and 200 au. GF-a02-Vf20 and GBFc-a02-Vf20 are able to reach of a couple of centimetres in a large portion of the disc, even if GBFc-a02-Vf20 has compaction during fragmentation. The effect of disruption can be seen between 50 to 150 au where grains do not suffer from compaction. The maximum size is about 1 cm, while without disruption, the maximum is about 8 cm. Finally, the simulation with a snow-line shows compacted grains up to 100 au with $\phi \sim 0.1 - 0.5$ and $s \geq 1$mm, up to 1 cm at the snow-line at 100 au.

4 Conclusions

We have implemented a complete model of dust porosity evolution in Phantom. We performed several simulations with different processes to see their effect on dust evolution. When taking into account growth, fragmentation, bouncing and compaction (GBFc), simulations show it is possible to form grains with $\phi \sim 0.1 - 0.5$ and $s \sim 1$ mm, compatible with observations (Güttler et al. 2019; Guidi et al. 2022; Zhang et al. 2023). Bouncing is negligible and disruption does not play a huge role, as we excepted (Michoulier & Gonzalez 2022), while compaction during fragmentation is the mechanism that allows results closer to observations. Synthetic images are the next step to compare with observations and better understand how planets form.

We would like to thank the SF2A and the organizers of "Latest insights on dust evolution" for letting us present our work to the "Journées de la SF2A 2023". Figures in the results section were made using the *matplotlib* library (Hunter 2007).

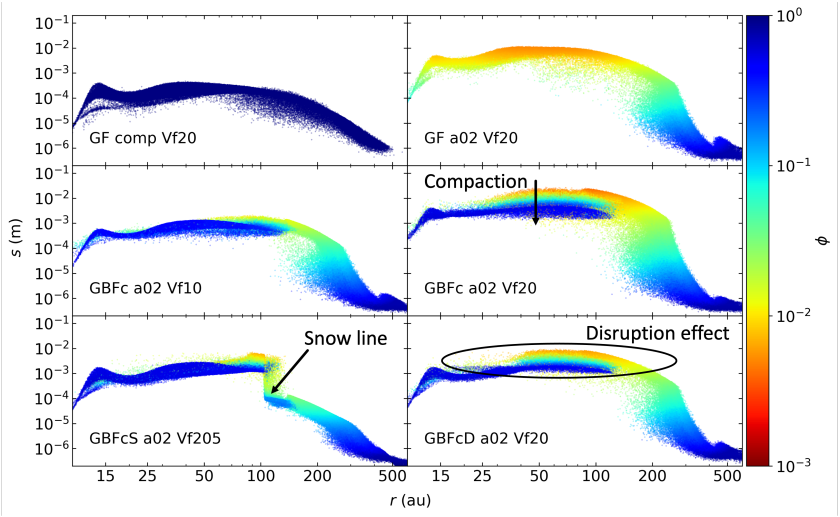

Fig. 3. Same as figure 2, but the grain size s is given as a function of r and color indicates the filling factor.

References

Arakawa, S., Okuzumi, S., Tatsuuma, M., et al. 2023, arXiv e-prints, arXiv:2306.04070
Barge, P. & Sommeria, J. 1995, A&A, 295, L1
Garcia, A. 2018, Theses, Université de Lyon
Garcia, A. J. L. & Gonzalez, J.-F. 2020, MNRAS, 493, 1788
Gonzalez, J.-F., Laibe, G., & Maddison, S. T. 2017, MNRAS, 467, 1984
Gonzalez, J.-F., Laibe, G., Maddison, S. T., Pinte, C., & Ménard, F. 2015, Planet. Space Sci., 116, 48
Guidi, G., Isella, A., Testi, L., et al. 2022, A&A, 664, A137
Gunkelmann, N., Ringl, C., & Urbassek, H. M. 2016, A&A, 589, A30
Güttler, C., Mannel, T., Rotundi, A., et al. 2019, A&A, 630, A24, arXiv: 1902.10634
Hunter, J. D. 2007, Computing in Science & Engineering, 9, 90
Kataoka, A., Tanaka, H., Okuzumi, S., & Wada, K. 2013, A&A, 557, L4
Kimura, H., Wada, K., Yoshida, F., et al. 2020, MNRAS, 496, 1667, arXiv: 2006.05107
Kobayashi, H. & Tanaka, H. 2010, Icarus, 206, 735
Kretke, K. A. & Lin, D. N. C. 2007, The Astrophysical Journal, 664, L55
Laibe, G., Gonzalez, J. F., Fouchet, L., & Maddison, S. T. 2008, A&A, 487, 265
Meheut, H., Keppens, R., Casse, F., & Benz, W. 2012, A&A, 542, A9
Michoulier, S. & Gonzalez, J.-F. 2022, MNRAS, 517, 3064
Okuzumi, S., Tanaka, H., Kobayashi, H., & Wada, K. 2012, ApJ, 752, 106
Okuzumi, S., Tanaka, H., & Sakagami, M.-a. 2009, ApJ, 707, 1247
Price, D. J., Wurster, J., Tricco, T. S., et al. 2018, Publications of the Astronomical Society of Australia, 35, e031
Ringl, C., Bringa, E. M., Bertoldi, D. S., & Urbassek, H. M. 2012, ApJ, 752, 151, aDS Bibcode: 2012ApJ...752..151R
Schäfer, U., Yang, C.-C., & Johansen, A. 2017, A&A, 597, A69
Shimaki, Y. & Arakawa, M. 2012, Icarus, 218, 737, aDS Bibcode: 2012Icar..218..737S
Stepinski, T. F. & Valageas, P. 1996, A&A, 309, 301
Suyama, T., Wada, K., & Tanaka, H. 2008, ApJ, 684, 1310
Tatsuuma, M. & Kataoka, A. 2021, ApJ, 913, 132
Tazaki, R. & Dominik, C. 2022, A&A, 663, A57
Vericel, A. & Gonzalez, J.-F. 2020, MNRAS, 492, 210
Vericel, A., Gonzalez, J.-F., Price, D. J., Laibe, G., & Pinte, C. 2021, MNRAS, 507, 2318
Wada, K., Tanaka, H., Suyama, T., Kimura, H., & Yamamoto, T. 2011, ApJ, 737, 36
Williams, J. P. & Best, W. M. J. 2014, ApJ, 788, 59, aDS Bibcode: 2014ApJ...788...59W
Yamamoto, T., Kadono, T., & Wada, K. 2014, ApJ, 783, L36
Youdin, A. N. & Goodman, J. 2005, ApJ, 620, 459, aDS Bibcode: 2005ApJ...620..459Y
Zhang, S., Zhu, Z., Ueda, T., et al. 2023, arXiv e-prints, arXiv:2306.00158

SF2A 2023
M. N'Diaye, A. Siebert, N. Lagarde, O. Venot, K. Baillié, M. Béthermin, E. Lagadec, J. Malzac, J. Richard (eds)

INSIGHT FROM LABORATORY MEASUREMENTS ON DUST IN DEBRIS DISCS

J. Milli[1], O. Poch[1], J. B. Renard[2], J. C. Augereau[1], P. Beck[1], E. Choquet[3], J. M. Geffrin[4], E. Hadamcik[5], J. Lasue[6], F. Menard[1], A. Peronne[1], C. Baruteau[6], R. Tazaki[1] and V. Tobon Valencia[1]

Abstract. Extreme adaptive optics instruments have revealed exquisite details on debris discs, allowing to extract the optical properties of the dust particles such as the phase function, the degree of polarisation and the spectral reflectance. These are three powerful diagnostic tools to understand the physical properties of the dust : the size, shape and composition of the dust particles. This can inform us on the population of parent bodies, also called planetesimals, which generate those particles through collisions. It is however very rare to be able to combine all those three observables for the same system, as this requires different high-contrast imaging techniques to suppress the starlight and reveal the faint scattered light emission from the dust. Due to its brightness, the ring detected around the A-type star HR 4796 is a notable exception, with both unpolarised and polarised images covering near-infrared wavelengths. Here, we show how measurements of dust particles in the laboratory can reproduce the observed near-infrared photo-polarimetric properties of the HR 4796 disc. Experimental characterisation of dust allows to bypass the current limitations of dust models to reproduce simultaneously the phase function, the degree of polarisation and the spectral reflectance.

Keywords: HR 4796, light scattering, debris disc, cosmic dust

1 Introduction

Debris discs represent an evolutionary stage of a planetary system after a few million years when the primordial gas-rich protoplanetary disc has dissipated, and leaves behind planetesimals that are thought to be leftovers from the planetary formation (see Wyatt 2008, for a review). Their mutual collisions produce an optically thin dust disc that is detectable through the infrared excess emission above the stellar photosphere. The initial reservoir of planetesimals depletes with time, hence also the amount of dust. The detection rate of debris discs is indeed 75% in the young 18 Myr β Pictoris moving group (Pawellek et al. 2021), but goes down to $\sim$ 20% around Gyr-old stars (e.g. Sibthorpe et al. 2018). With an age of 10 ± 3 Myrs, the A-type star HR 4796 located at 70.8 pc (Gaia Collaboration 2020) hosts a particularly well studied debris disc with a large infrared excess of 0.5% (Moór et al. 2006). Most of the dust is located in a narrow ring at $\sim$ 80 au from the central star and a width of about $\sim$ 10 au (Kennedy et al. 2018). Because of its relatively high surface brightness compared to other debris discs, this system has been extensively studied in many wavelengths, as visible in Fig. 1.

Despite this extensive spectral coverage, the composition, shape and size of the particles remain a mystery since the high-contrast imagers VLT/SPHERE and Gemini/GPI have revealed the scattering phase function (hereafter SPF) and degree of polarisation (hereafter DoLP) of the particules (Perrin et al. 2015; Milli et al. 2017). We will focus here on the near-infrared scattering properties of the disc to show how laboratory measurements of dust analogues can be used to shed light on the nature of the particles in this system.

[1] Univ. Grenoble Alpes, CNRS, IPAG, F-38000 Grenoble, France
[2] LPC2E, Université d'Orléans, CNRS, Orléans, France
[3] Aix Marseille Université, CNRS, CNES, LAM, Marseille, France
[4] Aix Marseille Univ, CNRS, Centrale Marseille, Institut Fresnel, Marseille, France
[5] LATMOS, Sorbonne Université, CNRS, CNES, Paris, France
[6] IRAP, Université de Toulouse, CNES, CNRS, UPS, Toulouse, France

© Société Française d'Astronomie et d'Astrophysique (SF2A) 2023

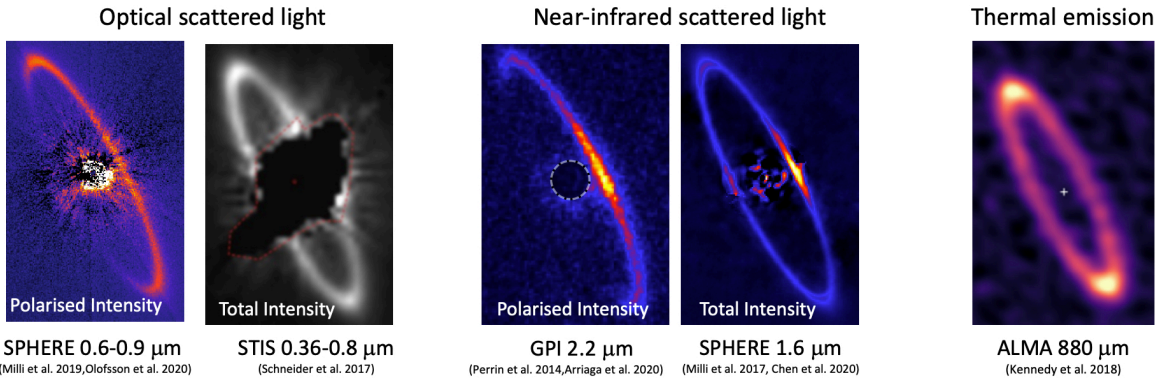

Fig. 1. The HR 4796 disc at various wavelengths. The semi-major axis of the disc is ~ 1". North is up, East to the left.

2 The scattered light near-infrared properties of the dust

Thanks to the polarimetric capabilities of the high-contrast instruments SPHERE (Beuzit et al. 2018) and GPI (Macintosh et al. 2014), the surface brightness of the ring can be measured at almost all azimuth angles, even along the minor axis. Each position along the ring corresponds to a unique angle between the illumination direction and the line of sight, called the scattering angle. The ring is inclined by $\sim 76.5°$ from pole-on, meaning that the minor axes correspond to scattering angles of 13.5° and 166.5° respectively for the bright North-West forward-scattering side, and the faint South-East backward scattering side. One can therefore extract the SPF and DoLP of the dust particles in this range of scattering angles, as shown in Fig 2.

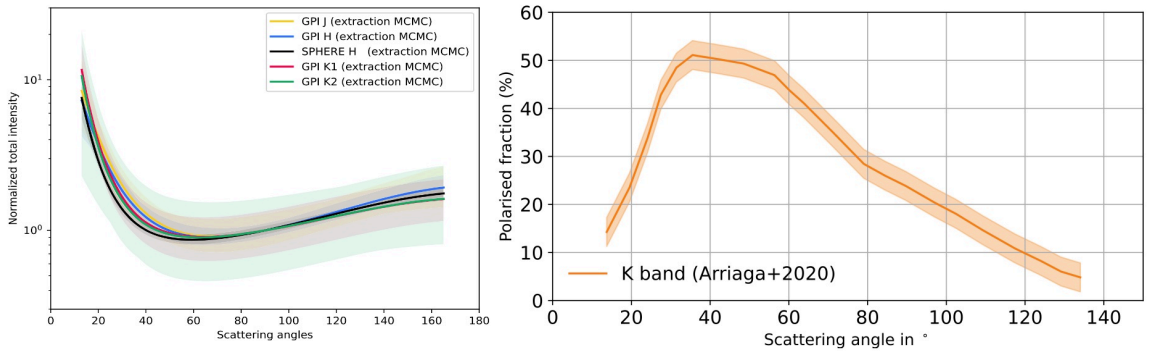

Fig. 2. Left: Total intensity scattering phase function of the disc, as extracted from GPI and SPHERE using a parametric modelling (double-component Heyney Greenstein model) in the J (1.2 µm), H (1.6 µm) and K (2.2 µm) band (Chen et al. 2020). **Right:** Degree of linear polarisation as extracted from GPI in the K band (Arriaga et al. 2020)

Modelling of the dust particles assuming compact spheres (Mie theory) made of basic cometary-like materials used traditionally for debris disc, e.g. silicates, amorphous carbon, water ice and porosity (see for instance Augereau et al. 1999), could not reproduce the total intensity scattering phase function of the dust particles (Milli et al. 2017). If one relaxes the assumption on the composition of the particles, Chen et al. (2020) showed that the total intensity SPF can be fit using the Distribution of Hollow Spheres (DHS, Min et al. 2005) but required a relatively high volume fraction of metallic iron of 37^{+15}_{9}%, a highly absorbing mineral, in addition to amorphous carbon and silicates. However, when adding the DoLP as a constraint, no model using the Mie nor the DHS theory could simultaneously reproduce the SPF and the DoLP (Arriaga et al. 2020). This points out that one of our initial assumption is wrong, either particles in the HR 4796 disk cannot be modelled by compact spheres, as suggested already in Milli et al. (2014), or a simple differential power-law size distribution is too simplistic. We decided to use laboratory experiments rather than numerical experiments to find good terrestrial analogues to the HR 4796 dust. The choice of the sample was driven by the fact that there are few micron-size particles with a peak in DoLP at scattering angles as small as 40°, while larger mm-size pebbles can do so (e.g. Muñoz et al. 2021) but are incompatible with the spectral energy distribution of the disk that requires a

minimum particle size of ~ 2 µm. We found an interesting sample in the PROGRA^2 database*, pyrrhotite, a non-stoichiometric form of iron sulphide $Fe_{1-x}S$ ($0 < x \leq 0.125$).

3 Laboratory measurements of dust particles with PROGRA^2

3.1 The PROGRA^2 instrument and pyrrhotite sample

The PROGRA^2 instrument is dedicated to the study of light scattered by solid particles deposited on a surface or lifted in clouds (Worms et al. 2000; Hadamcik et al. 2002). We used here a sample of pyrrhotite (Fig. 3) that was lifted in clouds in microgravity conditions during parabolic flights that took place between 2018 and 2021. The sample is contained in a vial where it receives the light from a laser. The light scattered by the particles is split using a polarised beam splitter in two channels where it is measured on two detectors.

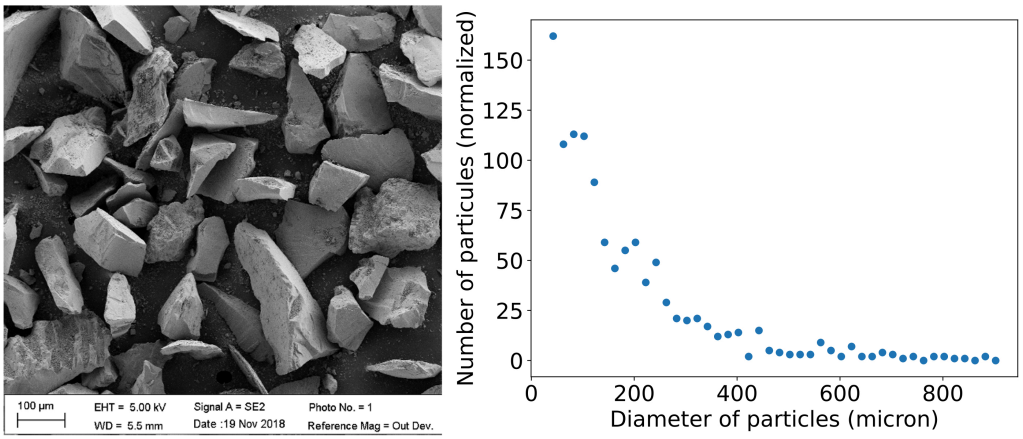

Fig. 3. Left: Scanning Electron Microscope view of the sample . **Right:** Granulometry of the sample as measured using the camera onboard PROGRA^2 in the R band. The resolution of the camera is limited to 40 µm.

3.2 Measurements and conclusions

PROGRA^2 allows measurements of the total intensity SPF at optical wavelengths, and the DoLP at both optical and NIR wavelengths. The comparison to the HR 4796 particles are shown in Fig. 4. We notice that the peak in DoLP around a scattering angle of 40° is well reproduced by the sample. There are very few samples with particles with sizes in the 1-200 µm range that can reproduce a peak at so small scattering angles in the large PROGRA^2 database: only silicon carbides (CSi) could also produce this behaviour, with an overall match not as good as pyrrhotite. The maximum DoLP as measured in the optical and near-infrared (NIR) is in the range 35-45% for the pyrrhotite, slightly smaller than the HR 4796 particles at 2.2 µm, but the maximum DoLP can increase with wavelength for large levitating grains (Renard et al. 2014) and can also largely dependent on the minimum particle size or size distribution (Milli et al. in prep.). Regarding the total intensity SPF (Fig. 4 right), the backward scattering behaviour seen on HR 4796 in the NIR is well reproduced by the pyrrhotite sample measured in the optical. Unfortunately, PROGRA^2 does not have the capability to measure the SPF in the NIR for a rigorous comparison at the same wavelength.

Overall, the pyrrhotite sample is an interesting candidate material to reproduce simultaneously the total intensity SPF and DoLP of the particles in HR 4796. In this study, no attempt to adjust the sample to match exactly the HR 4796 properties has been made, in particular the particle sizes, but we present here for the first time archival PROGRA^2 measurements done on a sample of pyrrhotite with sizes dominated by particles smaller than 100 µm. The presence of a highly absorbing material such as iron sulphide confirms the finding of Chen et al. (2020) using the total intensity SPF alone and bring guidance in the attempt to reconcile the SPF and DoLP with more irregular particles than the compact spheres tested in Arriaga et al. (2020). The presence of iron sulphides would not be surprising in circumstellar dust. Stratospheric interstellar dust particles,

*https://www.icare.univ-lille.fr/progra2-en/?noredirect=en_US

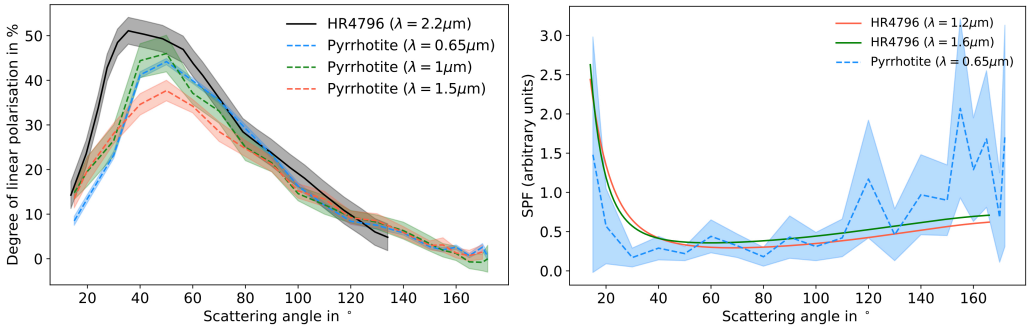

Fig. 4. Left: DoLP of the measured pyrrhotite sample compared to the DoLP of HR4796 in the K band (Arriaga et al. 2020). **Right:** Optical SPF of the pyrrhotite sample compared to the NIR SPF of HR4796 (Chen et al. 2020)

Antarctica Micro-Meteorites, comet Wild 2 samples, all contain sulphides in the form of troilite FeS (Dobrica et al. 2009). Iron is also present in the comet 67P/Churyumov-Gerasimenko, with a mass fraction of 7.5% (Bardyn et al. 2017). Moreover, opaque minerals (such as iron sulphides, or Fe-Ni alloys) are responsible for the dark reflectance (from optical to NIR wavelengths) of cometary and primitive asteroids surfaces (Quirico et al. 2016), they could therefore also be present on the surface of the HR 4796 particles, explaining at the same time the red reflectance spectrum of the disk (Milli et al. 2017).

We dedicate this paper to the memory of Anny-Chantal Levasseur-Regourd (ACLR), who encouraged and inspired our efforts to compare remote observations of exoplanetary dust to laboratory measurements. This work was carried out as part of the EPOPEE project (Etude des POussières Planétaires Et Exoplanétaires) project. This research group is funded by the Programme National de Planétologie (PNP) of CNRS-INSU in France, from which we acknowledge financial support. ACLR was one of the most enthusiastic members, always willing to share her wide expertise with the younger generation, and she has vastly contributed to this scientific collaboration between the disc and solar system community. She sadly passed away only a few weeks after attending our June 2022 EPOPEE working group meeting in Grenoble.

References

Arriaga, P., Fitzgerald, M. P., Duchêne, G., et al. 2020, AJ, 160, 79
Augereau, J. C., Lagrange, A. M., Mouillet, D., Papaloizou, J. C. B., & Grorod, P. A. 1999, A&A, 348, 557
Bardyn, A., Baklouti, D., Cottin, H., et al. 2017, MNRAS, 469, S712
Beuzit, J.-L., Mouillet, D., Sauvage, J.-F., Fusco, T., & Dohlen, K. 2018, in Adaptive Optics Systems VI, Proc. SPIE
Chen, C., Mazoyer, J., Poteet, C. A., et al. 2020, ApJ, 898, 55
Dobrica, E., Engrand, C., Duprat, J., et al. 2009, Meteoritics and Planetary Science, 44, 1643
Gaia Collaboration. 2020, VizieR Online Data Catalog, I/350
Hadamcik, E., Renard, J. B., Worms, J. C., Levasseur-Regourd, A. C., & Masson, M. 2002, Icarus, 155, 497
Kennedy, G. M., Marino, S., Matrà, L., et al. 2018, MNRAS, 475, 4924
Macintosh, B., Graham, J. R., Ingraham, P., et al. 2014, Proceedings of the National Academy of Science, 111, 12661
Milli, J., Lagrange, A.-M., Mawet, D., et al. 2014, A&A, 566, A91
Milli, J., Vigan, A., Mouillet, D., et al. 2017, A&A, 599, A108
Min, M., Hovenier, J. W., & de Koter, A. 2005, A&A, 432, 909
Moór, A., Ábrahám, P., Derekas, A., et al. 2006, ApJ, 644, 525
Muñoz, O., Frattin, E., Jardiel, T., et al. 2021, ApJS, 256, 17
Pawellek, N., Wyatt, M., Matrà, L., Kennedy, G., & Yelverton6, B. 2021, MNRAS, 502, 5390
Perrin, M. D., Duchene, G., Millar-Blanchaer, M., et al. 2015, ApJ, 799, 182
Quirico, E., Moroz, L. V., Schmitt, B., et al. 2016, Icarus, 272, 32
Renard, J. B., Hadamcik, E., Couté, B., Jeannot, M., & Levasseur-Regourd, A. C. 2014, J. Quant. Spec. Radiat. Transf., 146, 424
Sibthorpe, B., Kennedy, G. M., Wyatt, M. C., et al. 2018, MNRAS, 475, 3046
Worms, J. C., Renard, J. B., Hadamcik, E., Brun-Huret, N., & Levasseur-Regourd, A. C. 2000, Planet. Space Sci., 48, 493
Wyatt, M. C. 2008, ARA&A, 46, 339

SF2A 2023
M. N'Diaye, A. Siebert, N. Lagarde, O. Venot, K. Baillié, M. Béthermin, E. Lagadec, J. Malzac, J. Richard (eds)

DYNAMICAL STUDY OF THE COLLAPSE OF A CLOUD OF GAS AND PARTICLES: WHAT ARE THE THERMODYNAMICAL PROPERTIES OF THE FORMED PLANETESIMALS?

P. Segretain[1], H. Méheut[1] and M. Moreira[2]

Abstract. We present work that aims to confront geochemical information on the formation of planetesimals with dynamical studies of the nebula in which they grow from pebbles of around cm in size. A possible scenario consists of the concentration of these pebbles through interaction with the gas in the disc to form clumps, leading to a gravitational collapse and the formation of planetesimals. On the other hand, the geochemical approach of planet formation constrains these conditions as it shows that high temperatures should be reached to form the material of meteorites or to allow the incorporation of gas into planetesimals. In particular, the origin of noble gases in the terrestrial mantle is still debated and might ultimately provide a unique clue on this stage of planet formation. We study numerically the gravitational collapse of a cloud of particles and gas coupled by fluid friction. Our goal is to determine how the gravitational energy relaxed during the collapse will be divided into the different components of the system, and how this constrains the physical and thermodynamical conditions at the surface of the planetesimal.

We present here the numerical tools used for this study and the first results.

Keywords: gravitational collapse, pebbles, gas, fluid friction

1 Introduction

The ubiquity of planets shows that planet formation is a standard process. Protoplanetary disks with sizes of hundreds of AU are factories able to convert dust 20 orders of magnitude smaller into planets. This necessarily involves many different physical and chemical processes. In the incremental growth scenario, the micrometric dust grains agglomerate to form pebbles of around cm sizes (e.g. Armitage (2020)). The following step, the formation of kilometer size objects, planetesimals, is one of the major open questions in this domain. A possible scenario consists of the concentration of these pebbles through interaction with the gas in the disc to form clumps (Drazkowska et al. 2023) which would collapse to form planetesimals. Whereas the step of pebble concentration in the disc is often studied, for example with the process of streaming instability (e.g. Carrera & Simon (2022)) or of dust trapping in vortical structures (e.g. Gerosa et al. (2023), Chavanis (2000)), the step of the gravitational collapse has rarely been studied, mainly to know how one can form binary planetesimals (). On the other hand, the geochemical approach of planet formation shows that high temperature should be reached to form the material of meteorite, or to incorporate gas into planetesimals. Indeed, the origin of noble gas in the terrestrial mantle is still debated and should be consistent with the dynamical processes involved in planet formation. However, the coupling between the dynamics of solids and the gas temperature during the gravitational collapse of a pebble clump in a gaseous environment has rarely been taken into account. This work aims to study numerically the gravitational collapse of a cloud of particles and gas coupled through fluid friction. The aim is to estimate how the gravitational energy relaxed during collapse will be divided into the different components of the system and therefore the temperature the system can reach.

[1] Université Côte d'Azur, Observatoire de la Côte d'Azur, CNRS, Laboratoire Lagrange, Nice, France
[2] ISTO, Institut de Sciences de la Terre d' Orléans, Orléans, France

© Société Française d'Astronomie et d'Astrophysique (SF2A) 2023

2 Numerical Methods

2.1 Model

This numerical study of the collapse requires to model the coupled evolution of gas and particles. The gas is modelled as an Eulerian fluid for which the Euler equations are solved:

$$\frac{\partial \rho}{\partial t} + \nabla \cdot (\rho u) = 0 \tag{2.1}$$

$$\frac{\partial}{\partial t}(\rho u) + \nabla \cdot (\rho u \otimes u) = -\rho \nabla \phi_g - f_{\text{drag}} \tag{2.2}$$

$$\frac{\partial}{\partial t}(\rho e) + \nabla \cdot \left(\rho u (e + \frac{p}{\rho}) \right) = \rho u \cdot \nabla \phi_g + E_{\text{drag}} \tag{2.3}$$

The pebbles are modelled as Lagrangian particles for which we solved Newton's law of motion :

$$\frac{\mathrm{d}^2 x}{\mathrm{d}t^2} = -\nabla \phi_g + f_{\text{drag}} \tag{2.4}$$

The self-gravity of the system is taken into account by solving the Poisson equation :

$$\Delta \phi_g = 4\pi G \rho_t \tag{2.5}$$

where ρ_t is the total mass density of gas and pebbles. In these equations, f_{drag} corresponds to the drag force exerted by the gas on pebbles and its feedback onto the gas. We choose to use Epstein drag law (Epstein 1924) such that, for a lagrangian particle with speed v_p :

$$f_{\text{drag}} = -\frac{v_p - u}{\tau} \tag{2.6}$$

where τ is the dust stopping time, depending on the density and the sound speed of the gas.

These equations are solved by using the Idefix code (Lesur et al. 2023). This new numerical code allows us to solve hydrodynamical equations on a grid with a finite-volume Godunov method. A self-gravity module solving the Poisson equation through algebraic methods and a Lagrangian particles module (including gas friction) are currently developed and allow us to take into account the different physics needed for the simulations.

2.2 Initial and Boundary Conditions

All the simulations presented are 1D in spherical geometry. Thus, only the radial movement of the collapsing pebble clump is followed. In the initial state, the Lagrangian particles modelling the dust have no initial speed, and with a density profile chosen as follows:

$$\rho_p(r) = \begin{cases} \rho_c \text{ if } r \leq r_c \\ \rho_c \exp\left(\dfrac{(r - r_c)^2}{\sigma^2} \right) \text{ else} \end{cases} . \tag{2.7}$$

The initial radius of the pebble clump is defined as $R_0 = r_c + \sigma$ and $\sigma = \dfrac{r_c}{5}$. The total mass of pebbles is $M_{tot} = \displaystyle\int_0^{+\infty} 4\pi r^2 \rho_p(r) \mathrm{d}r$. The gas is also initially static, with a uniform density ρ_g and temperature T_g across the grid. It is supposed to be perfect. The characteristic time of the drag law was chosen equal to 9×10^4 s which corresponds (with the chosen gas density and sound speed) to pebbles with a size of about 10 cm.

We choose to explore the variations of the final temperature with the total mass of pebbles and the initial density of the gas. M_{tot} goes from 1 to 15×10^{16} kg and ρ_g goes from 3 to 21×10^{-6} kg $\cdot$ m^{-3}.

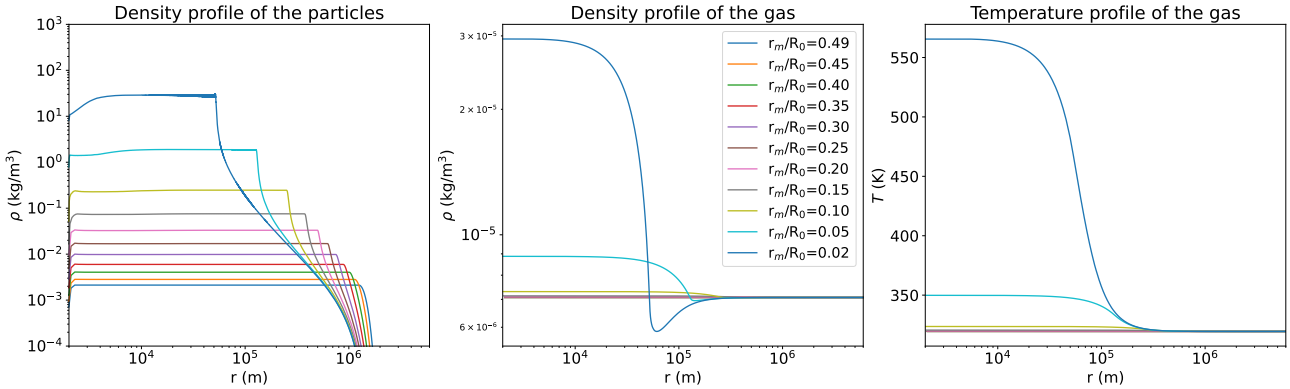

Fig. 1: Radial profile of the particle cloud's density (left), of the gas density (centre) and temperature (right) during the collapse, for $M = 3 \times 10^{16}$ kg, $R_0 = 1,5 \times 10^6$ m, $\rho_g = 7 \times 10^{-6}$ kg/m^3.

3 Results

3.1 Time evolution

We study the evolution of the cloud properties during the collapse. This evolution is shown on the figure 1, in our fiducial case with $R_0 = 1.5 \times 10^6$ m, $M_{tot} = 3 \times 10^{16}$ kg, $\rho_g = 7 \times 10^{-6}$ kg$\cdot$m^{-3} and $T_g = 320$ K. From left to right, this figure shows the density of the particle cloud, the density of the gas and its temperature. Each curve corresponds to a different time, characterised by the mean radius r_m of the pebble clump at that time, defined as

$$r_m = \frac{\int_0^{+\infty} r\rho_p(r)\mathrm{d}r}{\int_0^{+\infty} \rho(r)\mathrm{d}r}. \tag{3.1}$$

The density of pebble clump, shown on the left of figure 1, increases regularly with time during the collapse, to reach 3×10^1 kg$\cdot$m^{-3}. The core of the cloud has a uniform density during nearly all the collapse but the concavity of the tail changes and the edge of the cloud becomes steeper. On the contrary, the density of the gas (at the centre of the figure) and its temperature (on the right) are nearly constant during the collapse and change only at the end of the collapse, with finally a multiplication by 4 of the central density, and an increase of about 240 K of the central temperature of the gas.

3.2 Parameter Space Exploration

We studied the evolution of the final central temperature of the gas with two main parameters: the total mass of the cloud M_{tot} and the initial density of gas ρ_g. As shown in the left panel of Fig. 2, the final temperature is approximately inversely proportional to the initial density of gas. However, we see that the slope of the curves varies slightly with the initial mass of the cloud. To better understand this behaviour, we also plotted the final temperature as a function of the initial mass, as shown on the right panel of 2. We see that the final temperature is approximately proportional to the initial mass, but again, the slope depends slightly on the density of the gas. These slight variations are not for now fully understood and we project to explore in more detail the parameter space to explain that.

These behaviours are consistent with those we can expect theoretically: the more massive the pebble clump is, the more energy the system will release and so the hotter the gas will be in the vicinity of the forming planetesimal. Likewise, if less gas is surrounding the clump, then, for the same energy released, the gas will be hotter. These results show that, to dissolve gas from the disc into the forming planetesimal (i.e. reach a temperature of about 1200 K), we need to have a quite massive clump (mass of around 10^{17} kg that is a planetesimal of around 10 km in size) with low surrounding gas density (initial dust-to-gas ratio of around 1000 and above).

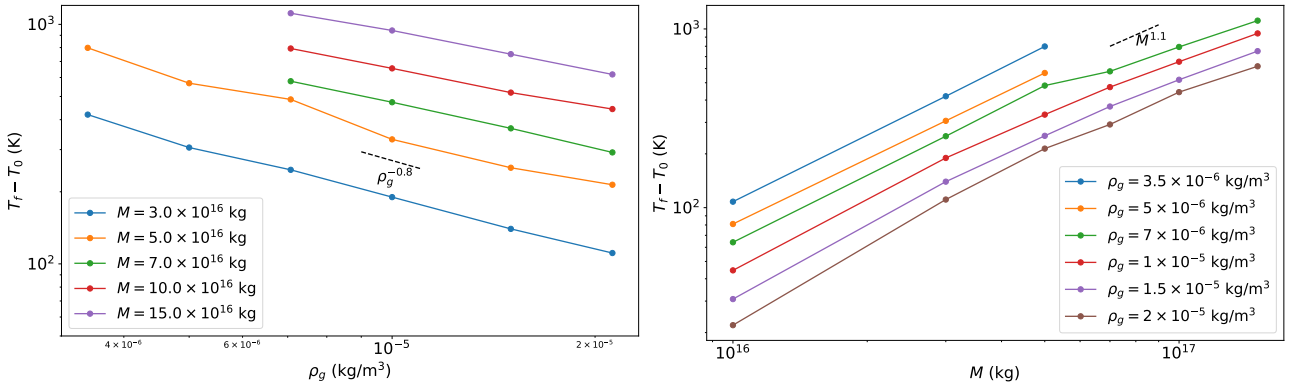

Fig. 2: **Left:** Gas central temperature as a function of the initial gas density for different values of the initial mass of the particles cloud ($R_0 = 1,5 \times 10^6$ m). **Right:** Gas central temperature as a function of the initial mass of particles for different values of initial gas density

4 Conclusion

Through these simulations of gravitationally collapsing pebble clumps, we were able to demonstrate the importance of the heating of the gas surrounding the clump. We expose the main dependencies of this heating with the clump mass and the gas density. We show that the clump should be sufficiently massive in order that the temperature of the gas is enough to dissolve itself in the forming planetesimal. This is consistent with small bodies of the solar system for which the smallest bodies do not have traces of heating processes during their history.

However, the simulations present several limits which could nuance our results. First, as we were doing 1D simulations, we completely neglected collisions and thus neglected the process of redistribution of kinetic energy and momentum between pebbles, which could then impact the temperature profile of the gas. Second, we made the hypothesis that only the gas is heated and not the pebbles, but if the gas is at around 1000 K but the pebbles are at the initial temperature of 300 K, thermal exchanges between them will cool the gas.

This work opens new paths for the exploration of the gravitational collapse of a pebble clump in a gaseous environment: first by extending the simulations to 2D or 3D, allowing to take into account initial velocity dispersion and collisions, and second by modelling better the thermal exchanges between pebbles and gas.

References

Armitage, P. J. 2020, Astrophysics of Planet Formation (Cambridge: Cambridge University Press), oCLC: 1155321290

Carrera, D. & Simon, J. 2022, Bulletin of the AAS, 54

Chavanis, P. H. 2000, A&A, 356, 1089

Drazkowska, J., Bitsch, B., Lambrechts, M., et al. 2023, Planet Formation Theory in the Era of ALMA and Kepler: from Pebbles to Exoplanets, arXiv:2203.09759 [astro-ph]

Epstein, P. S. 1924, Phys. Rev., 23, 710

Gerosa, F. A., Méheut, H., & Bec, J. 2023, European Physical Journal Plus, 138, 9, aDS Bibcode: 2023EPJP..138....9G

Lesur, G. R. J., Baghdadi, S., Wafflard-Fernandez, G., et al. 2023, IDEFIX: a versatile performance-portable Godunov code for astrophysical flows, arXiv:2304.13746 [astro-ph]

Session S12

Origine de l'eau et de la vie: Quels défis astrophysiques et instrumentaux pour demain ?

SF2A 2023
M. N'Diaye, A. Siebert, N. Lagarde, O. Venot, K. Baillié, M. Béthermin, E. Lagadec, J. Malzac, J. Richard (eds)

ORIGIN OF WATER AND LIFE: WHAT ASTROPHYSICAL AND INSTRUMENTAL CHALLENGES FOR TOMORROW?

G. Chauvin[1], S. Raymond[2], D. Mouillet[3], J.-P. Berger[3], I. Boisse[4], E. Choquet[4], H. Cottin[5], X. Delfosse[3], M. Ferrari[4], E. Huby[6], S. Lacour[6], M. Langlois[7], L. Leboulleux[3], F. Martinache[1], M. N'Diaye[1], A. Santerne[4], A. Vigan[4] and V. Vinogradoff[8]

Abstract. Our goal is to present here a brief summary of the background, objectives, presented talks, discussions and conclusions of the splinter session organized on June 20^{th} and 21^{st}, 2023 during the Journées 2023 de la Société Française d'Astronomie & d'Astrophysique (SF2A). This session has been a nice opportunity to be informed about current theoretical, observing and instrumental developments, initiate the discussion on how to organize and structure the French community around these astrophysical themes, finally to initiate a coordinated response to the call of ideas of CNES 2023 to organize and structure our community with a proposed roadmap for 2024.

Keywords: exoplanets, habitability, exobiology, ground based instrumentation, space missions

1 Context

Understanding how giant and telluric planets form and evolve, their internal structure and that of their atmosphere, represents one of the major challenges of modern astronomy, and is directly linked to the ultimate search for life by 2050. However, several astrophysical (understanding the formation and physics of giant and telluric exoplanets), biological (identification of the best biomarkers) and technological (technical innovations for new-generation telescopes and instruments). We now know that rocky exoplanets are ubiquitous in the Milky Way, and very probably in the immediate vicinity of the Sun too. Detecting these closest planets, understanding the diversity the (atmospheric) diversity of other worlds, and the search for clues to habitability and biological activity, particularly that of water, are essential to understanding the origin of life. With this in mind, the coming decades will be rich in instrumental projects in space and on the ground, exploiting the various techniques for detecting and characterizing exoplanets in highly complementary ways. Within the next 10 years, major systematic surveys using velocimetry, transit, astrometry and imaging will provide a virtually complete census of exoplanetary systems in the near-solar environment. This will usher in an observational era dedicated primarily to characterizing the conditions conducive to the formation of habitable worlds, and to the physical and atmospheric characterization of known exoplanets, particularly temperate telluric planets suitable for the emergence of life. This phase, already initiated with Hubble and Spitzer, and with the first ground-based spectrographs, will intensify with the JWST, Roman and ARIEL space telescopes, and from 2028 with the new generation of extremely large telescopes that will offer unique spatial and spectral resolution, , as well as versatile multi-decade instrumentation for characterization of giant and rocky planets and the search for the first clues of habitability and life activity. However, it is very likely that a systematic atmospheric study of dozens of Earth analogues and a quantitative assessment of their habitability and the possible existence of biomarkers will require large-scale, highly optimized space missions.

[1] Laboratoire J.-L. Lagrange, Université Cote d'Azur, CNRS, Observatoire de la Cote d'Azur, 06304 Nice, France
[2] Laboratoire d'Astrophysique de Bordeaux, CNRS and Université de Bordeaux, Allée Geoffroy St. Hilaire, 33165 Pessac, France
[3] Univ. Grenoble Alpes, CNRS, IPAG, F-38000 Grenoble, France
[4] Aix Marseille Univ, CNRS, CNES, LAM, Marseille, France
[5] LISA, Universités Paris-Est Créteil, Paris Cité, UMR 7583 CNRS, IPSL, France
[6] LESIA, Observatoire de Paris, PSL Research University, CNRS, Sorbonne Universités, UPMC Univ. Paris 06, Univ. Paris Diderot, Sorbonne Paris Cité, 5 place Jules Janssen, 92195 Meudon, France
[7] CRAL, UMR 5574, CNRS, Université de Lyon, ENS, 9 avenue Charles André, 69561 Saint Genis Laval Cedex, France
[8] Aix-Marseille Université, CNRS, PIIM, UMR 7345, Marseille, France

© Société Française d'Astronomie et d'Astrophysique (SF2A) 2023

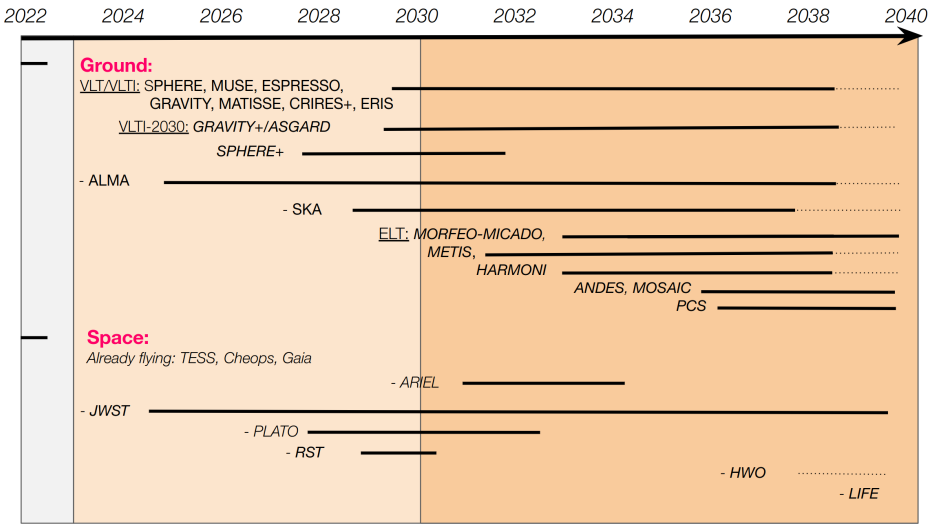

Fig. 1. Timeline for key ground and space-based instruments and missions dedicated to studying exoplanets and planetary formation.

2 Objectives

Our workshop was divided into two sub-sessions with the aim of addressing the following three themes:

- theme 1 - delivering water to planets: from the interstellar medium to planetary formation and exoplanets (S12a). Life as we know it requires water, but there is considerable uncertainty as to the steps required for a planet in the habitable zone to be formed with an abundant water budget. To address the question of the origin of water on Earth and other rocky planets, we need to gather expertise from many fields of study: modeling of planet formation, meteorite measurements, observations of exoplanets and planet-forming disks, and studies of the chemistry of ice in the interstellar medium and during star formation. Recent theoretical and observational advances are conducive to the organization of a workshop on the cosmic pathways that carry water to planets. This first part will cover all the phases in the origin of water, from astrochemistry to the study of meteorites and exoplanets.

- theme 2 - the current state of scientific knowledge on the conditions of habitability, biological activity and indications of life for astrophysical observation (S12b). The second part of the workshop will deal more generally with the most recent results and prospects concerning the study of the population of telluric planets, the properties and influence of host stars in promoting the existence of habitability conditions conducive to the formation of life, the physical and atmospheric properties of telluric planets, and current knowledge on biological activity and the best life tracers for future dedicated observations,

- theme 3 - technological challenges (S12b). Finally, we will look at future projects on the ground (VLT/I and ELTs) and in space (Roman, PLATO, ARIEL, HWO, LIFE) dedicated to the research and characterization of telluric planets, and particularly the observation of the first signs of life in their atmosphere. This second session will enable us to revisit together an ambitious roadmap for the preparation of future space and ground missions, identifying the most important technological obstacles and the best strategy for the French community to play a key role in the detection and characterization of the first signs of life in the atmospheres of temperate extrasolar telluric planets.

3 Addressed topics

During the first day, the question of the origin of stars in the Galaxy and the impact on the composition of planets was presented (N. Cabral), together with the observations of water in solar-type protostars (A. Andreu). This was followed by focused talks and discussions on the potential sources of terrestrial water in the context of the Solar system formation (L. Piani), the loss of volatiles by geological and astrophysical effects (N. Cowan),

the modeling of the primitive Earth's atmosphere (B. Charnay), the case of the water-dominated atmospheres, their structure, signatures, and the implication for habitability (F. Selsis), and finally the importance of a proper consideration of condensation front in current simulation of planetary habitability (M. Turbet). From the observational perspective, the water content of detected exoplanets (L. Acuña) was presented, together with the SOPHIE results for the specific system HD88986 (N. Heidari) and the latest results of JWST about the thermal emission from the Earth-sized Exoplanet TRAPPIST-1 b (E. Ducrot). Finally, J. Moran highlighted the need for some additional dynamical ingredients to go from prebiotic chemistry to life.

On the second day, the status of current atmospheric retrievals of terrestrial planets was discussed (E. Alei). This was followed by a summary of the current status of ground-based instruments: the VLT/RISTRETTO and ELT/ANDES spectrographs, aimed at characterizing the first atmospheres of very nearby rocky worlds at high spectral resolution and in reflected light (C. Lovis), and the VLT/SPHERE+ and ELT/PCS projects, designed to optimally combined spatial, spectral and temporal diversity to detect and characterize more systematically these rocky worlds in the case of PCS (M. Kasper). The prospect to identify the best rocky worlds for future characterization with extreme precision radial velocity surveys ws also reported (N. Hara). In the perspective of space missions, the status of direct imaging below the diffraction limit with JWST via phase kernel interferometry was shown (T. Vandal), together with the status of the coronographic mode of the Roman Space Telescope (J. Mazoyer), the LUVOIR-POLLUX instrument (A. Ines Gomez), and the ambitious developments of the HWO and LIFE missions (L. Pueyo and S. Quanz, respectively).

4 Discussion

Finally, the splinter session was concluded by a focused discussion about the preparation and the contribution of the French community to future long-term instruments and missions for exoplanet and exobiology (D. Mouillet). The scientific stakes and the size of the community mean that we need to start coordinating and structuring now, to ensure that we are strategically positioned ahead of the actual mission choices made by NASA or ESA for HWO and LIFE. The French community's involvement in this long-term strategic orientation is a major one, covering both i/ involvement in long-term scientific preparation, and ii/ the technological innovations and instrumental expertise required for future instruments, whose actions need to be pursued, stimulated and coordinated as of now. The PEPR-Origins program, due to start in 2023, fully illustrates the major commitment of our supervisory bodies and our community to studying these fundamental issues.

In the scientific field of exoplanetology, the French community, comprising several hundred researchers, has played a major role in exploiting the five main observational techniques used (radial velocity, transit, μ-gravitational lensing, direct imaging and astrometry). Our community is at the forefront of the search for low-mass planets, sub-Neptunes and super-Earths, using radial velocity methods, a position further strengthened by the new SPIRou, NIRPS and ANDES instruments, but also in space with PLATO in transit. It has also played a pioneering role in the first discoveries in direct imaging and interferometry with ground-based instruments such as SPHERE and GRAVITY, and is ideally positioned at European level for future instruments on major observatories. It has also developed world-renowned theoretical expertise in the study of planetary formation, the structure of giant and rocky planets, and the modeling of their atmospheres, enabling it to play a key role in the operation of current and future JWST programs, and in preparations for the ARIEL mission.

On the instrumental side, the involvement and position of the French community is also major, with around a hundred researchers active in these fields, in a closely-knit community led in particular by ASHRA, and spread across a dozen or so laboratories. In the field of interferometry, France's leading role in the first VLTI instruments continues with the current developments Gravity+ and the ASGARD instrument suite, both of which include a strong focus on exoplanets, with optimization of the exoGravity or nulling mode. Similarly, high-contrast imaging has emerged in Europe from French laboratories, with a complete overhaul of system analysis, calibration and signal processing. The result is the best international high-contrast instrument currently available to the community (VLT/SPHERE). This expertise continues with the development of high-contrast modules for the future ELT (in the MICADO and HARMONI instruments), as well as very active R&D on components, demonstrations and innovative concepts. In space, the needs, constraints and final objectives are different, but the expertise involved benefits from a strong synergy with the ground. CNES has indeed supported innovative developments in components (such as coronagraphs, but a high level of expertise in photonics also has enormous potential for space applications), key technological masteries (such as advanced polishing of aspheric and/or active optics), and signal processing. We must also emphasize the importance of supporting laboratory testing capabilities (such as the THD test bench at LESIA), with the high level of stability and

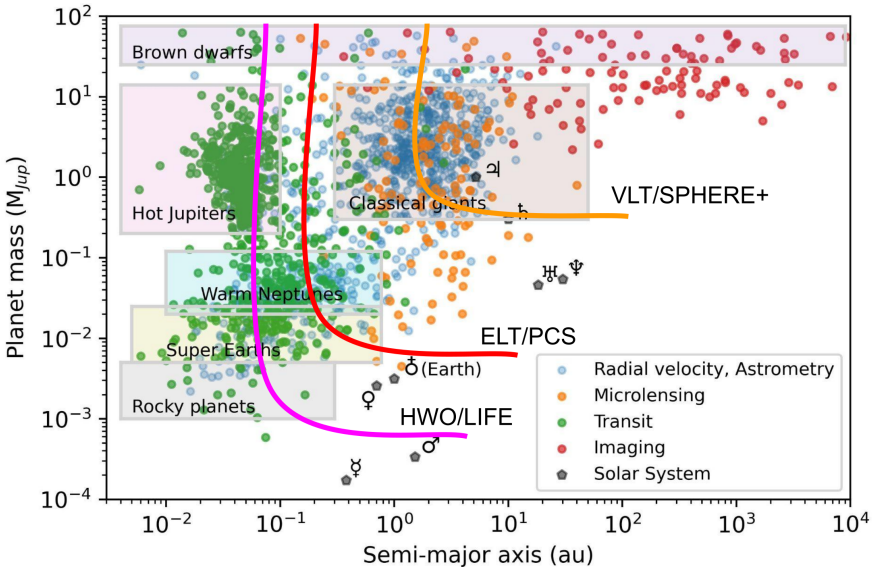

Fig. 2. Indicative detection limits for future instruments (*VLT/SPHERE+, ELT/PCS*) and space missions (*HWO, LIFE*) dedicated to the search for and the characterization exoplanets.

calibration control required for space applications, as an essential step in the final testing of concepts and in the ramp-up to maturity. This combination has opened up opportunities for effective, high-impact contributions to the high-contrast modes of JWST (MIRI) and the Roman Space Telescope.

The take away messages of the discussion were that the discovery of rocky worlds and the characterization of their atmospheres is a major goal for the French community. We need to find collectively a programmatic way to reach that goal under discussion (missions, collaborations, instruments) including intermediate steps and synergies. The technology maturation can be worked-on now to be ready for decisions in 2030, to be organized coherently based on a wealth of expertise in France and in Europe. The timing is good with the CNRS/INSU and CNES prospectives starting in 2023.

5 Conclusions and perspectives

The "Origin of water and life" splinter session has been a nice opportunity and a first stone: i/ to be informed about current theoretical, observing and instrumental developments, including the two long-term HWO and LIFE projects, ii/ to initiate the discussion on how to organize and structure the French community around these astrophysical themes, finally iii/ to discuss on how to respond with a coordinated position to current requests, and future calls for proposals in a coordinated fashion (CNES, ESA, INSU...). The key action resulting from the splinter has been to submit a coordinated proposal to the call of ideas of CNES 2023 to organize structure our community with a proposed roadmap: 1/ The first phase (2023-2024) should enable us to establish a collective determination to position and organize ourselves in the indicated approach, in France, in a visible and coordinated way with our partners in Europe and the United States, with identified points of contact. We will also need to define a detailed action plan, identifying the specific developments to be carried out in France, in line with the expertise on hand, and the complementarity with other partners. A 2-3 days workshop (CNES-APR and INSU-AA proposals submitted in 2023) should conclude this first phase to propose a coordinated roadmap for our community. 2/ The following 4 years (2025-2028) will be the effective time for focused theoretical, modelling, and technological development. These conclusions will be essential for positioning the 2029 project for potential effective contributions, in line with NASA's milestone for the next decadal 2030. The potential application of this know-how to other areas of space instrumentation will also need to be analyzed, and could be anticipated in earlier years, possibly in conjunction with industrial partners.

The SF2A-S12 scientific organizing committee would like to warmly thank all the speakers and the SF2A organizing committee for assisting and supporting the organization of this splinter session which was a real trigger for opening a first series of discussions on this unifying theme for our community.

SF2A 2023
M. N'Diaye, A. Siebert, N. Lagarde, O. Venot, K. Baillié, M. Béthermin, E. Lagadec, J. Malzac, J. Richard (eds)

WATER CONTENT TRENDS IN LOW-MASS MULTIPLANETARY SYSTEMS

L. Acuña[1,2], M. Deleuil[2,3], O. Mousis[2,3], T. A. Lopez[2], T. Morel[4], A. Aguichine[2,5], E. Marcq[6] and A. Santerne[2]

Abstract. Both rocky super-Earths and volatile-rich sub-Neptunes have been found simultaneously in multi-planetary systems, suggesting that these systems are appropriate to study different composition and formation pathways within the same environment. To estimate their composition, we present an interior structure model that includes self-consistently an atmosphere in radiative-convective equilibrium. We use our interior-atmosphere model within a Bayesian adaptive Markov Chain Monte Carlo (MCMC) for the detailed analysis of individual planets, allowing to estimate the uncertainties of the compositional parameters, core mass fraction and water mass fraction, given the error bars of the observed mass and radius. In this talk, I will present the development of this compositional model for super-Earths and sub-Neptunes, as well as its application to different planetary systems. I will focus in particular on the homogeneous analysis of a sample of multi-planetary systems hosting 5 or more exoplanets. Their composition gives us clues about their possible formation site in the protoplanetary disk and their formation mechanisms, including atmospheric escape. I will also discuss the uncertainties and degeneracies interior models face when estimating the volatile content of low-mass planets, and how JWST and future telescopes can help narrow down their possible compositions.

Keywords: Planetary interiors, Planetary composition, Numerical methods

1 Introduction

Low-mass exoplanets ($M < 20\ M_\oplus$) present two sub-populations based on their radius: super-Earths and rocky Earth-sized planets ($R \sim 1.3\ R_\oplus$) and sub-Neptunes ($R \sim 2.4\ R_\oplus$). The composition of the former sub-population is dominated by Fe and silicates that are found in the core and mantle, respectively, whereas sub-Neptunes are mostly composed by volatiles (Fulton et al. 2017; Fulton & Petigura 2018). It is still an open question whether super-Earths present a thin, low-mass atmosphere, or a bare rocky surface. If a thin atmosphere exists, the atmospheric composition would not present H_2, but high molecular weight species such as H_2O, CO_2, O_2 or N_2. In contrast, sub-Neptunes can be constituted by: 1) a rocky core underneath a supercritical or ice water layer (depending on the irradiation of the planet), 2) a H-dominated envelope, or 3) an intermediate atmospheric composition with both H_2O and H_2 in significant concentrations.

The first assessment of the composition of a planet is carried out by comparing its mass and radius to interior models. These models generate mass-radius relations that estimate the radius of a planet given its mass for a fixed composition. The mass and radius of a planet can be matched with mass-radius relations at different compositions, showing that there are degeneracies between the Fe and volatile content for super-Earths, and between the atmospheric mass and metallicity for sub-Neptunes. Therefore, atmospheric characterization observations are necessary to break these degeneracies in planetary interiors. Nonetheless, there are several instances where the characterization of the atmosphere may be difficult. This is the case of planets that present

[1] Max-Planck Institut für Astronomie, Königstuhl 17, 69117 Heidelberg, Germany. e-mail: acuna@mpia.de
[2] Aix-Marseille Université, CNRS, CNES, Institut Origines, LAM, Marseille, France.
[3] Institut universitaire de France (IUF), France
[4] Space sciences, Technologies and Astrophysics Research (STAR) Institute, Université de Liège, Quartier Agora, Allée du 6 Août 19c, Bât. B5C, 4000 Liège, Belgium
[5] Department of Astronomy and Astrophysics, University of Califor- nia, 1156 High St, Santa Cruz, CA 95064, USA
[6] LATMOS/CNRS/Sorbonne Université/UVSQ, 11 boulevard d'Alembert, Guyancourt, 78280, France

© Société Française d'Astronomie et d'Astrophysique (SF2A) 2023

clouds and hazes, and whose transmission spectrum is flat (i.e GJ1214 b, Gao et al. 2023), and planets whose stellar host is active and presents stellar contamination (TRAPPIST-1, see Ducrot et al. 2018; Zhang et al. 2018). In addition, the transmission spectrum may present a degeneracy to explain a particular spectral feature between two different opacity sources, making it difficult to set constraints on their abundances (see the case of water and methane in K2-18 b, Tsiaras et al. 2019; Bézard et al. 2022). Therefore, in these cases, interior models may be combined with atmospheric models to support the characterization of the bulk composition. In this talk, I will present an interior-atmospheric model applicable to terrestrial and water-rich compositions for low-mass planets (see Sect. 2). We apply this model to a sample of high multiplicity systems ($n_{planets} \geq 5$) and connect their composition to different planet formation processes (see Sect. 3). We conclude with our final remarks on the water content of super-Earths and sub-Neptunes (see Sect. 4).

2 Model

2.1 Interior

Our one-dimensional (1D) interior structure model is differentiated in three layers: a hydrosphere, a silicate-rich mantle, and a Fe-rich core. Along the 1D grid that represents the radius, we solve a set of differential equations to obtain the planetary profiles: pressure, temperature, gravity, density and enclosed mass. These are computed by assuming hydrostatic equilibrium, an adiabatic profile, the gravitational force produced by the enclosed mass, the equation of state (EOS), and conservation of mass, respectively. The total mass of the planet, as well as the mass fraction of the core (CMF), and the water mass fraction (WMF) are the input parameters. The boundary conditions include the pressure and temperature at the top interface of the outermost layer, P_{base} and T_{base}. The model iterates the planetary profiles until these and the masses of all layers converge to constant values, obtaining as output the total planetary radius (Brugger et al. 2016, 2017).

For highly irradiated planets, the surface conditions cannot maintain water in its liquid or ice phases. Instead, the expected phases of water at high temperatures are vapour and supercritical. Therefore, we use an EOS that is valid within the supercritical and plasma pressure and temperature range. Furthermore, we couple an atmospheric model with the interior to determine self-consistently its boundary temperature since the density of the supercritical water layer is sensitive to the temperature. For water-rich planets, the supercritical envelope is massive enough to sustain high pressures at the interface between the hydrosphere and the mantle. For these volatile-rich planets, the interior and the atmosphere are coupled at a fixed pressure level of 300 bars because this is close enough to 1) the critical point of water, to prevent unphysical behaviour of the EOS, and 2) the maximum limit for which the opacity data used in atmospheric models is available. For planets whose atmospheric surface pressure is less than 300 bar, we couple the interior and the atmosphere at the physical planetary surface, which is the interface between the silicate mantle and the atmosphere. Further details on the coupling scheme between the interior and the atmospheric models can be found in Acuña et al. (2021).

2.2 Atmosphere

To obtain self-consistently the temperature at the base of the atmosphere, we use RADCONV1D, a 1D k-correlated atmospheric model that calculates low-resolution emission and reflection spectra of water-dominated atmospheres (Marcq et al. 2017; Pluriel et al. 2019). The thermal structure of the atmosphere is prescribed as a near-surface convective layer that is unsaturated, which means that the temperature gradient follows a dry adiabat. For the atmospheric layers where the pressure is below the saturation pressure of water, vapor condenses to form water clouds. Consequently, in the convective layer immediately above the near-surface unsaturated one, the temperature is computed with a wet adiabat. The topmost layer in the atmosphere is a radiative isothermal mesosphere.

The atmospheric model takes as input the surface pressure and temperature, and the enclosed mass and radius between the center and the surface of the planet. For our calculations, we consider a water-dominated envelope with 99% vapor and 1% CO_2. Once the atmospheric structure is calculated, we solve the radiative transfer equation with DISORT (Stamnes et al. 2017) to obtain the outward emission at the top of the atmosphere and the reflection spectrum. Then these are integrated over wavelength to compute the outgoing longwave radiation (OLR) and the Bond albedo, A_B (Pluriel et al. 2019). With these two parameters, we solve with a root-finding method for the surface temperature at which the OLR and the absorbed flux are equal. The absorbed flux is calculated as $F_{abs} = \sigma\ T_{eq}^4$, where σ is the Stefan-Boltzmann constant. The equilibrium

temperature is defined as $T_{eq} = (1 - A_B)^{0.25}(R_\star/2a_d)^{0.5}\ T_\star$, where $R_\star$ and $T_\star$ are the stellar radius and effective temperature, and a_d is the planetary semi-major axis.

3 Multiplanetary systems

We combine our forward interior structure model with a Markov chain Monte-Carlo (MCMC) and apply it to a sample of multiplanetary systems. Multiplanetary systems are environments suitable to explore the compositional diversity of low-mass planets, as well as their formation and evolution. The aim of this work is to perform a homogeneous analysis, in other words, use the same interior-atmosphere model under similar assumptions, to obtain the WMF and CMF of planets in different systems, and compare their compositions. The MCMC retrieval on mass and radius data allows us to obtain the posterior distribution functions of the CMF and WMF, which determines the mean and uncertainties of these two compositional parameters.

We select multiplanetary systems that host low-mass planets only ($M < 20\ M_\oplus$), with 5 or more planets. Our final sample consists of 6 multiplanetary systems, including TRAPPIST-1 (Agol et al. 2021; Acuña et al. 2021), K2-138 (Lopez et al. 2019), TOI-178 (Leleu et al. 2021), Kepler-11, Kepler-102 and Kepler-80.

From our interior analysis, we find that TRAPPIST-1 b and c most likely have no atmosphere. For planet b, this is in agreement with JWST's emission photometry data (Greene et al. 2023; Ih et al. 2023). For planet c, the emission flux at 15 μm discards a thick CO_2 atmosphere, although it is still compatible with a thin atmosphere of other compositions, such as N_2, O_2 and water vapor (Zieba et al. 2023). With our interior structure retrieval, we constrain the maximum 1σ surface pressure for TRAPPIST-1 c as $P_{surf,max} = 80$ bar (Acuña et al. 2023). For TRAPPIST-1 d, a liquid water envelope is unlikely based on the surface temperature estimated by 1D radiative-convective and climate models. Nonetheless, water could still be present in the form of vapor mixed in a CO_2-dominated envelope. We calculate mass-radius relations for this scenario in planet d, and find that the density of TRAPPIST-1 d would be compatible with a maximum surface pressure of 300 bars. This is also in agreement with the maximum surface pressure that can be outgassed by a magma ocean in small planets (Baumeister et al. 2023). Furthermore, TRAPPIST-1 e to h present a trend where the WMF grows as the distance from the star increases. The system K2-138 also presents this trend in the WMF. The rest of the planetary systems show a diversity on their WMF vs incident irradiation trend (see Fig. 1). Nonetheless, all multiplanetary systems have in common that: 1) the inner planets are dry, and 2) the volatile-rich planets (water or H/He envelopes) are found in the outer part of the system. This can be explained by formation of the volatile-rich, outer planets in the vicinity of the water ice line, where volatile are more abundant for accretion than in the inner part of the protoplanetary disk. Many of these systems present mean motion resonances, which is indicative of later inward migration to their current location.

Moreover, some of the planets in our sample are not compatible with water envelopes in hydrostatic equilibrium because their observed radius is larger than the radius of a pure water planet by more than 1σ. For these planets, we estimate Jeans and XUV atmospheric escape in the energy-limited approximation (Aguichine et al. 2021) to discern whether their envelopes are H/He-dominated and in equilibrium, or are undergoing atmospheric escape. K2-138 g, TOI-178 g, and Kepler-11 c to e are candidates to having H/He-rich envelopes without atmospheric escape, whereas TOI-178 d, Kepler-11 f, Kepler-102 f and Kepler-80 g have lost more than 0.1 $M_\oplus$ due to Jeans escape. This escape mechanism is caused by the low surface gravity due to a small planetary core.

Regarding the Fe content of the planets in multiplanetary systems, planets whose CMF is larger than that of Mercury, are found in the innermost part of their respective systems. Collisions, mantle stripping and mantle evaporation have been proposed to explain their high Fe content. In addition, formation in the vicinity of refractory lines, particularly Fe and Si, explains how these planets could have accreted material that is rich in Fe (Aguichine et al. 2020).

4 Conclusions

We perform an interior structure, homogeneous analysis of the composition of planets hosted in multiplanetary systems. Our retrieval on mass and radius data provides the posterior distributions functions of the water and Fe content, allowing us to compare the composition of planets within a system. From our analysis, we find that: 1) multiplanetary systems show a clear separation between the inner, dry planets, and the outer, volatile-rich planets, 2) our CMF and WMF can be used to constrain formation site with respect to ice and refractory lines, as well as evolution mechanisms, such as Jeans escape. The typical water content of the inner,

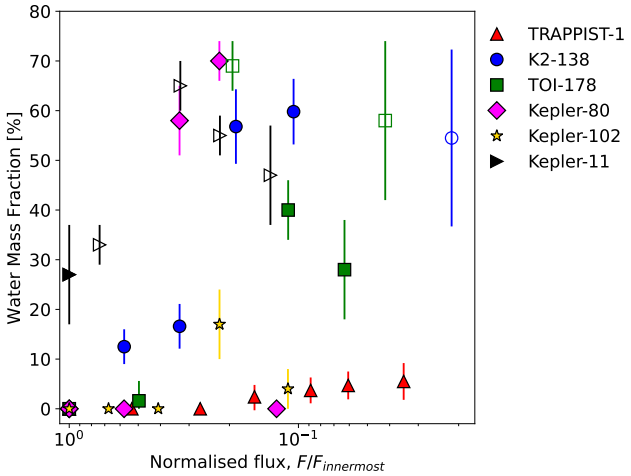

Fig. 1. Water mass fraction trends in multiplanetary systems as a function of the stellar incident flux. The fluxes are normalised to the flux of the innermost planet in their respective system.

dry planets is WMF $< 5\%$. Moderately volatile-rich sub-Neptunes have WMF $= 10$ to 25%. Sub-Neptunes whose water content is estimated as WMF $> 30\%$ with our interior model are good candidates for planets with H/He envelopes. Atmospheric characterization data is necessary to break the degeneracy between water and H/He for these sub-Neptunes.

M.D. and O.M. acknowledge support from CNES. This research has made use of the services of the ESO Science Archive Facility, the AAVSO Photometric All-Sky Survey (APASS), the Two Micron All Sky Survey, the Wide-field Infrared Survey Explorer, the K2 mission, the Exoplanet Follow-up Observation Program website, NASA's Astrophysics Data System Bibliographic Services. ESA's mission Gaia, the VizieR catalogue access tool.

References

Acuña, L., Deleuil, M., & Mousis, O. 2023, A&A, 677, A14
Acuña, L., Deleuil, M., Mousis, O., et al. 2021, A&A, 647, A53
Agol, E., Dorn, C., Grimm, S. L., et al. 2021, PSJ, 2, 1
Aguichine, A., Mousis, O., Deleuil, M., & Marcq, E. 2021, ApJ, 914, 84
Aguichine, A., Mousis, O., Devouard, B., & Ronnet, T. 2020, ApJ, 901, 97
Baumeister, P., Tosi, N., Brachmann, C., Grenfell, J. L., & Noack, L. 2023, A&A, 675, A122
Bézard, B., Charnay, B., & Blain, D. 2022, Nature Astronomy, 6, 537
Brugger, B., Mousis, O., Deleuil, M., & Deschamps, F. 2017, ApJ, 850, 93
Brugger, B., Mousis, O., Deleuil, M., & Lunine, J. I. 2016, ApJ, 831, L16
Ducrot, E., Sestovic, M., Morris, B. M., et al. 2018, AJ, 156, 218
Fulton, B. J. & Petigura, E. A. 2018, AJ, 156, 264
Fulton, B. J., Petigura, E. A., Howard, A. W., et al. 2017, AJ, 154, 109
Gao, P., Piette, A. A. A., Steinrueck, M. E., et al. 2023, ApJ, 951, 96
Greene, T. P., Bell, T. J., Ducrot, E., et al. 2023, Nature, 618, 39
Ih, J., Kempton, E. M. R., Whittaker, E. A., & Lessard, M. 2023, ApJ, 952, L4
Leleu, A., Alibert, Y., Hara, N. C., et al. 2021, A&A, 649, A26
Lopez, T. A., Barros, S. C. C., Santerne, A., et al. 2019, A&A, 631, A90
Marcq, E., Salvador, A., Massol, H., & Davaille, A. 2017, Journal of Geophysical Research (Planets), 122, 1539
Pluriel, W., Marcq, E., & Turbet, M. 2019, Icarus, 317, 583
Stamnes, K., Tsay, S. C., Jayaweera, K., et al. 2017, DISORT: DIScrete Ordinate Radiative Transfer, Astrophysics Source Code Library, record ascl:1708.006
Tsiaras, A., Waldmann, I. P., Tinetti, G., Tennyson, J., & Yurchenko, S. N. 2019, Nature Astronomy, 3, 1156
Zhang, Z., Zhou, Y., Rackham, B. V., & Apai, D. 2018, AJ, 156, 178
Zieba, S., Kreidberg, L., Ducrot, E., et al. 2023, Nature, 620, 746

SF2A 2023
M. N'Diaye, A. Siebert, N. Lagarde, O. Venot, K. Baillié, M. Béthermin, E. Lagadec, J. Malzac, J. Richard (eds)

PREPARATION TO FUTURE LONG-TERM SPACE MISSIONS FOR EXOPLANETS HIGH CONTRAST DIRECT CHARACTERIZATION

D. Mouillet[1], I. Laginja[2] and M. Ferrari[3]

Abstract. A wide international community has clearly expressed the need to plan as a priority very deep and accurate space-based observations in order to characterize a sizeable sample of telluric temperate exoplanet atmospheres. Such a characterisation will necessitate complementary information in reflected light, from near UV to near IR (as proposed for the Habitable Worlds Observatory, the first priority flagship mission as identified in the US decadal survey) and in thermal emission (as identified as a priority in the ESA Voyage2050 prospective, and proposed in a mission such as LIFE). The considered timeline targets a mission in the 2040+ decade, after the current and upcoming continuous effort on further exploring the vast diversity and statistics of planetary systems, and the characterization of the easier (and mostly at shorter separations) exoplanets. This timeline is practically also needed in order to mature the technologies and the key instrumental concepts which are absolutely needed for such an ambitious observational goal. We intend to precise here such a need, together with the actual expertise and the role that should be taken within the French community on this topic. We conclude on the importance of a strong push and coordination on the specific R&D actions to be handled in a timely manner within the next 5 years.

Keywords: exoplanets, space missions, research and development, high-contrast

1 Space-based high contrast characterization capability: an identified community priority

Exoplanet research has been impressively active over the past decades, combining both observational and theoretical studies, using ground-based and space-based facilities. Our understanding of the subject and the focus of the main questions evolve correspondingly. After the detection of the first exoplanet around a solar-type star in 1995, large multi-technique surveys have revealed a wide diversity of planet types, and have informed us on the statistics and the structures of planetary systems. The planet formation scenarios are now discussed in the combined perspective of theoretical models and observational evidences such as the directly imaged young systems, including the interaction between disks and forming planets, or as the statistics, the physical and chemical properties of the resulting planets. The atmosphere characterization of exoplanets has also progressed a lot, starting with the most favorable cases, as for transiting planets at very shot separations or massive young (still warm) very distant giant planets.

All these studies need to be pursued and they will be with both major ground-based instruments such as ELT or space missions such as JWST, Roman Space Telescope, PLATO and ARIEL. This will be of highest importance to provide a more complete (and less biased) view of the planetary systems and of their dynamics, to identify the population of the probably best targets around nearby stars, and to enter the field of comparative exoplanetology, to probe and to understand the diversity of exoplanet atmospheres. This will definitely require a > decade-long work. However, it is already possible now to identify the following step in the 2040+ timescale. This is not only possible ; this is actually done within an international perspective, and we argue this is indeed mandatory for a practical technological preparation towards such a goal.

Both the American and European communities have explicitly identified the fine characterization of earth-like exoplanets as a programmatic priority. It will provide objective and significant information on the likelihood

[1] Univ. Grenoble Alpes, CNRS, IPAG, 38000 Grenoble, France
[2] LESIA, Observatoire de Paris, Université PSL, Sorbonne Université, Université Paris Cité, CNRS, 92195 Meudon, France
[3] Laboratoire d'Astrophysique de Marseille, Aix-Marseille Univ / CNRS / CNES, Marseille, France

© Société Française d'Astronomie et d'Astrophysique (SF2A) 2023

that ubiquitous conditions would be met for emerging life elsewhere. Quoting the US Astronomical decadal survey*: *"We are on a path to exploring worlds resembling Earth and answering the question: "Are we alone?" The task for the next decades will be finding the easiest of such planets to characterize, and then studying them in detail, searching for signatures of life."* The US community has defined as a priority flagship mission: *"A large space-based IR/O/UV telescope with high contrast imaging and spectroscopy capable of observing planets 10 billion times fainter than their host star"*, aka Habitable Worlds Observatory (HWO). The scientific goal is also clearly identified in the European community, as expressed in the Astronet perspective†, and more specifically for the space community, as a conclusion of the Voyage2050 prospective‡, for which: *"launching a Large mission enabling the characterisation of the atmosphere of temperate exoplanets in the mid-infrared should be a top priority for ESA within the Voyage 2050 timeframe."* A corresponding mission, LIFE, has been proposed and studied, both on the instrument basic concept aspects, the reasonable expected level of performance, and the corresponding science case (see Quanz et al. (2022b) and the following paper serie)

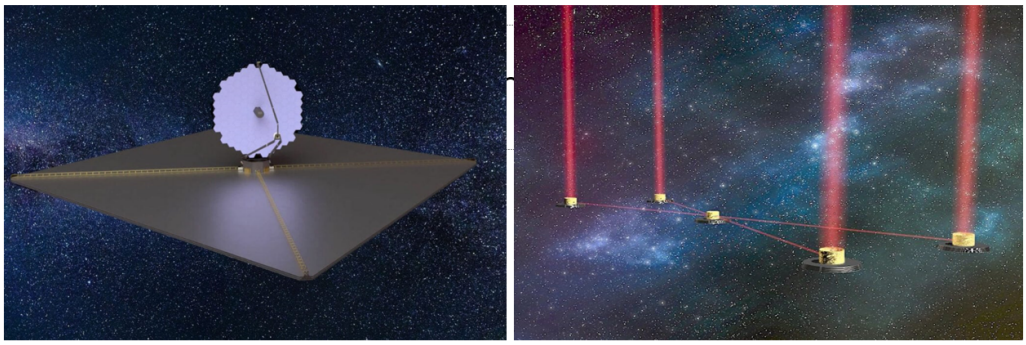

Fig. 1. Artist view of the future high contrast space missions. Left: Habitable World Observatory for UV/Vis/NIR high contrast imaging of exoplanets reflected light (NASA). Right: LIFE mission for IR interferometric high contrast detection of exoplanets thermal emission (proposed to ESA)

Such a goal for exo-earths characterization is very stimulating and ambitious. It also appears achievable, assuming the international community provides the appropriate effort in a timely and coordinated manner. This evaluation is made much stronger than it could have been a few decades ago, thanks to the impressive progress on both the scientific knowledge on exoplanetary systems. and on the instrumentation side. On the astronomical side, the game-changing information is the frequency of exoplanets. Now, we know that low-mass planets are very frequent, in a variety of stellar systems (single or binary, various stellar masses, planet multiplicity,...). It is possible to focus some very deep searches on the nearest stellar systems, with the most favorable angular separations and enough photons to be collected on large telescopes to envision high SNR spectral characterization. Concerning the instrumental aspects, we further detail hereafter the considered key domains which are involved.

2 Need for technological preparation coordinated in the international context

The actual definition of the 2040+ instrument architectures, and the formal development plans are not expected by now, but rather around 2030. The important point by then is to mature the relevant technologies and to provide some demonstrating proto-types for the key elements than may deeply impact the future design. It is also mandatory to properly evaluate the corresponding risk, the cost and the management organisation of the future missions. These are critical inputs at the stage of the mission decision. The envisioned future high contrast instruments are quite far some a direct extension or upgrade of already operating systems in space: it is clear that R&D must start very early-on. It must feed and inform rather than follow the formal programmatic decision.
Following such an analysis, NASA has explicitly defined a needed a "Great Observatory Maturation Program" (GOMAP) in order to identify and to carry on the critical R&D. This maturation shall bring all the critical

*https://www.nationalacademies.org/our-work/decadal-survey-on-astronomy-and-astrophysics-2020-astro2020
†https://www.astronet-eu.org
‡https://www.cosmos.esa.int/web/voyage-2050

aspects of the future concept to a safe readiness level (TRL 6) by 2029. A similar approach is perfectly relevant for a high-contrast IR interferometric mission such as LIFE.

This situation has been presented to ESA Science and Technological directorate members, by a small group of European representatives of the high contrast imaging community[§]. This dedicated meeting was also open through visioconference to international attendance. This actually offered the opportunity for the US partners (including the GOMAP Program Executive, within NASA HQ) to explicitly support the interest for known contacts and contributions in this R&D phase, from both individuals, institutes, and agencies. Within the need for coordination at international level, France has a leading role and a recognized expertise on a number of relevant topics for high contrast imaging or interferometry (see next section). This emphasizes the interest of a good preparation at this level.

A list of contacts covering a broad range of laboratories has been set up in order to exchange and coordinate such a preparation[¶]. This coordination initiative is supported by CNES-APR and INSU/AA, and a corresponding workshop is in preparation for Spring 2024. This group has also emphasized the need for an early technological preparation to future HWO-LIFE missions, as a contribution to CNES prospective.

At European scale, ground-based projects are in practice strongly stimulating some coordination across international teams. This happens for instance in the context of the developments of future instruments for the ELT (each first-light instrument includes a high-contrast mode), and for the VLTI (including enhanced adaptive optics correction and a nulling interferometric mode within the ASGARD instrumentation suite) ; longer term plans also motivate some coordinated R&D plans under construction for European INFRATECH calls, including the specific needs driven by an ELT instrument dedicated to high contrast (PCS). High contrast from space also gathers some strong communities as witnessed in the responses to the Voyage2050 calls (Quanz et al. 2022a; Snellen et al. 2022)[‖]. Some of the expertise is shared and offers strong synergies between the ground and space. The level of space-based performance also sets some specific requirements and challenges. Some of them will be addressed in the ESA-organized WITSO workshop[**] and, more specifically, a workshop dedicated to technological developments required for future exoplanet high contrast detection from space is foreseen for spring 2024.

3 Critical domains of instrumentation research and expertise in Europe and France

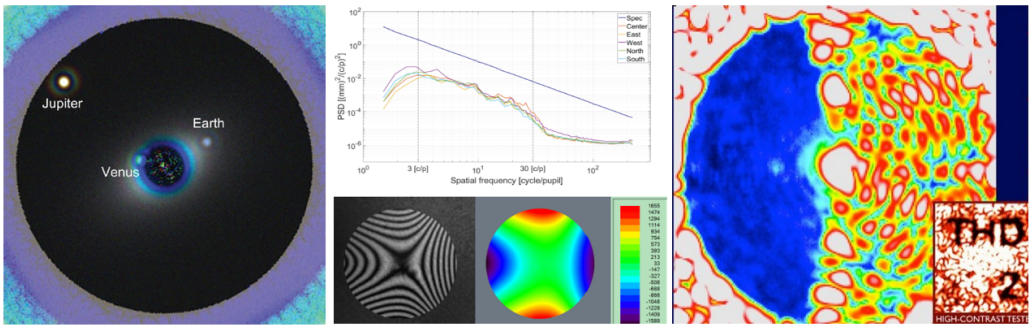

Fig. 2. Examples of advanced R&D for high contrast imaging. Left: Simulated performance of coronagraphic capability to rejected the stellar diffracted light down to imaging capability of a solar system twin from 10 pc away (N'Diaye et al. 2016). Middle: Super polishing of aspheric optics down to 5 nm rms, for Roman Space Telescope off-axis parabolae (courtesy M. Ferrari, LAM). Right: Wavefront sensing and control for dark-hole down to 10^{-8} level on the LESIA test bench (courtesy I. Laginja)

High contrast imaging or interferometry is very demanding for the exquisite goal performance, and they

[§]2023 May 30th. Slides: https://drive.google.com/file/d/1MTxuyb7fAitsAZe_fYykhNjG1KLRsxOv/view?usp=sharing

[¶]hwo-life-france@univ-grenoble-alpes.fr, contact Gael.Chauvin@oca.fr

[‖]see corresponding presentations at ESA Voyage2050 workshop on https://www.cosmos.esa.int/web/voyage-2050/workshop-programme

[**]https://atpi.eventsair.com/witso-2023/

require many different fields of expertise to be gathered for a successful development. The analysis of such requirements has been strongly supported by recent high contrast ground-based instruments, and also benefits from the inheritance of space-based missions, such as JWST (demonstrating the deployment, co-phasing and stability of its large segmented mirror up to a level of wavefront quality well above specifications) and in the near future Roman space telescope including very fine wavefront control for high contrast on a smaller mirror. In order to reach the future performance goals, we can at least mention the following aspects to be further matured and developed:

- system and trade-offs analysis at instrument level, based on large scale simulations and fundamental optical limitations, in order to include the many coupled sources of contrast degradation within a model. The general approach is known, but the considered level of performance has never been addressed
- experimental testbed capabilities, at a level of stability, calibration, and accuracy needed to address the required level of limitations.
- at component level: further key developments concerning integrated optics, coronographs, correcting optics, low-noise detectors in space environment, and/or very high wavefront quality on complex optics.
- operations and auto-calibration procedures: internal metrology, real-time wavefront sensing and control, and dark-hole procedures
- advanced signal processing for optimal real-time operation and a posteriori signal extraction, studied early on in a co-conception approach together with the instrument definition.

In each of these items, European (and in particular French) actors have demonstrated a very strong expertise with the potential of significant possible progress. In a context of limited time and resource, it will be definitely important to identify the most important items and to set some specific and quantified goals for corresponding R&D developments. The distribution of the effort should be discussed worldwide within typically 2 years for a consistent and efficient plan. The following 4 years should be devoted to the actual developments and demonstrations by the end of the decade. This will provide a clear and strong technological support to programmatic decisions on future missions, the instrument architecture definitions and the development plans.

4 Conclusion

The high-level scientific goal to characterize exo-earths and to evaluate the occurence of conditions favorable to the emergence of life is strongly expressed at international level both in US and in Europe. This very ambitious goal appears reachable within the 2040+ decade, but requires a strong and concerted R&D plan concerning high contrast capabilities to be organized now. France is in a recognized position to play a major role in this plan, based on very successful ground-based instruments in imaging and interferometry, and based on continuous R&D. The next 2 years will be important to identify the key technological items for be strongly matured, with a consistent and complementary workload distribution worldwide, in order to practically deploy such R&D actions up to 2029. Coordination work has been started in particular at the French level with a group and workshop foreseen in spring 2024 (INSU/AA and CNES), and another ESA workshop at European scale.

References

N'Diaye, M., Soummer, R., Pueyo, L., et al. 2016, ApJ, 818, 163

Quanz, S. P., Absil, O., Benz, W., et al. 2022a, Experimental Astronomy, 54, 1197

Quanz, S. P., Ottiger, M., Fontanet, E., et al. 2022b, A&A, 664, A21

Snellen, I. A. G., Snik, F., Kenworthy, M., et al. 2022, Experimental Astronomy, 54, 1237

Session S13

Atelier général du PCMI

SF2A 2023
M. N'Diaye, A. Siebert, N. Lagarde, O. Venot, K. Baillié, M. Béthermin, E. Lagadec, J. Malzac, J. Richard (eds)

SHAPING THE CO SNOWLINE IN PROTOPLANETARY DISKS

S. Gavino[1], J. Kobus[2], A. Dutrey[3], S. Guilloteau[3], S. Wolf[2], J. K. Jörgensen[1] and R. Sharma[1]

Abstract. Characterizing the dust thermal structure in protoplanetary disks is a fundamental task as the dust temperature can affect both the disk chemical evolution and planet formation. It is a challenging task, however, since the temperature is strongly dependent on many parameters, including the grain size distribution. We investigate the effects of the radiative interactions between multiple dust populations on the CO distribution using dedicated thermochemical disk models. We find that the interaction of the dust scattered light between at least two dust grain populations can produce a complex temperature structure. In particular, the scattered light is sufficient to significantly raise the temperature of micron-sized grains in the midplane. This results in the splitting of the CO snowline that can strongly reshuffle the distribution of both CO in the gas-phase and on the grain surface.

Keywords: protoplanetary disks, astrochemistry, radiative transfer, planet formation

1 Introduction

It is now expected that grain growth in protoplanetary disks occurs fast (e.g. Testi et al. 2014; Harsono et al. 2018; Ohashi et al. 2023), implying the presence of a large grain-size range. The extinction opacities are therefore difficult to characterize. Most recent studies consider a dust model composed of two-grain populations, a small dust population and a large dust population (e.g. Du & Bergin 2014; Ballering et al. 2021; Zhang et al. 2021) meant to fit observationally constrained evidence of grain growth and size-dependent distribution (Gräfe et al. 2013; Pérez et al. 2015; Villenave et al. 2020). Each population has its opacity averaged over a given size range, but a single resulting temperature is usually extracted for chemistry post-processes, However, since surface chemistry is strongly sensitive to dust surface temperatures, this treatment may overlook possible chemical effects by not considering the two dust structures independently. Indeed, real disks are most likely composed of grains of multiple sizes with independent optical properties, resulting in a complex radiative interaction between each grain species, and in a size-dependent temperature structure. In this work, we reproduce a typical two-size dust model as in recent studies, but we keep the dust structures independent so we can analyze the size-dependent temperature structures in the disk computed using dust continuum radiative transfer simulations and investigate the effect on the resulting CO distribution by treating the various dust populations simultaneously and independently in chemistry post-processes.

2 Model

2.1 Disk physical structure

The model is a static protoplanetary disks, consisting of a 2-D parametric smooth, axisymmetric and geometrically flared structure. Additionally, only passive heating is assumed. The disk is in Keplerian rotation. A more detailed description is given in Gavino et al. (2021). The radial gas surface density follows a simple truncated power-law,

[1] Niels Bohr Institute and Centre for Star and Planet Formation, University of Copenhagen, Öster Voldgade 5-7, 1350, Copenhagen K, Denmark
[2] University of Kiel, Institute of Theoretical Physics and Astrophysics, Leibnizstrasse 15, 24118 Kiel, Germany
[3] Laboratoire d'Astrophysique de Bordeaux, Université de Bordeaux, CNRS, B18N, Allée Geoffroy Saint-Hilaire, F-33615 Pessac

© Société Française d'Astronomie et d'Astrophysique (SF2A) 2023

$$\Sigma_g = \Sigma_{g,0}\left(\frac{r}{R_0}\right)^{-p}. \tag{2.1}$$

we allow for a warmer disk atmosphere using the formulation of Williams & Best (2014)

$$T_{\rm g}(r,z) = T_{\rm mid}(r) + (T_{\rm atm}(r) - T_{\rm mid}(r))\sin\left(\frac{\pi z}{2z_{\rm atm}}\right)^{2\sigma} \tag{2.2}$$

We solve the gas density by considering the (non-isothermal) vertical hydrostatic pressure equilibrium, that we solve iteratively following Hersant et al. (2009),

$$ln(\rho_g(z_i)) = ln(\rho_g(z_i - 1)) - (\Omega^2 \frac{\mu m_H}{k_B T_g(z_i)} + (ln(T_g(z_i)) - ln(T_g(z_{i-i}))) \tag{2.3}$$

The vertical density distribution of any dust component is defined by a vertical Gaussian profile. The dust scale height is size-dependent and is defined following (see Youdin & Lithwick 2007; Fromang & Nelson 2009; Dong et al. 2015),

$$H_d(a,r) = H_g(r)\frac{1}{\sqrt{1+{\rm St}\frac{S_c}{\alpha}}} \tag{2.4}$$

where $S_{\rm c}$ is the Schmidt number and α the turbulent viscosity coefficient, set to 1 and 0.01, respectively, in the whole study. The dust scale height therefore represents a fraction of the gas scale height, depending on the Stokes number, St which can be defined near the midplane as

$${\rm St} = \frac{a\rho_m}{\Sigma_g}\frac{\pi}{2} \tag{2.5}$$

where ρ_m is the dust material density and under the assumption of Epstein regime and spherical particles (see Birnstiel et al. 2012). The dust-to-gas surface density ratio is 1/100 at all radii but varies along the altitude. The model does not include radial drift. The disk is composed of two separate dust populations, each with its own size, settling factor, and temperature structure.

2.2 Dust opacity

We adopt the standard size-averaged smoothed optical properties with the mixed mie coefficients used for the DSHARP project as described in Birnstiel et al. (2018). For each population, we use a size-averaged opacity derived from a dust grain size distribution following the MRN distribution with a power-law index q = 3.5. The small grain and large population have an upper grain radius of 1 μm and 1 mm, respectively. Both populations have a lower grain radius of 0.005 μm. The resulting dust absorption opacities, dust scattering and the g parameter of anisotropy are hown in Fig. 1. The disk thermal structure is computed using the Monte-Carlo radiative transfer code RADMC-3D and it is later post-processed using the gas-grain code NAUTILUS to obtain the evolution of the chemical abundances.

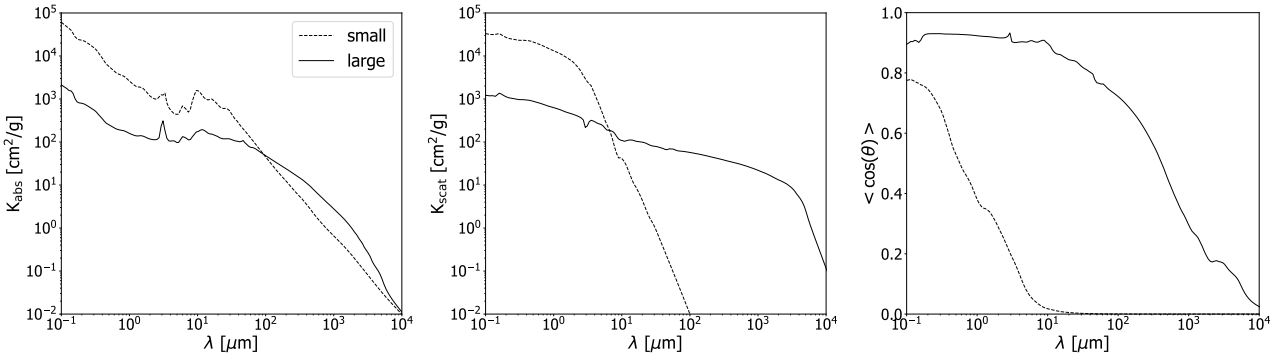

Fig. 1. Dust optical properties. **Left:** absorption coefficients. **Middle:** scattering coefficients. **Right:** Henyey-Greenstein g parameter of anisotropy (g = <cos(θ)>).

3 Results

3.1 Thermal structure

Figure 2 shows the dust temperature radial profiles in the midplane. The small grains are warmer than the large grains of approximately 13 K at almost all radii, even in the midplane. Moreover, the small dust population temperature shows a surprising bump between $\sim$ 30 au and $\sim$ 80 au. Such temperature spread cannot exist in a model with a unique dust structure. This bump originates from the radiative interaction between the two populations: the scattered light from a grain species is absorbed by the other grain species. Note that the emission comes from the stellar light scattered from the upper layers.

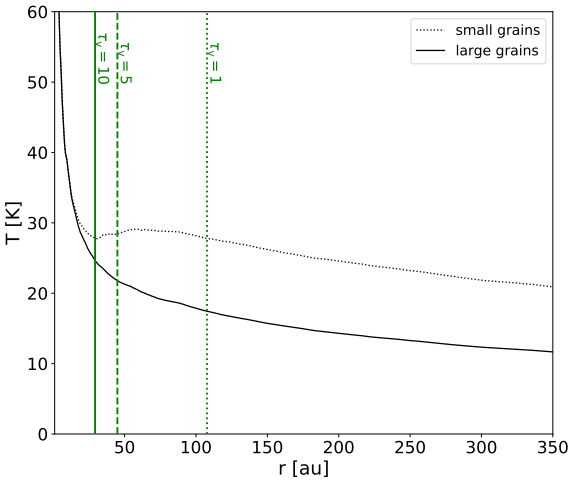

Fig. 2. Disk midplane radial profiles of dust temperatures. The black curves are the temperature profiles of the small grains (dotted line) and the large grains (solid line). The solid red curve is the temperature profile of a model with a single grain population. The vertical green solid, dashed, and dotted lines represent the radial distances from which the vertical optical depth (at 1 μm) becomes smaller than 10, 5, and 1, respectively.

3.2 CO snowline

Figure 3 shows the CO ice adsorbed into each population separately. We see that the CO snowline for the small grains is located further away ($\sim$ 250 au) from the star because the grains are warmer than the large grains, whereas the snowline for the large grains is much closer ($\sim$ 25 au) because their surface is globally colder. Inside $\sim$ 250 au, CO ice on the small grains is virtually non-existent because the temperature is above the freeze-out threshold for this population. There is thus a snowline segregation due to the presence of two temperature profiles. This, in principle, should affect the global chemical distribution in the disk. In particular, since the dynamical behaviour of the grains is also size-dependent, this could act as a segregated chemical delivery towards planetary embryos in more evolved disks.

4 Conclusions

We tested the impact of size-dependent vertical settling, dust densities, and dust opacities on the resulting dust temperatures and CO distribution in a protoplanetary disk model. We find that using different optical properties generates a systematic dust temperature spread, where the smaller grains are always warmer than the larger grains, in regions where the dust can be thermally decoupled. Most interestingly, the temperature of micron-sized grains can show a radial bump due to scattered stellarlight coming from the upper layers of the disk. The different temperatures affect the CO distribution in the disk because the CO condensation/evaporation balance is different from a grain species to another. The CO snowline is split since the temperature spread creates multiple condensation fronts. This effect does not require any radial drift process nor additional UV

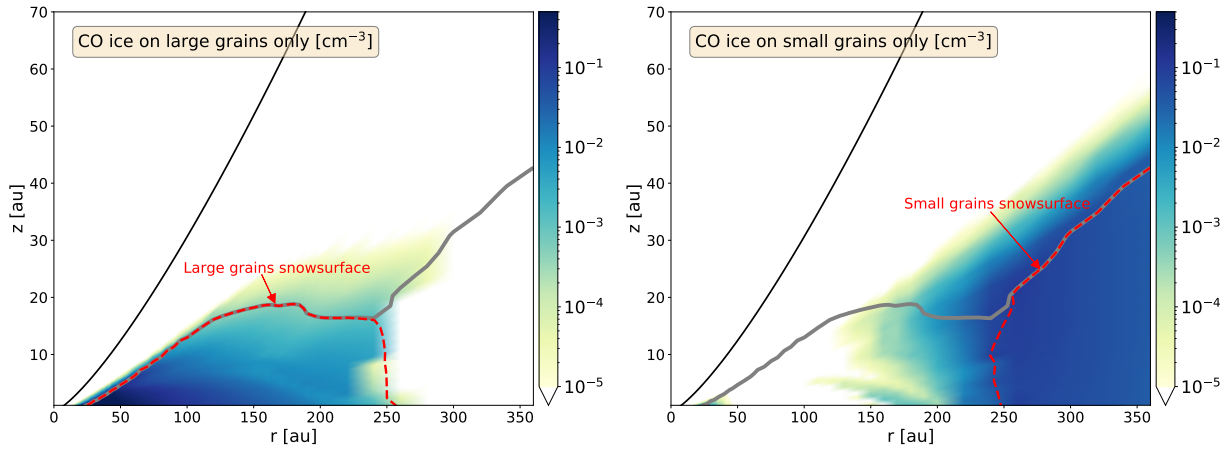

Fig. 3. 2-D maps of CO ice number density [cm^{-3}]. The solid grey line corresponds to the total CO snowline. The dashed red lines correspond to the snowline of each population independently. The black line is the maximum scale height below which chemistry is computed. **Left:** CO ice adsorbed onto the small dust population only. **Right:** CO ice adsorbed onto the large dust population only.

irradiation due to a change of dust-to-gas mass ratio, although radial drift should also reshape the CO snowline similarly. This result also shows that a size-dependent temperature has implication for chemical evolution during planet formation. Indeed, the formation pathway to more complex molecules via CO ice surface reactions is size-segregated. The small grains have virtually no CO ice on their surface inside the large grain snowline, and vice-versa, so that the formation of complex molecules via surface processes only occurs on the larger grains in the inner region of the disk, where planet formation is expected to take place. Later on, drifting pebbles from the outer disk, after the small grains have grown, should bring a different chemistry to the inner disk. Overall, this work suggests that it is not possible to create a 'fit-all' dust opacity model that can account for the dust temperature spread existing in a realistic size distribution.

S.G., J.K.J, and R.S acknowledge support from the Independent Research Fund Denmark (grant No. 0135-00123B). This work was supported by A. Dutrey and S. Guilloteau thank the French CNRS programs PNP, PNPS and PCMI. J. Kobus and S. Wolf acknowledge support from the DFG grant WO 857/19-1.

References

Ballering, N. P., Cleeves, L. I., & Anderson, D. E. 2021, ApJ, 920, 115
Birnstiel, T., Dullemond, C. P., Zhu, Z., et al. 2018, ApJ, 869, L45
Birnstiel, T., Klahr, H., & Ercolano, B. 2012, A&A, 539, A148
Dong, R., Zhu, Z., & Whitney, B. 2015, ApJ, 809, 93
Du, F. & Bergin, E. A. 2014, ApJ, 792, 2
Fromang, S. & Nelson, R. P. 2009, A&A, 496, 597
Gavino, S., Dutrey, A., Wakelam, V., et al. 2021, A&A, 654, A65
Gräfe, C., Wolf, S., Guilloteau, S., et al. 2013, A&A, 553, A69
Harsono, D., Bjerkeli, P., van der Wiel, M. H. D., et al. 2018, Nature Astronomy, 2, 646
Hersant, F., Wakelam, V., Dutrey, A., Guilloteau, S., & Herbst, E. 2009, A&A, 493, L49
Ohashi, N., Tobin, J. J., Jørgensen, J. K., et al. 2023, ApJ, 951, 8
Pérez, L. M., Chandler, C. J., Isella, A., et al. 2015, ApJ, 813, 41
Testi, L., Birnstiel, T., Ricci, L., et al. 2014, in Protostars and Planets VI, ed. H. Beuther, R. S. Klessen, C. P. Dullemond, & T. Henning, 339–361
Villenave, M., Ménard, F., Dent, W. R. F., et al. 2020, A&A, 642, A164
Williams, J. P. & Best, W. M. J. 2014, ApJ, 788, 59
Youdin, A. N. & Lithwick, Y. 2007, Icarus, 192, 588
Zhang, K., Booth, A. S., Law, C. J., et al. 2021, ApJS, 257, 5

SF2A 2023
M. N'Diaye, A. Siebert, N. Lagarde, O. Venot, K. Baillié, M. Béthermin, E. Lagadec, J. Malzac, J. Richard (eds)

MACHINE LEARNING TO FACILITATE THE STUDY OF COMPLEX ORGANIC MOLECULES IN HOT CORES

N. Kessler[1], T. Csengeri[1], D. Cornu[2] and S. Bontemps[1]

Abstract. The proper analysis of (sub)millimeter spectra containing emission from complex organic molecules is challenging for large samples. We study here a deep learning method to facilitate the analysis of molecular signatures for wide-band spectroscopic data for large samples. We demonstrate the feasibility of using neural network algorithms to identify the molecular content of synthetic spectra based on LTE models. Applying such tools to observational data could be a game changer in exploiting large datasets, and thereby help us to better understand the physical and chemical processes in star forming regions.

Keywords: star formation, astrochemistry, radioastronomy, machine learning

1 Introduction

During star formation complex organic molecules (COMs) form, and lead to the emergence of chemically rich regions such as hot cores, hot corinos, and shocks. State-of-the-art interferometers such as ALMA and NOEMA give us access to a large bandwidth at high spectral resolution in the (sub)millimeter domain, where most of the molecular emission is observed. They make it possible to search for new molecules in the interstellar medium, and to reveal a high complexity of the molecular gas in these regions (Belloche et al. 2014) with a significant increase in abundance of COMs towards chemically active regions (Csengeri et al. 2019; McGuire 2022). Nevertheless, the inspection of (sub)millimeter spectra that is rich in COMs is often time consuming and current analysis techniques are challenged by the arrival of large surveys, that require a systematic analysis. It is therefore necessary to develop new tools based on machine learning to automate the detection and the analysis of molecular emission. We present our first results in this area, as well as challenges and future prospects for the progression of machine learning in radioastronomy.

2 Artificial neural networks to study complex organic molecules in radioastronomy

The scientific community has proved that artificial neural networks (ANNs) can model complex functions to detect and recognize objects with a high accuracy, even in real time (LeCun et al. 2015). These machine learning models then appear as a way to automate the extraction of features from (sub)millimeter spectra.

2.1 Neural networks and training sets

We implemented a neural network using the framework of CIANNA (Convolutional Interactive Artificial Neural Networks by/for Astrophysicists) developed by Cornu (2020). The use of convolutional neural networks (CNNs) makes it possible to extract relevant patterns in 1D spectra that are determined by the receptive field of the convolutional layers. Thus, small scale information such as clusters of emission lines or their line profile can be taken into account, or large scale patterns such as the distance between two lines. This extracted data is treated by dense layers to learn the spectroscopic signature of each involved molecule. We developed an architecture optimised for recognizing the spectral pattern of a certain molecule. The structure of such a neural network is shown in Fig. 2 as an illustration. We used Local thermodynamic equilibrium (LTE) models over a wide range of parameters as a training set, an example of a spectrum from the training set for methanol detection is shown Fig. 1.

[1] Laboratoire d'Astrophysique de Bordeaux, Univ. Bordeaux, CNRS, UMR 5804, F-33615 Pessac, France
[2] LERMA, Observatoire de Paris, PSL Research University, CNRS, Sorbonne Univ., UMR 8112, F-75014 Paris, France

© Société Française d'Astronomie et d'Astrophysique (SF2A) 2023

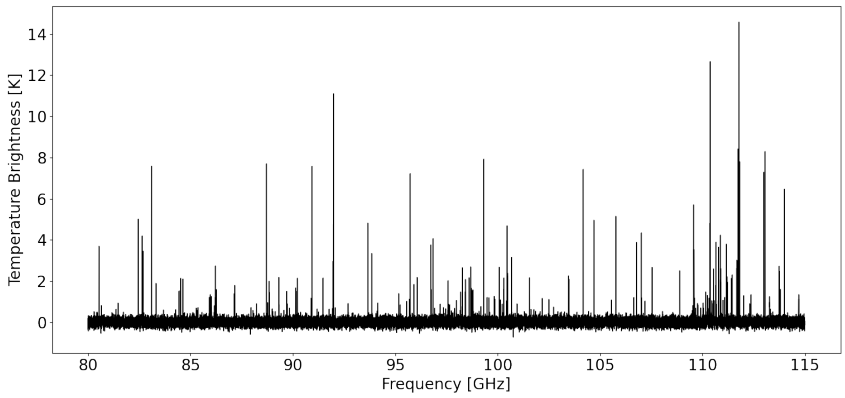

Fig. 1. Example spectra used as for the training set for methanol detection. The spectral signatures of four molecules, and noise, compose this spectrum : CH_3OH ($N = 6.6 \times 10^{15}$ cm^{-2}, $T_{ex} = 30.0$ K), CH_3OCH_3 ($N = 8.9 \times 10^{16}$ cm^{-2}, $T_{ex} = 107.8$ K), CH_3CN ($N = 6.7 \times 10^{14}$ cm^{-2}, $T_{ex} = 38.7$ K), CH_3OCHO ($N = 8.9 \times 10^{16}$ cm^{-2}, $T_{ex} = 232.2$ K).

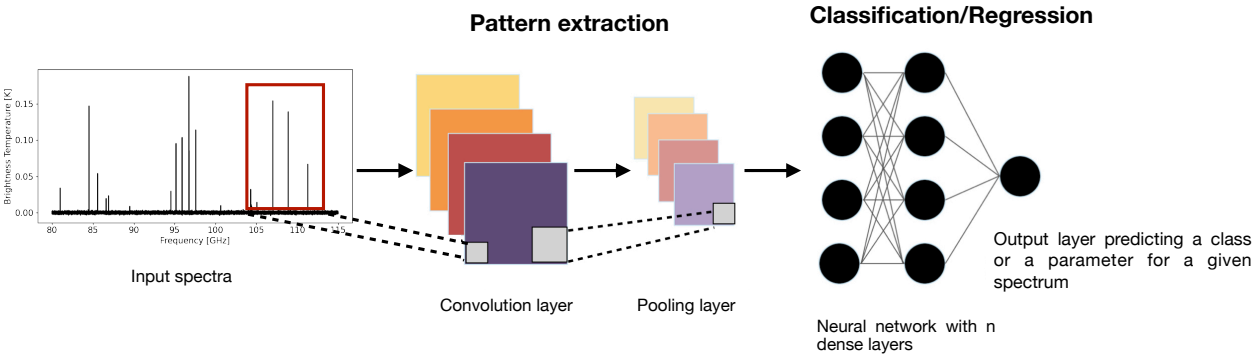

Fig. 2. Scheme of the structure of a convolutional neural network used for spectra classification or regression. The CNN takes as input a 1D spectrum. Convolutional layers extract patterns. These patterns are taken as input by dense layers. The last dense layer gives a classification or a parameter prediction depending on the use of the CNN.

2.2 First results on the detection of COMs with CNNs

The developed convolutional neural network is tested for the detection of methanol emission lines. On a data set of 2000 synthetic spectra – disjoint from the training set –, of which 1340 contain the molecule to be detected, the CNN performs a true detection for 1267 spectra with a 50% confidence threshold, and 26 false detections as shown on the left part of Fig. 3. These false detections correspond to cases with a strong confusion, and to cases located in a region of the parameter space poorly known by the CNN as suggests the histogram of Fig. 3.

3 Conclusions and perspectives

Artificial neural networks are able to learn the spectroscopic signature of molecules. Based on this principle, we developed a CNN capable of learning the information present in LTE models to then detect and identify complex organic molecules within rotational spectra. This tool will be improved for a more versatile use for recognizing more species, and will be highly beneficial for the efficient exploitation of large spectroscopic surveys, such as the NASCENT-Stars large program that aims to constrain the molecular composition of star forming regions in the Cygnus-X molecular complex with NOEMA over the next years.

Nina Kessler acknowledges financial support from the AAP DOCTORAT INTELLIGENCE ARTIFICIELLE, from the RRI ORIGINS, and the use of the Mesocentre de Calcul Intensif Aquitain (MCIA). T. Cs. has received financial support from the French State in the framework of the IdEx Université de Bordeaux Investments for the future Program. This work was supported by the Programme National "Physique et Chimie du Milieu Interstellaire" (PCMI) of CNRS/INSU with INC/INP co-funded by CEA and

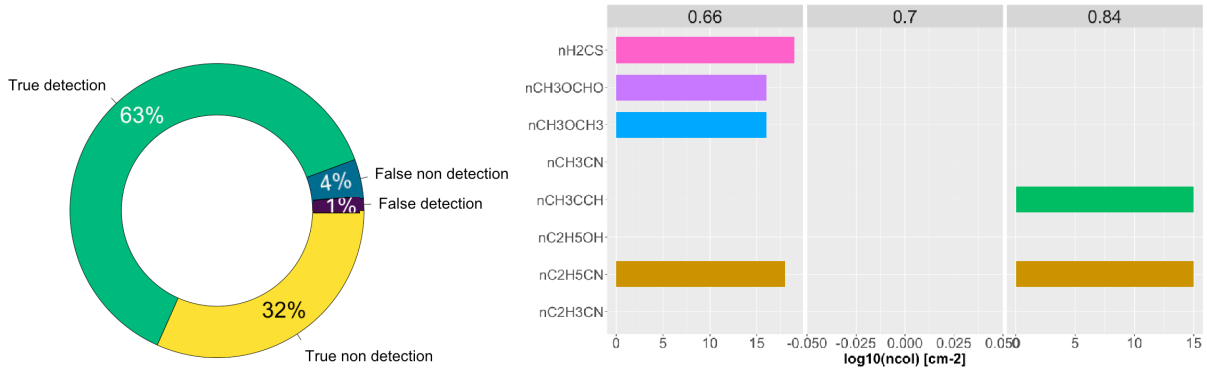

Fig. 3. Left: Doughnut chart of the CNN predictions on the presence or absence of the methanol spectral signature. **Right:** Histograms of the chemical composition with their respective column density of three spectra with false detection. The number on the top of each column is the probability given by the CNN that these spectra are composed of methanol.

CNES. This work was supported by the ""Programme National de Physique Stellaire"" (PNPS) of CNRS/INSU co-funded by CEA and CNES. The speaker expresses gratitude to the organizers of the SF2A annual meeting for gathering the French community and giving the opportunity to discuss the progress and challenges of astronomy and astrophysics.

References

Belloche, A., Garrod, R. T., Müller, H. S. P., & Menten, K. M. 2014, Science, 345, 1584

Cornu, D. 2020, arXiv e-prints, 251

Csengeri, T., Belloche, A., Bontemps, S., et al. 2019, A&A, 632, A57

LeCun, Y., Bengio, Y., & Hinton, G. 2015, Nature, 521, 436

McGuire, B. A. 2022, ApJS, 259, 30

SF2A 2023
M. N'Diaye, A. Siebert, N. Lagarde, O. Venot, K. Baillié, M. Béthermin, E. Lagadec, J. Malzac, J. Richard (eds)

DISCOVERY AND STUDY OF THE PHYSICAL PROPERTIES OF MASSIVE STARS PRECURSORS

M. Valeille-Manet[1], S. Bontemps[1] and T. Csengeri[1]

Abstract. The search for massive prestellar core (MPSC) candidates is essential to elucidate what physical processes lead to the formation of high mass stars. We build here an automatic method to detect protostellar outflows to discriminate prestellar from protostellar cores in the large statistical sample of dust cores of the ALMA-IMF large program. We find 40 MPSC candidates, ranging from 8 to 63 solar masses. This unique sample of cores will allow us to better understand the process leading to the formation of high-mass stars and their time-scales.

Keywords: ISM : outflows, stars : formation, stars : prestellar and protostellar cores

1 Introduction

The study of the early phases of high-mass star formation is a major topic in astrophysics that is still poorly understood. Several formation scenarios are still in competition (McKee & Tan (2003), Bonnell & Bate (2006)). To elucidate which precise processes of formation are in action, it is necessary to identify the youngest precursors of massive stars ($M > 8M_{\odot}$), on the verge of collapse (so-called pre-stellar cores), within high-mass star-forming regions. Here we search for MPSC candidates in a large sample of dust cores at a resolution of $\sim 2700\,au$ in the large program ALMA-IMF dataset (Motte et al. (2022)). To deal with such high statistics, we build a new method to detect protostellar outflows. We use ALMA Band 6 datacubes to study the CO and SiO lines. The data reduction process is presented in Cunningham et al. (2023) for the linecubes and in Ginsburg et al. (2022) for the continuum maps.

2 A new automatic method to detect protostellar outflows

2.1 On-Off spectra

Comparing the spectra On the source (computed in its ellipse) with the spectra Off the source, i.e. of its environment (computed in an annulus around the source), we search automatically for blue and red-shifted line wings, representative of a protostellar outflow. CO(2-1) and SiO(5-4) lines are used, as they are the best tracers of protostellar ejections. We use the On-Off spectra to detect automatically the protostellar outflows, which is the best spectra to trace the emission from the source as the environment contribution has been retrieved. Figure 1 presents the CO and SiO On, Off and On-Off spectra of a protostellar core showing clear line wings.

2.2 Molecular outflow maps

In addition to the automatic spectral analysis, moment 0 maps of the blue- and red-shifted CO(2-1) and SiO(5-4) lines overlaid to the continuum emission are used. This classical method has already been used in several studies to identify protostellar cores (see e.g. Duarte-Cabral et al. (2013), Nony et al. (2020), Nony et al. (2023)). It gives spatial information on the possible outflows that are driven by the continuum cores in the field. Figure 2 presents the molecular outflow maps of the two lines (CO on the left panel and SiO on the right one) for the W43-MM2 region. Using these two complementary tools, we search for MPSC candidates in the ALMA-IMF continuum cores catalogs.

[1] Laboratoire d'astrophysique de Bordeaux, Univ. Bordeaux, CNRS, B18N, allée Geoffroy Saint-Hilaire, 33615 Pessac, France

© Société Française d'Astronomie et d'Astrophysique (SF2A) 2023

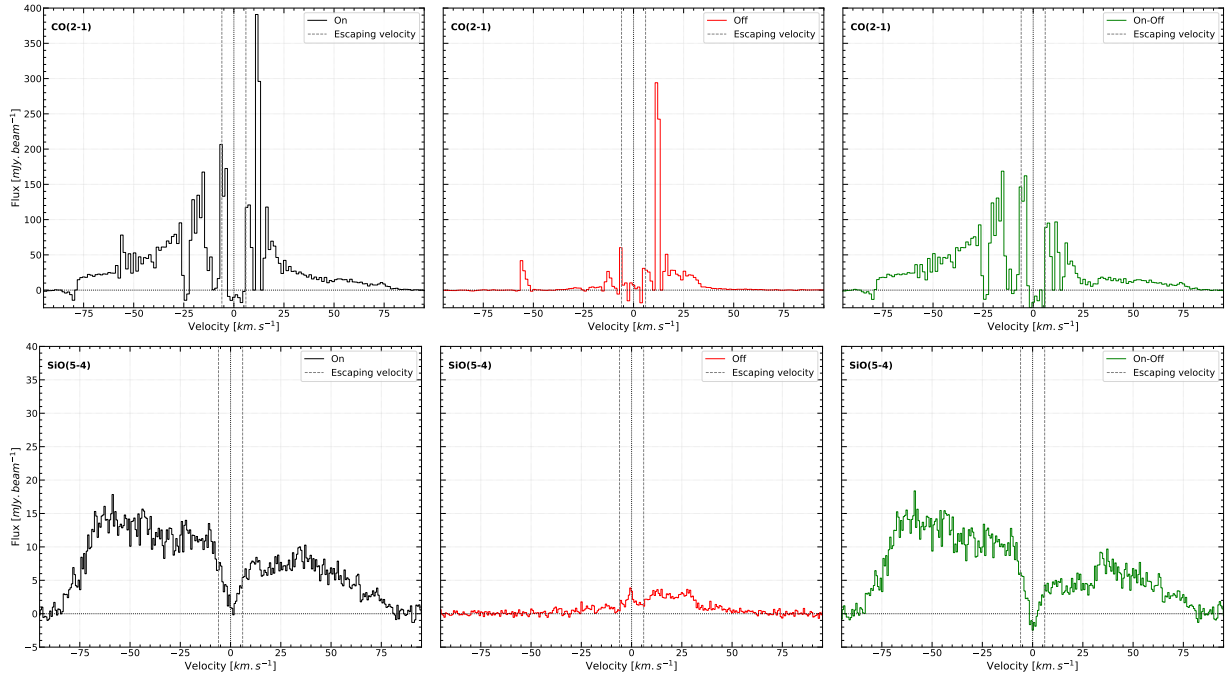

Fig. 1. On (black), Off (red), and On-Off (green) spectra of the CO(2-1) and SiO(5-4) lines of a protostellar core. The On-Off spectar displays line wings which are representative of the protostellar ejections of this core.

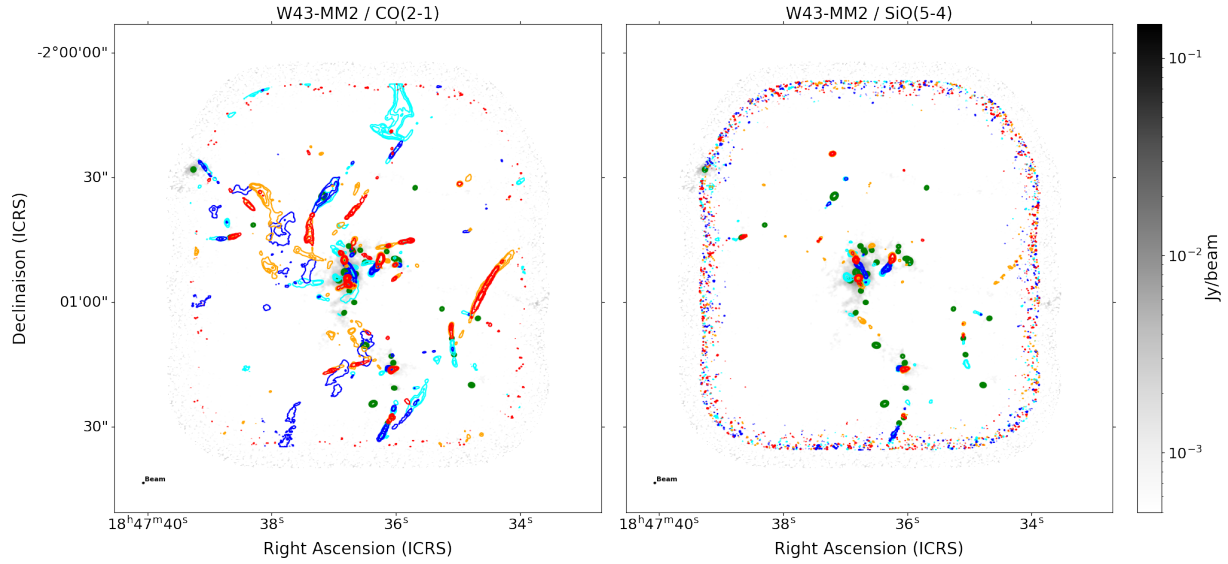

Fig. 2. CO and SiO molecular outflow maps of the W43-MM2 region. Cyan and blue contours represent low and high velocities blue-shifted lobes. Orange and red contours represent low and high velocities red-shifted lobes.

3 A unique sample of MPSC candidates

Using this automatic method we find 40 MPSC candidates in the ALMA-IMF dataset. It is the first sample of MPSC candidates, with such statistic and at a resolution high enough to study the candidates individually. The distribution in mass versus size of the candidates is presented in Fig. 3. The cores range in mass from 8 to 63 $M_{\odot}$, and in radii from $\sim 1200\,au$ to $\sim 2700\,au$. Candidates are found in young, intermediate, and evolved regions in terms of evolutionary status. This suggests that several star formation bursts are possible in a massive protocluster, and that subregions in one protocluster could present different evolutionary stages.

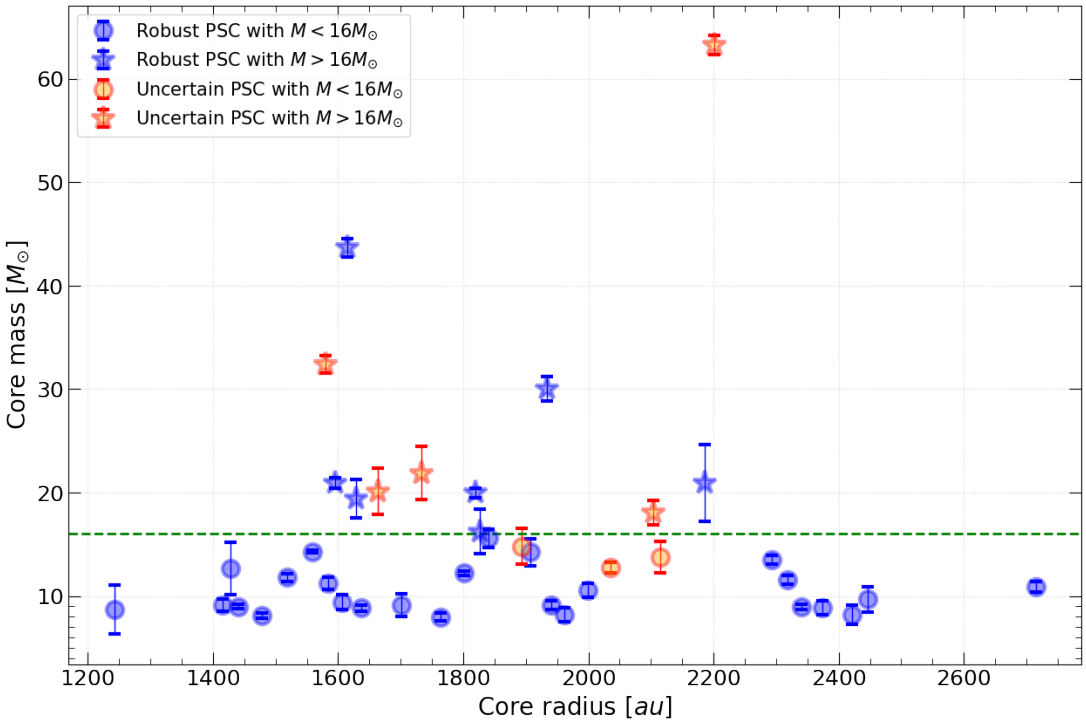

Fig. 3. Mass distribution versus core radius of the MPSC candidates.

4 Conclusions

Using this new automatic method of outflow detection, we detect 40 MPSC candidates in the ALMA-IMF massive protoclusters. This new sample will lead to new massive prestellar lifetime estimates and thus to a new vision of massive star formation.

T. Cs. has received financial support from the French State in the framework of the IdEx Université de Bordeaux Investments for the future Program. This work was supported by the Programme National "Physique et Chimie du Milieu Interstellaire" (PCMI) of CNRS/INSU with INC/INP co-funded by CEA and CNES. This work was supported by the "Programme National de Physique Stellaire" (PNPS) of CNRS/INSU co-funded by CEA and CNES.

References

Bonnell, I. A. & Bate, M. R. 2006, MNRAS, 370, 488
Cunningham, N., Ginsburg, A., Galván-Madrid, R., et al. 2023, arXiv e-prints, arXiv:2306.14710
Duarte-Cabral, A., Bontemps, S., Motte, F., et al. 2013, A&A, 558, A125
Ginsburg, A., Csengeri, T., Galván-Madrid, R., et al. 2022, A&A, 662, A9
McKee, C. F. & Tan, J. C. 2003, ApJ, 585, 850
Motte, F., Bontemps, S., Csengeri, T., et al. 2022, A&A, 662, A8
Nony, T., Galván-Madrid, R., Motte, F., et al. 2023, A&A, 674, A75
Nony, T., Motte, F., Louvet, F., et al. 2020, A&A, 636, A38

SF2A 2023
M. N'Diaye, A. Siebert, N. Lagarde, O. Venot, K. Baillié, M. Béthermin, E. Lagadec, J. Malzac, J. Richard (eds)

ATOMIS, AN ALMA ARCHIVE TOOL FOR MOLECULAR INVESTIGATIONS IN SPACE

A. Coutens[1], S. Ben Hmida[1] and J.-M. Glorian[1]

Abstract. Over the last decade, the amount of data in astrochemistry has exponentially increased. The Atacama Large Millimeter/submillimeter Array (ALMA) has played an important role in this rise. Indeed, about 500 Tb of raw and reduced data are produced per year and stored on the ALMA Science Archive (ASA). Tools are important to promote the use of these data. To facilitate the search for specific species in the ASA, we developed a web application called ATOMIS (ALMA archive TOol for Molecular Investigations in Space). Through this tool, the user can find all the observations covering the transitions of given species in lists of sources. From the list of results, the user can download the corresponding ALMA fits files or go to the ASA to retrieve the raw data. Currently, the fits files can be directly visualized in the ALADIN software through ATOMIS. Future improvements and direct visualization of the datacubes with other softwares are planned.

Keywords: Astrochemistry, Observations: ALMA, Submillimeter/millimeter, Molecules, Archive data

1 Introduction

The Atacama Large Millimeter/submillimeter Array (ALMA) has led to a revolution in astrochemistry thanks to its outstanding sensitivity and angular resolution. The amount of data produced by ALMA is also extremely high (∼500 Tb per year). All the raw and reduced data are stored on the ALMA Science Archive (ASA) and these data usually become public after one year. To make the best use of these archive data, solutions are needed to facilitate their exploitation. In particular, researchers can be interested in searching for a given molecule or a group of molecules in a list of sources. The search through the ASA is currently limited to frequencies, which makes the search more complicated when the molecule has a very high number of observable transitions. We developed a tool called ATOMIS (ALMA archive TOol for Molecular Investigations in Space) to facilitate the search for molecules in lists of sources.

2 ATOMIS design and implementation

The ATOMIS tool is publicly available at the following address: `https://atomis.irap.omp.eu`. It uses Flask framework and is written in Python, JavaScript, and HTML. It consists in four steps summarized in Fig. 1 and described below:

1. **Searching for ALMA observations**
   In the first step, ATOMIS asks the user to specify a source or a list of sources with their known velocities ($v_{\rm LSR}$) or redshift (z) as well as observation parameters such as the angular and spectral resolutions, the sensitivity, the ALMA receiver bands, the property rights of the data (only public data or all data) and the QA2 status. To search for the corresponding ALMA observations, ATOMIS uses the Astropy package (Astropy Collaboration et al. 2022) and features of the ALminer tool (Ahmadi & Hacar 2023). Some ALminer functions were adapted to achieve the desired results. ADQL(Astronomical Data Query Language) TAP query is used and sent to the PyVo TAP service. ATOMIS calculates the corresponding rest frequencies based on the values of $v_{\rm LSR}$ or redshift that are provided. A table of the filtered observations is then produced. It can be downloaded before getting to the next step.

[1] Institut de Recherche en Astrophysique et Planétologie (IRAP), Université de Toulouse, UT3-PS, CNRS, CNES, 9 av. du Colonel Roche, 31028 Toulouse Cedex 4, France

© Société Française d'Astronomie et d'Astrophysique (SF2A) 2023

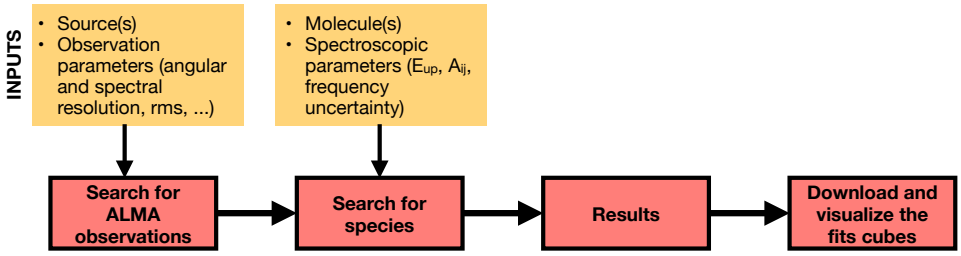

Fig. 1. Schematic view of the ATOMIS tool.

2. **Searching for species**
   The second step corresponds to the spectroscopic search. The user can select one or several species from the CASSIS database, which includes the public spectroscopic databases JPL (Pickett et al. 1998), CDMS (Müller et al. 2005), and LSD (Lille Spectroscopic Database) as well as the VASTEL* database. If the desired species is not present in this database, the user can also upload spectroscopic files (.cat file and partition function) or a private database with the CASSIS database format. Different criteria can be applied on the selected species: the minimum and the maximum values of $E_{\rm up}$ and $A_{\rm ij}$ and the maximum frequency uncertainty for the transitions. ATOMIS searches for all the corresponding transitions that are covered in the filtered observations and presents the results under a table format (third step).

3. **Displaying results**
   The results are displayed in a table which contains all the ALMA observations (spectral windows) that cover the selected transitions. The table can be adapted with the desired columns (source name, coordinates, project code, covered lines, sensitivity, angular resolution, spectral resolution, ...). The displayed observations can be modified based on the sensitivity and the angular resolution and by deselecting species. Also, ATOMIS provides three additional options to filter the results: only display observations for which all selected species are covered in the same source, in the same project or in the same spectral window. From this table, the user can select an observation and access to the corresponding project in the ALMA archive or click on the link to download the fits files (fourth step).

4. **Downloading and visualizing the datacubes**
   The fits files covering the requested transitions available on the ASA are listed on ATOMIS and can be downloaded directly by the user. They can also be directly visualized with Aladin-CASSIS (Glorian et al. 2021), as long as the software Aladin is installed and opened. The interoperability and the communication between ATOMIS and Aladin are ensured by the use of SAMP (Simple Application Messaging Protocol).

3 Conclusion

ATOMIS is a public tool that could present an interest for the astrochemistry community. Future improvements are planned. In particular, interoperabilities with other softwares used to visualize and analyse ALMA data cubes (CARTA, YAFITS, ...) would be useful.

This project has received funding from the European Research Council (ERC) under the European Union's Horizon 2020 research and innovation programme (Chemtrip, grant agreement 949278).

References

Ahmadi, A. & Hacar, A. 2023, Astrophysics Source Code Library, record ascl:2306.025
Astropy Collaboration, Price-Whelan, A. M., Lim, P. L., et al. 2022, ApJ, 935, 167
Glorian, J.-M., Fernique, P., Allen, M., et al. 2021, in ADASS XXXI Conference Oct 2021, ASP Conferences Series
Müller, H. S. P., Schlöder, F., Stutzki, J., & Winnewisser, G. 2005, Journal of Molecular Structure, 742, 215
Pickett, H. M., Poynter, R. L., Cohen, E. A., et al. 1998, J. Quant. Spec. Radiat. Transf., 60, 883

*http://cassis.irap.omp.eu/?page=catalogs-vastel

SF2A 2023
M. N'Diaye, A. Siebert, N. Lagarde, O. Venot, K. Baillié, M. Béthermin, E. Lagadec, J. Malzac, J. Richard (eds)

STATISTICAL ANALYSIS OF THE RELATIVE ORIENTATIONS BETWEEN FILAMENTS AND MAGNETIC FIELDS IN STAR FORMING REGIONS

J. Oers[1], I. Ristorcelli[1], K. Ferrière[1] and L. Montier[1]

Abstract. Filamentary structures are ubiquitous in the interstellar medium (ISM). This is particularly true in molecular clouds, with most clumps and cores forming inside the densest regions of filaments. Both simulations and observations suggest that magnetic fields play a key role in the formation and evolution of filaments and in the process of star formation. In this context, the study of the relative orientations between filaments and magnetic fields has become a go-to method to obtain new insight. Here, we use a dedicated method, FilDReaMS, to detect and extract filaments at multiple scales in the 116 fields of the *Herschel* 'Galactic Cold Cores' (GCC) key-project (18"−36" resolution), which measures dust emission in star-forming regions located in various Galactic environments. We then compare the filament orientations to the orientation of the plane-of-sky magnetic field ($\boldsymbol{B}_\perp$), inferred from *Planck* observations of the dust polarized emission (7' resolution). We present the results of our statistical analysis of these relative orientations as functions of filament spatial scale, gas column density ($N_{\mathrm{H_2}}$) and Galactic environment. In most *Herschel* fields, we find that small, low-$N_{\mathrm{H_2}}$ filaments tend to be roughly parallel to the magnetic field, while large, high-$N_{\mathrm{H_2}}$ filaments tend to be roughly perpendicular. Although this trend is not systematically observed, it is still prevalent, which confirms the existence of a coupling between magnetic fields at cloud scales and filaments at smaller scales.

Keywords: ISM: clouds - ISM: structures - ISM: magnetic fields - dust - infrared - ISM: submillimiter - ISM: techniques - image processing

1 Introduction

In star-forming regions, prestellar and protostellar cores are mostly located in dense filaments (André et al. 2014). Hence, the early stages of star formation are linked to the formation and evolution of filaments. The main physical actors involved are gravity, turbulence and magnetic fields. However, their actual roles and interplay are still poorly understood (McKee & Ostriker 2007). To make progress in our physical understanding, different scales must be probed, from molecular clouds to filaments, clumps and cores. Statistical analyses based on the *Planck* survey show that filaments in the diffuse ISM are mostly parallel to the plane-of-sky magnetic field ($\boldsymbol{B}_\perp$), while in molecular clouds, there appears to be a transition from parallel to perpendicular relative orientations at a column density $N_{\mathrm{H}} \sim 5.0 \times 10^{21}\,\mathrm{cm}^{-2}$ (Planck Collaboration et al. 2016a,b). In a combined *Herschel-Planck* analysis of a high-latitude star-forming cloud, Malinen et al. (2016) found evidence for a similar transition at $N_{\mathrm{H}} \sim 1.6 \times 10^{21}\,\mathrm{cm}^{-2}$; they would have found a value consistent with *Planck*'s had they used the same convention for dust opacity.

Our purpose is to study the statistics of the relative orientations between filaments and $\boldsymbol{B}_\perp$ as functions of the physical properties of the local gas and Galactic environment.

2 Method: FilDReaMS

We use our new filament detection method FilDReaMS, for Fil*ament* D*etection and* R*econstruction* at M*ultiple* S*cales*, presented in Carrière et al. (2022a,b). We apply FilDReaMS to the 116 fields of the *Herschel* GCC program (18"−36" resolution; Juvela et al. 2010). In short, FilDReaMS uses a rectangular template (a bar of width W_{b}) to search for filamentary structures in an image, then repeats this process over a whole range of

[1] IRAP, Université de Toulouse, CNRS, 9 avenue du Colonel Roche, BP 44346, 31028 Toulouse Cedex 4, France

© Société Française d'Astronomie et d'Astrophysique (SF2A) 2023

bar widths. Thus, FilDReaMS provides information on the widths of filaments, their column densities, their orientations and the robustness of the detection.

In a second step, we study the filaments' orientations relative to the orientation of $\boldsymbol{B}_\perp$ inferred from *Planck* observations of the dust polarized emission (7' resolution), and we do so at multiple scales.

3 Results

In Fig. 1, we present an example of the analysis performed for one of the GCC fields. We show the N_{H_2} map of the *Herschel* G132 field as well as all the filaments obtained with FilDReaMS, together with their bar widths W_b. In Fig. 2, we show 2D histograms of the relative orientation angles between filaments and $\boldsymbol{B}_\perp$ ($\psi_f^* - \psi_B$) as functions of N_{H_2}, for all the detected filaments. The filaments are split into 3 ranges of W_b defined by the smallest (S), largest (L) and all intermediate (M) values of W_b.

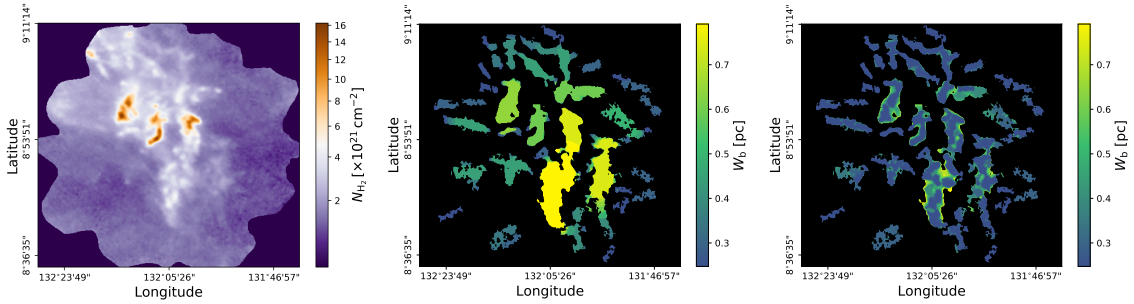

Fig. 1. G132 - **Left:** N_{H_2} map. Detected filaments, with the larger (**Middle**) and the smaller **Right** in the foreground.

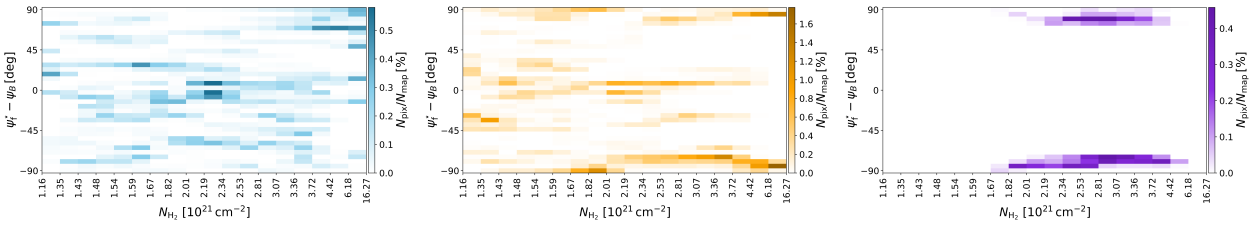

Fig. 2. 2D histograms for G132 - **Left:** S filaments. **Middle:** M filaments. **Right:** L filaments.

We combine the analyses of all 116 fields in order to identify statistical trends in the relative orientations between filaments and $\boldsymbol{B}_\perp$. The general trends we find agree with previous studies: smaller filaments at lower N_{H_2} are mostly parallel to $\boldsymbol{B}_\perp$, while filaments at higher N_{H_2} are mostly perpendicular to $\boldsymbol{B}_\perp$, with a transition from parallel to perpendicular to $\boldsymbol{B}_\perp$ occurring at $N_{\mathrm{H}_2} \in [0.8, 2] \times 10^{21}$ cm^{-2}. However, over 30% of the GCC maps show different results, with either filaments mostly parallel to $\boldsymbol{B}_\perp$ at all scales and N_{H_2}, or opposite transitions from perpendicular to parallel to $\boldsymbol{B}_\perp$ at higher N_{H_2}, or absence of clear preferred orientations.

This is work in progress. What we would like to do is identify the actors responsible for the different trends, such as dust polarisation fraction, large-scale magnetic field orientation, evolutionary stage of cores, etc.

References

André, P. et al. 2014, in Protostars and Planets VI, 27–51
Carrière, J.-S. et al. 2022a, A&A, 668, A41
Carrière, J.-S. et al. 2022b, A&A, 668, A42
Juvela, M. et al. 2010, A&A, 518, L93
Malinen, J. et al. 2016, MNRAS, 460, 1934
McKee, C. F. & Ostriker, E. C. 2007, ARA&A, 45, 565
Planck Collaboration et al. 2016a, A&A, 586, A135
Planck Collaboration et al. 2016b, A&A, 586, A138

Session S14

Galaxy evolution in the era of JWST (atelier du PNCG)

SF2A 2023
M. N'Diaye, A. Siebert, N. Lagarde, O. Venot, K. Baillié, M. Béthermin, E. Lagadec, J. Malzac, J. Richard (eds)

PRELIMINARY RESULTS ON JWST CYCLE 1 GO #2180: THE CIRCUMGALACTIC MEDIUM OF NGC 891

J. Chastenet[1], I. Looze[1,], M. Relaño[2,3], T. Williams[4], E. Xilouris[5] and the proposing team

Abstract. We present the latest maps of the edge-on galaxy NGC 891 observed by JWST, and preliminary results. The NIRCam instrument observed the northern half of the disk in the F150W and F277W filters, while MIRI observed a portion of the circum-galactic medium (CGM) in F770W. The mid-infrared image at 7.7 μm tracing aromatic-rich grains shows filamentary structures, expanding as far as $\sim$ 4 kpc, together with a large number of small clumps, also visible in the image. These dust-rich structures give us insights to identify the feedback processes responsible for the ejection of mid-plane material out to the CGM.

Keywords: Dust composition, Polycyclic aromatic hydrocarbons, Galactic and extragalactic astronomy, Circumgalactic medium

1 Introduction & Presentation of the proposal

The focus of this proceeding is the JWST Cycle 1 GO #2180 program (PI De Looze), entitled "Structure formation and baryonic cycling in the edge-on galaxy NGC891".

1.1 Introduction

The circum-galactic medium (CGM) is the interface between the large halo and the main disk of spiral galaxies. That is where in- and outflows happen, and the recycling of baryonic material that fuels galaxies takes place. Understanding these exchanges also requires to understand the stratification of disks, at various wavelengths. The determination of disks of various sizes (thin to thick, and even extra-thin disks) can only be done unambiguously in edge-on galaxies. This eventually can help understanding the inflow and outflow processes, making edge-on galaxies the best laboratories to study how feedback processes shape galaxy evolution.

These processes appear to be somewhat insufficiently understood, since the simulations often show discrepancies when compared to observational data. In particular, an overestimation of feedback processes in cosmological simulations tend to overestimate the scale-heights of galactic disks (Governato et al. 2004; Grand et al. 2016; Trayford et al. 2017). With numerous recent observations of these outflows, their importance is no longer questioned, but their exact nature and efficiency need to be refined. What drives these mechanisms, e.g., supernovae, stellar winds, ionizing radiation, cosmic rays, is not well understood.

This study focuses on the disk and CGM of NGC 891, a nearly perfectly edge-on galaxy ($i \sim 89.7°$; Xilouris et al. 1999), located at $\sim$ 9.6 kpc (Strickland et al. 2004). Its proximity and inclination, combined with the high-sensitivity and spatial resolution of JWST, this target is an excellent choice to investigate the main issues related to the feedback processes in spiral galaxies.

[1] Sterrenkundig Observatorium, Ghent University, Krijgslaan 281-S9, B9000 Gent, Belgium
[2] Departamento Física Teórica y del Cosmos, Universidad de Granada, E-18071 Granada, Spain
[3] Instituto Universitario Carlos I de Física Teórica y Computacional, Universidad de Granada, E-18071 Granada, Spain
[4] Sub-department of Astrophysics, Department of Physics, University of Oxford, Keble Road, Oxford OX1 3RH, UK
[5] Institute for Astronomy, Astrophysics, Space Applications & Remote Sensing, National Observatory of Athens, P. Penteli, 15236 Athens, Greece

© Société Française d'Astronomie et d'Astrophysique (SF2A) 2023

1.2 Data

We present the first data taken as part of the proposal. The NIRCam F150W and F277W observations were taken on August, 15$^{\rm th}$ 2022, and MIRI F770W observation were taken on December, 23$^{\rm rd}$ 2022. Figure 1 shows these observations. Additionally, we collected parallel NIRCam observations during the MIRI pointings, not shown here.

The NIRCam data cover the northern half of the disk, out to $\sim$ 3 kpc on both sides. We can notice visible absorption features in the mid-plane at both wavelengths, more prominent at 1.5 μm (top left panel of Figure 1). The data was reduced using the modified pipeline from the PHANGS Team (Lee et al. 2023, Williams et al., in prep). The short- and long-wavelength arrays do show conspicuous differences. While the background appears relatively smooth in F277W, the F150W image shows visible large structures, stripes and offsets between dithers that we have not yet corrected. Note that the small squares in F150W are due to a lack of overlap in the short-wavelength sub-array mode.

The MIRI F770W observations cover a strip off the main disk from $\sim$ 1 to $\sim$ 10 kpc (thus not covering the disk directly), to trace the 7.7 μm mid-IR emission feature from large aromatic molecules (Polycyclic Aromatic Hydrocarbons, PAHs, or Hydrogenatic Amorphous Hydrocarbons Jones et al. 2013; Li 2020, for a review). We mark the distances at 1, 2, 3, 5, and 10 kpc in the MIRI panel of Figure 1. With the high sensitivity and spatial resolution of JWST, bright, fine structures are visible. The presence of arcs, filaments, and potential galactic fountains are detected at reasonable signal-to-noise ratio.

2 Early analysis

This section presents preliminary results from a first analysis of the data products.

2.1 Mid-IR radial profiles

We use literature driven assumptions to estimate the scale-height of the dust distribution as seen in the MIRI image. In earlier work, a dust scale-height of $\sim$ 0.10 kpc was found using a single exponential disk or $\sim$ $0.13 - 0.6$ kpc with a double-exponential disk in the *Spitzer*/IRAC 8 μm image (e.g., Bocchio et al. 2016). Our analysis reveals a scale-height of $z_{\rm d} \sim 0.4 - 0.5$ kpc using a single disk. Since we do not cover the mid-plane, our estimate is closer to the thick disk that was found in other studies.

2.2 Clumps

The insets in Figure 1 show zoom-ins on a few regions, to highlight the presence of small bright clumps. Cold, dense gas clumps have been predicted in simulations (e.g., Lan & Fukugita 2017; Hirashita & Lan 2021; Farber & Gronke 2022).

We focus on these clumps throughout the image in a preliminary analysis. To identify them, we use the ASTRODENDRO package. However, as visible in Figure 1, there is a strong gradient close to the disk out to further distances. This gradient makes it difficult to adjust the parameters of ASTRODENDRO to conservatively, but accurately detect the right sources. To alleviate that effect, we use an unsharp-masked version of the MIRI image. Unsharp-masking is an edge enhancement technique. This allows us to focus on bright clumps and remove the more diffuse filaments and the gradient. The bulk of the detected clumps has a radius ranging between $\sim$ 10 and $\sim$ 30 pc, slightly smaller than what is predicted in simulations. The number of clumps peaks around 1 kpc from the disk, with a rapid decrease in number to further distances.

2.3 Filaments

Multiple filaments are visible in the first $\sim 2 - 2.5$ kpc. Filaments have been identified in the CGM of other edge-on galaxies, at different wavelengths (e.g., Rand et al. 1990; Howk & Savage 1997; Rossa et al. 2004; Irwin et al. 2007), showing that they exist in several phases of the gas component.

Unfortunately, since our observations do not cover the main disk, we cannot directly connect these filaments to the mid-plane of NGC 891. Instead, we combine our new data with the *Spitzer*/IRAC 8 μm image. We apply unsharp-masking to that image, and enhance dusty filaments and the disk. We compare these IRAC filaments with the ones identified in the (convolved) MIRI image using FILFINDER (Koch & Rosolowsky 2015). The agreement is very good, and we can connect these MIRI structures all the way back to the disk. Using

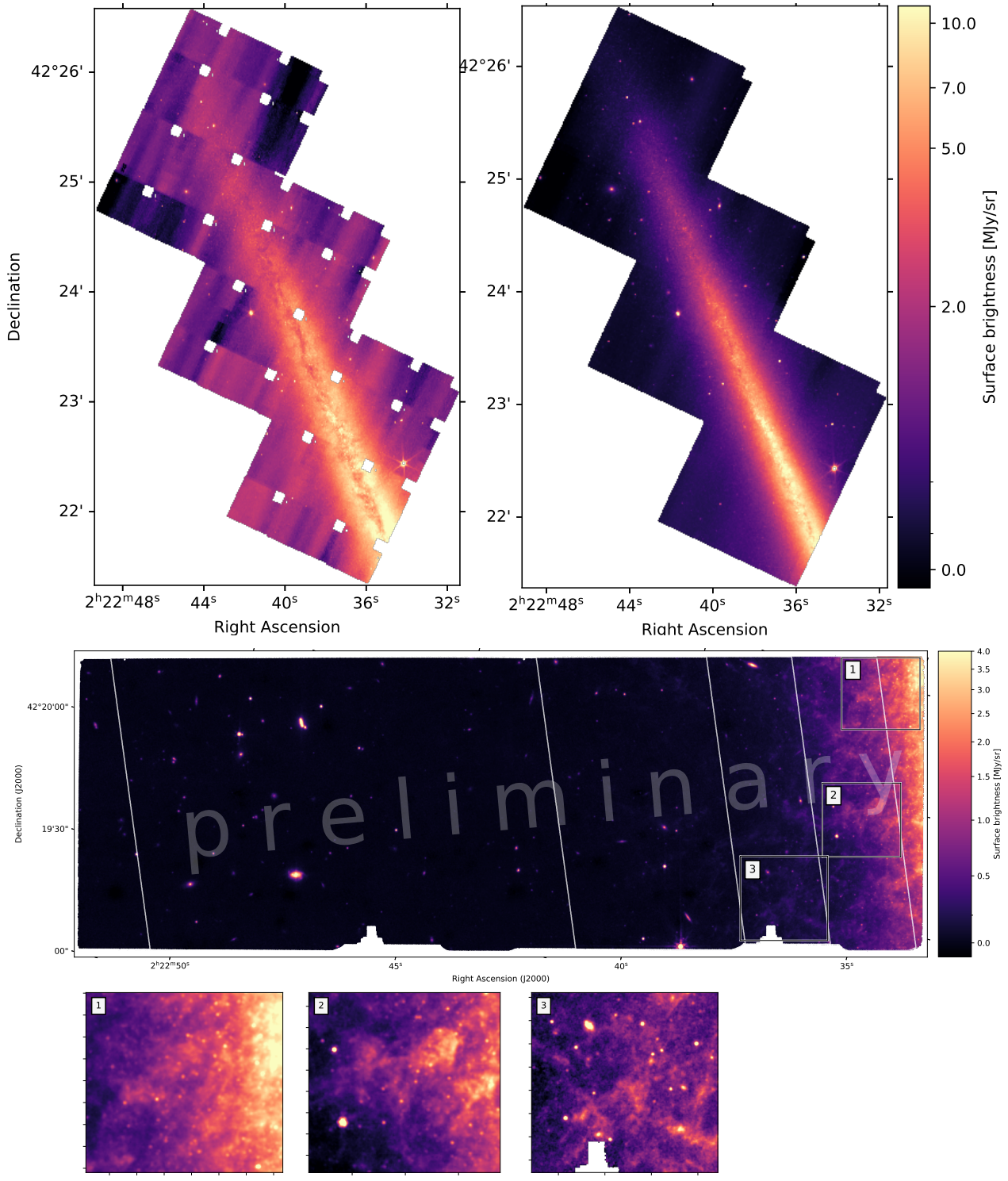

Fig. 1. *Top panels:* NIRCam F150W (left) and F277W (right) of the northern half of the disk. Conspicuous absorption structures are visible in both images. *Bottom panel:* MIRI F770W image, with distance marks at 1, 2, 3, 5, and 10 kpc from the mid-plane. The three insets (shown with a different color-stretch show detailed filaments and clumps.

mid-IR data to derive star formation rates (SFRs; e.g., Leroy et al. 2019), we find that these filaments are often linked to high SFRs. This has been studied in several works as well (e.g., Heckman 2002; Yoon et al. 2021). Additional work will attempt to precisely estimate the lower-limit on SFR that can birth extensive filaments.

3 Conclusions

We present new observations of NGC 891, a nearby edge-on galaxy. NIRCam data in the F150W and F277W filters trace the stellar content in the northern half. MIRI/F770W data shows the distribution of PAHs in the CGM of NGC 891, out to 4 kpc away from the mid-plane. We focus our early analysis on prominent filaments and small dense clumps, visible at 7.7 μm. Identifying the properties of these structures will allow us to estimate the amount of mid-IR features carriers (PAHs) in the CGM, put constrains on their formation outside of the mid-plane, and/or the stellar/supernova processes responsible for their ejection in the CGM through galactic outflows.

JC acknowledges support from ERC starting grant #851622 DustOrigin, and funding from the Belgian Science Policy Office (BELSPO) through the PRODEX project "JWST/MIRI Science exploitation" (C4000142239). MR acknowledges financial support by the research projects AYA2017-84897-P and PID2020-113689GB-I00, financed by MCIN/AEI/10.13039/501100011033. This research made use of astrodendro, a Python package to compute dendrograms of Astronomical data (`http://www.dendrograms.org/`)

References

Bocchio, M., Bianchi, S., Hunt, L. K., & Schneider, R. 2016, A&A, 586, A8

Farber, R. J. & Gronke, M. 2022, MNRAS, 510, 551

Governato, F., Mayer, L., Wadsley, J., et al. 2004, ApJ, 607, 688

Grand, R. J. J., Springel, V., Gómez, F. A., et al. 2016, MNRAS, 459, 199

Heckman, T. M. 2002, in Astronomical Society of the Pacific Conference Series, Vol. 254, Extragalactic Gas at Low Redshift, ed. J. S. Mulchaey & J. T. Stocke, 292

Hirashita, H. & Lan, T.-W. 2021, MNRAS, 505, 1794

Howk, J. C. & Savage, B. D. 1997, AJ, 114, 2463

Irwin, J. A., Kennedy, H., Parkin, T., & Madden, S. 2007, A&A, 474, 461

Jones, A. P., Fanciullo, L., Köhler, M., et al. 2013, A&A, 558, A62

Koch, E. W. & Rosolowsky, E. W. 2015, MNRAS, 452, 3435

Lan, T.-W. & Fukugita, M. 2017, ApJ, 850, 156

Lee, J. C., Sandstrom, K. M., Leroy, A. K., et al. 2023, ApJ, 944, L17

Leroy, A. K., Sandstrom, K. M., Lang, D., et al. 2019, ApJS, 244, 24

Li, A. 2020, Nature Astronomy, 4, 339

Rand, R. J., Kulkarni, S. R., & Hester, J. J. 1990, ApJ, 352, L1

Rossa, J., Dettmar, R.-J., Walterbos, R. A. M., & Norman, C. A. 2004, AJ, 128, 674

Strickland, D. K., Heckman, T. M., Colbert, E. J. M., Hoopes, C. G., & Weaver, K. A. 2004, ApJ, 606, 829

Trayford, J. W., Camps, P., Theuns, T., et al. 2017, MNRAS, 470, 771

Xilouris, E. M., Byun, Y. I., Kylafis, N. D., Paleologou, E. V., & Papamastorakis, J. 1999, A&A, 344, 868

Yoon, J. H., Martin, C. L., Veilleux, S., et al. 2021, MNRAS, 502, 969

SF2A 2023
M. N'Diaye, A. Siebert, N. Lagarde, O. Venot, K. Baillié, M. Béthermin, E. Lagadec, J. Malzac, J. Richard (eds)

JWST PROBES THE ROLE OF STELLAR MASS AND MORPHOLOGY IN OBSCURING GALAXIES

C. Gómez-Guijarro[1]

Abstract. In the last years a population of galaxies missed in optical surveys but bright at far-infrared/millimeter wavelengths has been discovered. These optically dark/faint galaxies (OFGs, among other nomenclatures) are of great interest as they are seen as a key population of galaxies that dominate the contribution of massive ($M_* > 10^{10.3}\,M_\odot$) galaxies to the star formation rate density of the universe at $z > 3$. However, their high-redshift, massive nature, and the reason behind their elusiveness are still uncertain. We present a *JWST*-based study investigating the drivers of dust attenuation in massive galaxies in the *JWST* era, focusing on understanding what is the nature of these OFGs that resulted in missing them in the pre-*JWST* observations. Stellar mass appears as the primary proxy of dust attenuation among those studied. However, there is a subset of highly dust attenuated ($A_V > 1$, typically) star-forming galaxies (SFGs), of which OFGs are a specific case. For this subset, we find that the key distinctive feature is their compact size. OFGs are dark because their dust content is associated to more compact stellar profiles, when compared to similarly massive SFGs at the same epoch.

Keywords: galaxies: evolution – galaxies: high-redshift – galaxies: photometry – galaxies: star formation – galaxies: structure – infrared: galaxies

1 Introduction

Prior the *JWST*, our insights into the early cosmic history of galaxies, especially those with $z > 3$, largely depended on samples chosen from their rest-frame ultraviolet (UV) light (see Madau & Dickinson 2014, for a review). Traditional selection methods, like those for Lyman break galaxies (LBGs) (LBGs; e.g., Steidel et al. 1996), often overlooked redder dusty star-forming galaxies (SFGs). Recent observations from the Spitzer Space Telescope (*Spitzer*) and the Atacama Large Millimeter/submillimeter Array (ALMA) revealed a subset of massive dusty SFGs not captured in previous optical/near-infrared (IR) surveys (e.g., Franco et al. 2018; Wang et al. 2019; Gómez-Guijarro et al. 2022). These galaxies differ from extreme dusty starbursts and are believed to play a significant role in the star-forming rate density of the universe around $z \sim 3$–6. Their precise role and characteristics, especially in terms of stellar morphologies, have been hard to uncover due to their faintness in optical/near-IR wavelengths.

With the *JWST*, light has been shed on these elusive galaxies, revealing diverse properties across multiple studies (e.g., Barrufet et al. 2022; Nelson et al. 2023; Pérez-González et al. 2023). In our study, we delve into the factors influencing dust attenuation in the *JWST* epoch, striving to discern the nature of these obscured galaxies and to elucidate why they remained elusive in the pre-*JWST* era. We emphasize the impact of stellar mass and morphology as proxies of dust attenuation and outline our methods and findings in the subsequent sections.

In this text the main results from Gómez-Guijarro et al. (2023) are outlined, to which the reader is referred for further details.

[1] Université Paris-Saclay, Université Paris Cité, CEA, CNRS, AIM, 91191, Gif-sur-Yvette, France

© Société Française d'Astronomie et d'Astrophysique (SF2A) 2023

2 Methodology

2.1 Data and catalog

We utilized data from the *JWST*, specifically from the Cosmic Evolution Early Released Science (CEERS) survey in the Extended Groth Strip (EGS) field (Finkelstein et al. 2022), along with complementary data from the Hubble Space Telescope (*HST*) and ground-based imaging from the Canada-France-Hawaii Telescope (CFHT). For cataloging, source detection was conducted using `SExtractor` in the F444W-band, following procedures similar to the CANDELS catalog in the EGS field (Stefanon et al. 2017). Photometry was carried out across 13 *JWST* and *HST* bands using dual image mode in `SExtractor`, and on five ground-based CFHT bands using aperture photometry.

2.2 Estimation of redshift, stellar mass, dust attenuation, and morphology

We used the `EAZy` code to calculate photometric redshifts from spectral energy distribution (SED) fitting across 18 bands in our catalog, utilizing the Flexible Stellar Population Synthesis (FSPS) templates. Where high-quality spectroscopic redshifts were available, we replaced the photometric redshifts, and used them to refine the zero point corrections iteratively in the `EAZy-py` run, improving photometric redshift accuracy.

For estimating stellar masses and dust attenuation, we used the `FAST++` SED fitting code, keeping the redshifts fixed at the previously obtained values. The used stellar population models, star formation histories, and metallicity values are standard in similar studies, facilitating comparisons.

Star formation rate (SFR) values were derived from a ladder of SFR estimators. We initially checked for counterparts in mid-IR-to-mm bands. For galaxies with significant signal in the IR, we applied the `CIGALE` code to dust emission templates to derive total IR luminosity estimates. For other cases, we re-normalized IR templates to *Spitzer*/MIPS 24 μm fluxes, or used the UV term alone corrected for dust attenuation to estimate the total SFR, depending on the available data. The SFR takes into account both obscured and unobscured star formation, combining IR and UV luminosity contributions.

For morphological analysis, we employed the `statmorph` code to fit surface brightness profiles to *JWST*/NIRCam F444W images. This band was chosen as it reliably probes optical-to-near-IR rest-frame morphologies across our redshift range of interest, minimizing morphological variances observed at shorter wavelengths. Our analysis was confined to good fit quality cases to ensure reliable morphological measurements.

2.3 Sample definitions

In this, we used a selective redshift range of $3 < z < 7.5$ to incorporate insights from the *JWST*/NIRCam into the rest-frame UV analysis, with the lower limit enabling coverage of the rest-frame UV at all redshifts using at least two NIRCam bands. The study also sets a stellar mass lower limit of $\log(M_*/M_\odot) \geq 9.0$ to focus on intermediate-to-massive galaxies. Three distinct galaxy samples were classified: SFGs, LBGs, and OFGs:

Star-Forming Galaxies (SFGs) parent sample: Identified within the defined redshift and stellar mass limits using a UVJ classification (e.g., Williams et al. 2009), yielding a total of 1490 galaxies. This parent sample aimed to serve as a benchmark for comparative analysis.

Lyman Break Galaxies (LBGs): Recognized by their prominent break beyond the Lyman limit due to intervening hydrogen absorption, facilitating the identification of high-redshift SFGs. The LBGs sample encapsulated 1182 galaxies, applying specific color criteria (Bouwens et al. 2015) to identify them within the parent SFGs sample.

Optically Dark/Faint Galaxies (OFGs): Defined by their intrinsic faintness in optical/near-IR wavelengths, yet bright at longer near-IR bands, with a total of 35 galaxies classified under this category. Using specific magnitude cuts (Xiao et al. 2023), this sample exposed a complementary selection of bright galaxies, missed by the LBG criteria.

3 Results

We explored the stellar and morphological characteristics of the parent sample of SFGs, LBGs, and OFGs. We find that while all galaxy samples share similar redshift distributions, OFGs are notably more massive and dust-attenuated. Morphologically, a distribution around smaller effective radii was observed in OFGs (Fig. 1).

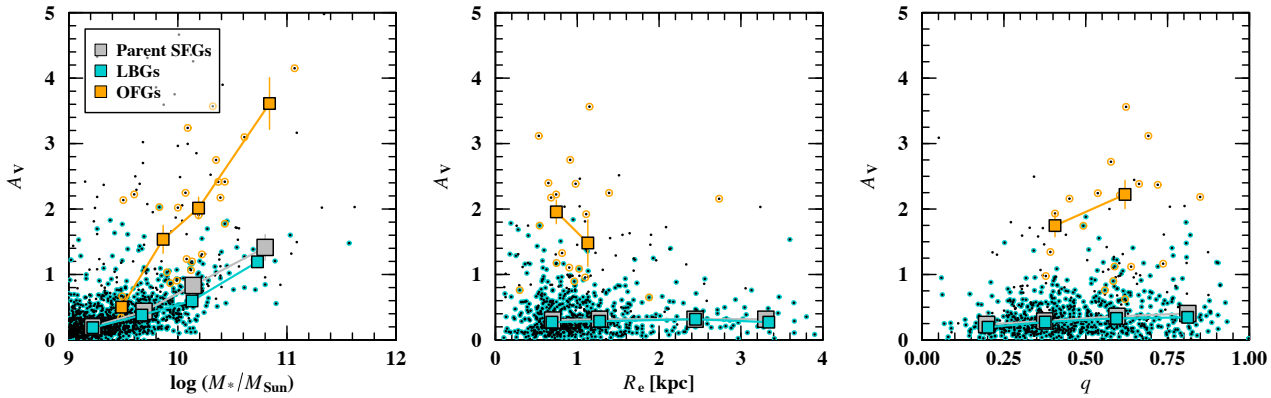

Fig. 1. From Gómez-Guijarro et al. (2023). Dust attenuation as a function of stellar mass, (circularized) effective radius, and axis ratio. Sliding medians for the different galaxy types shown in the legend are displayed with colored squares.

3.1 Drivers of dust attenuation

We investigated the impact of stellar mass and morphology on dust attenuation, particularly focusing on highly dust-attenuated galaxies like OFGs (Fig. 1). Stellar mass shows a correlation with dust attenuation in SFGs, establishing a general trend (see also e.g., Garn & Best 2010; Zahid et al. 2013; Pannella et al. 2015), with OFGs indicating a steeper trend towards a higher dust attenuation regime. This correlation stems from the mass-metallicity relation (e.g., Tremonti et al. 2004), where massive SFGs retain metals more efficiently, making them dustier compared to low mass SFGs. However, when it comes to morphology, the correlation is not as pronounced. In the case of OFGs, we find that the effective radii are generally smaller and associated with higher dust attenuation values, but no significant increase in dust attenuation is observed with lower axis ratios (edge-on galaxies). Our analysis reveals that at a common redshift and stellar mass, the $A_V > 1$ and OFGs samples are notably smaller than the parent sample of SFGs, $\sim 30\%$ smaller efective radius (Fig. 2).

The results highlight stellar mass as a key indicator of dust attenuation, while the effective radius and axis ratio do not exhibit a significant role, generally. However, among massive galaxies at similar redshifts, those with higher dust attenuation tend to have more compact stellar light profiles. To validate these observations, a Random Forest analysis was conducted (see e.g., Bluck et al. 2022, for a similar analysis). The Random Forest, a machine learning technique, aids in pinpointing the dominant parameter influencing a specified quantity, especially amidst inter-correlated parameters. This analysis was executed by segregating a target quantity and the associated features, further splitting them into training and testing samples for model training and validation respectively. Our investigation, utilizing a random forest regressor, aimed to identify the most predictive parameter of dust attenuation (A_V) among stellar mass (M_*), SFR, effective radius (R_e), and axis ratio (q). Stellar mass emerged as the most predictive parameter followed by SFR, aligning with our initial findings. Meanwhile, the morphological parameters effective radius and axis ratio did not stand out as strong predictors for dust attenuation, thereby reaffirming the observations made earlier (Fig. 2).

4 Discussion and conclusions

The findings of this work highlight the prominence of stellar mass in predicting dust attenuation. As stellar mass encapsulates a galaxy star formation history, and consequently its metal and dust composition, it plays a pivotal role in understanding dust attenuation. The data reveals that in addition to stellar mass, SFR also serves as a substantial predictor for dust attenuation.

When examining the role of orientation, it is observed that inclination holds minimal role in affecting dust attenuation at $z > 3$, close to a random variable, contrary to previous interpretations linking higher dust attenuation levels to edge-on disk galaxies (Nelson et al. 2023). The findings suggest a transition, where at such redshifts, dust attenuation is primarily governed by dust within dense star-forming regions as opposed to dust in the diffuse ISM, rendering inclination effects negligible (Lorenz et al. 2023).

Distinctly, a subset of galaxies dubbed OFGs, despite similar stellar mass, SFR, and redshift, exhibit fainter

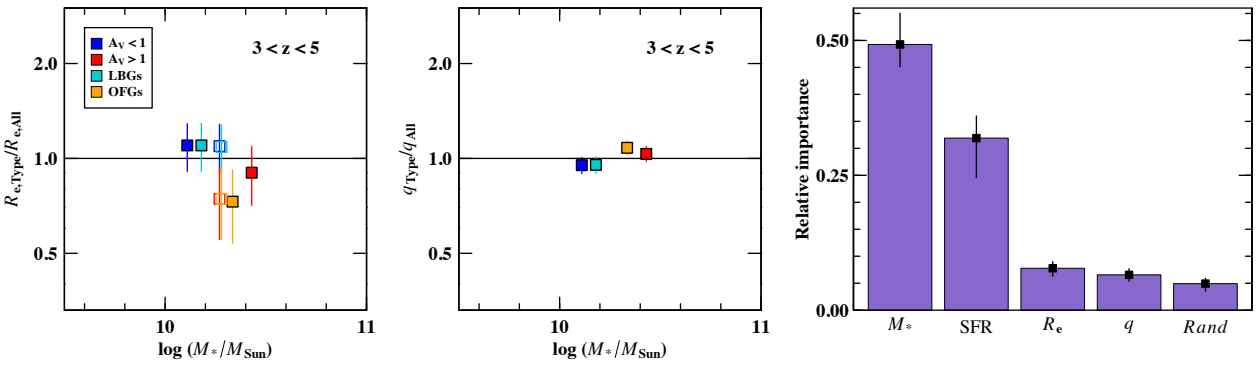

Fig. 2. From Gómez-Guijarro et al. (2023). **Left panel**: Ratio of the (circularized) effective radius for different galaxy types over those of the parent SFGs sample. Ratios after applying a correction to a common redshift and stellar mass are displayed with open squares. **Right panel**: Same as left panel for the axis ratio.

UV light, indicative of higher dust attenuation. The defining trait of these galaxies is their compact size, characterized by smaller effective radii when consider against the broader SFGs population. This compactness points to a denser distribution of their stellar profiles, which in turn, might aid in retaining metals and dust more efficiently. Moreover, the compactness of OFGs mirrors that of quiescent galaxies (QGs), suggesting a possible evolutionary linkage between the two. The condensed stellar light profiles of OFGs, coupled with their elevated SFR surface densities, echo a step towards the progressive buildup of compact QGs stellar profiles. This ties into broader galaxy evolution narratives (e.g., Barro et al. 2013; Toft et al. 2014; Gómez-Guijarro et al. 2018), hinting at the potential of OFGs serving as progenitors to massive compact QGs.

This work was carried out in collaboration with the CEERS team. CGG acknowledges support from CNES.

References

Barro, G., Faber, S. M., Pérez-González, P. G., et al. 2013, ApJ, 765, 104
Barrufet, L., Oesch, P. A., Weibel, A., et al. 2022, arXiv e-prints, arXiv:2207.14733
Bluck, A. F. L., Maiolino, R., Brownson, S., et al. 2022, A&A, 659, A160
Bouwens, R. J., Illingworth, G. D., Oesch, P. A., et al. 2015, ApJ, 803, 34
Finkelstein, S. L., Bagley, M. B., Arrabal Haro, P., et al. 2022, ApJ, 940, L55
Franco, M., Elbaz, D., Béthermin, M., et al. 2018, A&A, 620, A152
Garn, T. & Best, P. N. 2010, MNRAS, 409, 421
Gómez-Guijarro, C., Elbaz, D., Xiao, M., et al. 2022, A&A, 658, A43
Gómez-Guijarro, C., Magnelli, B., Elbaz, D., et al. 2023, A&A, 677, A34
Gómez-Guijarro, C., Toft, S., Karim, A., et al. 2018, ApJ, 856, 121
Lorenz, B., Kriek, M., Shapley, A. E., et al. 2023, arXiv e-prints, arXiv:2304.08521
Madau, P. & Dickinson, M. 2014, ARA&A, 52, 415
Nelson, E. J., Suess, K. A., Bezanson, R., et al. 2023, ApJ, 948, L18
Pannella, M., Elbaz, D., Daddi, E., et al. 2015, ApJ, 807, 141
Pérez-González, P. G., Barro, G., Annunziatella, M., et al. 2023, ApJ, 946, L16
Stefanon, M., Yan, H., Mobasher, B., et al. 2017, ApJS, 229, 32
Steidel, C. C., Giavalisco, M., Pettini, M., Dickinson, M., & Adelberger, K. L. 1996, ApJ, 462, L17
Toft, S., Smolčić, V., Magnelli, B., et al. 2014, ApJ, 782, 68
Tremonti, C. A., Heckman, T. M., Kauffmann, G., et al. 2004, ApJ, 613, 898
Wang, T., Schreiber, C., Elbaz, D., et al. 2019, Nature, 572, 211
Williams, R. J., Quadri, R. F., Franx, M., van Dokkum, P., & Labbé, I. 2009, ApJ, 691, 1879
Xiao, M. Y., Elbaz, D., Gómez-Guijarro, C., et al. 2023, A&A, 672, A18
Zahid, H. J., Yates, R. M., Kewley, L. J., & Kudritzki, R. P. 2013, ApJ, 763, 92

SF2A 2023
M. N'Diaye, A. Siebert, N. Lagarde, O. Venot, K. Baillié, M. Béthermin, E. Lagadec, J. Malzac, J. Richard (eds)

UNVEILING GALAXY EVOLUTION WITH THE COSMOS-WEB SURVEY

L. Paquereau[1], C. Laigle [1], H. J. McCracken [1] and M. Shuntov[2]

Abstract. Since the beginning of the observations in 2022, JWST has revealed the faintest and furthest galaxies ever observed. However, to push forward our understanding of early mass assembly and processes driving star formation efficiency, there is a need for wider extragalactic surveys, large enough to eliminate cosmic variance and probe the filamentary large-scale structures. The COSMOS-Web survey is the largest imaging program in JWST's first cycle of observations, with a contiguous coverage of 0.54 deg^2 in the COSMOS field. Thanks to its deep and high-resolution photometry in near and mid infrared and the combination of multiwavelength data available in COSMOS, it will provide a valuable resource for the study of the evolution of galaxies and their environments back to the universe's earliest epochs. We present an overview of this survey and discuss the creation process of the COSMOS-Web catalog, from the detection of sources in the images to the determination of galaxy properties such as their magnitude, redshift or stellar mass. We highlight the catalog's first results, including remarkable depth, redshift coverage and precision, surpassing those obtained by previous deep surveys of similar area. Furthermore, we demonstrate how this key resource can be used to investigate galaxy evolution, such as the study of galaxy clustering across the cosmic web.

Keywords: galaxy evolution, galaxy catalog, photometry, observations, galaxy clustering, galaxy environment

1 Introduction

One of the fundamental goals in galaxy evolution is to unravel the link between star formation and the environment of galaxies, back to the earliest epochs of the universe. To explore this connection, it becomes essential to investigate the influence of galaxy environment at various scales, ranging from dark matter halos hosting galaxies to the largest cosmic structures.

At the scale of the halo or smaller scales, galaxy growth is regulated by cold gas inflows and mergers, that can provide fuel for star formation. In the other hand, a spectrum of phenomena arises, such as feedback processes (AGN or stellar feedback) or ram pressure stripping, capable of inducing quenching of galaxies. At larger cosmic scales, it has become evident that not only do immediate galactic surroundings play a role over star formation, but also the filamentary cosmic web and the underlying dark matter density field has influence on galaxy evolution. These cosmic structures, which are the large-scale gas reservoir, can for example determine key parameters such as the accretion rate of galaxies.

Thus, the goal of our investigation is to answer this fundamental question: What is the role of the environment, spanning from the largest cosmic scales to the smallest galaxy neighborhood, in determining galaxy evolution up to the early universe? To answer these questions, the COSMOS-Web survey emerges as a valuable tool, enabling us to study a broad array of different galaxies and their environments at various scales.

2 The COSMOS-Web survey

2.1 Overview of the survey

COSMOS-Web is the largest extragalactic survey conducted during the first cycle of observations with JWST (Casey et al. 2023). It covers an expansive region of 0.5 square degrees situated within the well-known COSMOS

[1] Institut d'Astrophysique de Paris, UMR 7095, CNRS, and Sorbonne Universite, 98 bis boulevard Arago, 75014 Paris, France
[2] Cosmic Dawn Center (DAWN), and Niels Bohr Institute, University of Copenhagen, Jagtvej 128, 2200 Copenhagen, Denmark

© Société Française d'Astronomie et d'Astrophysique (SF2A) 2023

field. The survey operates across four NIRCam filters (F115W, F150W, F277W, F444W) in the near-infrared spectrum, alongside one MIRI filter (F770W) at longer wavelength. Thanks to prior observations in the COSMOS field by various telescopes, a wealth of multi-band data from HST or ground-based telescopes as HSC, UltraVISTA, and Spitzer is also available. This multi-wavelength dataset allows us to probe a diverse range of galaxies, including those at high redshift, quiescent or dusty galaxies. COSMOS-Web offers this unique combination of wide spatial coverage, high-resolution and deep infrared imaging, and multi-band resources.

Figure 1 shows the first observations conducted in January 2023, representing only 5% of the final area of the survey. Despite this limited coverage, we have already identified intriguing objects, including gravitational lenses and a large sample of galaxies at the highest redshifts (Franco et al. 2023; Mercier et al. 2023). This mosaic is already accessible to the public. Recently, in April, half of the survey field has been observed, while the remaining area is scheduled for December 2023.

It is worth noticing the significant contribution of MIRI data at 7.7 microns. Over 35% of the COSMOS-Web field is covered by MIRI observations, marking a notable advancement compared to prior mid-infrared surveys such as Spitzer IRAC observations. The depths in COSMOS-Web reaches impressive limits, with the 5σ depth of extended objects for NIRCam reaching approximately 28 magnitude (AB) and around 25 magnitude for MIRI.

The COSMOS-Web survey is driven by several primary scientific objectives. Firstly, it aims to detect and study galaxies from the epoch of reionization and map the large-scale structure during the Universe's first billion years. Additionally, the wide and multi-band coverage (including optical/NIR data from on-ground facilities) of the survey allows to identify and explore the characteristics of rare massive quiescent galaxies, and constrain their star formation history. Furthermore, the survey seeks to investigate the relationship between galaxy evolution and dark matter halos thanks to the statistical power offered by its large galaxy sample.

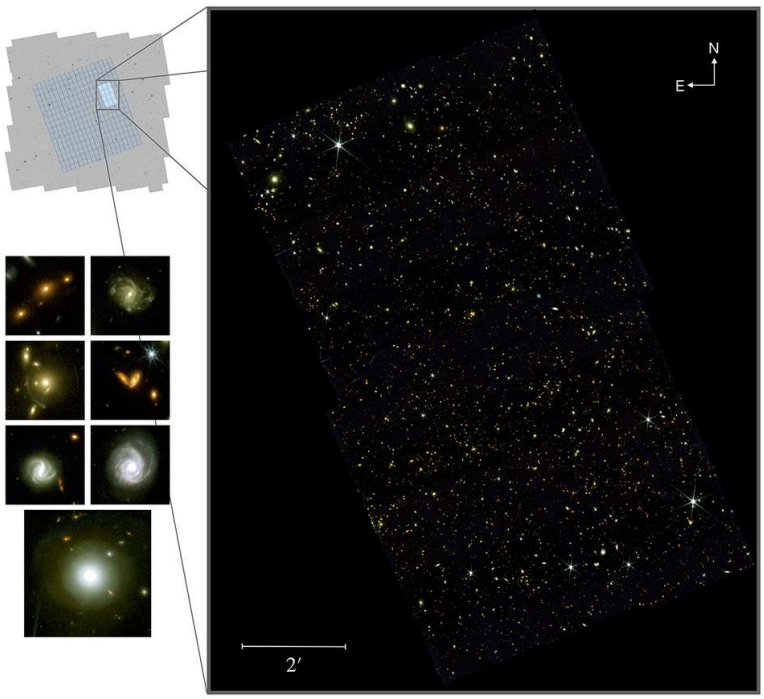

Fig. 1. COSMOS-Web first mosaic of NIRCam images, representing 5% of the total intended survey area, observed in January 2023. Figure from Casey et al. (2023).

2.2 Building COSMOS-Web catalogs

In COSMOS-Web, a significant challenge to create photometric catalogs arises from the necessity to merge high-resolution data from JWST with low-resolution data from ground-based telescopes within the COSMOS field. This implies dealing with varying PSFs and resolutions across the datasets, making it impractical to

consistently extract photometric measurements as typically done in previous studies or in JWST surveys with a wide range of filters. To overcome this challenge, we use a model-fitting code named `SourceXtractor++`, based upon the well-known detection algorithm `SExtractor`. This approach begins by the initial detection of all sources within the NIRCam images. Then, a morphological model is fitted to each source across the wavelength bands, and fluxes will be measured based on these models.

In addition to the model-fitting catalog, we also produce a more conventional catalog based on `SExtractor` aperture photometry on PSF-homogenized images. This catalog, created on only JWST and HST data, serves both as validating the SE++ catalog and as a complementary alternative for accurate color measurements or the study of high-redshift sources that may be more complicated to model.

Following detection and photometry procedures, we employ SED fitting codes, `LePhare` and `Eazy`, to derive photometric redshift estimates. Our analysis indicates an average accuracy of approximately 3%. For the determination of galaxy physical parameters, including stellar mass, star formation rate and others, the code CIGALE using non-parametric SFH is employed. A comprehensive description of these catalogs will be provided in a forthcoming paper by Shuntov et al. (in prep.), and these catalogs will be made accessible to the scientific community within the year.

3 First scientific results with COSMOS-Web

3.1 Galaxy clustering

We present a preliminary analysis of galaxy clustering in the COSMOS-Web field, that will be extended and described in the forthcoming paper Paquereau et al. (in prep.). Galaxy clustering is a measurement of the number of galaxy pairs in excess, compared to a random distribution, across the observed field. This is a valuable tool for constraining various aspects of galaxy evolution and even cosmological parameters. For instance, it helps us inferring dark matter halos masses and investigating how galaxy environment influences star formation activity.

In essence, clustering is the two-point correlation function between galaxy positions. In our preliminary analysis, we used the Landy-Szalay estimator, which involves comparing our observed galaxy catalog with a randomly distributed one. It is important to note that the measurements presented here are based on the initial 50% of the total survey area, but it still offers a strong demonstration of the potential of JWST data in this context.

Figure 2 presents preliminary results, with clustering measurements from COSMOS-Web and previous result from the catalog COSMOS2020 before the inclusion of JWST data, in one redshift bin. COSMOS-Web measurements agrees well with previous work, but a notable achievement here is our ability to measure clustering at exceptionally small scales, smaller than what was previously attainable. These scales are much smaller than the typical size of dark matter halos that host galaxies, meaning that this high-resolution data from JWST enable the study of how galaxies are distributed within a single halo and how they connect.

Our next steps involve exploring which types of galaxies or populations are found within these halos and what their physical properties indicate, as their star formation rate or morphology. For example, the second panel in Figure 2 depicts the difference in clustering between quiescent and star-forming galaxies, suggesting that the environment of galaxies has an impact on star formation. Additionally, we aim to identify galaxy satellites and examine the processes that lead to their quenching, to answer how their environment influences their evolution.

3.2 Other contributions

Furthermore, it should be noted that several papers based on COSMOS-Web observations have already been submitted at the time of this presentation, while more are currently in preparation. Two of these forthcoming papers will delve into the study of dusty galaxies. For instance, the work conducted by (Akins et al. 2023) is about the discovery of two exceptionally massive, compact, and dust-obscured galaxies around redshift 8. This discovery has the potential to significantly advance our understanding of dust buildup and star formation processes in the early universe.

Another upcoming paper will present a sample of EoR bright galaxies observed within the COSMOS-Web survey (Franco et al. 2023). According to preliminary findings, it suggests that the stellar populations of these galaxies were formed within an already metal-enriched environment, even at the higher redshifts.

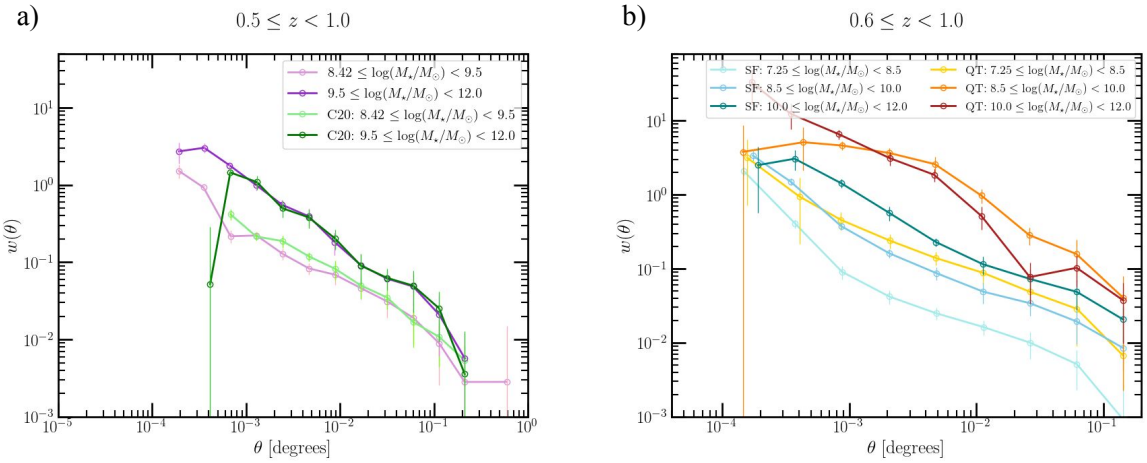

Fig. 2. Preliminary clustering results from half of the COSMOS-Web survey, in one redshift bin and different stellar mass bins. Panel (a) shows clustering of all COSMOS-Web galaxies in purple, compared to the COSMOS2020 catalog's measurements (before JWST data), in the same area, in green. The second panel (b) shows the variations in clustering for star-forming galaxies (noted SF) and quiescent galaxies (QT) in COSMOS-Web.

4 Conclusions

In summary, our study focuses on the link between the environment and galaxy evolution, spanning from the scales of dark matter halos to the largest cosmic web structures. We explored this connection using the COSMOS-Web survey, which is the largest extragalactic survey in the first cycle of observations of JWST.

Our preliminary findings indicate that COSMOS-Web offers unprecedented opportunities for studying galaxy clustering, at scales smaller than typical dark matter halo sizes. This high-resolution data allows us to investigation of how galaxies are connected within a single halo, as well as studying the influence of large cosmic web structures on star formation. Moving forward, our research will expand to explore the types of galaxies found within these halos, their morphologies or star formation rate, and the identification of galaxy satellites. We aim to uncover the processes that lead to the quenching of satellite galaxies and how their environment at various scales influences their evolution.

Furthermore, COSMOS-Web has already generated significant scientific interest, with several papers submitted and more in preparation. First discoveries include the study of massive dust-obscured galaxies at high redshifts, or samples of EoR bright galaxies. These findings mark just the beginning of the exploration of COSMOS-Web observations, with a lot more discoveries yet to come.

References

Akins, H. B., Casey, C. M., Allen, N., et al. 2023
Casey, C. M., Kartaltepe, J. S., Drakos, N. E., et al. 2023
Franco, M., Akins, H. B., Casey, C. M., et al. 2023
Mercier, W., Shuntov, M., et al. 2023
Paquereau, L. et al. in prep.
Shuntov, M., Paquereau, L., et al. in prep.

SF2A 2023
M. N'Diaye, A. Siebert, N. Lagarde, O. Venot, K. Baillié, M. Béthermin, E. Lagadec, J. Malzac, J. Richard (eds)

PROBING THE ATTENUATION CURVE OF 1 < Z < 3 GALAXIES WITH THE JWST/CEERS PROGRAM

L.-M. Seillé[1], V. Buat[1,2], V. Fernandez[3] and the CEERs team

Abstract. Stellar emission and hydrogen recombination lines reflect the star formation process at very different timescales and their combination should allow to get the star formation history of galaxies. However dust attenuation hampers any simple comparison because of the variable shape of dust attenuation curves and the differential amount of attenuation of the continuum and line emission. We aim to determine the respective amount of attenuation and the attenuation law at work in the combined ISM and birth clouds inspired by the original Charlot & Fall (2000) recipe. We select 14, $1 < z < 3$ galaxies observed by the CEERS/JWST program and we combine NIRCam photometry with Paschen and Balmer emission lines from NIRSpec. CFHT, HST and Spitzer measurements are added to obtain a multi-wavelength dataset. We will show that we are able to simultaneously fit the spectroscopic and photometric data of these objects using a new method based on equivalent widths (EWs) and we calculate consistent dust attenuation parameters.

Keywords: galaxies, ISM, SED fitting, JWST, EWs

1 Introduction

Hydrogen recombination lines provide critical constraints on the star-formation rates (SFRs) and dust reddening towards the ionised regions of star-forming galaxies. The lines are less extinguished than the far-UV continuum, and can even be measured from the ground with high signal-to-noise (SNR) for individual star-forming objects up to redshift $z \sim 2.6$. Multi-object near-IR spectrographs (e.g., Keck/MOSFIRE, VLT/KMOS) and space-based instruments (e.g., HST/WFC3 grism) provided scientists with hydrogen lines and nebular reddening measurements for a large number of sources up to $z \sim 2.6$ (e.g., Reddy et al. (2020), Battisti et al. (2022)).

On average, the nebular reddening exceeds that of the stellar continuum and these differences are usually attributed to higher dust column densities located around young massive stars which are still embedded in their birth molecular clouds as shown in Charlot & Fall (2000). The recently-launched James Webb Space Telescope (JWST) and its NIRSpec instrument now offer the wavelength coverage and sensitivity to detect Paschen lines. Paschen lines can track the SFR more closely as they are less affected by dust attenuation than the Balmer lines.Combining Paschen and Balmer lines can provide also help on constraining the nebular reddening and the associated characteristics of the ISM.

2 Sample selection

Our sample of 14 galaxies includes measurements over the full NIRCam wavelength range in the F115W, F150W, F200W, F277W, F356W, F410M, and F444W filters, HST/CANDELS ACS_WFC3 F606W and F814W bands, CFHT/Megacam u* and g'. Some objects have additional detections in the far-infrared which are also used when avalaible. To be able to probe the shape of the attenuation curve, Balmer and Paschen lines observed with NIRSpec gratings are necessary as they probe vastly different stellar populations so we require our objects to have at least one Balmer and one Paschen line with an equivalent width (EW) $S/N \geq 5$ (other Balmer and Paschen lines are allowed a $SNR \geq 3$). Finally, we exclude all objects hosting a potential active galactic nucleus (AGN) by checking their [NII]λ658/Hα.

[1] Aix-Marseille Univ, CNRS, CNES, LAM, Marseille, France
[2] Institut Universitaire de France (IUF)
[3] University of Michigan (Schmidt Futures), USA

© Société Française d'Astronomie et d'Astrophysique (SF2A) 2023

ID	Redshift	log NII(658)/Hα	Usable line EWs
23542	1.277	-0.78	**Hα, Hβ, Paα, Paβ, Paγ**
5113	1.402	-0.79	**Hα, Paα**
8736	1.553	-0.66	**Hα, Hβ,** Hγ, **Paα,** Paβ
8515	1.567	-0.77	**Hα, Hβ, Hγ, Hδ, Paα, Paβ,** Paγ
5430	1.676	-0.31	**Hα, Hβ, Paβ** , Paγ
10293	1.676	-0.53	**Hα, Hβ, Paα**
6563	1.699	-0.63	**Hα, Hβ, Hγ, Paα, Paβ, Paγ**
5409	1.699	×	**Hα, Hβ, Paα, Paβ**
5300	2.136	×	**Hα, Hβ, Hγ, Hδ, Paβ, Paγ**
3788	2.295	-1.23	**Hα, Hβ, Hγ, Hδ, Paβ, Paγ**
8588	2.336	-0.35	**Hα, Hβ,** Hγ, **Paβ, Paγ**
8710	2.337	-1.05	**Hα, Hβ, Hγ, Paγ**
16991	2.540	-1.28	**Hα,** Hβ, **Hδ,** Paβ, **Paγ**
18294	2.635	×	**Hα, Hβ,** Hγ, **Paβ**

Table 1. Characteristics of the objects used for the study. The spectroscopic redshifts are the mean of the estimated spectroscopic redshift of each line. A cross indicates an absence of [NII]λ(658) detection. Available lines with an EW S/N ≥ 5 are in bold.

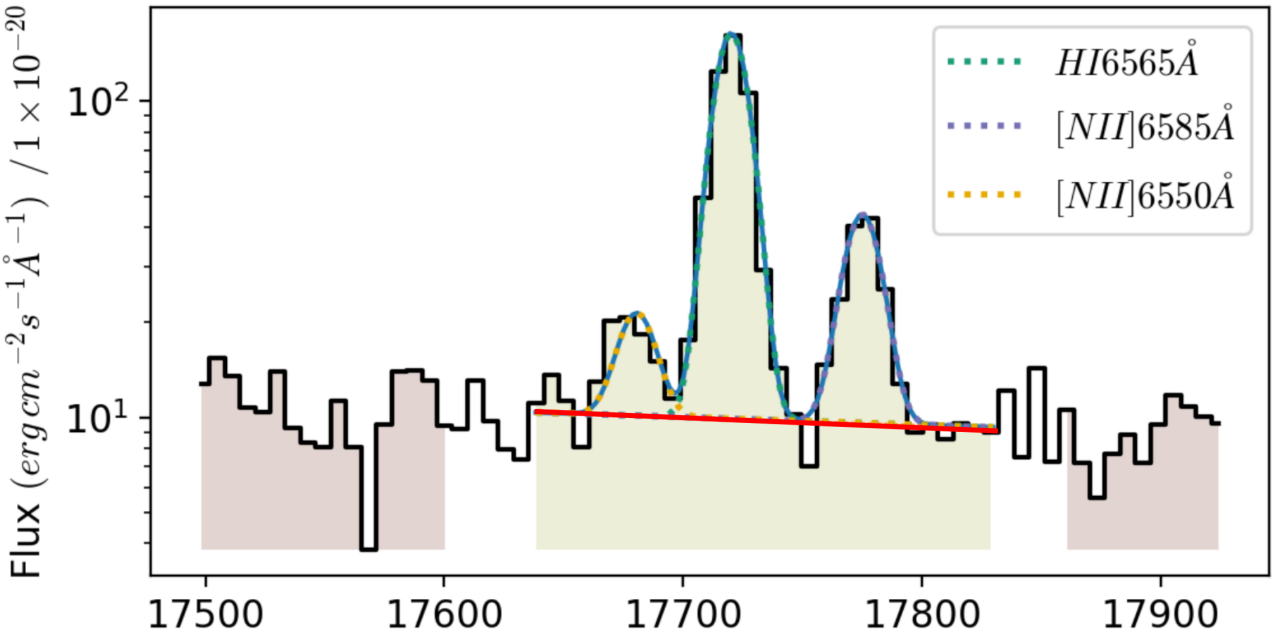

Fig. 1. An example of the new computation method for the [NII] doublet and Hα line. Continua regions are coloured in pink with their linear fit in red while line regions are in green. Note that we can easily deblend all three lines with this computation. Credit to V. Fernandez for the plot.

3 Spectral energy distribution fitting

In this work, we are fitting photometric data and EWs at the same time using the the modelling software CIGALE. We developped a new SED fitting module to reproduce the exact measurements of the EWs made by the CEERs team. The line fluxes are measured using the beta release of LiMe by Fernández et al. (2023). The reported flux uncertainty comes from the standard error definition of the least-squares trust-region method. This uncertainty is propagated to the equivalent width calculation. In this computation, the linear continuum flux and its standard deviation, is derived from two adjacent continua bands. These continua regions are manually adjusted for every line, to guarantee a representative linear continuum measurement and to avoid artefacts (see Fig. 1). With this method, non-symmetrical lines are now accurately modelled and the continuum can be

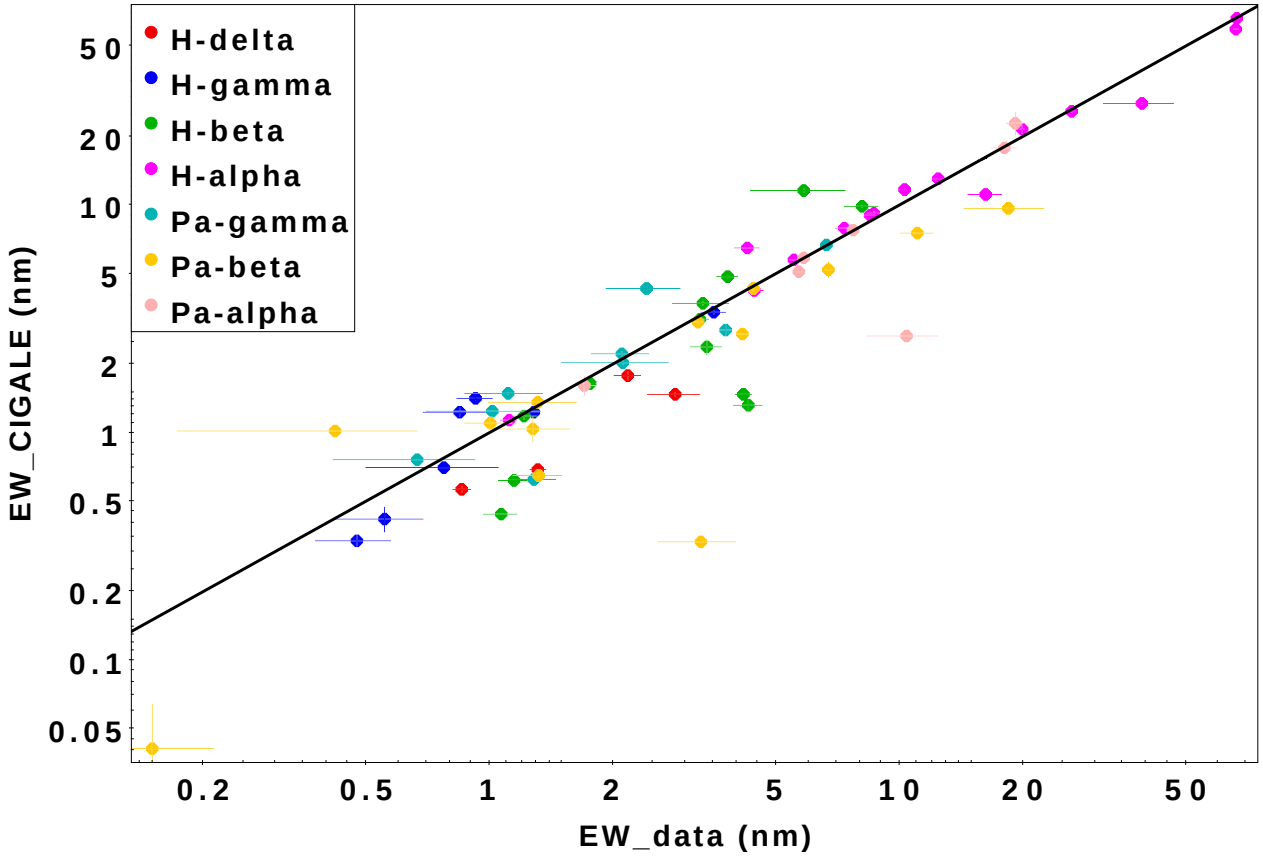

Fig. 2. Result of the fitting of the EWs. Data are on the x-axis while the fit of the EW made by CIGALE is on the y-axis. The black line is the 1:1 relation.

taken anywhere, thus making sure that absorption and other emission lines are avoided. The LiMe fittings for these spectra can be found at the interactive repository at `https://ceers-data.streamlit.app/`, using the corresponding Object ID.

4 Results of SED fitting

As can be seen in Fig. 2, the new method used to fit the EWs in CIGALE is very powerful at reproducing the data of our 14 galaxies. We notice that the fainter a line gets, the more difficult it is to fit it accurately. We can also use CIGALE to get the total attenuation curve of an object from the UV to the near-infrared. We show in Fig. 3 that we are able to reconstruct this curve and different galaxies are exhibiting different dust attenuation parameters. We are seeing a spread in the UV but no extreme values for the power law exponent. However, there is a clear separation between steep and flat curves in the IR part of the spectrum.

5 Conclusions

We are studying 14 objects between 1 < z < 3 observed by JWST to probe the shape of the total attenuation curve. To do this, we implemented a new EWs fitting method in CIGALE to reproduce exactly the line measurements and computations done by the CEERs team. With this method, we obtain an overall very good agreement between the fits and the data. We are able to reconstruct the total attenuation curve of every object in our sample and also to get the differential amount of attenuation between young and old stars. However, we still need to address the possible attenuation parameters degeneracy.

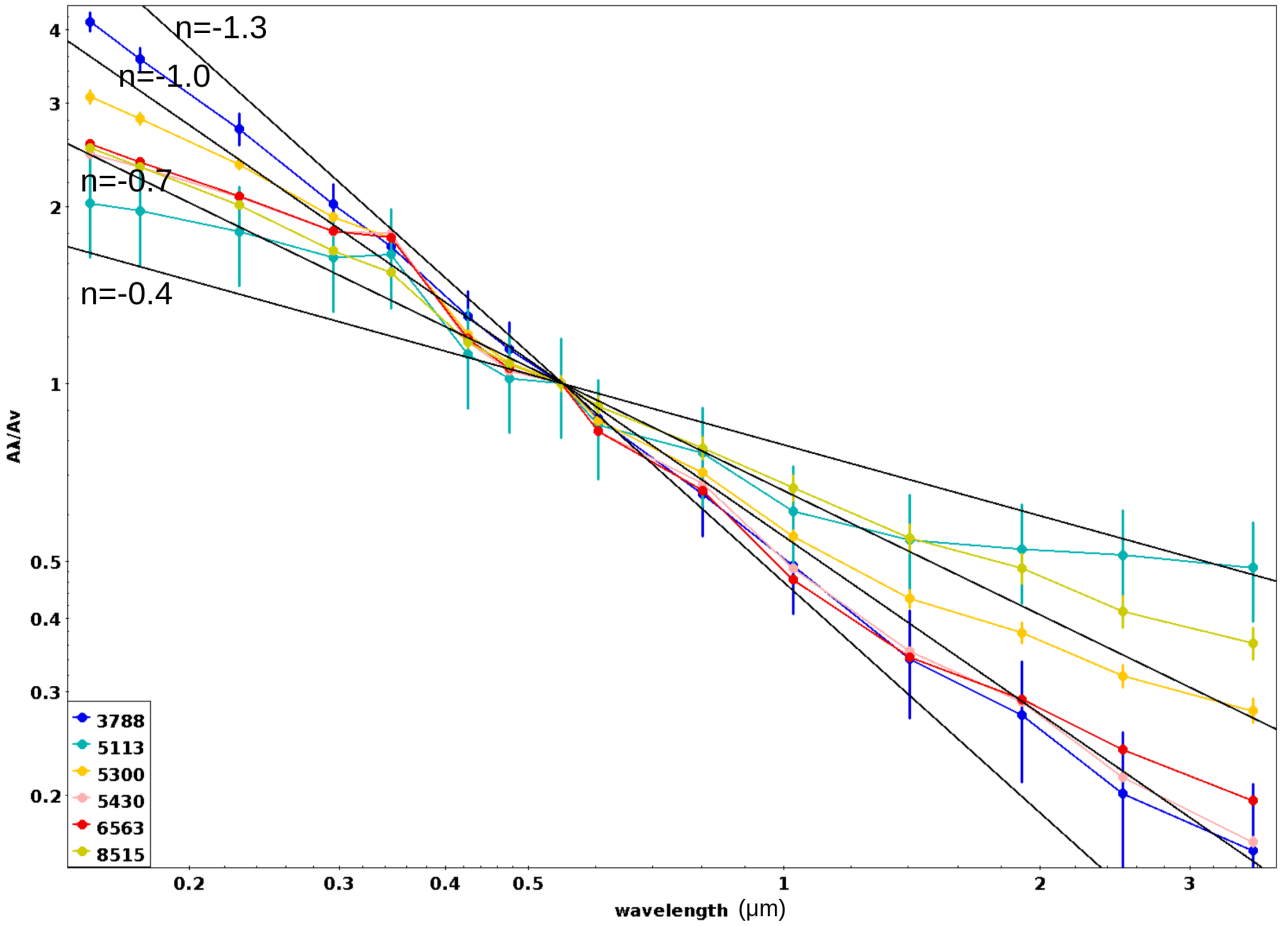

Fig. 3. Examples of total attenuation curves from objects in our sample compared to power laws with varying exponents in black.

References

Battisti, A. J., Bagley, M. B., Baronchelli, I., et al. 2022, MNRAS, 513, 4431

Charlot, S. & Fall, S. M. 2000, ApJ, 539, 718

Fernández, V., Amorín, R., Sanchez-Janssen, R., del Valle-Espinosa, M. G., & Papaderos, P. 2023, MNRAS, 520, 3576

Reddy, N. A., Shapley, A. E., Kriek, M., et al. 2020, ApJ, 902, 123

Session S15

PNGRAM Géodésie Spatiale

SF2A 2023
M. N'Diaye, A. Siebert, N. Lagarde, O. Venot, K. Baillié, M. Béthermin, E. Lagadec, J. Malzac, J. Richard (eds)

MODELING THE LUNAR TIDES IN INPOP

D. Baguet[1], N. Rambaux[1], A. Fienga[2], A. Briaud[2], H. Hussmann[3], M. Gastineau[1], X. Hu[4], J. Laskar[1], A. Mémin[2] and A. Stark[3]

Abstract. The Moon is affected by tides, mainly exerted by the Earth and the Sun, that deforms its shape. Studies of its tide through its rotation allows to probe its inner structure. In current planetary and lunar ephemerides, the lunar visco-elastic tides are computed with a time delay model in order to take into account the phase lag of the tidal bulge. The time-delay is introduced in the lunar moment of inertia through the distortion coefficients of the harmonics of degree two of the gravitational potential. We use an alternative method in the INPOP ephemerides which consists in formulating the distortion coefficients with the Fourier series introduced by Williams & Boggs (2015). This formulation allows to introduce any variation of the Love numbers with respect to the period of the tidal forcing. We show that we need to have around five hundred terms in the Fourier series in order to reach an amplitude of the residual caused by the truncation of the series at the level of the observational accuracy of Lunar Laser Ranging data.

Keywords: Moon, tides, ephemerides, INPOP

1 Introduction

Since the start of the Artemis program, interest in lunar studies has been renewed. The Lunar Laser Ranging (LLR) experiment measures the Earth-Moon distance with an accuracy of around two centimeters and the Moon's librations at a one milliarcsecond accuracy (Viswanathan et al. 2018). This allows to provide a refined description of the tidal deformation of the Moon. The ephemeris INPOP of the Paris Observatory is a joint numerical integration of the orbits of the Moon and the planets as well as the lunar rotation, which is fitted to the LLR data. Studying the lunar tides allows us to probe the internal composition of the Moon. For example, recent results from tidal constraints highlight the presence of a solid inner core (Briaud et al. 2023b). The tidal response depends on the density and the rheology of the layers, and on the dissipation due to the viscosity of the lunar interior (e.g. Williams & Boggs (2015), Briaud et al. (2023a)). The tidal Love number k_2 and the dissipation inside the Moon depend on the period of the tidal forcing.

In INPOP the tidal deformation accounts for a k_2 independent of the excitation frequency and a unique time delay (Viswanathan et al. 2018). The formulation in Fourier series of the distortion coefficients (also called variation of the Stokes coefficients) by Williams & Boggs (2015) allows us to describe the tidal gravitational variation by taking into account the frequency dependency. We introduce the distortion coefficients as Fourier series in order to test the impact of the variation of the Love number and of the dissipation on libration measurements.

2 Method

In the case of an elastic lunar tides, the deformation of the Moon is instantaneous and the tidal bulge is oriented in the Earth-Moon direction. However, in the case of the visco-elastic deformation, the tidal bulge is shifted with respect to the Earth-Moon direction. In order to take into account this shift, in current ephemerides, the distortion coefficients are computed with the time-delay model. The tidal Love number k_2 quantifies the tidal deformation of the gravitational potential at harmonics of degree 2. In the visco-elastic case, the tidal Love number is complex and noted k_2^*. Its real and imaginary parts can be written

$$Re(k_2^*) = |k_2^*| \sqrt{1 - 1/Q^2}, \tag{2.1}$$

[1] IMCCE/Observatoire de Paris, Sorbonne Université, Paris, France
[2] AstroGéo/GéoAzur - Observatoire de la Côte d'Azur, Valbonne, France
[3] Institute of Planetary Research, German Aerospace Center (DLR), Berlin, Germany
[4] Institute of Geodesy and Geoinformation Science, Technical University Berlin, Berlin, Germany

© Société Française d'Astronomie et d'Astrophysique (SF2A) 2023

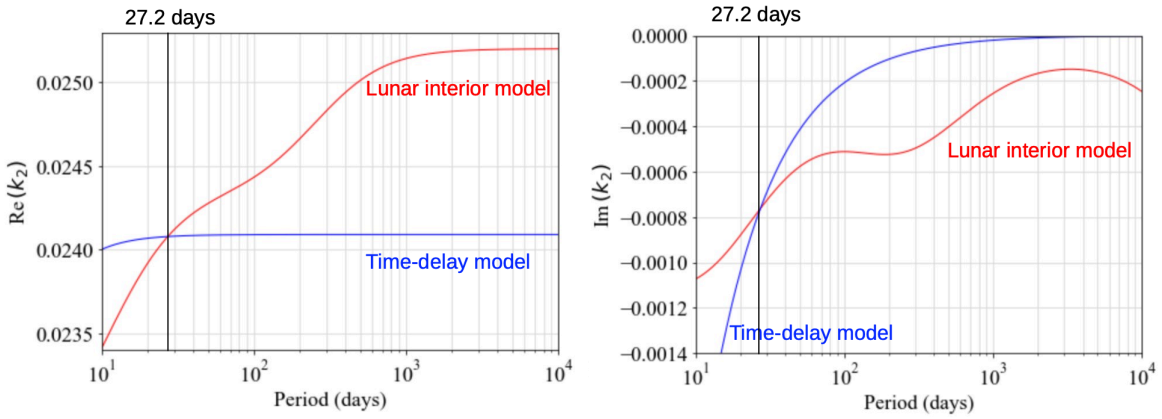

Fig. 1. Left: Variation of the real part of the tidal Love number with respect to the period of the tidal forcing. **Right:** Variation of the imaginary part of the tidal Love number with respect to the period of the tidal forcing..

$$Im(k_2^*) = -\frac{|k_2^*|}{Q}, \tag{2.2}$$

where Q is a dissipation factor. In the time-delay model, the dissipation factor is linked to the time-delay parameter through the relation

$$Q = \frac{1}{\sin(f\tau)}, \tag{2.3}$$

where f is the frequency of the tidal forcing.

The figure 1 shows the variation of the Love number with respect to the period of the tidal forcing. The left and right figures show respectively the variation of the real part and of the imaginary part. The blue curves show the variation for the time-delay model and the red curves show the variation from a solution provided by a lunar interior model computed by Briaud et al. (2023a). The time delay model does not allow to reproduce a Love number variation similar as in a solution from a lunar interior model. The time-delay model allows to have a realistic value of the Love number only for the dominant terms near 27 days.

The tidal contribution in the moment of inertial I_{tides} is related to the gravitational potential through the relation :

$$I_{tides} = MR^2 \begin{pmatrix} \frac{1}{3}\Delta C_{20} - 2\Delta C_{22} & -2\Delta S_{22} & -\Delta C_{21} \\ -2\Delta S_{22} & \frac{1}{3}\Delta C_{20} + 2\Delta C_{22} & -\Delta S_{21} \\ -\Delta C_{21} & -\Delta S_{21} & -\frac{2}{3}\Delta C_{20} \end{pmatrix} \tag{2.4}$$

where ΔC_{2m} and ΔS_{2m} (with $m = 0$, 1 or 2), are the distortion coefficients of the gravitational potential for the harmonics of degree two, M is the mass of the Moon and R its radius. Williams & Boggs (2015) provided a Fourier series formulation of the distortion coefficients :

$$\Delta C_{2m}(t) = \sum_q C_{2mq} \left(Re\{k_2^*(P_q)\} \cos\zeta_q(t) - Im\{k_2^*(P_q)\} \sin\zeta_q(t) \right), \tag{2.5}$$

$$\Delta S_{2m}(t) = \sum_q S_{2mq} \left(Re\{k_2^*(P_q)\} \cos\zeta_q(t) - Im\{k_2^*(P_q)\} \sin\zeta_q(t) \right). \tag{2.6}$$

The advantage of such a formulation is that it allows to separate the different periods of the tidal forcing and to associate for each term its associated Love number.

3 Results

Figure 2 shows the residual for the distance to the retroreflector Apollo 11 (A11) between the solution of INPOP19a and the solution of the version of INPOP with the distortion coefficients computed in Fourier series. The Fourier series contain the terms presented in Williams & Boggs (2015). The amplitude of the residual reach two meters, which is well above the observational accuracy of two centimeters provided by the LLR data.

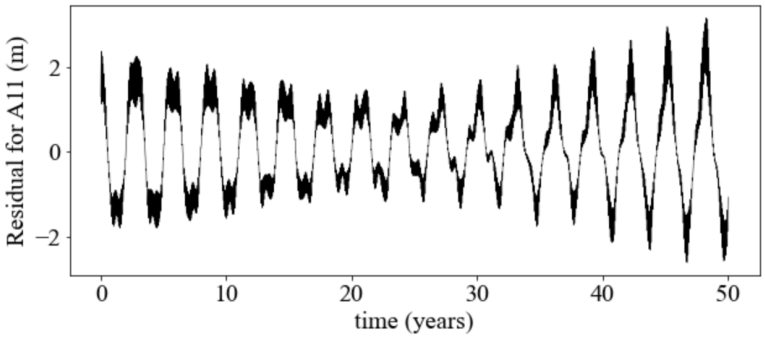

Fig. 2. Residual of the distance to the retroreflector A11 in the case where the Fourier series contain the termes of Williams & Boggs (2015).

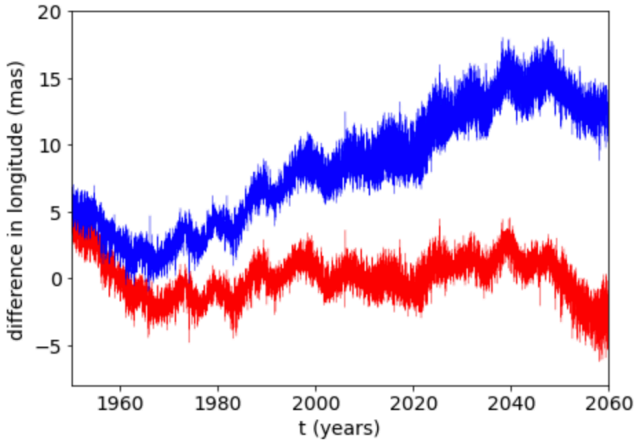

Fig. 3. Residual of the longitude of the Moon in spherical coordinates. The blue and red curves are for the cases with the secular parameters fitted respectively to DE405 and INPOP19a.

The terms of the series computed by Williams & Boggs (2015) are based on the ephemerides DE of JPL. We computed the terms of the series based on the solution of INPOP19a. In order to do so, we used the Paris Lunar Ephemeris (ELP) which is a semi-analytical representation of the lunar orbit. The last version of ELP is called ELP/MPP02 and has been fitted to DE405 (Chapront & Francou 2003). We fit the secular parameters of the Moon of ELP to the solution of INPOP19a. Figure 3 shows the residual of the longitude of the Moon in spherical coordinates between the solution of INPOP19a and the solution of ELP. The slope of the residual for the case of ELP fitted to DE405 is eliminated thanks to the fit of the secular parameters. However, the difference induced on the distance to the retroreflector by this latter solution with respect to the solution with the series of Williams & Boggs (2015) is only at the submillimeter level.

We shown that the amplitude of the residual in figure 2 is mainly due to the truncation of the series. Figure 4 shows the residual for different cases with different number of terms in the series. We need to include around five hundred terms in the Fourier series of each distortion coefficient in order to have a residual on the distance to the retroreflectors that is at the level of the accuracy of the Lunar Laser ranging data.

Now that we have reduced the residual due to the truncation of the series, we can introduce the frequency variation of the Love number according to a solution from a lunar interior model. Figure 5 shows that the effect on the proper rotation of the Moon introduced by the variation of the Love number according to a solution from a lunar interior model is much more important than the effect of the truncation of the Fourier series. The terms at 206 days, 365 days and 1095 days are in particular excited because of the difference of their associated Love number.

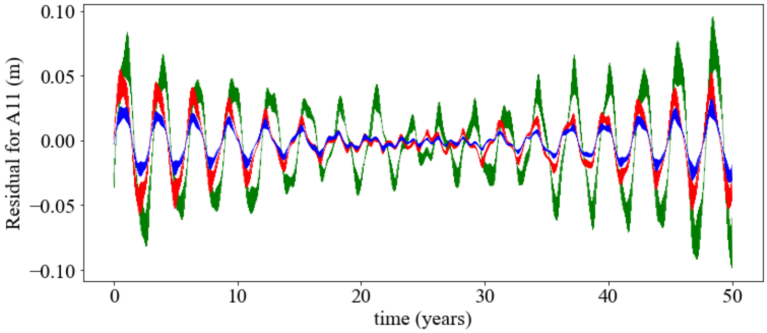

Fig. 4. Residual of the distance to the retroreflector A11. The green, red and blue curves are respectively for the cases with one hundred terms, two hundred terms and five hundred terms.

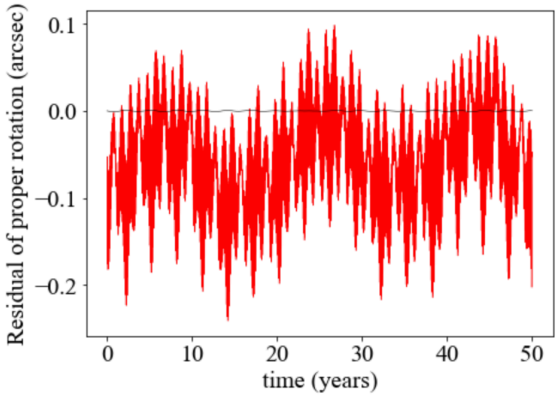

Fig. 5. The black curve shows the residual only due to the effect of the truncation of the Fourier series and the red curve shows the residual due to the effect of the variation of the complex tidal Love number according to a solution from a lunar interior model

4 Conclusions

We introduced in the ephemerides INPOP, the formulation in Fourier series of the distortion coefficients of Williams & Boggs (2015). We have fitted secular parameters of ELP to the solution of INPOP19a. From this solution of ELP fitted to INPOP19a, we have computed the terms of the Fourier series of the distortion coefficients. We find that the difference induced by this last solution of the series with respect to those of Williams & Boggs (2015) is at the submillimeter level and is negligible. We shown that we need to add up to around five hundred terms in the series in order to reduce the residual of the distance to the retroreflectors at the level of the observational accuracy. We are able to introduce the Love number variation with respect to the period of the tidal forcing according to lunar interior models. In future work we will test several solutions of Love number variation provided by interior models in order to test which models are abe to absorb the residuals.

This work has been funded by the French National Research Agency (ANR), France and by the German Research Foundation (DFG), Germany joined project ANR-19-CE31-0026.

References

Briaud, A., Fienga, A., Melini, D., et al. 2023a, Icarus, 394, 115426

Briaud, A., Ganino, C., Fienga, A., Mémin, A., & Rambaux, N. 2023b, Nature, 617, 743

Chapront, J. & Francou, G. 2003, A&A, 404, 735

Viswanathan, V., Fienga, A., Minazzoli, O., et al. 2018, MNRAS, 476, 1877

Williams, J. G. & Boggs, D. H. 2015, Journal of Geophysical Research (Planets), 120, 689

SF2A 2023
M. N'Diaye, A. Siebert, N. Lagarde, O. Venot, K. Baillié, M. Béthermin, E. Lagadec, J. Malzac, J. Richard (eds)

NAROO PROGRAM : ANALYSIS OF USNO GALILEAN OBSERVATIONS 1967-1998

V. Robert[1,2], D. Pascu[3], J.-E. Arlot[1] and V. Lainey[1]

Abstract. The New Astrometric Reduction of Old Observations (NAROO) program is dedicated to the measurement of astrophotographic plates and the analysis of old observations for scientific purposes. One of the main objectives is to provide accurate positional measurements of planets and satellites to improve our knowledge of their orbits and dynamics, and to infer the accuracy of the planet and satellite ephemerides. We digitzed 553 astronegatives of the Galilean satellites taken with the McCormick and the U.S. Naval Observatory 26-inch refractors from 1967 to 1998, resulting in 2650 individual observations. We measured and reduced these observations through an optimal process that includes image, instrumental, and spherical corrections using Gaia-DR3 catalogue to provide the most accurate equatorial (RA, Dec) ICRS positions. We compared the observed positions of the satellites with the theoretical positions from different planetary ephemerides and satellite ephemerides. 4819 positions of the Galilean satellites have been determined with an accuracy of 55 mas or 160 km at Jupiter, indicating that the limits of the photographic techniques were now reached.

Keywords: Astrometry - Ephemerides - Instrumentation: high angular resolution

1 Introduction

The New Astrometric Reduction of Old Observations (NAROO) facilities have been built as a unique center dedicated to the measurement of astrophotographic plates and the analysis of old observations for scientific purposes (Robert et al. 2021). The framework is the study of the dynamics of Solar System bodies, in particular, that require astrometric observations sampled over a long time span to quantify the long period terms which may help to analyze the evolution of the motion. One of the main objectives of the NAROO program is to provide accurate positional measurements of planets and satellites to improve our knowledge of their orbits and dynamics, and to infer the accuracy of the planet and satellite ephemerides.

We obtained the large photographic plate archive of the Galilean satellites taken at the U. S. Naval Observatory (USNO) from 1967 to 1998 for remeasurement and reanalysis. In fact, most of these plates had been measured with the USNO automatic StarScan measuring machine (Zacharias et al. 2008), reduced by the trail/scale scheme (Pascu 1977) and used by Jet Propulsion Lab (JPL) for the navigation of the Voyager and Galileo space probes to successful reconnaissance with the Jovian system. The expectation was that the astrometric positions of the planets, as well as the Galilean satellites, could now be obtained to the absolute limits of the photographic technique.

2 Measurement and reduction

We selected 553 photographic plates to be transmitted at Meudon and digitized with the NAROO machine. Each plate contains four to six exposures shifted in the declination direction. The exposure times of the photographic plates are 20-60 s. The field of view is 57 arcmin on the x-axis and 43 arcmin on the y-axis. Figure 1 shows the center of the digitized (positive) USNO Galilean plate No. 21014, which is a typical digitized image. Five 20 s exposures of the Jovian system were taken with the USNO 26-inch refractor on 18 June 1994. Non visible

[1] IMCCE, Observatoire de Paris, PSL Research University, CNRS UMR 8028, Sorbonne Universités, UPMC, Univ. Lille 1, 77 avenue Denfert- Rochereau, 75014 Paris, France
[2] Institut Polytechnique des Sciences Avancées IPSA, 63 bis Boulevard de Brandebourg, 94200 Ivry-sur-Seine, France
[3] United States Naval Observatory USNO (retired), 3458 Massachusetts Ave NW, Washington, DC 20392, USA

© Société Française d'Astronomie et d'Astrophysique (SF2A) 2023

by eye, the small special filter covers the planet and satellites, reducing their light and providing a measurable image of Jupiter and the Galileans. From left to right, Callisto, Ganymede, Europa, Jupiter, and Io. North is up, east to the left.

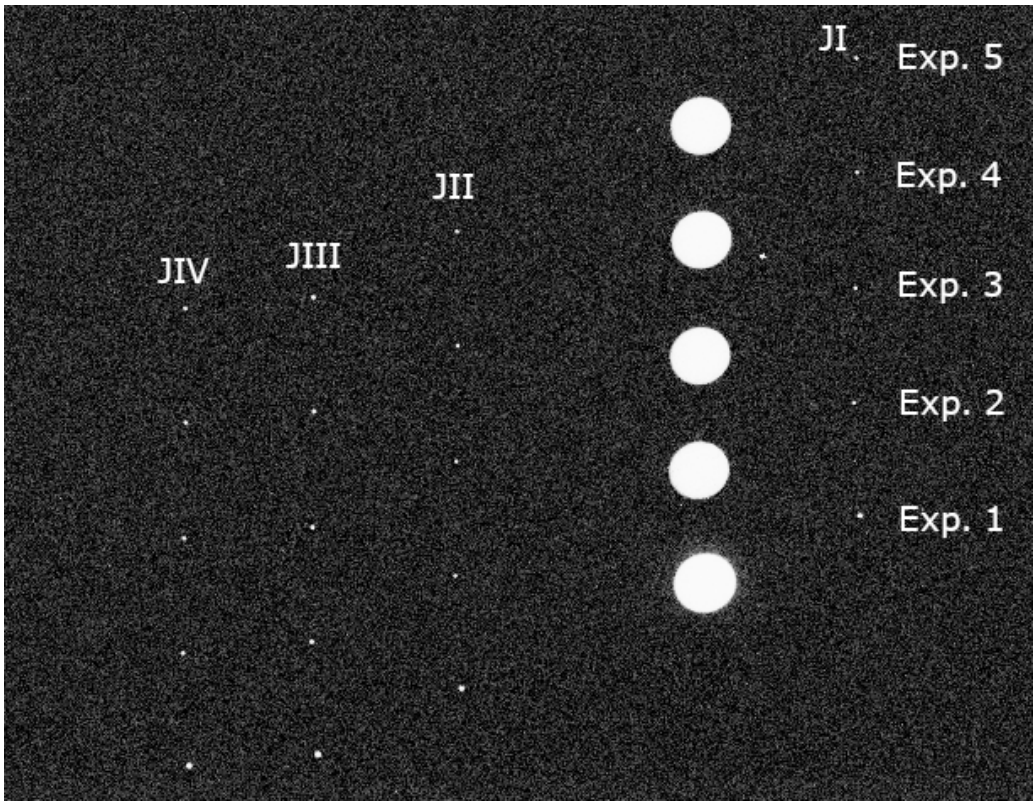

Fig. 1. Center of the digitization (positive) of the USNO 26-inch Galilean plate No. 21014. Five exposures shifted in the declination direction, from left to right: Callisto, Ganymede, Europa, Jupiter, and Io. North is up, east to the left.

2.1 Positioning results

We re-processed the analysis of the 553 NAROO images using the Gaia-DR3 reference star catalogue (Gaia Collaboration et al. 2016, 2022) to compare the positions of the Galilean satellites with their theoretical computed positions given by the INPOP21a planetary ephemeris (Fienga et al. 2021) and newest NOE-5-2021-JUP satellite ephemerides. All of the Gaia reference stars and the satellite images were centered using the shapelet decomposition method (Refregier 2003). This concerns 1145 positions of Io, 1178 positions of Europa, 1274 positions of Ganymede, and 1222 positions of Callisto. We also computed 1355 positions of Jupiter as the barycenter of the observed satellites, when at least two of them were available on the same date. The distributions of the (O-C)s and residuals in equatorial right ascension and declination are provided in Table 1. It shows the difference of (RA, Dec) coordinates for individual satellites, hence the observed positions versus positions calculated from INPOP21a and NOE-5-2021-JUP models with NAROO digitizations.

The key point is that the NOE-5-2021-JUP/INPOP21a rms (O-C) for all observations is 54.1 mas for Io, 53.0, mas for Europa, 57.2 mas for Ganymede, and 54.3 mas for Callisto. These average rms (O-C)s and residuals correspond to our observation accuracies over twenty-six oppositions in the series, or 31 years. The main improvement consisted in using the Gaia-DR3 star catalogue for the positioning of the stellar references for the astrometric reduction. In fact, we were able to decrease the residuals by about of 7 mas in both right ascension and declination, by comparison to the same analysis using the UCAC2 catalogue (Zacharias et al. 2008). With regard to the quadratic differences between the average residuals, we may conclude that we eliminated an error contribution about of 28 mas, indicating that our first measurements were degraded by unmodeled uncertainties. This result is consistent with the expected mean error of 15-30 mas of the UCAC2 catalogue, and we may deduce that the error contribution of the Gaia DR3 catalogue is negligible for our needs,

Table 1. Details of the equatorial mean (O-C)s and residuals for the Galilean satellites in mas, according to NOE-5-2021-JUP and INPOP21a ephemerides, with NAROO digitizations.

Satellite	$\overline{(O-C)_{\alpha\cos\delta}}$	$SEM_{\alpha\cos\delta}$ +/−	$\sigma_{\alpha\cos\delta}$ +/−	$\overline{(O-C)_{\delta}}$	SEM_{δ} +/−	σ_{δ} +/−
JI	-4.8	1.6	55.7	0.3	1.5	52.5
JII	-0.5	1.5	53.3	-0.1	1.5	52.7
JIII	-2.4	1.6	57.0	1.0	1.6	57.4
JIV	-1.0	1.6	56.2	0.9	1.5	52.5
Average	-2.1	0.8	55.6	0.5	0.8	53.9

as expected. Finally, we may conclude that astrometric positions derived from photographic plates could now be obtained to the absolute limits of the photographic technique since our results are very close to those derived from mutual phenomena techniques (Emelyanov et al. 2022).

2.2 Atmospheric limitations

With Fig. 2, we investigate the astrometric limitation in external precision due to the atmosphere. Lindegren (1980) discussed the influence on the astrometry of the wave-front distortion due to the atmospheric turbulence, and he expressed the mean astrometric error as a function of the measured angle between two objects. Thus, we plotted rms residuals in the (satellite-satellite) separations against the separations for Io, Europa, Ganymede and Callisto. For comparison, we also plotted Lindegren's function above.

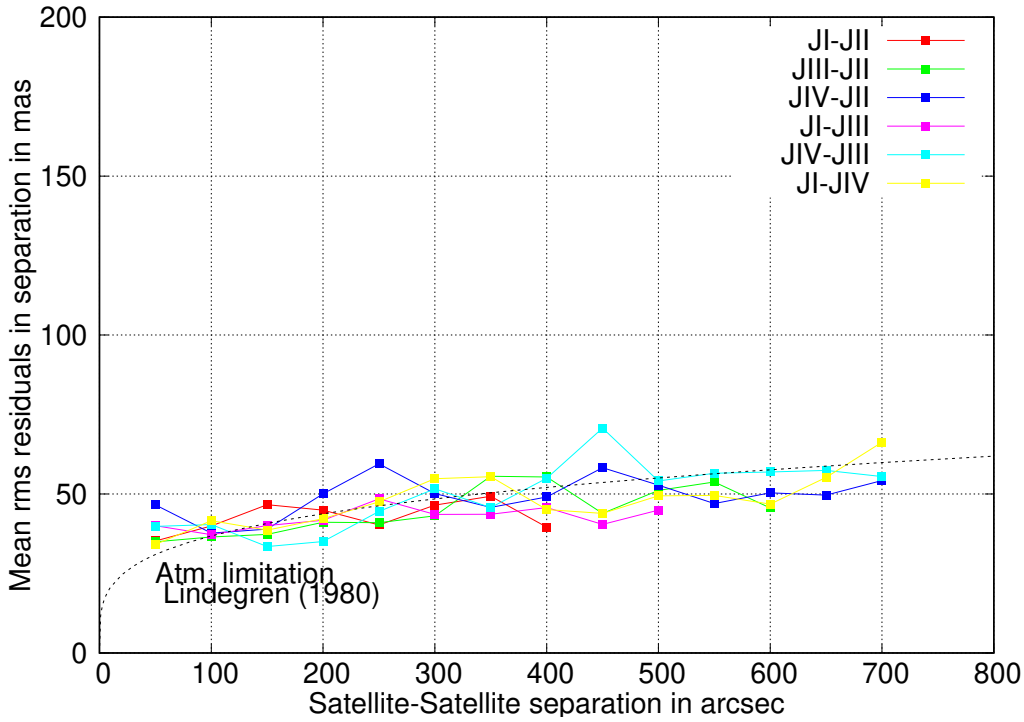

Fig. 2. Mean rms residuals in the (satellite-satellite) separations according to NOE-5-2021-JUP ephemerides. The x-axis shows the satellite-satellite separation and the y-axis the mean rms residuals in separation. Atmospheric limitation is given by Lindegren (1980).

Lindegren's function is referenced to the measured angle between two objects near the zenith and would not apply exactly to our observations, but this comparison is a first approach to assess the quality of our results. The curves for all satellite pairs are near coincident, and there is no excess variance in the separations. We may conclude that we have reached the limit in precision for these observations based on the Gaia-DR3, and confirm that we g-have reached the limits of the photographic techniques here.

2.3 The case of Amalthea

We compared the positions of the Galilean satellites with their theoretical computed positions given by the INPOP21a planetary ephemeris and former NOE-5-2010-JUP satellite ephemerides. In fact and by its definition, NOE-5-2010-JUP satellite model did not introduce the motion of the inner satellites. Their influence was taken into account by adding their mass to that of Jupiter. Thus, considering that Io is the main Galilean disturbed by the gravitational potential of the inners, we should be able to detect such an additional signal in its (O-C)s, in particular. We performed a frequency analysis of these data normalized by the Earth/satellite distance to reduce extra signals (motion of the observer, planetary ephemeris...) over 31 years, at the known frequencies of the four inner satellites. We assumed that the measured signals corresponded to variations in longitude since we were looking for mass estimations. Therefore, we were able to extract a 0.5016 ± 0.0022-days periodic signal of 20 ± 2 km of magnitude.

Table 2. Comparison of the mass of Amalthea.

Source	Amplitude (km)	Mass ($.10^{18}$kg)
USNO plates	20.00 ± 2	2.00 ± 0.20
Galileo	—	2.08 ± 0.15

Table 2 shows the comparison between the mass of Amalthea we estimated from our observations, and the mass that was calculated from Galileo flybys by Anderson et al. (2005). Both results are in the same order of magnitude. The differences are mainly due to the hypotheses of our estimation method. Although, our measuring error is a resulting indicator of these uncertainties. The key point is that we confirm that direct observation is not the only way to determine the physical characteristics of celestial bodies, and a new analysis of photographic plates could help to get more information about various bodies to contribute to a more fundamental physics.

3 Conclusions

We analyzed a full series of astrophotographic plates of the Galilean satellites taken at USNO from 1967 to 1998. Using the NAROO machine for the digitization and the Gaia-DR3 reference star catalogue allowed us to increase the precision and more important, to finally reach the limit in astrometric accuracy for the photographic technique. Thus, we were able to provide astrometric (RA, Dec) ICRS positions of the satellites, allowing us to deduce positions of the planet indirectly, with overall rms residuals of about 55 mas or 160 km at Jupiter.

We confirm the high interest in continuing the analysis of old observations, especially photographic plates, in the framework of the NAROO program. Since digitization time is reserved for external users, we remind that the NAROO machine is available for researchers to digitize their own collections following our call for proposals, issued every six months via our project website at `https://naroo.imcce.fr/`.

The NAROO program was supported by the DIM-ACAV of Île-de-France region, PSL Research University, the Programme National GRAM (PNGRAM), the Programme National de Planétologie (PNP) and the Programme National Soleil-Terre (PNST) of CNRS/INSU with INP and IN2P3, co-funded by CNES, and the Gaia Specific Action (AF Gaia) of Paris Observatory.

References

Anderson, J. D., Johnson, T. V., Schubert, G., et al. 2005, Science, 308, 1291

Emelyanov, N., Arlot, J. E., Anbazhagan, P., et al. 2022, MNRAS, 516, 3685

Fienga, A., Deram, P., Di Ruscio, A., et al. 2021, Notes Scientifiques et Techniques de l'Institut de Mecanique Celeste, 110

Gaia Collaboration, Prusti, T., de Bruijne, J. H. J., et al. 2016, A&A, 595, A1

Gaia Collaboration, Vallenari, A., Brown, A. G. A., et al. 2022, arXiv e-prints, arXiv:2208.00211

Lindegren, L. 1980, A&A, 89, 41

Pascu, D. 1977, in IAU Colloq. 28: Planetary Satellites, 63

Refregier, A. 2003, MNRAS, 338, 35

Robert, V., Desmars, J., Lainey, V., et al. 2021, A&A, 652, A3

Zacharias, N., Winter, L., Holdenried, E. R., et al. 2008, PASP, 120, 644

SF2A 2023
M. N'Diaye, A. Siebert, N. Lagarde, O. Venot, K. Baillié, M. Béthermin, E. Lagadec, J. Malzac, J. Richard (eds)

CONSTRAINTS ON EARTH'S CORE PROCESSES BY SPACE GRAVIMETRY

S. Rosat[1], H. Lecomte[1] and M. Mandea[2]

Abstract. Space gravimetric missions such as GRACE and GRACE Follow-On (hereafter denoted as GRACE) have been measuring the temporal mass variations within the Earth since 2002. GRACE products have been widely used to study continental water mass redistributions bringing additional constraints to hydrological models. GRACE solutions have also enabled to study internal mass redistributions before, during and after large earthquakes, putting some new constraints on the seismic cycle. In the deeper Earth's interior, the core also possesses a broad range of dynamical mechanisms involving mass variations. We compute the gravity perturbations expected for several core processes using the gravito-elastic equations governing the Earth's response to any internal forcing. We focus on the interannual signals generated by the dynamic pressure changes at the Core Mantle Boundary (CMB) associated with core flows reconstructed from geomagnetic observations, the reorientation of the inner core controlled by gravitational coupling with the Earth's mantle and time-varying topography changes at the CMB associated with dissolution and crystallization processes for instance. We then confront the predicted signatures with the current uncertainties linked to the GRACE data. New constraints on these core processes are finally obtained from space gravimetry. Some of the current limitations in the search for Earth's core signatures in space gravity records could be lifted with the future space gravimetric missions.

Keywords: time-variable gravimetry, Earth's core

1 Introduction

The Earth's core possesses a large part of complexity, that only a multi-disciplinary approach can resolve. While seismology provides fundamental information about the Earth's structure and composition, dynamical processes at play in the Earth's deep interior are hardly accessible. Geomagnetism and magneto-hydro-dynamic (MHD) simulations provide information about the core flow dynamics at time-scales longer than a few years. Despite the progress made to reach Earth's like conditions in MHD simulations and to inverse core flows from observed variations of the Earth's magnetic field, provided at a global scale by satellites carrying magnetometers, we still lack information about the density properties inside the core and about the coupling processes acting at its boundaries with the mantle and solid inner-core. Geodesy has here a complementary role to play.

Dynamical processes acting in the Earth's core give rise to mass redistributions and elastic deformation that perturb the gravity field. Space gravimetry measurements provide a global image of the time-varying gravity field at the Earth's surface. Earth's gravity field fluctuations are obtained from precise orbit determination by tracking satellites orbiting the Earth (Satellite Laser Ranging technique - SLR) or by accurate measurement of the distance between two satellites on the same orbit, like for the Gravity Recovery and Climate Experiment (GRACE) and GRACE Follow-On (-FO) satellites, after correcting from non-gravitational motions.

Since 2002, GRACE and GRACE-FO missions have been recording the gravity field fluctuations (Tapley et al. 2004; Landerer et al. 2020) associated with a wide range of processes (Fig. 1), which signatures are superposed on various spatial and temporal scales. The main sources of gravity changes are tidal effects, post-glacial rebound (Purcell et al. 2011), hydrology (Rodell et al. 2018), atmospheric (Kusche & Schrama 2005) and oceanic (Dobslaw et al. 2017) loading, water mass redistribution (Pfeffer et al. 2022), pre-seismic (Bouih et al. 2022), co-seismic and post-seismic (Deggim et al. 2021) mass redistributions, seismic pre-cursors (Panet

[1] Institut Terre et Environnement de Strasbourg, UMR7063, CNRS et Université de Strasbourg, EOST, 67084 Strasbourg, France
[2] Centre National d'Etudes Spatiales, Paris, France

© Société Française d'Astronomie et d'Astrophysique (SF2A) 2023

et al. 2018; Bouih et al. 2022), sea-level changes (Peltier 2009; Adhikari et al. 2019; Horwath et al. 2022) and core processes (Dumberry 2010b; Dumberry & Mandea 2021; Lecomte et al. 2023). Separation betwen these contributions is a very challenging task.

In this work, we review the precision of gravity field solutions in terms of dispersion of the existing gravity field products proposed by various analysis centers, in terms of dispersion of the surface mass loading models, with respect to predicted gravity changes produced by major core processes. Most of the results shown here can be found in Lecomte et al. (2023) but we consider an additional core process not included in the later work, which is topographic loading at the core-mantle boundary (CMB). We first start by a review of the precision of space gravity solutions and loading models. Then, predicted gravity perturbations for major core processes are presented. We finally conclude by some perspectives related to the future space gravimetric missions like the Mass-change And Geosciences International Constellation (MAGIC) in the frame of NASA's Mass Change Designated Observable (MCDO) and ESA's Next Generation Gravity Mission (NGGM) (Haagmans & Tsaoussi 2020).

2 Precision of time-variable gravity field measurements vs amplitude of core processes

Core-induced gravity perturbations are the largest for the degree-2 spherical harmonic component (Dumberry 2010a). In the following, we then focus only on the degree-2 component of the perturbed gravity field.

2.1 Precision of gravity field measurements

Lecomte et al. (2023) have estimated the dispersion for GRACE solutions as about 0.34 cm of equivalent water height (EWH) or 20% of the total signal, 0.2 cm for the degree 2 alone. Moreover, they have shown that the largest uncertainty in loading models comes from hydrology with a dispersion as large as 0.89-2.10 cm of EWH and 0.37 cm for the degree 2 alone.

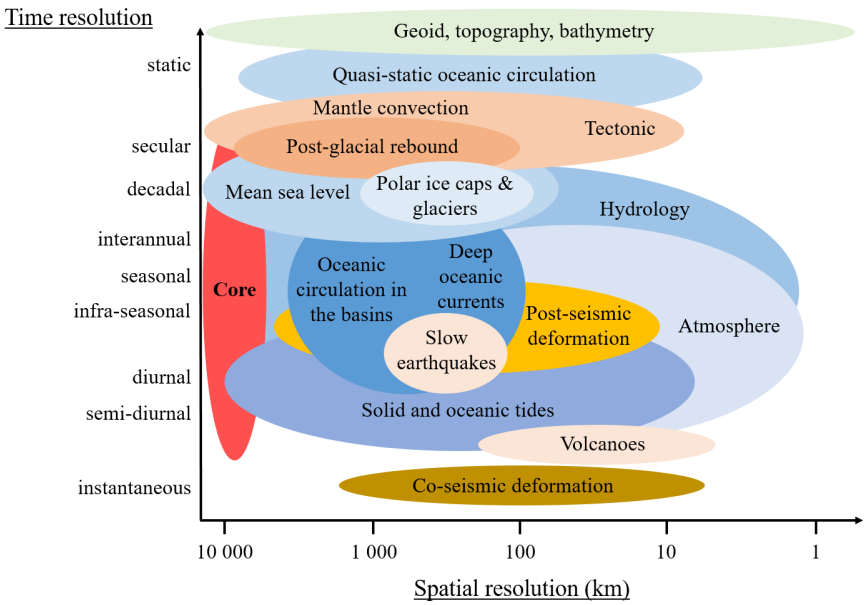

Fig. 1. Spatio-temporal fluctuations of the Earth's gravity field (after Lecomte et al. 2023).

2.2 Earth's core processes

Computation of the gravity field perturbation by core processes is performed using the classical Love numbers approach by integration of the gravito-elastic equations (Greff-Lefftz et al. 2004; Dumberry & Bloxham 2004) for a spherically symetric radial Earth's PREM (Dziewonski & Anderson 1981) model. We consider three core

processes: density and pressure anomalies associated with core flows, mass redistribution and deformation associated with the inner-core rotation, topographic loading at the CMB associated with cristallization-dissolution for instance.

Core flows Core flows are associated with density anomalies at the order of 10^{-5} kg.m^3, as an upper bound, (Dumberry 2010b) and pressure anomalies at the CMB between 20 to 100 Pa from a few years to decadal timescales (Gillet et al. 2020). Degree-2 Stokes coefficient variation for a 10^{-5} kg.m^3 density anomaly is 2×10^{-11} or 0.1 cm EWH. For inter-annual and decadal pressure anomalies of 20 and 100 Pa, the respective degree-2 Stokes coefficient variations are 2×10^{-12} or 0.1 cm EWH and 3×10^{-11} or 0.5 cm EWH (Lecomte et al. 2023).

Reorientation of the inner core When the inner core is tilted by an angle α, it creates a variation on the Stokes coefficient approximated by $\Delta S \approx 10^{-10} h\alpha$ under the hypothesis of a non-convecting inner core and with a density almost uniform at hydrostatic equilibrium (Dumberry 2010a). h is the degree-2 topography of the inner core. Dumberry & Mandea (2021) have estimated $\alpha = 0.4°$ and $h = 18$ m on decadal time scales. It gives a degree-2 Stokes coefficient variation of 10^{-11} or 0.2 cm EWH (Lecomte et al. 2023).

Topographic loading Dissolution and crystallization processes have been proposed to continuously reshape the topography of the CMB on a decadal time period (Mandea et al. 2015). Such processes would give rise to surface gravity perturbation through a density load $V^{c,s}_{n,m} = \frac{4\pi G b}{2n+1}\Delta\rho \times h^{c,s}_{n,m}$ at the CMB computed as

$$\Delta C, S_{n,m} = -\frac{a}{GM}\left[\left(\frac{b}{a}\right)^{n+1} + k'_n\right] V^{c,s}_{n,m}, \tag{2.1}$$

where $k'_2 = -0.2$, $\Delta\rho \approx 5\times10^3$ kg.m^{-3} the density jump at the CMB, $h^{c,s}_{n,m}$ the harmonic coefficient of the topography at the CMB, b and a are respectively the CMB and Earth's surface radii. We have noted $C_{n,m}$ and $S_{n,m}$ the degree$-n$, order$-m$ fully normalized Stokes coefficients of the spherical harmonic representation of the Earth's gravitational potential. A degree-2 topographic loading of 1 cm would induce a Stokes coefficient variation of 2×10^{-11} or 0.1 cm EWH (Fig. 2).

3 Conclusions

Earth's core processes affect the Earth's gravity field at time-scales ranging from a few years to a few decades. These perturbations occur under various mass redistributions associated with inner-core reorientation, topographic loading at the core interfaces or dynamic core flows. The surface effect increases with the time-scales. Decennal time-varying gravity records are then required to better constrain density anomalies associated with such core processes. The continuity of space gravimetric observation after GRACE-FO will be reached with the Next Generation Gravity mission (Cesare et al. 2016). The MAGIC mission is a planned National Aeronautics and Space Administration (NASA) and European Space Agency (ESA) joint venture. The MAGIC mission will provide greater temporal resolution with a substantial reduction in spatial and temporal aliasing (Haagmans & Tsaoussi 2020), and better determination of the low-degree Stokes coefficients (Technische Universität München & et al. 2023). If high accuracy (signals amplitude of 0.1 cm EWH in 10 years) can be reached at long wavelengths (thousands km) and decadal timescales, on-going deep Earth dynamics may become observable (Fig. 2). Continuity in time of the monitoring of the time-variable Earth's gravitational field is essential to constrain deep Earth's dynamics.

This work is supported by the Centre national d'études spatiales (CNES) and by the Doctoral School Earth and Environmental Sciences (ED 413) of the University of Strasbourg in the Institut Terre et Environnement de Strasbourg (ITES, CNRS UMR7063). This project has received funding from the European Research Council (ERC) under the European Union's Horizon 2020 research and innovation program (GRACEFUL Synergy Grant agreement 855677).

References

Adhikari, S., Ivins, E. R., Frederikse, T., Landerer, F. W., & Caron, L. 2019, Earth System Science Data, 11, 629

Bouih, M., Panet, I., Remy, D., Longuevergne, L., & Bonvalot, S. 2022, Earth and Planetary Science Letters, 584, 117465

Cesare, S., Allasio, A., Anselmi, A., et al. 2016, Advances in Space Research, 57, 1047

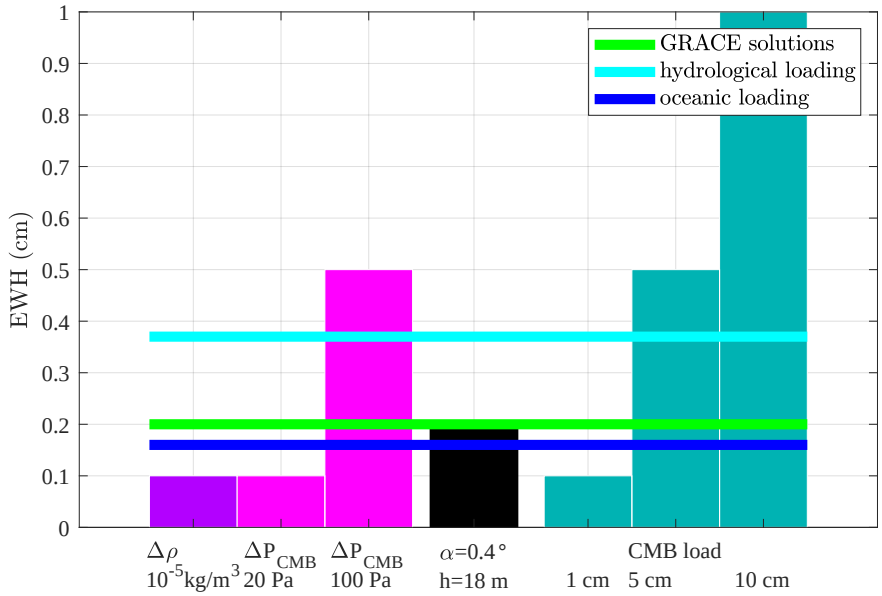

Fig. 2. Uncertainties of degree-2 GRACE solutions (green) and of hydrological (cyan) and oceanic (blue) loading with respect to expected degree-2 surface gravity perturbations by some dynamical core processes: density anomalies and pressure anomalies at the CMB associated with core flows (magenta and pink color), reorientation of the inner core (black) and topographic loading at the CMB for various degree-2 topographic heights (1, 5 and 10 cm) (turquoise). Amplitudes are given in Equivalent Water Height (EWH) in cm.

Deggim, S., Eicker, A., Schawohl, L., et al. 2021, Earth System Science Data, 13, 2227
Dobslaw, H., Bergmann-Wolf, I., Dill, R., et al. 2017, Geophysical Journal International, 211, 263
Dumberry, M. 2010a, Geophysical Journal International, 180, 635
Dumberry, M. 2010b, Earth and Planetary Science Letters, 297, 387
Dumberry, M. & Bloxham, J. 2004, Geophysical Journal International, 159, 417
Dumberry, M. & Mandea, M. 2021, Surveys in Geophysics
Dziewonski, A. & Anderson, D. 1981, Physics Earth Planetary Interior, 25, 297
Gillet, N., Dumberry, M., & Rosat, S. 2020, Geophysical Journal International, 224, 216
Greff-Lefftz, M., Pais, M., & Le Mouel, J.-L. 2004, Journal of Geodesy, 78, 386
Haagmans, R. & Tsaoussi, L. E. 2020, Earth and Mission Science Division, European Space Agency; NASA Earth Science Division
Horwath, M., Gutknecht, B. D., Cazenave, A., et al. 2022, Earth System Science Data, 14, 411
Kusche, J. & Schrama, E. J. O. 2005, Journal of Geophysical Research: Solid Earth, 110
Landerer, F. W., Flechtner, F. M., Save, H., et al. 2020, Geophysical Research Letters, 47, e2020GL088306
Lecomte, H., Rosat, S., Mandea, M., Boy, J.-P., & Pfeffer, J. 2023, Journal of Geophysical Research: Solid Earth, 128
Mandea, M., Narteau, C., Panet, I., & Le Mouël, J.-L. 2015, Journal of Geophysical Research: Solid Earth, 120, 5983
Panet, I., Bonvalot, S., Narteau, C., Remy, D., & Lemoine, J.-M. 2018, Nature Geoscience, 11, 367
Peltier, W. R. 2009, Quaternary Science Reviews, 28, 1658
Pfeffer, J., Cazenave, A., Blazquez, A., et al. 2022, EGUsphere, 2022, 1
Purcell, A., Dehecq, A., Tregoning, P., et al. 2011, Geophysical Research Letters, 38
Rodell, M., Famiglietti, J. S., Wiese, D. N., et al. 2018, Nature, 557, 651
Tapley, B. D., Bettadpur, S., Ries, J. C., Thompson, P. F., & Watkins, M. M. 2004, Science, 305, 503
Technische Universität München, T. & et al. 2023, Simulation studies for a Mass change And Geosciences International Constellation (MAGIC), Tech. rep., TUM

SF2A 2023
M. N'Diaye, A. Siebert, N. Lagarde, O. Venot, K. Baillié, M. Béthermin, E. Lagadec, J. Malzac, J. Richard (eds)

FREQUENCY DRIFT INTERFEROMETRY FOR STRAY LIGHT MEASUREMENT ON THE LISA SPACE INSTRUMENT

A. Roubeau-Tissot[1], M. Lintz[1], M. Nardello[1], M. Pichot[1] and J.-P. Coulon[1]

Abstract. Coherent stray light in intricate optical systems such as interferometers, impacts measurement accuracy, particularly in interferometric space missions such as GRACE-FO. The aim of our project is to create an instrument inspired by the FMCW method, utilizing a frequency-swept laser to detect stray light in LISA's optical system. The current demonstrator accurately quantifies stray light and fulfills the precision challenges asked for the LISA space mission with a <2 mm resolution in OPD.

Keywords: LISA France, instrumentation, OGSE, prototype, stray light, interferometry, FMCW, frequency-drift interferometry

1 Introduction

On a complex optical system such as an interferometer, coherent Stray Light is a pitfall in many ways because it can affect the accuracy and resolution of the measurements or their dynamics. This is all the more true with space interferometers as in the GRACE (Gravity Recovery And Climate Experiment) Follow-On space mission, which uses the LRI (Laser Ranging Interferometer) to track the Earth's mass distribution across the planet (Abich et al. 2019). The GRACE-FO mission employs high accuracy and high resolution laser interferometry, similar to the LISA space mission. Achieving precise optical phase measurements requires addressing and reducing coherent stray light issues. This involves using a reliable method at the system level to ensure that stray light limits are not exceeded after instrument integration. Simply measuring overall amplitude isn't effective, as individual stray light amplitudes for different components must be determined. This is because these components have varying stability and noise allocations, and their contributions must be identified separately. For example, stable components connected to a Zerodur baseplate differ from less stable ones like movable wave plates, which have lower acceptable stray light amplitudes.
This work aims to develop the demonstrator of an instrumentation that can measure the stray light optical amplitude, whatever its origin, in the photoreceivers of the LISA (Laser Interferometer Space Antenna) space mission's interferometric system MOSA (Moving Optical SubAssembly) before sending it into space. The instrumentation is based on the method known under the name of FMCW (Frequency Modulated Continuous Wave, Zheng (2004)) but is of more general application.

2 Experimental set-up

2.1 Method used

Utilizing a single-mode laser source, we sweep the optical frequency over time and introduce this beam into the optical system under test. Throughout the optical frequency scan, we capture all outgoing signals, encompassing both optical and electrical signals. Should any of these signals exhibit a fringe-like pattern, we attribute this modulation to the existence of stray light amplitude, which interferes with the nominal light amplitude.The optical path difference (OPD) between the nominal and stray light (SL) is deduced from the frequency of these interference fringes ($\mathbf{f_{itf}}$), as in coherent reflectometry, using:

$$f_{itf} = \frac{\Delta L}{c} \frac{\Delta \nu_{opt}}{\Delta t} \tag{2.1}$$

[1] Université Côte d'Azur, Laboratoire ARTEMIS, Nice

© Société Française d'Astronomie et d'Astrophysique (SF2A) 2023

where $\Delta L = nL_{SL} - nL_{nom}$ the SL/nom OPD, n the medium index and $\frac{\Delta\nu_{opt}}{\Delta t}$ the frequency scan rate.

So by doing spectral analysis of the recorded photo signals, we will retrieve the list [**SL amplitude** vs. **OPD**] of the different SL contributions. The setup must fulfill the requirements for MOSA stray light tests by reaching a measurement floor in fractional amplitude SL/nom under $\mathbf{2,2.10^{-6}}$ on the measurement range **[0–200 Hz]** and by achieving a resolution in SL/nom OPD under **2 mm**.

2.2 Demonstrator Implementation

The current demonstrator is composed of five main parts:

- **Frequency swept laser**: 1 064 nm fibered laser diode to be swept over at least 1 nm (swept optical frequency $\Delta\nu_{opt}$= 265 GHz) allowing a resolution of 1 mm on the OPD SL/nominal
- **Frequency Ramp Control**: Offset phase-locked loop that achieves linear optical frequency drift ($\frac{d\nu_{opt}}{dt}$=Cte) using an unbalanced fibered heterodyne Mach-Zehnder interferometer.(Kéfélian et al. (2009) and Jiang et al. (2010))
- **Frequency Scan rate measurement**: Measurement of the beat frequency between the frequency swept laser and a fixed frequency laser (method inspired by Chiodo et al. (2013)).
- **Frequency Ramp Monitoring**: A fibered interferometer to check the quality of the frequency ramp by doing a real-time interference measurement simultaneously with the MOSA tests.
- **MOSA simulator**: Free space setup where stray light contributions with known OPD and amplitude are used to test the efficiency and accuracy of our demonstrator.

The work presented here will focus on measurements made on the MOSA simulator test bench. This bench, as shown in Fig. 1, is composed of a silica wedge plate allowing us to generate multiple reflections/transmissions in R≈ 4% and T=1-R (SL beams), mirrors M1 and M2 reflecting the stray beams: some reflections finally reach the photoreceiver placed on the nominal beam and thus appear as "stray light contributions".

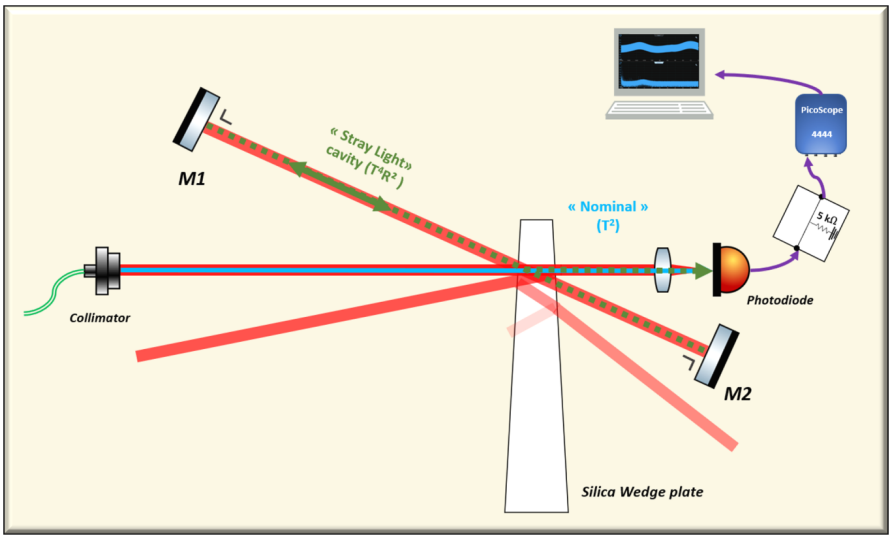

Fig. 1. Scheme of the MOSA simulator with a nominal optical path and several stray light contributions coming from the first reflection on the wedge and the M1-M2 cavity

In our scenario, we have a primary beam as the initial transmission through the wedge's output (depicted as light blue in the scheme, with a power ratio of T^2). Additionally, there's a stray light contribution from the first wedge reflection (green path, power ratio T^2R^2), and echoes of this stray light within the M1-M2 cavity (resulting in a T^2 power loss in the round trip).
The anticipated optical path difference (ΔL) between the stray light and the nominal beam is 1,402 2 m. This value is derived from the reconstruction of the optical path in the FRED simulation software, using measurements conducted with a mechanical arm on the optical bench.

3 Results on the MOSA simulator

After recording the photo signals, we calculate the FFT (Fast Fourier Transform) using a Python code and we obtain the spectrum shown in Fig. 2Left. We're making all our measurements with two frequency ramp velocities: 5,1 GHz/s (510 GHz in 100 s) or/and 5,3 GHz/s (530 GHz in 100 s) to scan the laser over around 2 nm and improve the OPD resolution.

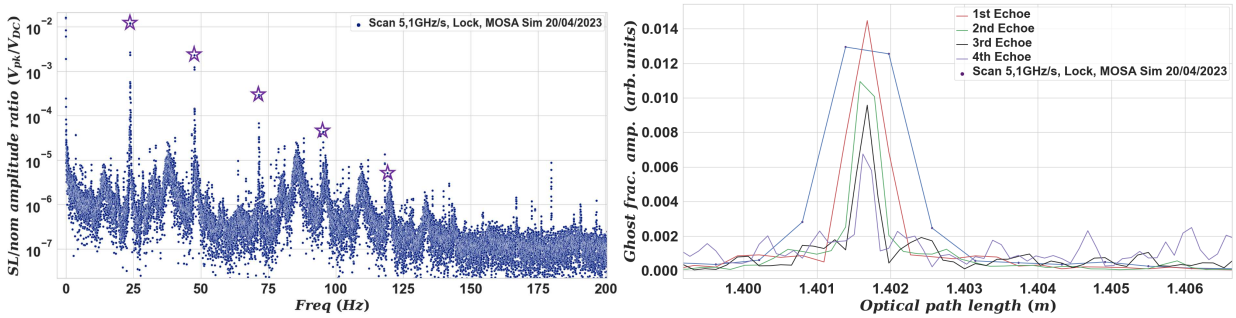

Fig. 2. Left: Example fractional amplitude spectrum of the photoreceiver signals recorded on the MOSA-simulator set-up as a function of the Fourier frequency during a **5,1 GHz/s** laser frequency scan. Stars indicate expected SL peaks at the output of the MOSA Sim. **Right:** The N-th Echoes, at $N * \Delta L_{M1M2}$ overlaps with the main SL contribution as a function of the OPD computed from 2.1

We retrieve the expected main SL contribution and his echoes in the M1-M2 cavity with an amplitude loss of factor 6 due to the beam's divergence (purple stars). And if we overlap all the echoes over the main SL peak as a function of the OPD and we compute their barycenters we see that, first, the peaks overlap pretty well on Fig. 2Right ($\leq$0,1 mm accuracy and then that the mean barycenter, 1,401 6 m, is 0,6 mm away from the theoretical value which is one of the main proof of the precision quality of our measurement.

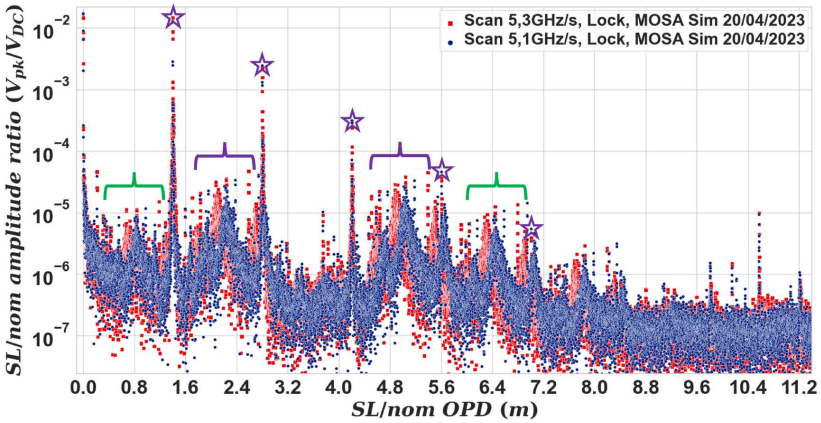

Fig. 3. Fractional amplitude spectra as a function of the OPD (computed from 2.1) during two laser scans. In red (resp. blue): data obtained with an optical frequency ramp rate of **5,3 GHz/s** (resp. **5,1 GHz/s**). Stars indicate SL peaks and brackets parasitic noise peaks

The presence of additional peaks related to mechanical noise, such as acoustic and seismic disturbances, can be observed alongside the stray light (SL) peaks. By employing a straightforward technique (Roubeau-Tissot et al. 2022), which involves overlaying spectra from two sequential measurements with varying frequency scan rates (**5,1 GHz/s** and **5,3 GHz/s**) as illustrated in Fig.3 in terms of optical path difference (using 2.1 to convert the Fourier frequency), it becomes possible to differentiate authentic SL peaks from the rest (parasitic peaks). Peaks that overlap are stray light contributions, while others represent noise contributions (depicted within brackets). Importantly, these noise patterns are exclusively evident in the MOSA simulator's output and do not directly affect our fiber instrument (e.g., the output of frequency ramp monitoring, a fiber interferometer). This distinction arises because mechanical noise only perturbs the cavity's optical path (mirrors or wedge).

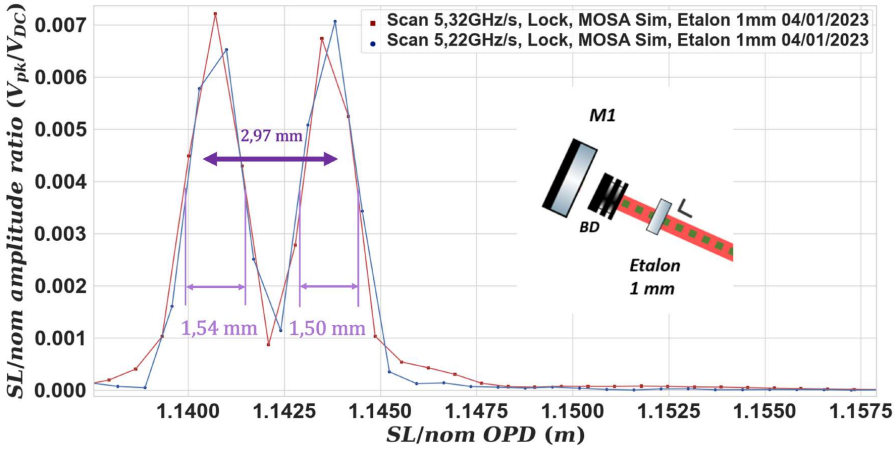

Fig. 4. Main stray light contributions in the MOSA simulator with the mirror M1 in Fig.1 replaced by an 1 mm silica etalon

To assess the demonstrator's OPD resolution (minimum discernible distance between two nearby stray light peaks), the M1 mirror is substituted with a 1 mm silica etalon. This introduces two SL contributions: one from the etalon's front reflection and another from the rear. The anticipated OPD between these peaks is **2,9 mm** (twice the thickness of the etalon multiplied by the silica index 1,45). Notably, in Fig.3,the experimental OPD measures **2,94 mm**, providing an adequate data points for the desired differentiation of the two peaks.

4 Conclusions

The spectral analyses of the MOSA simulator signals show the existence of the SL beams that we have prepared, and allow the measurement of the SL/nominal path difference, confirming the device's functionality for the measurement of the coherent stray light amplitude and OPD. The resolution in OPD is at the expected level of **2 mm** considering the amplitude **>500 GHz** of the frequency sweeps. The measurement floors demonstrate that we reach the currently required $\mathbf{2,2.10^{-6}}$ in SL/nom fractional amplitude above **1 Hz**. The residual noise at low frequency could possibly be removed by normalizing the photoreceiver signal by the laser power signal, obtained from a pick-up of the incoming laser beam.
We observe the presence of stray peaks (due to acoustic and seismic perturbations) and parasitic SL contributions coming from our fibered setup which we have to study and, if possible, remove. Also, we must understand and take into account all the physical phenomena which can affect the linearity of frequency ramp such as: the chromatic dispersion, the slow dependence in temperature and humidity of the fiber's effective optical index, the polarization variations in a strong birefringence medium as the fibers that we use...

Acknowledgements: This work is carried out within the LISA France Collaboration, and benefits from the funding of the Région Sud and the CNES (Centre National d'Etudes Spatiales) for the AIVT (Assembly, Integration, Validation and Test) of the MOSA of the LISA mission.

References

Abich, K., Abramovici, A., Amparan, B., et al. 2019, Physical Review Letters 123, 3
Chiodo, N., Djerroud, K., Acef, O., Clairon, A., & Wolf, P. 2013, Appl. Opt., 52, 7342
Jiang, H., Kéfélian, F., Lemonde, P., Clairon, A., & Santarelli, G. 2010, Opt. Express, 18, 3284
Kéfélian, F., Jiang, H., Lemonde, P., & Santarelli, G. 2009, Opt. Lett., 34, 914
Roubeau-Tissot, A., Lintz, M., Nardello, M., Pichot, M., & Coulon, J.-P. 2022, in Poster for Optique Nice 2022, SFO
Zheng, J. 2004, Appl. Opt., 43, 4189

SF2A 2023
M. N'Diaye, A. Siebert, N. Lagarde, O. Venot, K. Baillié, M. Béthermin, E. Lagadec, J. Malzac, J. Richard (eds)

CLAIRAUT'S EQUATION EXTENDED TO FAST ROTATORS

C. Staelen[1] and J.-M. Huré[1]

Abstract. In the theory of Nested Spheroidal Figures of Equilibrium (NSFoE, see Huré 2022), rotating bodies are decomposed into thick, homogeneous layers bounded by spheroids. The associated set of equations, which uses Maclaurin's formula for the homogeneous spheroid, admit accurate solutions, provided the interfaces between layers are very close to confocal (in the sense of spheroidal oblate coordinates). In this contribution, we present a few results obtained in the continuous limit, i.e. when the number of spheroidal layers is infinite, thereby enabling to model full heterogeneity. In particular, we derive an integro-differential equation which basically contains Clairaut's fundamental equation, but which works also for fast rotators (Staelen & Huré 2023). The solutions compare very well to numerical solutions obtained from the Self-Consistent-Field method. A few examples are given.

Keywords: Gravitation, stars: interiors, planets and satellites: interiors, Methods: analytical

1 Introduction

Two hundred and eighty years ago, Clairaut (1743) published a major theory for the figure of the Earth as a heterogeneous fluid mass in slight deviation from sphericity. He showed that, in the limit of small flattenings, the isopycnic surfaces are very close to spheroids (i.e. ellipsoids of revolution). Clairaut was able to derive a powerful second-order differential equation for the eccentricity ε as a function of the equatorial radius a, namely

$$\frac{\mathrm{d}^2\varepsilon^2}{\mathrm{d}a^2}+\frac{2}{a}\frac{a^3\rho(a)}{\int_0^a \mathrm{d}a'\rho(a')a'^2}\frac{\mathrm{d}\varepsilon^2}{\mathrm{d}a}+\frac{2}{a^2}\left[\frac{a^3\rho(a)}{\int_0^a \mathrm{d}a'\rho(a')a'^2}-3\right]\varepsilon^2(a)=0, \tag{1.1}$$

where ρ the mass density along the given isopycnic. So, provided the mass-density profile is known in advance (which is generally not the case), the eccentricity can be determined with appropriate boundary conditions (BCs). We have typically $\mathrm{d}\varepsilon^2/\mathrm{d}a=0$ at the center and a value ε_s can be prescribed at the surface. The internal structure is then fully solved. Clairaut's equation is valid only for small values of ε^2, i.e. for slow rotators. If this is justified for the Earth ($\varepsilon_\mathrm{s}^2\sim 7\times10^{-3}$) and for the Sun ($\varepsilon_\mathrm{s}^2\sim 2\times10^{-5}$), objects like Ceres ($\varepsilon_\mathrm{s}^2\sim 1\times10^{-1}$), Saturn ($\varepsilon_\mathrm{s}^2\sim 2\times10^{-1}$) and Achernar ($\varepsilon_\mathrm{s}^2\sim 4\times10^{-1}$) are clearly not accessible by Clairaut's theory. Lanzano (1974) has considered faster rotators by expanding both the shape and the gravitational potential on Legendre polynomials P_{2m} for any order m; thus the ellipsoidal shape is forsaken for a more general one. This method has been used at second-order for the Earth by Chambat et al. (2010), and at third-order for Ceres by Rambaux et al. (2015). In this work, however, we keep the spheoridal shape for all isopycnic surfaces and we study the quality of this approximation for fast rotators.

2 An integro-differential equation for the general problem

As early formulated by Poincaré and prolongated by Hamy (1890), a spheroidal stratification can not represent an exact physical equilibrium for any rotation rotation rate, mainly because this would require both an confocal stratification of layers and a density inversion from centre to surface. This is Hamy's "no-go" theorem. Both classical theories and modern models predict a fully reversed situation: for real systems isopycnic surfaces are more spherical at the centre than close to the surface and the mass-density gradient is essentially negative. We

[1] Univ. Bordeaux, CNRS, LAB, UMR 5804, F-33600 Pessac, France

© Société Française d'Astronomie et d'Astrophysique (SF2A) 2023

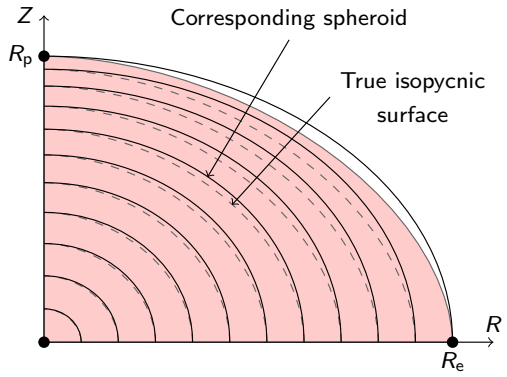

Fig. 1. Schematic diagram of the spheroidal approximation made in this work.

have build a $\mathcal{L}$-layer theory by superposing homogeneous spheroids with different mass densities and ellipse parameters (Huré 2022). Actually, in this kind of problem, the calculation of the gravitational potential is a major difficulty, and considering such structures is particularly attractive as the potential is exceptionnally known in closed-form. This is also widely supported by the numerical experiments which show that isopycnic surfaces are very close to spheroids (Kong et al. 2015; Basillais & Huré 2021). In the limit $\mathcal{L} \to \infty$, the body becomes continuously inhomogeneous, instead of piece-wise inhomogeneous. By converting discrete summations and differences to integrals and derivatives, we can derive a new equation relating the mass density and the eccentricity profile. This is an integro-differential equation (IDE) of the form

$$\frac{\mathrm{d}\varepsilon^2}{\mathrm{d}a} = \frac{2\int_{\rho(0)}^{\rho(a)} \mathrm{d}\rho(a')\chi(a',a;\varepsilon)}{\int_{\rho(0)}^{\rho(1)} \mathrm{d}\rho(a')\mu(a',a;\varepsilon)}, \tag{2.1}$$

which is tends to Clairaut's equation for $\varepsilon^2 \ll 1$. The two functions χ and μ (not reported here; see Staelen & Huré 2023) are continuous and smooth on the whole domain of interest, i.e. for $a \in [0, R_e]$, where R_e is the equatorial radius.

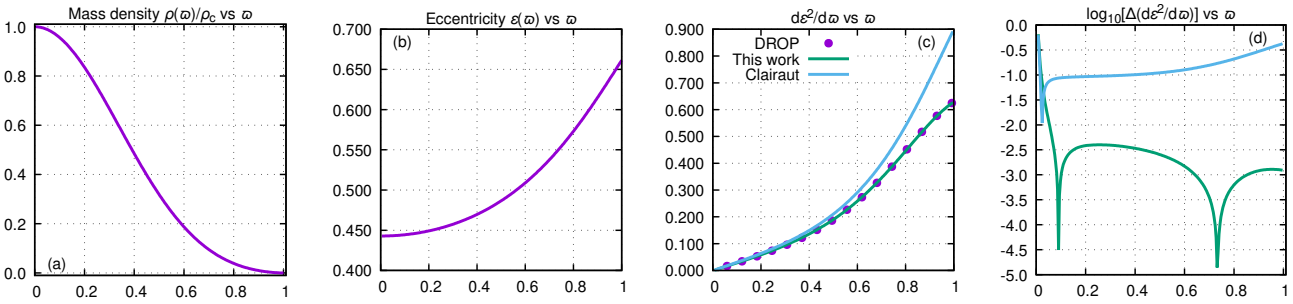

Fig. 2. The mass density obtained with the DROP-code (see in the text) in the equatorial plane (panel a) and the eccentricity profile (panel b) versus the normalised radius $\varpi = a/R_e$ obtained for a polytrope with axis ratio 0.75 and index $n = 1.5$. The self-consistency check of the IDE (panel c) compares both side of (2.1) computed from these reference profiles. Also shown is the derivative computed from Clairaut's equation, and the absolute deviations (panel d).

3 Validation of the IDE by a numerical reference

Regardless of any physical solution of (2.1) that could be produced for a given objets, it is possible to check its precision simply by comparing the LHS and th RHS when fed by a numerial solution. In this purpose, we use the multilayer version of the DROP code (Basillais & Huré 2021), which solves the equilibrium of self-gravitating fluid a from the self-consistent field method. Without loss of generality, we work under axisymmetry and use a

polytropic fluid*. Once a solution is obtained, we first extract the mass-density along the equatorial plane $\rho(a)$, and compute a pseudo-eccentricity $\sqrt{1-b^2/a^2}$ defined as the eccentricity of the isopycnic surfaces (which are not perfect spheroids) that hits the polar axis at $Z=b$ and the equatorial axis at $R=a$. We then inject these profiles into the integrals in the RHS of the IDE, and we then get $(\mathrm{d}\varepsilon^2/\mathrm{d}a)^{1\mathrm{D}}$. Second, we compute directly the derivative of the pseudo-eccentricity still output by the 2D-code, and we get directly $(\mathrm{d}\varepsilon^2/\mathrm{d}a)^{2\mathrm{D}}$. These two derivatives can then be compared. As an illustration, we give in Fig. 2 the results obtained in the case where the ratio between the polar radius and the equatorial radius is 0.75 (a fast rotator) and where the polytropic index is $n=1.5$ (this value corresponds for instance to a fully convective star). We see that the discrepancy between the IDE and the DROP-code is below 3×10^{-3}, typically (against 3×10^{-1} for Clairaut), which is very good. The IDE thus allows to access easily fast rotators, as the error is still low for highly flatten objects.

4 The case of mass-density jumps. An application to the Earth

We have tested the behaviour of the IDE in the case of the Earth, by using the Preliminary Reference Earth Model (PREM, Dziewonski & Anderson 1981). This is a seismologic model assuming *a spherical* (i.e. non-rotating) planet. As a matter of fact, (2.1) is able to account for mass-density jumps (the PREM presents several discontinuities; see Fig 3a), but this requires an additional technical effort. We first write the mass density as

$$\rho(\varpi)=\sum_{k=1}^{\mathcal{K}}\left[\rho_k(\varpi)-\rho_{k+1}(\varpi)\right]\mathcal{H}(\varpi_k-\varpi), \tag{4.1}$$

with ρ_k as the mass density inside domain k, ϖ_k as the position of the mass density jump between domains k and $k+1$ and $\mathcal{H}$ as Heaviside's distribution. Remembering that the derivative (in the sense of distributions) of $\mathcal{H}(x)$ is Dirac's distribution $\delta(x)$, we obtain for any continuous function f on $[0,1]^2$

$$\int_{\rho(0)}^{\rho(1)}\mathrm{d}\rho(\varpi')f(\varpi',\varpi)=\sum_{k=1}^{\mathcal{K}}\int_{\rho(\varpi_{k-1})}^{\rho(\varpi_k)}\mathrm{d}\rho_k(\varpi')f(\varpi',\varpi)-\sum_{k=1}^{\mathcal{K}}\frac{\alpha_k-1}{\alpha_k}\rho_k(\varpi_k)f(\varpi_k,\varpi) \tag{4.2}$$

where $\alpha_k=\rho_k(\varpi_k)/\rho_{k+1}(\varpi_k)$ is the mass density jump at the interface between domains k and $k+1$, which occurs at ϖ_k. Thus, (4.2) can be used to compute the RHS of (2.1). Then, we have written an algorithm to solve iteratively (2.1) with the mass density profile given by Dziewonski & Anderson (1981) as an input. We first initialise the eccentricity profile with a generic parabola (from center to surface), then compute $\mathrm{d}\varepsilon^2/\mathrm{d}a$ from (2.1), and deduce a new eccentricity profile by integration. This is repeated until the ε-profile converges. As BCs, we impose $1-\sqrt{1-\varepsilon_\mathrm{s}^2}=1/298.257\ldots$ as the flatenning. To make the numerical treatment easier, the mass density is normalised by its central value ρ_c, i.e. $\rho_\mathrm{c}=13088.5\ \mathrm{kg}\cdot\mathrm{m}^{-3}$.

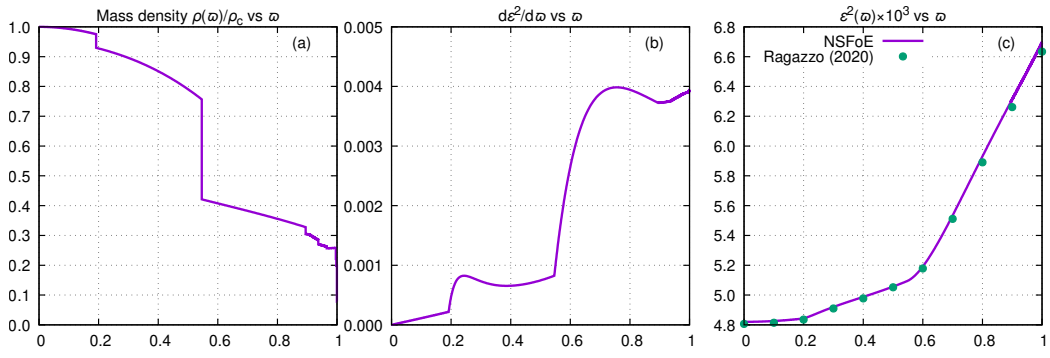

Fig. 3. Numerical solution for the eccentricity profile (panels b and c) versus the normalised radius inside the Earth using the "normalised PREM" as an input (panel a). Data computed by Ragazzo (2020) is also plotted.

The results are plotted in figure 3. We show in panel (a) the mass-density (the main input), and in panels (b) and (c) $\mathrm{d}\varepsilon^2/\mathrm{d}a$ and ε^2 respectively. We have also reported the results obtained by Ragazzo (2020) scanned,

*The pressure P is related to the mass density ρ by $P=K\rho^{1+1/n}$, where K and n are positive constants.

Quantity (unit)	(Chambat et al. 2010)	This work
Mass (kg)	5.97218×10^{24}	
Equatorial radius (m)	6.378137×10^{6}	
Normalised MOI (−)	3.3069×10^{-1}	3.3151×10^{-1}
Rotation rate (s^{-1})	7.2921×10^{-5}	7.3104×10^{-5}
2nd degree gravitational moment (−)	1.0826×10^{-3}	1.0771×10^{-3}
4th degree gravitational moment (−)	-1.620×10^{-6}	-2.8233×10^{-6}
Relative Virial parameter		6×10^{-7}

Table 1. Physical properties of the Earth rescaled on the observed mass and equatorial radius and comparison with the data from Chambat et al. (2010).

who has solved Clairaut's equation, i.e. (1.1), with the same mass density prescription. We see that both solutions are in excellent agreement, with a slight deviation at large radii (i.e. close to the outermost surface).

The main output data are listed on Tab. 1, where we have also listed the values given by Chambat et al. (2010). Our dimensionless results have been rescaled with the mass and the radius given therein. The agreement with our approach is good, within a few 10^{-3}. The discrepancies have a priori two origins: the mass-density profile, which, in our case, comes from the *non-rotating* PREM (i.e. $\varepsilon^2 = 0$, while we find $\varepsilon^2 \sim 5 \times 10^{-3}$), and the slight deviation to spheroids assumed in Chambat et al. (2010). As the Virial parameter[†] of our solution is about 10^{-6}, this means the spheroidal approximation is very good; thus the use of a non-rotating model for a rotating planet seems to be the main source of error.

5 Conclusions

We have derived an integro-differential equation (IDE) describing the equilibrium of a spheroidally stratified body in the framework of the NSFoE theory, which is based on Maclaurin's formula. Although such equilibria remain approximate (see Hamy's "no-go" theorem), we have shown that this IDE was a reliable approximation even for fast rotators, with errors about 10^{-3} in relative. We then have built a code solving numerically the IDE in the case of a prescribed mass-density profile, which may contain several discontinuities. We have then computed the eccentricity profile for a rotating Earth, with the mass density obtained by seismologic models for a non-rotating Earth as an input. Our results were in accordance with Chambat et al. (2010), with an accuracy of much less than a percent.

We would like to thank J. Lambert, N. Rambaux and S. Rosat for fruitful comments and discussions during the session.

References

Basillais, B. & Huré, J.-M. 2021, MNRAS, 506, 3773
Chambat, F., Ricard, Y., & Valette, B. 2010, Geophysical Journal International, 183, 727
Clairaut, A. C. 1743, Théorie de la figure de la Terre tirée des principes de l'hydrostatique (David Fils)
Dziewonski, A. M. & Anderson, D. L. 1981, Physics of the Earth and Planetary Interiors, 25, 297
Hamy, M. 1890, Journal de mathématiques pures et appliquées. Tome VI, Gauthier-Villars et Fils, 69
Huré, J.-M. 2022, MNRAS, 512, 4047
Kong, D., Zhang, K., & Schubert, G. 2015, Physics of the Earth and Planetary Interiors, 249, 43
Lanzano, P. 1974, Ap&SS, 29, 161
Ragazzo, C. 2020, São Paulo Journal of Mathematical Sciences, 14, 1
Rambaux, N., Chambat, F., & Castillo-Rogez, J. C. 2015, A&A, 584, A127
Staelen, C. & Huré, J.-M. 2023, MNRAS, under revision

[†]The relative Virial parameter RVP is defined as RVP $= (W + 2T + U)/|W|$, where W, T and U are the gravitational, kinetic and internal energies, respectively. The lower |RVP|, the closer the solution is to exact equilibrium.

Session S16

Atelier général du Programme National de Planétologie (PNP)

SF2A 2023
M. N'Diaye, A. Siebert, N. Lagarde, O. Venot, K. Baillié, M. Béthermin, E. Lagadec, J. Malzac, J. Richard (eds)

CHEMICAL CHARACTERISATION OF WARM EXOPLANETARY ATMOSPHERES: REVELATIONS FROM JWST ABOUT WASP-39B AND MUCH MORE

O. Venot[1], S.-M. Tsai[2, 3], R. Veillet[1], B. Fleury[4] and M. Poveda[1]

Abstract. The first observations of WASP-39b by JWST permitted important discoveries concerning exoplanetary atmospheres. With this single target, JWST detected for the first time carbon dioxide, but also sulfur dioxide. Importantly, this latter detection (and its analysis) permitted to obtain the first evidence of photochemical processes in an exoplanet atmosphere. In this context, the EXACT project is particularly timely as it will provide physico-chemical data validated at high temperature enabling reliable modelling of warm exoplanet atmospheres. Such data are mandatory to analyse future data from the next generation of instruments.

Keywords: planets and satellites, stars planetary systems, atmosphere, astrochemistry, techniques spectroscopic

1 Introduction

After a perfect launch on December, 25^{th} and six months of commissioning, JWST began its first scientific operations. In order for the community to become fully familiar with the telescope as swiftly as possible and exploit its full capabilities, the Director's Discretionary - Early Release Science (DD-ERS) program has been set up. The particularity of the observations performed during this program is to be released publicly immediately.

To answer to the call, The Transiting Exoplanet Community (gathering hundreds of researchers) submitted a proposal with the aim of accelerating the acquisition and diffusion of technical expertise for transiting exoplanet observations with JWST. This accepted proposal (ERS Program 1366) is divided in 3 sub-programs, with one target each (Bean et al. 2018):
- Primary transit observation of WASP-39b with NIRISS, NIRCam and NIRSpec
- A single phase curve observation of WASP-43b with MIRI/LRS
- A secondary eclipse observations of WASP-18b with NIRISS

We'll focus in this proceeding on the observations of WASP-39b and the results derived from them (Sect. 2). In view of these discoveries, the EXACT project (funding by ANR) is really timely. We'll present the goal of this project in Sect. 3 and advertise for the very first results.

2 Observations and characterisation of WASP-39b

The warm exoplanet WASP-39b (Faedi et al. 2011) has the mass of Saturn and is slightly larger than Jupiter. It orbits very close (0.048 AU) from his solar-type star. It has been observed by JWST on July 2022. More specifically, observations with NIRSpec PRISM (0.5–5.5 μm) has been performed on July, 10; with NIRCam (2–4 μm) on July, 22–23, with NIRISS (0.6–2.8 μm) on July, 26, and with NIRSpec G395H (3–5 μm) on July, 30–31. The analysis of these different sets of observations lead to a series of six publications (JWST Transiting Exoplanet Community Early Release Science Team et al. 2023; Ahrer et al. 2023; Alderson et al. 2023; Feinstein et al. 2023;

[1] Université de Paris Cité and Univ. Paris Est Creteil, CNRS, LISA, F-75013 Paris, France
[2] Atmospheric, Oceanic and Planetary Physics, Department of Physics, University of Oxford, Oxford, UK.
[3] Department of Earth Sciences, University of California, Riverside, Riverside, CA, USA.
[4] Univ Paris Est Creteil and Université Paris Cité, CNRS, LISA, F-94010 Créteil, France

© Société Française d'Astronomie et d'Astrophysique (SF2A) 2023

Rustamkulov et al. 2023; Tsai et al. 2023). The observations of this single planet lead to important results: the first conclusive detection of carbon dioxide (CO_2) and the first detection of a sulfur species, sulfur dioxide (SO_2).

While several other species have been detected in the atmosphere of WASP-39b, a particular focus has been made to understand the origin of SO_2 in this atmosphere. Indeed, this species is not predicted by thermochemical equilibrium at such high amount (1–10 ppm) and disequilibrium processes must be invoked to explain such abondances. In Tsai et al. (2023), four different 1D kinetics models have been used in order to reproduce the observations and understand the chemical composition: ARGO (Rimmer & Helling 2016; Rimmer & Rugheimer 2019; Rimmer et al. 2021), ATMO (Tremblin et al. 2015), KINETIC (Moses et al. 2011) and VULCAN (Tsai et al. 2017, 2021). They all used their own chemical network containing sulfur species. From the atmospheric composition derived, the synthetic observations have been calculated with the 3D Monte Carlo radiative-transfer code gCMCRT (Lee et al. 2022). The nominal model reproducing the best the observations is a model assuming a metallicity 10×solar, and a C/O ratio of 0.55 (solar). According to the outputs of all the models, the maximum abundance of SO_2 is found to be at 0.01–1 mbar, with a value of 10–100 ppm (see Fig. 1 of Tsai et al. 2023). This is slightly higher than the values derived from the observations, but still consistent (especially the column-integrated number densities above 10 mbar, see Tsai et al. 2023 for more details).
The analysis of the chemical pathways occurring in the atmospheric models permitted to understand that the production of sulfur dioxide in the upper atmosphere of this planet came from H_2S and was initiated by the photolysis of water, according to:

$$\begin{aligned} H_2O + h\nu &\longrightarrow OH + H \\ H_2O + H &\longrightarrow OH + H_2 \\ H_2S + H &\longrightarrow SH + H_2 \\ SH + H &\longrightarrow S + H_2 \\ S + OH &\longrightarrow SO + H \\ SO + OH &\longrightarrow SO_2 + H \\ \hline \text{net : } H_2S + 2\,H_2O &\longrightarrow SO_2 + 3\,H_2. \end{aligned}$$

This result is very important for exoplanet atmospheric science as it represents the first evidence of photolysis processes in the atmosphere of an exoplanet.
As can be seen on Fig. 1 of Tsai et al. (2023), the several models used in this study do not predict strictly the same abundance of SO_2. The peak of production varies by a factor 10 in term of abundance and by a factor 100 in term of pressure level. These deviations are due to the chemical data used by the models, which are not identical. In particular, the chemical schemes and the UV physico-chemical data are different, because coming from different sources. Indeed, there is no consensus in the community about which data to use and the lack of data at high temperature is an important source of uncertainty (Fortney et al. 2019).

Given the high quality of spectroscopic data that is now provided by JWST, it is urgent to address this point and obtain reliable data at high temperatures. This is the main focus of the ANR project EXACT, presented in Sect. 3.

3 The EXACT project

The EXACT project (EXoplanetary Atmospheric Chemistry at high Temperature, PI: O. Venot) aims at improving the study of warm exoplanet atmospheres. One of the objectives of the project is to reduce the uncertainties of kinetics models by providing physico-chemical data adapted to the high temperatures prevailing in exoplanets such as hot Jupiters and warm Neptunes. On this aspect, the project aims at 1. developing chemical schemes validated in high temperature conditions (Sect. 3.1) and 2. study experimentally the thermal dependency of VUV absorption cross section (Sect. 3.2). All the data developed or obtained in the frame of the project are available on the EXACT website*.

3.1 High temperature validated chemical schemes

Most of chemical schemes used in exoplanetology are developed 'ad-hoc', by picking reactions that seemed relevant from combustion literature, and adding them to existing chemical networks used to study giant planets

*https://www.anr-exact.cnrs.fr/.

(e.g. Moses et al. 2011; Rimmer & Helling 2016). This historically well-used method does not guarantee the completeness of the chemical schemes neither their validity. In an interdisciplinary collaboration with the Laboratoire Réaction et Génie des Procédés (LRGP), an original approach has been adopted, which consists of building comprehensive new chemical networks adapted from combustion studies and validated as a whole (not only individual reactions) against experimental data of the literature. These data correspond to combustion experiments performed on large ranges of temperatures (300-2500 K) and pressures (0.01-500 bars). This unique specificity allows these schemes to be highly robust and reliable. With this approach, several chemical schemes have already been developed (Venot et al. 2012, 2015, 2020). We have recently revisited our last chemical scheme in order to publish the most up-to-date CHON chemical scheme (Veillet et al. accepted, 2023). When used in a kinetic model, this new chemical scheme leads to quite important variations compared to what was obtained with our last chemical scheme (Venot et al. 2020). In particular in the case of warm Neptunes, such as GJ 436b, for which the abundance of CO_2 and HCN are particularly affected (see Fig. 1 and Fig. 5 of Veillet et al. accepted, 2023). This network will serve as basis for developing the first sulfur network validated on experimental combustion points (Veillet et al. in prep.).

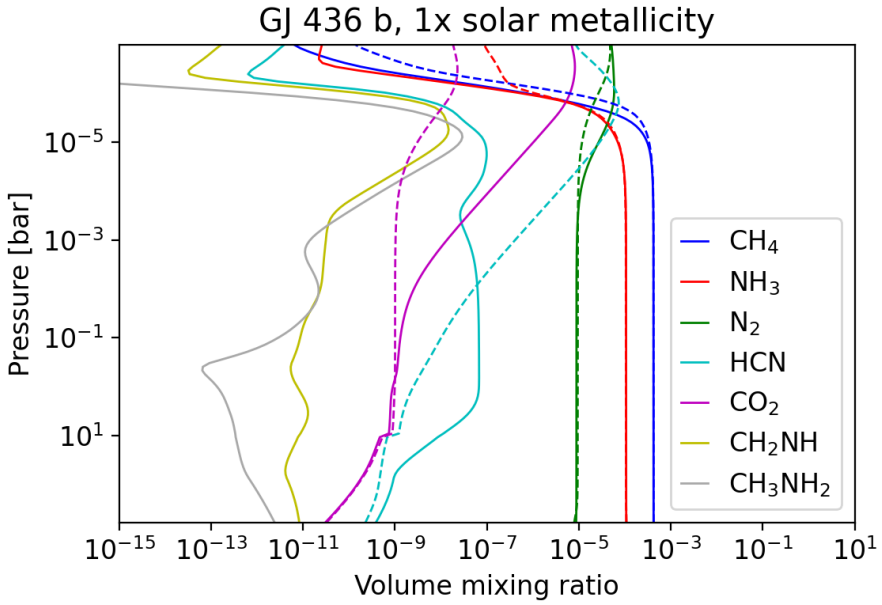

Fig. 1. Abundance profiles of GJ 436 b assuming solar metallicity and a constant eddy coefficient of 10^9 $cm^2.s^{-1}$. Dashed lines are when the kinetic model is using the chemical scheme from Venot et al. (2020), while solid lines are when using the new chemical scheme from Veillet et al. (accepted, 2023). Adapted from Veillet et al. (accepted, 2023).

3.2 Thermal dependency of VUV absorption cross sections

The other source of uncertainty addressed in the EXACT project concerns the VUV absorption cross-sections and their thermal dependency. Indeed, these physico-chemical data, fundamental to calculate the photolysis rates of species and the actinic flux depend on temperature but are poorly known. In the absence of data, room temperature data are often used, which is a major source of uncertainty. Venot et al. (2013, 2018) studied the absorption of CO_2 at various temperatures from 150 to 800 K and observed a strong increase of the absorption with temperature (about four orders of magnitude at 200 nm !). The use of correct data in atmospheric kinetic model has important implication for the chemical composition calculated, modifying by several orders of magnitude the abundance of some (other) species (NH_3, CH_4,...). All the species are indeed linked through chemical reactions, and thus the study of all absorbing species is necessary to have reliable chemical models. After the study of this first molecule, the EXACT project will permit to study the absorption cross sections of many other molecules, thanks to the VUV spectroscopic platform developed at the Laboratoire Interuniversitaire des Systèmes Atmosphériques (LISA) (Fig. 2). This platform permits acquisition of spectra in the range [50–300] nm with a resolution of 0.01 nm.

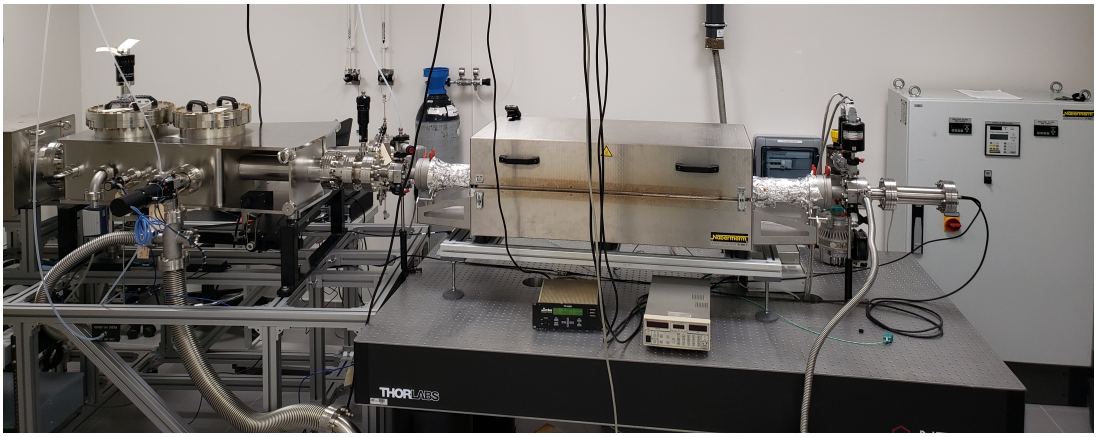

Fig. 2. VUV platform developed at LISA for absorption cross section measurements.

The first molecule for which we studied the absorption cross-section is acetylene (C_2H_2). As expected, we observed that the absorption increases together with temperature (see the Proceeding of Fleury et al. in this Edition and Fleury et al. in prep.).

4 Conclusion

During his first year of life, and with his very first observations, JWST showed us its huge potential. With only one target, the quality of his data and his large spectral covering permits to obtain very important results for exoplanetary atmospheric science : 1) the first firm detection of CO_2 in an atmosphere (JWST Transiting Exoplanet Community Early Release Science Team et al. 2023); 2) the first detection of a sulfur species (Tsai et al. 2023); 3) the first observational evidence of photochemical processes in an atmosphere (Tsai et al. 2023). Given the high quality of JWST data, it is mandatory to have reliable physico-chemical data to study exoplanetary atmospheres. It is the aim of the EXACT project (PI: O. Venot) to provide such data.

O.V. thanks the Conseil de la SF2A for the organisation of this week and the SOC of the PNP workshop to invite her to give a talk. O.V. and R.V. acknowledge funding from the ANR project EXACT (ANR-21-CE49- 0008-01). O. V. also thanks the Centre National d'Études Spatiales (CNES) and the CNRS/INSU Programme National de Planétologie (PNP). S.-M.T. acknowledges support from the University of California at Riverside.

References

Ahrer, E.-M., Stevenson, K. B., Mansfield, M., et al. 2023, Nature, 614, 653

Alderson, L., Wakeford, H. R., Alam, M. K., et al. 2023, Nature, 614, 664

Bean, J. L., Stevenson, K. B., Batalha, N. M., et al. 2018, PASP, 130, 114402

Faedi, F., Barros, S. C. C., Anderson, D. R., et al. 2011, A&A, 531, A40

Feinstein, A. D., Radica, M., Welbanks, L., et al. 2023, Nature, 614, 670

Fleury, B., Poveda, M., Venot, O., & Bénilan, Y. in prep.

Fortney, J., Robinson, T. D., Domagal-Goldman, S., et al. 2019, Astro2020: Decadal Survey on Astronomy and Astrophysics, 2020, 146

JWST Transiting Exoplanet Community Early Release Science Team, Ahrer, E.-M., Alderson, L., et al. 2023, Nature, 614, 649

Lee, E. K. H., Wardenier, J. P., Prinoth, B., et al. 2022, ApJ, 929, 180

Moses, J., Visscher, C., Fortney, J., et al. 2011, ApJ, 737, 15

Rimmer, P. & Rugheimer, S. 2019, Icarus, 329, 124

Rimmer, P. B. & Helling, C. 2016, ApJS, 224, 9

Rimmer, P. B., Jordan, S., Constantinou, T., et al. 2021, The Planetary Science Journal, 2, 133

Rustamkulov, Z., Sing, D. K., Mukherjee, S., et al. 2023, Nature, 614, 659

Tremblin, P., Amundsen, D. S., Mourier, P., et al. 2015, ApJ, 804, L17

Tsai, S.-M., Lee, E. K. H., Powell, D., et al. 2023, Nature, 617, 483
Tsai, S.-M., Lyons, J. R., Grosheintz, L., et al. 2017, ApJS, 228, 20
Tsai, S.-M., Malik, M., Kitzmann, D., et al. 2021, ApJ, 923, 264
Veillet, R., Venot, O., Sirjean, B., Bounaceur, R., & Glaude, P.-A. in prep.
Veillet, R., Venot, O., Sirjean, B., et al. accepted, 2023, A&A
Venot, O., Bénilan, Y., Fray, N., et al. 2018, A&A, 609, A34
Venot, O., Cavalié, T., Bounaceur, R., et al. 2020, A&A, 634, A78
Venot, O., Fray, N., Bénilan, Y., et al. 2013, A&A, 551, A131
Venot, O., Hébrard, E., Agúndez, M., Decin, L., & Bounaceur, R. 2015, A&A, 577, A33
Venot, O., Hébrard, E., Agúndez, M., et al. 2012, A&A, 546, A43

SF2A 2023
M. N'Diaye, A. Siebert, N. Lagarde, O. Venot, K. Baillié, M. Béthermin, E. Lagadec, J. Malzac, J. Richard (eds)

PLANET-GAS INTERACTIONS IN DEBRIS DISKS: OBSERVABLE STRUCTURES

C. Bergez-Casalou[1] and Q. Kral [1]

Abstract. Since recently, consequent amounts of CO gas were observed in old debris disks which were expected to be gas-free. At this stage, planet formation already occurred and planets are expected to be evolving in these discs. In this presentation, we show how these planets might form observable substructures in the gas of these debris disks. We focus specifically on a recent method developed in protoplanetary disks: when a planet is embedded in a gas disk, it perturbs its normally keplerian velocity, forming a kink. By simulating an already known debris disk hosting a large amount of CO, we show that these features can also be observed in debris disks. This leads to a new way to indirectly detect exoplanets and to better characterize the interactions between the already formed planets and the old observed gas.

Keywords: debris disks, synthetic observations, CO gas, planet-gas interactions, kinks

1 Introduction

1.1 Substructures observed in protoplanetary disks and their origin

Planets form in gas-rich (99% of gas for 1% of dust) disks surrounding new-born stars. Recent ALMA observations of the birth environment of planets show different kinds of substructures, like gaps, rings or asymmetries, both in the dust (e.g., as seen in the analysis from the DSHARP survey, Huang et al. 2018) and in the gas (e.g., in the CO distribution of the MAPS survey, Zhang et al. 2021). Simulations show that these substructures might have several different origins, as for example, zonal flows (Flock et al. 2015), secular gravitational instabilities (Takahashi & Inutsuka 2016; Tominaga et al. 2020) or sintering-induced rings (Okuzumi et al. 2016).

Another possible origin for these substructures is from the interactions between growing planets and their birth environment (e.g., Zhang et al. 2018; Teague et al. 2021). However, it is complicated to directly detect these planets due to the very dusty environment around them (Sanchis et al. 2020), forcing us to rely on the indirect impact that the planets leave on their environment.

When planets are embedded in their gaseous disks, they can create gaps if they are massive enough but also spiral arms, due to resonances with the gas in differential rotation. The characteristics of the spiral arms depend on the properties of both the planet and the gas. They impact the rotational velocity of the gas, which normally follows a keplerian profile. These deviations from the keplerian profiles are called **kinks** (for a review see Pinte et al. 2022). As shown in Fig.1, they are the strongest at the planet location and then dissipate in amplitude further away in the disk. It is possible to observe the velocity structure of disks thanks to the Doppler effect, making these kinks observable. They can therefore help to indirectly detect planets which are not massive enough to open a deep gap and/or to determine if a gap is indeed linked to the presence of a planet or not.

These kinks have been observed in CO gas by ALMA on multiple occasions: for example, in Pinte et al. (2018), they detected a perturbation of the gas rotational velocity in HD163296, consistent with a two-Jupiter-mass planet located at ≈ 260 AU from its host star. In Teague et al. (2018), they find two other deviations from the keplerian rotation of CO isotopologues, consistent with the presence of two Jupiter mass planets located at ≈ 83 and 137 AU. More recently, in Stadler et al. (2023), they find a non-keplerian feature in RXJ1604.3-2130A, consistent with a planet of ≈ 2 M_J located at roughly 41 AU. These detections prove that ALMA has the capacity to find such perturbations of the rotational velocity in a gaseous disk.

[1] LESIA, Observatoire de Paris, Université PSL, CNRS, Sorbonne Université, Univ. Paris Diderot, Sorbonne Paris Cité, 5 place Jules Janssen, 92195 Meudon, France

© Société Française d'Astronomie et d'Astrophysique (SF2A) 2023

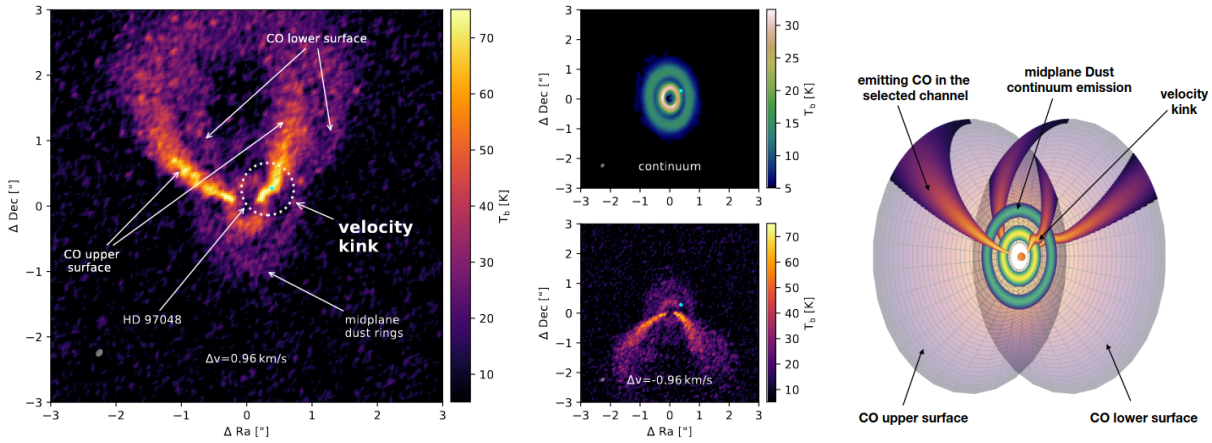

Fig. 1. From Pinte et al. (2019): **Left:** ALMA observations of the dust and gas disc surrounding HD 97048. a) ^{13}CO 3-2 emission at velocity +0.96km.s^{-1} from the systemic velocity. The velocity kink revealing the presence of an embedded perturber is marked by a dotted circle and the cyan dot represents the location of the putative planet. The kink is located above the gap detected in continuum.b) 885 μm continuum emission using all the continuum channels b) and c) ^{13}CO 3-2 emission at the opposite velocity −0.96km.s^{-1}from the systemic velocity, where the emission displays a smooth profile. Line observations were not continuum subtracted. The ALMA beam is 0.07" × 0.11" and is indicated by the grey ellipse. **Right:** Schematic view of the disc as seen by ALMA in a single channel. The CO emission originates from the disc surfaces, while the continuum is mostly emitted from the disc midplane.

1.2 Observed CO rich gas during the debris disk phase

The gaseous phase of the protoplanetary disk is estimated to last up to 10 Myrs due to different dispersal mechanisms (e.g., viscous accretion, disk winds, photoevaporation, see review by Lesur et al. 2022). After then, the system becomes a debris disk, mostly composed of dust, planetesimals and the formed planets. Since recently, gas has been observed in these old disks too (e.g., Moór et al. 2017). This gas seems to be highly enriched in metals compared to protoplanetary disks with the gas abundances being dominated by CO, C and O. Some models suggest that this might indicate that the gas is not primordial and originates from the collision of planetesimals (Kral et al. 2019) . It could then viscously evolve similarly to the protoplanetary disk phase, perhaps through an efficient MRI effect thanks to the high ionisation rate present in debris disks (Kral & Latter 2016). Some of the observed debris disks can host up to a few tenth of Earth masses in CO gas (Cataldi et al. 2020), similar to the amount of CO seen in some protoplanetary disks (Zhang et al. 2021).

2 Applying CO kinks analysis to debris disks

While we have some direct observations of planets in debris disks - as for example in the β Pictoris system, hosting a 9 M_J planet at 2.7 AU and a 10 M_J planet at 9.2 AU (Lagrange et al. 2019) or in the GJ504 system, hosting a 4 M_J planet at around 43 AU (Bonnefoy et al. 2018) - the direct detection method is able to probe mostly the most massive (and therefore more luminous) planets with masses larger than a few Jupiter masses. The debris disks might host smaller planets that cannot be observed directly. However, these hidden planets might interact with their surrounding environment and leave characteristic substructures that we can observe, such as the CO kinks observed in the protoplanetary disks. As the amount of CO observed in the debris disks is similar to some protoplanetary disks, we show here that such kinks can be observed in debris disks too.

Applying this analysis to the gas present in debris disks can lead to a new way to detect exoplanets, at an intermediate stage during the life of the planetary system where the majority of the primordial gas is gone but the planetesimal belts are still massive. In case of detection, we can start to then characterize then the interactions between the planets and this CO enriched gas: indeed, if this gas can approach the planets, then it might be accreted by them too, enriching their metallicity compared to the metallicity of the host star, as investigated by Kral et al. (2020).

2.1 The example of HD138813

As mentioned earlier, the CO kinks depend on the properties of both the planet and the gas. In order to test if such kinks are indeed observable in debris disk-like conditions, we based part of our study on a known debris disk. We selected a luminous and massive disk where CO was already detected and characterized: the disk around HD138813 (A0V star, located at 137.5 pc). Thanks to the analysis of previous observations, the disk around HD138813 is expected to host a quite significant mass of CO gas ($\sim 3 \times 10^{-3}$ $M_\oplus$, Hales et al. 2019). Its CO ring is estimated to spread between 5 AU and 210 AU, with a surface density profile constrained to follow $\Sigma_0(65\ \mathrm{AU}) = 10^{-5}\mathrm{g/cm^2}$ with a power law profile in $r^{-0.5}$ for the inner part ($r < 65$ AU) and in $r^{-4.0}$ for the outer part ($r > 65$ AU).

The advantage of HD138813 is its intermediate inclination (29° with a polar angle of 49.6°), which allows us to have a good representation of the isovelocities geometry (Pinte et al. 2022). It exists more massive disks that are more luminous than HD138813, however their inclination does not fit our constraints (such as HD32297 for example, with an estimated CO mass of 1.6 $M_\oplus$ but with a high inclination of 78°). Among the CO bearing debris disk population with an ideal inclination, HD138813 (inclination of 29° with a polar angle of 49.6°) is the one with the highest estimated CO mass, making it the best benchmark for our study.

Furthermore, in HD138813, the dust ring was observed to be ranging from 70 AU to 150 AU, which is smaller than the gas extent. This could be explained by the efficient viscous spreading of the gas as presented in Kral et al. (2016). If a planet is indeed embedded in the gas around HD138813, it would be more likely located at the edge of the dust belt: during the protoplanetary disk phase, the dust could have been accumulated at the edge of the planet gap where it could grow to planetesimal sizes. After the dispersal of the primordial gas, the collisions in the planetesimal belt would release dust and gas to the extent that we observe nowadays. In this scenario, as the planet is completely embedded in the gas, it would produce the strongest CO kinks (i.e., gas located closer to the planet will be more deviated from its keplerian rotation), making the detection easier.

2.2 Simulated observations of CO kinks in HD138813 to test their observability

In order to determine if CO kinks are observable in HD138813, we used different kind of simulations to produce synthetic ALMA images. Based on the characteristics of the gas presented earlier, we first run hydro-simulations with `FARGO2D1D`, with a Jupiter mass planet (arbitrary) located at the edge of the dust ring (i.e., at 70 AU). In this simulation, the gas is estimated to be only CO gas and its viscosity is intermediate (the turbulent viscosity parameter α is set to 10^{-3}). After integrating for $\sim 10^5$ years, the perturbed gas distribution is used as an input in a radiative transfer model called `RADMC3D`. Using the `simobserve` and `tclean` routines from `CASA`, we can therefore estimate under which ALMA configuration the CO kinks are observable.

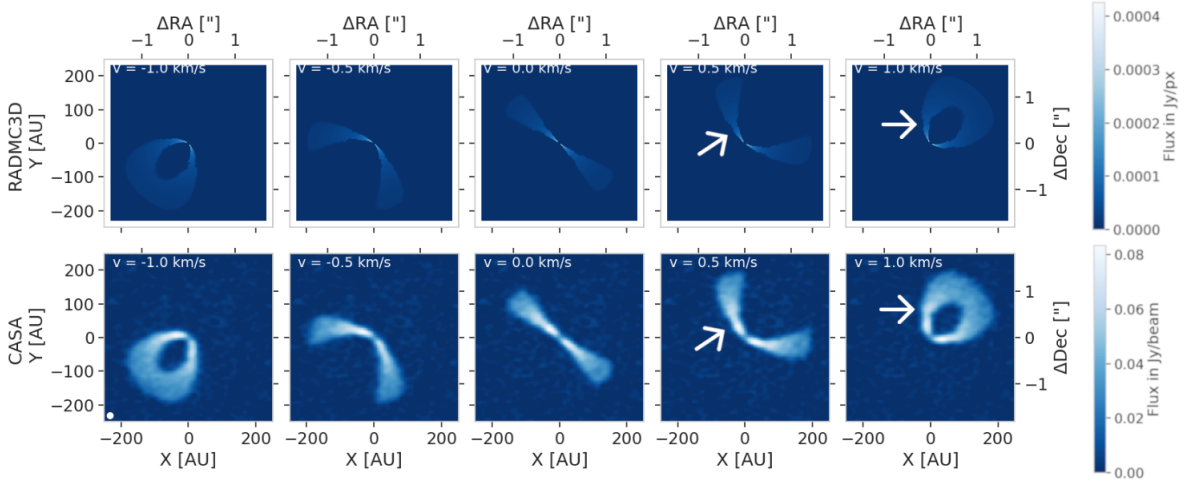

Fig. 2. *Top row: RADMC3D model of channels maps. The deviation from the center of the line is given in the top left corner of each plot. The CO kinks are marked by a white arrow. Bottom row: corresponding CASA simulated observation. In this case, the shown images are a combination of the C6 and C3 observations, the beam size is shown in the lower left corner of the first panel. The total integrated flux is 1.528 Jy.km/s, similar to the previous observations by Lieman-Sifry et al. 2016 (1.4 Jy.km/s).*

In Fig. 2, we show 5 channel maps of the CO(J=2-1) emission in our perturbed disk (the deviation from the center of the line is written in the top left corner of each map). The top row shows the total flux image coming from `RADMC3D` and the bottom row shows the corresponding image simulated in `CASA`. In the top row, we see that the typical size of the rotational velocity deviation is around 0.15" - 0.2", requiring a minimal resolution of 0.13" to be resolved. The C6 configuration allows for such observations at a reasonable integration time. However, with the combined observations in the C6 and C3 configurations, after 4h of integration in C6 and 1.36h in C3, we clearly start to distinguish the CO kinks.

3 Conclusions

As mentioned earlier, it is only since recently that gas has been discovered in debris disks. Observations as simulated here for HD138813 can help us better understand what kind of interactions the already formed planets might have with this old gas. The constraints derived from such future observations will help us improve our models for the description and evolution of this gas, which is fundamental to determine its origin. Furthermore, we are currently extending our study of HD138813 to different characteristics of debris disks in order to determine a more global observability study.

References

Bonnefoy, M., Perraut, K., Lagrange, A. M., et al. 2018, A&A, 618, A63
Cataldi, G., Wu, Y., Brandeker, A., et al. 2020, ApJ, 892, 99
Hales, A. S., Gorti, U., Carpenter, J. M., Hughes, M., & Flaherty, K. 2019, ApJ, 878, 113
Huang, J., Andrews, S. M., Dullemond, C. P., et al. 2018, ApJ, 869, L42
Kral, Q., Davoult, J., & Charnay, B. 2020, Nature Astronomy, 4, 769
Kral, Q. & Latter, H. 2016, MNRAS, 461, 1614
Kral, Q., Marino, S., Wyatt, M. C., Kama, M., & Matrà, L. 2019, MNRAS, 489, 3670
Kral, Q., Wyatt, M., Carswell, R. F., et al. 2016, MNRAS, 461, 845
Lagrange, A. M., Meunier, N., Rubini, P., et al. 2019, Nature Astronomy, 3, 1135
Lesur, G., Ercolano, B., Flock, M., et al. 2022, arXiv e-prints, arXiv:2203.09821
Lieman-Sifry, J., Hughes, A. M., Carpenter, J. M., et al. 2016, ApJ, 828, 25
Moór, A., Curé, M., Kóspál, Á., et al. 2017, ApJ, 849, 123
Okuzumi, S., Momose, M., Sirono, S.-i., Kobayashi, H., & Tanaka, H. 2016, ApJ, 821, 82
Pinte, C., Price, D. J., Ménard, F., et al. 2018, ApJ, 860, L13
Pinte, C., Teague, R., Flaherty, K., et al. 2022, arXiv e-prints, arXiv:2203.09528
Pinte, C., van der Plas, G., Ménard, F., et al. 2019, Nature Astronomy, 3, 1109
Sanchis, E., Picogna, G., Ercolano, B., Testi, L., & Rosotti, G. 2020, MNRAS, 492, 3440
Stadler, J., Benisty, M., Izquierdo, A., et al. 2023, A&A, 670, L1
Takahashi, S. Z. & Inutsuka, S.-i. 2016, AJ, 152, 184
Teague, R., Bae, J., Aikawa, Y., et al. 2021, ApJS, 257, 18
Teague, R., Bae, J., Bergin, E. A., Birnstiel, T., & Foreman-Mackey, D. 2018, ApJ, 860, L12
Tominaga, R. T., Takahashi, S. Z., & Inutsuka, S.-i. 2020, ApJ, 900, 182
Zhang, K., Booth, A. S., Law, C. J., et al. 2021, ApJS, 257, 5
Zhang, S., Zhu, Z., Huang, J., et al. 2018, ApJ, 869, L47

SF2A 2023
M. N'Diaye, A. Siebert, N. Lagarde, O. Venot, K. Baillié, M. Béthermin, E. Lagadec, J. Malzac, J. Richard (eds)

SIMULATED METHANE CLOUDS IN THE TITAN TROPOSPHERE WITH THE TITAN PLANETARY CLIMATE MODEL

B. de Batz de Trenquelleon[1,2], P. Rannou[1] and S. Lebonnois[2]

Abstract. On Titan, methane plays a central role in the climatic characteristics and prebiotic chemical processes taking place on this moon. In addition, methane and minor gases from photochemical reactions generate clouds and precipitation that shape the satellite's landscape. We have coupled the Titan PCM with a new microphysical model of haze and clouds, enabling us to include phenomena hitherto omitted from 3D simulations, such as the nucleation and condensation of methane clouds, which contribute significantly to the observable cloud cover on Titan. The results of the current model more accurately reflect the different distributions present on Titan, notably that of gas, haze and clouds. This substantial improvement translates into more accurate atmospheric wind and temperature profiles, as well as a better description of the satellite's cycles and related processes.

Keywords: Planetary Science, Titan, Atmosphere, Model, Climate, Clouds

1 Introduction

Observations of Titan by the Cassini probe have mapped the thermal structure and composition of Saturn's moon's stratosphere over almost a year of Titan (Mathé et al. 2020; Vinatier et al. 2020). Analysis of these observations has revealed numerous seasonal variations in the thermal structure and atmospheric composition of the stratosphere, as well as the planet's global circulation and its inversion over the course of the year showing the presence of seasonal cycles on Titan. Despite radio-occultations of the lower stratosphere probed by Cassini (Schinder et al. 2012) and CIRS observations of its composition (Sylvestre et al. 2020), most of the phenomena that occur in the troposphere remain unexplained. In particular, the impact of clouds on thermal profiles and the distribution of haze in the satellite's lower atmosphere.

The last few years have seen major improvements to the IPSL Titan GCM from Lebonnois et al. (2012), now called Titan Planetary Climate Model (Titan PCM). A new microphysical model for haze (Burgalat & Rannou 2017) and clouds (Burgalat et al. 2014) has been implemented in moment, in contrast to conventional bin-distribution models, to overcome the problem of excessive computational resources of bin models. We therefore have a description of aerosol distributions in terms of moments of distribution. We are now able to model the methane clouds and the mist of minor species present in Titan's trposphere, in order to then study the methane cycle, its sources, sinks and related processes including clouds and rains.

2 Methode : The Titan PCM

2.1 Overview of the model

The Titan PCM is based on the IPSL Titan GCM presented in Lebonnois et al. (2012). This new model features numerous improvements and modifications. Its dynamics have been upgraded, we now use the LMDZ5 dynamical core from Hourdin et al. (2013) (previously the LDMZ4). We continue to use an horizontal resolution of 32 longitudes by 48 latitudes, with each grid covering $11.25° \times 3.75°$. This resolution is destined to be increased for more accurate simulations. The vertical extension is also unchanged, with 55 levels extending up to $\sim$500 km, a surface pressure of $\sim$1.467 bar, but now with a topography.

[1] GSMA, UMR CNRS 6089, Université de Reims Champagne-Ardenne, 51100 Reims, France
[2] Laboratoire de Météorologie Dynamique, IPSL, CNRS/UPMC, 75005 Paris, France

© Société Française d'Astronomie et d'Astrophysique (SF2A) 2023

The physical parameterization of the model has also been improved. A new correlated-k radiative transfer scheme has been implemented in the model. It enables us to better describe the thermal structure of the upper stratosphere, in particular by modeling the stratopause, never before simulated in the Titan PCM. We have increased the number of radiative transfer calls per Titan day to 50 in order to better take these new phenomena into account. The photochemistry has also been improved thanks to the efforts of (Vuitton et al. 2019), enabling a better description of the gas cycles. We won't dwell on these last two points, as an article in prep. is dedicated to them. Above all, we have now coupled the radiative transfer to a new microphysical model of haze and clouds in moment. A more detailed description of this microphysical model is given in sections 2.2 and 2.3.

2.2 Microphysical model of haze

The equation governing the evolution of aerosols in the atmosphere is written as follows :

$$\frac{d}{dt}C(r,z) = Q(r,z) + \frac{d}{dt}C(r,z)|_{sedimentation} + \frac{d}{dt}C(r,z)|_{coagulation} \tag{2.1}$$

Where $C(r,z)$ is the concentration of particles of radius r at altitude z. $Q(r,z)$ corresponds to the particle production function, while the other two terms correspond respectively to the evolution of concentration under the effect of sedimentation and coagulation.

The model of Burgalat & Rannou (2017) describes these phenomena in terms of distribution moments. Here we present the main elements of this model, described for two aerosol populations, "small" spherical aerosols (denoted S) and "large" fractal aerosols (denoted F), interacting by Brownian coagulation.

The k^{th} moment of the distribution law of aerosols in radius $n(r)$, is defined by :

$$M_k(n) = \int_0^\infty x^k n(r) dr \tag{2.2}$$

In this model, we only deal with two selected moments (particle number density M_0 and particle volume concentration M_3), which are used in the most part of the microphysical processes discussed here.

The main phenomenon involved in aerosol microphysics is intra-modal or inter-modal coagulation. The equation describing the temporal evolution of the moments through coagulation depends on the flow regime in which we are working. On Titan, we're in a transition regime, with the flow regime shifting continuously from the molecular regime in the upper stratosphere to the continuous regime in the troposphere. The details of the calculations are given in Burgalat & Rannou (2017), we will recall here only the final form of the equations :

$$\frac{dM_0^S}{dt} \propto \beta_1 \times {M_0^S}^2 - \beta_2 \times M_0^S M_0^F \quad ; \quad \frac{dM_3^S}{dt} \propto \delta_1 \times {M_3^S}^2 - \delta_2 \times M_3^S M_3^F \tag{2.3}$$

$$\frac{dM_0^F}{dt} \propto \gamma_1 \times {M_0^S}^2 - \gamma_2 \times {M_0^F}^2 \quad ; \quad \frac{dM_3^F}{dt} \propto -\delta_1 \times {M_3^S}^2 + \delta_2 \times M_3^S M_3^F \tag{2.4}$$

Where the prefactors β_i, γ_i and δ_i depend on the atmospheric properties of the environment, and shape properties of aerosols.

Sedimentation process is implemented in the model using a flux method as presented by Toon et al. (1988). Its equation depends on the fractal dimension of the particle, and uses the first order approximation of the slip-flow correction. It is expressed in moment as :

$$\frac{d}{dt}M_k(z) = -\vec{\nabla}.\vec{\Phi}_{sed} = -\frac{d}{dz}\frac{2\rho_p g}{9\eta E}\left(M_{\frac{D_f(k+3)-3}{D_f}} + \frac{A\lambda_g}{E}M_{\frac{D_f(k+3)-6}{D_f}}\right) \tag{2.5}$$

Where $E = r_m^{\frac{D_f-3}{D_f}}$, with D_f the fractal dimension of the aerosol and r_m the monomer radius. ρ_p is the aerosols bulk density, η the air viscosity, A the coefficient used in the first order slip-flow correction, and λ_g the atmospheric mean free path.

2.3 Microphysical model of clouds

Like aerosols, clouds are subject to microphysical laws. In this section, we present the phenomena of nucleation and condensation, the two "first steps" in cloud formation and the evolution of the droplets that characterize

them. As far as sedimentation is concerned, this process follows the same principle whether we're dealing with aerosols or drops, with the difference that drops here are considered to be perfect spheres ($D_f = 3.0$).

We have adapted the microphysical cloud model in moment of Burgalat et al. (2014). This model gives us the nucleation equation expressed in moment :

$$\frac{d}{dt}M_k^{core} = 4\pi J_{het} r_m^{-1} \times M_{k+3}^{aer} \tag{2.6}$$

Where M_k^{aer} and M_k^{core} are the k-order moments of aerosols and nucleation core respectively. J_{het} is the heterogeneous nucleation rate given by Keesee (1989). On Titan, nucleation is effective mainly in the troposphere, where only fractal particles remain. We therefore consider here that all the moments associated with aerosols are those of the fractal mode, and the k-order moment evolution of aerosols is the opposite of that for core.

Condensation only controls the evolution of drop size. It affects the volume of condensate making up the drop, while the number of core remains constant. In the current model, each of the condensable species χ is considered independent and there is no mixing between species. The evolution of the total volume of condensate M_3^χ associated with the drops corresponds to the product of the evolution of the volume of an effective drop and the total number of available core M_0^{core} :

$$\frac{dM_3^\chi}{dt} = 4\pi r_g \times \frac{S - S^*}{R_c + R_d} M_0^{core} \tag{2.7}$$

Where r_g is the droplet radius, S corresponds to the environment saturation (far from the drop), and S^* the saturation at the surface of the drop. R_c and R_d are resistance terms that will slow down condensation.

3 Results : Model Cycles

3.1 The seasonal haze cycle

In the stratosphere, there is a predominant meridional circulation pattern characterized by a vast cell extending from one pole to the other. During the summer hemisphere, this cell features ascending winds, while during the winter pole's season, it experiences descending winds. This pole-to-pole circulation pattern undergoes a change in direction approximately every twelve Earth years (a Titan year $\sim$ 30 Earth years). In figure 1, the meridional

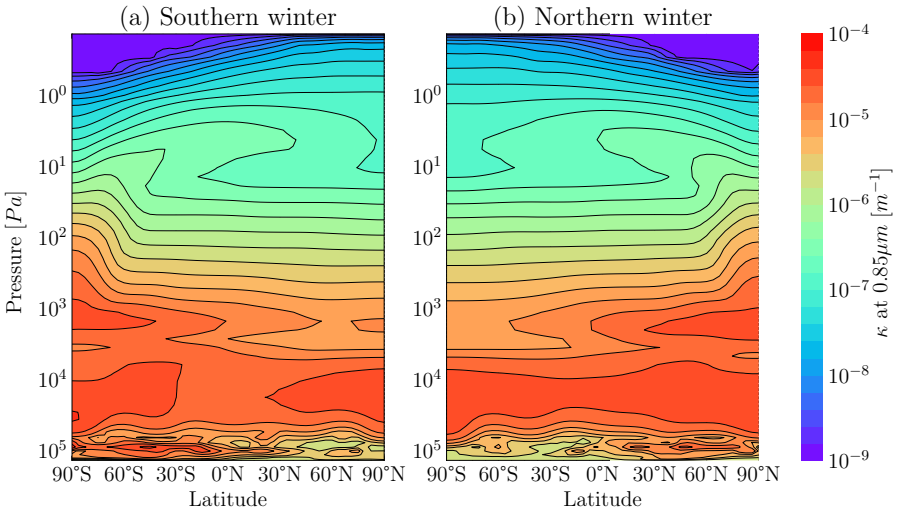

Fig. 1. Modeled latitude-pressure distribution of the extinction coefficient at $0.85\mu m$, for (a) southern winter ($L_S = 155°$) and (b) northern winter ($L_S = 335°$).

distribution of haze and clouds is shown during the northern and southern winters. It mainly highlights the seasonal variation of the main haze layer and its detached layer. More precisely, the haze follows the pole-to-pole stratospheric circulation, enriching the winter poles with aerosols. We also note the reversal of circulation that occurs at the northern spring equinox. This transition period leads to a haze cycle, which has a direct impact

on temperature profiles (not shown here), accentuating temperature differences between northern and southern regions. This influences atmospheric circulation and contributes to reinforcing atmospheric superrotation. A final point to note is the presence of an almost aerosol-free layer near the surface. This layer has been depleted of aerosols by precipitation from clouds higher up in the troposphere.

3.2 Tropospheric clouds

Consistently, our model produces clouds where clouds are actually observed (Fig. 2), but it also predicts clouds that have not (or not yet) been observed. Only clouds present in southern mid-latitudes between 2008 and 2010 (at the time of the circulation inversion) are not predicted by our model. In general, clouds form where methane is transported upwards by the circulation and condenses in the coldest regions. Methane clouds frequently appear in the rising branch of the tropospheric Hadley cell in the summer hemisphere (south in 2004). The mixing process produces a large region where the methane ratio is almost uniform and close to

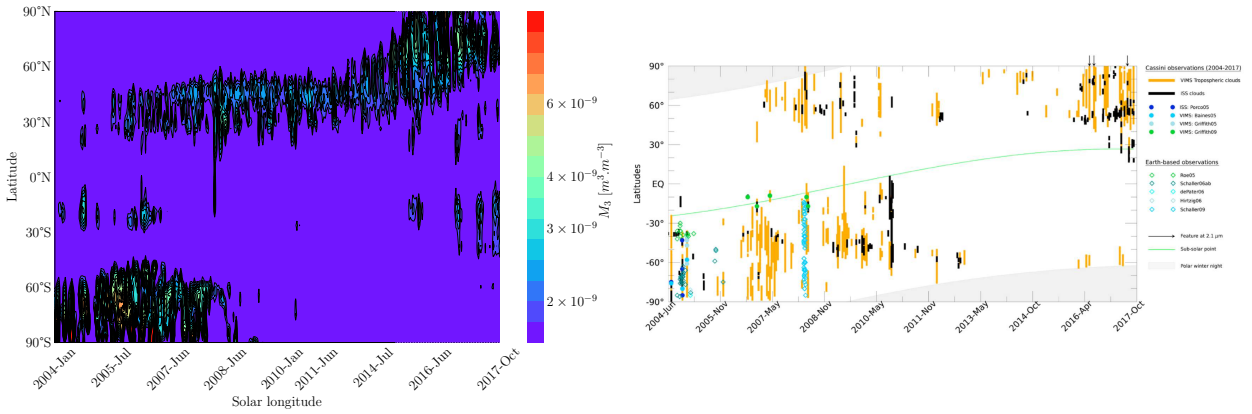

Fig. 2. Left: Modeled timescale-latitude distribution of the total volume of methane clouds. **Right:** Latitudes of tropospheric clouds observed from June 2004 through the end of the Cassini mission in September 2017 : Imaging Science Subsystem (ISS; black), Visual and Infrared Mapping Spectrometer (VIMS; orange), and Earth-based telescopes. From Turtle et al. 2018.

5%. In winter, temperature falls sharply with latitude, producing a zone of oversaturation. This pocket of supersaturation is fed by mixing, and the clouds that form at the lower edge of the region do not effectively remove the excess methane. These conditions are conducive to frequent cloud formation at mid-latitudes in winter. With radii of few tens of μm, methane droplets quickly sediment to the surface or evaporate a few kilometers lower down, in undersaturated layers. The time scale of sedimentation is much smaller than the time scale to restore, by upward mixing or advection, the methane saturation ratio to the critical saturation ratio (the ratio at which nucleation is triggered). As a result, methane clouds appear essentially as sporadic clouds rather than as a set of permanent clouds. Their lifespan is limited by their sedimentation timescale (several Earth days).

4 Conclusions

Based on the work of IPSL's Titan GCM, we have implemented a new microphysical model, which includes phenomena related to haze but now also includes clouds. Compared to the previous version of the model, we now have a better description of haze distribution, reinforcing temperature contrasts and thus super-rotation. We are also able to model clouds realistically, with a full description of their properties such as volume, drop size, or optical properties. The model can still be improved, taking into account deep convective clouds in the model. This type of phenomenon plays an important role in the global methane cycle. These developments will allow to go further in the understanding of the major cycles of Titan (methane, minor species, haze, etc.).

Thanks to the LOC and the SOC !

References

Burgalat, J. & Rannou, P. 2017, Journal of Aerosol Science, 105, 151
Burgalat, J., Rannou, P., Cours, T., & Rivière, E. D. 2014, Icarus, 231, 310
Hourdin, F., Grandpeix, J.-Y., Rio, C., et al. 2013, Climate Dynamics, 40, 2193
Keesee, R. G. 1989, J. Geophys. Res., 94, 14,683
Lebonnois, S., Burgalat, J., Rannou, P., & Charnay, B. 2012, Icarus, 218, 707
Mathé, C., Vinatier, S., Bézard, B., et al. 2020, Icarus, 344, 113547
Schinder, P. J., Flasar, F. M., Marouf, E. A., et al. 2012, Icarus, 221, 1020
Sylvestre, M., Teanby, N. A., Vatant d'Ollone, J., et al. 2020, Icarus, 344, 113188
Toon, O. B., McKay, C. P., Courtin, R., & Ackerman, T. P. 1988, Icarus, 75, 255
Turtle, E. P., Perry, J. E., Barbara, J. M., et al. 2018, Geophysical Research Letters, 45, 5320
Vinatier, S., Mathé, C., Bézard, B., et al. 2020, A&A, 641, A116
Vuitton, V., Yelle, R. V., Klippenstein, S. J., Hörst, S. M., & Lavvas, P. 2019, Icarus, 324, 120

SF2A 2023
M. N'Diaye, A. Siebert, N. Lagarde, O. Venot, K. Baillié, M. Béthermin, E. Lagadec, J. Malzac, J. Richard (eds)

HYDRODYNAMICAL MODELLING OF TIDAL DISSIPATION IN GAS GIANT PLANETS AT THE TIME OF SPACE MISSIONS

H. Dhouib[1], C. Baruteau[2], S. Mathis[3], F. Debras[2], A. Astoul[4] and M. Rieutord[2]

Abstract. Gas giant planets are differentially rotating magnetic objects that have strong and complex interactions with their environment. In our Solar system, they interact with their numerous moons while exoplanets with very short orbital periods (hot Jupiters), interact with their host star. The dissipation of waves excited by tidal forces in their interiors shapes the orbital architecture and the rotational dynamics of these systems. Recently, astrometric observations of Jupiter and Saturn systems have challenged our understanding of their formation and evolution, with stronger tidal dissipation in these planets than previously predicted, in contrast to what appears to be weaker in gas giant exoplanets. These new constraints are motivating the development of realistic models of tidal dissipation inside these planets. At the same time, the Juno and Cassini space missions have revolutionised our knowledge of the interiors of Jupiter and Saturn, whose structure is a combination of stably stratified zones and convective regions. In this work, we present results of hydrodynamical calculations modelling tidal waves and their dissipation in Jupiter, taking for the first time the latest, state-of-the-art interior model of the planet. We performed 2D numerical simulations of linear tidal gravito-inertial waves that propagate and dissipate within Jupiter interior by taking into account viscous, thermal and chemical diffusions. This new model allows us to explore the properties of the dissipation and the associated tidal torque as a function of all the key hydrodynamical and structural parameters.

Keywords: planets and satellites: gaseous planets, hydrodynamics, waves, methods: numerical

1 Introduction

Tides dissipate energy through various mechanisms, such as turbulent friction and heat diffusion (e.g. Ogilvie 2014; Mathis 2019). This dissipation impacts the evolution of planet-moon systems. Jupiter and Saturn display unexpectedly strong tidal dissipation, driving rapid orbital migration revealed by precise astrometric data (Lainey et al. 2009, 2012, 2017, 2020). For example, Lainey et al. (2009) determined a tidal dissipation rate of $k_{22}/Q = (1.1 \pm 0.2) \times 10^{-5}$ * for Io's asynchronous tide. This is one order of magnitude stronger than previous theoretical predictions based on moon formation scenarios (Goldreich & Soter 1966). In addition, the space missions Juno and the grand finale of the Cassini mission have completely changed our vision of the interiors of Jupiter and Saturn (Wahl et al. 2017; Guillot et al. 2018; Galanti et al. 2019). They revealed that these planets are structured by a central stably stratified core, a convective metallic shell, a potential intermediate stable layer in the case of Jupiter, and an outer differentially rotating molecular convective envelope. These new constraints motivate the development of realistic models of tidal dissipation inside these planets. That is why we develop a method to compute the dissipation of the dynamical tidal response of a self-gravitating, rotating fluid body composed of alternating convective layers and stably stratified layers (i.e. tidally-excited gravito-inertial waves; see also Lin 2023; Dewberry 2023) and which takes into account the viscous, thermal and chemical dissipation processes. We focus here on the latest Jupiter interior models built by Debras & Chabrier (2019), which matches constraints obtained by the Juno space mission.

[1] Université Paris Cité, Université Paris-Saclay, CEA, CNRS, AIM, F-91191, Gif-sur-Yvette, France
[2] IRAP, Université de Toulouse, CNRS, UPS, F-31400 Toulouse, France
[3] Université Paris-Saclay, Université Paris Cité, CEA, CNRS, AIM, F-91191, Gif-sur-Yvette, France
[4] Department of Applied Mathematics, School of Mathematics, University of Leeds, Leeds LS2 9JT, UK

* $k_{\ell m}$ is the tidal Love numbers which quantitatively characterises the planet's adiabatic hydrostatic response to the (ℓ, m) component of the tidal forcing, where ℓ and m are the latitudinal degree and azimuthal order of the corresponding spherical harmonics. Q is the tidal quality factor which evaluates the ratio between the maximum energy stored in the tidal distortion and the energy dissipated during an orbital period.

© Société Française d'Astronomie et d'Astrophysique (SF2A) 2023

2 Tidally forced waves in gas giant planet interiors

We investigate the linear excitation of (gravito-)inertial waves induced by external tidal forces. The dynamics of these waves are governed by Coriolis acceleration and buoyancy in stable layers and they undergo dissipative processes (assumed to be uniform here), namely viscosity (ν), thermal diffusion (κ), and molecular diffusion (D_μ). First, we linearise the hydrodynamic system around the hydrostatic steady-state. Each scalar field $X \coloneqq \{\rho, \Phi, T, \mu, P\}$[†] is expanded as the sum of its hydrostatic value X_0 and of the Eulerian perturbations associated with the tides X': $X(r,\theta,\varphi,t) = X_0(r) + X'(r,\theta,\varphi,t)$ and the velocity field, $\vec{V}$, is expanded as the sum of the large-scale azimuthal velocity associated with the uniform rotation Ω[‡] and of the wave velocity $\vec{v}$: $\vec{V}(r,\theta,\varphi,t) = r\sin\theta\,\Omega\,\vec{e}_\varphi + \vec{v}(r,\theta,\varphi,t)$, where t is time and (r,θ,φ) are the usual spherical coordinates with their associated unit vector basis $(\vec{e}_r, \vec{e}_\theta, \vec{e}_\varphi)$. Afterwards, we decompose the fluctuations associated with the tides into non-wavelike and wavelike parts: $Y = Y^{\mathrm{nw}} + Y^{\mathrm{w}}$, where $Y \coloneqq \{v_r, v_\theta, v_\varphi, X'\}$, Y^{nw} is the non-wavelike (equilibrium) tide that satisfies the hydrostatic equilibrium, and Y^{w} the wavelike (dynamical) tide that describes the propagation of tidal waves. The forcing term ($f^{\ell,m}$) arises when solving the wavelike tide as a residual force coming from the subtraction of the hydrostatic balance verified by the non-wavelike tide from the complete momentum equation (Ogilvie 2014). This force encompasses the acceleration of the non-wavelike tide and the Coriolis acceleration applied to it, which forces the (gravito-)inertial tidal waves. Finally, by assuming Boussinesq and Cowling approximations as a first step and by expanding on (vectorial) spherical harmonics (Rieutord 1987) the velocity field ($u_\ell^m, v_\ell^m, w_\ell^m$), temperature ($t_\ell^m$), molecular weight ($\mu_\ell^m$), reduced pressure ($p_\ell^m$) and the forcing vector ($f_{\mathrm{R}}^{\ell,m}, f_{\mathrm{S}}^{\ell,m}, f_{\mathrm{T}}^{\ell,m}$), we can write the dimensionless system that describe the wavelike tides as :

$$\mathrm{d}_r u_\ell^m + \frac{2}{r}u_\ell^m - \ell(\ell+1)\frac{v_\ell^m}{r} = 0, \tag{2.1}$$

$$\mathrm{E}\Delta_\ell u_\ell^m - \left(\frac{2\mathrm{E}}{r^2} - i\tilde{\omega}\right)u_\ell^m + \left(im + \frac{2\mathrm{E}}{r^2}\ell(\ell+1)\right)v_\ell^m - \beta_{\ell-1}^\ell w_{\ell-1}^m - \beta_{\ell+1}^\ell w_{\ell+1}^m - \mathrm{d}_r p_\ell^m + \frac{\delta g_0^*}{T_0^*}t_\ell^m - \frac{\phi g_0^*}{\mu_0^*}\mu_\ell^m = -f_{\mathrm{R}}^{\ell,m}, \tag{2.2}$$

$$\mathrm{E}\Delta_\ell v_\ell^m + \left(i\tilde{\omega} + \frac{im}{\ell(\ell+1)}\right)v_\ell^m + \left(\frac{2\mathrm{E}}{r^2} + \frac{im}{\ell(\ell+1)}\right)u_\ell^m - \gamma_{\ell-1}^\ell w_{\ell-1}^m - \gamma_{\ell+1}^\ell w_{\ell+1}^m - \frac{p_\ell^m}{r} = -f_{\mathrm{S}}^{\ell,m}, \tag{2.3}$$

$$\mathrm{E}\Delta_\ell w_\ell^m + \left(i\tilde{\omega} + \frac{im}{\ell(\ell+1)}\right)w_\ell^m + \gamma_{\ell-1}^\ell v_{\ell-1}^m + \gamma_{\ell+1}^\ell v_{\ell+1}^m - \frac{\alpha_{\ell-1}^\ell}{\ell}u_{\ell-1}^m + \frac{\alpha_{\ell+1}^\ell}{\ell+1}u_{\ell+1}^m = -f_{\mathrm{T}}^{\ell,m}, \tag{2.4}$$

$$\frac{\mathrm{E}}{\mathrm{Pr}}\Delta_\ell t_\ell^m - u_\ell^m\frac{T_0^* N_{\mathrm{t}}^{*2}}{g_0^*\delta} + i\tilde{\omega}t_\ell^m = 0, \quad \frac{\mathrm{E}}{\mathrm{Sc}}\Delta_\ell \mu_\ell^m + u_\ell^m\frac{\mu_0^* N_\mu^{*2}}{g_0^*\phi} + i\tilde{\omega}\mu_\ell^m = 0, \tag{2.5}$$

where $\tilde{\omega}$ is the normalised tidal forcing frequency, g_0^* is the normalised gravitational acceleration, $N_{\mathrm{t}}^{*2} = N_{\mathrm{t}}^2/4\Omega^2$ is the normalised Brunt-Väisälä frequency linked to the thermal stratification squared, $N_\mu^{*2} = N_\mu^2/4\Omega^2$ is the normalised Brunt-Väisälä frequency linked to the chemical stratification squared, and

$$\Delta_\ell = \mathrm{d}_{r^2} + \frac{2}{r}\mathrm{d}_r - \frac{\ell(\ell+1)}{r^2}, \quad \alpha_{\ell-1}^\ell = \alpha_\ell^{\ell-1} = \sqrt{\frac{\ell^2-m^2}{(2\ell-1)(2\ell+1)}}, \quad \beta_{\ell-1}^\ell = (\ell-1)\alpha_{\ell-1}^\ell, \tag{2.6}$$

$$\beta_{\ell+1}^\ell = -(\ell+2)\alpha_{\ell+1}^\ell, \quad \gamma_{\ell-1}^\ell = \frac{\ell-1}{\ell}\alpha_{\ell-1}^\ell,\ \gamma_{\ell+1}^\ell = \frac{\ell+2}{\ell+1}\alpha_{\ell+1}^\ell,\ \delta \coloneqq -\left(\frac{\partial\ln\rho}{\partial\ln T}\right)_{P,\mu},\ \phi \coloneqq \left(\frac{\partial\ln\rho}{\partial\ln\mu}\right)_{P,T}. \tag{2.7}$$

We define also the following dimensionless numbers : the Prandtl number $\mathrm{Pr} = \nu/\kappa$, the Schmidt number $\mathrm{Sc} = \nu/D_\mu$ and the Ekman number $\mathrm{E} = \nu/2\Omega R^2$[§] (the ratio between the viscous force and the Coriolis force).

[†] ρ, Φ, T, μ and P are the density, the gravitational potential, the temperature, the mean molecular weight, and the pressure, respectively.

[‡] As a first step we neglect differential rotation, since Jupiter's relative differential rotation is 4% (Guillot et al. 2018).

[§] R is Jupiter's radius.

3 Jupiter's interior model matching the constraints provided by Juno

The internal structure model that we consider here is computed by Debras & Chabrier (2019); Chabrier & Debras (2021) to reproduce Jupiter's multipolar gravitational moments as measured by Juno. As illustrated in Fig. 1, starting from its surface and moving towards the core, Jupiter is thought to exhibit the following layers : a gaseous convective envelope, a transitional stably stratified zone considered to be potentially semi-convective, an internal convective zone composed of metallic hydrogen and helium, a stably stratified zone located closer to the core which may exhibit double diffusion convection or a diluted core structure due to stabilising composition gradients, and a potential unstable solid core of size 1.4% of the radius made up of rock or ice ¶.

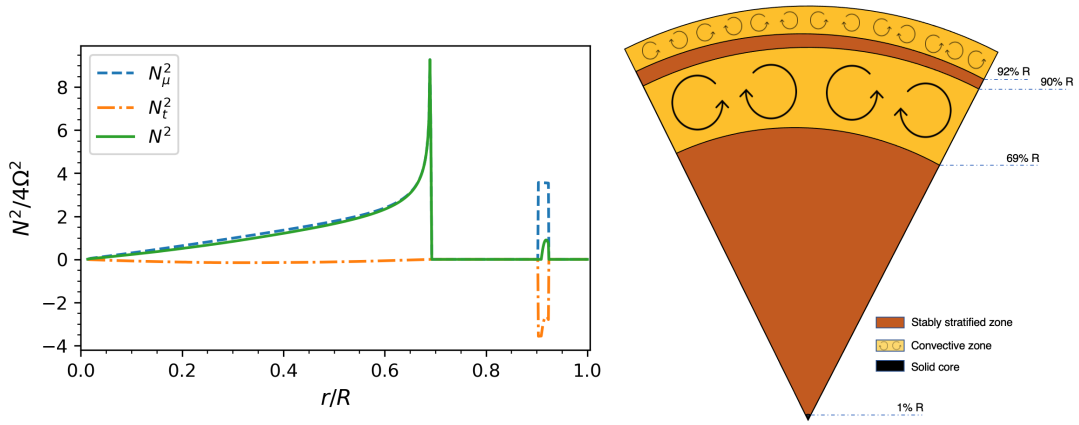

Fig. 1. Left: Radial profiles of the normalised compositional (N_μ^2), thermal (N_t^2), and total (N^2) buoyancy frequencies squared of Jupiter's interior used in this study. **Right:** Schematic of this model.

4 Dissipation spectra and imaginary part of the Love number

We solve the system (2.1)-(2.5) numerically using the 2D pseudo-spectral linear code LSB (Linear Solver Builder, Valdettaro et al. 2007). These equations are discretised in the radial direction on the Gauss-Lobatto collocation nodes associated with the Chebyshev polynomials. They are truncated to order N_r for the Chebyshev basis and to order N_ℓ for the spherical harmonics basis. We specifically investigate the quadrupolar tidal components ($\ell = m = 2$). The top panel of the Fig. 2 shows the viscous ($\widetilde{D}_{\rm visc}$), thermal ($\widetilde{D}_{\rm th}$), molecular ($\widetilde{D}_{\rm ch}$) and total ($\mathcal{D}$) dissipation rates integrated over the volume as a function of the normalised forcing frequency ($\tilde{\omega}$) for $\mathrm{E} = 10^{-7}$ and $\mathrm{Pr} = \mathrm{Sc} = 1$. We observe a significant frequency dependence, indicating a strong relationship between dissipation and forcing frequency. Moreover, for our set of E, Sc and Pr, the dominant mechanism contributing to dissipation is viscosity, surpassing both thermal and chemical dissipations in magnitude. We also represent the dissipation spectra for the standard vision of Jupiter's interior before Juno's results, where there is a single purely convective zone extending from $r = \eta = 0.014$ to $r = 1$. We can see that the spectra in this case exhibit a smooth profile with weaker magnitude, devoid of any pronounced peaks at specific frequencies. The bottom panel of Fig. 2 shows significant discrepancy between computed values of the imaginary part of the Love number due to Io and the observed ones, differing by roughly two orders of magnitude. Consequently, our calculations tend to overestimate the amplitude of tidal dissipation. Conversely, when examining the purely convective model, we observe an underestimation of tidal dissipation by approximately one and a half orders of magnitude. This shows the key role played by stably stratified layers in controlling the strength of the dissipation.

5 Conclusions

We examine the dissipation of dynamical tides in the latest Jupiter interior multi-layer model with alternating convective and stably stratified regions. We take into consideration various types of dissipations such as turbulent viscosity, thermal dissipation, and molecular diffusivity. This enables a more comprehensive and realistic

¶Note that as a first step, we neglected in this study the differential rotation in the outer convective region and the magnetic field in the internal one.

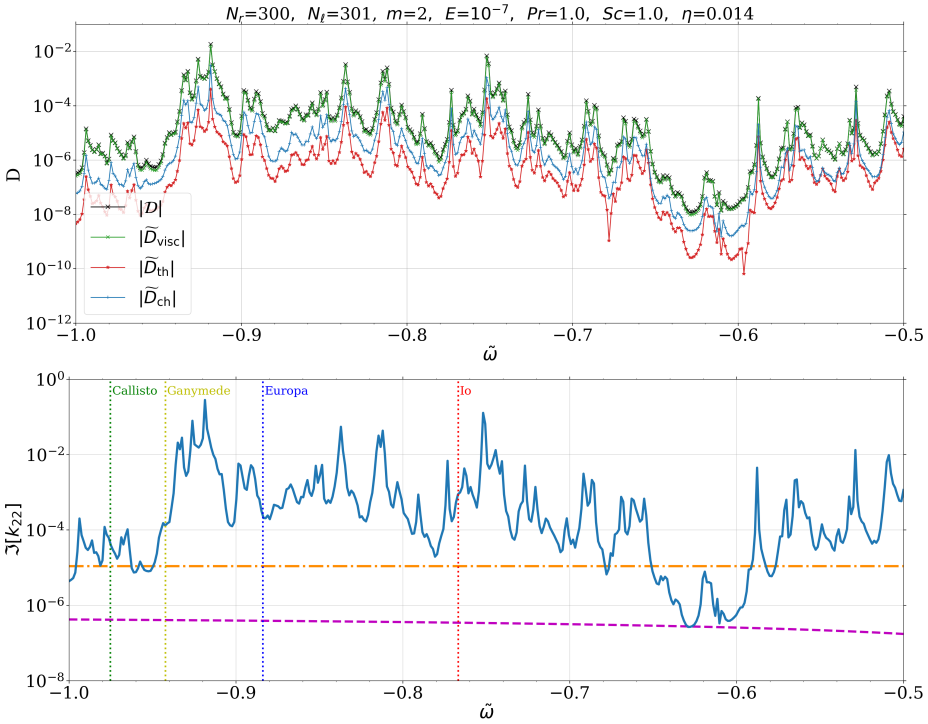

Fig. 2. Dissipations (Top) and imaginary part of the Love number (Bottom) as a function of the tidal frequency for $m = 2$, Pr = Sc = 1, E = 10^{-7} and $(N_r, N_\ell) = (300, 301)$. The magenta dashed line indicates the values of these quantities in the case of a purely convective interior. Vertical dotted lines indicate the tidal frequencies for the four Galilean Moons of Jupiter. The dash-dotted orange line marks the observed value due to Io (Lainey et al. 2009).

representation of the physical processes occurring within giant gas planets' interiors. We find that the presence of stably stratified regions plays a significant role in explaining the strong dissipation observed in Jupiter when compared to the case of a sole convective envelope. It is important to note that our model is not limited to Jupiter but can also be applied to other giant planets such as Saturn, as well as exoplanets.[‖]

References

Chabrier, G. & Debras, F. 2021, ApJ, 917, 4
Debras, F. & Chabrier, G. 2019, ApJ, 872, 100
Dewberry, J. W. 2023, MNRAS, 521, 5991
Galanti, E., Kaspi, Y., Miguel, Y., et al. 2019, Geophys. Res. Lett., 46, 616
Goldreich, P. & Soter, S. 1966, Icarus, 5, 375
Guillot, T., Miguel, Y., Militzer, B., et al. 2018, Nature, 555, 227
Lainey, V., Arlot, J.-E., Karatekin, Ö., & van Hoolst, T. 2009, Nature, 459, 957
Lainey, V., Casajus, L. G., Fuller, J., et al. 2020, Nature Astronomy, 4, 1053
Lainey, V., Jacobson, R. A., Tajeddine, R., et al. 2017, Icarus, 281, 286
Lainey, V., Karatekin, Ö., Desmars, J., et al. 2012, ApJ, 752, 14
Lin, Y. 2023, A&A, 671, A37
Mathis, S. 2019, in EAS Publications Series, Vol. 82, EAS Publications Series, 5–33
Ogilvie, G. I. 2014, ARA&A, 52, 171
Rieutord, M. 1987, Geophysical and Astrophysical Fluid Dynamics, 39, 163
Valdettaro, L., Rieutord, M., Braconnier, T., & Fraysse, V. 2007, J. Comput. Appl. Math., 205, 382
Wahl, S. M., Hubbard, W. B., Militzer, B., et al. 2017, Geophys. Res. Lett., 44, 4649

[‖]Acknowledgments: this work has been supported by PNP (CNRS/INSU) and the PLATO CNES grant at CEA/DAp and by the Leverhulme Trust for the award of an Early Career Fellowship to AA (ECF-2022-362).

SF2A 2023
M. N'Diaye, A. Siebert, N. Lagarde, O. Venot, K. Baillié, M. Béthermin, E. Lagadec, J. Malzac, J. Richard (eds)

HIGH TEMPERATURE MEASUREMENT OF ACETYLENE UV ABSORPTION CROSS SECTION FOR THE STUDY OF HOT EXOPLANET ATMOSPHERES

B. Fleury[1], M. Poveda[1,2], Y. Bénilan[1] and O. Venot[3]

Abstract. The interpretation of exoplanet atmospheres' observations relies on the used of atmospheric models requiring fundamental physico-chemical data as inputs. To improve the accuracy of these models, it is therefore essential to obtain physico-chemical data in conditions relevant to the observed atmospheres. For this purpose, we have studied experimentally the thermal dependency of the ultraviolet (UV) absorption cross section of acetylene (C_2H_2) between 296 and 673 K. Our first results reveal that the absorption cross section of C_2H_2 increases with the temperature, the increase being more important at longer wavelengths ($\lambda > \sim$180 nm) than at shorter ones.

Keywords: Exoplanet atmospheres, laboratory astrophysics, techniques spectroscopic, planets and satellites: atmospheres

1 Introduction

The understanding of the chemical composition of observed exoplanet atmospheres largely relies on the used of kinetic atmospheric models. This has been illustrated recently with the observation of sulfur dioxide (SO_2) in the atmosphere of the hot Jupiter WASP-39 b by JWST (Alderson et al. 2023). Indeed, the presence of SO_2 in this atmosphere has been explained, thanks to atmospheric 1D thermo-photochemical models, as the result of photochemical reactions (Tsai et al. 2023). To implement photochemistry, these models require fundamental physico-chemical data and in particular the UV absorption cross sections of molecules to calculate their photodissocation rates. Therefore, the use of inaccurate absorption cross sections lead to uncertainties in the calculation of the molecular abundances by these models (Ranjan et al. 2020; Venot et al. 2013, 2018).

Although most observed exoplanets have high equilibrium temperatures (500 - 2000 K), available data of the UV absorption cross sections of molecules of interest for exoplanet atmospheres are generally limited to the relatively low temperatures ($T < 400$ K) encounters in the atmospheres of the Solar System (see e.g., Bénilan et al. 2000; Chen & Wu 2004; Wu et al. 2001, 2007; Rufus et al. 2009). However, Venot et al. (2013, 2018) have determined the absorption cross section of carbon dioxide (CO_2) for a wider range of temperature (150 to 800 K) and shown that the absorption cross section of CO_2 increases of several orders of magnitude with the temperature. This increase of the absorption cross section significantly affects the molecular abundances calculated by kinetic model (Venot et al. 2018) and demonstrates the importance of using cross section determined at a temperature relevant for the studied atmospheres. It is therefore essential to study the thermal dependency of the UV absorption cross sections of molecules of interest in order to improve the accuracy of models used to study exoplanet atmospheres.

In this proceeding, we present the study of the thermal dependency of the UV absorption cross section of acetylene from 115 to 230 nm and for temperatures between 296 and 673 K. The experimental methodology is described in Sect. 2 and the first results are presented in Sect. 3.

[1] Univ Paris Est Creteil and Université Paris Cité, CNRS, LISA, F-94010 Créteil, France
[2] Université Paris-Saclay, UVSQ, CNRS, CEA, Maison de la Simulation, 91191, Gif-sur-Yvette, France
[3] Université Paris Cité and Univ Paris Est Creteil, CNRS, LISA, F-75013 Paris, France

© Société Française d'Astronomie et d'Astrophysique (SF2A) 2023

2 Experimental methods and protocols

2.1 Measurements of acetylene UV absorption spectra

The thermal dependency of the UV absorption cross section of C_2H_2 was studied thanks to a new UV spectroscopy plateform developed at the Laboratoire Interuniversitaire des Systèmes Atmosphériques (LISA, France). Briefly, the setup consists in a high temperature absorption cell composed of a quartz tube closed at each extremity by MgF_2 windows. The cell is warmed up by a tube furnace and its temperature is monitored with 3 type-K thermocouples. In this study, spectra of C_2H_2 were measured at 296 (ambient temperature), 373, 473, 573, and 673 K.

UV spectra of C_2H_2 were measured from 115 to 230 nm with an instrumental spectral resolution of 0.046 nm. As acetylene cross section in the 115-230 nm range spans five orders of magnitude (see Fig.1), it is necessary to adjust the pressure of the gas inside the cell (1×10^{-3} to 80 mbar) depending on the region of the spectrum measured in order to avoid any saturation of the absorption bands. For simplicity, we divided the full spectrum (115-230 nm) into 10 spectra covering a few nm each. Then, each spectrum was measured by introducing in the cell gaseous acetylene (purity > 99.5%) at an appropriate pressure.

As shown by Bénilan et al. (1995), acetone inside the gas bottle (used as a stabilizer) can affect the spectra of C_2H_2 recorded in the UV. To prevent this issue, acetone present in the injected gas was trapped by circulating the gas before injection into a cold trap made of a stainless-steel coil immersed in a mixture of liquid nitrogen and acetone at ∼183 K.

2.2 Calculation of the absorption cross section

The absolute absorption cross section of C_2H_2 was calculated from the measured spectra using the Beer-Lambert law:

$$\sigma(\lambda, T) = \frac{1}{nL} \times \ln\left(\frac{I}{I_0}\right) \tag{2.1}$$

where $\sigma(\lambda,\ T)$ is the absorption cross section (cm^2) at a given wavelength and temperature, L is the optical pathlength (cm), n the volume density of the gas in the cell (cm^{-3}), I_0 the intensity of the light transmitted through an empty cell and I the intensity of the light transmitted through the cell containing a density n of gas. Considering the gas as a perfect gas, the density of the gas in the cell n can be calculated using the equation $n = P\ /\ k_b\, T$ where P is the pressure of C_2H_2 inside the cell (Pa), T the temperature (K), and k_b the Boltzmann constant.

For each measured spectrum, data were filtered to eliminate noisy or saturated points and then the absorption cross section was calculated using Eq.2.1. Finally, the 10 spectra obtained were concatenated to reconstruct the full spectrum ranging from 115 to 230 nm.

3 Evolution of C_2H_2 absorption cross section with the temperature

We started our study by measuring the absorption cross section of C_2H_2 at 296 K, which will serve as a reference to compare the evolution of the absorption cross section of C_2H_2 as a function of the temperature. Then, we measured the absorption cross section of C_2H_2 at 373, 473, 573, and 673 K. Fig.1 presents the evolution of the absolute absorption cross section of C_2H_2 as a function of the temperature.

At 296 K, we observe that the spectrum has two components: a background continuum and the band system, which is superimposed on the continuum.

When the temperature of the gas increases, we observe an increase of the background continuum while the intensities of the bands tend to decrease. It results that there is a net increase of the absorption cross section of C_2H_2 with the temperature. This effect varies as a function of the wavelength. For $\lambda < 150$ nm, the increase of the continuum intensity is limited to a factor of ∼1.8 when the temperature increases from 296 to 673 K. For longer wavelength, the increase of the continuum intensity is more important with a factor of 2 at 174 nm and of a factor of 5 at 230 nm. Moreover, the decrease of the intensities of the absorption bands is more important at longers wavelength for which less structures are visible at 673 K compared to 296 K.

In addition, a new absorption band appears at ∼156.8 nm at high temperatures compared to ambient temperature and its intensity increases when the temperature increases. This can be attributed to the apparition of a "hot band". In the UV, transitions occur between two different electronic states. Each of the electronic

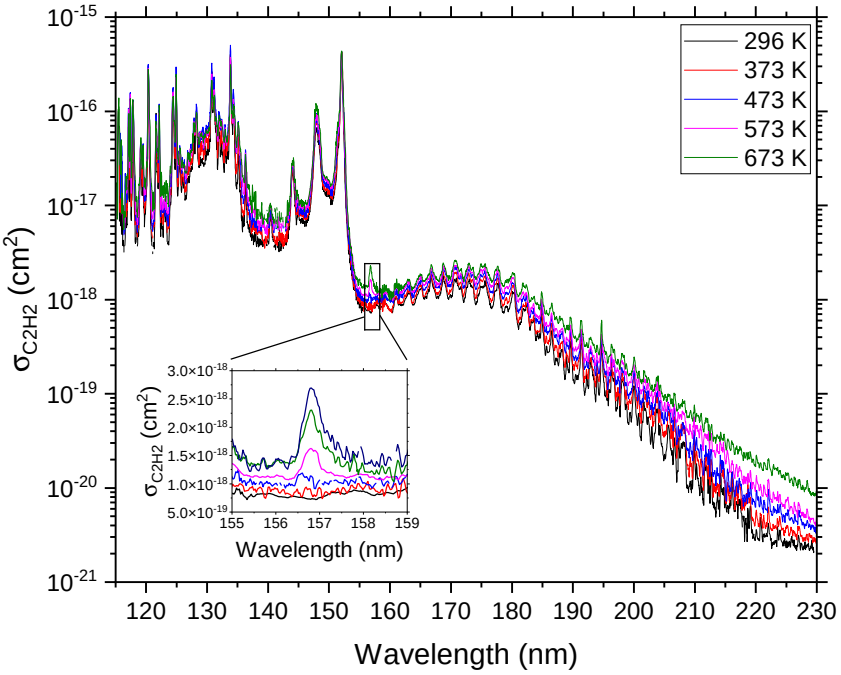

Fig. 1. Evolution of the absolute absorption cross section of C_2H_2 as a function of the temperature. Spectra were measured from 115 to 230 nm at LISA with an instrumental resolution of 0.046 nm.

states is subdivided into vibrational levels. Fundamental transitions occur between the vibrational ground level of the lower electronic state and a vibrational level of the higher electronic state, forming the "cold bands". When the temperature increases, vibrational levels of higher energy of the lower electronic state become more populated, and the intensities of the bands corresponding to transitions from these excited vibrational levels of the lower electronic state to vibrational levels of the higher electronic state increases. These bands are named "hot bands" and their intensities depends on the temperature of the gas.

Additional work will be needed to quantify how the observed increase of the absorption cross section of C_2H_2 with the temperature would affect the abundances calculated by kinetic models (see Fleury et al. in preparation).

4 Conclusions

We have studied experimentally the thermal dependency of the UV absorption cross section of C_2H_2 in a large range of temperatures relevant for exoplanet atmospheres. We determined the absorption cross section of C_2H_2 from 115 to 230 nm and from the ambient temperature to 673 K by increment of 100 K.

We found that the absorption cross section of C_2H_2 increases with the temperature. We also found that this increase is more important at longer wavelengths ($\lambda > 180$ nm) than for shorter ones.

Additional simulations with an atmospheric kinetic model will be done to quantify the impact of the observed increase of the absorption cross section of C_2H_2 with the temperature on the predicted abundances.

B.F. thanks the Université Paris-Est Créteil (UPEC) for funding support (postdoctoral grant). O.V. acknowledges funding from the ANR project 'EXACT' (ANR-21-CE49-0008-01), from the Centre National d'Etudes Spatiales (CNES), and from the CNRS/INSU Programme National de Planétologie (PNP).

References

Alderson, L., Wakeford, H. R., Alam, M. K., et al. 2023, Nature, 614, 664

Bénilan, Y., Andrieux, D., & Bruston, P. 1995, Geophysical Research Letters, 22, 897

Bénilan, Y., Smith, N., Jolly, A., & Raulin, F. 2000, Planetary and Space Science, 48, 463

Chen, F. Z. & Wu, C. Y. R. 2004, Journal of Quantitative Spectroscopy and Radiative Transfer, 85, 195

Ranjan, S., Schwieterman, E. W., Harman, C., et al. 2020, The Astrophysical Journal, 896, 148
Rufus, J., Stark, G., Thorne, A. P., et al. 2009, Journal of Geophysical Research: Planets, 114
Tsai, S.-M., Lee, E. K. H., Powell, D., et al. 2023, Nature, 617, 483
Venot, O., Bénilan, Y., Fray, N., et al. 2018, A&A, 609, A34
Venot, O., Fray, N., Bénilan, Y., et al. 2013, A&A, 551, A131
Wu, C. Y. R., Chen, F. Z., & Judge, D. L. 2001, Journal of Geophysical Research: Planets, 106, 7629
Wu, Y.-J., Lu, H.-C., Chen, H.-K., et al. 2007, The Journal of chemical physics, 127, 154311

SF2A 2023
M. N'Diaye, A. Siebert, N. Lagarde, O. Venot, K. Baillié, M. Béthermin, E. Lagadec, J. Malzac, J. Richard (eds)

A NEW SCENARIO FOR THE FORMATION OF PLANETARY ATMOSPHERES

P. Huet[1], Q. Kral[1] and P. Thébault[1]

Abstract. The observation of large quantities of CO in many debris disk systems means that we can study its potential impact on the atmospheres of planets embedded in this gas. An analytical model suggests that the accretion of the late gas (>10 Myr) in debris disks onto the planets is really efficient (Kral et al. 2020). In this regard, we are currently developing a code that can confirm this result numerically and determine more precisely the impact of different parameters such as core mass or luminosity on the overall accretion rate in this late phase. Late gas accretion could be one of the missing ingredients in completing (or totally modifying) the atmosphere of terrestrial planets and/or providing volatile substances to giant planets that have already formed.

Keywords: debris disks, exoplanets, atmospheres

1 Introduction

All present models of atmospheric evolution ignore any external source of gas after the evaporation of the protoplanetary disk, which occurs at the very beginning of the system's lifetime (10 Myr at the latest). However, intensive observations have shown that a significant fraction of dusty debris disks, akin to our own asteroid or Kuiper belts made of remnant material that has not been used in the planet-formation process and is collisionally eroding, do host an important amount of gas (Moór et al. 2017), despite being much older than the ∼10 Myr it takes for the primordial gas disk to dissipate. Therefore, the already-formed planets will be bathed in this late gas from the debris disk era for tens or hundreds of Myr, which may affect their atmospheres over long timescales (Kral et al. 2020).

2 Gas in debris disks

2.1 On the origin of the gas

As of today, gas has been detected in about 30 debris disks, mostly in the form of CO, but also as atomic species (C, C^+, O), and some more metallic elements (e.g., Fe, Na) that may not have the same origin (grazing exocomets rather than planetesimals at great distances). The estimated CO masses (which usually dominate the total gas mass in debris disks, Cataldi et al. 2023) can be as much as 1 $M_\oplus$ in some cases (Cataldi et al. 2020), but the origin of the gas remains unknown for the most massive systems, especially when considering the fact that CO should be very quickly (< 120 yr, Visser et al. 2009) photodissociated by stellar and interstellar UV radiations. For the least massive systems, the quantities of CO observed are so small that they can be explained as being constantly released from large planetesimals in exo-Kuiper belts but for the most massive gaseous systems, one would have to deplete the whole belt of volatiles at an incredibly unphysical high rate to explain observations. In this case, those gas disks could then not survive for more than a few thousand years and we would not be able to explain their omnipresence around the most luminous debris belts (Moór et al. 2017).

There are basically two competing models to explain these significant quantities of gas around mature stars on the main sequence. One scenario is that these disks are hybrids, meaning that despite having secondary collisionally eroding debris disks, they still contain primordial gas leftover from the protoplanetary disk phase. This would imply that the CO we detect has been shielded from stellar radiation by large amounts of H_2.

[1] LESIA, Observatoire de Paris, 92190 Meudon, France

© Société Française d'Astronomie et d'Astrophysique (SF2A) 2023

However, a new model, put forward by Kral et al. (2019) and subsequently refined and adapted by Moór et al. (2019), suggests that this gas is actually of secondary origin (similar to the less massive belts) and released from solids in planetesimal belts. In this scenario, hydrogen is not enough to protect carbon monoxide from photodissociation caused by interstellar radiation. However, the gas is shielded by CO itself and the neutral carbon gas produced during CO photodissociation. This model can explain most gaseous debris disks and makes predictions that could be checked in the near future by ALMA observations (e.g. Marino et al. 2020).

2.2 Accretion onto planets

Debris disks are, by definition, older than protoplanetary disks, which are the environments in which planets form and whose typical lifetime is only a few million years. This means that, if planets should form in a given system, they are already there by the time the debris disk phase is reached. These planets should have a significant effect on disk morphology (when massive enough) but observing them directly remains challenging due to their faintness and high contrast with the central star. However, a few Jovian planets have been directly imaged in some debris disks at large distances from their host stars (a few to tens of au). In the archetypal β Pic system, for example, two massive planets of roughly 10 and 9 Jupiter masses exist at distances of 9.2 and 2.7 au, respectively (Lagrange et al. 2009, 2019).

For systems in which gas has been detected, this gas should interact with the already formed planets, potentially resulting in gaseous accretion onto the planets, as outlined in Kral et al. (2020). This accretion could be very effective, as the gas produced in the belt spreads viscously towards the planet (Kral & Latter 2016), which in some cases can accrete most of the gas that spreads inwards. It is expected that a gap will form in the gas disk due to the planet's gravitational influence. In this scenario, most of the migrating gas would be stopped at the planet's orbit, so that the radial density profile of the gas disk would end up with a steep inward slope. However, this model has so far been explored with a simplified analytical approach, and it would require validation through more sophisticated numerical simulations. Such sophisticated models would for instance help us quantify the amount of gas that the planet accretes. It would also allow us to estimate important consequences of this gas-accretion phase, notably the effect of the core luminosity. Moreover, we can also explore the impact of some of the disk's key characteristics, such as its density, temperature, and composition, as well as the influence of initial conditions related to the planet, such as core mass and previously accreted atmosphere.

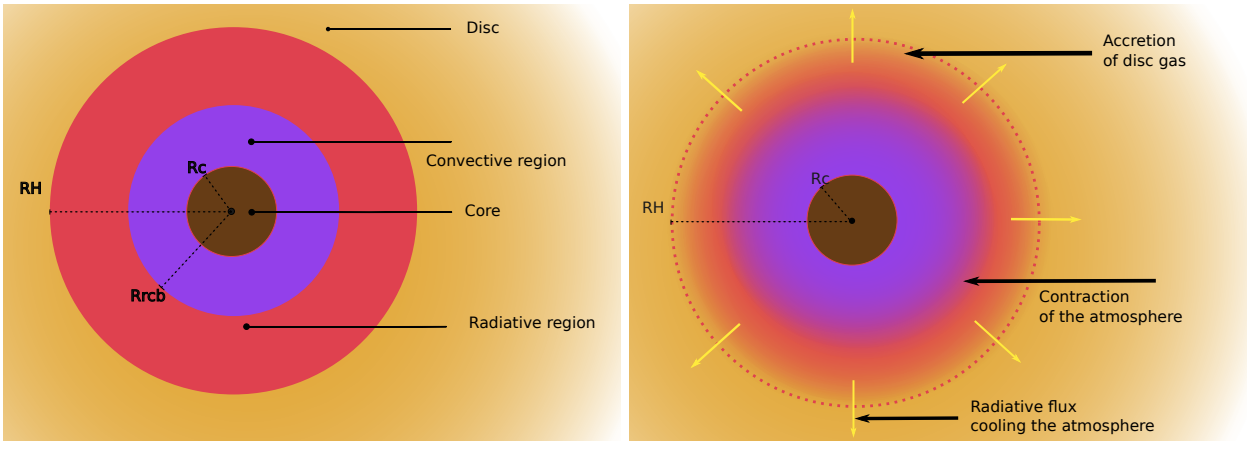

Fig. 1. Left: Structure of the modeled atmosphere and the disk that surrounds it. **Right:** Principle of the gas accretion onto the planet. R_c, R_{rcb}, and R_H are respectively the core radius, the radius at the radiative-convective boundary, and the Hill radius which is our outer integration limit.

3 The numerical model

3.1 General Principle

Our code is based on methods developed for gas accretion in protoplanetary disks (e.g. Piso & Youdin 2014, and references therein). Because of the timescale involved (> 100 Myr), we cannot use hydrodynamical simulations.

Similarly to previous work, we will solve the 1D stellar structure equations to handle accretion onto a planet's atmosphere:

$$\begin{cases} \frac{dr}{dm} &= \frac{1}{4\pi r^2 \rho} \\ \frac{dP}{dm} &= \frac{-\mathcal{G}m}{4\pi r^4} \\ \frac{dT}{dm} &= \nabla \frac{T}{P} \frac{dP}{dm} \\ \frac{dL}{dm} &= -T \frac{\partial S}{\partial t}\Big|_m \end{cases} \tag{3.1}$$

with m, $r(m)$, $P(m)$, $T(m)$, $L(m)$, $S(m)$ the mass, the radius, the pressure, the temperature, the luminosity, and the entropy, respectively (see Figure 1 left to see the structure of the atmospheres we model).

Through the radiative zone, the atmosphere cools down and then contracts. The gas from the disk takes up the space vacated by the contraction and the atmosphere grows and its composition evolves (see Figure 1 right).

In the system of differential equations we have to solve, we have four main parameters: r, P, T, and L. However, we do not have access to their four boundary conditions on the same side of the integration domain. We know the radius and the luminosity at the core $r(M_c) = R_c$, $L(M_c) = L_c$, and the temperature and pressure at the disk boundary: $T(M) = T_D, P(M) = P_D$ with M the total mass and M_c the core mass. Therefore, we use the shooting method to determine the missing parameters and integrate the system (see Figure 2 left).

To integrate the entire problem, we successively solve each spatial snapshot at each time step. The initial spatial state is the adiabatic state, which is time-independent because the adiabatic gradient does not depend on luminosity, so we do not need to solve for the last equation (as it is only the last equation, characterizing the energy transfer, which contains the time dependency). After the initial step, we have to estimate the time derivative of the entropy. To do so, we discretize it in the first order by using the entropy at the previous snapshot. We then have a method to solve the whole problem from the beginning to the end of the disk life (~ 100 Myr)

3.2 Adaptation for debris disks

The gas in debris disks is thought to have a different composition (dominated by CO, C, O) compared to that of protoplanetary disks (dominated by H_2). Moreover, the total gas mass in debris disks is expected to be much smaller than in their younger counterparts. All of this could easily be implemented in the code developed for protoplanetary disks though the timescales of accretion would drastically change. However, in the case of debris disks, we expect from models (e.g. Kral et al. 2019) that the gas release rate from the planetesimal belt is small (at most 1 $M_\oplus$/Myr), and hence the possible accretion rate onto the planets is also smaller than for protoplanetary disks. We end up with the code wanting to accrete more than the total gas that can arrive per unit time, which is a major issue.

We modified the code to handle this matter in the following way. In protoplanetary disks, the density and temperature are fixed at the disk level, and the mass and luminosity are calculated by the shooting method used to solve the set of differential equations above. For debris disks, the temperature at the disk level is fixed and the mass at $t + dt$ is given by the accretion rate τ: $m(t + dt) = m(t) + \tau dt$. The density (instead of mass) and luminosity are now calculated using the shooting method (see Figure 2 right) so that the disk density can decrease if too much gas gets accreted compared to what is refilled. This is more physical and will allow us to make predictions for the 1-D radial profile of gas at the inner boundary of the disk in the presence of different types of planets (and then compare with ALMA observations at high resolution).

3.3 Work in progress

We reproduced the result of Piso & Youdin (2014) for protoplanetary disks in order to test the first version of our code. We had to adjust their method because the technique they used to get rid of one of the two boundary parameters was not accurate. Hence, we solved a problem that appears when using the Piso & Youdin (2014) method, which is one of the consequences of the inaccuracy of their method: the luminosity should decrease when the atmospheric mass decreases (given that the core luminosity is small, see Figure 3).

We also calculated a mass constant equivalent of the energy conservation for isolated systems to test our code further. We are currently adapting this code to the debris disk-specific constraints, and we expect to run many simulations with different parameters when it is ready.

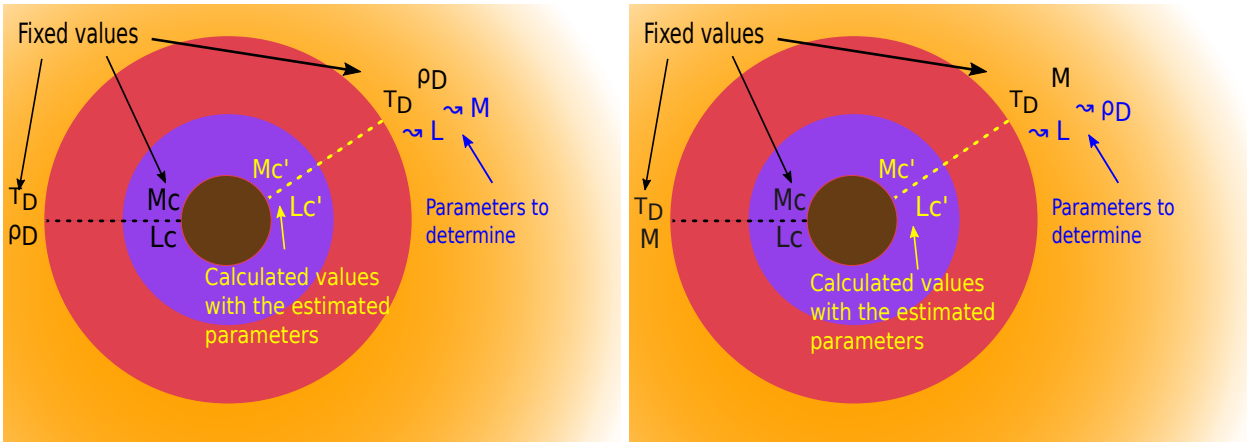

Fig. 2. Left: Boundary conditions for the case of protoplanetary disk conditions. **Right:** Boundary conditions for the case of debris disks with, e.g., lower disk density.

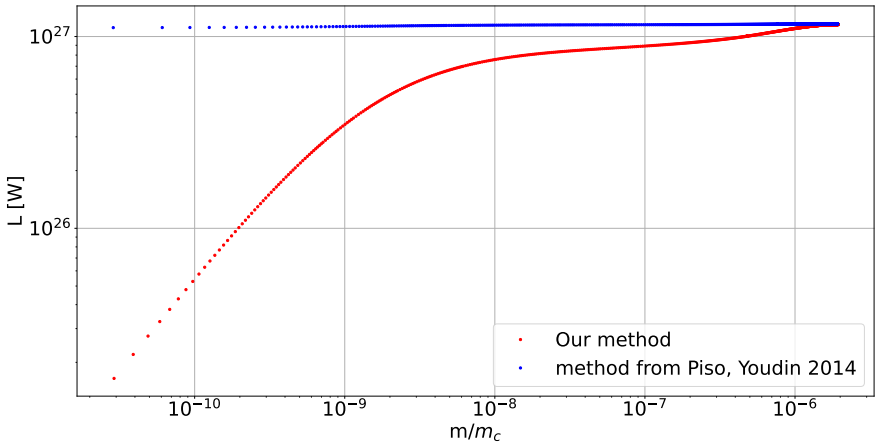

Fig. 3. Luminosity as a function of the mass ratio between the atmosphere and the core for a snapshot calculated by Piso & Youdin's method and by ours. With our method, the luminosity tends to 0 as the atmosphere's mass tends to 0. With the Piso & Youdin (2014)'s method, the luminosity tends to a constant of the order of the outer border luminosity, which is unphysical.

4 Conclusions

We are updating methods developed for protoplanetary disks to model planetary accretion of late gas in debris disks that can occur for hundreds of millions of years after the disappearance of the protoplanetary disk. We have validated the code against other published accretion models and are now in the process of including debris disk specificities including low gas density, lower accretion rates, and the effect of the core luminosity that may become important in this regime. The aim of this project is to gain a better understanding of the importance of late gas accretion in the final composition of the atmospheres of the planets affected. To do so, we will study the influence of the main parameters on the accretion rate: the temperature of the disk, both the compositions of the late gas and atmosphere, the gas production rate in the belt, and its density. Some other effects will be thoroughly investigated such as the effect of the core luminosity, and the influence of the initial conditions: mass of the solid core, and accretion onto an existing atmosphere...

References

Cataldi, G., Aikawa, Y., Iwasaki, K., et al. 2023, ApJ, 951, 111
Cataldi, G., Wu, Y., Brandeker, A., et al. 2020, ApJ, 892, 99
Kral, Q., Davoult, J., & Charnay, B. 2020, Nature Astronomy, 4, 769
Kral, Q. & Latter, H. 2016, MNRAS, 461, 1614
Kral, Q., Marino, S., Wyatt, M. C., Kama, M., & Matrà, L. 2019, MNRAS, 489, 3670
Lagrange, A. M., Gratadour, D., Chauvin, G., et al. 2009, A&A, 493, L21
Lagrange, A. M., Meunier, N., Rubini, P., et al. 2019, Nature Astronomy, 3, 1135
Marino, S., Flock, M., Henning, T., et al. 2020, MNRAS, 492, 4409
Moór, A., Curé, M., Kóspál, Á., et al. 2017, ApJ, 849, 123
Moór, A., Kral, Q., Ábrahám, P., et al. 2019, ApJ, 884, 108
Piso, A.-M. A. & Youdin, A. N. 2014, ApJ, 786, 21
Visser, R., van Dishoeck, E. F., & Black, J. H. 2009, A&A, 503, 323

SF2A 2023
M. N'Diaye, A. Siebert, N. Lagarde, O. Venot, K. Baillié, M. Béthermin, E. Lagadec, J. Malzac, J. Richard (eds)

MODELING THE RECENT (<5 MYRS) MARTIAN ICE AGES

J. Naar[1], F. Forget[1], E. Millour[1], A. Bierjon[1], L. Lange[1], E. Vos[1] and R. Vandemeulebrouck[1]

Abstract. In spite of its present-day arid climate, in which ice is unstable outside polar regions, planet Mars exhibits remnants of glacial landforms dated of a few hundred million years. Numerical Global Climate Models (GCMs) have been used to address the climate conditions in which these glacial structures were formed, driven by variations in orbital forcing. However, GCMs have struggled to explain the recent formation of a water-ice mantle down to the mid latitudes within the last few hundred thousand years. During this period, the obliquity of Mars (the angle between the rotational axis and the plane of revolution around the sun) has risen from its current value of 25.19° to 35° at most.
The previous paleoclimatic studies did not consider the radiative effect of clouds, which dramatically affects the thermal structure and circulation of the atmosphere at higher obliquity. They also did not account for the latent heat of ground ice sublimation/condensation, negligible in today's climate but critical at higher obliquity since the Northern Polar Cap, the main source for atmospheric water, is warmed during summer by the increased insolation. Latent heat cooling is also crucial to the persistence of seasonal mid-latitude ice over the summer and the formation of a thick ice mantle.
With our new state-of-the-art physic, including radiatively active clouds, improved cloud microphysics, and the latent heat of ground ice sublimation, we have performed numerical experiments at 35° obliquity. We find that radiatively active clouds have a mean global positive greenhouse effect of $\sim$ 20 K. But, despite increased summer surface temperatures, the combination of latent heat cooling and thermo-physical parameterizations for ice allows the inter-annual preservation of seasonal frost. The associated accumulation rates are compatible with the formation of a hundreds-of-meters thick latitude-dependent mantle over the duration of recent 35° obliquity excursions.

Keywords: Planet Mars, climate modeling, water cycle, Ice Ages

1 Introduction

Remnants of glaciers are visible at all latitudes on Mars, thought to be of atmospheric origin and deposited during high obliquity excursions (Forget et al. 2006). Finer geomorphological evidences point to the existence of a recent "Latitude-Dependent Mantle" (LDM), a thick layered ice deposit covering Mars from the polar regions down to the tropics (Head et al. 2003).
The climatic scenarios leading to the accumulation of surface ice outside the polar regions in the last hundreds thousand years remained unsatisfactory in previous GCM studies. Only the destabilization of tropical surface water ice reservoirs, deposited millions of years ago at even higher obliquity, allowed for transient high latitude deposition (Levrard et al. 2004; Madeleine et al. 2009).
The subsequent inclusion of radiatively active clouds in the models disrupted our previous understanding of high obliquity climates (Madeleine et al. 2014). Here, we present our new physical package of the Mars Planetary Climate Model (PCM, previously LMD-GCM) with the latent heat of ground ice and improved cloud microphysics, using radiatively active clouds.

The simulated climate at 35° obliquity results in a thicker seasonal frost mantle deposition in the winter hemisphere than present day. We use simple parameterizations for the physical properties of this exotic ice mantle, with increased albedo and thermal inertia. Doing so, we find that the seasonal ice is preserved from sublimation and forms a LDM at 35° of obliquity, which happened for the last time 0.4 Myrs ago.

[1] Laboratoire de Météorologie Dynamique, UMR CNRS 8539, Institut Pierre-Simon Laplace, Sorbonne Universités, UPMC Univ Paris 06, 4 place Jussieu, 75005, Paris, France

© Société Française d'Astronomie et d'Astrophysique (SF2A) 2023

2 Improved physics of the Mars PCM

2.1 Latent heat of ground water ice sublimation/condensation

In present-day Mars GCMs, ground water ice is sublimed/condensed either on top of the Northern Polar Cap or as diurnal and seasonal frost. In both cases, the associated latent heat flux is low, respectively because the ice deposits are cold or the mass budget is small. This is why latent heat of ground ice deposits has been neglected in the Mars PCM until now, as well as in other GCMs (Haberle et al. 2019). At 35° obliquity high latitude summer insolation is increased, the surface of the Northern Polar Cap is warmer and sublimes further, and the latent heat associated with sublimation becomes relevant.
Figure 1 depicts a validation experiment conducted under typical Martian conditions at the Phoenix Lander location (Lat=70°N), during the Norther summer solstice. In this experiment, latent heat release cools the martian surface by 8 K, with a corresponding decrease in the diurnal ice surface variation of 40%. Exposed water ice does not exist at this latitude and time of year in present-day climate but the insolation is comparable to the one received at the edge of the Northern Polar Cap at 35° obliquity at this time of year.

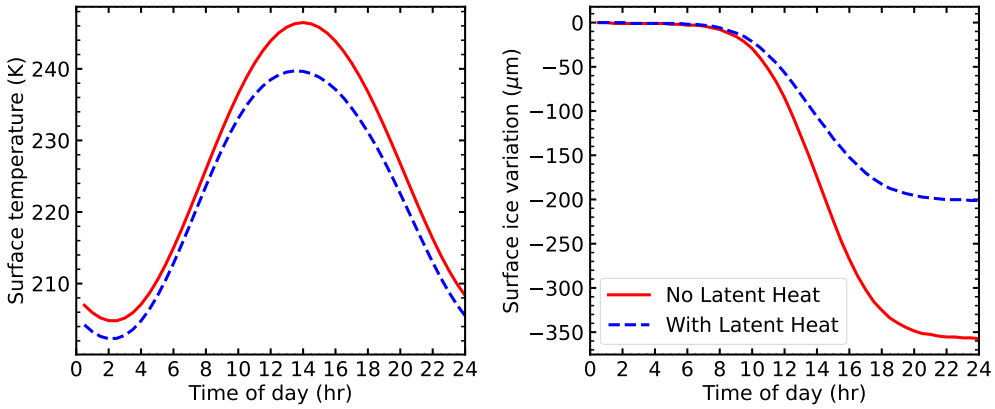

Fig. 1. Influence of latent heat on surface temperature and instantaneous sublimation rate with exposed surface ice in the model (for present-day conditions), at Phoenix lander location (Lat=70°N) at summer solstice (L_S=90°), with a prescribed integrated atmospheric water vapor of 10 precipitable microns. Extracted from Naar et al. (2023b)

2.2 Cloud microphysics

The radiative effect of clouds was implemented in the PCM and investigated in Madeleine et al. (2012). The global water cycle was tuned to match the Thermal Emission Spectrometer (TES) retrievals of seasonal water vapor and ice behavior Navarro et al. (2014). However, the model still was still biased in the representation of clouds. We implement a temperature-dependent contact parameter which improves our modeled water ice cloud cycle, especially in the polar regions (Naar et al. 2023b).
In addition, we identified that the numerical scheme of cloud microphysics was not well-resolved in the model. This is especially relevant at high obliquity where cloud activity is enhanced with the intensification of the global water cycle. We have developed an adaptive scheme to address this issue.
Using the new physical package, we tune the global water cycle in the model against TES observations. Our best simulation is presented in figure 2

3 High obliquity climate

Starting from the reference simulation presented in figure 2, we conduct 35° obliquity experiments.

3.1 Greenhouse effect of clouds

At 35° of obliquity, the insolation is increased in the high latitudes during the summer. The surface temperatures over the Northern Polar Cap (NPC) rise, and along with the sublimation rates of surface water ice. The increased

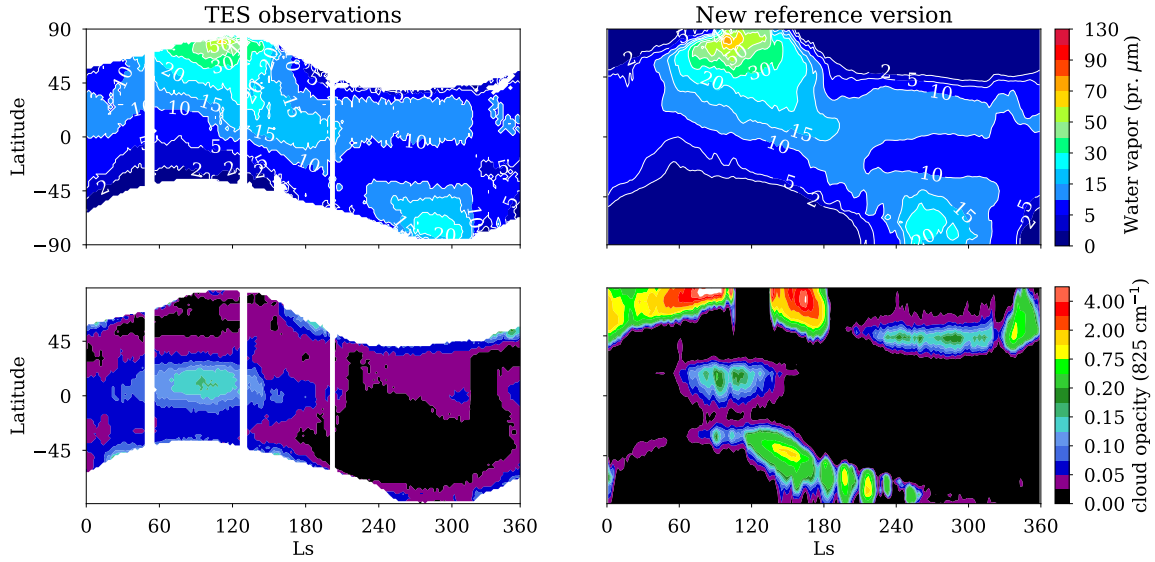

Fig. 2. Column-integrated water vapor (top panels) and cloud opacity (bottom panels) at 2 pm local time for TES observations (left panels) and our best numerical simulation of present-day Martian climate (right panels), corresponding to Martian year 26. Adapted from Naar et al. (2023a).

amount of water vapor in the atmosphere leads to the formation of water-ice cloud. In turn, their net radiative effect is to warm both the atmosphere and the surface. Clouds initiate a positive feedback via their greenhouse effect, further warming the surface and enhancing summertime sublimation of the NPC.
However, this positive feedback is dampened by the latent heat cooling associated with sublimation of the Northern Polar Cap. The corresponding energy flux reaches over 10 W.m^{-2}, more than an order of magnitude higher than in present-day climate.
The combination of these two effects leads to a climate regime approximately two order of magnitude wetter than today, with the mean atmospheric water vapor column reaching over 1000 precipitable microns when orbital configuration favors extended sublimation of the NPC. The resulting thick water-ice cloud coverage has a net greenhouse effect of about 20 K on global average.

3.2 Entering the Ice Age phase

In our present-day simulations, the seasonal frost in the winter hemisphere of Mars is formed via direct sublimation of atmospheric humidity on the surface. In our high obliquity simulations, the increased cloud activity leads to intense snowfall in the winter hemisphere, and thus a seasonal ice mantle several millimeters thick. The latent heat cooling of this seasonal ice sublimation reaches up to 30 W.m^{-2} but it still is not sufficient to preserve any ice from disappearing completely.
However, the thermo-physical properties of the seasonal ice mantle at high obliquity should be very different than the present-day winter frost. Specifically, snowy precipitations may have a high albedo, and millimeters-thick ice may have a higher thermal inertia than present-day microns-thick frost.
We conduct additional simulations, using conservative parameterizations for these two possible feedbacks. In those experiments, the seasonal frost albedo and thermal inertia feedbacks diminish the summertime temperature increase. The resulting water cycle is less intense than in the high obliquity simulation described above, as NPC sublimation is decreased. The latitudinal extent of the seasonal ground ice mantle is reduced, but the summer temperature decrease allows for the inter-annual accumulation of high-latitude ice, at tens of millimeters per year (figure 3).

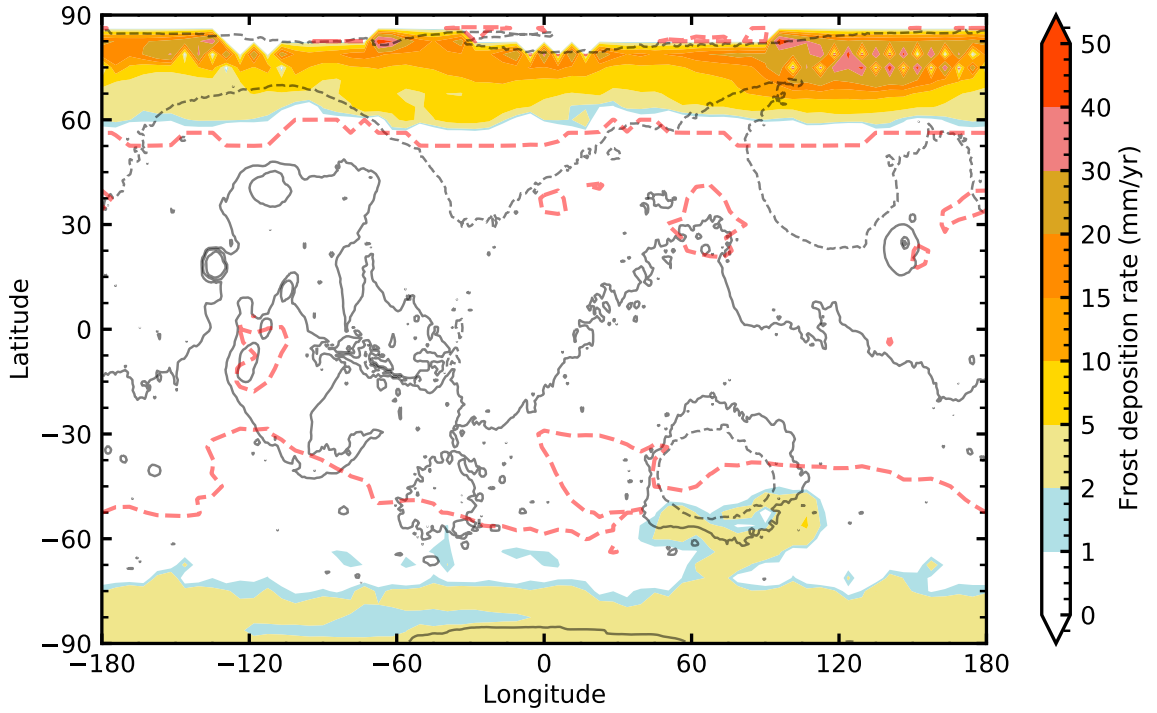

Fig. 3. Year by year accumulation of frost outside the Northern Polar Cap in a 35° obliquity numerical simulation, with the solar longitude of perihelion corresponding to the Northern summer solstice (L_S=90°) and with a ground ice albedo of 0.7 and a thermal inertia of 1200 J.m^2.K^{-1}.s$^{-1/2}$. The red dashed line is the extension of the seasonal ice mantle (1 mm thickness).

4 Conclusions

The 35° obliquity excursions of Mars occurred about 30 times in the last 5 million years, for tens of thousands of years at a time. The accumulation rates that we find with our conservative hypothesis provide a climatic explanation for the formation of the "Latitude-Dependent Mantle" in the recent past of Mars, during the high obliquity excursions, in agreement with geological observations. The climate regime corresponding to the emplacement of such "Ice Ages" is driven by the feedbacks of radiatively active clouds on the whole climate system and is one of a warmer and more cloudy planet.
Future work includes the development of an asynchronous "Planetary Evolution Model" which would allow for a self-consistent evolution of the water cycle with the location of surface water-ice deposits and the atmospheric pressure cycle. In addition, the interaction of atmospheric water with the regolith will be accounted for and may play a key role in the stability of surface water ice outside the polar regions.

References

Forget, F., Haberle, R. M., Montmessin, F., Levrard, B., & Head, J. W. 2006, Science, 311, 368
Haberle, R. M., Kahre, M. A., Hollingsworth, J. L., et al. 2019, Icarus, 333, 130
Head, J. W., Mustard, J. F., Kreslavsky, M. A., Milliken, R. E., & Marchant, D. R. 2003, Nature, 426, 797
Levrard, B., Forget, F., Montmessin, F., & Laskar, J. 2004, Nature, 431, 1072
Madeleine, Forget, F., Millour, E., Navarro, T., & Spiga, A. 2012, Geophysical Research Letters, 39
Madeleine, JB., Forget, F., Head, J. W., et al. 2009, Icarus, 203, 390
Madeleine, JB., Head, J. W., Forget, F., et al. 2014, Geophysical Research Letters, 41, 4873
Naar, J., Forget, F., Bierjon, A., et al. 2023a, In prep., Earth and Space Sciences
Naar, J., Forget, F., Bierjon, A., et al. 2023b, Submitted, Earth and Space Sciences
Navarro, T., Madeleine, J.-B., Forget, F., et al. 2014, Journal of Geophysical Research: Planets, 119, 1479

SF2A 2023
M. N'Diaye, A. Siebert, N. Lagarde, O. Venot, K. Baillié, M. Béthermin, E. Lagadec, J. Malzac, J. Richard (eds)

MULTIWAVELENGTH OBSERVATIONS OF THE EXO-COMETARY DUST AROUND β PICTORIS.

P. Priolet[1], J.-C. Augereau[1], J. Milli[1], A. Matter[2] and J.-B. Le Bouquin[1]

Abstract. Since the discovery of its edge-on debris disk in 1984, β Pictoris has become a laboratory for studies on planet formation and planet-disk interactions, especially around the outer disk (from $\sim$ 10 au to $\sim$ 100 au). Nevertheless, the inner region ($<$ 4 au) remains fairly unconstrained. VLTI/PIONIER observations first revealed the presence of a small circumstellar emission in the H-band which is probably due to hot dust in the inner regions of the system.

We present in this study the first detection of the circumstellar emission from hot dust around β Pictoris in the L-band using VLTI/MATISSE. We also present preliminary results showing the presence of spatial information in the interferometric fringe visibility data, supporting previous models which suppose that the hot dust is confined close to the sublimation distance ($\sim$0.1–0.2 au).

Keywords:
debris disk, exozodiacal dust, interferometry, VLTI, β Pictoris

1 Introduction

β pictoris (HD 39060, HIP 27321) is a classic example of a young planetary system. Its host star is a young ($18.5^{+2.0}_{-2.4}$ Myr Miret-Roig et al. 2020), A6V type, main-sequence star. Its edge-on, cold debris disk located at tens to hundreds of astronomical units (au) was discovered in 1984 (Aumann 1984; Smith & Terrile 1984) and since then it has been thoroughly studied in search of planets. As of right now, two planets have been detected: β Pictoris b (semi-major axis $\sim$10 au, Lagrange et al. 2009, 2010) and β Pictoris c (semi-major axis $\sim$3 au, Lagrange et al. 2019). An excess circumstellar emission was also detected in the H-band representing $1.37 \pm 0.16\%$ of the photospheric emission (Defrère et al. 2012a). This excess has been attributed to hot dust in the inner regions of the debris disk, inside the orbits of the detected exoplanets.

To study in depth the properties of the hot and warm dust in the inner parts of this system, we propose to combine VLTI/PIONIER observations in the H-band with VLTI/MATISSE observations in the L-band. We present here the results of these near- and mid-infrared interferometric observations, including the first detection of an L-band excess in this system, as well as preliminary results indicating that valuable information on the dust location might be present in the data.

2 Detection of circumstellar emission

2.1 Observations

Multiwavelength interferometric observations of β pic were obtained in October 2022 using VLTI/MATISSE* in the L-band (Lopez et al. 2022) and VLTI/PIONIER† in the H-band (Le Bouquin et al. 2011). These observations were taken using the small configuration of the AT array at the VLTI and they were interleaved with observations of reference stars to calibrate the instrumental effects in the observed quantities. These calibrators were chosen close to β Pic both in terms of position and magnitude. In this study we also use archival data taken with

[1] Univ. Grenoble Alpes, CNRS, IPAG, F-38000 Grenoble, France
[2] Université Côte d'Azur, Observatoire de la Côte d'Azur, CNRS, Laboratoire Lagrange, France
*Program ID: 110.246D.003
†Program ID: 110.246D.001

© Société Française d'Astronomie et d'Astrophysique (SF2A) 2023

PIONIER (H-band, 3 data sets [‡]) and MATISSE (L-band, 3 data sets [§]). For information on the H-band archival data obtained with PIONIER, refer to Ertel et al. (2014, 2016).

We focus here on the interferometric fringe squared visibilities (V^2) and not on the closure phase since it is close to 0 for all the datasets used. This however, allows us to rule out a bright companion in the FOV of the instrument.

2.2 Method

To search for circumstellar emission, we compare our data sets to the expected squared visibilities (V^2) of a purely photospheric model. For this stellar model we use the analytical model for a limb darkened photosphere by Hanbury Brown et al. (1974) using the linear H- and LM-band limb-darkening coefficients from Claret et al. (1995) and the stellar angular diameter calculated in Defrère et al. (2012b) using surface brightness relations (SBR, see Kervella et al. 2004) which give a limb darkened angular diameter $\theta_{LD} = 0.712 \pm 0.010$ mas. We see that both the MATISSE L-band and PIONIER H-band squared visibilities $V^2(B)$ show a deficit with respect to the stellar squared visibility $V^2_\star(B)$. This implies that an object is at least partially resolved in the FOV of the instruments.

First, we assume that this emission is homogeneous and over-resolved for the shortest baselines (ie: $V_{\rm CSE}$ close to $0, \forall B$, where $V_{\rm CSE}$ is the visibility of the circumstellar emission), an assumption which is commonly used in such studies (e.g. Ertel et al. 2014, 2016; Absil et al. 2021). This approximation, combined with the fact that the extended emission is faint relative to the star, strongly simplifies our approach (since we do not have to model the spatial distribution of the dust) and can lead to reasonable results as shown by Absil et al. (2009) and Defrère et al. (2011). In this case, the observed squared visibility $V^2(B)$ can be expressed as:

$$V^2(B) \simeq (1-f)^2 V^2_\star(B) \tag{2.1}$$

where $V_\star$ is the stellar visibility and f is the flux ratio between the circumstellar emission and the total emission (photospheric + circumstellar). We also suppose that the flux ratio f does not depend on the wavelength for a given band, which allows us to fit all spectral channels together. We then do a least squares minimization to find the parameter f.

2.3 Results

MATISSE : we detect the circumstellar emission in all the L-band data taken with MATISSE (including in archival data). The preliminary measured flux ratios f are : $2.36 \pm 0.42\%$, $2.37 \pm 0.27\%$, $2.52 \pm 0.08\%$ and $1.3 \pm 0.37\%$ for the following dates of observations, 08/01/2021, 16/01/2021, 28/01/2021 and 14/10/2022 respectively. It is to be noted that the 08/01/2021 dataset was taken using the UT array while the others were taken using the AT array.

PIONIER : we also detect circumstellar emission in the H-band data taken with PIONIER. We measure a preliminary flux ratio f of $1.6 \pm 0.11\%$ for the 2022 data. We repeated this methodology on already published archival data (Ertel et al. 2016) to confirm correct data processing and ensure homogeneity. We find that our values are consistently larger than the archival ones (see Fig. 1); this could be due in part to different calibration procedures between the data used in the study and the archival data we retrieved.

[‡]Program IDs: 088.C-0266(A), 090.C-0526(A) and 094.C-0232(A)
[§]Program IDs: 106.21Q8.006, 106.21Q8.004 and 106.21Q8.001

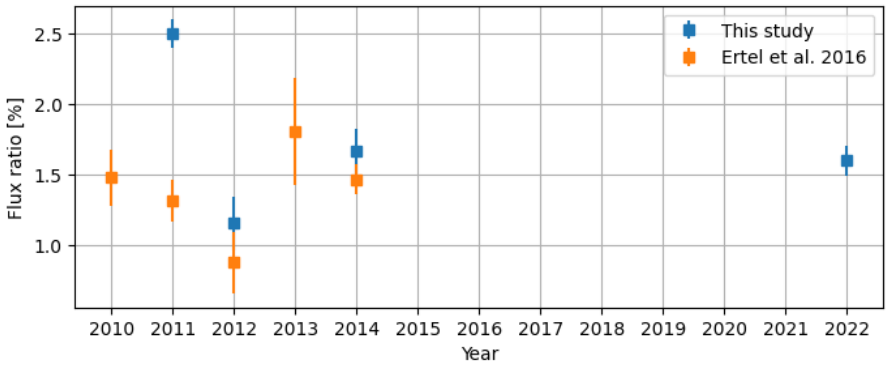

Fig. 1. Archival flux ratios from Ertel et al. (2016) compared to this study's estimates (VLTI/PIONIER data, H-band).

3 Spatial information

As hinted in Absil et al. (2021), approximating the circumstellar emission as homogeneous and over-resolved might lead to a miss estimation of the flux ratio. We therefore set out to test the presence of spatial information in the data by comparing it to the interferometric fringe visibilities of a geometrical model of an inclined flat ring.

3.1 Method

As in the previous section we use the analytical model for a limb darkened photosphere from Hanbury Brown et al. (1974) and we add a circumstellar emission in the form of a flat homogeneous geometrical ring. The visibility of such an object is analytical and allows for fast model fitting to the data. The free parameters of this model are: the internal radius ($r_{\rm in}$), the external radius (which we parametrize by a factor A such that $r_{\rm out} = A \times r_{\rm in}$ where $r_{\rm out}$ is the external radius), the inclination (i, such that $i = 0°$ for a pole-on disk and $i = 90°$ for edge-on), the position angle (PA) and finally the ratio between the flux of the flat ring and the total flux (f).

We then use an MCMC algorithm to fit this model to the dataset and extract the most likely parameters given our data set (supposing that this is a valid model for the circumstellar emission). This approach was employed for each of the PIONIER and MATISSE datasets separately.

3.2 Results

The free parameters remain unconstrained for most datasets; however, for certain datasets we find convergence of the free parameters (we do seem to constrain fairly well the internal radius), although some parameters are degenerated. One of the possible models has the same position angle (PA) as that of the external disk (29.5°, Boccaletti et al. 2009). We therefore decided to fix the PA of our model to that of the external disk to lift some of the degeneracies. As an example, the marginalized posterior probabilities for each parameter for the MATISSE dataset from 08/01/2021 when fixing the PA to 29.5° are shown in Figure 2.

These preliminary results show that thinner rings are preferred (small A values) and that the internal radius of the ring is close to the sublimation radius of both carbonaceous grains ($\sim$ 0.18 au for 10 nm-sized grains, $\sim$ 0.06 au for 1 μm-sized grains and $\sim$ 0.08 au for 1 mm-sized grains) and astronomical silicates ($\sim$ 0.23 au for 10 nm-sized grains, $\sim$ 0.17 au for 1 μm-sized grains and $\sim$ 0.13 au for 1 mm-sized grains).

It is also interesting to note that the fitted flux ratio in Figure 2 is higher than the one found in section 2.3.

4 Conclusions and discussion

This article presents preliminary work on the exozodi of β Pictoris. We show the detection of circumstellar emission in new H-band data and in the L-band data. This is the first time that the hot dust around β Pictoris is detected in the L-band and only one detection has been published so far with MATISSE in the L-band (κ

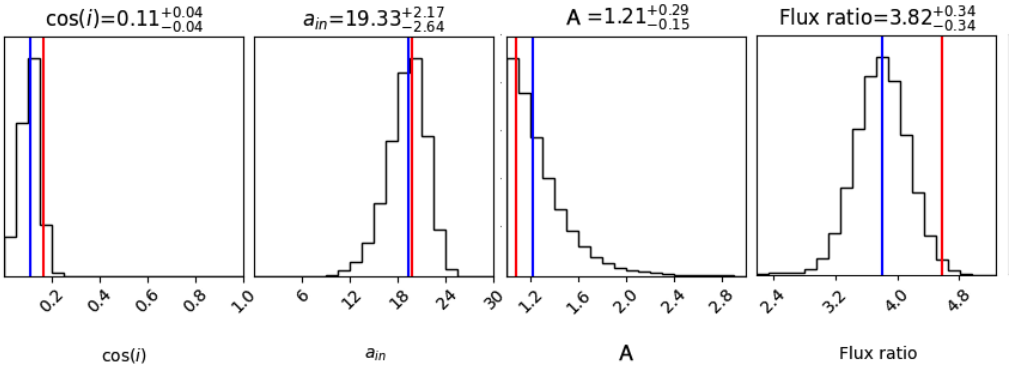

Fig. 2. Marginalized posterior probabilities for the free parameters using an archival MATISSE dataset (08/01/2021). The internal diameter of the ring ($a_{\rm in} = 2 \times r_{\rm in}$) is in mas and the flux ratio in % of the total flux. For more details on the definition of these parameters see section 3.1. The red lines represent the best fit values while the blue lines represents the median values of the posterior distribution.

Tuc Kirchschlager et al. 2020). In addition to the detection and measurement of the excess in the L- and H-bands, we indicate the possible presence of spatial information in these data sets. This could help alleviate a common degeneracy in SED modeling where smaller grains further from the star (including grains out of thermal equilibrium) have the same emission profile as larger grains closer to the star.

Since β Pic is viewed edge-on, a flat ring model might not be the best to reproduce the observed visibilities; this might lead to a best fitting model that is less inclined (less edge-on) than the actual dust to correctly reproduce the visibility signatures. A more detailed analysis is in preparation to take this effect into account.

This work was founded by the EPOPEE (Etude des POussières Planétaires Et Exoplanétaires) project supported by the French Planetology National Program (Programme National de Planétologie, PNP) and the Origin of life project supported by the Université Grenoble Alpes.

References

Absil, O., Marion, L., Ertel, S., et al. 2021, A&A, 651, A45
Absil, O., Mennesson, B., Le Bouquin, J.-B., et al. 2009, ApJ, 704, 150
Aumann, H. H. 1984, in Bulletin of the American Astronomical Society, Vol. 16, 483
Boccaletti, A., Augereau, J. C., Baudoz, P., Pantin, E., & Lagrange, A. M. 2009, A&A, 495, 523
Claret, A., Diaz-Cordoves, J., & Gimenez, A. 1995, A&AS, 114, 247
Defrère, D., Absil, O., Augereau, J. C., et al. 2011, A&A, 534, A5
Defrère, D., Lebreton, J., Le Bouquin, J. B., et al. 2012a, A&A, 546, L9
Defrère, D., Lebreton, J., Le Bouquin, J. B., et al. 2012b, A&A, 546, L9
Ertel, S., Absil, O., Defrère, D., et al. 2014, A&A, 570, A128
Ertel, S., Defrère, D., Absil, O., et al. 2016, A&A, 595, A44
Hanbury Brown, R., Davis, J., Lake, R. J. W., & Thompson, R. J. 1974, MNRAS, 167, 475
Kervella, P., Thévenin, F., Di Folco, E., & Ségransan, D. 2004, A&A, 426, 297
Kirchschlager, F., Ertel, S., Wolf, S., Matter, A., & Krivov, A. V. 2020, MNRAS, 499, L47
Lagrange, A. M., Bonnefoy, M., Chauvin, G., et al. 2010, Science, 329, 57
Lagrange, A. M., Gratadour, D., Chauvin, G., et al. 2009, A&A, 493, L21
Lagrange, A. M., Meunier, N., Rubini, P., et al. 2019, Nature Astronomy, 3, 1135
Le Bouquin, J. B., Berger, J. P., Lazareff, B., et al. 2011, A&A, 535, A67
Lopez, B., Lagarde, S., Petrov, R. G., et al. 2022, A&A, 659, A192
Miret-Roig, N., Galli, P. A. B., Brandner, W., et al. 2020, A&A, 642, A179
Smith, B. A. & Terrile, R. J. 1984, Science, 226, 1421

SF2A 2023
M. N'Diaye, A. Siebert, N. Lagarde, O. Venot, K. Baillié, M. Béthermin, E. Lagadec, J. Malzac, J. Richard (eds)

NAROO PROGRAM : ANALYSIS OF USNO GALILEAN OBSERVATIONS 1967-1998

V. Robert[1,2], D. Pascu[3], J.-E. Arlot[1] and V. Lainey[1]

Abstract. The New Astrometric Reduction of Old Observations (NAROO) program is dedicated to the measurement of astrophotographic plates and the analysis of old observations for scientific purposes. One of the main objectives is to provide accurate positional measurements of planets and satellites to improve our knowledge of their orbits and dynamics, and to infer the accuracy of the planet and satellite ephemerides. We digitzed 553 astronegatives of the Galilean satellites taken with the McCormick and the U.S. Naval Observatory 26-inch refractors from 1967 to 1998, resulting in 2650 individual observations. We measured and reduced these observations through an optimal process that includes image, instrumental, and spherical corrections using Gaia-DR3 catalogue to provide the most accurate equatorial (RA, Dec) ICRS positions. We compared the observed positions of the satellites with the theoretical positions from different planetary ephemerides and satellite ephemerides. 4819 positions of the Galilean satellites have been determined with an accuracy of 55 mas or 160 km at Jupiter, indicating that the limits of the photographic techniques were now reached.

Keywords: Astrometry - Ephemerides - Instrumentation: high angular resolution

1 Introduction

The New Astrometric Reduction of Old Observations (NAROO) facilities have been built as a unique center dedicated to the measurement of astrophotographic plates and the analysis of old observations for scientific purposes (Robert et al. 2021). The framework is the study of the dynamics of Solar System bodies, in particular, that require astrometric observations sampled over a long time span to quantify the long period terms which may help to analyze the evolution of the motion. One of the main objectives of the NAROO program is to provide accurate positional measurements of planets and satellites to improve our knowledge of their orbits and dynamics, and to infer the accuracy of the planet and satellite ephemerides.

We obtained the large photographic plate archive of the Galilean satellites taken at the U. S. Naval Observatory (USNO) from 1967 to 1998 for remeasurement and reanalysis. In fact, most of these plates had been measured with the USNO automatic StarScan measuring machine (Zacharias et al. 2008), reduced by the trail/scale scheme (Pascu 1977) and used by Jet Propulsion Lab (JPL) for the navigation of the Voyager and Galileo space probes to successful reconnaissance with the Jovian system. The expectation was that the astrometric positions of the planets, as well as the Galilean satellites, could now be obtained to the absolute limits of the photographic technique.

2 Measurement and reduction

We selected 553 photographic plates to be transmitted at Meudon and digitized with the NAROO machine. Each plate contains four to six exposures shifted in the declination direction. The exposure times of the photographic plates are 20-60 s. The field of view is 57 arcmin on the x-axis and 43 arcmin on the y-axis. Figure 1 shows the center of the digitized (positive) USNO Galilean plate No. 21014, which is a typical digitized image. Five 20 s exposures of the Jovian system were taken with the USNO 26-inch refractor on 18 June 1994. Non visible

[1] IMCCE, Observatoire de Paris, PSL Research University, CNRS UMR 8028, Sorbonne Universités, UPMC, Univ. Lille 1, 77 avenue Denfert- Rochereau, 75014 Paris, France
[2] Institut Polytechnique des Sciences Avancées IPSA, 63 bis Boulevard de Brandebourg, 94200 Ivry-sur-Seine, France
[3] United States Naval Observatory USNO (retired), 3458 Massachusetts Ave NW, Washington, DC 20392, USA

© Société Française d'Astronomie et d'Astrophysique (SF2A) 2023

by eye, the small special filter covers the planet and satellites, reducing their light and providing a measurable image of Jupiter and the Galileans. From left to right, Callisto, Ganymede, Europa, Jupiter, and Io. North is up, east to the left.

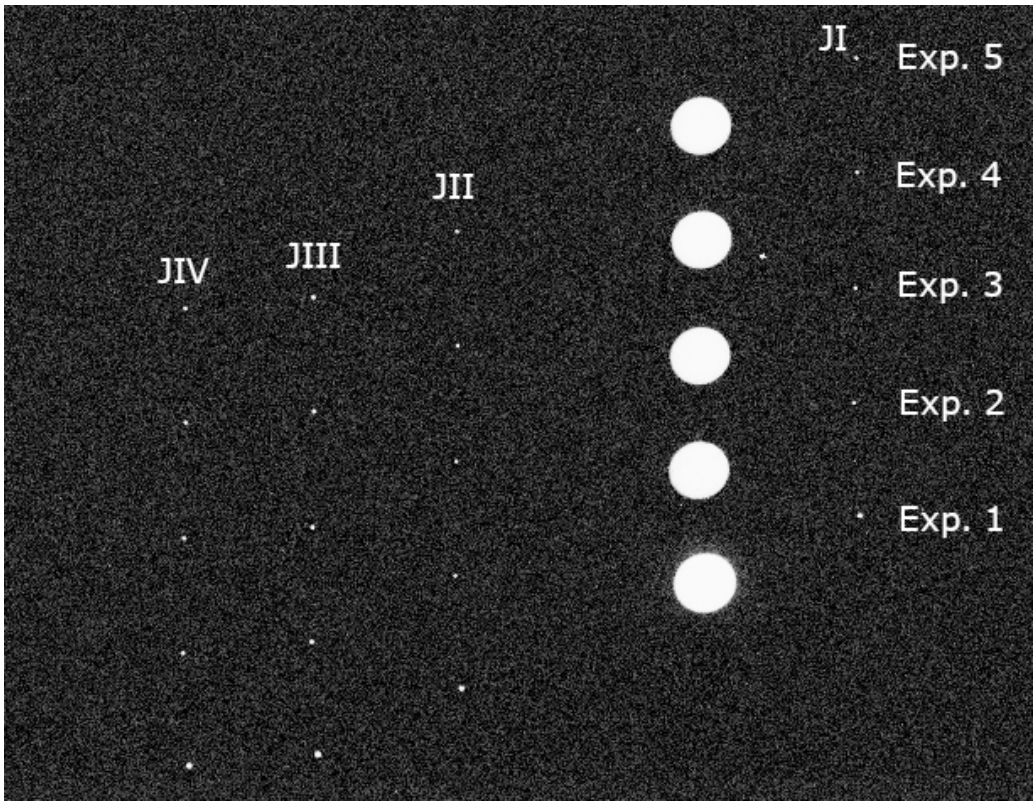

Fig. 1. Center of the digitization (positive) of the USNO 26-inch Galilean plate No. 21014. Five exposures shifted in the declination direction, from left to right: Callisto, Ganymede, Europa, Jupiter, and Io. North is up, east to the left.

2.1 Positioning results

We re-processed the analysis of the 553 NAROO images using the Gaia-DR3 reference star catalogue (Gaia Collaboration et al. 2016, 2022) to compare the positions of the Galilean satellites with their theoretical computed positions given by the INPOP21a planetary ephemeris (Fienga et al. 2021) and newest NOE-5-2021-JUP satellite ephemerides. All of the Gaia reference stars and the satellite images were centered using the shapelet decomposition method (Refregier 2003). This concerns 1145 positions of Io, 1178 positions of Europa, 1274 positions of Ganymede, and 1222 positions of Callisto. We also computed 1355 positions of Jupiter as the barycenter of the observed satellites, when at least two of them were available on the same date. The distributions of the (O-C)s and residuals in equatorial right ascension and declination are provided in Table 1. It shows the difference of (RA, Dec) coordinates for individual satellites, hence the observed positions versus positions calculated from INPOP21a and NOE-5-2021-JUP models with NAROO digitizations.

The key point is that the NOE-5-2021-JUP/INPOP21a rms (O-C) for all observations is 54.1 mas for Io, 53.0, mas for Europa, 57.2 mas for Ganymede, and 54.3 mas for Callisto. These average rms (O-C)s and residuals correspond to our observation accuracies over twenty-six oppositions in the series, or 31 years. The main improvement consisted in using the Gaia-DR3 star catalogue for the positioning of the stellar references for the astrometric reduction. In fact, we were able to decrease the residuals by about of 7 mas in both right ascension and declination, by comparison to the same analysis using the UCAC2 catalogue (Zacharias et al. 2008). With regard to the quadratic differences between the average residuals, we may conclude that we eliminated an error contribution about of 28 mas, indicating that our first measurements were degraded by unmodeled uncertainties. This result is consistent with the expected mean error of 15-30 mas of the UCAC2 catalogue, and we may deduce that the error contribution of the Gaia DR3 catalogue is negligible for our needs,

Table 1. Details of the equatorial mean (O-C)s and residuals for the Galilean satellites in mas, according to NOE-5-2021-JUP and INPOP21a ephemerides, with NAROO digitizations.

Satellite	$\overline{(O-C)_{\alpha\cos\delta}}$	$SEM_{\alpha\cos\delta}$ +/−	$\sigma_{\alpha\cos\delta}$ +/−	$\overline{(O-C)_{\delta}}$	SEM_{δ} +/−	σ_{δ} +/−
JI	-4.8	1.6	55.7	0.3	1.5	52.5
JII	-0.5	1.5	53.3	-0.1	1.5	52.7
JIII	-2.4	1.6	57.0	1.0	1.6	57.4
JIV	-1.0	1.6	56.2	0.9	1.5	52.5
Average	-2.1	0.8	55.6	0.5	0.8	53.9

as expected. Finally, we may conclude that astrometric positions derived from photographic plates could now be obtained to the absolute limits of the photographic technique since our results are very close to those derived from mutual phenomena techniques (Emelyanov et al. 2022).

2.2 Atmospheric limitations

With Fig. 2, we investigate the astrometric limitation in external precision due to the atmosphere. Lindegren (1980) discussed the influence on the astrometry of the wave-front distortion due to the atmospheric turbulence, and he expressed the mean astrometric error as a function of the measured angle between two objects. Thus, we plotted rms residuals in the (satellite-satellite) separations against the separations for Io, Europa, Ganymede and Callisto. For comparison, we also plotted Lindegren's function above.

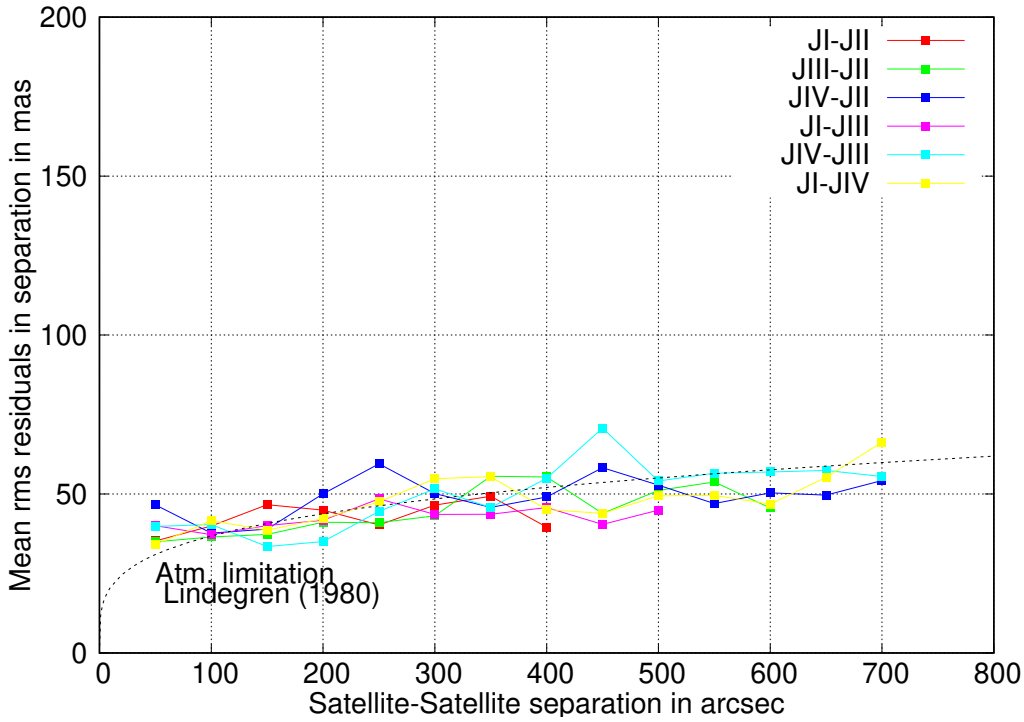

Fig. 2. Mean rms residuals in the (satellite-satellite) separations according to NOE-5-2021-JUP ephemerides. The x-axis shows the satellite-satellite separation and the y-axis the mean rms residuals in separation. Atmospheric limitation is given by Lindegren (1980).

Lindegren's function is referenced to the measured angle between two objects near the zenith and would not apply exactly to our observations, but this comparison is a first approach to assess the quality of our results. The curves for all satellite pairs are near coincident, and there is no excess variance in the separations. We may conclude that we have reached the limit in precision for these observations based on the Gaia-DR3, and confirm that we g-have reached the limits of the photographic techniques here.

2.3 The case of Amalthea

We compared the positions of the Galilean satellites with their theoretical computed positions given by the INPOP21a planetary ephemeris and former NOE-5-2010-JUP satellite ephemerides. In fact and by its definition, NOE-5-2010-JUP satellite model did not introduce the motion of the inner satellites. Their influence was taken into account by adding their mass to that of Jupiter. Thus, considering that Io is the main Galilean disturbed by the gravitational potential of the inners, we should be able to detect such an additional signal in its (O-C)s, in particular. We performed a frequency analysis of these data normalized by the Earth/satellite distance to reduce extra signals (motion of the observer, planetary ephemeris...) over 31 years, at the known frequencies of the four inner satellites. We assumed that the measured signals corresponded to variations in longitude since we were looking for mass estimations. Therefore, we were able to extract a 0.5016 ± 0.0022-days periodic signal of 20 ± 2 km of magnitude.

Table 2. Comparison of the mass of Amalthea.

Source	Amplitude (km)	Mass ($.10^{18}$kg)
USNO plates	20.00 ± 2	2.00 ± 0.20
Galileo	—	2.08 ± 0.15

Table 2 shows the comparison between the mass of Amalthea we estimated from our observations, and the mass that was calculated from Galileo flybys by Anderson et al. (2005). Both results are in the same order of magnitude. The differences are mainly due to the hypotheses of our estimation method. Although, our measuring error is a resulting indicator of these uncertainties. The key point is that we confirm that direct observation is not the only way to determine the physical characteristics of celestial bodies, and a new analysis of photographic plates could help to get more information about various bodies to contribute to a more fundamental physics.

3 Conclusions

We analyzed a full series of astrophotographic plates of the Galilean satellites taken at USNO from 1967 to 1998. Using the NAROO machine for the digitization and the Gaia-DR3 reference star catalogue allowed us to increase the precision and more important, to finally reach the limit in astrometric accuracy for the photographic technique. Thus, we were able to provide astrometric (RA, Dec) ICRS positions of the satellites, allowing us to deduce positions of the planet indirectly, with overall rms residuals of about 55 mas or 160 km at Jupiter.

We confirm the high interest in continuing the analysis of old observations, especially photographic plates, in the framework of the NAROO program. Since digitization time is reserved for external users, we remind that the NAROO machine is available for researchers to digitize their own collections following our call for proposals, issued every six months via our project website at `https://naroo.imcce.fr/`.

The NAROO program was supported by the DIM-ACAV of Île-de-France region, PSL Research University, the Programme National GRAM (PNGRAM), the Programme National de Planétologie (PNP) and the Programme National Soleil-Terre (PNST) of CNRS/INSU with INP and IN2P3, co-funded by CNES, and the Gaia Specific Action (AF Gaia) of Paris Observatory.

References

Anderson, J. D., Johnson, T. V., Schubert, G., et al. 2005, Science, 308, 1291

Emelyanov, N., Arlot, J. E., Anbazhagan, P., et al. 2022, MNRAS, 516, 3685

Fienga, A., Deram, P., Di Ruscio, A., et al. 2021, Notes Scientifiques et Techniques de l'Institut de Mecanique Celeste, 110

Gaia Collaboration, Prusti, T., de Bruijne, J. H. J., et al. 2016, A&A, 595, A1

Gaia Collaboration, Vallenari, A., Brown, A. G. A., et al. 2022, arXiv e-prints, arXiv:2208.00211

Lindegren, L. 1980, A&A, 89, 41

Pascu, D. 1977, in IAU Colloq. 28: Planetary Satellites, 63

Refregier, A. 2003, MNRAS, 338, 35

Robert, V., Desmars, J., Lainey, V., et al. 2021, A&A, 652, A3

Zacharias, N., Winter, L., Holdenried, E. R., et al. 2008, PASP, 120, 644

Session S17

Atelier général du Programme National de Physique Stellaire (PNPS)

SF2A 2023
M. N'Diaye, A. Siebert, N. Lagarde, O. Venot, K. Baillié, M. Béthermin, E. Lagadec, J. Malzac, J. Richard (eds)

SECULAR STABILITY OF THE DIPOLE-DIPOLE INTERACTION IN MAGNETIC BINARIES

C. Aykroyd[1], A. Bourgoin[1,2], C. Le Poncin-Lafitte[1], S. Mathis[2] and M.-C. Angonin[1]

Abstract. The existence of robust, extensive, and stable magnetic fields in a substantial fraction of early-type stars (mainly Ap, Bp, and O spectral types), white dwarfs, and neutron stars, has been firmly established. However, the mechanisms that give rise to these fields continue to be actively explored, with proposed explanations ranging from fossil fields to mergers and shear-driven dynamos. It is possible that the interplay between magnetism and binarity could provide insights into the origin of these fields, given the significant impact of magnetic fields on the long-term dynamics of binary systems. The purpose of this investigation is to analyze the secular spin precession behavior of binary systems under the influence of purely magnetic dipole-dipole interactions, focusing on stars with predominantly dipolar, strong, and stable magnetic fields. We utilise the Lie series approach to develop an effective secular model for the spin precession equations. The spin equilibrium configurations and their associated stabilities are obtained by minimizing the magnetic interaction energy of the system. Our findings demonstrate the existence of a single globally stable secular state among the four possible equilibrium states. This state corresponds to the configuration where the magnetic axes of one star are reversed relative to those of the companion, and are orthogonal to the orbital plane. We compare our results to conventional methods of determining instantaneous equilibrium states, which typically neglect the effects of orbital motion.

Keywords: magnetic fields, celestial mechanics, massive stars, white dwarfs, neutron stars

1 Introduction

Strong magnetic fields are found across a range of massive main-sequence stars (MMSs), white dwarfs (WDs), and neutron stars (NSs), and play a role in their evolution. Yet, understanding the origins of these fields remains a debated topic. Pure dynamo hypotheses are discouraged, since the transport of magnetic fields from the convective core across radiative zones of massive stars is a formidable challenge, with diffusivity timescales estimated to be longer than the main-sequence lifetime of the star (Moss, D. 2003). On the converse side, spectropolarimetry observations support the presence of strong and stable fields, more famously in the case of Ap and Bp stars (Ferrario et al. 2015). The so-called fossil mechanisms propose magnetic fields that are relics of a previous stage of a star's evolution and preserved by flux conservation. In the most basic scenario, this would be flux trapped in an interstellar cloud at the time of the star's birth. Nevertheless, for WDs and NSs, fossil magnetic fields are thought to be inherited from their progenitor stars, often A, B, or O-type stars. While this hypothesis seems to account for the observed strong magnetic fields, it raises intriguing questions. Notably, observations have revealed a dearth of weakly magnetic MMSs, indicating that these stars typically possess either strong fields or none at all. To potentially explain such bimodal distribution, studies have suggested the existence of thresholds to field strength, below which shear or convection instabilities develop (see e.g. Aurière et al. 2007); or that, in some stars, the time needed to reach an equilibrium becomes longer than the age in the main sequence, due to the Coriolis force produced by rapid rotation (Braithwaite & Cantiello 2013). Observations seem to indicate significantly lower magnetic incidence in binary systems, which may point towards other field formation mechanisms, specifically those linked to binarity. Commerçon et al. (2010) argues that interstellar clouds with strong magnetic fields are harder to fragment, yielding selection biases towards

[1] SYRTE, Observatoire de Paris, Université PSL, CNRS, Sorbonne Université, LNE, 61 avenue de l'Observatoire, 75014 Paris, France
[2] Université Paris-Saclay, Université Paris Cité, CEA, CNRS, AIM, F-91191, Gif-sur-Yvette, France

© Société Française d'Astronomie et d'Astrophysique (SF2A) 2023

less magnetic binary systems. Vidal et al. (2019) suggests instead that tidal instabilities in binary pairs can disrupt the magnetic fields via turbulent Joule diffusion within a few millions years, potentially explaining the scarcity of strong-field binaries. The merging scenario posits an alternative explanation: that the shear produced during the coalescence of protostars leads to magnetic field generation that subsequently settles into stable configurations. For WDs, this process is thought to occur during the common envelope phase. Such fields would only be present on the merged product, potentially explaining why single magnetic stars outnumber their binary counterparts. Many further routes for magnetic field generation have been proposed. For example, in the case of WDs, dynamos previously operating at the core of progenitor main-sequence stars may be compressed during core collapse (Stello et al. 2016).

While each hypothesis offers valuable insights, current observational data are insufficient to definitively favor one over another, and it is plausible that multiple mechanisms are at work simultaneously. Future observations of binary systems may offer a pathway to distinguish between scenarios. In particular, the next generation of gravitational wave detectors such as the Laser Interferometer Space Antenna (LISA; see Amaro-Seoane et al. 2017) or the Einstein Telescope (ET; see Maggiore et al. 2020) can provide enough sensitivity to characterise the magnetic properties of compact systems of WDs and NSs (Bourgoin et al. 2022; Carvalho et al. 2022; Lira et al. 2022).

In this work, we study the binary interaction of the fields themselves. Following Paper I (Aykroyd et al. 2023), we consider stars that have strong and stable magnetic fields, which are modulated by rotation. We investigate the dynamics of the interacting magnetic fields, concerning ourselves with the stability of the different configurations.

Notation and conventions. For each vector $\vec{u} = (u^1, u^2, u^3) \in \mathbb{R}^3$, we represent its norm without arrows $u = \|\vec{u}\|$ and its direction by a hat $\hat{u} = \vec{u}/u$. We adopt the summation convention on repeated indices, for example $a_i b^i = a_1 b^1 + a_2 b^2 + a_3 b^3$. We shall adopt the following constants: G the gravitational constant, μ_0 the permeability of free space.

2 Binary dynamics

We shall be considering a pair of stars in closed orbit: either a MMS binary or WD / NS binary. We assign an index $a \in \{1, 2\}$ to each star, and define a mass m_a, a spin vector $\vec{s}_a$, and a magnetic moment $\vec{\mu}_a$. We assume a stable magnetostatic field that is rigidly frozen into each star, compatible with general observations in massive stars and compact objects. We consider the topology to be predominantly dipolar (see e.g. Borra et al. 1982), aligned with the stellar spin. The aim is to study systems under strong magnetic interaction, where magnetism drives the stellar orientation. For this we also assume that the timescales of magnetic dynamics are much larger than the orbital period.

2.1 Hamiltonian formulation

We begin by formulating the dynamics of the system under a Hamiltonian formalism. We introduce a two-body Hamiltonian in the centre-of-mass frame:

$$\mathcal{H}(\vec{r}, \vec{p}\,; \vec{s}_1, \vec{s}_2) = \mathcal{H}_{\rm kep}(\vec{r}, \vec{p}) + \varepsilon \mathcal{H}_{\rm mag}(\vec{r}\,; \vec{s}_1, \vec{s}_2), \tag{2.1}$$

with $\vec{r}$ the separation between the two stars and corresponding phase-space momentum $\vec{p}$. The spin degrees-of-freedom $\vec{s}_1$ and $\vec{s}_2$ are non-canonical and satisfy the Poisson bracket relations $\{s_a^i, s_a^j\} = \epsilon_{ijk} s_a^k$, where ϵ_{ijk} is the Levi-Civita symbol. The constant ε is for bookkeeping and we shall later take $\varepsilon = 1$. The first term $\mathcal{H}_{\rm kep}$ represents the Keplerian gravitational interaction between two point-particles and is fully-integrable:

$$\mathcal{H}_{\rm kep}(\vec{r}, \vec{p}) = \frac{p^2}{2\beta} - \frac{G m_1 m_2}{r}, \tag{2.2}$$

with $\beta = m_1 m_2/(m_1 + m_2)$ the reduced mass. The second term $\mathcal{H}_{\rm mag}$ describes the magnetic interaction between two dipolar fields (Pablo et al. 2019), which we express in tensor form:

$$\mathcal{H}_{\rm mag} = -\mathcal{B}_{ij} \mu_1^i \mu_2^j, \qquad \text{with } \mathcal{B}_{ij} = \frac{\mu_0}{4\pi r^3}(3\,\hat{r}^i \hat{r}^j - \delta_{ij}), \tag{2.3}$$

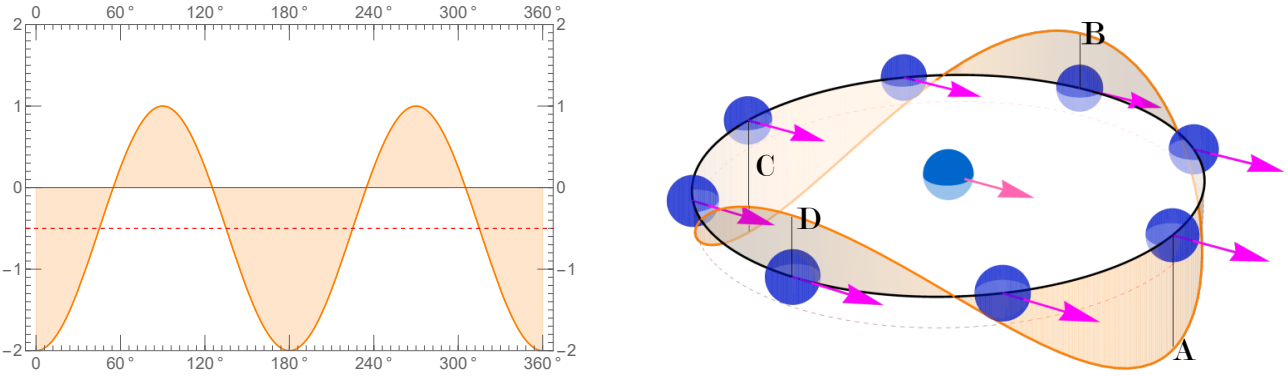

Fig. 1: Magnetic energy $\mathcal{H}_{\rm mag}$ (orange) as a function of the orbital phase, for a binary with two aligned dipole axes. Stationary points are labelled A through D. Energy oscillations emerge throughout the orbit. On longer timescales, such configuration is unstable to perturbations of the magnetic moments $\vec{\mu}_a$.

with δ_{ij} the Kronecker delta. We include a rigidbody constraint, enforcing alignment between the spin and moment, $\vec{\mu}_a = \mu_a \hat{s}_a$. Then, the evolution of the magnetic axes (or equivalently, of the spins) can be obtained from Hamilton's equations in Poisson bracket form:

$$\frac{\mathrm{d}\mu_a^i}{\mathrm{d}t} = \{\mu_a^i, \mathcal{H}\} = \epsilon_{ijk}\mu_a^j \left(\frac{\mu_a}{s_a}\mathcal{B}_{k\ell}\mu_b^\ell\right), \tag{2.4}$$

which corresponds to a precession of the vector $\vec{\mu}_a$. We remark that since the magnetic field tensor $\mathcal{B}_{ij}$ depends on the separation $\vec{r}$, the precession and orbital dynamics are coupled. We shall thus have two interacting timescales, the orbital period $P_{\rm orb}$ and the precession timescale $\tau \sim 8\pi a^3 s_a/(\mu_0\mu_1\mu_2)$ [see Eq. (2.4)]. As illustrated in Fig. 1, the (normalised) magnetic Hamiltonian exhibits oscillations in the orbital timescale. In the next step we search for magnetic configurations that are stable to perturbations. For this we employ an orbit-averaging procedure to eliminate small-timescale oscillations and obtain an effective description of the system at precession timescale τ.

2.2 *Secular stability*

We introduce a 'secular system', where the effects of orbital translation are averaged out from the potentials. In this new description, the precession dynamics and orbital motion will become naturally decoupled. The transformed Hamiltonian is computed by expanding Eq. (2.1) in a Lie series to first order in ε, yielding a new magnetic term which is integrable in the orbital variables:

$$\mathcal{H}^* = \mathcal{H}_{\rm kep} + \varepsilon\bar{\mathcal{H}}_{\rm mag} + O(\varepsilon^2). \tag{2.5}$$

The new magnetic term $\bar{\mathcal{H}}_{\rm mag}$ is computed by averaging $\mathcal{H}_{\rm mag}$ over the flow of the zero order term,

$$\bar{\mathcal{H}}_{\rm mag} = \lim_{T\to\infty}\frac{1}{T}\int_{-T/2}^{T/2}\mathcal{H}_{\rm mag}\circ\phi_t^{\mathcal{H}_{\rm kep}}\mathrm{d}t, \tag{2.6}$$

where $\phi_t^{\mathcal{H}_{\rm kep}}$ is the flow along $\mathcal{H}_{\rm kep}$. By plugging the solutions for the Keplerian two-body problem we get:

$$\bar{\mathcal{H}}_{\rm mag} = \bar{\mathcal{B}}_{ij}\mu_a^i\mu_b^j, \qquad \text{with } \bar{\mathcal{B}}_{ij} = \frac{\mu_0}{8\pi a^3(1-e^2)^{3/2}}\left(3\hat{L}^i\hat{L}^j - \delta_{ij}\right), \tag{2.7}$$

where a is the semi-major axis, e the eccentricity, and $\vec{L} = \vec{r}\times\vec{p}$ is the conserved angular momentum of the orbit. Following Paper I, we search for the magnetic configurations $\vec{\mu}_a$ that are stationary for $\mathcal{H}^*$. These are 'secular' or long-term equilibrium states and are unaffected by the short-period orbital perturbations. Conversely, equilibrium states obtained from system (2.1) (see Pablo et al. 2019) would only be stationary at a given orbital phase (cf. Fig. 1). There are four secular equilibrium states satisfying $\dot{\vec{\mu}}_a = \{\vec{\mu}_a, \mathcal{H}^*\} = 0$, illustrated in Fig. 2. From the Hessian of $\bar{\mathcal{H}}_{\rm mag}$ (computed in Paper I), we show that only a single of these states is stable: the configuration in which the dipole axes are orthogonal to the orbital plane and anti-aligned. Binaries with orientations controlled by magnetic interactions are expected to converge to this state.

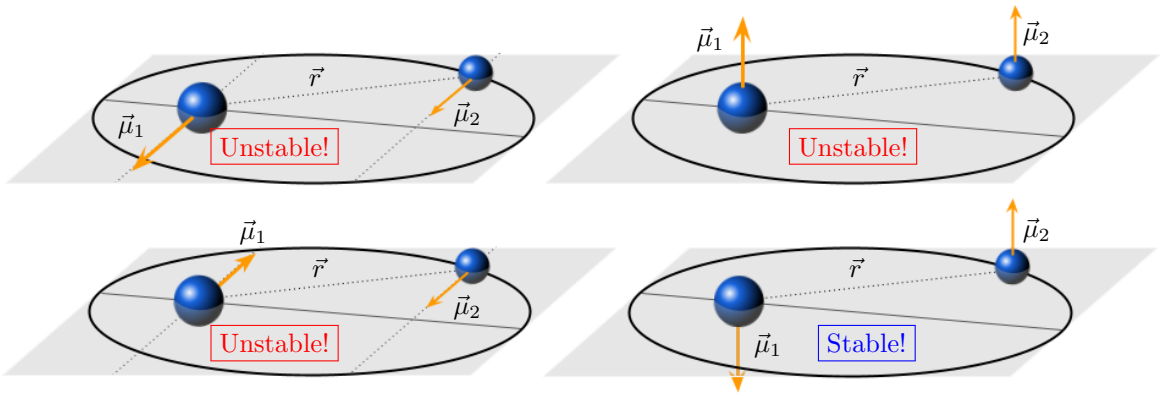

Fig. 2: Secular spin equilibrium states and their respective stabilities. These correspond to directions that are either inside the orbital plane, in some arbitrary direction (**left** column), or orthogonal to the orbital plane (**right** column). In each scenario, the two spins must be either parallel (**top** row) or anti-parallel (**bottom** row).

3 Conclusions

We have determined the secular dynamics and equilibrium of a pair of stars under the magnetic dipolar interaction. For that we have assumed that the fields are fixed with respect to the object's frame, and that the magnetic moments are aligned with the stellar spin. The method we have presented predicts a set of equilibrium states that are stationary throughout the whole orbit. We have found that there is a single state which is stable, where the stars have anti-aligned moments which are perpendicular to the orbital plane. This is a minimum of secular energy towards which we expect the system to converge. Our results are applicable for binaries of both compact objects (WD, NS) and massive stars. We remark that the ϵ-Lupi system, the only known doubly-magnetic MMSs binary system, is found in our stable state (cf. Pablo et al. 2019).

C.A. acknowledges the joint finantial support of Centre National d'Études Spatiales (CNES) and École Doctorale Astronomie et Astrophysique d'Île-de-France (ED127 AAIF). This work was also supported by the Programme National GRAM, by PNPS (CNRS/INSU), by INP and IN2P3 co-funded by CNES, and by CNES LISA grants at CEA/IRFU.

References

Amaro-Seoane, P., Audley, H., Babak, S., et al. 2017, Laser Interferometer Space Antenna
Aurière, M., Wade, G. A., Silvester, J., et al. 2007, A&A, 475, 1053
Aykroyd, C., Bourgoin, A., Poncin-Lafitte, C. L., Mathis, S., & Angonin, M.-C. 2023, A&A, 675, A32
Borra, E. F., Landstreet, J. D., & Mestel, L. 1982, ARA&A, 20, 191
Bourgoin, A., Poncin-Lafitte, C. L., Mathis, S., & Angonin, M.-C. 2022
Braithwaite, J. & Cantiello, M. 2013, MNRAS, 428, 2789
Carvalho, G. A., Anjos, R. C. d., Coelho, J. G., et al. 2022, ApJ, 940, 90
Commerçon, B., Hennebelle, P., Audit, E., Chabrier, G., & Teyssier, R. 2010, A&A, 510, L3
Ferrario, L., Melatos, A., & Zrake, J. 2015, Space Science Reviews, 191, 77
Lira, M., Degollado, J. C., Moreno, C., & Núñez, D. 2022, Gen. Rel. Grav., 54, 146
Maggiore, M., Broeck, C. V. D., Bartolo, N., et al. 2020, JCAP, 2020, 050
Moss, D. 2003, A&A, 403, 693
Pablo, H., Shultz, M., Fuller, J., et al. 2019, MNRAS, 488, 64
Stello, D., Cantiello, M., Fuller, J., et al. 2016, Nature, 529, 364
Vidal, J., Cébron, D., ud-Doula, A., & Alecian, E. 2019, A&A, 629, A142

SF2A 2023
M. N'Diaye, A. Siebert, N. Lagarde, O. Venot, K. Baillié, M. Béthermin, E. Lagadec, J. Malzac, J. Richard (eds)

PHOTOCENTRE DISPLACEMENT OF RHD SIMULATIONS OF AGB STARS AND CORRELATION WITH STELLAR PARAMETERS

E. Béguin[1], A. Chiavassa[1], B. Freytag[2], A. Ahmad[2] and S. Uttenthaler[3]

Abstract.
The evolution of stars with low to intermediate masses culminates in the Asymptotic Giant Branch (AGB) phase. During this phase, these stars undergo intricate dynamics marked by several processes, including convection, pulsation, and shockwaves. These processes give rise to strong stellar winds that significantly enhance the interstellar medium with various chemical elements. Over time, this enrichment has implications for astronomical measurements, amplifying uncertainties in the determination of essential stellar parameters. Furthermore, the development of convection-related structures on the surfaces of evolved stars leads to temporal fluctuations in the position of the photocentre. This variability influences Gaia measurements, where it contributes substantially to the uncertainties associated with parallax. In this work, we used 3D radiative-hydrodynamics simulations of stellar surface convection, computed with CO^{5}BOLD, to study the photocentre displacement and possible correlations with stellar parameters. This is done for 31 AGB simulations. Ultimately, our objective is to develop a systematic approach, a roadmap, for quantitatively determining the surface gravities of AGB stars from Gaia data, taking into account the inherent uncertainties, and leveraging tailored radiative-hydrodynamics simulations to enhance precision.

Keywords: stars: atmospheres, stars: AGB and post-AGB, astrometry, parallaxes, hydrodynamics

1 Introduction

After the main sequence, low- to intermediate-mass stars evolved into the Asymptotic Giant Branch (AGB). Their effective temperature is around $3300K$ and their luminosity ranges from 2000 to $10000L_\odot$ (Decin 2021). They are characterized by dynamics encompassing convective motions, pulsation, shockwaves... which induce strong winds, at a $10^{-8} - 10^{-5} M_\odot/yr$ mass-loss rate (De Beck et al. 2010) that enrich massively the interstellar medium in gas and dust (Höfner & Olofsson 2018).

Mira stars are peculiar AGB stars whose envelope is pulsating over a period from 100 to 1000 days, resulting in large-amplitude variations in radius, brightness and temperature of the star, above 2.5 magnitude in the V band for example (Decin 2021). As a consequence, it is difficult to accurately measure their stellar parameters and astrometric properties (Gaia Collaboration et al. 2019).

Chiavassa et al. (2018, 2022) used three-dimensional (3D) radiative hydrodynamic simulations of convection with CO^{5}BOLD and determined the impact of temporal variability of convection-related surface structures on the position of the photocentre. Its position does not coincide with the barycentre of the star as the surface pattern changes with time. These movements are up to $5 - 10\%$ of the stellar radius, depending on the stellar parameters, in particular the surface gravity. Moreover, Chiavassa et al. argued that this variability accounts for a substantial part of the Gaia parallax uncertainty.

These earlier works demonstrated the principle but were limited by the number of 3D simulations used. In this paper, we provide an extension of their works based on a larger grid of simulations with stellar parameters covering a larger portion of the Hertzsprung-Russell diagram. The objective is to obtain analytical laws allowing the extraction of the surface gravity from Gaia parallax uncertainty.

[1] Université Côte d'Azur, Observatoire de la Côte d'Azur, CNRS, Lagrange, CS 34229, Nice, France
[2] Department of Physics and Astronomy at Uppsala University, Regementsvägen 1, Box 516, SE-75120 Uppsala, Sweden
[3] Institute of Applied Physics, TU Wien, Wiedner Hauptstraße 8-10, 1040 Vienna, Austria

© Société Française d'Astronomie et d'Astrophysique (SF2A) 2023

2 Methods

We used radiative-hydrodynamics (RHD) simulations of AGB stars (from Freytag et al. 2017; Chiavassa et al. 2018; Ahmad et al. 2023, and private communication) computed with CO^{5}BOLD code (Freytag 2012). The code solves the coupled non-linear equations of compressible hydrodynamics and non-local radiative energy transfer, assuming solar abundances. The configuration is a "star-in-a-box" which describes the dynamics of the convective envelope and the inner atmosphere. Additionally, the simulations covers the range 2500 to $3300K$ in effective temperature, $\log(g)$ (surface gravity) spans values between -0.85 and 0.16, $2000 - 10000L_{\odot}$ in luminosity, 130 to $440R_{\odot}$ in stellar radius and 100 to 600 days in pulsation period (see details for computation of stellar parameters in Ahmad et al. 2023).

We post-processed a set of temporal snapshots using the radiative transfer code Optim3D (Chiavassa et al. 2009), which takes into account the Doppler shifts, partly due to convection, in order to compute intensity maps (Figure 1) integrated over the Gaia G band [320-1050 nm].

For each map, we then calculated the position of the photocentre as the intensity-weighted mean of the x-y positions of all emitting points tiling the visible stellar surface according to :

$$P_x = \frac{\sum_{i=1}^{N}\sum_{j=1}^{N} I(i,j) * x(i,j)}{\sum_{i=1}^{N}\sum_{j=1}^{N} I(i,j)} \tag{2.1}$$

$$P_y = \frac{\sum_{i=1}^{N}\sum_{j=1}^{N} I(i,j) * y(i,j)}{\sum_{i=1}^{N}\sum_{j=1}^{N} I(i,j)} \tag{2.2}$$

where $I(i,j)$ is the emerging intensity for the grid point (i,j), with coordinates $x(i,j)$, $y(i,j)$ of the intensity map in solar radii, and N the total number of grid points in the simulated box (from 281 to 637). The position of the photocentre doesn't coincide with the barycentre of the star as large convective cells result in intensity asymmetries.

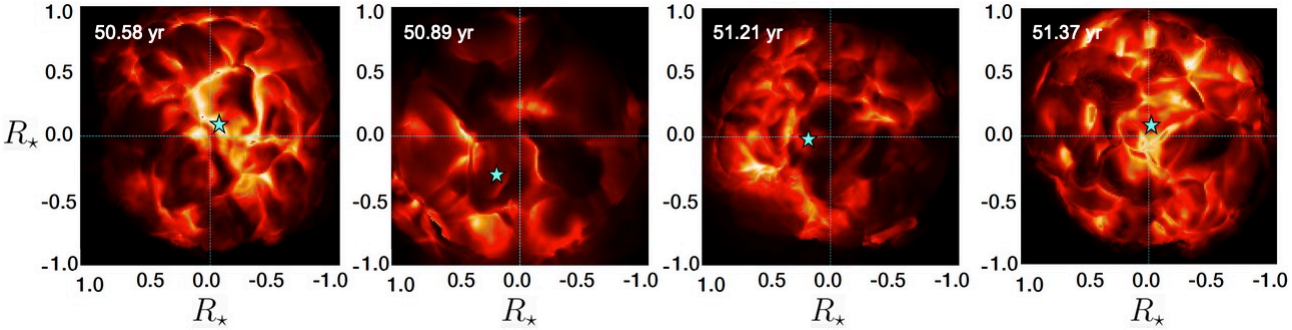

Fig. 1. Intensity maps of an AGB simulation in $erg.s^{-1}.\mathring{A}^{-1}$. The dashed lines intersect at the geometric center of the image. The star indicates the position of the photocentre at the given time.

Each snapshot of the simulation is spaced by ~ 60 days, for the simulations we used. We use ~ 100 snapshots for each simulation which gives the temporal variability of the photocentre moving across the stellar surface. We also computed the mean position of the photocentre and its standard deviation σ_P. Figure 2 displays an example of how the photocentre changes its position, the red dot indicates the mean position and the red circle the standard deviation. Figure 2 also displays how the photocentre displacement is correlated with the surface gravity. The displacements are larger when $\log(g)$ is lower ($\log(g)$=-0.36, left panel) with respect to a more compact behaviour with larger gravity ($\log(g) = 0.16$, right panel).

3 Correlation between the photocentre displacement and stellar parameters

From the study of the 31 simulations, the standard deviation of the photocentre displacement ranges from ~ 4 to 13% of the corresponding stellar radius, consistent with Chiavassa et al. (2018).

Figure 3 (left panel) displays that the logarithm of the pulsation period is decreasing with the logarithm of the surface gravity. Moreover, a correlation between the logarithm of the pulsation period and σ_P is visible in

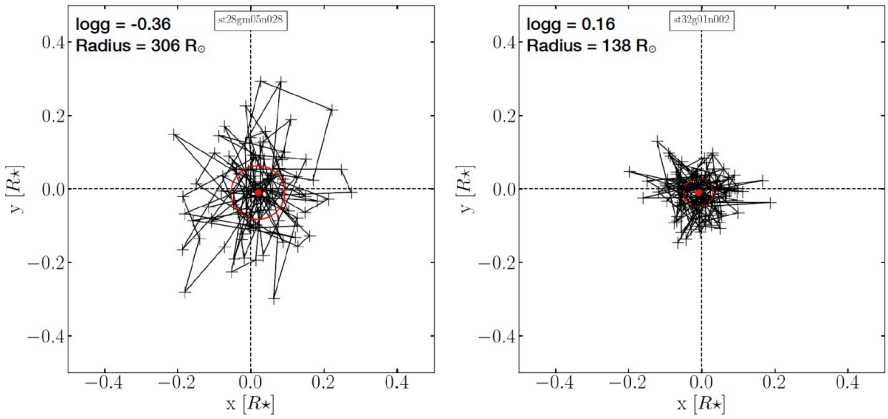

Fig. 2. Photocenter displacement of two different simulations: the red dot corresponds to its mean position and the red circle to its standard deviation. **Left:** Low surface gravity. **Right:** High surface gravity.

Figure 3 (right panel). The pulsation period gives important information about stellar interior (density) with hints on global shocks induced by large-amplitude, radial, and fundamental-mode pulsations.

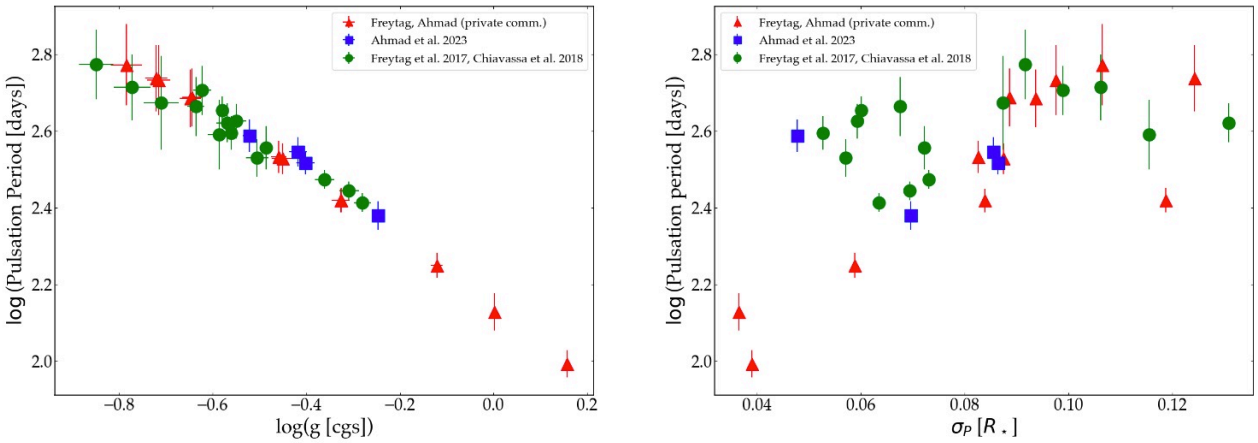

Fig. 3. Left: Log-log plot of pulsation period against surface gravity. We observe a correlation between the two parameters. **Right:** The pulsation period in logarithmic scale against σ_P. We suggest a fit with a power law whose parameters still need to be properly determined.

Figure 4 (left panel) displays a mild correlation between σ_P and stellar luminosity that further analysis will help characterise. Finally, we see a mild correlation between σ_P and the surface gravity (see Figure 4 right panel and Figure 2) as it is expected from the relations inferred in Figure 3. Interplay between large-scale convection and radial pulsations results in the formation of giant and bright convective cells at the surface. Freytag et al. (2017), and references therein, argue the size of the cells is governed by the pressure scale height. Thus, lower surface gravity means larger cells. Then, large convective cells result in intensity asymmetries, directly causing temporal fluctuations of the photocentre.

4 Followings project : exploitation of Gaia data

The next steps in our project concern the comparison of the 3D simulation predictions to Gaia data, aiming at characterising the photocentre variability hidden in Gaia uncertainty on parallax measurements of AGB stars, where convection-related variability accounts for a substantial part of it (Chiavassa et al. 2018, 2022). The final idea is to quantitatively extract the fundamental properties of AGB stars, such as surface gravity and pulsation, directly from Gaia parallax uncertainty thanks to appropriate RHD simulations. We will proceed as follows:

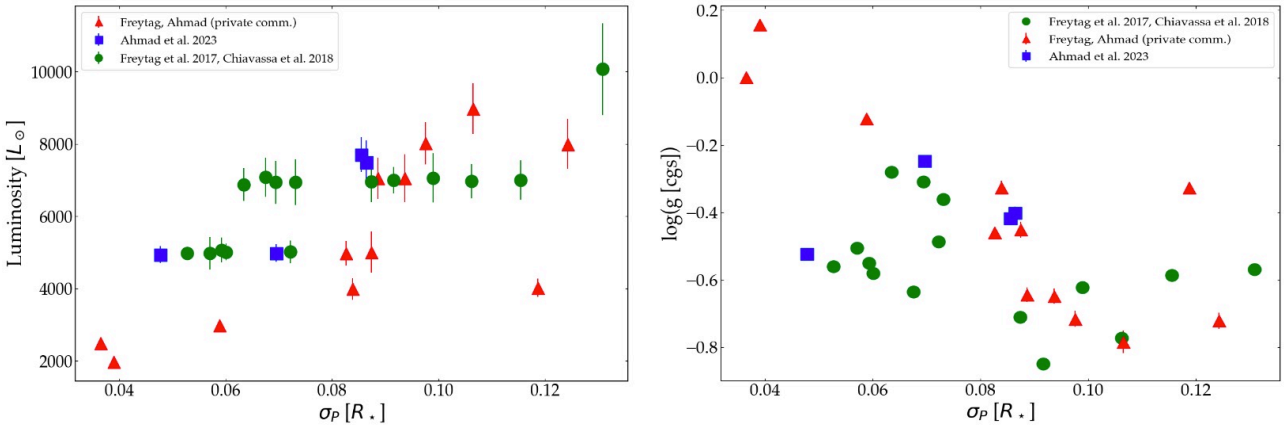

Fig. 4. Left: Luminosity against σ_P. We might find a mild correlation. **Right:** Surface gravity in logarithmic scale against σ_P. We can observe some correlation as it is expected.

- Starting from the simulations, we will provide analytical laws based on the photocentre displacement (σ_P) versus surface gravity and pulsation period ;
- Secondly, we will provide a comparison of the measured Gaia DR3 (Gaia Collaboration et al. 2016, 2023) uncertainty on parallax measurements of a sample of Mira stars (Uttenthaler et al. 2019) to our predictions of photocentre displacement ;
- Eventually, thanks to the analytical laws based on the RHD simulations, we will provide the $\log(g)$ of the observed stars.

In the end, combining our global 3D simulations with Gaia data will make it possible to systematically provide stellar parameters (surface gravity and pulsation) of AGB stars in an unique way. This work is on-going (Béguin et al., in prep.).

Acknowledgements: This work is funded by the French National Research Agency (ANR) project PEPPER (ANR-20-CE31-0002). BF acknowledges funding from the European Research Council (ERC) under the European Union's Horizon 2020 research and innovation programme Grant agreement No. 883867, project EXWINGS. The computations were enabled by resources provided by the Swedish National Infrastructure for Computing (SNIC). This work was granted access to the HPC resources of Observatoire de la Côte d'Azur Mésocentre SIGAMM.

References

Ahmad, A., Freytag, B., & Höfner, S. 2023, A&A, 669, A49
Chiavassa, A., Freytag, B., & Schultheis, M. 2018, A&A, 617, L1
Chiavassa, A., Kudritzki, R., Davies, B., Freytag, B., & de Mink, S. E. 2022, A&A, 661, L1
Chiavassa, A., Plez, B., Josselin, E., & Freytag, B. 2009, A&A, 506, 1351
De Beck, E., Decin, L., de Koter, A., et al. 2010, A&A, 523, A18
Decin, L. 2021, Annual Review of Astronomy and Astrophysics, 59, 337
Freytag, B. 2012, Journal of Computational Physics, 231, 919
Freytag, B., Liljegren, S., & Höfner, S. 2017, A&A, 600, A137
Gaia Collaboration, Eyer, L., Rimoldini, L., et al. 2019, A&A, 623, A110
Gaia Collaboration, Prusti, T., de Bruijne, J. H. J., et al. 2016, A&A, 595, A1
Gaia Collaboration, Vallenari, A., Brown, A. G. A., et al. 2023, A&A, 674, A1
Höfner, S. & Olofsson, H. 2018, Astronomy and Astrophysics Review, 26, 1
Uttenthaler, S., McDonald, I., Bernhard, K., Cristallo, S., & Gobrecht, D. 2019, A&A, 622, A120

SF2A 2023
M. N'Diaye, A. Siebert, N. Lagarde, O. Venot, K. Baillié, M. Béthermin, E. Lagadec, J. Malzac, J. Richard (eds)

NEBULAR SPECTRA FROM TYPE Ia SUPERNOVA EXPLOSION MODELS COMPARED TO JWST OBSERVATIONS OF SN 2021aefx

S. Blondin[1], L. Dessart[2], D. J. Hillier[3], C. A. Ramsbottom[4] and P. J. Storey[5]

Abstract. Recent *JWST* observations of the Type Ia supernova (SN Ia) 2021aefx in the nebular phase have paved the way for late-time studies covering the full optical to mid-infrared (MIR) wavelength range, and with it the hope to better constrain SN Ia explosion mechanisms. We investigate whether public SN Ia models covering a broad range of progenitor scenarios and explosion mechanisms can reproduce the full optical-MIR spectrum of SN 2021aefx at $\sim$270 days post explosion. We performed 1D steady-state non-local thermodynamic equilibrium simulations with the radiative-transfer code CMFGEN, and compared the predicted spectra to SN 2021aefx. Taken as a whole, the models can explain the main features of this SN over the full wavelength range. However, no single model emerges as a preferred match. We discuss possible causes for the mismatch of the models, including ejecta asymmetries and ionisation effects. Our models suggest that key physical ingredients are missing from either the explosion models, or the radiative-transfer post-processing, or both. Nonetheless, they also show the potential of the near- and MIR to uncover new spectroscopic diagnostics of SN Ia explosion mechanisms.

Keywords: supernovae: general, Radiative transfer, Atomic data, Line: identification, supernovae: individual: SN 2021aefx

1 Introduction

Current models for Type Ia supernovae (SNe Ia) invoke variations in the mass of the exploding carbon-oxygen white dwarf (WD) and in the conditions of the thermonuclear runaway. These models include delayed detonations in near-Chandrasekhar-mass ($M_{\rm Ch}$) WDs double detonations in sub-$M_{\rm Ch}$ WDs, and violent mergers of two sub-$M_{\rm Ch}$ WDs. However, due to numerous degeneracies in SN Ia light curves and spectra, distinguishing between these various models has been a challenge (e.g. Maoz et al. 2014).

While the early high-brightness phase of SNe Ia ($\lesssim 50$ d post explosion) yields constraints on the ejecta mass and kinetic energy, as well as the yields of intermediate-mass elements (IMEs) and ^{56}Ni, the late nebular phase (> 100 d post explosion) can provide complementary information. At such times, the ejecta have expanded and diluted to become optically thin, revealing their innermost layers. The cooling is then dominated by forbidden lines that provide key nucleosynthetic information. In particular, the abundance of stable iron-group elements (IGEs) synthesised during the explosion has been proposed to distinguish sub-$M_{\rm Ch}$ from $M_{\rm Ch}$ progenitors, since their production increases with the central density (and hence initial mass) of the exploding WD (e.g. Flörs et al. 2020). Accurate abundance determinations are however difficult to obtain given the amount of line overlap and the sensitivity of line strengths to small variations in the ionisation state (Blondin et al. 2022). The advent of *JWST* has paved the way for systematic studies of SNe Ia in the mid-infrared (MIR), where lines are typically less blended (and less sensitive to the electron temperature) than in the optical and near-infrared

[1] Aix Marseille Univ, CNRS, CNES, LAM, Marseille, France
[2] Institut d'Astrophysique de Paris, CNRS-Sorbonne Université, 98 bis boulevard Arago, 75014, Paris, France
[3] Department of Physics and Astronomy & Pittsburgh Particle Physics, Astrophysics, and Cosmology Center (PITT PACC), University of Pittsburgh, 3941 O'Hara Street, Pittsburgh, PA 15260, USA
[4] Astrophysics Research Centre, School of Mathematics and Physics, Queen's University Belfast, Belfast BT7 1NN, Northern Ireland, UK
[5] Department of Physics and Astronomy, University College London, Gower Street, London WC1E 6BT, UK

© Société Française d'Astronomie et d'Astrophysique (SF2A) 2023

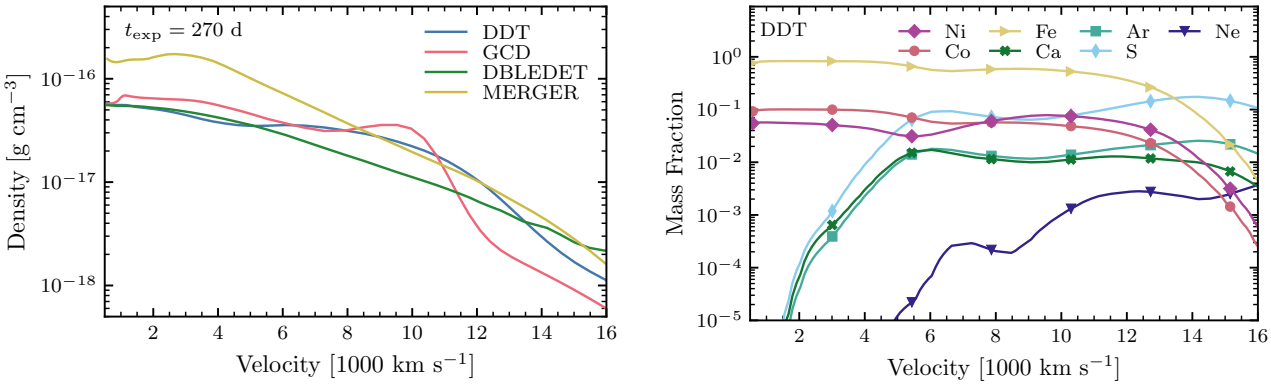

Fig. 1. Density profiles at 270 d post explosion for all models (*left*) and abundance profiles for the DDT model (*right*).

(NIR). This allows for a more secure identification of lines as well as detailed studies of their morphology, which may constrain the spatial distribution of the emitting material.

The Type Ia SN 2021aefx was recently observed with *JWST* using the Near Infrared Spectrograph (NIRSpec) and the Mid Infrared Instrument (MIRI) (Kwok et al. 2023a). Its nebular spectrum at +255 d past maximum light ($\sim$270 d post explosion) revealed the presence of numerous forbidden lines of IGEs and a distinct line due to argon ([Ar III] 8.99 μm), whose flat-topped profile was interpreted as indicative of a chemically stratified ejecta. Here we compare a diverse set of state-of-the-art, public SN Ia explosion models with the full optical-MIR nebular spectrum of SN 2021aefx, and evaluate which one, if any, fares better. All model outputs are publicly available online*, and the results presented here are taken from a recently accepted paper (Blondin et al. 2023).

2 Numerical approach

We select previously-published models from the Heidelberg Supernova Model Archive (HESMA; Kromer et al. 2017). These include the $M_{\rm Ch}$ delayed-detonation model N100 of Seitenzahl et al. (2013) [hereafter DDT], the $M_{\rm Ch}$ pulsationally assisted gravitationally-confined detonation model r10_d1.0 of Lach et al. (2022) [hereafter GCD], the sub-$M_{\rm Ch}$ double-detonation model M1002 of Gronow et al. (2021) [hereafter DBLEDET], and the violent merger model of Pakmor et al. (2012) [hereafter MERGER]. All models correspond to spherically-averaged versions of a 3D simulation. This averaging causes a systematic overestimate of the total mass by 3–8% and a difference of up to $\pm$10% for several isotopic and elemental yields compared to the original 3D models. The spherically-averaged density and representative abundance profiles at 270 d post explosion are shown in Fig. 1. We then solve the 1D non-local thermodynamic equilibrium (non-LTE) radiative transfer with CMFGEN (see Blondin et al. 2023, for details).

3 Results

Figure 2 shows the synthetic spectra for the four models compared to SN 2021aefx at 270 d post explosion in the wavelength range 0.35–14 μm. The models predict all the observed spectral features of SN 2021aefx from the blue end of the optical until the red end of the *JWST* range. Unfortunately, no single model produces a perfect match. The modest difference between the spectral properties of these four distinct explosion models reflects the similarity in composition for the dominant coolants in the ejecta. There are, however, numerous offsets in specific lines or features that result from differences in the abundance and ionisation of specific elements.

Throughout the optical and IR ranges, the spectrum is dominated by forbidden lines. Some exhibit clearly a broad flat top, e.g. [Ar III] 8.99 μm (except in the MERGER model), indicating a formation starting at large velocities and possibly extending to even larger velocities (the corresponding models have little Ar below about 5000 km s^{-1} or exhibit an ionisation stratification). Numerous lines show a Gaussian-like profile because they form throughout the ejecta (e.g. [Fe III] 0.47 μm). All lines from IGEs have typical line widths in the range $\sim$8000–14000 km s^{-1}, while those of IMEs, which tend to be present at large velocities only, exhibit significantly

*https://zenodo.org/record/8290155

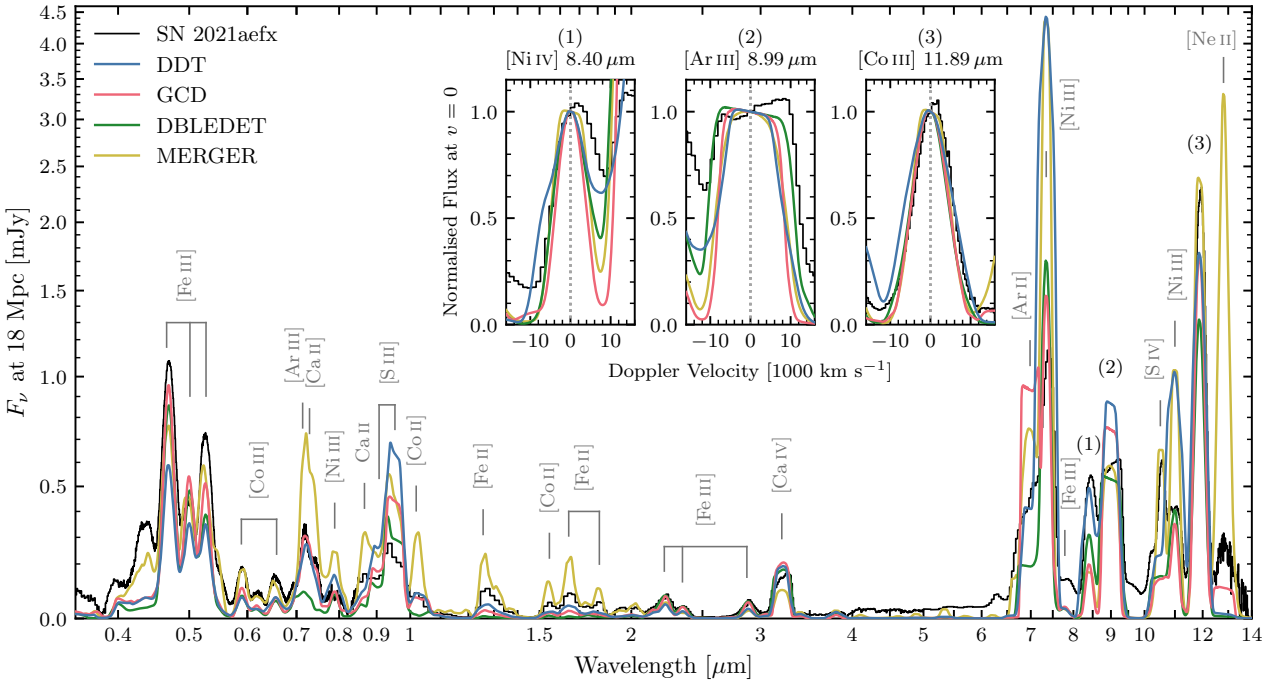

Fig. 2. Spectra of our four models at 270 days post explosion compared to SN 2021aefx over the wavelength range 0.35–14 μm. The SN 2021aefx spectrum has been corrected for redshift and extinction (assuming a host-galaxy reddening of 0.097 mag and a MW reddening of 0.008 mag). The synthetic fluxes correspond to the same assumed distance to SN 2021aefx of 18 Mpc; they have not been rescaled or normalised in any way. We include selected line identifications based on their maximum Sobolev equivalent width. The insets show normalised line profiles in velocity space for selected transitions, illustrating variations in line widths and morphology.

larger widths (FWHM $\gtrsim 20000\,\mathrm{km\,s^{-1}}$). The inset in Figure 2 gives the typical profile morphologies in our model spectra, using [Ni IV] 8.40 μm, [Ar III] 8.99 μm, and [Co III] 11.89 μm.

Our MERGER model displays a very strong line due to [Ne II] 12.81 μm, whose peaked profile reflects the presence of neon all the way to the innermost region of the ejecta. This is a natural expectation of this model as the central ejecta is dominated by the ashes of the secondary WD which burns to O and IMEs (Pakmor et al. 2012). While inconsistent with SN 2021aefx, this line was recently detected in the nebular spectrum of another SN Ia, which was interpreted as a violent merger event (SN 2022pul; Kwok et al. 2023b).

We attempted to qualitatively evaluate the impact of ejecta asymmetries on our 1D modelling approach by considering different directions in the original 3D version of the DDT model (I. Seitenzahl, priv. comm.). Specifically we considered the three orthogonal axes of their Cartesian grid ($\hat{\mathbf{x}}, \hat{\mathbf{y}}, \hat{\mathbf{z}}$) in both positive and negative directions, resulting in six distinct radial profiles. The variation in spectral properties along the six directions compared to the spherically-averaged model partly reflects variations in abundance (Fig. 3). The remaining variation results from differences in the temperature and ionisation structures due to variations in the ^{56}Co distribution along the different directions, in particular above $\sim 4000\,\mathrm{km\,s^{-1}}$. The impact is most readily seen in the optical Fe III-dominated complex around $\sim 0.5\,\mu$m. By comparing Figs. 2 and 3 we see that the spectroscopic variation along different lines of sight in the DDT model can be as large as when considering different explosion models. This impacts the accuracy of abundance determinations when using spherically-averaged ejecta as well as our ability to make quantitative comparisons with observations.

4 Conclusions

We have compared four classes of public state-of-the-art SN Ia explosion models to nebular observations of SN 2021aefx covering the full 0.35–14 μm range. Our main result is that no single model emerges as an obvious candidate for SN 2021aefx based on these data alone. All models predict the same set of spectroscopic features, all of which have an observed counterpart. Conversely, all models lack specific characteristics of the observed

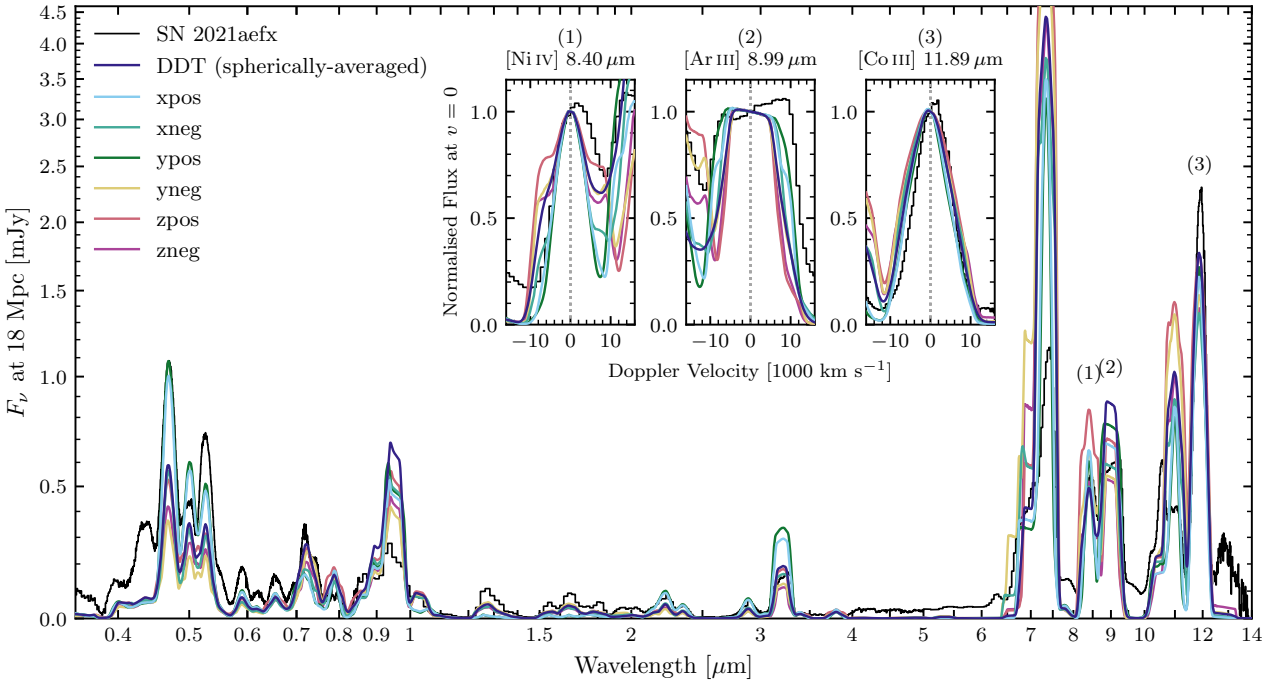

Fig. 3. Similar to Fig. 2 but for the DDT model along the three orthogonal axes of the original 3D Cartesian grid, in both positive ({x,y,z}pos) and negative ({x,y,z}neg) directions. We also show the original (spherically-averaged) DDT model.

spectrum, such as the overall mismatch in lines of singly-ionised IGEs throughout the optical and infrared. The largest variations in our model spectra result from differences in ionisation. A larger density, such as in the inner ejecta of the MERGER model, results in a lower ejecta temperature and ionisation state, further enhanced by the increased recombination rate.

In Blondin et al. (2023) we also discuss the use of lines of Ni I–IV in constraining the stable nickel mass, which could serve as a tracer of the mass of the exploding WD. Our investigation led to the computation of new collisional strengths for Ni III, available at the CDS.

Inferring reliable constraints on the progenitor mass and explosion mechanism of SNe Ia remains a formidable challenge, even with the extended wavelength coverage and exquisite data quality offered by *JWST*. Combined with early-time and optical observations, nebular infrared spectra of SNe Ia provide an additional validation criterion when comparing a diverse set of SN Ia models to observations.

This work was supported by the 'Programme National de Physique Stellaire' (PNPS) of CNRS/INSU co-funded by CEA and CNES. This research has made use of computing facilities operated by CeSAM data centre at LAM, Marseille, France.

References

Blondin, S., Bravo, E., Timmes, F. X., Dessart, L., & Hillier, D. J. 2022, A&A, 660, A96
Blondin, S., Dessart, L., Hillier, D. J., Ramsbottom, C. A., & Storey, P. J. 2023, arXiv e-prints, arXiv:2306.07116
Flörs, A., Spyromilio, J., Taubenberger, S., et al. 2020, MNRAS, 491, 2902
Gronow, S., Collins, C. E., Sim, S. A., & Röpke, F. K. 2021, A&A, 649, A155
Kromer, M., Ohlmann, S., & Röpke, F. K. 2017, Mem. Soc. Astron. Italiana, 88, 312
Kwok, L. A., Jha, S. W., Temim, T., et al. 2023a, ApJ, 944, L3
Kwok, L. A., Siebert, M. R., Johansson, J., et al. 2023b, arXiv e-prints, arXiv:2308.12450
Lach, F., Callan, F. P., Sim, S. A., & Röpke, F. K. 2022, A&A, 659, A27
Maoz, D., Mannucci, F., & Nelemans, G. 2014, ARA&A, 52, 107
Pakmor, R., Kromer, M., Taubenberger, S., et al. 2012, ApJ, 747, L10
Seitenzahl, I. R., Ciaraldi-Schoolmann, F., Röpke, F. K., et al. 2013, MNRAS, 429, 1156

SF2A 2023
M. N'Diaye, A. Siebert, N. Lagarde, O. Venot, K. Baillié, M. Béthermin, E. Lagadec, J. Malzac, J. Richard (eds)

HOW MUCH DO MAGNETIC FIELDS IMPACT STELLAR CHARACTERIZATION?

P. I. Cristofari[1] and J.-F. Donati[2]

Abstract. With our new tool, `ZeeTurbo`, used to model spectra of magnetic stars, we devised a process to simultaneously constrain the atmospheric parameters and average magnetic fields ($< B >$) of M dwarfs. Our process was applied to 6 targets observed with the near-infrared spectropolarimeter SPIRou, installed at the Canada-France-Hawaii Telescope, in the context of the SPIRou Legacy Survey. We derived atmospheric parameters and $< B >$ in agreement with previous studies and reported rotation periods. We further assessed the influence of magnetic fields on the characterization of M dwarfs, and show that neglecting them can lead to significant offsets in the estimated effective temperature, surface gravity and metallicity of the stars.

Keywords: spectroscopy, low-mass stars, magnetic fields, infrared

1 Introduction

The study of magnetic fields hosted by M dwarfs is essential to better constrain the properties of planets orbiting them, and to better understand their formation and evolution. In the recent years, several studies relied on high-resolution near-infrared (nIR) spectroscopy to estimate the atmospheric properties (such as the effective temperature $T_{\rm eff}$, log surface gravity $\log g$ and metallicity [M/H]) of M dwarfs (e.g., Passegger et al. 2019; Marfil et al. 2021; Cristofari et al. 2022a,b). At the same time, several studies relied to high-resolution spectroscopy to measure the Zeeman broadening of the line profiles (see, e.g., Kochukhov 2021), allowing one to probe magnetic fields on smaller scales than with Zeeman-Doppler-Imaging techniques (Donati & Brown 1997; Donati et al. 2006).

Studies aimed at characterizing the magnetic properties of stars typically assume a set of atmospheric parameters. Conversely, studies attempting to constrain atmospheric parameters tend to avoid active targets, to neglect the effect of magnetic fields, or to focus on lines with near to zero Landé factors. With the improvement of spectroscopic observations and models, it now becomes possible to assess the impact of magnetic fields on the estimation of stellar properties, by relying on spectral lines with different Landé factors in order to constrain both magnetic fields and atmospheric parameters at once.

We rely on our new tool, `ZeeTurbo` (Cristofari et al. 2023), built from the `Turbospectrum` (Plez 2012) and `Zeeman` (Landstreet 1988) codes, to compute high-resolution nIR spectra of M dwarfs from MARCS model atmospheres (Gustafsson et al. 2008). We fit our models to spectra recorded with SPIRou (Donati et al. 2020) in the context of the SPIRou Legacy Survey (SLS) to estimate both the average magnetic field ($< B >$) and atmospheric parameters of 6 magnetic M dwarfs: AU Mic, Gl 388, Gl 410, EV Lac, Gl 406 and PM J18482+0741 (PM J18 in the rest of this manuscript).

2 Characterizing magnetic M dwarfs

Our magnetic fields estimates place our targets in the unsaturated dynamo regime of the Rossby (Ro) – $< B >$ diagram (see Fig. 1, Left). Furthermore, we found that our estimates are consistent with those of previous studies (Reiners et al. 2022), with differences that can be attributed to the choice of selected lines, models, assumed atmospheric parameters or even with the evolution of magnetic fields with time.

[1] Center for Astrophysics — Harvard & Smithsonian, 60 Garden street, Cambridge, MA 02138, United States
[2] Université de Toulouse, CNRS, IRAP, 14 avenue Belin, 31400 Toulouse, France

© Société Française d'Astronomie et d'Astrophysique (SF2A) 2023

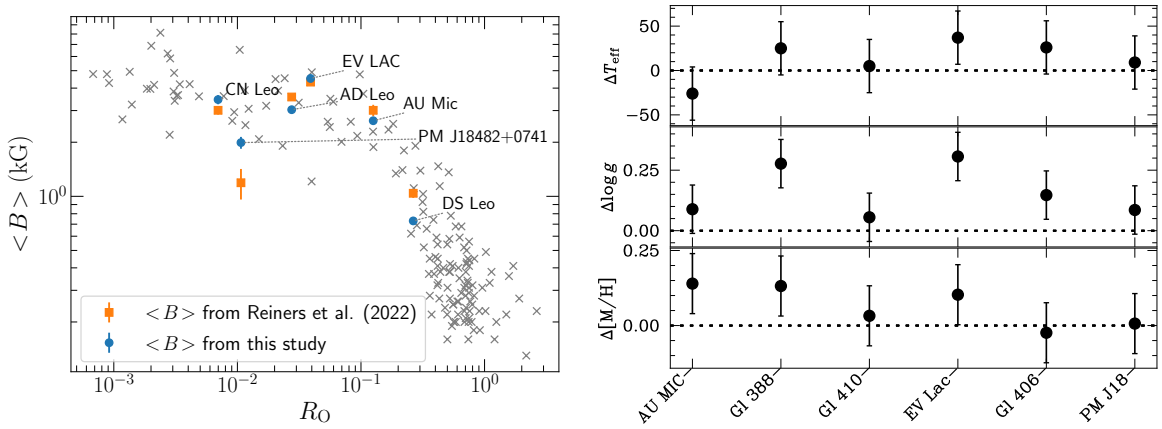

Fig. 1. Left: Rossby–< B > diagram for 6 magnetic M dwarfs observed with SPIRou. The gray crosses mark the position of stars studied in (Reiners et al. 2022). **Right:** Residuals between values derived with magnetic and non-magnetic models.

We compared the derived atmospheric parameters recovered with magnetic models to those obtained with non-mangnetic models in Fig. 1 (Right). Our analysis relied on about 30 atomic lines with Landé factors ranging 0 to 2, and about 40 magnetically insensitive molecular lines mainly from one CO band. We obtained significant differences in the results, with an overall tendency to find larger estimates of $T_{\rm eff}$, $\log g$ and [M/H] with non-magnetic models, with the exception of AU Mic whose temperature is found smaller with non-magnetic models. The difference between the two sets of parameters reach values comparable to our error bars on $T_{\rm eff}$ and [M/H] (~ 30 K and ~ 0.10 dex, respectively), and up to two times our error bars on $\log g$, estimated to ~ 0.05 dex. The significant impact on $\log g$, in particular, can result from the broadening of the spectral lines caused both by this parameters and magnetic fields. We note that $\log g$ is among the most difficult parameters to accurately constrain, even for weakly-active M dwarfs (Cristofari et al. 2022b). The inclusion of magnetic fields in the modeling of moderately active stars is, therefore, likely to influence the atmospheric parameters estimates, and can be used to provide better constraints on the stellar properties overall.

Our method can be applied to a larger sample of M dwarfs with slower rotations (see Donati et al. 2023b) in order to detect and quantify the strength of their small-scale magnetic fields (Cristofari et al., submitted). By analyzing spectra on a nightly basis, we will also study the temporal evolution of the detected fields, and search for rotational modulation in the obtained time series, such as what was done in Donati et al. (2023a).

We acknowledge funding from the European Research Council under the H2020 & innovation program (grant #740651, NewWorlds)

References

Cristofari, P. I., Donati, J. F., Masseron, T., et al. 2022a, MNRAS, 511, 1893

Cristofari, P. I., Donati, J.-F., Folsom, C. P., et al. 2023, MNRAS, 522, 1342

Cristofari, P. I., Donati, J. F., Masseron, T., et al. 2022b, MNRAS, 516, 3802

Donati, J. F. & Brown, S. F. 1997, A&A, 326, 1135

Donati, J. F., Catala, C., Landstreet, J. D., & Petit, P. 2006, in Astronomical Society of the Pacific Conference Series, Vol. 358, Solar Polarization 4, ed. R. Casini & B. W. Lites, 362

Donati, J. F., Cristofari, P. I., Finociety, B., et al. 2023a, MNRAS, 525, 455

Donati, J. F., Kouach, D., Moutou, C., et al. 2020, MNRAS, 498, 5684

Donati, J. F., Lehmann, L. T., Cristofari, P. I., et al. 2023b, MNRAS, 525, 2015

Gustafsson, B., Edvardsson, B., Eriksson, K., et al. 2008, A&A, 486, 951

Kochukhov, O. 2021, A&A Rev., 29, 1

Landstreet, J. D. 1988, ApJ, 326, 967

Marfil, E., Tabernero, H. M., Montes, D., et al. 2021, A&A, 656, A162

Passegger, V. M., Schweitzer, A., Shulyak, D., et al. 2019, A&A, 627, A161

Plez, B. 2012, Turbospectrum: Code for spectral synthesis, Astrophysics Source Code Library, record ascl:1205.004
Reiners, A., Shulyak, D., Käpylä, P. J., et al. 2022, A&A, 662, A41

SF2A 2023
M. N'Diaye, A. Siebert, N. Lagarde, O. Venot, K. Baillié, M. Béthermin, E. Lagadec, J. Malzac, J. Richard (eds)

A LANDSCAPE OF MAIN SEQUENCE COOL STARS ACTIVITY THOUGHT PHOTOMETRIC OBSERVATIONS

L. Degott[1,2], F. Baudin[1], R. Samadi[2], C. Damiani[3], B. Perri[4] and C. Pinçon[1]

Abstract. The magnetic activity of stars presents a large diversity that is still poorly understood. With the recent discovery of a massive number of exoplanets has emerged the need to better characterize their interactions with their host stars. Therefore, we need to better understand their internal and external magnetism. Using Kepler, we computed the Fourier spectra of the data and used an analytical description of spot transits in light-curves to look at global trends. We thus recovered two proxies to identify activity regimes: a proxy which estimates the lifetime of the spots and a second which estimates the activity, in terms of surface coverage and light contrast of the spots on the stellar disk.Using these proxies, we propose a distribution of low-mass stars into four different activity regimes.

Keywords: Stars: activity, low-mass stars, magnetic field

1 Introduction

Stellar activity is a direct consequence of the internal and external magnetism of stars and is characterized by the appearance of magnetic structure like dark spots on the surface of stars, and their destabilization which can lead to flares and therefore massive release of energy. There are several methods used to study this activity: one can look at the coronal X-rays emission (Wright et al. 2011; Reinhold et al. 2019) or to the CaII K or Hα lines (West et al. 2008) which are related to variations respectively in the corona or the chromosphere. Photometric variability can also provide information on stellar activity (Mathur et al. 2014; García et al. 2010) since the transit of spots on the surface of the star induces a temporary drop in its luminosity.Thanks to space missions, increasingly precise photometric data such as Kepler can provide information on the properties of these spots, which are a direct expression of magnetic activity. The study of photometric variability in the temporal domain to determine properties of spots has unfortunately highlighted the degeneracy of this problem (position of the spots on the disk, their sizes, their temperatures, inclination of the star, possible rotation differential...).

However, the Fourier domain makes it possible to extract global trends about spots. Harvey (1985) has shown that the impact of activity in photometric data could be seen in low frequencies and could be approximated by a pseudo-Lorentzian. Later, Aigrain et al. (2004) suggested that the parameters of this function can be related to spots properties like their characteristic lifetime.

The aim of this work is to build on this concept and go beyond with a new analytical approach and apply it on the large sample of stars provided by McQuillan et al. (2014).

2 Method

This section gives a analytical description of the signature and mean properties of spots as seen in the Fourier spectrum of the light curves analyzed. This description is based on Harvey (1985), Harvey et al. (1993) and Aigrain et al. (2004).

[1] Université Paris-Saclay, CNRS, Institut d'Astrophysique Spatiale, 91405 Orsay, France
[2] LESIA, CNRS, Université Pierre et Marie Curie, Université Denis Diderot, Observatoire de Paris, 92195 Meudon Cedex, France
[3] Max-Planck-Institut fur Sonnensystemforschung, Justus-von-Liebig-Weg 3, 37077 Gottingen, Germany e-mail: damiani@mps.mpg.de
[4] Université Paris-Saclay, Université Paris Cité, CEA, CNRS, AIM, 91191, Gif-sur-Yvette, France

© Société Française d'Astronomie et d'Astrophysique (SF2A) 2023

2.1 Model

We consider a single spot transiting on a star with a rotation period P_{rot}, which is characterized by an area S_{spot} and a temperature T_{spot}. This spot is assumed to always rotate at the same rotation period and to remain at the same latitude. Its transits on the stellar disk can be described using three normalized components:

- ш_{Prot}: a Dirac comb with a spacing of one rotation period which represents the periodicity of the transit,
- $T_{transit}(t)$: the mean shape of the transit, it is associated to the characteristic time τ_{tr}, proportional to $P_{rot}/2$. The shape of the transit can vary depending on the inclination of the star relative to the line of sight and its position on the disk, but we consider here an average transit shape,
- $E_{life}(t)$: the intrinsic evolution with time of the spot, with a characteristic time τ_{life} which represents the spot lifetime. This function reflects the possible variations of the size and temperature of the spot during its lifetime.

By combining these three components, the impact of the spot in the light curve (Eq. 2.1) can be reproduced: coevolving ш_{Prot} and $T_{transit}(t)$ replicates the repetition of the spot transit. Then, multiplying by $E_{life}(t)$ represents the intrinsic evolution of the spot during its lifetime:

$$S_0(t) = [\text{ш}_{Prot} * T_{transit}(t)] \times E_{life}(t) \tag{2.1}$$

The transit photometric depth is given by $A(T_{spot}, S_{spot})$ which depends on the temperature contrast and the area of the spot. Therefore: $S(t) = A(T_{spot}, S_{spot}) \cdot S_0(t)$.

Two types of spots can be distinguished: if $\tau_{life} > P_{rot}$, the spot shows multiple transits, it is then categorized as *long spots*; if $\tau_{life} < P_{rot}$, the spot shows only one transit, it is then the **short spot** case.

When shifting to the Fourier domain, we obtain:

$$\widehat{S_0}(\nu) = [\frac{\text{ш}_{1/P_{rot}}}{P_{rot}} \times \widehat{T_{transit}}] * \widehat{E_{life}}(\nu); \tag{2.2}$$

The convolution between the Fourier comb $\text{ш}_{1/P_{rot}}$ and the Fourier transform of E_{life} yields the rotation peaks that are seen in the light curve spectrum. These peaks are multiplied by the Fourier transform of the transit component, $T_{transit}$, giving the final shape of the spectrum. The information about the spot lifetime, τ_{life}, appears thus in the rotation peaks whereas the width of the spectrum part just above the zero frequency, described by a pseudo-lorentzian in Harvey et al. (1993), provides information on the transit time, τ_{tr}. In the case of short spots ($\tau_{life} < \tau_{tr}$), the peaks are wider than the rest of the profile and overlap each other. As a result, the rotation peaks disappear and the spectrum corresponds to the description of Harvey (1985) and (1993) for the solar case.

In summary, three proxies linked directly with the spots physical properties can be extracted from the spectra of a light curve:

1. The *transit proxy*, τ_{tr}: the inverse of the width of the very low frequency part of the spectrum. It is the characteristic time of the transit and is thus proportional to $P_{rot}/2$,
2. The *lifetime proxy*, τ_{life}: the inverse of the width of the rotation peaks. It gives an information about the mean lifetime of the spots transiting on the stellar disk,
3. The *coverage proxy*, A: the amplitude of the spectrum. This proxy gives an information about the spot coverage of the stellar disk but is linked to two spot properties: their surface and their temperature. This gives degenerate information about whether the spots are cold or hot, small or large, and provides only an estimate of the global activity of the star over the duration of the observation.

3 Application to Kepler data

The data used here are the sample of 34 040 stars from McQuillan et al. (2014). This sample is composed of main sequence stars observed by the Kepler mission, with an effective temperature below 6500 K. There are no binary stars or stars with exoplanets visible in the light curves in this sample. McQuillan et al. (2014) also give an estimate of the rotation period and the mass of these stars. After removing the data where the fit has not converged, the sampling used here is made of 33 200 stars.

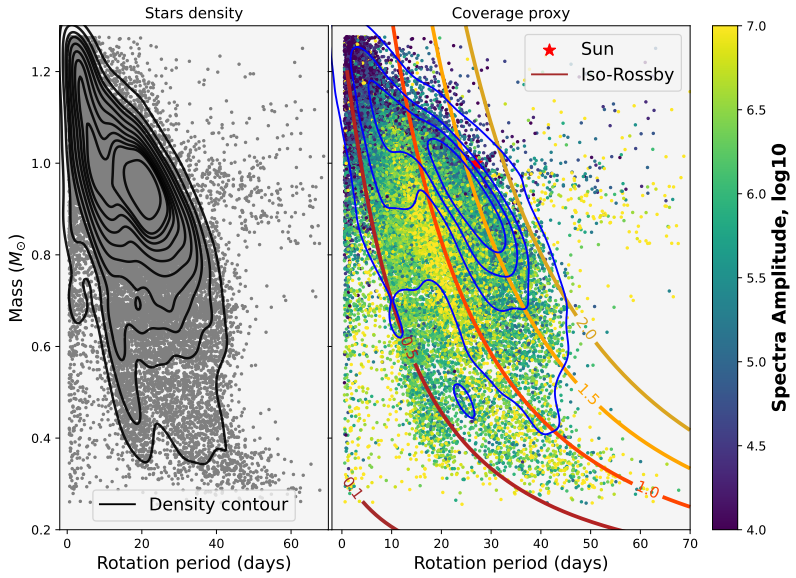

Fig. 1. The left figure show the density of stars in the diagram. Right : All of the star sample as a function of mass and rotation period. The color scale shows the surface proxy: yellow is for a large spot coverage (active stars), blue for low spot coverage (less active stars). The colored lines show iso-Rossby values. The red star symbol indicates the position of the Sun in this diagram. Blue lines represent the density of point from the short spots stars sample (ie. $\tau_{life} < P_{rot}$) from the fig. 2.

3.1 Coverage proxy

The results of the estimate of the coverage proxy are shown in Figure 1. The colored lines in hot colored with values from 0.1 to 2 are iso-Rossby lines, computed from the turn-over time estimated with the mass dependent relation from Wright et al. (2011) (Ro = P_{rot} / $\tau_{turnovertime}$). We can see a first regime of intense activity around Ro = 1: we can see a banana-shaped cloud for which the proxy is the highest. A second regime is emerging for high mass stars (top of the diagram): here the proxy coverage is relatively weak (dark purple area). This corresponds to fairly low activity, which is in line with current theory: the most massive stars have a weaker convective zone and therefore less magnetic activity (Berdyugina 2005). Finally, on either side of the Ro = 1 regime, stars show a similar activity (green areas).

3.2 Lifetime proxy

Figure 2 shows the results for the lifetime proxy. The density lines in black highlight two points of accumulation in this diagram: the short spots stars, below a lifetime of $\tau_{life} < 10$ days (in dark blue), and the long spots stars (in yellow). The sample of long spots stars represent 77 % of the initial sample. Most of these stars have higher coverage proxy than the short spot stars, and are thus more active. However, a small group of stars with a short spot lifetime shows a higher coverage proxy than the rest of the sample (bottom of the diagram).

4 Discussion and conclusion

Figure 1 highlight two regimes: one made of very active stars at Ro = 1 and another made of low active stars. By superposing the samples of short-lived stars in Figure 1 (blue contour lines) we can observe that they correspond to the massive stars from the low activity regime and the stars above the high activity regime. When we compile all of these results together, we can therefore identify four activity regimes:

- A high activity regime at Ro = 1 with long spots, corresponding to the elongated shape in Figure 1,
- A low activity regime with short spots, for the more massive stars,

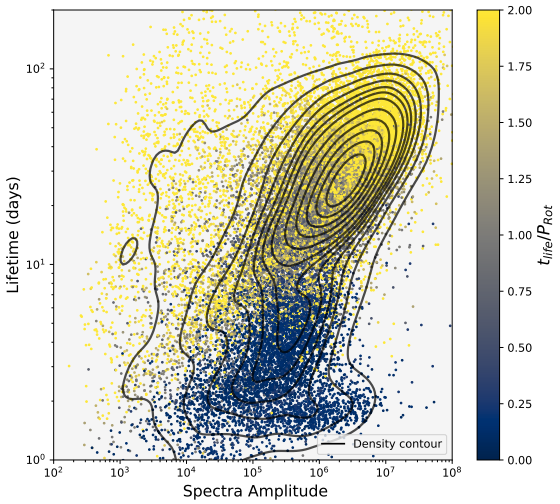

Fig. 2. The star sample shown as a function of the lifetime proxy and the coverage proxy. The color scale shows the ratio between the rotation periods estimated by McQuillan et al. (2014) and the lifetime proxy. Blue is for short spots ($\tau_{life} < P_{rot}$) and the yellow for long spots. The black lines represent the density of stars in this figure.

- A regime of intermediate activity with long spots, corresponding to the iso-Rossby Ro = 0.5 ,
- A second intermediate regime activity with short spots above the one of high intensity.

However, there remains a number of biases that can influence these results such as differential rotation and the appearance of faculae or plages . These biases will be discussed in more detail in a futur publication. This work can alredy be put into perspective with the results found by Reinhold et al. (2019) who suggest the existence of spotdominated stars and faculaedominated stars. The two regimes of stars with long spots may correspond to regions with spot-dominated stars and the two other regimes to stars dominated by faculae, like the Sun, which reinforces the idea of several types of activity linked to different types of magnetism at the surface of the star.

Looking at the global characteristics of the spots using the Fourier domain thus makes it possible to highlight different types of stellar activity, which will eventually provide information on the magnetism of stars such as stellar dynamo. More results and interpretations are coming !

This paper includes data collected by the Kepler mission and obtained from the MAST data archive at the Space Telescope Science Institute (STScI). Funding for the Kepler mission is provided by the NASA Science Mission Directorate. STScI is operated by the Association of Universities for Research in Astronomy, Inc., under NASA contract NAS 5-26555.

References

Aigrain, S., Favata, F., & Gilmore, G. 2004, A&A, 414, 1139

Berdyugina, S. V. 2005, Living Reviews in Solar Physics, 2, 8

García, R. A., Mathur, S., Salabert, D., et al. 2010, Science, 329, 1032

Harvey, J. 1985, in ESA Special Publication, Vol. 235, Future Missions in Solar, Heliospheric & Space Plasma Physics, ed. E. Rolfe & B. Battrick, 199

Harvey, J. W., Duvall, T. L., J., Jefferies, S. M., & Pomerantz, M. A. 1993, in Astronomical Society of the Pacific Conference Series, Vol. 42, GONG 1992. Seismic Investigation of the Sun and Stars, ed. T. M. Brown, 111

Mathur, S., Salabert, D., García, R. A., & Ceillier, T. 2014, Journal of Space Weather and Space Climate, 4, A15

McQuillan, A., Mazeh, T., & Aigrain, S. 2014, ApJS, 211, 24

Reinhold, T., Bell, K. J., Kuszlewicz, J., Hekker, S., & Shapiro, A. I. 2019, A&A, 621, A21

West, A. A., Hawley, S. L., Bochanski, J. J., et al. 2008, AJ, 135, 785

Wright, N. J., Drake, J. J., Mamajek, E. E., & Henry, G. W. 2011, ApJ, 743, 48

SF2A 2023
M. N'Diaye, A. Siebert, N. Lagarde, O. Venot, K. Baillié, M. Béthermin, E. Lagadec, J. Malzac, J. Richard (eds)

THE SCIENTIFIC PROJECTS OF THE INTERFEROMETRIC SURVEY FOR STELLAR PARAMETERS WITH CHARA/SPICA

R. Ligi[1], D. Mourard[1], P. Bério[1], O. Creevey[1], S. Deheuvels[2], A. Domiciano de Souza[1], N. Ebrahimkutty[1], R. Ibañez-Bustos[1], J. Jonak[1], N. Nardetto[1], D. Salabert[1], M. Vrard[1] and M. Wittkowski[3]

Abstract. To date, around 200 stars have a measured angular diameter with a precision at the 1% level. These measurements have been made with different instruments, using different techniques, and different spectral bands, which provide scattered and sometimes inconsistent results. The angular diameter is a key quantity to measure because it allows the determination of many other physical properties, like the stellar radius (if combined with the distance to the star), the effective temperature (when combined with the bolometric flux), or the radius of a planet if it transits its star.

The Interferometric Survey for Stellar Parameters (ISSP) is dedicated to the measurement of a thousand stars with a homogeneous data and analysis approach, and this will provide the largest catalogue of stellar diameters with a 1% precision. The main objectives of this survey are 1) the determination of exoplanet host star's radii, thus of exoplanetary parameters, 2) the determination of parameters of asteroseismic targets, to refine scaling laws and determine accurate ages, and 3) the calibration of surface brightness-color relations (SBCR). Five additional programs of this survey focus on limb-darkening, rotation, binarity, stellar winds and environments, with an additional objective to study these phenomena and control the systematics in the three main programs.

The survey exploits the new CHARA/SPICA instrument that combines light from the six telescopes of the array in the optical band. Here, we present the scientific objectives of the survey, the status of the instrument after first commissioning and the initial results of the observing campaign.

Keywords: Visible interferometry, stellar parameters

1 Introduction

Interferometry is a high angular resolution technique which measures the complex visibility of an object, a quantity composed of the modulus (often taken to the square), which yields the angular diameter of a star, and the closure phase, that gives information on the asymetries of an object. Today, 1478 stellar angular diameters have been measured with various interferometers (from the JMDC, the JMMC Measured Stellar Diameters Catalog, Duvert 2016), but the precision reached (1% for only 11% of the measurements) is not enough to obtain precise stellar parameters at the large scale (Mourard et al. 2022). These measurements have been performed with different methods, analysis, instruments, and the full star sample does not constitute a homogeneous set of angular diameters.

The development of the Stellar Parameters and Images with a Cophased Array (SPICA, Mourard et al. 2018) instrument on the Centre for High Angular Resolution Array (CHARA, ten Brummelaar et al. 2005) will be a turning point in optical interferometry for stellar physics. This new instrument takes advantage of the adaptive optics recently installed on CHARA, and is based on spatial filtering with single mode fibers. It potentially allows to measure the angular diameter of thousands of stars with 1% precision, but also to do image reconstruction of stars.

[1] Observatoire de la Côte d'Azur, CNRS, Laboratoire Lagrange, Bd de l'Observatoire, CS 34229, 06304 Nice Cédex 4, France
[2] IRAP, Université de Toulouse, CNRS, CNES, UPS, 14 avenue Edouard Belin, 31400 Toulouse, France
[3] ESO, Karl-Schwarzschild-Str. 2, 85748 Garching bei München, Germany

© Société Française d'Astronomie et d'Astrophysique (SF2A) 2023

2 The Interferometric Survey for Stellar Parameters (ISSP)

The ISSP – an ERC-funded project – aims at measuring the angular diameter of 800 stars and obtain the images of 200 stars (Fig.1, right). With the angular resolution allowed by CHARA, and the use of the SPICA instrument, the goal is to reach 1% precision on the diameters for stars with an angular diameter $\theta > 0.2$ mas and magV< 9. These data will be used to cover three important problematics in stellar physics : the characterisation of exoplanets host stars (Sec. 3.1), the calibration of asteroseismic scaling relation (Sec. 3.2) and the calibration of surface brightness-color relations (SBCR, Sec. 3.3). These objectives will be reached by the detailed control of the systematics (caused by stellar rotation, stellar wind, limb-darkening, binarity, see Sec. 3.4), that perturbs the interferometric measurements. On the other hand, better understanding these phenomena will bring valuable and unprecedented insight to stellar physics.

The survey can be achieved with a large amount of observing time : 4000 individual observations (which includes the observation of one target star surrounded by the observation of calibration stars) over 200 nights covering 3 years are required. This implies preparing an optimal observing strategy by observing stars that are close in hour angle and declination during each allocated night.

3 Objectives of the survey

3.1 Exoplanet host stars characterisation

Exoplanetary properties and stellar properties are closely linked. The radial velocity (RV) and the transit detection methods yields the ratio of the planetary to the stellar mass $M_{\rm p}\sin(i)/M_\star$, with i the inclination of the system, and the planetary to the stellar radius $R_{\rm p}/R_\star$, respectively. For the transit method in particular, interferometry can play a major role because measuring the angular diameter, combined with the parallax usually given by the *Gaia* satellite, provides $R_\star$.

The focus on transiting exoplanet host stars (EHS) has another important advantage: from the transit light curve, one can derive the density of the star (Seager & Mallén-Ornelas 2003). With a direct measurement of the radius, we can then estimate the stellar mass, which is a parameter usually obtained through modelling. As many transiting exoplanetary systems are often followed in RV, we can also derive the exoplanets densities $\rho_{\rm p}$. These three parameters are mandatory to infer the internal structure of exoplanets, and to learn about their habitability. This kind of analysis has already been applied to two systems (Crida et al. 2018b,a; Ligi et al. 2019), where the mass was derived, allowing to confront the models with the data, and to constrain in detail the internal structure of the exoplanets (Fig.1, left).

Up to now, only a handful of transiting EHS could be measured with interferometry, mainly because of the limiting magnitude of interferometers. The vast majority of *Kepler* targets are faint, and their angular diameter is smaller than what CHARA allows. With SPICA, we expect to push the limiting magnitude, and to reach at the end of the survey magV<9. Moreover, the current and future missions dedicated to exoplanetary search, like PLATO and TESS, are aiming at bright stars in order to characterize them and will constitute a large amount of SPICA potential targets. We already identified 42 transiting exoplanets host stars accessible by SPICA, and more than 200 hundreds exoplanets hosts (without transits), and expect many more when PLATO is on sky. We will also benefit from the progresses made on SBCR that will provide angular diameters of stars for which a direct measurement is not possible, and thus characterize even the stars that are very faint and angularly small.

3.2 Asteroseismic stars

Scaling relations in asteroseismology link oscillation frequencies and global oscillation parameters ($\Delta\nu$, $\nu_{\rm max}$) to stellar parameters ($T_{\rm eff}$, R$_\star$, M$_\star$, $\rho_\star$, age). This domain has grown, in particular since the *Kepler* and CoRoT missions, and have led to the studies of several thousands of stars. Yet, these relations need to be calibrated by direct radius estimations. The advantages of combining interferometry and asteroseismology has been known for a long time (Creevey et al. 2007; Cunha et al. 2007; Huber et al. 2012, e.g.). The angular size provided by interferometry can be used with the bolometric flux to derive the effective temperature of stars. These parameters, obtained independently of models, are inputs to scaling laws, and help derive the mass and evolutionary stage with little model dependence.

The accuracy of the stellar diameter is important in this context, as reaching 1% on the radius is necessary to bring enough constraints on atmospheric and internal structure models of stars. With SPICA, we have the chance to measure the angular diameter of a selection of 400 seismic targets, spanning FGK dwarfs subgiants

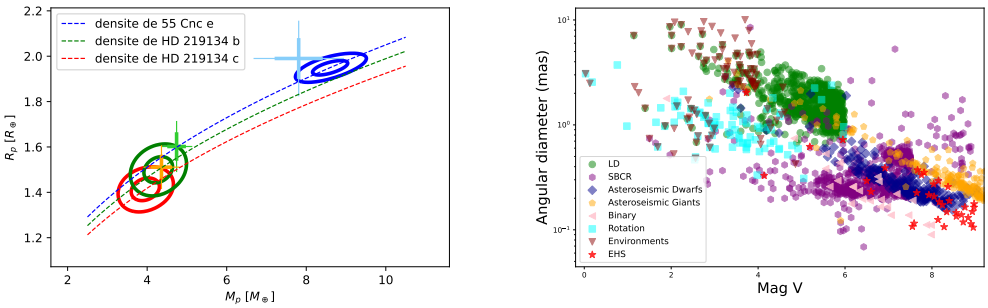

Fig. 1. Left: Contours at 1 and 2 σ of the joint likelihood M_p -R_p (Crida et al. 2018b,a; Ligi et al. 2019). The ellipses are flattened along the iso-densities (dashed lines), showing the correlations M_p -R_p. The crosses indicate previous values in the literature. **Right:** Angular diameter (in mas) according to the magnitude in the V band of the stars of the ISSP survey. The different colors and symbols show the stars of the different programs.

and giants. The primary objectives are 1) the calibration of the radius-seismic scaling relations covering a range of masses and metallicities, and to obtain independently derived masses by exploiting $\Delta\nu$, 2) detailed seismic analysis for providing high precision stellar parameters, and 3) testing different physical ingredients in stellar models. This analysis will also be applied to PLATO targets.

3.3 Calibration of surface brightness-color relations (SBCR)

SBCRs are key tools for easily estimating the angular diameter of a star from photometric measurements. The SBCRs are used, for instance, to derive the distances of eclipsing binaries in the Magellanic clouds (Pietrzyński et al. 2013, 2019; Graczyk et al. 2020). The distance estimate of LMC was used by the SHOES team to constrain the Hubble-Lemaître constant, H_0, and tackle the difficult issue of the Hubble tension (Riess et al. 2019). The SBCRs are also of high interest for the study of transiting EHS (see Sec. 3.1). Our initial SBCRs, extracted from VEGA programs, are currently implemented in the pipeline of the PLAnetary Transits and Oscillation of stars (PLATO) space mission (Gent et al. 2022). Additionally, the physics of SBCRs is under deeper analysis. By applying a homogeneous approach on a large sample of data, recent studies have shown that the SBCRs depend not only on the temperature of stars, but also on their luminosity class (Salsi et al. 2020, 2021), a result corroborated using atmospheric models (Salsi et al. 2022). The SBCRs are also used to derive the distance to Cepheids (Nardetto et al. 2023), to estimate the angular diameter of interferometric calibrators, and for microlensing surveys.

The ISSP has 4 focussed objectives : 1) calibrate the SBCR to 2% or better for stars later than F5 (IV/V), to be applied in the context of the PLATO space mission, 2) calibrate the SBCR for KIII stars at the 1% level in order to verify and potentially improve the distance to LMC, 3) open a new road to H_0 by calibrating an SBCR at the 1-2% level for early-type stars (B1-3 IV/V). Such a relation will be used in the context of the Araucaria Project to derive the distance of eclipsing binaries in M31 and M33, 4) calibrate the SBCR all over the HR diagram in the most homogeneous way as possible with a precision of 1 to 2% in order to study the impact of spectral type, class and weak stellar activity (rotation, binarity, wind and environment). To reach these objectives our goal is to observe 2 stars per sub-spectral channels [B0-M3] and per class (V, IV, >III) which corresponds to a total of 324 stars.

3.4 Studying stellar physics all over the HR diagram : toward a control of systematics

Limb-darkening (LD), binarity, rotation, winds and environment are crucial phenomena to understand various specific physical processes, leading to an improved determination of stellar parameters, directly or through a better definition of stellar models.

If their effect on the interferometric signal is weak, they can potentially perturb the visibility curve at high spatial frequencies, and then bias the derived angular diameters or the estimate of the LD. Indeed, the LD can only be measured if the star is resolved beyond the first visiblity minimum. For this reason, it has only been done a handful of times, e.g. for α Cen A and B Kervella et al. (2017). Yet, it can cause a variation of a few % in the angular diameter. LD is taken into account through correction grids computed from atmospheric models, which

lack direct measurements for accurate calibration. Moreover, the LD is also important in exoplanet transit light curve exploitation, where it has to be accounted for (Maxted 2023). In addition, the knowledge of binarity constitutes a rare opportunity to directly measure the stellar mass, which is crucial to constrain evolution models. Moreover, rotation can generate surface flattening and gravity darkening that should be considered in detail when calibrating the SBCR (in particular for early-type stars) and when deriving the stellar diameter (50 km/s of $v \sin(i)$ corresponds to a flattening of about 1%). Rotation also has an important impact on the physical structure and evolution of stars and thus, is a key ingredient of stellar evolution models. Finally, studying wind and environments give information on mass loss, which has an impact of stellar evolution.

A direct measurement of all these phenomena through interferometry brings valuable constraints for stellar models, and the comprehension of systematics in the interferometric signal. For this reason, the ISSP survey forsees: 1) direct measurements of the LD of $\sim$ 160 targets for giants and dwarfs, 2) the observation of 50 detached eclipsing and spectroscopic binaries, with angular separations ranging from 0.15 to 10 mas, and covering the HR diagram, 3) the measurement of the rotation for hundreds of stars, 4) high spectral resolution observations of the CaII triplet to probe the presence and extension of the chromosphere of cool giants and supergiants, and low spectral resolution observations to constrain the visibility function and the fundamental stellar parameters.

4 First fringes and conclusion

The ISSP project officially started in September 2021 and will end in August 2026. It began with engineering nights with the SPICA instrument, and the scientific commissioning began in 2022. Even though the first commissioning months have been paved with bad luck (in particular, 2 meters of snow at CHARA!), the instrument is now working routinely. We obtained the first 15 fringes during the observing run of June 2023. In Fig. 2, we show the 2D Fourier Transform of the 15 dispersed fringes obtained by recombining the light from 6 telescopes. This is the first time that this many fringes have been obtained in the visible domain. The August observation run demonstrated that the instrument is now ready to work routinely. However, some improvements are still necessary, in particular in the injection process, in order to reach the magnitude limit of the survey, and in the routine operation of the fringe tracker SPICA-FT (Pannetier et al. 2022).

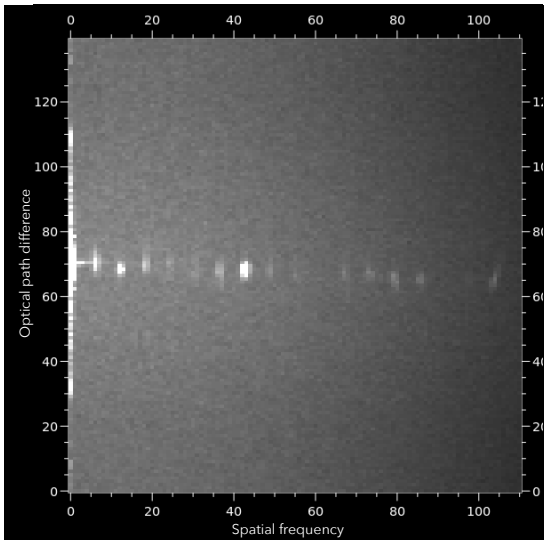

Fig. 2. 2D Fourier Transform of the dispersed fringes obtained during 20-second integrations, for the 15 baselines available at CHARA.

The ISSP covers wide aspects of stellar physics. It will provide very accurate and precise interferometric measurements of 1000 stars obtained with homogeneous data reduction, that will serve exoplanetary science, the determination of new SBCR, astroseismology, while tackling the problems linked to stellar activity. These topics are closely related to the current and future spatial missions dedicated to exoplanets search and characterisation (PLATO, TESS, CHEOPS...), to the Auraucaria project, and will certainly reach many domains of Astrophysics.

The development of SPICA (SPICA-VIS and SPICA-FT) has been made possible thanks to the funding support of CNRS, Université Côte d'Azur, Observatoire de la Côte d'Azur, University of Aarhus, Région Sud, and the CHARA Array. This program has made use of the Jean-Marie Mariotti Center services. This research has made use of the VizieR catalogue access tool, CDS, Strasbourg, France. This project has received funding from the European Research Council (ERC) under the European Union's Horizon 2020 research and innovation programme (Grant agreement No. 101019653). This work is based upon observations obtained with the Georgia State University Center for High Angular Resolution Astronomy Array at Mount Wilson Observatory. The CHARA Array is supported by the National Science Foundation under Grant No. AST-1636624 and AST-2034336. Institutional support has been provided from the GSU College of Arts and Sciences and the GSU Office of the Vice President for Research and Economic Development.

References

Creevey, O. L., Monteiro, M. J. P. F. G., Metcalfe, T. S., et al. 2007, ApJ, 659, 616

Crida, A., Ligi, R., Dorn, C., Borsa, F., & Lebreton, Y. 2018a, Research Notes of the American Astronomical Society, 2, 172

Crida, A., Ligi, R., Dorn, C., & Lebreton, Y. 2018b, ApJ, 860, 122

Cunha, M. S., Aerts, C., Christensen-Dalsgaard, J., et al. 2007, A&A Rev., 14, 217

Duvert, G. 2016, VizieR Online Data Catalog, II/345

Gent, M. R., Bergemann, M., Serenelli, A., et al. 2022, A&A, 658, A147

Graczyk, D., Pietrzyński, G., Thompson, I. B., et al. 2020, ApJ, 904, 13

Huber, D., Ireland, M. J., Bedding, T. R., et al. 2012, ApJ, 760, 32

Kervella, P., Bigot, L., Gallenne, A., & Thévenin, F. 2017, A&A, 597, A137

Ligi, R., Dorn, C., Crida, A., et al. 2019, A&A, 631, A92

Maxted, P. F. L. 2023, MNRAS, 519, 3723

Mourard, D., Berio, P., Pannetier, C., et al. 2022, in Society of Photo-Optical Instrumentation Engineers (SPIE) Conference Series, Vol. 12183, Optical and Infrared Interferometry and Imaging VIII, ed. A. Mérand, S. Sallum, & J. Sanchez-Bermudez, 1218308

Mourard, D., Nardetto, N., ten Brummelaar, T., et al. 2018, in Society of Photo-Optical Instrumentation Engineers (SPIE) Conference Series, Vol. 10701, Optical and Infrared Interferometry and Imaging VI, ed. M. J. Creech-Eakman, P. G. Tuthill, & A. Mérand, 1070120

Nardetto, N., Gieren, W., Storm, J., et al. 2023, A&A, 671, A14

Pannetier, C., Bério, P., Mourard, D., et al. 2022, in Society of Photo-Optical Instrumentation Engineers (SPIE) Conference Series, Vol. 12183, Optical and Infrared Interferometry and Imaging VIII, ed. A. Mérand, S. Sallum, & J. Sanchez-Bermudez, 1218309

Pietrzyński, G., Graczyk, D., Gallenne, A., et al. 2019, Nature, 567, 200

Pietrzyński, G., Graczyk, D., Gieren, W., et al. 2013, Nature, 495, 76

Riess, A. G., Casertano, S., Yuan, W., Macri, L. M., & Scolnic, D. 2019, ApJ, 876, 85

Salsi, A., Nardetto, N., Mourard, D., et al. 2020, A&A, 640, A2

Salsi, A., Nardetto, N., Mourard, D., et al. 2021, A&A, 652, A26

Salsi, A., Nardetto, N., Plez, B., & Mourard, D. 2022, A&A, 662, A120

Seager, S. & Mallén-Ornelas, G. 2003, ApJ, 585, 1038

ten Brummelaar, T. A., McAlister, H. A., Ridgway, S. T., et al. 2005, ApJ, 628, 453

SF2A 2023
M. N'Diaye, A. Siebert, N. Lagarde, O. Venot, K. Baillié, M. Béthermin, E. Lagadec, J. Malzac, J. Richard (eds)

A MAGNETIC FIELD STUDY IN THE ENVELOPE OF COOL EVOLVED STARS

L. Marinho[1], F. Herpin[1], H. Wiesemeyer[2], A. López-Ariste[3], A. Baudry[1], A. Asensio Ramos[4] and the PEPPER team

Abstract. Evolved cool stars exhibit a massive mass loss, which contributes to the enrichment of the interstellar medium and therefore to the recycling of matter in the Universe. The mechanisms (e.g. the stellar magnetic field) behind this mass loss phenomena are not understood, but can be constrained thanks to observations of the star and its circumstellar envelope (CSE). Here, we focus on the SiO maser line emission, which probes the inner region of the envelope (2-4 stellar radii from the photosphere) and can reveal the presence of a magnetic field. With radio-astronomical polarimetric observations, we derive the angle of polarization, the linear and circular polarization, which according to theories can lead to an estimate of the magnetic field strength along the line of sight. The magnetic field strength is hence estimated at between 0.1 and 10 G. A global poloidal field can be excluded. There are still questions about the origin of the magnetic field (solar-type dynamo, turbulent dynamo ...) and its evolution.

Keywords: masers – polarization – stars: evolution, late-type, magnetic field

1 Introduction

Over 95% of the stars in the Galaxy are low- or intermediate-mass star (under $8M_{\odot}$; Salpeter (1955); Chabrier (2003)). After the Main Sequence, these stars will evolve through different stages, including the Asymptotic Giant Branch (AGB) phase. During the few million years they will spend on the AGB, their circumstellar envelope (CSE) will become an impressive chemical factory, where more than 80 molecules and 15 dust species have been discovered (Höfner & Olofsson 2018; Decin et al. 2018). The important mass loss that these stars experience ($10^{-4} - 10^{-6}$ $M_{\odot}$/yr, Höfner & Olofsson 2018; Decin et al. 2018) makes them important actors in the recycling in the Universe, contributing at 85% to the gas enrichment of all stellar sources and at 35% of the total enrichment of the ISM. What triggers and shapes those strong winds is still debated and not fully understood. The magnetic field is expected to be a potential agent in the mass loss process (Pascoli & Lahoche 2008) and in shaping the wind. It has already been detected in the CSE through observations of different maser lines, probing the magnetic field at different distances from the star: SiO in the inner region of the CSE (Herpin et al. 2006), OH and H_2O in the more outer regions (Rudnitski et al. 2010). Optical spectropolarimeters (ESPaDOnS@CFHT, Narval@TBL) have contributed a lot of information on the magnetic activity on the stellar surface.

2 Observations

We observed the SiO v=1, J=2-1 maser line at 86.2434277 GHz with the IRAM-30m telescope in March and May 2022. Our sample is made of 6 evolved stars: 5 Mira-type AGB (χ Cyg, o Ceti, R Aql, R Leo and U Her) and one RSG (Red super giant) μ Cep, described in Table 1. We obtained the Stokes parameters with instrument XPol (Thum et al. 2008), using the EMIR receiver (E90 frontend band), and VESPA backend.

We verified the polarization angle calibration with the Crab Nebula, a well-known, strongly linearly polarized source. The instrumental polarization on the optical axis was verified on a planet (Uranus) as a non-polarized

[1] Laboratoire d'astrophysique de Bordeaux, Univ. Bordeaux, CNRS, B18N, allée Geoffroy Saint-Hilaire, 33615 Pessac, France.
[2] Max-Planck-Institut für Radioastronomie, Auf dem Hüugel 69, 53121 Bonn, Germany
[3] IRAP, Université de Toulouse, CNRS, CNES, UPS, 14 Av. E. Belin, 31400 Toulouse, France,
[4] Instituto de Astrofísica de Canarias, La Laguna

© Société Française d'Astronomie et d'Astrophysique (SF2A) 2023

Star	RA (J2000) [h m s]	DEC (J2000) [° ’ ”]	Type	d [pc]	L [$L_\odot$]	T_{eff} [K]	Mass-Loss rate [$M_\odot$/yr]
o Ceti[a]	02:19:20.79	-02:58:39.50	Mira	107	6099	2193	2.5×10^{-7}
R Leo[b]	09:47:33.49	+11:25:43.82	Mira	100	5617	2890	9.2×10^{-7}
U Her[b,c]	16:25:47.47	18:53:32.86	Mira	271	8000	3000	5.9×10^{-7}
R Aql[b,c]	19:06:22.25	08:13:48.01	Mira	308	4900	2800	1.1×10^{-6}
χ Cyg[b]	19:50:33.92	+32:54:50.61	Mira	180	7813	2000	2.4×10^{-7}
μ Cep[d,e]	21:43:30.46	+58:46:48.16	RSG	390/1818	35000	3750	2.0×10^{-6}

Table 1. List of the observed sources, data from [a]De Beck et al. (2010), [b] Andriantsaralaza et al. (2022), [c]Gottlieb et al. (2022), [d]Montargès et al. (2019), [e]Maercker et al. (2022)

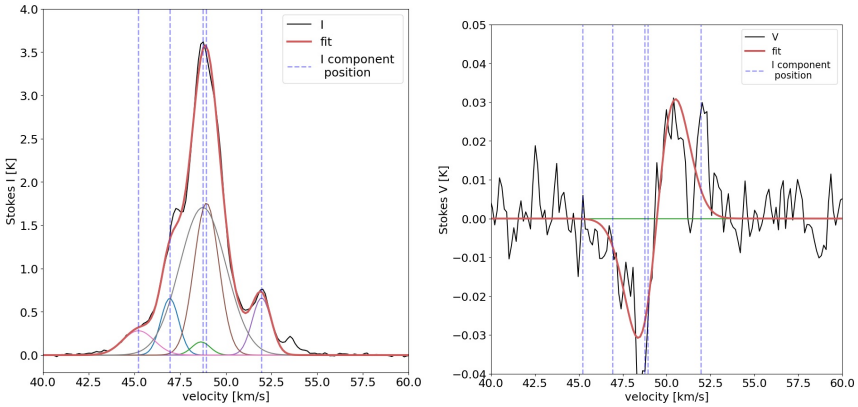

Fig. 1. Decomposition by the *rvm* code. **Left:** Stokes I decomposition, the data are in black and the fit in red is the sum of all the Gaussian components (in color). The dashed purple vertical lines are the position of the central velocity of the Gaussian functions. **Right:** Stokes V decomposition with the same color as before.

source. From the Stokes parameters I, Q, V and U we can compute the circular polarization rate ($p_{\rm C}$), the linear polarization rate ($p_{\rm L}$), and the angle of polarization (χ). The instrumental and astronomical contributions to the linear polarization were separated thanks to the modulation of the former in the celestial reference frame. For the circular polarization, we developed a method to remove the instrumental contamination from the data.

3 Data analysis and method

3.1 Stokes I and V decomposition

For an analysis based on the Zeeman theory, we first decomposed Stokes I into a combination of Gaussian functions.

$$I(v) = \sum_{k=1}^{n} A_k e^{-\frac{(v-v_{0,k})^2}{\Delta v_{D,k}^2}} \tag{3.1}$$

with $v_{0,k}$ and $v_{D,k}$ respectively the central velocity and Doppler width for each component k, and A_k a weight. We develop a code based on the relevant vector machine (Tipping & Faul 2003). The *rvm* code finds the best linear combination of entries from a dictionary. In our case, it will find the best number of Gaussians from a dictionary of parameters that we fixed. The dictionary is made of 200x50 parameters, with 200 central velocities and 50 line-width ranges. We can do the same for Stokes V. Based on the Zeeman theory, V can be written as $V(\lambda) = f(B)\frac{dI}{d\lambda}$ with $f(B)$ a function of the magnetic field. An example of decomposition of Stokes V in a sum of the derivative of Gaussian functions is shown in Figure 1.

3.2 Magnetic field estimate

We compute the magnetic field strength at the two V peaks of each Zeeman component found by the code: $\lambda_{peak} = \lambda_0 \pm \frac{1}{\sqrt{2}}\Delta\lambda_{\rm D}$. This calculation depends on the saturation level of the maser emission. To estimate

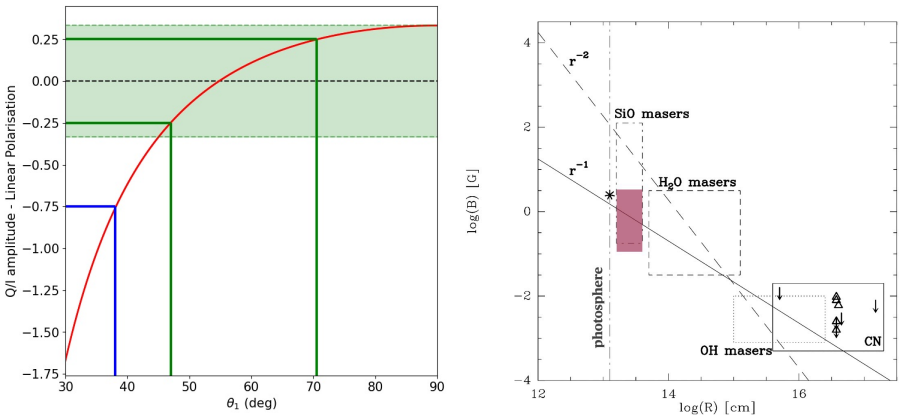

Fig. 2. Left: Linear polarization vs the angle for B=1G. The blue solution represents a case where $|q| > q_c$, the green one where $|q| < q_c$. The green-shaded area indicates the loci where two solutions exist. **Right:** The magnetic field strength as a function of the distance. The dotted squares are previous observations (Herpin et al. 2006; Rudnitski et al. 2010; Duthu et al. 2017) and the red one is the new results computed here, constraining the magnetic field in r^{-1}.

this saturation level, we compute the stimulated emission rate $R = \frac{AkT_b\Delta\Omega}{4\pi h\nu}$, with A the Einstein coefficient for spontaneous emission of the transition, k the Boltzmann constant, T_b the brightness temperature, and $\Delta\Omega$ the solid beaming angle (the ratio of the surface area of the maser spot area to that of the masing cloud). This parameter is not well known and we adopt a minimal value: 5×10^{-2} from Assaf et al. (2013). Considering R and the linear polarization fraction(Nedoluha & Watson 1990), we consider two strongly saturated sources (χ Cyg and U Her), two not strongly saturated (R Aql and μ Cep), and two sources where we can't conclude (o Ceti and R Leo.)

We thus consider two cases:

$$\textbf{Saturated maser (Elitzur 1996):}\quad \frac{B}{\cos\theta_1} \simeq 65\Delta v_{\rm D}\frac{V(v_{peak})}{I(v_{peak})} \tag{3.2}$$

$$\textbf{Unsaturated maser (Zeeman weak field theory):}\quad B\cos\theta_2 \simeq 33.73\frac{V(v_{peak})}{\partial_v I(v_{peak})} \tag{3.3}$$

B is in Gauss and $\Delta v_{\rm D}$ is the width of the Gaussian used in the *rvm* code to fit the Stokes V. In Both formula, there is still a dependence on the angle (θ_1 is the angle between $\vec{B}$ and the incident beam, θ_2 is the angle between $\vec{B}$ and the refracted beam). We can't derive the angle from the Zeeman weak field theory, but we can for the strongly saturated maser. Following Elitzur (1996), in a coordinate system that is aligned with the sky-plane projected magnetic field, $q = Q/I$ is given by: $q = 1 - 2\frac{3-R_1}{(2R_1+1)\sin^2\theta_1}$ with $R_1 = 1 - x_B^2(1-2\lambda^2)$ and x_B the ratio of the Zeeman splitting Δv_B to the Doppler line-width $\Delta v_{\rm D}$. So $R_1 = 1 - 14^2 g^2 \lambda_0^2 B^2 (1-2\lambda^2)/\Delta\lambda_D^2$ where g is the Landé factor, λ_0 the wavelength of the maser emission, and B the magnetic field strength in Gauss. This equation is plotted in Figure 2, left. As we only have the absolute value of $p_{\rm L}$ in the observations, depending on the values of $p_{\rm L}$, we have two possibilities. There is a critical value q_c defined by $\lim_{\theta\to+90^\circ} q = 0.333$. If $|q| > q_c$: the solution for the angle θ_2 is unique (see example in blue in the Figure 2, left). And if $|q| < q_c$, there are two solutions for θ_2 (see the example in green), and hence two solutions for the magnetic field strength.

Uncertainties computation: There are two main sources of uncertainties. 1/ A remaining instrumental polarization in the data that we quantified, $\delta V_{\rm inst} = 7$ mK for the sample. 2/ The difference between the fit and the observational data ($\delta V_{\rm noise}$).

4 Results and Discussion

Applying this, we compute the magnetic field for all the sources (see Fig. 3) and the results were added in red in Figure 2 right. The magnetic field seems to evolve in r^{-1} in agreement with the point on the photosphere, measured for χ Cyg (Lèbre et al. 2014). We also have two periods of observation for U Her, and we can see that the magnetic field has changed in two months. So far we have no stringent explanation for this change,

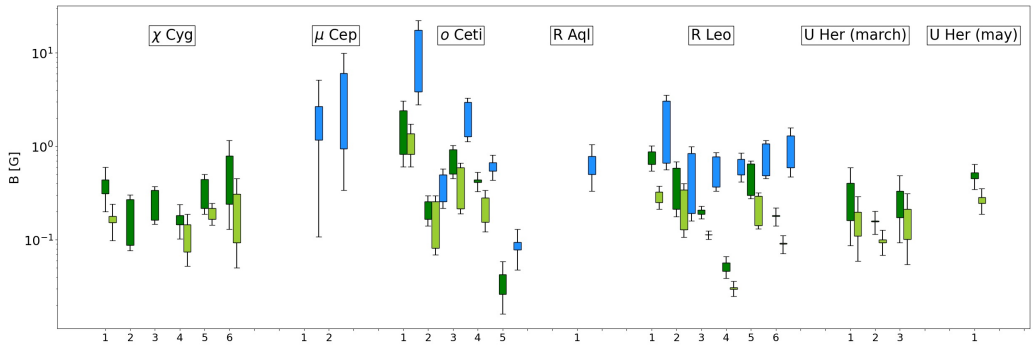

Fig. 3. Magnetic field strength for all sources, depending on the Gaussian component as indicated on the x-axis. The blue results are for mildly strongly saturated maser, the green ones are the strongly saturated solution. Two green bars for the same Gaussian component indicate that p_L is under 33%, entailing two magnetic-field solutions. For μ Cep and R Leo, the strongly saturated and the not strongly saturated solution are shown.

but it is probably correlated with the stellar activity and the presence of cool spots on the stellar surface (Soker 2002). A turbulent dynamo mechanism ($\alpha^2 - \omega$) can generate a weak magnetic field at the stellar surface, that is amplified by shocks and convection above the cool spots.

5 Conclusions

We developed a method to estimate the magnetic field in the inner region of the envelope of cool evolved stars. We were able to remove the instrumental contamination. We found a magnetic field between 0.1 and 10 Gauss. This result suggests that the magnetic field evolves in r^{-1} in the envelope. There is still work to be done to understand the temporal evolution and the origin of the magnetic field.

Acknowledgements: This work is funded by the French National Research Agency (ANR) project PEPPER (ANR-20-CE31- 0002)

References

Andriantsaralaza, M., Ramstedt, S., Vlemmings, W. H. T., & De Beck, E. 2022, A&A, 667, A74
Assaf, K. A., Diamond, P. J., Richards, A. M. S., & Gray, M. D. 2013, Monthly Notices of the Royal Astronomical Society, 431, 1077
Chabrier, G. 2003, PASP, 115, 763
De Beck, E., Decin, L., de Koter, A., et al. 2010, A&A, 523, A18
Decin, L., Richards, A. M. S., Danilovich, T., Homan, W., & Nuth, J. A. 2018, A&A, 615, A28
Duthu, A., Herpin, F., Wiesemeyer, H., et al. 2017, A&A, 604, A12
Elitzur, M. 1996, The Astrophysical Journal, 457, 415
Gottlieb, C. A., Decin, L., Richards, A. M. S., et al. 2022, A&A, 660, A94
Herpin, F., Baudry, A., Thum, C., Morris, D., & Wiesemeyer, H. 2006, A&A, 450, 667
Höfner, S. & Olofsson, H. 2018, A&A Rev., 26, 1
Lèbre, A., Aurière, M., Fabas, N., et al. 2014, A&A, 561, A85
Maercker, M., Khouri, T., Mecina, M., & De Beck, E. 2022, A&A, 663, A64
Montargès, M., Homan, W., Keller, D., et al. 2019, MNRAS, 485, 2417
Nedoluha, G. E. & Watson, W. D. 1990, ApJ, 354, 660
Pascoli, G. & Lahoche, L. 2008, PASP, 120, 1267
Rudnitski, G. M., Pashchenko, M. I., & Colom, P. 2010, Astronomy Reports, 54, 400
Salpeter, E. E. 1955, ApJ, 121, 161
Soker, N. 2002, MNRAS, 336, 826
Thum, C., Wiesemeyer, H., Paubert, G., Navarro, S., & Morris, D. 2008, PASP, 120, 777
Tipping, M. E. & Faul, A. C. 2003, in Proceedings of Machine Learning Research, Vol. R4, Proceedings of the Ninth International Workshop on Artificial Intelligence and Statistics, ed. C. M. Bishop & B. J. Frey (PMLR), 276–283, reissued by PMLR on 01 April 2021.

Abstract. Most massive stars are in binaries. Binarity can drastically alter their evolution, which can result in the formation of X-ray binaries or binary black hole systems, the dominant sources of gravitational waves. While single star formation is increasingly well understood, the detailed physics of binary/multiple massive star formation has received less attention. In particular, a good understanding of the combined influence of birth environmental conditions such as rotation, turbulence, magnetic fields, on (massive) stellar multiplicity is still lacking. In this proceeding, we summarize recent numerical efforts to clarify these points, using radiation-magneto-hydrodynamical simulations of massive pre-stellar core collapse with the RAMSES code, including the relevant physics to identify several fragmentation processes. We find magnetic fields to limit disk fragmentation in several ways: they remove angular momentum via outflows and magnetic braking, thereby limiting (and/or delaying) disk growth, self-gravitational effects and fragmentation. In binaries linked by a gaseous filament, magnetic pressure impedes gas concentration in the filament, thus suppressing fragmentation via spiral arm-filament, a fragmentation channel ubiquitous in hydrodynamical runs. On the opposite, core rotation and turbulence carry angular momentum, favouring disk growth and fragmentation. Moreover, turbulence reduces magnetic braking and outflows, again favoring disk fragmentation. We conclude that the environmental conditions (rotation, turbulence, magnetic fields) are keys to understand (massive) stellar multiplicity.

Keywords: stars: formation, stars: massive, accretion, magnetohydrodynamics(MHD), methods: numerical, binaries: general

1 Introduction

The majority of stars is in binary or higher-multiple systems. Moreover, the multiplicity fraction (i.e. frequency of multiple systems) and companion fraction (average number of companions) increases with the primary stellar mass, so that at least 90% of Main-Sequence massive stars ($\geq 8 M_\odot$) are in multiple systems, and massive stars have, on averaged, at least 1.6 companion (Offner et al. 2022). Various mechanisms can influence the final multiplicity of a stellar system, at distinct stages of the stellar system formation (see e.g. the reviews by Lee et al. 2020 and Offner et al. 2022). In the final stages, the system's multiplicity can be affected by stellar capture; in the earliest stages, core (or turbulent) fragmentation (e.g. Gingold & Monaghan 1983, Machida et al. 2005) and gravitational fragmentation of accretion disks (e.g. Bonnell & Bate 1994) are at play to form stars and increase the system's multiplicity; in this proceeding, we focus on disk fragmentation.

Several attempts to identify the dominant fragmentation channel in astrophysical environments have been undertaken. For instance, Tobin et al. (2018) searched for rotation signatures in the circum-multiple gas in the Perseus molecular cloud, targeting low-mass stellar systems; the detection of these signatures would suggest that the youngest stars were born out of disk fragmentation. They found that, in their sample, 8 out of 12 stars were consistent with disk fragmentation origin, the remaining 4 being attributed to core fragmentation. Thus, those results suggest at the very least that disk fragmentation is at play, in addition to core fragmentation. Although the extrapolation of these results to high-mass stars is not straightforward, disk fragmentation is not found to be inhibited around massive protostars in numerical simulations (e.g. Krumholz et al. 2009, Mignon-Risse et al. 2020, Oliva & Kuiper 2020).

Disk fragmentation occurs in two stages. First, non-axisymmetric instability in (axisymmetric) disks is triggered when the disk self-gravity becomes sufficiently important; when occuring, the disk grows spiral arms. The associated unstable state of a disk is expressed via the condition $Q > 1$, where Q is the Toomre parameter Q (Toomre 1964). It compares the relative importance of self-gravity, which triggers the instability, and shear and pressure supports (of radiative, magnetic and thermal origin), that prevent it. Under some circumstances, this condition can be re-formulated as $Q \approx M_{\rm disk} \,/\, M_\star > H/R$, where $M_{\rm disk}$ is the primary disk mass, $M_\star$ the primary star mass, and H/R the primary disk aspect ratio (of the order 0.1); thus, disk growth can lead to disk self-gravitational instability. Second, these spiral arms can lead to gravitationally unstable structures (e.g. via collision of spiral arms) that collapse to form a stellar companion.

In this proceeding, we address the influence of the birth environmental conditions (rotation, turbulence, magnetic fields) of stars on disk fragmentation and on the subsequent stellar multiplicity, in the context of massive star formation. Since accretion disks around massive young stars are found to be supported by thermal pressure rather than radiative (Mignon-Risse et al. 2020) or magnetic (Mignon-Risse et al. 2021, Commerçon et al. 2022) pressure, we will be mainly interested in how these environmental conditions influence the self-gravitational instabilities triggering via the disk growth. For this, we will be following the collapse of a massive pre-stellar core using the `RAMSES` (Teyssier 2002) to solve the equations of radiation-magneto-hydrodynamics (Fromang et al. 2006, Masson et al. 2012, Mignon-Risse et al. 2020).

2 First experiment: impact of magnetic fields on multiplicity

In this first experiment, we compare two sets of calculations: one set without magnetic fields (referred to as "hydrodynamical" runs) and one set with magnetic fields, including ambipolar diffusion. We use an axisymmetric numerical setup identical to Mignon-Risse et al. (2023b). It consists of a core of 200 $M_\odot$, radius = 0.1 pc, density profile $\rho(r) \propto r^{-3/2}$, rotation profile defined by the angular frequency $\Omega(R) \propto R^{-3/4}$, with R the cylindrical radius, with a rotational-to-gravitational energy ratio of 5% in the core midplane. The dust-to-gas ratio 1%, with a dust sublimation model at high (> 1000 K) temperature. In the magnetized runs, the mass-to-flux to critical-mass-to-flux ratio is $\mu = 2$ at the core border. Finest resolution is varied between 10 AU and 1.25 AU. When a gas parcel is gravitationally-bound and Jeans-unstable, it is replaced by a sink particle that mimics a star (Bleuler & Teyssier 2014).

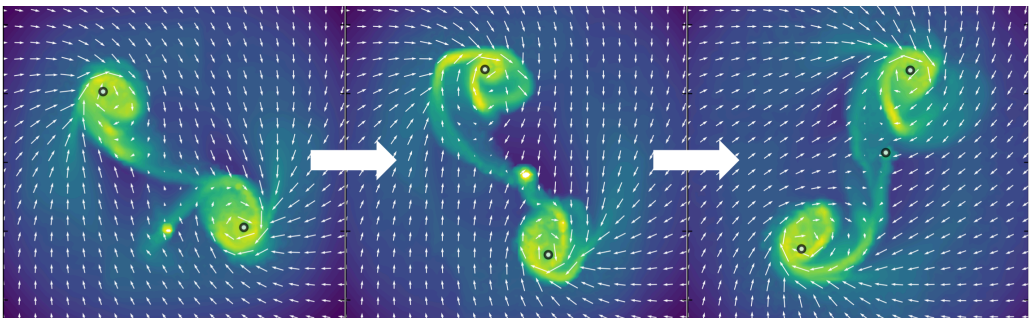

Fig. 1. Time sequence of density slices with sink particles overplotted, illustrating the arm-filament collision mode of fragmentation, in one of the hydrodynamical runs. The slices cover 1000 AU ×1000 AU. This mode of fragmentation, ubiquitous in the hydrodynamical runs, is absent in the magnetized runs.

In both magnetized and hydrodynamical runs, a binary system is formed after a few kyr. Figure 1 shows a time sequence in one of the hydrodynamical runs at the time when the third star forms. It can be seen that, initially, each star is surrounded by an accretion disk, and the two systems are linked by a filament (left panel of Fig. 1). The disks exhibit large spiral arms. The collision of one disk's arm with the filamentary structure linking the binary leads to the formation of the third star, as illustrated on Fig. 1. This mode of fragmentation is reported in all the hydrodynamical runs and is absent in the magnetized runs. Indeed, the impact of magnetic fields on this fragmentation mode is twofold. First, before fragmentation, disks are about twice larger in hydrodynamical (≈150 AU) than in magnetic runs, in which case their disk size is consistent with magnetic regulation. Indeed, magnetic braking removes angular momentum and thereby limits disk growth and therefore self-gravitational effects such as spiral arm formation. In the hydrodynamical case, only disk fragmentation can limit disk growth. Second, the filament is much more diffuse in the magnetized case. This is visible in Fig. 2, which shows the column density map at the end of the same hydrodynamical run as Fig. 1 and in the resolution-equivalent magnetized run. Indeed, the filament is located in a region where magnetic pressure dominates over thermal and radiative pressures and certainly limits mass concentration.

To sum up, magnetic fields limit massive stellar multiplicity by reducing disk fragmentation because they limit disk growth (provided by the angular momentum of the infalling gas) – while only disk fragmentation can limit disk growth otherwise –, and in binaries, they lead to more diffuse inter-binary filamentary structures (as observed by e.g. Sadavoy et al. 2018). More details can be found in Mignon-Risse et al. (2023a).

3 Second experiment: relative influence of magnetic fields and turbulence on multiplicity

In this second experiment, we only consider magnetized runs (with ambipolar diffusion) and address the relative impact of magnetic fields and turbulence in setting massive stellar multiplicity. The setup (see Commerçon et al. 2022) is similar to the previous one except for the following: the core has a mass 100 $M_\odot$, radius 0.2 pc, a density profile $\rho(r) \propto 1/(1+(r/r_c)^2)$ with a central plateau of radius $r_c = 0.02$ pc, in solid-body rotation with rotation-to-gravitational energy ratio 1% at the core border. On top of this, an initial velocity distribution is set so as to mimic turbulence (in turbulent runs), set by the Mach number $\mathcal{M}$, and we vary the level of magnetization. The relative importance of turbulence with respect to magnetic fields is, thus, set by the Alfvénic Mach number

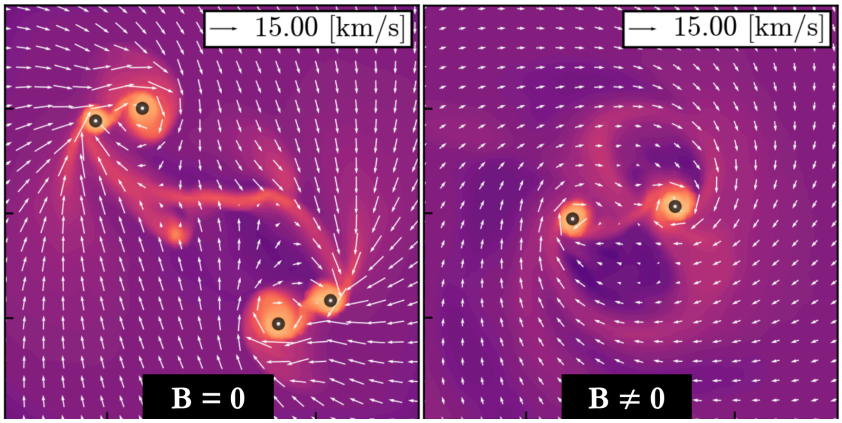

Fig. 2. Column density maps at the end of one of the hydrodynamical runs (left panel) and magnetized runs (right panel). Sink particles are indicated by white dots. The maps cover 2000 AU ×2000 AU. The stellar system is a quadruple in the hydrodynamical run while it is a binary in the magnetized run.

$\mathcal{M}_{\rm A}$ ($\mathcal{M}_{\rm A} > 1$ means turbulence dominating over magnetic fields). The magnetization level is varied between $\mu = 2$ and $\mu = 5$ at the core border. The finest numerical resolution is set to be 5 AU.

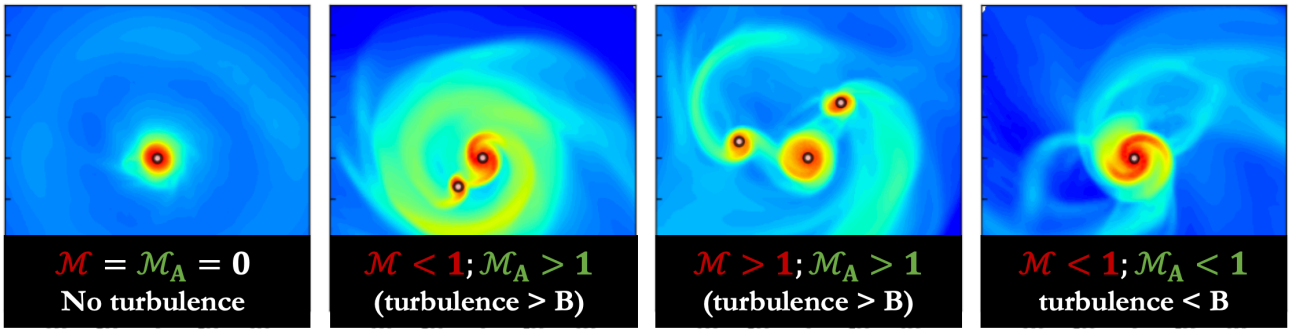

Fig. 3. Column density maps at the same time in the four runs. Sink particles are overplotted as white circles. The maps cover 1500 AU ×1500 AU. Magnetic-dominated runs ($\mathcal{M}_{\rm A} < 1$) lead to single star formation; turbulence-dominated runs ($\mathcal{M}_{\rm A} > 1$) lead to multiple systems.

Figure 3 shows the column density and multiplicity outcome of this set of simulations at $t = 50$ kyr. Magnetic-dominated (i.e. "sub-Alfvénic" turbulence) runs lead to single stars; turbulence-dominated (i.e. "super-Alfvénic" turbulence) runs lead to multiple systems – binaries at the end of the run, when accounting for sink mergers. On top of the core/turbulent initial fragmentation found to occur in turbulence-dominated runs, we report disk fragmentation in these same runs. These events occur after a 'spike' in disk size is reported, thus a spiral arm forming. In one of these two runs, we observe disk growth followed by spiral arm formation, and spiral arms collision to produce the fragment that will eventually become gravitationally-unstable and lead to sink particle creation. For a given $\mathcal{M}$ value, the run with higher magnetization exhibits a delayed disk growth, spiral arm formation and collision, and the formed fragment falls down onto the disk, which we attribute to angular momentum removal by magnetic fields. Angular momentum transport is found to be dominated by magnetic braking. Magnetic braking weakens as turbulence increases, which we attribute to the turbulence deorganizing the magnetic fields topology.

To sum up, environmental turbulence carries angular momentum and therefore contributes to disk growth, while magnetic fields remove it and limit disk fragmentation (more details in Mignon-Risse et al. 2021).

4 Conclusions

We have studied various ways in which the environmental conditions (rotation, turbulence, magnetic fields) could influence the multiplicity of a young massive stellar system via disk fragmentation, using non-ideal radiation-

magnetohydrodynamical calculations. Rotation and turbulence, because they carry angular momentum, contribute to disk growth, self-gravitational instability and subsequent fragmentation. Magnetic fields seem to play an opposite role: they remove angular momentum (via outflows and magnetic braking; whose amplitude is reduced by turbulence), thereby limiting disk fragmentation. In binaries, which are linked by a gas filament, they also add an extra pressure support, thereby suppressing arm-filament collision as another fragmentation channel. In their absence, and in the case of a disk embedded in a reservoir of rotating gas, disk growth would be theoretically unlimited: fragmentation appears as the natural mechanism to limit it. Finally, the aforementioned mechanisms are not only valid for massive stars and could also matter for low-mass star formation. Environmental conditions are, therefore, important in setting (massive) stellar multiplicity.

This work was supported by the CNRS "Programme National de Physique Stellaire" (PNPS). This work has received funding from the French Agence Nationale de la Recherche (ANR) through the project COSMHIC (ANR-20- CE31-0009). The numerical simulations we have presented in this paper were produced on the CEA machine Alfvén and using HPC resources from GENCI-CINES (Grant A0080407247)

References

Bleuler, A. & Teyssier, R. 2014, MNRAS, 445, 4015

Bonnell, I. A. & Bate, M. R. 1994, MNRAS, 271, 999

Commerçon, B., González, M., Mignon-Risse, R., Hennebelle, P., & Vaytet, N. 2022, A&A, 658, A52

Fromang, S., Hennebelle, P., & Teyssier, R. 2006, A&A, 457, 371

Gingold, R. A. & Monaghan, J. J. 1983, MNRAS, 204, 715

Krumholz, M. R., Klein, R. I., McKee, C. F., Offner, S. S. R., & Cunningham, A. J. 2009, Science, 323, 754

Lee, Y.-N., Offner, S. S. R., Hennebelle, P., et al. 2020, Space Sci Rev, 216, 70, arXiv: 2006.05778

Machida, M. N., Matsumoto, T., Hanawa, T., & Tomisaka, K. 2005, MNRAS, 362, 382

Masson, J., Teyssier, R., Mulet-Marquis, C., Hennebelle, P., & Chabrier, G. 2012, ApJSS, 201, 24

Mignon-Risse, R., González, M., & Commerçon, B. 2023a, A&A, 673, A134

Mignon-Risse, R., González, M., Commerçon, B., & Rosdahl, J. 2020, A&A, 635, A42

Mignon-Risse, R., González, M., Commerçon, B., & Rosdahl, J. 2021, A&A, 652, A69

Mignon-Risse, R., Oliva, A., González, M., Kuiper, R., & Commerçon, B. 2023b, A&A, 672, A88

Offner, S. S. R., Moe, M., Kratter, K. M., et al. 2022, The Origin and Evolution of Multiple Star Systems, arXiv:2203.10066 [astro-ph]

Oliva, G. A. & Kuiper, R. 2020, A&A, 644, A41

Sadavoy, S. I., Myers, P. C., Stephens, I. W., et al. 2018, ApJ, 869, 115

Teyssier, R. 2002, A&A, 385, 337

Tobin, J. J., Looney, L. W., Li, Z.-Y., et al. 2018, ApJ, 867, 43

Toomre, A. 1964, ApJ, 139, 1217

SF2A 2023
M. N'Diaye, A. Siebert, N. Lagarde, O. Venot, K. Baillié, M. Béthermin, E. Lagadec, J. Malzac, J. Richard (eds)

A NEW 12C+12C REACTION RATE FROM THE STELLA COLLABORATION: HOW TO DETERMINE ASTROPHYSICAL PARAMETERS WITH NUCLEAR EXPERIMENTS?

E. Monpribat[1], T. Dumont[1], A. Bonhomme[1], M. Heine[1], J. Nippert[1] and S. Courtin[1,2]

Abstract. Among the nuclear reactions driving stellar evolution, $^{12}C + ^{12}C$ fusion is the key ingredients to describe the carbon burning. This system is known to show many resonances, and the low energy region might be affected by fusion hindrance. The reaction was recently measured by the STELLA collaboration making use of the gamma-particle coincidence technique for measurement of cross-sections with unprecedent accuracy, reaching energies of astrophysical interest. Reaction rates were extracted from experimental data by approximating a hindrance trend, or by adding on top a resonance at the lowest measured energy. The impact of these new rates on the evolution of massive stars was explored using the stellar evolution code GENEC, and a more detailed study of the nucleosynthesis with a large isotopes network was performed. The sensitivity of the STELLA experiment on the temperature range for C- burning has been thoroughly investigated, showing that the reaction rates determined by this experience are ideally suited for astrophysical studies and simulations.

Keywords: Nuclear reaction, Nucleosynthesis, Stars: evolution

1 Introduction

The origin of chemical elements, known as nucleosynthesis, has always been a significant and fundamental subject in modern physics. Nuclear physics plays a crucial role in this process as it governs composition of stars. These processes are closely tied to stellar evolution, the various types of stars, and the combustion phase.

Among these phases, the one of utmost interest for the STELLA collaboration is the carbon-burning phase. It is of a pivotal importance in stellar evolution, occurring only in massive stars and playing a significant role in type Ia supernovae. It is during this phase that the fusion reaction between ^{12}C and ^{12}C takes place. This reaction leads to several nuclear processes, such as heavy-ion fusion and the generation of neutron seeds.

Over the past few decades, numerous experiments have been conducted with the aim of directly measuring the carbon fusion cross-section at sub-barrier energies (see e.g. Patterson et al. 1969; High & Čujec 1977; Becker et al. 1981; Aguilera et al. 2006; Barrón-Palos et al. 2006; Spillane et al. 2007; Bucher et al. 2015). These experimental measurements have revealed the presence of resonances in the energy range well above and below the Coulomb barrier, possibly associated to molecular configurations of ^{12}C within the ^{24}Mg nucleus (Jenkins & Courtin 2015). The most recent results also suggest the occurrence of fusion hindrance (Fruet et al. 2020; Tan et al. 2020), a behavior at deep sub-barrier energy, observed in many heavier systems (Jiang et al. 2002).

However, at astrophysical energies, specifically deep sub-barrier energies within the Gamow window, experimental results exhibit substantial uncertainties. Different theoretical models, such as fusion hindrance (Jiang et al. 2007) and the CF88 model – commonly used in astrophysics (Caughlan & Fowler 1988) –, show orders of magnitude discrepancy. The lack of precise data is primarily due to the huge experimental challenges imposed by this system. Tiny cross-sections of the picobarn range necessitates extended beam exposure at high intensity, and spectra are often dominated by background noise originating from contaminant reactions, natural radioactivity, and cosmic rays. To address these challenges, a coincidence method for the $^{12}C + ^{12}C$ fusion reaction has been developed for deep sub-barrier energies (Jiang et al. 2012).

[1] Université de Strasbourg, CNRS, IPHC UMR 7178, F-67000 Strasbourg, France
[2] University of Strasbourg, Institut of Advanced Studies (USIAS), Strasbourg, France

© Société Française d'Astronomie et d'Astrophysique (SF2A) 2023

2 Measurements with the STELLA UK-FATIMA Experiment

The STELLA station addresses the formidable experimental challenges associated with direct measurements of the $^{12}C + ^{12}C$ cross-section through the use of a coincidence method combined with nano-seconds timing gates (Heine et al. 2018). This approach relies on the simultaneous detection of emitted light particles, specifically alpha particles or protons, and the associated gamma rays emitted during de-excitation.

To generate the $C^{2+,3+}$ beam required for the $^{12}C + ^{12}C$ cross-section measurement, the Andromède facility at IJCLab, located in Orsay, France, is used, able to deliver a beam with an intensity of up to 6 pμA. To facilitate heat dissipation and prevent target deterioration, a rotating system has been implemented. These targets are composed of carbon graphite, with a diameter of 5 cm and a thickness ranging from 20 to 70 $\mu g/cm^2$, spinning at a maximum rate up to 1000 rpm, depending of the heat input from the intense beam. Carbon buildup on these targets is monitored and effectively mitigated due to the high vacuum conditions (10^{-8} mbar) maintained within the reaction chamber.

The detection of light particles is achieved through the use of two annular charged-particle silicon detectors, characterized by high granularity and nanosecond triggering capability. Gamma rays, on the other hand, are detected by $LaBr_3$(Ce) scintillators, which are part of the UK-FATIMA (FAst TIMing Array) collaboration's equipment.

3 Reaction rate

In Monpribat et al. (2022), two distinct fusion scenarios concerning the excitation functions of the $^{12}C+^{12}C$ fusion reaction have been investigated. These scenarios were derived from direct measurements conducted as part of the STELLA experiment (Fruet et al. 2020). The first scenario follows the fusion hindrance model (referred to as Hin model), as described in Jiang et al. (2007), while the second scenario combines fusion hindrance with an additional resonance at $E_{cdm} = 2.14$ MeV, proposed by Spillane et al. (2007) (referred to as HinRes model). During the fitting procedure, parameters related to the fusion hindrance were not constraint, and these fits were performed simultaneously in both exit channels, assuming a common underlying explanation for hindrance (Jiang et al. 2013). The obtained fitting parameters align with previous findings (Jiang et al. 2018), and there is notable agreement between the resonance and the experimental data collected by STELLA.

The study also determined reaction rates for each of these fusion scenarios. These rates are generally lower than the rates that have been used in astrophysical simulations over the past few decades, as determined by the CF88 model (Caughlan & Fowler 1988). The resonance impacts the reaction rate, significantly increasing it to a level comparable with the CF88 model rate at a temperature of approximately T = 0.85 GK, right in the astrophysics region of interest of massive stars according to Hin and HinRes predictions (Monpribat et al. 2022).

Furthermore, the STELLA sensitivity was defined in Monpribat et al. (2022). This sensitivity corresponds to the temperature range in which reaction rates are determined solely by interpolating the excitation functions provided by the STELLA collaboration. By considering the energy at which the cross sections are measured and employing the Gamow window definition, along with an approximation proposed in Illiadis (2015), the STELLA sensitivity was found to reach a minimum temperature of T = 0.6 GK at 1σ uncertainties. In this temperature range, relative uncertainties are approximately 15% and 30% for the Hin and HinRes models, respectively.

4 Impact on stellar evolution

To investigate the effects of the presented reaction rates, hydrodynamics and nucleosynthesis simulations were conducted using the GENeva stellar Evolution Code GENEC (Eggenberger et al. 2008). Two stellar models were considered, one with a mass of $12\,M_\odot$ and the other with $25\,M_\odot$, both starting with initial solar metallicity and without accounting for rotation. The evolution of these models was tracked until the end of the carbon burning phase.

During this phase, it is observed that the fusion temperature for the $12\,M_\odot$ model (referred to as Hin) was approximately 10% higher than for the $25\,M_\odot$ model (referred to as HinRes), resulting in shorter carbon burning lifetime by a factor of two. This is attributed to the significantly lower reaction rate in the Hin model, which led to lower heat output. Consequently, the star undergoes contraction and eventually reaches higher temperature for carbon burning. This seemingly counter-intuitive finding indicates that lower reaction rates will cause higher core temperatures (see also Pignatari et al. 2013), as the star continuously adjusts itself, within hydrostatic equilibriuum.

The Kippenhahn diagram shows at the culmination of the core carbon burning phase in the 25 $M_\odot$ star (as depicted in Fig.4 in Monpribat et al. (2022)). Both reaction rate models exhibit similar evolutionary trends, except for the fact that the convective region in the Hin model extends much farther compared to HinRes. This difference is attributed to the higher temperature in the former case, resulting in a stronger temperature gradient and dynamic behavior.

Furthemore, the cooling of the star due to neutrino emission (as shown in Fig.7 in Monpribat et al. (2022)) is influenced by variations in carbon burning lifetime. This, in turn, will leave repercussions on the dynamics during core collapse and ultimately impacts the nature of the stellar remnant.

The 25 $M_\odot$ model was investigate using the complementary "One-Layer" nucleosynthesis code by Choplin et al. (2016). This code was used to create a single-layer model of the star, but with an expanded nuclear reaction network that accounts for more than one thousand isotopes and their reactions. The temperature and density trajectory in this model was adjusted to match that of the CF88 model.

In Figure 9 of Monpribat et al. (2022), minor difference in the final abundances were observed when comparing the CF88, Hin, and HinRes models for elements such as sodium, aluminum, phosphorus, and some heavier elements. These variations could potentially have implications for the subsequent phases of stellar evolution, as s-process, although a more in-depth investigation would be required to fully understand their effects and significance.

It is worth noting that in the GENEC simulations, the results obtained with the CF88 and HinRes models are very similar, which is expected given their comparable reaction rates at the temperatures during carbon burning (as shown in Figure 2 of Monpribat et al. (2022)). However, there is a discrepancy in the abundances derived from the One-Layer code for CF88 and Hin, with somewhat different pattern. This could be attributed to the branching ratios involving α- and proton-emission, which were adjusted in the One-Layer code based on experimental data presented in Table 1 of Monpribat et al. (2022), but could only be indirectly accounted for in the GENEC package (Hirschi 2004). Indeed, the branching ratios during carbon burning, as illustrated in Figure 1 of Monpribat et al. (2023), indicate a situation where CF88 and Hin (with a ratio of 0.65/0.35, Bennett et al. (2012)) are closer to each other than for HinRes. The latter is caused by the ratio of strengths of the resonance at $E = 2.14$ MeV in the carbon-carbon system, where α emission dominates. However, it is important to exercise caution when interpreting these results, as the temperature trajectories must be tailored to the specific hydrodynamics constraints of CF88, Hin, and HinRes individually, where different nucleosynthesis pathways may open up with more realistic assumptions.

In conclusion, these results emphazise the sensitivity of nucleosynthesis calculations to resonance branching in reaction rates, particularly for key reactions. It highlights that straightforward factorization of entire energy region may only provide general results, and a more detailed consideration of branching ratios may be necessary for a comprehensive understanding of nucleosynthesis process.

5 Conclusions

Crucial parameters used in stellar simulation models, like reaction rates, are established through values derived from nuclear physics, particularly from experiments conducted under conditions relevant to stellar physics. Achieving these conditions represents a significant challenge, leading to the development of experimental systems dedicated to such measurements. The STELLA experiment has contributed to the determination of new reaction rates for the $^{12}C + {}^{12}C$ reaction, considering two different physical scenarios. Notably, the results obtained generally indicate lower rates than those commonly employed in the field. The sensitivity range of the measurements extends to the carbon-burning regions within stellar evolution models, notably 1 $M_\odot$ and 25 $M_\odot$. Preliminary studies of the consequences of these revised reaction rates have already been conducted, revealing various effects on nucleosynthesis and the duration of the carbon combustion phase, among other factors. Beyond their influence on the carbon-burning phase of massive stars, further investigations should explore their impacts in scenarios where carbon fusion reactions are critical at lower temperatures. This is particularly significant in cases where discrepancies with older rate data are most pronounced, such as in the context of carbon burning in the study of limit between intermediate-mass and massive stars (Gerónimo et al. 2023), type Ia supernovae, or even in superbursts (Strohmayer & Brown 2002).

STELLA was funded by the University of Strasbourg IdEX program and CNRS IN2P3. JN acknowledges support from the Interdisciplinary Thematic Institute QMat, as part of the ITI 2021 2028 program of the University of Strasbourg, CNRS and Inserm, which was supported by IdEx Unistra (ANR 10 IDEX 0002), and by SFRI STRAT'US project (ANR 20 SFRI 0012)

and EUR QMAT ANR-17-EURE-0024 under the framework of the French Investments for the Future Program. This work was supported by the European Union (ChETEC-INFRA, project no. 101008324).

References

Aguilera, E. F., Rosales, P., Martinez-Quiroz, E., et al. 2006, Phys. Rev. C, 73, 064601

Barrón-Palos, L., Aguilera, E., Aspiazu, J., et al. 2006, Nuclear Physics A, 779, 318

Becker, H. W., Kettner, K. U., Rolfs, C., & Trautvetter, H. P. 1981, Zeitschrift für Physik A Atoms and Nuclei, 303, 305

Bennett, M. E., Hirschi, R., Pignatari, M., et al. 2012, Monthly Notices of the Royal Astronomical Society, 420, 3047

Bucher, B., Tang, X. D., Fang, X., et al. 2015, Phys. Rev. Lett., 114, 251102

Caughlan, G. R. & Fowler, W. A. 1988, Atomic Data and Nuclear Data Tables, 40, 283

Choplin, A., Maeder, A., Meynet, G., & Chiappini, C. 2016, A&A, 593, A36

Eggenberger, P., Meynet, G., Maeder, A., et al. 2008, Astrophysics and Space Science, 316, 43

Fruet, G., Courtin, S., Heine, M., et al. 2020, Phys. Rev. Lett., 124, 192701

Gerónimo, F. C. D., Bertolami, M. M. M., Catelan, M., & Battich, T. 2023, Uncertainties in the 12C+12C reaction rate and their impact on the composition of ultra-massive WDs

Heine, M., Courtin, S., Fruet, G., et al. 2018, Nuclear Instruments and Methods in Physics Research Section A: Accelerators, Spectrometers, Detectors and Associated Equipment, 903, 1

High, M. & Čujec, B. 1977, Nuclear Physics A, 282, 181

Hirschi, R. 2004, Massive rotating stars : the road to supernova explosion (Université de Genève. Thèse)

Illiadis, C. 2015, Nuclear Physics of Stars, 2nd edn. (Wiley-VCH)

Jenkins, D. & Courtin, S. 2015, Journal of Physics G: Nuclear and Particle Physics, 42, 034010

Jiang, C. L., Back, B. B., Esbensen, H., et al. 2013, Phys. Rev. Lett., 110, 072701

Jiang, C. L., Esbensen, H., Rehm, K. E., et al. 2002, Phys. Rev. Lett., 89, 052701

Jiang, C. L., Rehm, K. E., Back, B. B., & Janssens, R. V. F. 2007, Phys. Rev. C, 75, 015803

Jiang, C. L., Rehm, K. E., Fang, X., et al. 2012, Nuclear Instruments and Methods in Physics Research Section A: Accelerators, Spectrometers, Detectors and Associated Equipment, 682, 12

Jiang, C. L., Santiago-Gonzalez, D. and Almaraz-Calderon, S., Rehm, K. E., et al. 2018, Phys. Rev. C, 97, 012801

Monpribat, E., Choplin, A., Martinet, S., et al. 2023, EPJ Web Conf., 279, 11016

Monpribat, E., Martinet, S., Courtin, S., et al. 2022, A&A, 660, A47

Patterson, J., Winkler, H., & Zaidins, C. 1969, The Astrophysical Journal, 157, 367

Pignatari, M., Hirschi, R., Wiescher, M., et al. 2013, ApJ, 762, 31

Spillane, T., Raiola, F., Rolfs, C., et al. 2007, Phys. Rev. Lett., 98, 122501

Strohmayer, T. E. & Brown, E. F. 2002, ApJ, 566, 1045

Tan, W. P., Boeltzig, A., Dulal, C., et al. 2020, Phys. Rev. Lett., 124, 192702

SF2A 2023
M. N'Diaye, A. Siebert, N. Lagarde, O. Venot, K. Baillié, M. Béthermin, E. Lagadec, J. Malzac, J. Richard (eds)

THE GRAVITY VIEW OF THE INNERMOST REGIONS OF PROTOPLANETARY DISKS

K. Perraut[1], L. Labadie[2], J. Bouvier[1] and the GRAVITY Collaboration[3]

Abstract. Probing the innermost regions of the protoplanetary disks where micron-sized dust grains grow to pebbles and larger bodies producing the first building blocks of planets, and investigating star-disk interactions at sub-astronomical unit (sub-au) scale are of utmost interest as they define the initial and environmental conditions for planet formation. Since its installation in 2016, VLTI/GRAVITY has brilliantly illustrated the potential of the high angular and spectral resolutions to constrain the processes at play in the central au's of protoplanetary disks in the near-infrared K-band (around 2.2 μm). With a sample of a hundred young stellar objects (YSO), from solar-like (namely the T Tauri) to high-mass YSO, the YSO GTO Large Program has gathered a large homogeneous data set allowing us to simultaneously study the emission of dust and of the hot (e.g., Brγ Hydrogen I line) and warm (e.g., CO bandheads) gas. In this talk, I will review the most striking results obtained with GRAVITY during its first 5 years of operation and illustrate the opportunities opened by the future upgrade GRAVITY+.

Keywords: Pre-main sequence stars, protoplanetary disks, optical long-baseline interferometry

1 Introduction

With more than 5300 exoplanets detected so far, it is clear that planet formation is a robust and efficient process. Statistically, most solar-mass stars should host at least one planet. The current population of known exoplanets shows an incredible diversity, both in the nature (mass, radius) of the planets themselves, but also in the architecture of these systems. More striking, the majority of exoplanetary systems revealed by Kepler transits consist of chains of low-mass planets, super-Earths and mini-Neptunes alike, located close to their host stars. The origin of this diversity, its connection to planetary migration, and whether it is inherited from the initial stages of planet formation is still unclear. These observational results question what are the initial conditions that would favour the formation of compact, short-period planetary systems in the inner disk of young stars, at distances ranging from 0.1 astronomical units (au) to a few au from the central star (e.g., Mishra et al. 2023; Batygin & Morbidelli 2023; Li et al. 2022).

Understanding the origin of such a diversity requires exploring the birth environment of these planets, namely the planet-forming protoplanetary disk, that plays a crucial role as the mass reservoir of gas and dust from which matter is accreted onto the star and from which planets are built. The accretion of disk material onto the stellar surface directly impacts the star's properties and early evolution. It also produces high-energy radiation that illuminates the circumstellar disk and the proto-atmosphere of nascent planets, thus drastically affecting their physical and chemical evolution. Star formation, planet formation, and disk evolution processes occur simultaneously and influence each other. These mutual influences last for only a few million years but they set stellar and planetary properties that persist for billions of years. Thus, a deep understanding of the structure and evolution of protoplanetary disks, on both local and global scales, is required to comprehend the diverse outcome of the planet formation process. Thanks to its deep sensitivity in the near-infrared K-band and its exquisite spatial resolution of a fraction of au, GRAVITY (GRAVITY Collaboration et al. 2017) at the combined focus of the Very Large Telescope Interferometer (VLTI) of the European Southern Observatory (ESO) allows us to probe their inner au-scales.

[1] Univ. Grenoble Alpes, CNRS, IPAG, 38000 Grenoble, France

[2] I. Physikalisches Institut, Universität zu Köln, Zülpicher Str. 77, 50937, Köln, Germany

[3] GRAVITY is developed in a collaboration by the Max Planck Institute for Extraterrestrial Physics, LESIA of Paris Observatory and IPAG of Université Grenoble Alpes / CNRS, the Max Planck Institute for Astronomy, the University of Cologne, the Centro de Astrofísica e Gravitação and the European Southern Observatory.

© Société Française d'Astronomie et d'Astrophysique (SF2A) 2023

2 Probing the dust distribution in the innermost regions of the protoplanetary disks

Since its start of operation in 2016, about 60 Herbig Ae-Be stars and 40 G-K-M T Tauri stars have been observed within the GRAVITY YSO Large Program, which allowed the inner disk radius - stellar luminosity relation to be explored over more than 4 decades in stellar luminosity, and to look for trends between the properties of the central star and the disk morphology. Combined with the previous PIONIER surveys (Lazareff et al. 2017; Kluska et al. 2020), our GRAVITY data sets have enabled us to constrain the geometry and the temperature of sublimation fronts (GRAVITY Collaboration et al. 2019, 2021), highlighting their widening, which could trace a highly differentiated particle size distribution. These studies provide unique inputs to test advanced simulations of the inner disk rim, notably regarding the presence of a dead-zone at the inner edge (Flock et al. 2016, 2017).

With our large sample, the origins of gaps in the innermost regions were put into test through a comparison between the dust emission sizes measured with GRAVITY and size predictions from photoevaporation models. In the model of Gorti et al. (2009), heating by the stellar radiations in the Extreme and Far UV, and the X-rays induces the opening of a gap in the protoplanetary disk with a peak efficiency at a critical radius r_c; this gap formation takes ∼4 Myr for solar-type masses and is likely shorter for masses larger than 3 $M_\odot$, while the clearing of the whole cavity takes ∼0.5 Myr. All GRAVITY measurements (but for one object) lie below the critical radius computed for a standard 10^4 K gas temperature (Fig. 1). For the younger objects of our sample (blue symbols), the smaller sizes compared to r_c are compatible with a scenario where photo-evaporation has just started and the cavity is not totally void of dust, but for the older sources (yellow, green, and red symbols), EUV/FUV/X-ray photoevaporation seems not to be the dominant process that clears the inner cavity and other scenarios might be invoked (EUV/X-ray photoevaporation, dynamical clearing by young planets, ...).

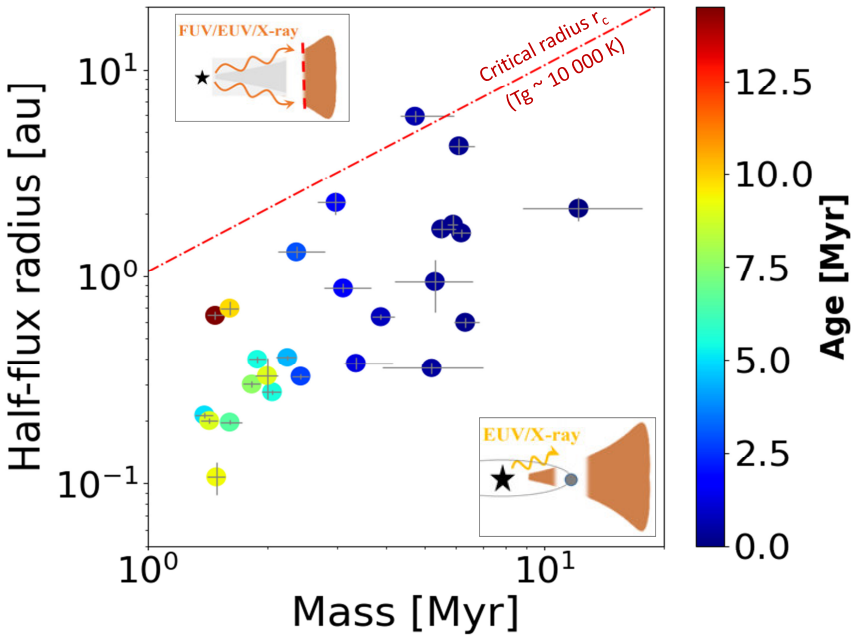

Fig. 1. K-band half-flux radii measured with GRAVITY of a function of the mass and age (color) of the Herbig stars of the GRAVITY YSO sample, compared to the critical radius (red dash-dotted line) when gaps are opened by X-EUV-FUV photoevaporation as modeled by Gorti et al. (2009). Adapted from GRAVITY Collaboration et al. (2019).

3 Probing the magnetospheric accretion flows

Thanks to its spectroscopic ability with a spectral resolution of about 4000 over the whole K band, GRAVITY has led to the spatial resolution of the Hydrogen Brγ emitting regions around a sample of Herbig and T Tauri

stars. The GRAVITY measurements allow the size of the emitting region to be determined: this region is in most of the case more compact than the continuum emitting region, and corresponds to a few stellar radii. The comparison between these sizes, the corotation radius, and the truncation radius derived from spectro-polarimetric observations allows the dominant driver of the Brγ line to be investigated: if the magnetospheric accretion process dominates, the Brγ emitting region is expected to be on the order of the corotation radius, or even slightly more compact, which is what we observed for the weakest accretors in our sample DoAr 44 (Bouvier et al. 2020), TW Hya (Gravity Collaboration et al. 2020), and CI Tau (Gravity Collaboration et al. 2023a). For most of the other objects, the Brγ half flux radii extend to scales outside the corotation radius, suggesting a wind contribution (Gravity Collaboration et al. 2023b). More interestingly, the interferometric differential phases provided by GRAVITY across the Brγ line are proxies of offsets between the photocenters of the continuum and of the Brγ line emitting regions, that could be interpreted as the first resolution of an accretion flow onto the central star as in the case of DoAr 44 (Bouvier et al. 2020).

Within the framework of the ERC SPIDI project*, huge efforts were made to develop advanced Radiative Transfer codes (Tessore et al. 2021) and Magneto-HydroDynamical simulations (Pantolmos et al. 2020) to model the inner disk rim and the accretion flows onto the central star. These tools produce intensity maps from which synthetic interferometric observables could be computed and compared with our GRAVITY observations (Tessore et al. 2023).

4 Prospects for GRAVITY+

While the unique, homogeneous data set obtained with the GRAVITY instrument has already enabled us to carry out statistical studies, the current instrumental context is even more promising, particularly with the imminent arrival (2025) of the GRAVITY+ instrument at the VLTI. GRAVITY+ is an upgrade of the entire VLTI infrastructure, which will equip the 4 unit telescopes (UTs) with modern adaptive optics (new deformable mirrors, new wavefront sensors) and laser guide stars. Both instrumental improvements will have an impact on all the interferometric instruments currently in operation or planned for the future. As far as GRAVITY is concerned, they will significantly increase its sensitivity and sky coverage, by enabling telescope guidance on stars of magnitude as low as 18 in G band (compared to 14 today), and fringe tracking on sources of magnitude 13 in K band with UTs (compared with 10 at present) and possibly separated by 30" (instead of 2" at present). GRAVITY+ will enable us to spatially resolve for the first time in the near-infrared range the environment of most T Tauri stars (over 300 stars in the Taurus star-forming region alone), and thus extend our observations to several star-forming regions (Fig. 2), such as Serpens (1-3 Myr old), σ Ori (3-5 Myr old), and Upper Sco (5-10 Myr old). The future sample will thus cover a wider range of parameters in terms of mass, luminosity, age, and accretion regime.

In addition, this increase in performance will provide a better overlap with other observational techniques, particularly spectro-polarimetry. This technique, notably with the ESPaDOnS (Donati et al. 2006) and SPIRou (Donati et al. 2020) instruments at the Canada-France-Hawaii-Telescope, enables us to determine the topology of the stellar magnetic field, follow its temporal evolution, and study its impact on the inner disk. Combining these observations with the new GRAVITY+ observations will allow the magnetospheric accretion scenario to be tested for a more representative set of young stars, including lower-mass, and younger embedded sources that would become observable with near-infrared interferometry for the first time.

5 Conclusions

The GRAVITY Young Stellar Object Large Program has already provided an invaluable homogeneous data set enabling demographic studies, variability follow-up, and test of inner disk and star-disk interaction advanced models. Combined within multi-technique and multi-wavelength campaigns, and with advanced radiative transfer and MHD simulations, the GRAVITY+ observations will be key to obtain a global picture of the inner parts of the protoplanetary disks and provide clues to the conditions prevailing over the formation of close-in planets.

We acknowledge the funding of the French National Program of Stellar Physics (PNPS) and support from the European Research Council (ERC) under the European Union's Horizon 2020 research and innovation programme (grant agreement No 742095; *SPIDI*: Star-Planets-Inner Disk-Interactions), and from LabEx OSUG@2020 (Investissements d'avenir - ANR10LABX56).

*spidi-eu.org

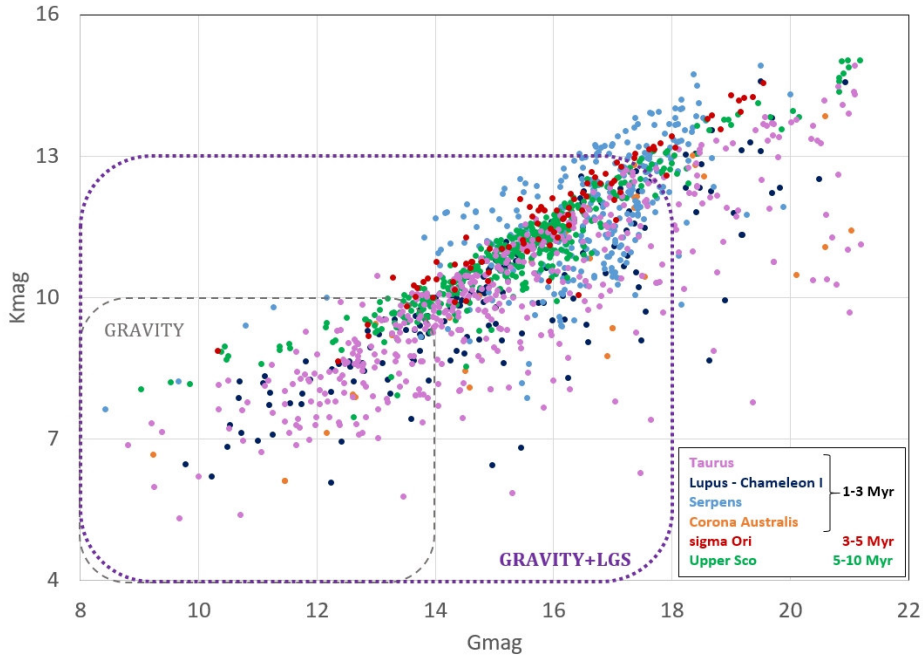

Fig. 2. Color-color diagram of the YSOs currently observable with GRAVITY (in the gray dashed area) and observable in the future with GRAVITY+ when equipped with the Laser Guide Stars (LGS; purple dotted area). The color codes the star-forming regions of different ages.

References

Batygin, K. & Morbidelli, A. 2023, Nature Astronomy, 7, 330

Bouvier, J., Perraut, K., Le Bouquin, J. B., et al. 2020, A&A, 636, A108

Donati, J. F., Catala, C., Landstreet, J. D., & Petit, P. 2006, in Astronomical Society of the Pacific Conference Series, Vol. 358, Solar Polarization 4, ed. R. Casini & B. W. Lites, 362

Donati, J. F., Kouach, D., Moutou, C., et al. 2020, MNRAS, 498, 5684

Flock, M., Fromang, S., Turner, N. J., & Benisty, M. 2016, ApJ, 827, 144

Flock, M., Fromang, S., Turner, N. J., & Benisty, M. 2017, ApJ, 835, 230

Gorti, U., Dullemond, C. P., & Hollenbach, D. 2009, ApJ, 705, 1237

GRAVITY Collaboration, Abuter, R., Accardo, M., et al. 2017, A&A, 602, A94

Gravity Collaboration, Garcia Lopez, R., Natta, A., et al. 2020, Nature, 584, 547

GRAVITY Collaboration, Perraut, K., Labadie, L., et al. 2021, A&A, 655, A73

GRAVITY Collaboration, Perraut, K., Labadie, L., et al. 2019, A&A, 632, A53

Gravity Collaboration, Soulain, A., Perraut, K., et al. 2023a, A&A, 674, A203

Gravity Collaboration, Wojtczak, J. A., Labadie, L., et al. 2023b, A&A, 669, A59

Kluska, J., Berger, J. P., Malbet, F., et al. 2020, A&A, 636, A116

Lazareff, B., Berger, J. P., Kluska, J., et al. 2017, A&A, 599, A85

Li, R., Chen, Y.-X., & Lin, D. N. C. 2022, MNRAS, 510, 5246

Mishra, L., Alibert, Y., Udry, S., & Mordasini, C. 2023, A&A, 670, A68

Pantolmos, G., Zanni, C., & Bouvier, J. 2020, A&A, 643, A129

Tessore, B., Pinte, C., Bouvier, J., & Ménard, F. 2021, A&A, 647, A27

Tessore, B., Soulain, A., Pantolmos, G., et al. 2023, A&A, 671, A129

SF2A 2023
M. N'Diaye, A. Siebert, N. Lagarde, O. Venot, K. Baillié, M. Béthermin, E. Lagadec, J. Malzac, J. Richard (eds)

DO NONLINEAR EFFECTS DISRUPT TIDAL DISSIPATION PREDICTIONS IN CONVECTIVE ENVELOPES?

A. Astoul[1] and A. J. Barker[1]

Abstract. Most prior works studying tidal interactions in tight star/planet or star/star binary systems have employed linear theory of a viscous fluid in a uniformly-rotating two-dimensional spherical shell. However, compact systems may have sufficiently large tidal amplitudes for nonlinear effects to be important. We compute tidal flows subject to nonlinear effects in a 3D, thin (solar-like) convective shell, spanning the entire frequency range of inertial waves. Tidal frequency-averaged dissipation predictions of linear theory with solid body rotation are approximately reproduced in our nonlinear simulations (though we find it to be reduced by a factor of a few), but we find significant differences, potentially by orders of magnitude, at a fixed tidal frequency corresponding to a specific two-body system at a given epoch. This is largely due to tidal generation of differential rotation (zonal flows) and their effects on the waves.

Keywords: tidal interaction, astrophysical fluid dynamics, star-planet interactions, close binary stars, low mass stars, extrasolar gaseous giant planets

1 Introduction

Tidal interactions play an important role in driving spin-orbit evolution in close planetary and stellar binary systems. A key mechanism in low-mass stars and giant planets is tidal dissipation of inertial waves (restored by the Coriolis acceleration) in their convective envelopes (e.g. Ogilvie & Lin 2004; Barker 2022). For sufficiently compact systems, like for Hot Jupiter-like planets orbiting in a day or less around their host stars, the tidal flows are likely to be sensitive to nonlinear effects (e.g. Ogilvie 2014). We build upon the numerical model of Astoul & Barker (2022) to simulate the nonlinear hydrodynamical dissipation of tidally-excited inertial waves in a 3D spherical shell containing an incompressible, viscous and adiabatically-stratified fluid. We aim to investigate the robustness of linear estimates of tidal dissipation derived for solid body rotation. For this purpose, we compute the imaginary part of the Love number $\mathrm{Im}\left[k_2^2(\omega)\right]$ and the associated modified tidal quality factor $Q'_\omega = 3/\left|2\,\mathrm{Im}\left[k_2^2(\omega)\right]\right|$ over the entire range of frequencies allowed for inertial waves. Here, we focus on large tidal forcing amplitudes relevant for close giant gaseous planets, and a thin (solar-like) convective shell (representing either the star or the outer envelope of a giant planet) with fractional inner radius $\alpha = 0.7$.

2 Tidal dissipation with nonlinear effects

Using the pseudo-spectral code MagIC (`https://magic-sph.github.io/`) amended to study tidally-excited inertial waves (of velocity $\boldsymbol{u}$ and forcing frequency ω) in convective envelopes, we compute the volume-averaged ($\langle\cdot\rangle$) dimensionless tidal dissipation $D_\nu(\omega) = -\langle \nu \boldsymbol{u}\cdot\Delta\boldsymbol{u}\rangle$ with (atomic or turbulent) viscosity ν (see Astoul & Barker 2022; Astoul & Barker 2023, for more details). In our simulations, the emergence of cylindrical differential rotation triggered by nonlinear self-interactions of inertial waves causes large departures from linear predictions with solid body rotation. This is particularly true for a thin shell with high tidal forcing amplitudes and a low viscosity, as shown in Fig. 1. We display the frequency-dependent and frequency-averaged tidal dissipation:

$$\left|\mathrm{Im}\left[k_2^2(\omega)\right]\right| = \frac{6}{5}\frac{D_\nu(\omega)}{|\omega|}\frac{\epsilon_\mathrm{t}^2}{C_\mathrm{t}^2}, \quad \text{and} \quad \Lambda \equiv \int_{-\infty}^{+\infty} \mathrm{Im}\left[k_2^2(\omega)\right]\,\frac{\mathrm{d}\omega}{\omega}, \tag{2.1}$$

with the tidal forcing amplitude $C_\mathrm{t} = \left(1+\mathrm{Re}\left[k_2^2\right]\right)(M_2/M_1)(R/a)^3$, and $\epsilon_\mathrm{t} = \left(1+\mathrm{Re}\left[k_2^2\right]\right)\Omega/\sqrt{GM_1/R^3}$. For a homogeneous convective shell, $\Lambda_\mathrm{l} = 16\pi\,\epsilon_\mathrm{t}^2\alpha^5/[63(1-\alpha^5)]$ in linear theory (Ogilvie 2013).

[1] Department of Applied Mathematics, School of Mathematics, University of Leeds, Leeds, LS2 9JT, UK

© Société Française d'Astronomie et d'Astrophysique (SF2A) 2023

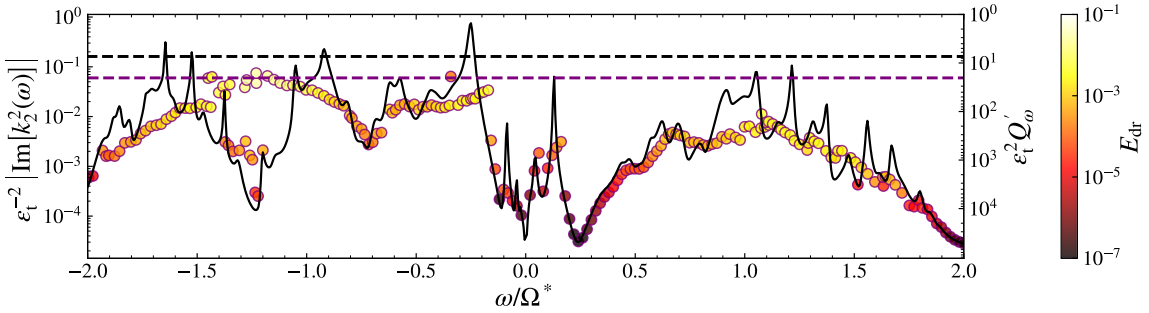

Fig. 1. Imaginary part of the Love number Im $\left[k_2^2(\omega)\right]$, or equivalently, modified tidal quality factor Q'_ω, both re-scaled (so system-independent), versus the Doppler-shifted frequency ω in the rotating frame with mean rotation Ω^*. Parameters are $\alpha = 0.7$, $C_t = 5 \cdot 10^{-2}$, and Ekman number $E = \nu/(\Omega R^2) = 10^{-5}$ (with R the radius and Ω the initial rotation). Linear predictions are shown in black (the black dashed line is Λ_l), while nonlinear ones are shown in reddish colour (E_{dr} quantifies the strength of zonal flows), while the frequency-averaged nonlinear Λ is shown by the purple dashed line.

2.1 Tidal dissipation in HAT-P-65 b

As an example, we calculate the tidal dissipation due to eccentricity tides in the Hot Jupiter HAT-P-65 b, which may have an eccentricity up to $e \approx 0.3$*. By assuming the planet's rotation is quasi-synchronised with its orbit, we have $\omega/\Omega^* = \pm 1$ for the dominant tidal component. By setting Re $\left[k_2^2\right] = 0.6$ (Dewberry & Lai 2022), we estimate that the dominant amplitude for eccentric tides is $7e\,C_t/2 \approx 5 \cdot 10^{-2}$ (Astoul & Barker 2023), and $\epsilon_t \approx 0.27$ which means the planet is strongly deformed by its rotation. Then, using Fig. 1 (i.e. assuming the planet has a convective shell with $\alpha = 0.7$), the linear and nonlinear frequency-dependent tidal quality factors are, respectively, $Q'_\omega \sim 8 \cdot 10^2$ and $Q'_\omega \sim 3 \cdot 10^3$ for $\omega = 1$. Therefore, taking into account nonlinear effects reduces tidal dissipation in HAT-P-65 b by almost a factor 4. For comparison, the linear frequency-averaged tidal quality factor, $Q' \sim 10^2$, being dominated by the most dissipative resonant peaks, is more than 1 order of magnitude smaller than the frequency-dependent nonlinear value (hence the latter is less dissipative).

3 Conclusions

We have performed a nonlinear exploration of tidal dissipation estimates in convective envelopes representing low-mass stars or giant gaseous planets in close systems, over a large range of forcing frequencies (different shell thicknesses, tidal amplitudes, and viscosities, are discussed in Astoul & Barker 2023). Though nonlinear frequency-averaged tidal dissipation estimates are only moderately attenuated from prior linear predictions, nonlinear frequency-dependent rates can strongly differ from the linear ones (and from the frequency-averaged value), particularly when the shell is thin (large α), the viscosity is low, and the tidal forcing is strong, as evidenced for our application to HAT-P-65 b. Differential rotation, especially the interactions between inertial waves and zonal flows, play a key role in smoothing and mitigating the highly frequency-dependent peaky tidal dissipation spectra (see Fig. 1). Our results indicate that a more realistic treatment of tidal flows including nonlinear effects/differential rotation is necessary to model the spin/orbit evolution of a close two-body system.

Funded by STFC grants ST/S000275/1 and ST/W000873/1, and by a Leverhulme Trust Early Career Fellowship to AA.

References

Astoul, A. & Barker, A. J. 2022, MNRAS, 516, 2913
Astoul, A. & Barker, A. J. 2023, The Astrophysical Journal Letters, 955, L23
Barker, A. J. 2022, ApJ, 927, L36
Dewberry, J. W. & Lai, D. 2022, ApJ, 925, 124
Ogilvie, G. I. 2013, MNRAS, 429, 613
Ogilvie, G. I. 2014, ARA&A, 52, 171
Ogilvie, G. I. & Lin, D. N. C. 2004, ApJ, 610, 477

*From the `http://exoplanet.eu/` database, also used to calculate C_t and ϵ_t.

SF2A 2023
M. N'Diaye, A. Siebert, N. Lagarde, O. Venot, K. Baillié, M. Béthermin, E. Lagadec, J. Malzac, J. Richard (eds)

IMPACT OF THE MAGNETIC FIELD ON THE STOCHASTIC EXCITATION OF P-MODES

L. Bessila[1] and S. Mathis[1]

Abstract. We model the stochastic excitation of p-modes to take into account magnetic fields. First, we derive the forced wave equation with a magnetic field and compute the source terms which inject energy into the oscillations. We make use of magnetized convection Mixing Length Theory (hereafter noted MLT) to assess how the convective velocity is modified by the magnetic field. Finally, we derive scaling laws for the modes amplitudes depending on the ratio between the local Alfvén and MLT convective velocities.

Keywords: helioseismology, asteroseismology, Sun, Stars, pulsations (including oscillations), convection, magnetic field

1 Introduction

Amplitudes of acoustic modes in solar-like stars are intrinsically linked to the properties of turbulent convection, which acts as their excitation source. Their detection is the best way to determine the key global properties of these stars (i.e. their masses and their radius) and their age (e.g. García & Ballot 2019). Recent observational works using results of the *Kepler* space mission, showed that acoustic modes' signal is not detected in a large fraction of solar-type stars (Chaplin et al. 2011; Mathur et al. 2019), where they are nevertheless expected because of their convective envelope. This non-detection is a function of both stellar magnetism and rotation. One hypothesis is that the excitation source term is too low to trigger the oscillations. In addition, observations of solar-type stars show that the amplitudes of stellar acoustic modes are modulated along their magnetic activity cycles (Garcia et al. 2010). Rotation and magnetic fields strongly influence convection (e.g. Stevenson 1979), but their action is most of the time ignored in the models. For the first time, we extend the theoretical formalism for stochastic excitation of p-modes (Samadi & Goupil 2001) to assess the impact of the magnetic field.

2 Stochastic wave excitation with a magnetic field

Following the method of Samadi & Goupil (2001), we derive the inhomogeneous wave equation :

$$\rho_0 \left(\partial_{\mathrm{tt}} - \mathcal{L}\right)\left(\boldsymbol{u}_{\mathrm{osc}}, \boldsymbol{b}_{\mathrm{osc}}\right) + \mathcal{D}(\boldsymbol{u}_{\mathrm{osc}}, \boldsymbol{b}_{\mathrm{osc}}, \boldsymbol{U}_{\mathrm{t}}, \boldsymbol{B}_{\mathrm{t}}) = \partial_t \mathcal{S}(\boldsymbol{U}_t, \boldsymbol{B}_t), \tag{2.1}$$

where $\boldsymbol{u}_{\mathrm{osc}}$ (resp. $\boldsymbol{U}_t$) is the oscillation velocity (resp. turbulent velocity), $\boldsymbol{b}_{\mathrm{osc}}$ (resp. $\boldsymbol{B}_t$) is the wave magnetic field (resp. turbulent magnetic field), $\mathcal{L}$ is the linear wave operator, $\mathcal{D}$ is a damping term, and the oscillations source term is $\mathcal{S} = \mathcal{S}_R + \mathcal{S}_B$. $\mathcal{S}_R = -\nabla : (\rho_0 \boldsymbol{U}_t \boldsymbol{U}_t)$ is the Reynolds-stresses source term, and $\mathcal{S}_B = \nabla : \left(B_i B_j/\mu_0 - \delta_{ij} B^2/2\mu_0\right)$ is the source term due to the Maxwell-stresses, where δ_{ij} is the Kronecker symbol, and we use Einstein convention for the tensorial form of the stresses. Furthermore, as demonstrated in Samadi & Goupil (2001), the temporal average of the squared modes amplitudes is proportional to the squared source term : $\langle |A(t)|^2 \rangle \propto \mathcal{S}^2$.

[1] Université Paris-Saclay, Université Paris Cité, CEA, CNRS, AIM, F-91191, Gif-sur-Yvette, France

© Société Française d'Astronomie et d'Astrophysique (SF2A) 2023

3 Scaling laws for p-modes amplitudes

We derive scaling laws for the source terms, taking the magnetic field into account. We introduce the ratio between the mode's amplitude with and without magnetic field : $\frac{\langle |A(t)|^2 \rangle_{\rm mag}}{\langle |A(t)|^2 \rangle_0} \propto \frac{\mathcal{S}^2_{\rm mag}}{\mathcal{S}^2_0}$, where $\langle . \rangle$ denotes the statistical average on an infinite number of independent realisations. $\mathcal{S}_{\rm mag}$ (resp. $\mathcal{S}_0$) is the source term with a magnetic field (resp. with no magnetic field). Not only does the magnetic field add up a new source term through the Maxwell-stresses, but it also changes the Reynolds-stresses source term through the modification of convection by the magnetic field. To account for this modification, we use Stevenson (1979) scaling laws in magnetized convection, with MLT. These make use of the inverse Alfvén number : $A = v_A^2/u_0^2$, where $v_A = B^2/\sqrt{\mu_0 \rho_0}$ is the Alfvén velocity and u_0 the convective velocity when the magnetic field is ignored. For values of $A < 1$, which is the case at the top of the convective zone where the acoustic modes are excited in solar-type stars, one has : $\frac{\mathcal{S}^2_{\rm mag}}{\mathcal{S}^2_0} \sim \left(1 - \frac{11A}{75}\right)^2 \left(1 - \frac{A}{\left(1 - \frac{11}{75A^2}\right)^2}\right)$. For values of $A > 1$, $\frac{\mathcal{S}^2_{\rm mag}}{\mathcal{S}^2_0} \sim \frac{0,92^2}{A}\left(1 - \frac{A^2}{2 \cdot 0,92^2}\right)$. As shown in Fig. 1, there are two different regimes : when increasing the magnetic field, the modes amplitudes tend to be lower and lower, thus it is the tendency found in observations. Above $A = 1$, the Maxwell-stresses become the dominant source and the modes amplitudes increase with the magnetic field.

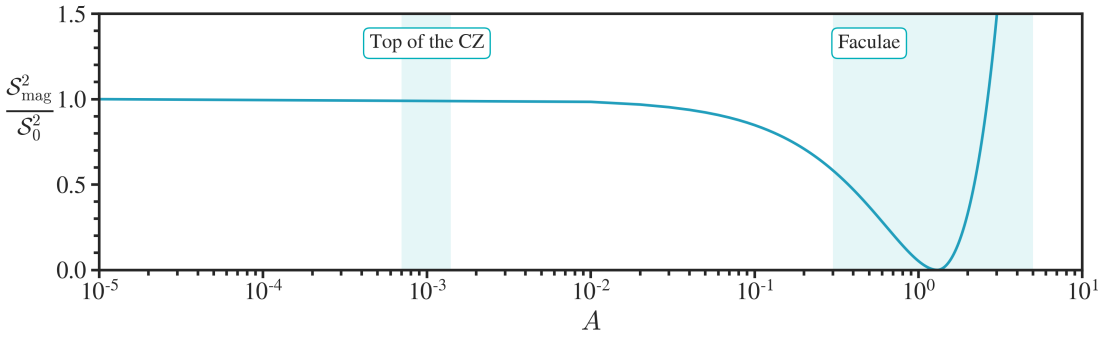

Fig. 1. Scaling of the relative modes amplitude as a function of the inverse Alfvén number A.

4 Conclusions

In this work, we have derived the inhomogeneous wave equation, which allows us to study the stochastic excitation of stellar oscillation modes in the presence of magnetic fields. We identify the supplementary source term due to magnetic Maxwell stresses and account for the modification of convection using the Magnetic MLT. We show that in the weak magnetic field regime the injection of energy diminishes when the field amplitude increases because of the inhibition of Reynolds-stresses by the magnetic field. In the strong field regime, the Maxwell-stresses dominate and the power injection of energy in stellar oscillation is increased.

L. B. and S. M. acknowledge support from the CNES SOHO/GOLF and PLATO grants at DAp/AIM at CEA and from PNPS (CNRS/INSU).

References

Chaplin, W. J., Bedding, T. R., Bonanno, A., et al. 2011, The Astrophysical Journal, 732, L5

Garcia, R. A., Mathur, S., Salabert, D., et al. 2010, Science, 329, 1032, arXiv:1008.4399 [astro-ph]

García, R. A. & Ballot, J. 2019, Living Reviews in Solar Physics, 16, 4, aDS Bibcode: 2019LRSP...16....4G

Mathur, S., Garcia, R. A., Bugnet, L., et al. 2019, Frontiers in Astronomy and Space Sciences, 6, 46, arXiv:1907.01415 [astro-ph]

Samadi, R. & Goupil, M.-J. 2001, Astronomy & Astrophysics, 370, 136

Stevenson, D. J. 1979, Geophysical & Astrophysical Fluid Dynamics, 12, 139, publisher: Taylor & Francis

SF2A 2023
M. N'Diaye, A. Siebert, N. Lagarde, O. Venot, K. Baillié, M. Béthermin, E. Lagadec, J. Malzac, J. Richard (eds)

MEASURING STELLAR ROTATION AND ACTIVITY WITH PLATO

S. N. Breton[1], A. F. Lanza[1], S. Messina[1], R. A. García[2], S. Mathur[3], A. R. G. Santos[4], L. Bugnet[5], E. Corsaro[1] and I. Pagano[1]

Abstract. Due to be launched late 2026, the PLATO mission will bring the study of main-sequence solar-type and low-mass stars into a new era. In particular, PLATO will provide the community with a stellar sample with solar-type oscillations and activity-induced brightness modulation of unequalled size. We present here the main features of the analysis module that will be dedicated to measure stellar surface rotation and activity in the PLATO Stellar Analysis System.

Keywords: PLATO, stellar physics, stellar rotation, stellar activity

1 Introduction

The Planetary Transit and Oscillations of stars (PLATO, Rauer et al. 2014) mission will provide high-cadence photometric light curves for hundreds of thousand of solar-type stars. The Module for Stellar Astrophysics number 4 (MSAP4), currently under development, is the PLATO pipeline component dedicated to analyse stellar surface rotation and surface magnetic activity including magnetic cycles in the light curves acquired by the mission.

2 The MSAP4 module

2.1 General framework

The flow diagram of the MSAP4 module is shown in Fig. 1. Using the stellar light curve and corresponding periodogram, MSAP4 will perform several analyses in order to provide values for the spectral background components (Corsaro & De Ridder 2014; Corsaro et al. 2015), the logarithm of surface gravity, log g (Bugnet et al. 2018), the average surface rotation period, $P_{\rm rot}$, the photometric activity index, $S_{\rm ph}$ (Mathur et al. 2014), the Rossby number, *Ro* (Noraz et al. 2022), and long-term variability periods, $P_{\rm cycle}$. The demonstration code for MSAP4 is fully open-source* and modular, with dedicated documentation and tutorials†.

2.2 Extracting rotation

For stars ranging from M- to F- type, MSAP4 will measure surface rotation periods. To ensure robustness of the analysis, rotation-related parameters are extracted with several methods. In MSAP4-01, Fourier analysis is performed with the generalised Lomb-Scargle (GLS, Zechmeister & Kürster 2009). In MSAP4-02, a time series analysis is performed by computing the autocorrelation function (ACF, McQuillan et al. 2013) In MSAP4-03, the two methods are combined to enhance common periodicities, yielding the composite spectrum (CS, Ceillier et al. 2016). These results are combined using the machine-learning methodology Random fOrests Over STEllar Rotation (ROOSTER, Breton et al. 2021). In particular, ROOSTER will provide a reliability score for the measured period. $S_{\rm ph}$ and *Ro* are finally computed using the measured $P_{\rm rot}$.

[1] INAF - Osservatorio Astrofisico di Catania, Via S. Sofia, 78, 95123 Catania, Italy
[2] Université Paris-Saclay, Université Paris Cité, CEA, CNRS, AIM, F-91191, Gif-sur-Yvette, France
[3] Instituto de Astrofísica de Canarias, 38205 La Laguna, Tenerife, Spain
Departamento de Astrofísica, Universidad de La Laguna (ULL), 38206 La Laguna, Tenerife, Spain
[4] Instituto de Astrofísica e Ciências do Espaço, Universidade do Porto, CAUP, Rua das Estrelas, PT4150-762 Porto, Portugal
[5] Institute of Science and Technology Austria (IST Austria), Am Campus 1, Klosterneuburg, Austria
*The source code can be downloaded here: `https://gitlab.com/sybreton/plato_rotation_pipeline`.
†The documentation is hosted here: `https://plato-rotation-pipeline.readthedocs.io/en/latest/`.

© Société Française d'Astronomie et d'Astrophysique (SF2A) 2023

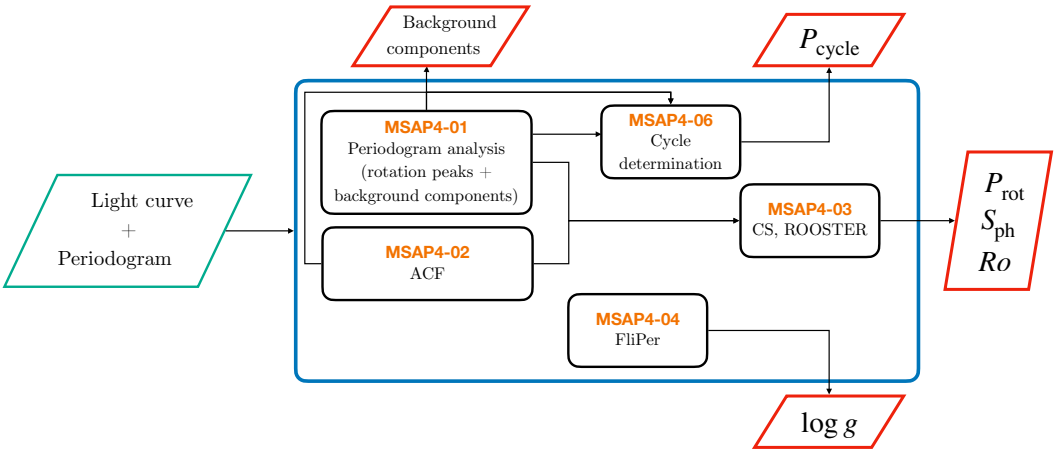

Fig. 1. Flow diagram of the MSAP4 module.

2.3 Looking for cyclic modulations

In addition to surface rotation measurements, long-term variability in the light curves will be searched: solar-type magnetic activity cycle, but also shorter cycle such as Rieger-like cycles (Rieger et al. 1984). To this purpose, measurements from the GLS, the ACF, and the $S_{\rm ph}$ modulation will be combined.

3 Conclusions

PLATO will enable to obtain new insights on the interaction between rotation and activity in main-sequence low-mass stars. Combined with the asteroseismic measurements that the mission will also perform, it will provide an unprecedented sample of stars with exquisite characterisation.

S.N.B, A.F.L., Se.M., E.C., and I.P. acknowledge support from PLATO ASI-INAF agreement n. 2015-019-R.1-2018. R.A.G acknowledges support from PLATO and GOLF CNES grants. Sa.M. acknowledges support from the Spanish Ministry of Science and Innovation (MICINN) with the Ramón y Cajal fellowship no. RYC-2015-17697, grant no. PID2019-107187GB-I00 and PID2019-107061GB-C66, and through AEI under the Severo Ochoa Centres of Excellence Programme 2020–2023 (CEX2019-000920-S). A.R.G.S. acknowledges the support by FCT through national funds and by FEDER through COMPETE2020 by these grants: UIDB/04434/2020 & UIDP/04434/2020. A.R.G.S. is supported by FCT through the work contract No. 2020.02480.CEECIND/CP1631/CT0001.

References

Breton, S. N., Santos, A. R. G., Bugnet, L., et al. 2021, A&A, 647, A125
Bugnet, L., García, R. A., Davies, G. R., et al. 2018, A&A, 620, A38
Ceillier, T., van Saders, J., García, R. A., et al. 2016, MNRAS, 456, 119
Corsaro, E. & De Ridder, J. 2014, A&A, 571, A71
Corsaro, E., De Ridder, J., & García, R. A. 2015, A&A, 579, A83
Mathur, S., Salabert, D., García, R. A., & Ceillier, T. 2014, Journal of Space Weather and Space Climate, 4, A15
McQuillan, A., Aigrain, S., & Mazeh, T. 2013, MNRAS, 432, 1203
Noraz, Q., Breton, S. N., Brun, A. S., et al. 2022, A&A, 667, A50
Rauer, H., Catala, C., Aerts, C., et al. 2014, Experimental Astronomy, 38, 249
Rieger, E., Share, G. H., Forrest, D. J., et al. 1984, Nature, 312, 623
Zechmeister, M. & Kürster, M. 2009, A&A, 496, 577

SF2A 2023
M. N'Diaye, A. Siebert, N. Lagarde, O. Venot, K. Baillié, M. Béthermin, E. Lagadec, J. Malzac, J. Richard (eds)

IMPROVING STELLAR MODELING WITH NEW PRECISE NUCLEAR REACTION RATES DETERMINED FROM NUCLEAR EXPERIMENT

T. Dumont[1], E. Monpribat[1,], A. Choplin[2], A. Bonhomme[1,], M. Heine[1,], J. Nippert[1,] and S. Courtin[1,3]

Abstract. The origin of elements in the Universe is still a challenging question today. From the Big Bang nucleosynthesis that formed the lightest elements (essentially H and He), all the heavier were since synthesized through the stellar nucleosynthesis involving different processes with mainly nuclear fusion or particle capture and the subsequent reactions. The knowledge about nuclear reaction rates that drive these reactions is, however, still inaccurate. Their determination by new nuclear experiments is pursued for the main nuclear reactions of the stellar fusion phases, i.e. H- He-, C-burning phases. In order to improve stellar modelling, we now need to take into account these new results that might be key to understand stellar evolution. We implemented new $^{12}C + ^{12}C$ nuclear reaction rates and explore their impact.

Keywords: Nuclear reactions, Stars: evolution, Star: interiors, Nucleosynthesis, Stars: rotation

1 Introduction

In recent years, numerous nuclear reaction rates relevant for astrophysics have been determined experimentally via direct and indirect methods, highlighting specific trends like the unexpected fusion hindrance phenomenon (steep fall of the fusion cross-section at very low energies) and multiple resonances. In particular, a precise determination of the nuclear reaction rates is a crucial ingredient in understanding stellar evolution. New nuclear reaction rates have been determined for the different cycles of H- He-, C-burning phases by nuclear experiments (e.g. Broggini et al. 2018), leading to significant changes in the nucleosynthesis. In particular, measurements for the $^{12}C + ^{12}C$ nuclear reaction have been obtained at the low energies of astrophysical interest by the STELLA collaboration in France (Fruet et al. 2020) and open the way to improvements in stellar evolution modelling. This reaction is indeed the main nuclear reaction during the advanced C-burning phase of massive stars ($\geq$ 8 $M_\odot$). Monpribat et al. (2022) showed these new rates impact the burning lifetime as well as the production of C-burning products and s-process elements changing later stages of the evolution. In continuation of this work, using the stellar evolution code GENEC (Ekström et al. 2012), we computed new models for a larger range of masses and metallicities, and including rotation-induced mixing ($V_{ini}/V_{crit} = 0.4$).

2 Nuclear reaction rates $^{12}C + ^{12}C$

$^{12}C + ^{12}C$ nuclear rates are often taken from the so-called CF88 reference (Caughlan & Fowler 1988) in stellar evolution codes. New measurements are available for the p and α channels (Fruet et al. 2020) and for the n channel (Bucher et al. 2015). They consider the hindrance phenomenon (steep fall of the cross-section, HIN model) which is observed for certain energies in this reaction, as well as a resonance close to the astrophysics region of interest and observed for the α exit channel (HINRES model, Fruet et al. 2020). Figure 1, left panel, shows reaction rates normalised to the CF88 rates, as a function of the central temperature for these two new cases: HIN, HINRES. The temperature location of the resonance may impact differently the stars depending on their C-burning temperature, or in other words, depending on their mass and metallicity.

[1] University of Strasbourg, CNRS, IPHC UMR 7178, F-67000 Strasbourg, France
[2] Institut d'Astronomie et d'Astrophysique, Université Libre de Bruxelles, CP 226, 1050, Brussels, Belgium
[3] University of Strasbourg, Institute of Advanced Studies (USIAS), Strasbourg, France

© Société Française d'Astronomie et d'Astrophysique (SF2A) 2023

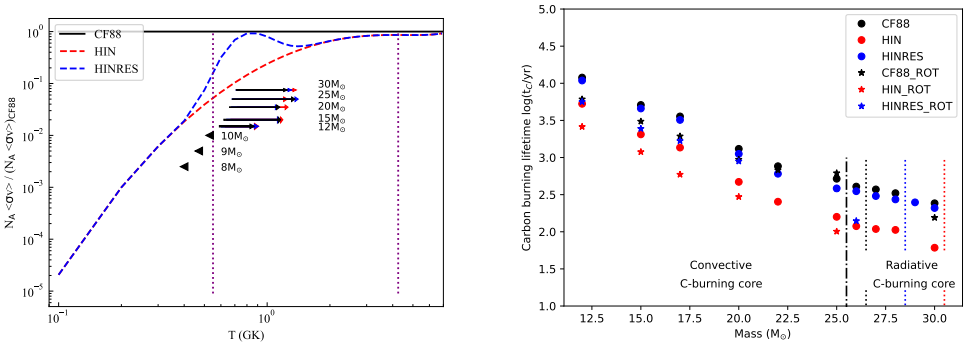

Fig. 1. Left: Reactions rates following CF88, HIN, and HINRES reference in black, red, and blue, respectively, and normalised to CF88 rates ($N_A < \sigma v >_{CF88}$). Black, red, and blue arrows show the temperature regions where carbon fusion takes place for classical models of 12, 15, 20, 25, and 30 $M_\odot$. Black triangles give the maximum core temperature reached by the 8, 9, and 10 $M_\odot$ stars. The area between purple dotted-lines was explored by the STELLA experiment. **Right:** Core C-burning lifetimes for stellar models of different masses without/with rotation (circle/star, respectively). Dotted-lines and dotted-dashed lines indicate the transitions between convective and radiative core for models without/with rotation, respectively.

A lower reaction rate (HIN) results in a higher central temperature and density, and a shorter lifetime during the C-burning phase (see right panel of Fig. 1). This trend was already shown by (Pignatari et al. 2013; Chieffi et al. 2021) for different rates. The difference between the HIN and HINRES models is due to the resonance observed in Fig. 1, left panel. Rotation leads in both cases to a shift to higher T_c/ρ_c and shorter lifetime. The effects on nucleosynthesis remain small on classical models but should be further explored for rotation models, as well as during the C-burning shell phase (Raiteri et al. 1991).

3 Conclusions

New nuclear reaction rates for ^{12}C $+^{12}$ C are driving changes in the C-ignition and C-burning in massive stars (core temperature, lifetime). Preliminary results show that the resulting effects are multiple impacting nucleosynthesis, intermediate/massive stars mass limit, core structure (convective or radiative), end-of-life (e.g. Chieffi et al. 2021; Monpribat et al. 2022; De Gerónimo et al. 2023). Thanks to new measurements, accurate nuclear rates are currently obtained for a large set of fundamental reactions. In this context, results for ^{12}C+^{12}C support the need to test and update stellar evolution codes for the different nuclear fusion phases. A better nuclear description is indeed one of the key for improving the stellar modelling and is especially relevant in the context of asteroseismic constraints on stellar interiors.

This work was supported by the European Union (ChETEC-INFRA, project no. 101008324). The authors thank S. Ekström, and G. Meynet for helpful discussions. TD thanks the Department of Astronomy of the University of Geneva for numerical resources access. This research has made use of NASA's Astrophysics Data System Bibliographic Services.

References

Broggini, C., Bemmerer, D., Caciolli, A., & Trezzi, D. 2018, Progress in Particle and Nuclear Physics, 98, 55
Bucher, B., Tang, X. D., Fang, X., et al. 2015, Phys. Rev. Lett., 114, 251102
Caughlan, G. R. & Fowler, W. A. 1988, Atomic Data and Nuclear Data Tables, 40, 283
Chieffi, A., Roberti, L., Limongi, M., et al. 2021, ApJ, 916, 79
De Gerónimo, F. C., Miller Bertolami, M. M., Catelan, M., & Battich, T. 2023, arXiv e-prints, arXiv:2303.00060
Ekström, S., Georgy, C., Eggenberger, P., et al. 2012, A&A, 537, A146
Fruet, G., Courtin, S., Heine, M., et al. 2020, Phys. Rev. Lett., 124, 192701
Monpribat, E., Martinet, S., Courtin, S., et al. 2022, A&A, 660, A47
Pignatari, M., Hirschi, R., Wiescher, M., et al. 2013, ApJ, 762, 31
Raiteri, C. M., Busso, M., Gallino, R., & Picchio, G. 1991, ApJ, 371, 665

SF2A 2023
M. N'Diaye, A. Siebert, N. Lagarde, O. Venot, K. Baillié, M. Béthermin, E. Lagadec, J. Malzac, J. Richard (eds)

DETECTION OF A STEEP HEIGHT GRADIENT OF THE ROTATIONAL VELOCITY IN THE LOW PHOTOSPHERE OF THE SUN

M. Faurobert[1], T. Corbard[1], B. Gelly[2], R. Douet[2] and D. Laforgue[2]

Abstract. We present a new method to measure the rotational height gradient in the solar photosphere. The method is inspired from differential interferometric techniques, it is applied to spectroscopic observations in the FeI 630.15 nm obtained at the solar telescope THEMIS equipped with an efficient adaptative optics system. At the center of the solar disk, we measured systematic retrograde shifts between images of the granulation pattern obtained at different line cords that are formed at different heights. The shift varies linearly with height. We interprete this as the signature of a steep decrease of the rotational velocity in the low photosphere.

Keywords: Techniques: high angular resolution - Techniques: spectroscopic - Sun: photosphere

1 Introduction

Rotational shear plays a major role in driving the stellar dynamo. For the Sun helioseismic observations have revealed two regions that show a strong height-gradient of the rotation rate, namely, the tachocline at the base of the convective zone and the near surface shear layer (NSSL). Heliosismic technics do not allow us to explore the photospheric layer. Previous spectroscopic observations by Livingston & Milkey (1972) failed to find any evidence of a depth gradient but more recently Cunnyngham et al. (2017) using 3 years of the Helioseismic and Magnetic Imager (HMI) data could measure a steep rotational shear of the latitudinal average of the rotational velocity in the upper photosphere. Here we show that the rotation profile in the photosphere may be probed by high resolution spectroscopic methods and we report the detection of a steep decrease of the rotational velocity in the low photosphere.

2 Observations and method

Our detection method relies on the measurements of systematic shifts between simultaneous images of the granulation taken at different altitudes. Systematic shifts may arise from two different effects, namely, a perspective effect in the radial direction when the images are taken away from the center of the solar disk or horizontal shifts that are induced by a height-gradient of large scale horizontal velocities projected on the plane of the sky. The perspective effect allowed us to measure the formation height of line-cord images with respect to the continuum layer, whereas at the center of the solar disk where the perspective effect vanishes we measured systematic retrograde shifts along the solar equator of the images formed higher up in the photosphere.

We used spectroscopic observations obtained at the solar telescope THEMIS dating from July, 18 to July 22, 2022, in the FeI 630.15 nm line. To measure the perspective shift we also used HINODE Solar Optical Telescope (SOT) spectropolarimetric (SP) data from the irradiance program, HOP79, performed on July 21, 2022. We defined 25 cords in the line profile from the continuum (level 25) to the line core (level 1). To measure a very small displacement between images in the continuum and in the line wings, we used the phase of their cross-spectrum. This method requires us to consider the power spectra of intensity fluctuations in images taken rigorously at the same time in the continuum and in the line. To extract statistical information we performed ensemble averages of the cross-spectra obtained at a large number of slit positions. Actually, 2D images are not

[1] University Cote d'Azur, Lagrange Laboratory, CNRS UMR7293, Parc Valrose. 06108 Nice cedex 2
[2] CNRS-IRL2009, c/o IAC Via Lactea s/n, ES38205 La Laguna, Tenerife, Spain

© Société Française d'Astronomie et d'Astrophysique (SF2A) 2023

needed as far as the spectrograph slit is oriented in the direction of the displacement. In practice, we used 1D power spectra of the intensity variations along the spectrograph slit and we summed over all the slit positions. A shift between the images gives rise to a linear phase term in their cross-spectrum, the slope of this linear phase term allows us to determine the shift between the images. The details are given in Faurobert et al. (2023). We stress here that this method allows us to measure shifts that much smaller than the resolution of the telescope.

3 Retrograde shift measured at the center of the solar disk along the equator

Figure 1 shows a schematic representation of the drag of the granular pattern at a height z by the rotational height-gradient. This gives rise to a shift Δx of the intensity distribution along the spectrograph slit if we align it with the equator.

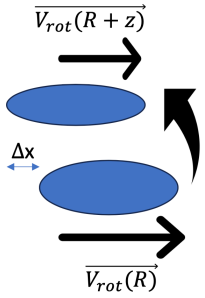

Fig. 1. Schematic representation of the drag of the upper layer at height z due to the rotational depth-gradient.

Figure 2 shows as an example, the cross-spectrum phase of images at line-cord 15 with images at the continuum level, when the slit is oriented along the north/south polar axis (left panel) and when its is oriented along the equator (right panel). In the last case we show the results obtained for three different observing days. No shift of the images is observed along the polar axis (the phase is noisy but remains close to 0), whereas we do observe a linear behavior of the cross-spectrum phase when the slit is along the equator. This allows us to measure the shift Δx, that it is negative meaning that the rotational velocity decreases with height. For the line cord shown here we get $\Delta x = -22.3 \pm 1.3$ km. In Faurobert et al. (2023) it is shown, using several line cords that Δx is proportional to the height z (obtained from the perspective effect) in the low photosphere.

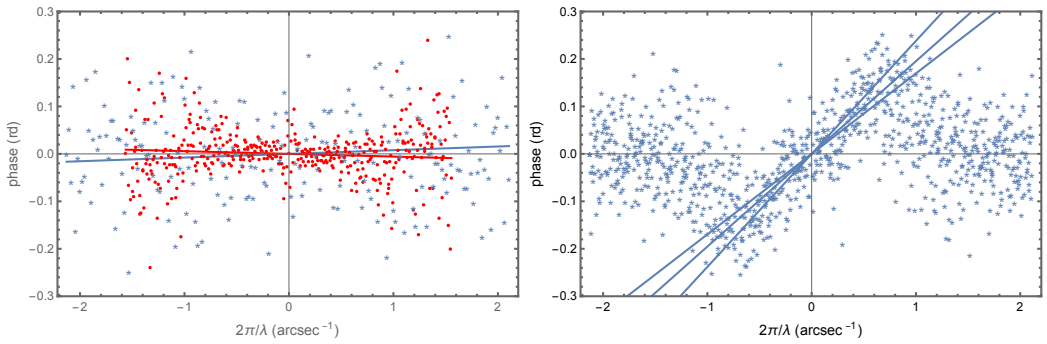

Fig. 2. Left: Phase of the cross-spectrum of images at cords 15 and 25 (continuum) with the slit along the polar axis. Blue symbols: from Themis data, red symbols: from Hinode data. **Right:** Phase of the cross-spectrum with the slit along the equator for three different observing days. The straight lines show linear fits at spatial frequencies smaller than 0.6 arcsec^{-1}.

References

Cunnyngham, I., Emilio, M., Kuhn, J., Scholl, I., & Bush, R. 2017, Phys. Rev. Lett., 118, 051102
Faurobert, M., Corbard, T., Gelly, B., Douet, R., & Laforgue, D. 2023, A&A, 676, L4
Livingston, W. & Milkey, R. 1972, Sol. Phys., 25, 267

SF2A 2023
M. N'Diaye, A. Siebert, N. Lagarde, O. Venot, K. Baillié, M. Béthermin, E. Lagadec, J. Malzac, J. Richard (eds)

STUDYING BROWN DWARF DUST CLOUD DISTRIBUTION THROUGH POLARISATION

E. González[1], B. Goldman[1,2], M. R. Zapatero Osorio[3], V. J. Sánchez Bejar[4], T. Henning[5] and J. Pitann[6]

Abstract. Variations in the cloud cover of brown dwarfs have been detected through photometry monitoring and polarisation observations. This project aims at detecting the time dependence of the polarization for LHS102B, 2MASS J1507−16 and 2MASS J0036+18, which could be then explained by large-scale cloud coverage variations. We have obtained high SNR images with 16 retarder-plate angles using the VLT/FORS2 instrument and reduced the data using the method described in Patat & Romaniello (2006), achieving a level of precision of $\sim 0.04\%$. Our results give evidence of a variation in the polarisation degree in all three targets, and a significant correlation between the flux variability of 2MASS J1507 and the measured polarisation.

Keywords: Brown Dwarfs, Polarimetry, Atmospheres, LHS102B, 2MASS J1507−16, 2MASS J0036+18

1 Introduction

Brown dwarfs (BDs) are compact objects with masses between those of stars and planets. They are not massive enough to sustainably burn hydrogen, and eventually cool down due to the lack of an energy source. Cool BDs host low-temperature atmospheres, favouring molecules over single atoms, and dust grains. Those dust grains may form clouds in their atmosphere, leading to polarised light through scattering and flux variations if the cloud deck is heterogeneous.

Variations in the cloud cover of BDs have been detected through photometry monitoring and polarisation observations. This project aims at detecting the time dependence of the polarisation for 2MASS J00361617+1821104 (L3.5), LHS 102BC (L4.5), and 2MASS J15074769-1627386 (L5), which could be then explained by rotation and large-scale cloud coverage variations. Our sample, located close enough (within 12 pc) that there is no polarisation from interstellar dust, was previously observed in polarisation and showed convincing signs of polarisation variability.

Our goal is to extract new polarimetric information to better understand if the variation of the signal with time can be related to the rotation of the BD.

2 Observations and Data Reduction

Our data consists of unique observations obtained between Oct-2010 and Mar-2011, using FORS2 (ESO 2022), which is mounted on the Cassegrain focus of the 8.2-m ANTU telescope at the ESO VLT in Chile.

When used in the IPOL mode (Imaging POLarimetry), FORS2 works as dual-beam polarimeter. This means that the incident light beam (I) is split by a Wollaston prism (WP) into two perpendicular beams: the ordinary (fo,i) and extraordinary beams (fe,i). In this setup, a rotating half-wave retarder plate (HWP) placed before the WP, allows to measure the intensity of both beams at different angles (θ_i). FORS2 has a FoV of 6.8' x 6.8'

[1] International Space University (ISU), 1 rue Jean-Dominique Cassini, 67400 Illkirch-Graffenstaden, France
[2] Astronomical Observatory of Strasbourg, 11 rue de l'Université, 67000 Strasbourg, France
[3] Centro de Astrobiología (CSIC-INTA), Crta. Ajalvir km 4, 28850 Torrejón de Ardoz, Madrid, Spain
[4] Instituto de Astrofísica de Canarias (IAC), Calle Vía Láctea s/n, 38200 La Laguna, Tenerife, Spain
[5] Max Planck Institute for Astronomy, Königstuhl 17, 69117 Heidelberg, Germany
[6] Space Operations and Astronaut Training (DLR), 82234 Wessling, Germany

© Société Française d'Astronomie et d'Astrophysique (SF2A) 2023

imaged into two identical CCD detectors, with a pixel size of 0.25 arcsec with the standard binning of 2x2. For each target, we obtained 16 observations with a different θ_i (step=22.5°), in the I band. The 16-angle set allows to obtain the highest accuracy and to minimise and understand the noise sources (Patat & Romaniello 2006).

We applied the standard calibration process using the associated flat and bias frames, for each night. The photometry phase consists of measuring the flux for both the ordinary and extraordinary beams using aperture photometry. Our analysis shows that the polarisation results are not significantly dependent on the chosen aperture radius. Depending on the observation conditions we selected 4 to 6 pixels (1" to 1".5). Regarding the polarimetry analysis, we followed the steps and formulae presented in Patat & Romaniello (2006).

Uncertainties were estimated at every single step within the process and propagated accordingly. Moreover, we performed the Fourier analysis suggested in Patat & Romaniello (2006) to assess our error results, which can be estimated with the signal included in the harmonics with k= 3, 5-8. The estimated uncertainties were consistent with the systematics obtained through the harmonics power spectrum.

The whole data reduction steps were implemented through an original pipeline developed in Python specifically for this research project, based on the *astropy*, *photutils*, and *ccdproc* packages.

3 Results

We report our measurements in Figs. 1- 3. 2MASS J0036 shows a variation on the polarisation over the three nights (Fig. 1), reaching a significant degree of polarisation (DOP) of (0.26±0.08)% at the end of the first night. In the case of LHS 102BC (Fig. 2), our results also show variations on the polarisation measurements but in this case the highest DOP were obtained in the first two nights (0.18±0.07; 0.15±0.07)%. As to 2MASS J1507 (Fig. 3), the variation in the polarisation shows a peak by the end of the night, with a DOP of (0.25±0.05)%.

In addition, for 2MASS J1507 we performed a variability analysis. Atmospheric models predict that cloud patches that could lead to polarisation would also lead to flux variability. We normalized the sum of the ordinary and extraordinary beam fluxes by the average flux of its reference stars, and compare it with our polarimetry results (Fig. 3). Our results show no significant correlation between the DOP and the flux: r=-0.15 (p-value=0.74).

Furthermore, we compared the results of 2MASS J0036 against other polarisation measurements. The amplitude of variations that we tentatively detected matches with previous observations: (0.199 ±0.028)% in 12/2001 (Ménard et al. 2002) vs. (0.077 ±0.029)% in 08/2005 (Goldman et al. 2009).

In addition, for the same target we looked for photometric variability in the literature, with the intention of understanding the relation between photometry and polarisation variations. Photometric variability has been reported in I band (Croll et al. 2021) as well as radio emission (Berger et al. 2005) but the ∼3h period couldn't be confirmed in our polarimetry observations, as the polarisation peak detected at MJD-5494=0.23d is not observed 3h before, due to a lack of data.

We note that Vos et al. (2017) determined the inclination of 2MASS J0036 and 2MASS J1507 at 51±9deg and 23±2deg resp. A lower inclination, together with a higher rotational velocity, increases the effect of the flattening on the DOP.

4 Conclusions

We tentatively observed a variation of the polarisation degree in all three targets. Yet, we detected significant polarisation measurements in only ≈ 15% of the data points obtained and even then the polarisation significance is low. For 2MASS J1507 we compared the polarisation results with the flux variability and found no correlation.

Over the past decade, there has been a dramatic improvement in the sensitivity of photometric monitoring of BDs and in the understanding of their cloud structure thanks to photometric variability studies (Luna & Morley 2021). Polarimetric measurements of high quality like ours and others (Millar-Blanchaer et al. 2020) provide us with an additional set of constraints related specifically to the dust distribution.

Our analysis puts strong constraints on the level of polarisation in L-type BDs over time and illustrates the difficulty to detect it. However, the degeneracies that affect the polarisation signal can be partly lifted thanks to those independent photometric measurements (Vos et al. 2017), which paves the way for a more accurate interpretation of polarimetric observations of brown dwarfs.

This research is based on observations collected at the European Organisation for Astronomical Research in the Southern Hemisphere under ESO programme 086.C-0812(A/C/D/F), and has made use of the SIMBAD database and VizieR catalogue access tool, both operated and maintained at the CDS, Strasbourg, France.

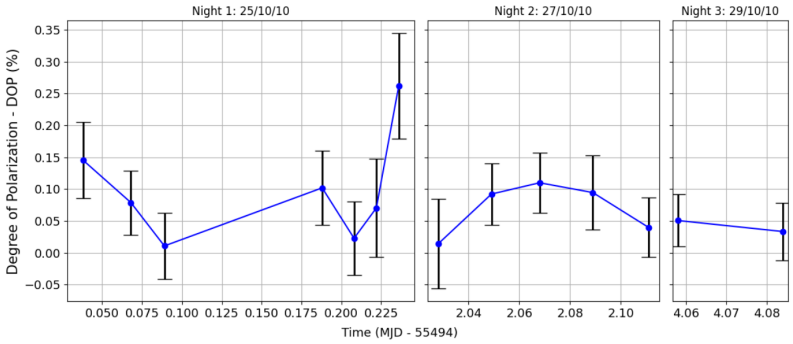

Fig. 1. Polarimetry results for 2MASS J0036

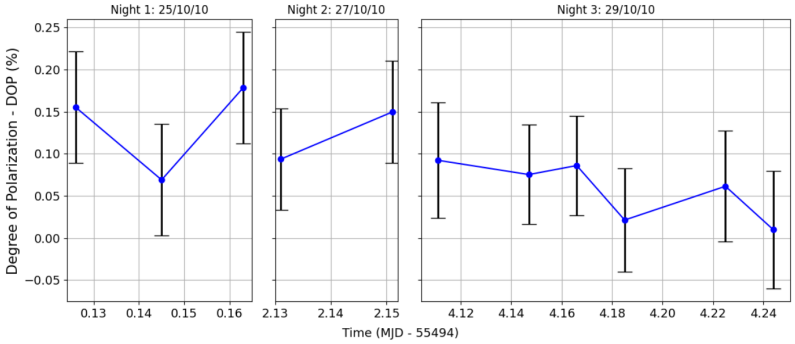

Fig. 2. Polarimetry results for LHS 102BC

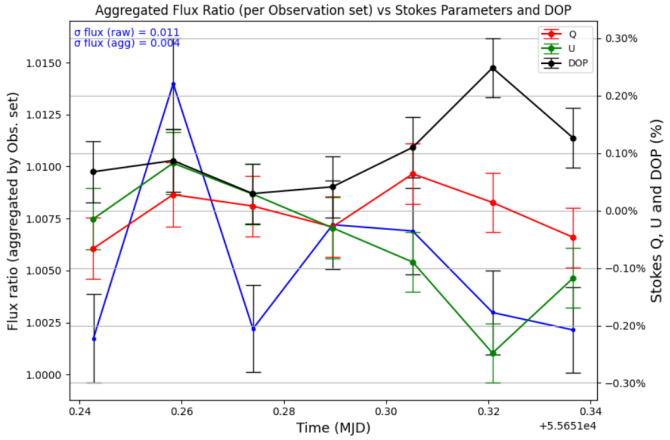

Fig. 3. Polarimetry results for 2MASS J1507 along with flux variability

References

Berger et al. 2005, ApJ, 627, 960
Croll et al. 2021, arXiv preprint arXiv:1609.03586
ESO. 2022, FORS2 FOcal Reducer/low dispersion Spectrograph 2, `https://www.eso.org/sci/facilities/paranal/instruments/fors/overview.html`
Goldman et al. 2009, A&A, 502(3), 929:936
Luna, J. & Morley, C. 2021, ApJ, 920(2), 146
Millar-Blanchaer et al. 2020, ApJ, 894, 42
Ménard et al. 2002, A&A, 396(3), L35:L38
Patat, F. & Romaniello, M. 2006, PASP, 118(839), 146
Vos et al. 2017, ApJ, 842, 78

SF2A 2023
M. N'Diaye, A. Siebert, N. Lagarde, O. Venot, K. Baillié, M. Béthermin, E. Lagadec, J. Malzac, J. Richard (eds)

MASSES AND LUMINOSITIES OF SB2 COMPONENTS DEDUCED FROM OHP SPECTROSCOPIC OBSERVATIONS AND GAIA-DR3 ASTROMETRIC ORBITS

J.-L. Halbwachs[1], F. Kiefer[2,3], Y. Lebreton[3,4], F. Arenou[5], B. Famaey[1], P. Guillout[1], T. Mazeh[6], D. Pourbaix[7] and J.-B. Salomon[8]

Abstract. The masses and luminosities of 10 binary components are derived from accurate SB2 orbital elements and from Gaia DR3 astrometric orbits.

Keywords: binaries:spectroscopic, Astrometry, stars: fundamental parameters

1 Introduction

A selection of double-lined spectroscopic binaries (SB2s) have been observed since 2010 with the 193 cm-telescope and the "Spectrographe pour l'Observation des PHénomènes des Intérieurs Stellaires et des Exoplanètes" (Sophie) at the Observatoire de Haute-Provence (OHP), in order to obtain precise orbital elements (see Halbwachs et al. 2020, and references therein). The third Data Release of the Gaia satellite (Gaia-DR3) includes the elements of nearly 165500 astrometric orbits (Gaia Collaboration et al. 2016; Halbwachs et al. 2023; Holl et al. 2023), including 10 SB2s of the OHP programme, out of 34 whose orbits we have already published: HIP 20601, 21946, 61100, 61732, 62935, 95575, 100046, 101382, 116160 and HD 98031. The combination of the SB2 and astrometric orbital elements is used here to estimate the masses and luminosities of the components of these binaries, where possible.

2 Selection of binaries of compatible orbital elements

It is not possible to calculate a joint solution for our spectroscopic measurements and the astrometric measurements of the DR3, as the latter have not been included in Gaia-DR3. We therefore must ensure that the spectroscopic and astrometric orbital elements are compatible, and exclude stars for which they are not. We checked the compatibility of the periods, eccentricities, arguments and epochs of periastron at the 2 σ threshold, and finally retained HIP 20601, 21946, 61732, 95575 and 101382.

3 Calculation of the masses and luminosities

The calculation of the masses is trivial, since we have already calculated and published the quantities $\mathcal{M}_1 \sin^3 i$ and $\mathcal{M}_2 \sin^3 i$ and their uncertainties (see references in Table 1; $\mathcal{M}_1$ and $\mathcal{M}_2$ are the primary mass and the

[1] Université de Strasbourg, CNRS, Observatoire astronomique de Strasbourg, UMR 7550, F-67000 Strasbourg, France
[2] Institut d'Astrophysique de Paris,CNRS/UMR7095, F-75014 Paris, France
[3] LESIA, Observatoire de Paris, PSL Research University, CNRS, Sorbonne Université, UPMC Univ. Paris 06, Univ. Paris Diderot Sorbonne Paris Cité, F-92195 Meudon, France
[4] Univ Rennes, CNRS, IPR (Institut de Physique de Rennes) - UMR 6251, F-35000 Rennes, France
[5] GEPI, Observatoire de Paris, PSL Research University, CNRS, Université Paris Diderot, Sorbonne Paris Cité, Place Jules Janssen, F-92195 Meudon, France
[6] School of Physics and Astronomy, Tel Aviv University, Tel Aviv 69978, Israel
[7] FNRS, Institut d'Astronomie et d'Astrophysique, Université Libre de Bruxelles, Bruxelles, Belgium. Deceased on 14/11/2021.
[8] Institut UTINAM, CNRS UMR6213, Université Bourgogne Franche-Comté, OSU THETA, Observatoire de Besançon, BP 1615, F-25010 Besançon Cedex, France

© Société Française d'Astronomie et d'Astrophysique (SF2A) 2023

Table 1. Masses and absolute magnitudes derived from our SB2 orbits and from Gaia-DR3.

Ident. HIP	SB2 orbit reference	$\mathcal{M}_1$ ($\mathcal{M}_\odot$)	$\sigma_{\mathcal{M}_1}$ ($\mathcal{M}_\odot$)	$\mathcal{M}_2$ ($\mathcal{M}_\odot$)	$\sigma_{\mathcal{M}2}$ ($\mathcal{M}_\odot$)	$M_{G\ 1}$ (mag)	$\sigma_{M_{G\ 1}}$ (mag)	$M_{G\ 2}$ (mag)	$\sigma_{M_{G\ 2}}$ (mag)
20601	Halbwachs et al. (2020)	1.015	0.019	0.753	0.014	4.964	0.033	7.09	0.23
21946	Kiefer et al. (2018)	0.792	0.016	0.560	0.010	6.4739	0.0057	8.796	0.031
61732	Halbwachs et al. (2020)	1.414	0.086	0.995	0.060	3.485	0.012	5.506	0.052
95575	Kiefer et al. (2016)	0.773	0.028	0.690	0.025	6.1876	0.0051	7.0225	0.0094
101382	Kiefer et al. (2018)	0.8374	0.0024	0.6584	0.0017	5.3276	0.0036	7.189	0.012

secondary mass, respectively, and i is the inclination of the orbital plane). So all we have to do is calculate i and its uncertainty from the Thiele-Innès elements given in DR3, applying the relations given by Halbwachs et al. (2023), and deduce the masses. The uncertainties of the masses are calculated by a simple quadratic sum, since the elements of the astrometric orbits are not correlated with those of the spectroscopic orbits.

To calculate luminosities, we consider the quantities $a_1 \sin i$ and $a_2 \sin i$ from the spectroscopic orbits, where a_1 and a_2 are the semi-major axes of the orbits of the components around the barycentre. The luminosity ratio is derived from the formula:

$$\frac{\mathcal{F}_1}{\mathcal{F}_1 + \mathcal{F}_2} = \frac{a_1 - a_0}{a_1 + a_2} \tag{3.1}$$

where $\mathcal{F}$ refers to a flux and where a_0 is the semi-major axis of the photocentre orbit, converted into km using the trigonometric parallax. Knowing the magnitude of the binary in Gaia's G band, we can deduce the absolute magnitudes of the components. Uncertainties are calculated by simulation to take into account the different correlation coefficients. The results are presented in Table 1.

4 Comparison with previous results

The masses of the components of 3 binaries have already been calculated from our spectrocopic observations and interferometric orbits. These are HIP 20601 (Halbwachs et al. 2020), 95575 (Docobo et al. 2018) and 101382 (Kiefer et al. 2018). The results are all compatible within 2 σ with those from Gaia-DR3.

The masses and absolute magnitudes of the stars considered here were all derived from the same data in Chevalier et al. (2023), but with different results, since they have re-evaluated the elements of the astrometric orbit by assigning elements from the spectroscopic orbit with the Template Model Builder code.

5 Discussion and conclusion

We used the Gaia-DR3 to calculate the masses and absolute magnitudes of the components of 5 binaries that we had observed spectroscopically at the Haute-Provence Observatory with the T193/Sophie. The Gaia-DR4 will include the astrometric transits, allowing the calculation of combined astrometric and spectroscopic solutions. The 34 binaries that we had already monitored at the T193/Sophie should then all obtain more accurate results.

We made use of the Vizier database, operated at CDS, Strasbourg, France.

References

Chevalier, S., Babusiaux, C., Merle, T., & Arenou, F. 2023, arXiv e-prints, arXiv:2307.16719
Docobo, J. A., Campo, P. P., Gomez, J., & Horch, E. P. 2018, AJ, 156, 185
Gaia Collaboration, Prusti, T., de Bruijne, J. H. J., et al. 2016, A&A, 595, A1
Halbwachs, J. L., Kiefer, F., Lebreton, Y., et al. 2020, MNRAS, 496, 1355
Halbwachs, J.-L., Pourbaix, D., Arenou, F., et al. 2023, A&A, 674, A9
Holl, B., Sozzetti, A., Sahlmann, J., et al. 2023, A&A, 674, A10
Kiefer, F., Halbwachs, J. L., Arenou, F., et al. 2016, MNRAS, 458, 3272
Kiefer, F., Halbwachs, J. L., Lebreton, Y., et al. 2018, MNRAS, 474, 731

SF2A 2023
M. N'Diaye, A. Siebert, N. Lagarde, O. Venot, K. Baillié, M. Béthermin, E. Lagadec, J. Malzac, J. Richard (eds)

ACCRETION PROPERTIES OF CLASS 0 PROTOSTARS STUDIED WITH NEAR-INFRARED SPECTROSCOPY

V. Gouellec[1], T. Greene[1,], L. Hillenbrand[2] and Z. Yates[1,]

Abstract. Sun-like stars are thought to accrete most of their final mass during the protostellar phase, where the protostellar embryo is surrounded by an infalling dense envelope. The so-called Class 0 phase designates the youngest protostellar stage, where the accretion is the most vigorous. Because these objects are highly embedded, it is difficult to retrieve direct diagnostics from the accretion, whose observational imprint lie at small wavelengths, in the near-infrared and below. Therefore, little is known about the accretion mechanisms occurring in the Class 0 phase because of high extinction. However, in rare cases the blueshifted cavity created by the outflow is sufficiently close to pole-on to liberate enough near-infrared scattered light for us to probe the immediate surroundings of the central object. We present a new set of K-band spectra of 26 Class 0 protostars recently observed with Keck MOSFIRE. Br_γ, several H_2 and $\Delta\nu = 2$ CO lines are detected and analyzed. We detect Br_γ in several sources, which suggests a good fraction but not all of Class 0s may accrete via magnetospheric accretion. The H_2 lines are consistent with shock excitation indicating jets/outflows. Stella CO lines are seen in absorption in 6 sources suggesting recent vigorous accretion episodes. CO is seen in emission in 13 sources, tracing the heated inner accretion disk. We find that a significant higher fraction of Class 0 objects tend to exhibit CO in emission than in archival K-band spectra of later-evolved, Class I protostars. We also perform and discuss statistical tests comparing the near-IR line parameters of Class 0 and I objects. Our results suggest that the near-IR accretion properties of Class 0s tend to be different that of Class I objects. Upcoming JWST observations shall constrain further the accretion mechanisms of Class 0 protostars.

Keywords: ISM: jets and outflows - stars: formation - stars: protostars - accretion

1 New sample of K-band spectroscopy of low-mass Cass 0 protostars

Figure 1 presents the new observations of medium resolution (R $\sim$ 3300) NIR K-band spectroscopy for a sample of 26 Class 0 protostars in the Perseus, Serpens, and Orion molecular clouds. The H_2, Br_γ, and CO overtone emission bands features are detected toward $\sim$ 90, 65, and 50 % of the sample, respectively. [Fe II] lines, a common jet tracer, as well as Ca I and Na I emission lines, are also detected in several sources. The photosphere is detected in 6 sources, exhibiting CO, Na and Ca absorption features consistent with dwarf spectra, and indicative of low-veiling. We perform statistical comparisons with a sample of Class I K-band spectra taken from the literature.

Analysis of the Br_γ and CO overtone emission equivalent width and luminosity values shows that the accretion luminosity is on average higher in Class 0 systems, suggesting that Class 0s accrete more vigorously. The much higher detection rate of CO overtone in Class 0s (50 % against $\leq$15 % in Class Is) indicates that episodes of high accretion activity is more frequent in Class 0 systems. The H_2 excitation is similar between Class 0s and Is, pointing toward outflow/jet shock origin collisionally exciting H_2. However, the H_2 emission lines are much brighter in Class 0s, suggesting stronger shocks, *i.e.*larger shock velocity and pre-shock density. The Class 0 CO overtone emission is either consistent with redshifted emission or no shift. While the latter would suggest an inner disk origin, clear redshifted emission suggests that the dense and hot gas associated with the CO emitting regions can correspond to infalling material at $\sim$15-40 km s^{-1}. Br_γ emission lines usually attributed to the magnetospheric accretion column in T-Tauri systems exhibits clearly different velocity profiles

[1] NASA Ames Research Center Space Science and Astrobiology Division M.S. 245-6 Moffett Field, CA 94035, USA
[2] Department of Astronomy, MC 249-17, California Institute of Technology, Pasadena, CA 91125, USA

© Société Française d'Astronomie et d'Astrophysique (SF2A) 2023

between the two protostellar phases: while Class Is systems have blueshifted centroids and in a few sources a clear redshifted absorption, Class 0s exhibit symmetric Br_γ profiles with no velocity shifts. This could point toward an accretion mechanism of different nature in Class 0 systems.

This study reveals the NIR accretion properties of a statistically relevant sample of Class 0 protostellar systems. These objects exhibit systematic difference with the more evolved Class I objects: Class 0 accretion appears more vigorous and episodes of high accretion activity more frequent. Further modeling of the emission can reveal relevant further insights on the kinematics of the CO and Br_γL emission line regions. JWST diagnostics of the spatial location of these emissions and the extinction of these embedded regions will enable more quantitative analysis of the actual mass accretion rate of these systems.

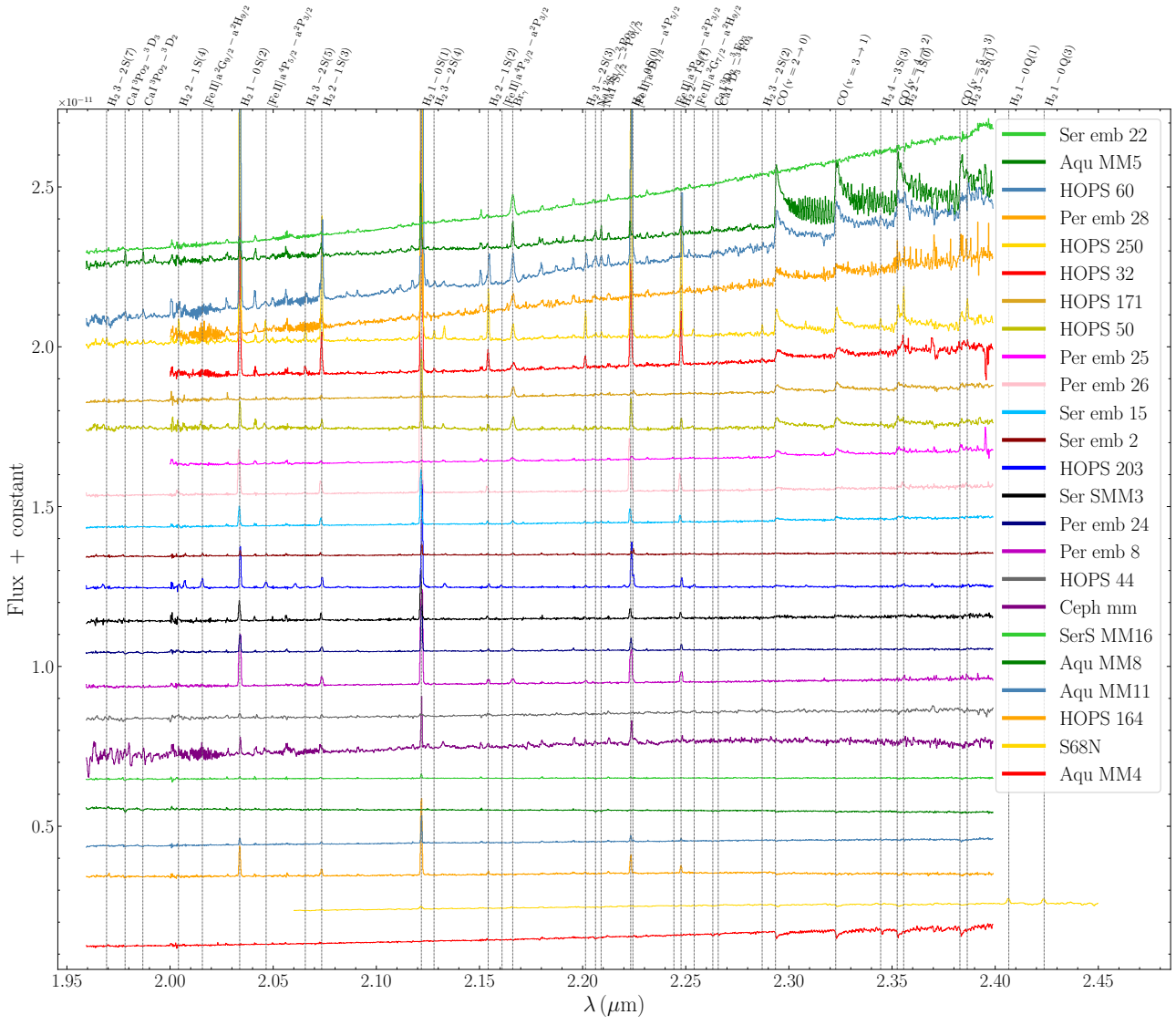

Fig. 1. Extracted 1D K band spectra of our sample of Class 0 protostars. We sorted the spectra such as the reddest spectra and the CO overtone emitting sources are at the top, while the sources exhibiting photospheric features are at the bottom. These spectra are not corrected for extinction. The grey vertical dashed line report all the detected lines in the sample. Per emb 21 and HOPS 87 are not shown here because no continuum has been detected in these sources. However, their spectra show bright emission lines for nearly all of the H2 lines outlined in this Figure.

SF2A 2023
M. N'Diaye, A. Siebert, N. Lagarde, O. Venot, K. Baillié, M. Béthermin, E. Lagadec, J. Malzac, J. Richard (eds)

MAGNETISED WINDS IN TRANSITION DISCS

E. Martel and G. Lesur[1]

Abstract. Protoplanetary discs (PPDs) have been widely observed around young stars and are supposed to be the birth cradle of planets. These objects are cold, dense and magnetised. Among them stand the so-called transition discs (TDs) characterised by a dust cavity in their inner regions, whose diameter varies from a few AU to a few hundreds AU. The formation of such cavities remains unexplained. Moreover, such cavities are not only detected in the dust radial density profiles, but they are also observed in the gas radial density profiles.

A striking observation, challenging the intuition, states that in spite of their diminished surface density profile, TDs accrete merely as much as full PPDs. Their accretion rates are similar to one measured in standard PPDs ($\dot{M}_{\rm PPD} \sim 10^{-7}\,M_\odot\,{\rm yr}^{-1}$). Such an observation suggests a fast inward motion of matter inside the cavity.

A possible explanation for these high accretion rates is the presence of magnetised winds that would allow matter to fall onto the star at high radial velocity.

The aim of my work is to address this observational discrepancy using magnetohydrodynamic (MHD) winds to account for the accretion in TDs. With my contribution, I showed with global numerical simulations how wind-emitting cavity-hosting discs could support a fast inner accretion.

I present the results of 2.5 D and 3 D simulations modelling TDs with non-ideal magnetic winds. I focus on mass accretion through the cavity and on the 3 D stability of this cavity against hydro and magnetohydrodynamic instabilities.

Keywords: accretion, accretion discs - protoplanetary discs - non-ideal magnetohydrodynamics (MHD) - numerical simulations

1 Introduction

Transition discs are the subjects of many surveys (see for example van der Marel et al. 2018) that investigate in particular the gas repartition in their cavities. Interestingly, many TDs exhibit high accretion rates, that are comparable to the one of full PPDs. These strongly-accreting TDs have cavities of various widths, some of which having very large ones, up to 100 AU such as in González-Ruilova et al. (2020).

The work I present aims at describing global numerical models of TDs whose cavities are sustained by magnetic winds, which enable a strong accretion.

The link between TDs and magnetic winds was first proposed by Combet & Ferreira (2008), while Wang & Goodman (2017) studied the magnetic diffusion properties of TDs cavities in the non-ideal MHD framework. I report the results of the first global numerical simulations (2.5 D and 3 D) of TDs sustained by magnetic winds. The MHD winds are launched with the Blandford & Payne process (Blandford & Payne 1982). The cavity is added by hand in the initial state. My model does not enforce any effective viscosity and focuses exclusively on the gas. The work presented here is based on Martel & Lesur (2022), and is a short insight on my thesis work (Martel 2022).

2 2.5 D simulations: secular evolution

I used a set of 2.5 D axisymmetric simulations to check the stability of a TD with magnetic winds on long period of time. I show the corresponding spatio-temporal profile of the surface density in the left panel of fig. 1.

[1] Univ. Grenoble Alpes, CNRS, IPAG, 38000 Grenoble, France

© Société Française d'Astronomie et d'Astrophysique (SF2A) 2023

The cavity remains through time and the disc reaches a quasi-stationary state. The corresponding order of magnitude for the accretion rate is $\dot{M}_{\rm TD} \sim 10^{-7}\ M_\odot\,{\rm yr}^{-1}$. Such a strong accretion rate in the depleted cavity implies that the accretion is transsonic in this region.

The accretion rate of the cavity connects to the one of the external part of the disc. The transport of angular momentum outwards occurs throughout the whole disc in an homogeneous fashion.

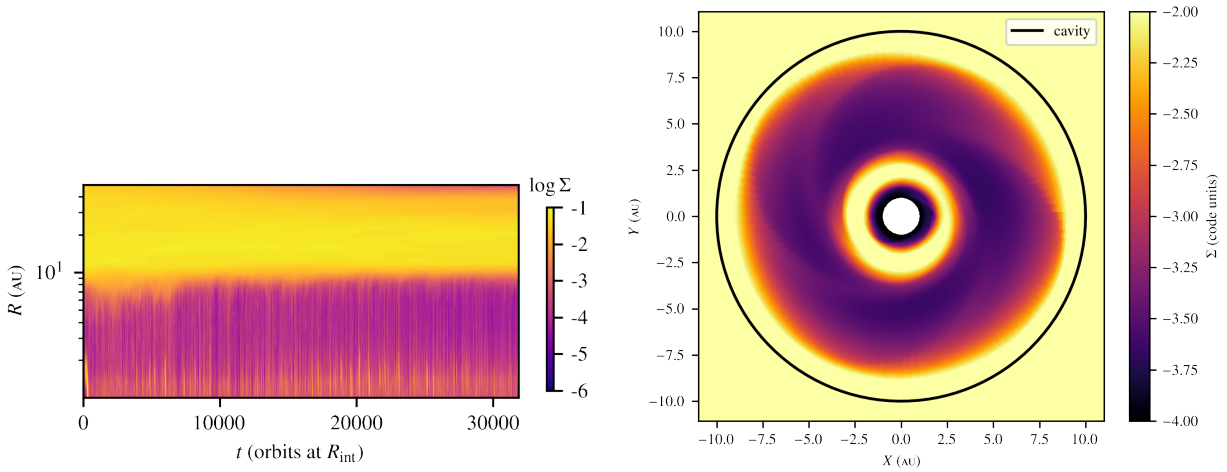

Fig. 1. Left: Spatio-temporal diagram of the surface density for the fiducial 2.5 D simulation. **Right:** Surface density in the midplane and at a given time for the fiducial 3 D simulation. The black circle indicates the location of the outer edge of the cavity.

3 3 D simulations: stability of the cavity

I ran another set of 3 D simulations to investigate the stability of the cavity under hydro- and magnetohydrodynamic instabilities. These 3 D simulations are restarted from the corresponding 2.5 D ones. After a fast transitory state, the disc remains in a similar dynamical state as it was in 2.5 D.

Nevertheless, an inner ring forms close to the inner boundary and a set of 4 spirals develops inside the cavity. These spirals can be seen in the right panel of fig. 1. I checked various stability criteria (Magnetic Rayleigh-Taylor instability, Rossby wave instability, rotational instability), but could not identify the occurring instability with certainty.

4 Conclusions

All these numerical simulations proove that magnetic winds are efficient to sustain stable inner cavities of TDs. They enable a strong accretion in the cavity as well as the radial transport of angular momentum. In essence, the simulated cavities recalls the physics of Magnetically Arrested Discs (MADs, see Narayan et al. 2003) that are studied in the context of black-holes physics.

References

Blandford, R. D. & Payne, D. G. 1982, 199, 883
Combet, C. & Ferreira, J. 2008, 479, 481
González-Ruilova, C., Cieza, L. A., Hales, A. S., et al. 2020, 902, L33
Martel, E. 2022, PhD thesis, 2022GRALY058
Martel, E. & Lesur, G. 2022
Narayan, R., Igumenshchev, I. V., & Abramowicz, M. A. 2003, 55, L69
van der Marel, N., Williams, J. P., Ansdell, M., et al. 2018, 854, 177
Wang, L. & Goodman, J. J. 2017, 835, 59

SF2A 2023
M. N'Diaye, A. Siebert, N. Lagarde, O. Venot, K. Baillié, M. Béthermin, E. Lagadec, J. Malzac, J. Richard (eds)

ASGARD: THE REALM OF HIGH ANGULAR RESOLUTION

M.-A. Martinod[1], D. Defrère[1], M. Ireland[2], S. Kraus[3], F. Martinache[4] and Asgard consortium

Abstract. Asgard promises significant advances in diverse astrophysical fields such as the formation of the binaries and multiple systems, the formation and evolution of exoplanets and the characterization of their atmospheres, the observation of mass accretion around YSOs and AGNs, the study of protoplanetary or exozodiacal disks. To do so, Asgard embeds four natively collaborating instruments: HEIMDALLR, Baldr, BIFROST and NOTT.

Keywords: integrated-optics, wavefront control, infrared, high contrast imaging, high angular resolution, optical fibers, long baseline interferometry, exoplanets, AGN, protoplanetary disk, spectroscopy

1 Introduction

The emphatic triumph of the Very Large Telescope Interferometer (VLTI) of the European Southern Observatory (ESO) and its second-generation instruments (namely General Relativity Analysis via Vlt InTerferometrY –GRAVITY– (Eisenhauer et al. 2011) and Multi AperTure mid-Infrared SpectroScopic Experiment –MATISSE– (Lopez et al. 2022)) in delivering unique science has set European astronomy apart. The Asgard instrument suite will extend the scientific capabilities of the VLTI following its priorities for the next decade (Mérand 2018). Asgard was approved during the first semester of 2023 for integration and commissioning from 2024 to mid-2026.

2 Instrument overview

The Asgard suite (Martinod et al. 2023) mainly consists of four instruments which are:

- HEIMDALLR (High-Efficiency Multiaxial Do-it ALL Recombiner): a remapped interferometer + wavefront sensor operating in K band (Ireland et al. 2018);
- Baldr: an active injection controller (Zernike wavefront sensor) operating in H band;
- BIFROST (Beam-combination Instrument for studying the Formation and fundamental paRameters of Stars and planeTary systems): a stellar interferometer with high resolution spectroscopy operating in Y, J and H bands with spectral resolutions of R=50, 1000, 5000, 25000 (Kraus et al. 2022);
- NOTT (Nulling Observations of dusT and planeTs): a photonic nuller operating in the L band (Defrère et al. 2022).

HEIMDALLR and Baldr are mostly dedicated to correcting atmospheric aberrations and atmospheric pistons; BIFROST and NOTT are mostly science-driven. Asgard will operate from Y to L bands (1 to 4 microns). The current design of Asgard is shown in Figure 1.

[1] Institute of Astronomy, KU Leuven, Celestijnenlaan 200D, 3001 Leuven, Belgium
[2] The Australian National University, Canberra, Australia
[3] University of Exeter, School of Physics and Astronomy, Stocker Road, Exeter, EX4 4QL, United Kingdom
[4] Observatoire de la Côte d'Azur, Nice, France

© Société Française d'Astronomie et d'Astrophysique (SF2A) 2023

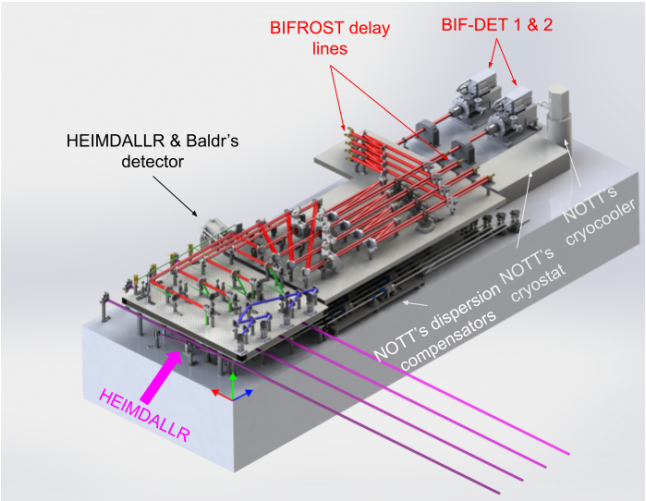

Fig. 1. Preliminary version of the optomechanical design of Asgard.

3 Science cases

Asgard science cases are diverse (Martinod et al. 2023; Kraus et al. 2022; Defrère et al. 2022), such as the formation process of binary systems, mass accretion and ejection, formation and evolution of exoplanetary systems and exoplanet atmospheres, protoplanetary and circumplanetary disks, exozodiacal dust.

4 Conclusions

Asgard is a new instrument suite proposed to ESO as a visitor instrument to open new unique scientific capabilities at the VLTI (YJH high-spectral resolution and L-band high-contrast nulling interferometry at milli-arcsecond angular separation). It consists of 4 different modules: BIFROST, Baldr, HEIMDALLR, and NOTT. The suite is currently in the design and preparation phases.

M-A.M. has received funding from the European Union's Horizon 2020 research and innovation program under grant agreement No. 101004719. S.K. acknowledge support from an ERC Consolidator Grant ("GAIA-BIFROST", grant agreement No. 101003096) and from STFC Consolidated Grant (ST/V000721/1).. This research was partially funded by the Australian Government through the Australian Research Council. (LE220100126). SCIFY has received funding from the European Research Council (ERC) under the European Union's Horizon 2020 research and innovation program (grant agreement CoG - 866070). We are grateful for the kind support and constructive interactions with colleagues at ESO, in particular Frédéric Gonte, Xavier Haubois, Antoine Mérand, Nicolas Schuhler, and Julien Woillez.

References

Defrère, D., Bigioli, A., Dandumont, C., et al. 2022, in Society of Photo-Optical Instrumentation Engineers (SPIE) Conference Series, Vol. 12183, Optical and Infrared Interferometry and Imaging VIII, ed. A. Mérand, S. Sallum, & J. Sanchez-Bermudez, 121830H

Eisenhauer, F., Perrin, G., Brandner, W., et al. 2011, The Messenger, 143, 16

Ireland, M. J., Defrère, D., Martinache, F., et al. 2018, in Society of Photo-Optical Instrumentation Engineers (SPIE) Conference Series, Vol. 10701, Optical and Infrared Interferometry and Imaging VI, ed. M. J. Creech-Eakman, P. G. Tuthill, & A. Mérand, 1070111

Kraus, S., Mortimer, D., Chhabra, S., et al. 2022, in Society of Photo-Optical Instrumentation Engineers (SPIE) Conference Series, Vol. 12183, Optical and Infrared Interferometry and Imaging VIII, ed. A. Mérand, S. Sallum, & J. Sanchez-Bermudez, 121831S

Lopez, B., Lagarde, S., Petrov, R. G., et al. 2022, A&A, 659, A192

Martinod, M.-A., Defrère, D., Ireland, M., et al. 2023, Journal of Astronomical Telescopes, Instruments, and Systems, 9, 025007

Mérand, A. 2018, The Messenger, 171, 14

SF2A 2023
M. N'Diaye, A. Siebert, N. Lagarde, O. Venot, K. Baillié, M. Béthermin, E. Lagadec, J. Malzac, J. Richard (eds)

PROBING THE SECULAR EVOLUTION OF EMBEDDED PROTOPLANETARY DISCS

J. Mauxion[1]

Abstract. We perform a large timescale core collapse simulation to explore the secular evolution of embedded protoplanetary discs. The secular evolution properties point towards evolved discs. The disc experiments three accretion phases where the magnetic braking is the main accretion driver in the pseudo-disc while self-gravity is the main accretion driver in the disc via Toomre instability.

Keywords: Stars: formation – Protoplanetary discs – Magnetohydrodynamics – Methods: numerical

1 Introduction

During the early class 0/I stages of their evolution, protoplanetary discs are embedded in an infalling envelope. They are small, massive and strongly magnetized. In class II discs however, the envelope is depleted. The disc is large and weakly magnetized, its mass being dominated by the protostar. This gap is reflected in numerical models, with core collapse models tracking the physics up to early class I while class II disc models assume hydrostatic equilibrium and power-law physics. We bridge this gap by performing core collapse simulations up to the end of class I ($\sim$ 100 kyr after first core formation) while resolving the disc vertical structure ($\sim$ 10 cells/H).

2 Model parameters

The setup is inspired from Masson et al. (2016). We start from an initial uniformly rotating supercritical ($\mu = 2$) 1 $M_\odot$ core of radius $R_0 = 2500$ au at $T_0 = 10$ K. The thermal behavior is handled using a barotropic equation of state following Marchand et al. (2016). The non-ideal effects of the magnetohydrodynamics are accounted using a chemical network adapted from Kunz & Mouschovias (2009).

3 Secular evolution properties

Left panel of figure 1 shows midplane radial profiles of surface density, rotation rate and poloidal magnetic field through the long-term evolution. Surface density has first a sharp transition between a high Σ disc and a low Σ pseudo-disc, then flattens to a power-law. Gas is first Keplerian over $\approx$ 10 au then circularizes up to a few 100 au. The poloidal magnetic field is a plateau in the disc and decreases from 100 mG down to roughly 1 mG.

4 Accretion history

Right panel of figure 1 shows spacetime diagrams of the surface density, poloidal magnetic flux and Toomre parameter, along with the disc radius. When Toomre parameter is near one, it predicts gravitational instability. The pseudo-disc region is always associated to high magnetic flux: there, accretion is driven by magnetic braking. There are three accretion phases in the disc: first, a small disc accretes via gravitational instability. Second, it is growing and stable. Third, it stagnates, the outer part is unstable and accretes.

[1] Univ. Grenoble Alpes, CNRS, IPAG, 38000 Grenoble, France

© Société Française d'Astronomie et d'Astrophysique (SF2A) 2023

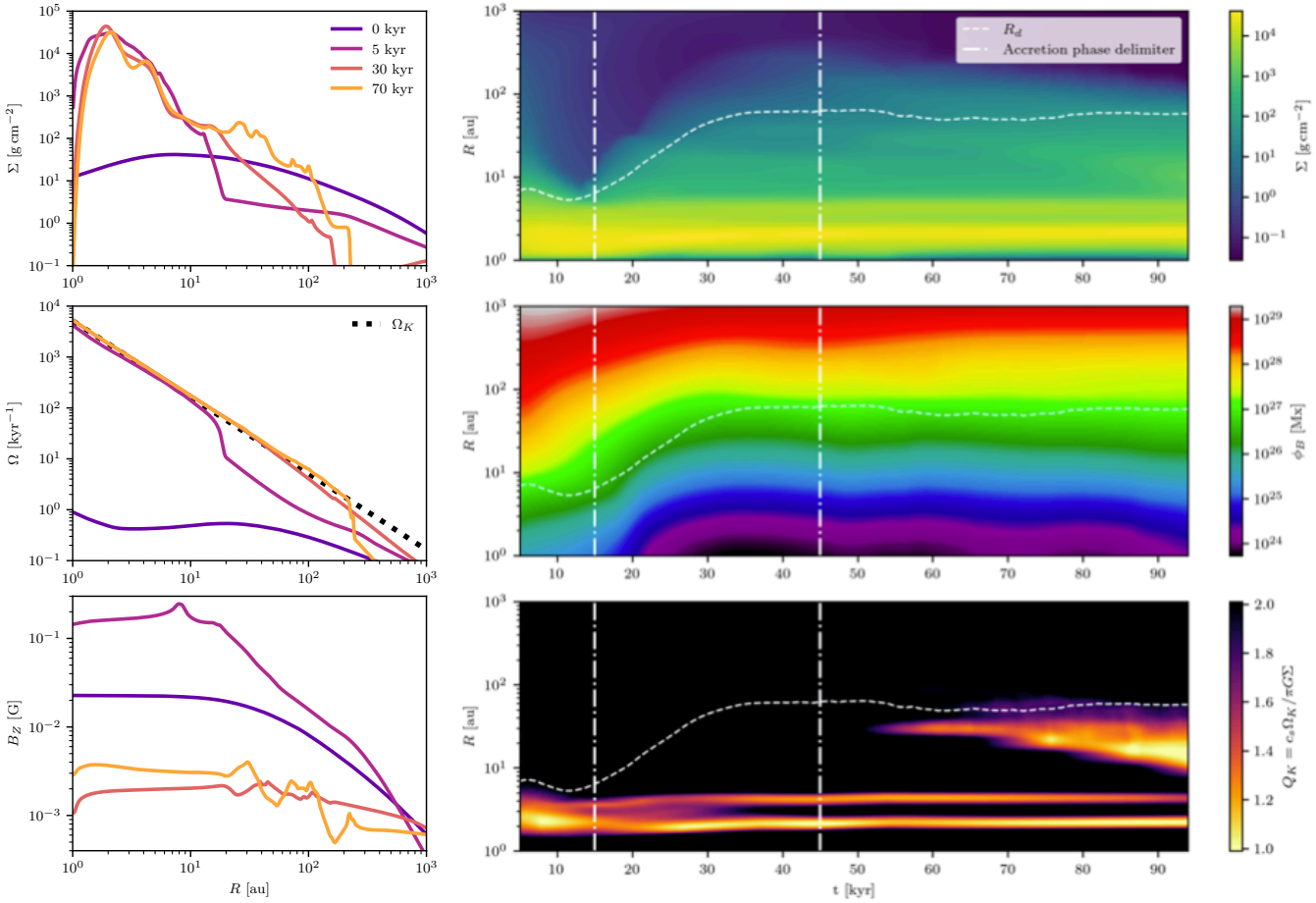

Fig. 1. Left: Radial profiles of the surface density (top), rotation rate (middle), and poloidal magnetic field (bottom) in the midplane, spanning over the whole secular evolution (the lighter, the later). In the middle panel, the black dashed line is the theoretical Keplerian rotation rate. **Right:** Spacetime diagrams of the surface density (top), poloidal magnetic flux (middle) and Toomre parameter (bottom). The dashed white line corresponds to the disc radius, and dash-dotted white lines delimit the three accretion phases.

5 Conclusions

The model is integrated for 100 kyr after disc formation and resolves the vertical structure ($dZ \sim 10^{-2}$ au). The secular evolution properties point towards evolved discs : realization of a surface density power law, magnetic field diffusion from 100 down to 1 mG and gas circularization from 10 up to a few 100 au. There are three phases in the disc accretion history : first a small, spiral-driven accreting disc. Second, an expanding smooth disc. Third an outer, spiral-driven accreting disc. Once a disc has settled, magnetic braking is mainly important in the pseudo-disc where it drives accretion while self-gravity controls the disc accretion through spiral-density waves triggered by Toomre instability.

References

Kunz, M. W. & Mouschovias, T. C. 2009, The Astrophysical Journal, 693, 1895

Marchand, P., Masson, J., Chabrier, G., et al. 2016, Astronomy & Astrophysics, 592, A18

Masson, J., Chabrier, G., Hennebelle, P., Vaytet, N., & Commerçon, B. 2016, Astronomy & Astrophysics, 587, A32

SF2A 2023
M. N'Diaye, A. Siebert, N. Lagarde, O. Venot, K. Baillié, M. Béthermin, E. Lagadec, J. Malzac, J. Richard (eds)

USING ARTIFICIAL INTELLIGENCE TO IMPROVE THE PERFORMANCE OF RADIATIVE HYDRODYNAMICS SIMULATIONS

G. Radureau[1], C. Michaut[1], A. I. Comport[2] and R. Drouilly[1]

Abstract. Radiation hydrodynamics models the coupling between the dynamics of a hypersonic hot plasma and the radiation it produces or external radiation. Radiation hydrodynamics enables us to understand the flow of matter under the extreme conditions present in many astrophysical objects. Various simplified models exist, but in most cases they are limited or even wrong. It was in this context that the HADES code, which stands for "Hydrodynamics Adapted to the Description of Supersonic Flows", was developed (Nguyen (2011), Michaut et al. (2011), Michaut et al. (2017)). This code solves the general equations of radiative hydrodynamics in the 2D case and uses the M1 model for radiation transfer (Turpault 2003). However, calculating the radiative pressure remains a constraint that slows down the code and also requires search algorithms that do not always converge. We are therefore using "Multi-layer Perceptron" neural network architectures, which are among the simplest and most conventional, because we hope that they will reduce computing time and solve convergence problems. These architectures are composed of "perceptrons", the basic cells of neural networks containing parameters to be set, arranged in layers. The parameters of the perceptrons are adjusted so that the neural network gives the right answers to known examples. At the SF2A conference, I will be presenting my work on the use of these neural networks to calculate the Eddington tensor linking radiative pressure to radiative energy, work inspired by what has been done in the case of the study of the interaction of neutrinos with matter, in the case of supernovae (Harada et al. 2022). Preliminary results show a gain in computation time using these neural networks, but we obtain a loss of precision, which is unacceptable for radiative hydrodynamics simulations. On the other hand, a hybrid method using neural networks to initialise the search algorithms is much more interesting. The neural networks then help these algorithms to converge more quickly and more reliably. This latter solution is the most promising for the HADES code.

Keywords: Radiation hydrodynamics, machine learning

1 Introduction

In this work, we describe the fluid's mechanics with Euler's equations taking into account a source term $\overrightarrow{\mathbf{S}}$ and $c\mathrm{S}^0$, coming from the interaction of the fluid with light. We model the radiative transfer with the M1 multi-group model, which namely in cutting the frequency spectrum into groups of frequencies $\mathcal{G} = \{[\nu_1, \nu_2], [\nu_2, \nu_3], ...\}$, giving us one equation describing the evolution of the radiative energy, flux and pressure for each group :

$$\begin{cases} \partial_t \rho + \overrightarrow{\nabla} \cdot (\rho \overrightarrow{\mathbf{u}}) = 0 \\ \partial_t (\rho \overrightarrow{\mathbf{u}}) + \overrightarrow{\nabla} \cdot (\rho \overrightarrow{\mathbf{u}} \otimes \overrightarrow{\mathbf{u}} + p\mathbb{I}) = \overrightarrow{\mathbf{S}} \\ \partial_t E + \overrightarrow{\nabla} \cdot ((E+p)\overrightarrow{\mathbf{u}}) = c\mathrm{S}^0 \end{cases}$$

Euler equations

$$\begin{cases} \forall g \in \mathcal{G}, \quad \partial_t \mathrm{E_g} + \overrightarrow{\nabla} \cdot \overrightarrow{\mathbf{F}_g} = -c\mathrm{S}^0_\mathrm{g} \\ \forall g \in \mathcal{G}, \quad \partial_t (c^{-2}\overrightarrow{\mathbf{F}_g}) + \overrightarrow{\nabla} \cdot \mathbb{P}_g = -\overrightarrow{\mathbf{S}_g} \\ \mathrm{S}^0 = \sum_{g\in\mathcal{G}} \mathrm{S}^0_\mathrm{g} \quad ; \quad \overrightarrow{\mathbf{S}} = \sum_{g\in\mathcal{G}} \overrightarrow{\mathbf{S}_g} \end{cases}$$

M1 multi-group radiative transfer equations

Our model also relies on the assumption that light propagates in preferentially in the direction of the radiative flux, which leads to the following relation (Levermore 1984) :

$$\forall g \in \mathcal{G}, \quad \mathbb{P}_g = \mathbb{D}_g \mathrm{E_g} = \begin{bmatrix} \mathbb{D}_{g,xx} & \mathbb{D}_{g,xy} \\ \mathbb{D}_{g,xy} & \mathbb{D}_{g,yy} \end{bmatrix} \mathrm{E_g}$$

[1] Université Côte d'Azur, CNRS, OCA, Lagrange, France
[2] Laboratoire I3S, Université Côte d'Azur, CNRS, Sophia Antipolis, France

© Société Française d'Astronomie et d'Astrophysique (SF2A) 2023

Where $\mathbb{D}_g$ is the Eddington tensors for the group g and $\mathbb{D}_{g,xx}$, $\mathbb{D}_{g,yy}$ and $\mathbb{D}_{g,yy}$ are its components. In radiation hydrodynamics simulations we compute this tensor, but it requires expensive numerical algorithms. We thus have explored the use of MLPs to compute the Eddington tensor in a more efficient way.

2 Our Machine learning approach

2.1 Multi-Layer Perceptron (MLP)

Neural networks are composed of elementary blocks, the *perceptrons*, which are mathematical functions, containing parameters that need to be adjusted to solve a given problem. These elementary structures can be assembled into layers to reproduce more complex functions.

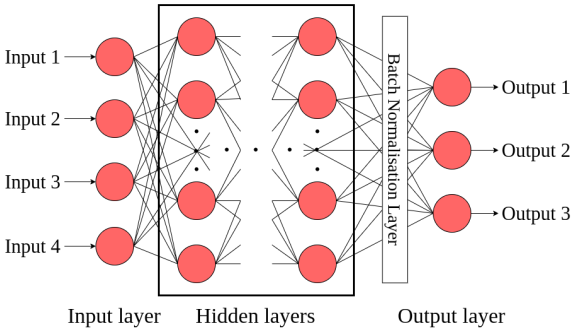

In our case we have used an MLP containing 4 hidden layers, 36 neurons per hidden layer and we have trained the network for 500 epochs. The inputs of our neural network are the radiative energy $\mathrm{E_g}$, the x and y components of the radiative flux $\mathrm{F}_{x,g}$ and $\mathrm{F}_{y,g}$ and the frequency bounds of the group ν_1 and ν_2. The outputs are the components of the Eddington tensor $\mathbb{D}_{g,xx}$, $\mathbb{D}_{g,yy}$ and $\mathbb{D}_{g,xy}$.

2.2 Use of machine learning algorithms : Eddington tensor

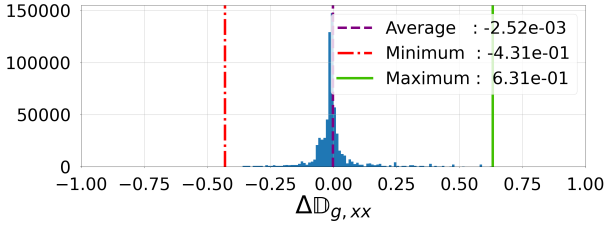

Fig. 1: Prediction error on $\mathbb{D}_{g,xx}$

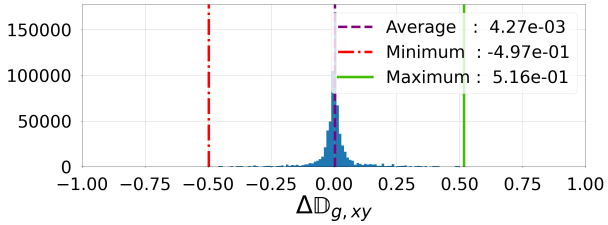

Fig. 2: Prediction error on $\mathbb{D}_{g,yy}$

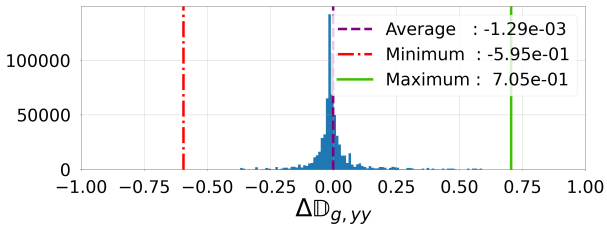

Fig. 3: Prediction error on $\mathbb{D}_{g,xy}$

We have trained an MLP to replace the current algorithm that computes the Eddington tensor in the M1 multi-group case, using random inputs. The error is centered on 0, yet we can get errors that reach 0.7, which is very significant, since $\mathbb{D}_{g,xx}$ and $\mathbb{D}_{g,yy}$ vary in [0, 1] and $\mathbb{D}_{g,xy}$ varies in [-1, 1].

3 Conclusions and perspectives

Our preliminary estimations have shown that using an MLP to compute the Eddington tensor can reduce by a factor 10 the computation time, yet they can introduce large numeric errors. In our future work, we will explore a hybrid method using an MLP and search algorithms to enhance the accuracy of the neural network.

This work was supported by a French government grant managed by the Agence Nationale de la Recherche under the Investissement d'avenir program, reference ANR-19-P3IA-0002.

References

Harada, A., Nishikawa, S., & Yamada, S. 2022, The Astrophysical Journal, 925, 117
Levermore, C. 1984, Journal of Quantitative Spectroscopy and Radiative Transfer, 31, 149
Michaut, C., Di Menza, L., Nguyen, H., Bouquet, S., & Mancini, M. 2017, High Energy Density Physics, 22, 77
Michaut, C., Nguyen, H., & Di Menza, L. 2011, Astrophysics and Space Science, 336, 175
Nguyen, H. C. 2011, PhD thesis, Paris 11
Turpault, R. 2003, Theses, Université Sciences et Technologies - Bordeaux I

SF2A 2023
M. N'Diaye, A. Siebert, N. Lagarde, O. Venot, K. Baillié, M. Béthermin, E. Lagadec, J. Malzac, J. Richard (eds)

NEAR-INFRARED SPECTROSCOPIC FOLLOW-UP OF GAIA ULTRA-COOL DWARFS CANDIDATES

T. Ravinet[1], C. Reylé[1], A. Burgasser[2], R. L. Smart[3], J. G. Fernández-Trincado[4] and W. H. Moya[5]

Abstract. Ultra-cool dwarfs are red, cool and low-luminosity objects, with spectral types later than M7. They encompass the stellar-substellar boundary, and their faintness make them an elusive population. In the solar neighbourhood, their census is incomplete, despite representing an important fraction of local objects in the Milky Way. Numerous new ultra-cool dwarfs candidates have been identified thanks to the Gaia survey, and have to be spectroscopically confirmed to complete a census.

We analyse the near-infrared spectra, obtained with the SOFI spectrograph between 0.93 and 2.5 microns (R$\sim$ 600), of 61 ultra-cool dwarf candidates in the solar neighbourhood. We confirm that all are ultra-cool dwarfs from their spectral types, except one. Their near-infrared spectral types are close to what was expected from their photometric spectral types, derived using their absolute magnitude. We find that objects identified in previous surveys have similar published spectral types.

In our UCD sample, we detected binary candidates, from common parallaxes and proper motions. We also find unresolved binaries from features in their spectra, revealing the presence of a cool companion.

Keywords: Brown dwarfs, Stars: late-type, Stars: low-mass, Infrared: stars, surveys

1 Introduction

M dwarfs ($\lesssim 0.6\,M_\odot$) are the most prominent stars in the Galaxy, and account for $\sim 60\%$ of the stellar budget in the solar neighbourhood (Bochanski et al. 2010; Reid & Gizis 1997; Reyl'e et al. 2021b). Objects with spectral types later than M7, with a temperature lower than 2800 K (e.g Rajpurohit et al. 2013) have been defined as Ultra-Cool Dwarfs (hereafter UCDs) by Kirkpatrick et al. (1999), a name used to designate the less massive stars, as well as brown dwarfs, encompassing the stellar-substellar transition.

UCDs form an elusive population, due to their faintness. Large photometric surveys of objects found red, cold, and low luminosity in colour-absolute magnitude diagrams allow to statistically study UCDs. Thanks to its complete sky coverage, the *Gaia* satellite permits to unveil the optical emissions of UCDs down to a G-magnitude of ~ 20.5. With *Gaia* Data Release 2, Reylé (2018) compiled a set of 14 200 UCD candidates, and additional candidates have been identified within the data release by Smart et al. (2019); Scholz (2020). The DR3 acquired new parallaxes and new candidates (Gaia Collaboration, Smart et al. 2021; Sarro et al. 2023).

The Spectral Energy Distribution of the candidates, together with stellar atmosphere and evolutionary models, permit to estimate their temperatures Filippazzo et al. (2015). Their space-density can be estimated using luminosity functions (Cruz et al. 2007; Reyl'e et al. 2010; Bochanski et al. 2010).

With the acquisition of UCD candidates spectra in the near-infrared, where the objects radiate most of their energy, we can determine their spectral types, and confirm their nature that was estimated from their *Gaia* G-band absolute magnitude. These new spectra also allow improving our understanding of the physics and atmospheric processes occurring in these cool objects, and to search for unresolved binaries.

[1] Université de Franche-Comté, Institut UTINAM, CNRS UMR6213, OSU THETA Franche-Comté-Bourgogne, Observatoire de Besançon, BP 1615, 25010 Besançon Cedex, France

[2] Department of Astronomy & Astrophysics, University of California San Diego, La Jolla, CA 92093, USA

[3] Istituto Nazionale di Astrofisica, Osservatorio Astrofisico di Torino, Strada Osservatorio 20, I-10025 Pino Torinese, Italy

[4] Instituto de Astronomía, Universidad Católica del Norte, Av. Angamos 0610, Antofagasta, Chile

[5] Instituto Multidisciplinario de Investigación y Postgrado, Universidad de La Serena, Raúl Bitrán 1305, La Serena, Chile ; Departamento de Astronomía, Universidad de La Serena, Av. Cisternas 1200, La Serena, Chile

© Société Française d'Astronomie et d'Astrophysique (SF2A) 2023

2 Method

Using the SOFI spectrometer (Moorwood et al. 1998, NTT, la Silla), we acquire near-infrared spectra of 61 *Gaia* UCD candidates that were found in Reylé (2018); Smart et al. (2019); Scholz (2020). The resulting spectra are low-resolution ($R \sim 600$), within the $0.90 - 2.53\,\mu$m wavelength range.

Using the *SpeX Prism Library Analysis Toolkit* (SPLAT, Burgasser & Splat Development Team 2017), we determine the spectral types of the SOFI spectra by comparing the SOFI spectra to spectra with spectral types already assigned from the SpeX Prism Library (SPL). The library includes standard objects, such as the ones defined by Kirkpatrick et al. (2010), but also peculiar ones : low and very-low gravity objects classified following β, γ indices of Cruz et al. (2009), or low metallicity subdwarfs (Lodieu et al. 2019).

We also search for binaries, by looking for objects with common parallaxes and proper motions (Smart et al. 2019; Reyl'e et al. 2021a), as well as objects showing signs of spectral (unresolved) binarity (Burgasser et al. 2010, 2011; Bardalez Gagliuffi et al. 2014).

3 Results

On Fig. 1, we present the distribution of spectral types of observed objects. We confirm that 57 objects have a spectral type later than M7, and that 3 have a spectral type of M6 or M6.5, compatible with being UCDs. The last object, that was expected to be a M8, is found to be a M4. This unexpected spectral type could be caused by a pointing error, or by a *Gaia* photometry error that led to the selection of this object as a UCD candidate. The overall agreement between the photometric spectral types published by Reylé (2018) and those derived in this study, which agree by less than one subtype, gives confidence in the nature of the objects detected by *Gaia*, even without spectroscopic follow-up.

Amongst the observed objects, two to four objects are potential low-metallicity subdwarfs, as they have blue colours or are similar to already-classified low-metallicity UCDs. We find seven that have common parallaxes and proper motions with brighter objects or other UCDs. One of them is in a binary system with a white dwarf spotted by *Gaia*, *Gaia* DR2 4757030391786232576. We also find spectra that show indices of unresolved binarity. Analysing these spectra following the method proposed by Bardalez Gagliuffi et al. (2014), we find seven sources that are likely to be unresolved UCDs accompanied by even cooler companions, T-dwarfs.

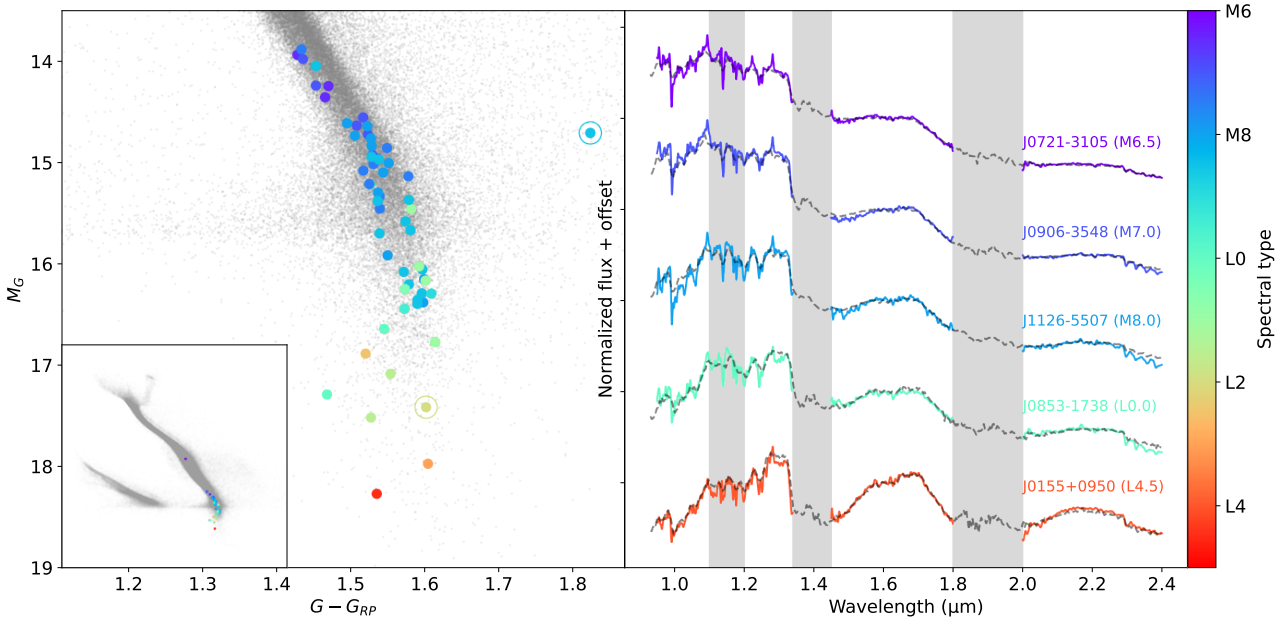

Fig. 1. Left: Observed UCD candidates on a zoomed *Gaia* M_G - $G - G_{RP}$ diagram. UCDs are coloured by their obtained spectral type. The two circled UCDs have peculiar colours due to poor photometry or partially resolved binarity. Right: Example spectra issued from our observed sample, coloured by their spectral type. In dashed grey, we present the best matching standard used to derive the classification. The shaded area are telluric absorption regions of the Earth atmosphere.

This work has made use of data from the European Space Agency (ESA) mission Gaia (https://www.cosmos.esa.int/gaia), processed by the Gaia Data Processing and Analysis Consortium (DPAC, https://www. cosmos.esa.int/web/gaia/dpac/consortium). This research has made use of the SIMBAD database, operated at CDS, Strasbourg, France. Based on observations collected at the European Organisation for Astronomical Research in the Southern Hemisphere under ESO programmes 106.214E.001 and 108.22G4.001. This research has been supported by the Centre National d'Etudes Spatiales (CNES) PhD grant 2021-262, and a PhD grant from the Région Bourgogne-Franche-Comté.

References

Bardalez Gagliuffi, D. C., Burgasser, A. J., Gelino, C. R., et al. 2014, The Astrophysical Journal, 794, 143

Bochanski, J. J., Hawley, S. L., Covey, K. R., et al. 2010, The Astronomical Journal, 139, 2679

Burgasser, A. J., Bardalez-Gagliuffi, D. C., & Gizis, J. E. 2011, The Astronomical Journal, 141, 70, aDS Bibcode: 2011AJ....141...70B

Burgasser, A. J., Cruz, K. L., Cushing, M., et al. 2010, The Astrophysical Journal, 710, 1142

Burgasser, A. J. & Splat Development Team. 2017, 14, 7, conference Name: Astronomical Society of India Conference Series Place: eprint: arXiv:1707.00062 ADS Bibcode: 2017ASInC..14....7B

Cruz, K. L., Kirkpatrick, J. D., & Burgasser, A. J. 2009, The Astronomical Journal, 137, 3345

Cruz, K. L., Reid, I. N., Kirkpatrick, J. D., et al. 2007, The Astronomical Journal, 133, 439

Filippazzo, J. C., Rice, E. L., Faherty, J., et al. 2015, The Astrophysical Journal, 810, 158

Kirkpatrick, J. D., Looper, D. L., Burgasser, A. J., et al. 2010, The Astrophysical Journal Supplement Series, 190, 100

Kirkpatrick, J. D., Reid, I. N., Liebert, J., et al. 1999, The Astrophysical Journal, 519, 802

Lodieu, N., Allard, F., Rodrigo, C., et al. 2019, Astronomy & Astrophysics, 628, A61

Moorwood, A., Cuby, J. G., & Lidman, C. 1998, The Messenger, 91, 9, aDS Bibcode: 1998Msngr..91....9M

Rajpurohit, A. S., Reyl'e, C., Allard, F., et al. 2013, Astronomy & Astrophysics, 556, A15

Reid, I. N. & Gizis, J. E. 1997, The Astronomical Journal, 113, 2246

Reylé, C. 2018, Astronomy & Astrophysics, 619, L8

Reyl'e, C., Delorme, P., Willott, C. J., et al. 2010, Astronomy & Astrophysics, 522, A112

Reyl'e, C., Gimenez Sanchez, V., & Lagarde, N. 2021a, Ultra-cool dwarfs in wide binaries from Gaia, conference Name: The 20.5th Cambridge Workshop on Cool Stars, Stellar Systems, and the Sun (CS20.5) Pages: 320 ADS Bibcode: 2021csss.confE.320R

Reyl'e, C., Jardine, K., Fouqu'e, P., et al. 2021b, Astronomy & Astrophysics, 650, A201

Sarro, L. M., Berihuete, A., Smart, R. L., et al. 2023, Astronomy & Astrophysics, 669, A139, publisher: EDP Sciences

Scholz, R.-D. 2020, Astronomy & Astrophysics, 637, A45

Smart, R. L., Marocco, F., Sarro, L. M., et al. 2019, Monthly Notices of the Royal Astronomical Society, 485, 4423

Smart, R. L., Sarro, L. M., Rybizki, J., et al. 2021, Astronomy & Astrophysics, 649, A6

Session S18

Prédiction et suivi des signaux multi-messagers

SF2A 2023
M. N'Diaye, A. Siebert, N. Lagarde, O. Venot, K. Baillié, M. Béthermin, E. Lagadec, J. Malzac, J. Richard (eds)

SVOM CONTRIBUTION TO MULTI-MESSENGER ASTRONOMY

J.-L. Atteia[1], B. Cordier[2] and J. Y. Wei, on behalf of the SVOM collaboration[3]

Abstract. Few months before the launch of the *SVOM* satellite, this short contribution describes the mission and its expected contribution to the rapidly developing field of multi-messenger astronomy.

Keywords: SVOM, gamma-ray bursts, multi-messenger astronomy.

1 Overview of the mission

SVOM (Space-based multiband astronomical Variable Objects Monitor) is a Sino-French mission committed to Gamma-Ray Burst (GRB) studies and, in general, to the discovery and multi-wavelength follow-up of cosmic transients. The mission includes a satellite and a dedicated ground segment. The satellite carries two wide-field monitors for GRB detection, called ECLAIRs and GRM (Gamma-Ray Monitor), and two narrow-field telescopes for GRB follow-up, called MXT (Microchannel X-ray Telescope) and VT (Visible Telescope). The Ground segment encompasses two 1-m class robotic telescopes (C-GFT and F-GFT), a network of wide-field visible cameras (GWACs) and an ensemble of ~ 45 VHF receivers distributed in tropical zones at the footprint of *SVOM* orbit to receive the alerts and forward them to the French Science Center. *SVOM* is expected to be launched in the first semester of 2024 for a nominal mission of three years, possibly extended by two additional years. An important effort is on-going to prepare the science tools needed for data analysis before the launch.

While the two wide-field monitors will survey large fractions of the sky ($\sim 15\%$ for ECLAIRs and $\sim 20\%$ for GRM) to look for new high-energy transients, the narrow-field instruments will simultaneously perform multi-wavelength observations of selected sources. The detection and localisation of a new transient will result in the sending of an alert and the automatic repointing of the satellite, allowing its observation with the on-board X-ray and visible telescopes in minutes. *SVOM* will adopt a pointing strategy optimized for ground-based follow-up, by observing the sky above the Earth's night hemisphere. This allows for a large fraction (up to 75 %) of the real-time GRB alerts broadcast by *SVOM* to be quickly observed by ground-based instruments, fostering space - ground collaborations.

When in operation, *SVOM* will provide many of the capabilities expected from a modern HE transient mission, such as on-board localizations in seconds and quick alert dissemination, automatic satellite slew, on-board multi-wavelength follow-up, refined localizations in minutes, and a the possibility to quickly adjust the observing plan to point targets of opportunity. The interested reader will find more detailed information, including a complete list of the mission partners, instrument performance and detailed science goals, in the mission reference paper(Wei et al. 2016) and in recent reviews (Yu et al. 2020; Bernardini et al. 2021; Atteia et al. 2022).

Tables 1 and 2 summarize the main characteristics of *SVOM* instruments. These characteristics are not discussed here, but the reader will find extensive information on the instruments in the references given in each table. One unique strength of *SVOM* is its combination of space and ground instruments, which aims at providing the broad temporal and spectral coverage required to clarify the complex physical processes at work in GRBs, especially during the prompt emission and early afterglow. In an ideal case a GRB detected and localized by ECLAIRs, will benefit from observations of its prompt emission from 4 keV to 5 Mev, with simultaneous optical observations with one of the GWACs. The afterglow of this ideal GRB will be simultaneously detected by MXT and VT in space and by one of the GFTs on Earth, allowing to follow the full spectro-temporal evolution of the afterglow from eV to keV. The benefits of this approach are discussed in Bernardini et al. (2017).

[1] Université de Toulouse, CNRS, CNES, UPS, (Toulouse), France

[2] Lab AIM - CEA, CNRS, Université Paris-Saclay, Université de Paris, 91191, Gif-sur-Yvette, France

[3] Key Laboratory of Space Astronomy and Technology, National Astronomical Observatories, Chinese Academy of Sciences, Beijing 100101, People's Republic of China

© Société Française d'Astronomie et d'Astrophysique (SF2A) 2023

Fig. 1. Pictures of various components of the mission. **From top left to bottom right:** The satellite in August 2023, before thermal vacuum tests in Shanghai - The 1.3 meter French Ground Follow-up Telescope at Haute Provence Observatory in June 2023, about to leave for Mexico (credit CNRS, Cyril Frésillon) - A VHF receiving ground station installed on the roof of one building of the Martin-de-Viviès base in the Amsterdam Island in South Pacific - A set of GWAC cameras at the Xinglong Observatory in China.

2 SVOM and multi-messenger astronomy

The crucial role of high-energy transient detectors has been stressed by the simultaneous detection of GW 170817 and GRB 170817A (Abbott et al. 2017). Since it is clearly beyond the scope of this paper to list all the possible science contributions of the mission, we prefer to indicate below some areas where *SVOM* will bring new observing capabilities:

= **First**, *SVOM* will expand the zoo of high-energy transients to poorly studied events. ECLAIRs will be sensitive to soft GRBs (X-Ray Flashes and high-z GRBs) and ultra-long GRBs (with stable long pointings) (Arcier et al. 2020; Dagoneau et al. 2020), while the GRM will favor the detection of short GRBs and SGRs over a large field of view. The history of the field has shown that the diversity of high-energy transients can only be fully explored with instruments with diverse capabilities and observing strategies.

= **Second**, sub-threshold searches for excesses coincident with other signals (e.g. gravitational waves) will be fostered by the recording of all photons detected by ECLAIRs and GRM. This post-processing capability is especially important in the multi-messenger era.

= **Third**, *SVOM* will greatly enhance follow-up capabilities and redshift measurements, thanks to the detection of high-energy transients immediately observable from the ground, to a sensitive Visible Telescope on-board the satellite and to two 1-meter class fast follow-up telescopes, one of which is equipped with a near-infrared camera.

= **Fourth**, *SVOM* will offer valuable target of opportunity (ToO) capabilities to the community, with the

possibility of performing single pointings as well as tiled observations optimized for large error boxes (Ducoin et al. 2023), a few hours only after the decision.

***SVOM* and O4.** The launch of *SVOM* in the first semester of 2024 will provide the first occasion to test these new capablities for real during the O4 run of the gravitational wave interferometers of the LVK collaboration We are currently working hard to have *SVOM* ready to contribute to multi-messenger astrophysics during the second half of O4 (`https://observing.docs.ligo.org/plan/`).

3 SVOM status

The satellite is currently (october 2023) undergoing environment testing in the premises of the Shanghai Micro Satellite Engineering Center (SECM) on line for a launch in the first semester of 2024. Regarding the ground segment, most of the VHF network has been deployed (see `https://www.svom.eu/en/reseau-dalerte-en/` for a status), the C-GFT telescope and the GWAC network are already observing (Turpin et al. 2020, e.g.), and the F-GFT will be operational at the San Pedro Mártir Observatory (Mexico) in the first semester of 2024. Within few months, *SVOM* will give us a new window on the high-energy sky and contribute to the fast growing fields of multi-messenger astronomy and time domain astronomy

The authors gratefully acknowledge the support of *SVOM* funding agencies: CNES, CEA and CNRS in France ; CNSA and CAS in China.

References

Abbott, B. P., Abbott, R., Abbott, T. D., et al. 2017, ApJ, 848, L13

Arcier, B., Atteia, J. L., Godet, O., et al. 2020, Ap&SS, 365, 185

Atteia, J. L., Cordier, B., & Wei, J. 2022, International Journal of Modern Physics D, 31, 2230008

Basa, S., Lee, W. H., Dolon, F., et al. 2022, in Society of Photo-Optical Instrumentation Engineers (SPIE) Conference Series, Vol. 12182, Ground-based and Airborne Telescopes IX, ed. H. K. Marshall, J. Spyromilio, & T. Usuda, 121821S

Bernardini, M. G., Cordier, B., & Wei, J. 2021, Galaxies, 9, 113

Bernardini, M. G., Xie, F., Sizun, P., et al. 2017, Experimental Astronomy, 44, 113

Dagoneau, N., Schanne, S., Atteia, J.-L., Götz, D., & Cordier, B. 2020, Experimental Astronomy, 50, 91

Ducoin, J. G., Desoubrie, B., Daigne, F., & Leroy, N. 2023, MNRAS, 524, 4000

Fan, X., Zou, G., Wei, J., et al. 2020, in Society of Photo-Optical Instrumentation Engineers (SPIE) Conference Series, Vol. 11443, Society of Photo-Optical Instrumentation Engineers (SPIE) Conference Series, 114430Q

Godet, O., Atteia, J. L., Amoros, C., et al. 2022, in Society of Photo-Optical Instrumentation Engineers (SPIE) Conference Series, Vol. 12181, Society of Photo-Optical Instrumentation Engineers (SPIE) Conference Series, ed. J.-W. A. den Herder, S. Nikzad, & K. Nakazawa, 121815O

Godet, O., Nasser, G., Atteia, J. ., et al. 2014, in Society of Photo-Optical Instrumentation Engineers (SPIE) Conference Series, Vol. 9144, Space Telescopes and Instrumentation 2014: Ultraviolet to Gamma Ray, ed. T. Takahashi, J.-W. A. den Herder, & M. Bautz, 914424

Götz, D., Boutelier, M., Burwitz, V., et al. 2023, Experimental Astronomy, 55, 487

Han, X., Xiao, Y., Zhang, P., et al. 2021, PASP, 133, 065001

He, J., Sun, J.-C., Wen, X., et al. 2020, Ap&SS, 365, 167

Mao, Q., Qiu, Y., Zhang, Y., et al. 2022, in Society of Photo-Optical Instrumentation Engineers (SPIE) Conference Series, Vol. 12181, Society of Photo-Optical Instrumentation Engineers (SPIE) Conference Series, ed. J.-W. A. den Herder, S. Nikzad, & K. Nakazawa, 121815S

Meuris, A., Arhancet, A., Bachet, D., et al. 2023, Nuclear Instruments and Methods in Physics Research A, 1049, 167908

Nouvel de la Flèche, A., Atteia, J.-L., Boy, J., et al. 2023, Experimental Astronomy

Schneider, B., Renault-Tinacci, N., Götz, D., et al. 2023, Experimental Astronomy, 56, 77

Turpin, D., Wu, C., Han, X.-H., et al. 2020, Research in Astronomy and Astrophysics, 20, 013

von Kienlin, A., Meegan, C. A., Paciesas, W. S., et al. 2020, ApJ, 893, 46

Wei, J., Cordier, B., Antier, S., et al. 2016, arXiv e-prints, arXiv:1610.06892

Wen, X., Sun, J., He, J., et al. 2021, Nuclear Instruments and Methods in Physics Research A, 1003, 165301

Xu, Y., Xin, L. P., Wang, J., et al. 2020, PASP, 132, 054502

Yu, S.-j., Gonzalez, F., Wei, J.-y., Zhang, S.-n., & Cordier, B. 2020, Chinese Astron. Astrophys., 44, 269

Table 1. Main characteristics of space instruments .

	GRM	**ECLAIRs**
Energy range	15 – 5000 keV	4 – 150 keV
Number of detectors	3	6400
Detection area	3 $\times$200 cm^2	1000 cm^2
Field of View	2.6 sr (all 3 modules)	total: 2.0 sr ; half-coded: 1.0 sr
Localisation accuracy	$\sim 5^\circ$ (with 3 GRDs)	12'
Expected GRB rate	$\sim$110 yr^{-1} ($\sim$ 17% short, von Kienlin et al. (2020))	$\sim$65 yr^{-1}
Additional features	Includes a particle monitor	Mask open fraction: 40%
References	He et al. (2020); Wen et al. (2021)	Godet et al. (2014, 2022) Bernardini et al. (2021)
	MXT	**VT**
Energy range	0.2 – 10 keV	400 – 1000 nm
Focal length	1150 mm	3600 mm
Optics dimension	200 mm (side)	400 mm (diameter)
Number of detectors	1 (Si pnCCD)	2 (2k $\times$ 2k CCD)
Effective area	35 cm^2 @ 1.5 keV	
Sensitivity	10 mCrab in 10 s ; 150 μCrab in 10 ks	$m_V = 22$ (300 s)
Field of View	$58' \times 58'$	$26' \times 26'$
Localisation accuracy	$< 2'$	$1''$
Additional features	Micro-pores optics with square 40 μm pores. 100 ms time resolution.	Covers the full ECLAIRs error boxes.
References	Götz et al. (2023); Meuris et al. (2023) Schneider et al. (2023)	Fan et al. (2020); Mao et al. (2022)

Table 2. Main characteristics of ground-based instruments.

	C-GFT	**F-GFT (aka Colibri)**
Diameter	1200 mm	1300 mm
Focal ratio	8	3.75
Number of channels	3 (g ; r ; i)	3 (g/r/i ; z/y ; J/H)
Field of View	$21' \times 21'$	$26' \times 26'$ (grizy) ; $21' \times 21'$ (JH)
Limiting magnitude (r channel, 300 s, 10σ)	$m_{AB} \approx 20$	$m_{AB} \approx 22$
References	`https://www.svom.eu/en/..` `ground-follow-up-telescope-gft/`	Basa et al. (2022) Nouvel de la Flèche et al. (2023)
	GWAC	
Number of units	5 (Xinglong) + 4 (Muztagh Ata)	
Number of telescopes / unit	Joint Field of View (JFoV): 4 – Full Field of View (FFoV): 1	
Diameter	JFoV: 180 mm – FFoV: 35 mm	
Detector	JFoV: 4k x 4k CCD – FFoV: 3k x 3k CCD	
Field of View	JFoV: $12.8^\circ \times 12.8^\circ$ – FFoV: $30^\circ \times 30^\circ$	
Limiting magnitude	JFoV: $m_R \sim 16$ – FFoV: $m_R \sim 12$ (r channel, 10 s)	
Location	Xinglong and Muztagh Ata Observatories	
Additional features	Self triggering capability ; The FFoV performs guiding.	
References	Turpin et al. (2020); Xu et al. (2020); Han et al. (2021)	

SF2A 2023
M. N'Diaye, A. Siebert, N. Lagarde, O. Venot, K. Baillié, M. Béthermin, E. Lagadec, J. Malzac, J. Richard (eds)

THE IMPACT OF ROTATION AND DYNAMOS ON THE MULTI-MESSENGER EMISSION OF CORE-COLLAPSE SUPERNOVAE

M. Bugli[1,2], J. Guilet[2], T. Foglizzo[2], M. Obergaulinger[3], M. Reichert[3], M. Bendahman[4], S. El Hedri[4] and I. Goos[4]

Abstract. The gravitational collapse of a massive star leads to the strong emission of gravitational waves and neutrinos during the first few seconds of the supernova event. Multi-messenger observations offer, thus, a unique window on the dynamics that regulate the explosion mechanism and the physical properties of the still-forming central proto-neutron star (PNS). In recent years, numerical models of core-collapse supernovae (CCSN) have started to produce quantitative predictions of both gravitational waves and neutrino emissions which provide the key ingredients necessary to constraint the physics of the explosion engine from actual observational data. Despite the fundamental role that strong magnetic fields play in the case of exceptionally energetic stellar explosions (e.g. long GRBs, hypernovae, superluminous supernovae), their impact on the multi-messenger emission from CCSN remains still largely unknown. We present results from recent studies aimed at quantifying the impact of dynamo-generated magnetic fields on the neutrino and gravitational waves emitted at the formation of a stellar compact object. We show how magnetic fields, by modifying the rotational profile of the proto-neutron star, weaken the development of large-scale instabilities connected to strong multi-messenger signals. However, this can also lead to a broadening of the spectral shape of the GW signal due to the magnetic field's impact on rotation and possibly the onset of the kink instability within the PNS. We finally display how current and upcoming neutrino detectors (e.g. KM3Net, DUNE, DarkSide) will be sensitive to the effects of rotation and strong magnetic fields predicted by our numerical models.

Keywords: supernovae, magnetic fields, gravitational waves, neutrinos, multi-messenger astronomy

1 Introduction

Core-collapse supernovae (CCSN) play a fundamental role in the formation of stellar-sized compact objects. The vast majority of CCSN can be explained by the so-called *neutrino-heating* mechanism, where a small fraction of the neutrinos emitted by the proto-neutron star (PNS) is absorbed by the shocked material (Janka 2012). At this stage of the explosion hydrodynamic phenomena such as the Standing Accretion Shock Instability (SASI) (Buellet et al. 2023; Walk et al. 2023) and the post-shock convection stirred by the neutrino absorption are crucial to aid the expansion of the shock further (Foglizzo et al. 2015). On the other hand, outstanding stellar explosions such as hypernovae, superluminous supernovae or long gamma-ray bursts require some additional energy reservoir to account for their exceptional kinetic energies and luminosities (Kasen & Bildsten 2010; Nicholl et al. 2013). A popular explanation relies on the *magneto-rotational* mechanism, where the combination of fast rotation (which provides an additional source of energy) and strong large-scale magnetic fields (which allow to tap into that reservoir) leads to powerful bipolar explosions with collimated outflows propagating along the rotational axis of the star (Bugli et al. 2020; Obergaulinger & Aloy 2021; Bugli et al. 2021).

Regardless of the specific explosion mechanism, the emission of both neutrinos and gravitational waves during this early stage of the explosion provides a unique window on the physical properties of the central PNS and the shock dynamics (Kuroda & Umeda 2010; Kuroda et al. 2016; Torres-Forné et al. 2019). Fast rotation can induce the onset of the so-called low-$T/|W|$ instability, whose action leads to large-scale non-axisymmetric

[1] Dipartimento di Fisica, Università di Torino, via Pietro Giuria 1, 10125 Torino, Italy
[2] Université Paris-Saclay, Université Paris Cité, CEA, CNRS, AIM, 91191, Gif-sur-Yvette, France
[3] Departament d'Astonomia i Astrofísica, Universitat de València, C/Dr. Moliner, 50, E-46100 Burjassot (València), Spain
[4] Université Paris Cité, CNRS, Astroparticule et Cosmologie, 10 rue Alice Domon et Léonie Duquet, Paris, France

© Société Française d'Astronomie et d'Astrophysique (SF2A) 2023

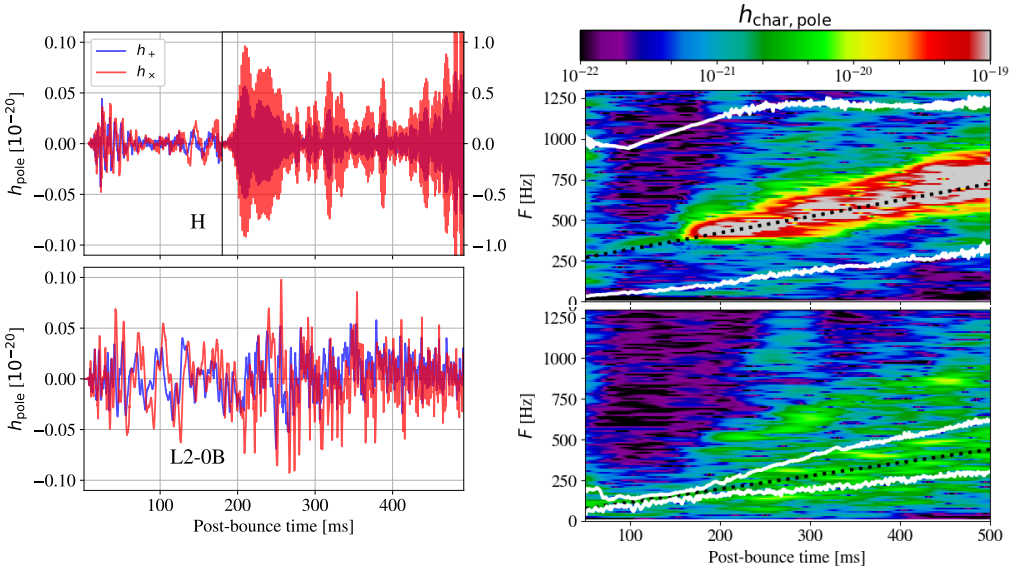

Fig. 1. On the left, GW strains observed along the polar axis for the unmagnetized model (top panel) and the model with an aligned quadrupolar magnetic field (bottom). On the right, time-frequency spectrograms for the corresponding characteristic strain $h_{\rm char}$. White lines represent twice the minimum and maximum rotational frequency of the PNS, while the black dotted line is twice the frequency of the $m = 1$ mode in the PNS density (from Bugli et al. 2023).

modes that can produce a strong emission of gravitational waves and modulations in the neutrino lightcurves (Takiwaki et al. 2021). However, the impact that strong magnetic fields can have on the multi-messenger emission of CCSN is still not very clear, due to the high computational cost of 3D magnetohydrodynamic (MHD) simulations of a stellar collapse and the consequent limitation in the number of models available. In the present work we show the analysis on the GW and neutrino emission from highly magnetized and fast rotating CCSN models (Bugli et al. 2023), highlighting in particular the signatures of fluid instabilities such as SASI and the low-$T/|W|$ instability. We will present the effects of the intense magnetic fields within the PNS on the neutrino luminosity curves and comment on their detectability with current and next-generation neutrino detectors (Bendahman et al. 2023). Finally, we will show the impact of strong magnetic fields on the ejecta composition and the effects on the explosive nucleosynthesis and the production of r-process elements (Bugli et al. 2023; Reichert et al. 2023).

2 Gravitational waves

The results shown here were obtained from 3D MHD numerical models of CCSN with the massive stellar progenitor `350C` in fast rotation. The different initial magnetic field configurations (an aligned dipolar, aligned quadrupolar, and equatorial dipolar field; for more details, see Bugli et al. 2021) are meant to take into account the complex field structures that typically arise during the dynamo processes that can occur within the PNS during the collapse (Raynaud et al. 2020; Reboul-Salze et al. 2021; Reboul-Salze et al. 2022; Guilet et al. 2022) but are not resolved in large-scale CCSN models.

Model H represents a hydrodynamic benchmark without a magnetic field, and it is the only one amongst the simulations we are considering that develops the low $T/|W|$ instability within the first few hundreds of ms after shock formation. This is evident from Fig. 1 (top panel on the left), where the GW strain observed along the rotational axis exhibits a strong and long lasting emission after $\sim$ 200 ms post-bounce (p.b.) which coincides with the formation of a spiral structure in the density distribution within the PNS. The frequency of this emission increases steadily with time (top right panel of Fig. 1), due to the contraction of the PNS and the conservation of angular momentum. On the other hand, none of the magnetized models show a distinctive sign of the onset of the instability. The GW emission remains overall weaker than the hydrodynamic case, with no clear bursts over time. The spectral shape of the signal is generally broader, with features appearing at frequencies higher than the PNS rotational one, suggesting a significant contribution by mechanisms not induced by rotation itself (e.g. proper oscillation modes of the PNS). The main reason behind this qualitative

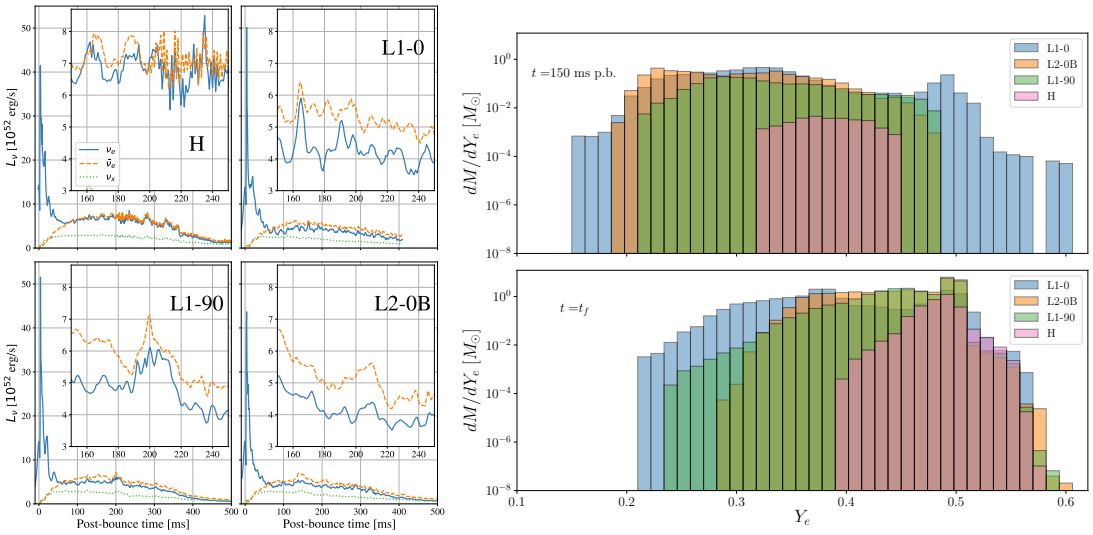

Fig. 2. Neutrino luminosities along the equatorial plane for all 3 neutrino species and four different magnetic field configurations (left) and ejecta compositions at two different times (right; from Bugli et al. 2023).

difference is the high efficiency of outward transport of angular momentum in presence of strong large-scale magnetic fields. As the rotation profile flattens, the PNS becomes stable against the low-$T/|W|$ instability and the formation of large-scale non-axisymmetric structures is disfavoured (Bugli et al. 2023).

3 Neutrinos and explosive nucleosynthesis

The neutrino emission from the magnetized models also presents qualitative differences w.r.t. the hydrodynamic case (left panels of Fig. 2). Similarly to GW, only for model H the luminosity curves observed along the equatorial plane have a distinctive high-frequency modulation at ~ 200 ms p.b. caused by the onset of the low-$T/|W|$ instability. Moreover, all magnetized models systematically have a lower luminosity in ν_e and $\bar{\nu}_e$, which stems from the more oblate shape of the PNS induced by the strong magnetic transport of angular momentum. Another effect of the extraction of rotational energy from the PNS via magnetic torques is a tendency to increase the amount of neutron-rich material in proximity of the PNS surface in the equatorial region, which would be otherwise accreted on the PNS without the additional rotational support. This phenomenon tends to increase the size of the region where ν_e are absorbed, pushing the electron neutrino-sphere further out, thus decreasing both the mean energy and the corresponding luminosity of ν_e w.r.t. $\bar{\nu}_e$.

The systematic decrease in the equatorial ν_e and $\bar{\nu}_e$ fluxes due to the action of strong magnetic fields can have a clear impact on neutrino observations (Bendahman et al. 2023). The left panel of Fig. 3 shows the number of events expected in the ARCA detector from the KM3NeT experiment (Adrian-Martinez et al. 2016; Aiello et al. 2021; Bendahman et al. 2022) for a CCSN event located at a distance of 5 kpc. Even considering the finite efficiency of the instrument and the presence of significant background, there is a clear suppression of the neutrino fluxes between 200 and 400 ms p.b. for the model with an aligned dipolar magnetic field. The significance of this effect, measured for several next-generation neutrino detectors, is instead shown in the right panel of Fig. 3. While KM3NeT could observe the suppression up to the galactic center at 3σ, experiments such as Hyper-Kamiokande, DUNE, and DarkSide-20k will have full galactic sensitivity.

Magnetic fields can also have a strong impact on the nuclear composition of the ejecta and the prospects for the production of heavy elements via explosive nucleosynthesis. Fig. 2 shows how magnetized models tend to expel more neutron-rich material than the hydrodynamic case, with model L1 (aligned dipolar field) producing the ejecta with the lower electron fraction Y_e. This effect is mainly due to the magneto-rotational explosion mechanism being able to eject material on shorter time-scales than in the hydrodynamic scenario, thus preventing the accretion of this material on the PNS or its irradiation by ν_e, which would increase Y_e accordingly. Since the presence of more neutron-rich ejecta favours the production of r-process elements (Reichert et al. 2021, 2023), the magnetized models here presented also produce heavier elements than model H, with the aligned dipolar case being the most efficient and capable of producing, to a certain extent, elements up to the second

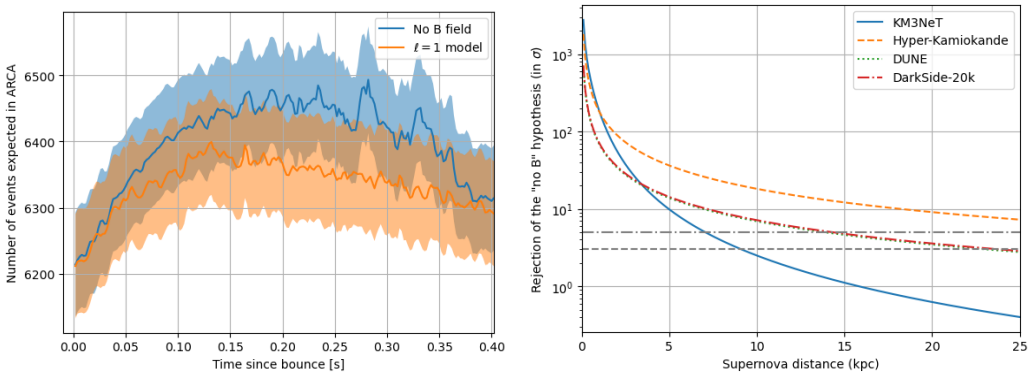

Fig. 3. On the left panel, neutrino event counts in the window 200-400 ms p.b. expected at KM3NeT-ARCA for the dipolar model L1-0. On the right panel, significance of the difference between the hydrodynamic model and the magnetic dipole model as a function of the CCSN distance (from Bendahman et al. 2023).

r-process peak (Reichert et al., in prep.).

4 Conclusions

We presented a series of 3D MHD models of fast rotating and highly-magnetized CCSN that showcase the impact of strong magnetic fields on the multi-messenger emission of CCSN. We have shown distinctive signatures arising both in GW and neutrinos (in some cases with similar features) and the qualitative effect that magnetic fields have on the production of new elements during the explosion. In forthcoming studies we will explore more in detail the correlations that GW and neutrino signals can display in virtue of common physical processes responsible for their production, while we will also quantitatively assess to what extent different magnetic fields configurations can have a role in the explosive nucleosynthesis.

References

Adrian-Martinez, S., Ageron, M., Aharonian, F., et al. 2016, JPhysG, 43, 084001
Aiello, S., Albert, A., Alves Garre, S., et al. 2021, European Physical Journal C, 81, 445
Bendahman, M., Buellet, A.-C., Bugli, M., et al. 2023, in EPJ Web Conf, Vol. 280, 05002
Bendahman, M., Bugli, M., Coleiro, A., et al. 2022, in 37th International Cosmic Ray Conference, 1090
Buellet, A. C., Foglizzo, T., Guilet, J., & Abdikamalov, E. 2023, A&A, 674, A205
Bugli, M., Guilet, J., Foglizzo, T., & Obergaulinger, M. 2023, MNRAS, 520, 5622
Bugli, M., Guilet, J., & Obergaulinger, M. 2021, MNRAS, 507, 443, aDS Bibcode: 2021MNRAS.507..443B
Bugli, M., Guilet, J., Obergaulinger, M., Cerdá-Durán, P., & Aloy, M. Á. 2020, MNRAS, 492, 58
Foglizzo, T., Kazeroni, R., Guilet, J., et al. 2015, Publications of the Astronomical Society of Australia, 32, e009
Guilet, J., Reboul-Salze, A., Raynaud, R., Bugli, M., & Gallet, B. 2022, MNRAS
Janka, H.-T. 2012, Annual Review of Nuclear and Particle Science, 62, 407
Kasen, D. & Bildsten, L. 2010, ApJ, 717, 245
Kuroda, T., Kotake, K., & Takiwaki, T. 2016, ApJ, 829, L14
Kuroda, T. & Umeda, H. 2010, ApJS, 191, 439
Nicholl, M., Smartt, S. J., Jerkstrand, A., et al. 2013, Nature, 502, 346
Obergaulinger, M. & Aloy, M. A. 2021, MNRAS, 503, 4942
Raynaud, R., Guilet, J., Janka, H.-T., & Gastine, T. 2020, Science Advances, 6, eaay2732
Reboul-Salze, A., Guilet, J., Raynaud, R., & Bugli, M. 2021, A&A, 645, A109
Reboul-Salze, A., Guilet, J., Raynaud, R., & Bugli, M. 2022, A&A, 667, A94
Reichert, M., Obergaulinger, M., Aloy, M. Á., et al. 2023, MNRAS, 518, 1557
Reichert, M., Obergaulinger, M., Eichler, M., Aloy, M. Á., & Arcones, A. 2021, MNRAS, 501, 5733
Takiwaki, T., Kotake, K., & Foglizzo, T. 2021, MNRAS, 508, 966
Torres-Forné, A., Cerdá-Durán, P., Obergaulinger, M., Müller, B., & Font, J. A. 2019, Phys. Rev. Lett., 123, 051102
Walk, L., Foglizzo, T., & Tamborra, I. 2023, Phys. Rev. D, 107, 063014

SF2A 2023
M. N'Diaye, A. Siebert, N. Lagarde, O. Venot, K. Baillié, M. Béthermin, E. Lagadec, J. Malzac, J. Richard (eds)

FOLLOW-UP OF GRAVITATIONAL WAVES ALERTS WITH IACTS USING ASTRO-COLIBRI

M. de Bony de Lavergne[1], H. Ashkar[2], A. K. Alkan[1 3], J. Mourier[1], P. Reichherzer[4], F. Schüssler[1] and M. Seglar-Arroyo[5]

Abstract. Follow-up of gravitational wave alerts has proven to be challenging in the past due to the large uncertainty on the localisation, much larger than the field of view of most instruments. A smart pointing strategy helps to increase the chance of observing the true position of the underlying compact binary merger event and so to detect an electromagnetic counterpart.

To tackle this, a software called tilepy has been developed and was successfully used by the H.E.S.S. collaboration to search for very-high energy gamma-ray emission from GWs during the O2 and O3 runs. The optimised tiling strategies implemented in tilepy allowed H.E.S.S. to be the first ground facility to point toward the true position of GW 170817. Here we will present the main strategy used by the software to compute an optimal observation schedule.

The Astro-COLIBRI platform helps to plan follow-up of a large range of transient phenomena including GW alerts. The integration of tilepy in this tool allow for an easy planning and visualisation of of follow-up of gravitational wave alert helping the astronomer to maximise the chance of detecting a counterpart. The platform also provides an overview of the multi-wavelength context by grouping and visualising information coming from different observatories alongside GW alerts.

Keywords: gravitational wave, tiling, observation tool

1 Introduction

Since the first detection of gravitational waves in 2015, the LIGO and Virgo interferometers have identified more than a hundred of mergers. Despite continuous enhancements to the detectors, the localisation of these events remain uncertain, with uncertainties spanning hundreds to even thousands of square degrees. This challenge is particularly pronounced when attempting to follow up on these gravitational wave alerts using Imaging Atmospheric Cherenkov Telescopes (IACTs), which typically have a limited field of view, typically covering only a few tens of square degrees.

To increase the likelihood of accurately observing the event's precise location, a smart pointing strategy is essential. This strategy involves observing multiple sky fields, often referred to as tiles. To facilitate the scheduling and computation of these tiles, a software tool named *tilepy* has been developed and seamlessly integrated into the Astro-COLIBRI platform. This platform serves as a comprehensive solution for collecting alerts from various channels and efficiently scheduling observations, especially in the context of gravitational wave events, where *tilepy* plays a pivotal role.

2 tilepy: A software for efficient gravitational wave follow-up

2.1 Working principle

tilepy was originally developed for the purpose of following up on Gravitational Wave (GW) events using the H.E.S.S. telescopes (Ashkar et al. 2021). Especially the tool allowed H.E.S.S. to be first ground facility

[1] IRFU, CEA, Université Paris-Saclay, F-91191 Gif-sur-Yvette, France
[2] Laboratoire Leprince-Ringuet, Ecole Polytechnique, CNRS, Institut Polytechnique de Paris, Palaiseau, France
[3] Université Paris-Saclay, CNRS, Laboratoire intersdisciplonaire des sciences du numérique, 91045, Orsay France
[4] Department of Physics, University of Oxford, Oxford OX1 3PU, United Kingdom
[5] Institut de Fisica d'Altes Energies (IFAE), Barcelona Institute of Science and Technology, E-08193 Barcelona, Spain

© Société Française d'Astronomie et d'Astrophysique (SF2A) 2023

pointing towards the real position of GW 170817 (Abdalla et al. 2017), the first coincidence event between gravitational wave and electromagnetic signal. The software is also used by LST-1, the first telescope of CTA, for the follow-up of gravitational waves during the O4 observation run (CTA-LST Project et al. 2022). Today, the code of *tilepy* is accessible to everyone through its GitHub repository at the following address: `https://github.com/astro-transients/tilepy`. Furthermore an API to allow an easy access is accessible at the following address : `https://tilepy.com`.

tilepy operates on the basis of a grid of pointing directions that cover the entire sky. Its primary objective is to optimize scheduling to maximize coverage within the uncertainty region of a GW event by choosing the best pointing possible. Two main strategies are implemented in *tilepy* to achieve this goal.

The first strategy, called "2D" approach, directly utilizes the sky localization map provided by LIGO/Virgo. *tilepy*'s algorithm searches for the pointing direction that provides the most extensive coverage of the uncertainty region. Once identified, this position is removed from the map, and a new pointing direction can be computed in a similar manner. It's worth noting that this method can also be adapted for other types of alerts, such as Gamma-Ray Bursts (GRBs) detected by Fermi/GBM.

Gravitational wave interferometers not only provide sky localizations but also estimate the distance at each position in the sky, enabling a so called "3D" algorithm. This distance information can be cross-referenced with a galaxy catalog, with the current catalog of choice being GLADE+ (Dálya et al. 2022). *tilepy* assigns a probability to each galaxy and then searches for the field of view that encompasses the highest cumulative probabilities by summing the probabilities of all galaxies within it. It is important to note that this strategy is applicable only up to distances of a few hundred megaparsecs, as the completeness of galaxy catalogs diminishes for larger distances.

For a more in-depth understanding of the algorithms used in *tilepy*, please refer to the detailed description provided in Ashkar et al. (2021).

2.2 An HTTP API for an easy use of tilepy

To simplify the use of *tilepy*, a REstful API has been developed. This API allows users to perform tiling for a specific alert through an easy to use and publicly available endpoint. Most of *tilepy*'s essential parameters, such as telescope location, size of the field of view, maximum zenith angle, moon separation, and more, can be configured via the parameters when making a query. The results are returned in JSON format to be easily parsed by an automatic system. The API is accessible with it's documentation at the following address: `https://tilepy.com`. The system is currently hosted on AWS, which assures a high availability.

3 Astro-COLIBRI, a tool for transient astronomy

3.1 The tool for transient astronomy

Fig. 1. Web interface of Astro-COLIBRI

Fig. 2. Smartphone interface of Astro-Colibri

Astro-COLIBRI is a platform for simplifying the study of transient astronomical events. It is integrating real-time multi-messenger observation tools in a simple and user-friendly graphical interface. This platform collects and consolidates information and alerts from various channels, providing astronomers with a comprehensive overview of the current transient phenomena across the sky and facilitating observation planning.

Astro-COLIBRI accommodates a wide range of astrophysical phenomena, making it a versatile tool for astronomers. It includes Active Galactic Nuclei (AGN), Gamma-ray Bursts (GRBs), Fast Radio Bursts (FRBs), Gravitational Waves (GWs), High-energy Neutrinos, Optical Transients (OT), Supernovae (SN), ...

The platform is accessible through two main interfaces. Firstly, a RESTful API hosted on AWS provides programmatic access to its features. You can access this API at the following address: `https://astro-colibri.science`, where comprehensive documentation is also available. Furthermore, Astro-COLIBRI offers a user-friendly graphical interface, which can be accessed through a Web browser (Figure 1) or a dedicated smartphone application (Figure 2). This last option also allows one to receive notification on your smartphone when a specific category of events is detected.

A more detailed presentation of Astro-COLIBRI and together with the presentation of other use cases other than gravitation waves can be found in (Schüssler et al. 2023).

3.2 *Integration of* tilepy

Fig. 3. Web interface of Astro-COLIBRI when using the tiling function. The maps on the left shows the position uncertainty contour of the gravitational wave alert alongside with the position of each tile. On the right, a table with the detailed information about each tile, including the time at which it should be observed is given.

Fig. 4. Smartphone interface of Astro-COLIBRI when using the tiling function. At the top a map illustrates the position uncertainty contour of the gravitational wave alert alongside the position of each observation tile. The latter are also given in the list below.

To enhance the capabilities of Astro-COLIBRI to facilitate the follow-up of gravitational wave events, we have integrated the *tilepy* API into the Astro-COLIBRI platform. This integration simplifies the process of requesting and visualizing tile-based observations. When using this functionality, users can retrieve detailed information about each tile, including its optimal observation time. The platform also provides a visual representation of the uncertainty contours of the gravitational wave alongside the positions of each tile (cf. Figure 3). Users of the smartphone interfaces can enjoy a similar experience through the available apps (Figure 4).

4 Conclusion

In this contribution, we have presented Astro-COLIBRI, an advanced platform for real-time multi-messenger astrophysics. Astro-COLIBRI integrates multi-messenger observation tools into a comprehensive and user-friendly graphical interface, empowering astronomers to swiftly access critical information related to transient events.

One notable feature is the platform's ability to visualize recent gravitational wave events. Furthermore, with the recent integration of *tilepy*, astronomers can efficiently plan follow-up observations, significantly enhancing their capabilities in responding to these phenomena.

tilepy is a powerful tool for scheduling follow-up observations of GW events. It offers diverse strategies to optimize the coverage of the localization region, taking into account telescope specifications and visibility conditions. As an open source project, *tilepy* is accessible to a large number of researchers. We firmly believe

that *tilepy* has the potential to become an indispensable resource for multi-messenger follow-up observations. With continued community-driven development, it could play a pivotal role in increasing the likelihood of detecting counterparts to GW events.

tilepy and Astro-COLIBRI are still under active development, with various planned enhancements. These include the incorporation of novel strategies to further refine observation scheduling within *tilepy* and improved filtering and notification capabilities for Astro-COLIBRI.

The Astro-COLIBRI and *tilepy* development team welcomes comments and feedback from the community to further improve the platform and can be contacted, respectively, at astro.colibri@gmail.com and astro.tilepy@gmail.com.

The authors acknowledge the support of the French Agence Nationale de la Recherche (ANR) under reference ANR-22-CE31-0012. This work was also supported by the Programme National des Hautes Energies of CNRS/INSU with INP and IN2P3, co-funded by CEA and CNES and we acknowledge support by the European Union's Horizon 2020 Programme under the AHEAD2020 project (grant agreement n. 871158). MSA acknowledges the support of Grant FJC2020-044895-I funded by MCIN/AEI/10.13039/501100011033 and by the European Union NextGenerationEU/PRTR.

References

Abdalla, H., Abramowski, A., Aharonian, F., et al. 2017, The Astrophysical Journal Letters, 850, L22

Ashkar, H., Brun, F., Füßling, M., et al. 2021, J. Cosmology Astropart. Phys., 2021, 045

CTA-LST Project, T., Abe, H., Aguasca, A., et al. 2022, in 37th International Cosmic Ray Conference, 838

Dálya, G., Díaz, R., Bouchet, F. R., et al. 2022, Monthly Notices of the Royal Astronomical Society, 514, 1403

Schüssler, F., de Bony de Lavergne, M., Kaan Alkan, A., Mourier, J., & Reichherzer, P. 2023, PoS, ICRC2023, 1469

SF2A 2023
M. N'Diaye, A. Siebert, N. Lagarde, O. Venot, K. Baillié, M. Béthermin, E. Lagadec, J. Malzac, J. Richard (eds)

PROBING BINARY EVOLUTION IN ACCRETING HIGH-MASS SYSTEMS

F. Fortin[1], F. Garcia[2], A. Simaz-Bunzel[2], S. Chaty[1] and E. Chassande-Mottin[1]

Abstract. High-mass X-ray binaries (HMXBs) are stellar couples that undergo mass exchange between a massive star and a compact object. They are ideal candidates to be the progenitors of compact binaries, composed of neutron stars and/or black holes, which can end up merging resulting in a burst of gravitational waves. Evolutionary mechanisms such as supernova explosions or the common envelope phase have a strong impact on whether or not these systems can coalesce within a time lower than the age of the universe.

I will present the observational state of the art on HMXBs in the Milky Way, aiming to bring constraints to their evolutionary past. After building the latest and most up to date catalogue of Galactic HMXBs, I use astrometric data from Gaia EDR3 to infer the strenght of the natal kick these HMXBs received, as well as integrate their motion 100 Myr back in time to find their birthplace whithin the Galaxy.

Keywords: binaries: general; stars: formation; stars: evolution; astrometry; stars: kinematics and dynamics; stars: neutron; stars: black holes;

1 Introduction

High-mass X-ray binaries are stellar couples composed of a compact object –usually a neutron star (NS) and seldom a black hole (BH) – accreting from a massive O-B companion ($M \geq 8\,M_{\odot}$, see a broad review in Chaty (2022)). Mass transfer can occur through a decretion disk around a Be companion in BeHMXBs (Rivinius et al. 2013), or via intense stellar wind from an evolved, supergiant companion in sgHMXBs (Chaty 2013).

X-ray binaries have been observed for more than 60 years now, yet they require multiwavelength observations as well as time series to be properly constrained. Hence, we still unveil new systems today and keep observing known ones to better constrain their properties: orbital periods, spectral type of the companion, nature of the compact object, etc. Not only they are of interest because of the extreme, high-energy physics of accretion-ejection they display, they also are of key importance in the scope of stellar evolution. It is likely that most massive stars spend at least part of their lives in binaries, and by the end of their lives some could be the progenitors of compact mergers now seen by LIGO/Virgo (and later by LISA).

With the advent of new observational facilities (SVOM, LSST, eROSITA, Athena, LISA) in the high-energy/gravitational/transient sky astronomy, it is high time we have an updated view of the population of X-ray binaries in the Galaxy in a modern, community-driven database. This HMXB catalogue (Fortin et al. 2023), available online*, is designed to be a starting base for population studies and and tool to help with targeting the right HMXBs to revisit in observing time proposals. I will present the catalogue in Section 2, then review how it has already been used to valorize astrometric data from Gaia by probing the past history of those HMXBs, inferring their natal kick (Section 3) and finding their birthplace in the Milky Way (Section 4).

2 The catalogue of HMXBs in the Galaxy from the INTEGRAL to the Gaia era

The latest catalogue dedicated to Galactic HMXBs was compiled by Liu et al. (2006), a few years after the launch of the *INTEGRAL* satellite. Back then, the census counted 114 HMXBs and candidates in the Milky Way.

[1] Université Paris Cité, CNRS, Astroparticule et Cosmologie, F-75013 Paris, France
[2] Instituto Argentino de Radioastronomía (CCT La Plata, CONICET; CICPBA; UNLP), C.C.5, (1894) Villa Elisa, Buenos Aires, Argentina
*`https://binary-revolution.github.io/HMXBwebcat/`

© Société Française d'Astronomie et d'Astrophysique (SF2A) 2023

However, *INTEGRAL* was particularly adapted to the observation of HMXBs and even discovered a new subclass, the obscured sgHMXBs, thanks to its sensitivity in hard X-rays. Hence, in the past 17 years, *INTEGRAL* has triggered many multi-wavelength followup campaigns to identify hard X-ray sources and constrain their nature (Fortin et al. 2018).

All of this observational knowledge, produced by independent teams of researchers over many years, is not easy to collect together in a coherent and updated database because of the many new systems discovered each year and new constraints brought on their nature and intrinsic parameters (orbital period, companion spectral type, presence of pulsations...). It is necessary to have an accurate picture of the current population of X-ray binaries if we want to be able to link them to the growing population of compact binaries, and bring constraints to the evolutionary mechanisms that govern the life of massive stars.

2.1 Building an updated database

For this work, we have extensively used the services of the Centre de Données Astronomiques de Strasbourg (CDS), mainly Simbad and Vizier. First, we retrieved the last HMXB catalogue from Liu et al. (2006), that we supplemented by adding hard X-ray sources detected by INTEGRAL (Bird et al. 2016). We crossmatched the two catalogues, and at this stage kept all INTEGRAL sources labelled either HMXB, LMXB or CV since misidentification is common.

Then, we queried Simbad for all sources labelled "HXB", and performed a spatial selection on the plane of the sky to discard extragalactic sources (which are densely clustered in their host galaxies, contrary to Galactic HMXBs which are mainly spread whithin the Galactic plane). After crossmatching the Simbad HMXBs with the sample from Liu et al. (2006) and Bird et al. (2016), we added 66 new candidates to review.

At this point, we performed an individual, minute search in the literature for each source to retrieve the original references for already published data on their parameters, find out if anything new was publised since the last catalogues and confirm they are indeed HMXBs. For this, we queried NASA's ADS using a combination of a variety of keywords. This process is quite lengthy but necessary to ensure the quality of the data presented in the catalogue and have a proper track of references for each listed parameter.

Finally, we performed a semi-automatic search for counterparts of each HMXB at various wavelengths, including the detections from Gaia EDR3 in order to also retrieve a distance estimation whevever possible.

2.2 Contents of the catalogue and availability

At the time of publication, the finished catalogue counted 153 HMXBs in the Milky Way (Fortin et al. 2023). That was a 33% increase compared to the sample in Liu et al. (2006), or a 100% increase if we limit to the confirmed systems (hard X-ray detection and early spectral type confirmed for the optical counterpart). 111 HMXBs had a Gaia counterpart, which offer an unprecendented opportunity to precisely locate them whithin the Milky Way. We compiled astrometric information, orbital data, spectral types and spin periods, which allows us to draw the most up to date picture of the Galactic HMXB population (see e.g. the Corbet diagram of Galactic HMXBs in Figure 1, left panel).

The catalogue is hosted at the CDS in a fixed version; but in order to take into account new discoveries (or correct the few mistakes that are unavoidable on such a large, manually built database), we host the catalogue on an independent website, HMXBwebcat[†]. The database itself is hosted on our GitHub collaboration, and is able to receive updates from the community as new observations are performed. This is why, at the time of writing, the catalogue now counts 159 HMXBs and the numbers keep steadily growing. New versions of the catalogue are published regularly, with a track reccord of each modifications to ensure continuity. The database can be browsed directly in a navigator, or downloaded in various formats to be explored (we recommend Topcat).

3 Constraints to neutron star kicks in HMXBs

All the HMXBs present in the catalogue contain a compact object, and most of them are NSs. Hence, most of HMXBs, prior to their X-ray phase, underwent a supernova event. Not only the explosion induces a sudden mass loss that affects the orbit of the binary, the supernova may happen with a certain degree of asymetry, kicking the center of mass in a random direction and adding to the eccentricity of the system. Because we have

[†]`https://binary-revolution.github.io/HMXBwebcat/index.html`

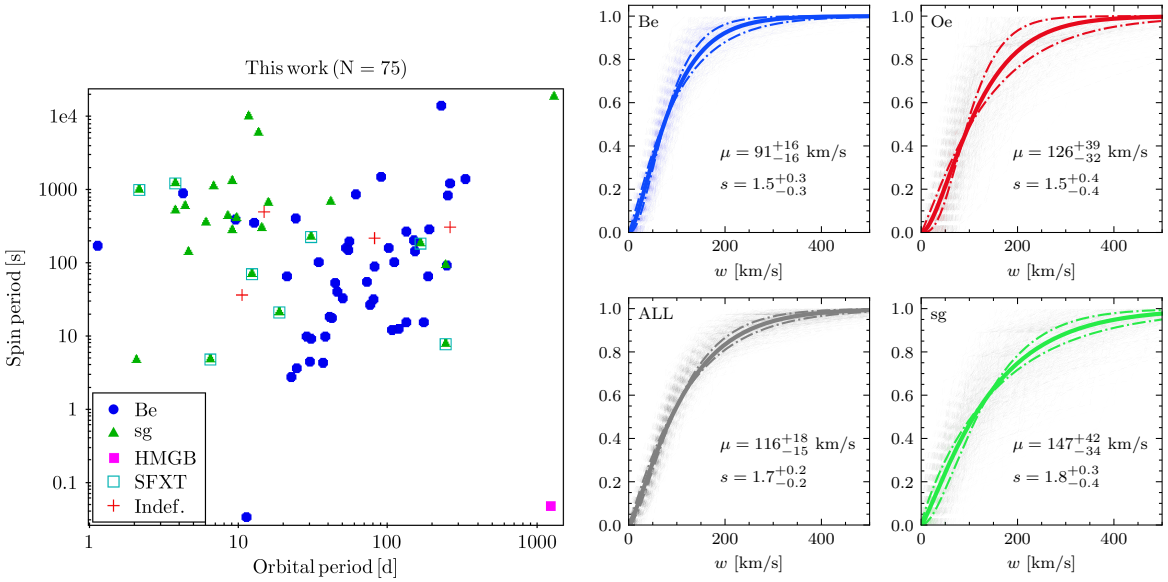

Fig. 1. Left: Corbet diagram of the Galactic HMXBs in the catalogue. Right: Cumulative distribution of neutron star kicks in Galactic HMXBs.

compiled intrinsic parameters such as orbital periods, eccentricities and stellar masses in HMXBs, and retrieved astrometric measurements from Gaia, it is possible to observe the effects of this natal kick in HMXBs and thus allow us to estimate the strength of the supernova explosion and its effect on the binaries.

The information on the natal kick is indeed contained within the peculiar velocity of HMXBs, which is the proper motion corrected for the Galactic co-rotation velocity. Hence, we can compute the peculiar velocity of HMXBs on the condition of them having a precise distance determination from Gaia data (Bailer-Jones et al. 2021) as well as having an independent radial velocity measurement. The peculiar velocity is used as an input the the equations that describe the effects of an asymetric supernova explosion on the center of mass of a binary system (Brandt & Podsiadlowski 1995; Kalogera 1996). Using Monte-Carlo Markov-Chain simulations, we can compute the posterior probability of the natal kick strength in each of the neutron stars of our HMXB sample. Because a complete set of orbital parameters, masses and astrometry of high quality are necessary, we were able to perform this on 35 Galactic HMXBs.

On top of deriving the kick strength for each system, we agregated those results to get average kick distributions across sub-types of HMXBs, namely the BeHMXBs, OeHMXBs (slightly more massive than Be) and sgHMXBs (Figure 1, right panel).

4 Finding the birthplace of HMXBs in the Milky Way

For the few HMXBs that have exquisite astrometry and radial velocity measurements, it is possible to look even further back in time to search for their birthplace in the Milky Way. Not only this would provide an estimation of their age, this can also give an estimation of the initial masses of the stars whithin the binaries, which is of prime importance to understand what is the population of star that are the progenitors of HMXBs.

We are looking for birthplaces in the Galactic spiral arms as well as the open clusters in the Galaxy. Recent publications, also using Gaia EDR3 astrometry, bring very good constraints on the shape, pitch angle and rotation velocity of the spiral arms (Castro-Ginard et al. 2021), and the precise location of 2000 open clusters whithin the Milky Way (Cantat-Gaudin et al. 2018). To find birthplace candidates, we integrate the motion of the HMXBs, clusters and spiral arms 100 Myr back in time and look for spatio-temporal coincidences.

When a coincidence is found, the time at which it happened provides an estimation of the time since supernova. In the case of a candidate birthplace in a cluster, since we have access to the age of the cluster via isochrone fitting, we can assume the binary formed at the same time as the cluster and thus have access to the full age of the binary. Combined with the knowledge of the time since supernova, and currently measured mass of the companion star, we can infer the initial masses of the two stars, the mass gained by the companion during the initial mass transfer as well as the pre-supernova mass of the primary star.

5 Conclusion

The building of an up to date catalogue of Galactic HMXBs lead to getting an accurate view of their population, and is a tool that can be used in various ways to explore the history and ecology of X-ray binaries in the Milky Way. Combined with recent astrometric data from Gaia, we can constrain the evolution of massive binaries from their formation (Fortin et al. 2022a) up to the supernova event that preceeds the X-ray phase (Fortin et al. 2022b). Multiple other evolutionary mechanisms punctuate the life of massive stars in binaries, e.g. the common envelope event, and are of prime importance to understand how massive stars reaching the endpoint of their lives coalesce as double compact systems.

Double compact mergers were, up until a few years ago, almost invisible to our eyes (except the ones leading to the emergence of short gamma ray bursts). Now, with the gravitational observatories LIGO and Virgo (currently under their fourth observation run), the population of observed double compact binaries is steadily growing, which in time will give us a description of the endpoint of the population of binary stars. This will be an opportunity to link the population of massive binaries, HMXBs and compact binaries and study the complex mechanisms responsible for the evolution of massive stars.

The authors were supported by the LabEx UnivEarthS, Interface project I10, "From evolution of binaries to merging of compact objects" and Interface project "Binary rEvolution". The authors would like to thank Thierry Foglizzo, Jérôme Guillet and Thomas Tauris for fruitful discussions. This research has made use of the SIMBAD database, operated at CDS, Strasbourg, France. This work has made use of data from the European Space Agency (ESA) mission *Gaia* (`https://www.cosmos.esa.int/Gaia`), processed by the *Gaia* Data Processing and Analysis Consortium (DPAC, `https://www.cosmos.esa.int/web/Gaia/dpac/consortium`). Funding for the DPAC has been provided by national institutions, in particular the institutions participating in the *Gaia* Multilateral Agreement.

References

Bailer-Jones, C. A. L., Rybizki, J., Fouesneau, M., Demleitner, M., & Andrae, R. 2021, AJ, 161, 147

Bird, A. J., Bazzano, A., Malizia, A., et al. 2016, ApJS, 223, 15

Brandt, N. & Podsiadlowski, P. 1995, MNRAS, 274, 461

Cantat-Gaudin, T., Jordi, C., Vallenari, A., et al. 2018, A&A, 618, A93

Castro-Ginard, A., McMillan, P. J., Luri, X., et al. 2021, A&A, 652, A162

Chaty, S. 2013, Advances in Space Research, 52, 2132

Chaty, S. 2022, Accreting Binaries, 2514-3433 (IOP Publishing)

Fortin, F., Chaty, S., Coleiro, A., Tomsick, J. A., & Nitschelm, C. H. R. 2018, A&A, 618, A150

Fortin, F., García, F., & Chaty, S. 2022a, A&A, 665, A69

Fortin, F., García, F., Chaty, S., Chassande-Mottin, E., & Simaz Bunzel, A. 2022b, A&A, 665, A31

Fortin, F., García, F., Simaz Bunzel, A., & Chaty, S. 2023, A&A, 671, A149

Kalogera, V. 1996, ApJ, 471, 352

Liu, Q. Z., van Paradijs, J., & van den Heuvel, E. P. J. 2006, A&A, 455, 1165

Rivinius, T., Carciofi, A. C., & Martayan, C. 2013, A&A Rev., 21, 69

SF2A 2023
M. N'Diaye, A. Siebert, N. Lagarde, O. Venot, K. Baillié, M. Béthermin, E. Lagadec, J. Malzac, J. Richard (eds)

UPDATE IN THE SEARCH FOR CLOSE MASSIVE BINARY BLACK HOLES: A LIST OF NEW CANDIDATES

V. Foustoul[1] and N. A. Webb[1]

Abstract. Supermassive black holes are found in the center of galaxies. However, their formation and evolution is still obscure. Even though they are thought to be formed from lower mass seed black holes, the merger and accretion rate of these black holes is still unconstrained. The next space-based gravitational wave observatory LISA will constrain the merger rate of massive black holes, and thus shed light on how they are formed. We conducted a search for MBBHs candidates using Catalina Real-Time Transient Survey (CRTS) and Zwicky Transient Facility (ZTF) observations. We searched for long-term sinusoidal modulation emanating from the centres of galaxies, which may be evidence of MBBHs or coming from a circumbinary disk. We found 36 MBBHs candidates. We present here the results of this study.

Keywords: Gravitational waves - Black hole physics - Catalogs - Galaxy: evolution - Galaxy: formation - quasars: supermassive black holes

1 Introduction

Observations revealed the presence of supermassive black holes ($M \sim 10^{5-10} M_{\odot}$) in the center of galaxies (Vestergaard & Osmer 2009). However, their formation and evolution is still unclear. In a hierarchical model, we expect them to be created from lower mass black holes seeds, stellar ($M \sim 5-60 M_{\odot}$; Mapelli et al. (2020)) or intermediate ($\sim 10^2 M_{\odot} < M < 10^5 M_{\odot}$; Greene et al. (2020)) mass black holes. These seeds may evolve through different processes, periods of intense accretion and/or successive mergers (Volonteri et al. 2003). The importance of these two scenarios and when they dominated is still obscure. As two galaxies merge, when the orbital separation is sufficiently small, the inspiral of the two supermassive black holes generates gravitational waves. The next space-based gravitational waves observatory LISA (Laser Interferometer Space Antenna) will be able to probe the mili-hertz regime of the gravitational wave spectrum (Amaro-Seoane et al. 2017). Massive binary black hole (MBBHs) of mass $M \approx 10^{4-7} M_{\odot}$ are expected to be loud mHz gravitational wave sources. LISA will detect these objects up to a redshift $z \sim 20$ (Amaro-Seoane et al. 2012) and thus, this will bring constraints on the evolutionary paths of supermassive black holes. Numerical simulations showed that when the binary hardens, mini-disks around each black hole are created and a circumbinary disk forms at a radius r $\sim 2a(1+e)$, with a and e respectively the semi-major axis and eccentricity of the binary. A cavity is established between the circumbinary disk and the mini-disks, accretion streams coming from the circumbinary disk cross the cavity to fuel each mini-disk (d'Ascoli et al. 2018; Shi & Krolik 2015; Combi et al. 2021). Therefore, we expect to detect long-term sinusoidal modulation either from the orbiting mini-disks or from a blob of matter in the circumbinary disk. Mignon-Risse et al. (2023) showed that an over-density can grow in the circumbinary disk which could explain the observed variability. This variability could also come from periodic accretion flow, as the lower mass black hole in the orbit is closer to the inner edge of the circumbinary disk, more gas is accreted by the secondary black hole (Artymowicz & Lubow 1996). Another origin for this variability is periodic Doppler boosting, as the two black holes orbit, the light emitted from the mini-disks is periodically boosted (D'Orazio et al. 2015). Sub-parsec scale orbital separation MBBHs are still to be confirmed and only candidates have been proposed. Graham et al. (2015) made a systematic search for long-term optically variable objects in the Catalina Real-Time Transient Survey (CRTS) and reported 111 quasars that could harbor a MBBH. Nevertheless, quasars exhibit an intrinsic optical variability due to the turbulent accretion process in

[1] IRAP, Université de Toulouse, CNRS, 9 avenue du Colonel Roche, Toulouse, France

© Société Française d'Astronomie et d'Astrophysique (SF2A) 2023

such systems. This variability is well modelled by a red noise process and, as described in Vaughan et al. (2016). It is therefore necessary to observe a sufficient number of periods to ensure that the periodicity is caused by an orbital motion and not due to a stochastic modulation. So as to verify that the periodicity of the candidates discovered by Graham et al. (2015) is sustained over enough periods, we added Zwicky Transient Facility (ZTF) observations, when available, to the CRTS lightcurves. Additionally, we searched for other candidates using both CRTS and ZTF data. CRTS observations were made between 2005 and 2015 in the V-band using three telescopes, respectively the Mt Lemmon Survey, Catalina Sky Survey and Siding Spring Survey. The CRTS catalog contains around 500 million objects and covers nearly 26000 square degrees in the northern sky (Drake et al. 2009). ZTF observations debuted in 2017 and are still ongoing. They are performed at the Palomar observatory in r, g and i filters. The ZTF catalog is much bigger than CRTS and includes around 7 billion objects located in 30000 square degrees in the northern sky (Bellm et al. 2019).

2 Methods

We extended the lightcurves of sources with CRTS only data shown in Graham et al. (2015) adding ZTF observations when available. Also, we investigated the Chen et al. (2020) list of variable sources to search for sinusoidal modulation. This catalog contains 2 163 129 objects detected with the Zwicky Transient Facility (ZTF) Data Release 2 (DR2). Firstly, we cross-correlated this catalog with Glade2, a galaxy catalog, which includes 3.26 million galaxies and quasars. This catalog is complete to a luminosity distance of 37 Mpc (Dálya et al. 2018). We extracted ZTF DR16 lightcurves of galaxies and kept the ones with at least 400 ZTF measurements to ensure reliable statistical results. We grouped data points into bins of 4 days and modelled a sinusoidal function to test the variability of the lightcurves. We then calculated the reduced chi-squared to evaluate the goodness of the fit. We selected objects for which the value of the reduced chi-square was lower than 1.3. Where CRTS data was available for the ZTF variable sources, we also added it to the lightcurves to extend the baseline, and selected the ones with at least 25 data points after binning to limit stochastic effects. However, CRTS observations were made in the V band whilst ZTF observations were done in r, g and i filters making it difficult to model both data sets simultaneously. As we are interested in the timescale of the variability and not its amplitude, we scaled ZTF observations to the CRTS data using the average magnitude and amplitude of the CRTS variability, as we assume the periodicity to be achromatic. After scaling ZTF observations to CRTS data, we fitted a sine function to the ZTF and CRTS data sets altogether. To find the best fit, we used the nested sampling package Ultranest (Buchner 2021b,a, 2016) to derive posterior probability distributions of the sinusoidal model. This method evaluates the posterior distribution by calculating the marginal likelihood Z over the whole parameter space. In order to further validate the identified periods determined through the fitting techniques, we also computed the Lomb-Scargle periodogram. The Lomb-Scargle is a technique to find periodicities in irregularly sampled observations (Lomb 1976; Scargle 1982). This technique calculates the Power Spectral Density (PSD) for a given data set, where most likely periods in the observations are represented by the highest peaks in the PSD. Moreover, to evaluate the peak significance we calculated the false alarm level for each periodogram. This corresponds to the minimum power a peak must reach to be considered significant for a given confidence interval. We computed the 5σ false alarm level and only considered peaks above this threshold.

3 Results

3.1 Lightcurves

We searched for interesting candidates in the Graham et al. (2015) sample. We found ZTF observations for 89 objects out of the initial 111 sources. We modelled CRTS and ZTF data simultaneously and recognized 26 candidates with a similar variability in both CRTS and ZTF observations. We discarded 58 candidates as the variability observed in CRTS data was inconsistent with the one in ZTF observations. Finally, there were not enough ZTF observations for 5 sources to confirm that the modulation continued on the long-term. Additionally, we investigated the Chen et al. (2020) catalog and cross-matched it with the galaxy catalog Glade2 (Dálya et al. 2018), reducing the sample to 21 862 galaxies. We fitted ZTF data and selected sources with a $\chi^2_\nu < 1.3$, identifying 1010 variable galaxies. We found 10 objects with analogous modulations in CRTS and ZTF data. The calculated Lomb-Scargle periodogram for each of the 36 selected candidates exhibit a maximum peak corresponding to the periodicity of the best fitted sine function, supporting the proposed variability. We show in 1 the optical lightcurve and Lomb-Scargle periodogram of one of the candidates.

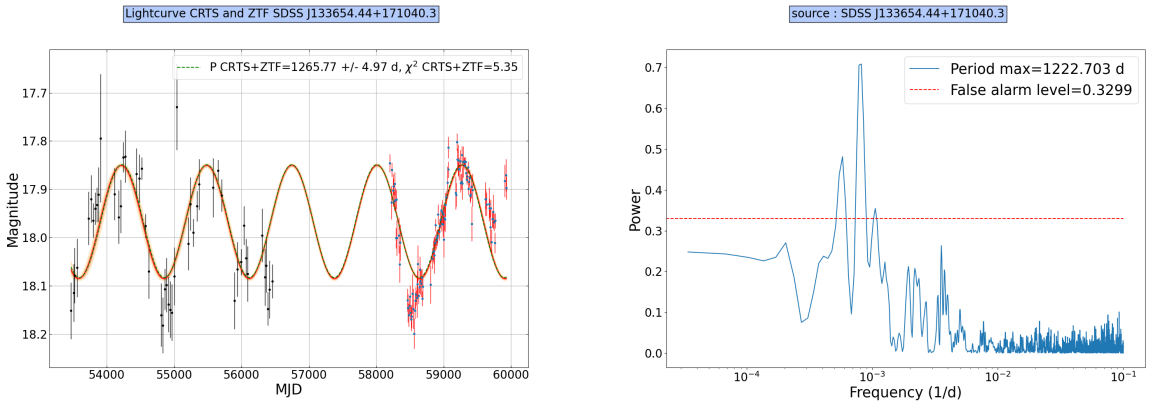

Fig. 1. Left: CRTS (black) and ZTF (red) optical lightcurve of one of the 36 candidates : SDSS J133654.44+171040.3. Orange line is 3σ best fitted sine function **Right:** Lomb-Scargle periodogram of SDSS J133654.44+171040.3 panel.

In our final sample of 36 candidates, we observe between 3 and 5 periods, which may indicate the presence of a MBBH in these galaxies. Moreover, out of the 1099 sources we inspected (1010 from Chen et al. (2020) catalog and 89 from Graham et al. (2015) sample), we focused our study on objects with both CRTS and ZTF data, and objects with too few or no CRTS observations have been removed from our final sample. Insufficient cycles are available in the current data to confirm the modulation, but 261 objects merit further follow-up to confirm the modulation. We therefore provide a second catalog of proposed candidates.

3.2 Optical Spectra

We investigated the SDSS optical spectra when available of the sources we identified as MBBH candidates. MBBH candidates are expected to display double-peaked emission lines, due to the accretion around the two black holes, each having their own broad-line (BL) and narrow-line (NL) regions (Begelman et al. 1980; De Rosa et al. 2019). However, this is not an indisputable way to confirm MBBH candidates as it may be due to a recoiling supermassive black hole (e.g. Komossa et al. 2008) or a background AGN (e.g. Heckman et al. 2009). Nonetheless, observing both long-term sinusoidal variability and double-peaked emission lines lends weight to the MBBH scenario. One of the objects in our sample of MBBHs candidates seems to have double-peaked emission lines in its optical spectra. We show in Fig 2 the SDSS optical spectra of quasar SDSS J122616.70+504205.9 with identified double-peaked H_β and Mg_{II} emission lines. This may indicate that this source possesses two BL regions and further support the idea that this galaxy may host a MBBH.

4 Conclusions

We report 36 MBBHs candidates through the identification of 3 to 5 periods of sinusoidal variability in their optical lightcurve. These periodicities have been found using a fitting technique and confirmed by their Lomb-Scargle periodogram. In this work, we also could reject 58 objects previously proposed as MBBHs candidates, because the observed variability in CRTS observations was not sustained in later ZTF data. Additionally, we investigated the SDSS optical spectrum of these candidates and found double-peaked emission lines for one candidate, favoring the MBBH hypothesis. Also, we created a catalog of possible MBBH candidates which require further follow-up observations to confirm the long-term sinusoidal modulation. Upcoming surveys, such as the Rubin observatory Legacy Survey of Space and Time (LSST, Ivezić et al. 2019), will help us to confirm or discard current MBBHs candidates and discover many more of them.

The authors acknowledge the support of the French Agence Nationale de la Recherche (ANR), under the grant of the MBH Waves group.

References

Amaro-Seoane, P., Aoudia, S., Babak, S., & et al. 2012, eLISA: Astrophysics and cosmology in the millihertz regime
Amaro-Seoane, P., Audley, H., Babak, S., et al. 2017, arXiv e-prints, arXiv:1702.00786

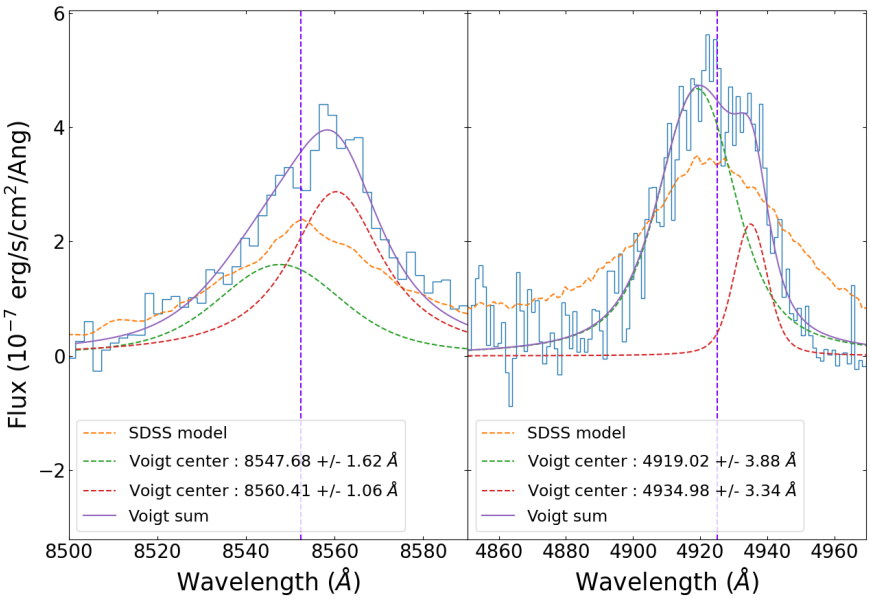

Fig. 2. Normalized flux of identified double-peaked emission lines H_β (left) and Mg_{II} in SDSS optical spectra of quasar SDSS J122616.70+504205.9

Artymowicz, P. & Lubow, S. H. 1996, The Astrophysical Journal Letters, 467, L77
Begelman, M. C., Blandford, R. D., & Rees, M. J. 1980, Nature, 287, 307
Bellm, E. C., Kulkarni, S. R., Graham, M. J., et al. 2019, Publications of the Astronomical Society of the Pacific, 131, 018002
Buchner, J. 2016, Statistics and Computing, 26, 383
Buchner, J. 2021a, arXiv e-prints, arXiv:2101.09675
Buchner, J. 2021b, The Journal of Open Source Software, 6, 3001
Chen, X., Wang, S., Deng, L., et al. 2020, The Astrophysical Journal Supplement Series, 249, 18
Combi, L., Lopez Armengol, F., Campanelli, M., et al. 2021, The Astrophysical Journal
Dálya, G., Galgóczi, G., Dobos, L., et al. 2018, Monthly Notices of the Royal Astronomical Society, 479, 2374
d'Ascoli, S., Noble, S. C., Bowen, D. B., et al. 2018, The Astrophysical Journal, 865, 140
De Rosa, A., Vignali, C., Bogdanović, T., et al. 2019, New Astronomy Review, 86, 101525
D'Orazio, D. J., Haiman, Z., & Schiminovich, D. 2015, Nature, 525, 351
Drake, A. J., Djorgovski, S. G., Mahabal, A., et al. 2009, The Astrophysical Journal, 696, 870
Graham, M. J., Djorgovski, S. G., Stern, D., et al. 2015, Monthly Notices of the Royal Astronomical Society, 453, 1562
Greene, J. E., Strader, J., & Ho, L. C. 2020, Annual Review of Astronomy and Astrophysics, 58, 257
Heckman, T. M., Krolik, J. H., Moran, S. M., Schnittman, J., & Gezari, S. 2009, Th Astrophysical Journal, 695, 363
Ivezić, Ž., Kahn, S. M., Tyson, J. A., et al. 2019, The Astrophysical Journal, 873, 111
Komossa, S., Zhou, H., & Lu, H. 2008, The Astrophysical Journal Letters, 678, L81
Lomb, N. R. 1976, Astrophysics and Space Science, 39, 447
Mapelli, M., Spera, M., Montanari, E., et al. 2020, The Astrophysical Journal, 888, 76
Mignon-Risse, R., Varniere, P., & Casse, F. 2023, Monthly Notices of the Royal Astronomical Society
Scargle, J. D. 1982, Astrophysical Journal, 263, 835
Shi, J.-M. & Krolik, J. H. 2015, The Astrophysical Journal, 807, 131
Vaughan, S., Uttley, P., Markowitz, A. G., et al. 2016, Monthly Notices of the Royal Astronomical Society, 461, 3145
Vestergaard, M. & Osmer, P. S. 2009, The Astrophysical Journal, 699, 800
Volonteri, M., Madau, P., & Haardt, F. 2003, The Astrophysical Journal, 593, 661

SF2A 2023
M. N'Diaye, A. Siebert, N. Lagarde, O. Venot, K. Baillié, M. Béthermin, E. Lagadec, J. Malzac, J. Richard (eds)

PREDICTING THE ELECTROMAGNETIC SIGNATURES OF PRE-MERGER BINARY BLACK HOLES

R. Mignon-Risse[1,2], P. Varniere[2,3] and F. Casse[2]

Abstract. The many recent detections of gravitational waves (GWs) of binary black hole (BBHs) mergers, and the first detection of an EM counterpart to neutron star merger, have opened the way for future multi-messenger compaigns. One expected result, not achieved yet, is the detection of the electromagnetic (EM) counterpart to BBH merger, ideally in the pre-merger phase to ensure optimal follow-up. However, the pre-merger EM signal is not firmly identified because few numerical codes are able not only to model the gravitational impact of the BBH on its circumbinary disk but also to compute its observational consequences, in General Relativity (GR). In this proceeding, we use `e-NOVAs` ("extended Numerical Observatory for Violent Accreting systems") to compute the circumbinary disk evolution in GR-hydrodynamics in an analytical BBH metric, and to compute synthetic observations in the same metric via GR ray- tracing. We find the central region to be cleared of material by the BBH torques, thus forming a low-density cavity. As a consequence, the energy spectrum resembles that of a truncated disk. The circumbinary disk hosts several non-axisymmetries: spiral arms and an overdensity, the so-called 'lump'. They produce a two-timescale modulation of the EM lightcurve for non-face-on observers; this could be the smoking-gun for pre-merger BBHs.

Keywords: black hole physics, accretion discs, hydrodynamics, gravitational waves, multi-messenger astronomy

1 Introduction

While the gravitational wave (GW) detection associated with a neutron star merger (Abbott et al. 2017a) and the associated gamma-ray burst observation (Abbott et al. 2017b) have set the stage for a new era in multi-messenger astrophysics, the electromagnetic (EM) counterpart to binary black hole (BBH) pre- and post-merger remains undetected. A pre-merger detection would allow for optimal EM follow-up, and a subsequent GW-EM co-detection would be precious in many ways, for several branches of physics/astrophysics. It would allow us to test General Relativity (GR) in strong and dynamical spacetimes and to measure the speed of gravity by comparing the arrival time of GW and photons, thus testing GR. In the case of supermassive BBHs, systems evolving on longer timescales and more likely to offer opportunities for pre-merger EM detection, it would also benefit cosmology: measuring the host galaxies' redshift together with the GW luminosity distance could help relieving the Hubble tension (e.g. Piro et al. 2022).

Currently, stellar-mass BBH mergers are being detected by ground-based GW detectors (LIGO/Virgo/Kagra). The future Laser Interferometer Space Antena (LISA, Amaro-Seoane et al. 2017) and Pulsar Timing Arrays (PTA, e.g. Babak et al. 2016) are/will be sensitive to the low-frequency GWs produced during supermassive BBH mergers of total mass $M{\sim}10^{4-7}\mathrm{M}_\odot$ and $M > 10^8\mathrm{M}_\odot$, respectively. While a new generation of EM facilities is being under preparation (e.g. Athena in X-ray, THESEUS in IR/X-ray/gamma) or becoming available (Vera Rubin Observatory in optical), the EM signature of pre-merger BBHs to look for in the location box given by the GW signal for sufficiently slowly inspiralling systems remains elusive, and relies on theoretical predictions.

This problem has been addressed via numerical simulations of the circumbinary, gaseous environment around pre-merger BBHs, or more generally, binaries. Artymowicz & Lubow (1994) have shown that binary systems accreting from a circumbinary disk clear a central cavity of low-density gas, from which two accretion streams

[1] Institutt for fysikk, NTNU, Trondheim, Norway
[2] Université Paris Cité, CNRS, Astroparticule et Cosmologie, F-75013 Paris, France
[3] Université Paris-Saclay, Université Paris Cité, CEA, CNRS, AIM, 91191, Gif-sur-Yvette, France

© Société Française d'Astronomie et d'Astrophysique (SF2A) 2023

can feed the individual objects. As a consequence, several authors reported a deficit at high energy in the thermal SED of the circumbinary disks and mini-disks surrounding the individual objects (e.g. Roedig et al. 2014). Circumbinary disks are far from axisymmetric: they develop two spiral arms and their inner edge is the site of an orbiting overdensity dubbed 'lump' (Shi et al. 2012), whose origin is not fully understood yet although we found its appearance to be concomitant with the development of the Rossby Wave Instability (Mignon-Risse et al. 2023a). The observational appearance of circumbinary disks is rarely obtained from a (computationally- and memory-expensive) full GR treatment in the same BBH spacetime, and rather relies on approximations. Those include cooling/heating models to compute the luminosity (Farris et al. 2015), applying relativistic boosts analytically in post-processing rather than ray-tracing (Tang et al. 2018), or computing ray-tracing assuming that light travels faster than the fluid and the spacetime (D'Ascoli et al. 2018, Gutiérrez et al. 2022). Here we propose to fill this gap by studying circumbinary disks surrounding pre-merger BBHs in the full GR framework provided by `e-NOVAs`.

2 GRHD simulations of the circumbinary disk

In the first step of `e-NOVAs`, we follow the circumbinary disk evolution in 2D GRHD with the `GR-AMRVAC` code (Casse et al. 2017) incorporating an approximate, analytical BBH spacetime (Mignon-Risse et al. 2022). In this spacetime, we solve the equations of conservation of baryon density and momentum on a spherical grid, at the center of which the BBH is located (see Fig. 1). The circumbinary material is initially axisymmetric, close to gravito-centrifugal equilibrium (on an equivalent single BH of mass M). We use an adiabatic equation-of-state. Several setups are considered, varying the orbital separation, circular-orbit versus GW-driven inspiral, or mass ratio.

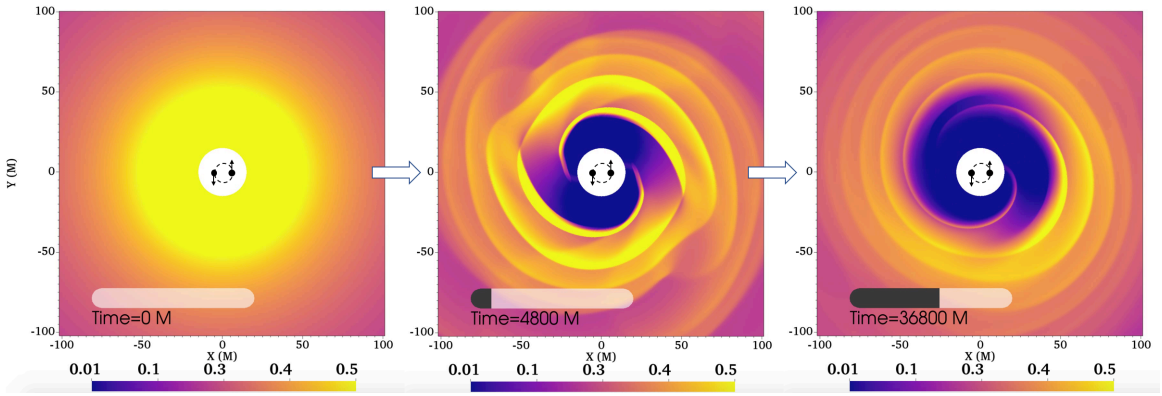

Fig. 1. Time sequence of the density (given in code units) in the mass ratio $q = 1$, circular-orbit, $b = 20\,\mathrm{r_g}$, case. The BBH is located within the inner boundary of the domain.

Figure 1 shows the time-evolution of the density in the circumbinary disk in the $q = 1$, circular-orbit, $b = 20\,\mathrm{r_g}$ case ($\mathrm{r_g}$ being defined with the total BBH mass M). This orbital separation value, if accounting for GW-driven inspiral, corresponds to a time-to-merger $\sim 1\,(M/10^6 \mathrm{M}_\odot)$ day. In less than one binary period, axisymmetry is broken. We recover accretion structures already reported in the literature: a low-density *cavity* of radius about twice the orbital separation, *accretion streams* crossing the cavity to feed the BBH, *spiral arms*, and after more than 50 binary orbits, an azimuthal $m = 1$ overdensity becomes visible: this is *the lump* feature, which orbits at the local Keplerian frequency $\Omega_{\rm lump}$, a fraction of the binary orbital frequency.

The accretion rate through the surface $r = 2$ b which roughly corresponds to the cavity surface is shown in the top-left panel of Fig. 2. It is modulated at twice the beat frequency between the mean orbital frequency of the lump $\bar{\Omega}_{\rm lump}$ and the orbital frequency of the binary $\Omega_{\rm orb}$, i.e. $2\,\Omega_{\rm beat} = 2\,(\Omega_{\rm orb} - \Omega_{\rm lump}) \approx 1.7\,\Omega_{\rm orb}$.

3 Electromagnetic counterparts

3.1 Variability

In order to investigate whether any of these accretion structures would translate into observable EM signatures of pre-merger BBHs, we post-process those simulations in `e-NOVAs` with the `GYOTO` code (Vincent et al. 2011) in

the same BBH spacetime, assuming thermal emission. From this, we obtain multi-wavelength thermal emission maps (right panel of Fig. 2) and lightcurves (bottom-left panel of Fig. 2), here for an inclination angle 70° (0° being face-on). In order to make this lightcurve mass-independent, we have integrated the flux around the SED peak frequencies, then we normalized it to the averaged flux. The SED peak is typically located in the optical to UV bands; the peak frequency increases with the accretion rate normalized to the Eddington value, with the decreasing orbital separation (hence time-to-merger), with the decreasing BBH mass. The most prominent feature of the lightcurve is the modulation at the lump orbital period, on top of a second modulation, smaller in amplitude, at the binary semi-orbital period. It is amplified by relativistic beaming: a non-axisymmetric feature (azimuthal $m = 2$: spiral arms; or azimuthal $m = 1$: the lump) appears brighter as it approaches the observer and dimmer as it gets away from the observer (see e.g. Vincent et al. 2013). Since the lump is also responsible for the SED peak emission, the lightcurve modulation originates from the highest-energy part of the circumbinary disk spectrum only. These results apply qualitatively for q ranging between 0.1 and 1, $b = 20\,\mathrm{r_g}$ and $b = 36\,\mathrm{r_g}$.

Most notably, there is a mismatch between the accretion rate and lightcurve modulations, as visible in Fig. 2. Therefore, the accretion rate variability is not a good proxy for the EM variability. More details can be found in Mignon-Risse et al. (2023b).

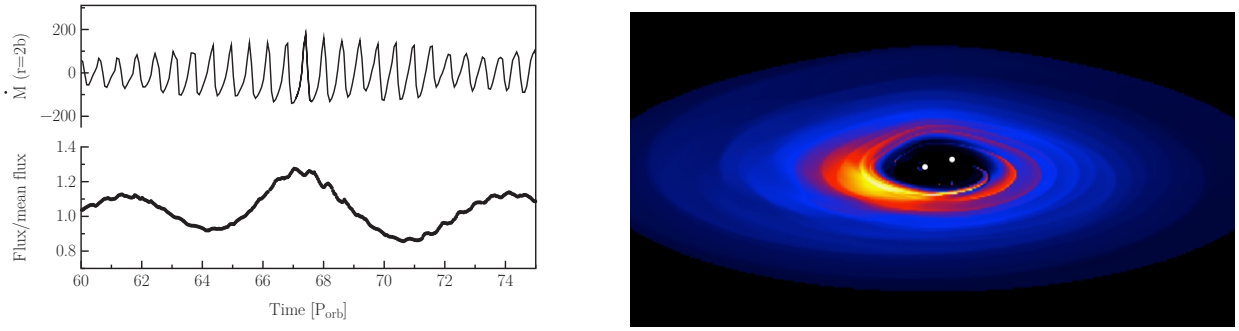

Fig. 2. Accretion rate through the surface $r = 2$ b (similar to that found at the domain inner boundary) and lightcurve (left panel); thermal emission map (right panel). Those are given for the simulation shown in Fig. 1, with an observer inclination angle of 70°.

3.2 Spectral energy distribution

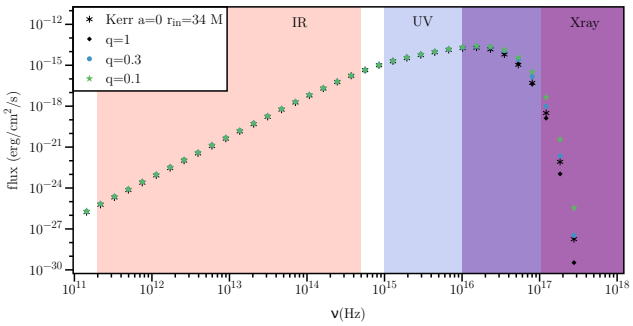

Fig. 3. Energy spectrum of: a circumbinary disk around a $10^5\,\mathrm{M_\odot}$ BBH with $q = [0.1, 0.3, 1]$ (here shown for a BBH inspiralling from $b = 15\,\mathrm{r_g}$ to $b = 8\,\mathrm{r_g}$) and a single $10^5\,\mathrm{M_\odot}$ BH disk of inner radius located at $34\,\mathrm{r_g}$.

Here we investigate the observational impact of the cavity, that is the lack of emitting material in the central region of the circumbinary disk. The energy spectrum of a circumbinary disk around a $10^5\,\mathrm{M_\odot}$ is shown in Fig. 3 for q varying between 0.1 and 1. Interestingly, the spectrum is hardly distinguishable between different values of q, and with a single BH disk whose edge would be set at 34 M, which roughly corresponds to twice the initial separation $b = 15\,\mathrm{r_g}$, i.e. the approximate cavity radius. Thus, compared to a single BH (of mass equal

to the total BBH mass) disk that would reach the innermost stable circular orbit (ISCO), located at a few r_g (depending on the BH spin), the spectrum appears as that of a truncated disk. This has been often referred to as a 'notch' between the circumbinary disk spectrum and the mini-disk spectrum when accounted for (e.g. Shi & Krolik 2016), that the streams do not compensate. In other words: a single BH source whose disk inner radius – as given from spectrum fitting – is away from the ISCO, could actually be a BBH. More details can be found in Mignon-Risse et al. (2022).

4 Conclusions

In this proceeding, we reported recent efforts to predict the EM signatures of circumbinary disks around pre-merger BBHs. To do so, we have computed the fluid evolution and emission in a full GR framework provided by the numerical observatory `e-NOVAs`, incorporating an approximate BBH spacetime. We have recovered the main accretion structures already reported in the literature: *a low-density cavity, accretion streams, spiral arms*, and the orbiting overdensity, *the lump* feature. In thermal emission, we found the circumbinary disk lightcurve to be dominated by the orbiting spiral arms and lump emission, thus producing a two-timescale modulation. This modulation is observer-dependent and cannot be obtained via scalar arguments (still valid for face-on views) assuming a one-to-one correspondance between the accretion rate variability and the EM variability. Meanwhile, as a consequence of the cavity, the spectrum is similar to that of a truncated disk around a single BH (of mass equal to the total BBH mass). Thus, the energy spectrum of a single BH disk whose inner edge would be away from the ISCO is hardly distinguishable from a BBH circumbinary disk spectrum. To allow for such a comparison, an accurate BBH mass measurement from GW signal and/or EM observations is required.

RMR acknowledges funding from Centre National d'Etudes Spatiales (CNES) through a postdoctoral fellowship. This work was supported by CNES, the LabEx UnivEarthS, ANR-10-LABX-0023 and ANR-18-IDEX-000, and by the 'Action Incitative: Ondes gravitationnelles et objets compacts' and the Conseil Scientifique de l'Observatoire de Paris. The numerical simulations we have mentioned in this proceeding were run on the platform DANTE (AstroParticule & Cosmologie, Paris, France) and on the high-performance computing resources from Grand Equipement National de Calcul Intensif (GENCI) - Centre Informatique National de l'Enseignement Supérieur (CINES, grants A0100412463, A0130412463).

References

Abbott, B., Abbott, R., Abbott, T., et al. 2017a, Physical Review Letters, 119

Abbott, B. P., Abbott, R., Abbott, T. D., et al. 2017b, ApJ, 848, L13

Amaro-Seoane, P., Audley, H., Babak, S., et al. 2017, publisher: arXiv Version Number: 3

Artymowicz, P. & Lubow, S. H. 1994, ApJ, 421, 651

Babak, S., Petiteau, A., Sesana, A., et al. 2016, Mon. Not. R. Astron. Soc., 455, 1665

Casse, F., Varniere, P., & Meliani, Z. 2017, MNRAS, 464, 3704

D'Ascoli, S., Noble, S. C., Bowen, D. B., et al. 2018, The Astrophysical Journal, 865, 140

Farris, B. D., Duffell, P., MacFadyen, A. I., & Haiman, Z. 2015, Monthly Notices of the Royal Astronomical Society: Letters, 446, L36

Gutiérrez, E. M., Combi, L., Noble, S. C., et al. 2022, ApJ, 928, 137

Mignon-Risse, R., Varniere, P., & Casse, F. 2022, MNRAS, 519, 2848

Mignon-Risse, R., Varniere, P., & Casse, F. 2023a, Monthly Notices of the Royal Astronomical Society, 520, 1285

Mignon-Risse, R., Varniere, P., & Casse, F. 2023b, To be submitted

Piro, L., Ahlers, M., Coleiro, A., et al. 2022, Exp Astron

Roedig, C., Krolik, J. H., & Miller, M. C. 2014, ApJ, 785, 115

Shi, J.-M. & Krolik, J. H. 2016, ApJ, 832, 22

Shi, J.-M., Krolik, J. H., Lubow, S. H., & Hawley, J. F. 2012, ApJ, 749, 118

Tang, Y., Haiman, Z., & MacFadyen, A. 2018, Monthly Notices of the Royal Astronomical Society, 476, 2249, arXiv: 1801.02266

Vincent, F. H., Meheut, H., Varniere, P., & Paumard, T. 2013, A&A, 551, A54, arXiv: 1301.1147

Vincent, F. H., Paumard, T., Gourgoulhon, E., & Perrin, G. 2011, Classical and Quantum Gravity, 28, 225011

SF2A 2023
M. N'Diaye, A. Siebert, N. Lagarde, O. Venot, K. Baillié, M. Béthermin, E. Lagadec, J. Malzac, J. Richard (eds)

JACOBI CAPTURES : A FIRST STEP IN THE FORMATION OF OFF-CENTERED MASSIVE BLACK HOLE BINARIES IN DWARF GALAXIES

T. François[1], C. Boily[1] and J. Freundlich[1]

Abstract. The discovery of early-time supermassive black holes by JWST has rekindled interest in black hole mass assembly. Additionally, simulations and observations suggest a substantial population of off-centered intermediate-mass black holes in dwarf galaxies, potentially impacting black hole mass assembly, provided their capacity to merge beyond galactic cores. This study examines off-centered black hole dynamics in dwarf galaxies with cored dark matter haloes which can lead to long infall times and core stalling. By integrating off-centered black holes into the gravitational potential of a dwarf galaxy and exploring the phase space of initial conditions, we quantify the number of captures, which are a crucial step in off-center black hole mergers. Our analysis indicates captures in about 11% of cases. Such captures could be maintained over time within structures such as stripped nuclei or globular clusters.

Keywords: black hole physics - galaxies: dwarf - galaxies: kinematics and dynamics - software: simulations.

1 Introduction

Over the last decades, black holes have been discovered at the centers of both massive and dwarf galaxies, suggesting a shared history between them and their hosts (e.g., Gebhardt et al. 2000; Reines et al. 2013). The conventional picture of black hole mergers involves a three-phase process starting by their infall towards the galaxy center due to dynamical friction (cf. top panel of Fig. 1). However, this picture may not hold in low-density systems like dwarf galaxies, where the infall time can significantly exceed the Hubble time or black holes may be halted by core stalling (Kaur & Sridhar 2018; Banik & van den Bosch 2021), which would result in a large population of off-centered intermediate mass black holes (Bellovary et al. 2019, 2021; Pfister et al. 2019; Reines et al. 2020). Hence, it is essential to inquire whether merging beyond the central region is possible, as this could bear notable consequences for the assembly of black hole mass. We investigate the first anticipated step of this process: the Jacobi capture, namely the capture between the two black holes when they enter their sphere of influence (cf. lower panel of Fig. 1, and Francois et al. in prep., for more details). In this effect, we integrate two off-centered black holes in a dwarf galaxy gravitational potential. Our study aims to provide simplified yet general insights applicable to various scenarios, paving the way for more complex simulations.

2 Method

We use a simplified setup where we integrate two black holes on coplanar circular orbits in an external gravitational potential representing the dark matter halo of a dwarf galaxy. We explore the 5-parameter space of the encounter (cf. Fig. 1 right) to quantify the occurrences of capture, investigating how the different parameters affect this process. We then focus on core stalling as the cause for off-centering, reducing the parameters to 3 ($M_1, M_2, \Delta\varphi_i$). Subsequently, we employed a semi-analytical model to generate merger trees (Jiang et al. 2021), yielding a representative sample of black hole masses which enables us to derive a merger probability in the case of black holes stemming from major mergers.

[1] Université de Strasbourg, CNRS, Observatoire astronomique de Strasbourg, UMR 7550, F-67000 Strasbourg, France

© Société Française d'Astronomie et d'Astrophysique (SF2A) 2023

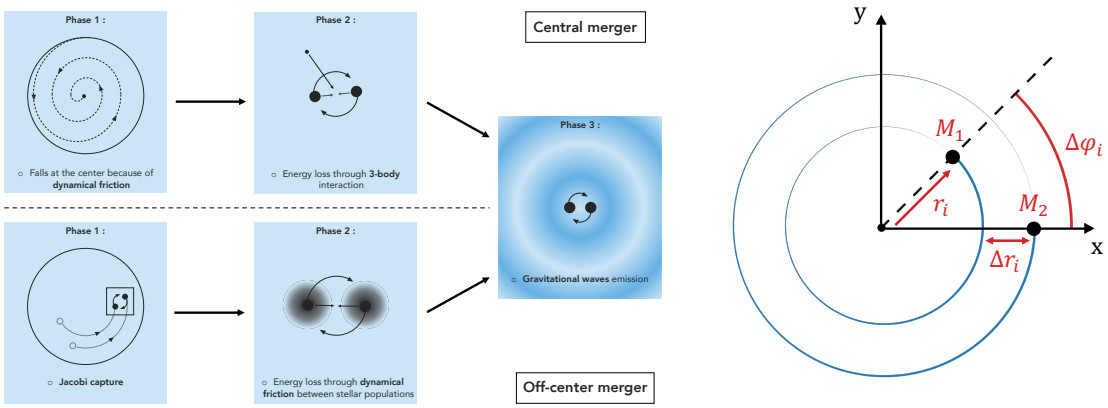

Fig. 1. Left: Top panel: classical black holes merger scenario in the galactic centre. Bottom panel: anticipated scenario for an off-center merger. **Right:** Parameters of an initial configuration : r_i the initial radius of the inner BH, Δr_i the radial separation between BHs, $\Delta\varphi_i$ the phase difference and M_1, M_2 the two masses.

3 Results

The general 5-parameter case highlights a preference for capture when the outer black hole surpasses the inner one in mass. We find bonding bands in terms of initial separation between the orbits (Δr_i); below these bands (small radial separation between black holes), either initial proximity enables binding, or insufficient orbital frequency difference hinders the catch-up with the initial phase difference, preventing binding. Conversely, beyond these bands (associated with larger radial separations), the black holes remain too distant for binding. Core stalling typically places the BHs at very close radii, namely in the regime of small radial separations, where BHs bind when their initial separation is small enough. This results in a moderate mass disparity (closely matched masses are synonymous with closely matched stalling radii) and a low phase difference. Subsequently, using merger trees to sample masses, we derived a capture probability of 11% when BHs stem from major mergers.

4 Conclusions

In this study, we explored the possibility for black holes to merge outside galactic centers in dwarf galaxies. Using an idealized setup, we quantified the probability of Jacobi capture, a fundamental step in forming an off-centered binary and examined the effects of various parameters. We find that capture occurs in about 11% of cases. This result carries significant implications for the assembly of black hole masses, especially if these captures can be prolonged over time through dissipative forces. Further investigations into the effectiveness of these forces, particularly within stripped nuclei or globular clusters, are warranted. These findings shed light on the importance of captures in these environments and are perhaps an important step in the ongoing quest to understand the origins and growth of black holes in the Universe.

References

Banik, U. & van den Bosch, F. C. 2021, ApJ, 912, 43
Bellovary, J. M., Cleary, C. E., Munshi, F., et al. 2019, MNRAS, 482, 2913
Bellovary, J. M., Hayoune, S., Chafla, K., et al. 2021, MNRAS, 505, 5129
Francois, T. L., Boily, C., Freundlich, J., et al. in prep.
Gebhardt, K., Bender, R., Bower, G., et al. 2000, ApJ, 539, L13
Jiang, F., Dekel, A., Freundlich, J., et al. 2021, MNRAS, 502, 621
Kaur, K. & Sridhar, S. 2018, ApJ, 868, 134
Pfister, H., Volonteri, M., Dubois, Y., Dotti, M., & Colpi, M. 2019, MNRAS, 486, 101
Reines, A. E., Condon, J. J., Darling, J., & Greene, J. E. 2020, ApJ, 888, 36
Reines, A. E., Greene, J. E., & Geha, M. 2013, ApJ, 775, 116

Session S19

Sixième réunion des utilisateurs des télescopes français (TBL/OHP193)

SF2A 2023
M. N'Diaye, A. Siebert, N. Lagarde, O. Venot, K. Baillié, M. Béthermin, E. Lagadec, J. Malzac, J. Richard (eds)

SPECTRO-IMAGING FOLLOW-UP OF GAMMA-RAY BURSTS WITH THE OHP/T193

B. Schneider[1,2], E. Le Floc'h[2], C. Adami[3], D. Turpin[2], S. Basa[3], D. Götz[2], J. T. Palmerio[4], A. Saccardi[4], S. D. Vergani[4] and B. Cordier[2]

Abstract. Gamma-ray bursts (GRBs) are the most powerful explosions known in the Universe produced by the death of massive stars or the coalescence of two compact objects such as a binary system of two neutron stars. Due to their transient nature, rapid follow-up observations are the unique chance to fully characterize their radiative processes and better understand these violent phenomena. The upcoming Sino-French SVOM mission will monitor the gamma-ray sky and detect new transient sources such as GRBs. In addition to previous GRB missions, SVOM will benefit from an improved synergy with ground telescopes to perform fast and efficient follow-up observations. As part of this effort, we proposed a target of opportunity program using the spectro-imager MISTRAL instrument mounted on the OHP/T193 to follow-up GRB alerts. Our program was granted for 10-15 alerts (20-30 hours) over the past three semesters since March 2022. We present our first GRB follow-up observations with MISTRAL using Swift alerts. In particular, we report the observations of the brightest of all time GRB (GRB 221009A) and a first GRB redshift tentative with the OHP/T193. These preliminary MISTRAL triggers prepare the SVOM community to react quickly to alerts, and rapidly reduce, analyze and interpret the MISTRAL data, essential to fully exploit the imminent SVOM alerts.

Keywords: Gamma-ray bursts, Follow-up, MISTRAL, SVOM

1 Introduction

Gamma-ray bursts (GRBs) are brief flashes of γ-photons produced by extragalactic explosions. Observationally, two main emissions are detected, a prompt emission mainly composed of gamma-ray radiations from mili-seconds to minutes followed by a longer (hours to days) and spectrally broader (X-ray to radio) afterglow emission. The GRB population is traditionally divided into two main classes according to their hardness and duration considering a separation at $T_{90} \sim 2$ s (e.g., Sakamoto et al. 2011). Short and hard GRBs are thought to be produced by the coalescence of two compacts objects (e.g., a binary neutron star system) (Abbott et al. 2017) while long GRBs are thought to be associated with the core-collapse of a fast rotating massive stars (Hjorth et al. 2003). Rapid and efficient follow-up observations represent the only way to further characterize the transient by improving its localization, inferring its distance (i.e., redshift), and sampling the evolution of its light curve. The forthcoming Sino-French SVOM (Space-based multiband astronomical Variable Objects Monitor) mission will be dedicated to the study of GRBs (Wei et al. 2016). The mission includes a major follow-up network to improve the space-ground synergy and the wavelength coverage of the afterglow emission. SVOM is expected to provide a more homogeneous and complete sample (e.g., $\sim$2/3 redshift) than previous missions. In this work, we report the first follow-up observations of GRBs carried out by the spectro-imager MISTRAL mounted on the OHP/T193 telescope. These observations provide valuable experience for preparing upcoming SVOM alerts.

[1] Kavli Institute for Astrophysics and Space Research, Massachusetts Institute of Technology, 77 Massachusetts Ave, Cambridge, MA 02139, USA
[2] Université Paris-Saclay, Université Paris Cité, CEA, CNRS, AIM, 91191 Gif-sur-Yvette, France
[3] Aix Marseille Université, CNRS, CNES, LAM, Marseille, France
[4] GEPI, Observatoire de Paris, Université PSL, CNRS, 5 Place Jules Janssen, 92190 Meudon, France

© Société Française d'Astronomie et d'Astrophysique (SF2A) 2023

2 Spectro-imager MISTRAL

The Haute-Provence Observatory (OHP) is located in the south-eastern of France at about 650 m altitude with observational conditions favorable in more than 60% of the nights. The main telescope still in operation for science is the T193 with a primary mirror of diameter 1.93m. Two main instruments are permanently mounted on the telescope and can be switched in less than one minute, the high resolution SOPHIE spectrograph and the Multi-purpose InSTRument for Astronomy at Low-resolution (MISTRAL) spectro-imager. MISTRAL offers an imagery mode as well as a low-resolution spectroscopy mode using an elongated and narrow slit ($R \sim 750$) through two independent settings, a blue grism (4200-8000 Å), and red grism (5800-9950 Å)*. Since 2022, the instrument was opened to the community for visitor mode and target-of-opportunity (ToO) mode limited at 2 hours per trigger with one ToO maximum every 3 nights. Given the unpredictable nature of GRBs, the ToO mode is ideal for GRB science and commonly used with ground telescopes to perform follow-up observations of new sources detected by gamma-ray space missions.

3 Scientific motivation

Two meters type telescopes are more likely to be available than large (>8 m) ground telescopes. The OHP/T193 is also ideally located between two others SVOM follow-up telescopes (in China and Mexico). MISTRAL can reach in a reasonable time a magnitude of about 20.5 mag for photometry (∼20 mins) and 19 mag for spectroscopy (∼60 mins) with a minimal signal-to-noise ratio (S/N) of 3. Moreover, considering previous observed GRBs in the R-band (Kann et al. 2010), we expect to be able to detect with MISTRAL most of GRBs, if observed relatively soon after their first detection from space satellites (typically <4 hours). In a small number of cases, if the afterglow is bright enough (<19 mag) or if observations are carried out promptly after the GRB trigger time, we can obtain a spectrum of the source with a good S/N and infer its redshift using absorption lines in the afterglow emission. Finally, for local events, we might also constrain the presence of a possible supernova (SN) as previously observed with long GRBs (Hjorth et al. 2003), as well as deeply characterize the host galaxy after the fading of the transient.

4 Follow-up strategy

Multiple GRB alerts are reported every day by various gamma-ray spacecrafts with diverse localization accuracy, from arcseconds up to several degrees. Given the field-of-view of MISTRAL (5 arcmin) and the expected localization of SVOM GRBs (<2 arcmin in the majority of cases thanks to MXT, Götz et al. 2023; Schneider et al. 2023), we limit our program to GRBs detected by the *Swift* satellite with sub-arcmin localization provided by the X-Ray Telescope (XRT). This maximizes our ability to find the optical transient and practice ToO observations in similar conditions than during the SVOM operations. Our trigger criteria can be summarized as follow: (1) *Swift* alert with at least an XRT detection (error box $\lesssim$10 arcsec), (2) Visibility >1 hour above 30° at OHP, (3) $T_{\rm obs} < T_0 + 4$ hours, (4) Low Galactic extinction: $A_V < 0.5$, (5) No nearby bright stars. In practice, these criteria can be relaxed for interesting events or regarding information reported by other teams via Gamma-ray Coordination Network (GCN) circulars†. During observations, a quicklook of the data are performed in real-time by the burst advocates in shift using static data calibration files. This allows us to rapidly adapt the observational strategy and maximize the scientific results. A typical observation sequence starts by ∼20 mins of imaging in the R-band. If a bright counterpart is identified (<19 mag), MISTRAL switches to spectroscopic mode for 60 minutes. Alternatively, imaging mode is continued to increase the S/N, and eventually observations in additional bands can be performed to further constrain the afterglow light curve.

5 First GRB follow-up and results

Over the three past semesters, MISTRAL was triggered a total of nine times with a mean response time of ∼15 hours and included imaging and spectroscopy observations. Our resulting photometry and analysis were reported to the GRB community via GCN circulars. We have detected 3 optical transients (Schneider et al. 2022a; Turpin et al. 2023a; Adami et al. 2023a), inferred 2 redshifts (Adami et al. 2023b,c), and derived 5

*http://www.obs-hp.fr/guide/mistral/MISTRAL_spectrograph_camera.shtml
†https://gcn.nasa.gov/circulars/

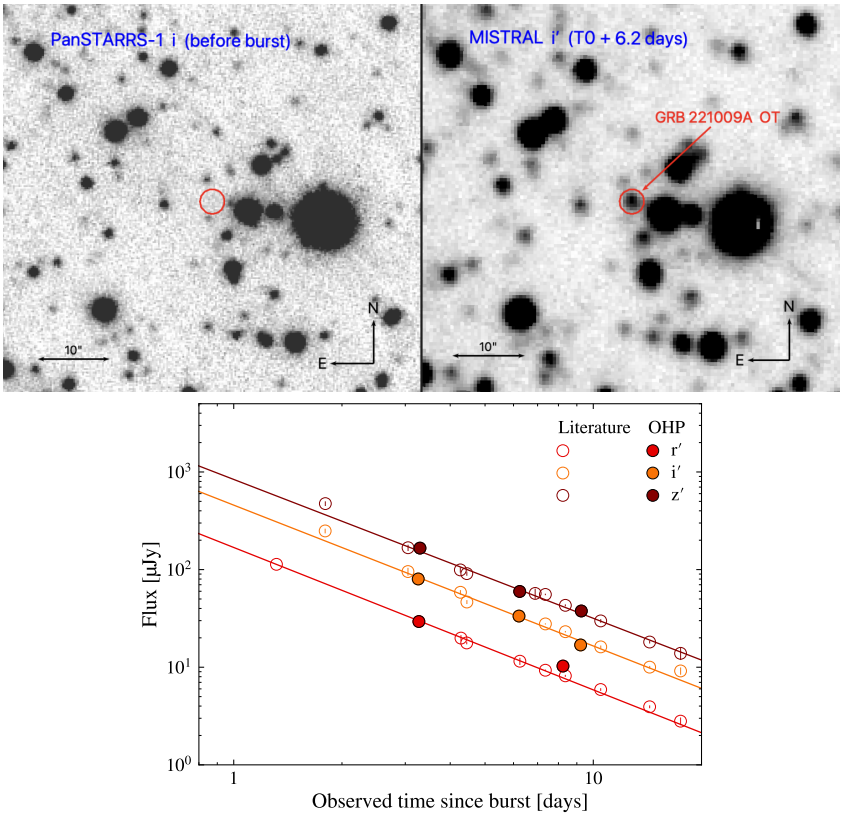

Fig. 1. **Top:** Optical counterpart of GRB 221009A (the BOAT) detected by MISTRAL. The left panel shows the PanSTARRS-1 image of the GRB 221009A field before the burst and the right panel is the image obtained by MISTRAL of the same field ∼6 days after the detection of the burst by the Fermi satellite. The expected optical transient position is highlighted by a red circle. **Bottom:** Light curve of GRB 221009A combining literature (empty circles) values and measured obtained at the OHP with MISTRAL and OHP/T120 telescope at different epochs for r′, i′ and z′ filters.

upper-limits up to r > 22.3 AB mag (Schneider et al. 2022b; Turpin et al. 2022, 2023b; Adami et al. 2023a,d). Among them, GRB 221009A (also called the BOAT for the brightest of all time) was observed at two different epochs ($T_0 + 6$ and $T_0 + 10$ days) by MISTRAL in multiple filters. The optical afterglow was clearly detected in both epochs, as visible in the top panel of Fig. 1. Our magnitudes contributed to the extensive follow-up of this source and confirmed the power law decay expected for a pure afterglow fading (Fig. 1). This further helped to investigate the possible raising of the SN, widely debated within the community for this burst. GRB 230506C was rapidly observed after the *Swift* trigger (about $T_0 + 4$ hours). A clear optical transient at ∼20.9 mag in the r-band was detected in the XRT error circle (top panel of Fig. 2). We then obtained a spectroscopy observation of 30 mins using the MISTRAL blue setting. The spectrum revealed a faint continuum consistent with the source. A refined analysis of the 1D spectrum revealed break at ∼6000 Å (Fig. 2). We interpreted it as the Lyman-α break, commonly observed in GRB afterglow spectrum due to neutral hydrogen absorption within the host galaxy. This suggests that the redshift of this source is around $3.7 \leq z \lesssim 4$. This represents the most distant redshift measured at OHP and confirm the capability of MISTRAL to infer the redshift of GRBs.

6 Conclusions

We reported the first follow-up observations performed with the MISTRAL instrument as part of our GRB program. A total of nine observations were carried out based on *Swift* alerts and our data analysis were reported to the community via GCN circulars. These triggers demonstrated the potential of MISTRAL to constrain the light curve or redshift of GRBs, and its possible key role for the SVOM follow-up network. These first ToO observations also provided valuable training, from initial reaction to data interpretation, in order to be ready for the imminent SVOM alerts.

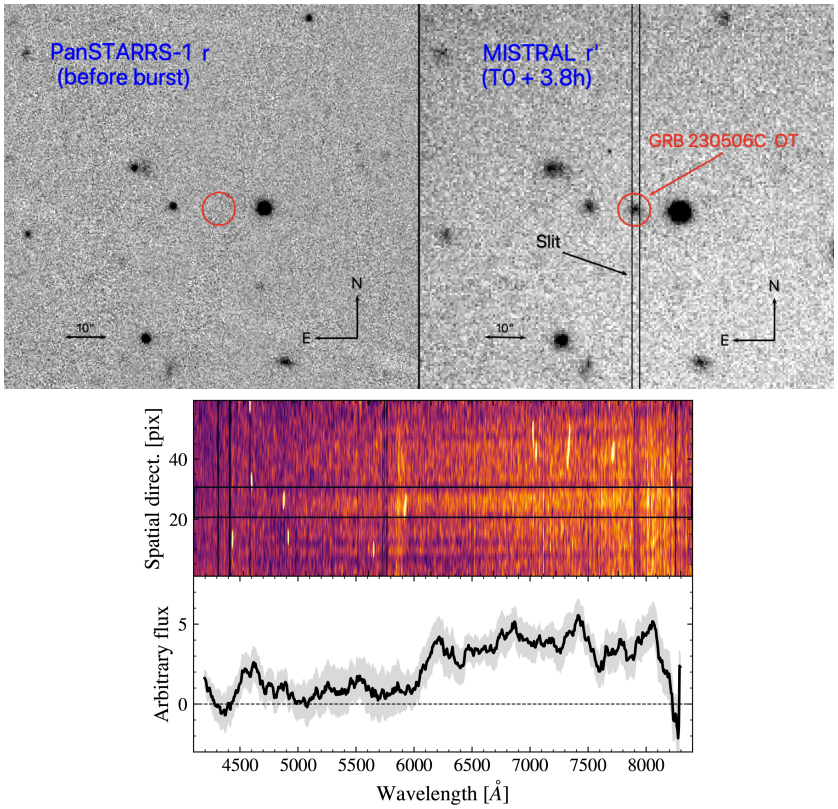

Fig. 2. **Top:** Optical counterpart of GRB 230506C detected by MISTRAL. The left panel is the PanSTARRS-1 image of the GRB 230506C field where no source is visible in the red circle. The right panel shows the image obtained by MISTRAL of the same field at ∼4 hours after the detection of the burst by *Swift*. The long slit position used for spectroscopy observation is visible as a black box and the expected optical transient position is highlighted by a red circle. **Bottom:** 2D spectrum (top panel) obtained by MISTRAL of GRB 230506C in blue setting. The black box shows the extraction region considered for the 1D spectrum visible in the bottom panel.

We acknowledge the OHP staff for their excellent observations and the support of the OHP for this program. BS additionally acknowledges the grant provided by the SF2A and the SVOM mission for participation at the Journées SF2A 2023. MISTRAL was jointly funded by the Région Sud and the French Government through its CPER.

References

Abbott, B. P., Abbott, R., Abbott, T. D., et al. 2017, ApJ, 848, L13
Adami, C., Basa, S., Le Floc'h, E., et al. 2023a, GRB Coordinates Network, 33741, 1
Adami, C., Garnichey, M., Michel, F., et al. 2023b, GRB Coordinates Network, 33707, 1
Adami, C., Palmerio, J., Vergani, S. D., et al. 2023c, GRB Coordinates Network, 33749, 1
Adami, C., Schneider, B., Basa, S., et al. 2023d, GRB Coordinates Network, 33607, 1
Götz, D., Boutelier, M., Burwitz, V., et al. 2023, Experimental Astronomy, 55, 487
Hjorth, J., Sollerman, J., Møller, P., et al. 2003, Nature, 423, 847
Kann, D. A., Klose, S., Zhang, B., et al. 2010, ApJ, 720, 1513
Sakamoto, T., Barthelmy, S. D., Baumgartner, W. H., et al. 2011, ApJS, 195, 2
Schneider, B., Adami, C., Le Floc'h, E., et al. 2022a, GRB Coordinates Network, 32753, 1
Schneider, B., Renault-Tinacci, N., Götz, D., et al. 2023, Experimental Astronomy, 56, 77
Schneider, B., Turpin, D., Le Floc'h, E., et al. 2022b, GRB Coordinates Network, 32271, 1
Turpin, D., Adami, C., Le Floc'h, E., et al. 2023a, GRB Coordinates Network, 33282, 1
Turpin, D., Adami, C., Schneider, B., et al. 2023b, GRB Coordinates Network, 33696, 1
Turpin, D., Adami, C., Schneider, B., Le Floch, E., & Basa, S. 2022, GRB Coordinates Network, 32360, 1
Wei, J., Cordier, B., Antier, S., et al. 2016, arXiv e-prints, arXiv:1610.06892

SF2A 2023
M. N'Diaye, A. Siebert, N. Lagarde, O. Venot, K. Baillié, M. Béthermin, E. Lagadec, J. Malzac, J. Richard (eds)

A NEW NEONARVAL PIPELINE WITH PYREDUCE

K. Thomson-Paressant[1], C. Gutteridge[1], C. Neiner[1] and C. Catala[1]

Abstract. After the upgrade of the Narval instrument at TBL to NeoNarval, concerns have been raised regarding the quality of results in polarimetry and precision in velocimetry. Investigations into the topic have hinted at both instrumental and software issues that must be resolved in order to accurately exploit the data. We present our discoveries of issues and subsequent work performed to improve the reduction of NeoNarval data. We aim to provide comparisons between the DRS and a pipeline utilised for similar instruments, as well as initial attempts to implement new methods. PyReduce, an open-source reduction pipeline for echelle spectrographs, has modules already designed for a variety of currently-used instruments as well as initialisation of a number of options allowing for the evolution and expansion of its functions, which is of great benefit for integrating the specifics of the NeoNarval instrument.

Keywords: instrumentation, spectropolarimeter, stellar magnetism

1 Introduction

1.1 The NeoNarval instrument

After 13 years of operation, the Narval spectropolarimeter installed at the Télescope Bernard Lyot (TBL) in the Observatoire Midi-Pyrénées was upgraded to NeoNarval in 2019. The aim of this upgrade was to achieve increased stability in radial velocity measurements (< 3 m.s^{-1} goal), at the cost of reduced instrumental resolution (68,000 →53,000). This would allow the instrument to obtain high precision velocimetry for exoplanet research, in addition to the stellar spectropolarimetric studies it was already performing. To achieve this, efforts were focused on improving calibration, as well as thermal and mechanical stability (Böhm et al. 2016).

The data taken by the previous Narval instrument was reduced by the LibreEsprit pipeline (Donati et al. 1997), however this software is not open-source and modifications were necessary for operation with NeoNarval. In particular, a super-resolution algorithm was required to theoretically recover the resolution lost by the upgrade of the hardware. As a result, it was decided that a new open-source pipeline should be designed from the ground up for NeoNarval, called the Data Reduction Software (DRS).

Since the upgrade of the instrument, concerns have been raised regarding the quality of the spectropolarimetric results and the precision in velocimetry. Independent investigations hint at both instrumental and software issues, both of which would require correction in order to accurately exploit the science data coming from the instrument. A workshop was organised in January 2023 to discuss the instrument and the problems being observed, during which a science team was formed to assess these concerns, and we were tasked with investigating software-related issues. To this end, we elected to utilise PyReduce to diagnose these problems and to perform reduction of the spectropolarimetric data in an isolated environment, independent of the DRS.

A new release of the DRS (version 3) became operational in May 2023. However all comparisons between our adaptation of PyReduce and the DRS presented here will be regarding DRS version 2.

1.2 PyReduce software

PyReduce is a data reduction pipeline designed for echelle spectrographs (Piskunov et al. 2021), based on the IDL Reduce package (Piskunov & Valenti 2002) that has been ported to Python3. It is open source

[1] LESIA, Paris Observatory, PSL University, CNRS, Sorbonne University, Université Paris Cité, 5 place Jules Janssen, 92195 Meudon, France

© Société Française d'Astronomie et d'Astrophysique (SF2A) 2023

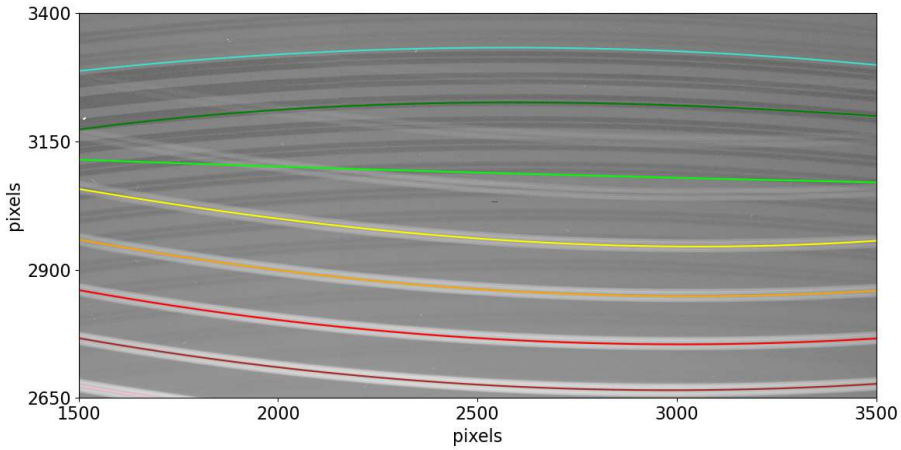

Fig. 1. Example of the order tracing method performed by the DRS version 2. Note the blue and green curves at the top of the image that are incorrectly tracing the ghost orders.

and available on GitHub*, albeit with limited support from the original authors. Nevertheless, it is under development by a number of independent groups, each with their own goals e.g. SALT (Crause et al. 2022) and MIKE (Das & Banyal 2021). The software already operates for a variety of spectroscopic instruments (e.g. UVES, XSHOOTER, HARPS, NIRSpec, etc.), and was designed with the intention of eventually adding polarimetric methods, though they had yet to be implemented. Using this tried and tested tool, we are steadily progressing on implementing polarimetry, in addition to the instrument configuration for NeoNarval.

2 Issue resolution

During the process of applying PyReduce to the NeoNarval data, a number of key issues have arisen on which we have elected to focus our efforts. These are detailed in the following sections, but this is far from an exhaustive list of areas we are currently investigating in the operation of the DRS and the NeoNarval instrument.

2.1 Spurious Inverted Orders

Visible on the CCD, most clearly on the flat field exposures, are inverted ghost orders. This instrumental issue originates from an electronic crosstalk between the 4 amplifiers, but ultimately needs to be considered in the data reduction as it causes errors in the flux recorded in the far blue orders and in the order tracing as seen in Fig. 1. This ultimately led to DRS version 2 having large errors in the wavelength calibration for the bluest orders, as these spurious orders were being calibrated rather than the true orders.

To solve this problem, we identify clusters of points along the bright beams and fit a second-order polynomial to each region. Any fit with an inverted sign in the leading term, with respect to the majority, is isolated and removed from the list. Additionally, each fit is only allowed minor variations to those around it, preventing any deviations where the spurious orders intercept. Unfortunately, the proportion of overlap of true and ghost orders results in the inability to extract quality data from the far blue orders. A potential solution to maximise the extracted data would be to trace these inverted orders to mask out the regions they interfere with.

2.2 Background scatter subtraction

When looking at the raw data files, it becomes quickly apparent that there is flux that appears between the spectral orders. This is a result of scattered light inside the instrument, and causes issues when attempting to determine the flux ratio in each order as it contributes unevenly across the beams. This feature is particularly

*See `https://github.com/AWehrhahn/PyReduce`

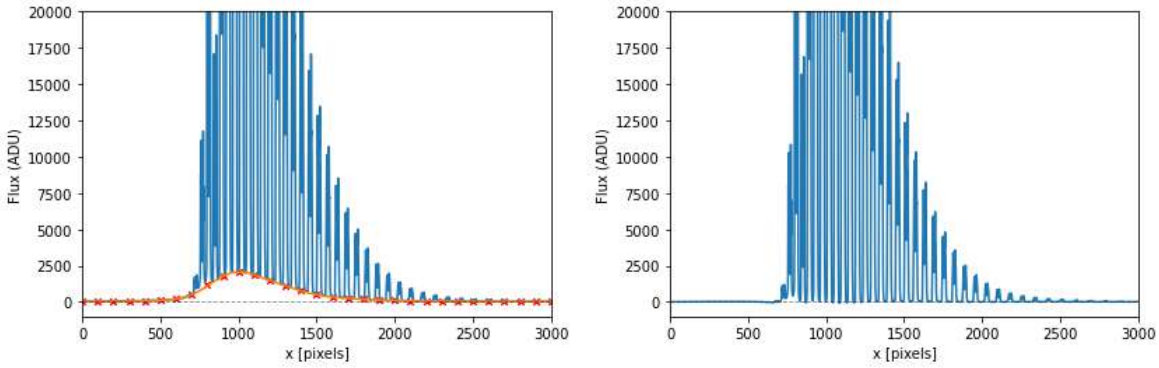

Fig. 2. Slice of a CCD image perpendicular to the orders (blue), before (left panel) and after (right panel) subtraction of the fit to the background scatter (red and orange).

visible when looking at the flat-field calibration files, as the overall flux in the image is larger, and so too is the amount of scattered light, but it is also present in all illuminated exposures.

To resolve this issue, we utilise a window function that runs perpendicular to the orders to search for local minima. These minima correspond to the zero-points between orders, from which we can perform a 2D fit over the entire image to determine the overall contribution of background scatter to the image. We utilise a linear combination of four Gaussian profiles, as this was the most consistently performing shape. A least-squares algorithm determines the best fit parameters, which we then use to subtract the fit from the image.

We first perform this fit to the flat-fields, then apply the given parameters as a first guess for the fit on the science files. While the amplitude will differ, the overall shape of the function should remain roughly constant. As an example, a 2D slice of this fit is shown in Fig. 2. One should note that the NeoNarval DRS currently only performs this step on science files and not on the calibration files.

2.3 Beam separation and order extraction

Illuminated images taken by NeoNarval exhibit curved spectral orders consisting of two beams, one for each perpendicular polarisation state. Unfortunately, there is a slight overlap in the areas illuminated by each beam. While this is not an issue for spectroscopy, it is problematic in polarimetry, as one polarisation state pollutes the other. We therefore opted to design a new extraction algorithm to minimise the contribution of each beam to the other.

Each beam is split into 3 separate peaks due to the slicer it passes through. The central peak of each beam is the brightest, and one (and always the same one) of the side lobes is brighter than the other. Looking at the left panel of Fig. 3, we can see that a simple double-Gaussian profile does a poor job of fitting these peaks, and that rather two sets of three Gaussians (labelled 'Hex Gaussian') is a much more accurate representation. This can be extrapolated quite easily to 2-dimensions to fit the two beams of an entire order at once, as seen in the right panel of Fig. 3.

Once the fit to the flat-corrected science files has been determined, we can then exclude all pixels between the two beams with $\geq$5% contribution from both beams. Typically, this corresponds to an exclusion region of up to three columns (out of $\sim$ 30 columns per order).

3 Conclusions

We are implementing polarimetry into PyReduce, with new and improved methods for e.g. order tracing, blending removal, background scatter subtraction, wavelength calibration, and Stokes profiles generation. Here, we present preliminary results of our efforts to integrate some of these into the software, taking into account the specific configuration of the NeoNarval instrument.

PyReduce produces encouraging results, though there is still work to be done in order to accurately and precisely exploit the spectropolarimetric data coming from NeoNarval. The next steps in this process are:

- Consider vignetting at the extremities of each order to prevent error being introduced into the order tracing and background scatter steps.

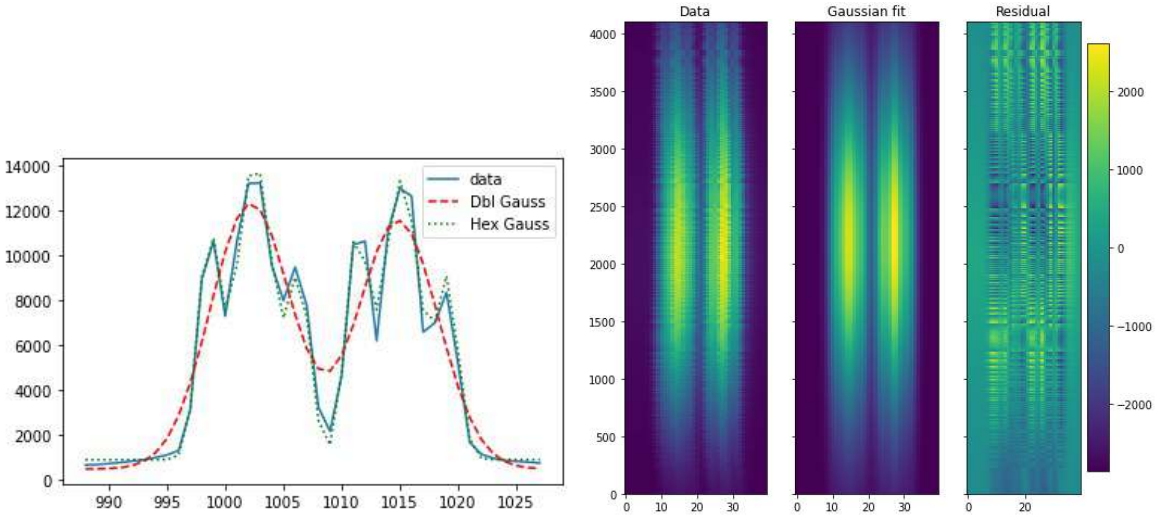

Fig. 3. Gaussian fits to the two beams of a given order, **left:** in one dimension and **right:** in two dimensions. The latter also provides the residuals of the fit to the data, with corresponding value range.

- Transition from the rigid pixel grid currently in operation to a non-linear grid to improve precision of order tracing.
- Integrate 2D wavelength calibration, to be performed on each polarisation state separately.
- Ensure the validity of the cosmic ray removal method inside of PyReduce on NeoNarval data.
- Implement multi-threading/parallelisation for the most computationally expensive steps, particularly the various fitting steps such as background scatter and inter-beam exclusion.
- Ensure universality/portability of packages for Python 3.X, so that the code operates on a maximum of devices.

We emphasise that the implementation of these methods into PyReduce will not solve the instrumental problems, but rather will help to diagnose such issues and improve the operation of the instrument as a whole, while maximising the quality of both past and future reduced data.

The branch of PyReduce that we are currently working on is not yet openly available, but can be made so for anyone willing to test the methods on their own data, and will be open access in the future, with the hopes that other members of the community can contribute to its operation and improve its function.

We thank the TBL team for providing us with the DRS source code and raw data, as well as for useful discussions. We also thank the PyReduce team for making their code publicly available.

References

Böhm, T., Cabanac, R., & Lopez Ariste, A. 2016, Neo-Narval Technical Specifications, Tech. rep., Obs. Midi-Pyrénées

Crause, L. A., McCracken, R. A., Reid, D. T., et al. 2022, in Ground-based and Airborne Instrumentation for Astronomy IX, ed. C. J. Evans, J. J. Bryant, & K. Motohara, Vol. 12184, 121844V

Das, T. & Banyal, R. K. 2021, Appl. Opt., 60, 9906

Donati, J.-F., Semel, M., Carter, B. D., Rees, D. E., & Cameron, A. C. 1997, MNRAS, 291, 658

Piskunov, N. E. & Valenti, J. A. 2002, A&A, 385, 1095

Piskunov, N. E., Wehrhahn, A., & Marquart, T. 2021, A&A, 646, A32

SF2A 2023
M. N'Diaye, A. Siebert, N. Lagarde, O. Venot, K. Baillié, M. Béthermin, E. Lagadec, J. Malzac, J. Richard (eds)

MISTRAL OBSERVATIONS OF THE C/2022 E3 (ZTF) COMET BY THE AIX-MARSEILLE M2 STUDENTS: FIRST SCIENCE RESULTS

C. Adami[1], E. Jehin[2], K. Aravind[3], Y. Ahmad[4], A. Roy[4], C. Carvajal-Bohorquez[4], M. Garnichey[4], M. Hasan[4], D. Hassaine[4], N. E. Jimenez de la Vega[4], A. Kaddour[4], V. Kueviakoe[4], R. Mendil[4], F. Michel[4], S. Anderson[1], A. Delsanti[1], H. LeCoroller[1], D. Russeil[1], S. Lazzarini[5] and A. Litman[6]

Abstract. The bright long period comet C/2022 E3 (ZTF) was observed using the MISTRAL spectrograph camera on the 1.93 m OHP telescope on 2023-02-10. We derived the production rates of (2.61+/-0.04)E26 and (2.51+/-0.07)E26 for C2 ($\Delta\nu = 0$) from our two sets of observations. These values are in close agreement with those reported for the same comet from previous independant observations. The Afρ dust proxy of 5100±80 cm is also in agreement with literature values at similar epochs.

Keywords: MISTRAL, OHP, Comet

1 Observations and reductions

The bright comet C/2022 E3 (ZTF) was observed in manual tracking mode for different exposure times, 120s and 240s, using the MISTRAL spectrograph camera on the 1.93 m OHP telescope on 2023-02-10 when the comet was at a distance of 1.20 au from the Sun and 0.39 au from the Earth. We used the blue mode covering the ∼4200-8000A range at resolution ∼750 with a 1.9arcsec width slit. All the acquired frames for different exposures were bias subtracted and then flat fielded using the spectral flat lamp present in the instrument (Tungsten). The cosmic rays were removed using the LACOSMIC package (van Dokkum 2001). The reduced and extracted 1D spectrum is shown in Fig.1.

Both the 120s and 240s spectra, even if slightly trailed, were used to compute the production rates of C2 ($\Delta\nu = 0$) emission band using a single aperture (200 pixel aperture) with the comet at the centre, as mentioned in Aravind et al. (2021). The 120s spectra that were better guided with a narrower dust continuum were used to extract spectra with apertures of equal widths moving away from the photo centre to compute spatial profile of the column density and hence the production rates with the help of Haser (1957) modelling. The HgArXe lamp available in the instrument was used in both cases to wavelength calibrate all the extracted spectra. The spectrophotometric standard, Hiltner600, observed on the same night using the same configuration was used to produce the sensitivity curve of the instrument and then flux calibrate the comet spectra. The Solar analog standard star HD19445 was observed on the same night to remove the dust reflected solar continuum present in the optical spectra. Even though, ideally, a separate sky frame of similar exposure is required to remove the sky background from the comet frames, we used the sky from a point source observed with a similar exposure time on the same night to remove the sky lines.

[1] Aix Marseille Univ, CNRS, CNES, LAM, Marseille, France
[2] Space sciences, Technologies & Astrophysics Research (STAR) Institute, Allée du Six Août, 19C, University of Liège, 4000 Liège, Belgium
[3] Physical Research Laboratory, Navarangpura, Ahmedabad, 380058, Gujarat, India
[4] Aix Marseille Univ, Marseille, France
[5] Aix Marseille Univ, Université de Toulon, CNRS, CPT, IPhU, Marseille, France
[6] Aix Marseille Univ, Institut Fresnel, Marseille, France

© Société Française d'Astronomie et d'Astrophysique (SF2A) 2023

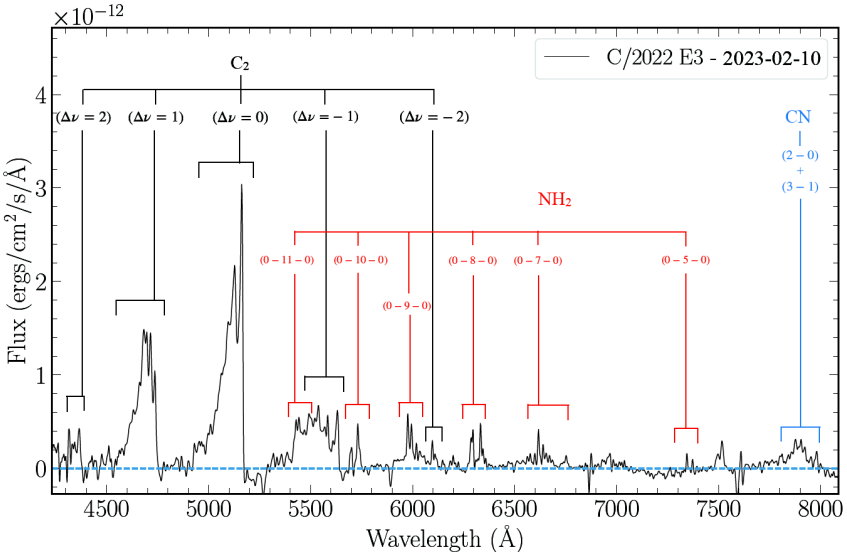

Fig. 1. Optical spectrum of comet C/2022 E3 (ZTF) observed using the MISTRAL spectrograph camera on the OHP telescope. The spectrum, obtained from the 240s frame, was extracted using a 29.2arcsec x 1.93arcsec aperture with the comet at the centre. The main cometary emissions are labelled.

2 Analysis

Several usual cometary emission bands were detected from C2, NH2 and CN radicals. The production rate of (2.61+/-0.04)E26 and (2.51+/-0.07)E26 for C2 ($\Delta\nu = 0$) were computed for the 240s frame and 120s respectively and are in good agreement with the values reported for the same comet from the TRAPPIST telescopes ((Jehin et al. 2022); ATel 15822). The Afρ, a proxy to the dust production (A'Hearn et al. 1984) computed for the green continuum narrow band filter (Farnham et al. 2000), from spectroscopic data using techniques as mentioned in (Aravind et al. 2022), was found to be around 5100±80 cm, which is again in agreement with the values reported from TRAPPIST for the comet at similar observational epochs.

3 Conclusions

With the help of these observations, the MISTRAL spectrograph camera on the OHP telescope proves to be reliable for cometary observations for a wavelength range of 4200A - 8000A. With proper differential tracking and required frames acquired in an orderly manner, longer exposure observation of fainter and more distant comets could be used to effectively analyse the column density profiles of the various emission bands marked in the figure, which can further be used to compute their production rates.

We acknowledge OHP staff for its support during the AMU M2-Physics 2023 observationnal internship. We thank M. Dennefeld for his help. This work received support from the French government under the France2030 investment plan, as part of the initiative d'Excellence d'Aix-Marseille Université- A*MIDEX (AMX-19-IET-008). We were also supported by the IPhU Graduate School program at Aix-Marseille University. EJ is a FNRS Senior Research Associate. TRAPPIST is a project funded by the Belgian Fonds (National) de la Recherche Scientifique (F.R.S.-FNRS) under grant T.0120.21. We also acknowledge the support by Master Erasmus Mundus Europhotonics (599098-EPP-1-2018-1-FR-EPPKA1-JMD-MOB) financed by EACEA (European Education and Culture Executive Agency). Authors thanks the SF2A organizers.

References

A'Hearn, M. F., Schleicher, D. G., Millis, R. L., Feldman, P. D., & Thompson, D. T. 1984, AJ, 89, 579

Aravind, K., Ganesh, S., Venkataramani, K., et al. 2021, MNRAS, 502, 3491

Aravind, K., Halder, P., Ganesh, S., et al. 2022, Icarus, 383, 115042

Farnham, T. L., Schleicher, D. G., & A'Hearn, M. F. 2000, Icarus, 147, 180

Haser, L. 1957, Bulletin de la Societe Royale des Sciences de Liege, 43, 740

Jehin, E., Vander Donckt, M., Manfroid, J., et al. 2022, The Astronomer's Telegram, 15822, 1
van Dokkum, P. G. 2001, PASP, 113, 1420

SF2A 2023
M. N'Diaye, A. Siebert, N. Lagarde, O. Venot, K. Baillié, M. Béthermin, E. Lagadec, J. Malzac, J. Richard (eds)

SPECTROSCOPY OF TRANSIENTS WITH MISTRAL AT OHP

M. Dennefeld[1]

Abstract. The many on-going sky surveys, on ground or space, reveal dozen of variables or transients per night which require a spectrum to be properly caracterised. This includes Novae and SNe (in particular, the Ic's associated with some GRBs), FBOT's, FRB's, etc...TDE's help to detect otherwise quite AGN's and CLQ's challenge the standard unified scheme of AGN's. The advent of the LSST/Rubin telescope and of the SVOM satellite will multiply such events and the brighter ones can be studied with Mistral at OHP.

Keywords: Supernovae, AGN, Quasars

1 Introduction

The many on-going sky surveys from ground (ZTF, Atlas, ASAS-SN, Pan-STARRS, YSE) or space (Swift, Gaia...) reveal dozen of variables or transients per night which need to be caracterised. While the long-term lightcurve can eventually allow classification for standard objects, like classical Ia SNe, to catch peculiarities and understand the physics behind the event requires spectroscopy, even before the maximum if possible. Among explosive events, this includes superluminous SNe (SLSN), whose energy source is still unknown, or Luminous Red Novae or other types of objects: in a diagram showing the peak luminosity versus the caracteristic timescale of the event, the full space is progressively filled in with new events (Fig.1), following efforts by the ZTF consortium at Palomar, or the PESSTO survey at ESO (Smartt et al. 2015), and recently at OHP with Mistral (Fig.2). GRB's are discussed elsewhere in this volume (Schneider et al.).

2 The variety of events

When the event is occuring close to the nucleus of the host galaxy, it is a-priori difficult to distinguish between a SLSN or a Tidal Disruption Event (TDE) or an occurrence in the nucleus itself, without a sequence of follow-up spectroscopy. Initially, the spectrum often just shows a featureless, blue continuum (which is also the case for a classical type II SN when the enveloppe is still optically thick), but then develops some lines: OII lines typical of a SLSN ; or H or He emission lines (or no lines at all) for TDE's, depending on its class. Particularly caracteristic of some TDE's is the early presence of a broad emission complex around 4640 Å, which is a mix of NIII and HeII excited by Bowen fluorescence, lines which progressively vanish with time. The TDE could eventually be identified later when the full lightcurve is available, but it is then to late to get the physical parameters.

Some other, new types of rapid transients have been identified in the last decade, but are not yet understood. Fast Blue Optical Transients (FBOTs) show a rapidly raising light-curve, followed by an as-fast decay, with timescales of a few days: the few spectra obtained so far show only a featureless continuum, whose temperature is however decreasing with time. They may be the initial phase of explosion of a massive star with an optically thick envelope, which then collapses directly to a blackhole. Fast Radio Bursts (FRB's), detected in radio waves, are now detected by dozens with the CHIME instrument: only few of them have been located so far within an identified host galaxy, but we have no details about their immediate environment; they could be due to bursts in a magnetar. After the first detection by gravitational waves of a neutron stars merger and its location in a nearby galaxy (GW170817, Abbott et al. (2017)), more such events are expected: some could even be detected in the optical without the signature of GW's, but none has been detected this way

[1] IAP, CNRS & Sorbonne University, Paris

© Société Française d'Astronomie et d'Astrophysique (SF2A) 2023

so far. When more precise GW locations become available in the future, all those objects will deserve a detailed spectroscopic follow-up to understand the on-going mechanisms and the production of r-process elements.

Now talking not about transients, but about variable objects, Active Galactic Nuclei (AGN's) or Quasars deserve a special mention. A number of cases of changing spectra, the so-called Changing Look Quasars (CLQ's), have been identified (under others by Gaia Alerts, whose angular resolution is essential, e.g. Huo et al. (2020)), where Broad Lines appear with an increase of the central brightness, or disappear with dimming of the nucleus (e.g. MacLeod et al. (2016)). This is at odds with the standard model of AGN's, where the absence of broad lines (in Seyfert 2's) is thought to be due to obscuration of the central engine by the so-called torus lying on the line of sight. The timescale of such changes (from months to a few years) is not compatible with a change of orientation. Instead, it could be due to changes in obscuration towards, or in luminosity of, the central engine. In support of this idea is the recent detection of dormant AGN's which wake-up thanks to the fuel brought by a TDE: an example is AT2022cmc (Pasham et al. 2023) which reached an absolute magnitude of -25, typical of an AGN, but it was unknown before. The survey of variable galactic nuclei can thus reveal more AGN's, particularly those with intermediate mass black holes which are hard to detect otherwise, and nearly similtaneous observations in the optical (OHP) and the X-rays (SVOM) will be essential to understand them.

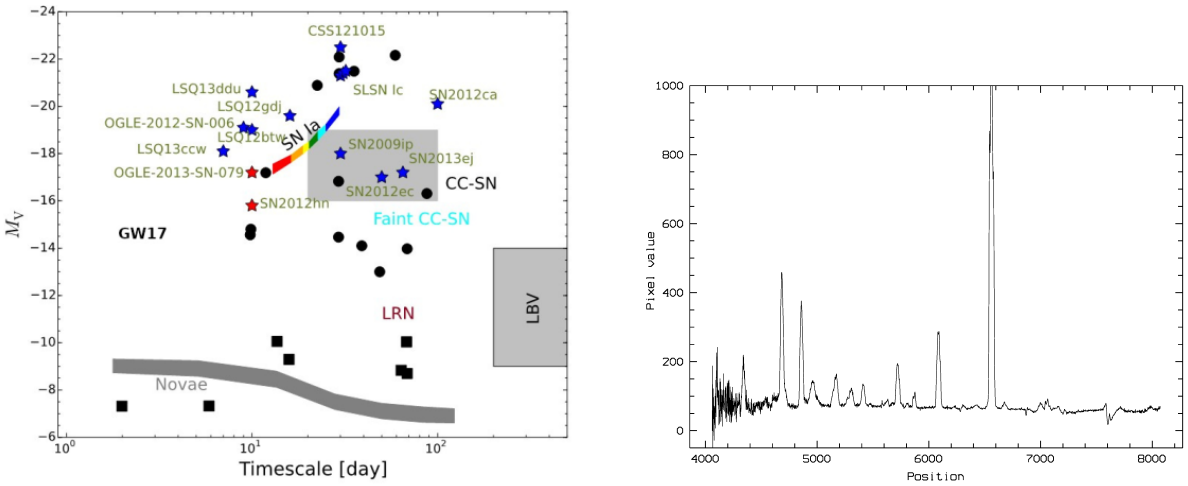

Fig. 1. Left: Some PESSTO results, after Smartt et al. (2015). **Right:** OHP spectrum of NovaCas 2021.

3 Conclusions

It is thus clear that rapid (within a few nights) spectroscopic follow-up of newly detected transients or variables is key to understand their physics. More important than just an initial classification is the obtention of a time-series of spectra which reveal the evolution of the object. To be able to do this, we need to lift the present limitation at OHP, which limits the number of ToO's and prevents from obtaining more than one ToO spectrum every three nights ! This will become particularly sensitive with the launch of SVOM early next year, which is expected to provide many transients of various nature. Or even more so when the next Galactic SN will be detected...

References

Abbott, B.P., & al. 2017, ApJ, 848, L12
Huo, Z., Dennefeld, M. Liu, X. et al. 2020, Ap & Sp. Sci., 365, 89
MacLeod, C.L., Ross, N.P., Lawrence, A. et al. 2016, MNRAS, 457, 389
Pasham, D.R., Lucchini, M., Laskar, T. et al., 2023, Nature Astronomy, 7, 88
Smartt, S.J., Valenti, S., Fraser, M. et al., 2015, A &A, 579, 40

SF2A 2023
M. N'Diaye, A. Siebert, N. Lagarde, O. Venot, K. Baillié, M. Béthermin, E. Lagadec, J. Malzac, J. Richard (eds)

OPTICAL AND X-RAY VARIABILITY IN THE ACTIVE CGCG 077-102 NED02 GALAXY

K. Parra Ramos[2,1], C. Adami[2], J. T. Harry[3], M. Ulmer[3], G. B. Lima Neto[1] and P. Amram[2]

Abstract. Supermassive black holes are known to play an essential role during the evolution of their galaxy host due to the close connection between their properties, which makes the study of the active galactic nuclei (AGN) activity essential to understand the processes behind the galaxy formation and evolution. In this work, we used the spectrograph MISTRAL to obtain optical spectra of the galaxy pair CGCG 077-102 localized within the Abell 2063 cluster. We used Chandra and XMM-Newton archival data to derive its X-ray spectral shape and variability, and the Zwicky Transient Facility time-domain survey to obtain light curves in g and r-bands. We classified the galaxy CGCG 077-102 NED02 as a Seyfert, and we confirmed the passive state of its companion. We found that CGCG 077-102 NED02 light curve (g-band) shows a significant variability and is well described by a damped random walk model, with the best-fitted damping timescale parameter $\tau_{\rm DRW} = 30^{+28}_{-12}$ days, which points toward a moderately massive black hole of $\sim 10^6$ $M_\odot$. In the X-ray counterpart, we found that the $0.5 - 10$ keV flux varied between observations by factors up to ~ 2, which is likely non-random. In the future, we will characterize the spectral variability of CGCG 077-102 NED02 and search for quasi-periodic oscillations in the X-ray flux to obtain a deeper insight into the processes related to the AGN activity.

Keywords: galaxy pair, active galactic nuclei, x-ray, optical, variability, supermassive black hole

1 Introduction

Several works have shown that nuclear activity is related to galaxy interactions, where a high fraction of active galactic nuclei (AGNs) are observed in close pair of galaxies (e.g., Ellison et al. 2011). However, a fraction of AGNs can be missed in the optical selection due to the high obscuration resulting from the merging process, which makes it difficult to understand the role of mergers in nuclear activity (Pfeifle et al. 2019; Guainazzi et al. 2021). Moreover, the variability is an important characteristic observed in all wavelength ranges of the electromagnetic emission of AGNs, as it can be related to physical processes that occur in their accretion disk and jets that still need to be better understood. In this context, our attention was brought to the galaxy pair CGCG 077-102 (members: CGCG 077-102 NED01 and CGCG 077-102 NED02, NED01 and NED02 hereafter) because we discovered a variable X-ray source in the nucleus of one galaxy of the pair, which was never reported in the literature as an AGN before.

2 Optical Spectroscopy of the CGCG 077-102 Pair

We mapped the galaxy pair at the *Observatoire de Haute Provence* in order to investigate its spectral characteristics with the instruments MISTRAL and GHASP. We classified the galaxy NED02 as a Seyfert, and we confirmed the passive state of its companion NED01 with the spectrograph MISTRAL. Based on the GHASP observations, we estimated a lower black hole mass limit of $M_{BH} > 1.2 \times 10^5$ $M_\odot$ for NED02.

[1] Instituto de Astronomia, Geoféisica e Ciências Atmosféricas, Universidade de São Paulo, São Paulo, Brazil
[2] Aix-Marseille Université, CNRS, CNES, Laboratoire d'Astrophysique de Marseille, Marseille, France
[3] Department of Physics and Astronomy, CIERA, Northwestern University, Evanston, IL 60208-3112, USA

© Société Française d'Astronomie et d'Astrophysique (SF2A) 2023

3 Optical Variability

We used the public Zwicky Transient Facility data to investigate the optical variability of NED02 in g and r filters. After applying a noise correction to the data, we did not detect short-term variability on time scales from weeks to months in any filter. However, we found that NED02 has aperiodic stochastic variability in long timescales in the g-band that can be well described by the Damped Random Walk (DRW) model (Fig. 1). From the best-fitted DRW model, we found a characteristic damping timescale of $\tau_{\rm DRW} = 30^{+28}_{-12}$ days, and using the $\tau_{\rm DRW} - M_{BH}$ relation (Burke et al. 2021), we found $M_{BH} = 10^{6.65^{+0.72}_{-0.55}}$ M$_\odot$.

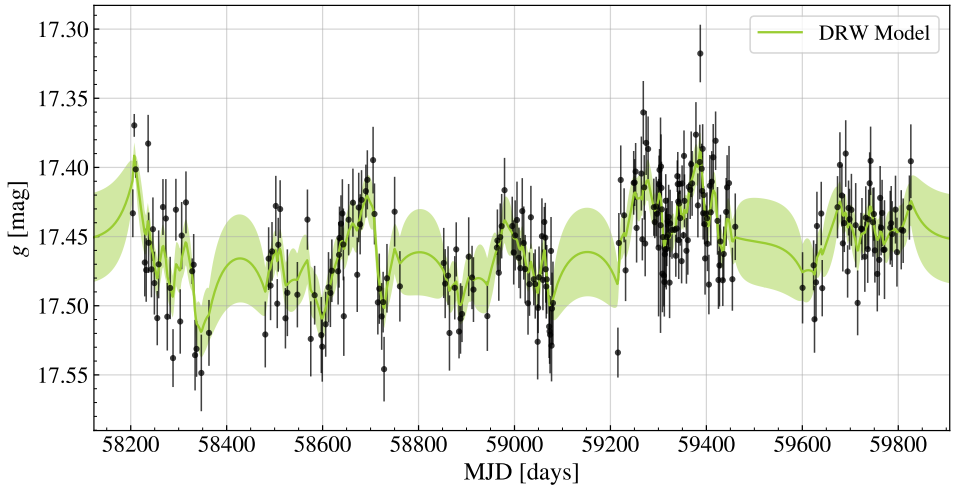

Fig. 1. The detrended light curve of NED02 in g-band (black dots). The best-fitted DRW model with a 1σ of uncertainty (shaded area) is shown in green.

4 X-Ray Analysis

We used Chandra and XMM-Newton archival data, and we did not find evidence of multiple X-ray sources or an extended component within NED02. However, we detected a significant non-random variation in the $0.5-10$ keV X-ray flux inter-observations between $\sim$ 4 days for short-term variations up to $\sim$ 700 days for long-term variations.

5 Conclusions

Our results show that NED02 is a Seyfert hosting a black hole moderately massive of 10^6 M$_\odot$. Moreover, NED02 shows surprising signs of variability in the optical as well as likely non-random variations in X-rays. In the future, we expect to obtain follow-up X-ray data to investigate its possible non-random variability and understand its correlations with the optical one. Also, our findings encourage us to characterize the spectral variability of NED02 with follow-up MISTRAL data. A complete and detailed version of this work can be found in Adami et al. (2023).

K.P.R. acknowledges financial support of the *Coordenação de Aperfeiçoamento de Pessoal de Néivel Superior* (CAPES), Grant No. 88887.694541/2022 – 00

References

Adami, C., Parra Ramos, K., Harry, J. T., et al. 2023, arXiv e-prints, arXiv:2307.10772
Burke, C. J., Shen, Y., Blaes, O., et al. 2021, Science, 373, 789
Ellison, S. L., Patton, D. R., Mendel, J. T., & Scudder, J. M. 2011, MNRAS, 418, 2043
Guainazzi, M., De Rosa, A., Bianchi, S., et al. 2021, MNRAS, 504, 393
Pfeifle, R. W., Satyapal, S., Secrest, N. J., et al. 2019, ApJ, 875, 117

SF2A 2023
M. N'Diaye, A. Siebert, N. Lagarde, O. Venot, K. Baillié, M. Béthermin, E. Lagadec, J. Malzac, J. Richard (eds)

MISTRAL@OHP OBSERVATIONS OF BOW-SHOCK STAR CANDIDATES

D. Russeil[1], A. Zavagno[1], J. C. Bouret[1], C. Adami[1] and M. Dennefeld[2]

Abstract. Assuming that bow-shocks are produced by the interaction of the stellar winds with the interstellar medium we observed 47 bow-shock driving star candidates with the MISTRAL spectrograph at OHP. The goal is to confirm that OB stars are the main sources leading to the bow-shocks observed in the infrared.

Keywords: Stars, ISM:bow-shock

1 Introduction

Bow-shocks are arc-shaped structures located ahead a star and generally observed at mid-to-far IR wavelength. They are expected to result from the interaction of the stellar wind with the ambient interstellar medium (ISM). Two main categories can be distinguished: in-situ bow-shock and bow-shock due to a run-away star. When the star is a run-away it is its relative supersonic motion respectively to the ambient medium which creates the bow-shock. For in-situ bow-shock it is the flow of the local ISM in the direction of the star which creates it. In this poster we present a spectroscopic follow-up of a sample of 47 bow-shock driving star candidates in order to confirm the O or B spectral type of the driving star and to check, from GAIA DR3 astrometric data, their run-away status.

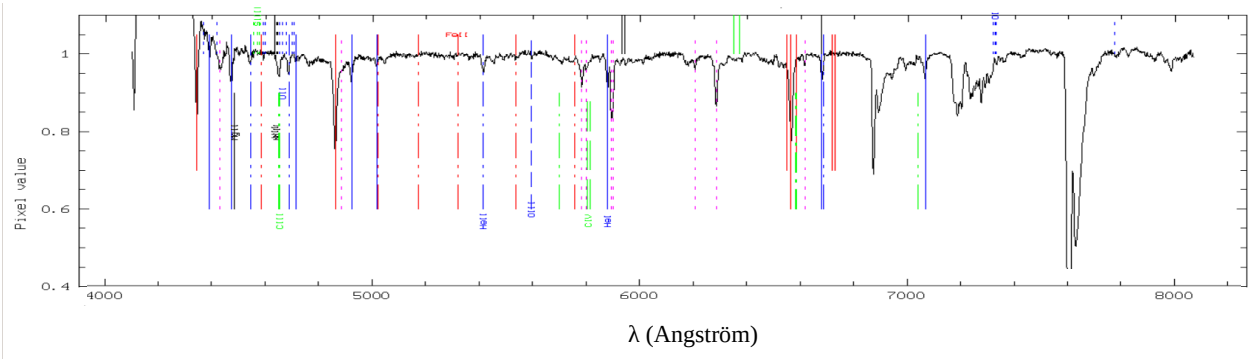

Fig. 1. Typical continuum normalised spectra observed with MISTRAL. The position of the lines (e.g. red, blue and blue dash-dot-dot labels for Hydrogen, HeI and HeII respectively) and diffuse interstellar bands (in magenta dashed) are identified.

The sample consists of 47 candidate bow-shock (BS) stars selected from the Jayasinghe et al. (2019) catalog and selected to be observable with the MISTRAL instrument (`http://www.obs-hp.fr/guide/mistral/MISTRAL_spectrograph_camera.shtml`) mounted at the T193 telescope to the Haute-Provence Observatory. The observations have been led with the blue objective. The spectral resolution is R = 709 at 6000Å. The data reduction has been led using the dedicated pipeline.

[1] Aix Marseille Univ., CNRS, CNES, LAM, 1388 Marseille, France
[2] Institut d'Astrophysique de Paris, 98bis Boulevard Arago, 75014 Paris, France

© Société Française d'Astronomie et d'Astrophysique (SF2A) 2023

2 Spectral Classification

The spectral classification is commonly done from lines in the 4000-5000Å domain but, due to the low S/N (< 3) we have in this spectral range we performed the spectral classification from lines in the red part (4500-7000Å) of the spectrum. Figure 1 shows a typical spectra with the main spectral features identified. We find that among the 47 candidates we have: 2 unclassifiable stars, 3 cool stars, 1 A-type star, 10 O stars and 31 B (mainly giants and super-giants) stars. **We confirm that bow-shocks are mainly driven by hot stars.**

3 Tranverse Velocity

From the Gaia EDR3 (`https://www.cosmos.esa.int/web/gaia/early-data-release-3`) we retreived the proper motions and the parallaxes for the sample stars which are used, following Russeil et al. (2020), to calculate the transverse velocity component of the stars in its local reference frame. We adopt the distance estimated from parallaxes by Bailer-Jones et al. (2021). If not available, the adopted distance is the spectro-photometric one. To ensure good quality, the transverse velocity (Vtan) vector is calculated only for stars with $\pi > 0$, RUWE* ≤ 1.4, and $\sigma_\pi \leq 0.2$. In this way, the transverse velocity could have been determined for 34 out of 47 sources. Figure 2 shows two examples of the tranverse velocity vector respectively to the bow-schock. Regarding the angle (α) between the bow-schock axis and the Vtan direction the following results are obtained:
- 8 stars are well aligned and we note that they have the largest velocities (mean Vtan = 54.4 km s^{-1}) suggesting they are run-away.
- 15 stars have $30° \leq \alpha \leq 90°$ (mean Vtan = 33.5 km s^{-1}).
- 11 move at the oppposite direction (mean Vtan = 24.2 km s^{-1}), suggesting that in this case the bow-shock is an in-situ one.

Our analysis indicates that bow-shocks are not only formed by run-away stars.

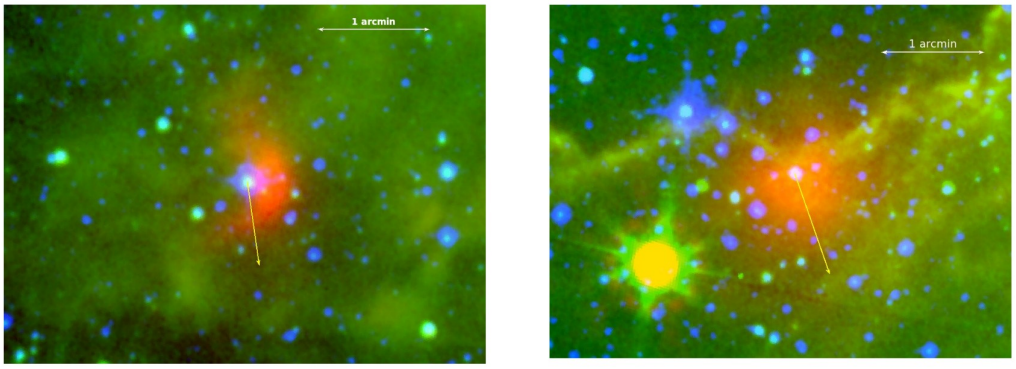

Fig. 2. Examples of the tranverse velocity vector (yellow arrow, arbitrary scale) respectively to the bow-schock seen on the images as the red arc-shaped emission. The images combine the Spitzer-MIPS 24 μm (red), Spitzer-IRAC 8 μm (green) and DSS-RED (blue) images. The pictures show G0609757-0034412 (at 2 kpc) and G0629904-0043101 (at 4 kpc) respectively. With Vtan = 11.5 km/s and Vtan = 55.3 km/s respectively, only the second one is a run-away star.

4 Conclusion

Following these preliminary results we are dealing now with the ISM characterisation to clarify the context of each of these bow-shocks formation.

References

Bailer-Jones, C. A. L., Rybizki, J., Fouesneau, M., Demleitner, M., & Andrae, R. 2021, AJ, 161, 147
Jayasinghe, T., Dixon, D., Povich, M. S., et al. 2019, MNRAS, 488, 1141
Russeil, D., Zavagno, A., Nguyen, A., et al. 2020, A&A, 642, A21

*The RUWE value is a measure of the reliability of the astrometric solution

SF2A 2023
M. N'Diaye, A. Siebert, N. Lagarde, O. Venot, K. Baillié, M. Béthermin, E. Lagadec, J. Malzac, J. Richard (eds)

OBSERVATIONS OF THE XMM X-CLASS CLUSTERS OF GALAXIES WITH MISTRAL AT OHP

G. Soucail[1], N. Clerc[1], R. Cabanac[1], L. Paquereau[1,2], Q. Moysan[1], B. Altieri[3] and F. Sarron[1]

Abstract. We present the preliminary results of a spectroscopic follow-up of a sub-sample of low redshift clusters and groups of galaxies identified in the XMM Cluster Archive Super Survey (X-CLASS). These clusters were observed with MISTRAL at OHP over 16 nights allocated between October 2021 and January 2023. A semi-automatic data reduction pipeline was developed and all data are fully reduced. 130 redshifts of galaxies are measured and 46 new structures (clusters or groups) have a confirmed redshift ($0.1 < z < 0.4$). Further studies of the physical properties of low mass and low redshift structures will be addressed.

Keywords: catalogues, galaxies: clusters: general, cosmology: observations, X-rays: galaxies: clusters

1 Introduction

The XMM CLuster Archive Super Survey (X-CLASS) is a complete sample of clusters of galaxies detected serendipitously in the full XMM-Newton archive, using dedicated source detection algorithms (Clerc et al. 2012). This sample has already been used to test cosmological models through the mass function of large scale structures and and to put constraints on the σ_8 and Ω_m cosmological parameters. After reprocessing the archive with improved algorithms for detection (Faccioli et al. 2018), the present sample contains 1688 clusters observed within an area of 269 deg^2 (Koulouridis et al. 2021). But only 60% have a confirmed redshift and complementary spectroscopic identifications are on-going.

The new instrument MISTRAL mounted on the T193 telescope at OHP is well suited to our follow-up program, limiting ourselves to relatively bright objects ($V < 21.0$) to fit its performances (Adami et al. 2018). We have set-up a spectroscopic survey aimed at measuring cluster redshifts for Northern candidates extracted from the X-CLASS database ($z < 0.3$ and $\delta > -5°$). We present in this poster the first results of the survey.

2 Observations and data reduction

A total of 16 observing nights was allocated to the program, split into 5 runs from October 2021 to January 2023. Observing conditions were acceptable for 66% of the time (low extinction and seeing $< 4''$). Exposure time was limited to at most 30 minutes and duplicated if needed to get total integration times of 1 to 2 hours.

Several technical difficulties were encountered, in particular with the slit rotation. It was quasi impossible to rotate the bonette over the 2022 runs and even if it is now functional, the rotation is still manually applied on the instrument. This difficulty generated large overheads for the objects positioning. We are confident that significant improvements are possible to reduce these overheads and allow a more efficient use of telescope time.

A semi-automatic pipeline was developed to reduce the data in the Pyraf environment. Spectra are extracted manually for each object and then rebinned with a 2Å/pixel step, from 4000 to 8000Å typically. Final spectra were processed by adding individual ones when several observations were available.

In total, 130 new redshifts of galaxies are measured, mostly through the identification of absorption features because the galaxies are mainly early-type galaxies. The redshift accuracy is $\simeq 0.001$, limited by the resolution of the spectrograph and the low S/N spectra. The redshift histogram (Fig 1 – left) shows a distribution ranging from 0.05 to 0.4+ for the most distant clusters and a median value of 0.21. The limiting magnitudes for these galaxies is measured as $V = 21.0$ and $R = 20.0$. This gives robust values for the real performances of MISTRAL and are in close agreement with the expectations.

[1] IRAP, Université de Toulouse, UT3, CNRS, CNES, 14 Av. Edouard Belin, 31400 Toulouse, France
[2] IAP, CNRS, Sorbonne Université, 98 bis boulevard Arago, 75014 Paris, France
[3] ESAC/ESA, Villafranca del Castillo, 28692 Madrid, Spain

© Société Française d'Astronomie et d'Astrophysique (SF2A) 2023

3 Galaxies identification and cluster/group redshift validation

A long work of galaxy identification was done because centering images provided by MISTRAL do not contain accurate information on the telescope coordinates and orientation. We used the DESI Legacy Imaging Surveys interface (`https://www.legacysurvey.org/`) to identify the observed galaxies (Fig 1 – right). We also retrieved photometric information when available (g and r photometry, photometric redshifts and SDSS redshifts). For Northern fields or fields that were not observed in DESI, we used PanSTARRS imaging, also available in the ESASky interface (`http://sky.esa.int/`) to get similar information.

The last step is to assess a redshift for each observed X-CLASS source, including a quality flag that depends on the number of measured redshifts in the structure, with or without the Brightest Cluster Galaxy. Redshifts of 48 X-CLASS sources were measured, more than 60% of the sources having a secure redshift coming from 3 or more redshifts. The results of our survey will be ingested in the X-CLASS database (`https://xmm-xclass.in2p3.fr/`).

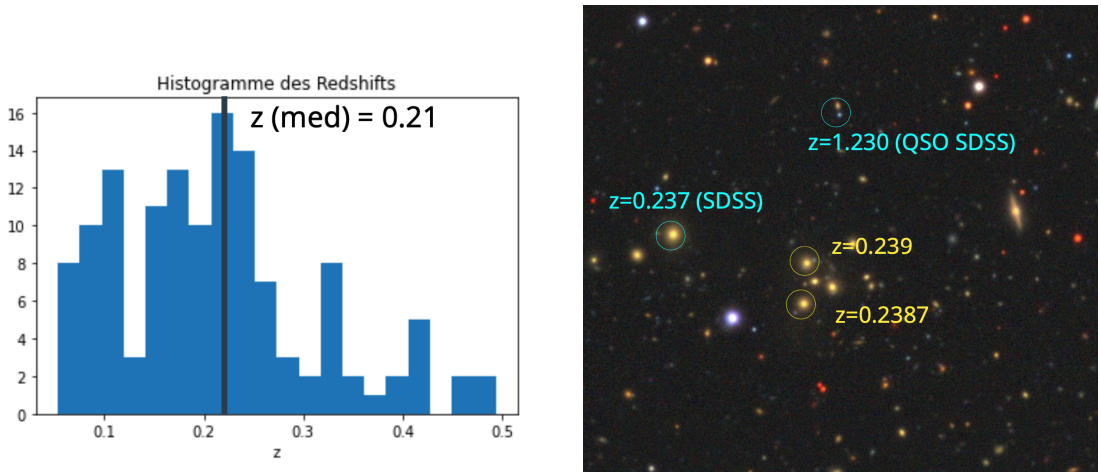

Fig. 1. Left: Redshift histogram of the measured redshifts. **Right:** Galaxy identification for the sources observed with MISTRAL (yellow) as well as existing data in the field (cyan) – X-CLASS 3135, $z = 0.239$.

4 Conclusions and future work

We have performed a successful survey of faint galaxies with the T193 at OHP equipped with MISTRAL. Pushing the instrument to its limits we were able to validate galaxy redshifts up to $z \simeq 0.4$ and $V \simeq 21.0$. The redshift confirmation of about 50 clusters and groups at low redshift will be completed by photometric information for the remaining clusters that could not be observed. This is also the case for more distant clusters for which spectroscopic identification is still pending. With the arrival of new large spectroscopic surveys like DESI we expect to reach a completeness fraction of 80 to 90% for the redshift identification. This allows us to measure accurately some physical parameters such as the X-ray luminosity, the R500 physical radius and also the X-ray temperature that can be properly extracted from the XMM image.

References

Adami, C., Basa, S., Brunel, J. C., et al. 2018, in SF2A-2018: Proceedings of the Annual meeting of the French Society of Astronomy and Astrophysics, ed. P. Di Matteo, F. Billebaud, F. Herpin, N. Lagarde, J. B. Marquette, A. Robin, & O. Venot

Clerc, N., Sadibekova, T., Pierre, M., et al. 2012, MNRAS, 423, 3561

Faccioli, L., Pacaud, F., Sauvageot, J. L., et al. 2018, A&A, 620, A9

Koulouridis, E., Clerc, N., Sadibekova, T., et al. 2021, A&A, 652, A12

Session S20

The future of micro- and nanosatellites for astronomy

SF2A 2023
M. N'Diaye, A. Siebert, N. Lagarde, O. Venot, K. Baillié, M. Béthermin, E. Lagadec, J. Malzac, J. Richard (eds)

THE FRENCH RESEARCH FEDERATION FOR NANOSATELLITES IN UNIVERSE AND EARTH SCIENCES

C. Neiner[1]

Abstract. In January 2023 a research federation for nanosatellites in Universe and Earth sciences was created in France. It includes ∼130 members from 14 different laboratories and space centers in the Paris region, and it is planned to be extended in the future to the rest of France. The goal is to organize this community, share technical, financial, and human resources, and better communicate within the community and outside, to be more efficient at developing robust scientific nanosatellites.

Keywords: nanosatellites, newspace

1 Context

Over the last ten years, more and more French laboratories have developped scientific nanosatellites or technologies for such satellites. More and more projects are under study, and more and more universities have their own space center for nanosatellites. This is particularly true in the Paris region. These laboratories and space centers often develop similar tools and technologies, face the same challenges, but unfortunately do not communicate much with each others. This is why the need for a research federation emerged. This federation, called Research Federation for Nanosatellites in Universe and Earth Sciences (or Nanosats Federation) initially concentrates on the Paris region, but it is planned to be extended to the rest of France in a few years.

2 Organization

The Nanosats Federation* has six governing bodies: CNRS, Paris Observatory, Ecole Normale Supérieure, Sorbonne University, Université Paris Cité, and Université Paris-Est Créteil (UPEC). It includes 14 CNRS entities (mostly laboratories) and space centers: LESIA, IMCCE, LERMA, LP-ENS, APC, IPGP, LISA, IAP, LATMOS, Observatoire de Paris, CENSUS (the space center of the PSL university), PSUP (the space center of Université Paris Cité), CS-UPEC (the space center of UPEC), and CurieSat (the space center of Sorbonne University). About ∼130 people from these 14 entities are currently registered as members of the federation. Additional employees of these 14 entities can join the federation every year, other entities from the six governing bodies in the Paris region will likely be able to join in 2025, other entities in France should be able to join in 2028.

The federation is led by its director (C. Neiner) and co-director (G. Hulot), with the help of a steering committee and a council. The steering committee is composed of representatives of the six governing bodies, one representative from the French space agency CNES, two representative from academia, four representative from industry, one observer from ONERA, and the federation directors. Its role is to define the strategic directions the federation shoudl follow and it typically meets once per year. The council is composed of six elected and four nominated persons among the members of the federation, and the directors. Its role is to coordinate the actions of the federation and it typically meets every three months.

[1] LESIA, Paris Observatory, PSL University, CNRS, Sorbonne University, Université Paris Cité, 5 place Jules Janssen, 92195 Meudon, France
*`https://federation-nanosats`

© Société Française d'Astronomie et d'Astrophysique (SF2A) 2023

3 Goals

The goals of the Nanosats Federation is to organize the community of the various participating laboratories and space centers. For this we plan to share technical resources, such as test facilities, components off-the-shelf (COTS), pieces of home-made hardware or software. The federation has its own budget which will also allow us to buy common equipment, fund meetings, and publish calls for the community. Ultimately we hope that the various laboratories and space centers will also share human resources, e.g. having an engineer from one laboratory help on a specific task for a nanosatellite project from another laboratory which would not have the required expertise or available manpower otherwise.

In addition, we aim to improve communication and collaboration amongst the community with dedicated workshops, project reviews, common answers to calls, etc. We will also be active in making this community more visible and known to our potential partners, e.g. industrials, and funding agencies.

The final goal is to be more efficient in the development of more robust scientific nanosatellites.

To reach these goals, we have already set up working groups dedicated to specific topics of interest for the federation and its community. In particular, a group is working on the pooling of test facilities: census of existing and already shared resources, of existing resources that could be pooled, and on missing resources that should be bought. Another group is working on interconnecting ground stations of the various entities of the federation and their partners, including industrial partners. Several other working groups are currently being set up, e.g. on sharing technological developements and on having a common catalog and open library of COTS available in our laboratories and space centers.

4 Ongoing nanosatellites projects

Three scientific nanosatellites have already been launched by entities participating in the Nanosats Federation:

- PicSat[†] was launched by LESIA in 2018 with the aim to detect the transit of an exoplanet around the star β Pic and demonstrate tracking with a mono-mode fiber. The science goal was not reached, first because of pointing issues and then because of a high-energy proton hit above the South Atlantic Anomaly that causes hardware damage, but the technological demonstration with the mono-mode fiber succeeded.
- UVSQ-Sat[‡] was launched by LATMOS in 2021 to demonstrate technologies for broadband measurements of Earth radiation budget and for solar spectral irradiance in the Herzberg continuum (200 – 242 nm). It is still flying and providing data.
- Inspire-Sat 7[§] was launched by LATMOS in 2023. It will contribute to the science of UVSQ-Sat but also measure perturbations in the ionosphere of the Earth.

Many more nanosatellite projects are currently under study within the federation. A non-exhaustive list of examples in solar system, astrophysics, and Earth science domains is provided here:

- BIRDY for the exploration of the internal structure of small bodies
- Meteorix for the detection and characterization of meteors and space debris
- TeraCube for the sdudy of planetary atmospheres at THz radio frequencies
- Vamos for the seismic activity of Venus
- NOIRE for radio-interferometric imaging with a swarm behind the Moon
- CASSTOR for UV spectropolarimetry of hot stars
- CosmoCal for the calibration of ground-based and space-based cosmic microwave background measurements
- CIRCUS for the study of the ionospheric dynamics of the Earth

[†] https://picsat.obspm.fr
[‡] https://www.uvsq.fr/uvsq-sat
[§] https://www.uvsq.fr/inspire-sat-7

- IGOSat for the characterization of the gamma environment and high-energy electrons in the South Atlantic Anomaly
- NanoMagSat for the Earth magnetic field
- OGMS-SA for radiations studies in low altitude orbits and testing of safe softwares
- MacroPlastic for the cartography of macroplastics in Earth oceans

These nanosatellites will allow for very diverse and competitive science as well as technological innovation.

5 Conclusions

The Research Federation for Nanosatellites in Universe and Earth Sciences only started in January 2023 and already includes ∼130 members from 14 laboratories or space centers from the Paris region. In the near future the Nanosats Federation will be open to more French entities. Sharing efforts and resources will allow us to more efficiently develop nanosatellites for solar system studies, astrophysical research, and Earth investigations. French entities wishing to join the Nanosats Federation are encouraged to contact the federation director[¶].

[¶]directrice.FRnanosats@obspm.fr

Session S21

Transition environnementale : quels leviers d'actions pour réduire l'empreinte environnementale de l'astronomie ?

SF2A 2023
M. N'Diaye, A. Siebert, N. Lagarde, O. Venot, K. Baillié, M. Béthermin, E. Lagadec, J. Malzac, J. Richard (eds)

ENVIRONMENTAL TRANSITION: OVERVIEW OF ACTIONS TO REDUCE THE ENVIRONMENTAL FOOTPRINT OF ASTRONOMY

L. Leboulleux[1], F. Cantalloube[2], M.-A. Foujols[3], M. Giard[4], J. Guilet[5], J. Knödlseder[4], A. Santerne[2], L. Todorov[2], D. Barret[5], O. Berne[4], A. Crida[6], P. Hennebelle[5], Q. Kral[7], E. Lagadec[6], F. Malbet[1], J. Milli[1], M. N'Diaye[6] and F. Roques[7]

Abstract. To keep current global warming below 1.5°C compared with the pre-industrial era, measures must be taken as quickly as possible in all spheres of society. Astronomy must also make its contribution. In this proceeding, and during the workshop to which it refers, different levers of actions are discussed through various examples: individual efforts, laboratory-level actions, impact evaluation and mitigation in major projects, institutional level, and involvement through collectives.

Keywords: SF2A-2023, S21, Societal, Environmental Transition, Astronomy Community Responsibilities, Community

1 Introduction

The Paris Climate Agreement, ratified by all countries during the COP21 in 2015, aims to keep global warming at 1.5°C-2.0°C compared to the pre-industrial era. This objective is based on strategies to reduce greenhouse gas emissions, mainly due to the use of fossil fuels, which must be implemented at all levels of society. The French community of astronomy has also taken up this issue, by multiplying greenhouse gas emissions assessments and actions to limit its own impact on global warming: a dozen astronomy laboratories have calculated their greenhouse gas emissions. Several initiatives have been launched, as a result of these diagnostics, including: (i) founding collectives of academic researchers, such as *Labos 1point5*[*], a cross-disciplinary group in France (Ben Ari 2023), and *Astronomers for Planet Earth*[†], an international movement of astronomy students, educators, amateurs and scientists, (Cantalloube & Burtscher 2021; Wagner et al. 2023; Stevens & Moss 2023), (ii) setting up hybrid or remote meetings and conferences (Kral 2021; Sarabipour et al. 2021; Moss et al. 2021), (iii) introducing a system for tracking greenhouse gas emissions when booking business trips (at LESIA), etc.

In 2023, during the annual conference of the Société Française d'Astronomie et d'Astrophysique (SF2A), we organized the third edition of a special session dedicated to the environmental transition within the professional astronomy community. In this special half-day session, we addressed the question of how our research projects are evolving in the context of the Paris Climate Agreement. The aim of the discussions was to address the opportunities and implications for individuals, laboratories, institutions and major scientific projects, as well as the impact and recognition of these actions.

The content of this proceeding is broken down according to the topics addressed by the speakers, each focusing on a different level of action: institutional level with Martin Giard (Deputy director Head of Astronomy

[1] Univ. Grenoble Alpes, CNRS, IPAG, 38000 Grenoble, France
[2] Aix Marseille Univ, CNRS, CNES, LAM, Marseille, France
[3] Institute Pierre-Simon Laplace (IPSL), Sorbonne University, CNRS, Paris, France,
[4] Institut de Recherche en Astrophysique et Planétologie, Université de Toulouse, CNRS, CNES, Toulouse, France
[5] Université Paris-Saclay, Université Paris Cité, CEA, CNRS, AIM, 91191, Gif-sur-Yvette, France
[6] Univ. Côte d'Azur, Observatoire de la Côte d'Azur, CNRS, Lagrange (UMR7293), 06304 Nice, France
[7] LESIA, Observatoire de Paris, Université PSL, CNRS, Sorbonne Université, Univ. Paris Diderot, Meudon, France
[*] https://labos1point5.org
[†] https://astronomersforplanet.earth/

© Société Française d'Astronomie et d'Astrophysique (SF2A) 2023

& Astrophysics Division of the CNRS, section 2), involvement through collectives with Marie-Alice Foujols (CNRS engineer at IPSL in climate science numerical modeling, core member of Labos1point5, section 3), assessing and mitigating the impact of major astronomical projects with Jürgen Knödlseder (researcher at IRAP, author of *The carbon footprint of astronomical research infrastructures*, section 4), laboratory-level actions with Lilia Todorov (ITA CNRS in the administrative department, leader of the sustainability group at LAM, section 5) and Alexandre Santerne (researcher at LAM, member of Labos1point5), and individual implication in collective actions with Jérôme Guilet (researcher at CEA, member of Scientist Rebellion, section 6).

2 Institutional level: the french astronomy and astrophysics community prospective

In 2024, as every five years, the Centre National de Recherche Scientifique (CNRS) will realize a new community prospective exercise in the field of astronomy and astrophysics. This will be the occasion to collectively decide the french scientific priorities in the domain and our roadmap for the period 2025-2030. The situation of our professional activities in the society will also be reviewed in detailed with a focus on three different topics attached to social progress within our community and in relation with our social and ecological environment: 1) Equity, Diversity, and Inclusion, 2) Carbon and ecology transition, and 3) astronomy and territories and participative science. Even regarding the yet ongoing work at CNRS and in laboratories, this prospective and its preparatory discussions and team work plan to evaluate, support, encourage and, guide the ecological transition of research. Between others, the impact of research and formation as a tool for social progress will be discussed, in addition with the gestion of decarbonation of already existing projects and infrastructures and the ongoing development of new ones.

3 Collectives: the success of Labos1point5

Labos1point5 (Ben Ari 2023) is a pioneering project started in 2019 in France by a collective of academic researchers, whose goal is to better understand and reduce the environmental impact of research, especially on the Earth's climate. One of the main highlight of Labos 1point5 is the development of an online open source tool to assess the carbon footprint of a research institute *GES 1point5*[‡] (Mariette et al. 2022). The associated tool *Scenario 1point5* enables mitigation scenarios to be explored by means of more than 15 reduction measures in the various areas. The networking platform *Transition 1point5* enables labs in transition to exchange ideas. To date, over 800 research institutes in France have used *GES 1point5*, representing thousands of employees, producing a unique database that can be studied to assess in detail the origin and determinants of the carbon footprint of French research. Several papers related to the carbon footprint of research using the *GES 1point5* database and the Labos 1point5 survey have been published or submitted for publication in international peer reviewed journals (Mariette et al. 2022; Berné et al. 2022; De Paepe et al. 2023). *GES 1point5* is currently being adapted in the USA with expected applications at the Space Telescope Science Institute and NoirLab.

Since 2022, Labos 1point5 is an official research consortium supported by several national institutions in France: CNRS, ADEME, INRAE and INRIA. Labos 1point5 is also a think tank, organizing monthly webinars and producing texts and reports on various topics relating to the ecological transition in research and teaching. Among other actions, Labos 1point5 sent to national recruitment committees in France a text in which it is asked that environmental activities are taken into consideration in the hiring and career evaluation.

4 Major astronomical projects: example of CTAO

The Cherenkov Telescope Array Observatory (CTAO) is the next generation ground-based instrument for gamma-ray astronomy at very high energies. With 64 telescopes located in the northern and southern hemispheres, the CTAO will be the first open ground-based gamma-ray observatory and the world's largest and most sensitive instrument to study high-energy phenomena in the Universe.

Recently, an Office for the Reduction of the Environmental Footprint of CTAO was created with the mission of ensuring that the environmental footprint of CTAO does not exceed the planetary limits within which humanity can continue to develop and thrive for generations to come (Richardson et al. 2023). The Office was established under the initiative of the CTAO Managing Director and approved by the administrative Council of the Observatory. Bringing the Office into life is however challenging, since the environmental footprint is

[‡]https://labos1point5.org/ges-1point5

conceived as an additional constraint on top of a wealth of managerial and technical challenges that are already tricky to cope with in a complex international environment. Also, it is difficult to obtain the financial resources needed to commission studies or recruit staff in a context where project costs are already tightly constrained.

A first rough estimate of sources of greenhouse gas emissions reveals that CTAO operations are likely to dominate the life-cycle carbon footprint, due to the observatory's 30 years lifetime. Electricity consumption will be a major source of emissions during operations, underscoring the need to implement renewable energy solutions. Telescope construction is likely to be another major source of emissions, which is challenging to control owing to their provision in form of in-kind contributions.

To go beyond this first rough estimate, it is planned to perform an environmental life cycle assessment (LCA) of the observatory, in order to develop plans for powering CTAO using renewable energy sources, as well as to conduct optimisation efforts that will reduce the environmental footprint of CTAO during the construction and operations phases. Hopefully, the financial resources will soon become available to start these activities.

5 Laboratory-level actions: focus on LAM

The Laboratoire d'Astrophysique de Marseille is a joint research unit (UMR 7326) under the supervision of the CNRS, the Aix-Marseille University and the CNES. The sustainable development group was created in November 2018, with about 10 volunteer staff from different backgrounds: doctoral students, researchers, lecturers, engineers and administrative staff. The aim of this group approach is to implement solutions to effectively reduce the impact of our activities on the environment and make daily life in the laboratory more eco-responsible.

The above-mentioned actions are structured around several themes: 1) From 2020 onwards, the group has set itself the target of quantifying its greenhouse gas emissions using the methodology common to all laboratories proposed by Labos1point5. The group intends to continue this analysis over the next few years in order to implement a multi-year action plan aimed at reducing the LAM's carbon footprint. The results were presented at a LAM seminar and an article is currently being prepared (Santerne et al., in prep.). 2) The group writes 2-3 articles in the laboratory's monthly science newsletter, highlighting the actions and informing the staff. To raise awareness and popularise the issue, the group organises seminars at the laboratory with external speakers. It also provides an in-house training for staff through *Ma Terre en 180 minutes* activity (Gratiot et al. 2023). 3) To promote biodiversity and engage against soil artificialization in the laboratory, a communal vegetable garden was created in the LAM's patio. 4) The group has introduced recycling bins for paper, cardboard, ink cartridges and IT equipment. To combat the misuse of plastic, the group has also worked to eliminate plastic cups and bottles, as well as installing water fountains and distributing water bottles, mugs and coffee cups.

6 Civil disobedience

Non-violent civil disobedience is widely considered to be an efficient means of achieving social and political change. It has therefore been used for more than a century by citizens fighting for various causes (antislavery, women or black people rights, anticolonialism, ecology, etc.). The failure of other means of actions to foster a reduction of greenhouse gas emission has pushed a growing number of citizens and scientists to turn to non-violent civil disobedience in the fight against climate change. The active engagement of scientists in such actions can be justified by several reasons. Recent developments in the philosophy and sociology of science show that neutrality is neither attainable nor desirable (Fragnière 2022). Scientists need to engage actively with society because producing and supplying information is not sufficient to ensure that this information will be taken into account and produce adequate changes (Oreskes 2022). The failure of climate mitigation is caused in large parts by opposing political and economical interests (Stoddard et al. 2021) that make power relationships unavoidable in the fight against climate change. Finally, protests against fossil fuel projects have been shown to be more effective when they include multiple strategies including civil disobedience (Thiri et al. 2022). More and more academic publications therefore call for scientists to engage in civil disobedience (Capstick et al. 2022) and for the universities, research institutions and unions to support researchers that do so (Gardner et al. 2021). Scientist Rebellion, and its french branch *Scientifiques en rébellion* [§], is an international collective of scientists funded in 2020 that engages in non-violent civil disobedience in order to demand emergency decarbonisation and degrowth, facilitated by wealth redistribution.

[§]https://scientifiquesenrebellion.fr

7 Discussions and conclusions

The multi-scale panel covered by J. Guilet, L. Todorov, J. Knödlseder, M. Giard, and M.-A. Foujols during the SF2A special session S21 prompted many questions and discussions with the audience. Among others, the topic of decision-making and decision-makers was discussed, with the example of the carbon footprint of business trips: the audience and speakers pointed out a profound discrepancy between 1) what is expected or required from researchers (e. g. PhD candidates and postdoctoral researchers feel compelled to travel a lot to attend conferences and give talks in order to increase their visibility and foster collaborations with a view to obtaining grants, scholarships or permanent positions), 2) the resources provided to reduce the trip's carbon footprint (e. g. the booking platform does not offer train trips abroad and/or trains travel is more expensive than flights...), 3) individual and collective determination to actively reduce our carbon footprint.

In this context, which decisions could be made and how to implement them, with what level of compromise? The first option is bottom-up, driven by employees, as is the case in many laboratories. But sometimes, opposition to change can also stem from other employees: for instance at LERMA, carbon quota could not be implemented since the adoption of this measure required the support of a large majority of employees ($> 80\%$ of employees). Conversely, other actions can be imposed by employers or research infrastructures on the community, for instance, before using data from the Hawaiian telescope, watching informational videos about sacred land use in Hawaiian observatories despite protests from the local population. For reference, the Labos 1point5 collective has compiled a list of actions carried out in laboratories, together with the processes for obtaining their approval.

The weight of research infrastructures was mentioned, along with the idea that today's science has become highly specialized, dependent on research institutes that produce large quantities of greenhouse gases and are only accessible to an exclusive few. Others spoke of the need for citizens to regain access to knowledge through participatory science.

At a less structural level, the discussions evoked the weight of individual decisions and actions: for instance, protesting or civil disobedience involves only the citizen, not their employer. Some junior researchers attending the round table expressed their frustration and concern that a career in astronomy does not seem compatible with a reduction of the individual or collective carbon footprints. These young researchers also reported suffering from solastalgia (also known as eco-anxiety).

In the end, there seems to be a general desire for change at various levels in our community. It was indeed one of the most attended SF2A special sessions, with an explicitly large proportion of junior researchers, despite parallel sessions about future large astronomical facilities that may have attracted more audience. To conclude, one can quote J. Knödlseder, explaining that this huge challenge ahead of us is also an opportunity for change: "*when did we have such an opportunity to start from a blank page and write a new chapter in history?*". As a community, we sincerely hope that decisions will be rapidly taken and implemented in the years to come, at all possible levels, in order to do our part to achieve the goal set by the Paris Climate Agreement and limit the impact of astronomical research on the health of the planet.

The authors thank the SF2A organization committees (SOC and LOC) who made this conference a large success. The SOC of the Environmental Transition session is also grateful for the panel of speakers for their implication during the talks and during the discussions with the audience, and to Pierre Kern for taking and sharing notes.

References

Ben Ari, T. 2023, Nature Reviews Physics

Berné, O., Agier, L., Hardy, A., et al. 2022, Environmental Research Letters, 17, 124008

Cantalloube, F. & Burtscher, L. 2021, in SF2A-2021: Proceedings of the Annual meeting of the French Society of Astronomy and Astrophysics. Eds.: A. Siebert, 310–312

Capstick, S., Thierry, A., Cox, E., et al. 2022, Nat. Clim. Chang. 12, 773–774

De Paepe, M., Jeanneau, L., Mariette, J., Aumont, O., & Estevez-Torres, A. 2023, bioRxiv, 2023

Fragnière, A. 2022, Université de Lausanne

Gardner, C. J., Thierry, A., Rowlandson, W., & Steinberger, J. K. 2021, Frontiers in Sustainability, 2

Gratiot, N., Klein, J., Challet, M., et al. 2023, PLOS Sustainability and Transformation, 2, e0000049

Kral, Q. 2021, in SF2A-2021: Proceedings of the Annual meeting of the French Society of Astronomy and Astrophysics. Eds.: A. Siebert, 317–319

Mariette, J., Blanchard, O., Berné, O., et al. 2022, Environmental Research: Infrastructure and Sustainability, 2, 035008

Moss, V. A., Adcock, M., Hotan, A. W., et al. 2021, Nature Astronomy, 5, 213
Oreskes, N. 2022, Proc. Indian Natl. Sci. Acad., 88(4):824–8
Richardson, K., Steffen, W., Lucht, W., et al. 2023, Science Advances, 9, eadh2458
Sarabipour, S., Khan, A., Seah, Y. F. S., et al. 2021, Nature Human Behaviour, 5, 296
Stevens, A. R. H. & Moss, V. A. 2023, Communicating Astronomy with the Public Journal, 32, 15
Stoddard, I., Anderson, K., Capstick, S., et al. 2021, Annual Review of Environment and Resources, 46, 653
Thiri, M. A., Villamayor-Toms, S., Scheidel, A., & Demaria, F. 2022, Ecological Economics, 195, 107356
Wagner, S. M., Mingo, B., Majidi, F. Z., et al. 2023, Nature Astronomy, 7, 244

Author Index

Acuña, L., 289
Adam, R., 223
Adami, C., 55, 503, 511, 517, 519
Aguichine, A., 289
Aguilera–Gómez, C., 105
Ahmad, A., 405
Ahmad, Y., 511
Alkan, A. K., 483
Allen, M., 3
Allouch, A., 183
Altieri, B., 521
Amram, P., 517
Anderson, S., 511
Angonin, M.-C., 401
Aravind, K., 511
Arenou, F., 457
Arlot, J.-E., 339, 395
Asensio Ramos, A., 427
Ashkar, H., 483
Ashkar, K., 171
Astoul, A., 373, 443
Atteia, J.-L., 475
Auchère, F., 171
Augereau, J.-C., 391
Augereau, J. C., 275
Aykroyd, C., 401

Béguin, E., 405
Bénilan, Y., 377
Bério, P., 421
Baguet, D., 335
Ballot, J., 15
Bamba, A., 255
Barbotin, E., 199
Barker, A. J., 443
Barlow, M., 263
Barrère, P., 167
Barrere, P., 119
Barret, D., 531
Barroy, P., 199, 209
Bartlett, J., 59
Baruteau, C., 275, 373
Basa, S., 503
Bastian, N., 99
Baudin, F., 417
Baudoz, P., 239
Baudry, A., 427
Baylet, M., 213
Beaudoin, E., 215
Beck, P., 275
Bellier, J.-B., 209
Ben Hmida, S., 311
Bendahman, M., 479
Bergé, J., 31
Berger, J.-P., 285
Bergez-Casalou, C., 363
Bernard, D., 155
Berne, O., 531
Berta, V., 167
Berteaud, J., 125
Bessila, L., 445
Bierjon, A., 387
Bilek, M., 63
Blaizot, J., 227
Blondin, S., 409
Boily, C., 499
Boisse, I., 285
Bonhomme, A., 435, 449
Bontemps, S., 303, 307
Bot, C., 25, 183, 267
Boughelilba, M., 129
Bouret, J. C., 519
Bourgoin, A., 401
Bouvier, J., 439
Brau-Nogué, S., 25
Breton, S. N., 447
Briaud, A., 335
Briot, D., 25
Brouillet, N., 105
Bruel, P., 155
Buat, V., 329
Buchlin, E., 171
Bugli, M., 167, 479
Bugnet, L., 447
Buil, C., 199
Burgasser, A., 469

Cabanac, R., 521
Calore, F., 125
Caminade, S., 171
Cantalloube, F., 531
Carlier, D., 209
Carvajal-Bohorquez, C., 511
Casamiquela, L., 105
Casse, F., 495
Catala, C., 507
Cecconi, B., 3
Cerardi, N., 51
Chambers, K. C., 55
Chassande-Mottin, E., 87, 487
Chastenet, J., 263, 267, 317
Chaty, S., 87, 487
Chauvin, G., 239, 285
Chiavassa, A., 405

© Société Française d'Astronomie et d'Astrophysique (SF2A) 2023

Choplin, A., 449
Choquet, E., 275, 285
Chu, A., 55
Ciesla, L., 25
Clarke, F., 243
Clavel, M., 125
Clerc, N., 521
Cognard, I., 137
Colas, F., 195
Coliac, J.-F., 213
Commercon, B., 431
Comport, A. I., 467
Contini, T., 233
Contursi, G., 83
Corbard, T., 451
Cordier, B., 475, 503
Cornu, D., 303
Correia, L., 267
Corsaro, E., 447
Cottin, H., 285
Coulon, J.-P., 347
Courson, C., 209
Courtin, S., 435, 449
Coutens, A., 311
Creevey, O., 105, 421
Crida, A., 531
Cristofari, P. I., 413
Csengeri, T., 303, 307
Cuillandre, J.-C., 55

Dallier, R., 137
Dalton, G., 233
Damiani, C., 417
Dauvergne, J. L., 215
de Batz de Trenquelleon, B., 367
de Boer, T., 55
de Bony de Lavergne, M., 203, 483
de Brito Silva, D., 105
de Laverny, P., 25, 83
De Simone, M., 9
Debras, F., 373
Decoene, V., 137
Defrère, D., 463
Degott, L., 417
Deheuvels, S., 15, 421
Del Zanna, L., 167
Delaveau, B., 213
Delcroix, M., 215
Deleuil, M., 289
Delfosse, X., 285
Delisle, Y., 199, 209
Delsanti, A., 243, 511
Dennefeld, M., 199, 515, 519
Desmars, J., 195
Desormiere, O., 209
Dessart, L., 409
Dhouib, H., 373
Diakogiannis, F. I., 107
Diez, C. M., 143
Domiciano de Souza, A., 421
Donati, J.-F., 413
Donati, N., 183
Douet, R., 451
Douté, S., 243
Drouilly, R., 467
Dubois, Y., 227
Dufourg, N., 171
Dumont, T., 435, 449
Dupouy, P., 199
Duqué, R., 147
Durand, E., 213
Durret, F., 55
Dutrey, A., 299

Ebrahimkutty, N., 421
El Hadi, K., 233
El Mellah, I., 143
Eliott, R., 219
Ellien, A., 55
El Hedri, S., 479

Fürst, F., 143
Famaey, B., 63, 91, 95, 457
Farcy, M., 227
Faurobert, M., 451
Fernández-Trincado, J. G., 469
Fernandez, V., 329
Ferrari, M., 285, 293
Ferrière, K., 313
Fienga, A., 335
Fletcher, L. N., 243
Fleury, B., 357, 377
Foglizzo, T., 479
Forget, F., 387
Fortin, F., 87, 487
Foujols, M.-A., 531
Foustoul, V., 491
François, T., 499
Freundlich, J., 63, 499
Freytag, B., 405

Götz, D., 503
Gómez-Guijarro, C., 321
García, R. A., 447
Garcia, F., 87, 487
Garnichey, M., 511
Garrel, C., 51
Gaspari, P., 137
Gastineau, M., 335
Gavino, S., 299
Geffrin, J. M., 275
Gelly, B., 451

Genova, F., 175
Giard, M., 531
Girardat, J., 183
Glorian, J.-M., 311
Godard, J.-P., 209
Goldman, B., 453
Gomez, H., 263
Gonneau, A., 3
González, E., 453
González, M., 431
Gonzalez, J.-F., 271
Goos, I., 479
Gouellec, V., 459
Grand, M., 195
Grandidier, M., 209
Grebel, E. K., 99
Greene, T., 459
Griessmeier, J.-M., 137
Grinberg, V., 143
Groussin, O., 243
Guiderdoni, B., 67, 71
Guilet, J., 119, 167, 479, 531
Guilloteau, S., 299
Guillout, P., 457
Gutteridge, C., 507
Gwyn, S., 55

Hadamcik, E., 275
Halbwachs, J.-L., 191, 457
Harry, J. T., 517
Hasan, M., 511
Hasan, P., 255
Hassaine, D., 511
Hassanin, A. S., 255
Heine, M., 435, 449
Heiter, U., 105
Hennebelle, P., 531
Henning, T., 453
Hensley, B., 263
Herpin, F., 427
Hillenbrand, L., 459
Hillier, D. J., 409
Hu, X., 335
Huby, E., 239, 285
Huet, P., 381
Hugo, T., 219
Huré, J.-M., 351
Hussmann, H., 335

Iba, R., 421
Ibata, R., 107
Ireland, M., 463
Irzyk, M., 209

Jörgensen, J. K., 299
Jehin, E., 511
Jimenez de la Vega, N. E., 511
Jofré, P., 105
Jonak, J., 421

Kaan Alkan, A., 203
Kaddour, A., 511
Kessler, N., 303
Khalil, Y., 91
Kiefer, F., 191, 457
King, O., 243
Kirchschlager, F., 263
Knödlseder, J., 531
Kobus, J., 299
Kou, R., 59
Kral, Q., 363, 381, 531
Kraus, S., 463
Kretschmar, P., 143
Kueviakoe, V., 511

Labadie, L., 439
Lacour, S., 285
Laforgue, D., 451
Lagadec, E., 531
Lagarde, N., 25, 105
Laginja, I., 293
Lagos, C. D. P., 255
Laigle, C., 325
Laine, U., 137
Lainey, V., 339, 395
Lange, L., 387
Langin, G., 195
Langlois, M., 285
Lanza, A. F., 447
Laouisset, A., 213
Lardo, C., 99
Laskar, J., 335
Lasue, J., 275
Laviron, A., 155
Lazzarini, S., 511
Lazzaro, D., 255
Le Bouquin, J.-B., 391
Le Floc'h, E., 503
Le Poncin-Lafitte, C., 401
Lebonnois, S., 367
Leboulleux, L., 19, 25, 285, 531
Lebreton, Y., 191, 457
Lecomte, H., 343
LeCoroller, H., 511
Leibacher, J., 255
Lekic, A., 209, 213
Leroy, A., 195, 199
Lesur, G., 461
Li, C., 95
Li, G., 15
Ligi, R., 421
Lignières, F., 15

Lilensten, J., 215
Lima Neto, G. B., 517
Lintz, M., 347
Litman, A., 511
Looze, I., 263, 317
Lopez, J. M., 199
Lopez, T. A., 289
Losse, F., 199
López-Ariste, A., 427

Méheut, H., 279
Mémin, A., 335
Métris, G., 31
Macías-Pérez, J., 263
Magnier„ E. A., 55
Mahler, G., 47
Malbet, F., 531
Malchirand, G., 213
Malzac, J., 25
Manchon, L., 25
Mandea, M., 343
Marchand, M., 3
Marcowith, A., 67, 71
Marcq, E., 289
Marinho, L., 427
Maris, E., 199
Marquez, I., 55
Martínez Núñez, S., 143
Martel, E., 461
Martell, S., 99
Martin, L., 137
Martin-Alvarez, S., 227
Martinache, F., 285, 463
Martinet, N., 55
Martinez, P., 199
Martinod, M.-A., 463
Martocchia, S., 99
Masegosa, J., 255
Mathis, S., 373, 401, 445
Mathur, S., 447
Matsuura, M., 263
Matter, A., 391
Mattia, G., 167
Mauxion, J., 465
Mazeh, T., 457
McConnachie, A. W., 55
McCracken, H. J., 325
Mei, S., 183
Menard, F., 275
Mendil, R., 511
Merc, J., 213
Merlin, F., 243
Messina, S., 447
Michaut, C., 467
Michel, F., 511
Michoulier, S., 271
Midavaine, T., 195, 199, 209
Mignon-Risse, R., 431, 495
Mignone, A., 167
Milli, J., 275, 391, 531
Millour, E., 387
Monari, G., 91, 95
Monpribat, E., 435, 449
Montier, L., 313
Moreira, M., 279
Morel, T., 289
Mottez, F., 137, 159
Mouillet, D., 285, 293
Moukaddem, N., 137
Mourard, D., 421
Mourier, J., 203, 483
Mousis, O., 289
Moya, W. H., 469
Moysan, Q., 521
Musolino, C., 147
Muthumariappan, C., 71

N'Diaye, M., 285, 531
Naar, J., 387
Nagesh, S. T., 63
Nardello, M., 347
Nardetto, N., 421
Nastula, J., 255
Neichel, B., 243
Neiner, C., 507, 525
Nesvadba, N., 25
Neveu, S., 199, 209
NG, C., 37, 111
Ng, C., 137
Nippert, J., 435, 449
Noble, J. A., 43
Norman, D. J., 255

Obergaulinger, M., 479
Oers, J., 313
Ouazzani, R.-M., 25, 251

Pétri, J., 115
Pagano, I., 447
Paladini, R., 267
Palicio, P. A., 77
Palicio, P. A., 83
Palma-Bifani, P., 239
Palmerio, J. T., 503
Pandey-Pommier, M., 67, 71, 255
Pantacchini, C., 199
Paquereau, L., 325, 521
Parenti, S., 171
Parra Ramos, K., 517
Pascu, D., 339, 395
Pattle, K., 263
Paufique, J., 209

Paul, S., 67
Pellier, C., 215
Pello, R., 233
Peronne, A., 275
Perraut, K., 439
Perri, B., 171, 417
Piccialli, A., 255
Pichot, M., 347
Pierre, M., 51
Pinçon, C., 417
Pitann, J., 453
Poch, O., 275
Ponthieu, N., 263
Porte, T., 213
Pourbaix, D., 457
Poveda, M., 357, 377
Priestley, F., 263
Prieto, E., 233
Priolet, P., 391
Puech, M., 233

Quéant, D., 209
Quintin, E., 163

Radureau, G., 467
Rambaux, N., 335
Ramsbottom, C. A., 409
Rannou, P., 367
Rashid„ M., 71
Ravi, A., 263
Ravinet, T., 469
Raymond, S., 285
Raynaud, R., 119, 167
Reboul-Salze, A., 119, 167
Recio-Blanco, A., 83
Reichert, M., 479
Reichherzer, P., 203, 483
Relaño, M., 263, 317
Renard, J. B., 275
Reylé, C., 469
Rezzolla, L., 147
Rho, J., 263
Rieutord, M., 373
Ristorcelli, I., 313
Ritacco, A., 263
Robert, V., 339, 395
Rocci, P.-F., 209
Rodrigues, M., 31, 233
Rodriguez, J., 209
Roman, M., 243
Roques, F., 531
Rosat, S., 343
Rosdahl, J., 227
Roubeau-Tissot, A., 347
Rousselot, P., 243
Roy, A., 511
Roy, N., 67, 71
Roy, S., 71
Rozier, S., 95
Russeil, D., 511, 519
Rymar, A., 267

Sánchez Bejar, V. J., 453
Saccardi, A., 503
Salabert, D., 421
Salomon, J.-B., 457
Samadi, R., 417
Sanchez-Janssen, R., 233
Santangelo, A., 143
Santerne, A., 285, 289, 531
Santos, A. R. G., 447
Sarron, F., 55, 521
Savino, A., 99
Schüssler, F., 203, 483
Schneider, B., 503
Seglar-Arroyo, M., 483
Segretain, P., 279
Seillé, L.-M., 329
Serrau, M., 199, 209
Sethuram, R., 71
Sharma, R., 299
Shetrone, M., 99
Shuntov, M., 325
Siebert, A., 91, 95
Simaz-Bunzel, A., 87, 487
Sivet, L., 213
Smart, R. L., 469
Soubiran, C., 105
Soucail, G., 521
Staelen, C., 351
Stark, A., 335
Storey, P. J., 409

Targa, F., 209
Tazaki, R., 275
Tenachi, W., 107
Thébault, P., 381
Tharakan, C. M., 213
Thatte, N., 243
Thomson-Paressant, K., 507
Thuillot, W., 199
Tobon Valencia, V., 275
Todorov, L., 531
Traoré, N., 171
Traverse, P., 209
Tsai, S.-M., 357
Turpin, D., 503

Ulmer, M., 517
Uttenthaler, S., 405

Valageas, P., 51

Valeille-Manet, M., 307
Valls-Gabaud, D., 255
Vandemeulebrouck, R., 387
Vandenbroucke, B., 263
Vargas Dominguez, S., 255
Varniere, P., 495
Vasseur, S., 213
Vauglin, I., 25, 251
Veillet, R., 357
Venot, O., 25, 357, 377
Vergani, S. D., 503
Vienney, J.-M., 209
Vigan, A., 285
Vincendon, M., 215
Vinogradoff, V., 285
Vitali, S., 105
Voisin, G., 137
Vos, E., 387
Vrard, M., 421

Wünsche, A., 199
Wagh, S., 71
Webb, N. A., 163, 183, 491
Wesson, R., 263
Wiesemeyer, H., 427
Wilkes, B. J., 255
Williams, T., 317
Wittkowski, M., 421
Wolf, S., 299
Worley, C., 105
Wullaert, P., 213

Xilouris, E., 317

Yang, L., 255
Yates, Z., 459

Zapatero Osorio, M. R., 453
Zarka, P., 137
Zavagno, A., 519